Springer Series in Optical Sciences 166

Rainer Michalzik *Editor*

VCSELs

Fundamentals, Technology and Applications of Vertical-Cavity Surface-Emitting Lasers

Springer

Springer Series in Optical Sciences

Volume 166

Founded by
H. K. V. Lotsch

Editor-in-Chief:
W. T. Rhodes

Editorial Board:
Ali Adibi, Atlanta
Toshimitsu Asakura, Sapporo
Theodor W. Hänsch, Garching
Takeshi Kamiya, Tokyo
Ferenc Krausz, Garching
Bo A. J. Monemar, Linköping
Herbert Venghaus, Berlin
Horst Weber, Berlin
Harald Weinfurter, München

For further volumes:
http://www.springer.com/series/624

Springer Series in Optical Sciences

The Springer Series in Optical Sciences, under the leadership of Editor-in-Chief William T. Rhodes, Georgia Institute of Technology, USA, provides an expanding selection of research monographs in all major areas of optics: lasers and quantum optics, ultrafast phenomena, optical spectroscopy techniques, optoelectronics, quantum information, information optics, applied laser technology, industrial applications, and other topics of contemporary interest.
With this broad coverage of topics, the series is of use to all research scientists and engineers who need up-to-date reference books.
The editors encourage prospective authors to correspond with them in advance of submitting a manuscript. Submission of manuscripts should be made to the Editor-in-Chief or one of the Editors. See also www.springer.com/series/624

Editor-in-Chief
William T. Rhodes
School of Electrical and Computer Engineering
Georgia Institute of Technology
Atlanta, GA 30332-0250
USA
e-mail: bill.rhodes@ece.gatech.edu

Editorial Board
Ali Adibi
Georgia Institute of Technology
School of Electrical and Computer Engineering
Atlanta, GA 30332-0250
USA
e-mail: adibi@ee.gatech.edu

Toshimitsu Asakura
Hokkai-Gakuen University
Faculty of Engineering
1-1, Minami-26, Nishi 11, Chuo-ku
Sapporo, Hokkaido 064-0926, Japan
e-mail: asakura@eli.hokkai-s-u.ac.jp

Theodor W. Hänsch
Max-Planck-Institut für Quantenoptik
Hans-Kopfermann-Straße 1
85748 Garching, Germany
e-mail: t.w.haensch@physik.uni-muenchen.de

Takeshi Kamiya
Ministry of Education, Culture, Sports,
Science and Technology
National Institution for Academic Degrees
3-29-1 Otsuka Bunkyo-ku
Tokyo 112-0012, Japan
e-mail: kamiyatk@niad.ac.jp

Ferenc Krausz
Ludwig-Maximilians-Universität München
Lehrstuhl für Experimentelle Physik
Am Coulombwall 1
85748 Garching, Germany *and*
Max-Planck-Institut für Quantenoptik
Hans-Kopfermann-Straße 1
85748 Garching, Germany
e-mail: ferenc.krausz@mpq.mpg.de

Bo A. J. Monemar
Department of Physics and Measurement Technology
Materials Science Division
Linköping University
58183 Linköping, Sweden
e-mail: bom@ifm.liu.se

Herbert Venghaus
Fraunhofer Institut für Nachrichtentechnik
Heinrich-Hertz-Institut
Einsteinufer 37
10587 Berlin, Germany
e-mail: venghaus@hhi.fhg.de

Horst Weber
Optisches Institut
Technische Universität Berlin
Straße des 17. Juni 135
10623 Berlin, Germany
e-mail: weber@physik.tu-berlin.de

Harald Weinfurter
Sektion Physik
Ludwig-Maximilians-Universität München
Schellingstraße 4/III
80799 München, Germany
e-mail: harald.weinfurter@physik.uni-muenchen.de

Rainer Michalzik
Editor

VCSELs

Fundamentals, Technology and Applications of Vertical-Cavity Surface-Emitting Lasers

Springer

Editor
Rainer Michalzik
Institute of Optoelectronics
Ulm University
Ulm
Germany

ISSN 0342-4111 ISSN 1556-1534 (electronic)
ISBN 978-3-642-24985-3 ISBN 978-3-642-24986-0 (eBook)
DOI 10.1007/978-3-642-24986-0
Springer Heidelberg New York Dordrecht London

Library of Congress Control Number: 2012938353

© Springer-Verlag Berlin Heidelberg 2013
This work is subject to copyright. All rights are reserved by the Publisher, whether the whole or part of the material is concerned, specifically the rights of translation, reprinting, reuse of illustrations, recitation, broadcasting, reproduction on microfilms or in any other physical way, and transmission or information storage and retrieval, electronic adaptation, computer software, or by similar or dissimilar methodology now known or hereafter developed. Exempted from this legal reservation are brief excerpts in connection with reviews or scholarly analysis or material supplied specifically for the purpose of being entered and executed on a computer system, for exclusive use by the purchaser of the work. Duplication of this publication or parts thereof is permitted only under the provisions of the Copyright Law of the Publisher's location, in its current version, and permission for use must always be obtained from Springer. Permissions for use may be obtained through RightsLink at the Copyright Clearance Center. Violations are liable to prosecution under the respective Copyright Law.
The use of general descriptive names, registered names, trademarks, service marks, etc. in this publication does not imply, even in the absence of a specific statement, that such names are exempt from the relevant protective laws and regulations and therefore free for general use.
While the advice and information in this book are believed to be true and accurate at the date of publication, neither the authors nor the editors nor the publisher can accept any legal responsibility for any errors or omissions that may be made. The publisher makes no warranty, express or implied, with respect to the material contained herein.

Printed on acid-free paper

Springer is part of Springer Science+Business Media (www.springer.com)

To Professor Kenichi Iga
and Professor Fumio Koyama
for pioneering contributions
to VCSEL research

Preface

Vertical-cavity surface-emitting lasers (VCSELs) are firmly established in the laser diode market for about 15 years meanwhile. It took about 17 years before these devices were commercialized. Multimode fiber optical networks with data rates in the 1 Gbit/s range were the initial market. In 2004, VCSELs were first incorporated in optical computer mice. Today, these two application areas approximately equally share a production volume of almost 100 million units per year. In future, high volumes can be expected also, e.g., for diverse sensing and illumination purposes, the latter using high-power laser arrays.

Enormous progress in VCSEL performance has been witnessed over the last ten years. In particular, digital data rates of 10 Gbit/s are now routinely achieved, and 25 Gbit/s is the next step to be taken very soon. As for the first commercial devices, emission wavelengths of 850 nm are still dominating both for optical datacom and optical mice. However, also 1.3 and 1.55 μm wavelength VCSELs for telecommunications have reached a high level of maturity. On the long-wavelength side, electrically pumped devices are available up to about 2.4 μm. For short wavelengths, a major breakthrough was achieved in the year 2008 with the first continuous-wave room-temperature operation of a GaN-based VCSEL at about 414 nm wavelength. A pulse-mode electrically driven VCSEL with green emission at 503 nm was demonstrated in the year 2011. Large-area two-dimensional arrays are now exceeding previous expectations with conversion efficiencies of about 50% and continuous-wave output powers of some hundred watts for wavelengths of approximately 800 to 1100 nm.

This book covers basic VCSEL concepts as well as the state of the art in modelling, performance, and application areas of VCSELs. Single-mode emission, polarization dynamics and control, high-speed operation, high-power generation, high-contrast grating devices, blue, red, and long-wavelength spectral regimes, wavelength tuning, fiber-optic transceiver, video link and parallel optical link technologies, as well as optical mouse sensors and laser printing are described in some detail by distinguished experts in the respective fields. The text is not only suited for scientists and engineers who develop and apply VCSELs, but also for

graduate students who strive to deepen their knowledge about most modern semiconductor laser diodes.

I am very grateful to all authors for having squeezed the extra writing task into their busy schedules. I wish to thank explicitly Claus Ascheron and Adelheid Duhm from Springer-Verlag in Heidelberg for supporting this book project and for succor while I had to deal with the numerous problems during the typesetting process, respectively. Special thanks go to Professor Fumio Koyama from Tokyo Institute of Technology for the help with the definition of this project and the kind invitation of many contributors.

Ulm, July 2012 Rainer Michalzik

Contents

Part I Basic VCSEL Characteristics

1 VCSELs: A Research Review . . . 3
Rainer Michalzik
1.1 Research History Reflected in VCSEL Books . . . 3
1.2 New Developments Motivating This Book . . . 7
1.3 Other Research Not Covered by the Chapters . . . 9
1.4 The Future . . . 12
References . . . 15

2 VCSEL Fundamentals . . . 19
Rainer Michalzik
2.1 Introduction . . . 19
2.2 VCSEL Design and Operation Parameters . . . 21
2.2.1 VCSEL Types and General Properties . . . 21
2.2.2 Bragg Reflectors . . . 24
2.2.3 Relative Confinement Factor . . . 27
2.2.4 Threshold Gain and Photon Lifetime . . . 28
2.2.5 Threshold Current . . . 30
2.2.6 Matrix Method and Standing-Wave Pattern . . . 32
2.2.7 Energy Flux and Differential Quantum Efficiency . . . 35
2.2.8 Conversion Efficiency . . . 38
2.3 Emission Characteristics of Oxide-Confined VCSELs . . . 40
2.3.1 Device Structure . . . 40
2.3.2 Experimental Operation Characteristics . . . 41
2.3.3 Temperature Behavior . . . 43
2.3.4 Transverse Modes . . . 46
2.4 Dynamic and Noise Behavior . . . 50
2.4.1 Rate Equations . . . 50
2.4.2 Small-Signal Modulation Response . . . 52

2.4.3 Relative Intensity Noise 55
2.4.4 Emission Linewidth 57
2.5 VCSEL-Based Optical Interconnects 59
2.5.1 Fiber Coupling 59
2.5.2 Large-Signal Modulation Effects 60
2.5.3 High-Speed Optical Data Transmission 61
2.6 Conclusion 66
References 67

3 Three-Dimensional Modeling of VCSELs 77
Pierluigi Debernardi
3.1 Introduction 77
3.2 Interplay of the Different Effects 78
3.3 Optical Part 79
3.3.1 The Coupled-Mode Approach 80
3.3.2 Comparing Different Models 83
3.3.3 Comparisons with Experimental Results 84
3.4 Thermal Part 93
3.5 Major Temperature Related Phenomena 97
3.6 Electrical Part 99
3.6.1 Approximated Current Profiles 99
3.6.2 Current Leakage 101
3.7 Rate Equations 103
3.7.1 Carrier Expansion and Projection Technique 105
3.7.2 Light Output Curve Computation 106
3.8 Example of Results 107
3.8.1 Model Validation 109
3.8.2 Additional Examples of Numerical Results 111
3.9 Summary 115
References 115

4 Single-Mode VCSELs 119
Anders Larsson and Johan S. Gustavsson
4.1 Introduction 119
4.2 Applications and Requirements 120
4.3 Optical Fields and Modes in VCSELs 122
4.3.1 Longitudinal Fields 122
4.3.2 Transverse Fields 122
4.3.3 Polarization 126
4.4 Techniques for Single-Mode Emission 127
4.4.1 Inherently Single-Mode VCSELs 127
4.4.2 Single-Mode Emission from Inherently
Multimode VCSELs 132
4.5 A Specific Example 138

4.6 Summary 140
References 140

Part II Device Technology and Performance

5 Polarization Control of VCSELs 147
Johannes Michael Ostermann and Rainer Michalzik
5.1 Introduction 147
5.2 VCSELs and Their Polarization 148
5.2.1 Experimental Findings 149
5.2.2 Some Theoretical Explanations 153
5.3 Need for Polarization Control of VCSELs 155
5.4 Approaches to Polarization Control 156
5.4.1 Polarization-Dependent Gain 157
5.4.2 Polarization-Dependent Mirror 158
5.4.3 Asymmetric Resonators 159
5.4.4 External Optical Feedback 159
5.4.5 Intentional Polarization Switches 159
5.5 Surface Gratings for Polarization Control 160
5.5.1 Gratings with Wavelength-Scale Periods 161
5.5.2 Sub-Material-Wavelength Surface Gratings 167
5.5.3 High-Index-Contrast Subwavelength Gratings 168
5.6 Conclusion 168
References 169

6 Polarization Dynamics of VCSELs 181
Krassimir Panajotov and Franco Prati
6.1 Background 182
6.2 Overview of the Experimental Results on Polarization Dynamics of a Solitary VCSEL 184
6.2.1 Alignment of Polarization Axis to [110] or $[1\bar{1}0]$ Axes: Elasto-Optic and Electro-Optic Effects 184
6.2.2 Type I Polarization Switching 186
6.2.3 Polarization Mode Hopping 189
6.2.4 Type II Polarization Switching and Double Polarization Switching 192
6.2.5 Impact of QW Anisotropic Strain on Polarization Switching Behavior 195
6.2.6 Polarization Fluctuations and Nonlinear Birefringence and Dichroism 196
6.2.7 Pitchfork Type of Polarization Switching in VCSELs 202

6.2.8 Voltage Controlled Polarization Switching in Coupled-Cavity VCSELs 203
6.2.9 Polarization Dynamics of Optically Pumped VCSELs 204
6.3 Physical Mechanisms and Theoretical Modeling of Polarization Dynamics in VCSELs 206
6.3.1 Polarization Bistability in Edge-Emitting Semiconductor Lasers and Gain Compression Model 206
6.3.2 Different Physical Mechanisms Can Lead to Net Gain Equalization in VCSELs 210
6.3.3 Polarization Dynamics in VCSELs: The Spin-Flip Model (SFM) 214
6.4 Conclusions and Perspective Applications 223
References 225

7 Design and Performance of High-Speed VCSELs 233
Yu-Chia Chang and Larry A. Coldren
7.1 Introduction 233
7.2 Theoretical Background 235
7.2.1 Intrinsic Laser Response 236
7.2.2 Extrinsic Parasitic Response 239
7.3 Design of High-Speed VCSELs 241
7.3.1 Active Region 241
7.3.2 Lateral Mode Confinement and Single Modeness 242
7.3.3 Chip Parasitics 243
7.3.4 Pad Parasitics 245
7.3.5 Thermal Management 246
7.4 Performance of High-Speed VCSELs 247
7.4.1 850-nm VCSELs 248
7.4.2 980-nm VCSELs 249
7.4.3 1.1-μm VCSELs 251
7.4.4 Long-Wavelength VCSELs 253
7.5 Loss-Modulated High-Speed VCSELs 255
7.5.1 Principle of Operation 255
7.5.2 VCSELs with an Electroabsorption Modulator 256
7.5.3 VCSELs with an Electrooptical Modulator 257
7.6 Conclusion 257
References 257

8 High-Power VCSEL Arrays 263
Jean-François P. Seurin
8.1 Introduction 263
8.2 Development of High-Efficiency VCSEL Devices 266

8.2.1 Device Structure and Fabrication 266
8.2.2 Results and Discussion 267
8.3 2D VCSEL Array Fabrication 276
8.4 Results 279
8.5 High-Brightness VCSEL Arrays 282
8.6 High-Energy VCSEL Arrays 284
8.6.1 VCSEL-Based Active Q-Switch 284
8.6.2 Short Pulse VCSEL Array Modules 286
8.7 Conclusions 286
References 287

9 High-Contrast Grating VCSELs 291
Connie J. Chang-Hasnain
9.1 Introduction 291
9.2 High-Contrast Subwavelength Grating (HCG) 292
9.2.1 HCG as Broadband Reflector 293
9.2.2 Physics of HCG 295
9.3 HCG-VCSEL Design and Fabrication 296
9.4 Optical Characteristics of HCG-VCSEL 298
9.4.1 Light–Current and Near Field Characteristics 298
9.4.2 Lithographically-Defined Polarization Control 300
9.4.3 Transverse Mode Control 302
9.4.4 HCG Size Dependence 303
9.5 Fabrication Tolerance 304
9.6 Lithographically-Defined Multi-Wavelength HCG-VCSELs . . . 306
9.7 Tunable HCG-VCSELs 309
9.7.1 Design and Fabrication 309
9.7.2 Characteristics of Tunable HCG-VCSEL 311
9.8 Summary 313
References 314

Part III From Infrared to Violet Emission

10 Long-Wavelength VCSELs with Buried Tunnel Junction 321
Markus Ortsiefer, Werner Hofmann, Jürgen Rosskopf
and Markus-Christian Amann
10.1 Special Issues for Long-Wavelength VCSELs 322
10.2 The Buried Tunnel Junction Concept 324
10.3 Device Structures and Characteristics 327
10.3.1 InP-Based VCSELs 327
10.3.2 GaSb-Based VCSELs 341
10.4 Applications 343
10.4.1 Optical Communication 343
10.4.2 VCSEL-Based Optical Gas Sensing 346

10.5 Conclusion. 348
References 349

11 GaInNAs(Sb) Long-Wavelength VCSELs 353
James S. Harris, Hopil Bae and Tomás Sarmiento
11.1 Introduction 353
11.2 Growth Issues of GaInNAs(Sb) 358
11.3 1.3 μm GaInNAs VCSELs 362
11.4 1.55 μm GaInNAsSb VCSELs 364
11.5 Summary 369
References 370

12 Red Emitting VCSEL 379
Michael Jetter, Robert Roßbach and Peter Michler
12.1 Introduction 379
12.2 VCSEL Structure 381
12.2.1 AlGaInP Active Zone 381
12.2.2 Distributed Bragg Reflectors 381
12.2.3 Oxide Aperture. 383
12.2.4 In-Situ Reflection Measurement 384
12.3 Device Characteristics of Red VCSEL 385
12.3.1 Heat Dissipation Model. 386
12.3.2 High Temperature Results 389
12.3.3 Modulation Bandwidth 389
12.3.4 Modulation Limits 390
12.3.5 Data Transmission 392
12.3.6 Reliability 393
12.4 Quantum Dot Based Red Emitting VCSEL 394
12.5 Conclusion. 396
12.6 Outlook 396
References 397

13 GaN-Based VCSELs 403
Shing-Chung Wang, Tien-Chang Lu, Hao-Chung Kuo and Jun-Rong Chen
13.1 Introduction 403
13.2 Design and Fabrication of GaN-Based VCSELs 406
13.3 Optically Pumped GaN-Based VCSELs. 410
13.3.1 Hybrid DBR VCSEL 410
13.3.2 Dielectric DBR VCSEL 413
13.4 Electrically Pumped GaN-Based VCSELs 416
13.4.1 Hybrid DBR VCSEL 416
13.4.2 Dielectric DBR VCSEL 421
13.5 Future Perspectives 423

13.6 Summary 423
References 424

Part IV VCSEL Applications

14 VCSEL-Based Transceivers for Data Communications 431
Kenneth P. Jackson and Clint L. Schow
14.1 Introduction 431
14.2 Early Datacom Transceivers 432
14.3 The Need for VCSELs 435
14.4 VCSEL Technology and the Drive for Lower Costs 436
14.5 Today's VCSEL-Based Transceivers 441
14.6 Future of VCSEL-Based Transceivers 444
References 448

15 Low-Cost Optical Video Links Based on VCSELs 449
Hyun-Kuk Shin
15.1 Introduction 449
15.2 Optical Video Link Modules for DVI and HDMI 450
15.3 VCSEL in Display Interconnection Module 458
15.4 Applications of Optical Video Links 461
15.4.1 Train Display System 461
15.4.2 Elevator System 462
15.4.3 Medical Application 464
15.5 Reduction of the Number of Fibers 465
15.6 Optical Video Link for a Mass Market 466
15.7 Conclusion 470
References 470

16 Progress in VCSEL-Based Parallel Links 473
Daniel M. Kuchta
16.1 Introduction 473
16.2 Commercial VCSEL-based Parallel Links Since ~2000 475
16.3 Research Activities in VCSEL-Based Parallel Links 485
16.4 Deployment of Parallel Links in Large Systems and Test Beds 497
16.5 Fibers and Connectors for Parallel Links 505
16.6 Reliability for Parallel Links 507
16.7 Outlook 510
References 512

17 VCSELs for Optical Mice and Sensing 521
Martin Grabherr, Holger Moench and Armand Pruijmboom
17.1 Introduction 521
17.2 VCSELs as Ideal Illumination Source for the Optical Mouse 522
17.2.1 General Requirements and Benefits of VCSELs Over Edge Emitters 523
17.2.2 VCSEL Production and Typical Characteristics 523
17.2.3 Polarization Stabilization 527
17.3 SMI Laser Doppler Interferometry 528
17.3.1 Velocity Measurement 528
17.3.2 Direction of Motion and Distance 529
17.4 VCSEL as Integrated Laser Doppler Interferometer 531
17.4.1 VCSEL with Integrated Photodiode 531
17.4.2 Single-Mode VCSEL 533
17.4.3 $d\lambda/dI$ Requirements 534
17.4.4 Philips “Twin-Eye” Product 534
17.5 More SMI Applications 536
17.6 Summary 537
References 537

18 VCSEL-Based Laser Printing System 539
Nobuaki Ueki and Naotaka Mukoyama
18.1 Introduction 539
18.2 VCSELs for Printer Applications 541
18.3 Structure and Characteristics of VCSEL Array 542
18.4 VCSEL Driver IC 545
18.5 Image Quality 546
18.6 VCSEL-Based Printer Products 547
18.7 Summary 548
References 548

Index 549

Contributors

Markus-Christian Amann Walter Schottky Institut, Technische Universität München, Am Coulombwall, 85748 Garching, Germany, e-mail: amann@wsi.tum.de

Hopil Bae Department of Electrical Engineering, Stanford University, 420 Via Ortega, Stanford, CA 94305, USA, e-mail: hopilbae@gmail.com

Yu-Chia Chang Department of Electrical and Computer Engineering, University of California, Santa Barbara, CA 93106, USA, e-mail: yuchia@engineering.ucsb.edu

Connie J. Chang-Hasnain Department of Electrical Engineering and Computer Science, University of California, Berkeley, CA 94720, USA, e-mail: cch@berkeley. edu

Jun-Rong Chen Department of Photonics and Institute of Electro-Optical Engineering, National Chiao Tung University, 1001 University Road, Hsinchu 300, Taiwan, e-mail: jrchen.eo95g@nctu.edu.tw

Larry A. Coldren Department of Electrical and Computer Engineering, University of California, Santa Barbara, CA 93106, USA, e-mail: coldren@ece.ucsb.edu

Pierluigi Debernardi IEIIT-CNR c/o Politecnico di Torino Corso Duca degli Abruzzi 24, 10129 Torino, Italy, e-mail: pierluigi@polito.it

Martin Grabherr Philips Technologie GmbH U-L-M Photonics, Lise-Meitner-Str. 13, 89081 Ulm, Germany, e-mail: martin.grabherr@ulm-photonics.de

Johan S. Gustavsson Department of Microtechnology and Nanoscience, Photonics Laboratory, Chalmers University of Technology, 41296 Göteborg, Sweden, e-mail: johan.gustavsson@chalmers.se

James S. Harris Jr. Department of Electrical Engineering Stanford University, 420 Via Ortega, Stanford, CA 94305, USA, e-mail: harris@snow.stanford.edu

Werner Hofmann Walter Schottky Institut, Technische Universität München, Am Coulombwall, 85748 Garching, Germany, now: Institut für Festkörperphysik, Technische Universität Berlin, Hardenbergstr. 36, 10623 Berlin, Germany, e-mail: werner.hofmann@tu-berlin.de

Kenneth P. Jackson Emcore Corporation, 10420 Research Road SE, Bldg 2, Albuquerque, NM 87123, USA, e-mail: kenneth_jackson@emcore.com

Michael Jetter Institut für Halbleiteroptik und Funktionelle Grenzflächen, Universität Stuttgart, Allmandring 3, 70569 Stuttgart, Germany, e-mail: michael.jetter@ihfg.uni-stuttgart.de

Daniel M. Kuchta IBM T. J. Watson Research Center, 1101 Kitchawan Rd., M.S. 38-123, Yorktown Heights, NY 10598, USA, e-mail: kuchta@us.ibm.com

Hao-Chung Kuo Department of Photonics and Institute of Electro-Optical Engineering, National Chiao Tung University, 1001 University Road, Hsinchu 300, Taiwan, e-mail: hckuo@faculty.nctu.edu.tw

Anders Larsson Department of Microtechnology and Nanoscience, Photonics Laboratory, Chalmers University of Technology, 41296 Göteborg, Sweden, e-mail: anders.larsson@chalmers.se

Tien-Chang Lu Department of Photonics and Institute of Electro-Optical Engineering National Chiao Tung University, 1001 University Road, Hsinchu 300, Taiwan, e-mail: timtclu@mail.nctu.edu.tw

Rainer Michalzik Institute of Optoelectronics, Ulm University, Albert-Einstein-Allee 45, 89081 Ulm, Germany, e-mail: rainer.michalzik@uni-ulm.de

Peter Michler Institut für Halbleiteroptik und Funktionelle Grenzflächen, Universität Stuttgart, Allmandring 3, 70569 Stuttgart, Germany, e-mail: p.michler@ihfg.uni-stuttgart.de

Holger Moench Philips Research Laboratories, Weisshausstr.2, 52066 Aachen, Germany, e-mail: holger.moench@philips.com

Naotaka Mukoyama Optical System Business Development, Fuji Xerox Company, Ltd., 430 Sakai, Kanagawa 259-0157, Japan

Johannes Michael Ostermann Institute of Optoelectronics, Ulm University, Albert-Einstein-Allee 45, 89081 Ulm, Germany, e-mail: johannes-michael.ostermann@alumni.uni-ulm.de

Markus Ortsiefer VERTILAS GmbH, Lichtenbergstr. 8, 85748 Garching, Germany, e-mail: ortsiefer@vertilas.com

Krassimir Panajotov Department of Applied Physics and Photonics, Vrije Universiteit Brussel, Pleinlaan 2, 1050 Brussels, Belgium and Institute of Solid State Physics, Bulgarian Academy of Sciences, 72 Tzarigradsko Chaussee blvd., 1784 Sofia, Bulgaria, e-mail: kpanajot@b-phot.org

Franco Prati CNISM and Dipartimento di Fisica e Matematica, Università dell'Insubria, via Valleggio 11, 22100 Como, Italy, e-mail: franco.prati@uninsubria.it

Armand Pruijmboom Philips Laser Lighting Systems, Hurksestraat 2c, 5652 AJ Eindhoven, The Netherlands, e-mail: armand.pruijmboom@philips.com

Jürgen Rosskopf VERTILAS GmbH, Lichtenbergstr. 8, 85748 Garching, Germany, e-mail: rosskopf@vertilas.com

Robert Roßbach Institut für Halbleiteroptik und Funktionelle Grenzflächen, Universität Stuttgart, Allmandring 3, 70569 Stuttgart, Germany, now: Robert Bosch GmbH, 72703 Reutlingen, Germany, e-mail: robert.rossbach@de.bosch.com

Tomás Sarmiento Department of Electrical Engineering, Stanford University, 420 Via Ortega, Stanford, CA 94305, USA, e-mail: tsarmie@stanford.edu

Clint L. Schow IBM T. J. Watson Research Center, 1101 Kitchawan Rd., M.S. 38-127, Yorktown Heights, NY 10598, USA, e-mail: cschow@us.ibm.com

Jean-François P. Seurin Princeton Optronics, 1 Electronics Drive, Mercerville, NJ 08619, USA, e-mail: jfseurin@princetonoptronics.com

Hyun-Kuk Shin OPTICIS Co., Ltd., Suite 304, Byucksan Technopia, 434-6 Sangdaewon-dong, Jungwon-Gu, Sungnam, Gyunggi-Do 462-120, Korea, e-mail: hkshin@opticis.com

Nobuaki Ueki (Deceased) Optical System Business Development, Fuji Xerox Company, Ltd., 2274 Hongo, Ebina, Kanagawa 243-0494, Japan

Shing-Chung Wang Department of Photonics and Institute of Electro-Optical Engineering, National Chiao Tung University, 1001 University Road, Hsinchu 300, Taiwan, e-mail: scwang@mail.nctu.edu.tw

Part I
Basic VCSEL Characteristics

Chapter 1
VCSELs: A Research Review

Rainer Michalzik

Abstract This chapter attempts to briefly review the research history of vertical-cavity surface-emitting lasers (VCSELs). Based on the contents of previous monographs on VCSELs written in English, we motivate the selection of topics in the present book and give an introduction to the individual chapters. Moreover, we mention some other research that is not covered in a dedicated chapter in order to provide the readers with even deeper insights into VCSEL research. Future directions and opportunities are also indicated.

1.1 Research History Reflected in VCSEL Books

VCSEL research started with the suggestion of this novel type of semiconductor laser by Prof. Kenichi Iga in the year 1977 and in particular with the first publication in Dec. 1979 [1]. Even before that, in 1965 Ivars Melngailis published a remarkable paper [2] reporting longitudinal lasing operation at about 5.2 µm wavelength in a 220 µm long cavity made from n^+pp^+-doped InSb. The surfaces were polished and a Ag–Au contact was evaporated on the p^+-side. At a temperature of about 10 K, current pulses with a duration of 50 ns and an amplitude of at least 20 A (corresponding to a current density of 60 kA/cm^2) were injected parallel to the direction of emission. An external longitudinal magnetic field was needed for focusing. Interestingly, the author already lists a number of advantages inherent to such a structure: Array formation, coherent emission over large areas with associated small beam divergence, and large output powers, all of which we know from VCSELs today.

The importance of VCSELs is reflected in the fact that they have the second largest production volume among all types of semiconductor lasers today—only exceeded by

R. Michalzik (✉)
Institute of Optoelectronics, Ulm University,
Albert-Einstein-Allee 45, 89081 Ulm, Germany
e-mail: rainer.michalzik@uni-ulm.de

R. Michalzik (ed.), *VCSELs*, Springer Series in Optical Sciences 166,
DOI: 10.1007/978-3-642-24986-0_1, © Springer-Verlag Berlin Heidelberg 2013

Fabry–Pérot-type edge-emitting lasers for use in optical disk drives for data storage. They are the most versatile laser diode, have enormous market growth potential, and will most probably soon become number one. Thus by now we are faced with a huge number of publications on VCSELs. In addition to research papers and review articles there are several books with an exclusive focus on VCSELs [3–8], where two of them were written by single authors and four are edited multi-author volumes. About nine years have passed since the last book was produced. The contribution of the present book to the field can be best appreciated by browsing the contents of its predecessors.[1]

A book by G.A. Evans and J.M. Hammer from the year 1993 [9] already contains a chapter on VCSELs and arrays, whereas its main purpose was to present the progress with horizontal-cavity lasers and two-dimensional arrays in which surface emission is achieved with grating couplers or integrated beam deflectors. In their chapter, K. Iga and F. Koyama describe the many advantages of VCSELs and the early research progress. Expected performances are analyzed theoretically and experimental results are summarized both in the InGaAsP–InP and AlGaAs–GaAs material systems. At that time, continuous-wave room-temperature lasing and sub-mA threshold currents had already been achieved with GaAs-based devices.

In 1995, T.E. Sale presented a comprehensive book [3] as an extended version of his own Ph.D. Thesis on VCSELs [10]. Distributed Bragg reflectors (DBRs) are described in some detail, including the challenge to achieve low ohmic resistances. An entire chapter deals with gain calculations for compressively strained InGaAs–GaAs quantum wells (QWs) which became very popular as active region since J. Jewell demonstrated first full-monolithic VCSELs with epitaxial DBRs and those QWs in 1989 [11]. Such devices typically have emission wavelengths in the range of 950–1,000 nm. Sale discusses and analyzes own experimental results on devices grown by molecular beam epitaxy (MBE) as well as metal-organic chemical vapor deposition (MOCVD). These lasers had a resonant period gain (RPG) structure with three InGaAs QWs separated by GaAs barriers with half a material wavelength thickness and showed moderate performance. The RPG concept was demonstrated for VCSELs in 1989 [12, 13] but turned out to be inferior to a regular multiple-QW (MQW; mostly three QWs are used) concept with thin barriers. It is interesting to note that somewhat more elaborate RPG structures with a larger number of periods are nowadays applied in optically pumped semiconductor disk lasers, also known as vertical-external-cavity surface-emitting lasers (VECSELs) [14]. VCSEL types considered by Sale use etched mesas and proton implantation for current confinement. The selective oxidation of AlGaAs with close to 100% Al content to produce current apertures of just a few ten nanometers thickness and quasi arbitrary diameter was not yet considered because pioneering demonstrations [15] were done just before publication of the book. Polarization effects in VCSELs find no mention and little attention is given to the dynamic VCSEL properties.

---

[1] Readers who are not very familiar with VCSELs yet will find it helpful to study also Chap. 2 of this book, where we discuss many of the terms that are mentioned here in much greater detail.

In the same year, T.P. Lee edited a book containing seven chapters [4] which was a reprint of a special issue of the International Journal of High Speed Electronics and Systems. It starts with an overview of InGaAsP–InP VCSELs for 1.3 and 1.55 μm operation. At that time, continuous-wave room-temperature lasing of such devices had not yet been achieved. The preparation of dielectric mirrors for VCSELs is presented next, addressing the difficulties with epitaxial DBR formation especially for long-wavelength devices. The third chapter presents a buried-heterostructure-type antiguided VCSEL targeted for single-mode emission as well as two-dimensional multiple-wavelength VCSEL arrays for wavelength division multiplexing (WDM) applications, which were obtained by tailoring the spatial growth temperature pattern in MBE. The performance of optimized MOCVD-grown proton-implanted 850 nm VCSELs suitable for mass production is reported next. Record performance data were obtained. The devices were applied in a first 32-channel parallel-optical link with 500 Mbit/s individual data rate. The first (and extensive) chapter on red emitting InAlGaP–GaAs VCSELs is also part of this book. The devices already showed continuous-wave room-temperature lasing with remarkable output power and conversion efficiency. Thermal effects in VCSELs are then discussed in great detail and various thermal models are presented. Chapter 7 deals with the reliability of proton-implanted 850 and 980 nm VCSELs. The mean-time-to-failure was then still in the range of 10^5 h. Improvements by about two orders of magnitude were seen in the years after these initial observations.

The book edited by C. Wilmsen, H. Temkin, and L.A. Coldren in 1999 [5] very well reflects in 12 chapters the rapid progress in VCSEL research at that time. It contains comprehensive introduction and design chapters with much emphasis on oxide-confined VCSELs, which had already outperformed the other device types with all key performance parameters. Microcavity effects which are very important for understanding spontaneous emission in resonant-cavity light-emitting diodes (RCLEDs) are treated in detail in another chapter. For the first time, full attention is given to the epitaxy of VCSELs, recognizing the fact that the high crystal quality of epitaxial layers is the indispensable prerequisite of every high-performance semiconductor laser. Likewise, VCSEL fabrication issues are excellently covered in the book. VCSEL polarization effects are also mentioned, however, with a main focus on free-space optical data links with polarization-selective losses. The need for polarization stability is stressed. The authors come to the conclusion ([16], p. 265): “Therefore, we believe that the most promising way of achieving complete polarization stability is to use VCSEL structures with anisotropic gain or integrated polarization-selective reflectors”. We will get back to this statement later. Chapter 7 deals with visible light emitting VCSELs, in particular in the red spectral regime. First optically pumped lasing had been observed from GaN-based VCSEL structures but no electrically pumped devices were then feasible. A chapter on 1.3 and 1.55 μm emission long-wavelength VCSELs showed that these devices were still relatively immature when compared with already commercially available 850 nm devices. Wafer fusion combining AlGaAs-based DBRs with an InGaAsP-based cavity region seemed to be a promising approach. In the book, VCSEL applications are introduced in Chap. 9, followed by three chapters on aspects of optical interconnection. Extended temperature

operation, polarization control through anisotropically etched mesas, WDM arrays, two-dimensional fiber-optic and free-space interconnects, as well as smart pixels through hybrid or monolithic integration of optoelectronic and electronic components are among the topics. A detailed overview of VCSEL-based fiber-optic transceivers is given. Data rates of such modules were mainly in the range of 0.5–1.25 Gbit/s.

Shortly after this, in the year 2000 J. Cheng and N.K. Dutta presented an edited book with a short overview and six chapters [6]. Chapter 1 gives much insight into oxide aperture formation in AlGaAs–GaAs VCSELs, which allows to produce microcavities with very small active areas and associated threshold currents below 100 μA. It is followed by a review of the technology and performance of such oxide-confined lasers. Chapter 3 investigates proton-implanted 850 nm VCSELs for optical data links in terms of small-signal, noise, and large-signal properties including turn-on delays. The latter topic received some attention at that time because the low threshold currents of VCSELs even seemed to allow bias-free data transmission (see also Sect. 2.5 of this book). A commercial fiber-optic transceiver for 1 Gbit/s data rate is introduced. The concept of a 32-channel, 1 Gbit/s-range parallel-optical interconnect module including receiver and driver electronics as well as packaging is presented next. Chapter 5 treats VCSEL modulation aspects, parallel-optical links, WDM VCSEL and photodetector arrays, optical switching, and reconfigurable and multi-access network scenarios in some detail. Again, data rates range from a few 100 Mbit/s–1 Gbit/s. Finally an overview of 950 nm range micromechanical tunable VCSELs using a movable cantilever is given in the last chapter.

In 2003, S.F. Yu autored a remarkable VCSEL book focusing on modeling aspects [7]. It briefly outlines recent VCSEL developments and the commercial status. Then it covers in much detail the one-dimensional design of VCSEL resonators, the transverse mode characteristics, the polarization properties, the thermal and electrical behavior, the dynamic characteristics, spontaneous emission, as well as nonlinear effects in VCSELs.

Finally, also in 2003 the (to the author's knowledge) last, 12-chapter-long monograph on VCSELs was published [8]. The project was initiated by H. Li who passed away a little later. Kenichi Iga then became the co-editor. The text starts with a historical account and an overview of VCSEL operation in different wavelength regimes. Details of optical gain calculations are presented, followed by the third chapter which explains the operation principles of oxide-confined VCSELs including state-of-the-art static, noise, and dynamic behavior. Digital data transmission over single-mode and multimode fibers is shown up to data rates of 12.5 Gbit/s. Chapter 4 deals with the theory of anisotropic optical gain of QWs grown on non-(001)-oriented substrates. The corresponding experimental VCSEL work is reviewed and polarization stability of lasers is demonstrated. Thus, here the above statement ([16], p. 265) on anisotropic gain in [5] is addressed. VCSEL modeling is represented in two chapters in terms of a static three-dimensional coupled electrical–optical–thermal model and comprehensive dynamic models with high complexity up to a quasi-three-dimensional case. Microcavity oxidized VCSELs and light-emitting diodes are discussed in Chap. 7. The use of quantum dots in the active region is emphasized for improved carrier confinement and for reaching longer wavelengths on GaAs

substrates. Various designs of DBRs for VCSELs and cavity effects including external optical feedback are presented in the next chapter. The problems associated with the realization of 1.3 and 1.55 μm long-wavelength VCSELs in various material systems including dilute nitride GaInNAs–GaAs are summarized in Chap. 9, whereas Chap. 12 focuses on a rather successful approach in InAlGaAs–InP material employing a buried tunnel junction for current confinement. Continuous-wave lasing at elevated temperatures is demonstrated at 1.5 and 1.8 μm wavelengths. Chapter 10 introduces the design of special radiation-tolerant 0.04 and 1.28 Gbit/s VCSEL-based multimode fiber data links in a particle collider environment. The progress in GaN-based blue and near-ultraviolet wavelength vertical-cavity emitters is presented in Chap. 11. A quasi-continuous-wave optically pumped VCSEL at 355 nm and electrically pumped RCLEDs with emission in the range of 410–440 nm wavelength are shown.

1.2 New Developments Motivating This Book

Enormous progress of VCSEL performance and applications has been achieved since the last two VCSEL books have been published in 2003. In what follows we introduce the contents of the present book with respect to the previous work discussed in the preceding section. In a certain sense, this book is related to [8], which was also published by Springer-Verlag. Owing to a largely different selection of subjects it can nevertheless not be considered simply a second edition.

The 18 chapters are arranged into four groups. Entirely new contributions are made to the fields of vectorial three-dimensional optical modeling, single-mode VCSELs, polarization control, polarization dynamics, very-high-speed design, high-power emission, use of high-contrast gratings, GaInNAsSb long-wavelength VCSELs, optical video links, VCSELs for optical mice and sensing, as well as VCSEL-based laser printing.

The first group on “Basic VCSEL Characteristics” contains:

1. This chapter, which shall give a general overview of the field.
2. A text about VCSEL fundamentals outlining laser design principles and (static, noise, and dynamic) operation characteristics of oxide-confined GaAs-based VCSELs in the 850 and 980 nm wavelength regions. It is meant to make the book accessible to a broad range of readers with different technical background.
3. A chapter on three-dimensional modeling of VCSELs, considering coupled optical, electrical, and thermal phenomena. Strong emphasis is put on a vectorial optical model with the ability to handle non-circular geometries which are vital to the performance of, e.g., polarization-stable surface grating VCSELs introduced in Chap. 5.
4. The first book chapter dealing specifically with single-mode VCSELs, reviewing different cavity designs that have been presented in the literature. Transverse single-mode emission has become important in recent years in particular for

optical sensing. Whereas until the year 2004, almost all commercial VCSELs were designed for multimode emission, nowadays single-mode devices have about half the market volume.

The second group is concerned with "Device Technology and Performance":

5. A chapter on polarization control of VCSELs addresses the fact that the light output polarization is inherently unstable in most types of VCSELs. On the other hand, a stable polarization is required for most optical sensing applications. Different stabilization methods are reviewed. It is shown that monolithic semiconducting surface gratings provide a convenient solution to the polarization problem. Such VCSELs are commercial products today. The use of "integrated polarization-selective reflectors", as stated above [5] ([16], p. 265) is indeed most promising, whereas anisotropic gain currently is too difficult to incorporate into high-performance VCSEL structures.
6. Another "first" of this book is a chapter devoted to the rich variety of polarization dynamics of VCSELs. The authors provide a very detailed overview of the literature, both from theoretical and experimental points of view and thus contribute to a deeper understanding of the nonlinearities inherent these semiconductor lasers.
7. In recent years, VCSELs have been optimized for high-speed operation at data rates of as much as 40 Gbit/s. This chapter analyzes the modulation bandwidth which is determined by the intrinsic laser response and extrinsic parasitic effects. The state of the art at wavelengths from 850 nm to 1.6 μm is reviewed. Alternative modulation schemes are also considered.
8. Another breakthrough over the past several years is the demonstration and commercialization of high-power, high-efficiency two-dimensional VCSEL arrays, mainly in the 808 and 980 nm spectral domains. This chapter is the first to summarize the progress in this field. The devices feature high reliability, wavelength stability, low-divergence circular output beams, and low-cost manufacturing. They thus enable a number of new applications and have become a strong contender to edge-emitting diode lasers which presently dominate the market.
9. More in the research stage is the fascinating work on high-contrast gratings that have the prospects to replace an entire DBR stack with a single nanostructured layer of semiconductor material. Lithographic control of polarization, transverse mode structure, and emission wavelength is provided. Also wavelength tuning can be much more efficient.

The third group of chapters is concerned with VCSELs showing "From Infrared to Violet Emission":

10. The first chapter is essentially an update of Chap. 12 in [8]. Long-wavelength VCSELs with buried tunnel junctions show excellent characteristics meanwhile and are commercial products. The chapter discusses InP- and GaSb-based devices for applications in optical communications and gas sensing. Maximum emission wavelengths exceed 2.3 μm.
11. An alternative promising approach to long-wavelength VCSELs is the growth of GaInNAsSb compounds on GaAs substrates. Such research is described in this

chapter. Edge-emitting laser diodes and first monolithic 1500 nm VCSELs are demonstrated.

12. Since the last book chapter was written in [5], a lot of progress has been achieved with red emitting VCSELs. This chapter presents the crystal growth issues in AlGaAs and AlGaInP on GaAs, electrical, optical, thermal, and dynamic laser characteristics as well as optical data transmission over polymer optical fibers. The incorporation of InP quantum dots allows to reach record-low threshold current densities and reduced temperature sensitivity.
13. Compared to the status in [5, 8], the new developments on GaN-based blue and near-ultraviolet emitting VCSELs are even more dramatic. The chapter describes the challenge of DBR formation and different microcavity configurations. First electrically pumped VCSELs emitting continuously at room temperature have been fabricated. Future prospects and emerging applications are discussed.

The final group named “VCSEL Applications” covers single-fiber and parallel-optical data transmission, sensing in optical mice, as well as printing:

14. We start with a very valuable review of the 850 nm VCSEL-based transceiver market for data communications over multimode optical fibers, which has grown tremendously over the last decade.
15. A special application of VCSEL-based transceivers in optical video links is described next. History, current status, and technical issues for mass market rollout are discussed.
16. A comprehensive overview of the advancements in VCSEL-based parallel-optical links is given in this chapter. Commercial and research activities, deployment in large computing systems and test beds, fiber connectorization, reliability, and future applications are all covered extensively.
17. For the first time, VCSEL use in optical computer mice is described in the present book chapter. Comparisons to LEDs as illumination source are made and an advanced interference sensor based on laser self-mixing is introduced. Such sensors employ optoelectronic chips in which VCSELs are monolithically integrated with intra-cavity PIN-type photodiodes. Aspects of mass production are also addressed.
18. Finally, also for the first time a VCSEL book chapter specifically addresses laser printing. Two-dimensional 8×4 VCSEL arrays at 780 nm wavelength enable 2,400 dots per inch resolution, high printing speed, and reduced power consumption. Key technologies for achieving high image quality are pointed out.

1.3 Other Research Not Covered by the Chapters

In this section we briefly list some VCSEL research that is not explicitly mentioned in the individual chapters. Hereby the versatility of this type of laser becomes very apparent. In addition, a few recent references on selected topics of this book are provided.

- In-depth overviews of the *history* of VCSEL research have been compiled by K. Iga [17–19], see also Chap. 1 in [4], Chap. 1 in [8], and (together with F. Koyama) Chap. 3 in [9].
- Particularly rapid progress is currently seen in the field of *high-speed* VCSELs. Complementing Chap. 7 of this book, [20] presents the state of the art as of Dec. 2010. A focus on 980 nm high-speed VCSELs is put in [21].
- *Bidirectional* single-wavelength (no WDM) Gbit/s-rate data transmission over multimode fiber [22–24] (see also the end of Chap. 2 of this book) can lead to cost-effective transceiver solutions for some application areas and thus might be considered for commercialization. For this, VCSELs are monolithically integrated with metal–semiconductor–metal (MSM) or PIN-type photodetectors.
- The *nonlinear dynamics* of VCSELs induced by optical injection, optical feedback, current modulation, and mutual coupling are reviewed in a recent paper [25], supplementing the nonlinear polarization effects described in Chap. 6 of this book.
- A very good overview of advances in *long-wavelength* VCSELs is given in [26]. References are provided for various approaches based on highly strained InGaAs–GaAs QWs, InGaAs quantum dots, GaAsSb QWs, dilute nitride GaInNAs QWs on GaAs, and InAlGaAs–InP QWs. Besides the use of buried tunnel junctions (see Chap. 10 of this book), wafer fusion has led to devices with excellent performance [27]. High-speed modulation at 25 Gbit/s of a 1.1 μm VCSEL at 100°C [28] and at 35 Gbit/s (25°C) and 25 Gbit/s (55°C) of a 1.53 μm device [29] were achieved.
- Multiple-wavelength VCSEL arrays for *WDM applications* have been realized by epitaxial MOCVD growth on patterned substrates. A maximum lasing span of 192 nm [30] and a 110-channel VCSEL array centered at 1,226 nm with a thermally tuned wavelength spacing of 0.1 nm [31] have been reported. A novel hollow-waveguide multiplexer [32] might enable the coupling of such arrays to multimode fibers in a very compact way.
- Impressive results on micromechanically actuated 1.55 μm VCSELs with larger than 100 nm *tuning range* have recently been obtained [33] (see also Chaps. 9 and 10 of this book).
- *Athermal operation* with a tuning coefficient as small as 0.002 nm/K has been achieved with a cantilever-type 840 nm-range VCSEL [34, 35].
- Up-to-date insights into *red emitting* VCSELs from an industrial point of view are provided in [36].
- *Quantum dot* VCSELs have been developed and show very good operation characteristics [37, 38]. However, at present there is no compelling advantage of these devices that would lure an established VCSEL company to incorporate such active regions into their designs.
- *Photonic crystals* have been much explored for use in VCSELs [39], with an initial focus on increasing the single-mode output power (see also Chap. 4 of this book). Coherently coupled arrays with low beam divergence are among the more recent prospects [40].
- A self-consistent *VCSEL model* is presented in [41] and applied to various resonator configurations and wavelength regimes, with much attention paid to single-mode operation.

- As reviewed in [42], the integration with *micro-optical elements* provides many opportunities for the beam control of VCSELs.
- Beam control is also achieved particularly well with *VECSELs* [14]. For electrically pumped devices, up to now the laser community was not able to rival the amazing work done by Novalux a few years ago (reviewed in [43, 44]). More recent results on frequency doubling to the blue spectral region [45] are by far inferior to tens of milliwatts at 490 nm or hundreds of milliwatts continuous-wave Gaussian mode emission at 980 nm that were reported by the company. Anyhow, manufacturing the extended cavity mirror at the back side of the substrate has enabled to achieve fundamental mode powers of up to 15 mW [46]. VECSELs at 850 nm with a short external cavity length of only 25 μm were fabricated with the goal of obtaining higher output power and reduced emission linewidth [47]. Moreover, electrically pumped VECSELs are also considered for particle sensing in microfluidics [48].
- *All-optical signal processing*—if accomplished in a viable way—is of much interest for optical telecommunications. Contributions to this field have also been made with VCSEL-type devices. Among these are an *optical inverter* based on transverse mode switching (induced by mode locking) in a two-mode VCSEL [49], a *polarization converter* to a fixed polarization state based on similar principles [50], and an optical *nonlinear phase-shifter* [51] (enabling both positive and negative shifts to compensate laser chirp and fiber nonlinearities, respectively [52]) based on a VCSEL structure with a saturable absorber.
- An extensive review of *cavity soliton* effects in broad-area VCSELs is provided in [53]. Applications might be found in the fields of all-optical information processing and VCSEL characterization.
- *Slow-light* effects have been exploited in a Bragg waveguide as part of a 1.5 μm VCSEL structure to achieve efficient electro-absorption in an only 20 μm long device [54].
- The paper [55] reports a metal nano-apertured GaAs-based VCSEL in which a 100 nm diameter Au nanoparticle leads a *plasmon enhancement* of the optical field. Potential applications are in sub-wavelength optical near-field probing. Related research in [56] has even shown field enhancements in a 970 nm VCSEL suitable for *near-field optical recording*.
- Recent progress with metal-coated *nanocavity* pillar-type surface-emitting lasers is summarized in [57].
- Concepts of *spin-controlled* VCSELs are discussed in [58]. Those devices could enable much faster dynamics. Both optical excitation and electrical spin injection are considered.
- VCSELs are also being investigated as light sources in *optical tweezers* and traps used in biophotonics. In particular there are opportunities for the integration with *microfluidic chips* [59].

1.4 The Future

As is well known, predictions are difficult to make, especially when they concern the future.[2] It is much easier to check to which degree previous predictions have materialized.

Interestingly, from the beginning, optical data storage has been listed as a future VCSEL application. A miniaturized 780 nm VCSEL-based compact disk (CD) pickup head had been developed in Korea [60]. However, the available single-mode powers even nowadays are too small for data writing which has been an essential feature of every optical disk drive for a long time. Thus in reality the VCSEL never entered the optical storage market. Near-field optical recording as mentioned in the previous section might be a new option but right now it seems to be more likely that optical disks will altogether be replaced by solid-state silicon-based memory technologies in future.

Also VCSEL-based displays have been prophesied again and again. Optical displays today are extremely advanced but visible (i.e., visible radiation emitting) VCSELs are not. Their brightness is simply insufficient for projection displays. Pico projectors for mobile devices are equipped with high-power LEDs [61]. For larger-scale, laser-based projection, VECSELs are better candidates [14].

As a third example, in the past there was much speculation about optical computing. For instance, two-dimensional image processing with VCSEL arrays was praised and some nice demonstrations were made. Many papers have also been published on all-optical logic. A striking underestimation of the creativity and capabilities of the silicon electronics industry was usually behind such optimism.

Optical computing is dead but optics in computing is alive. In particular this is true for supercomputers. As detailed in Chap. 16 of this book, e.g., more than five million VCSELs transmit data in a fully configured modern IBM high-performance computing system, mostly in parallel-optical links using multimode fiber ribbon cable. This is where VCSELs are really good at. The penetration further down into the system, i.e., from the rack-to-rack level to the backplane and printed-circuit board levels and to the inter-chip level is much harder. Research in this direction is ongoing for at least two decades [62, 63]. Current projections say that optical interconnects are much needed at these levels [64]. A huge number of devices would be required, i.e., annual VCSEL production volumes would exceed 10^9 (one billion) units. On the other hand, the price pressure is enormous. The price of an 850 nm VCSEL now approaches 0.10 US dollars for high-volumes, but it is an open question if a one-cent VCSEL can be made. VCSEL production currently moves from 3-inch toward 4-inch diameter GaAs substrates. Further improving the yield and decreasing the footprint of the chips are essential issues.

Concerning VCSEL use in mainstream computing, in the year 2010 there was much enthusiasm about *Light Peak*, a converged I/O (input/output) technology demonstrated by Intel in Sept. 2009 and at that time supported by the big

---

[2] In similar form, this quote can be attributed to Mark Twain, Winston Churchill, Karl Valentin, and perhaps others.

players Sony, Nokia, and Apple. It was designed to work with 850 nm VCSELs and multimode fiber with data rates of 10 Gbit/s initially and up to 100 Gbit/s later. Target devices were PCs (personal computers), handhelds, workstations, consumer electronics, and so on. Through the economies of scale, Light Peak was expected to change the cost structures for optical links. A multi-hundred-million annual VCSEL market was predicted. First devices were said to be available to the public even in late 2010. Just a few months later, searching for Light Peak resulted in finding *Thunderbolt*, an *electrical* solution at 20 Gbit/s, limited to 3 m cable length. As often before, optics could not meet the cost target. Moreover, the optical connectors were found not to be consumer-compliant. This is a very good example for the usual fight of "copper versus optical". An optical physical layer for Thunderbolt is still planned, but predictions are difficult to make... A so-called active optical cable (AOC) would be the most viable implementation. Such a cable has electrical connectors and the electrical-to-optical-to-electrical conversions and the optical transmission over fiber are entirely hidden from the user. In general, a growing importance of AOCs for VCSEL-based optical links can be expected. More information on AOCs is provided in Chap. 16 of this book.

With respect to optical technologies at the intra-chip level, there is enormous activity in the silicon photonics community for several years. Still the goal is to overcome the electrical interconnection bottleneck that is on the horizon. It is difficult to see where a regular VCSEL would find a place here. Most scenarios envisage external (i.e., outside of the chip) continuous-wave emitting WDM light sources. Wavelengths should be at least 1.2 μm to avoid absorption in Si, and high optical power would probably be needed to compensate the propagation and splitting losses in the optical circuits.

Having mentioned long wavelengths just before, we may ask why we are still waiting for the real breakthrough of long-wavelength VCSELs on the market. As written in Chaps. 10 and 11 of this book, very good devices are commercially available. On the other hand, volumes are comparatively low. First of all, it is hard to beat the price of a Fabry–Pérot edge-emitting laser produced in a highly automated laser factory. Then, there has been a strong cost reduction for distributed feedback (DFB) laser diodes in recent years. At this point it needs to be mentioned that the most successful long-wavelength VCSEL structures to date, e.g., based on buried tunnel junctions or wafer fusion, are more difficult to fabricate than short-wavelength 850 or 980 nm devices. Yield is thus also an issue. Moreover, optical telecommunication specifications are very demanding. Finally, if all telecom specifications are met, lower power consumption might indeed become the winning argument for long-wavelength VCSELs. This is what VCSEL lovers are hoping for.

Gas sensing is a good market for long-wavelength VCSELs with much opportunity for growth. Here much higher prices are paid per device compared to optical interconnects. The wide adoption of VCSEL-based gas sensors will be strongly correlated with the cost of such units.

Talking about optical sensing, the VCSEL mouse is a great invention. Chapter 17 explains that, compared to previous generations of computer mice, it has better resolution, higher speed and acceleration, enhanced surface compatibility (i.e., works

on almost all surfaces), and also lower power consumption, which is important for cordless mice to improve battery lifetime. However, unfortunately, for regular office applications (in contrast to, e.g., computer-aided design work or advanced gaming), LED mice do a fine job. When you buy a computer and it comes with a mouse, it is most probably an LED mouse. Of course, if you have to purchase a mouse yourself, the VCSEL community expects you to honor the achievements of the pioneers in the field by *not* buying an LED mouse (even if you would save a dollar)—and not a mechanical mouse.

With regard to other consumer products, it remains to be seen if, e.g., VCSELs become part of mobile phones, which would be a huge market. Data transmission between display and processing unit, optical finger navigation,[3] or proximity sensing are among the opportunities.

In addition to position sensing in general, not only in computer mice (or, more general, computer input devices) but also in various kinds of encoders, VCSELs are likewise well suited for contactless distance and velocity measurements for a wide range of applications. This is described in Chap. 17 of this book. Much growth can be expected in this field.

With the advent of high-efficiency, high-power VCSELs, as described in Chap. 8 of this book, a whole new range of applications are now in within reach and should be exploited. Tailored illumination [65] is just one of them.

About 8 years ago there was much hope to bring 850 nm VCSELs into automotive systems. The use of these lasers (instead of red emitting LEDs) in combination with 200 μm core diameter polymer-clad silica (PCS) fibers in data buses was strongly promoted by the car manufacturer Daimler [66] (see also [22] for a bidirectional transmission solution using this medium). Suitable high-temperature-compatible VCSELs had been developed for that purpose. Nevertheless the next-generation data bus at 150 Mbit/s data rate was still LED-based [67]. Data rates in cars will continue to increase and the VCSEL will thus remain on the agenda—another arena for "copper versus optical". Apart from optical networks, potential high-volume opportunities for VCSELs in automotive systems are LIDAR (light detection and ranging) units as well as speed-over-ground and lane-keeping sensors. None of them, however, is close to market introduction.

Getting back to data storage from above, in fact the magnetic storage density has experienced tremendous growth over the last decades. However, the current approach is soon reaching its superparamagnetic limit where the magnetic state becomes thermally unstable. Heat-assisted magnetic recording (HAMR) is a future technique for hard disk drives proposed by Seagate with which the recording density can potentially be increased by two orders of magnitude [68, 69]. It relies on the effect that local heating above the Curie point lowers the resistance to magnetic polarization. In practice this requires a temperature increase by more than 300 K in about 1 ns for a spot size of, e.g., 25 nm. A possible approach is to use near-field

---

[3] Based on similar physical principles as the laser mouse, optical finger navigation in mobile phones is gaining acceptance and might find widespread use in electronic equipment like music players, digital cameras, or keyboards.

optics with surface plasmon resonance. Initial experiments have been carried out with 830 nm edge-emitting lasers at power levels of 80 mW and 35 μm incident spot size. If we would find a VCSEL-based solution, we had a new, gigantic market. Just imagine a VCSEL in every future magnetic writing head!

Other remarks about future opportunities for VCSELs in addition to "it's all about cost" are made by the authors of the individual chapters of this book. I would like to close this section by reminding the readers of the observation that the wisest prophets make sure of the event first.[4]

References

1. H. Soda, K. Iga, C. Kitahara, Y. Suematsu, GaInAsP/InP surface emitting injection lasers. Jpn. J. Appl. Phys. **18**, 2329–2330 (1979)
2. I. Melngailis, Longitudinal injection-plasma laser of InSb. Appl. Phys. Lett. **6**, 59–60 (1965)
3. T.E. Sale, *Vertical Cavity Surface Emitting Lasers* (Taunton Research Studies Press, Somerset, 1995)
4. T.P. Lee (ed.), *Current Trends in Vertical Cavity Surface Emitting Lasers* (World Scientific Publishing, Singapore, 1995)
5. C. Wilmsen, H. Temkin, L.A. Coldren (eds.), *Vertical-Cavity Surface-Emitting Lasers* (Cambridge University Press, Cambridge, 1999)
6. J. Cheng, N.K. Dutta (eds.), *Vertical-Cavity Surface-Emitting Lasers: Technology and Applications* (Gordon and Breach Publishing, Amsterdam, 2000)
7. S.F. Yu, *Analysis and Design of Vertical Cavity Surface Emitting Lasers* (Wiley, Hoboken, 2003)
8. H. Li, K. Iga (eds.), *Vertical-Cavity Surface-Emitting Laser Devices* (Springer, Berlin, 2003)
9. G.A. Evans, J.M. Hammer (eds.), *Surface Emitting Semiconductor Lasers and Arrays* (Academic Press, San Diego, 1993)
10. T.E. Sale, Vertical Cavity Surface Emitting Lasers. Ph.D. Thesis, University of Sheffield, 1993
11. J.L. Jewell, A. Scherer, S.L. McCall, Y.H. Lee, S. Walker, J.P. Harbison, L.T. Florez, Low-threshold electrically pumped vertical-cavity surface-emitting microlasers. Electron. Lett. **25**, 1123–1124 (1989)
12. S.W. Corzine, R.S. Geels, J.W. Scott , R.-H. Yan, L.A. Coldren, Design of Fabry-Perot surface-emitting lasers with a periodic gain structure. IEEE J. Quantum Electron. **25**, 1513–1524 (1989)
13. M.Y.A. Raja, S.R.J. Brueck, M. Osiński, C.F. Schaus, J.G. McInerney, T.M. Brennan, B.E. Hammons, Resonant periodic gain surface-emitting semiconductor lasers. IEEE J. Quantum Electron. **25**, 1500–1512 (1989)
14. O.G. Okhotnikov (ed.), *Semiconductor Disk Lasers* (Wiley-VCH, Weinheim, 2010)
15. D.L. Huffaker, D.G. Deppe, K. Kumar, T.J. Rogers, Native-oxide defined ring contact for low threshold vertical-cavity lasers. Appl. Phys. Lett. **65**, 97–99 (1994)
16. D. Kuksenkov, H. Temkin, Polarization related properties of vertical-cavity lasers, Chap. 6 in *Vertical-Cavity Surface-Emitting Lasers*, ed. by C. Wilmsen, H. Temkin, L.A. Coldren (Cambridge University Press, Cambridge, 1999), pp. 233–267
17. K. Iga, Surface-emitting laser—its birth and generation of new optoelectronics field. IEEE J. Select. Topics Quantum Electron. **6**, 1201–1215 (2000)
18. K. Iga, Vertical cavity surface emitting lasers photonics. Jpn. J. Appl. Phys. **45**, 6541–6543 (2006)

[4] This quote is attributed to Horace Walpole.

19. K. Iga, Vertical-cavity surface-emitting laser: its conception and evolution. Jpn. J. Appl. Phys. **47**, 1–10 (2008)
20. A. Larsson, Advances in VCSELs for communication and sensing. IEEE J. Select. Topics Quantum Electron. **17**, 1552–1567 (2011)
21. A. Mutig, D. Bimberg, Progress on high speed 980 nm VCSELs for short reach optical interconnects. Advances in Optical Technologies, Special Issue on *Recent Advances in Semiconductor Surface-Emitting Lasers*, Article ID 290508 (2011)
22. R. Michalzik, A. Kern, M. Stach, F. Rinaldi, D. Wahl, True bidirectional optical interconnects over multimode fiber, in *Optoelectronic Interconnects and Component Integration X*, ed. by A.L. Glebov, R.T. Chen, Proceedings of SPIE, vol. 7607 (2010), pp. 76070B-1–76070B-17
23. A. Kern, S. Paul, D. Wahl, R. Blood, W. Schwarz, R. Michalzik, Bidirectional multimode fiber interconnection at Gbit/s data rates with monolithically integrated VCSEL–PIN transceiver chips. IEEE Photon. Technol. Lett. **23**, 1058–1060 (2011)
24. A. Kern, S. Paul, D. Wahl, A. Al-Samaneh, R. Michalzik, Single-fiber bidirectional optical data links with monolithic transceiver chips. Advances in Optical Technologies, Special Issue on *Recent Advances in Semiconductor Surface-Emitting Lasers*, Article ID 729731 (2012)
25. K. Panajotov, M. Sciamanna, I. Gatare, M. Arteaga, H. Thienpont, Nonlinear dynamics of vertical-cavity surface-emitting lasers. Advances in Optical Technologies, Special Issue on *Recent Advances in Semiconductor Surface-Emitting Lasers*, Article ID 469627 (2011)
26. F. Koyama, Recent advances of VCSEL photonics. J. Lightwave Technol. **24**, 4502–4513 (2006)
27. A. Mereuta, G. Suruceanu, A. Caliman, V. Iacovlev, A. Sirbu, E. Kapon, 10-Gb/s and 10-km error-free transmission up to 100°C with 1.3-μm wavelength wafer-fused VCSELs. Opt. Exp. **17**, 12981–12986 (2009)
28. H. Hatakeyama, T. Anan, T. Akagawa, K. Fukatsu, N. Suzuki, K. Tokutome, M. Tsuji, Highly reliable high-speed 1.1-μm range VCSELs with InGaAs/GaAsP-MQWs. IEEE J. Quantum Electron. **46**, 890–897 (2010)
29. W. Hofmann, M. Müller, P. Wolf, A. Mutig, T. Gründl, G. Böhm, D. Bimberg, M.-C. Amann, 40 Gbit/s modulation of 1550 nm VCSEL. Electron. Lett. **47**, 270–271 (2011)
30. M. Arai, T. Kondo, A. Onumura, A. Matsutani, T. Miyamoto, F. Koyama, Multiple-wavelength GaInAs–GaAs vertical cavity surface emitting laser array with extended wavelength span. IEEE J. Select. Topics Quantum Electron. **9**, 1367–1373 (2003)
31. Y. Uchiyama, T. Kondo, K. Takeda, A. Matsutani, T. Uchida, T. Miyamoto, F. Koyama, 1.2 μm band GaInAs/GaAs high-density multiple-wavelength vertical cavity surface emitting laser array. Jpn. J. Appl. Phys. **44**, L214–L215 (2005)
32. A. Imamura, A. Matsutani, F. Koyama, Multi-wavelength 1060 nm-band VCSEL array with tapered hollow waveguide multiplexer, in *Proceedings of the 22nd IEEE International Semiconductor Laser Conference*, paper MB3, two pages, Kyoto, Japan, Sept. 2010
33. C. Gierl, T. Gruendl, P. Debernardi, K. Zogal, C. Grasse, H.A. Davani, G. Böhm, S. Jatta, F. Küppers, P. Meißner, M.-C. Amann, Surface micromachined tunable 1.55 μm VCSEL with 102 nm continuous single-mode tuning. Opt. Exp. **19**, 17336–17343 (2011)
34. H. Sano, A. Matsutani, F. Koyama, Athermal and tunable operations of 850 nm VCSEL with thermally actuated cantilever structure, in *Proceedings of the 35th European Conference on Optical Communication, ECOC 2009*, paper P2.26, two pages. Vienna, Austria, Sept. 2009
35. H. Sano, A. Matsutani, F. Koyama, A thermal 850 nm vertical cavity surface emitting lasers with thermally actuated cantilever structure. Appl. Phys. Exp. **2**, 072101-1–072101-3 (2009)
36. K. Johnson, M. Hibbs-Brenner, W. Hogan, M. Dummer, Advances in red VCSEL technology. Advances in Optical Technologies, Special Issue on *Recent Advances in Semiconductor Surface-Emitting Lasers*, Article ID 569379 (2012)
37. F. Hopfer, A. Mutig, G. Fiol, M. Kuntz, V.A. Shchukin, V.A. Haisler, T. Warming, E. Stock, S.S. Mikhrin, I.L. Krestnikov, D.A. Livshits, A.R. Kovsh, C. Bornholdt, A. Lenz, H. Eisele, M. Dähne, N.N. Ledentsov, D. Bimberg, 20 Gb/s 85°C error-free operation of VCSELs based

on submonolayer deposition of quantum dots. IEEE J. Select. Topics Quantum Electron. **13**, 1302–1308 (2007)
38. N.N. Ledentsov, F. Hopfer, D. Bimberg, High-speed quantum-dot vertical-cavity surface-emitting lasers. Proc. IEEE **95**, 1741–1756 (2007)
39. K.D. Choquette, D.F. Siriani, A.M. Kasten, M.P. Tan, J.D. Sulkin, P.O. Leisher, J.J. Raftery Jr., A.J. Danner, Single mode photonic crystal vertical cavity surface emitting lasers. Advances in Optical Technologies, Special Issue on *Recent Advances in Semiconductor Surface-Emitting Lasers*, Article ID 280920 (2012)
40. D.F. Siriani, K.D. Choquette, In-phase, coherent photonic crystal vertical-cavity surface-emitting laser arrays with low divergence. Electron. Lett. **46**, 712–714 (2010)
41. R. Sarzala, T. Czyszanowski, M. Wasiak, M. Dems, L. Piskorski, W. Nakwaski, K. Panajotov, Numerical self-consistent analysis of VCSELs. Advances in Optical Technologies, Special Issue on *Recent Advances in Semiconductor Surface-Emitting Lasers*, Article ID 689519 (2012)
42. V. Bardinal, T. Camps, B. Reig, D. Barat, E. Daran, J.B. Doucet, Collective micro-optics technologies for VCSEL photonic integration. Advances in Optical Technologies, Special Issue on *Recent Advances in Semiconductor Surface-Emitting Lasers*, Article ID 609643 (2011)
43. A. Mooradian, A. Shchegrov, A. Tandon, G. Yoffe, External-cavity surface-emitting diode lasers, Chap. 7 in *Semiconductor Disk Lasers*, ed. by O.G. Okhotnikov (Wiley-VCH, Weinbeim, 2010), pp. 263–304
44. J.G. McInerney, A. Mooradian, Optimizing electrically pumped vertical extended cavity surface emitting semiconductor lasers (E-VECSELs), in *Vertical External Cavity Surface Emitting Lasers (VECSELs)*, ed. by U. Keller, Proceedings of SPIE, vol. 7919 (2011), pp. 79190L-1–79190L-15
45. I. Kardosh, F. Demaria, F. Rinaldi, M.C. Riedl, R. Michalzik, Electrically pumped frequency-doubled surface emitting lasers operating at 485 nm emission wavelength. Electron. Lett. **44**, 524–525 (2008)
46. I. Kardosh, F. Demaria, F. Rinaldi, S. Menzel, R. Michalzik, High-power single transverse mode vertical-cavity surface-emitting lasers with monolithically integrated curved dielectric mirrors. IEEE Photon. Technol. Lett. **20**, 2084–2086 (2008)
47. D.K. Serkland, K.M. Geib, G.A. Keeler, G.M. Peake, Fully micro-fabricated VECSEL at 850 nm, in *Vertical-Cavity Surface-Emitting Lasers XV*, ed. by J.K. Guenter, C. Lei, Proceedings of SPIE, vol. 7952 (2011), pp. 79520L-1–79520L-8
48. W. Schwarz, A.J. Márquez del Pino, D. Rimpf, F. Rinaldi, T. Mappes, R. Michalzik, Hybrid-integrated optofluidic microparticle sensor using a vertical-extended-cavity surface-emitting laser, in *Proceedings of the 4th EOS Topical Meeting on Optical Microsystems* ($O\mu S$'11), paper 4550, two pages, Capri, Italy, Sept. 2011
49. Y. Onishi, N. Nishiyama, C. Caneau, F. Koyama, C.-E. Zah, Dynamic behavior of an all-optical inverter using transverse-mode switching in 1.55-μm vertical-cavity surface-emitting lasers. IEEE Photon. Technol. Lett. **16**, 1236–1238 (2004)
50. K. Hasebe, F. Koyama, N. Nishiyama, C. Caneau, C.-E. Zah, All-optical polarization controller using elliptical-apertured 1.5 μm VCSEL, in *Proceedings of the Conference on Lasers and Electro-Optics 2006*, *CLEO 2006*, paper CWP1, two pages, Long Beach, CA, May 2006
51. S. Suda, F. Koyama, N. Nishiyama, C. Caneau, C.-E. Zah, Optical nonlinear phase shifter using vertical micro-cavity with saturable absorber, in *Proceedings of the Conference on Lasers and Electro-Optics 2006*, *CLEO 2006*, paper CWK3, two pages, Long Beach, CA, May 2006
52. S. Suda, F. Koyama, N. Nishiyama, C. Caneau, C.-E. Zah, High speed response of nonlinear optical phase-shifter based on vertical micro-cavity saturable absorber. IEICE Electron. Exp. **5**, 131–135 (2008)
53. S. Barbay, R. Kuszelewicz, J. Tredicce, Cavity solitons in VCSEL devices. Advances in Optical Technologies, Special Issue on *Recent Advances in Semiconductor Surface-Emitting Lasers*, Article ID 628761 (2011)

54. G. Hirano, F. Koyama, K. Hasebe, T. Sakaguchi, N. Nishiyama, C. Caneau, C.-E. Zah, Slow light modulator with Bragg reflector waveguide, in *Proceedings of the Optical Fiber Communication Conf. (OFC)*, paper PDP34, Anaheim, CA, Mar. 2007
55. J. Hashizume, F. Koyama, Plasmon enhanced optical near-field probing of metal nanoaperture surface emitting laser. Opt. Exp. **12**, 6391–6396 (2004)
56. Z. Rao, L. Hesselink, J.S. Harris, High-intensity bowtie-shaped nano-aperture vertical-cavity surface-emitting laser for near-field optics. Opt. Lett. **32**, 1995–1997 (2007)
57. M. Hill, M. Marell, Surface emitting metal nano cavity lasers. Advances in Optical Technologies, Special Issue on *Recent Advances in Semiconductor Surface-Emitting Lasers*, Article ID 314952 (2011)
58. N.C. Gerhardt, M.R. Hofmann, Spin controlled vertical-cavity surface-emitting lasers. Advances in Optical Technologies, Special Issue on *Recent Advances in Semiconductor Surface-Emitting Lasers*, Article ID 268949 (2012)
59. R. Michalzik, A. Kroner, A. Bergmann, F. Rinaldi, VCSEL-based optical trapping for microparticle manipulation, in *Vertical-Cavity Surface-Emitting Lasers XIII*, ed. by K.D. Choquette, C. Lei, Proceedings of SPIE, vol. 7229 (2009), pp. 722908-1–722908-13
60. Y.H. Lee, Y.G. Ju, I.Y. Han, 780-nm VCSELs for CD applications, in *Proceedings of the IEEE Lasers and Electro-Optics Society Annual Meeting, LEOS '98*, vol. 1, Orlando, FL, Dec. 1998, p. 214
61. S. Morgott, S. Groetsch, W. Schnabel, D. Wiener, LED light sources for mobile embedded projection, in *Optics, Photonics, and Digital Technologies for Multimedia Applications*, ed. by P. Schelkens, T. Ebrahimi, G. Cristóbal, F. Truchetet, P. Saarikko, Proceedings of SPIE, vol. 7723 (2010) pp. 77230W-1–77230W-9
62. R. Michalzik, Optical backplanes, board and chip interconnects, Chap. 6 in *Fiber Optic Data Communication: Technological Trends and Advances*, ed. by C. DeCusatis (Academic Press, San Diego, 2002), pp. 216–269
63. R. Michalzik, Optical backplanes, board and chip interconnects, Chap. 26 in *Handbook of Fiber Optic Data Communication: A Practical Guide to Optical Networking*, ed. by C. DeCusatis, 3rd edn. (Elsevier, San Diego, 2008), pp. 657–676
64. R. Dangel, R. Beyeler, N. Meier, T. Lamprecht, F. Horst, D. Jubin, J. Weiss, B.J. Offrein, Optical interconnects for board level applications, in *Optoelectronic Integrated Circuits XI*, ed. by L.A. Eldada, E.-H. Lee, Proceedings of SPIE, vol. 7219 (2009), pp. 721904-1–721904-7
65. H. Moench, S. Gronenborn, M. Miller, P. Loosen, High power VCSEL systems for tailored intensity distributions, in *Vertical-Cavity Surface-Emitting Lasers XV*, ed. by J.K. Guenter, C. Lei, Proceedings of SPIE, vol. 7952 (2011), pp. 795207-1–795207-11
66. T. Kibler, S. Poferl, G. Böck, H.-P. Huber, E. Zeeb, Optical data buses for automotive applications. J. Lightwave Technol. **22**, 2184–2199 (2004)
67. MOST Cooperation provides new physical layer specification, MOST Cooperation, press release, March 10, 2008. See also MOST Informative, Issue 2, March 2008. Both available at http://www.mostcooperation.com/
68. L. Pan, D.B. Bogy, Data storage: heat-assisted magnetic recording. Nat. Photon. **3**, 189–190 (2009)
69. W.A. Challener, C. Peng, A.V. Itagi, D. Karns, W. Peng, Y. Peng, X. Yang, X. Zhu, N.J. Gokemeijer, Y.-T. Hsia, G. Ju, R.E. Rottmayer, M.A. Seigler, E.C. Gage, Heat-assisted magnetic recording by a near-field transducer with efficient optical energy transfer. Nat. Photon. **3**, 220–224 (2009)

Chapter 2
VCSEL Fundamentals

Rainer Michalzik

Abstract In this chapter we outline major principles of vertical-cavity surface-emitting laser (VCSEL) design and operation. Basic device properties and generally applicable cavity design rules are introduced. Characteristic parameters like threshold gain and current, differential quantum efficiency and power conversion efficiency, as well as thermal resistance are discussed. We describe the design of Bragg reflectors and explain the transfer matrix method as a convenient tool to compute VCSEL resonator properties in a one-dimensional approximation. Experimental results illustrate the emission characteristics of high-efficiency VCSELs that apply selective oxidation for current and photon confinement. Both the 850 and 980 nm wavelength regions are considered. The basic treatment of laser dynamics and noise behavior is presented in terms of the small-signal modulation response as well as the relative intensity noise. Finally we give some examples of VCSEL applications in fiber-based optical interconnects, i.e., optical data transmission over short distances.

2.1 Introduction

VCSELs have undergone an extraordinary evolution over the past three decades. Suggested by Prof. Kenichi Iga and first demonstrated by the research group at Tokyo Institute of Technology in the late 1970s [1–3], VCSELs are a commodity item today [4] and already serve millions of computer users as the key component in modern navigation devices such as the optical mouse. In even larger quantity, this laser type has entirely replaced edge-emitting laser diodes for use in multimode fiber-based Gbit/s speed optical data transmission in premises networks and for the interconnection of various kinds of computer clusters. Several books entirely devoted

R. Michalzik (✉)
Institute of Optoelectronics, Ulm University,
Albert-Einstein-Allee 45, 89081 Ulm, Germany
e-mail: rainer.michalzik@uni-ulm.de

R. Michalzik (ed.), *VCSELs*, Springer Series in Optical Sciences 166,
DOI: 10.1007/978-3-642-24986-0_2, © Springer-Verlag Berlin Heidelberg 2013

to VCSELs have been published meanwhile [5–9]. Early VCSELs were based on the technologically challenging InGaAsP–InP material system [10]. A major breakthrough occurred in the late 1980s with the demonstration of the first continuous-wave operating GaAs-based VCSEL using metal and dielectric mirrors [11, 12]. Full-monolithic InGaAs–GaAs lasers incorporating epitaxial distributed Bragg reflectors with emission wavelengths of about 960 nm and pulsed threshold currents of 1.3 mA were demonstrated in 1989 [13]. VCSELs were first commercially offered by Honeywell in 1996. As a result of standardization, these first-generation lasers were made from GaAs–AlGaAs mixed compound semiconductors for emission close to 850 nm and relied on proton implantation [14, 15] for current confinement. During the years to follow, in particular 1999–2002, many companies were founded, aiming to capitalize on the enormous projected growth in the optical datacom and telecom markets. Reality showed that those projections contained gross overestimation and several companies had to go out of business. Fortunately, the market recovered a few years later [16]. The 850 nm spectral region has remained dominant until today, including optical mouse applications. The production volume nowadays is about 100 million lasers per year.

The success of the VCSEL arises from a combination of unique properties. With a main emphasis on optical data transmission, the most important are

- low threshold currents of smaller than 1 mA and correspondingly small driving currents for required optical output powers in the milliwatt range, thus minimizing power consumption and making the design of electronic driver circuits more easy,
- excellent digital modulation behavior for data rates nowadays approaching 40 Gbit/s,
- high power conversion efficiencies of larger than 50% and thus low power dissipation,
- circular beam profiles with small divergence angles, simplifying the design of beam-shaping optics,
- a wide ambient temperature range exceeding $+125°\mathrm{C}$ that enables uncooled operation even in automobiles,
- the straightforward formation of homogeneous one- and two-dimensional laser arrays as the key to compact space division multiplexed data transmission,
- complete testing and device selection on the wafer level, yielding enormous cost reduction compared to edge-emitting laser diodes,
- the use of mounting and packaging technology well known from light-emitting diode (LED) production, and finally
- very high reliability with projected lifetimes of the order of ten million hours at room temperature.

Moreover, for optical sensing, VCSELs can be designed to feature single-mode emission with a linearly polarized quasi-Gaussian transverse mode pattern as well as wide and continuous wavelength tuning.

This chapter is intended to provide the reader with the basic knowledge necessary to understand VCSEL benefits and limitations and at the same time give examples of performance data obtained experimentally. We start with basic studies of the laser

cavity, such as amplification in the active region and laser mirror properties, where essential differences to edge-emitting laser operation are underlined. A better insight into field distributions and energy flux in the VCSEL cavity is then obtained from numerical calculations with the transfer matrix method. Power conversion efficiency is of particular interest and briefly treated separately. Focusing on the most successful kind of high-performance VCSEL manufacturing, we then deal with the emission characteristics of oxide-confined devices, including the temperature behavior. An intuitive understanding of transverse mode guiding effects is provided. In order to treat dynamic and noise properties, we briefly write down the laser rate equations to obtain the small-signal modulation response as well as relative intensity noise spectra. A concise subsection is devoted to the emission linewidth, basically determined by random spontaneous emission processes. Especially with respect to noise phenomena, advantages of single-mode compared to multi-transverse-mode emission become apparent. As an important application area of VCSELs, fiber-based optical interconnects are finally discussed, where the emphasis is put on fiber coupling properties, large-signal modulation effects, and high-speed optical data transmission over various types of fiber.

2.2 VCSEL Design and Operation Parameters

In this section we will discuss basic VCSEL properties, the design of Bragg reflectors used as laser mirrors, and device parameters such as threshold gain, photon lifetime, threshold current, differential quantum efficiency, and power conversion efficiency. To illustrate reflectivity spectra, standing-wave patterns, and the energy flow in the resonator, the transfer matrix method serves as a versatile tool.

2.2.1 VCSEL Types and General Properties

Figure 2.1 illustrates the typical layout of a VCSEL. The inner cavity containing the amplifying layers is surrounded by electrically conductive layer stacks that form the laser mirrors which provide optical feedback. VCSELs designed for emission wavelengths in the 850–980 nm spectral range require about 8 μm of epitaxially grown material, whereas the active region is composed of just a few quantum wells (QWs) with some 10 nm thickness. Metal-organic chemical vapor deposition (MOCVD) or molecular beam epitaxy (MBE) are preferred for crystal growth. The PIN-type doping configuration is similar to conventional edge-emitting laser diodes (EELs). In the most simple device layouts, electric current is injected from ohmic contacts on the top epitaxial side and the back side of the substrate, where the bottom contact is omitted in Fig. 2.1. A p-on-n doping sequence is preferred to n-on-p owing to usually lower defect densities of n-type substrates (which is beneficial for the device yield on a given wafer and for laser reliability) and reduced absorption loss of n-type mirrors

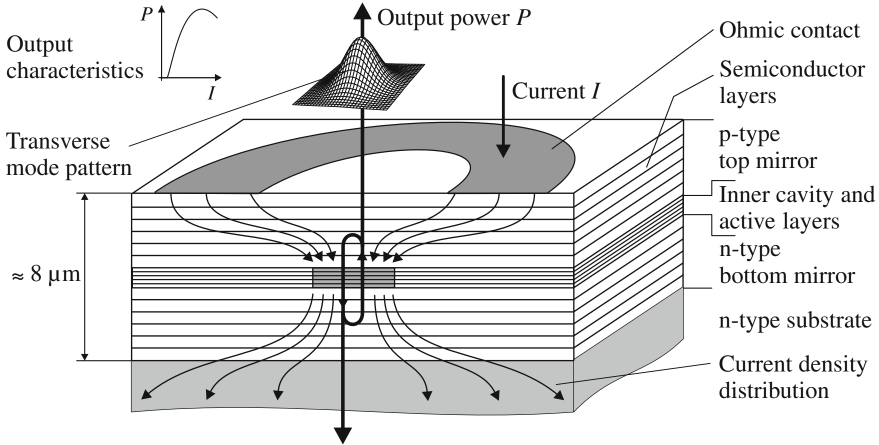

Fig. 2.1 Schematic layer structure and operating principle of a VCSEL

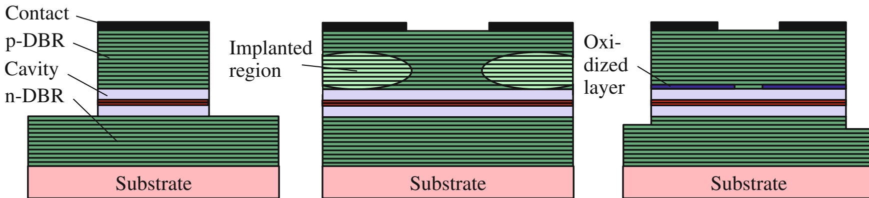

Fig. 2.2 Major approaches to current confinement in VCSELs. Air-post or mesa-etched (*left*), proton-implanted (*center*), and oxide-confined VCSEL (*right*)

(see footnote on free-carrier loss on p. 37). In the figure, the current is somewhat miraculously confined to the center of the inner cavity. As shown in Fig. 2.2, several methods have been successfully employed to achieve current confinement to a predefined active area. Among those are simple mesa etching of the top mirror [13, 17] (often called air-post VCSELs), ion implantation (predominantly using protons) to create highly resistive semiconductor regions [14, 15], or selective lateral oxidation [18] of a some 10 nm thick semiconductor layer with high aluminum content like $Al_{0.98}Ga_{0.02}As$ or even AlAs. Mesa etching incurs scattering losses of the optical field and may cause reliability problems if the active region is exposed to air. Proton implantation has been the first method employed to fabricate commercial VCSELs of outstanding producibility and reliability [19, 20]. On the other hand, selective oxidation introduces less optical losses in the cavity and has led to a leap of VCSEL performance [21–24].[1] The vast majority of commercial VCSELs nowadays relies on oxide confinement. These lasers will be in the focus of this chapter; their fabrication principles being explained in Sect. 2.3.

[1] The high wallplug efficiency result in [24] was first presented in [25].

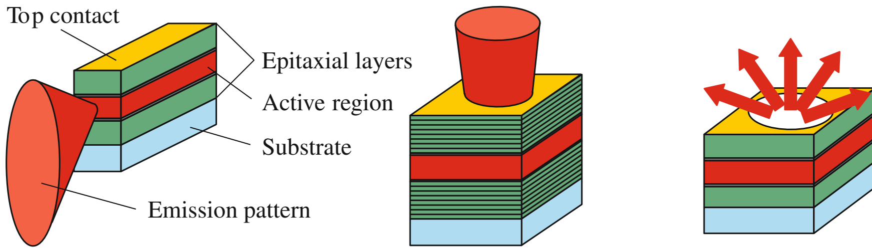

Fig. 2.3 EEL (*left*), VCSEL (*center*), and LED (*right*) schemes

Table 2.1 Advantages of VCSELs compared to EELs (left) and communication-type LEDs (right)

VCSELs vs. EELs	VCSELs vs. LEDs
Low threshold current	High modulation bandwidth
High efficiency at low power	Focused output beam
Slowly divergent circular beam	Narrow spectrum
Wafer-level testing, low cost	Small operating current
Simplified mounting and packaging	High output power
Two-dimensional arrays	High power conversion efficiency

The active diameter of the VCSEL can be reduced to just a few micrometers in order to obtain single transverse mode operation together with lowest threshold currents in the sub-100 μA range [26], but can also exceed 100 μm to get high output powers beyond 100 mW [27–29]. Chapter 8 of this book is entirely devoted to high-power VCSELs and arrays. As a rule of thumb, planar, selectively oxidized VCSELs without (internally [30, 31] or externally [32–34]) extended cavity emit in a single transverse mode with approximately Gaussian shape, as indicated in Fig. 2.1, up to active diameters of about 4 μm. Chapter 4 of this book deals with different approaches to such single-mode VCSELs. Larger devices start lasing on several higher (radial and azimuthal) order modes right above or even at threshold. The light versus current curve has a constant slope above threshold, as is common for laser diodes, but shows a characteristic rollover for higher currents due to internal heating (see sketch in Fig. 2.1). Unlike for EELs it is uncritical to operate VCSELs up to their maximum output powers since power densities remain in the lower kW/cm^2 range and cannot induce optical damage to the semiconductor material or the laser facet. Of course, device reliability is lower at higher operating temperatures [35]. Depending on the wavelength and material composition, VCSELs can be designed for top emission through a ring contact or bottom emission through a transparent substrate (as in Fig. 2.1). In case of a GaAs substrate, bottom emission with low absorption loss is possible for wavelengths exceeding ≈ 920 nm.

VCSELs are schematically contrasted to conventional edge-emitting lasers and communication-type light-emitting diodes [36] in Fig. 2.3 and their advantages are summarized in Table 2.1.

2.2.2 Bragg Reflectors

The VCSEL mirrors in Fig. 2.1 are realized as distributed Bragg reflectors (DBRs) which consist of an alternating sequence of high and low refractive index layers with thicknesses of one quarter of the material wavelength. If these conditions are met, the partial reflections at each interface add constructively, and the peak reflectivity of the mirror continuously increases by adding more Bragg pairs. Because of the short amplification length in a VCSEL, the average reflectivity must exceed $\approx 97\%$, and typically more than 20 semiconductor layer pairs are required for each mirror. Electric field distributions and reflectivity spectra are suitably calculated by the transfer matrix method described in Sect. 2.2.6. Properties of Bragg reflectors are treated in more detail in [37, 38]. Here we will restrict ourselves to some basic analytical discussions applied to AlGaAs-based semiconducting mirrors. In several special VCSEL designs, mainly for long-wavelength emission, also dielectric DBRs together with intra-cavity contacts are used (see, e.g., [39] and Chaps. 10 and 11 of this book).

In an EEL with a Fabry–Pérot resonator, the mirrors are most simply formed by cleaving the crystal along natural cleaving planes [40]. Each discrete mirror thus consists of a high-to-low refractive index step, as seen from the resonator. In analogy, the first layer of the top or bottom mirror in Fig. 2.1, as seen from the inner cavity, has to have a lower refractive index than the neighboring carrier confinement layer.[2] The requirement of an alternating index sequence then leads to an integer number of Bragg pairs for the top mirror of an AlGaAs-based VCSEL, whereas a single low-index quarter-wave layer adjacent to the high-index GaAs substrate has to be added to the bottom mirror. Here we assume that the top mirror is terminated by a low-index material such as air.

Referring to index sequences $\bar{n}_\mathrm{c}|(\bar{n}_1|\bar{n}_2)^{M_\mathrm{Bt}}|\bar{n}_\mathrm{s}$ or $\bar{n}_\mathrm{c}|(\bar{n}_1|\bar{n}_2)^{M_\mathrm{Bb}}|\bar{n}_1|\bar{n}_\mathrm{s}$ for the Bragg reflectors and assuming a wave that is incident from a cladding material with refractive index $\bar{n}_\mathrm{c}$ and is transmitted into a substrate of index $\bar{n}_\mathrm{s}$, the peak reflectivity of a top or bottom mirror with M_Bt or M_Bb layer pairs is found at the Bragg wavelength λ_B and is written as [41]

$$R_\mathrm{t,b} = \left(\frac{1 - b_\mathrm{t,b}}{1 + b_\mathrm{t,b}}\right)^2 \tag{2.1}$$

with

$$b_\mathrm{t} = \frac{\bar{n}_\mathrm{s}}{\bar{n}_\mathrm{c}} \left(\frac{\bar{n}_1}{\bar{n}_2}\right)^{2M_\mathrm{Bt}} \quad \text{and} \quad b_\mathrm{b} = \frac{\bar{n}_1^2}{\bar{n}_\mathrm{c}\bar{n}_\mathrm{s}} \left(\frac{\bar{n}_1}{\bar{n}_2}\right)^{2M_\mathrm{Bb}}, \tag{2.2}$$

where $\bar{n}_1 < \bar{n}_2$. Layer thicknesses $d_{1,2}$ have to be chosen as $d_{1,2} = \lambda_\mathrm{B}/(4\bar{n}_{1,2})$. It should be pointed out that for each mirror, the quantities $\bar{n}_1$, $\bar{n}_2$, $\bar{n}_\mathrm{c}$, and $\bar{n}_\mathrm{s}$ have to be identified separately. For instance, in most cases the "substrate" (i.e., the terminating layer) of the top mirror is air.

---

[2] This will become clearer from Fig. 2.7 presented later.

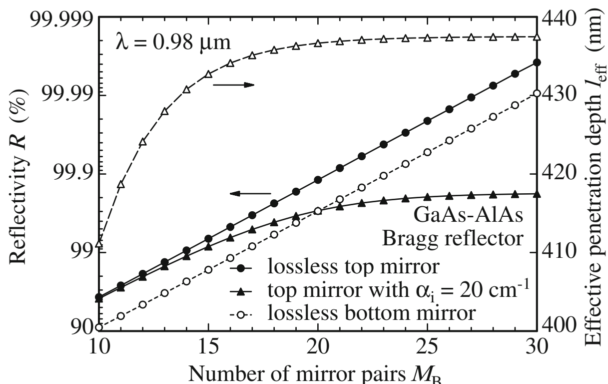

Fig. 2.4 Peak reflectivities of 980 nm GaAs–AlAs Bragg reflectors versus the number of mirror pairs. Data for the absorptive top mirror are calculated analytically from (2.15). The right-hand ordinate shows the effective penetration depth according to (2.4) which is very similar for all three reflectors

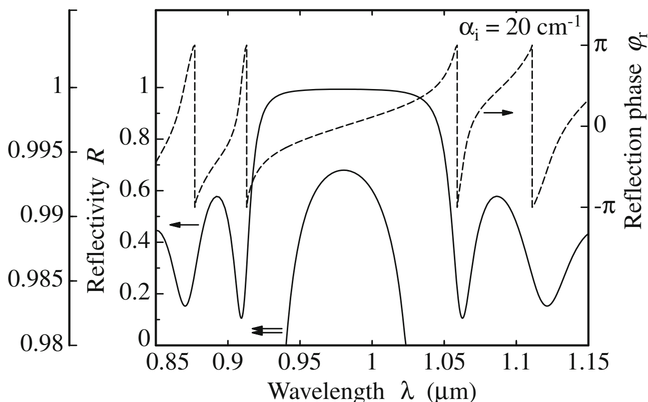

Fig. 2.5 Spectral dependence of the intensity reflection coefficient R and the phase φ_r of the amplitude reflection coefficient for the lossy top Bragg mirror from Fig. 2.4 with $M_{Bt} = 16$. The outer left-hand ordinate presents details in the center of the stop-band, revealing substantial curvature of $R(\lambda)$

Figure 2.4 shows top and bottom GaAs–AlAs Bragg mirror reflectivities as a function of the number of layer pairs calculated according to (2.1) and (2.2). Waves are incident from $Al_{0.3}Ga_{0.7}As$ and are transmitted to air or GaAs in case of the top or bottom mirror, respectively, the latter having an additional AlAs quarter-wave layer. It can be seen that in case of a lossless top mirror, peak reflectivities exceeding 99.9% are to be expected for more than 21 mirror pairs. Lower reflectivities of the bottom mirror arise from the smaller index contrast at the output interface.

Figure 2.5 displays the numerically determined spectral reflectivity $R(\lambda)$ and phase $\varphi_r(\lambda)$ for a top Bragg mirror from Fig. 2.4. A broad spectral plateau of high

reflectivity, often denoted as stop-band, appears around the Bragg wavelength λ_B, the width of which can be roughly estimated from [40, 42]

$$\Delta\lambda_{stop} \approx \frac{2\lambda_B \Delta\bar{n}_B}{\pi \langle \bar{n}_{gr} \rangle}. \tag{2.3}$$

The stop-band width is proportional to the refractive index step $\Delta\bar{n}_B = |\bar{n}_1 - \bar{n}_2|$, yielding $\Delta\lambda_{stop} \approx 100\,\text{nm}$ for the GaAs–AlAs composition from Fig. 2.4 with $\Delta\bar{n}_B = 0.56$ [43] and $\langle \bar{n}_{gr} \rangle \approx 3.6$ for the spatial average of the group index $\bar{n}_{gr} = \bar{n} - \lambda \mathrm{d}\bar{n}/\mathrm{d}\lambda$ at $\lambda_B = 980\,\text{nm}$. It has to be noted that only lossless mirrors or those with homogeneous absorption provide identical reflectivity spectra for waves being incident from the top or bottom side.

For incidence from a high-index material, the phase φ_r of the complex amplitude reflection coefficient $r = \sqrt{R}\exp\{i\varphi_r\}$ is zero at the Bragg wavelength, as to be expected for a high-to-low refractive index step. By writing $\varphi_r = -2\beta l_{eff}$ with a propagation constant β, we assume that the reflection effectively originates from a hard mirror with identical peak reflectivity placed at a distance l_{eff}. Since the phase in Fig. 2.5 varies almost linearly with wavelength deviation from λ_B (or inverse wavelength deviation corresponding to the phase coefficient β), such a model actually makes sense. The new parameter l_{eff} has the meaning of an effective mirror length, considering the phase penetration depth of the incident wave into the Bragg reflector. From the phase change, the penetration depth is obtained as

$$l_{eff} = -\frac{1}{2}\frac{\mathrm{d}\varphi_r}{\mathrm{d}\beta} = \frac{\lambda^2}{4\pi \langle \bar{n}_{gr} \rangle}\frac{\mathrm{d}\varphi_r}{\mathrm{d}\lambda} \approx \frac{\tanh(\kappa L_B)}{2\kappa} \tag{2.4}$$

$$= \frac{\sqrt{R}}{2\kappa} = \frac{\sqrt{R}\lambda_B}{4\Delta\bar{n}_B} \approx \frac{\lambda_B}{4\Delta\bar{n}_B}, \tag{2.5}$$

where coupled-mode theory [40] is applied to obtain the first approximation, which can be further simplified to the last result in case of high reflectivities $\sqrt{R} \approx 1$. The coupling length (i.e., the physical length over which the coupling takes place) equals $L_B = M_B(d_1 + d_2)$, and the coupling coefficient is $\kappa = 2\Delta\bar{n}_B/\lambda_B$ for a simple quarter-wave stack. The slow variation of l_{eff} with the number of mirror pairs M_B according to (2.4) is plotted in Fig. 2.4, leading to $l_{eff} \approx 0.44\,\mu\text{m}$ for the binary mirror under consideration. It should be noted that a more rigorous treatment of Bragg mirror properties distinguishes between phase and energy penetration depths [44], which, however, turn out to be very similar for usual semiconductor mirrors with small index steps. With the length L of the inner VCSEL cavity (i.e., the distance between the Bragg mirrors), the total effective cavity length is finally determined as

$$L_{eff} = L + l_{eff,t} + l_{eff,b} \tag{2.6}$$

and can be used to estimate the longitudinal mode spacing as

$$\Delta\lambda_l \approx \frac{\lambda^2}{2L_{eff}\langle \bar{n}_{gr} \rangle}, \tag{2.7}$$

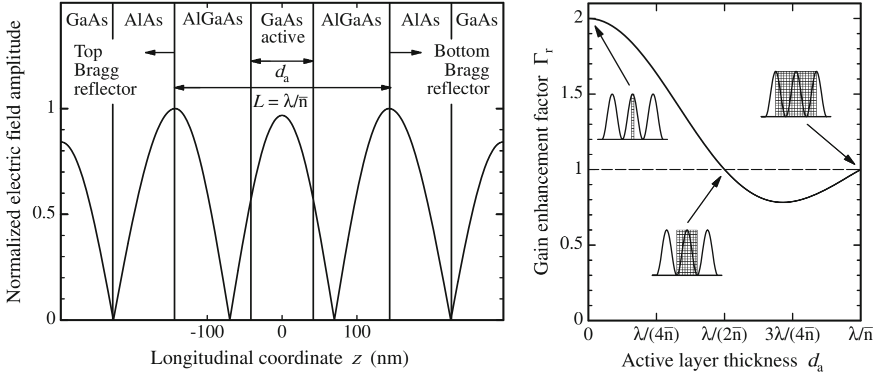

Fig. 2.6 Spatial distribution of the normalized electric field amplitude in the center region of a simplified VCSEL with active layer thickness d_a (*left*). Dependence of the relative confinement factor Γ_r on the active layer thickness (*right*). The three insets show exemplary overlaps of intensity profile and gain region

which is obtained from (2.8) for $L \rightarrow L_{\rm eff}$. In the next section, we will learn that the inner VCSEL cavity is mostly one material wavelength thick. With $L_{\rm eff} \approx 1.3\,\mu$m we then get $\Delta\lambda_l \approx 110$ nm. Thus the neighboring longitudinal modes are positioned outside both the mirror stop-band and the spectral gain bandwidth [40, 45] of the QW material. Therefore just a single longitudinal mode can oscillate in a VCSEL with a thin inner cavity. The spectral position of this mode can readily be theoretically or experimentally determined by localizing the sharp dip appearing in the reflectivity spectrum of the complete layer stack, as shown in more detail in Fig. 2.9. Note, however, that depending on the lateral size of the VCSEL several transverse modes may oscillate simultaneously (so-called multimode VCSELs), as discussed later.

2.2.3 Relative Confinement Factor

Figure 2.6 shows the layer structure and the standing-wave pattern of the electric field in the inner part of a simplified VCSEL cavity realized in the AlGaAs material system. The field is calculated with the transfer matrix method described in Sect. 2.2.6. Analogously to a simple Fabry–Pérot-type EEL with its mirrors composed of abrupt semiconductor–air interfaces, maxima of the electric field amplitude are found at both ends of the inner cavity of length L. With a positive integer m and the spatially averaged refractive index $\langle\bar{n}\rangle$, the resonance condition for the emission wavelength λ is then simply written as

$$\langle\bar{n}\rangle L = m\lambda/2. \tag{2.8}$$

The active layers have to be placed in an antinode of the standing-wave pattern in order to provide good coupling between electrons and photons.[3] For $m = 1$,there would be a field null in the cavity center so that the active layers were to be placed asymmetrically at an edge of the inner cavity or be split into two groups approximately separated by $\lambda/(2\langle\bar{n}\rangle)$. Both variants are likely to incur lower carrier injection efficiencies. Thus the shortest cavity with centered active layers is just one wavelength thick, equivalent to $m = 2$.

An important difference between a VCSEL cavity and a conventional EEL cavity arises from the fact that the active gain region does not extend over the full cavity length L but is enclosed by larger bandgap layers to form a double-heterostructure. Therefore, for an arbitrary position and total thickness d_a of the active layers, we have to take the overlap with the standing-wave pattern $E(z)$ into account in order to obtain the average gain in the cavity [46]. We define the relative confinement factor or gain enhancement factor by

$$\Gamma_r = \frac{L}{d_a} \frac{\int_{d_a} |E(z)|^2 dz}{\int_L |E(z)|^2 dz}, \tag{2.9}$$

which is the average intensity in the active layers normalized to that in the inner cavity. For all further considerations, the material gain coefficient g of the QWs has to be modified to $\Gamma_r g$. The electric field profile in the central $\lambda/(2\langle\bar{n}\rangle)$ part of the cavity in Fig. 2.6 (left) is very well approximated by

$$E(z) = E_0 \cos(2\pi \langle\bar{n}\rangle z/\lambda) \tag{2.10}$$

if $z = 0$ is centered in the inner cavity, resulting in

$$\Gamma_r = 1 + \frac{\sin(2\pi \langle\bar{n}\rangle d_a/\lambda)}{2\pi \langle\bar{n}\rangle d_a/\lambda} \tag{2.11}$$

for a single gain segment. The gain enhancement factor of a perfectly aligned active layer is thus expressed as a raised-sinc function, as illustrated in Fig. 2.6 (right). For a thin QW we have $\Gamma_r \to 2$. For $d_a = m\lambda/(2\langle\bar{n}\rangle)$ we obtain $\Gamma_r = 1$. Thus, in EELs Γ_r does not have to be taken into account. In the general case of M_a active sections (usually multiple QWs) with equal gain, located at positions $z_{i1} \le z \le z_{i2}$ with $i = 1, \ldots, M_a$ we find

$$\Gamma_r = 1 + \frac{\lambda}{4\pi \langle\bar{n}\rangle} \frac{\sum_{i=1}^{M_a} \sin(4\pi \langle\bar{n}\rangle z_{i2}/\lambda) - \sin(4\pi \langle\bar{n}\rangle z_{i1}/\lambda)}{\sum_{i=1}^{M_a} z_{i2} - z_{i1}}, \tag{2.12}$$

where $z = 0$ is located as before. For the more detailed VCSEL structure from Fig. 2.7 with three centered 8 nm thick QWs separated by 10 nm barriers we get $\Gamma_r = 1.8$. By exploiting the standing-wave effect, one can therefore almost double the available amount of optical amplification.

[3] In the rate equations, the amount of stimulated emission is determined by the product of optical gain coefficient and photon density, the latter being proportional to the intensity of the electromagnetic field; see (2.59), (2.60).

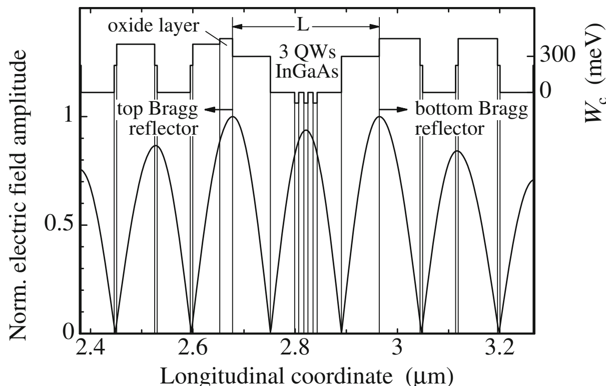

Fig. 2.7 Normalized electric field amplitude in the center region of a quantum well VCSEL together with the conduction band edge W_c, neglecting band bending effects. Details of the plot are discussed in connection with Fig. 2.10

2.2.4 Threshold Gain and Photon Lifetime

For lasing, the gain in the cavity has to balance the losses. With internal losses α_i and α_a in the passive and active sections, respectively, considerations of gain enhancement and penetration of the waves into the Bragg reflectors lead to the round-trip condition

$$R_t R_b \exp\{2\Gamma_r(g_{th} - \alpha_a)d_a - 2\alpha_i(L_{eff} - d_a)\} = 1 \tag{2.13}$$

for VCSEL operation, from which the threshold gain is obtained as

$$g_{th} = \alpha_a + \frac{1}{\Gamma_r d_a}\left[\alpha_i(L_{eff} - d_a) + \ln\frac{1}{\sqrt{R_t R_b}}\right]. \tag{2.14}$$

In general, α_i is a spatial average over the locally varying loss coefficient, where weighting with the standing-wave intensity profile has to be applied. In this case, however, it is more convenient to determine the threshold gain g_{th} with the transfer matrix method from Sect. 2.2.6. More in general, the loss coefficient α_i comprises potential scattering and diffraction loss components in addition to free-carrier absorption in doped semiconductors. The intensity reflection coefficients R_t and R_b are valid for lossless top and bottom mirrors, respectively, and can, in the most simple cases, be determined from (2.1). Alternatively, the threshold condition can be formulated using the maximum reflectivity

$$R_\alpha \approx R\exp\{-2\alpha_i l_{eff}\} \approx R(1 - 2\alpha_i l_{eff}) \tag{2.15}$$

of a Bragg mirror with small losses $2\alpha_i l_{eff} \ll 1$, assuming that the wave traverses the distance l_{eff} back and forth. From (2.15) and the example in Fig. 2.4 it is seen that

absorption imposes an upper limit on the achievable reflectivity of Bragg mirrors. Increasing the number of mirror pairs beyond ≈ 25 in Fig. 2.4 hardly improves the reflectivity but in contrast decreases the transmissivity and thus the available light output. It should be noted that the assumed absorption coefficient $\alpha_i = 20\,\text{cm}^{-1}$ is rather high. Using (2.6), the threshold condition (2.14) is now rewritten as

$$g_{th} = \alpha_a + \frac{1}{\Gamma_r d_a}\left[\alpha_i(L - d_a) + \ln\frac{1}{\sqrt{R_{t\alpha}R_{b\alpha}}}\right], \tag{2.16}$$

where the effective length L_{eff} is replaced by the inner cavity length L.

Having determined the threshold gain, the photon lifetime τ_p is expressed as

$$\frac{1}{\tau_p} = \frac{d_a}{L_{eff}} v_{gr}\Gamma_r g_{th} \approx v_{gr}\left[\alpha_i + \frac{1}{L_{eff}}\ln\frac{1}{\sqrt{R_t R_b}}\right] = v_{gr}(\alpha_i + \alpha_m)$$
$$\approx v_{gr}\left[\alpha_i\frac{L}{L_{eff}} + \frac{1}{L_{eff}}\ln\frac{1}{\sqrt{R_{t\alpha}R_{b\alpha}}}\right], \tag{2.17}$$

with the mirror loss α_m and the first approximation holding for the usually satisfied conditions $\alpha_a \ll g_{th}$ and $d_a \ll L_{eff}$. For the second approximation, moreover we demand $d_a \ll L$ in addition to (2.15). The group velocity of the laser mode is related to the vacuum velocity of light c as $v_{gr} = c/\langle\bar{n}_{gr}\rangle$. In more generalized form we may write (2.17) as

$$v_{gr}\Gamma\Gamma_r g_{th}\tau_p = 1, \tag{2.18}$$

where

$$\Gamma = \Gamma_l\Gamma_t = \frac{d_a}{L_{eff}}\Gamma_t \tag{2.19}$$

is the total confinement factor, considering a transverse overlap Γ_t between intensity profile of the laser emission and active area in addition to a longitudinal overlap Γ_l. Usually $0.5 < \Gamma_t < 1$. For a given active volume $V_a = A_a d_a$ with the active area A_a, the effective volume occupied by the lasing mode (or the "photon volume") is determined as

$$V_p = V_a/\Gamma. \tag{2.20}$$

As an example, with $\langle\bar{n}_{gr}\rangle = 3.6$, $L_{eff} = 1.3\,\mu\text{m}$, $R_t = R_b = 99.5\%$, and $\alpha_i = 10\,\text{cm}^{-1}$ we obtain $\tau_p = 2.5$ ps and $g_{th} = 1{,}460\,\text{cm}^{-1}$ for $d_a = 24$ nm and $\Gamma_r = 1.8$. Despite drastically different resonator length and mirror reflectivities, VCSELs have very similar photon lifetimes as EELs.

2.2.5 Threshold Current

Knowing the threshold gain, the required threshold carrier density $n_{\rm th}$ depends on the chosen active material. For QWs one can approximate the peak gain coefficient as [47]

$$g_{\rm p} \approx g_1 \ln \frac{n}{n_{\rm t}} \tag{2.21}$$

or [45]

$$g_{\rm p} \approx g_2 \ln \frac{n + n_{\rm s}}{n_{\rm t} + n_{\rm s}}, \tag{2.22}$$

where n is the carrier (electron or hole; assuming charge neutrality in the active region) density, and $g_{1,2}$, $n_{\rm t,s}$ are constants determined from curve fits to numerically calculated functions $g_{\rm p}(n)$ [45]. The term $n_{\rm t}$ has the meaning of a transparency carrier density, namely $g_{\rm p}(n = n_{\rm t}) = 0$. For 8 nm thick GaAs–$Al_{0.2}Ga_{0.8}As$ QWs suitable for 850 nm range VCSELs, one has $g_1 = 2{,}400\,{\rm cm}^{-1}$, $n_{\rm t} = 2.6 \cdot 10^{18}\,{\rm cm}^{-3}$, $g_2 = 3{,}000\,{\rm cm}^{-1}$, $n_{\rm s} = 1.1 \cdot 10^{18}\,{\rm cm}^{-3}$. Emission wavelengths in the 980 nm range are obtained with, e.g., 8 nm thick $In_{0.2}Ga_{0.8}As$–GaAs QWs characterized by $g_1 = 2{,}100\,{\rm cm}^{-1}$, $n_{\rm t} = 1.8 \cdot 10^{18}\,{\rm cm}^{-3}$, $g_2 = 1{,}800\,{\rm cm}^{-1}$, $n_{\rm s} = -0.4 \cdot 10^{18}\,{\rm cm}^{-3}$ [45].

Similarly as in DBR or distributed feedback (DFB) laser diodes, the emission wavelength of a VCSEL is dictated by the resonator and not by the spectral position of the gain peak. When there is an offset $\delta\lambda_{\rm g}$ between lasing wavelength λ and gain peak wavelength $\lambda_{\rm p}$ (see also Fig. 2.17), the shape of the gain spectrum needs to be considered[4] to obtain $n_{\rm th}$ for a given $g_{\rm th}$. For perfect alignment with $\delta\lambda_{\rm g} = 0$, we have $g_{\rm th} = g_{\rm p}$ and (2.21) or (2.22) can be applied with $n = n_{\rm th}$. The threshold current density then follows as

$$j_{\rm th} = \frac{q d_{\rm a}}{\eta_I \tau_{\rm sp}} n_{\rm th}, \tag{2.23}$$

where q is the elementary charge and η_I is the current injection efficiency accounting for lateral leakage currents and carrier overflow over confining barriers. In well-designed VCSELs with high-quality active regions, $\eta_I > 95\%$ can be achieved. The spontaneous recombination lifetime $\tau_{\rm sp}$ depends on the carrier density as

$$\frac{1}{\tau_{\rm sp}(n)} = \frac{1}{\tau_{\rm sp,r}(n)} + \frac{1}{\tau_{\rm sp,n}(n)} = A + Bn + Cn^2 \tag{2.24}$$

[4] In a simple approach, spectral deviations $\delta\lambda_{\rm g}$ of gain peak and laser resonance can be treated by approximating $g(n,\lambda) = g(n)(1 + a_{g\pm}(\delta\lambda_{\rm g})^2)$, where a_{g+} and a_{g-} are the (negative) curvatures of $g(\lambda)$ at both sides of the gain peak. Higher degrees of accuracy are obtained by considering the carrier density dependence of $a_{g\pm}$.

with the A-, B-, and C-terms characterizing non-radiative surface or interface recombination, radiative bimolecular recombination, and Auger recombination, respectively. The non-radiative lifetime $\tau_{\mathrm{sp,n}}$ is thus described by A and C. Owing to the proportionality [45] $C \propto \mathrm{e}^{-W_{\mathrm{g}}/(k_{\mathrm{B}}T)}$ with the bandgap energy W_{g} and Boltzmann's constant k_{B}, the non-radiative Auger effect is an important carrier loss mechanism in long-wavelength lasers operating at elevated temperature T.

If j_{th} is constant over the active area A_{a}, the threshold current is

$$I_{\mathrm{th}} = A_{\mathrm{a}} j_{\mathrm{th}} = \frac{qV_{\mathrm{a}}}{\eta_I \tau_{\mathrm{sp}}} n_{\mathrm{th}} \approx \frac{qV_{\mathrm{a}}B}{\eta_I} n_{\mathrm{th}}^2 \approx \frac{qV_{\mathrm{a}}B}{\eta_I} n_{\mathrm{t}}^2 \exp\{2g_{\mathrm{th}}/g_1\} \tag{2.25}$$

with the active volume $V_{\mathrm{a}} = A_{\mathrm{a}} d_{\mathrm{a}}$, where for simplicity the approximations assume $A = C = \delta\lambda_{\mathrm{g}} = 0$ and the validity of (2.21).

Using the example from the end of the previous section with $g_{\mathrm{th}} = 1{,}460\,\mathrm{cm}^{-1}$ and $d_{\mathrm{a}} = 24\,\mathrm{nm}$, we expect a threshold current density of $j_{\mathrm{th}} = 0.88\ \mathrm{kA/cm^2}$ and a threshold current of $I_{\mathrm{th}} = 0.44\,\mathrm{mA}$ for an 850 nm wavelength VCSEL with an active diameter $D_{\mathrm{a}} = \sqrt{4A_{\mathrm{a}}/\pi} = 8\,\mu\mathrm{m}$, assuming $B \approx 10^{10}\,\mathrm{cm^3/s}$ and perfect current injection with $\eta_I = 1$.

Small active volumes allow to obtain very low threshold currents of VCSELs. When the active diameter is reduced to below $\approx 4\,\mu\mathrm{m}$ in oxide-confined VCSELs, increased diffraction and scattering losses [48] as well as a decreased transverse confinement factor Γ_{t} lead to an increase of I_{th}. The ultimate limit is reached with vanishing internal losses and mirror losses. When $g_{\mathrm{th}} \to 0$, $n_{\mathrm{th}} \to n_{\mathrm{t}}$ in (2.21). With a single 8 nm thick GaAs–$\mathrm{Al_{0.2}Ga_{0.8}As}$ QW, from (2.25) (with $\eta_I = 1$) one calculates $j_{\mathrm{th}} = 87\ \mathrm{A/cm^2}$ and $I_{\mathrm{th}} = 11\,\mu\mathrm{A}$ for $D_{\mathrm{a}} = 4\,\mu\mathrm{m}$.

It should be noted that all relationships summarized in this section are not specific to VCSELs but are identical to those for QW-based EELs.

2.2.6 Matrix Method and Standing-Wave Pattern

For the design of high-performance VCSELs it is important to know the reflectivity spectra of the Bragg mirrors and the electric field distribution in the resonator. Assuming linearly polarized waves in a one-dimensional scalar approach, we have to solve the Helmholtz equation

$$\frac{\mathrm{d}^2 E(z)}{\mathrm{d}z^2} + \gamma^2 E(z) = 0 \tag{2.26}$$

for the phasor[5] of the transverse electric field component $E = E_x$ (or $E = E_y$) in the multilayer system depicted in Fig. 2.8. The complex propagation constant

---

[5] From the complex $E(z)$, the real, time-dependent electric field is obtained as $\tilde{E}(z,t) \propto \mathrm{Re}\{E(z) \cdot \exp\{\mathrm{i}\omega t\}\}$ with the time t and the angular frequency ω.

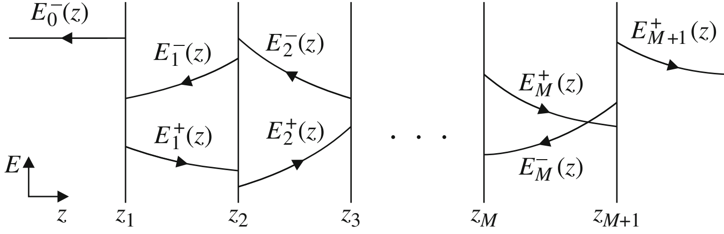

Fig. 2.8 Multilayer structure and traveling wave components in the one-dimensional transfer matrix method for a resonator under lasing operation with $E_0^+(z) = E_{M+1}^-(z) = 0$. In the example, layer zero is assumed to be lossless and layer two is amplifying

$$\gamma_m = \beta_m - \mathrm{i}\alpha_m/2 \tag{2.27}$$

with the imaginary unit $\mathrm{i} = \sqrt{-1}$ is space-independent in each homogeneous layer of index m, and the loss coefficient fulfills $\alpha_m \geq 0$ except for the QW layers, where gain leads to $\alpha_m < 0$. The real part β_m of the propagation constant is related to the refractive index $\bar{n}_m$ by

$$\beta_m = 2\pi\bar{n}_m/\lambda. \tag{2.28}$$

In each layer, the electric field is the superposition

$$\begin{aligned} E_m(z) &= E_m^+(z) + E_m^-(z) \\ &= E_m^+ \exp\{-\mathrm{i}\gamma_m(z - z_m)\} + E_m^- \exp\{+\mathrm{i}\gamma_m(z - z_m)\} \end{aligned} \tag{2.29}$$

of two monochromatic plane waves counter-propagating in z-direction. According to Fig. 2.8, E_m^+ and E_m^- denote the complex field amplitudes of the waves at the interface $z = z_m$ in section m with $z_m \leq z \leq z_{m+1}$, where $m = 1, \ldots, M$ with M as the total number of layers.

The continuity conditions for the transverse components of electric and magnetic (see (2.36)) fields lead to the relations

$$\begin{aligned} E_m^+ &= (\gamma_m^+ E_{m+1}^+ + \gamma_m^- E_{m+1}^-) \exp\{\mathrm{i}\gamma_m d_m\}, \\ E_m^- &= (\gamma_m^- E_{m+1}^+ + \gamma_m^+ E_{m+1}^-) \exp\{-\mathrm{i}\gamma_m d_m\} \end{aligned} \tag{2.30}$$

between amplitudes in subsequent layers with thicknesses $d_m = z_{m+1} - z_m$, where the abbreviations

$$\gamma_m^+ = \frac{\gamma_m + \gamma_{m+1}}{2\gamma_m} \quad \text{and} \quad \gamma_m^- = \frac{\gamma_m - \gamma_{m+1}}{2\gamma_m} \tag{2.31}$$

have been introduced. The relations (2.30) can be written in matrix form

$$\begin{pmatrix} E_m^+ \\ E_m^- \end{pmatrix} = \overline{T}_m \cdot \begin{pmatrix} E_{m+1}^+ \\ E_{m+1}^- \end{pmatrix} \tag{2.32}$$

and thus establish the well-known transfer matrix method [49] for calculating the electric field in a multilayer stack. Through matrix multiplications, the field amplitudes in layer one are related to the amplitudes in layer $M+1$. Equivalent continuity conditions apply at $z = z_1$. To determine the reflectivity R, i.e., the intensity reflection coefficient of a wave incident in positive z-direction, we assume an arbitrary finite amplitude E^+_{M+1}, compute the amplitude reflection coefficient $r = E^-_0(z_1)/E^+_0(z_1)$ and then $R = |r|^2$.

Self-oscillation of the layer structure exclusively allows emergent waves in the terminating sections $m = 0$ and $m = M + 1$, i.e.,

$$E^+_0 = 0 \quad \text{and} \quad E^-_{M+1} = 0. \tag{2.33}$$

These kinds of solutions are possible only for sufficiently large gain in the active layers. Conditions (2.30)–(2.33) thus simultaneously fix the lasing wavelength and threshold gain of all longitudinal modes [50].

As an application example of the transfer matrix method, Fig. 2.9 (left) depicts the calculated reflectivity spectrum of a full 980 nm VCSEL structure, where the wave is incident from air. Compared to Fig. 2.5, the combined effect of both Bragg reflectors produces a broader plateau of high reflectivity, and additional oscillations appear in the spectrum. The dip in the center of the stop-band clearly proves the presence of a cavity mode in a resonator. Just like in a simple Fabry–Pérot resonator, a local minimum in the reflectivity spectrum occurs at the lasing wavelength of a longitudinal mode. For an incident wave, the laser behaves like a transmission line with a length of multiples of $\lambda/(2\langle\bar{n}\rangle)$. As seen in Fig. 2.9 (right), the dip becomes narrower with decreasing absorption in the active quantum wells, which indicates an increase of the resonator's quality factor. In practice, a measurement of the reflectivity spectrum after epitaxial growth of the VCSEL structure is extremely helpful. On the one hand, it provides immediate information about the lasing wavelength to be expected from the sample. On the other hand, the shape of the spectrum and the amount of offset of the dip from the center of the stop-band tell about unwanted deviations from the target layer structure. These can subsequently be corrected without wasting time during laser processing.

Figure 2.10 shows the result of a numerical calculation of the electric field distribution for a model VCSEL that contains three active InGaAs QWs in the center, an 18 pairs GaAs–$Al_{0.7}Ga_{0.3}As$ top and a 24.5 pairs GaAs–AlAs bottom Bragg reflector. It is seen that, due to the high reflectivities of the mirrors, a pronounced resonant enhancement of the field amplitude is built up. In the given example, the half-width of the envelope is 1.7 µm, and the field amplitude in the antinode at the surface is less than 10% of the maximum value found near the center. Details of the standing-wave pattern together with the conduction band edge profile in flat-band approximation were already displayed in Fig. 2.7. In the Bragg reflectors, single-step grading of the heterointerfaces has been introduced to reduce the potential barrier and thus the electrical resistance. Grading is especially important at those heterojunctions that are electrically driven in backward direction, which, in the present design, just occur at nodes of the standing-wave pattern. It is thus possible to

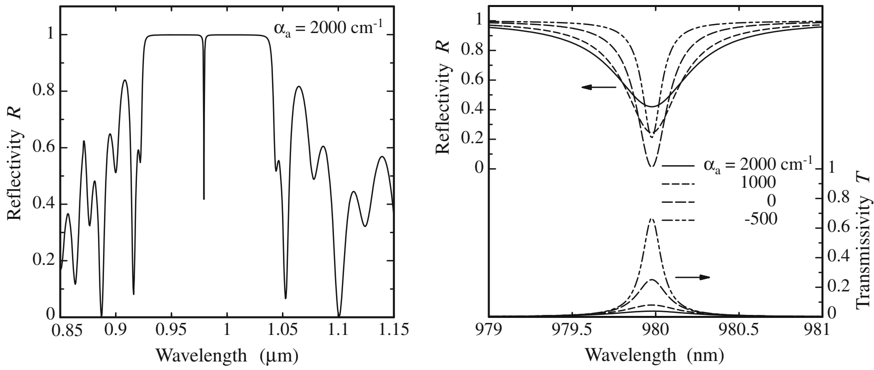

Fig. 2.9 Reflection spectrum of a 980 nm wavelength VCSEL with 16 top and 22.5 bottom GaAs–AlAs Bragg mirror pairs (*left*). Detailed plot of both reflectivity and transmissivity in the vicinity of the resonance dip for different loss coefficients α_a in the three active quantum wells (*right*). In all cases, the passive layers are assumed to have losses of $\alpha_i = 20\,\text{cm}^{-1}$

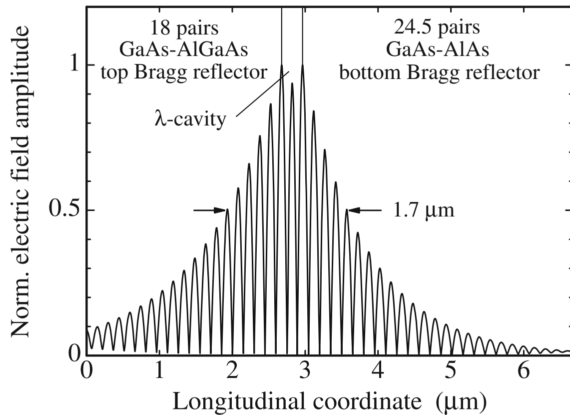

Fig. 2.10 Standing-wave pattern of the electric field in a VCSEL. Details of the one-wavelength thick cavity region are displayed in Fig. 2.7

apply modulation doping in the mirrors in order to optimize the current–voltage characteristics without significantly increasing the threshold gain [51]. It should be noted that several bandgap engineering techniques like multi-step, superlattice-type, or continuous gradings have been successfully applied in practice. Adverse effects on the mirror reflectivities can be kept small with thin intermediate layers or can be compensated for by increasing the mirror thickness. The AlAs layer in the top Bragg reflector in Fig. 2.7 serves to provide current and photon confinement after selective oxidation, which will be discussed in Sects. 2.3.1 and 2.3.4.

2.2.7 Energy Flux and Differential Quantum Efficiency

Above the threshold current I_{th}, top and bottom light output powers P_t and P_b, respectively, increase linearly with driving current I [40, 45], which follows from the

laser rate equations (see Sect. 2.4.1). We write

$$P_{t,b} = \eta_{dt,b} \frac{\hbar\omega}{q}(I - I_{th}), \tag{2.34}$$

where we have defined the differential quantum efficiency $\eta_{dt,b}$ describing the fraction of injected electrons that produce coherent emission in the top or bottom external beam, and $\hbar\omega$ (with the reduced Planck's constant $\hbar = h/(2\pi)$ and the optical angular frequency ω) denotes the photon energy. Laser heating and higher-order effects such as spatial hole burning or thermal lensing (see Chap. 3 of this book) lead to deviations from the simple relationship (2.34). The differential quantum efficiency contains the current injection efficiency η_I from (2.23) as

$$\eta_{dt,b} = \hat{\eta}_{dt,b}\eta_I, \tag{2.35}$$

where the photonic quantum efficiency $\hat{\eta}_{dt,b}$ characterizes the percentage of generated coherent light that is available as top or bottom emission. Owing to loss in the resonator we always[6] find $\hat{\eta}_{dt} + \hat{\eta}_{db} < 100\%$. The emitted coherent power is related to the time-averaged Poynting vector [40] $\vec{S} = Re\{\vec{E} \times \vec{H}^*\}$ with $*$ denoting complex conjugation. In the one-dimensional scalar approach used in the preceding section, from the corresponding Maxwell equation, the (linearly polarized) magnetic field is proportional to the longitudinal spatial derivative of the electric field as

$$H = H_y = \frac{\mathrm{i}}{\omega\mu_0}\frac{\mathrm{d}E}{\mathrm{d}z}, \tag{2.36}$$

where μ_0 is the vacuum permeability. With field components E_x and H_y only, energy flux exclusively occurs in $\pm z$-directions, i.e., $S_x = S_y = 0$. Using (2.29) and (2.36) yields the expression

$$\begin{aligned} S_m(z) = {} & \frac{\beta_m}{\omega\mu_0}|E_m^+|^2\exp\{-\alpha_m(z - z_m)\} - \frac{\beta_m}{\omega\mu_0}|E_m^-|^2\exp\{\alpha_m(z - z_m)\} \\ & + \frac{\alpha_m}{\omega\mu_0}\mathrm{Im}\left\{E_m^+(E_m^-)^*\exp\{-\mathrm{i}2\beta_m(z - z_m)\}\right\} \end{aligned} \tag{2.37}$$

for the energy flux in section m of the multilayer structure. The first and second terms describe the energy flux of the forward and backward propagating waves, respectively, which are mutually coupled by the third term whenever the material exhibits gain or loss, i.e., when $\alpha_m \neq 0$.

Figure 2.11 depicts the energy flux for the standing-wave patterns of Figs. 2.7 and 2.10. It becomes clear that power is generated in the QWs only, as characterized by

[6] Locally, in transition regions between predominant oscillation on different transverse modes, $\eta_d = \eta_{dt} + \eta_{db} > 1$ arising from redistributions of the carrier density profile can be observed (see, e.g., [52]). Moreover, differential quantum efficiencies $\eta_d > 1$ can regularly be obtained in laser diodes with cascaded pn-junctions (by means of tunnel junctions), at the expense of higher operating voltages [53, 54].

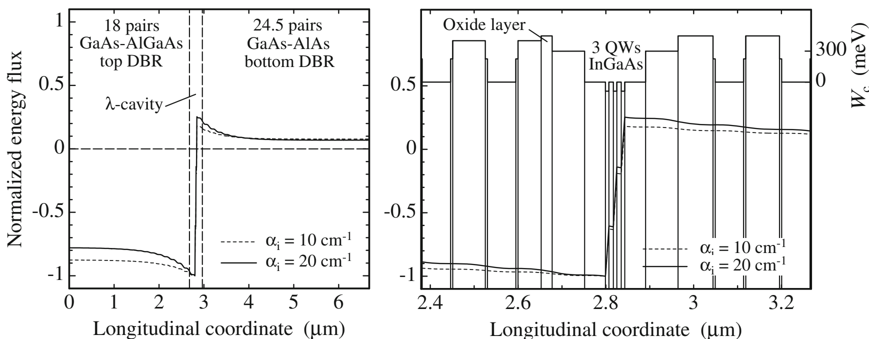

Fig. 2.11 Normalized energy flux density in a VCSEL cavity corresponding to the electric field distributions in Figs. 2.10 (*left*) and 2.7 (*right*)

$\mathrm{d}S/\mathrm{d}z > 0$. Extrema in the energy flux are found on both sides of the three-QW system, and power flux occurs toward the Bragg reflectors ($S < 0$ signifies energy transport in $-z$-direction), where the flux is diminished due to the distributed loss. Closer inspection of the right-hand diagram shows that in the passive layers, regions with high negative slope of $S(z)$ alternate with regions in which the slope is close to zero, where the period length is half a material wavelength. A comparison with Fig. 2.7 reveals that high and low slopes correspond to antinodes and nodes of the standing-wave pattern $E(z)$, respectively. In other words, the losses close to a field node contribute much less to a decrease of the efficiency of a VCSEL. This finding gave rise to the concept of modulation doping [51], i.e., the doping level[7] is increased in the vicinity of a field node and correspondingly decreased in regions of high field strength.

The photonic quantum efficiency for top and bottom emission $\hat{\eta}_\mathrm{d} = \hat{\eta}_\mathrm{dt} + \hat{\eta}_\mathrm{db}$ is identified as the fraction of the generated flux that is emitted through the top or bottom mirrors, i.e., [56]

$$\hat{\eta}_\mathrm{d} = \frac{g_\mathrm{th}}{g_\mathrm{th} + \alpha_\mathrm{a}} \left(1 + \frac{\sum_{i,\mathrm{pass.}} \Delta S_i}{\sum_{i,\mathrm{act.}} \Delta S_i} \right) \quad \text{with} \quad \Delta S_i = S(z_{i+1}) - S(z_i), \tag{2.38}$$

where g_th is the threshold gain previously determined by the transfer matrix method (in which loss in the active layers is not taken into account). The sum in the numerator or denominator extends over all passive or active segments, respectively. Obviously, loss leads to flux increments $\Delta S_i < 0$ and thus to $\hat{\eta}_\mathrm{d} < 1$. Denoting the top and bottom emitted energy flux by $S_\mathrm{t} = S(z_1) < 0$ and $S_\mathrm{b} = S(z_{M+1}) > 0$, respectively

[7] Free carriers cause optical absorption losses which have been found to scale as $\alpha_\mathrm{fc} = (3 \cdot 10^{-18} n + 7 \cdot 10^{-18} p)\ \mathrm{cm}^2$ for GaAs (see [55], p. 175), where n and p are the electron and hole densities, respectively.

(see Fig. 2.8 for the labeling of the layers), the corresponding photonic quantum efficiencies are

$$\hat{\eta}_{\mathrm{dt}} = \hat{\eta}_{\mathrm{d}} \frac{|S_{\mathrm{t}}|}{|S_{\mathrm{t}}| + |S_{\mathrm{b}}|} \quad \text{and} \quad \hat{\eta}_{\mathrm{db}} = \hat{\eta}_{\mathrm{d}} \frac{|S_{\mathrm{b}}|}{|S_{\mathrm{t}}| + |S_{\mathrm{b}}|}. \tag{2.39}$$

Figures 2.7 and 2.10 have been calculated with constant $\alpha_{\mathrm{i}} = 20\,\mathrm{cm}^{-1}$. In general, spatially varying absorption can accurately be taken into account in the transfer matrix computation. To illustrate the effect of reduced average absorption on the energy flux distribution, as to be achieved by modulation doping, a curve with $\alpha_{\mathrm{i}} = 10\,\mathrm{cm}^{-1}$ has been included in Fig. 2.11. Compared to values $g_{\mathrm{th}} = 1{,}820\,\mathrm{cm}^{-1}$ and $\hat{\eta}_{\mathrm{d}} = 67\%$ before, threshold gain and differential efficiency are modified to $g_{\mathrm{th}} = 1{,}520\,\mathrm{cm}^{-1}$ and $\hat{\eta}_{\mathrm{d}} = 80\,\%$, respectively, such that $g_{\mathrm{th}} \cdot \hat{\eta}_{\mathrm{d}} \approx const$. Without any loss, horizontal lines $S(z)$ would appear in the passive layers in Fig. 2.11.

Employing the simple formalism from Sect. 2.2.4, the photonic differential quantum efficiency results from (2.17) as

$$\hat{\eta}_{\mathrm{d}} = \frac{\tau_{\mathrm{p}}}{\tau_{\mathrm{p,m}}} \approx \frac{\alpha_{\mathrm{m}}}{\alpha_{\mathrm{i}} + \alpha_{\mathrm{m}}} = \frac{1}{1 - \alpha_{\mathrm{i}} L_{\mathrm{eff}} / \ln \sqrt{R_{\mathrm{t}} R_{\mathrm{b}}}}, \tag{2.40}$$

where $\tau_{\mathrm{p,m}}$ is the photon lifetime related to mirror losses. In analogy to edge-emitting lasers, the top- and bottom-side quantum efficiencies have to be written as (see [57, Chap. 2])

$$\hat{\eta}_{\mathrm{dt,b}} = \hat{\eta}_{\mathrm{d}} \cdot \eta_{\mathrm{ut,b}} \tag{2.41}$$

with the unbalance factors

$$\eta_{\mathrm{ut,b}} = \frac{T_{\mathrm{t,b}} \sqrt{R_{\mathrm{b,t}}}}{T_{\mathrm{t,b}} \sqrt{R_{\mathrm{b,t}}} + T_{\mathrm{b,t}} \sqrt{R_{\mathrm{t,b}}}} = \frac{T_{\mathrm{t,b}} \sqrt{R_{\mathrm{b,t}}}}{(\sqrt{R_{\mathrm{t}}} + \sqrt{R_{\mathrm{b}}})(1 - \sqrt{R_{\mathrm{t}} R_{\mathrm{b}}})} \tag{2.42}$$

which satisfy $\eta_{\mathrm{ut}} + \eta_{\mathrm{ub}} = 1$ and assume the values $\eta_{\mathrm{ut}} = \eta_{\mathrm{ub}} = 0.5$ for $R_{\mathrm{t}} = R_{\mathrm{b}}$. In (2.42), $T_{\mathrm{t,b}} = 1 - R_{\mathrm{t,b}}$ are the transmissivities of the lossless mirrors. The ratio between top and bottom emitted powers is thus[8]

$$\frac{P_{\mathrm{t}}}{P_{\mathrm{b}}} = \frac{\eta_{\mathrm{ut}}}{\eta_{\mathrm{ub}}} = \frac{(1 - R_{\mathrm{t}}) \sqrt{R_{\mathrm{b}}}}{(1 - R_{\mathrm{b}}) \sqrt{R_{\mathrm{t}}}}. \tag{2.43}$$

In this analytical approach (2.40)–(2.43), however, the effects of optimization techniques like modulation doping cannot be easily assessed.

[8] In other texts one often finds $\alpha_{\mathrm{m}} = \alpha_{\mathrm{mt}} + \alpha_{\mathrm{mb}}$ with $\alpha_{\mathrm{mt,b}} = -L_{\mathrm{eff}}^{-1} \ln \sqrt{R_{\mathrm{t,b}}}$ (compare with (2.17)) and thus $\eta_{\mathrm{ut,b}} = \alpha_{\mathrm{mt,b}} / \alpha_{\mathrm{m}} = \ln R_{\mathrm{t,b}} / \ln(R_{\mathrm{t}} R_{\mathrm{b}})$. For VCSELs we have $R_{\mathrm{t,b}} \approx 1$, and with the approximation $\ln x \approx x - 1$ we get $\eta_{\mathrm{ut,b}} \approx T_{\mathrm{t,b}} / (T_{\mathrm{t}} + T_{\mathrm{b}})$, which is also obtained from (2.42) when setting $\sqrt{R_{\mathrm{t}}} \approx \sqrt{R_{\mathrm{b}}} \approx 1$. In both cases, the ratio (2.43) is then $P_{\mathrm{t}} / P_{\mathrm{b}} \approx T_{\mathrm{t}} / T_{\mathrm{b}}$.

From (2.14) while assuming $\alpha_\mathrm{a} \ll g_\mathrm{th}$ and $d_\mathrm{a} \ll L_\mathrm{eff}$ we obtain

$$g_\mathrm{th} \cdot \hat{\eta}_\mathrm{d} \approx \frac{L_\mathrm{eff}}{\Gamma_\mathrm{r} d_\mathrm{a}} (\alpha_\mathrm{i} + \alpha_\mathrm{m}) \cdot \frac{\alpha_\mathrm{m}}{\alpha_\mathrm{i} + \alpha_\mathrm{m}} = -\frac{\ln \sqrt{R_\mathrm{t} R_\mathrm{b}}}{\Gamma_\mathrm{r} d_\mathrm{a}}, \tag{2.44}$$

which is independent of the internal losses, as found in the numerical example at the end of the previous paragraph.

2.2.8 Conversion Efficiency

The wallplug or conversion efficiency η_c for emission through the top or bottom mirror is defined as the ratio of coherent light output power and electrical input power, namely

$$\eta_\mathrm{ct,b} = \frac{P_\mathrm{t,b}}{IV}, \tag{2.45}$$

where V is the voltage applied across the VCSEL. Usually the current–voltage characteristic can be approximated by

$$V \approx V_\mathrm{k} + R_\mathrm{d} I, \tag{2.46}$$

where $R_\mathrm{d} = \mathrm{d}V/\mathrm{d}I$ denotes the differential resistance, and the kink voltage V_k is related to the separation of quasi-Fermi energies but can be approximated by $V_\mathrm{k} \approx \hbar\omega/q$. Non-perfect grading of heterointerfaces induces a larger voltage offset accompanied by a pronounced curvature of the I–V characteristic [58]. Using (2.34), (2.45), and (2.46) leads to

$$\eta_\mathrm{ct,b} = \eta_\mathrm{dt,b} \frac{\hbar\omega}{q} \frac{I - I_\mathrm{th}}{I V_\mathrm{k} + I^2 R_\mathrm{d}}, \tag{2.47}$$

showing that for $I \gg I_\mathrm{th}$ the series resistance is responsible for the decrease of $\eta_\mathrm{ct,b}$ with increasing current. In the limit $R_\mathrm{d} \to 0$ and $I \gg I_\mathrm{th}$ we have approximately $\eta_\mathrm{ct,b} \to \eta_\mathrm{dt,b}$. The efficiency is maximized at the laser current

$$\hat{I}_\mathrm{c} = I_\mathrm{th} \cdot \left(1 + \sqrt{1 + \xi}\right) \qquad \text{with} \qquad \xi = \frac{V_\mathrm{k}}{I_\mathrm{th} R_\mathrm{d}}, \tag{2.48}$$

from which the peak conversion efficiency is obtained as

$$\hat{\eta}_\mathrm{ct,b} = \eta_\mathrm{dt,b} \frac{\hbar\omega}{q V_\mathrm{k}} \frac{\xi}{(1 + \sqrt{1 + \xi})^2} = \eta_\mathrm{dt,b} \frac{\hbar\omega}{q V_\mathrm{k}} f_\mathrm{c}(\xi). \tag{2.49}$$

Figure 2.12 shows the conversion function $f_\mathrm{c}(\xi)$, approaching $f_\mathrm{c}(\xi) \to 1$ only slowly with increasing ξ. Even for perfect injection and photonic quantum efficiencies as well as a kink voltage close to the photon energy equivalent voltage $\hbar\omega/q$,

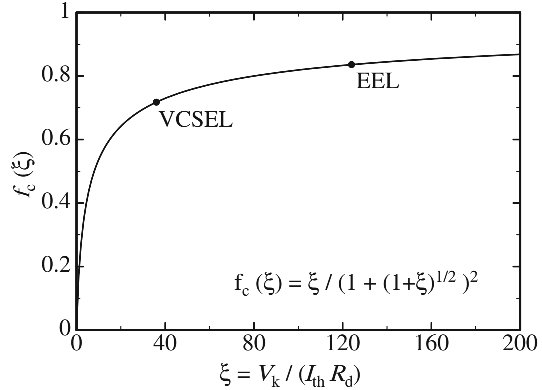

Fig. 2.12 Electrical-to-optical conversion function for laser diodes with linear current–voltage characteristics. Data for the 1.06 μm wavelength VCSEL ($V_k = 1.27$ V, $I_{th} = 0.7$ mA, $R_d = 50\,\Omega$, $\xi = 36$) and the 808 nm EEL ($V_k = 1.56$ V, $I_{th} = 180$ mA, $R_d = 0.07\,\Omega$, $\xi = 124$) are taken from [24, 25] and [59], respectively

maximum obtainable conversion efficiencies cannot exceed f_c. For high-efficiency lasers it is certainly desired to strive for small products $I_{th} R_d$ or equivalently $j_{th} \bar{R}_d$ with the sheet resistance $\bar{R}_d = R_d A_a$. Unfortunately for VCSELs, the usually thick multilayer stack leads to higher sheet resistances compared to EELs.[9] Likewise, thin QW gain regions with small round-trip gain induce higher threshold current densities. For these reasons, VCSEL conversion efficiency curves, as displayed below, show rollover at smaller ratios $\hat{I}_c / I_{th}$ compared to, e.g., broad-area EELs for high-power applications. Figure 2.12 contains data points for a record EEL with $\hat{\eta}_c = 75\%$ and $\hat{I}_c / I_{th} \approx 12$ [59] and an optimized VCSEL with $\hat{\eta}_c = 62\%$ and $\hat{I}_c / I_{th} \approx 7$ [24, 25]. Since there exists a tradeoff between increasing layer conductivity (leading to small R_d) and decreasing threshold gain (leading to small I_{th}) while maintaining high differential efficiencies, it becomes clear that obtaining peak conversion efficiencies above 70% is one of the most challenging topics in VCSEL research. In [24, 25], undoped DBRs and a double intra-cavity contact scheme are employed to minimize optical losses. On the other hand, due to low threshold currents, VCSELs readily offer fairly high η_c at low output powers even in the sub-mW range, which is of special importance for parallel-optical interconnect applications and not at all easily achieved with EELs.

2.3 Emission Characteristics of Oxide-Confined VCSELs

This section illustrates exemplary experimental data of selectively oxidized VCSELs. Device layout and fabrication are described, the operation behavior of multimode as well as single transverse mode VCSELs and arrays are shown, and the origins of the observed temperature characteristics are investigated. Transverse modes are

[9] Although small-area VCSELs appear to have fairly competitive sheet resistances, threshold current densities tend to be in the kA/cm^2 range.

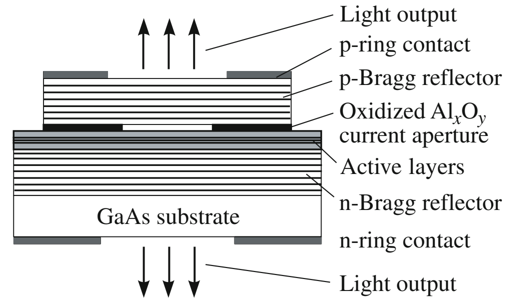

Fig. 2.13 Schematic cross-sectional view of a selectively oxidized VCSEL

introduced in a general Laguerre–Gaussian approximative manner, and effective index guiding in oxidized VCSELs is quantified.

2.3.1 Device Structure

Figure 2.13 illustrates the general configuration of the investigated selectively oxidized VCSELs. The multilayer system is grown by solid-source molecular beam epitaxy on n-GaAs substrate. For emission wavelengths in the 980 nm (850 nm) spectral region, the active region consists of half-wavelength thick GaAs ($Al_{0.2}Ga_{0.8}As$) with three, each 8 nm thick compressively strained $In_{0.2}Ga_{0.8}As$ (unstrained GaAs) QWs separated by 10 nm barriers in the center. Quarter-wavelength $Al_{0.4}Ga_{0.6}As$ ($Al_{0.5}Ga_{0.5}As$) cladding layers are introduced on both sides of the active region to improve longitudinal carrier confinement and to make the inner region one wavelength thick. Top and bottom mirrors contain $Al_{0.7}Ga_{0.3}As$–GaAs ($Al_{0.9}Ga_{0.1}As$–$Al_{0.2}Ga_{0.8}As$) quarter-wavelength Bragg stacks. Single-step grading with 5 nm thick layers of intermediate bandgap energy is used to reduce the electrical series resistance. Current is supplied through the carbon p-doped top and silicon n-doped bottom reflectors, where modulation and δ-doping is required for high performance devices [58]. Current confinement is achieved by means of selective lateral oxidation [18] of an about 30 nm thick AlAs layer placed directly above the top cladding layer (see Fig. 2.7). Oxidation is done in an about 400°C hot water vapor atmosphere [22], leading to lateral oxidation rates in the 1 μm/min range. Semiconductor layers with lower Al content have much lower oxidation rates [60]. Before oxidation, a mesa is formed by wet or dry etching. Applying TiPtAu top and AuGeNi bottom ring contacts, simultaneous top and bottom laser emission from InGaAs QWs is obtained. The etched mesa size might be chosen several 10 μm larger than the envisaged active diameter which can be adjusted from, e.g., 1 μm to above 100 μm by proper choice of mesa diameter and oxidation time.

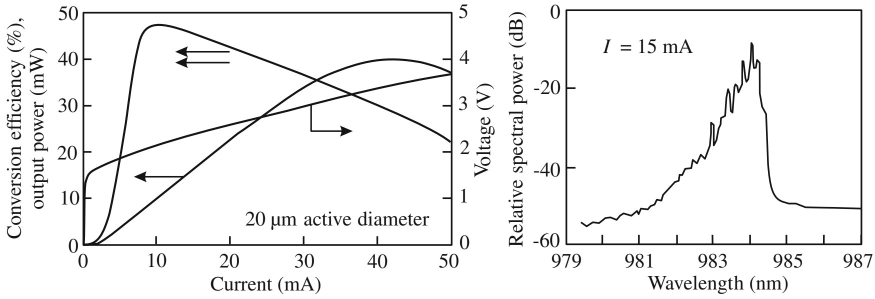

Fig. 2.14 Output power, conversion efficiency, and current–voltage characteristics of a high-efficiency selectively oxidized InGaAs QW VCSEL with 20 µm active diameter (*left*). Emission spectrum at $I = 15$ mA driving current (*right*) [61]

2.3.2 Experimental Operation Characteristics

Figure 2.14 shows the operation characteristics of an InGaAs QW VCSEL with 20 µm diameter of the oxide aperture [61]. Threshold current and threshold voltage are 3 mA and 1.65 V, respectively. Since the differential resistance is less than 40 Ω under lasing conditions, the driving voltage remains below 3.5 V up to the maximum output power of 40 mW which is limited by thermal rollover. No dedicated heat-sinking was applied. The peak conversion efficiency of $\hat{\eta}_{ct} = 47\%$ is observed for a driving current of 10 mA at an output power of 10 mW, where several transverse modes oscillate simultaneously. The mode spacing is about 0.2 nm, and the total −10 dB spectral emission bandwidth is less than 2 nm. The emission spectrum changes rapidly with increasing bias current and higher-order, shorter-wavelength modes become more dominant. The high wallplug efficiency is related to the favorable top-side differential quantum efficiency of $\eta_{dt} \approx 90\%$. Owing to the comparatively large driving voltage at optimum power conversion, the electrical series resistance consumes about 40% of the total input power. Other sources of loss are bottom emission, carrier escape, spontaneous emission, and internal absorption and scattering in the mirrors as well as the active region. Highest power conversion efficiencies reported to date are above 50% [21–25]. The present record device with $\hat{\eta}_{ct} = 62\%$ is a multimode laser with a 7 µm diameter oxide aperture [24, 25].

Top-emitting VCSELs with larger active size begin to suffer from laterally inhomogeneous current supply due to current crowding at the oxide aperture edge and tend to develop ring-shaped near- and far-field patterns. Homogeneous large-area emission can be achieved from bottom-emitting devices with appropriate heat-sinking [62].

In contrast to transverse multimode devices, Fig. 2.15 illustrates the operation behavior of a small-diameter oxide-confined VCSEL exhibiting high single-mode output powers [63]. The GaAs QW device is designed for emission in the 850 nm spectral region, being defined as a standard for short-distance optical interconnects. The threshold current is about 500 µA, and the maximum fundamental mode out-

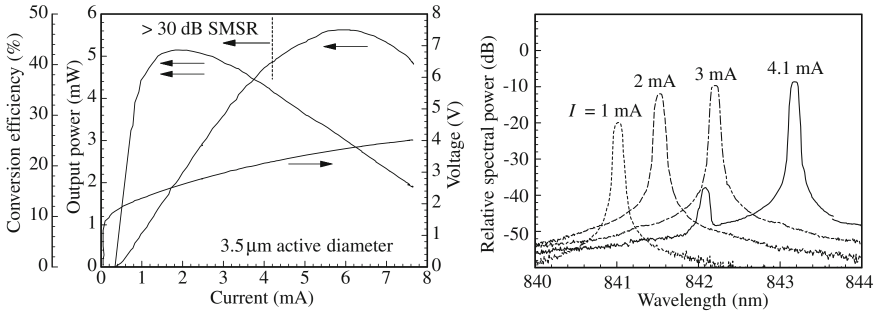

Fig. 2.15 Operation characteristics (*left*) and current-dependent emission spectra (*right*) of a 3.5 µm active diameter GaAs QW single-mode VCSEL [63]

put power of 4.8 mW is achieved at a driving current of 4.1 mA, corresponding to a wallplug efficiency of 35%. Usually, the single-mode emission limit is defined through a side-mode suppression ratio (SMSR) of larger than 30 dB. Maximum power conversion of $\hat{\eta}_{ct} = 42\%$ occurs at $I = 2$ mA and $P_t = 2.2$ mW. The red-shift of the emission spectrum with increasing current indicates internal heating of the VCSEL, which is discussed in Sect. 2.3.3. The onset of the higher azimuthal order, donut-shaped transverse mode for high currents is initiated by fundamental mode spatial hole burning and thermally induced waveguiding. It should be mentioned that VCSELs with much smaller threshold currents in the sub-100 µA range have already been demonstrated [26] by choosing small active diameters and high mirror reflectivities which, however, greatly limits the achievable output power and conversion efficiency levels.

Owing to their surface-normal emission, VCSELs especially lend themselves to form one- and two-dimensional arrays for various applications including highly parallel optical interconnects. Some early work is found in [64–70]. An extensive discussion is contained in Chap. 16 of this book. Figure 2.16 presents layout and characteristics of a VCSEL array consisting of 32 individually addressable devices arranged in a 4×8 matrix, designed for hybrid integration by direct flip-chip bonding onto Si CMOS circuits [71, 72]. The particular array shows transverse multimode emission at 990 nm wavelength with excellent homogeneity of L–I and I–V curves. The device pitch of 250 µm is well suited for direct coupling to dense arrays of silica or plastic optical fibers to establish inter- and intra-cabinet data links down to optical backplanes in advanced computer environments that require channel data rates in the 10 Gbit/s regime. Single-channel digital data transmission at 12.5 Gbit/s has been reported with such arrays [71].

2.3.3 Temperature Behavior

Caused by the short optical resonator, the emission wavelength λ of a VCSEL is determined by the cavity resonance and not by the gain peak as in conventional

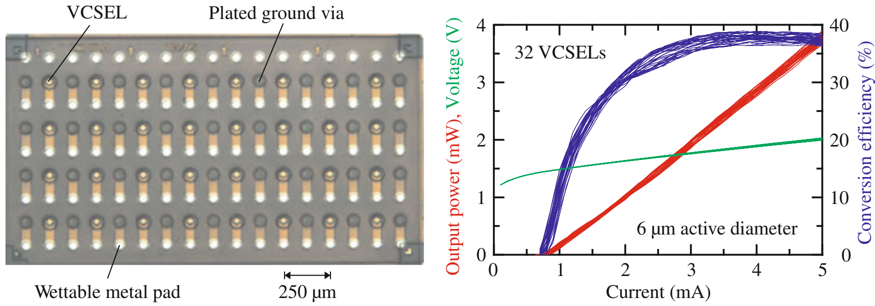

Fig. 2.16 Layout (*left*) [71] and static operation characteristics (*right*) [72] of a 4 × 8 elements, 6 μm individual device diameter bottom-emitting VCSEL array suitable for flip-chip mounting

Fabry–Pérot-type EELs. The thermal wavelength shift is thus mainly governed by changes of the average refractive index in the resonator and to a smaller extent (about 10%) by the thermal expansion of the semiconductor layers. Consequently, the wavelength shift of the mode depends on the material composition of the Bragg reflectors and the inner cavity. For VCSELs in the 800–1,000 nm emission wavelength range, the mode shift is typically found to be $\partial\lambda/\partial T \approx 0.07$ nm/K. With this ratio, internal temperature rises can be estimated from measured spectral red-shifts as in Fig. 2.15.

On the other hand, the active QWs show a shift of the peak material gain wavelength λ_p according to $\partial\lambda_\mathrm{p}/\partial T \approx 0.32$ nm/K mainly due to bandgap shrinkage. Because of differing gain and mode shifts with increasing current (and thus device temperature), a mutual shift of lasing mode and gain spectrum occurs. Figure 2.17 illustrates the resulting material gain experienced by the VCSEL mode as a function of temperature T. The calculations are performed for an 8 nm thick $\mathrm{In_{0.2}Ga_{0.8}As}$–GaAs QW at a fixed carrier density of $n = 3 \cdot 10^{18}\,\mathrm{cm^{-3}}$. Although the peak gain continuously decreases with increasing temperature, the modal material gain can decrease or increase depending on the amount of wavelength detuning at room temperature, which is characterized in Fig. 2.17 by the offset $\delta\lambda_\mathrm{g} = \lambda(T_\mathrm{ref}) - \lambda_\mathrm{p}(T_\mathrm{ref})$ with $T_\mathrm{ref} = 300$ K. The offset $\delta\lambda_\mathrm{g}$ can be adjusted during epitaxial growth of the VCSEL structure. Of great practical interest is the choice $\delta\lambda_\mathrm{g} > 0$. Starting from operation at room temperature, with increasing laser current or ambient temperature the gain available for the mode increases, thus compensating for the decay of the peak gain and temperature-dependent loss mechanisms in the active region. In this way, the output power of the VCSEL can be made rather temperature-insensitive.

As a result of the temperature-dependent detuning, the threshold current of a VCSEL usually varies with temperature as $I_\mathrm{th}(T) = I_\mathrm{th,min} \cdot (1 + C_T(T - T_\mathrm{min})^2)$ with a constant $C_T > 0$. An example can be seen in [22]. Within certain limits, a higher $\delta\lambda_\mathrm{g}$ leads to an increase of T_min. As expected from Fig. 2.17, the maximum modal material gain and thus the minimum VCSEL threshold current $I_\mathrm{th,min}$ is not obtained for optimum alignment of mode and gain peak but is found at lower temperatures with a negative detuning. Whereas this effect is relatively small in high-quality InGaAs or GaAs QW active material, it has to be taken into account for the design of long-wavelength VCSELs based on InP [73].

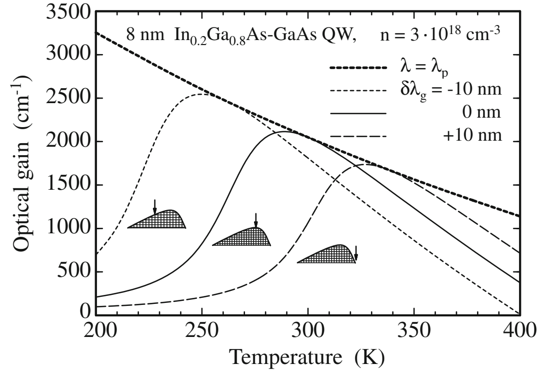

Fig. 2.17 Modal material gain coefficient as a function of temperature. The *upper dashed* curve for $\lambda = \lambda_p$ is the peak gain. The *lower* curves are calculated for different gain offsets $\delta\lambda_g$ at room temperature. Modal positions at $T_{ref} = 300$ K are indicated as *arrows* in the cross-hatched spectral gain profiles $g(\lambda)$ in the insets

Heating of the VCSEL is suitably described by the thermal resistance

$$R_{Th} = \frac{\Delta T}{P_{diss}}, \tag{2.50}$$

defined by the ratio of temperature increase ΔT in the device and dissipated electrical power P_{diss}. For VCSELs with high wallplug efficiency it is important to use

$$P_{diss} = IV - P_t - P_b = IV - P = IV(1 - \eta_c) \tag{2.51}$$

instead of the electrical input power since otherwise one would neglect "photon cooling" by the radiated optical power P. The thermal resistance often closely obeys the simple relation [74]

$$R_{Th} \approx \frac{1}{2\lambda_{Th} D_a}, \tag{2.52}$$

which is obtained assuming heat flow from a circular area with diameter D_a, here identified as the active diameter, into a half-space filled with a medium of thermal conductivity λ_{Th}. Thermal resistances plotted in Fig. 2.18 were measured for top- as well as bottom-emitting devices, both mounted substrate-down without dedicated heat sink. The thermal resistance is determined experimentally as $R_{Th} = C_1/C_2$ from two measurements, namely the wavelength shift with consumed power, $C_1 = \Delta\lambda/\Delta P_{diss}$, and the shift with varying heat-sink temperature, $C_2 = \Delta\lambda/\Delta T_{hs}$, usually at pulsed operation, i.e., with negligible dissipated power. As mentioned before, $C_2 \approx 0.07$ nm/K for short-wavelength VCSELs. The lines in Fig. 2.18 are curve fits according to (2.52), leading to average thermal conductivities of the multilayer stack close to that of the GaAs substrate. Thermal resistances of VCSELs can be considerably reduced by upside-down mounting on a heat-spreader, requiring, however, bottom emission through a transparent substrate or even substrate removal [75].

With increasing driving current above threshold or increasing ambient temperature, a typical rollover of the output power characteristics is observed. Higher carrier densities to maintain the threshold gain, carrier and current leakage effects, as well

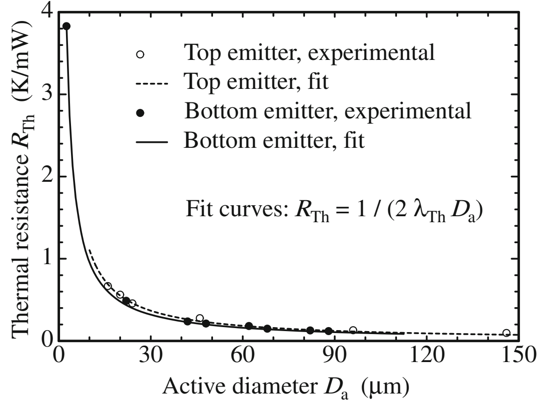

Fig. 2.18 Experimental and fitted thermal resistances of substrate-side-mounted top- and bottom-emitting VCSELs as a function of active diameter D_a. The data points are fitted according to (2.52)

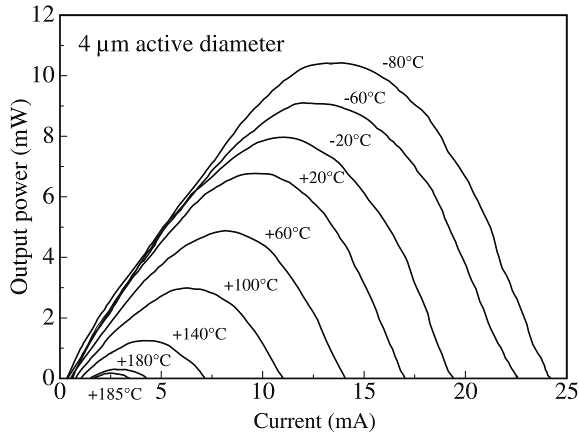

Fig. 2.19 Continuous-wave operation light–current curves of a VCSEL with 4 μm active diameter for various heat-sink temperatures from −80 to +185°C [22] (© 1997 IEEE)

as increased non-radiative recombination are generally made responsible for the deviation from the linear increase of output power with current. Figure 2.19 shows output characteristics of an oxidized VCSEL for various heat-sink temperatures up to $T_{hs} = 185°C$. By observing the red-shift of the emission spectrum, it is found [22] that for room temperature operation, rollover occurs at about $\Delta T = 90\,K$ internal temperature rise, whereas laser turn-off at $T \approx 200°C$ is fairly independent of T_{hs}. A more detailed analysis of the output characteristics in Fig. 2.19 shows that in a reduced temperature interval between −40 and +80°C that is of primary technical interest for datacom applications, the threshold current varies between 300 and 500 μA, while the laser current required for 1 mW output power ranges between 1.5 and 1.85 mA. The results clearly demonstrate that well-designed VCSELs can operate over an extremely wide temperature range, often even making external temperature control unnecessary.

2.3.4 Transverse Modes

Analyzing the transverse mode behavior of VCSELs is a rather complex subject. The purpose of this section is to give a rough idea of the modal properties; details can be found in Chap. 3 of this book. The number and intensity of oscillating modes is related to the balance between optical losses during round-trip propagation in the cavity and amplification in the short active section of the VCSEL. Losses are due to absorption, scattering, as well as diffraction and largely depend on the vertical waveguiding properties of the multilayer stack. Unfortunately, in the most promising, oxide-confined device designs to date, waveguide-like structures cannot be easily identified and are even inhomogeneous in the propagation direction. In the active layers, amplification is non-uniform among different modes owing to varying spatial overlaps between optical gain and mode intensity profiles (different Γ_t in (2.19)). Rather unimpressed by the amount of complexity involved, modes emitted from circularly symmetric VCSEL structures prefer to closely resemble the profiles of the Laguerre–Gaussian mode family [76], constituting the eigenfunctions for guided-wave propagation in a quadratic refractive index medium. In planar proton-implanted VCSELs, a correspondence to this refractive index distribution can be found in the thermally induced index profile that is established as a result of internal heating [56], and even the more step-like effective index profile in selectively oxidized VCSELs discussed below can be roughly approximated in this way.

The near-field intensity profiles of the modes are then written as

$$
\begin{aligned}
S_{lp}(r,\varphi) &\propto |E_{lp}(r,\varphi)|^2 \\
&\propto \left(\frac{2r^2}{w_0^2}\right)^l \left[L_{p-1}^{(l)}\left(\frac{2r^2}{w_0^2}\right)\right]^2 \left\{\begin{matrix}\cos^2(l\varphi)\\ \sin^2(l\varphi)\end{matrix}\right\} \exp\left\{-\frac{2r^2}{w_0^2}\right\},
\end{aligned} \tag{2.53}
$$

where (r,φ) are cylindrical coordinates and $L_{p-1}^{(l)}$ is the generalized Laguerre polynomial of kind l and order $p-1$, with integers l and p characterizing the azimuthal and radial mode orders, respectively. The nomenclature of mode orders is chosen in analogy to linearly polarized LP_{lp} optical fiber modes. From (2.53), the fundamental mode

$$
S_{01}(r) \propto \exp\left\{-\frac{2r^2}{w_0^2}\right\} \tag{2.54}
$$

is of simple Gaussian shape with azimuthal symmetry. All modes can oscillate in two orthogonal states of polarization. Including polarization, the degeneracy of modes with $l \geq 1$ is fourfold, whereas it is twofold for $l = 0$. The mode field radius or spot radius w_0 is expressed as

$$
w_0 = \sqrt{\frac{a\lambda}{\pi\sqrt{\bar{n}_0^2 - \bar{n}_\mathrm{a}^2}}}, \tag{2.55}
$$

introducing the distance a at which the refractive index profile

$$\bar{n}^2(r) = \bar{n}_0^2 - (\bar{n}_0^2 - \bar{n}_a^2) \cdot (r/a)^2 \tag{2.56}$$

has dropped from $\bar{n}(r=0) = \bar{n}_0$ at the waveguide center to the value $\bar{n}(r=a) = \bar{n}_a$. Near-field mode profiles according to (2.53) can be easily transformed into the far-field and thus be conveniently accessed experimentally. In particular for the fundamental mode, the full far-field angle at which the intensity has dropped to one-half of its maximum writes as $\Theta_{\mathrm{FWHM}} \approx \lambda\sqrt{2\ln 2}/(\pi w_0)$, where the approximation holds for angles satisfying $\tan\Theta \approx \Theta$.

As an example, Fig. 2.20 shows measured and calculated far-field distributions of a large-diameter planar proton-implanted VCSEL [77]. For the calculation, spot diameters (2.55) are determined self-consistently by taking the generated internal temperature profile into account. Far-fields are then obtained from a superposition of different mode intensities, the weighting of which is taken from the experimental emission spectra. In the insets in Fig. 2.20, the asterisks at the LP_{11} and LP_{12} modes indicate a superposition of the $\cos^2(l\varphi)$ and $\sin^2(l\varphi)$ terms in (2.53) to obtain the experimentally observed azimuthally symmetric mode profiles. Increasing the current leads to a red-shift of the overall spectrum due to pronounced heating. Stronger waveguiding and photon–carrier interactions like spatial hole burning favor oscillation of shorter-wavelength modes of increasingly higher order. In general, the Gaussian fundamental mode is followed by the LP_{11} donut mode with vanishing on-axis intensity. It is seen that an excellent correspondence between measurement and calculation is obtained, supporting the applicability of the simplified Laguerre–Gaussian field approach. In fact, thermally induced index guiding is a much stronger effect than gain guiding in proton-implanted VCSELs. It has to be noted that the prediction of the emission spectra itself is a much more demanding task.

When applying a similar approach to get a simple understanding of mode propagation in oxide-confined VCSELs, the main difficulty is the identification of a suitable refractive index profile in the planar cavity. The vital role that is played by the oxide layer can be inferred from the reduction of its refractive index from about 3.0 before to only $\bar{n}_{\mathrm{ox}} \approx 1.6$ after selective oxidation [78]. The local index decrease leads to a blue-shift $\Delta\lambda_{\mathrm{ox}} < 0$ of the cavity resonance wavelength in the oxidized section with respect to the active device center. The wavelength shift can be easily determined from transfer matrix calculations and be translated into an average cavity index variation

$$\Delta\bar{n}_{\mathrm{c}} = \langle\bar{n}\rangle\Delta\lambda_{\mathrm{ox}}/\lambda, \tag{2.57}$$

where λ and $\langle\bar{n}\rangle$ denote the resonance wavelength and average refractive index before oxidation [79]. In this way, we have used a perturbation-like approach to convert the inhomogeneous index profile into that of a homogeneous step-index fiber.[10]

[10] The effect of the oxide aperture on laser mode formation can also be understood as that of a focusing lens. Since the refractive index is higher in the active area compared to the oxidized region, a phase shift is induced in the traveling wave which reduces its diffraction losses [48].

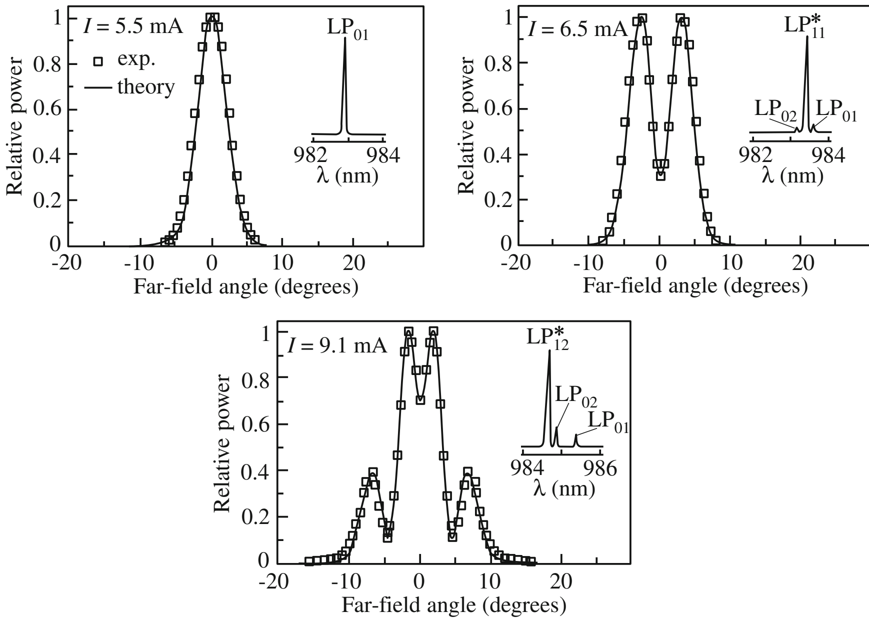

Fig. 2.20 Measured and calculated far-field distributions of a 19 μm diameter proton-implanted VCSEL as well as corresponding emission spectra for different driving currents above threshold current $I_{\mathrm{th}} = 4.9$ mA [77] (© 1995 IEEE)

Figure 2.21 shows calculated index variations for a model 980 nm VCSEL as a function of the oxide thickness d_{ox} for different positions of the oxide layer. Owing to the exponential-like decay of the longitudinal standing-wave pattern in Fig. 2.10, the detuning decreases with increasing distance from the active layers. Likewise, induced cavity index variations are larger when the oxide layer is located closer to an antinode of the electric field. On the other hand, placing the aperture right at a field node creates a weakly index-guided waveguide while still providing ideal current confinement. Intuitively it is clear that such a configuration should favor transverse single-mode emission of a VCSEL, which has indeed been proven experimentally [22]. Restrictions from oxidation technology and voltage breakdown behavior limit the minimum oxide thickness to 10–30 nm. Even with $d_{\mathrm{ox}} = 30$ nm, cavity index steps $|\Delta\bar{n}_{\mathrm{c}}|$ of just a few times 10^{-3} can be obtained. Weak-index-guiding designs and an appropriate choice of the active size have led to single-mode VCSELs like in Fig. 2.15 with output powers in the few mW range. Single-mode VCSELs are treated in much larger depth in Chap. 4 of this book.

The conversion of the longitudinally inhomogeneous refractive index profile of a VCSEL into that of a homogeneous quadratic or step-index waveguide also easily allows estimations of the transverse mode spacing $\Delta\lambda_{lp}$. From the propagation constant [80]

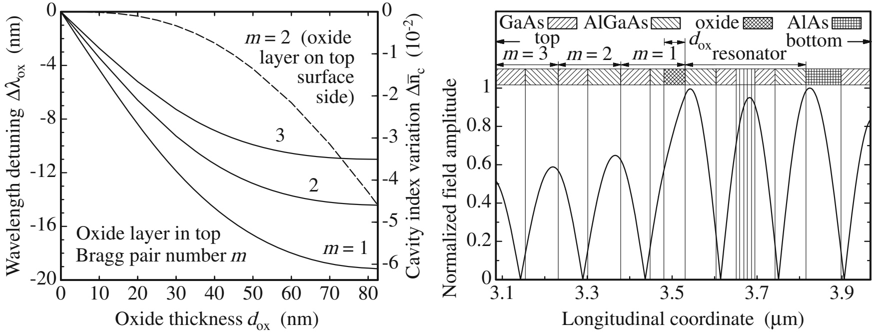

Fig. 2.21 Resonance wavelength detuning and corresponding cavity index variation versus thickness of the oxide layer that is located in the m-th Bragg pair of the VCSEL top mirror (*left*). The *dashed line* for $m = 2$ assumes an oxide layer starting at the node of the electric field. The virtual standing-wave pattern in the oxidized cavity section is illustrated in the *right-hand part* for $d_{\mathrm{ox}} = 50$ nm and $m = 1$

$$\beta_{lp} \approx \frac{2\pi \bar{n}_0}{\lambda} \left(1 - \frac{2p + l - 1}{2\pi} \frac{\lambda}{a} \frac{\sqrt{\bar{n}_0^2 - \bar{n}_a^2}}{\bar{n}_0^2} \right) \tag{2.58}$$

of a weakly guided mode in a quadratic index medium, one expects a proportionality $\Delta\lambda_{lp} \propto \lambda^2/D_{\mathrm{a}}$, whereas a step-index guide can even lead to $\Delta\lambda_{lp} \propto \lambda^3/D_{\mathrm{a}}^2$ [81]. In the first case, the characteristic profile diameter $2a$ is assumed to scale with the active diameter as $2a \propto D_{\mathrm{a}}$. As seen in Fig. 2.15, transverse mode spacings of small-diameter VCSELs can easily exceed 1 nm. In the emission spectrum, the influence of thermally induced index guiding is indicated by an increase of mode spacing with current. It should be added that any deviation of the refractive index profile (including the gain profile of the active layer) from the assumed symmetry, tracing back to, e.g., processing tolerances, thermal oxidation rates depending on the crystal orientation, induced stress, or built-in strain can break the degeneracy of modes with respect to both orientation and polarization, resulting in a more complex transverse mode spectrum. For more details, see Chap. 3 of this book.

2.4 Dynamic and Noise Behavior

Applications of VCSELs in data transmission systems rely on the dynamic and noise properties of the source. These characteristics are generally obtained from rate equations [40, 45] describing the time evolutions of electrons and photons in the laser cavity as well as their interaction. The dynamic behavior is most easily inferred from the small-signal current modulation transfer function. Noise originates from spontaneous emission whose statistic nature is expressed in the rate equations by Langevin

forces for carriers and photons. The amplitude noise is quantified by the relative intensity noise spectrum, and the phase noise is visible as a finite laser linewidth. Both processes occur in VCSELs in the same way as in EELs. For simplicity we will mostly restrict ourselves to single-mode laser oscillation and provide practical examples.

2.4.1 Rate Equations

The well-accepted laser rate equations characterize the carrier and photon reservoirs in terms of time derivatives $\mathrm{d}/\mathrm{d}t$ as

$$\frac{\mathrm{d}n}{\mathrm{d}t} = \frac{\eta_I j}{q d_\mathrm{a}} - \frac{n}{\tau_\mathrm{sp}(n)} - \Gamma_\mathrm{r} \sum_m g_m(n) N_m v_{\mathrm{gr},m} + F_n(t), \tag{2.59}$$

$$\frac{\mathrm{d}N_m}{\mathrm{d}t} = \Gamma_m \beta_{\mathrm{sp},m} \frac{n}{\tau_{\mathrm{sp,r}}(n)} + \Gamma_m \Gamma_\mathrm{r} g_m(n) N_m v_{\mathrm{gr},m} - \frac{N_m}{\tau_{\mathrm{p},m}} + F_N(t), \tag{2.60}$$

where n is the carrier (electron or hole) density and N_m is the photon density of the m-th laser mode. In regular VCSELs without extended cavity, only transverse modes with identical longitudinal mode order can oscillate. Particle densities are taken as spatial averages over the corresponding active volume V_a or the mode volume $V_{\mathrm{p},m}$. The current injection efficiency η_I was already introduced in (2.23) and (2.35).

The photon density of the considered mode is increased by spontaneous emission according to the spontaneous recombination rate $\beta_{\mathrm{sp},m} n/\tau_{\mathrm{sp,r}}$ (with the spontaneous emission factor $\beta_{\mathrm{sp},m}$ [82] and the radiative part $\tau_{\mathrm{sp,r}}$ of the spontaneous recombination lifetime according to (2.24)) and decreases due to optical losses and outcoupling, both included in the photon lifetime $\tau_{\mathrm{p},m}$. With the relative confinement factor Γ_r from Sect. 2.2.3, the stimulated emission terms in (2.59) and (2.60) take the spatial overlap between the QWs with material gain g_m and the standing-wave pattern in the resonator into account.

Corresponding to (2.20), $\Gamma_m = V_\mathrm{a}/V_{\mathrm{p},m} = \Gamma_\mathrm{l} \cdot \Gamma_{\mathrm{t},m}$ holds for the confinement factor of the m-th mode. The Langevin forces $F_n(t)$ for the electron density and $F_N(t)$ for the photon density have been added to account for the statistical nature of spontaneous emission events that are responsible for laser noise [40, 45].

In the rate equations (2.59) and (2.60) we have assumed that the laser modes do not interact and that stimulated emission takes place from an identical carrier reservoir for all modes. For the following discussion it is sufficient to restrict ourselves to the important case of single transverse mode emission, greatly simplifying the system of rate equations.[11] The modal material gain coefficient of the QWs at the spectral position of the lasing mode, which for VCSELs in general is not identical to the peak gain (see Fig. 2.17), is then approximated by

[11] Namely there is no sum anymore in (2.59), $g_m(n) \to g(n)$, $N_m \to N$, $v_{\mathrm{gr},m} \to v_\mathrm{gr}$, and there is only one equation (2.60), in which $\Gamma_m \to \Gamma$, $\beta_{\mathrm{sp},m} \to \beta_\mathrm{sp}$, and $\tau_{\mathrm{p},m} \to \tau_\mathrm{p}$.

$$g(n, N) = \frac{g(n)}{1 + \varepsilon N}, \tag{2.61}$$

where $g(n)$ was already introduced in (2.21) and (2.22). Gain compression [83] caused by spectral hole burning or carrier heating is quantified by the parameter ε.

In a more detailed rate equation model [84], transport effects are considered by assuming current injection into the barrier layers surrounding the QWs and by distinguishing between carrier reservoirs in the active QW region and in the adjacent barriers. Carrier exchange is then governed by supply and escape time constants. It is found experimentally that transport effects do not limit the VCSEL modulation speed up to frequencies of at least 20 GHz. In addition to carrier transport in the inner cavity region, the rate equations (2.59) and (2.60) neglect spatial hole-burning effects and the associated lateral carrier diffusion as well as the fact that many parameters depend on the temperature.

2.4.2 Small-Signal Modulation Response

From the rate equations we can infer the dynamic response of the VCSEL to a harmonic variation $\Delta I(t)$ of the current about an operating point $I_0 \gg |\Delta I(t)|$. The equations are first of all linearized with respect to the resulting variations $\Delta n(t)$ and $\Delta N(t)$ (which are small compared to n_0 and N_0, respectively) and after that Fourier transformed into quantities $\Delta\widetilde{I}(\nu)$, etc. to obtain the spectral fluctuations as a function of the modulation frequency ν. The carrier-dependent part of the gain coefficient is also linearized. As an example, for (2.21) we can write

$$g(n_0) = g_1 \ln \frac{n_0}{n_t} \approx \bar{a}(n_0 - \bar{n}_t) \tag{2.62}$$

with the differential gain coefficient $\bar{a}$ and the transparency carrier density $\bar{n}_t$ expressed as

$$\bar{a} = \frac{g_1}{n_0} \qquad \text{and} \qquad \bar{n}_t = n_0 \left(1 - \ln \frac{n_0}{n_t}\right). \tag{2.63}$$

The Langevin forces F_n, F_N are both set to zero since noise is not of interest here. Neglecting the spontaneous emission contribution in (2.60) owing to the small magnitude of β_{sp} [82], the resulting modulation transfer function that relates the photon density fluctuations to those of the modulating current is finally obtained as

$$H(\nu) = \frac{\Delta\widetilde{N}(\nu)}{\Delta\widetilde{I}(\nu)/q} = \frac{A}{4\pi^2(\nu_r^2 - \nu^2) + \mathrm{i}2\pi\gamma\nu} \tag{2.64}$$

with the amplitude factor

$$A = \frac{\eta_I v_{gr} \Gamma_r \bar{a} N_0}{V_p(1 + \varepsilon N_0)}, \tag{2.65}$$

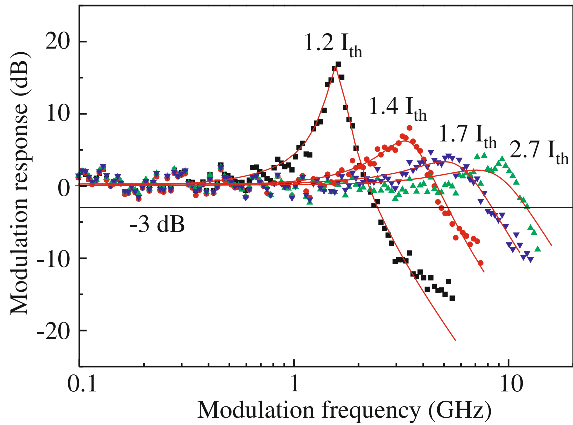

Fig. 2.22 Measured modulation transfer function $|H(\nu)|^2$ of a single-mode oxidized VCSEL for different currents above threshold current $I_{\mathrm{th}} = 1.1$ mA [86]. Solid lines are curve fits according to (2.64)

the damping coefficient

$$\gamma = \frac{1}{\tau_{\mathrm{sp}}} + AV_{\mathrm{p}} + \frac{\varepsilon N_0}{\tau_{\mathrm{p}}(1 + \varepsilon N_0)}, \tag{2.66}$$

and the resonance frequency

$$\nu_{\mathrm{r}} = \frac{1}{2\pi}\sqrt{A\frac{V_{\mathrm{p}}}{\tau_{\mathrm{p}}}\left(1 + \frac{\varepsilon}{\tau_{\mathrm{sp}} v_{\mathrm{gr}} \Gamma_{\mathrm{r}} \bar{a}}\right)} \approx \frac{1}{2\pi}\sqrt{A\frac{V_{\mathrm{p}}}{\tau_{\mathrm{p}}}}. \tag{2.67}$$

The damping coefficient can be rewritten as

$$\gamma = K\nu_{\mathrm{r}}^2 + \frac{1}{\tau_{\mathrm{sp}}} \tag{2.68}$$

with the so-called K-factor

$$K = 4\pi^2\left(\tau_{\mathrm{p}} + \frac{\varepsilon}{v_{\mathrm{gr}} \Gamma_{\mathrm{r}} \bar{a}}\right). \tag{2.69}$$

Its importance arises from the fact that the maximum 3-dB modulation corner frequency of $|H(\nu)|^2$ is related to K as [85]

$$\nu_{\max} = \sqrt{2}\frac{2\pi}{K}, \tag{2.70}$$

indicating the intrinsic modulation limit of the laser without any parasitic effects. The K-factor is usually determined by plotting the damping coefficient (2.68) as a function of the resonance frequency squared, where both γ and ν_{r} are obtained from curve fits to the measured data according to (2.64), as illustrated in Fig. 2.22.

Smallest K-factors observed for VCSELs so far are in the 0.15 to 0.2 ns range [87, 88] and 3-dB small-signal modulation bandwidths exceed 20 GHz [87]. More

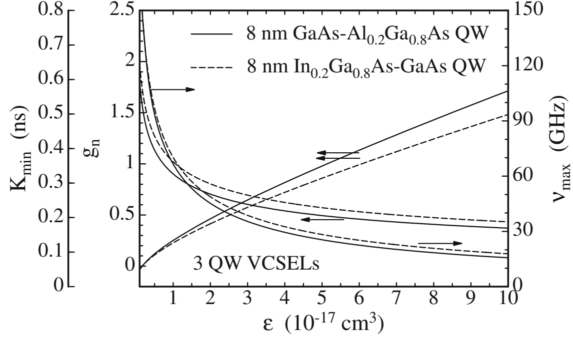

Fig. 2.23 Optimum normalized threshold gain g_n, minimum K-factor K_{min}, and corresponding modulation bandwidth ν_{max} versus the gain compression factor ε for GaAs and InGaAs three-QW VCSELs

details on the current state of the art and the design of high-speed VCSELs are found in Chap. 7 of this book. Speed-limiting effects are self-heating and the onset of multi-transverse-mode operation, where in the latter case power partitioning between the modes limits their individual photon densities. To further push the internal frequency damping limit, the K-factor has to be minimized, for which case a corresponding design rule can easily be derived. We start by writing the photon lifetime as $\tau_p = (\Gamma \Gamma_r g_{th} v_{gr})^{-1}$ in accordance with (2.18) or as obtained from (2.60) in the single-mode case when putting $d/dt = 0$ and neglecting spontaneous emission as well as the noise source. Recalling $\bar{a} = g_1/n_{th}$ with the threshold carrier density $n_{th} = n_0$ shows that there exists an optimum threshold gain g_{th} that minimizes K. Rearranging (2.62) as $n_{th} = n_t \exp\{g_n\}$ with the normalized threshold gain $g_n = g_{th}/g_1$ leads to the characteristic equation $\Gamma \varepsilon n_t g_n^2 = \exp\{-g_n\}$, from which g_n can be obtained numerically. The minimum K-factor then results as

$$K_{min} = \frac{4\pi^2}{v_{gr}\Gamma\Gamma_r g_1}\frac{g_n+1}{g_n^2} = 4\pi^2\tau_p\left(1+\frac{g_1}{g_{th}}\right). \tag{2.71}$$

Figure 2.23 shows calculated values of g_n, K_{min}, and ν_{max} for a reasonable interval of the gain compression factor ε, assuming parameters $\Gamma_t = 1$, a three-QW gain region with $d_a = 24$ nm and $\Gamma_r = 1.8$, $L_{eff} = 1.25\,\mu$m, as well as $v_{gr} = c/3.6$. As active layer, both InGaAs QWs with $n_t = 1.8 \cdot 10^{18}\,cm^{-3}$, $g_1 = 2{,}100\,cm^{-1}$ and GaAs QWs with $n_t = 2.6 \cdot 10^{18}\,cm^{-3}$, $g_1 = 2{,}400\,cm^{-1}$ [45] have been considered.

It is seen that for smaller gain compression ε, the optimum threshold gain increases, leading to a smaller K-factor and higher bandwidth, with the strained InGaAs QW system being slightly more advantageous. For $\varepsilon \approx 7 \cdot 10^{-18}\,cm^3$ with $g_n = 1$, the two terms of the sum in (2.69) or (2.71) contribute equally to the total K, whereas for higher ε the term corresponding to the gain nonlinearity prevails. The preceding discussion has shown that, equivalent to EELs [83], the optimum VCSEL cavity design for high-speed operation is closely related to nonlinear gain properties of the active layer, which have thus to be taken into account to obtain maximum internal modulation capability of the device. Minimizing nonlinearities is certainly helpful. A step in this direction can be taken by applying p-type doping of the QWs,

thus decreasing the contribution of spectral hole burning [89, 90]. Doping also assists to increase the differential gain, which is beneficial for the K-factor (2.69).

For applications in optical communications, it is of much interest to obtain high modulation bandwidths for small operating currents. Taking the approximation for ν_r in (2.67), neglecting gain compression and relating the photon density N_0 to the output power P as $\hat{\eta}_\mathrm{d} N_0 V_\mathrm{p} \hbar\omega = \tau_\mathrm{p} P$, we obtain the expression

$$\nu_\mathrm{r} \approx \frac{1}{2\pi}\sqrt{\frac{v_\mathrm{gr}\Gamma_\mathrm{r}\bar{a}P}{\hbar\omega\hat{\eta}_\mathrm{d}V_\mathrm{p}}} = \frac{1}{2\pi}\sqrt{\frac{\eta_I v_\mathrm{gr}\Gamma_\mathrm{r}\bar{a}}{qV_\mathrm{p}}} \cdot \sqrt{I - I_\mathrm{th}} = D \cdot \sqrt{I - I_\mathrm{th}}, \tag{2.72}$$

where furthermore (2.34) and (2.35) have been used. In semiconductor laser literature, the proportionality factor is often denoted as D-factor. As another figure of merit, the modulation current efficiency factor (MCEF) specifies the increase of the 3-dB corner frequency of $|H(\nu)|^2$ as

$$\mathrm{MCEF} = \frac{\nu_\mathrm{3dB}}{\sqrt{I - I_\mathrm{th}}}. \tag{2.73}$$

In the case of sufficiently low damping with $\gamma^2 \ll 8\pi^2\nu_\mathrm{r}^2$, one would expect a relation $\mathrm{MCEF} \approx \sqrt{1+\sqrt{2}}D \approx 1.55D$ which is usually not observed in practice (see, e.g., [87]). It is important to note from (2.72) that one should keep the differential gain high and the cavity volume $V_\mathrm{p} = L_\mathrm{eff}A_\mathrm{a}$ low in order to maximize the modulation efficiency. MCEFs exceeding $14\,\mathrm{GHz}/\sqrt{\mathrm{mA}}$ have already been reported [87], indicating that VCSELs can achieve modulation speeds in the multi-GHz regime even if driven only slightly above threshold.

Deviations from an ideal damping-limited modulation behavior especially occur due to parasitic elements found in the equivalent electric circuit of the laser. They can be accounted for by a parasitic modulation transfer function $H_\mathrm{p}(\nu)$, converting $H(\nu)$ from (2.64) into the total response

$$H_\mathrm{t}(\nu) = H(\nu) \cdot H_\mathrm{p}(\nu). \tag{2.74}$$

Even if bond wire and track inductances and bondpad capacitances are kept low, the RC low-pass filter composed of the ohmic series resistance R and the capacitance C (related to the etched mesa in oxide-confined VCSELs) can impose a serious frequency limit. In this simple case, $H_\mathrm{p}(\nu)$ is just expressed as $1/(1 + \mathrm{i}\nu/\nu_\mathrm{p})$ with $\nu_\mathrm{p} = 1/(2\pi RC)$. Elements of the equivalent circuit can conveniently be deduced from microwave impedance measurements [86, 87, 91]. Even if more than two elements are involved, $H_\mathrm{p}(\nu)$ can often be well approximated by a first-order low-pass [91] with the characteristic parameter ν_p. In total, the measured small-signal response of the VCSEL is approximated by the fit function

$$|H_\mathrm{t}(\nu)|^2 = \frac{B\nu_\mathrm{r}^4}{(\nu_\mathrm{r}^2 - \nu^2)^2 + (\gamma\nu/(2\pi))^2} \cdot \frac{1}{1 + (\nu/\nu_\mathrm{p})^2} \tag{2.75}$$

with the constant B. A parasitic first-order low pass with a 3-dB frequency $1/(2\pi\tau_\mathrm{s})$ is also expected from transport effects mentioned at the end of Sect. 2.4.1, where τ_s is the supply time constant [84].

2.4.3 Relative Intensity Noise

The spectral relative intensity noise (RIN) relates the photon density fluctuations to the mean photon density squared as [57]

$$\mathrm{RIN}(\nu) = 2\Delta\nu \frac{\langle|\Delta\widetilde{N}(\nu)|^2\rangle}{\langle N\rangle^2} = 2\Delta\nu \frac{\langle|\Delta\widetilde{P}(\nu)|^2\rangle}{\langle P\rangle^2} = 2\Delta\nu \frac{\langle|\Delta\widetilde{I}_{\mathrm{PD}}(\nu)|^2\rangle}{\langle I_{\mathrm{PD}}\rangle^2}, \tag{2.76}$$

where $\Delta\nu$ is the filter bandwidth, and the angular brackets denote an average over the observation time. $\mathrm{RIN}(\nu)$ is measured in units of dB/Hz. In (2.76) we have employed the proportionality between spectral components of photon density $\Delta\widetilde{N}(\nu)$, output power $\Delta\widetilde{P}(\nu)$, and detector photocurrent $\Delta\widetilde{I}_{\mathrm{PD}}(\nu)$ (assuming a large enough detector bandwidth) and correspondingly for the mean values $\langle N\rangle$, $\langle P\rangle$, and $\langle I_{\mathrm{PD}}\rangle$. In contrast to the previous section, here we assume the photon density to be modulated by spontaneous emission processes instead of the external current. Thus we put $\Delta\widetilde{I}(\nu) = 0$ after linearization and Fourier transformation of the single-mode versions of (2.59), (2.60) and insert proper expressions [40, 45] for the Langevin forces F_n, F_N. This leads to the result

$$\mathrm{RIN}(\nu) = \frac{4\beta_{\mathrm{sp}}\Gamma n_0}{\tau_{\mathrm{sp}}\langle N\rangle} \frac{4\pi^2\nu^2 + \gamma^{*2}}{16\pi^4(\nu_{\mathrm{r}}^2 - \nu^2)^2 + 4\pi^2\gamma^2\nu^2} \tag{2.77}$$

with the modified damping coefficient

$$\gamma^* = \gamma - \frac{\varepsilon\langle N\rangle}{\tau_{\mathrm{p}}(1+\varepsilon\langle N\rangle)} \approx \frac{1}{\tau_{\mathrm{sp}}} + 4\pi^2\nu_{\mathrm{r}}^2\tau_{\mathrm{p}}, \tag{2.78}$$

where we have used (2.66) and the approximation in (2.67) to obtain the expression on the right-hand side of (2.78) and more appropriately have written $\langle N\rangle$ instead of N_0 in conjunction with noise processes. Other than the modulation transfer function (2.75), $\mathrm{RIN}(\nu)$ does not include a parasitic roll-off term (since the laser is driven by a continuous-wave current) and also carrier transport effects play no role. Relative intensity noise measurements can therefore be employed to characterize intrinsic dynamic properties of laser diodes [91].

For small resonance frequencies we can approximate $\gamma^* \approx (\tau_{\mathrm{sp}})^{-1}$ in (2.78) to obtain a decrease of the RIN according to

$$\mathrm{RIN}(\nu) \propto \langle N\rangle^{-3} \propto \langle P\rangle^{-3} \qquad \text{for } \nu \ll \nu_{\mathrm{r}}, \tag{2.79}$$

since $\nu_{\mathrm{r}}^2 \propto \langle N\rangle$ for $\varepsilon\langle N\rangle \ll 1$. For large ν_{r}, i.e., far above threshold, we can neglect $(\tau_{\mathrm{sp}})^{-1}$ in (2.78), and the RIN only decreases as

$$\mathrm{RIN}(\nu) \propto \langle N\rangle^{-1} \propto \langle P\rangle^{-1}. \tag{2.80}$$

In the above treatment we have not considered that the emitted wave consists of single quanta of energy $\hbar\omega$, which, for thermal or ideally coherent radiation, are distributed

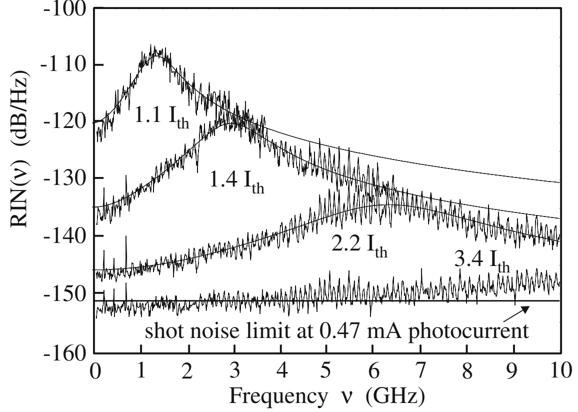

Fig. 2.24 Measured RIN spectra of a single-mode, single-polarization oxide-confined VCSEL for different pumping levels above threshold current $I_{\text{th}} = 0.5$ mA. The measurement system noise level is 2.5 dB below the shot noise level for 0.47 mA photocurrent. Theoretical curves are drawn as solid lines [93]

according to Poisson's statistics. In other words, we have to include the well-known fact that the quantum nature of light is the cause of the shot noise contribution in the photodetector, leading to a quantum noise limit of the RIN according to

$$\text{RIN}_{\text{Q}} = \frac{2q}{\langle I_{\text{PD}} \rangle} = \frac{2\hbar\omega}{\eta_{\text{PD}} \langle P \rangle} \tag{2.81}$$

with the detection efficiency η_{PD}. Concerning RIN measurements with a regular photodiode, we have to add the term (2.81) to the classical expression (2.77). For a mean photocurrent $\langle I_{\text{PD}} \rangle = 1$ mA, the quantum noise limit is found at -155 dB/Hz and can fall below only for non-Poissonian (squeezed) light [92]. It is now seen that the dependence $\text{RIN}(\nu) \propto \langle P \rangle^{-1}$ has to be considered as a fundamental limit although it was earlier obtained for a rather special case.

The predicted spectral behavior of the RIN is experimentally observed for single-mode VCSELs with high side-mode suppression, as indicated in Fig. 2.24 [93]. Above threshold, the noise level rapidly decreases with increasing current, and the resonance frequency is shifted beyond 10 GHz. At a current of only 1.7 mA, corresponding to 1 mW optical output power, the shot noise level of the detecting system is reached over almost the entire frequency interval from 0 to 10 GHz. For still higher currents, higher-order modes start to oscillate and mode competition severely increases the laser noise. Deteriorations of the RIN spectrum are also observed if lasing on the orthogonally polarized fundamental mode sets in.

2.4.4 Emission Linewidth

It is well known [40, 45, 94] that statistical phase fluctuations of the electric field introduced by spontaneous emission processes are responsible for the finite linewidth of laser diode oscillation. The spectral power density of a single-mode laser emission line is well approximated by the Lorentzian line-shape function

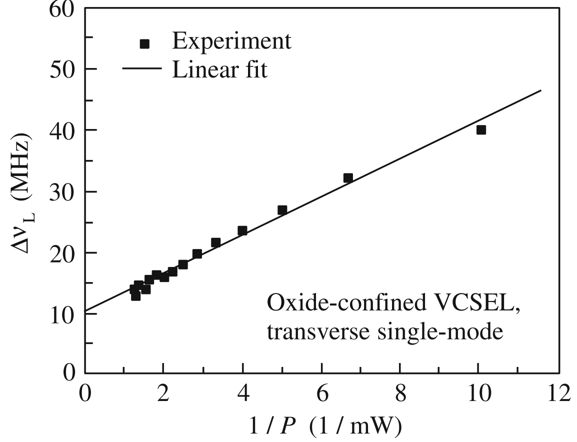

Fig. 2.25 Emission linewidth of a single-mode VCSEL as a function of the inverse optical output power P

$$|\widetilde{E}(\nu)|^2 = |\widetilde{E}(\nu_m)|^2 \frac{(\Delta\nu_{\mathrm{L}}/2)^2}{(\Delta\nu_{\mathrm{L}}/2)^2 + (\nu - \nu_m)^2} \tag{2.82}$$

with ν_m denoting the center frequency of the mode and $\Delta\nu_{\mathrm{L}}$ is the full linewidth at half maximum. The linewidth is given by

$$\Delta\nu_{\mathrm{L}} = \frac{\beta_{\mathrm{sp}} \Gamma \langle n \rangle}{4\pi \tau_{\mathrm{sp}} \langle N \rangle}(1 + \alpha_{\mathrm{H}}^2), \tag{2.83}$$

where α_{H} is the linewidth enhancement factor (also called Henry factor) that typically takes values between −2 and −7. As an example $\alpha_{\mathrm{H}} = -5$ has been determined for a single-mode proton-implanted 960 nm VCSEL [95].

Figure 2.25 shows measured linewidths for a single-mode oxide-confined VCSEL of about 4 µm diameter. As expected from (2.83), the linewidth increases linearly with inverse output power. However, a residual linewidth of $\Delta\nu_0 = 11$ MHz is observed for the extrapolation $P \to \infty$, which is attributed to mode competition with not perfectly suppressed side-modes or perhaps 1/*f*-noise contributions, similarly to EELs [57]. Considering the experimentally found residual linewidth $\Delta\nu_0$, relation (2.83) is rewritten as

$$\Delta\nu_{\mathrm{L}}^* = \Delta\nu_{\mathrm{L}} + \Delta\nu_0. \tag{2.84}$$

The onset of higher transverse order modes at higher currents generally leads to an increase of the fundamental mode linewidth due to the reduction of modal power, although the total power is still increasing. As seen in Fig. 2.25, VCSEL linewidths are usually in the some 10 MHz range [95, 96] but also just a few MHz have been reported [97].

Owing to their convenient, mode-hop-free tunability via the operating current, high modulation bandwidths, and sufficiently low linewidths, single-mode VCSELs

are good candidates for nonlinear spectroscopy [98] (and its use in optical interrogation for atomic sensors like clocks [91, 99] or magnetometers [100]) or gas sensing, with oxygen sensors operating in the 760 nm wavelength region as a prominent example [101–103]. Gas sensing with long-wavelength VCSELs is discussed in Chap. 10 of this book. In particular for optical sensing it is important to stabilize the polarization of VCSEL emission. This can be conveniently done by monolithically incorporating a surface grating [104]. Chapters 5 and 6 of this book are entirely devoted to polarization control and dynamics of VCSELs, respectively.

2.5 VCSEL-Based Optical Interconnects

In this section we discuss some aspects of VCSEL applications in optical interconnects and illustrate selected results of data transmission experiments. The term *optical interconnects* refers to information transport systems with short transmission distances and is thus to be distinguished from the optical telecommunication (often just "telecom") business. Sometimes the term *optical datacom* is used synonymously. Maximum distances are several hundred meters or at most very few kilometers, as required for in-building cabling or local-area networks with somewhat longer reach. On the other extreme, distances down to some centimeters are considered for the anticipated optical data transmission between or even within electronic integrated circuits. The optical pathway mostly consists of multimode waveguides. However, also free-space propagation is included, which in practice is either commercially applied on an inter-building distance level [105] or evaluated on the length scale of electronic multi-chip modules [106, 107]. Usually optical interconnect applications are very cost sensitive.

Among the attractive features of VCSELs for short-distance fiber transmission are low driving power, high-speed current modulation for multi-Gbit/s data generation, simple mounting technology similar as for light-emitting diodes, and parallel arrangements in one- or two-dimensional arrays. The performance of data links is commonly characterized by bit error ratio (BER, often called bit error rate) measurements [108]. Stringent demands for BERs of less than 10^{-12} or even down to 10^{-15} are required in computer interconnects. As described in Chap. 16 of this book, high aggregate bit rates are most easily achieved with parallel links making use of optical fiber ribbons, where bit rates of individual channels currently are in the 10 Gbit/s range and will soon exceed 20 Gbit/s [109, 110]. Since their emission wavelength can be adjusted during epitaxial growth, VCSELs are well suited for wavelength division multiplexing transmission [111], which has been exploited in optical telecommunications for many years. This advanced technique is expected to be unleashed in future generations of optical interconnect modules. VCSEL-based optical links are not only established with graded-index multimode fibers with lengths of a few meters up to a few hundred meters but more and more extend into the realm of optical backplanes, hybrid printed circuit boards, and multi-chip modules [112, 113].

2.5.1 Fiber Coupling

VCSEL radiation can be very efficiently coupled into optical fibers. Mostly, simple microoptics is used but also quasi or direct butt coupling can be employed, taking advantage of the circularly symmetric emission profile. Assuming Gaussian field distributions $E(r) \propto \exp\{-(r/w_{\mathrm{l,f}})^2\}$ for both the laser emission and the guided fiber mode with spot radii w_{l} and w_{f}, respectively, one can analytically calculate the power coupling efficiency η_{fc} for the general case of longitudinal displacement, radial offset, as well as tilt [114]. Without any misalignment, one finds $\eta_{\mathrm{fc}} = 4/(w_{\mathrm{l}}/w_{\mathrm{f}} + w_{\mathrm{f}}/w_{\mathrm{l}})^2$. Possible Fresnel reflection losses have not been taken into account. For a standard single-mode fiber with $2w_{\mathrm{f}} = 9\,\mu\mathrm{m}$, one expects coupling efficiencies exceeding 50% for single-mode VCSEL spot diameters $2w_{\mathrm{l}} \geq 3.8\,\mu\mathrm{m}$ or $\eta_{\mathrm{fc}} > 80\%$ for $2w_{\mathrm{l}} \geq 5.6\,\mu\mathrm{m}$. In these examples, no upper limits have been specified since VCSELs tend to emit higher-order transverse modes for large active diameters. Also it has to be noted that the assumed fiber carries two guided LP modes in the wavelength range between 800 and 1,000 nm discussed in this chapter, so that special measures like fiber mode filtering have to be taken in order to avoid intermodal dispersion limitations [115]. For sufficiently stable coupling arrangements, index matching fluid or fiber antireflection coating do not necessarily have to be applied with up to a few $10\,\mu\mathrm{m}$ wide air gaps, since the fiber end-face only slightly alters the properties of the highly reflective outcoupling mirror and thus the VCSEL threshold. Experimentally, a $\lambda = 980\,\mathrm{nm}$ proton-implanted VCSEL with about $4\,\mu\mathrm{m}$ spot diameter has been butt-coupled to a true single-mode fiber with $4.5\,\mu\mathrm{m}$ core diameter with a coupling efficiency of larger than 80% [116]. Coupling a single-mode VCSEL to a graded-index multimode fiber with $50\,\mu\mathrm{m}$ core diameter and a numerical aperture of 0.2 is easily obtained with $\eta_{\mathrm{fc}} > 80\%$. Multimode sources may show reduced fiber coupling efficiencies [117]. In the general case, the evaluation of VCSEL-to-fiber coupling efficiencies requires the calculation of all mode overlap integrals [40]. An additional difficulty lies in the fact that the modal power distribution of multimode VCSELs usually rapidly changes with the bias current.

2.5.2 Large-Signal Modulation Effects

Up to now we have discussed the dynamic VCSEL behavior in terms of small-signal modulation. The analytic solutions obtained provide important insight into the scaling behavior of the laser parameters. However, for digital modulation, large-signal effects come into play, which have to be considered for system design. To analyze large-signal behavior numerically, the time-dependent rate equations (2.59), (2.60) have to be solved (perhaps even in extended from to include lateral variations of particle densities as well as carrier diffusion). For systems employing single-mode

VCSELs, mainly three effects have an impact on the modulation performance and have been investigated experimentally in [86].

- As the first one, *turn-on delay* occurs if the VCSEL is biased below threshold and time is needed to build up the threshold carrier density in the active layer. Especially for bias-free operation [118], turn-on delays exceeding 100 ps are easily observed. In general, low threshold currents of VCSELs are very advantageous and bias-free data transmission at 2.5 Gbit/s data rate over 500 m of multimode fiber has been demonstrated [119] (see Fig. 2.26). However, for practical applications in low-cost uncooled modules, error-free transmission has to be ensured over a wide ambient temperature range. This can hardly be accomplished since the threshold current and thus the turn-on delay vary with temperature. Bias-free operation at 10 Gbit/s is not viable. Normally, the off-state bias is always set slightly above threshold.
- *Turn-on jitter* as the standard deviation of the turn-on delay is caused by fluctuations due to spontaneous emission and is found to be in the 10 ps range for single-mode VCSELs, thus imposing no limit even for 10 Gbit/s systems.
- Finally, so-called *pattern effects* which are caused by a memory-like behavior of the carrier reservoir and result in cavity build-up time variations play a major role in practice, even for bias points above threshold. To minimize bit pattern effects, it is desirable to have a very fast VCSEL response (small rise and fall times), i.e., high resonance frequencies in both the logical on- and off-states. Unfortunately, this rule interferes with the demand for high extinction ratios in the optical signal (see next section), so that optimum operating conditions have to be chosen.

It has to be mentioned that also the noise behavior can be quite different for large-signal modulation, especially if transverse modes of different order or polarization are only weakly suppressed and mode competition comes into play.

2.5.3 High-Speed Optical Data Transmission

In digital optical transmission, the bit error ratio is expressed as a function of the Q-factor by the well-known formula [108]

$$\mathrm{BER} = \frac{1}{2}\mathrm{erfc}\left(\frac{Q}{\sqrt{2}}\right) \approx \frac{1}{\sqrt{2\pi}\,Q}\exp\left\{-\frac{Q^2}{2}\right\}\left(1-\frac{1}{Q^2}\right) \tag{2.85}$$

with the complementary error function erfc, which is valid for Gaussian statistics of the logic level fluctuations. As examples, $Q = 6$ corresponds to $\mathrm{BER} = 10^{-9}$ and for $Q = 7$ one obtains $\mathrm{BER} = 1.3 \cdot 10^{-12}$. Denoting the average received power at the photodetector by $\langle P \rangle$ and the variance of the current noise by $\langle \delta I_\mathrm{N}^2 \rangle$ (including, among others, the thermal photodetector noise and the amplifier noise as the main contributions), the parameter Q is written as

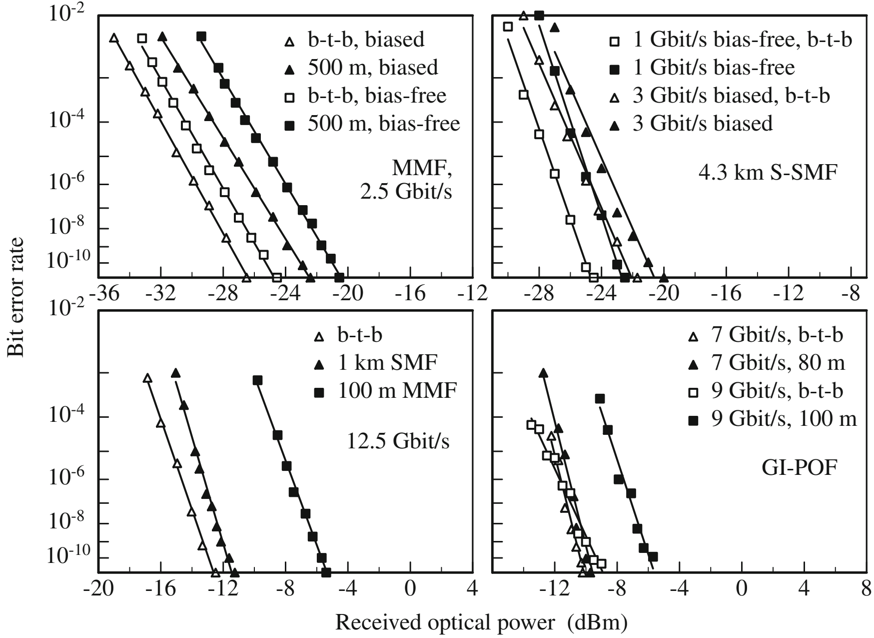

Fig. 2.26 Bit error rate performance as a function of received optical power for data transmission with oxide-confined single-mode VCSELs over various types of fiber as well as corresponding back-to-back (b-t-b) measurements. *Top left*: Biased and bias-free 2.5 Gbit/s transmission over 500 m MMF at 840 nm [119]. *Top right*: 3 Gbit/s biased and 1 Gbit/s bias-free transmission over 4.3 km standard single-mode fiber (S-SMF) at 820 nm [115] (© 1998 IEEE). *Bottom left*: 12.5 Gbit/s transmission over 100 m MMF and 1 km of 5 µm core diameter SMF at 850 nm [86] (© 1999 IEEE). *Bottom right*: 9 Gbit/s over 100 m GI POF at 830 nm and 7 Gbit/s over 80 m GI POF at 935 nm wavelength [153]

$$Q = \frac{\eta_e \eta_{PD} \langle P \rangle / (\hbar\omega)}{\sqrt{\langle \delta I_N^2 \rangle} / q} = \eta_e \frac{\langle I_{PD} \rangle}{\sqrt{\langle \delta I_N^2 \rangle}} \tag{2.86}$$

(cf. with (2.81) for η_{PD}, $\langle I_{PD} \rangle$, $\langle P \rangle$), where $\eta_e = (1 - r_{01})/(1 + r_{01})$ denotes an extinction efficiency of the optical signal, with $r_{01} = \langle I_0 \rangle / \langle I_1 \rangle$ being the ratio between average photocurrents in the off- and on-state. Vanishing modulation depth results in $\eta_e = 0$, whereas $\eta_e = 1$ is obtained for modulation down to the threshold current. Combining (2.85) and (2.86) gives a characteristic relation between BER and average received power $\langle P \rangle$. For sufficiently high Q, the Gaussian term in (2.85) dominates, and a plot of measured log(log(BER)) versus $\langle P \rangle$ (in dBm) is expected to result in a straight line.

Figure 2.26 summarizes the BER performance obtained for various single-mode VCSEL links employing multimode fiber (MMF) or single-mode fiber (SMF), all showing quasi error-free operation with BERs in the 10^{-11} range without indication of error floors. The combination of single-mode VCSEL and MMF has been dis-

cussed quite controversially due to modal noise related issues, and often the use of low coherence multimode VCSELs is suggested [120, 121]. However, at least for point-to-point interconnects or if small mode-selective transmission loss is present, the noise performance of fiber interconnects with single-mode VCSELs is found to be superior to those with multimode sources simply because mode competition noise in the laser does not occur. The large mode field mismatch moreover may lead to notably decreased sensitivity with regard to distant optical feedback [122].

In each part of Fig. 2.26 we compare the BER at the end of the fiber with back-to-back (b-t-b) measurements. The upper left diagram demonstrates biased as well as bias-free 2.5 Gbit/s data transmission over 500 m MMF (50 μm core diameter) using a nearly single-mode 840 nm VCSEL with 400 μA threshold current, where in the latter case modulation signals with 2 V peak-to-peak amplitude from a 50 Ω impedance pattern generator are applied [119]. Owing to lower average power consumption and less complex driving circuits, bias-free operation might be of interest for some niche applications but is generally limited by turn-on delay effects (see Sect. 2.5.2). The upper right diagram presents 3 Gbit/s biased and 1 Gbit/s bias-free data transmission results over 4.3 km of standard SMF with 8.3 μm core diameter [115]. At the emission wavelength of 820 nm, the fiber is operated in a dual-mode guiding regime, so that higher-order LP_{11} fiber mode filtering had to be applied to overcome intermodal dispersion limitations. Owing to weaker LP_{11} mode guiding, this transmission scheme is more easy to implement with 980 nm InGaAs QW-based lasers. Since 1.3 and 1.55 μm long-wavelength VCSELs are meanwhile available, the use of short-wavelength VCSELs in combination with SMFs is not much considered anymore. The lower left diagram displays results of 12.5 Gbit/s data transmission over 100 m MMF with 50 μm core diameter and 1 km of 5 μm diameter SMF with an 850 nm VCSEL [86]. Experiments at the same data rate have also been performed with a 980 nm VCSEL over 1.6 km standard SMF [86], where constraints were imposed by the available fiber length rather than fiber attenuation or dispersion effects. It is seen that MMF power penalties are considerably higher than those for SMF transmission as a result of intermodal dispersion and associated intersymbol interference. Although 10 Gbit/s operation over 500 m of 50 μm MMF was demonstrated as early as 1996 [123] (in this case with a 980 nm proton-implanted VCSEL), such experiments suffered from the lack of graded-index fibers with high bandwidth–distance products, providing alignment-tolerant power launch and decreased power penalties. Triggered by the work toward a 10-Gigabit Ethernet (10-GbE) standard[12] initiated in March 1999, such fibers with 50 μm core diameter and a bandwidth–distance product $B \cdot L$ exceeding 2 GHz· km in the 850 nm wavelength range have indeed been developed and have entered the market in the first few months of the year 2000.[13] In [125] (see also [112]), 10 Gbit/s data transmission over up to 1.6 km of high-performance

[12] IEEE Standard 802.3ae-2002, IEEE, Piscataway, NJ, USA, June 2002. See URL http://www.ieee802.org/3/ae/.

[13] In this case one speaks of OM3-grade fibers which guarantee 10 Gbit/s data transport over distances of at least 300 m [124]. Even more modern OM4-grade fibers have $B \cdot L \geq 4{,}700\,\text{MHz} \cdot \text{km}$ with $L \geq 550$ m at 10 Gbit/s.

MMF incurring less than 3 dB power penalty is reported. A single transverse mode VCSEL emitting at 830 nm was employed to circumvent the chromatic dispersion limit imposed by the high dispersion coefficient that exceeds 100 ps/(km · nm) in the short-wavelength regime. Moreover, this experiment took advantage of a transimpedance amplifier-based and MMF-compatible PIN-photodiode-based receiver with close to −18 dBm sensitivity, by which the high optical power levels seen in Fig. 2.26, largely arising from thermal noise of regular PIN-photodiodes, could be overcome. With a longer spool of almost ideal quality fiber, 10 Gbit/s transmission over even 2.8 km was possible [126].

Recently, a lot of progress was witnessed in the field of high-speed MMF transmission, including comprehensive link modeling [127]. Examples for high-bandwidth links using modern MMF are 15.6 Gbit/s transmission over 1 km in the 850 nm wavelength range with a directly modulated VCSEL [128], 40 Gbit/s over somewhat more than 400 m at 1270 . . . 1310 nm [129], and 40 Gbit/s over 3.4 km at 1,550 nm [130], where the two latter experiments employed externally modulated laser sources. Alternative research on high-capacity MMF transmission is motivated by the desire to use the installed low-bandwidth fiber base instead of investing in a new fiber infrastructure. Apart from the fiber cost, the special encircled flux conditions [131–133] for launching the light into the OM3 fiber add some complexity to the transceiver design. Subcarrier multiplexing [134] and in particular electronic dispersion compensation (EDC) have been successfully investigated. EDC by means of electronic equalization is usually applied after photodetection [135–140] but is expected to yield further improvements when implemented at the transmitter side of the link [141]. EDC is already incorporated in the 10-GbE standard[14] to allow link lengths of at least 220 m using MMFs with a bandwidth–distance product of 500 MHz · km. Moreover, mode group diversity multiplexing, i.e., parallel transmission using different groups of modes [142–144], spatially resolved detection with a segmented photodiode [145], the use of spatial light modulator-based adaptive optics to control the field launched into the MMF [146, 147], and even the combination of a conventional MMF and a dispersion-compensating MMF with an individually matched graded-index profile have been proposed [148]. In [149] it is pointed out that the integrated circuits required for signal processing, error correction and control methods have high power consumption, introduce latency and increase the cost. Thus direct detection and space-parallel transmission is usually more competitive for short-distance applications.

Similar to long-haul data transmission over single-mode fibers in the 1.55 μm wavelength window, wavelength division multiplexing (WDM) is another viable option to upgrade a MMF link. However, instead of dense WDM with narrow channel spacing in the 100 GHz regime, coarse WDM systems with several nm spacing to obviate the need for active wavelength stabilization are considered for low-cost MMF links. An integrated coarse WDM module that operates in the 820–865 nm wavelength interval and enables 4 × 2.5 Gbit/s data throughput over 100 m MMF

[14] IEEE Standard 802.3aq-2006, Clause 68, "10GBASE-LRM" (long reach multimode), IEEE, Piscataway, NJ, USA, Sept. 2006. See URL http://www.ieee802.org/3/aq/.

with 62.5 μm core diameter has been demonstrated in [150], whereas 8 × 155 Mbit/s have been transmitted in the 780–860 nm wavelength range over 2 km of 160 MHz·km low-bandwidth MMF in [151]. Even a first 40 Gbit/s system featuring four 815 to 835 nm high-speed single-mode VCSEL channels has been reported in [111] (see also [112]), where transmission over 310 m was made possible by a new high-bandwidth MMF.

Since the year 2005, the demand for 10 Gbit/s transport according to the 10-GbE standard has increased considerably [152], where MMF-based solutions have main applications in central offices and fiber-cabled backplanes of high-throughput switching systems. Future MMF developments are likely to target CWDM systems with increasing channel count and an aggregate data rate exceeding 100 Gbit/s. Channel data rates can be expected to lie in the 10–40 Gbit/s range and VCSELs as the signal source will remain the preferred choice.

As another fiber option, the bottom right diagram of Fig. 2.26 illustrates VCSEL-based data transmission over plastic optical fiber (POF). In particular, these are high-bandwidth graded-index (GI) POFs with 130 μm core diameter (9 Gbit/s transmission over 100 m distance at 830 nm wavelength) and 155 μm core diameter (7 Gbit/s over 80 m at 935 nm) [153] (see also [112]). Both fibers are made of perfluorinated material, showing promising attenuation coefficients below 50 dB/km over a wide spectral range, similar to losses of silica glass fibers in their early days. Minimum losses are in the 20 dB/km range. Although being among the best figures of merit reported so far [154], the achieved data throughput of 9 Gbit/s over 100 m is, however, much below the benchmark of today's OM3- or OM4-grade MMFs. Compared to previous projections by the POF community, the adoption of such fibers is far behind the expectations. Main graded-index POF installations are found in Japan. Very recently, 40 Gbit/s transmission over 100 m of a 50 μm core diameter GI POF was demonstrated using a 1,325 nm wavelength externally modulated Fabry–Pérot laser [155] (see also [156]), which may to some degree revive the interest in this fiber technology.

In contrast, the 1 mm diameter step-index PMMA POF has a high potential for very widespread use in short-distance, Gbit/s-range interconnects, e.g., in optical home networking. Owing to very high fiber losses at usual datacom wavelengths, the 650 nm wavelength range is preferred. More information on this topic is provided in Chap. 12 of this book, dealing with red-emitting VCSELs.

Figure 2.27 finally shows new concepts of AlGaAs-based transceiver chips suited for 850 nm range bidirectional optical data transmission over multimode fiber. The layer structures of metal–semiconductor–metal (MSM) or PIN-type photodiodes are monolithically grown over the VCSEL layers followed by selective material removal for individual contacting. The fibers can be butt-coupled to the chips, thus avoiding any external optics. Suitable fiber diameters range from 200 μm down to 50 μm. As an example, data rates of 2.5 Gbit/s were transmitted over 50 m of a 100 μm core diameter graded-index MMF in full-duplex mode [157]. More recently, half-duplex transmission of 9 Gbit/s in back-to-back mode and of 7 Gbit/s over a 500 m long 50 μm core diameter fiber was shown, both with a VCSEL–PIN photodiode

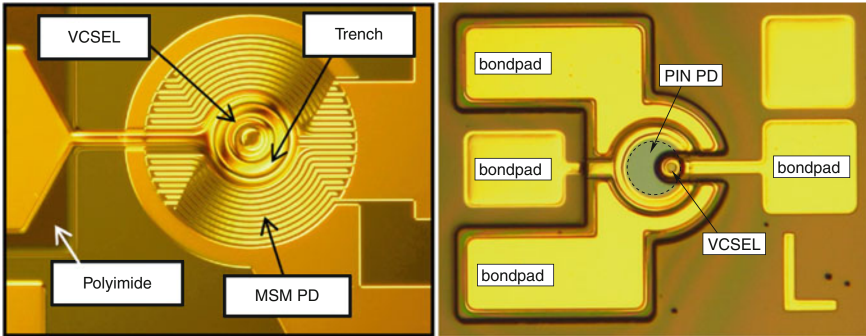

Fig. 2.27 *Left*: Transceiver chip consisting of an MSM photodiode with 110 μm diameter and a top-emitting 850 nm VCSEL at center position. Metal finger width and spacing are 1 and 2 μm, respectively. *Right*: Transceiver chip with a PIN-type photodiode with an active diameter of 73 μm and an off-center VCSEL. The dashed circle indicates the core of a 62.5 μm OM1-grade MMF [157]

chip [158]. Full-duplex operation could be demonstrated up to 8 Gbit/s back-to-back and 6 Gbit/s over 500 m of OM3 fiber [159].

2.6 Conclusion

The previous discussion has shown that oxide-confined VCSELs exhibit excellent properties with regard to threshold current, emission spectrum, temperature characteristics, as well as dynamic and noise behavior. The given analysis provides important guidelines for optimizing the device performance. Multimode VCSELs can provide tens of milliwatt output power and can be combined in two-dimensional arrays to generate Watt-level outputs from small-area chips. Continuous-wave operation at 180°C ambient temperature has been demonstrated, where material-dependent gain and carrier loss from the active region are limiting effects. Polarization-controlled single-mode devices with side-mode suppression ratios exceeding 30 dB and few-100 μA threshold currents show power conversion efficiencies above 30% in the below-1 mW range of interest for optical interconnection.

Datacom applications of VCSELs exploit the displacement-tolerant fiber coupling capabilities and the high modulation current efficiency of the source. Quasi error-free data transmission rates above 10 Gbit/s over single-mode fiber and silica glass or plastic optical multimode fiber have been obtained using linearly polarized single-mode VCSEL emission. Single-frequency devices have been shown to reach the shot noise limit of the relative intensity noise spectrum at milliwatt power levels over a frequency range exceeding 10 Gbit/s system requirements.

The results indicate that VCSELs in many respects outperform edge-emitting laser diodes. For at least ten years, these devices are the dominating transmitter

source for commercial high-speed optical interconnects operating preferentially at 850 nm wavelength. Other applications like parallel-optical links, 1.3 and 1.55 μm long-wavelength data transmission, surface or gas sensing, printing, or optical pumping are all covered in this book.

Acknowledgments The author would like to thank all former and present members of the VCSEL team of Ulm University for many years of successful device and systems research.

References

1. K. Iga, F. Koyama, S. Kinoshita, Surface emitting semiconductor lasers. IEEE J. Quantum Electron. **24**, 1845–1855 (1988)
2. K. Iga, Surface-emitting laser—its birth and generation of new optoelectronics field. IEEE J. Select. Topics Quantum Electron. **6**, 1201–1215 (2000)
3. K. Iga, Vertical-cavity surface-emitting laser: its conception and evolution. Jpn. J. Appl. Phys. **47**, 1–10 (2008)
4. R. Szweda, VCSEL applications diversify as technology matures. III-Vs Rev. **19**(1), 34–38 (2006)
5. T.E. Sale, *Vertical Cavity Surface Emitting Lasers* (Research Studies Press, Taunton, 1995)
6. C. Wilmsen, H. Temkin, L.A. Coldren (eds.), *Vertical-Cavity Surface-Emitting Lasers* (Cambridge University Press, Cambridge, 1999)
7. J. Cheng, N.K. Dutta (eds.), *Vertical-Cavity Surface-Emitting Lasers: Technology and Applications* (Gordon and Breach, Amsterdam, 2000)
8. S.F. Yu, *Analysis and Design of Vertical Cavity Surface Emitting Lasers* (Wiley, Hoboken, 2003)
9. H. Li, K. Iga (eds.), *Vertical-Cavity Surface-Emitting Laser Devices* (Springer, Berlin, 2003)
10. H. Soda, K. Iga, C. Kitahara, Y. Suematsu, GaInAsP/InP surface emitting injection lasers. Jpn. J. Appl. Phys. **18**, 2329–2330 (1979)
11. F. Koyama, S. Kinoshita, K. Iga, Room temperature cw operation of GaAs vertical cavity surface emitting laser. IEICE Trans. **E71-E**, 1089–1090 (1988)
12. F. Koyama, S. Kinoshita, K. Iga, Room-temperature continuous wave lasing characteristics of a GaAs vertical cavity surface-emitting laser. Appl. Phys. Lett. **55**, 221–222 (1989)
13. J.L. Jewell, A. Scherer, S.L. McCall, Y.H. Lee, S. Walker, J.P. Harbison, L.T. Florez, Low-threshold electrically pumped vertical-cavity surface-emitting microlasers. Electron. Lett. **25**, 1123–1124 (1989)
14. M. Orenstein, A.C. Von Lehmen, C. Chang-Hasnain, N.G. Stoffel, J.P. Harbison, L.T. Florez, E. Clausen, J.E. Jewell, Vertical-cavity surface-emitting InGaAs/GaAs lasers with planar lateral definition. Appl. Phys. Lett. **56**, 2384–2386 (1990)
15. B. Tell, Y.H. Lee, K.F. Brown-Goebeler, J.L. Jewell, R.E. Leibenguth, M.T. Asom, G. Livescu, L. Luther, V.D. Mattera, High-power cw vertical-cavity top surface-emitting GaAs quantum well lasers. Appl. Phys. Lett. **57**, 1855–1857 (1990)
16. R. Szweda, VCSELs resurgent. III-Vs Rev. **17**(8), 28–31 (2004)
17. R.S. Geels, S.W. Corzine, J.W. Scott, D.B. Young, L.A. Coldren, Low threshold planarized vertical-cavity surface-emitting lasers. IEEE Photon. Technol. Lett. **2**, 234–236 (1990)
18. D.L. Huffaker, D.G. Deppe, K. Kumar, T.J. Rogers, Native-oxide defined ring contact for low threshold vertical-cavity lasers. Appl. Phys. Lett. **65**, 97–99 (1994)
19. R.A. Morgan, J.A. Lehman, M.K. Hibbs-Brenner, Vertical-cavity surface-emitting lasers come of age, in *Fabrication, Testing, and Reliability of Semiconductor Lasers*, ed. by M. Fallahi, S.C. Wang. Proceedings of SPIE, vol. 2683 (1996), pp. 18–29

20. K.D. Choquette, H.Q. Hou, Vertical-cavity surface emitting lasers: moving from research to manufacturing. Proc. IEEE **85**, 1730–1739 (1997)
21. K.L. Lear, K.D. Choquette, R.P. Schneider, S.P. Kilcoyne, K.M. Geib, Selectively oxidised vertical cavity surface emitting lasers with 50% power conversion efficiency. Electron. Lett. **31**, 208–209 (1995)
22. B. Weigl, M. Grabherr, C. Jung, R. Jäger, G. Reiner, R. Michalzik, D. Sowada, K.J. Ebeling, High-performance oxide-confined GaAs VCSELs. IEEE J. Select. Topics Quantum Electron. **3**, 409–415 (1997)
23. J.-F. Seurin, C.L. Ghosh, V. Khalfin, A. Miglo, G. Xu, J.D. Wynn, P. Pradhan, L.A. D'Asaro, High-power high-efficiency 2D VCSEL arrays, in *Vertical-Cavity Surface-Emitting Lasers XII*, ed. by C. Lei, J.K. Guenter. Proceedings of SPIE, vol. 6908 (2008), pp. 690808-1–690808-14
24. K. Takaki, N. Iwai, S. Kamiya, H. Shimizu, K. Hiraiwa, S. Imai, Y. Kawakita, T. Takagi, T. Ishikawa, N. Tsukiji, A. Kasukawa, Experimental demonstration of low jitter performance and high reliable 1060 nm VCSEL arrays for 10Gbps x 12ch optical interconnection, in *Vertical-Cavity Surface-Emitting Lasers XIV*, ed. by J.K. Guenter, K.D. Choquette. Proceedings of SPIE, vol. 7615 (2010), pp. 761502-1–761502-8
25. K. Takaki, N. Iwai, K. Hiraiwa, S. Imai, H. Shimizu, T. Kageyama, Y. Kawakita, N. Tsukiji, A. Kasukawa, A recorded 62% PCE and low series and thermal resistance VCSEL with a double intra-cavity strucure, in *21st IEEE International Semiconductor Laser Conference*, postdeadline paper PD 1.1. Sorrento, Sept. 2008
26. D.L. Huffaker, L.A. Graham, H. Deng, D.G. Deppe, Sub-40 μA continuous-wave lasing in an oxidized vertical-cavity surface emitting laser with dielectric mirrors. IEEE Photon. Technol. Lett. **8**, 974–976 (1996)
27. M. Grabherr, M. Miller, R. Jäger, R. Michalzik, U. Martin, H. Unold, K.J. Ebeling, High-power VCSEL's: single devices and densely packed 2-D-arrays. IEEE J. Select. Topics Quantum Electron. **5**, 495–502 (1999)
28. M. Miller, M. Grabherr, R. King, R. Jäger, R. Michalzik, K.J. Ebeling, Improved output performance of high-power VCSELs. IEEE J. Select. Topics Quantum Electron. **7**, 210–216 (2001)
29. J.-F. Seurin, G. Xu, Q. Wang, B. Guo, R. Van Leeuwen, A. Miglo, P. Pradhan, J.D. Wynn, V. Khalfin, C. Ghosh, High-brightness pump sources using 2D VCSEL arrays, in *Vertical-Cavity Surface-Emitting Lasers XIV*, ed. by J.K. Guenter, K.D. Choquette. Proceedings of SPIE, vol. 7615 (2010), pp. 76150F-1–76150F-9
30. H.J. Unold, S.W.Z. Mahmoud, R. Jäger, M. Kicherer, M.C. Riedl, K.J. Ebeling, Improving single-mode VCSEL performance by introducing a long monolithic cavity. IEEE Photon. Technol. Lett. **10**, 939–941 (2000)
31. I. Kardosh, F. Demaria, F. Rinaldi, S. Menzel, R. Michalzik, High-power single transverse mode vertical-cavity surface-emitting lasers with monolithically integrated curved dielectric mirrors. IEEE Photon. Technol. Lett. **20**, 2084–2086 (2008)
32. A. Mooradian, High brightness cavity-controlled surface emitting GaInAs lasers operating at 980 nm, in *Optical Fiber Communication Conference, OFC*, postdeadline paper PD17. Anaheim, March 2001
33. M. Kuznetsov, F. Hakimi, R. Sprague, A. Mooradian, Design and characteristics of high-power (> 0.5-W CW) diode-pumped vertical-external-cavity surface-emitting semiconductor lasers with circular TEM_{00} beams. IEEE J. Select. Topics Quantum Electron. **5**, 561–573 (1999)
34. I. Kardosh, F. Demaria, F. Rinaldi, M.C. Riedl, R. Michalzik, Electrically pumped frequency-doubled surface emitting lasers operating at 485 nm emission wavelength. Electron. Lett. **44**, 524–525 (2008)
35. J.E. Cunningham, D.K. McElfresh, L.D. Lopez, D. Vacar, A.V. Krishnamoorthy, Scaling vertical-cavity surface-emitting laser reliability for petascale systems. Appl. Opt. **45**, 6342–6348 (2006)
36. E.F. Schubert, *Light-Emitting Diodes* (Cambridge University Press, Cambridge, 2005)

37. A.D. Rakic, M.L. Majewski, Cavity and mirror design for vertical-cavity surface-emitting lasers, Chap. 8 in *Vertical-Cavity Surface-Emitting Laser Devices*, ed. by H. Li, K. Iga (Springer, Berlin, 2003), pp. 259–301
38. P. Debernardi, R. Orta, Analytical electromagnetic solution for Bragg mirrors with graded interfaces and guidelines for enhanced reflectivity. IEEE J. Quantum Electron. **43**, 269–274 (2007)
39. D. Supper, G. Steinle, M. Ilzhöfer, C. Giuliani, C. Degen, A. Lima, A. Ramakrishnan, L. Korte, G. Ebbinghaus, G. Müller, Hybrid 1285 nm GaInNAs VCSELs with 1.2 mW singlemode output power at 85°C. Semicond. Sci. Technol. **21**, 1464–1466 (2006)
40. K.J. Ebeling, *Integrated Optoelectronics* (Springer, Berlin, 1993)
41. S.W. Corzine, R.H. Yan, L.A. Coldren, A tanh substitution technique for the analysis of abrupt and graded interface multilayer dielectric stacks. IEEE J. Quantum Electron. **27**, 2086–2090 (1991)
42. P. Yeh, *Optical Waves in Layered Media* (Wiley, New York, 1988)
43. S. Adachi, GaAs, AlAs, and $Al_xGa_{1-x}As$: material parameters for use in research and device applications. J. Appl. Phys. **58**, R1–R29 (1985)
44. D.I. Babić, S.W. Corzine, Analytic expressions for the reflection delay, penetration depth, and absorptance of quarter-wave dielectric mirrors. IEEE J. Quantum Electron. **28**, 514–524 (1992)
45. L.A. Coldren, S.W. Corzine, *Diode Lasers and Photonic Integrated Circuits* (Wiley, New York, 1995)
46. S.W. Corzine, R.S. Geels, J.W. Scott, R.-H. Yan, L.A. Coldren, Design of Fabry–Perot surface-emitting lasers with a periodic gain structure. IEEE J. Quantum Electron. **25**, 1513–1524 (1989)
47. P.W.A. McIlroy, A. Kurobe, Y. Uematsu, Analysis and application of theoretical gain curves to the design of multi-quantum-well lasers. IEEE J. Quantum Electron. **21**, 1958–1963 (1985)
48. E.R. Hegblom, D.I. Babic, B.J. Thibeault, L.A. Coldren, Scattering losses from dielectric apertures in vertical-cavity lasers. IEEE J. Select. Topics Quantum Electron. **3**, 379–389 (1997)
49. M. Born, E. Wolf, *Principles of Optics*, 6th edn. (Pergamon Press, Oxford, 1989)
50. K.J. Ebeling, L.A. Coldren, Analysis of multielement semiconductor lasers. J. Appl. Phys. **54**, 2962–2969 (1983)
51. M. Sugimoto, H. Kosaka, K. Kurihara, I. Ogura, T. Numai, K. Kasahara, Very low threshold current density in vertical-cavity surface-emitting laser diodes with periodically doped distributed Bragg reflectors. Electron. Lett. **28**, 385–387 (1992)
52. K.L. Lear, R.P. Schneider, K.D. Choquette, S.P. Kilcoyne, J. Figiel, J.C. Zolper, Vertical cavity surface emitting lasers with 21% efficiency by metalorganic vapor phase epitaxy. IEEE Photon. Technol. Lett. **6**, 1053–1055 (1994)
53. W. Schmid, D. Wiedenmann, M. Grabherr, R. Jäger, R. Michalzik, K.J. Ebeling, CW operation of a diode cascade InGaAs quantum well VCSEL. Electron. Lett. **34**, 553–555 (1998)
54. T. Knödl, M. Golling, A. Straub, R. Jäger, R. Michalzik, K.J. Ebeling, Multistage bipolar cascade vertical-cavity surface-emitting lasers: theory and experiment. IEEE J. Select. Topics Quantum Electron. **9**, 1406–1414 (2003)
55. H.C. Casey Jr., M.B. Panish, *Heterostructure Lasers, Part A: Fundamental Principles* (Academic Press, Orlando, 1978)
56. R. Michalzik, K.J. Ebeling, Modeling and design of proton-implanted ultralow-threshold vertical-cavity laser diodes. IEEE J. Quantum Electron. **29**, 1963–1974 (1993)
57. K. Petermann, *Laser Diode Modulation and Noise* (Kluwer Academic, Dordrecht, 1991)
58. G. Reiner, E. Zeeb, B. Möller, M. Ries, K.J. Ebeling, Optimization of planar Be-doped InGaAs VCSELs with two-sided output. IEEE Photon. Technol. Lett. **7**, 730–732 (1995)
59. L. Li, G. Liu, Z. Li, M. Li, H. Li, X. Wang, C. Wan, High-efficiency 808-nm InGaAlAs–AlGaAs double-quantum-well semiconductor lasers with asymmetric waveguide structures. IEEE Photon. Technol. Lett. **20**, 566–568 (2008)

60. K.D. Choquette, K.M. Geib, C.I.H. Ashby, R.D. Twesten, O. Blum, H.Q. Hou, D.M. Follstaedt, B.E. Hammons, D. Mathes, R. Hull, Advances in selective wet oxidation of AlGaAs alloys. IEEE J. Select. Topics Quantum Electron. **3**, 916–926 (1997)
61. B. Weigl, M. Grabherr, G. Reiner, K.J. Ebeling, High efficiency selectively oxidised MBE grown vertical-cavity surface-emitting lasers. Electron. Lett. **32**, 557–558 (1996)
62. R. Michalzik, M. Grabherr, R. Jäger, M. Miller, K.J. Ebeling, Progress in high-power VCSELs and arrays, in *Optoelectronic Materials and Devices*, ed. by M. Osiński, Y.-K. Su. Proceedings of SPIE, vol. 3419 (1998), pp. 187–195
63. C. Jung, R. Jäger, M. Grabherr, P. Schnitzer, R. Michalzik, B. Weigl, S. Müller, K.J. Ebeling, 4.8 mW single-mode oxide confined top-surface emitting vertical-cavity laser diodes. Electron. Lett. **33**, 1790–1791 (1997)
64. C.J. Chang-Hasnain, J.P. Harbison, C.-E. Zah, M.W. Maeda, L.T. Florez, N.G. Stoffel, T.-P. Lee, Multiple wavelength tunable surface-emitting laser arrays. IEEE J. Quantum Electron. **27**, 1368–1376 (1991)
65. J. Cheng, P. Zhou, S.Z. Sun, S. Hersee, D.R. Myers, J. Zolper, G.A. Vawter, Surface-emitting laser-based smart pixels for two-dimensional optical logic and reconfigurable optical interconnects. IEEE J. Quantum Electron. **29**, 741–756 (1993)
66. S.E. Swirhun, R.P. Bryan, W.S. Fu, W.E. Quinn, J.L. Jewell, G.R. Olbright, Commercial manufacturing of vertical-cavity surface-emitting laser arrays, in *Vertical-Cavity Surface-Emitting Laser Arrays*, ed. by J.L. Jewell. Proceedings of SPIE, vol. 2147 (1994), pp. 74–84
67. S. Matsuo, T. Nakahara, Y. Kohama, Y. Ohiso, S. Fukushima, T. Kurokawa, A monolithically integrated smart pixel using an MSM-PD, MESFET's, and a VCSEL. IEEE J. Select. Topics Quantum Electron. **2**, 121–127 (1996)
68. Y. Liu, M. Hibbs-Brenner, B. Morgan, J. Nohava, B. Walterson, T. Marta, S. Bounnak, E. Kalweit, J. Lehman, D. Carlson, P. Wilson, Integrated VCSELs, MSM photodetectors, and GaAs MESFETs for low cost optical interconnects, in *OSA Trends in Optics and Photonics, Advances in Vertical Cavity Surface Emitting Lasers*, vol. 15, ed. by C.J. Chang-Hasnain (Optical Society of America, Washington, DC 1997), pp. 196–198
69. H. Kosaka, M. Kajita, M. Yamada, Y. Sugimoto, K. Kurata, T. Tanabe, Y. Kasukawa, Plastic-based receptacle-type VCSEL-array modules with one and two dimensions fabricated using the self-alignment mounting technique, in *Proceedings of 47th Electronic Components and Technology Conference, ECTC*. San Jose, May 1997, pp. 382–390
70. S.Y. Hu, S.Z. Zhang, J. Ko, J.E. Bowers, L.A. Coldren, 1.5 Gbit/s/channel operation of multiple-wavelength vertical-cavity photonic integrated emitter arrays for low-cost multimode WDM local-area networks. Electron. Lett. **34**, 768–770 (1998)
71. R. King, R. Michalzik, D. Wiedenmann, R. Jäger, P. Schnitzer, T. Knödl, K.J. Ebeling, 2D VCSEL arrays for chip-level optical interconnects, in *Optoelectronic Interconnects VI*, ed. by J.P. Bristow, S. Tang. Proceedings of SPIE, vol. 3632 (1999), pp. 363–372
72. R. Michalzik, R. King, R. Jäger, S. Müller, K.J. Ebeling, VCSEL arrays for CMOS integrated optical interconnect systems, in *Optoelectronic and Wireless Data Management, Processing, Storage, and Retrieval*, ed. by R. Raymond, P.K. Srimani, R. Su, C.W. Wilmsen. Proceedings of SPIE, vol. 4534 (2001), pp. 101–113
73. J. Piprek, Y.A. Akulova, D.I. Babic, L.A. Coldren, J.E. Bowers, Minimum temperature sensitivity of 1.55 μm vertical-cavity lasers at −30 nm gain offset. Appl. Phys. Lett. **72**, 1814–1816 (1998)
74. W. Nakwaski, M. Osiński, Thermal resistance of top-surface-emitting vertical-cavity semiconductor lasers and monolithic two-dimensional arrays. Electron. Lett. **28**, 572–574 (1992) (corrected in Electron. Lett. **28**, 1283 (1992))
75. H. Roscher, R. Michalzik, Toward redundant 2-D VCSEL arrays for optical datacom, in *Micro-Optics, VCSELs, and Photonic Interconnects*, ed. by H. Thienpont, K.D. Choquette, M.R. Taghizadeh. Proceedings of SPIE, vol. 5453 (2004), pp. 170–181
76. A.E. Siegman, *Lasers* (University Science Books, Mill Valley, 1986)

77. E. Zeeb, B. Möller, G. Reiner, M. Ries, T. Hackbarth, K.J. Ebeling, Planar proton implanted VCSEL's and fiber-coupled 2-D VCSEL arrays. IEEE J. Select. Topics Quantum Electron. **1**, 616–623 (1995)
78. M.H. MacDougal, H. Zhao, P.D. Dapkus, M. Ziari, W.H. Steier, Wide-bandwidth distributed Bragg reflectors using oxide/GaAs multilayers. Electron. Lett. **30**, 1147–1148 (1994)
79. G.R. Hadley, Effective index model for vertical-cavity surface-emitting lasers. Opt. Lett. **20**, 1483–1485 (1995)
80. D. Marcuse, *Light Transmission Optics*, 2nd edn. (Van Nostrand Reinhold, New York, 1982)
81. R. Michalzik, K.J. Ebeling, Generalized BV diagrams for higher order transverse modes in planar vertical-cavity laser diodes. IEEE J. Quantum Electron. **31**, 1371–1379 (1995)
82. J.H. Shin, Y.G. Ju, H.E. Shin, Y.H. Lee, Spontaneous emission factor of oxidized vertical-cavity surface-emitting lasers from the measured below-threshold cavity loss. Appl. Phys. Lett. **70**, 2344–2346 (1997)
83. K.Y. Lau, Dynamics of quantum well lasers, in *Quantum Well Lasers*, ed. by P.S. Zory Jr. (Academic Press, Boston, 1993)
84. R. Nagarajan, M. Ishikawa, T. Fukushima, R.S. Geels, J.E. Bowers, High speed quantum-well lasers and carrier transport effects. IEEE J. Quantum Electron. **28**, 1990–2008 (1992)
85. R. Olshansky, P. Hill, V. Lanzisera, W. Powazniak, Frequency response of 1.3 μm InGaAsP high speed quantum-well semiconductor lasers. IEEE J. Quantum Electron. **23**, 1410–1418 (1987)
86. D. Wiedenmann, R. King, C. Jung, R. Jäger, R. Michalzik, P. Schnitzer, M. Kicherer, K.J. Ebeling, Design and analysis of single-mode oxidized VCSEL's for high-speed optical interconnects. IEEE J. Select. Topics Quantum Electron. **5**, 503–511 (1999)
87. K.L. Lear, V.M. Hietala, H.Q. Hou, M. Ochiai, J.J. Banas, B.E. Hammons, J.C. Zolper, S.P. Kilcoyne, Small and large signal modulation of 850 nm oxide-confined vertical cavity surface emitting lasers, in *OSA Trends in Optics and Photonics, Advances in Vertical Cavity Surface Emitting Lasers*, vol. 15, ed. by C.J. Chang-Hasnain (Optical Society of America, Washington, DC, 1997), pp. 69–74
88. B.J. Thibeault, K. Bertilsson, E.R. Hegblom, E. Strzelecka, P.D. Floyd, R. Naone, L.A. Coldren, High-speed characteristics of low-optical loss oxide-apertured vertical-cavity lasers. IEEE Photon. Technol. Lett. **9**, 11–13 (1997)
89. J.D. Ralston, S. Weisser, I. Esquivias, E.C. Larkins, J. Rosenzweig, P.J. Tasker, J. Fleissner, Control of differential gain, nonlinear gain, and damping factor for high-speed application of GaAs-based MQW lasers. IEEE J. Quantum Electron. **29**, 1648–1659 (1993)
90. T. Takahashi, M. Nishioka, Y. Arakawa, Differential gain of GaAs/AlGaAs quantum well and modulation-doped quantum well lasers. Appl. Phys. Lett. **58**, 4–6 (1991)
91. A. Al-Samaneh, S. Renz, A. Strodl, W. Schwarz, D. Wahl, R. Michalzik, Polarization-stable single-mode VCSELs for Cs-based MEMS atomic clock applications, in *Semiconductor Lasers and Laser Dynamics IV*, ed. by K.P. Panayotov, M. Sciamanna, A.A. Valle, R. Michalzik. Proceedings of SPIE, vol. 7720 (2010), pp. 772006-1–772006-14
92. D.C. Kilper, P.A. Roos, J.L. Carlsen, K.L. Lear, Squeezed light generated by a microcavity laser. Phys. Rev. A **55**, 3323–3326 (1997)
93. D. Wiedenmann, P. Schnitzer, C. Jung, M. Grabherr, R. Jäger, R. Michalzik, K.J. Ebeling, Noise characteristics of 850 nm single-mode vertical cavity surface emitting lasers. Appl. Phys. Lett. **73**, 717–719 (1998)
94. C.H. Henry, Phase noise in semiconductor lasers. J. Lightwave Technol. **4**, 298–311 (1986)
95. W. Schmid, C. Jung, B. Weigl, G. Reiner, R. Michalzik, K.J. Ebeling, Delayed self-heterodyne linewidth measurement of VCSEL's. IEEE Photon. Technol. Lett. **8**, 1288–1290 (1996)
96. D.K. Serkland, G.A. Keeler, K.M. Geib, G.M. Peake, Narrow linewidth VCSELs for high-resolution spectroscopy, in *Vertical-Cavity Surface-Emitting Lasers XIII*, ed. by K.D. Choquette, C. Lei. Proceedings of SPIE, vol. 7229 (2009), pp. 722907-1–722907-8

97. F. Monti di Sopra, H.P. Zappe, M. Moser, R. Hövel, H.-P. Gauggel, K. Gulden, Near-infrared vertical-cavity surface-emitting lasers with 3-MHz linewidth. IEEE Photon. Technol. Lett. **11**, 1533–1535 (1999)
98. C. Affolderbach, A. Nagel, S. Knappe, C. Jung, D. Wiedenmann, R. Wynands, Nonlinear spectroscopy with a vertical-cavity surface-emitting laser (VCSEL). Appl. Phys. B **70**, 407–413 (2000)
99. D.K. Serkland, G.M. Peake, K.M. Geib, R. Lutwak, R.M. Garvey, M. Varghese, M. Mescher, VCSELs for atomic clocks, in *Vertical-Cavity Surface-Emitting Lasers X*, ed. by C. Lei, K.D. Choquette. Proceedings of SPIE, vol. 6132 (2006), pp. 613208-1–613208-11
100. D.K. Serkland, K.M. Geib, G.M. Peake, R. Lutwak, A. Rashed, M. Varghese, G. Tepolt, M. Prouty, VCSELs for atomic sensors, in *Vertical-Cavity Surface-Emitting Lasers XI*, ed. by K.D. Choquette, J.K. Guenter. Proceedings of SPIE, vol. 6484 (2007), pp. 648406-1–648406-10
101. H.P. Zappe, F. Monti di Sopra, H.-P. Gauggel, K. Gulden, R. Hövel, M. Moser, High-spectral-purity VCSELs for spectroscopy and sensors, in *Laser Diodes and LEDs in Industrial, Measurement, Imaging, and Sensors Applications II*, ed. by G.T. Burnham, X. He, K.J. Linden, S.C. Wang. Proceedings of SPIE, vol. 3945 (2000), pp. 106–116
102. J.M. Ostermann, F. Rinaldi, P. Debernardi, R. Michalzik, VCSELs with enhanced single-mode power and stabilized polarization for oxygen sensing. IEEE Photon. Technol. Lett. **17**, 2256–2258 (2005)
103. B. Scherer, J. Wöllenstein, M. Weidemüller, W. Salzmann, J.M. Ostermann, F. Rinaldi, R. Michalzik, Measurement of the pressure broadening coefficients of the oxygen A-band using a low cost, polarization stabilized, widely tunable vertical-cavity surface-emitting laser. Microsyst. Technol. **14**, 607–614 (2008)
104. R. Michalzik, J.M. Ostermann, P. Debernardi, Polarization-stable monolithic VCSELs, in *Vertical-Cavity Surface-Emitting Lasers XII*, ed. by C. Lei, J.K. Guenter. Proceedings of SPIE, vol. 6908 (2008), pp. 69080A-1–69080A-16
105. H. Willebrand, B.S. Ghuman, *Free-Space Optics: Enabling Optical Connectivity in Today's Networks* (Sams Publishing, Indianapolis, 2001)
106. S. Sinzinger, J. Jahns, *Microoptics* (Wiley-VCH, Weinheim, 1999)
107. M. Vervaeke, C. Debaes, B. Volckaerts, H. Thienpont, Optomechanical Monte Carlo tolerancing study of a packaged free-space intra-MCM optical interconnect system. IEEE J. Select. Topics Quantum Electron. **12**, 988–996 (2006)
108. G.P. Agrawal, *Fiber-Optic Communication Systems*, 3rd edn. (Wiley, New York, 2002)
109. E. Mohammed, H. Au, 200 Gb/s 10-channel miniature optical interconnect transmitter module for high performance computing (HPC), in *Optoelectronic Interconnects and Component Integration X*, ed. by A.L. Glebov, R.T. Chen. Proceedings of SPIE, vol. 7607 (2010), pp. 760709-1–760709-12
110. K. Yashiki, Y. Hashimoto, M. Oda, N. Suzuki, K. Yamamoto, M. Kurihara, T. Sugimoto, H. Hatakeyama, J. Sakai, T. Akagawa, K. Narita, H. Ono, K. Fukatsu, K. Tokutome, H. Kouta, M. Tsuji, I. Ogura, A. Noda, T. Anan, Y. Suzuki, K. Kurata, 240-Gb/s on-board optical transmitters and receivers, in *Proceedings of Optical Fiber Communication Conference, OFC*, paper OTuM4. San Diego, March 2010
111. R. Michalzik, G. Giaretta, K.W. Goossen, J.A. Walker, M.C. Nuss, 40 Gb/s coarse WDM data transmission with 825 nm wavelength VCSELs over 310 m of high-performance multimode fiber, in *Proceedings of 26th European Conference on Optical Communications, ECOC*, vol. 4. Munich, Sept. 2000, pp. 33–34
112. R. Michalzik, Optical backplanes, board and chip interconnects, Chap. 6 in *Fiber Optic Data Communication: Technological Trends and Advances*, ed. by C. DeCusatis (Academic Press, San Diego, 2002), pp. 216–269
113. R. Michalzik, Optical backplanes, board and chip interconnects, Chap. 26 in *Handbook of Fiber Optic Data Communication: A Practical Guide to Optical Networking*, 3rd edn., ed. by C. DeCusatis (Elsevier, San Diego, 2008), pp. 657–676

114. S. Nemoto, T. Makimoto, Analysis of splice loss in single-mode fibres using a Gaussian field approximation. Opt. and Quant. Electron. **11**, 447–457 (1979)
115. P. Schnitzer, R. Jäger, C. Jung, R. Michalzik, D. Wiedenmann, F. Mederer, K.J. Ebeling, Biased and bias-free multi-Gb/s data links using GaAs VCSEL's and 1300-nm single-mode fiber. IEEE Photon. Technol. Lett. **10**, 1781–1783 (1998)
116. K.J. Ebeling, Optical interconnects and data links with vertical cavity surface emitting laser diodes (VCSEL), in *Proceedings of 21st European Conference on Optical Communications, ECOC*, vol. 4. Brussels, Sept. 1995, pp. 113–147
117. J. Heinrich, E. Zeeb, K.J. Ebeling, Transverse modes under external feedback and fiber coupling efficiencies of VCSEL's. IEEE Photon. Technol. Lett. **10**, 1365–1367 (1998)
118. R. Michalzik, P. Schnitzer, U. Fiedler, D. Wiedenmann, K.J. Ebeling, High-bit-rate data transmission with short-wavelength oxidized VCSEL's: toward bias-free operation. IEEE J. Select. Topics Quantum Electron. **3**, 396–404 (1997)
119. P. Schnitzer, M. Grabherr, R. Jäger, C. Jung, K.J. Ebeling, Bias-free 2.5 Gbit/s data transmission using polyimide passivated GaAs VCSELs. Electron. Lett. **34**, 573–575 (1998)
120. K.H. Hahn, M.R. Tan, Y.M. Houng, S.Y. Wang, Large area multitransverse-mode VCSELs for modal noise reduction in multimode fibre systems. Electron. Lett. **29**, 1482–1484 (1993)
121. D.M. Kuchta, C.J. Mahon, Mode selective loss penalties in VCSEL optical fiber transmission links. IEEE Photon. Technol. Lett. **6**, 288–290 (1994)
122. D. Wiedenmann, M. Grabherr, C. Jung, R. Jäger, R. Michalzik, P. Schnitzer, K.J. Ebeling, Feedback insensitive 3 Gb/s fiber interconnect with low noise single-mode VCSEL, in *Proceedings of 24th European Conference on Optical Communications, ECOC*, vol. 1. Madrid, Sept. 1998, pp. 457–458
123. U. Fiedler, G. Reiner, P. Schnitzer, K.J. Ebeling, Top-surface emitting vertical-cavity laser diodes for 10 Gbit/s data transmission. IEEE Photon. Technol. Lett. **8**, 746–748 (1996)
124. S. Bottacchi, *Multi-Gigabit Transmission Over Multimode Optical Fibre: Theory and Design Methods for 10GbE Systems* (Wiley, Chichester, 2006)
125. R. Michalzik, G. Giaretta, A.J. Ritger, Q.L. Williams, 10 Gb/s VCSEL based data transmission over 1.6 km of new generation 850 nm multimode fiber. *IEEE Lasers and Electro-Optics Society Annual Meeting, LEOS*, postdeadline paper PD1.6. San Francisco, Nov. 1999
126. G. Giaretta, R. Michalzik, A.J. Ritger, Long distance (2.8 km), short wavelength (0.85 μm) data transmission at 10 Gb/sec over new generation high bandwidth multimode fiber, *Conference on Lasers and Electro-Optics, CLEO*, postdeadline paper CPD13. San Francisco, May 2000
127. P. Pepeljugoski, S.E. Golowich, A.J. Ritger, P. Kolesar, A. Risteski, Modeling and simulation of next-generation multimode fiber links. J. Lightwave Technol. **21**, 1242–1255 (2003)
128. P. Pepeljugoski, D. Kuchta, Y. Kwark, P. Pleunis, G. Kuyt, 15.6-Gb/s transmission over 1 km of next generation multimode fiber. IEEE Photon. Technol. Lett. **14**, 717–719 (2002)
129. P. Matthijsse, G. Kuyt, F. Gooijer, F. Achten, R. Freund, L. Molle, C. Caspar, T. Rosin, D. Schmidt, A. Beling, T. Eckhardt, Multimode fiber enabling 40 Gbit/s multi-mode transmission over distances >400 m, in *Proceedings of Optical Fiber Communication Conference, OFC*, paper OWI13. Anaheim, March 2006
130. S.S.-H. Yam, F. Achten, Single wavelength 40 Gbit/s transmission over 3.4 km broad wavelength window multimode fibre. Electron. Lett. **42**, 592–594 (2006)
131. P. Pepeljugoski, M.J. Hackert, J.S. Abbott, S.E. Swanson, S.E. Golowich, A.J. Ritger, P. Kolesar, Y.C. Chen, P. Pleunis, Development of system specification for laser-optimized 50-μm multimode fiber for multigigabit short-wavelength LANs. J. Lightwave Technol. **21**, 1256–1275 (2003)
132. J.B. Schlager, M.J. Hackert, P. Pepeljugoski, J. Gwinn, Measurements for enhanced bandwidth performance over 62.5-μm multimode fiber in short-wavelength local area networks. J. Lightwave Technol. **21**, 1276–1285 (2003)
133. C.-A. Bunge, J.-R. Kropp, K. Petermann, Study of simplified test procedure for 10-GB-Ethernet fibers. IEEE Photon. Technol. Lett. **14**, 1539–1541 (2002)

134. A.M.E.-A. Diab, J.D. Ingham, R.V. Penty, I.H. White, 10-Gb/s transmission on single-wavelength multichannel SCM-based FDDI-grade MMF links at lengths over 300 m: a statistical investigation. J. Lightwave Technol. **25**, 2976–2983 (2007)
135. X. Zhao, F.S. Choa, Demonstration of 10-Gb/s transmission over a 1.5-km-long multimode fiber using equalization techniques. IEEE Photon. Technol. Lett. **14**, 1187–1189 (2002)
136. J.D. Ingham, R.V. Penty, I.H. White, D.G. Cunningham, Electronic equalisation for length extension of $\times 2$ to $\times 3$ in 10 Gbit/s multimode-fibre datacommunication links. Electron. Lett **40**, 1437–1439 (2004)
137. C. Xia, M. Ajgaonkar, W. Rosenkranz, On the performance of the electrical equalization technique in MMF links for 10-Gigabit Ethernet. J. Lightwave Technol. **23**, 2001–2011 (2005)
138. P. Pepeljugoski, J.A. Tierno, A. Risteski, S.K. Reynolds, L. Schares, Performance of simulated annealing algorithm in equalized multimode fiber links with linear equalizers. J. Lightwave Technol. **24**, 4235–4249 (2006)
139. K. Balemarthy, A. Polley, S.E. Ralph, Electronic equalization of multikilometer 10-Gb/s multimode fiber links: mode-coupling effects. J. Lightwave Technol. **24**, 4885–4894 (2006)
140. Y. Sun, P. Hallemeier, H. Ereifej, O.V. Sinkin, B.S. Marks, C.R. Menyuk, Statistics of electrical dispersion compensator penalties of 10-Gb/s multimode fiber links with offset connectors. IEEE Photon. Technol. Lett. **19**, 689–691 (2007)
141. J.D. Ingham, R.V. Penty, I.H. White, Transmitter-based equalisation for extended-reach multimode-fibre datacommunication links. Electron. Lett. **43**, 240–242 (2007)
142. H.R. Stuart, Dispersive multiplexing in multimode optical fiber. Science **289**, 281–283 (2000)
143. C.P. Tsekrekos, M. de Boer, A. Martinez, F.M.J. Willems, A.M.J. Koonen, Temporal stability of a transparent mode group diversity multiplexing link. IEEE Photon. Technol. Lett. **18**, 2484–2486 (2006)
144. M. Greenberg, M. Nazarathy, M. Orenstein, Data parallelization by optical MIMO transmission over multimode fiber with intermodal coupling. J. Lightwave Technol. **25**, 1503–1514 (2007)
145. K.M. Patel, A. Polley, K. Balemarthy, S.E. Ralph, Spatially resolved detection and equalization of modal dispersion limited multimode fiber links. J. Lightwave Technol. **24**, 2629–2636 (2006)
146. X. Shen, J.M. Kahn, M.A. Horowitz, Compensation for multimode fiber dispersion by adaptive optics. Opt. Lett. **30**, 2985–2987 (2005)
147. R.A. Panicker, J.P. Wilde, J.M. Kahn, D.F. Welch, I. Lyubomirsky, 10×10 Gb/s DWDM transmission through 2.2-km multimode fiber using adaptive optics. IEEE Photon. Technol. Lett. **19**, 1154–1156 (2007)
148. N. Guan, K. Takenaga, S. Matsuo, K. Himeno, Multimode fibers for compensating intermodal dispersion of graded-index multimode fibers. J. Lightwave Technol. **22**, 1714–1719 (2004)
149. D.G. Cunningham, I.H. White, Does multimode fibre have a future in data-communications? Electron. Lett. **43**, 63–65 (2007)
150. L.B. Aronson, B.E. Lemoff, L.A. Buckman, D.W. Dolfi, Low-cost multimode WDM for local area networks up to 10 Gb/s. IEEE Photon. Technol. Lett. **10**, 1489–1491 (1998)
151. E.B. Grann, K. Herrity, B.C. Peters, B. Wiedemann, Datacom applications for new VCSEL technologies, in *Vertical-Cavity Surface-Emitting Lasers IV*, ed. by K.D. Choquette, C. Lei. Proceedings of SPIE, vol. 3946 (2000), pp. 165–169
152. E. Wendt, Passing the test: the secret of success in 10 GbE, FibreSystems Europe/LIGHTWAVE Europe, pp. 16–19, May 2005
153. G. Giaretta, F. Mederer, R. Michalzik, W. White, R. Jäger, G. Shevchuk, T. Onishi, M. Naritomi, R. Yoshida, P. Schnitzer, H. Unold, M. Kicherer, K. Al-Hemyari, J.A. Valdmanis, M. Nuss, X. Quan, K.J. Ebeling, Demonstration of 500 nm-wide transmission window at multi-Gb/s data rates in low-loss plastic optical fiber, in *Proceedings of 25th European Conference on Optical Communications, ECOC*, vol. II. Nice, Sept. 1999, pp. 240–241
154. Y. Koike, T. Ishigure, High-bandwidth plastic optical fiber for fiber to the display. J. Lightwave Technol. **24**, 4541–4553 (2006)

155. A. Polley, S.E. Ralph, 100 m, 40 Gb/s plastic optical fiber link, in *Proceedings of Conference on Optical Fiber Communication/National Fiber Optic Engineers Conference 2008, OFC/NFOEC 2008*, paper OWB2. San Diego, Feb. 2008
156. A. Polley, S.E. Ralph, Mode coupling in plastic optical fiber enables 40-Gb/s performance. IEEE Photon. Technol. Lett. **19**, 1254–1256 (2007)
157. R. Michalzik, A. Kern, M. Stach, F. Rinaldi, D. Wahl, True bidirectional optical interconnects over multimode fiber, in *Optoelectronic Interconnects and Component Integration X*, ed. by A.L. Glebov, R.T. Chen. Proceedings of SPIE, vol. 7607 (2010), pp. 76070B-1–76070B-17
158. A. Kern, S. Paul, D. Wahl, R. Blood, W. Schwarz, R. Michalzik, Bidirectional multimode fiber interconnection at Gbit/s data rates with monolithically integrated VCSEL–PIN transceiver chips. IEEE Photon. Technol. Lett. **23**, 1058–1060 (2011)
159. A. Kern, S. Paul, D. Wahl, A. Al-Samaneh, R. Michalzik, Single-fiber bidirectional optical data links with monolithic transceiver chips. Advances in Optical Technologies, Special Issue on *Recent Advances in Semiconductors Surface-Emitting Lasers,* Article ID 729731 (2012)

Chapter 3
Three-Dimensional Modeling of VCSELs

Pierluigi Debernardi

Abstract VCSELs are complicated objects, also from a modeling point of view. In fact the computation of statical and dynamical operation implies the interaction of different physical phenomena: electrical, thermal and optical. All are strongly coupled and rule device operation. In this chapter the relevant effects and corresponding mutual interactions will be reviewed and possible ways to numerically address them discussed. Particular attention will be devoted to the optical solver, which is the core of any VCSEL simulation tool. In fact the optical characteristics determine the final device performance.

3.1 Introduction

In spite of good performance and appealing features of modern VCSELs, a lot has still to be done in view of new applications and optimized features. There is therefore an increasing demand for accurate and efficient tools for VCSEL design, simulation and optimization.

A lot of groups have been and are working at this topic; different methods have been proposed (see for example [1–10]), with different degrees of approximation, depending on the different balance between flexibility/precision and simulation runtime. In fact three different kinds of problems: *electrical, thermal* and *optical* have to be solved with their mutual couplings. Such still difficult tasks are even further complicated by the extremely complex structure of VCSELs, which also in the simplest structures comprises a lot of layers of different materials and with different physical properties.

P. Debernardi (✉)
IEIIT-CNR c/o Politecnico di Torino,
Corso Duca degli Abruzzi 24, 10129 Torino, Italy
e-mail: pierluigi@polito.it

R. Michalzik (ed.), *VCSELs*, Springer Series in Optical Sciences 166,
DOI: 10.1007/978-3-642-24986-0_3, © Springer-Verlag Berlin Heidelberg 2013

A comprehensive and self-consistent solution is hardly affordable with nowadays ordinary computation power by using full discretization techniques, especially for the electrical and optical solvers. This is even more true in devices where the circular symmetry is broken. In fact, within such simplified geometry, the solution of the aforesaid problems is greatly simplified by using cylindrical coordinates and invoking a complete rotational symmetry of the involved phenomena. In some models (see e.g. [2, 6]) the problem is reduced in the longitudinal dimension, thus focussing on the transverse effects in the active plane only.

In some cases the need is felt of modeling tools capable to handle non-circularly symmetric structures, which may arise from technological processes [11] or particular demands [12–15]. In such cases a really three dimensional (3D) model for all the variables of interest is required. To the best of my knowledge, such complete treatments has been attempted only recently [16, 17], due to the relevant computer power requirements and to the fact that many structures have a rotational symmetry or can be simplified as such.

3.2 Interplay of the Different Effects

The different effects acting in a VCSEL and their relevant mutual interactions are schematically depicted in Fig. 3.1. All phenomena refer to the rate equations which govern the carrier–photon exchanges (center of block diagram). All the parameters are supplied by the different solvers, which act on different spatial domains (see in Fig. 3.1 the details for a top-injected device).

As indicated in the sketch, the electrical part is relevant to two aspects: carrier injection into active region, the VCSEL drive force, and Joule heating, its side drawback. Heat generation and corresponding temperature increase in the device set the ultimate operation limit. It is therefore important to include all the main heat sources, that is Joule heating, carrier non-radiative recombinations and free carrier optical absorption. The 3D temperature profile affects all the important parameters: resonator characteristics, active region properties, transport and leakage features.

Optical properties depend not only on the VCSEL geometry, but also change during operation through 3D temperature profile, which induces related refractive index and loss profiles. The carrier density profile induces corresponding gain and refractive index changes in the active region and also modifies the optical modal features.

In the following sections the single phenomena will be reviewed and possible ways to numerically treat them will be discussed. A best order of discussing them can hardly be defined due to their tight interplays. The optical part will then be treated first. In fact it is by far the most demanding computationally in a VCSEL solver and determines to a large extent many important characteristics, such as threshold, differential efficiency, modal behavior. The other effects, mainly driven by temperature, play a role at higher pump rates, far above threshold. This is why the optical part

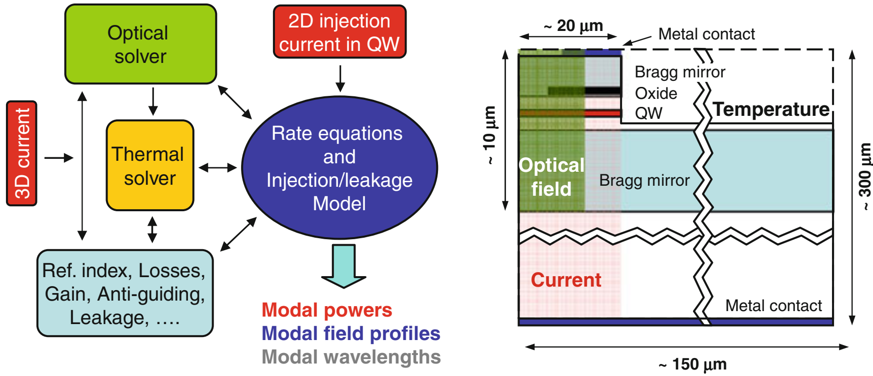

Fig. 3.1 *Left:* Block diagram of the various interacting phenomena. *Right:* Their spatial domains (half device): optical field (*green, inner area*), current flow (*red shaded area*) and temperature (whole domain)

is sometime referred as "cold cavity model" when it includes mainly the geometry and refractive indexes of the resonator.

3.3 Optical Part

To compute the optical modes supported by a VCSEL, Maxwell equations have to be solved for an open dielectric resonator, which comprises hundreds of layers with refractive index and loss transverse profiles. Full numerical approaches have been proven for circularly symmetrical structures first [7, 18] and lately [19] for arbitrary transverse geometries. Even so, it has to be pointed out such techniques are highly cumbersome computationally and are reported to require 20–30 hours to evaluate one mode in a fully 3D structure [19].

Therefore different techniques have been proposed. The very first and popular one is the effective index method by Hadley [20] which strongly simplifies the problem by decoupling the longitudinal and transverse problems. First the longitudinal fields are computed in the different transverse regions, providing an effective transverse index profile. The corresponding optical scalar modes are computed by solving the related 2D wave equation.

More refined techniques have been proposed later, based on wave expansion techniques. In [21] the device is put in a large metal cylinder with artificial perfectly matched boundary conditions to avoid spurious reflections from the metal interfaces. At each interface the field continuity is imposed, which leads to a generalized round-trip condition. A similar method is proposed in [22], with the limitation of using the vectorial modes of a circular fiber in each section, which definitely limits the possible transverse shapes. The method proposed in [23] solves the transverse structure in

the different sections numerically and then applies the field continuity at each interfaces, ending also up to a self-consistency round-trip matrix problem.

3.3.1 The Coupled-Mode Approach

To my knowledge, all available techniques are reported and tested for circularly-symmetric structures and from the published literature it is hard to say to which extent and numerical efficiency they could be generalized to complex transverse sections, such as arrays or gratings. For that purpose only the model presented first in [24] and developed within VELM (Vcsel ELectroMagnetics) code has been successfully demonstrated by comparisons to experimental results [13, 15, 25]. A modal expansion technique as in [21] is chosen, but the basis of the complete set of the vectorial mode $\mathbf{E}_\nu(\rho, \varphi)$ of an infinite reference medium in cylindrical coordinates is adopted instead. In that way the problem of transverse boundary conditions is completely avoided. Moreover, as a major difference, the coupled mode theory is used to propagate the field in the structure instead of applying the boundary conditions at each interface. We will summarize in the following the guidelines of the technique [24]. The electric field is expanded in the plane waves $\mathbf{E}_\nu(r)$ of a reference infinite medium as:

$$\mathbf{E}(\rho, \varphi, z) = \sum_{\nu'} \int dk A_{\nu'}(z)\mathbf{E}_{\nu'} \simeq \sum_{\nu} A_\nu(z) \Delta k \mathbf{E}_\nu \tag{3.1}$$

where the index ν labels the characteristics of the basis modes, which are expressed in terms of Bessel functions of the first kind (see Appendix of [24]). They are classified according to the continuous radial component of the wavevector k, azimuthal variation n, even or odd symmetry, TE or TM, forward and backward waves; Δk originates by approximating the integral over the continuous radial wavevector expansion by a finite sum of terms.

In each layer m of thickness L_m where the structure does not depend on the longitudinal coordinate z the vector $\mathbf{A} = A_\nu$ of mode amplitudes satisfies the coupled mode equations:

$$\frac{d\mathbf{A}}{dz} = \left(B + K'_m\right)\mathbf{A} \tag{3.2}$$

where B describes the free propagation in the reference material. It is a diagonal matrix of elements $(B)_{\nu\nu'} = -is_\alpha \beta_\nu \delta_{\nu\nu'}$, where $s_\alpha = \pm 1$ ($\alpha = f, b$ is an index which describes forward and backward propagation) and $\beta_\nu = \sqrt{k_r^2 - k^2}$ is the longitudinal wavevector component (k_r being the reference material wavevector). The corresponding coupling between the modes is introduced by the matrix $K' = K\Delta k$, where K is given by:

$$(K)_{\nu\nu'} = -\frac{i\omega}{C_\nu}\int_S dS\left\{\mathbf{E}_{\nu t}\cdot\left[\left(\underline{\Delta\epsilon}\cdot\mathbf{E}_{\nu'}\right)_t - \frac{\left(\underline{\Delta\epsilon}_{tz}\cdot\hat{z}\right)\left(\underline{\Delta\epsilon}\cdot\mathbf{E}_{\nu'}\right)_z}{\epsilon_c+\Delta\epsilon_{zz}}\right] + \frac{\epsilon_c E_{\nu z}}{\epsilon_c+\Delta\epsilon_{zz}}\left(\underline{\Delta\epsilon}\cdot\mathbf{E}_{\nu'}\right)_z\right\} \tag{3.3}$$

where the subscripts t and z indicate transverse and longitudinal components of the vectors and C_ν is the power normalization constant. The tensor $\underline{\Delta\epsilon}$ describes the difference with respect to the homogeneous and isotropic reference dielectric permittivity ϵ_r. Since coupled mode theory stems directly from the reciprocity theorem, any material can be treated, even metal layers. The tensorial forms in the preceding equation account for the possibility of non-isotropic media in the structures, which mainly originate from Pockels and elasto-optic effects. This topic is treated in details in [26] where the interested readers can find more details. It is however worth recalling here the important result that anisotropies induce coupling between the different azimuthal modes as non-circularly symmetric geometries do. Such a coupling is the cause of the almost linear polarization observed in real devices.

The information on the device transverse geometry is included in the model by defining, for each transversely inhomogeneous layer of the structure, the profile of $\underline{\Delta\epsilon}(\rho,\varphi)$. Very often one has to deal with step-like variations of the dielectric constant. All other loss or refractive index continuous variations, induced by temperature profiles and carrier distribution are included in the model on the same foot.

The solution of (3.2) can be expressed in the form of an exponential matrix and, hence, the mode amplitudes at the two interfaces of each discretization layer L_m are related by:

$$\mathbf{A}(z_{m+1}) = e^{(B+K_m')L_m}\mathbf{A}(z_m) = T_m\mathbf{A}(z_m) \tag{3.4}$$

where the transmission matrix T_m has been introduced.

The closure of the problem is obtained by imposing proper boundary conditions, i.e., the consistency of the forward and backward mode amplitudes at two reference interfaces. It is convenient to set these two sections to be the extreme lower ($z = z_1$) and upper ($z = z_n$) layers, beyond which the structure does not present any transverse perturbation and the geometry is planar (see Fig. 3.2). With this choice, since the layers above (below) $z = z_n$ ($z = z_1$) are multilayered stacks (or even a single medium), the chain matrix formalism can be applied to determine their reflectivity coefficients Γ_1 and Γ_n, which are nothing but diagonal matrices dependent on the wavevector k. Then the boundary conditions at these two sections explicitly read:

$$\mathbf{A}^f(z_1) = \Gamma_1\mathbf{A}^b(z_1), \quad \mathbf{A}^b(z_n) = \Gamma_n\mathbf{A}^f(z_n) \tag{3.5}$$

By introducing the global transmission matrix:

$$T = \prod_m T_m \tag{3.6}$$

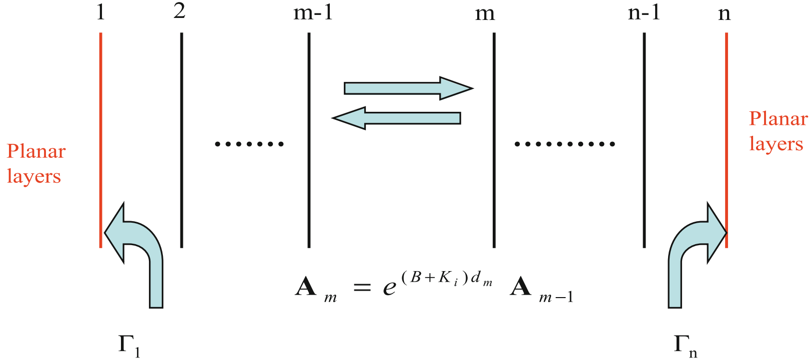

Fig. 3.2 Schematic of the layer structure of a VCSEL together with the coefficient progation scheme, and some notations

and considering explicitly its dependence on the index $\alpha = f, b$, the boundary conditions (3.5) can be rewritten only in terms of $\mathbf{A}^b(z_1)$:

$$\left(T^{bf}\Gamma_n + T^{bb}\right)\mathbf{A}^b(z_1) = \Gamma_1\left(T^{ff}\Gamma_n + T^{fb}\right)\mathbf{A}^b(z_1) \tag{3.7}$$

which becomes the unknown of the problem. A mode is then found when, after a complete round trip, the corresponding expansion coefficients exactly replicate themselves. This condition gives the frequency and the gain needed to fulfill the threshold condition of all the modes supported by the structure. Following the guidelines of (13–17) in [24], (3.7) can be expressed as a standard eigenvalue problem, by exploiting the small active region thickness:

$$\lambda\mathbf{A}^b(z_1) = M\mathbf{A}^b(z_1) \tag{3.8}$$

where the eigenvalue λ is related to QW permittivity by:

$$\lambda^{-1} = -ik_r d\frac{\Delta\epsilon_a}{\epsilon_r} \tag{3.9}$$

This relation links the eigenvalues to the active optical response and it allows to evaluate the threshold carrier density, once known its effects on $\Delta\epsilon_a$. The matrix of the eigenvalue problem is $M = M_c^{-1}M_a$, which in turn are defined as:

$$M_j = T_j^{bb} - \Gamma_1 T_j^{ff}\Gamma_n + T_j^{bf}\Gamma_n - \Gamma_1 T_j^{fb} \quad (j = c, a) \tag{3.10}$$

where T_c and T_a are respectively the cold cavity and active contribution to the global transmission matrix:

$$T = T_c + \lambda^{-1}T_a \tag{3.11}$$

They stem from the linearization of the transmission matrix with respect to the unknown QW permittivity due to carriers ($\Delta\epsilon_a$); this is a good approximation since the active thickness d is much smaller than the wavelength.

Numerically the method previously outlined is quite simple and straightforward. The evaluation of the coupling coefficients must be undertaken only once at the beginning of the computations and consists of an integral over the transverse section of the basis functions and the dielectric permittivity difference with respect to the reference medium. The computation of the exponential matrices is the more time consuming part of the numerical code and is comparable, as number of operations, to a matrix diagonalization. VELM has been optimized so as to reduce the computational effort as much as possible; a full exponential matrix calculation is needed only when the corresponding exponent is a full matrix (i.e. in layers with lateral variations). In the case of infinite layers, also including transversely constant anisotropies, one can optimize the computation of the exponential matrix by solving many smaller problems.

3.3.2 Comparing Different Models

In the framework of COST268 EU project a VCSEL modeling exercise was carried out; the results were presented in [29] and are summarized here for the reader's commodity. The benchmark 980 nm structure is very schematic and comprises a λ-cavity with only one quantum well (QW) as active region. The back (top) mirror is composed of 29.5 (24) GaAs/AlGaAs pairs. The oxide layer (16 nm thick) is placed within the first top-mirror pair. Many research groups joined and the different models could be compared on an equal foot.

In the following results are presented from a selection of vectorial models reported in [29]. In Fig. 3.3 the guiding effect of the oxide position, varied from the field node to antinode in 5 steps, is shown. Figure 3.5 reports the effect of varying the oxide aperture, positioned at a field anti-node. The numerical results for the threshold material gain, supposed to have the same transverse profile as the oxide aperture, are given in the tables (Fig. 3.4) for the fundamental and first order (TE_{01}) modes. The data of [29] are complemented by the results of a FEM (finite element method) approach, recently reported in [19]. It can be seen that such fully numerical method provides slightly underestimated threshold gains, while lasing frequencies deviate appreciably compared to all other models. This is probably the consequence of a compromise between discretization steps and computing resources. VELM shows its good performance, pretty comparable with all the other codes. As an advantage, it is available in both scalar and vectorial implementations [24]. This is achieved by only using a different expansion set: the vectorial basis functions (TE and TM plane waves) are set to their TEM limit. In that way one can compare within the same model scalar and vectorial treatments. As can be seen from the left table in Fig. 3.4, the difference is higher for smaller apertures, as expected from the increased scattering losses in the vectorial treatment.

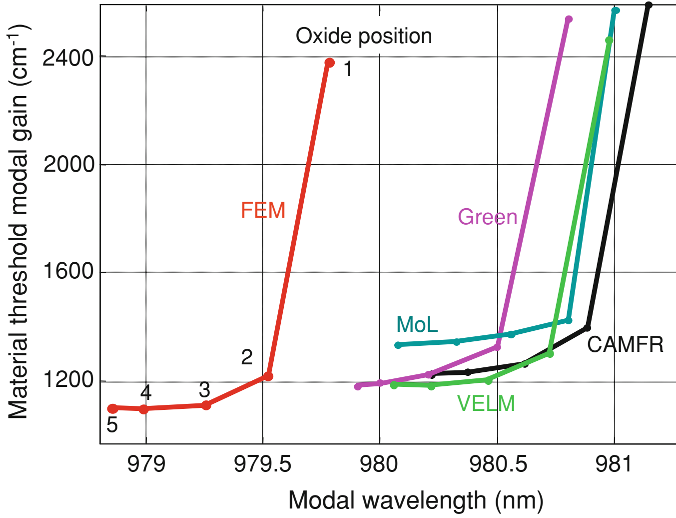

Fig. 3.3 Simulation results from different vectorial models: CAMFR [21], MoL [27], Green [28], VELM [24] and FEM [19]. Fundamental mode threshold material gains vs. modal wavelengths are reported for different positions of the oxide layer (1, field node; 5, field anti-node); the oxide aperture diameter is 8 μm. Data from [29] and [19]

Fund. mode threshold material gain (cm^{-1})					
Φ (μm)	CAMFR	Green	MoL	VELM	VELM-S
1	9925	8780	4813	6945	6818
2	2823	2340	2300	1769	1756
4	1437	1386	1450	1275	1274
6	1279	1231	1350	1217	1217
8	1224	1193	1300	1197	1196

First order mode threshold material gain (cm^{-1})					
Φ (μm)	CAMFR	Green	MoL	VELM	VELM-S
1	cutoff	cutoff	cutoff	cutoff	cutoff
2	cutoff	20679	cutoff	21765	21578
4	1696	1710	1750	1396	1453
6	1357	1361	1390	1233	1263
8	1252	1257	1320	1202	1221

Fig. 3.4 Threshold gains provided by different models (see Fig. 3.3) for different oxide sizes, having fixed its position at the anti-node. Also the first order mode TE_{01} is given. Data from [29]

3.3.3 Comparisons with Experimental Results

After the numerical validation previously reported, comparisons with real VCSELs are reported, by considering devices where the full capabilities of VELM are used. In the following some significant examples will be exemplarily given, related to VCSEL anisotropies, phase-coupled arrays and grating VCSELs.

Material and Shape Anisotropies

Spatially, frequency and polarization resolved measurements performed at Darmstadt University [11] revealed a clear signature of both shape and material anisotropies in

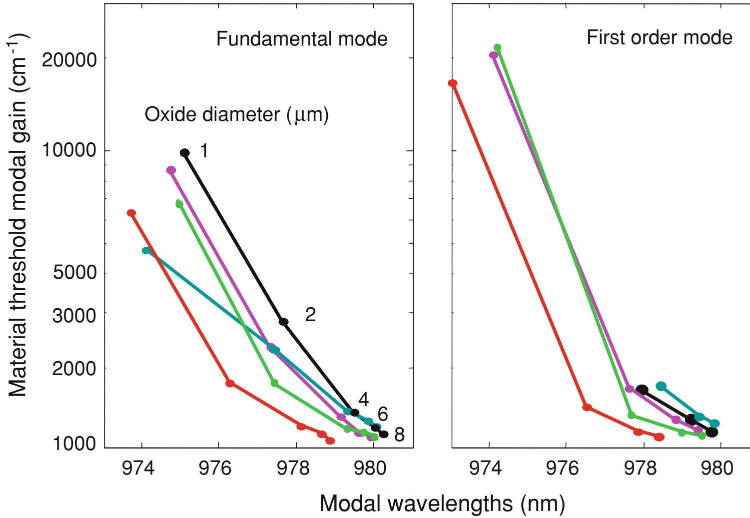

Fig. 3.5 As in Fig. 3.3, but varying the oxide aperture width, placed at the field anti-node. On the left (*right*) the results for the fundamental (first order, TE_{01}) are reported. Data from [29] and [19]

VCSELs made at Ulm University. The devices are typical 810 nm oxide-confined VCSELs with a λ-cavity containing three 8 nm GaAs quantum wells. The mirrors present graded interfaces; on the *p*-side a carbon δ-doping at the field nulls was used to improve the electrical characteristics. The oxide thickness is 30 nm, also close to a field node so as to reduce the number of transverse modes at a minimum. For the sake of a better understanding the experimental results are reported in Fig. 3.6 for a device with an oxide aperture of about 5 μm. The lowest order modes show a birefringence of about 23 GHz, due to material anisotropies. In fact, slightly deformed circular geometries give a very small contribution to birefringence, as also VELM shows. An *y*-oblong geometry is neththeless indicated by mode *h* at the r.h.s. of the spectrum (see Fig. 3.6, top-right) with three spots oriented along *y* and by the fact that, among the four first order modes, the ones with the two spots oriented along *y* exhibit the lower frequencies (modes *c, d*).

Material anisotropies: Since no intentional strain is put in the structure, the Pockels effect plays the major role. To this aim the static field profile, originating from the doping in the Bragg mirrors, is computed. This is accomplisheds by using the 1D transport model presented in [30], which results in the static electric field depicted in Fig. 3.7. It is a very rapidly varying function of the longitudinal position and is an effect of the doping in presence of band-gap discontinuities. Such a stiff profile requires, as a drawback, to finely discretize the structure in the longitudinal direction. The effect of the bias is noticeable mainly in the intrinsic cavity region. The overall computed birefringence is about 10 GHz, by introducing the anisotropy as:

$$\Delta\epsilon_{xx} = +n^4 r_{41} \mathcal{E}_z; \quad \Delta\epsilon_{yy} = -n^4 r_{41} \mathcal{E}_z \tag{3.12}$$

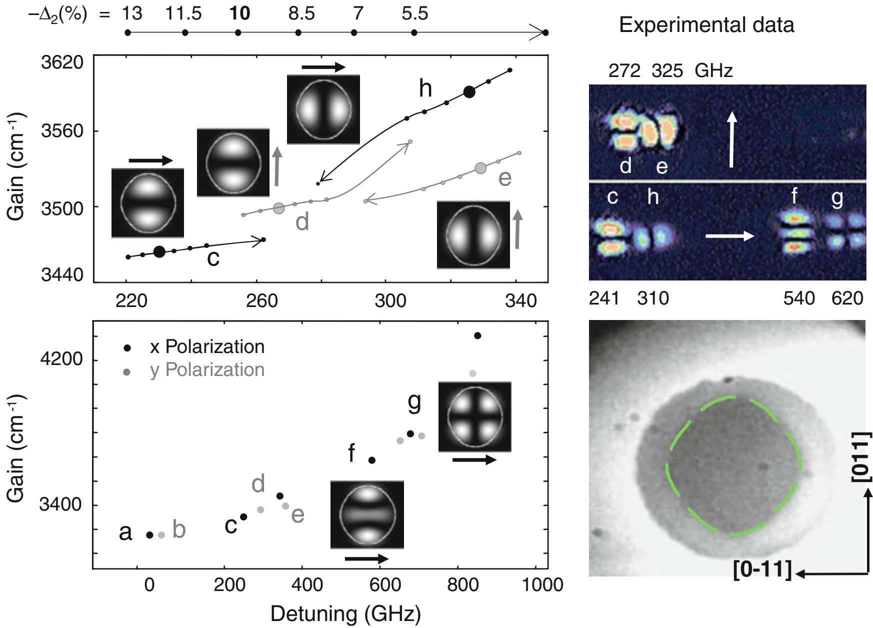

Fig. 3.6 Mode positions in the gain-detuning plane for an oxide aperture shape obtained by (3.13) with $r_0 = 2.5\,\mu\text{m}$ and $\Delta_4 = 3\%$. At top, parametric analysis of the modal positions of first order modes for different shape deviations, indicated above the figure. In the lower part, for $\Delta_2 = -10\%$, modal positions of all the supported modes. The ones with letters are detected by polarization and spectrally resolved near-field images [11], with mode positions in gigahertz (relative to the fundamental mode, not shown here). Below a typical infrared image of the oxide aperture from Ulm University; dashed line shows a fit by (3.13). Partially from [11] (© 2002 IEEE)

where $\mathcal{E}_z$ is the static field distribution, $r_{41} = -1.610^{-12}$ V/m for GaAs and -1.110^{-12} V/m for AlAs and $x(y)$ corresponds to [110] ($[1\bar{1}0]$) crystallographic direction that diagonalizes the permittivity tensor [26]. The discrepancy with the experimental value of 23 GHz is most probably due to some residual strain in the device, which is introduced in the simulations by increasing by a 2.3 factor the electro-optic effect. This is equivalent to look for an effective strain in the device, since the tensorial structure of the two anisotropies is formally the same [26].

Shape effects are due to the oblong oxide-window shape which may be a consequence of both an anisotropic oxidation speed and a non-perfectly circular mesa (reproduced later by the oxide aperture). I proposed a simple analytical shape:

$$r(\varphi) = r_0\,[1 + \Delta_2\cos(2\varphi) + \Delta_4\cos(4\varphi)] \tag{3.13}$$

where Δ_4 gives rise to a diamond shape for values in the range 0 to 6% and Δ_2 controls the ellipticity. Only three years after publication of [11] I became aware of the actual oxide aperture shape: an example and the corresponding fit with (3.13) is shown in Fig. 3.6.

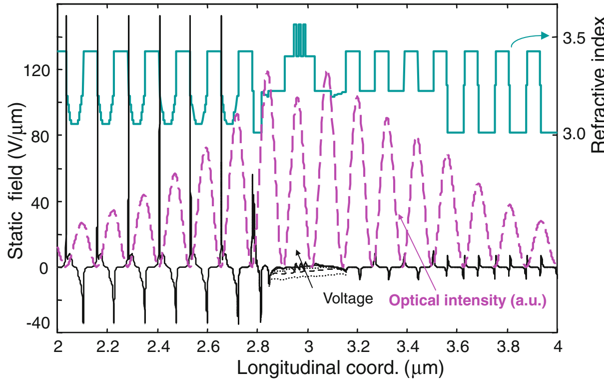

Fig. 3.7 Static field (*left scale, black lines*), refractive index (*right scale, green line*) and optical intensity (*dashed line, arbitrary units*) profiles for four values of applied bias: 0, 1, 1.5, 2.5 V. The doping levels are: 2.5 10^{18} cm^{-3} C-doping with δ-doping at the heterointerfaces for the p-mirror and 2 10^{18} cm $^{-3}$ Si-doping in the n-mirror. From [11] (© 2002 IEEE)

In [11] a parametric analysis on Δ_2 was performed to infer the actual oxide aperture shape. The results are shown in the upper plot of Fig. 3.6, where the evolution of the first order modes in the gain-frequency plain is reported. $\Delta_2 = -10\%$ provides the best fit with the experimental data. For a symmetric device (harrow points) the mode frequencies are mainly influenced by the material anisotropies that split x and y-polarized modes. Note by comparing these results with the experiments that all the modal characteristics are reproduced. So, the first two modes have y-aligned spots and the x-polarization has always smaller frequencies compared to y-polarization. Moreover, due to material anisotropies, the x-polarized mode with x-aligned spots (labeled h in the figure) has the highest threshold gain among these four modes, which in the experiments gives the weakest intensity.

By using the best-fit parameters previously determined the frequencies and the threshold gains of all the modes supported by the structure are computed and are presented in the lower part of Fig. 3.6. The three-spot mode f can be interpreted as a deformed second order mode; it closely compares with the experimental observations and appears at the right frequency and polarization. The frequency position of all the modes detected in the experiment fairly agree with the computations, without any other parameter adjustment.

Phase-Coupled Arrays

The model can handle not only slightly deformed circular geometries, as those of the previous example, but also much complicated geometries. To prove and test this capability VELM was applied to the structure described in [12]: a device with a square oxide aperture and a top metal grid, operating at 960 nm wavelength, as depicted in Fig. 3.8. The metal grid serves also as an electrode that makes the injected current more uniform. The 1 μm width multilayer PtTiPtAu grid stripes define 4×4 μm^2 openings which allow light escape, for a total array pitch of $d = 5\,\mu$m. Different

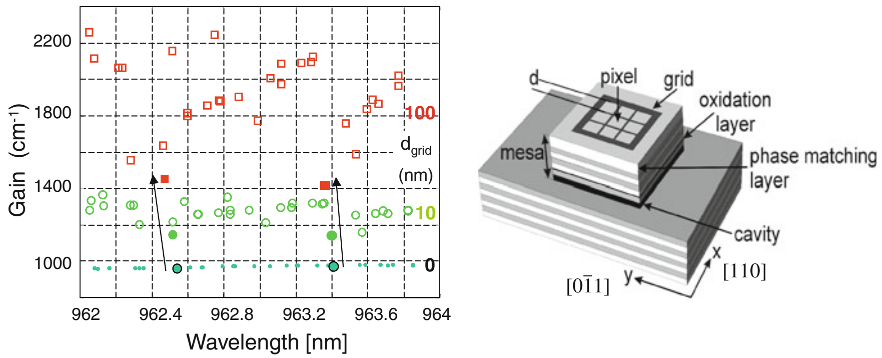

Fig. 3.8 *Left:* Computed threshold gains and wavelegths of the 4 × 4 array within the first two nanometer interval for 3 metal grid thicknesses: 0 (*dots*), 10 nm (*circles*) and 100 nm (*squares*), as in the actual devices. The modes observed in the experiments are put in evidence. *Right:* Schematics of the device. Partially from [13] (© 2003 IEEE)

array sizes have been made with $n \times n$ pixels. The structure is composed by an $Al_{0.15}Ga_{0.85}As$ λ-cavity with three InGaAs quantum wells, followed on the p-side by a $\lambda/2$-layer containing a 25 nm thick AlAs oxidation layer at the minimum of the optical field. The top-DBR consists of 19 periods of p-doped $GaAs/Al_{0.9}Ga_{0.1}As\lambda/4$-layers; the 30 periods of the bottom DBR are of the same composition but n-type. A special role is played by the last, phase-matching GaAs layer whose thickness of 180 nm was chosen so to maximize the reflectivity contrast between openings and metal stripe regions.

All the tested arrays display single mode operation on the same y-polarization over a certain current range (up to about 1.5 I_{th}), where a higher order mode appears. All pixels emit on the lowest order, bell-like modes, all at the same frequency. This is well demonstrated by the far-field distributions (see Fig. 3.9). Their characteristic four lobe radiation patterns indicate a 180° phase difference between adjacent pixels.

The far-fields distribution are obtained almost for free within VELM, since the expansion coefficients are closely related to the Fourier transform of the output field [24]. Figure 3.9 reports experimental and numerical far-field patterns, which fairly agree; this is also shown by the dependence of the lobe apertures vs. array size. Very narrow emissions are obtained, as low as one degree; the possibility of converting this far-field profile into a more practical central lobe emission is discussed extensively in [13].

The role of the metal grid is clarified by applying VELM to a 4 × 4 array and studying the effect of varying the grid thickness, as shown in Fig. 3.8. The dense distribution of the supported modes is shown for the first 2 nm wavelength interval. The very flat gain distribution without metal grid is expected for that large device size (20 × 20 μm^2 oxide aperture). By introducing the grid, threshold gains get larger and important differences among the various modes appear. Such higher losses are strongly dependent on the mode profiles and are minima for those modes whose intensity is null in correspondence of the grid lines. Such modes are put in

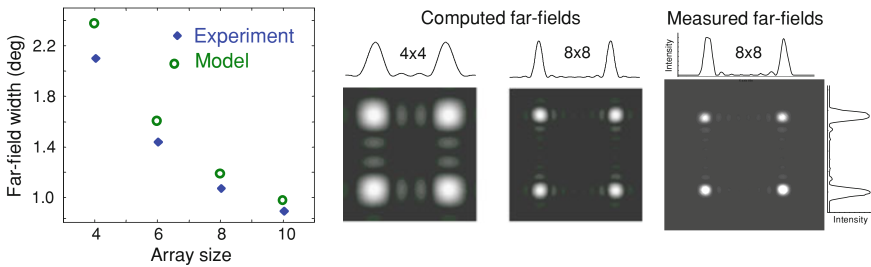

Fig. 3.9 *Left:* full width half maximum of the far-field lobes vs. array size. *Center:* computed far-field distributions of arrays of size 4 and 8 on 10 × 10 degree windows. *Right:* measured far-field distributions of an array of size 8 on a 12 × 12 degree window. Partially from [13] (© 2003 IEEE)

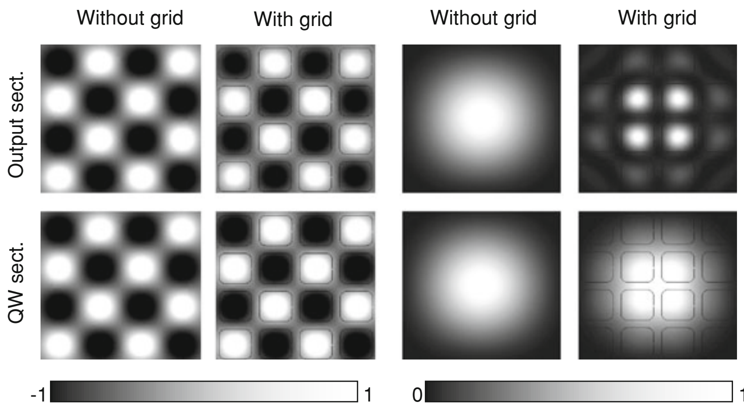

Fig. 3.10 Computed amplitude profiles of the TEM_{00} (*right*) and the lasing mode (*left*) at the output and QW sections, with and without the metal grid. The thin black lines represent the openings in the metallization and the profiles are normalized to their maxima. For the TEM_{00} mode, black corresponds to zero level, while the lasing mode amplitude swings from −1 to +1. Partially from [13] (© 2003 IEEE)

evidence by bold symbols in Fig. 3.8 and arrows show their evolution at increasing the grid thickness. These two modes correspond to those observed in the experiments. A second mode appears at increasing the current and displays a near-field characterized by two spots in every pixel.

The different selectivity of the metal grid on the modes is clarified by considering the lowest threshold mode and the gaussian-like mode. In Fig. 3.10 the amplitude profiles of these two modes are shown at the output (grid-air interface) and QW sections in the two cases with and without the metal grid. The array lasing mode is only marginally perturbed by the metal, while in all the other cases the field is strongly deformed by the grid, resulting in much higher losses. The gaussian-like mode experiences the highest losses, since it does not present any intensity minima in correspondence of the grid lines. Then the metal grid acts as a "*modal filter*".

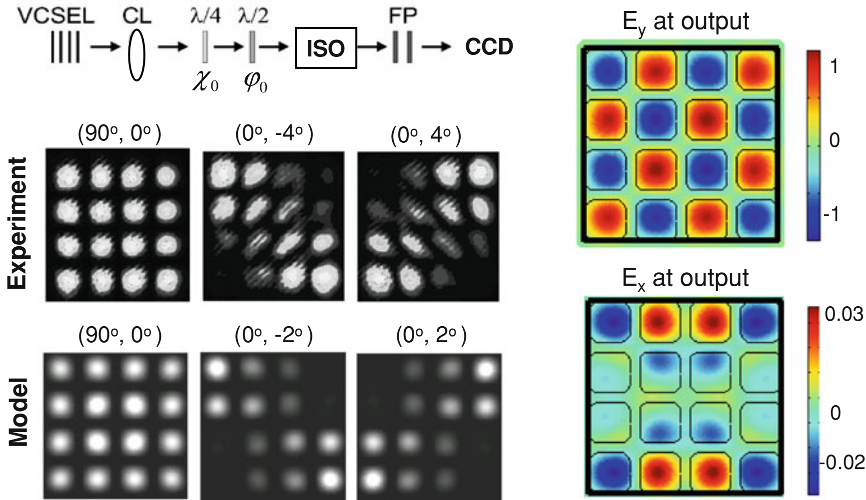

Fig. 3.11 *Left:* at top, experimental setup for detecting polarization patterns, shown below for a 4×4 array at $1.5 \times I_{th}$ with the corresponding numerical results. The polarization filter angles (φ_0, χ_0) are indicated above each map. *Right:* The output transverse field components used to compute the model polarization patterns. Thick lines show the $20 \times 20\,\mu\text{m}^2$ oxide aperture, thin lines the grid openings. Partially from [13] (© 2003 IEEE)

The terms "*supermodes*" and "*phase-coupled arrays*" have been used for such devices [12]. Both are misleading, since they recall solitary devices coupled in some way [31], instead of the actual high order mode of the large area device, selected by the reflectivity patterning. An even stronger evidence of that is given by the inhomogeneous polarization features of these devices [13]. The emitted light is first passed through a polarization filter, a $\lambda/4$ and a $\lambda/2$ waveplate that allow to measure the ellipticity (χ_0) and the polarization orientation (φ_0), as shown at top of Fig. 3.11. A scanning Fabry-Pérot (FP) is used to single out the fundamental mode; the corresponding output is then sent to a photo-diode or a CCD camera, for polarization, spectral and spatial near-field measurements.

The near-field CCD images behind the FP reported in Fig. 3.11, upper part, clearly show that the polarization state is inhomogeneously distributed over the array pixels. By playing with the quarterwave plate one can successfully block the light only on certain pixels, while other pixels display an increased output. This is clearly shown by the middle and left images, where for two opposite angles the resulting outputs are shown. Similar results are obtained for arrays with different sizes [13].

The origin of these polarization properties is readily understood by applying the full vectorial capabilities of VELM. Among the two transverse modal field components, one is generally dominating and determines what, commonly speaking, is the polarization of that mode. By accounting also for the anisotropy induced by the electro-optic effect, as previously discussed, the smallest gain solution is the y-polarized mode, as in the experiment. The resulting modal birefringence of

+10 GHz corresponds to the experimental values. The lower part of Fig. 3.11 shows the results obtained by performing the experiment "numerically", by varying φ_0 and χ_0 by an ideal polarization filter. Both experiment and the model show bow tie polarization patterns in fair agreement. The reason of this particular symmetry arises from the different parities of the strong and weak transverse components (see Fig. 3.11 on the right), which is a general feature of vectorial modes [24, 32].

Polarization-Stable Grating VCSEL

VCSELs with a dielectric monolithic grating, etched into the out coupling layer, are presented as a last example in this review of application of VELM to real devices; for a later application to tunable VCSEL with a curved top DBR, see [33]. The idea of grating VCSELs was first proposed by the author in [34], where the main guidelines of their design were outlined. The purpose of such devices is to exploit the well known properties of gratings so as to fix the VCSEL polarization. In fact unstable polarization characteristics were pointed out already in the early 90's [35]. Since then, a lot of different solutions have been proposed to overcome the unpredictable polarization behavior of VCSELs. They are due to the almost complete isotropic features of the gain material and of the circularly symmetric resonator transverse geometry. All attempted solutions were found problematic and not suitable for mass production. The encouraging results predicted in [34] were readily confirmed by the experimental findings by Dr. J.M. Ostermann at Ulm University (see Chap. 5 for more details).

The idea of using gratings to fix VCSEL polarization was pursued before, but with non conclusive results. In fact the behavior of a grating within a resonator is different from the free-standing case. Only a fully self-consistent solver can provide valuable and quantitative information. So the grating effects depend on many factors: thickness and position play a major role, period has smaller influence for values around the lasing wavelengths. In Fig. 3.12 an example of the field profile in a grating VCSEL is given. The near-field at the output section brings the grating fingerprints, showing maxima where the radiation losses are larger. As expected for a grating period larger than the emitted wavelength, the periodic near-field results in diffraction side lobes in the far-field. This is observed in the field longitudinal cross section (Fig. 3.12), shown on a large computation window compared to device size. The side lobe angle is directly linked to the grating period and excellent agreement between model and experiments has been shown [15]. What is relevant for these devices is their capability of providing very different modal losses for the two polarizations. As an example Fig. 3.13 shows the computed dichroism (the difference between the threshold gains in the two polarizations, see formula in the inset of left graph) vs. grating depth for different periods. The grating is etched into the whole out coupling section of the top-cladding layer of a standard device, with an oxide aperture of 4 μm. The stronger effect is given by the grating etch depth, which influences the strength and sign of the dichroism, that is the lasing polarization: negative (positive) values correspond to a perpendicular (parallel) polarization compared to the grating grooves. The grating period plays a minor role and may affect the selected polarization only where the grating thickness correspond to a change of the dichroism sign. The same parameter

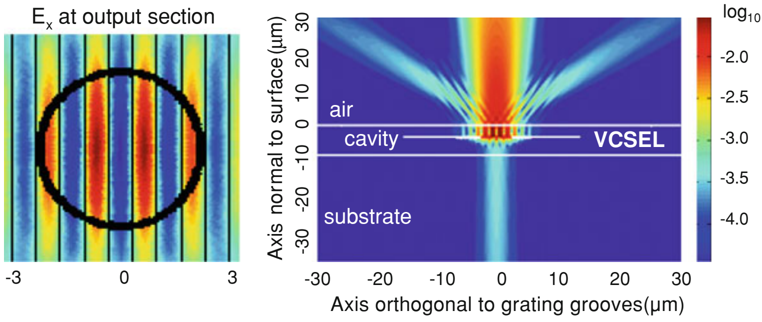

Fig. 3.12 *Left:* Field intensity distribution at the transverse output section. *Right:* Field intensity distribution (longitudinal cross section). Inverted grating (i.e. etched into an anti-phase cap-layer) with 1.2 μm period and 60 nm thickness. Lines on the left map show the 4 μm oxide aperture and the grating edges. White lines on the right indicate the active region and mirror positions

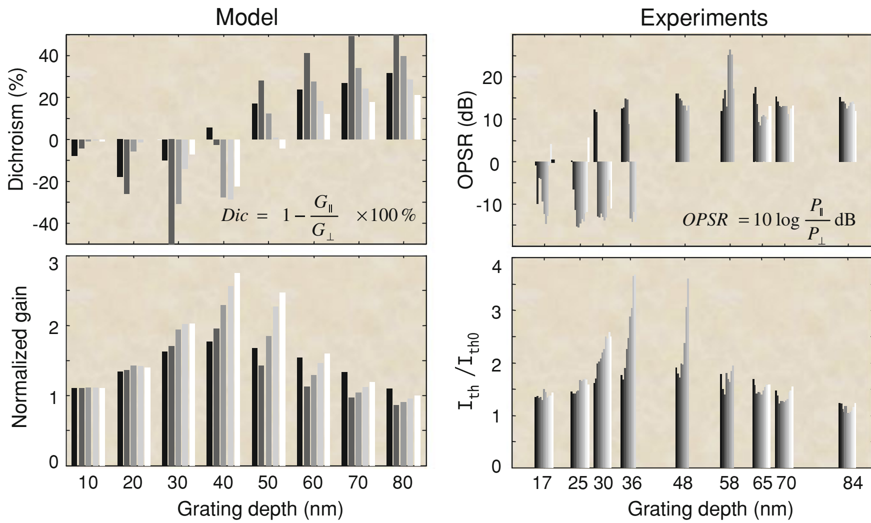

Fig. 3.13 *Left:* Model results: top, dichroism as defined in the *inset*; bottom, threshold gain normalized to the values without grating. *Right:* Experimental results: top, orthogonal polarization suppression ration (OPSR defined in the *inset*); bottom, threshold current normalized with an average value for devices with no grating. From [15] (© 2005 IEEE)

investigation was performed experimentally and a very good agreement was found for the detected polarization orientation, which changes direction at the same grating depth as predicted by the model. At the lower part a similar comparison is performed on the threshold features. Good agreement is found also here, with a threshold peak in the range of 30–50 nm.

From the preceding results, however, only indirect comparisons are possible: in fact the OPSR is not directly linked to dichroism, apart from its sign. Also,

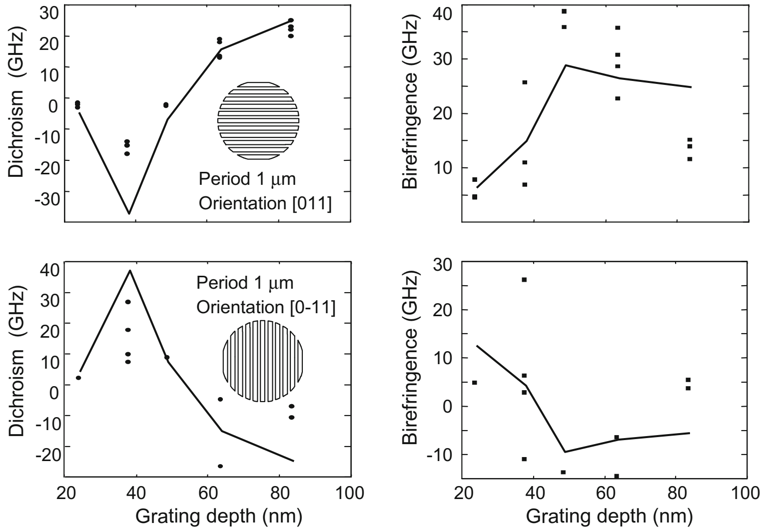

Fig. 3.14 *Left:* Comparison between computed (*line*) and measured (*dots*) dichroism. Different dots at the same grating depth refer to nominally equal devices. Two grating orientation are tested. *Right:* Corresponding modal birefringence

threshold current is only indirectly linked to threshold gain: the current has to be transformed into carriers and the latter to a gain profile. Therefore a set of measurements were performed aimed to directly measure the dichroism by detecting the polarization resolved spontaneous emission spectra close to threshold and taking their difference [25]. The corresponding results are shown in Fig. 3.14, both for dichroism and birefringence (the difference in modal emission wavelengths for modes with same transverse profiles). In these results gratings were oriented as the crystal axes, as shown in Fig. 3.14. In that way the combined effects of grating and material anisotropies (electro-optic effect, see first example of this section) can be better compared. In the modal birefringence the grating and electro-optic effects sum or subtract to each other. The computed and measured dichroism compare fairly well, giving then more solid proof that VELM is adequate also for grating VCSELs. Birefringence shows also quite accurate comparison; however experimental data are more scattered, as it has been observed also in previous studies [36]. Similarly we attribute the scattered experimental data to uncontrollable residual strain in the different devices.

3.4 Thermal Part

Thermal effects are of great relevance in VCSELs, since they are responsible, at increasing injection current, for an earlier power rollover in comparison to edge-emitting lasers. Moreover, the thermal profile produces in the whole device a variation

of refractive index which may have important consequences on the optical features. The temperature profile is obtained by solving the well know thermal conduction equation at steady state. In fact in most cases temperature dynamics is negligible, being thermal time constants at least one thousand times slower than all the other ones involved in VCSEL simulation. Temperature equation reads as:

$$\nabla \cdot (\kappa \nabla T) = -Q_{tot} \tag{3.14}$$

where $T(\mathbf{r})$ is the 3D temperature profile and $\mathbf{r} = (\rho, \varphi, z)$ the 3D position. The thermal conductivity $\kappa(\mathbf{r})$ is assumed also direction dependent [37–39], with two different values in the transverse (κ_ρ) and longitudinal (κ_z) directions. Solutions of (3.14) can be obtained by imposing appropriate boundary conditions, that is a fixed value of temperature (T_0) at the heat-sink (usually the lower metal contact on the substrate) and vanishing of its derivative normal to the boundary surfaces. This problem can be solved either numerically (by taking a mesh of the device) or by using techniques based on analytical formulations [40, 41]. The temperature variation compared to the heat-sink is written as:

$$\Delta T(\mathbf{r}) = \sum_{ijl} c_{ijl} J_l(\theta_j \rho) \cos l\varphi \sin \zeta_i z \tag{3.15}$$

and takes into account the major phenomena of the thermal problem in a largely analytical way. In fact it can include both the anisotropy of the thermal conductivity, induced by the layered mirrors [39] and its spatial dependence, which is important for the final temperature profile. For the transverse part, please refer also to section 3.7.1; the only change is the computation window, which for temperature is much lager, so as to cover all the device size. The choice of the sine basis for the longitudinal temperature profile assure the continuity of the temperature at the substrate-metal interface; moreover, the choice:

$$\theta_i = \pi/(2L_z)(2i - 1) \tag{3.16}$$

will ensure a zero derivative at the semiconductor-air interface ($z = L_z$).

Equation (3.14) is now considered in more details, to show how the expansion procedure works also in presence of an anisotropic and spatially dependent thermal conductivity κ, which leads to:

$$\nabla \cdot (\kappa \nabla T) = \nabla \kappa \cdot \nabla T + \kappa \nabla^2 T \tag{3.17}$$

The laplacian and gradient operators can then be split in their transverse and longitudinal parts to allow the introduction of the anisotropic thermal conductivity, which will be indicated as κ_t and κ_z respectively. The thermal problem will read then:

$$\nabla_t \kappa_t \cdot \nabla_t T + \frac{\partial \kappa_z}{\partial z} \frac{\partial T}{\partial z} + \kappa_t \nabla_t^2 T + \kappa_z \frac{\partial^2 T}{\partial z^2} = -Q_{tot} \tag{3.18}$$

By substituting (3.15) in (3.18) and projecting on the basis functions one can transform the second order differential equation (3.17) into the much simpler problem for the coefficients of the temperature expansion:

$$\underline{c} = \underline{\underline{P}}^{-1}\underline{Q} \tag{3.19}$$

To reach this final form, the three indices of expansion (3.15) are organized in a vector, i.e. $\underline{c} \equiv c_{ijl}$. The projected heat source vector elements read:

$$Q_{ijl} = \int_0^{L_z}\int_0^{2\pi}\int_0^{r_M} J_l(\theta_j\rho)\cos(l\varphi)\sin(\zeta_i z)Q_{tot}(\mathbf{r})\rho d\rho d\varphi dz \tag{3.20}$$

and P is a matrix, whose elements are computed as:

$$\begin{aligned} P_{(ijl),(ijl)'} = &\int_0^{L_z} dz \int_0^{2\pi} d\varphi \int_0^{r_M} (\kappa_t\theta_j^2 + \kappa_z\zeta_i^2) J_{l'}(\theta_j'\rho)\cos l'\varphi \sin\zeta_i' z J_l(\theta_j\rho)\cos l\varphi \sin\zeta_i z\rho d\rho \\ &- \sum_m \int_0^{2\pi}\int_0^{r_M} \Delta\kappa_{zm} k_i' \sin\zeta_i z_m \cos\zeta_i' z_m J_{l'}(\theta_j'\rho)\cos l'\varphi \; \rho d\rho d\varphi \\ &- \sum_n \int_0^{L_z} \sin\zeta_i z \sin\zeta_i' z\rho_n \Delta\kappa_{tn}\nabla_t \Big[J_{l'}(\theta_j'\rho)\cos l'\varphi\Big]_{\rho_n} dz \end{aligned} \tag{3.21}$$

In such projection matrix three different contributions appear; the first term account for the laplacian of the temperature profile and is composed by a combination of thermal conductivity profiles and laplacian of the basis functions. There are also contributions stemming from the gradient of thermal conductivity, i.e. the first term of rhs of (3.17). If piecewise profiles are assumed for thermal conductivity, the spatial integration over z can be performed analytically. Therefore the last two rows of (3.21) accounts for the discontinuities of κ at the longitudinal positions z_m (second term in rhs of (3.21)) and at the transverse surfaces ρ_n (third term in rhs of (3.21)). $\Delta\kappa_{zm}$ and $\Delta\kappa_{\rho n}$ accounts for the corresponding steps in the thermal conductivity. The gradient leads to delta functions $\Delta\kappa_{zm}\delta(z-z_m)$ and $\Delta\kappa_{\rho n}\delta(\rho-\rho_n)$, which simplify the projection integral over the corresponding variables. In this way κ discontinuities are easily introduced. In the approximation that thermal conductivity is constant with temperature, $\underline{\underline{P}}^{-1}$ has to be computed only once, at the beginning of the simulation. In current driven semiconductor lasers there are three main heat sources contributing to Q_{tot} (see for an extensive analysis [40] and references therein):

- *Joule heating*: $Q_J = \sigma^{-1}(\mathbf{r})J^2(\mathbf{r})$ due to current injection through resistive mirrors. This is a major effect during all operation range; σ is the electrical conductivity and J the current density distributions in the whole VCSEL volume (see previous section).
- *Optical free-carrier absorption* in the doped layers: $Q_{fca} = \alpha(\mathbf{r})S_{opt}(\mathbf{r})$ is caused by the photons reabsorbed in the semiconductor, mainly by *free carrier absorption* α induced by doping. The optical power density S is spatially depending and follows the 3D distributions of the modal fields.

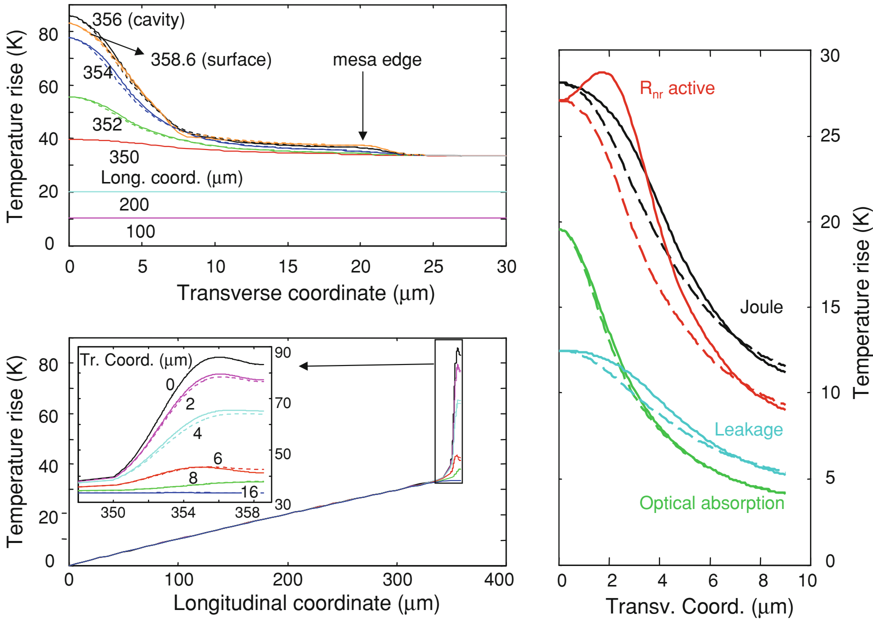

Fig. 3.15 *Left*: cuts of the temperature profile at 10 mA, from computation of the power versus current curve of Fig. 3.24. *Right:* Corresponding transversally resolved temperature contributions at the active section. The extreme angular positions (0 degree, *x*-axis, and 90 degree, *y*-axis) are shown by dashed and continuous lines. Partially from [42] (© 2009 IEEE)

- *Non-radiative recombinations*: $Q_{nri} = E_{gi} R_{nri}$, where E_{gi} is the band-gap energy of region i and $R_{nri} = N_i/\tau_i + CN_i^3$ the corresponding non-radiative recombination rate, see (3.29). Spontaneous recombinations take place not only in the active area, but also in other regions. Such contributions are very important to correctly simulate the laser power roll-off. In this model, different from preceding works, not only the active region, but also the cavity and the first Bragg mirror pairs serve as carrier reservoirs. Such latter contributions are negligible at low pumping, but become important at/above thermal rollover.

Some examples of temperature increase profiles are anticipated from the results section. Their cuts in the x-transverse plane at different longitudinal sections and in the longitudinal plane, at device center, for different x-positions, are shown in Fig. 3.15. In the 350 μm long substrate the temperature decreases linearly and has almost no transverse variations, thanks to the much higher heat conductivity of that region. Instead, in the transverse profiles the low heat conductivity of air surrounding the 20 μm radius mesa causes a fast decrease of the temperature at that interface. The richest features appear close to the active area, where temperature is maximum. Such transverse profile can qualitatively be compared to some experimental results recently published [43]. The single contributions to temperature increase show different transverse profiles, related to the corresponding heat sources. This can be

done thanks to the linearity of the heat diffusion problem (Eq. 3 of [42]). Only the recombination part has a small dip in the center, due to spatial hole-burning, which is completely compensated by the other contributions, all peaked at the center.

3.5 Major Temperature Related Phenomena

Most of the parameters introduced so far depend on temperature, at different degrees. In the following only the most important ones will be discussed in detail.

Thermal lensing: An important phenomenon related to temperature profiles in VCSELs is the so called "thermal lensing effect". It consists of a guiding effect induced by the refractive index increase at increasing temperature, which also gives rise to a red shift of the emission wavelengths. The dependence of refractive index on temperature is taken into account by the simple linear relation: $n(T) = n(T_0) + \frac{dn}{dT}\big|_{T_0}(T - T_0)$.
Therefore, since the temperature 3D profile has a maximum in the center of the device [43], that results in a guiding effect.

Absorption: The optical fields are directly influenced by temperature through refractive index and absorption increase, which is modeled by $\alpha = \alpha_0(T/T_0)^{2.2}$. In fact the major absorption source comes from free carrier absorption, which in the simple Drude model depends on the inverse of the carrier mobility. The latter, in turn, scales with approximately an inverse, nearly quadratic law with temperature [16]. Higher losses result at the center of the laser, favoring optical modes which are more intense at the device periphery. This effect counteracts the thermal-lensing, which by increasing guiding diminishes the modal losses. Therefore a minimum threshold gain is expected at certain operation conditions.

Optical gain and antiguiding: Lots of different optical models have been reported in the literature, either approximated (as e.g. [6]) or phenomenological [44] or directly derived from quantum-mechanical treatments [45]. For refined VCSEL simulations carrier, temperature and wavelength dependences must be carefully included. In this work the dielectric susceptibility induced by a 2D carrier density in a QW is computed with the model reported in [46] without coulomb effects. It provides at the same time the optical gain and the refractive index reduction induced by carriers in the active region, the so-called antiguiding effect. The QW band structure is included, accounting also for valence band mixing effects. The numerical costs are limited, since the computation is performed only once, creating look-up tables at varying carrier density, wavelength and temperature. These are later used in VCSEL simulation by appropriate fitting procedures.

Gain variations with temperature play an important role in a hot-cavity model, especially at high pumping. The temperature enters the optical gain model mainly through the quasi-Fermi levels and the bandgap red shift. The latter, which is the strongest effect, is introduced by the well-known relation: $E_g(T) = E_g(0) - aT^2/(T + b)$; where $a = 6.2 \times 10^{-4}$ eV/K, $b = 280$ K [47] for GaAs. An example of

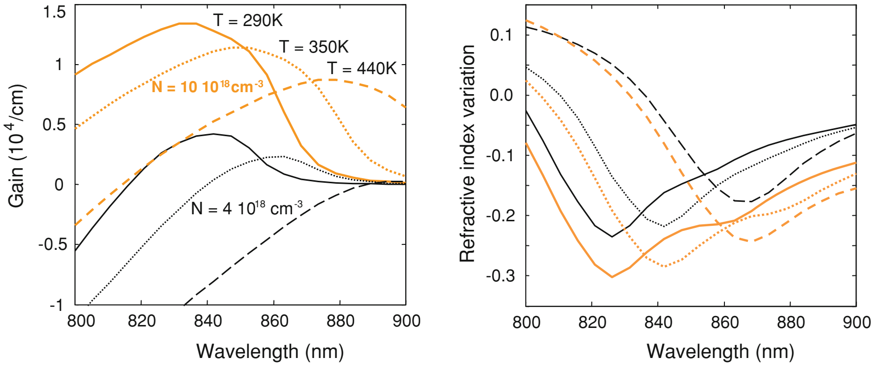

Fig. 3.16 Gain and refractive index variation spectra for different carrier densities and temperatures. Partially from [17] (© 2009 IEEE)

gain and refractive index variation spectra for an 8 nm GaAs/AlGaAs QW is shown in Fig. 3.16. The red shift induced by temperature is illustrated.

Carrier leakage: As previously discussed, a major phenomenon at high pumping is current leakage. In fact it exponentially depends on temperature, due to carrier thermionic escape from the QWs and from the potential walls of the cladding region [48]. This effect even goes beyond the usual drift-diffusion models [7], and has been introduced here in a phenomenological way. In [1] a dependence of the injection current on the quasi Fermi-levels is proposed. Temperature rises Fermi-levels and brings carrier closer to the potential barrier edges, thus increasing the escape probability. In this paper the dependence of injection/leakage on temperature and pumping is introduced via the escape and leakage times, τ_e and τ_L in system (3.28). To that end we introduce here the following *leakage factor*:

$$f_L = \frac{\tau_j}{\tau_{j0}} = \frac{2}{1 + \exp\left[I/(I_L - I_{th})\right]} \tag{3.22}$$

which shows a decreasing behavior at increasing pump rate, thus introducing increasing, pump dependent, leakage features. In $f_L,\ j = e, L,\ \tau_{j0}$ is the escape/leakage rate at room temperature and low pumping, I is the pump current, I_{th} is the threshold current and I_L is a current value close to the one where power roll-off occurs. It depends only on the longitudinal electrical design and must be found only once, by fitting an experimental power versus current curve. The different level of carriers involved in the laser action is taken into account by I_{th} in the denominator. The leakage factor f_L until slightly above threshold is close to unity, since $I \ll I_L - I_{th}$ and I_{th} can be neglected in the exponent. After threshold is reached I_{th} can be properly inserted in the leakage factor. This model is related to that of [1], but has more degree of freedom to fit the experimental findings. In fact I_L is linked to the height of the potential barriers which confine the carriers and it depends only on the band structure of the particular epilayer design.

Carrier recombinations: Also carrier recombinations increase with temperature; such effect adds to carrier leakage, since the number of carriers available for stimulated recombinations is diminished. In the model the recombinations are included as a function of the carrier density with the standard form of (3.29). The linear carrier lifetime τ is considered constant, while the spontaneous emission is computed in the same framework as for gain [49]. For Auger recombinations a cubic dependence on carrier density is usually assumed. The related coefficient C is the most sensitive on temperature and is particularly strong in InP-based devices, less for GaAs based ones. For temperature dependence of non-radiative recombinations one can refer e.g. to [50, 51].

3.6 Electrical Part

A good electrical model is very important since early design stages, so as to achieve not only good performance but simply lasing devices. Its main goal is to provide efficient carrier injection into the active area, keeping low the series resistance and optical losses due to free carrier absorption. Such issues are contradictory, so trade-offs must be pursued. The most common injection scheme, where the current is injected through the mirrors, is not so good in this respect. Therefore the electrical conductivity of the mirrors has to be improved by high doping levels, which in turn increase the free-carrier optical absorption. Modulation doping schemes and δ-doping at the optical field nodes are adopted to partly circumvent such issues [11]. Correspondigly a very complicated transport problem, comprising also complex band-gap profiles (see Fig. 3.7) has to be solved. That has never been attempted so far in full. To the best of my knowledge the approximate treatment presented in [7] is the most refined one. It solves accurately in a circularly symmetric structure the region close to the cavity, while approximates the outer mirror region by resistive bulk layers. This is still far from a fully 3D solution.

3.6.1 Approximated Current Profiles

Since here the main focus are the optical features, the electrical part will be kept at the simplest level as possible. Therefore only what affects directly the optical model is introduced, namely Joule heating and injection profile into the active region. To that purpose many groups [3, 16, 52] use a simplified model which is a fair approximation in the diode conducting regime. A resistive 3D problem described by a Laplace equation for the electrical potential has to be solved, namely:

$$\nabla \cdot \sigma(\mathbf{r}) \nabla V = 0 \tag{3.23}$$

where σ is the electrical conductivity and $\mathbf{r} = (\rho, \varphi, z)$ the 3D position. The current density distribution is simply given by $J(\mathbf{r}) = \sigma(\mathbf{r}) \nabla V$. In the results presented later

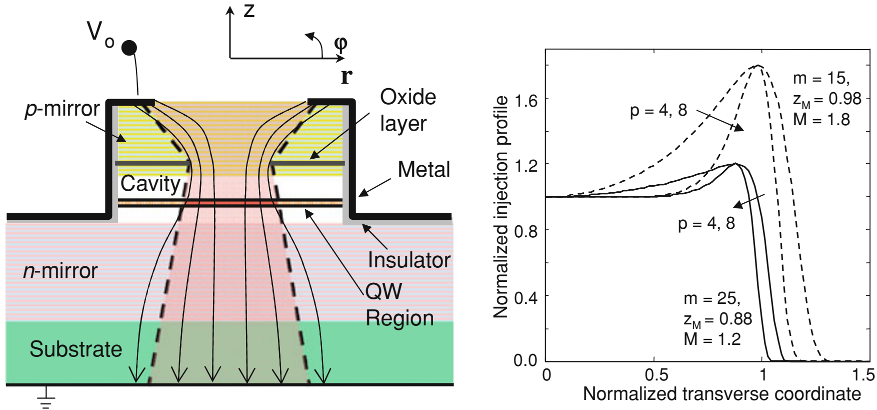

Fig. 3.17 *Left:* Scheme of a VCSEL electrically pumped through the mirrors. The thin, dashed lines are a sketch of the current paths; the thick, dashed ones the approximate profile. *Right:* Current profiles from (3.24) for different positions z_M and heights (M) of the injection overshoot and exponents m and p

an even more simplified approach is adopted. That may be convenient, allowing more degrees of freedom to fit the model to experimental results, in particular for the current injection profile into the quantum wells [6]. The latter has to be complemented by the 3D current distribution for Joule heating. To estimate it, one can take advantage of the following considerations. The semiconductor layer under the metal is heavily doped, to enhance current flow towards the device axis. Therefore the current is assumed to spread over a section related to the outer contour of the metal ring. Due to the oxide layer, the current is then forced to enter the oxide aperture, after which it can continue towards the ground metallization on the back side of the substrate. Such paths have a shape similar to a sand-glass (see Fig. 3.17) whose top and bottom parts are approximated by two truncated cones with straight walls. The upper part is fixed by the structural geometry (metal contact and oxide aperture shape), while the lower part is most influenced by carrier scattering and diffusion over the long path through the substrate (200−500 μm), during which the current can possibly spread. In this simplified view the current density is fully determined by the VCSEL geometry. That allows for any shape of the metal ring contact and, much importantly, of the oxide shape, which is never circular in real devices [11], but rather with a diamond shape (see Sect. 3.3.3).

The previous model, reasonable as Joule source, might be over-simplified to derive the carrier injection profile. In fact, the combination of a metal contact ring with a smaller oxide aperture causes the so called current crowding effect. It consist of a stronger injection close to the oxide aperture rim than in the center; the current tends always to follow the shortest path between the two electrodes. For all those cases when such effect is relevant, especially for large aperture devices, the constant injection profile can be modified by a phenomenological injection shape, suitable to describe the current crowding features, such as:

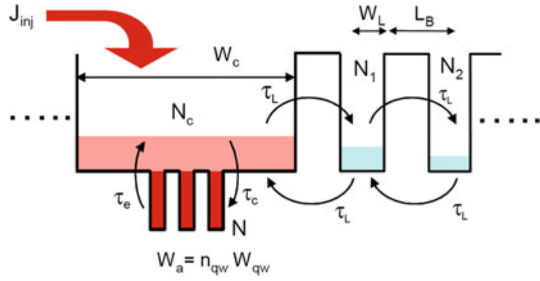

Fig. 3.18 Scheme of the introduced carrier reservoirs and their interactions

$$J_{inj}(z) = J_0 \exp(az^p - bz^m) \tag{3.24}$$

This super-Gaussian shape is a generalization of the one proposed in [6]. The second, negative term $(-bz^m)$ in the exponent accounts for the current confinement induced by the oxide aperture shape. The exponent m can be chosen so as to fit the injection decay in the outer region. For very large m values the shape can be made close to step like (constant in the center and zero in the outer region). The transverse profile is included via the normalized radial coordinate $z = r/r_s(\varphi)$, being $r_s(\varphi)$ the angularly (φ) dependent oxide aperture shape. Current crowding is represented by the first, positive term (az^p). Depending on the absolute size of the oxide aperture, the exponent p can be chosen to fit the injection overshoot which occurs slightly before the oxide edge $r_s(\varphi)$. An example of the possible different profiles can be seen in Fig. 3.17. For very deformed aperture shapes the four parameters may be assumed to vary azimuthally. They can be obtained e.g. from the experimental spontaneous emission, which is directly related to injection through carriers, as for example the ones measured and reported in [53].

3.6.2 Current Leakage

To provide a reliable simulation of laser action also at high pump rates, carrier leakage has been included in the model. This ingredient would enter automatically within a fully self-consistent electrical model, accounting for the full band-structure of the device. Here the carrier leakage is introduced in a phenomenological way, via capture and escape rates among different carrier reservoirs, as schematically illustrated in Fig. 3.18. This is somewhat similar to what proposed in [39], but including also the pairs of the Bragg mirrors closer to the cavity as carrier-drain regions. The need for such additional terms comes clear by considering the computed carrier profiles at high pumping rates, as exemplarily shown in Fig. 3.19, where the results of a 1D simulations obtained by Simwindows code [30] are reported. At high pump rates and temperatures, those regions can spill a significant fraction of current from the cladding region and effectively contribute to carrier leakage. The carrier densities in the different regions are supposed longitudinally constant, since of the small widths of

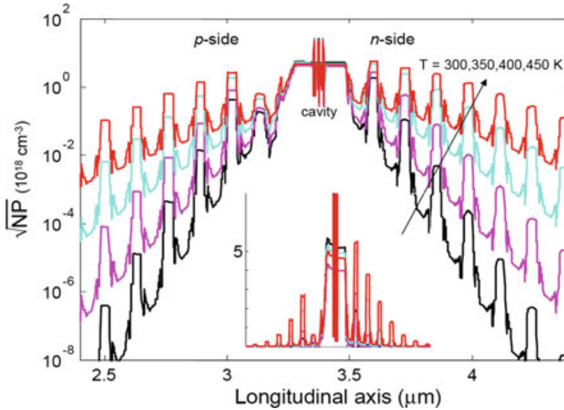

Fig. 3.19 Carrier profiles in a hard-pumped VCSEL, given as $\sqrt{NP}$ and in logarithmic scales so as to put in evidence the minority carrier in the *p*- and *n*-doped regions. N and P indicate the electron and hole densities. The inset shows the same information in linear scales; the carriers in the QW have values around $20 \times 10^{18}\text{cm}^{-1}$ and have been zoomed so as to put in better evidence their behavior in the lateral regions. The computations are performed by Simwindows [30] at different temperatures. Only the region around the cavity section is shown, where the effect of leakage in the Bragg mirror is stronger. Device structure as in [54]. From [42] (© 2009 IEEE)

the confinement potentials compared to diffusion lengths; this can be well observed in Fig. 3.19. The rate equations for the carrier densities N_l (in the *p*- and *n*-pairs, $l = 1, l_{max}$) and N_c (in the cladding) read as:

$$\begin{aligned}
\frac{\partial N_c}{\partial x} &= L_c^2 \nabla_t^2 N_c - N_c(1 + \frac{1}{x_c} + \frac{2}{x_L}) + \frac{2}{x_L}\frac{W_B}{W_c}N_1 + \frac{1}{x_e}\frac{W_a}{W_c}N + \frac{J_{inj}}{eW_c} \\
\frac{\partial N_1}{\partial x} &= L_1^2 \nabla_t^2 N_1 - N_1(1 + \frac{2}{x_L}) + \frac{W_c}{W_B}\frac{1}{x_L}N_c + \frac{1}{x_L}N_2 \\
\frac{\partial N_l}{\partial x} &= L_l^2 \nabla_t^2 N_l - (1 + \frac{2}{x_L})N_l + \frac{1}{x_L}(N_{l-1} + N_{l+1})
\end{aligned} \tag{3.25}$$

The first terms in the r.h.s. account for carrier transverse diffusion, being L_l the corresponding diffusion lengths. The time is normalized as $x = t/\tau$, being τ the linear contribution to carrier lifetime (see (3.29)). Also the model time constants τ_i are normalized as $x_i = \tau_i/\tau$. N is the carrier density in the active region. For a visual guide of the introduced variables and lifetimes governing their exchanges, refer to Fig. 3.18. The model (3.25) takes into account the different widths W_i of the involved carrier reservoirs: active (a), cladding (c) and Bragg mirrors (B). It introduces three time constants:

- τ_c capture time of carriers into the quantum wells from cladding
- τ_e escape time of carriers from the quantum wells to cladding
- τ_L leakage time; this is assumed for simplicity equal for all the carrier exchanges from cladding to mirror pairs and within different mirror pairs.

In practice the exchanges among the different Bragg pairs might not be ruled by a unique time constant, even supposed equal for escape and capture rates. This is assumed for the sake of simplicity. Also, the leakage in the mirrors is supposed symmetrical (same in p and n mirrors). The slight asymmetry (see Fig. 3.19), giving preference to the n-side does not justify a much higher numerical effort in a phenomenological model. By introducing some approximations, system (3.25) can be simplified and the number of unknowns reduced. Namely, one can observe that:

$$N_{l+1} - 2N_l + N_{l-1} \simeq L_B^2 \frac{d^2 N_l}{dz^2} \tag{3.26}$$

is the discretized form of a second derivative, being L_B the period of the Bragg mirror. By neglecting transverse diffusion in the outer Bragg pairs, one can then simply relate their carrier profiles to that of the first pair by:

$$N_l \simeq N_1 \exp[-(l-1)\sqrt{x_L}\ ] \quad l = 2, l_{max} \tag{3.27}$$

An exponential decay of minority carriers in the mirrors is clearly observed in Fig. 3.18, giving credit to the previous approximation, which strongly reduces the number of variables. Therefore only two variables, N_c and N_1, are added to the standard rate equations, which deals only with active carriers and photons.

3.7 Rate Equations

The rate equation model is derived in the standard way from quantum theory of semiconductor lasers [49], by performing the usual approximations (carrier neutrality, adiabatic elimination of the microscopic polarization). Including the improved injection scheme previously discussed, it reads as:

$$\begin{aligned}
\frac{\partial N_1}{\partial x} &= L_1^2 \nabla_t^2 N_1 - \frac{1}{x_{ef}} N_1 + \frac{W_c}{W_B} \frac{1}{x_L} N_c \\
\frac{\partial N_c}{\partial x} &= L_c^2 \nabla_t^2 N_c - N_c \left(1 + \frac{1}{x_c} + \frac{2}{x_L}\right) + \frac{2}{x_L} \frac{W_B}{W_c} N_1 + \frac{1}{x_e} \frac{W_a}{W_c} N + \frac{J_{inj}}{e W_c} \\
\frac{\partial N}{\partial x} &= L_a \nabla_t^2 N - \tau R(N) - \sum_q \tau R_{st,q} - \frac{1}{x_e} N + \frac{W_c}{W_a} N_c / x_c \\
\frac{\partial P_i}{\partial t} &= \left(\Gamma_z G_{m,i} - L_{m,i} - \sum_q \epsilon_{iq} P_q - \epsilon_{ii'} P_{i'} \right) P_i + S_i
\end{aligned} \tag{3.28}$$

The first two equations deal with the carrier reservoirs and constitute the injection model discussed previously. $x_{ef}^{-1} = 1 + (2 - e^{-\sqrt{x_L}})/x_L$ is an effective time which arizes from eliminating the outer outer Bragg pairs by (3.27). In the third dynamical equation for the carrier density in the active region, the recombination term is written as:

$$R(N) = N/\tau + CN^3 + R_{sp}(N) \tag{3.29}$$

and includes non radiative recombinations in the standard way as a linear term (N/τ) and a cubic one (CN^3) for Auger contributions. Radiative recombinations R_{sp} are instead computed out of the standard quadratic approximation, by means of a band-to-band model [55]. Within this injection model, the driving term for active carriers is $\frac{W_c}{W_a} N_c/\tau_c$. The standard, simpler rate equation model can be obtained by substituting this term by $J_{inj}/(eW_a)$ and neglecting carrier escape N/x_e from QW and all other carrier reservoirs.

In the photon equations:

- P_i is the output power into the i-th optical mode, defined both by its transverse and polarization features,
- $P_{i'}$ is the power into the orthogonally polarized mode compared to P_i,
- Γ_z is the longitudinal confinement factor of the multiple quantum well active region,
- $G_{m,i}$ is the transverse modal gain of the corresponding optical mode, defined as:

$$G_{m,i} = \frac{\int_S G_i I_i ds}{\int_S I_i ds} \tag{3.30}$$

  where G_i stands for the material gain in cm^{-1} for i-th mode, $\int_S (\cdot) ds$ the integral over the whole transverse surface, $I_i = |E_{act,i}|^2$ the field intensity profile at the active section,
- $L_{m,i}$ is the overall loss of mode i,
- ϵ_{iq} is the gain saturation and $\epsilon_{ii'}$ the cross-gain saturation coefficient between the two polarizations [56],
- S_i is the spontaneous emission in mode i [49].

The last two equations are directly coupled through gain $G_i(N)$ and the stimulated emission term, which is written as:

$$R_{st,q} = \omega_q \Im m(\Delta\varepsilon_{act}) I_q/(\omega_q \hbar) \tag{3.31}$$

By considering that $\Im m(\Delta\varepsilon_{act}) = G_q/(\omega_q Z_r)$ (being Z_r the reference impedance [24]) and that the output optical power of mode q can be written in terms of the electric field E_o at the output section as $P_q Z_r = \int_S |E_o|^2 ds$, (3.31) can be rewritten as:

$$R_{st,q} = \frac{G_q I_q}{\omega_q \hbar Z_r} \frac{P_q}{P_q} = \frac{G_q |E_{act,q}|^2}{\omega_q \hbar \int_S |E_{o,q}|^2 ds} P_q \tag{3.32}$$

In this way the quantities of major interest, the modal output powers, play the role of unknowns other than the field intensities in the active region. These two quantities are linked not simply by the Bragg mirror transmission coefficient as in most models, but

by the ratio of the modal field profiles at the output and active sections. For particular designs this factor can play an important role since it varies from one mode to another.

Carrier spin relaxation phenomena [57] are included in an approximate way [56], which allows to eliminate the equations for the spin-population difference and for the field phases. All the effects but phase nonlinearities are included through the nonlinear cross gain between the two polarizations; their explicit expressions can be found in [56] and have to be adjusted so as to account for the output power instead of the cavity photon number. The implementation of the full SFM model [57], as presented in [6], is relevant when polarization issues in quasi isotropic VCSELs are of main concern. In principle this might be done within the present model, but with higher computational costs (inclusion of the phases of the fields and the spin population difference). This is out of the scope of the present paper.

3.7.1 Carrier Expansion and Projection Technique

System (3.28) is a set of differential coupled equations. Its size and therefore the corresponding computer resources, are determined mainly by the carrier equation. In fact the system has one equation for each optical mode, while the usual way to handle spatial dependent carrier densities is to use a meshing technique. The latter results in as many coupled dynamical equations as the number of discretization points (see e.g. [7, 52]). In circularly symmetric devices this leads to a quite reasonable size of the system since accurate results can already be obtained with about one hundred of discretization points in the radial coordinate. However if one leaves the circular symmetry the number of carrier samples lays on a 2D mesh, leading to a much larger system of differential equations. This becomes three times larger, when accounting also for system (3.25). Therefore carrier densities are expanded by using 2D functions of the form:

$$N = \sum_{jlp} n_{jlp} J_l(k_j \rho) A_p(l\varphi) \tag{3.33}$$

where A_p stands for sin or cos angular variation and J_l is the Bessel function of the first order. This is a generalized form of what already proposed by [5, 8, 58], including also azimuthal variations that can handle any kind of carrier profile. If the geometry is symmetric with respect to the crystal axes as it occurs most of the times, only even azimuthal indices are involved. For circular devices and assuming a perfect azimuthal modal degeneracy (as is assumed most of the times in the literature), no angular variations occur and only the radial part is sufficient. The chosen basis (3.33) guarantees zero derivative of carrier densities at the center ($\rho = 0$). The choice of k_j is made by imposing the orthogonality of the basis in the computation window, which turns out to require a zero of the first derivative at the edge of computation window [42]:

$$J'_\nu(k_i r_\mathrm{M}) = 0 \quad \forall \;\; i \tag{3.34}$$

By means of (3.33) one can rewrite the dynamical system in terms of the coefficients of the expansions. In this way the size of the system is determined by the number of the elements of the basis and can be greatly reduced compared to other discretization techniques. The coefficients of the expansion are found by a projection technique. It is readily realized that a *full projection scheme*, that is using only the coefficients instead of the spatial variables, is cumbersome and numerically inefficient. In fact, since one has complex profiles of all the involved quantities (fields, temperatures, QW optical susceptibility) which in turn interact in nonlinear ways, one cannot handle the system as in [5] without either loosing most of the information or obtaining a huge amount of terms due to the nonlinear interactions. A huge number of projection coefficients arise in the linearized form of the laser rate equations [8]. Therefore this technique is not pursuable for a refined simulation, where also the field profiles changes during operation through thermal effects. It is proposed here, for the first time, what I call a *mixed technique*. It preserves the benefits of both the spatial and projection techniques: the accurate representation of all the interactions and the computational efficiency. The carrier expansion is used only to lower the size of the system and to analytically compute the diffusion terms in the carrier equations, which, by exploiting the properties of Bessel functions [59], reads as:

$$\nabla_t^2 N = \sum_{jlp} -k_j^2 n_{jlp} J_l(k_j \rho) A_p(l\varphi) \tag{3.35}$$

All the other variables at rhs of system (3.28) are kept in their spatial representations and only the final result is projected on the basis functions. This is done by numerical integration at every step of the integration of the nonlinear dynamical system. Examples of expansion coefficients and corresponding computation times are anticipated in Fig. 3.20 from Sect. 3.8. 125 expansion coefficients are able to well represent a complex carrier profile (see. Fig. 3.27). More than ten time faster computation times are achieved by the projection technique, as shown on the right plot, even if it comes clear that the most of the computing time is spent by the optical solver.

3.7.2 Light Output Curve Computation

To compute the power versus current curves of a VCSEL one has to solve all the above problems self-consistently. The core of the model is the rate-equation problem (3.28), which is treated by a Matlab ODE (ordinary differential equation) solver, until the steady-state is reached. Some approximations are introduced so as to stay within reasonable computation times. The following simple scheme is applied to compute a PI curve:

1. A current value is set,
2. The corresponding temperature profile is computed
3. The optical problem is solved by VELM, including all 3D thermal effects (refractive index and absorption profiles). Actual gain and refractive index distributions

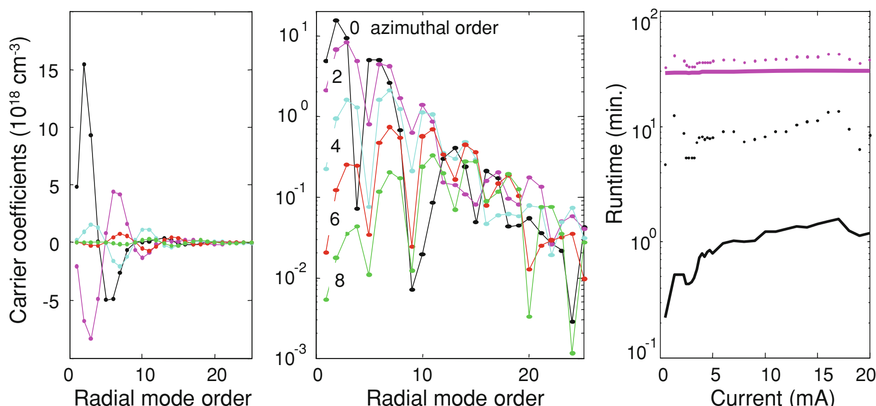

Fig. 3.20 *Left:* Example of expansion coefficients of the active region carrier density N at 15mA (see Sect. 3.8). The logscale puts in better evidence the small coefficients. *Right:* Computer runtimes (Intel Core 2 Extreme CPU Q6850@3GHz) vs. current within the two different carrier techniques: expansion (*lines*) and spatial sampling (*dots*). In black the runtime spent on the solution of the rate equation system, in magenta the total runtime, whose major contribution comes from the optical solver. Partially from [42] (© 2009 IEEE)

in the active region are included, using the carrier density profile of the preceding current value. This provides modal fields, frequencies and gains.

4. All preceding steps are used in system (3.28), which is solved up to steady-state.

Starting from zero current, steps 1 to 4 are passed until all the required current values are considered. Approximations are included at step 2, where to compute the thermal profile the actual current value is input, but for non-radiative recombinations and reabsorbed optical power the values of the preceding current step are used. The same is applied for gain profile and carrier antiguiding. By keeping the current steps sufficiently small, these are fairly good approximations and result in a huge increase of computational efficiency. In case one is not satisfied with this scheme, an iterative procedure can well be applied also in the framework of this model. The computation of a PI curve starts from below threshold, at weak injected currents. The latter define the 3D current path, according to the simple geometrical model described in [42]. Its important ingredients are the dimensions and shapes of the metal ring and the oxide aperture. Through the spatially dependent resistivities one can compute the Joule heating source.

3.8 Example of Results

The model has been first tested on real devices, by comparing the numerical results with the experimental findings [17]. It is then useful to briefly report on that, since also some of the model parameters have been achieved by that comparison. The same

	Parameter	Symbol	Value	Units
	Electrical properties			
*	Resistivity in the cladding	ρ_c	1	$\Omega\mu$m
*	Resistivity of substrate	ρ_s	10	$\Omega\mu$m
*	Resistivity of n-mirror	ρ_n	100	$\Omega\mu$m
*	Resistivity of p-mirror	ρ_p	1000	$\Omega\mu$m
	Thermal properties			
*	Ther. cond. mirrors (tran.)	κ_{Bt}	6	W m^{-1} K^{-1}
*	Ther. cond. mirrors (long.)	κ_{Bz}	5	W m^{-1} K^{-1}
	Ther. cond. substrate	κ_s	40	W m^{-1} K^{-1}
	Ther. cond. air	κ_a	0.025	W m^{-1} K^{-1}
	Ther. cond. metallization	κ_m	300	W m^{-1} K^{-1}
*	Ther. cond. cladding	κ_c	10	W m^{-1} K^{-1}
	Ther. cond. passivation	κ_p	0.5	W m^{-1} K^{-1}
	Carrier dynamics			
	Diffusion coefficient	D	20	s^{-1} cm^{-2}
	Linear carrier lifetime	τ	10	ns
	Auger coefficient	C	3.5 10^{-30}	s^{-1} cm^{6}
*	Capture time	τ_c	5	ps
*	Escape time	τ_e	150	ps
*	Leakage time	τ_L	100	ps
	Others			
	Refractive index var.	dn/dT	2.10^{-4}	K^{-1}
*	Leakage factor	I_L	9	mA

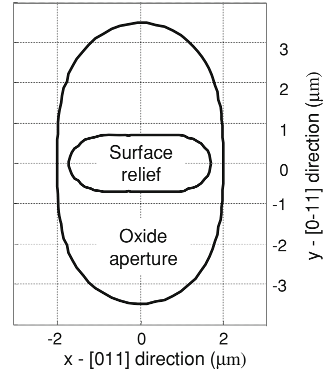

Fig. 3.21 Table of parameters (*left*) and transverse geometry used in the simulations. The parameters indicated by asterisks are used to fit the experimental results

structure is here used to investigate a more demanding transverse geometry, useful to better put in evidence all the relevant model features.

The VCSEL epilayer design is from the Ulm University [54] and is aimed for single mode operation. Therefore the built-in optical confinement is set to a minimum and thermal effects play a role also on the modal properties from the very beginning of operation. The 860 nm design comprises 23 AlGaAs layer pairs in the p-doped top Bragg mirror and 39.5 pairs in the n-type bottom mirror. The active region consists of 3 GaAs QWs placed at the center of the λ-cavity. The current is confined by a thin oxide aperture in the first top-mirror pair above the cavity, at a field node, so as to keep the optical guiding low and therefore to inhibit high order modes as much as possible. Current is injected through a top metal annular ring, 16 μm in diameter (see Fig. 3.17). The sample was designed with an out-of-phase cap-layer, so that the top mirror reflectivity is minimum. Later processing, etching away 60 nm or cap-layer, restores the high mirror reflectivity in a selected inner area, which results in the so called *inverse relief* technique [60]. In that way single transverse mode operation is possible and successfully achieved. Devices with a circular relief of 3 μm diameter show single mode operation over the full working range, attaining the very high power of 6.3 mW [54].

3.8.1 Model Validation

On the same inverted chip both surface-relief (see Chap. 5 for more details) and standard devices were processed for comparison. The latter are obtained by simply etching the whole out coupling section defined by the opening of the metal contact ring. A list of parameters used to simulate PI curves is given in the table of Fig. 3.21. Some of them are typical and taken from literature [52], some result from a parametric study to match the experimental results. In the two devices all parameters are the same, except for the surface relief. That single change produces all the differences, as shown in Fig. 3.22. The threshold is drastically reduced by a factor of five, the differential efficiency is smaller and the power rollover occurs at higher current. Moreover, at around 4 mA, first-order modes start to contribute to the laser action, as it is seen from the spectra at various currents [17]. All those experimental features are fully reproduced by the numerical results; this is a strong indication that the parameter set correctly describes the epitaxial design. The modally resolved output powers come for free from the simulations, since the total power is simply obtained by summing up all the modal contributions. In the experiments, that information can be accessed only indirectly, via the current-resolved optical spectra. Their peak values are extracted at different pump rates and plotted vs. current, showing a fairly good comparison. dB scales allows also non-lasing modes to be seen; the model can reproduce them thanks to the spontaneous emission terms S_i in (3.28) of the individual modes. The computed total power accounts for the sum of all the supported modes with the addition of the power related to radiative spontaneous recombinations; the latter is the dominating term below threshold, while it stays almost clamped above threshold.

For the surface relief VCSEL, one can see that first-order modes are well suppressed over the whole operation range. The suppression stays pretty constant, nearly at 40 dB, and compares very well with the computed results. The situation for the standard device is much more complicated, since many modes contribute to the lasing action in different amounts at varying current. For the first time to the best of my knowledge, a modally resolved PI curve is compared with the experimental data. In particular, the competition among the fundamental and the two first-order modes compares very well up to 10–12 mA, where in the measurements the higher-order modes come into play. In the lower injection range, the onsets of the first-order modes, their relative power share (induced by the oblong oxide aperture) and the current for which the power of the fundamental mode equals that of the first-order mode are well reproduced.

To better access the thermal behavior and see how the model compares with experiments, the positions of the modal peaks are extracted from the measured spectra. The comparison is shown in Fig. 3.23 for both analyzed devices. The agreement is very good even in the details. In particular one can observe a sort of thermal run-away at high pump rate above rollover, which is due to the conversion of carriers to heat instead of light and to the recombinations from leaked carriers.

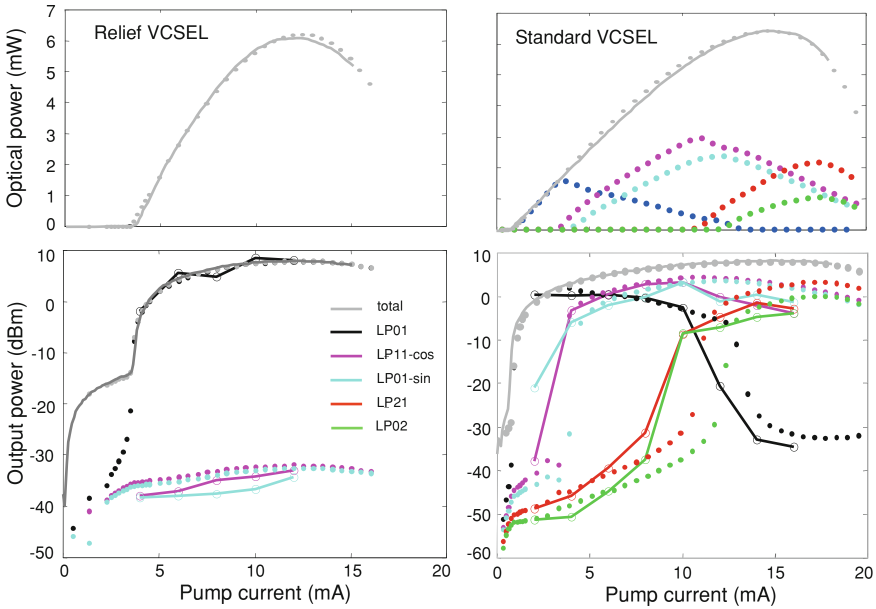

Fig. 3.22 Optical output characteristics in natural and logarithmic units (dBm) so as to clarify the features of weaker/non-lasing modes. In the lower plots also the modally resolved powers extracted from the peaks of the experimental spectra are given, which are displayed as open circles, connected by lines as a guide to the eye. The modally resolved powers are displayed by dotted lines of different gray tones. The total emitted power provided by computations (*dark gray dots*) includes spontaneous radiative recombinations and is compared to total experimental power (*dark gray lines*). From [17] (© 2009 IEEE)

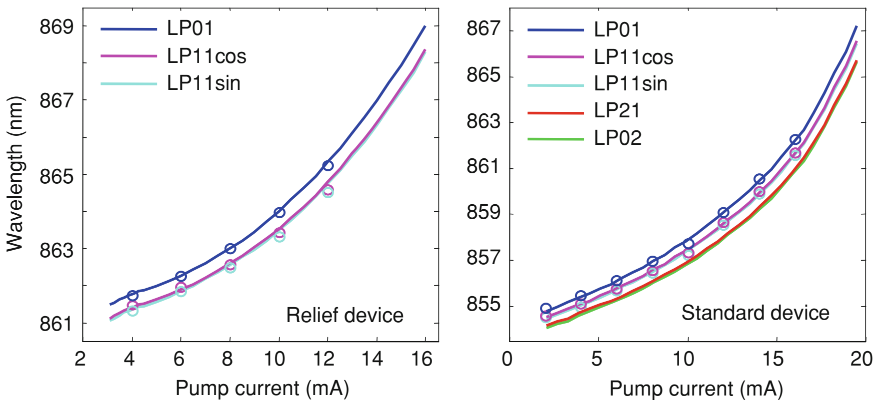

Fig. 3.23 Modal wavelength vs. current from the optical spectra (*open circles*) and from the computations (*continuous lines*). From [17] (© 2009 IEEE)

3.8.2 Additional Examples of Numerical Results

To illustrate all model features, a more computationally demanding structure is adopted where all the possible effects come into play. The epilayer design is the same of the real devices considered before, but the transverse geometry is strongly deformed and shown in Fig. 3.21. The inherent oblong oxide aperture shape which arises from wet oxidation (see Fig. 3.6), is here exaggerated on purpose so as to put in better evidence the model capabilities in handling non-circular symmetries. Additionally an oblong surface relief, $3.4 \times 1.7\,\mu m^2$ wide and 60 nm deep, is introduced as transverse and polarization mode filter, similarly to [61]. In the electromagnetic modeling, the electro-optic effect is included, according to Sect. 3.3.3. This results mainly in a frequency difference between the polarizations, which is taken into account in computing the optical gains. The x- and y-axes are oriented according to the crystal directions, as shown in Fig. 3.21. Both oxide aperture and surface relief are described by the analytical shape (3.13), with $r_0 = 2.67$ (3.1), $\Delta_2 = -0.281$ (0.454) and $\Delta_4 = 0.03$ (0.09) for the oxide aperture (surface relief).

As for the experimental case considered before, a flat injection profile is used ($m = 20$, $b = 1$, $a = 0$ in (3.24)). Figure 3.24 reports the computed PI curve. A major difference with previous results is that now the full vectorial treatment is used. The fingerprints of the non circular geometry in the active part and in the relief can be clearly seen. All the mode are non-degenerate, as concerns both the polarization and the spatial distribution (for first order modes). For the latter one can see that the cos-like modes (see Fig. 3.25) are preferred to the sin-like ones, due to their better superposition with the oblong surface relief. Since of the 90deg rotated oxide aperture, exactly the opposite happens for the modal gains, where the sin-like modes superimpose better with the gain shape. None of them succeed to reach threshold during operation and their emission powers stay always below 40 dB compared to the lasing mode. Due to the inherently stable resonator design with the oblong relief, all spin relaxation nonlinearities [56] have been omitted here for the sake of simplicity. The non-lasing x-polarization stays always below 20 dB the lasing mode.

The vectorial and 3D fields are computed accounting for the 3D thermal distribution and gain/refractive index profiles in the active region. The continuously varying thermal profiles (see Fig. 3.15) have been longitudinally discretized by a staircase approximation, accounting 20 steps within the 8 μm of the optically significant structure (Bragg mirrors and cavity). The different modal losses are extracted from the optical model, together with the relations between cavity and output intensities. Those are computed by making use of the field profiles at the corresponding two sections. The modal gains provided by the carriers in the active section are part of the dynamical system and are computed in the standard way, by superposition of the active field intensity and gain profile induced by carriers.

The modal gains and losses are shown in Fig. 3.25 for the six modes included in the simulation of the previously described device: the fundamental, gaussian-like mode and the two first-order modes, with their x and y dominant polarizations.

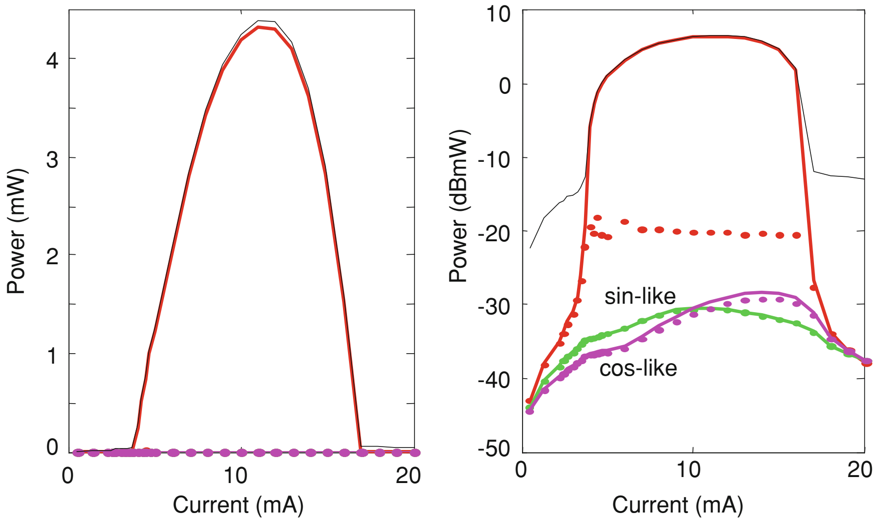

Fig. 3.24 Optical power vs. current in linear (*left*) and logarithmic (*right*) scales. Continuous (*dashed*) lines show the *y* (*x*)-polarized modes. The black, thin lines report the total emission (sum of all included modes and spontaneous emission, related to carrier density). Partially from [42] (© 2009 IEEE)

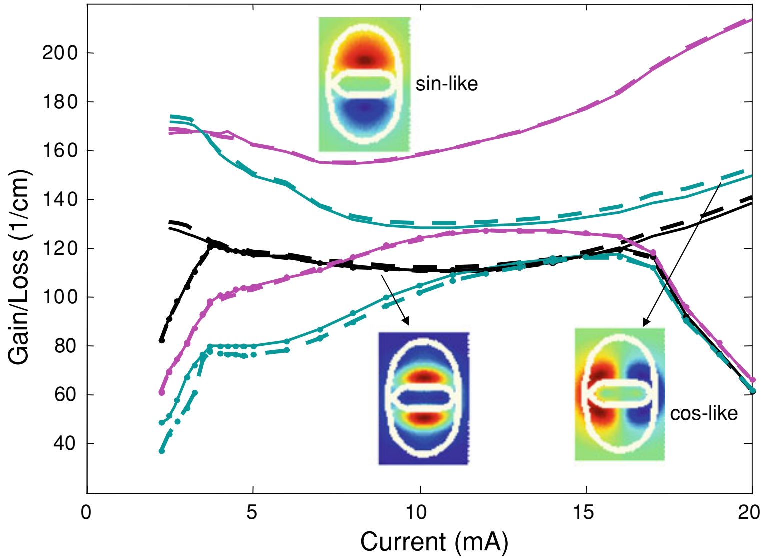

Fig. 3.25 Modal gains (*lines and dots*) and losses (*only lines*) vs. current. The continuous (*dashed*) lines show the *y* (*x*)-polarized modes, whose transverse profiles, rendered by the different colors, are shown at the output section by the insets. Partially from [42] (© 2009 IEEE)

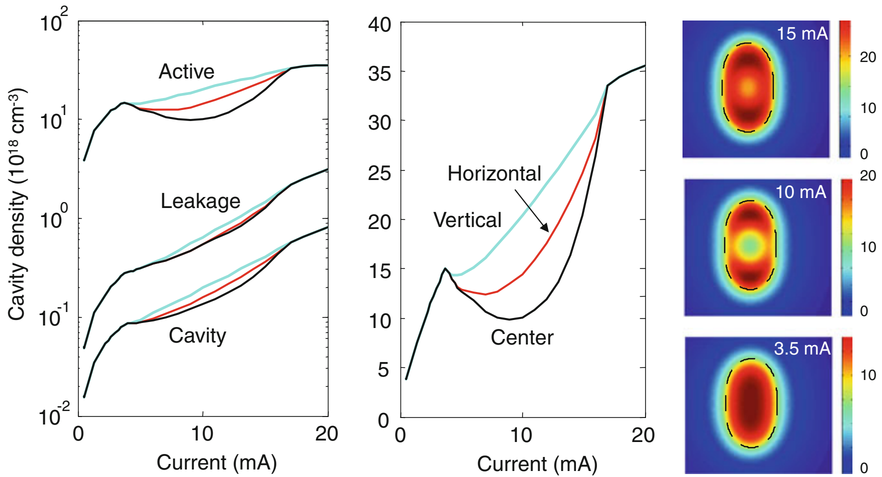

Fig. 3.26 *Left:* Carrier values vs. current at particular spatial places: center, maxima in x- and y-directions; logscales allow to show the small values related to cavity and leakage in the Bragg mirrors. *Center:* The same information for active carriers, in linear scales. *Right:* Corresponding carrier profiles for different injection currents. Dashed lines refer to oxide aperture

As soon as the injected current delivers enough gain so as to compensate for the lowest losses, threshold is reached for that mode, usually the fundamental mode, gaussian-like intensity profile. This happens also in our device over the whole range of operation. Here the modal gain of the lasing mode strictly follow the modal losses, which depend mainly on the thermal properties and vary during operation. In the figure one can see the opposite effects of the two main actors in the optical problem: thermal lensing and temperature dependent losses. At low pump rates the effect of the thermal lens (Eq. 17 of [42]) dominates and the losses diminish with current. This is due to the stronger optical confinement which reduces the field portion in the region outside the relief. Instead at high currents the increased losses (Eq. 18 of [42]) prevail, giving origin to minimum modal losses at certain current values.

In Fig. 3.26 one can compare the carrier values in the different zones: active, cavity, leakage. The carrier densities at device center and their maxima in the horizontal and vertical direction are shown vs. injection current. On the right side the corresponding carrier profiles in the active section are given at different currents; the spatial hole burning phenomenon clearly appears. Below threshold carrier are maxima at the center; above threshold carrier are converted to photons according to the intensity shape of the lasing mode. Therefore they diminish in the center and stay higher close to oxide aperture rim; in this case their values along the rim are varying, due to the different oblong shapes of carrier and optical intensity profiles.

The density in the cavity region is the lowest due to the its largest volume. In any case, the carrier densities other than the active ones stay small, as it has to be for a properly working device. They increase with pumping due to the injection-dependent

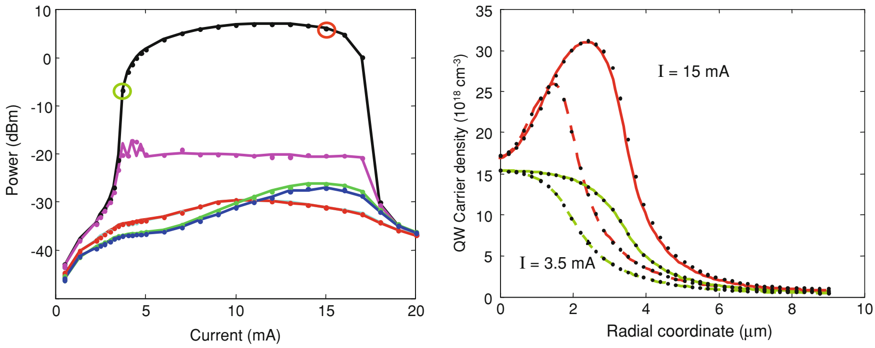

Fig. 3.27 *Left:* Modally resolved optical powers vs. current, computed with the simplified injection scheme (only active carriers included). The dots refer to results computed by using a spatial sampling technique. *Right:* corresponding carrier density profiles at 3.5 mA *(gray)* and 15 mA (*black*) in the *x*-(*continuous lines*) and *y*-(*dashed lines*) directions. Dots refer to results computed with the spatial sampling technique. From [42] (© 2009 IEEE)

leakage factor (Eq. 19 of [42]). This can be seen in the logscale plot, by comparing the active carrier increase with the ones of the other reservoirs.

In Fig. 3.27 one can see the same results of Fig. 3.24, but computed within the simplified injection scheme. This is done with the purpose of comparing the expansion technique adopted here with the common carrier sampling procedure. The two simulations provide very similar results, hardly distinguishable in the figures, with reference to both optical power and carrier profiles. An example of the latter is given for two injections. The maximum deviations are 50 μW in optical power and 2×10^{17} cm^{-3} for active carrier density. This provides an important validation to the expansion technique.

The temperature increase is caused by different heat sources, as discussed in Sect. 3.4. Figure 3.28 shows the contributions to temperature increase vs. current. It appears that Joule heating and carrier non-radiative recombinations are effective over the whole operation range while optical absorption contributes only where the laser action is stronger. Carrier non-radiative recombinations in the active area increase up to threshold, stay almost clamped in the first range of operation regime, than increase again to compensate for the lower gain and higher losses at increasing temperature. Finally, non-radiative recombinations of leakage carriers provide a contribution which becomes relevant at high pumping rates due to its exponential increase above thermal rollover (see Eq. 19 in [42]). Therefore the additional carrier reservoirs comes into play at strong pumping regimes and are useful to describe power rollover. All these saturation effects are caused by temperature, which is therefore a very important ingredient in VCSEL simulation.

In Fig. 3.28 the effects which contribute more to power rollover are also analyzed. To that end the simulation is run several times, by excluding each time a different, temperature dependent, phenomenon: dependence of the optical response of the QW material, dependence of the resonator properties (refractive index and loss),

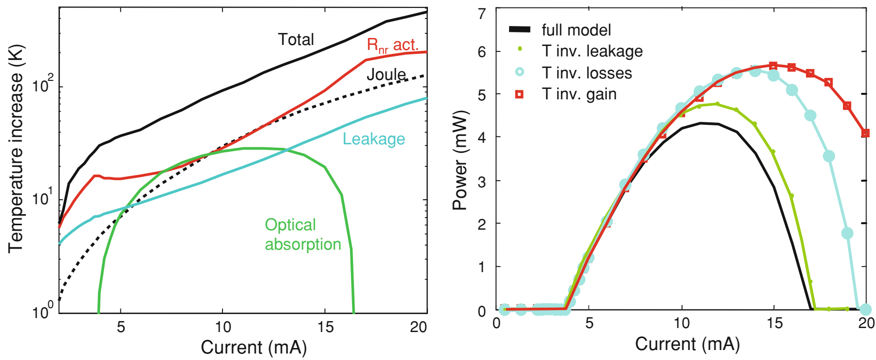

Fig. 3.28 *Left:* Contributions to temperature increase at active region center vs. current. *Right:* PI curves showing the influence of different effects, which are assumed temperature invariant, as indicated by the legend. Partially from [42] (© 2009 IEEE)

dependence of leakage. One can clearly see that the major role in power rollover is played by the gain dependence on temperature, followed by temperature dependent losses. The temperature dependence of leakage display the minor, even not negligible role.

3.9 Summary

Comprehensive models for VCSEL operation above threshold are very complex since of the many coupled interactions between optical, electrical and thermal phenomena. They act on different 3D spatial domains in the most general case and have been comprehensively described. Fully numerical techniques have been proposed, but so far they are still too cumbersome to be used to design or optimize actual devices. Therefore efficient expansion techniques have been used throughout this chapter; they were shown capable to handle fully 3D geometries and vectorial field features, at moderate costs in terms of memory and run times.

References

1. J.W. Scott, R.S. Geels, S.W. Corzine, L.A. Coldren, IEEE J. Quantum Electron. **29**, 1295 (1993)
2. A. Valle, J. Sarma, K.A. Shore, IEEE J. Quantum Electron. **31**, 1423 (1995)
3. G.R. Hadley, K.L. Lear, M.E. Warren, K.D. Choquette, J.W. Scott, S.W. Corzine, IEEE J. Quantum Electron. **32**, 607 (1996)
4. B. Klein, L.F. Register, M. Grupen, K. Hess, Opt. Express **2**, 163 (1998)
5. P.V. Mena, J.J. Morikuni, S.M. Kang, A.V. Harton, K.W. Wyatt, J. Lightwave Technol. **17**, 2612 (1999)
6. J. Mulet, S. Balle, IEEE J. Quantum Electron. **38**, 291 (2002)

7. M. Streiff, A. Witzig, M. Pfeiffer, P. Royo, W. Fichtner, IEEE J. Select. Topics Quantum Electron. **9**, 879 (2003)
8. M.X. Jungo, D. Erni, W. Bächtold, IEEE J. Select. Topics Quantum Electron. **9**, 939 (2003)
9. P.R. Sarzala, P. Mendla, M. Wasiak, P. Mackowiak, M. Bugajski, W. Nakwaski, Opt. Quantum Electron. **36**, 331 (2004)
10. J. Gustavsson, A. Haglund, J. Bengtsson, P. Modh, A. Larsson, IEEE J. Quantum Electron. **40**, 607 (2004)
11. P. Debernardi, G.P. Bava, C. Degen, I. Fischer, W. Elsäßer, IEEE J. Quantum Electron. **38**, 73 (2002)
12. F. Monti di Sopra, M. Brunner, H.P. Gauggel, H.P. Zappe, M. Moser, R. Hövel, E. Kapon, Appl. Phys. Lett. **77**, 2283 (2000)
13. P. Debernardi, G.P. Bava, F. Monti di Sopra, M.B. Willemsen, IEEE J. Quantum Electron. **39**, 109 (2003)
14. H.J. Unold, M.C. Riedl, R. Michalzik, K.J. Ebeling, Electron. Lett. **38**, 77 (2002)
15. P. Debernardi, J.M. Ostermann, M. Feneberg, C. Jalics, R. Michalzik, IEEE J. Select. Topics Quantum Electron. **11**, 107 (2005)
16. P. Nyakas, G. Varga, Z. Puskás, N. Hashizume, T. Kárpáti, T. Veszprémi, G. Zsombok, J. Opt. Soc. Am. B **23**, 1761 (2006)
17. P. Debernardi, A. Kroner, F. Rinaldi, R. Michalzik, IEEE J. Select. Topics Quantum Electron. **15**, 828 (2009)
18. J. Noble, J. Lott, J. Loehr, IEEE J. Quantum Electron. **34**, 2327 (1998)
19. P. Nyakas, J. Lightwave Technol. **25**, 2427 (2007)
20. G.R. Hadley, K.L. Lear, M.E. Warren, K.D. Choquette, J.W. Scott, S.W. Corzine, Opt. Lett. **20**, 1483 (1995)
21. P. Bienstman, R.G. Baets, IEE Proc. Optoelectronics **149**, 161 (2002)
22. D. Burak, R. Binder, IEEE J. Quantum Electron. **33**, 1205 (1997)
23. J.F.P. Seurin, S.L. Chuang, IEE Proc. Optoelectronics **149**, 174 (2002)
24. G.P. Bava, P. Debernardi, L. Fratta, Phys. Rev. A **63**, 023816 (2001)
25. P. Debernardi, J.M. Ostermann, M. Sondermann, T. Ackemann, G.P. Bava, R. Michalzik, IEEE J. Select. Topics Quantum Electron. **13**(5), 1340 (2007)
26. P. Debernardi, G.P. Bava, Phys. Status Solidi A **188**, 967 (2001)
27. E. Ahlers, S.F. Helfert, R. Pregla, in Techn. Digest *Integrated Photonics Research Conf. (IPR 1996)*, paper ITuE5, pp. 340–343 (Boston, USA, Apr. 1996)
28. B. Klein, L.F. Register, K. Hess, D.G. Deppe, Q. Deng, Appl. Phys. Lett. **73**, 3324 (1998)
29. P. Bienstman, R. Baets, J.A. Vukušić, A. Larsson, M.J. Noble, M. Brunner, K. Gulden, P. Debernardi, L. Fratta, G.P. Bava, H. Wenzel, O. Conradi, R. Pregla, J.F.P. Seurin, S.L. Chuang, IEEE J. Quantum Electron. **37**, 1618 (2001)
30. D.W. Winston, R.E. Hayes, IEEE J. Quantum Electron. **34**, 707 (1998)
31. F. Prati, D. Vecchione, G. Vendramin, Opt. Lett. **22**, 1633 (1997)
32. L. Fratta, P. Debernardi, G.P. Bava, C. Degen, J. Kaiser, I. Fischer, W. Elsäßer, Phys. Rev. A **64**, 031803(R) (2001)
33. P. Debernardi, B. Kogel, K. Zogal, P. Meissner, M. Maute, M. Ortsiefer, G. Bohm, M.C. Amann, IEEE J. Quantum Electron. **44**(4), 391 (2008)
34. P. Debernardi, G.P. Bava, IEEE J. Select. Topics Quantum. Electron. **9**, 905 (2003)
35. C.J. Chang-Hasnain, J.P. Harbison, G. Hasnain, A.C.V. Lehmen, L.T. Florez, N.G. Stoffel, IEEE Quantum Electron. **27**, 1402 (1991)
36. M.P. van Exter, A.K. Jansenvan Doorn, J.P. Woerdman, Phys. Rev. A **56**, 845 (1997)
37. A. Tsigopoulos, V. Paschos, C. Caroubalos, P. Salet, J. Jacquet, IEEE J. Quantum Electron. **33**, 2221 (1997)
38. A.A. Leal, M. Osinski, E. Conforti, IEEE Trans. Microwave Theory Tech. **46**, 208 (1998)
39. J.S. Gustavsson, J.A. Vukušić, J. Bengtsson, A. Larsson, IEEE J. Quantum Electron. **38**, 203 (2002)

40. W. Nakwaski, M. Osinski, in *Progress in optics XXXVIII*, chap. III, ed. by E. Wolf (Elsevier Science, BV, 1998), pp. 165–262
41. Y.G. Zhao, J.G. McInerney, IEEE J. Quantum Electron. **9**, 1668 (1995)
42. P. Debernardi, IEEE J. Quantum Electron. **45**, 979 (2009)
43. M. Farzaneh, R. Amatya, D. Luerszen, K.J. Greenberg, W.E. Rockwell, J.A. Hudgings, IEEE Photon. Technol. Lett. **19**, 601 (2007)
44. S.F. Yu, IEEE J. Quantum Electron. **32**, 1168 (1996)
45. H. Haug, S.W. Koch, *Quantum Theory of the Optical Properties of Semiconductors* (World Scientific, 1990)
46. P. Debernardi, A. Pisoni, G.P. Bava, IEEE J. Quantum Electron. **30**, 93 (1994)
47. H.C. Casey, M.B. Panish, *Heterostructure Lasers* (Academic Press, New York, 1978)
48. P.A. Andrekson, R.F. Kazarinov, N.A. Olsson, T. Tanbun-Ek, R.A. Logan, IEEE Quantum Electron. **30**(2), 219 (1994)
49. G.P. Bava, P. Debernardi, L. Fratta, JOSA B **16**, 2147 (1999)
50. E.P. O'Reilly, A.R. Adams, IEEE Quantum Electron. **30**, 366 (1994)
51. T.H. Gfroerer, L.P. Priestley, M.F. Fairley, M.W. Wanlass, J. Appl. Phys. **94**, 1738 (2003)
52. J.A. Vukušić, H. Martinsson, J.S. Gustavsson, A. Larsson, IEEE J. Quantum Electron. **37**, 108 (2001)
53. C. Degen, I. Fischer, W. Elsäßer, Opt. Express **5**, 38 (1999)
54. A. Kroner, F. Rinaldi, J.M. Ostermann, R. Michalzik, Optics Commun. **270**, 332 (2007)
55. G.P. Bava, P. Debernardi, IEE-J Optoelectron. **145**, 37 (1998)
56. G. van der Sande, J. Danckaert, I. Veretennicoff, T. Erneux, Phys. Rev. A **67**(1), 013809 (2003)
57. M. San Miguel, Q. Feng, J.V. Moloney, Phys. Rev. A **52**, 1728 (1995)
58. J. Dellunde, M.C. Torrent, J.M. Sancho, K.A. Shore, IEEE J. Quantum Electron. **33**(7), 1197 (1997)
59. M. Abramowitz, I.A. Stegun, *Handbook of Mathematical Functions* (Dover Publications, Inc., 1970)
60. H. Martinsson, J.A. Vukušić, M. Grabherr, R. Michalzik, R. Jäger, K.J. Ebeling, A. Larsson, IEEE Photon. Technol. Lett. **11**, 1536 (1999)
61. P. Debernardi, H.J. Unold, J. Maehnss, R. Michalzik, G.P. Bava, K.J. Ebeling, IEEE J. Select. Topics Quantum. Electron. **9**, 1394 (2003)

Chapter 4
Single-Mode VCSELs

Anders Larsson and Johan S. Gustavsson

Abstract The only active transverse mode in a truly single-mode VCSEL is the fundamental mode with a near Gaussian field distribution. A single-mode VCSEL produces a light beam of higher spectral purity, higher degree of coherence and lower divergence than a multimode VCSEL and the beam can be more precisely shaped and focused to a smaller spot. Such beam properties are required in many applications. In this chapter, after discussing applications of single-mode VCSELs, we introduce the basics of fields and modes in VCSELs and review designs implemented for single-mode emission from VCSELs in different materials and at different wavelengths. This includes VCSELs that are inherently single-mode as well as inherently multimode VCSELs where higher-order modes are suppressed by mode selective gain or loss. In each case we present the current state-of-the-art and discuss pros and cons. At the end, a specific example with experimental results is provided and, as a summary, the most promising designs based on current technologies are identified.

4.1 Introduction

The vertical-cavity surface-emitting laser (VCSEL) is an attractive light source for an expanding range of applications. Due to low cost manufacturing, low power consumption, simplified packaging, attractive beam properties (circular and low divergence beam) and excellent high-speed modulation characteristics at low currents, it has replaced the edge-emitting laser in short-reach optical communication links

A. Larsson (✉) · J. S. Gustavsson
Department of Microtechnology and Nanoscience,
Photonics Laboratory, Chalmers University of Technology,
41296 Göteborg, Sweden
e-mail: anders.larsson@chalmers.se

J. S. Gustavsson
e-mail: johan.gustavsson@chalmers.se

R. Michalzik (ed.), *VCSELs*, Springer Series in Optical Sciences 166,
DOI: 10.1007/978-3-642-24986-0_4, © Springer-Verlag Berlin Heidelberg 2013

and networks based on multimode fibers. VCSELs used in these applications are multimode which benefits manufacturability and reliability as well as system performance. However, new applications are emerging that require, e.g., improved spectral purity, higher degree of coherence and improved focusing capabilities. These requirements are met by single-mode VCSELs while still providing all the advantages listed above. The near Gaussian beam produced by a single-mode VCSEL also allows for the use of simple optics in the system.

In this chapter we discuss applications for single-mode VCSELs, introduce the basic concepts of optical fields and modes in VCSELs and review various techniques that have been implemented for achieving single-mode emission.

4.2 Applications and Requirements

Short-reach communication links and networks based on multimode fiber (local/storage area networks and optical interconnects) have been the main driver for the development of VCSELs since their commercial introduction in 1996 [1]. Such links and networks employ 850 nm multimode VCSELs with excellent high-speed and reliability performance. However, VCSELs are also being developed for *longer distance optical communication* such as access and metropolitan networks where wavelengths of 1,310 and 1,550 nm are used [2]. With such networks being based on single-mode fiber, the VCSEL has to be single-mode, i.e. supporting the fundamental transverse mode only, to enable sufficient coupling to the fiber. In addition, the spectral purity of the single-mode VCSEL is needed to prevent excessive pulse broadening over longer transmission distances due to chromatic dispersion in the fiber. Single-mode VCSELs may also find applications in short-reach multimode fiber links where, e.g. the low noise and good RF (radio frequency) linearity of single-mode VCSELs can improve the performance of radio-over-fiber links in distributed antenna systems [3].

The *optical computer mouse* has recently emerged as another high volume application for VCSELs where laser light is used to improve the resolution, sensitivity and speed of position tracking and to enable tracking on a larger variety of surfaces. Compared to other types of diode lasers, the low power consumption of VCSELs is attractive for cordless, battery-driven mice. High definition tracking requires a high degree of coherence and therefore the VCSEL has to be single-mode. In addition, the polarization of the laser field has to be stable to avoid coherence reduction due to polarization instabilities. The laser mouse is the first high-volume application of single-mode (850 nm) VCSELs [4].

Because VCSELs are surface emitting they can be monolithically integrated in two-dimensional arrays. Such components have found applications in *laser printing* where arrays of individually addressable VCSELs (780 nm) are used as light sources to simultaneously improve print resolution and speed [5]. The array has a large number (32) of closely spaced single-mode VCSELs with small beam divergence, enabling a print resolution as high as 2,400 dpi and fast color reproduction with print

speeds of several tens of pages per minute. More details can be found in Chap. 18 of this book.

Single-mode VCSELs are also used as compact and efficient, low-cost sources in optically pumped miniature *atomic clocks* where the emission lines of an RF modulated single-mode VCSEL interact with atomic transitions in the atomic vapor (Cs at 852 or 895 nm or Rb at 780 or 795 nm) [6]. This enables the construction of miniature, chip-scale atomic clocks for precise time synchronization. Such atomic clocks, with volumes < 1 cm^3, may become important time standards in, e.g. GPS receivers and for clock distribution in communication networks. The application requires the single-mode VCSEL to operate in a stable, linear state of polarization and to have low intensity and phase noise as well as a large modulation bandwidth.

Gas sensing and analysis through absorption spectroscopy by means of tunable diode lasers is of industrial importance in fields ranging from medicine to monitoring and control of combustion processes. Detection techniques based on sweeping the laser emission line through specific gas absorption lines (wavelength modulation spectroscopy) offer sensitivities in the ppm range or better. Gas species and wavelengths of interest range from, e.g., oxygen at 760 nm to CO, CO_2 and NO_2 in the mid-infrared (2–3.5 μm). The use of current-tuned single-mode VCSELs offers advantages over other types of diode lasers in terms of tuning range, response time, power consumption and beam quality [7]. In addition to being single-mode the VCSEL has to be polarization-stable.

In addition to the applications discussed above, there are numerous other applications for single-mode VCSELs in the area of *sensing*, all benefiting from the low power consumption, small form factor, low noise and excellent beam quality. This includes sensors operating in, e.g., reflection, transmission, absorption, or scattering modes for position sensing, motion control, bar code scanning and many other measurement tasks [8]. For instance, VCSEL-based optical encoders, for digital encoding of, e.g., linear and rotary positions, offer significantly improved performance in terms of precision and resolution compared to encoders based on light-emitting diodes or edge-emitting lasers. With single-mode VCSELs offering higher resolution than multimode VCSELs, high-definition optical encoding represents a growing market for high-power single-mode VCSELs. The higher degree of coherence of single-mode VCSELs also enable their use in measurement systems based on optical interference and statistical analysis of speckle patterns.

The performance requirements for single-mode VCSELs vary between applications. In most present applications the output power is quite modest, on the order of 1 mW or less. However, several applications such as communication, printing and gas sensing would benefit from higher power to increase transmission distance, improve print speed and enable faster, real-time measurements. Large efforts are therefore devoted to the development of high-power single-mode VCSELs. Suppression of higher-order transverse modes generally has to exceed 30 dB while the suppression of the orthogonal polarization state, in applications requiring polarization-stable VCSELs, should exceed 20 dB. Some applications, such as gas sensing and atomic clocks, require a precise wavelength which is demanding from a fabrication point of view. Other performance measures include the phase noise (which determines the

linewidth and the coherence length) and the intensity noise, with requirements being strongly application-dependent. Last, but not least, the single-mode VCSEL has to fulfill requirements in terms of reliability and manufacturability.

4.3 Optical Fields and Modes in VCSELs

Before reviewing various designs for single-mode emission we introduce the basic concepts of waveguiding and optical modes in VCSELs.

4.3.1 Longitudinal Fields

Field confinement in the longitudinal direction (the z-direction) is achieved by highly reflective distributed Bragg reflectors (DBRs) positioned below and above the active region (Fig. 4.1). Because of the short distance between the reflectors, forming a resonator with an effective length of only one or a few wavelengths, the resonator supports only one wavelength within the gain bandwidth of the active region. This corresponds to a single *longitudinal mode* with a field distribution as indicated in Fig. 4.1.

4.3.2 Transverse Fields

Field confinement in the transverse direction (the r-direction) can be achieved by various means. To introduce the concept of *transverse modes* we consider an oxide-confined VCSEL of circular symmetry as illustrated in Fig. 4.2. This design is frequently used for high-performance GaAs-based VCSELs emitting in the 0.65–1.3 μm range [9]. Oxide confinement implies that an AlGaAs layer, with a high Al-content (near 100%), close to the active region is partially oxidized through wet-chemical oxidation. The oxidized layer becomes electrically non-conducting, thus confining the injected current to the central region of the VCSEL (the oxide aperture of diameter d_{ox}). Oxidation also lowers the refractive index (from ~3 to ~1.6 at a wavelength of 850 nm [10]). This provides transverse optical confinement, thus forming a waveguide for light propagating in the longitudinal direction.

The formation of a waveguide can be understood by applying an effective index analysis [11], which shows that any modification of the VCSEL resonator that produces a local shift of the resonance wavelength ($\Delta\lambda_0$) produces a corresponding change of the effective index (Δn_{eff}) in that region:

$$\frac{\Delta n_{\mathrm{eff}}}{n_{\mathrm{eff}}} \approx \frac{\Delta\lambda_0}{\lambda_0} \qquad (4.1)$$

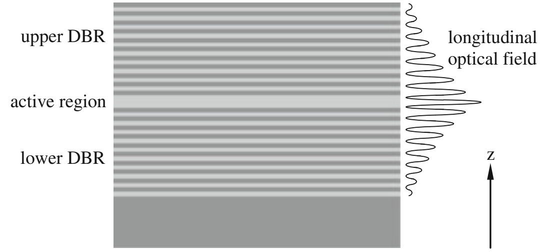

Fig. 4.1 Longitudinal optical field distribution in a VCSEL with two DBR mirrors for longitudinal field confinement

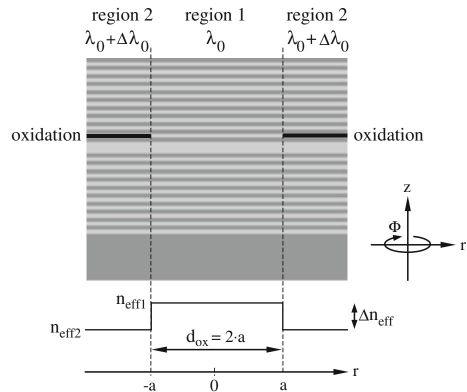

Fig. 4.2 An oxide-confined VCSEL with the shift of the resonance wavelength and lowering of the effective index in the oxidized region (region 2)

The change depends on the direction of the shift and is positive for red shifts and negative for blue shifts. Oxidation (which lowers the refractive index of the material) produces a blue shift of the resonance wavelength ($\Delta\lambda_0 < 0$) and therefore lowers the effective index in the oxidized region ($n_{\text{eff2}} < n_{\text{eff1}}$). Thus, a cylindrical waveguide is formed, having a core diameter of d_{ox} and an effective index difference between core and cladding of Δn_{eff}. This is similar to the waveguide of a step-index optical fiber and the guiding characteristics can be analyzed using standard methods applied to optical fibers [12].

Using Maxwell's equations and the boundary conditions at the core-cladding interface one can find the transverse electromagnetic modes supported by the waveguide, which are characterized by their propagation constants and characteristics field distributions in the transverse plane. In the weakly guiding approximation, where $\Delta n_{\text{eff}} << n_{\text{eff}}$, the modes can be expressed in terms of linearly polarized modes (polarized in the $r - \Phi$ plane), or LP_{mn} modes, where m is the azimuthal mode number and n is the radial mode number. In cylindrical coordinates we have for the electric field amplitude of an LP_{mn} mode:

$$E_{mn}(r, \Phi, z) \propto e^{jm\Phi} . e^{-j\beta_{mn}z} \cdot J_m(u_{mn}r) \quad \text{when } r < a \text{ (core)} \tag{4.2}$$

$$E_{mn}(r, \Phi, z) \propto e^{jm\Phi} . e^{-j\beta_{mn}z} \cdot K_m(v_{mn}r) \quad \text{when } r < a \text{ (cladding)} \tag{4.3}$$

where r, Φ and z are the cylindrical coordinates, β_{mn} is the propagation constant, J_m is a Bessel function of the first kind and order m and K_m is a modified Bessel function of the second kind and order m. The parameters u_{mn} and v_{mn} are given by:

$$u_{mn}^2 = k_0^2 n_{\text{eff1}}^2 - \beta_{mn}^2 \tag{4.4}$$

$$v_{mn}^2 = \beta_{mn}^2 - k_0^2 n_{\text{eff2}}^2 \tag{4.5}$$

where k_0 is the propagation constant in vacuum. The modes supported by the waveguide and the corresponding values for the u and v parameters, and therefore the propagation constants, are obtained by applying the boundary conditions which results in the following characteristic equation:

$$u \cdot \frac{J_{m-1}(ua)}{J_m(ua)} = -v \cdot \frac{K_{m-1}(va)}{K_m(va)} \tag{4.6}$$

For a given waveguide (radius a and index step Δn_{eff}), a discrete and finite number of guided modes exist which are the solutions of (4.6). With large radius and index step, a large number of modes exist. With sufficiently small radius and index step, only the fundamental LP_{01} mode exists.

The mode intensity, which is proportional to the square of the electric field amplitude, of some of the lowest order LP_{mn} modes are shown in Fig. 4.3. Note that each mode with $m \geq 1$ can be coupled with either a $\cos(m\Phi)$ or a $\sin(m\Phi)$ dependence, thus having two identical angular intensity distributions rotated with respect to each other. The LP_{01} mode is the fundamental mode of the waveguide and is the only active mode in a truly single-mode VCSEL. All other modes should be non-existing or strongly suppressed.

For the discussion of mode selectivity in VCSELs with a waveguide supporting multiple transverse modes (Sect. 4.4) it is important to note that the fundamental mode has its intensity confined to the central region (core) of the waveguide while higher-order modes have more of their intensity at the periphery of the waveguide, extending into the cladding region.

The fact that different transverse modes extend to various degree into the cladding region of the waveguide implies that their resonance wavelengths differ. Higher-order modes, which extend more into the region of lower effective index and therefore have a lower effective mode index, have shorter resonance wavelengths. However, the spectral mode separation of an 850 nm oxide-confined VCSEL is only one or a few Å's. Therefore, even in a VCSEL supporting several transverse modes, the spectral dependence of gain in the active region has a small effect on mode selectivity.

The relative strength (intensity) of the various transverse modes under current injection also depends on the overlap of the transverse intensity distribution with the transverse distribution of gain in the active region. Assuming that the transverse extent of gain is determined by the size of the oxide aperture (current confinement) and that the gain is uniform within the aperture, one can define a transverse optical confinement factor which determines the modal gain:

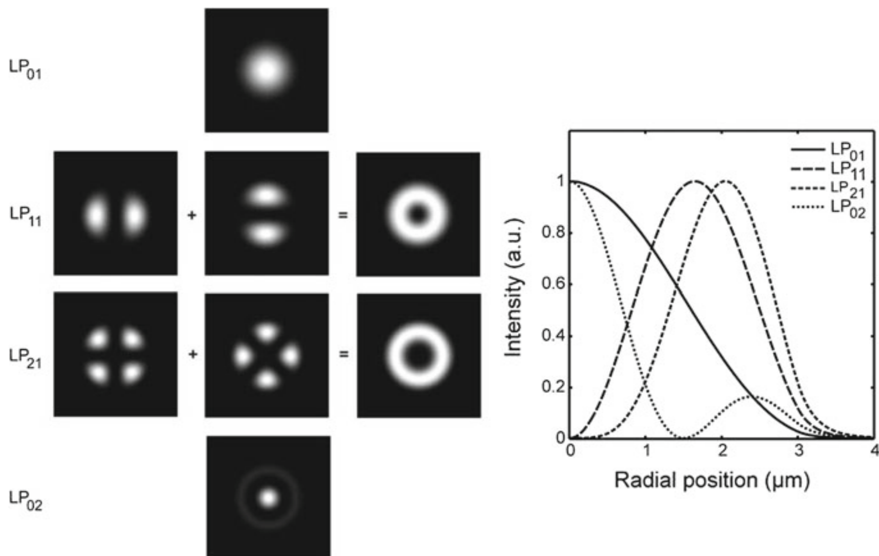

Fig. 4.3 Intensity distributions in the transverse plane (*left*) and in the radial direction (*right*) for the four lowest order LP_{mn} modes of a cylindrical step-index waveguide

$$\Gamma_{\text{trans},mn} = \int_0^a \int_0^{2\pi} E_{mn}^2 r d\Phi dr \Big/ \int_0^\infty \int_0^{2\pi} E_{mn}^2 r d\Phi dr \tag{4.7}$$

The fundamental LP_{01} mode, which has a larger transverse optical confinement factor, has the highest modal gain while for higher-order modes the modal gain decreases with increasing mode order. This results in mode selectivity, favouring the fundamental mode. In real VCSELs, the non-uniformity of current injection in the active region also introduces a certain degree of mode selectivity, favouring higher-order modes.

So far it has been assumed that only the index step provided by the oxide confinement defines the waveguide in the VCSEL. However, in a real VCSEL under current injection the properties of the waveguide are also affected by the presence of carriers in the active region and by self-heating. The presence of carriers, within the core of the waveguide, provides gain guiding (through the imaginary part of the refractive index). Just like index guiding, gain guiding confines the optical field to the core of the waveguide [13]. However, carriers also have an effect on the real part of the refractive index which is reduced with increasing carrier density (the plasma effect). Therefore, carriers also produce an antiguiding effect. Finally, self-heating due to the resistive loss in the VCSEL structure under current injection produces a convex radial temperature distribution. Through the temperature dependence of the refractive index this translates into a thermal lens [14] which further confines the transverse optical fields to the core of the waveguide and allows for additional

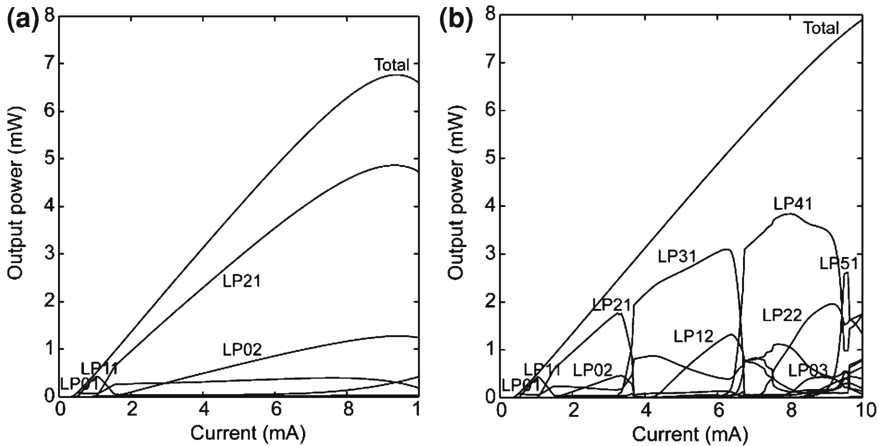

Fig. 4.4 Mode-resolved power-current characteristics for a 7 μm oxide-confined 850 nm VCSEL without (**a**), and with (**b**) effects of carriers and temperature accounted for

higher-order modes. All these effects are superposed on the built-in step-index waveguide and together define the modal characteristics of the VCSEL.

Above threshold, the strong stimulated emission rate in regions of high optical intensity results in a depletion of the carrier density in that region, an effect known as spatial hole burning [15]. This leads to a modification of the waveguiding properties and to strong competition between transverse modes with overlapping field distributions.

To illustrate the impact of carriers and temperature on the modal properties of VCSELs we have applied a quasi-three-dimensional numerical VCSEL model [15], which self-consistently treats all optical, electrical and thermal effects, to an oxide-confined 850 nm GaAs-based VCSEL with a 7 μm oxide aperture. Figure 4.4a shows mode-resolved power vs. current characteristics when the effects of carriers and temperature are neglected, while Fig. 4.4b shows the corresponding behaviour when these effects are included. Note the strikingly different behaviour and the mode competition and switching as the current is increased due to spatial hole burning and thermal lensing.

4.3.3 Polarization

In the weakly guiding approximation, the guided modes are transverse electromagnetic in nature with each mode having two linear and orthogonal states of polarization. If the optical properties of the VCSEL materials were isotropic, and the VCSEL geometry was perfectly cylindrical, the two polarizations of the LP_{mn} mode would propagate with the same propagation constant and have the same transverse

intensity distribution. In a real VCSEL, due to anisotropies, the two polarization states have slightly different propagation constants and therefore the resonance wavelengths are slightly different (corresponding to a frequency difference of a few GHz for an 850 nm VCSEL [16]). Since there is no strong intrinsic mechanism to select one of the polarization states, VCSELs often exhibit uncontrolled polarization instabilities [17], as discussed in Chap. 6.

In many applications of single-mode VCSELs a stable, linear state of polarization is required. Therefore, various techniques for polarization control in VCSELs have been developed. This is the subject of Chap. 5.

4.4 Techniques for Single-Mode Emission

In the remainder we review various single-mode VCSEL designs and their performance. We first discuss VCSELs designed to be inherently single-mode, which includes the special class of single-mode VCSELs based on photonic crystal and holey structures. Next we discuss VCSELs which are inherently multimode and where single-mode emission is obtained by introducing mode-selective loss or gain. In each case we present the current state-of-the-art and discuss pros and cons.

We limit the discussion to electrically driven, monolithic designs, which excludes, e.g. the use of external mirrors for mode-selective feedback. Such designs can produce very high single-mode power but at the expense of a more complex, hybrid arrangement [18].

In each case a simple schematic sketch is used to illustrate the design principle, with the injection current driven through conducting *p*- and *n*-doped DBRs and an *n*-doped substrate. Note, however, that in several designs the use of one dielectric DBR with one or two intra-cavity contacts is also common.

4.4.1 Inherently Single-Mode VCSELs

In its most simple form, an inherently single-mode VCSEL employs a waveguide sufficiently narrow to support the fundamental mode only, or at least being narrow enough for higher-order modes to suffer from considerably higher loss to prevent them from reaching threshold.

One of the most simple VCSEL designs, which has been applied to GaAs-based VCSELs at wavelengths $< 1\,\mu$m, uses proton implantation to provide transverse current confinement (Fig. 4.5). Since the refractive index change in the implanted region is very small, transverse optical confinement is provided mainly by gain guiding and thermal lensing. For truly single-mode emission (from threshold to thermal roll-over), the diameter of the implant aperture has to be on the order of $5\,\mu$m [19]. Proton-implanted VCSELs with a larger implant aperture ($8\,\mu$m) have demonstrated up to 4.4 mW of single-mode power with a higher-order mode

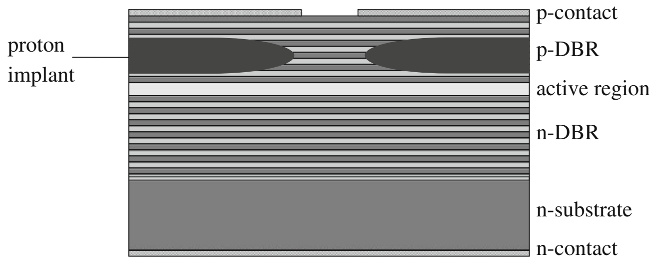

Fig. 4.5 A proton-implanted VCSEL where the implanted region provides transverse current confinement and thereby gain guiding

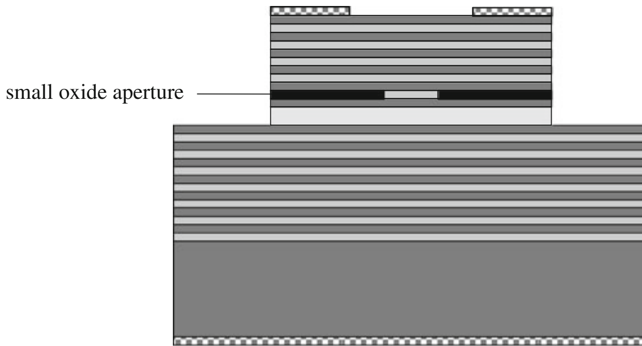

Fig. 4.6 An oxide-confined VCSEL where the oxide aperture provides transverse current and optical confinement

suppression ratio (MSR) of 40 dB, but with the onset of higher-order modes at high currents [20]. Since there is essentially no built-in index guide, the modal and beam characteristics of proton-implanted VCSELs are strongly affected by thermal lensing, carrier antiguiding and spatial hole burning. With these effects being dependent on current, the proton-implanted VCSEL exhibits unstable, current-dependent beam characteristics.

Much improved beam characteristics and higher single-mode power are obtained with oxide confinement, already discussed in Sect. 4.3. This technique has been successfully applied to GaAs-based VCSELs where partial oxidation of a high Al-content layer in one of the AlGaAs based DBRs, close to the active region, provides an aperture for efficient current and optical confinement (Fig. 4.6). The strength of the index guiding is controlled by the positioning of the oxide aperture with respect to the longitudinal optical field (standing wave) distribution. With the aperture close to a field minimum, for weak index guiding, and with a small enough aperture diameter, the built-in waveguide supports the fundamental mode only, thereby ensuring single-mode operation. With this technique a single-mode power of 4.8 mW with an MSR of 30 dB was obtained at a wavelength of 840 nm using a 3.5 μm diameter

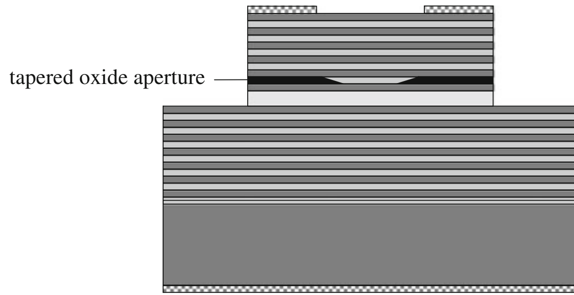

Fig. 4.7 An oxide-confined VCSEL with a tapered oxide aperture for transverse current and optical confinement

aperture [21]. The technique has also been applied to 1,300 nm GaInNAs VCSELs, with undoped semiconductor DBRs and intra-cavity contacts, to produce 1.4 mW of single-mode power [22].

The small-aperture, oxide-confined VCSEL provides improved beam quality and stability because of the built-in index guide which makes the transverse mode less susceptible to thermal lensing and effects of carriers. However, the small aperture leads to a high series resistance (typically $> 200\ \Omega$ for an 850 nm VCSEL) which limits the output power because of excessive current induced self-heating. The small oxide aperture is also of concern from manufacturing and reliability point of views since precise control of the small aperture size is necessary and the VCSEL operates at high current density and high internal temperature.

Higher single-mode power should in principle be possible to achieve from oxide-confined VCSELs with a tapered oxide aperture (Fig. 4.7). A tapered oxide aperture is obtained by varying the Al-content in the oxide layer and using the strong dependence of the oxidation rate on the Al-content [23]. The taper gradually reduces the volume of low-index material towards the aperture which reduces the effective index contrast between core and cladding regions. The mode then spreads in the transverse direction and the transverse confinement is reduced. By increasing the aperture size (to reduce resistance), higher-order modes become allowed and the VCSEL is no longer inherently single-mode. However, since the current injection aperture is defined by the tip of the tapered oxide layer, higher-order modes have even lower transverse confinement and single-mode emission is favored. With this technique a single-mode power of about 4 mW has been achieved at both 850 and 990 nm [24, 25], which is still not higher than that obtained with an ordinary oxide aperture.

Buried heterostructures (BHs) have also been used in attempts to produce high single-mode power. The design is illustrated in Fig. 4.8. After the formation of an air-post (mesa) structure, the BH VCSEL is realized by epitaxial regrowth. For current confinement, the regrowth material can be semi-insulating or contain a reverse-biased *pn*-junction. By an appropriate choice of regrowth material, the transverse effective index can in principle be tailored for single-mode emission from a large area with low resistance. Examples include BH VCSELs at 850 nm using regrowth of Fe-doped GaInP [26] and BH VCSELs at 1.55 μm using Fe-doped InP [27]. However, due to the limited availability of materials suitable for lattice-matched regrowth

Fig. 4.8 Buried heterostructure VCSEL where the regrowth material provides transverse current and optical confinement

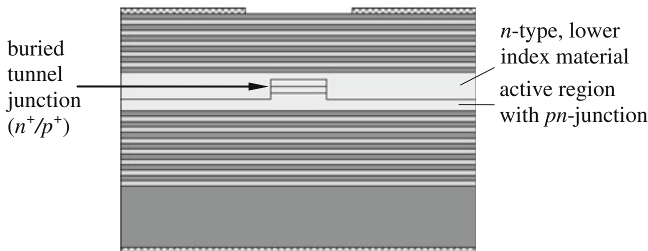

Fig. 4.9 A BTJ-VCSEL where current and optical confinement is provided by transverse structuring of the BTJ

and problems associated with the quality of the regrowth interface, the maximum single-mode power is typically limited to < 1 mW. In a somewhat different design, using regrowth only around the active region, before depositing the upper DBR, a single-mode power of 1 mW with an MSR of 45 dB was obtained at an emission wavelength of 1,310 nm [28].

Unlike the AlGaAs material system used for short-wavelength VCSELs, the InGaAsP material system used for long-wavelength VCSELs does not offer the possibility of easy formation of an oxide aperture. Therefore, other techniques have been developed for current and optical confinement. One of the most successful techniques is the use of a buried tunnel junction (BTJ). The design is illustrated in Fig. 4.9. Fabrication starts with epitaxial growth of the n-DBR, the active region (with a pn-junction) and the n^+/p^+-tunnel junction. After transverse structuring of the tunnel junction it is buried in n-type, lower index material. The top mirror is typically a dielectric DBR and an intra-cavity contact is used for current injection. The transverse structure provides current confinement through a blocking pn-junction and optical confinement through the effective index step induced by structuring of the

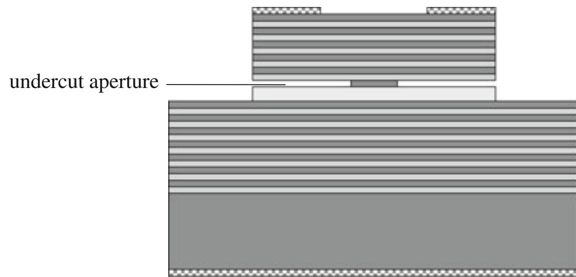

Fig. 4.10 A VCSEL with an air-gap aperture for transverse current and optical confinement

tunnel junction. With a small enough diameter of the BTJ, the waveguide supports the fundamental mode only and single-mode emission is obtained.

With BTJ diameters of around 5 μm, long-wavelength BTJ-VCSELs have produced single-mode powers exceeding 3 mW at 1.3 μm [29, 30] and approaching 4 mW at 1.55 mW [30, 31], with an MSR typically exceeding 40 dB. Using a somewhat different design based on wafer fusion of undoped AlGaAs-based DBRs, an InAlGaAs-based active region and intra-cavity contacts, BTJ-VCSELs have reached single-mode powers as high as 6 mW at 1.3 μm [32] and 6.5 mW at 1.55 μm, with an MSR exceeding 30 dB [33].

An alternative technique applied to long-wavelength, InP-based VCSELs is based on selective undercut etching where a thin layer, close to the active region, is selectively etched to form an air-gap aperture for transverse current and optical confinement (Fig. 4.10). Various designs with undoped DBRs based on InAlGaAs, AlGaAsSb or InP/air, intra-cavity contacts and a tunnel junction to minimize the amount of *p*-type material for low optical loss have been demonstrated. Achieved performance includes single-mode powers of 1.6 mW at both 1.3 μm [34, 35] and 1.55 μm [36] with an MSR generally exceeding 40 dB. The aperture size is typically 6−8 μm for single-mode emission. It is predicted that the undercut aperture causes a certain amount of scattering loss [37]. With the scattering loss being strongly mode-dependent, single-mode emission is obtained even from air-gap VCSELs with apertures large enough to support higher-order modes.

A more elaborate method for transverse mode control in VCSELs is the use of a two-dimensional, single defect photonic crystal (PhC) structure defined by a pattern of etched holes in the top DBR (Fig. 4.11). With a proper selection of hole depths, diameters and arrangement, index confinement can be exploited to create a single-mode waveguide, similar to the case in a photonic crystal fiber. After the first demonstration of a PhC-VCSEL [38], there has been steady progress towards higher single-mode power with best performance achieved using an oxide aperture for current confinement (Fig. 4.11). GaAs-based PhC-VCSELs have reached a single-mode power of 3.1 mW (MSR > 30 dB) at 850 nm [39], 5.7 mW (MSR > 35 dB) at 990 nm [40] and 1.7 mW (MSR > 30 dB) at 1.3 μm [41]. A particular problem for such PhC-VCSELs is the increased optical loss and electrical resistance caused by the deep holes, leading to relatively high threshold currents and low power efficiency. To combat these negative effects, there have been attempts to bury a PhC structure in

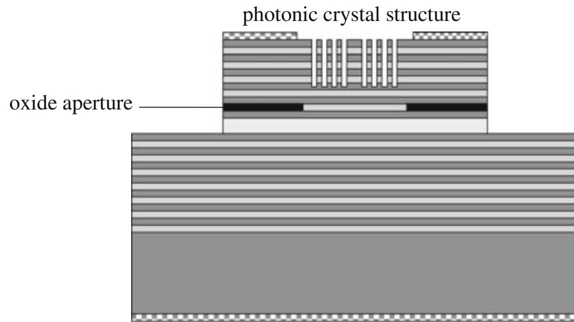

Fig. 4.11 A VCSEL with a photonic crystal structure etched in the top mirror for mode control. Current confinement is provided by the oxide aperture

the VCSEL by shallow etches in a layer close to the active region (where the optical field is strong), followed by the deposition of a dielectric top DBR. Such PhC-VCSELs have produced 3.7 mW of single-mode power (MSR > 40 dB) at 1.3 μm, although not being truly single-mode since higher-order modes reach threshold at high currents [42].

A similar concept is that of single-mode VCSELs with a holey structure. Using a wedge-shaped holey structure for tailoring the radial index profile, in combination with an oxide aperture for current confinement, single-mode emission at an output power of 7 mW (MSR = 40 dB) [43] was obtained for a GaAs-based 850 nm VCSEL. However, the mode is not the fundamental mode of the waveguide and the far-field contains side-lobes. This is due to the strong contribution to guiding by the oxide aperture when the penetration of the wedges into the aperture is small. With a larger penetration, lasing in the fundamental mode was achieved at an output power of 2 mW. The use of proton implantation, rather than an oxide aperture, for current confinement, allows for independent radial index profiling by the wedge-shaped structure and has enabled a single-mode power of 3.5 mW at 840 nm (MSR > 30 dB) [44]. As for the PhC-VCSELs, VCSELs with a holey structure suffer from increased optical loss and electrical resistance caused by the deep holes, leading to higher threshold currents and lower efficiencies.

4.4.2 Single-Mode Emission from Inherently Multimode VCSELs

Certain advantages can be gained by introducing mode-selective gain or loss in an otherwise multimode VCSEL to force it to oscillate in the lowest-order LP_{01} mode only. A fundamental issue for such designs is to what extent also the fundamental mode suffers from any mode-discriminating feature built into the VCSEL, which calls for certain design trade-offs. The various designs presented below have been applied primarily to GaAs-based VCSEL at wavelengths up to 1.3 μm.

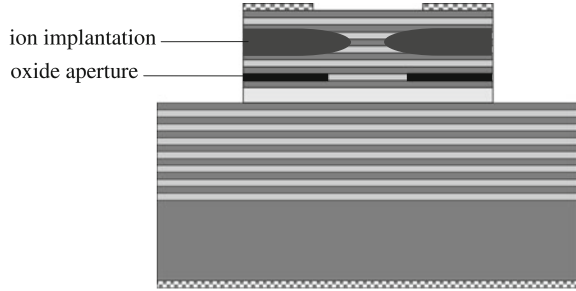

Fig. 4.12 A VCSEL where a large oxide aperture is used for optical confinement and a small implanted aperture is used for mode selective gain

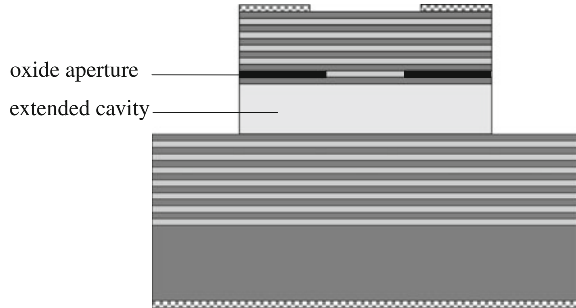

Fig. 4.13 A VCSEL with a large oxide aperture for optical confinement and an extended cavity for enhanced mode-selective loss

Mode-selective gain can be accomplished by combining selective oxidation with ion implantation (Fig. 4.12) to decouple the effects of current and optical confinement. With the oxide aperture defining and stabilizing the transverse modes, the smaller diameter implant aperture selectively funnels the current to the center of the cavity, thus preferentially feeding the fundamental mode with gain. Higher-order modes suffer from increased loss due to the unpumped regions around the periphery of the implant aperture. This results in sufficient mode discrimination for single-mode emission. At a wavelength of 850 nm a single-mode power of 4.5 mW (MSR $>$ 45 dB) has been achieved using proton implantation [45] and 3.8 mW (MSR $>$ 30 dB) was obtained using oxygen implantation [46]. The implant/oxide aperture diameters were 6/9 and 8/10 μm, respectively. The latter involves regrowth to enable positioning of the oxygen implant aperture close to the active region.

The use of an extended cavity (Fig. 4.13) allows for single-mode emission from oxide-confined VCSELs with a large oxide aperture because of increased diffraction losses for higher-order modes with larger propagation angles [47]. The large aperture reduces the electrical resistance which delays thermal roll-over and enables high single-mode power. Using a 9.2 μm thick lightly *n*-doped GaAs cavity spacer, a maximum single-mode power of 5.4 mW (MSR $>$ 30 dB) was obtained from a 980 nm VCSEL with a 6.5 μm oxide aperture [48]. However, such VCSELs are not truly single-mode since higher-order modes appear at high currents. With the thick cavity spacer needed for high single-mode power, such VCSELs are also

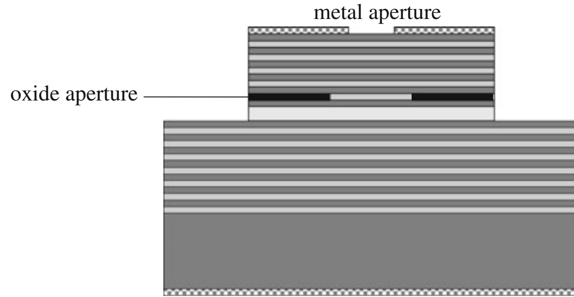

Fig. 4.14 A VCSEL with an oxide aperture for optical confinement and a small metal aperture for mode filtering

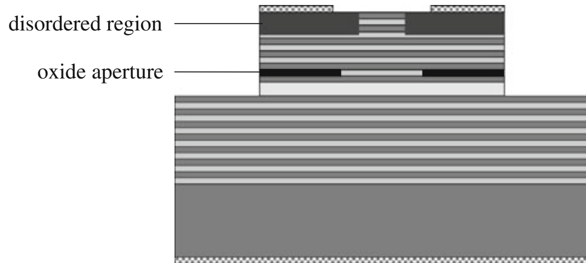

Fig. 4.15 A VCSEL with a large oxide aperture for optical confinement and a disordered region in the top DBR for mode-selective loss and reflectivity

susceptible to longitudinal mode switching because of the reduced longitudinal mode spacing [49].

Metal apertures have been successfully used for mode discrimination to enable single-mode emission from proton-implanted, gain-guided VCSELs as well as oxide-confined, index-guided VCSELs (Fig. 4.14). Higher-order modes are suppressed because of a phase-mismatched reflection at the metal/semiconductor interface which increases the cavity loss in the metalized region where the higher-order modes have more of their field intensity than the fundamental mode. The metal aperture also acts as a spatial filter, blocking higher-order modes. With a 5 μm metal aperture, a gain-guided VCSEL with a 15 μm implant aperture delivered 1.5 mW of single-mode power at a wavelength of 850 nm [50]. Much better performance have been obtained with oxide-confined VCSELs where the size of the metal aperture is similar to the size of the oxide aperture. At a wavelength of 780 nm, 3.4 mW of single-mode power (MSR > 30 dB) was achieved [51] while 4.7 mW of single-mode power (MSR ~ 30 dB) was achieved at 850 nm [52]. Truly single-mode emission, from threshold to thermal roll-over, was obtained for metal apertures slightly larger than the oxide aperture.

It was early recognized that selective-area, impurity-induced disordering of the top DBR (Fig. 4.15) can be used for suppression of higher-order modes [53]. Disordering creates a near uniform alloy, thereby effectively reducing the number of layer pairs in the DBR and therefore the DBR reflectivity. If Zn-diffusion is used for disordering, the high concentration of holes also increases the optical loss (through free-carrier absorption) in the disordered region. With the higher-order modes

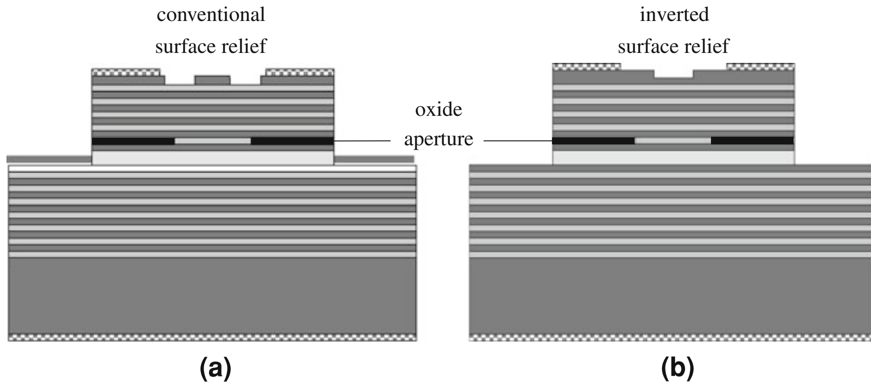

Fig. 4.16 A VCSEL with a large oxide aperture for optical confinement and **a** a conventional, and **b** an inverted surface relief for mode-selective loss

overlapping to a greater extent with the disordered region, they experience higher cavity loss due to the combined effect of reduced reflectivity and increased absorption loss. Zn-diffusion also has the advantage of reducing the series resistance which delays thermal roll-over to higher currents. Recently, this technique has been applied to an oxide-confined 850 nm VCSEL with a 6 μm oxide aperture and a 5 μm non-disordered aperture [54]. As much as 7.3 mW of single-mode power (MSR > 25 dB) was obtained with a low threshold current (0.5 mA), a high differential efficiency (80%) and a low series resistance (80 Ω).

One of the most successful techniques for single-mode VCSELs is the use of a shallow surface relief etched in the top DBR of an oxide-confined VCSEL (Fig. 4.16). The technique is based on the fact that the modal properties of a VCSEL with a sufficiently low reflectivity top DBR is very sensitive to surface modifications. By removing only the top layer ($\lambda/4$ thick, with λ being the material wavelength) from the top DBR, an anti-phase reflection is obtained from the semiconductor/air interface which results in a large increase of the cavity loss. If this layer is removed only at the periphery of the oxide aperture (Fig. 4.16a) higher-order modes suffer from excess loss and single-mode emission is achieved. An early demonstration showed the remarkable effect of the surface relief on the modal and beam characteristics of an oxide-confined VCSEL [55]. With further optimizations of oxide and surface relief diameters, and using a fabrication technique for self-alignment of the surface relief to the oxide aperture [56], a single-mode power of 3.4 mW was achieved at 850 nm [57].

A problem with the conventional surface relief technique (Fig. 4.16a) is that a very precise etch depth ($\pm$ a few nm's) is needed for large mode discrimination. This can be overcome by using an inverted surface relief (Fig. 4.16b). Here, the thickness of the top layer is increased by $\lambda/4$ during epitaxial growth. This extra layer acts as an anti-phase layer to increase the loss of the as-grown VCSEL resonator. By removing the anti-phase layer in the central part of the top DBR, a lower cavity

loss is obtained for the fundamental mode and single-mode emission is achieved. This relaxes the requirement for precision in etch depth (to $\pm$ a few tens of nm's) [57] while the precision in epitaxial growth is used to ensure a large loss contrast between etched and unetched areas. With this technique, single-mode emission from threshold to thermal roll-over, with a maximum single-mode power exceeding 6 mW (MSR > 30 dB), has been achieved at an emission wavelength of 850 nm [58, 59]. The VCSELs also remain single-mode under high-frequency, large-signal modulation [60]. An advantage of the surface relief technique, over many other techniques, is that the surface relief does not impair the electrical or thermal characteristics of the VCSEL. Therefore, high single-mode power can be obtained together with low threshold current, high efficiency and low series resistance. It also represents a small modification to standard VCSEL fabrication procedures.

The surface relief technique has also been applied to GaAs-based VCSELs operating at other wavelengths, such as 760 nm (with a single-mode power of 2 mW [61]) and 1.3 μm (with a single-mode power exceeding 1 mW [62, 63]). It should also be noted that, rather than etching a surface relief, a relief structure can be deposited to preferentially lower the cavity loss for the fundamental mode [64, 65].

The use of large current and optical apertures is advantageous for achieving high output power with reliable operation. However, with a positive index guide (where the effective index of the core is higher than that of the cladding, Fig. 4.2) single-mode emission can only be achieved with a small aperture and a small index step. By contrast, with a negative index guide (antiguide), where the effective index of the core is smaller than that of the cladding, single-mode emission can be achieved from a larger aperture with a larger index step since such waveguides provide strong higher-order mode discrimination due to transverse radiation losses [66]. The larger index step also provides for mode stability against thermal and carrier-induced index variations. Because all modes suffer from transverse radiation losses, the design of an antiguided VCSEL requires a balance between the excess losses of higher-order modes relative the fundamental mode loss.

Antiguided VCSELs can be based on the buried heterostructure design (Fig. 4.8) if the regrowth material has a higher refractive index than the core. However, the single-mode power is typically limited to <2 mW [67] because of the relatively large transverse radiation loss incurred for the fundamental mode, which is inherent to the antiguide structure. An antiguide can also be created by shifting the cavity resonance towards longer wavelengths outside the core region ((4.1) with $\Delta\lambda_0$ being positive), so-called cavity-induced antiguiding [68]. Various techniques based on etching and regrowth have been used to achieve the required transverse variation of the cavity resonance [69, 70] and to control the amount of antiguiding. However, as for the antiguided VCSEL based on bulk regrowth, the single-mode power is limited ($\sim$1 mW) because of large transverse radiation loss also for the fundamental mode.

In order to reduce the transverse radiation loss for the fundamental mode of an antiguide, an antiresonant reflecting optical waveguide (ARROW) can be employed (Fig. 4.17). The ARROW reflects back the radiated waves of the fundamental mode but higher-order modes still suffer from large transverse radiation loss. This improves the modal discrimination and a waveguide with a large core size and a large index

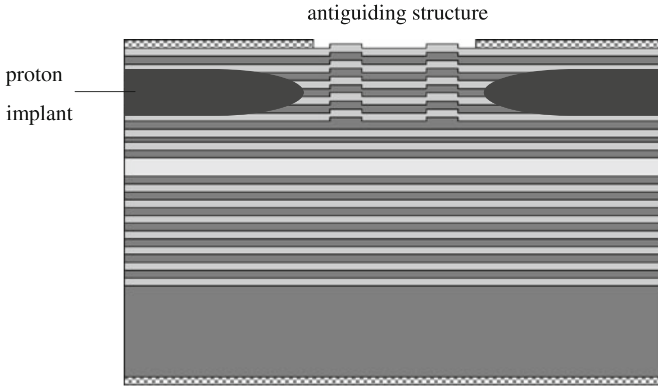

Fig. 4.17 A VCSEL with proton implantation for current confinement and an antiguiding structure for mode definition and discrimination

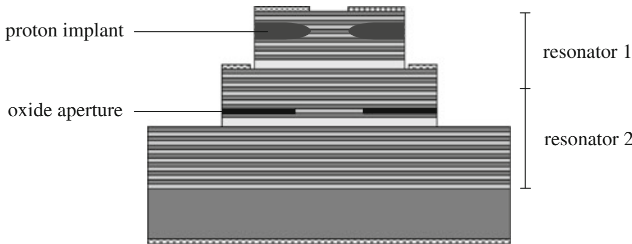

Fig. 4.18 A VCSEL with two coupled resonators for mode selectivity

step, suitable for high-power single-mode operation, is created [71]. Such ARROW VCSELs, with an 8 μm core size and proton implantation for current confinement, have produced 7.1 mW of single-mode power at a wavelength of 980 nm [72]. However, the suppression of higher-order modes is limited (MSR ~ 20 dB) and the threshold current is much higher than for most other high-power, single-mode VCSELs.

Finally, it has been shown that VCSELs with two coupled resonators (Fig. 4.18) can provide high single-mode power. The coupling between the two resonators is mediated by the middle DBR and by current tuning of the two active cavities, large mode discrimination can be obtained, allowing for single-mode operation at high power. Using an implanted current aperture (6 μm) in the upper resonator, an oxide-defined optical aperture (10 μm) in the lower resonator and a fixed current through the implant cavity, a maximum single-mode power of 6.1 mW (MSR > 30 dB) was achieved at 850 nm by varying the current through the oxide cavity [73]. However, this can only be achieved under critical biasing conditions and the complex design and fabrication procedure are of concern from a manufacturing point of view.

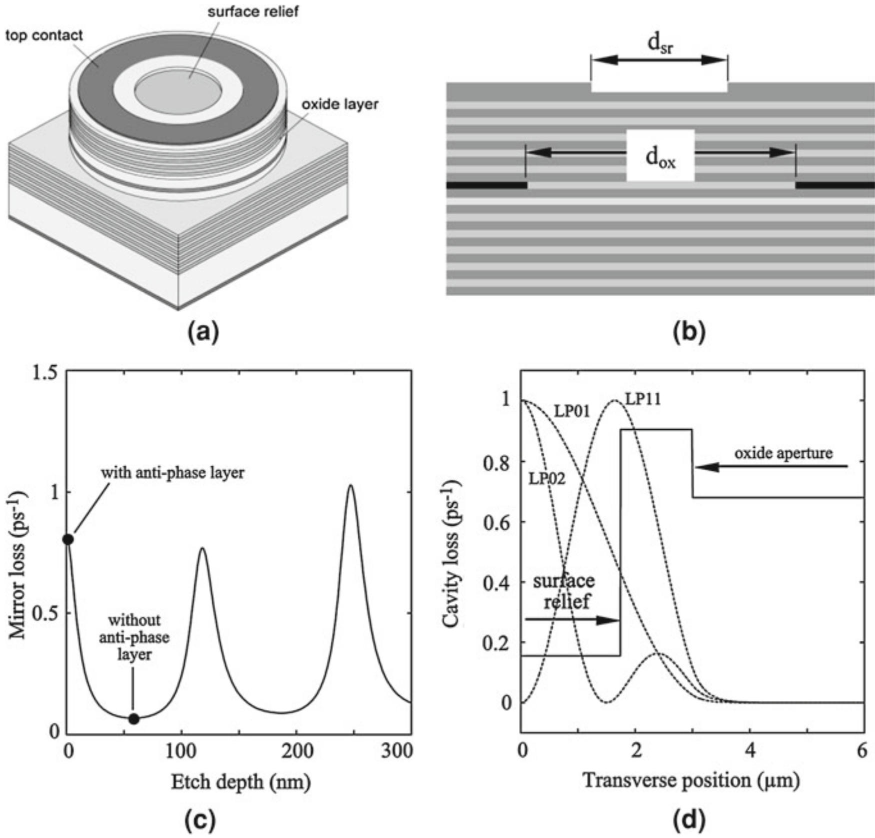

Fig. 4.19 **a** Schematic view of a VCSEL with an inverted surface relief for selecting the fundamental mode. **b** Cross-sectional view defining the diameters of the oxide aperture and the surface relief. **c** Top mirror loss as a function of etch depth. **d** Cavity loss as a function of the transverse position for a VCSEL with a 6 μm oxide aperture and a 3.5 μm surface relief. A loss rate of 1 ps^{-1} corresponds to a distributed loss of $\sim$110 cm^{-1}

4.5 A Specific Example

To provide a specific example of a high-power single-mode VCSEL we here present the design and performance of an oxide-confined 850 nm VCSEL with an inverted surface relief for selecting the fundamental mode (as described in Sect. 4.4.2). The work was performed at Chalmers University of Technology [58]. Similar performance has been demonstrated by Ulm University [59]. A schematic view of the device is shown in Fig. 4.19a. The cross-sectional view shown in Fig. 4.19b defines the diameters of the oxide aperture and the surface relief.

The design employs an epitaxial VCSEL structure with 22 and 34 $Al_{0.12}Ga_{0.88}As$/ $Al_{0.90}Ga_{0.10}As$ layer pairs in the top and bottom DBR, respectively. A $\lambda/4$ thick layer

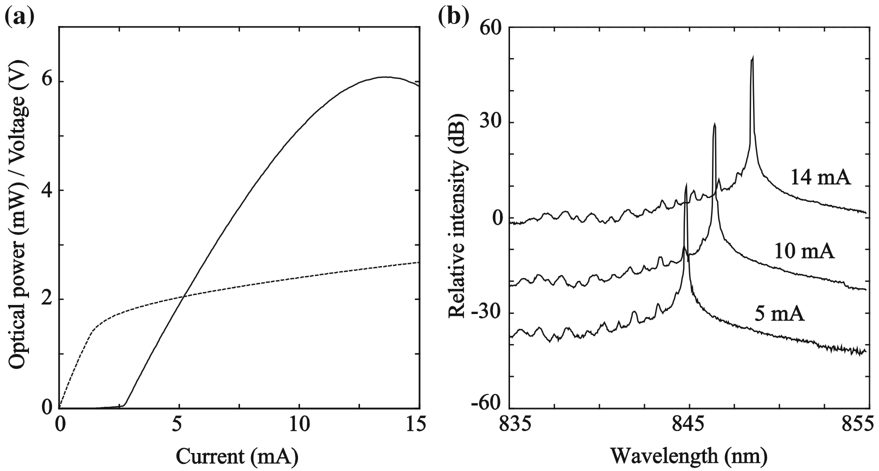

Fig. 4.20 **a** Output power (*solid line*) and voltage (*dashed line*) as a function of current for an 850 nm VCSEL with a 5 μm oxide aperture and a 2.5 μm surface relief. **b** Emission spectra recorded at three different drive currents

(57.5 nm) is added to the top layer of the top-DBR to provide an anti-phase reflection from the semiconductor/air interface. This increases the loss of the top-DBR by a factor ~10. By removing the anti-phase layer, using dry etching, the lower loss of the original top-DBR can be restored. The variation of the loss of the top-DBR with etch depth is shown in Fig. 4.19c, indicating that a loss contrast of ~10 can be obtained when etching to a depth of 57.5 nm. The graph also shows the relaxed requirement for precision in etch depth (±10 nm) offered by the inverted surface relief for achieving a high loss contrast.

The cavity loss for the fundamental mode is preferentially lowered by removing the anti-phase layer only in the central part of the top-DBR where the fundamental mode has most of its field intensity (Fig. 4.19d). This defines the diameter of the surface relief. Higher order modes have more of their field intensity in the unetched areas, close to the periphery of the oxide aperture, and therefore experience a higher cavity loss, thereby being suppressed.

The diameters of the oxide aperture and the surface relief (d_{ox} and d_{sr} in Fig. 4.19b) were optimized with respect to highest single-mode power using extensive numerical optical-electrical-thermal simulations [74]. It was generally found that oxide apertures of 4–6 μm, with surface reliefs of 2.5–3.5 μm (i.e. the surface relief diameter being roughly half of the oxide aperture diameter) produce the highest single-mode power. For such designs, single-mode operation was predicted at all currents, with a maximum single mode power of 6 mW.

Experimental results for an 850 nm VCSEL with a 5 μm oxide aperture and a 2.5 μm inverted surface relief are shown in Fig. 4.20 [58]. As predicted from simulations, 6 mW of single-mode power is obtained and single-mode operation, with a suppression of higher order transverse modes >30 dB, is obtained at all currents. The

Table 4.1 Summary of most successful long- and short-wavelength single-mode VCSEL technologies under consideration of low threshold current, high efficiency, manufacturability and potential for reliability

Technology	Wavelength (nm)	Single-mode power (mW)	Ref.
Surface relief	850	6.1	[58, 59]
Impurity-induced disordering	850	7.3	[54]
Metal aperture	850	4.7	[52]
Buried tunnel junction	1,310	6.0	[32]
	1,550	6.5	[33]

differential resistance of the VCSEL is 80 Ω and the beam divergence (full-width at half maximum) was measured to be 12°.

4.6 Summary

Progress in single-mode VCSEL technology has brought the output power to the multi-mW level. While several single-mode VCSEL designs have proved capable of producing several mW of output power, only a few meet requirements of low threshold current, high efficiency, manufacturability and reliability. The most successful techniques to date are summarized in Table 4.1.

At shorter wavelengths ($<1.3\,\mu$m), where VCSELs are based on the GaAs/AlGaAs/InGaAs material system, the use of a surface relief, a metal aperture or a partly impurity-disordered top DBR, together with an oxide aperture for current and optical confinement, have been most successful. Such designs can provide a single-mode power in the 5–7 mW range. At longer wavelengths ($>1.3\,\mu$m), where the InP/InGaAsP/InGaAlAs material system is used, the use of a buried tunnel junction for current and optical confinement has proved to be the most successful concept with a single-mode power in the range of 4–6 mW. It is likely that with further refinements of current technologies, a single-mode power exceeding 10 mW can be achieved at both shorter and longer wavelengths. New technologies may also emerge to bring the single-mode power from monolithic, current driven VCSELs to even higher levels.

References

1. J.A. Tatum, VCSEL proliferation, in *Vertical-Cavity Surface-Emitting Lasers XI*, ed. by K.D. Choquette, J.K. Guenter, Proceedings of SPIE, vol. 6484 (2007), p. 648403-1
2. W. Hofmann, M.C. Amann, 1.55 µm VCSEL arrays for high bandwidth WDM-PONs. IEEE Photon. Technol. Lett. **20**(4), 291 (2008)

3. K.A. Persson, C. Carlsson, A. Alping, Å. Haglund, J.S. Gustavsson, P. Modh, A. Larsson, WCDMA radio-over-fibre transmission experiment using singlemode VCSEL and multimode fibre. Electron. Lett. **46**(6), 372 (2006)
4. M. Grabherr, R. King, R. Jäger, D. Wiedenmann, P. Gerlach, D. Duckeck, C. Wimmer, Volume production of polarization controlled single-mode VCSELs, in *Vertical-Cavity Surface-Emitting Lasers XII*, ed. by C. Lei, J.K. Guenter, Proceedings of SPIE, vol. 6908 (2008), p. 690803-1
5. N. Mukoyama, H. Otoma, J. Sakurai, N. Ueki, H. Nakayama, VCSEL array based light exposure system for laser printing, in *Vertical-Cavity Surface-Emitting Lasers XII*, ed. by C. Lei, J.K. Guenter, Proceedings of SPIE, vol. 6908 (2008), p. 69080H-1
6. D.K. Serkland, G.M. Peake, K.M. Geib, R. Lutwak, R.M. Garvey, M. Varghese, M. Mescher, VCSELs for atomic clocks, in *Vertical-Cavity Surface-Emitting Lasers X*, ed. by C. Lei, K.D. Choquette, Proceedings SPIE, vol. 6132 (2006), p. 613208-1
7. W. Hofmann, G. Böhm, M. Ortsiefer, M. Görblich, C. Lauer, N.H. Zhu, M.C. Amann, Long wavelength VCSELs for optical networks and trace gas monitoring, in *Optoelectronic Devices: Physics, Fabrication and Application*, ed. by J. Piprek, J.J. Wang, Proceedings of SPIE, vol. 6766 (2007), p. 67660F-1
8. J. Tatum, R. Chandler, B. Stapleton, VCSEL based reflective sensors tackle more demanding applications. Laser Focus World **39**(9), 79 (2003)
9. K.D. Choquette, R.P. Schneider Jr., K.L. Lear, K.M. Geib, Low threshold voltage vertical cavity lasers fabricated by selective oxidation. Electron. Lett. **30**(24), 2043 (1994)
10. F.A. Kish, S.J. Carraci, N. Holonyak Jr., J.M. Dallesasse, K.C. Hsieh, M.J. Ries, S.C. Smith, R.D. Burnham, Planar native oxide index guided AlGaAs-GaAs quantum well heterostructure lasers. Appl. Phys. Lett. **59**(14), 1755 (1991)
11. G.R. Hadley, Effective index model for vertical cavity surface emitting lasers. Opt. Lett. **20**(13), 1483 (1995)
12. B.E.A. Saleh, M.C. Teich, *Fundamentals of Photonics*, 2nd edn. (Wiley, Hoboken, 2007), p. 325
13. J.P. Zhang, K. Petermann, Numerical analysis of transverse modes in gain guided vertical cavity surface emitting lasers. IEE Proc.-Optoelectron. **142**(1), 29 (1995)
14. M. Farzaneh, R. Amataya, D. Lürssen, K.J. Greenberg, W.E. Rockwell, J.A. Hudgings, Temperature profiling of VCSELs by thermoreflectance microscopy. IEEE Photon. Technol. Lett. **19**(8), 601 (2007)
15. J.S. Gustavsson, J.A. Vukusic, J. Bengtsson, A. Larsson, A comprehensive model for the modal dynamics of vertical cavity surface emitting lasers. IEEE J. Quantum Electron. **38**(2), 203 (2002)
16. A.K. Jansenvan Doorn, M.P. van Exter, J.P. Woerdman, Effects of transverse anisotropy on VCSEL spectra. Electron. Lett. **30**(23), 1941 (1994)
17. K.D. Choquette, R.P. Schneider Jr., K.L. Lear, R.E. Leibenguth, Gain dependent polarization properties of vertical cavity lasers. IEEE J. Select. Topics Quantum Electron. **1**(2), 661 (1995)
18. J.G. McInerney, A. Mooradian, A. Lewis, A.V. Shchegrov, E.M. Strzelecka, D. Lee, J.P. Watson, M. Liebman, G.P. Carey, B.D. Cantos, W.R. Hitchens, D. Heald, High power surface emitting semiconductor laser with extended vertical compound cavity. Electron. Lett. **39**(6), 523 (2003)
19. C.J. Chang-Hasnain, M. Orenstein, A. Von Lehmen, L.T. Florez, J.P. Harbison, N.G. Stoffel, Transverse mode characteristics of vertical cavity surface emitting lasers. Appl. Phys. Lett. **57**(3), 218 (1990)
20. K.L. Lear, R.P. Schneider, K.D. Choquette, S.P. Kilcoyne, J.J. Figiel, J.C. Zolper, Vertical cavity surface emitting lasers with 21% efficiency by metal organic vapour phase epitaxy. IEEE Photon. Technol. Lett. **6**(9), 1053 (1994)
21. C. Jung, R. Jäger, M. Grabherr, P. Schnitzer, R. Michalzik, B. Weigl, S. Müller, K.J. Ebeling, 4.8 mW single mode oxide confined top surface emitting vertical cavity laser diodes. Electron. Lett. **33**(21), 1790 (1997)

22. H. Riechert, A. Ramakrishnan, G. Steinle, Development of InGaAsN-based 1.3 μm VCSELs. Semicond. Sci. Technol. **17**(8), 892 (2002)
23. E.R. Hegblom, B.J. Thibeault, R.L. Naone, L.A. Coldren, Vertical cavity lasers with tapered oxide apertures for low scattering loss. Electron. Lett. **33**(10), 869 (1997)
24. K.D. Choquette, H.Q. Hou, G.R. Hadley, K.M. Geib, D. Mathes, R. Hull, High power single transverse mode selectively oxidized VCSELs, in *Proceedings 1997 LEOS Summer Topical Meeting*, Montreal, Canada (1997), p. 73
25. S.A. Blokhin, N.A. Maleev, A.G. Kuzmenkov, A.V. Sakharov, M.M. Kulagina, Y.M. Shernyakov, I.I. Novikov, M.V. Maximov, V.M. Ustinov, A.R. Kovsh, S.S. Mikhrin, N.N. Ledentsov, G. Lin, J.Y. Chi, Vertical cavity surface emitting lasers based on submonolayer InGaAs quantum dots. IEEE J. Quantum Electron. **42**(9), 851 (2006)
26. C. Carlsson, C.A. Barrios, E.R. Messmer, A. Lövqvist, J. Halonen, J. Vukusic, M. Ghisoni, S. Lourdudoss, A. Larsson, Performance characteristics of buried heterostructure VCSELs using semi-insulating GaInP:Fe regrowth. IEEE J. Quantum Electron. **37**(7), 945 (2001)
27. Y. Ohiso, H. Okamoto, R. Iga, K. Kishi, C. Amano, Single transverse mode operation of 1.55 μm buried heterostructure vertical cavity surface emitting lasers. IEEE Photon. Technol. Lett. **14**(6), 739 (2002)
28. D.A. Francis, D.B. Young, J. Walker, A. Verma, D. Gold, C. Decker, Monolithic 1310 nm buried heterostructure VCSEL using InGaAsP/InP DBR reflectors, in *Optoelectronic Devices: Physics, Fabrication and Application II*, ed. by J. Piprek, Proceedings of SPIE, vol. 6013 (2005), p. 60130A-1
29. M. Ortsiefer, W. Hofmann, E. Rönneberg, A. Boletti, A. Gatto, P. Boffi, R. Shau, C. Neumeyr, G. Böhm, M. Martinelli, M.C. Amann, High speed 1.3 μm VCSELs for 12.5 Gbit/s optical interconnects. Electron. Lett. **44**(16), 974 (2008)
30. N. Nishiyama, C. Caneau, M. Sauer, A. Kobyakov, C.E. Zah, InP-based long wavelength VCSELs: their characteristics and applications, in *Optoelectronic Materials and Devices II*, ed. by Y. Nakano, Proceedings of SPIE, vol. 6782 (2007), p. 67820M-1
31. M. Ortsiefer, S. Baydar, K. Windhorn, G. Böhm, J. Rosskopf, E. Rönneberg, W. Hofmann, M.C. Amann, 2.5 mW single mode operation of 1.55 μm buried tunnel junction VCSELs. IEEE Photon. Technol. Lett. **17**(8), 1596 (2005)
32. A. Syrbu, A. Mereuta, V. Iakovlev, A. Caliman, P. Royo, E. Kapon, 10 Gbps VCSELs with high single mode output in 1310 nm and 1550 nm wavelength bands, in *Proceedings Conference on Optical Fiber Communication*, paper OThS2, San Diego, CA, USA (2008)
33. A. Caliman, V. Iakovlev, A. Mereuta, A. Sirbu, G. Suruceanu, E. Kapon, 8 mW fundamental mode output of wafer-fused VCSELs emitting in the 1550 nm band, in *Proceedings Conference on Lasers and Electro Optics*, paper CMRR1, Baltimore, MD, USA (2009)
34. C.K. Lin, D.P. Bour, J. Zhu, W.H. Perez, M.H. Leary, A. Tandon, S.W. Corzine, M.R.T. Tan, High temperature continuous wave operation of 1.3 and 1.55 μm VCSELs with InP/air gap DBRs. IEEE J. Select. Topics Quantum Electron. **9**(5), 1415 (2003)
35. D. Feezell, L.A. Johansson, D.A. Buell, L.A. Coldren, Efficient modulation of InP-based 1.3 μm VCSELs with AsSb-based DBRs. IEEE Photon. Technol. Lett. **17**(11), 2253 (2005)
36. M.R. Park, O.K. Kwon, W.S. Han, K.H. Lee, S.J. Park, B.S. Yoo, All epitaxial InAlGaAs-InP VCSELs in the 1.3–1.6 μm wavelength range for CWDM band applications. IEEE Photon. Technol. Lett. **18**(16), 1717 (2006)
37. D. Feezell, D.A. Buell, D. Lofgreen, M. Mehta, L.A. Coldren, Optical design of InAlGaAs low loss tunnel junction apertures for long wavelength vertical cavity lasers. IEEE J. Quantum Electron. **42**(5), 494 (2006)
38. D.S. Song, S.H. Kim, H.G. Park, C.K. Kim, Y.H. Lee, Single fundamental mode photonic crystal vertical cavity surface emitting lasers. Appl. Phys. Lett. **80**(21), 3901 (2002)
39. A.J. Danner, T.S. Kim, K.D. Choquette, Single fundamental mode photonic crystal vertical cavity laser with improved output power. Electron. Lett. **41**(6), 20057841 (2005)
40. H.P. Yang, I.C. Hsu, Y.H. Chang, F.I. Lai, H.C. Yu, G. Lin, R.S. Hsiao, N.A. Maleev, S.A. Blokhin, H.C. Kuo, J.Y. Chi, Characteristics of InGaAs submonolayer quantum dot and

InAs quantum dot photonic crystal vertical cavity surface emitting lasers. J. Lightwave Technol. **26**(11), 1387 (2008)
41. R. Stevens, P. Gilet, A. Larrue, L. Grenouillet, N. Olivier, P. Grosse, K. Gilbert, B. Hladys, B.B. Bakir, J. Berggren, Mattias Hammar, A. Chelnokov, Microstructured photonic crystal for single mode long wavelength VCSELs, in *Semiconductor Lasers and Laser Dynamics III*, ed. by K.P. Panajotov, M. Sciamanna, A.A. Valle, R. Michalzik, Proceedings of SPIE, vol 6997 (2008), p. 69970X-1
42. F. Romstad, S. Bischoff, M. Juhl, S. Jacobsen, D. Birkedal, Photonic crystals for long wavelength single mode VCSELs, in *Vertical-Cavity Surface-Emitting Lasers XII*, ed. by C. Lei, J.K. Guenter, Proceedings of SPIE, vol 6908 (2008), p. 69080C-1
43. A. Furukawa, S. Sasaki, M. Hoshi, A. Matsuzono, K. Moritoh, T. Baba, High power single mode vertical cavity surface emitting lasers with triangular holey structure. Appl. Phys. Lett. **85**(22), 5161 (2004)
44. P.O. Leisher, A.J. Danner, J.J. Raftery Jr., K.D. Choquette, Proton implanted single mode holey vertical cavity surface emitting lasers. Electron. Lett. **41**(18), 20052394 (2008)
45. E.W. Young, K.D. Choquette, S.L. Chuang, K.M. Geib, A.J. Fischer, A.A. Allerman, Single transverse mode vertical cavity lasers under continuous and pulsed operation. IEEE Photon. Technol. Lett. **13**(9), 927 (2001)
46. F.I. Lai, T.H. Hsueh, Y.H. Chang, H.C. Kuo, S.C. Wang, L.H. Laih, C.P. Song, H.P. Yang, 10 Gb/s single mode vertical cavity surface emitting laser with large aperture and oxygen implantation. Semicond. Sci. Technol. **19**(8), L86 (2004)
47. H.J. Unold, S.W.Z. Mahmoud, R. Jäger, M. Kicherer, M.C. Riedl, K.J. Ebeling, Improved single mode VCSEL performance by introducing a long cavity. IEEE Photon. Technol. Lett. **12**(8), 939 (2000)
48. H.J. Unold, M.C. Riedl, S.W.Z. Mahmoud, R. Jäger, K.J. Ebeling, Long monolithic cavity VCSELs for high single mode power. Electron. Lett. **37**(3), 178 (2001)
49. S.W.Z. Mahmoud, H.J. Unold, W. Schmid, R. Jäger, R. Michalzik, K.J. Ebeling, Analysis of longitudinal mode wave guiding in vertical cavity surface emitting lasers with long monolithic cavity. Appl. Phys. Lett. **78**(5), 586 (2001)
50. R.A. Morgan, G.D. Guth, M.W. Focht, M.T. Asom, K. Kojima, L.E. Rogers, S.E. Callis, Transverse mode control of vertical cavity top surface emitting lasers. IEEE Photon. Technol. Lett. **4**(4), 374 (1993)
51. N. Ueki, A. Sakamoto, T. Nakamura, H. Nakayama, J. Sakurai, H. Otoma, Y. Miyamoto, M. Yoshikawa, M. Fuse, Single transverse mode 3.4 mW emission of oxide confined 780 nm VCSELs. IEEE Photon. Technol. Lett. **11**(12), 1539 (1999)
52. H. Otoma, A. Murakami, Y. Kuwata, N. Ueki, N. Mukoyama, T. Kondo, A. Sakamoto, S. Omori, H. Nakayama, T. Nakamora, Single mode oxide confined VCSEL for printers and sensors, in *Proceedings Electronics System Integration Technology Conference*, Dresden, Germany (2006), p. 80
53. P.D. Floyd, M.G. Peters, L.A. Coldren, J.L. Merz, Suppression of higher order transverse modes in vertical cavity lasers by impurity induced disordering. IEEE Photon. Technol. Lett. **7**(12), 1388 (1995)
54. J.W. Shi, C.C. Chen, Y.S. Wu, S.H. Guol, C. Kuo, Y.J. Yang, High power and high speed Zn-diffusion single fundamental mode vertical cavity surface emitting lasers at 850 nm wavelength. IEEE Photon. Technol. Lett. **20**(13), 1121 (2008)
55. H. Martinsson, J.A. Vukusic, M. Grabherr, R. Michalzik, R. Jäger, K.J. Ebeling, A. Larsson, Transverse mode selection in large area oxide confined vertical cavity surface emitting lasers using a shallow surface relief. IEEE Photon. Technol. Lett. **11**(12), 1536 (1999)
56. H.J. Unold, M. Grabherr, F. Eberhard, F. Mederer, R. Jäger, M. Riedl, K.J. Ebeling, Increased area oxidised single fundamental mode VCSEL with self-aligned shallow surface relief. Electron. Lett. **35**(16), 1340 (1999)

57. H.J. Unold, S.W.Z. Mahmoud, R. Jäger, M. Grabherr, R. Michalzik, K.J. Ebeling, Large area single mode VCSELs and the self-aligned surface relief. IEEE J. Select. Topics Quantum Electron. **7**(2), 386 (2001)
58. Å. Haglund, J.S. Gustavsson, J. Vukusic, P. Modh, A. Larsson, Single fundamental mode output power exceeding 6 mW from VCSELs with a shallow surface relief. IEEE Photon. Technol. Lett. **16**(2), 368 (2004)
59. A. Kroner, F. Rinaldi, J.M. Ostermann, R. Michalzik, High-performance single fundamental mode AlGaAs VCSELs with mode-selective mirror reflectivities. Opt. Commun. **270**(2), 332 (2007)
60. Å. Haglund, J.S. Gustavsson, P. Modh, A. Larsson, Dynamic mode stability analysis of surface relief VCSELs under strong RF modulation. IEEE Photon. Technol. Lett. **17**(8), 1602 (2005)
61. F. Rinaldi, J.M. Ostermann, A. Kroner, R. Michalzik, High-performance AlGaAs-based VCSELs emitting in the 760 nm wavelength range. Opt. Commun. **270**(2), 310 (2007)
62. H.C. Kuo, Y.H. Chang, Y.A. Chang, F.I. Lai, J.T. Chu, M.Y. Tsai, S.C. Wang, Single mode 1.27 μm InGaAs:Sb-GaAs-GaAsP quantum well vertical cavity surface emitting lasers. IEEE J. Select. Topics Quantum Electron. **11**(1), 121 (2005)
63. E. Söderberg, P. Modh, J.S. Gustavsson, A. Larsson, Z.Z. Zhang, J. Berggren, M. Hammar, High speed, high temperature operation of 1.28 μm singlemode InGaAs VCSELs. Electron. Lett. **42**(17), 978 (2006)
64. A.C. Lehman, E.A. Yamaoka, C.W. Willis, K.D. Choquette, K.M. Geib, A.A. Allerman, Variable reflectance vertical cavity surface emitting lasers. Electron. Lett. **43**(8), 460 (2007)
65. R. Marcks von Würtemberg, P. Sundgren, J. Berggren, M. Hammar, M. Ghisoni, E. Ödling, V. Oscarsson, J. Malmquist, 1.3 μm InGaAs vertical cavity surface emitting lasers with mode filter for single mode operation. Appl. Phys. Lett. **85**(21), 4851 (2004)
66. L.J. Mawst, “Anti” up the aperture. IEEE Circuits Devices Mag. **19**(2), 34 (2003)
67. Y.A. Wu, G.S. Li, W. Yuen, C. Caneau, C.J. Chang-Hasnain, High yield processing and single mode operation of passive antiguide region vertical cavity lasers. IEEE J. Select. Topics Quantum Electron. **3**(2), 429 (1997)
68. T.H. Oh, M.R. McDaniel, D.L. Huffaker, D.G. Deppe, Cavity-induced antiguiding in a selectively oxidized vertical cavity surface emitting laser. IEEE Photon. Technol. Lett. **10**(1), 12 (1998)
69. K.D. Choquette, G.R. Hadley, H.Q. Hou, K.M. Geib, B.E. Hammons, Leaky mode vertical cavity lasers using cavity resonance modifications. Electron. Lett. **34**(10), 991 (1998)
70. T.H. Oh, O.B. Shchekin, D.G. Deppe, Single mode operation in an antiguided vertical cavity surface emitting laser using low temperature grown AlGaAs dielectric aperture. IEEE Photon. Technol. Lett. **10**(8), 1064 (1998)
71. D. Zhou, L.J. Mawst, Simplified antiresonant reflecting optical waveguide type vertical cavity surface emitting lasers. Appl. Phys. Lett. **76**(13), 1659 (2000)
72. D. Zhou, L.J. Mawst, High power single mode antiresonant reflecting optical waveguide type vertical cavity surface emitting lasers. IEEE J. Quantum Electron. **38**(12), 1599 (2002)
73. A.J. Fischer, K.D. Choquette, W.W. Chow, A.A. Allerman, D.K. Serkland, K.M. Geib, High single mode power observed from a coupled resonator vertical cavity laser diode. Appl. Phys. Lett. **79**(25), 4079 (2001)
74. J.S. Gustavsson, Å. Haglund, J. Bengtsson, A. Larsson, Dynamic behaviour of fundamental-mode stabilized VCSELs using a shallow surface relief. IEEE J. Quantum Electron. **40**(6), 607 (2004)

Part II
Device Technology and Performance

Chapter 5
Polarization Control of VCSELs

Johannes Michael Ostermann and Rainer Michalzik

Abstract In most types of VCSELs, the light output polarization is inherently unstable. While, in case of single-mode oscillation, the emitted light is mainly linearly polarized, its orientation is not well defined. This is because both the resonator and the gain medium are quasi isotropic in the plane of the active layers. Since a stable polarization is required for almost all sensing and some datacom applications, extensive and in-depth investigations have been undertaken during the last twenty years in order to stabilize the polarization of VCSELs without affecting their favorable operation parameters. Polarization control of VCSELs can be achieved by introducing a polarization-dependent gain, an asymmetric resonator, or mirrors with a polarization-dependent reflectivity. It has turned out that the last approach is most promising. It can be realized by incorporating a shallow surface grating in the upper mirror of a top-emitting VCSEL. Several million grating VCSELs are in reliable operation meanwhile, mainly in optical computer mice.

5.1 Introduction

Shortly after the first successful demonstration of VCSELs [1, 2] it turned out that the orientation of the polarization of their emitted modes is not well defined [3]. While the modes of VCSELs are predominantly linearly polarized, the orientation

J. M. Ostermann (✉) · R. Michalzik
Institute of Optoelectronics, Ulm University,
Albert-Einstein-Allee 45, 89081 Ulm, Germany
e-mail: johannes-michael.ostermann@alumni.uni-ulm.de

R. Michalzik
e-mail: rainer.michalzik@uni-ulm.de

R. Michalzik (ed.), *VCSELs*, Springer Series in Optical Sciences 166,
DOI: 10.1007/978-3-642-24986-0_5, © Springer-Verlag Berlin Heidelberg 2013

of this linear polarization is not only unpredictable[1] from VCSEL to VCSEL, but it can also change during operation [4]. The latter is called a polarization switch.

Intensive research was done over the last two decades to characterize these polarization instabilities in VCSELs and to understand their physical origin. Some results will be presented briefly in Sect. 5.2. A deeper discussion and more details on this topic are given in Chap. 6 of this book.

While polarization switches are very interesting and exciting phenomena, they inhibit the use of VCSELs in a variety of datacom and sensing applications, as will be discussed in Sect. 5.3. To open these applications to VCSELs, a method to define and pin the polarization is needed. This method should not deteriorate other VCSEL properties like very small threshold current, high differential quantum efficiency, and circularly symmetric far-field profile. Quite some approaches to control the polarization of VCSELs have been suggested and investigated. These attempts will be the topic of Sect. 5.4. Among all ideas for polarization control, surface gratings have turned out to be the most promising method. Therefore, they will be discussed in more detail in Sect. 5.5.

5.2 VCSELs and Their Polarization

As pointed out above, there is no intrinsic and strong mechanism in VCSELs to select one specific orientation of the polarization.[2] This is the cause of unwanted polarization instabilities. Such instabilities are known from edge-emitting lasers (EELs) as well [5, 6], but a stable polarization can easily be achieved in properly designed EELs for three reasons: First, the transverse electric (TE) mode in an EEL, which is polarized in the plane of the active region, experiences a higher reflectivity at the cleaved facets than the orthogonally polarized transverse magnetic (TM) mode [7]. This difference already selects a stable polarization. Second, the TE modal gain is usually higher than the TM gain in bulk semiconductor laser structures owing to better confinement [8]. Third, unstrained or compressively strained quantum wells provide gain exclusively for the TE polarization [9–11].

In contrast, because of light propagation perpendicular to the active region, all polarization modes in VCSELs are TE polarized and thus experience basically the same gain. In addition, also the Bragg mirrors used for VCSELs do not select a specific polarization. Although their reflectivity is slightly higher for waves polarized normal to the plane of incidence than for those polarized parallel to this plane [12, 13], this neither results in a specific preference of any polarization nor in any specific orientation of the polarization at all, since the reflectivity of a distributed Bragg reflector (DBR) has a circular symmetry with no preferred crystal axis.

---

[1] Unpredictable without a very deep knowledge of all properties of the particular laser, including all imperfections.

[2] With the term "polarization" we refer to the orientation of the electric (not the magnetic) field vector, as is done in most publications.

Consequently, VCSELs suffer a priori from an unpredictable and instable polarization, as discussed in the following.

5.2.1 Experimental Findings

Owing to their short cavity combined with the finite spectral widths of the stop-bands of their Bragg reflectors and of their gain medium, standard VCSELs are longitudinal single-mode. However, their transverse dimension is larger than their effective longitudinal cavity length, which is usually in the order of 1–1.5 μm [14] (see also Chap. 2 of this book). Consequently, VCSELs emit several transverse modes if their active diameter exceeds approximately 3–4 μm in standard oxide-confined devices. In the model of a weakly guiding VCSEL structure (as is the case with large active diameters and a small effective transverse refractive index step), these transverse modes are frequently approximated by linearly polarized LP modes, as outlined in Chap. 2 of this book.

For every LP mode in a VCSEL, there exist two polarization modes with orthogonal polarizations [15]. In a VCSEL structure without an anisotropic refractive index, these two polarization modes would have identical emission wavelengths. However, due to the birefringence introduced by the electro-optic and elasto-optic effects in VCSELs, the emission wavelengths of the two polarization modes of one particular transverse mode differ by up to 100 pm [16]. In the context of research into VCSELs, the wavelength difference between two polarization modes is often called birefringence [17]. The slightly wavelength- and polarization-dependent complex refractive indices inside a VCSEL structure lead to a net modal gain difference between two polarization modes. This net modal gain difference is commonly called linear modal dichroism [17]. In the absence of a nonlinear modal dichroism, one expects lasing of the polarization mode with the higher net modal gain.

If in oxide-confined VCSELs the transverse index variation between the oxide aperture and the oxide itself can no longer be neglected or if the diameter of the oxide aperture is small, the LP approximation remains no longer valid [18]. In that case, a polarization mode in a VCSEL contains not only its dominant polarization but also orthogonal components [19]. Within a single polarization mode, the weaker polarization is thus only suppressed by at most about 35 dB [19]. The weaker polarization mode is in most cases only driven by spontaneous emission [20], but can also lase under certain circumstances [21, 22]. In both cases, the polarization extinction ratio is limited by the suppressed polarization mode. Even if the suppressed polarization mode does not lase, the modes in VCSELs are in general slightly elliptically polarized [20]. The ratio of the intensity in the long axis of the polarization ellipsoid to the intensity in its short axis depends on the alignment between birefringence and linear dichroism [23] and decreases with increasing angle enclosed by the axis of birefringence and the axis of linear dichroism. Consequently, even in single-mode VCSELs the suppression of the orthogonal polarization was found to be in most

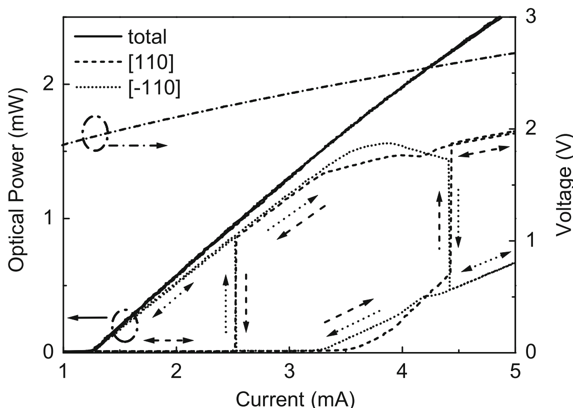

Fig. 5.1 Polarization-resolved light–current–voltage characteristics of a standard VCSEL showing a polarization switch with hysteresis, which means that the dominant polarization differs for increasing and decreasing current. The active diameter of this VCSEL is 4 μm. The sum of the measured powers in the two polarizations is lower than the total output power due to the losses in the Wollaston prism used in the measurement setup

cases about 17 dB [20]. For some VCSELs the measured suppression was even as low as 7–10 dB.

The polarization-resolved light–current–voltage (PR-LIV) characteristics of a standard VCSEL[3] with an active diameter of 4 μm and an emission wavelength of 860 nm can be seen in Fig. 5.1. The solid line represents the total optical output power of the VCSEL as it is measured without a polarizer, while the dashed and dotted lines represent the optical power measured behind a polarizer whose transmission direction is oriented along the [110] and $[\bar{1}10]$ crystal axis of the VCSEL, respectively. The device was grown on a (001)-oriented GaAs substrate. The dash-dotted line gives the voltage. Already in 1988, when research on VCSELs had just started, it was discovered that VCSELs are in most cases polarized along one of these two crystal axes [3]. This preference of the polarization could later be explained by the electro-optic effect [24], which causes a refractive index ellipsoid with [110] and $[\bar{1}10]$ as the principal axes.

While the total output power of the VCSEL in Fig. 5.1 increases continuously and monotonically, the polarization is not pinned along the main crystal axis selected at threshold. At two different drive currents, the distribution of the output power among the two polarizations changes abruptly. These events are called polarization switches. Such a polarization switch was observed in 1991 for the first time [4]. In the case of the VCSEL shown in Fig. 5.1, the polarization switch occurs at a drive current of 4.41 mA when the current is increased and at a current of 2.52 mA when the current

[3] In this chapter, VCSELs without any special measure for polarization control are denoted as standard VCSELs.

is decreased. Therefore the powers in the two polarizations pass through a hysteresis region [16] with first increasing and then decreasing current, as indicated by the arrows in Fig. 5.1.

The polarization switch at the lower current basically exchanges the complete output power between the two polarizations, while in the case of the switch at the higher current, the weaker polarization contains a significant amount of power before and after the polarization switch. This difference is due to higher-order transverse modes, which substantially contribute to the emission of the VCSEL in Fig. 5.1 for currents exceeding 3 mA. The polarization of the individual higher-order transverse modes seems to be arbitrary at first glance [4, 21], although it depends on the polarization of the other modes. The first higher-order mode is in most cases polarized orthogonal to the fundamental one. However, polarization switches are not limited to the fundamental mode. Instead, every higher-order transverse mode can also exhibit a polarization switch. The first two higher-order modes of the VCSEL shown in Fig. 5.1 are polarized along the [110] crystal axis and thus orthogonal to the fundamental mode with an increasing drive current smaller than 4.41 mA. If the current is raised further, the fundamental and the first higher-order mode change their polarization simultaneously. However, if the current is subsequently decreased to 4 mA, also the second higher-order mode exhibits a polarization switch and is then polarized parallel to the first higher-order mode again. This change in the polarization of the second higher-order transverse mode appears only as a small ripple in the PR-LIV characteristics, since in this VCSEL the second higher-order transverse mode is somewhat weaker than the fundamental one and additionally exhibits an even lower degree of suppression of the weaker polarization than the fundamental mode. In contrast, the polarization switch of the fundamental mode at 2.52 mA with decreasing current is very pronounced, since the laser is single-mode at that current.

Although a rotation of the polarization with current or temperature was observed as well [21], in most cases the orientation of the polarization changes by a polarization switch. Commonly one distinguishes between two different types of polarization switches [25]: If the switch occurs from the polarization with the shorter emission wavelength to the polarization with the longer emission wavelength for increasing current, it is called a type I switch. The opposite case is called a type II switch [16]. Type I polarization switches are found more frequently than type II switches [22] and can be followed by a type II polarization switch at higher current [26]. However, in addition to changes of the drive current, a polarization switch can also be caused by variations of the substrate temperature [21] or by intentionally introduced strain. The latter was done by either bending the VCSEL chip [27], by creating a local hot spot in the vicinity of the laser [28], or by introducing a permanent modification of the semiconductor material on one side of the VCSEL [29].

In contrast to the polarization switches observed in Fig. 5.1, a polarization switch can seem to occur gradually with current [30], if measured with a photodiode with a large time constant. However, this virtually gradual polarization switch is in reality a mode hopping between the two polarizations [16] with the average residence times in

the two polarization modes depending on the current [31]. In the vicinity of the polarization switch, the average residence time in the polarization that was dominant before the polarization switch decreases with increasing current, while simultaneously the average residence time in the initially suppressed polarization increases. The absolute values of the average residence times depend on the difference between the current at which the polarization switch occurs and the threshold current [32, 16]. If current noise is intentionally applied, the average residence time decreases [33].

The response of VCSELs to a small current modulation around a bias current at which a polarization switch occurs was investigated as well [34]. It turned out that the time delay between the edge of the modulation pattern and the polarization switch is stochastically distributed [35] and that the maximum modulation frequency at which the polarization switch still occurs depends on the underlying mechanism of the switch [36]. This stochastic nature of polarization switches appears as well in the turn-on characteristics of VCSELs under current or voltage pulses having a short rise time. Even for VCSELs with a stable polarization under continuous-wave (CW) operation, it can take several nanoseconds of polarization competition with two almost equally strong polarizations until the steady-state condition is reached [37].

The pronounced polarization switching found in VCSELs raises the question which influence these polarization instabilities have on their noise properties. First investigations were done on multimode VCSELs, and it was found that an increase of the relative intensity noise in the total output power by about 3–5 dB occurs as soon as the second polarization contributes to the lasing action [38, 39]. However, this increment of the noise in the total output power is quite small compared to the rise of the noise in the individual polarizations, which can even exceed 25 dB [39]. This effect is explained by the strong anti-correlation of the two polarizations which is observed in most cases [40]. Consequently, the noise properties of VCSELs in an optical setup are very sensitive to polarization-dependent absorption, reflection, and transmission along the optical path. Also in single-mode VCSELs, the noise in the individual polarizations exceeds the one of the total output power by 15–20 dB [30]. The birefringence and the consequently induced splitting of the emission wavelengths of the polarization modes determines to which degree the noise properties of single-mode VCSELs deteriorate due to polarization instabilities. If the wavelength splitting is small, the noise in the total optical output power of the VCSEL increases more than for a larger wavelength splitting [30].

Not surprisingly, optical feedback can have a strong and potentially crucial influence on the polarization properties of VCSELs [41]. The polarization of VCSELs can be switched by polarization-sensitive feedback [42, 43] or by varying the length of an extremely short external cavity [44, 45]. Pronounced laser dynamics in the emitted polarizations were observed under isotropic [46] as well as polarized [47] optical feedback or by injecting orthogonally polarized light from a master laser into a VCSEL [48]. Thus, feedback has to be avoided very carefully for many VCSEL applications if no measures have been taken to stabilize the laser intrinsically, as discussed in Sects. 5.4 and 5.5.

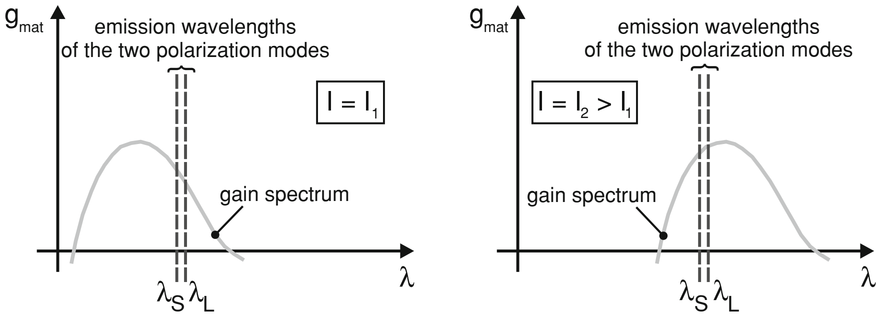

Fig. 5.2 Illustration of the wavelength shift of the material gain spectrum $g_{\mathrm{mat}}(\lambda)$ and the cavity resonances with increasing laser temperature, which might be caused, e.g., by a higher drive current I

5.2.2 Some Theoretical Explanations

The polarization instabilities summarized above call for explanations. The first one was presented in 1994, stating that polarization switches result from an interplay of the wavelength difference between the two polarization modes with the wavelength dependence of the gain [21]. In contrast to Fabry–Pérot-type EELs, the emission wavelength of VCSELs is determined by the laser cavity and not by the gain spectrum. With increasing temperature in the active region, usually caused by a higher drive current, the gain spectrum shifts to longer wavelengths at a rate of about 0.32–0.34 nm/K [12], whereas the cavity resonance shift is 0.056–0.09 nm/K. In a temperature-insensitive design, the gain spectrum has to be on the short-wavelength side of the cavity resonance at the target ambient operation temperature and zero drive current. Increasing the current, the gain spectrum then shifts from the short-wavelength side of the cavity resonance to the long-wavelength side, as illustrated in Fig. 5.2. Consequently, for small currents, the polarization mode with the smaller wavelength λ_{S} experiences a higher material gain on the long-wavelength side of the gain spectrum, while, for high currents on the short-wavelength side of the gain spectrum, the material gain is higher for the polarization mode with the longer wavelength λ_{L}.

This effect can explain the more frequently observed type I polarization switch, that is a switch from shorter to longer emission wavelengths, but not the type II. To be able to describe also those, the wavelength dependence of the absorption was included later [25]. Free-carrier absorption via transitions between the split-off band and the heavy-hole band in the p-doped DBR was identified as the dominant absorption mechanism. This absorption increases with increasing wavelength. Thus nothing changes if the cavity resonances are on the long-wavelength side of the gain spectrum. However, when the cavity resonances are on the short-wavelength side, the dominant polarization depends on the magnitude of the derivatives of the material gain and of the absorption with respect to the wavelength. In this way,

one can phenomenologically explain type I and type II polarization switches as well as—with some restrictions—a type I switch followed by a type II switch. The observation of polarization switches attributed to spatial hole burning [49] or thermal lensing [50] points out that instead of the net material gain the net modal gain has to be considered to describe polarization switches in VCSELs correctly. In addition, the polarization dependence of the gain and the absorption due to the electro-optic and especially the elasto-optic effect has to be included [11, 27].

The observation of hysteresis in the two orthogonal polarizations of VCSELs, that is the phenomenon that the dominant polarization differs for increasing and decreasing current (as shown in Fig. 5.1), makes clear that the net modal gain difference alone does not define the polarization. Thus, nonlinear effects like self- and cross-saturation of the gain with varying photon density have to be considered [51]. If the cross-saturation exceeds the self-saturation, bistability of the polarization and therefore a hysteresis like in Fig. 5.1 can be theoretically described. Even including these nonlinear effects, there are experimental observations which cannot be explained with a thermal model as discussed up to now. Among these observations are polarization switches at constant active region temperature [52], polarization switches to the gain-disfavored mode [53], and intermediate elliptically polarized dynamic states associated with a type II switch [22].

So far, the birefringence was mentioned as the cause of the frequency splitting of the two polarization modes, but has not been considered as a phase anisotropy in the rate equations. This is correct only if either the birefringence itself or the linewidth enhancement factor vanishes [54]. However, both quantities are different from zero in VCSELs. Including phase–amplitude coupling, as is typical for semiconductor lasers, polarization switching is predicted even in the absence of any net modal gain difference [55]. Furthermore, even polarization switches to the polarization mode with the smaller net modal gain can be explained [54]. Besides that, ranges for parameters like current and birefringence in which one polarization, both polarizations, or no polarization is stable can be identified by performing a stability analysis of the general solution of this so-called spin-flip model [55, 56]. Its name originates from the fact that the angular momentum of the conduction and valence band states is taken into account. Apart from two linearly polarized solutions, an elliptical polarization, a periodically modulated polarization, or a polarization assumed to be chaotically modulated can be found in the vicinity of the boundaries of the stability regions [54]. Also a double polarization switch, that is a type I switch followed by a type II switch, can be described by the spin-flip model if gain saturation is included [57].

In a second step, the spin-flip model was combined with the thermal aspects discussed before. This was done by introducing a more realistic gain behavior in the spin-flip model through a frequency-dependent susceptibility [58], which accounts for thermal effects by a varying detuning and substitutes the linewidth enhancement factor. The advanced model is known as the extended spin-flip model. Later, the frequency-dependent susceptibility was further generalized to include strain effects as well [59].

In this way, the repeatedly extended spin-flip model, which is discussed in much more detail in Chap. 6 of this book, became the most complete theory to describe

polarization switching. However, this could only be achieved at the expense of a high level of complexity. Therefore, several attempts have been made to reduce the spin-flip model without losing the ability to describe the most common experimental conditions. These simplifications are based on adiabatical elimination of the spin dynamics [17, 20] or on a multiple time scale analysis in combination with averaging methods [60].

To summarize the discussion on the polarization properties of VCSELs, it shall be pointed out that besides the net modal gain difference, nonlinear effects like phase–amplitude coupling play a major role in the selection of the dominant polarization as well. In general, the physical mechanisms which influence the polarization properties of VCSELs are so manifold that a stable polarization cannot be achieved by addressing them individually. Instead, one mechanism should be chosen for polarization selection and be pronounced so strongly that it dominates all other influences and thus guarantees a stable polarization.

5.3 Need for Polarization Control of VCSELs

As presented in the previous section, VCSELs a priori have an unstable and hardly predictable polarization. However, in several applications, a stable polarization is advantageous or even required. Polarization switches or an undefined polarization in general increase the relative intensity noise of VCSELs [38, 37, 61, 62], which is an important performance parameter in data communication and sensing. Especially in a setup with polarization-dependent transmission, the noise floor of the system is strongly raised [63].

Apart from a polarizer there are other optical elements like beam splitters, mirrors, or lenses which in most cases possess a polarization-dependent transmissivity or reflectivity. Therefore, all components in any optical setup in which a VCSEL with an unstable polarization is supposed to be used have to have polarization-independent properties if no variations of the transmitted power can be tolerated. This requires extra care and effort and leads to higher cost. Explicitly one cannot compensate the unstable polarization of a VCSEL with a polarizer inserted in the beam path of the laser. Besides the strongly increased noise, the total available power behind such a polarizer would vary or jump by potentially even more than 20 dB depending on the distribution of the laser output power among the two main polarizations.

While VCSELs were developed with a main focus on data communication, optical sensing and spectroscopy have become two very important application areas. Owing to the electro-optic and elasto-optic effects, a polarization switch of a VCSEL is accompanied by a shift of the emission wavelength. Such a shift can be as large as 100 pm [16], exceeding the spectral linewidths of common gases such as oxygen, which has absorption lines around 760 nm wavelength with a full width at half maximum (FWHM) of 7.5 pm at 1 bar [64]. In the case of a polarization switch, the spectral overlap of the absorption line and the laser emission would be lost. In the growing commercial field of microsensors using microoptics, single-mode and

simultaneously single-polarization VCSELs are required for atomic clocks [65, 66] as well as for other atomic sensors like magnetometers or gyroscopes [67]. Optical computer mice are a mass market for VCSELs [68, 69]. The sensing schemes usually require VCSELs with a well-defined and stable polarization [70]. The same is true for the potential use of VCSELs in magneto-optical, compact, or digital versatile disc drives.

Consequently, a reliable technique to control the polarization of VCSELs would open up new application areas and would make new products possible. Up to now, VCSELs with an accidentally polarization-stable emission were often handpicked from a large quantity. An intrinsic method for polarization control would make such a selection obsolete. Additionally, the emission of these handpicked VCSELs is not guaranteed to be polarization-stable for operating conditions differing from those used for testing. For example, a VCSEL which is polarization-stable when tested on-wafer is not necessarily polarization-stable after it has been mounted, since the mounting process can introduce additional stress. The same holds true if an apparently stable VCSEL is exposed to optical feedback. Furthermore, it is easier to guarantee a stable polarization of a VCSEL in CW operation than under high-speed modulation.

To be suitable for mass market consumer products like optical computer mice, polarization control must be realized without causing additional fabrication costs exceeding a few cents per device. The solution must thus be implemented monolithically. Polarization-stable VCSEL properties like threshold current, output power, differential quantum efficiency, circularly symmetric far-field, or high modulation bandwidth should be well comparable with those of standard devices. Since VCSELs are nowadays often used for spectroscopic applications which require a stable polarization, there is a high demand for a variety of different emission wavelengths. Therefore, the method of choice for polarization control of VCSELs has to be either wavelength-independent or easily adaptable to different wavelengths without individual optimization.

5.4 Approaches to Polarization Control

As early as 1991, first proposals and attempts to stabilize the polarization of VCSELs were made in the group of Prof. Iga at Tokyo Institute of Technology, Japan [71]. In the years to follow, his group and his successor Prof. Koyama made substantial contributions to the research into polarization-stable VCSELs [72–85]. Over the years, groups at several laboratories came up with new ideas in this research field: the group of Prof. Lee at the Korea Advanced Institute of Science and Technology [86–90], Dr. Choquette at Sandia National Laboratories, USA [91], the group of Prof. Bowers at the University of California, Santa Barbara, USA [92, 93], Prof. Chang-Hasnain's group at the University of California, Berkeley, USA [94, 95], the group of Prof. Thienpont at Vrije Universiteit Brussel, Belgium [96–98], Prof. White's group at the University of Bristol (now at Cambridge), UK [99, 100], the group of Prof. Larsson at Chalmers University of Technology, Sweden

[101–104], and the group of Prof. Ebeling [105, 106] and Dr. Michalzik at Ulm University, Germany in close collaboration with Dr. Debernardi at the Italian National Research Center at Politecnico di Torino, Italy [63, 107–122]. Since the issue of polarization control is of such high practical interest and importance, very active and in-depth research in this field was undertaken by several companies like NTT [123–127], Avalon Photonics [128], NEC [129–131], Nortel [132], Fuji Xerox [133, 134], Matsushita (Panasonic) [135], and Philips U-L-M Photonics [70] (based on research at Ulm University).

In what follows, we will discuss the major approaches to polarization control of VCSELs investigated up to now. They can be roughly divided in the use of polarization-dependent gain, polarization-dependent mirrors, asymmetric resonators, or external optical feedback.

5.4.1 Polarization-Dependent Gain

The gain of quantum wells grown on (001)-oriented substrates is equal for all polarization directions in the plane of the quantum wells if the direction of current flow is orthogonal to the quantum wells. However, this gain degeneracy is lifted as soon as the direction of the current flow is changed. Consequently, the idea of an inclined current path by using intra-cavity contacts came up [96, 97]. The polarization of the investigated VCSELs was indeed influenced by this asymmetric current injection, but the extinction of the suppressed polarization was rather small and the overall laser performance clearly suffered from the modified current distribution inside the active layers.

The above isotropy of the quantum well gain is broken on substrates with higher indices [136]. First attempts with GaAs substrates which were misoriented by two degrees towards the (111)A or (111)B plane[4] did not give the desired results [130]. The material gain anisotropy is enhanced strongly in VCSELs grown on GaAs (113)A substrates [75, 76, 78]. To avoid problems in the doping of layers with high aluminum content, GaAs (113)B substrates were chosen later [77, 79, 123]. With this method for polarization control, a very high orthogonal polarization suppression ratio (OPSR) of 30 dB was achieved [79], because already the spontaneous emission of such VCSELs is partially polarized. A drawback is the rather difficult processing [81]. Since the activation energies along the [$3\bar{3}\bar{2}$] and [$\bar{1}\bar{1}0$] crystal axes are different, the process temperature for lateral oxidation had to be increased up to 480°C, while commonly temperatures around 400°C are chosen for a better control of the oxidation rate. Nevertheless, single-mode emission was achieved [80], but with a rather moderate single-mode output power of less than 1 mW. Multimode VCSELs showed a stable polarization under 5 GHz sinusoidal modulation, but the peak-to-peak suppression of the weaker polarization in the spectra of single-mode VCSELs dropped from 30 dB for CW operation to 11 dB [81]. The reduction of polarization suppression in

[4] The symbols ‘A’ and ‘B’ indicate whether the surface layer contains gallium or arsenic atoms, respectively.

single-mode VCSELs on (113)B substrates under high-speed modulation was later reduced by using strained quantum wells in combination with an optimized AlAs layer for lateral oxidation.

The VCSELs grown on substrates with higher indices discussed so far had emission wavelengths of around 960 nm. In the year 1998, the IEEE 802.3z Gigabit Ethernet standard defined the use of 850 nm light sources for data communication over multimode fibers with lengths up to several hundred meters. A transfer of the 960 nm results to shorter wavelengths of 850 nm thus became necessary. These attempts were only partially successful [124, 125]. An improvement was again achieved by incorporating strained quaternary $In_{0.2}Al_{0.15}Ga_{0.65}As$ quantum wells [126]. While OPSRs of more than 20 dB were achieved for CW operation, the suppression of the orthogonal polarization decreased to below 10 dB during the first peak of relaxation oscillations.

Longer-wavelength VCSELs emitting at about 1.1 μm exhibited a stable polarization in CW operation [84]. An emission wavelength of 1.3 μm was realized with an optically pumped VCSEL by combining an active region grown on InP (113)B substrates with Bragg reflectors grown on GaAs (001)-substrates by wafer bonding [92, 93].

An active medium consisting of quantum wires [137] or structurally anisotropic quantum dots can provide a polarization-dependent gain under certain circumstances as well [138]. Recently, a 1.6 μm InP-based VCSEL with an active region containing InAs quantum dashes showed a stable polarization under optical pumping conditions [139]. The overall performance of VCSELs with quantum dots as active gain medium was rather poor for a long time. Although their performance has been strongly improved [140], no final judgment concerning the intrinsic polarization behavior can yet be made. The same statement holds for the attempt to define the polarization of VCSELs by controlling the spin of electrically injected or optically generated carriers [141, 142].

5.4.2 Polarization-Dependent Mirror

Besides anisotropic gain, the use of mirrors with a polarization-dependent reflectivity is an evident concept for polarization control of VCSELs. A polarization-dependent reflectivity can be realized by etching a shallow elliptic surface relief in the upper Bragg mirror of a VCSEL [106, 107]. However, the induced polarization control is rather weak. Several combinations of a Bragg mirror and a metallic or semiconductor grating have been tried to realize polarization-dependent mirrors [74, 86, 143, 144]. However, none of these attempts has been satisfactory, as will be discussed in more detail in Sect. 5.5. Instead of a grating, two-dimensional microstructures on top of the upper Bragg mirror making use of surface plasmon resonances were investigated as well. To enhance the reflectivity for one polarization and to reduce it for the other, the microstructure has to differ along the two main polarization directions in its dimension [85] or in its period [135]. Recently, photonic crystals have been studied to achieve single-mode oscillation of VCSELs [145–148].

An extension of this concept towards single-mode, polarization-stable VCSELs is obvious [89, 90, 149] but not straightforward: Up to now, the polarization control is insufficient and output powers are moderate.

5.4.3 Asymmetric Resonators

Introducing a transverse anisotropy into the VCSEL cavity has been a very popular idea. Dumbbell-shaped [91], rectangular [129], or elliptical [105, 133, 150] mesas were the first representatives of this technique. They all aimed at polarization-dependent scattering losses inside the laser cavity [151]. However, these polarization-dependent losses are so weak that a combination of an elliptic cavity and a special geometry of metal wires for current injection was tried [134]. Furthermore, an oxide slit with a width of less than 3 μm was manufactured in a proton-implanted VCSEL with an active diameter of 7 μm [88]. However, the slit distorted the circular far-field and thus cancelled a main advantage of standard VCSELs. Combining the existing birefringence in a VCSEL with an antiresonant reflecting optical waveguide for polarization control was proposed and theoretically investigated [152]. Moreover, a tilted mesa structure [153] and a zigzag pattern at two opposed mesa sidewalls [131] were tested. However, in all cases the polarization control achieved with such transverse anisotropies remained rather weak.

The material gain as well as the cavity losses of the two polarizations can be changed simultaneously when external stress is applied. Consequently, intentionally introduced stress seemed to be a promising possibility for polarization control [72, 73, 99, 100, 128, 132, 154]. However, it turned out that the applied stress has to be rather large to achieve a reliably stable polarization, and therefore this approach cannot be implemented easily in a manufacturing process.

5.4.4 External Optical Feedback

External optical feedback has proven to be a very powerful tool for pinning the polarization of VCSELs [43, 98, 155]. However, a major advantage of VCSELs is their compactness and very low price of much less than one US dollar for large volumes. In contrast, external optical feedback requires relatively bulky and expensive optical components as well as careful alignment and mounting. It has thus not much practical importance.

5.4.5 Intentional Polarization Switches

In addition to defining a polarization direction in VCSELs and to pin the polarization reliably along this direction, intentional switching of the polarization is of interest. Ideally this should happen without changing the drive current or the substrate

temperature such that the output power and the emission wavelength remain constant. Several of these attempts were based on optical feedback [43–45, 156] or optical injection [157, 158]. Other techniques utilized the dependence of the gain spectrum on the current direction [159, 160] or relied on the electro-optic effect. The latter was done using devices with three contacts, two of which were used to bias the laser and the third (together with one of the other two) to apply a voltage to one Bragg mirror [161] or to a second cavity [162, 163]. The first approach utilized the birefringence introduced by the electro-optic effect, while in the second one, a combination of the electro-optic effect and the quantum-confined Stark effect were made responsible for the observed partial polarization control.

5.5 Surface Gratings for Polarization Control

Over the last years, reliable polarization control of VCSELs by utilizing surface gratings has been proven not only in academic research [63, 94, 95, 101–104, 109–122, 164, 165], but has found its way into high-volume commercial products [70]. Therefore, surface gratings shall be discussed in more detail in this section.

It is well known from microwave theory that the reflectivity and transmissivity of linear gratings under specific conditions depend on the polarization of the incident electromagnetic wave [166]. Already thirty years ago, it was theoretically [167] as well as experimentally [168] proven that this also holds for infrared light. Thus it is evident to combine a grating with a Bragg mirror to obtain a laser mirror with a polarization-dependent reflectivity. This approach was investigated several times during the last fifteen years [74, 86, 143, 144]. An alternating gold and silicon dioxide grating on top of the upper mirror of a bottom-emitting device was intended to act as a birefringent medium [74]. For this purpose, the grating period has to be much smaller than the laser wavelength in the respective material. Due to technological restrictions, a larger grating period was chosen and consequently the approach failed. A gold–chrome sub-material-wavelength grating on top of the upper mirror of a bottom-emitting VCSEL fabricated later was neither completely convincing: Polarization control was indeed achieved, but the VCSELs could be operated only under pulsed excitation with very small output powers [144]. Promising results for single- and multimode VCSELs were obtained with metal-interlaced semiconductor gratings [86]. A grating was etched into the top quarter-wave layer of the upper DBR of a top-emitting VCSEL. Subsequently, a 20 nm thick aluminum film and a 4 nm thick gold–zinc film were deposited on the sidewalls of the grating ridges. These metal films were intended to act as polarization-dependent absorbers but complicated the manufacturing process significantly. This might be the reason why this promising approach was not pursued further. Pure semiconductor gratings with a rather large grating depth of approximately 0.5 μm were tried as well to achieve a high polarization-dependent reflectivity [143]. While their performance as a stand-alone mirror was satisfactory, these gratings were never incorporated successfully into an actual VCSEL structure.

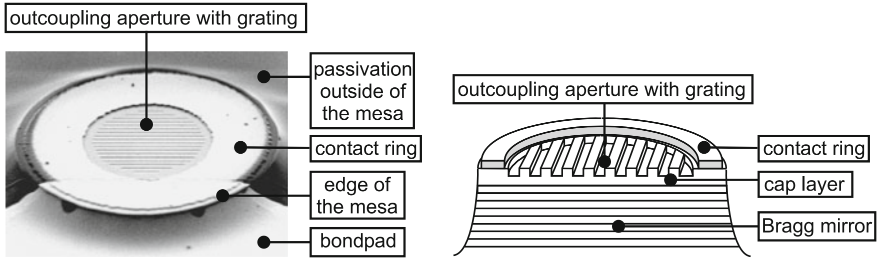

Fig. 5.3 Scanning electron micrograph of a VCSEL with a surface grating monolithically integrated into its outcoupling aperture (*left*) and schematic drawing of a corresponding upper Bragg mirror (*right*) [169]

Monolithically integrated shallow surface gratings were proposed by Pierluigi Debernardi in 2002 [108]. This concept differs from the previously mentioned approaches in several respects. First of all, such pure semiconductor–air gratings have very small absorption and a high refractive index contrast, which is of great importance. They yield a high polarization-dependent reflectivity but don't require a major modification of the VCSEL structure. Owing to the shallow semiconductor ridges, diffraction and absorption losses can be kept acceptable. Finally, monolithic integration with the VCSEL structure allows manufacturing with low additional cost.

The idea and the realization of these monolithically integrated surface gratings is demonstrated in Fig. 5.3 in terms of a scanning electron micrograph and a schematic sketch of an upper Bragg mirror. The grating is etched into the topmost layer of the DBR, where the etch depth is smaller than the thickness of this layer. Thus the material below the grating is the same as that of the grating ridges, while the medium above the grating is air, with which also the grating grooves are filled.

The fact that a Bragg mirror is located below the grating has to be kept in mind for the design, since the grating does not only influence the magnitude of the modes reflected at the semiconductor–air interface but also their phase. Especially the phase is of high relevance. The high reflectivity of a Bragg mirror results from the constructive interference of the reflections at the individual interfaces. The semiconductor–air interface on top of the VCSEL provides the highest reflectivity of all interfaces owing to the high refractive index contrast. Thus, the overall reflectivity of the upper Bragg mirror of a VCSEL depends strongly on the amplitude and the phase of the field reflected at the outcoupling aperture. This is also true for the case of an integrated surface grating, since, under certain circumstances, the reflectivity of a grating can even be higher than that of a planar interface. Consequently, the surface grating has to be designed together with the Bragg mirror below the grating.

5.5.1 Gratings with Wavelength-Scale Periods

While the fabrication of gratings with a period in the order of the wavelength is possible with a reasonable effort, their design is complicated, since full-vectorial,

three-dimensional calculations of the complete resonator are needed, as discussed in detail in Chap. 3 of this book. In these calculations, the transverse wavevectors of the incident modes strongly influence the interaction between the light and the grating. Therefore, plane waves as incident electric field are not a proper choice in the simulations of a surface grating combined with a Bragg mirror. Since the grating is part of a resonator, the reflection from the surface grating influences the field distribution of the incident light. This condition has to be addressed by a proper feedback loop in the computations or, equivalently, by simulating the complete VCSEL resonator in a full-vectorial, three-dimensional way.

The fabrication of the surface gratings can easily be combined with a standard VCSEL manufacturing sequence. Preferably the grating is defined in the first processing step. However, the widely used standard contact lithography is quite at its limit for the grating periods needed. Therefore, alternative lithographical techniques have to be used. In the research stage, the most flexible one is electron-beam lithography. However, this technique might be too expensive for mass production of very-low-cost VCSELs. Since optical projection lithography used for microelectronic integrated circuits fabrication requires major investments, nanoimprint lithography [170] is an attractive alternative.

Etching of the grating grooves is the second challenge in the fabrication process of grating VCSELs. Depending on the exact design, grating depths between 20 and 150 nm have to be realized with a tolerance of just a few nanometers in some cases. Wet-chemical as well as dry etching can be used for this purpose but require very good process control.

To illustrate the achievable polarization control with surface gratings [109–112, 114, 120–122, 164], the polarization-resolved light–current–voltage (PR-LIV) characteristics and the spectra of a multimode surface grating VCSEL are shown in Fig. 5.4. This VCSEL has an active diameter of 7 μm, a grating depth of 22 nm, a grating period of 1 μm, and a grating duty cycle (DC, the ratio between ridge width and grating period) of 65%. The polarization along the $[\bar{1}10]$ direction is clearly dominating over the entire current range from threshold until thermal rollover. Besides changing the drive current, a frequent reason for polarization switches is a change of the operating temperature, as can be easily understood from the thermal model presented in Sect. 5.2. However, while the output power, the threshold current, and the voltage are affected by the temperature change, the polarization of the grating VCSEL remains unchanged. The polarization control introduced by the surface grating is not restricted to the fundamental mode, as can be seen in the spectra in the right-hand graph recorded at room temperature. The orthogonal polarization suppression ratio (OPSR) easily exceeds 20 dB when calculated from the optical powers measured in the two polarizations (left graph), and even 28 dB when defined as peak-to-peak difference in the spectra (right graph).

However, finding a single polarization-stable VCSEL is no proof of a reliable polarization method, since the probability to have some polarization-stable VCSELs on a typical VCSEL wafer is quite high even without any specific measures for polarization control. The results of the study presented in Fig. 5.5 therefore give a much better evidence of the effectiveness of polarization control by surface gratings.

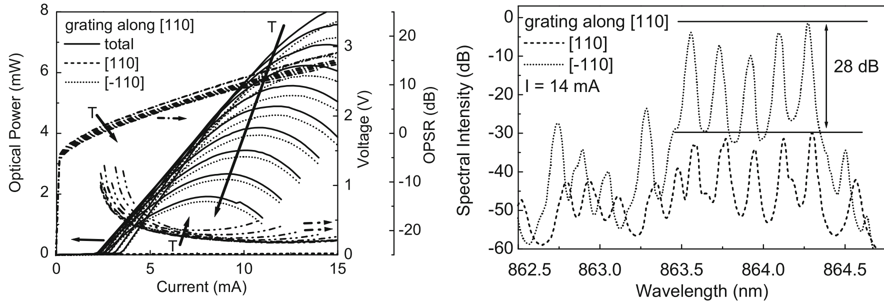

Fig. 5.4 PR-LIV characteristics (*left*) and spectra (*right*) of a grating VCSEL with an active diameter of 7 μm, a grating depth of 22 nm, a grating period of 1 μm, and a DC of 65%. While the spectra were recorded at room temperature, the LIV measurements were performed at substrate temperatures from 20 to 110°C in steps of 10°C. The arrows labelled with 'T' point towards higher temperature. The difference between the total output power and the power of the light polarized along the [$\bar{1}$10] direction indicates the transmission loss of the polarizer [169]

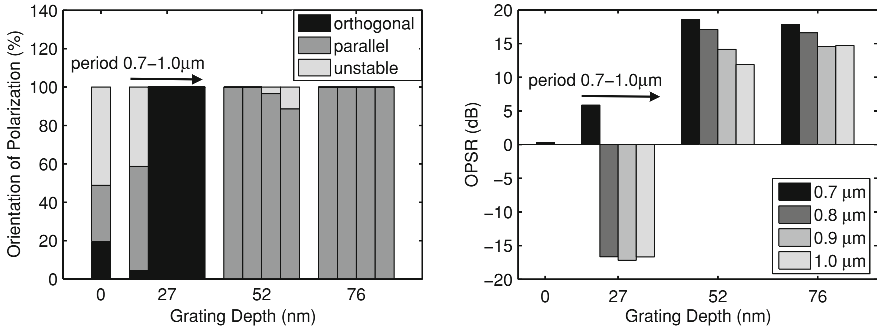

Fig. 5.5 Polarization behavior of 3574 VCSELs. The left chart gives the distribution of VCSELs with an unstable or a stable polarization parallel or orthogonal to the grating grooves, while the right chart displays the average OPSR. The active diameters range between 3 and 23 μm and the emission wavelength is about 850 nm [169, 122]

3574 VCSELs with an emission wavelength of about 850 nm were processed and measured on one wafer. The grating period of these VCSELs is varied between 0.7 and 1.0 μm, the grating depth between 0 and 76 nm, and the oxide diameter between 3 and 23 μm. The graphs in Fig. 5.5 reveal the dependence of the achieved polarization control and of the orientation of the polarization with respect to the grating grooves on the grating parameters. For small grating depths, the polarization is oriented orthogonal to the grating grooves, while it is parallel for larger grating depths. The transition from orthogonal to parallel polarization occurs at smaller grating depths for smaller grating periods. Every bar in the graphs represents at least 129 VCSELs. In total, 1374 VCSELs having a grating depth of 76 nm were measured. Not a single one exhibits a polarization orthogonal to the grating grooves or an unstable polarization. All these VCSELs have a well-defined polarization parallel to

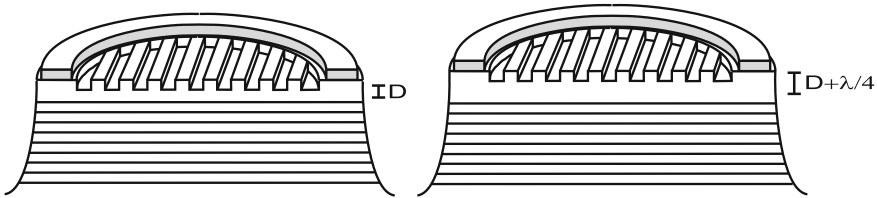

Fig. 5.6 Sketch of the upper Bragg mirror of a VCSEL structure incorporating a normal grating (*left*) and an inverted grating (*right*), where λ is the material wavelength (after [116])

the grating grooves independent of the orientation of the grooves along the $[\bar{1}10]$ or [110] crystal axis. This is in strong contrast to standard VCSELs, which are labelled in Fig. 5.5 with a grating depth of 0 nm.

The polarization control achieved by surface gratings has been tested under high-frequency modulation [63, 165] and externally applied strain [119]. In all investigations, the polarization remained fully defined and controlled through the grating. These observations are supported by the simulated and measured modal dichroism of such grating VCSELs [120], which exceeds the modal dichroism typically present in standard VCSELs by at least a factor of two. In another study, the grating VCSELs were tested under unpolarized and polarized feedback [118]. While unpolarized feedback had no influence on the selected polarization, polarized feedback could change the polarization. This is not surprising, since a surface grating is nothing else than a polarization-dependent reflector and thus influences the polarization of VCSELs similar to polarized external feedback. However, the observed instabilities introduced by polarized feedback are of no relevance for practical applications, since the external reflectivity had to exceed 25% to observe any influence on the polarization of the grating VCSEL. Moreover, the external cavity had to be aligned very carefully to match the mode inside the VCSEL with the mode in the external resonator.

While the polarization control provided by surface gratings is very reliable, independent of the emission wavelength of the VCSEL [122], the diffraction losses introduced by the grating are the drawback of surface gratings with a period in the order of or slightly smaller than the emission wavelength. Consequently, the threshold current is increased and the differential efficiency as well as the maximum output power are decreased. The magnitude of these losses depends very strongly on the chosen grating parameters. For grating periods smaller than the emission wavelength, no diffraction can be seen in the far-field. Nevertheless, the grating still leads to backward diffraction into the VCSEL. This diffraction is not easily accessible experimentally but can be proven by simulations [117].

To eliminate diffraction losses completely, the grating period must be reduced below the material wavelength of the VCSEL, as will be discussed in the next section. To avoid this complication of the processing, the diffraction losses can nevertheless be reduced by etching the grating not into the cap-layer of a standard VCSEL

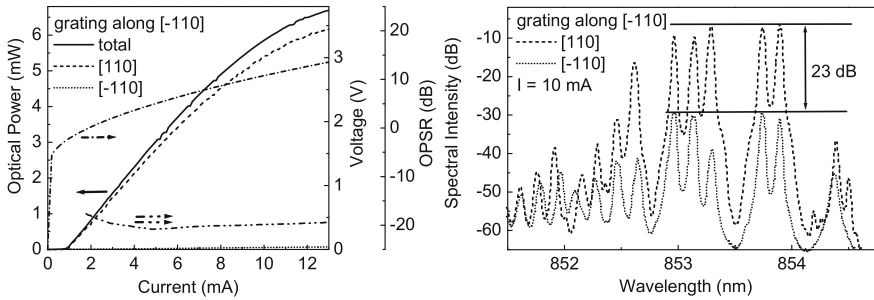

Fig. 5.7 PR-LIV characteristics (*left*) and polarization-resolved spectra (*right*) of an inverted grating VCSEL with 7 μm oxide aperture diameter. The grating period is 0.65 μm and the grating depth is 35 nm (after [116])

structure, but into a cap-layer with a thickness increased by one quarter of the material wavelength [116, 117, 121] (see Fig. 5.6). As illustrated in Fig. 5.7, the achieved suppression of the orthogonal polarization with such inverted gratings is comparable to the one of normal grating devices.

Controlling all modes of a multimode VCSEL is much more challenging compared to single-mode VCSELs and therefore is a better evidence for the degree of polarization control induced by a surface grating. However, most applications demanding a stable polarization of a VCSEL require single-mode emission. Since VCSELs tend to emit in multiple transverse modes, special measures have to be applied to ensure lasing of only the fundamental mode. Techniques to enhance the single-mode output power are discussed in Chap. 4 of this book. Among these techniques, the surface relief is one of the most promising [171–175]. For simultaneous mode and polarization control, the surface relief and surface grating concepts were combined to a grating relief [108, 113, 115], as depicted in Fig. 5.8. Also here one has to distinguish between a normal grating relief that is etched into the cap-layer of a standard VCSEL and an inverted grating relief in a cap-layer extended by one quarter of the material emission wavelength of the VCSEL. The latter approach is more favorable owing to increased design freedom and relaxed fabrication tolerances [113, 169].

Tunable diode laser absorption spectroscopy (TDLAS) is a prominent application requiring polarization-stable single-mode VCSELs [64, 177–180]. One example is the measurement of the oxygen concentration utilizing the absorption peaks at wavelengths of about 760 nm. The PR-LIV characteristics and the spectra of an inverted grating relief VCSEL optimized for oxygen spectroscopy are shown in Fig. 5.9. The laser is single-mode up to a drive current of 5 mA, where the side-mode suppression ratio is 30 dB. At a substrate temperature of 20°C, the maximum single-mode power is 2.6 mW, which is a factor of 2.5 larger than reported before in this wavelength regime [178]. Simultaneously the fundamental mode has a well-defined polarization. In TDLAS, the emission wavelength of the VCSEL is coarse tuned to match the absorption band of interest by adjusting the substrate temperature of the

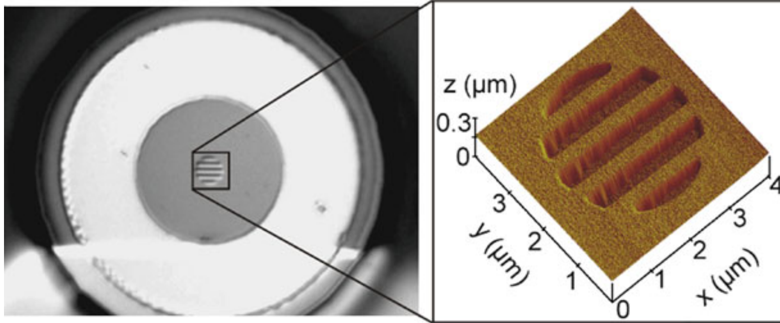

Fig. 5.8 Optical micrograph of an inverted grating relief VCSEL (*left*) and atomic force micrograph of the grating relief in more detail (*right*) [176] (© 2005 IEEE)

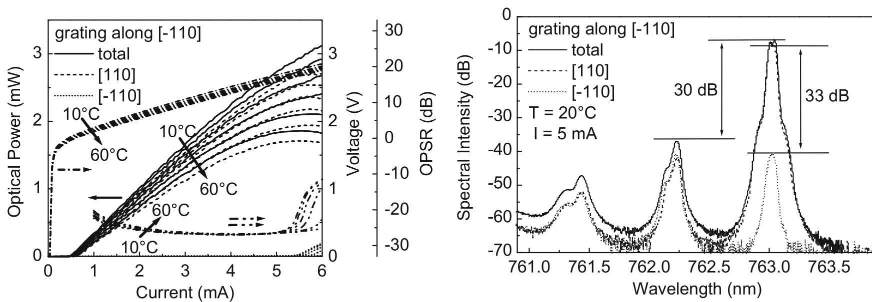

Fig. 5.9 PR-LIV characteristics of a grating relief VCSEL at substrate temperatures varied between 10 and 60°C in steps of 10°C (*left*) and polarization-resolved spectra at a substrate temperature of 20°C and a drive current of 5 mA (*right*). The device has an active diameter of 4.5 μm, a grating relief diameter of 3 μm, a grating period of 0.8 μm, and a grating depth of 44 nm (after [176])

laser. Stability of the polarization control against temperature variations is therefore of great importance. This issue is investigated in the left graph of Fig. 5.9.

As a conclusion of this section, surface gratings with grating periods similar to the emission wavelength have proven to provide very reliable polarization control for all kinds of top-emitting VCSELs. Combined with a surface relief, simultaneous polarization and mode control can be realized. The relatively simple additional processing steps make surface gratings attractive not only for academic investigations but also for industrial applications [70]. To completely avoid internal diffraction losses from the surface gratings at the expense of a more demanding fabrication process, the grating period has to be reduced below the material wavelength, as will be discussed in the next section.

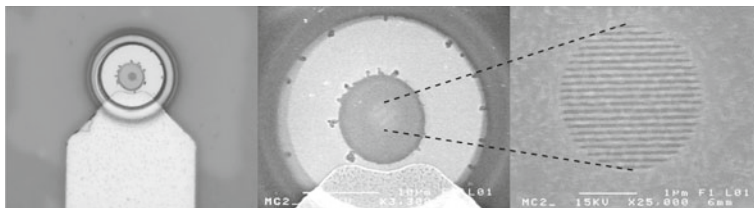

Fig. 5.10 Microscope image (*left*) and scanning electron micrographs (*middle* and *right*) of a VCSEL with an inverted sub-material-wavelength surface grating [103] (© 2006 IEEE)

5.5.2 Sub-Material-Wavelength Surface Gratings

If the grating period is much smaller than the laser wavelength in the grating material, the grating behaves like an artificial birefringent medium whose dielectric constants parallel and orthogonal to the grating grooves are given by [101, 181] respectively,

$$\epsilon_{||} = \frac{w_{\text{ridge}}\epsilon_{\text{ridge}} + w_{\text{groove}}\epsilon_{\text{groove}}}{w_{\text{ridge}} + w_{\text{groove}}} \quad \text{and} \quad \epsilon_{\perp} = \frac{(w_{\text{ridge}} + w_{\text{groove}})\epsilon_{\text{ridge}}\epsilon_{\text{groove}}}{w_{\text{ridge}}\epsilon_{\text{groove}} + w_{\text{groove}}\epsilon_{\text{ridge}}},$$

with w_{ridge} and w_{groove} as the widths of the grating ridges and grooves, respectively, and ϵ_{ridge} and ϵ_{groove} as the corresponding dielectric constants. Such a grating is also called zero-order grating, since only the zeroth transmitted and reflected order can propagate. Consequently, these gratings do not cause any diffraction (and therefore laser losses), which makes them very attractive. However, the fabrication of gratings with such a small period is more challenging. In the case of a VCSEL with an emission wavelength of 850 nm, the material wavelength inside GaAs having a refractive index of 3.65 [182] is 234 nm. Since the grating period has to be significantly smaller than the material wavelength for the surface grating to act as a birefringent medium, the required grating period for a sub-material-wavelength grating in a GaAs-based VCSEL with an emission wavelength of 850 nm is about 120 nm. Thus the grating ridge and groove widths have to be as small as about 60 nm. Nevertheless, such sub-material-wavelength grating VCSELs have been realized very successfully in the group of Prof. Larsson [102, 103].

Figure 5.10 depicts a microscope image and scanning electron micrographs of an inverted grating relief VCSEL with a grating period of 120 nm. The PR-LIV characteristics on the left side of Fig. 5.11 clearly indicate the polarization control provided by such sub-material-wavelength gratings. Independent of the orientation of the grating along the $[\bar{1}10]$ (top) or [110] (bottom) crystal direction, the polarization orthogonal to the grating grooves is dominating with an OPSR of about 20 dB. As can be seen from the spectra in the center column of Fig. 5.11, recorded at 4 and 7 mA, these VCSELs are even single-mode with a maximum output power of about 4 mW, since the grating is realized as a grating relief with a relief diameter of 2.5 µm.

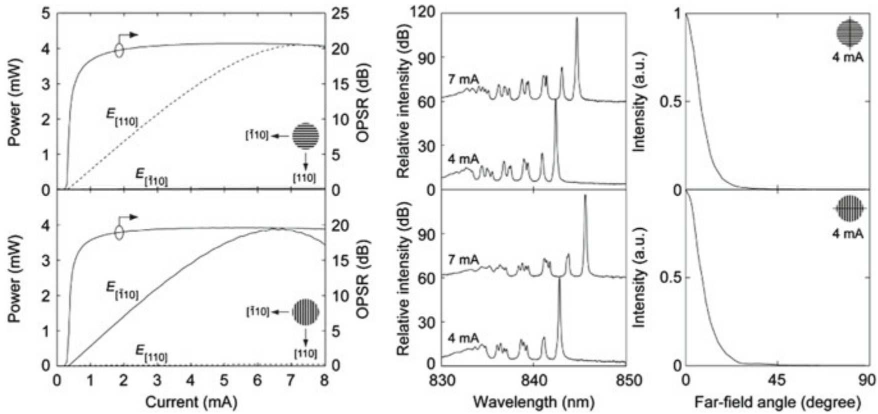

Fig. 5.11 PR-LIV characteristics, spectra, and far-fields of two sub-material-wavelength surface grating VCSELs with the grating grooves oriented along the [1̄10] direction (*top*) and along the [110] direction (*bottom*). The oxide aperture diameter is 4.5 μm, the grating diameter 2.5 μm, the grating duty cycle 60%, and the grating depth 60 nm [103] (© 2006 IEEE)

5.5.3 High-Index-Contrast Subwavelength Gratings

Investigating the concept of surface gratings and especially subwavelength gratings further, one comes to the conclusion that the grating can not only be used to define and control the polarization of VCSELs, but also to provide the high reflectivity of a DBR. To reach this, the grating period, grating depth, grating duty cycle, and the refractive indices of the materials of the grating and of its adjacent layers must be well matched. Thus in the extreme case, the complete upper Bragg mirror of a VCSEL can be replaced by just a single grating layer. Below the grating there can either be an air gap [95] or an oxide layer [183]. Besides controlling the polarization and providing the reflectivity of the upper Bragg mirror, such high-index-contrast subwavelength gratings (HCGs) can also be used to realize tunable VCSELs [94]. Chapter 9 of this book is entirely devoted to these novel concepts.

5.6 Conclusion

In this chapter we have addressed the issue of unstable VCSEL polarization and have reviewed various methods for polarization control in some detail. With the surface grating technique, the polarization problem has been entirely solved for commercial VCSELs.

References

1. H. Soda, K. Iga, C. Kitahara, Y. Suematsu, GaInAsP/InP surface emitting injection lasers. Jpn. J. Appl. Phys. **18**(12), 2329–2330 (1979)
2. K. Iga, F. Koyama, S. Kinoshita, Surface emitting semiconductor lasers. IEEE J. Quantum Electron. **24**(9), 1845–1854 (1988)
3. M. Shimizu, F. Koyama, K. Iga, Polarization characteristics of MOCVD grown GaAs/GaAlAs CBH surface emitting lasers. Jpn. J. Appl. Phys. **27**(9), 1774–1775 (1988)
4. C.J. Chang-Hasnain, J.P. Harbison, G. Hasnain, A. von Lehmen, L.T. Florez, N.G. Stoffel, Polarization characteristics of quantum well vertical cavity surface emitting lasers. Electron. Lett. **27**(2), 163–164 (1991)
5. Y.C. Chen, J.M. Liu, Direct polarization switching in semiconductor lasers. Appl. Phys. Lett. **45**(6), 604–606 (1984)
6. G. Berger, R. Müller, A. Klehr, M. Voss, Polarization bistability in strained ridge-waveguide InGaAsP/InP lasers: experiment and theory. J. Appl. Phys. **77**(12), 6135–6144 (1995)
7. T. Ikegami, Reflectivity of mode at facet and oscillation mode in double-heterostructure injection lasers. IEEE J. Quantum Electron **8**(6), 470–476 (1972)
8. J. Haes, B. Demeulenaere, T.D. Visser, D. Lenstra, H. Blok, R. Baets, How (not) to calculate the confinement factor for the modal gain of TM modes in amplifying waveguides, in *Proceedings of 21st European Conference on Optical Communication, ECOC*, vol. 2. Brussels, Belgium, Sept. 1995, pp. 729–732
9. W.W. Chow, S.W. Koch, M. Sargent III, *Semiconductor-Laser Physics* (Springer-Verlag, Berlin, 1994)
10. L.A. Coldren, S.W. Corzine, *Diode Lasers and Photonic Integrated Circuits* (Wiley, New York, 1995)
11. D. Burak, J.V. Moloney, R. Binder, Microscopic theory of polarization properties of optically anisotropic vertical-cavity surface-emitting lasers. Phys. Rev. A **61**(5), 053809-1–21 (2000)
12. A.D. Rakic, M.L. Majewski, Cavity and mirror design for vertical-cavity surface-emitting lasers. Chap. 8 in *Vertical-Cavity Surface-Emitting Laser Devices*, ed. by H. Li, K. Iga (Springer, Berlin, 2003), pp. 259–301
13. P. Debernardi, R. Orta, Analytical electromagnetic solution for Bragg mirrors with graded interfaces and guidelines for enhanced reflectivities. IEEE J. Quantum Electron. **43**(3), 269–274 (2007)
14. K. Iga, Surface-emitting laser—its birth and generation of new optoelectronics field. IEEE J. Select. Topics Quantum Electron. **6**(6), 1201–1215 (2000)
15. M.P. van Exter, M.B. Willemsen, J.P. Woerdman, Characterizing and understanding VCSEL polarization noise, in *Vertical-Cavity Surface-Emitting Lasers IV*, ed. by K.D. Choquette, C. Lei, Proceedings of SPIE, vol. 3946 (2000), pp. 58–68
16. G. Verschaffelt, K. Panajotov, J. Albert, B. Nagler, M. Peeters, J. Danckaert, I. Veretennicoff, H. Thienpont, Polarisation switching in vertical-cavity surface-emitting lasers: from experimental observations to applications. Opto-Electronics Rev. **9**(3), 257–268 (2001)
17. M.P. van Exter, R.F.M. Hendriks, J.P. Woerdman, Physical insight into the polarization dynamics of semiconductor vertical-cavity lasers. Phys. Rev. A **57**(3), 2080–2090 (1998)
18. G.P. Bava, P. Debernardi, L. Fratta, Three-dimensional model for vectorial fields in vertical-cavity surface-emitting lasers. Phys. Rev. A **63**(2), 023816-1–13 (2001)
19. L. Fratta, P. Debernardi, G.P. Bava, C. Degen, J. Kaiser, I. Fischer, W. Elsäßer, Spatially inhomogeneously polarized transverse modes in vertical-cavity surface-emitting lasers. Phys. Rev. A **64**(3), 031803-1–4 (2001)
20. M.P. van Exter, M.B. Willemsen, J.P. Woerdman, Polarization fluctuations in vertical-cavity semiconductor lasers. Phys. Rev. A **58**(4), 4191–4205 (1998)
21. K.D. Choquette, D.A. Richie, R.E. Leibenguth, Temperature dependence of gain-guided vertical-cavity surface emitting laser polarization. Appl. Phys. Lett. **64**(16), 2062–2064 (1994)

22. T. Ackemann, M. Sondermann, Characteristics of polarization switching from the low to the high frequency mode in vertical-cavity surface-emitting lasers. Appl. Phys. Lett. **78**(23), 3574–3576 (2001)
23. A.K. Jansen van Doorn, M.P. van Exter, A.M. van der Lee, J.P. Woerdman, Coupled-mode description for the polarization state of a vertical-cavity semiconductor laser. Phys. Rev. A **55**(2), 1473–1484 (1997)
24. M.P. van Exter, A.K. Jansen van Doorn, J.P. Woerdman, Electro-optic effect and birefringence in semiconductor vertical-cavity lasers. Phys. Rev. A **56**(1), 845–853 (1997)
25. B. Ryvkin, K. Panajotov, A. Georgievski, J. Danckaert, M. Peeters, G. Verschaffelt, H. Thienpont, I. Veretennicoff, Effect of photon-energy-dependent loss and gain mechanisms on polarization switching in vertical-cavity surface-emitting lasers. J. Opt. Soc. Am. B **16**(11), 2106–2113 (1999)
26. K.D. Choquette, R.P. Schneider, K.L. Lear Jr., R.E. Leibenguth, Gain dependent polarization properties of vertical-cavity lasers. IEEE J. Select. Topics Quantum Electron. **1**(2), 661–666 (1995)
27. K. Panajotov, B. Nagler, G. Verschaffelt, A. Georgievski, H. Thienpont, J. Danckaert, I. Veretennicoff, Impact of in-plane anisotropic strain on the polarization behavior of vertical-cavity surface-emitting lasers. Appl. Phys. Lett. **77**(11), 1590–1592 (2000)
28. A.K. Jansen van Doorn, M.P. van Exter, J.P. Woerdman, Elasto-optic anisotropy and polarization orientation of vertical-cavity surface-emitting semiconductor lasers. Appl. Phys. Lett. **69**(8), 1041–1043 (1996)
29. A.K. Jansen van Doorn, M.P. van Exter, J.P. Woerdman, Tailoring the birefringence in a vertical-cavity semiconductor laser. Appl. Phys. Lett. **69**(24), 3635–3637 (1996)
30. J. Kaiser, C. Degen, W. Elsäßer, Polarization-switching influence on the intensity noise of vertical-cavity surface-emitting lasers. J. Opt. Soc. Am. B **19**(4), 672–677 (2002)
31. B. Nagler, M. Peeters, I. Veretennicoff, J. Danckaert, Stochastic resonance in vertical-cavity surface-emitting lasers based on multiple time-scale analysis. Phys. Rev. E **67**(1), 056112-1–7 (2003)
32. M.B. Willemsen, M.U.F. Khalid, M.P. van Exter, J.P. Woerdman, Polarization switching of a vertical-cavity semiconductor laser as a Kramers hopping problem. Phys. Rev. Lett. **82**(24), 4915–4818 (1999)
33. G. Giacomelli, F. Marin, I. Rabbiosi, Stochastic and bona fide resonance: an experimental investigation. Phys. Rev. Lett. **82**(4), 675–678 (1999)
34. G. Verschaffelt, J. Albert, I. Veretennicoff, J. Danckaert, S. Barbay, G. Giacomelli, F. Marin, Frequency response of current-driven polarization modulation in vertical-cavity surface-emitting lasers. Appl. Phys. Lett. **80**(13), 2248–2250 (2002)
35. J. Danckaert, M. Peeters, C. Mirasso, M. San Miguel, G. Verschaffelt, J. Albert, B. Nagler, H. Unold, R. Michalzik, G. Giacomelli, F. Marin, Stochastic polarization switching dynamics in vertical-cavity surface-emitting lasers: theory and experiment. IEEE J. Select. Topics Quantum Electron. **10**(5), 911–917 (2004)
36. G. Verschaffelt, J. Albert, B. Nagler, M. Peeters, J. Danckaert, S. Barbay, G. Giacomelli, F. Marin, Frequency response of polarization switching in vertical-cavity surface-emitting lasers. IEEE J. Quantum Electron. **39**(10), 1177–1186 (2003)
37. D.V. Kuksenkov, H. Temkin, S. Swirhun, Polarization instability and relative intensity noise in vertical-cavity surface-emitting lasers. Appl. Phys. Lett. **67**(15), 2141–2143 (1995)
38. T. Mukaihara, N. Ohnoki, Y. Hayashi, N. Hatori, F. Koyama, K. Iga, Excess intensity noise originated from polarization fluctuation in vertical-cavity surface-emitting lasers. IEEE Photon. Technol. Lett. **7**(10), 1113–1115 (1995)
39. G. Giacomelli, F. Marin, M. Gabrysch, K.H. Gulden, M. Moser, Polarization competition and noise properties of VCSELs. Optics Commun. **146**(1–6), 135–140 (1998)
40. J.-L. Vey, C. Degen, K. Auen, W. Elsäßer, Quantum noise and polarization properties of vertical-cavity surface-emitting lasers. Phys. Rev. A **60**(4), 3284–3295 (1999)

41. C. Masoller, M.S. Torre, Influence of optical feedback on the polarization switching of vertical-cavity surface-emitting lasers. IEEE J. Quantum Electron. **41**(4), 483–489 (2005)
42. F. Robert, P. Besnard, M.L. Chares, G.M. Stephan, Polarization modulation dynamics of vertical-cavity surface-emitting lasers with extended cavity. IEEE J. Quantum Electron. **33**(12), 2231–2239 (1997)
43. C.I. Wilkinson, J. Woodhead, J.E.F. Frost, J.S. Roberts, R. Wilson, M.F. Lewis, Electrical polarization control of vertical-cavity surface-emitting lasers using polarized feedback and a liquid crystal. IEEE Photon. Technol. Lett. **11**(2), 155–157 (1999)
44. M. Arizaleta Arteaga, H.J. Unold, J.M. Ostermann, R. Michalzik, H. Thienpont, K. Panajotov, Investigation of polarization properties of VCSELs subject to optical feedback from an extremely short external cavity—part I: theoretical analysis. IEEE J. Quantum Electron. **42**(2), 89–101 (2006)
45. M. Arizaleta Arteaga, H.J. Unold, J.M. Ostermann, R. Michalzik, H. Thienpont, K. Panajotov, Investigation of polarization properties of VCSELs subject to optical feedback from an extremely short external cavity—part II: experiments. IEEE J. Quantum Electron. **42**(2), 102–107 (2006)
46. M. Sondermann, T. Ackemann, Correlation properties and drift phenomena in the dynamics of vertical-cavity surface-emitting lasers with optical feedback. Opt. Express **13**(7), 2707–2715 (2005)
47. G. Giacomelli, F. Marin, M. Romanelli, Multi-time-scale dynamics of a laser with polarized optical feedback. Phys. Rev. A **67**(5), 053809-1–4 (2003)
48. J.B. Altés, I. Gatare, K. Panajotov, H. Thienpont, M. Sciamanna, Mapping of the dynamics induced by orthogonal optical injection in vertical-cavity surface-emitting lasers. IEEE J. Quantum Electron. **42**(2), 198–207 (2006)
49. A. Valle, K.A. Shore, L. Pesquera, Polarization selection in birefringent vertical-cavity surface emitting lasers. J. Lightwave Technol. **14**(9), 2062–2068 (1996)
50. K. Panajotov, B. Ryvkin, J. Danckaert, M. Peeters, H. Thienpont, I. Veretennicoff, Polarization switching in VCSEL's due to thermal lensing. IEEE Photon. Technol. Lett. **10**(1), 6–9 (1998)
51. J. Danckaert, B. Nagler, J. Albert, K. Panajotov, I. Veretennicoff, T. Erneux, Minimal rate equations describing polarization switching in vertical-cavity surface-emitting lasers. Opt. Commun. **201**(1–3), 129–137 (2002)
52. J. Martin-Regalado, J.L.A. Chilla, J.J. Rocca, P. Brusenbach, Polarization switching in vertical-cavity surface emitting lasers observed at constant active region temperature. Appl. Phys. Lett. **70**(25), 3350–3352 (1997)
53. M. Sondermann, M. Weinkath, T. Ackemann, Polarization switching to the gain disfavored mode in vertical-cavity surface-emitting lasers. IEEE J. Quantum Electron. **40**(2), 97–104 (2004)
54. J. Martin-Regalado, F. Prati, M. San Miguel, N.B. Abraham, Polarization properties of vertical-cavity surface-emitting lasers. IEEE J. Quantum Electron. **33**(5), 765–783 (1997)
55. M. San Miguel, Q. Feng, J.V. Moloney, Light-polarization dynamics in surface-emitting semiconductor lasers. Phys. Rev. A **52**(2), 1728–1739 (1995)
56. M. San Miguel, Polarisation properties of vertical cavity surface emitting lasers, Chap. 10 in *Semiconductor Quantum Optoelectronics—from Quantum Physics to Smart Devices*, ed. by A. Miller, M. Ebrahimzadeh, D.M. Finlayson (SUSSP Publications, Edinburg, 1999), pp. 339–366
57. F. Prati, P. Caccia, F. Castelli, Effects of gain saturation on polarization switching in vertical-cavity surface-emitting lasers. Phys. Rev. A **66**(6), 063811-1–7 (2002)
58. S. Balle, E. Tolkachova, M. San Miguel, J.R. Tredicce, J. Martin-Regalado, A. Gahl, Mechanisms of polarization switching in single-transverse-mode vertical-cavity surface-emitting lasers: thermal shift and nonlinear semiconductor dynamics. Opt. Lett. **24**(16), 1121–1123 (1999)

59. G. Van der Sande, M. Peeters, I. Veretennicoff, J. Danckaert, G. Verschaffelt, S. Balle, The effects of stress, temperature, and spin flips on polarization switching in vertical-cavity surface-emitting lasers. IEEE J. Quantum Electron. **42**(9), 898–906 (2006)
60. G. Van der Sande, J. Danckaert, I. Veretennicoff, T. Erneux, Rate equations for vertical-cavity surface-emitting lasers. Phys. Rev. A **67**(1), 013809-1–7 (2003)
61. D.V. Kuksenkov, H. Temkin, S. Swirhun, Polarization instability and performance of free-space optical links based on vertical-cavity surface-emitting lasers. IEEE Photon. Technol. Lett. **8**(5), 703–705 (1996)
62. D. Kuksenkov, H. Temkin, Polarization related properties of vertical-cavity lasers, Chap. 6 in *Vertical-Cavity Surface-Emitting Lasers*, ed. by C. Wilmsen, H. Temkin, L.A. Coldren (Cambridge University Press, Cambridge, 1999), pp. 233–267
63. J.M. Ostermann, P. Debernardi, R. Michalzik, Surface grating VCSELs with dynamically stable light output polarization. IEEE Photon. Technol. Lett. **17**(12), 2505–2507 (2005)
64. P. Vogel, V. Ebert, Near shot noise detection of oxygen in the A-band with vertical-cavity surface-emitting lasers. Appl. Phys. B **72**(1), 127–135 (2001)
65. D.K. Serkland, G.M. Peake, K.M. Geib, R. Lutwak, R.M. Garvey, M. Varghese, M. Mescher, VCSELs for atomic clocks, in *Vertical-Cavity Surface-Emitting Lasers X*, ed. by C. Lei, K.D. Choquette, Proceedings of SPIE, vol. 6132 (2006), pp. 613208-1–11
66. A. Al-Samaneh, S. Renz, A. Strodl, W. Schwarz, D. Wahl, R. Michalzik, Polarization-stable single-mode VCSELs for Cs-based MEMS atomic clock applications, in *Semiconductor Lasers and Laser Dynamics IV*, ed. by K.P. Panayotov, M. Sciamanna, A.A. Valle, R. Michalzik, Proceedings of SPIE, vol. 7720 (2010), pp. 772006-1–14
67. D.K. Serkland, K.M. Geib, G.M. Peake, R. Lutwak, A. Rashed, M. Varghese, G. Tepolt, M. Prouty, VCSELs for atomic sensors, in *Vertical-Cavity Surface-Emitting Lasers XI*, ed. by K.D. Choquette, J.K.Guenter, Proceedings of SPIE, vol. 6484 (2007), pp. 648406-1–10
68. A. Pruijmboom, M. Schemmann, J. Hellmig, J. Schutte, H. Moench, J. Pankert, VCSEL-based miniature laser-Doppler interferometer, in *Vertical-Cavity Surface-Emitting Lasers XII*, ed. by C. Lei, J.K. Guenter, Proceedings of SPIE, vol. 6908 (2008), pp. 69080I-1–7
69. A. Pruijmboom, S. Booij, M. Schemmann, K. Werner, P. Hoeven, H. van Limpt, S. Intemann, R. Jordan, T. Fritzsch, H. Oppermann, M. Barge, VCSEL-based miniature laser-self-mixing interferometer with integrated optical and electronic components, in *Photonics Packaging, Integration, and Interconnects IX*, ed. by A.L. Glebov, R.T. Chen, Proceedings of SPIE, vol. 7221 (2009), pp. 72210S-1–12
70. M. Grabherr, R. King, R. Jäger, D. Wiedenmann, P. Gerlach, D. Duckeck, C. Wimmer, Volume production of polarization controlled single-mode VCSELs, in *Vertical-Cavity Surface-Emitting Lasers XII*, ed. by C. Lei, J.K. Guenter, Proceedings of SPIE, vol. 6908 (2008), pp. 690803-1–9
71. M. Shimuzi, T. Mukaihara, F. Koyama, K. Iga, Polarisation control for surface emitting lasers. Electron. Lett. **27**(12), 1067–1069 (1991)
72. T. Mukaihara, F. Koyama, K. Iga, Polarization control of surface emitting lasers by anisotropic biaxial strain. Jpn. J. Appl. Phys. **31**(5A), 1389–1390 (1992)
73. T. Mukaihara, F. Koyama, K. Iga, Engineered polarization control of GaAs/AlGaAs surface-emitting lasers by anisotropic stress from elliptical etched substrate hole. IEEE Photon. Technol. Lett. **5**(2), 133–135 (1993)
74. T. Mukaihara, N. Ohnoki, Y. Hayashi, N. Hatori, F. Koyama, K. Iga, Polarization control of vertical-cavity surface-emitting lasers using a birefringent metal/dielectric polarizer loaded on top distributed Bragg reflector. IEEE J. Select. Topics Quantum Electron. **1**(2), 667–673 (1995)
75. M. Takahashi, P. Vaccaro, K. Fujita, T. Watanabe, T. Mukaihara, F. Koyama, K. Iga, An InGaAs-GaAs vertical-cavity surface-emitting laser grown on GaAs (311)A substrate having low threshold and stable polarization. IEEE Photon. Technol. Lett. **8**(6), 737–739 (1996)

76. M. Takahashi, N. Egami, T. Mukaihara, F. Koyama, K. Iga, Lasing characteristics of GaAs (311)A substrate based InGaAs-GaAs vertical-cavity surface-emitting lasers. IEEE J. Select. Topics Quantum Electron. **3**(2), 372–378 (1997)
77. A. Mizutani, N. Hatori, N. Nishiyama, F. Koyama, K. Iga, MOCVD grown InGaAs/GaAs vertical cavity surface emitting laser on GaAs (311)B substrate. Electron. Lett. **33**(22), 1877–1878 (1997)
78. M. Takahashi, P. Vaccaro, N. Egami, A. Mizutani, A. Matsutani, F. Koyama, K. Iga, Oxide-confinement vertical-cavity surface-emitting lasers grown on GaAs (311)A substrates with dynamically stable polarisation. Electron. Lett. **34**(3), 276–278 (1998)
79. A. Mizutani, N. Hatori, N. Nishiyama, F. Koyama, K. Iga, A low-threshold polarization-controlled vertical-cavity surface-emitting laser grown on GaAs (311)B substrate. IEEE Photon. Technol. Lett. **10**(5), 633–635 (1998)
80. N. Nishiyama, A. Mizutani, N. Hatori, M. Arai, F. Koyama, K. Iga, Single-transverse mode and stable-polarization operation under high-speed modulation of InGaAs-GaAs vertical-cavity surface-emitting laser grown on GaAs (311)B substrate. IEEE Photon. Technol. Lett. **10**(12), 1676–1678 (1998)
81. N. Nishiyama, A. Mizutani, N. Hatori, M. Arai, F. Koyama, K. Iga, Lasing characteristics of InGaAs-GaAs polarization controlled vertical-cavity surface-emitting laser grown on GaAs (311)B substrate. IEEE J. Select. Topics Quantum Electron. **5**(3), 530–536 (1999)
82. M. Arai, N. Nishiyama, S. Shinada, A. Matsutani, F. Koyama, K. Iga, Vertical-cavity surface-emitting laser array on GaAs (311)B substrate exhibiting single-transverse mode and stable-polarization operation. Jpn. J. Appl. Phys **39**(6B), L588–L590 (2000)
83. M. Arai, N. Nishiyama, S. Shinada, A. Matsutani, F. Koyama, K. Iga, Highly stable single polarization operation of GaInAs/GaAs vertical-cavity surface-emitting laser on GaAs (311)B substrate under high-speed modulation. Jpn. J. Appl. Phys. **39**(8B), L858–L860 (2000)
84. N. Nishiyama, M. Arai, S. Shinada, M. Azuchi, T. Miyamato, F. Koyama, K. Iga, Highly strained GaInAs-GaAs quantum-well vertical-cavity surface-emitting laser on GaAs (311)B substrate for stable polarization operation. IEEE J. Select. Topics Quantum Electron. **7**(2), 242–248 (2001)
85. P.B. Dayal, F. Koyama, Polarization control of 0.85 μm vertical-cavity surface-emitting lasers integrated with gold nanorod arrays. Appl. Phys. Lett. **91**(11), 111107-1–3 (2007)
86. J.-H. Ser, Y.-G. Ju, J.-H. Shin, Y.-H. Lee, Polarization stabilization of vertical-cavity top-surface-emitting lasers by inscription of fine metal-interlaced gratings. Appl. Phys. Lett. **66**(21), 2769–2771 (1995)
87. Y.-G. Ju, J.-H. Ser, Y.-H. Lee, Analysis of metal-interlaced-grating vertical-cavity surface-emitting lasers using the modal method by modal expansion. IEEE J. Quantum Electron. **33**(4), 589–595 (1997)
88. K.-H. Ha, Y.-H. Lee, H.-K. Shin, K.-H. Lee, S.-M. Whang, Polarisation anisotropy in asymmetric oxide aperture VCSELs. Electron. Lett. **34**(14), 1401–1402 (1998)
89. D.-S. Song, Y.-J. Lee, H.-W. Choi, Y.-H. Lee, Polarization-controlled, single-transverse-mode, photonic-crystal, vertical-cavity, surface-emitting lasers. Appl. Phys. Lett. **82**(19), 3182–3184 (2003)
90. K.-H. Lee, J.-H. Baek, I.-K. Hwang, Y.-H. Lee, G.-H. Lee, J.-H. Ser, H.-D. Kim, H.-E. Shin, Square-lattice photonic-crystal vertical-cavity surface-emitting lasers. Opt. Express **12**(17), 4136–4143 (2004)
91. K.D. Choquette, R.E. Leibenguth, Control of vertical-cavity laser polarization with anisotropic transverse cavity geometries. IEEE Photon. Technol. Lett. **6**(1), 40–42 (1994)
92. Y.L. Okuno, J. Geske, K.-G. Gan, Y.-J. Chiu, S.P. DenBaars, J.E. Bowers, 1.3 μm wavelength vertical cavity surface emitting laser fabricated by orientation-mismatch wafer bonding: a prospect for polarization control. Appl. Phys. Lett. **82**(15), 2377–2379 (2003)

93. Y.L. Okuno, K.-G. Gan, H.-F. Chou, Y.-J. Chiu, C.S. Wang, S. Wu, J. Geske, E.S. Björlin, J.E. Bowers, Stable polarization operation of 1.3 μm wavelength vertical-cavity surface-emitting laser (VCSEL) fabricated by orientation-mismatched wafer bonding. IEEE J. Select. Topics Quantum Electron. **11**(5), 1006–1014 (2005)
94. M.C.Y. Huang, Y. Zhou, C.J. Chang-Hasnain, Nano electro-mechanical optoelectronic tunable VCSEL. Opt. Express **15**(3), 1222–1227 (2007)
95. M.C.Y. Huang, Y. Zhou, C.J. Chang-Hasnain, A surface-emitting laser incorporating a high-index-contrast subwavelength grating. Nature Photonics **1**(2), 119–122 (2007)
96. R.C. Strijbos, G. Verschaffelt, M. Creusen, W.C. van der Vleuten, F. Karouta , T.G. van de Roer, M. Buda, J. Danckaert, B. Ryvkin, I. Veretennicoff, H. Thienpont, Intra-cavity contacted VCSELs with polarization control, in *Vertical-Cavity Surface-Emitting Lasers IV*, ed. by K.D. Choquette, C. Lei. Proceedings of SPIE, vol. 3946 (2000) 69–77
97. G. Verschaffelt, W. van der Vleuten, M. Creusen, E. Smalbrugge, T.G. van de Roer, F. Karouta, R.C. Strijbos, J. Danckaert, I. Veretennicoff, B. Ryvkin, H. Thienpont, G.A. Acket, Polarization stabilization in vertical-cavity surface-emitting lasers through asymmetric current injection. IEEE Photon. Technol. Lett. **12**(8), 945–947 (2000)
98. M. Arizaleta Arteaga, O. Parriaux, M. López-Amo, H. Thienpont, K. Panajotov, Polarized optical feedback from an extremely short external cavity for controlling and stabilizing the polarization of vertical cavity surface emitting lasers. Appl. Phys. Lett. **90**(12), 121104-1–3 (2007)
99. P. Dowd, P.J. Heard, J.A. Nicholson, L. Raddatz, I.H. White, R.V. Penty, J.C.C. Day, G.C. Allen, S.W. Corzine, M.R.T. Tan, Complete polarisation control of GaAs gain-guided top-surface emitting vertical cavity lasers. Electron. Lett. **33**(15), 1315–1317 (1997)
100. L.J. Sargent, J.M. Rorison, M. Kuball, R.V. Penty, I.H. White, S.W. Corzine, M.R.T. Tan, S.Y. Wang, P.J. Head, Investigation of polarization-pinning mechanism in deep-line-etched vertical-cavity surface-emitting lasers. Appl. Phys. Lett. **76**(4), 400–402 (2000)
101. J. Gustavsson, Å. Haglund, J. Vukušić, J. Bengtsson, P. Jedrasik, A. Larsson, Efficient and individually controllable mechanisms for mode and polarization selection in VCSELs, based on a common, localized, sub-wavelength surface grating. Opt. Express **13**(17), 6626–6634 (2005)
102. Å. Haglund, J.S. Gustavsson, J. Vukušić, P. Jedrasik, A. Larsson, High-power fundamental-mode and polarisation stabilised VCSELs using sub-wavelength surface grating. Electron. Lett. **41**(14), 805–807 (2005)
103. Å. Haglund, J.S. Gustavsson, J. Bengtsson, P. Jedrasik, A. Larsson, Design and evaluation of fundamental-mode and polarization-stabilized VCSELs with a subwavelength surface grating. IEEE J. Quantum Electron. **42**(3), 231–240 (2006)
104. J. Gustavsson, Å. Haglund, E. Söderberg, J. Vukušić, P. Modh, P. Jedrasik, A. Larsson, Mode and polarization control in VCSELs using shallow surface structures. IET Optoelectron. **1**(5), 197–205 (2007)
105. B. Weigl, M. Grabherr, C. Jung, R. Jäger, G. Reiner, R. Michalzik, D. Sowada, K.J. Ebeling, High-performance oxide-confined GaAs VCSEL's. IEEE J. Select. Topics Quantum Electron. **3**(2), 409–415 (1997)
106. H.J. Unold, M.C. Riedl, R. Michalzik, K.J. Ebeling, Polarisation control in VCSELs by elliptic surface etching. Electron. Lett. **38**(2), 77–78 (2002)
107. P. Debernardi, H.J. Unold, J. Maehnss, R. Michalzik, G.P. Bava, K.J. Ebeling, Single-mode, single-polarization VCSELs via elliptical surface etching: experiments and theory. IEEE J. Select. Topics Quantum Electron. **9**(5), 1394–1404 (2003)
108. P. Debernardi, G.P. Bava, Coupled mode theory: a powerful tool for analyzing complex VCSELs and designing advanced device features. IEEE J. Select. Topics Quantum Electron. **9**(3), 905–917 (2003)
109. J.M. Ostermann, P. Debernardi, C. Jalics, A. Kroner, M.C. Riedl, R. Michalzik, Monolithic polarization control of multimode VCSELs by a dielectric surface grating, in *Vertical-Cavity*

Surface-Emitting Lasers VIII, ed. by C. Lei, S.P. Kilcoyne, Proceedings of SPIE, vol. 5364 (2004), pp. 201–212

110. R. Michalzik, J.M. Ostermann, P. Debernardi, C. Jalics, A. Kroner, M. Feneberg, M.C. Riedl., Polarization-controlled monolithic oxide-confined VCSELs, in *Micro-Optics, VCSELs and Photonic Interconnects*, ed. by H. Thienpont, K.D. Choquette, M.R. Taghizadeh, Proceedings of SPIE, vol. 5453 (2004), pp. 182–196
111. J.M. Ostermann, P. Debernardi, C. Jalics, A. Kroner, M.C. Riedl, R. Michalzik, Surface gratings for polarization control of single- and multi-mode oxide-confined vertical-cavity surface-emitting lasers. Optics Commun. **246**(4–6), 511–519 (2005)
112. P. Debernardi, J.M. Ostermann, M. Feneberg, C. Jalics, R. Michalzik, Reliable polarization control of VCSELs through monolithically integrated surface gratings: a comparative theoretical and experimental study. IEEE J. Select. Topics Quantum Electron. **11**(1), 107–116 (2005)
113. J.M. Ostermann, P. Debernardi, C. Jalics, R. Michalzik, Polarization-stable oxide-confined VCSELs with enhanced single-mode output power via monolithically integrated inverted grating reliefs. IEEE J. Select. Topics Quantum Electron. **11**(5), 982–989 (2005)
114. J.M. Ostermann, P. Debernardi, C. Jalics, R. Michalzik, Shallow surface gratings for high-power VCSELs with one preferred polarization for all modes. IEEE Photon. Technol. Lett. **17**(8), 1593–1595 (2005)
115. J.M. Ostermann, F. Rinaldi, P. Debernardi, R. Michalzik, VCSELs with enhanced single-mode power and stabilized polarization for oxygen sensing. IEEE Photon. Technol. Lett. **17**(11), 2256–2258 (2005)
116. J.M. Ostermann, P. Debernardi, R. Michalzik, Optimized integrated surface grating design for polarization-stable VCSELs. IEEE J. Quantum Electron. **42**(7), 690–698 (2006)
117. J.M. Ostermann, P. Debernardi, R. Michalzik, Optimization of polarization-stable single and multimode surface grating VCSELs towards high fabrication tolerance and superior performance, in *Semiconductor Lasers and Laser Dynamics II*, ed. by D. Lenstra, M. Pessa, I.H. White, Proceedings of SPIE, vol. 6184 (2006), pp. 618410-1–12
118. J.M. Ostermann, P. Debernardi, R. Michalzik, Polarization-controlled surface grating VCSELs under unpolarized and polarized optical feedback. IEEE Photon. Technol. Lett. **19**(18), 1359–1361 (2007)
119. J.M. Ostermann, P. Debernardi, A. Kroner, R. Michalzik, Polarization-controlled surface grating VCSELs under externally induced anisotropic strain. IEEE Photon. Technol. Lett. **19**(17), 1301–1303 (2007)
120. P. Debernardi, J.M. Ostermann, M. Sondermann, T. Ackemann, G.P. Bava, R. Michalzik, Theoretical-experimental study of the vectorial modal properties of polarization-stable multimode grating VCSELs. IEEE J. Select. Topics Quantum Electron. **13**(5), 1340–1348 (2007)
121. P. Debernardi, J.M. Ostermann, R. Michalzik, VCSEL polarization control by monolithic surface gratings: a survey of modelling and experimental activities, in *Second International Conference on Advanced Optoelectronics and Lasers*, ed. by I.A. Sukhoivanov, V.A. Svich, Y.S. Shmaliy, Proceedings of SPIE, vol. 7009 (2008), pp. 700903-1–10
122. R. Michalzik, J.M. Ostermann, P. Debernardi, Polarization-stable monolithic VCSELs, in *Vertical-Cavity Surface-Emitting Lasers XII*, ed. by C. Lei, J.K. Guenter, Proceedings of SPIE, vol. 6908 (2008), pp. 69080A-1–16
123. K. Tateno, Y. Ohiso, C. Amano, A. Wakatsuki, T. Kurokawa, Growth of vertical-cavity surface-emitting laser structures on GaAs (311)B substrates by metal-organic chemical vapor deposition. Appl. Phys. Lett. **70**(25), 3395–3397 (1997)
124. H. Uenohara, K. Tateno, T. Kagawa, Y. Ohiso, H. Tsuda, T. Kurokaw, C. Amano, Polarization-controlled 850-nm-wavelength vertical-cavity surface-emitting lasers grown on (311)B substrates by metal-organic chemical vapor deposition. IEEE J. Select. Topics Quantum Electron. **5**(3), 537–545 (1999)
125. H. Uenohara, K. Tateno, T. Kagawa, Y. Ohiso, H. Tsuda, T. Kurokawa, C. Amano, Investigation of dynamic polarization stability of 850-nm GaAs-based vertical-cavity surface-emitting

lasers grown on (311)B and (100) substrates. IEEE Photon. Technol. Lett. **11**(4), 400–402 (1999)
126. O. Tadanaga, K. Tateno, H. Uenohara, T. Kagawa, C. Amano, An 850-nm InAlGaAs strained quantum-well vertical-cavity surface-emitting laser grown on GaAs (311)B substrate with high-polarization stability. IEEE Photon. Technol. Lett. **12**(8), 942–944 (2000)
127. T. Kagawa, O. Tadanaga, H. Uenohara, K. Tateno, C. Amano, Polarization control of VCSEL on (311)B substrate and its effect on transmission characteristics. IEICE Trans. Electron. **E84-C**(3), 351–357 (2001)
128. F. Monti di Sopra, M. Brunner, R. Hövel, Polarization control in strained T-bar VCSELs. IEEE Photon. Technol. Lett. **14**(8), 1034–1036 (2002)
129. T. Yoshikawa, H. Kosaka, K. Kurihara, M. Kajita, Y. Sugimoto, K. Kasahara, Complete polarization control of 8×8 vertical-cavity surface-emitting laser matrix arrays. Appl. Phys. Lett. **66**(8), 908–910 (1994)
130. T. Numai, K. Kurihara, K. Kühn, H. Kosaka, I. Ogura, M. Kajita, H. Saito, K. Kasahara, Control of light-output polarization for surface-emitting-laser type device by strained active layer grown on misoriented substrate. IEEE J. Quantum Electron. **31**(4), 636–642 (1995)
131. T. Yoshikawa, T. Kawakami, H. Saito, H. Kosaka, M. Kajita, K. Kurihara, Y. Sugimoto, K. Kasahara, Polarization-controlled single-mode VCSEL. IEEE J. Quantum Electron. **34**(6), 1009–1015 (1998)
132. Y. Matsui, D. Vakhshoori, P. Wang, P. Chen, C.-C. Lu, M. Jiang, K. Knopp, S. Burroughs, P. Tayebati, Complete polarization mode control of long-wavelength tunable vertical-cavity surface-emitting lasers over 65-nm tuning, up to 14-mW output power. IEEE J. Quantum Electron. **39**(9), 1037–1048 (2003)
133. C.L. Chua, R.L. Thornton, D.W. Treat, R.M. Donaldson, Anisotropic apertures for polarization-stable laterally oxidized vertical-cavity lasers. Appl. Phys. Lett. **73**(12), 1631–1633 (1998)
134. N. Ueki, H. Nakayama, J. Sakurai, A. Murakami, H. Otoma, Y. Miyamoto, M. Yamamoto, R. Ishii, M. Yoshikawa, T. Nakamura, Complete polarization control of 12×8-bit matrix-addressed oxide-confined vertical-cavity surface-emitting laser array. Jpn. J. Appl. Phys. **40**(1A/B), L33–L35 (2001)
135. T. Onishi, T. Tanigawa, T. Ueda, D. Ueda, Polarization control of vertical-cavity surface-emitting lasers by utilizing surface plasmon resonance. IEEE J. Quantum Electron. **43**(12), 1123–1128 (2007)
136. T. Ohtoshi, T. Kuroda, A. Niwa, S. Tsuji, Dependence of optical gain on crystal orientation in surface-emitting lasers with strained quantum wells. Appl. Phys. Lett. **65**(15), 1886–1887 (1994)
137. Y. Higuchi, S. Osaki, Y. Sasahata, T. Kitada, S. Shimomura, M. Ogura, S. Hiyamizu, 830-nm polarization controlled lasing of InGaAs quantum wire vertical-cavity surface-emitting lasers grown on (775)B GaAs substrates by molecular beam epitaxy. Jpn. J. Appl. Phys. **46**(7), L138–L141 (2007)
138. H. Saito, K. Nishi, S. Sugou, Y. Sugimoto, Controlling polarization of quantum-dot surface-emitting lasers by using structurally anisotropic self-assembled quantum dots. Appl. Phys. Lett. **71**(5), 590–592 (1997)
139. J.M. Lamy, C. Paranthoen, C. Levallois, A. Nakhar, H. Folliot, J.P. Gauthier, O. Dehaese, A. Le Corre, S. Loualiche, Polarization control of 1.6 μm vertical-cavity surface-emitting lasers using InAs quantum dashes on InP(001). Appl. Phys. Lett. **95**(1), 011117-1–3 (2009)
140. S.A. Blokhin, N.A. Maleev, A.G. Kuzmenkov, A.V. Sakharov, M.M. Kulagina, Y.M. Shernyakov, I.I. Novikov, M.V. Maximov, V.M. Ustinov, A.R. Kovsh, S.S. Mikhrin, N.N. Ledentsov, G. Lin, J.Y. Chi, Vertical-cavity surface-emitting lasers based on submonolayer InGaAs quantum dots. IEEE J. Quantum Electron. **42**(9), 851–858 (2006)
141. S. Hövel, A. Bischoff, N.C. Gerhardt, M.R. Hofmann, T. Ackemann, A. Kroner, R. Michalzik, Optical spin manipulation of electrically pumped vertical-cavity surface-emitting lasers. Appl. Phys. Lett. **92**(4), 041118-1–3 (2008)

142. N.C. Gerhardt, M.R. Hofmann, Spin controlled vertical-cavity surface-emitting lasers. Advances in Optical Technologies, Special Issue on *Recent Advances in Semiconductor Surface-Emitting Lasers*, Article ID 268949 (2011)
143. S. Goeman, S. Boons, B. Dhoedt, K. Vandeputte, K. Caekebeke, P. Van Daele, R. Baets, First demonstration of highly reflective and highly polarization selective diffraction gratings (GIRO-gratings) for long-wavelength VCSEL's. IEEE Photon. Technol. Lett. **10**(9), 1205–1207 (1998)
144. C.-A. Berseth, B. Dwir, I. Utke, H. Pier, A. Rudra, V.P. Iakovlev, E. Kapon, Vertical cavity surface emitting lasers incorporating structured mirrors patterned by electron-beam lithography. J. Vac. Sci. Technol. B **17**(6), 3222–3225 (1999)
145. H.J. Unold, M. Golling, R. Michalzik, D. Supper, K.J. Ebeling, Photonic crystal surface-emitting lasers: tailoring waveguiding for single-mode emission, in *Proceedings of 27th European Conference on Optical Communication, ECOC*, vol. 4. Amsterdam, The Netherlands, Sept./Oct. 2001, pp. 520–521
146. D.-S. Song, S.-H. Kim, H.-G. Park, C.-K. Kim, Y.-H. Lee, Single-fundamental-mode photonic-crystal vertical-cavity surface-emitting lasers. Appl. Phys. Lett. **80**(21), 3901–3903 (2002)
147. A.J. Danner, T.S. Kim, K.D. Choquette, Single fundamental mode photonic crystal vertical cavity laser with improved output power. Electron. Lett. **41**(6), 325–326 (2005)
148. D.F. Siriani, P.O. Leisher, K.D. Choquette, Loss-induced confinement in photonic crystal vertical-cavity surface-emitting lasers. IEEE J. Quantum Electron. **45**(7), 762–768 (2009)
149. S. Noda, M. Yokoyama, M. Imada, A. Chutinan, M. Mochizuki, Polarization mode control of two-dimensional photonic crystal laser by unit cell structure design. Science **293**(5532), 1123–1125 (2001)
150. M. Ortsiefer, R. Shau, M. Zigldrum, G. Böhm, F. Köhler, M.-C. Amann, Submilliamp long-wavelength InP-based vertical-cavity surface-emitting laser with stable linear polarization. Electron. Lett. **36**(13), 1124–1126 (2000)
151. S. Riyopoulos, E. Nhan, Polarization selection due to scattering losses in nonaxisymmetric vertical cavity surface emitting laser cavities. Appl. Phys. Lett. **85**(15), 3038–3040 (2004)
152. S.F. Yu, Polarization selection in birefringent antiresonant reflecting optical waveguide-type vertical-cavity surface-emitting lasers. IEEE J. Quantum Electron. **39**(11), 1362–1371 (2003)
153. H.Y. Chu, B.-S. Yoo, M.S. Park, H.-H. Park, Polarization characteristics of index-guided surface-emitting lasers with tilted pillar structure. IEEE Photon. Technol. Lett. **9**(8), 1066–1068 (1997)
154. A.K. Dutta, K. Kasahara, Polarization control in vertical-cavity surface emitting laser using uniaxial stress. Solid-State Electron. **42**(6), 907–910 (1997)
155. S.J. Schablitsky, L. Zhuang, R.C. Shi, S.Y. Chou, Controlling polarization of vertical-cavity surface-emitting lasers using amorphous silicon subwavelength transmission gratings. Appl. Phys. Lett. **69**(1), 7–9 (1996)
156. F. Robert, P. Besnard, M.-L. Charès, G.M. Stephan, VCSEL-polarisation control with polarised feedback. IEE Proc.-Optoelectron **143**(1), 104–106 (1996)
157. H. Kawaguchi, I.S. Hidayat, Y. Takahashi, Y. Yamayoshi, Pitchfork bifurcation polarisation bistability in vertical-cavity surface-emitting lasers. Electron. Lett. **31**(2), 109–111 (1995)
158. H. Kawaguchi, I.S. Hidayat, Gigahertz all-optical flip-flop operation of polarisation-bistable vertical-cavity surface-emitting laser. Electron. Lett. **31**(14), 1150–1151 (1995)
159. L.M. Augustin, E. Smalbrugge, K.D. Choquette, F. Karouta, R.C. Strijbos, G. Verschaffelt, E.-J. Geluk, T.G. van de Roer, H. Thienpont, Controlled polarization switching in VCSELs by means of asymmetric current injection. IEEE Photon. Technol. Lett. **16**(3), 708–710 (2004)
160. Y. Sato, K. Furuta, T. Katayama, H. Kawaguchi, Polarization switching in vertical-cavity surface-emitting lasers by asymmetrical current injection. IEEE Photon. Technol. Lett. **20**(17), 1446–1448 (2008)

161. M.S. Park, B.T. Ahn, B.-S. Yoo, H.Y. Chu, H.-H. Park, C.J. Chang-Hasnain, Polarization control of vertical-cavity surface-emitting lasers by electro-optic birefringence. Appl. Phys. Lett. **76**(7), 813–815 (2000)
162. V. Badilita, J.-F. Carlin, M. Ilegems, M. Brunner, G. Verschaffelt, K. Panajotov, Control of polarization switching in vertical coupled-cavities surface emitting lasers. IEEE Photon. Technol. Lett. **16**(2), 365–367 (2004)
163. D.M. Grasso, K.D. Choquette, Polarization switching in composite-resonator vertical-cavity lasers. Appl. Phys. Lett. **83**(25), 5148–5150 (2003)
164. G.A. Keeler, K.M. Geib, D.K. Serkland, G.M. Peake, J.R. Wendt, Control of VCSEL polarization using deeply etched surface gratings, in *Proceedings of Conference on Lasers and Electro-Optics/Quantum Electronics and Laser Science Conference, CLEO/QELS 2006*, Long Beach, CA, USA, May 2006, paper CWP2
165. C. Fuchs, T. Gensty, P. Debernardi, G.P. Bava, J.M. Ostermann, R. Michalzik, Å. Haglund, A. Larsson, W. Elsäßer, Spatiotemporal turn-on dynamics of grating relief VCSELs. IEEE J. Quantum Electron. **43**(12), 1227–1234 (2007)
166. N. Marcuvitz, *Waveguide Handbook* (McGraw-Hill, New York, 1951)
167. J.-L. Roumiguieres, The rectangular-groove grating used as an infrared polarizer. Opt. Commun. **19**(1), 76–78 (1976)
168. K. Knop, Reflection grating polarizer for the infrared. Opt. Commun. **26**(3), 281–283 (1978)
169. J.M. Ostermann, *Diffractive Optics for Polarization Control of Vertical-Cavity Surface-Emitting Lasers* (Cuvillier Verlag, Göttingen, 2007)
170. M.D. Austin, H. Ge, W. Wu, M. Li, Z. Yu, D. Wasserman, S.A. Lyon, S.Y. Chou, Fabrication of 5 nm linewidth and 14 nm pitch features by nanoimprint lithography. Appl. Phys. Lett. **84**(26), 5299–5301 (2004)
171. H. Martinsson, J.A. Vukušić, M. Grabherr, R. Michalzik, R. Jäger, K.J. Ebeling, A. Larsson, Transverse mode selection in large-area oxide-confined vertical-cavity surface-emitting lasers using a shallow surface relief. IEEE Photon. Technol. Lett. **11**(12), 1536–1528 (1999)
172. H.J. Unold, M. Grabherr, F. Eberhard, F. Mederer, R. Jäger, M. Riedl, K.J. Ebeling, Increased-area oxidised single-fundamental mode VCSEL with self-aligned shallow etched surface relief. Electron. Lett. **35**(16), 1340–1341 (1999)
173. H.J. Unold, S.W.Z. Mahmoud, R. Jäger, M. Grabherr, R. Michalzik, K.J. Ebeling, Large-area single-mode VCSELs and the self-aligned surface relief. IEEE J. Select. Topics Quantum Electron. **2**(10), 386–392 (2001)
174. Å. Haglund, J.S. Gustavsson, J.A. Vukušić, P. Modh, A. Larsson, Single fundamental-mode output power exceeding 6 mW from VCSELs with a shallow surface relief. IEEE Photon. Technol. Lett. **16**(2), 368–370 (2004)
175. A. Kroner, F. Rinaldi, J.M. Ostermann, R. Michalzik, High-performance single fundamental mode AlGaAs VCSELs with mode-selective mirror reflectivities. Opt. Commun. **270**(2), 332–335 (2007)
176. J.M. Ostermann, F. Rinaldi, P. Debernardi, R. Michalzik, VCSELs with enhanced single-mode power and stabilized polarization for oxygen sensing. IEEE Photon. Technol. Lett. **17**(11), 2256–2258 (2005)
177. V. Weldon, J. O'Gorman, J.J. Pérez-Camacho, D. McDonald, J. Hegarty, J.C. Connolly, N.A. Morris, R.U. Martinelli, J.H. Abeles, Laser diode based oxygen sensing: a comparison of VCSEL and DFB laser diodes emitting in the 762 nm region. Infrared Phys. Technol. **38**(6), 325–329 (1997)
178. H.P. Zappe, M. Hess, M. Moser, R. Hövel, K. Gulden, H.-P. Gauggel, F. Monti di Sopra, Narrow-linewidth vertical-cavity surface-emitting lasers for oxygen detection. Appl. Opt. **39**(15), 2475–2479 (2000)
179. J. Wang, S.T. Sanders, J.B. Jeffries, R.K. Hanson, Oxygen measurements at high pressures with vertical-cavity surface-emitting lasers. Appl. Phys. B **72**(7), 865–872 (2001)
180. B. Scherer, J. Wöllenstein, M. Weidemüller, W. Salzmann, J.M. Ostermann, F. Rinaldi, R. Michalzik, Measurement of the pressure broadening coefficients of the oxygen A-band using

a low cost, polarization stabilized, widely tunable vertical-cavity surface-emitting laser. Microsyst. Technol. **14**(4–5), 607–614 (2008)

181. M. Born, E. Wolf, *Principles of Optics*, 6th edn. (Pergamon Press, Oxford, 1997)
182. S. Adachi, Optical properties of AlGaAs: transparent and interband-transition regions (tables), Chap. 5 in *Properties of Aluminium Gallium Arsenide*, ed. by S. Adachi (INSPEC, London, 1993), pp. 125–140
183. I.-S. Chung, J. Mørk, P. Gilet, A. Chelnokov, Subwavelength grating-mirror VCSEL with a thin oxide gap. IEEE Photon. Technol. Lett. **20**(2), 105–107 (2008)

Chapter 6
Polarization Dynamics of VCSELs

Krassimir Panajotov and Francesco Prati

Abstract In this chapter we wrap up the experimental and theoretical results on polarization dynamics of solitary vertical-cavity surface-emitting lasers. Experiments have shown that VCSELs emit a linearly polarized fundamental transverse mode either along the [110] or [$1\bar{1}0$] crystallographic direction. Polarization switching between these modes can occur when the injection current is increased, showing either a frequency shift from the higher to the lower frequency mode (type I) or the reverse (type II). The two modes of linear polarization are strongly anti-correlated. The switching can happen through a region of mode hopping, with a dwell time scaling over eight orders of magnitude with the switching current, or through a region of hysteresis. Thermal (carrier) effects influence the polarization behavior of VCSELs through a red (blue) shift of the gain maximum. Also, in-plane anisotropic strain can strongly modify the polarization behavior of VCSELs. All these experimental results call for explanations, as there is no a priori intrinsic polarization selection mechanism in VCSELs. We present different gain equalization models to explain type I, type II or double polarization switching. Alternatively, the spin-flip model can explain both types polarization switching by involving a microscopic spin-flip relaxation mechanism. Its predictive power has been experimentally established

K. Panajotov (✉)
Department of Applied Physics and Photonics, Vrije Universiteit Brussel,
Pleinlaan 2, 1050 Brussels, Belgium
e-mail: kpanajot@b-phot.org

Institute of Solid State Physics, Bulgarian Academy of Sciences,
72 Tzarigradsko Chaussee blvd., 1784 Sofia, Bulgaria

F. Prati
CNISM and Dipartimento di Fisica e Matematica,
Università dell'Insubria, via Valleggio 11, 22100 Como, Italy
e-mail: franco.prati@uninsubria.it

R. Michalzik (ed.), *VCSELs*, Springer Series in Optical Sciences 166,
DOI: 10.1007/978-3-642-24986-0_6, © Springer-Verlag Berlin Heidelberg 2013

as, e.g., polarization switching through elliptically polarized states and dynamical instabilities. Finally, we highlight some perspective applications using polarization dynamics of VCSELs.

6.1 Background

In contrast to the edge-emitting lasers (EELs) where light propagates along the active region and is emitted from the edge, in VCSELs light propagates perpendicular to the quantum wells (QWs) inside a high finesse cavity built by very high reflectivity distributed Bragg reflectors (DBRs) [1, 2]. This configuration of VCSELs provides several advantages, such as much smaller dimensions, inherent single longitudinal-mode emission, integration in 2-dimensional arrays, circular beam shape to facilitate coupling to optical fibers, on-wafer testing which significantly reduces the production cost. However, the surface emission and the cylindrical symmetry of the VCSEL cavity create some problems, namely multi transverse-mode emission and polarization unstable behavior.

The polarization properties of the light emitted by a semiconductor laser are determined by the polarization properties of: gain, i.e., by the interband transition matrix element (TME); and optical cavity. The TME, $|M_T|^2$, depends on the relative orientation of light polarization (with a unit vector $\boldsymbol{e}$) and electron wavevector (with a unit vector $\boldsymbol{k}$) as [3]

$$\frac{|M_T|^2}{|M|^2} = \begin{cases} 1/2\,(1 - |\boldsymbol{k}\cdot\boldsymbol{e}|) & \text{for HH band} \\ 1/2\,(1/3 + |\boldsymbol{k}\cdot\boldsymbol{e}|) & \text{for LH band}, \\ 1/3 & \text{for SO band} \end{cases} \tag{6.1}$$

where $|M|^2$ is the TME for bulk material [3] and HH, LH and SO stand for the heavy hole, light hole and split off bands, respectively. This TME enters the expression for the optical gain [3–5] providing a dependence on the angle between the light polarization unit vector and the electron wavevector $\boldsymbol{k}$. When calculating the optical gain one is averaging over all orientations of the $\boldsymbol{k}$ vector in the plane of the QW. For QW active material that is commonly used in contemporary VCSELs, an average on all possible directions of $\boldsymbol{k}$(in the first octant of a coordinate system with z-axis along the quantization axis) results in $\langle \boldsymbol{k} \rangle = k_z$. Substituting this in (6.1) determines the polarization anisotropy at the band edge due to quantum confinement (see Fig. 6.1). Therefore, the TME is different in EEL for light polarized in the plane of the QW (TE-polarization) and perpendicular to it (TM-polarization)—illustrated by the dumbbell shape in Fig. 6.1. Conduction band (CB)–HH transitions contribute dominantly to the gain for TE polarization with band-edge $|M_T|^2/|M|^2$ of 1/2 compared to 1/6 for CB–LH transitions. For TM polarization however, the CB–LH transitions mainly contribute to the gain: a band-edge value of the $|M_T|^2/|M|^2$ of 2/3 compared to 0 for CB–HH transitions according to (6.1). Because of VCSEL surface emission the

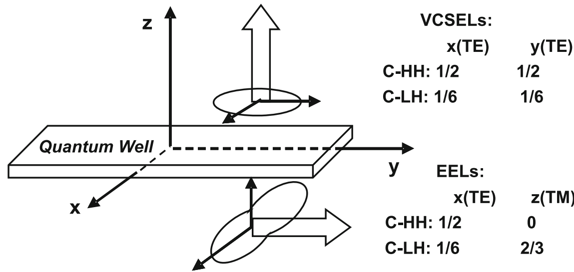

Fig. 6.1 Schematic drawing showing the polarization anisotropy of the transition matrix element in QWs. Light is emitted in the direction shown with *large arrows* (z in case of VCSELs and y in case of EELs). While in EELs there is large gain anisotropy due to different transitions involved for x (TE) and z (TM) polarization directions, in VCSELs the transition matrix elements are the same for linear polarization in any direction in the xy-plane of the QW (perpendicular to the direction of light emission)

TME will be the same for linear polarization in any direction in the xy-plane of the QW (perpendicular to the z-direction of light emission)—illustrated by the circle in Fig. 6.1. Moreover, the CB–HH transitions will dominantly contribute to the gain in VCSELs with band-edge $|M_T|^2/|M|^2$ of 1/2 compared to 1/6 for CB–LH transitions. The quantum confinement leads to coupling between the HH and the LH subbands for $\boldsymbol{k}$ different from 0 [3–5] so that the wave function exhibits both the HH and LH characteristics (the names of the subbands are according to their character at the band edge). Carrying out the averaging over all $\boldsymbol{k}$ vectors in the plane of the QW with energy dispersion calculated with the $\boldsymbol{k} \cdot \boldsymbol{p}$ method [3–5] results in equivalent gain for all [100] (or [110]) directions even for the case of lattice mismatch strained QWs. The reason is that biaxial strain, either compressive or tensile, is isotropic in the plane of the QW and does not modify the valence band symmetry in the QW plane. Therefore, we can conclude that *there is no intrinsic polarization gain anisotropy mechanism in conventional VCSELs.*

The optical confinement is also different in VCSELs and EELs: Usually a symmetric cylindrical or rectangular aperture is defined by oxidation, an air post or proton implantation in VCSELs. On the contrary, the much different lateral and transverse dimensions of the EEL waveguide give rise to waveguiding and reflectivity anisotropy. Thus, in contrast with EELs, neither gain nor cavity polarization anisotropy mechanism is present in conventional VCSELs.

As a result VCSELs show interesting polarization dynamics. In this chapter we will focus on the polarization dynamics of VCSELs with different structures in a single transverse-mode regime. In Sect. 6.2, we summarize the experimental results on polarization switching (PS) and dynamics in VCSELs. In Sect. 6.3, we discuss the physics behind these interesting polarization dynamics and their theoretical modeling. In Sect. 6.4, we conclude by giving some unique applications of polarization dynamics in VCSELs.

6.2 Overview of the Experimental Results on Polarization Dynamics of a Solitary VCSEL

6.2.1 Alignment of Polarization Axis to [110] *or* [$1\bar{1}0$] *Axes: Elasto-Optic and Electro-Optic Effects*

It has been found experimentally that both gain-guided [6–8] and index-guided [9] VCSELs emit fundamental transverse mode, linearly polarized (LP) along [110] or [$1\bar{1}0$] crystallographic axes. It has also been found that the degeneracy of the two orthogonal LP modes is lifted leading to a small frequency splitting of $\Delta\nu =$ 1–15 GHz [7–9]. The point group symmetry of III-V compound semiconductors is cubic T_d ($\bar{4}3m$) implying full rotational symmetry of the linear optical susceptibility. In the multilayer QW VCSELs grown on [100] substrate this symmetry is broken along the growth axis (z) but preserved in the orthogonal (xy) plane. It is therefore puzzling why the light polarization prefers the specific [110]/[$1\bar{1}0$] directions. In order to understand the origin of this preference and study the relation between strain and birefringence different experimental techniques have been used that introduce intentionally controlled QW in-plane strain in the VCSELs. In the “hot-spot” technique [8] a small hot spot is created on the VCSEL surface outside the metal contact by absorption of Ti-sapphire laser beam. The radial thermal gradient results in QW in-plane strain and in a change of the LP mode frequency splitting and orientation. The temperature rise can be determined from the spectral shift of the lasing mode. The orientation of the induced birefringence can be chosen by the hot spot position with respect to the VCSEL. It has been shown that due to the anisotropy of the elasto-optic effect even a random distribution of strain leads to LP orientation more likely near [110] than [100] axis.

A simpler way to introduce controllable anisotropic strain in VCSELs is by using its mechanical holder as shown in Fig. 6.2 [10]. The anisotropic strain is caused by pressing the upper metal plate on the VCSEL package and can be controlled by turning two screws that are positioned on the line A–B and supported by springs. A thin steel rod is inserted between the holder and the metal plate of the package perpendicular to the A–B line. The in-plane anisotropic strain is obtained by bending the metal plate of the laser package on which the VCSEL wafer is glued. This geometry introduces a tensile strain σ in the laser along line A–B and a compressive strain in the orthogonal direction. In Fig. 6.3 we show by a solid line the calculated orientation of the index ellipsoid with respect to the crystal coordinate system if the induced birefringence via elasto-optic effect is taken into account [11, 12]. The only input parameters are the experimentally measured residual birefringence $\Delta\nu_0 =$ 2 GHz and initial polarization orientation $\phi_0 = 15°$. The external strain σ is a dummy variable with a maximum value of 0.04%. The experimental LP state orientation is represented by triangles. A large birefringence tuning from -80 to $+80$ GHz is achieved using this techniques and except for the narrow range of very small birefringence around zero frequency splitting the orientation of the index ellipsoid remains along the [110]/[$1\bar{1}0$] crystallographic axes.

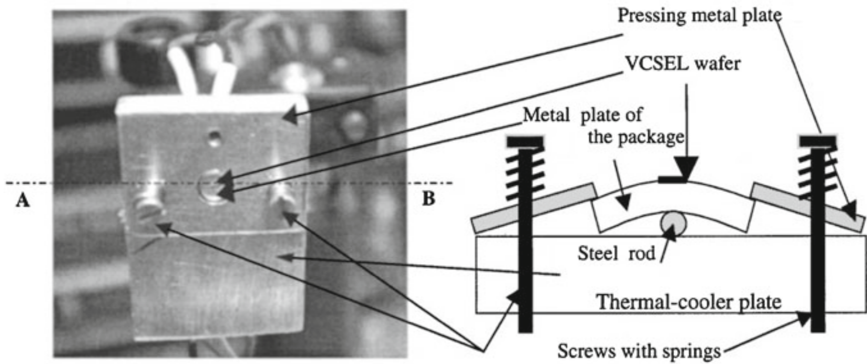

Fig. 6.2 Photograph (*left*) and schematic (*right*) drawing of the VCSEL holder used to apply a controllable QW in-plane strain. Reprinted with permission from [10]. Copyright 2000, American Institute of Physics

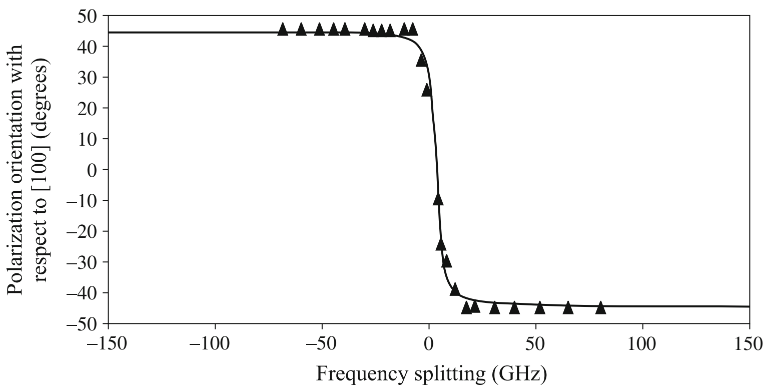

Fig. 6.3 Experimental (*triangles*) and theoretical (*solid line*) orientation with respect to the crystal axes of one LP mode as a function of frequency splitting between the two LP modes induced by QW in-plane uniaxial strain. After [12]

The hot-spot technique has been used to change VCSEL birefringence in a controllable and permanent way [13, 14]. To this aim a small hole is melted by the focused laser beam in the vicinity of the VCSEL. A small residual ellipticity ($|\chi| > 4°$) is measured for the lasing mode in [14]; i.e., light is better blocked (to 10^{-6}) after a combination of quarter-wave plate and polarizer than after a polarizer only (10^{-4}). This has been explained by misaligned linear birefringence and linear dichroism giving rise to orthogonal elliptically polarized modes with the same ellipticity and helicity [14].

Experimental characterization of 39 gain-guided VCSELs carried out in [15] showed that, almost all lasers lase on the higher frequency LP mode, oriented at 90° with respect to the VCSEL array axis (lately identified as $[1\bar{1}0]$ crystallographic axis). This systematic positive birefringence has been attributed in [15] to the linear electro-

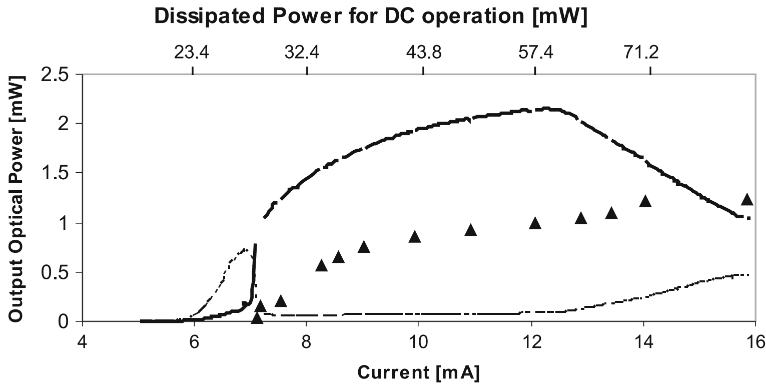

Fig. 6.4 Polarization-resolved light vs. current (LI) curve showing type I PS for DC current: ν_H (ν_L) mode is shown as *thin* (*thick*) line. No PS is observed for short-pulse current (*triangles*) [29] (© 1998 IEEE)

optic effect. The longitudinal (z) dependence of the static electric field in VCSELs has been considered with contributions from the built-in potential across the active layer, the series resistance of the device and the localized fields at the DBR heterojunctions (the last one being the most significant). For a typical GaAs/AlGaAs VCSEL the estimated birefringence due to the electro-optic effect is about 15 GHz with the higher frequency mode oriented along the [110] axis. The case of GaAs/AlGaAs oxide-confined VCSELs has been considered in [16] and the electro-optic birefringence has been shown to decrease almost twice (from about 18 to 10 GHz) as the forward voltage bias is increased from 0 to 2.5 V. More direct experimental confirmation of electro-optic effect induced birefringence is carried out in [17] where conventional asymmetrically doped VCSELs (pin-doped, 12 GHz birefringence) are compared to symmetrically doped ones (pip-doped, 0.7–1.6 GHz birefringence). The lack of birefringence in the last case is in accordance with the prediction of general symmetry considerations of polarization isotropy in VCSELs [18].

6.2.2 Type I Polarization Switching

Experimentally, it is found that the two orthogonal LP VCSEL fundamental modes do not lase simultaneously and that a switching between them may occur when changing the injection current [6, 7, 10–12, 19–46]. A polarization-resolved light versus current (LI) characteristic of a proton-implanted GaAs/AlGaAs QW VCSEL emitting around 850 nm is shown in Fig. 6.4 [29].

PS is observed in the fundamental Gaussian transverse mode when operating with direct current (DC) but not for short-pulse current operation. From the spectrum of the emitted light, we identify the PS to be, when increasing the injection current, from the higher frequency ν_H mode (thin line) to the lower frequency ν_L mode (thick line). We shall refer to such kind of PS as type I PS because it is the one first identified [7, 19, 23] and to distinguish from the opposite way of switching,

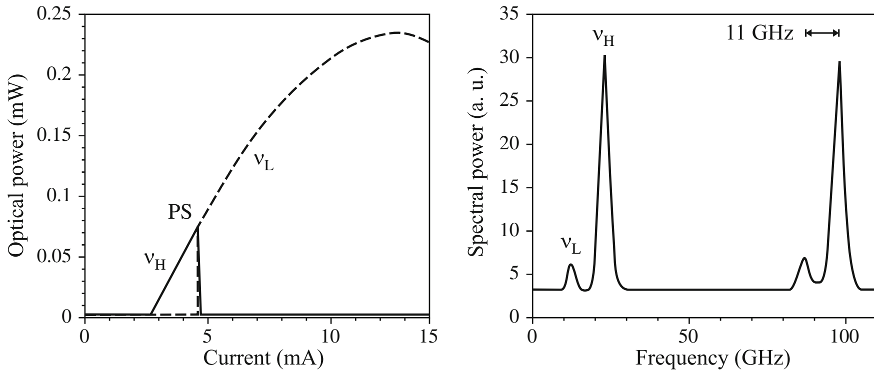

Fig. 6.5 *Left*: Polarization-resolved LI curve showing type I PS for InGaAs air-post VCSELs: The ν_H (ν_L) mode is shown as full (*dashed*) line. *Right*: High-resolution spectrum taken at a current before the PS. A polarizer in front of the Fabry–Perot interferometer is aligned to almost extinguish the lasing (ν_H) mode. After [12]

from lower to higher frequency polarization mode which we call type II PS [33]. A typical feature of VCSELs is that the LI curve is not linear: the slope of the LI curve saturates with current as seen in Fig. 6.4, and then may even become negative (a thermal rollover). This is due to the current self-heating of the VCSEL combined with the single longitudinal mode operation: the gain curve red-shifts about 3 times faster with temperature than the cavity mode, which results in misalignment between them and decrease of material gain. The kink in the LI curve, that is clearly visible in Fig. 6.4 around an injection current of 12.8 mA, is a signature of the appearance of the first order transverse mode. The appearance of higher-order transverse modes is due to the spatial hole burning effect, i.e., the decrease of the carrier density in the regions of high optical intensity as the carrier diffusion can not compensate for the fast removal of carriers by the stimulated emission recombination. The thermal gain–cavity misalignment and spatial hole burning will be discussed in Sect. 6.3.2 in relation to polarization switching in VCSELs.

Type I PS is not restricted to gain-guided VCSELs, it has also been observed in index-guided air-post [12, 24] and oxide-confined [12] VCSELs. The air-post VCSELs in [24] have three 8 nm thick InGaAs QWs and GaAs/AlAs mirrors lasing around 980 nm. Polarization-resolved LI curve and optical spectrum taken by a high-resolution Fabry–Perot interferometer of similar air-post VCSELs [12] are shown in Fig. 6.5 (left) and (right), respectively. The frequency splitting between the two LP modes is 11 GHz and does not change with the injection current and temperature. The experiments described in [24] revealed strong sidebands at the relaxation oscillation frequency ($\nu_{RO} = 2.6$ GHz) in the optical spectrum taken before the PS type I (the LP modes were 7.1 GHz apart). These sidebands abruptly disappear after the PS. The polarization-resolved LI curves of two oxide-confined VCSELs with different aperture size and with InGaAs QWs emitting around 960 nm are shown in Fig. 6.6.

When the oxide aperture is small (diameter 3–4 μm), the VCSELs are single-transverse mode up to the thermal rollover point at about five times the threshold

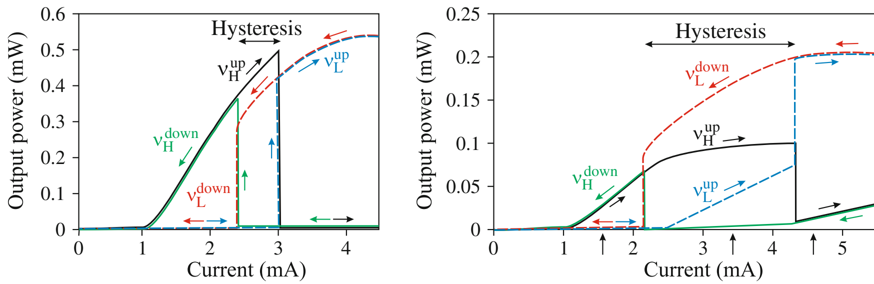

Fig. 6.6 Polarization-resolved LI curves for InGaAs oxide-confined VCSELs: The ν_H (ν_L) modes are shown as *full* (*dashed*) lines. Small (*left*) and large (*right*) oxide aperture. Type I PS is observed with a large hysteresis. After [12]

current. For these lasers PS of type I is observed between the two fundamental modes along [110] and [$1\bar{1}0$] directions, see Fig. 6.6 (left). In contrast to the case of proton-implanted and air-post VCSELs, the PS now happens through a large region of hysteresis. When the oxide-aperture is larger, VCSELs with the same structure operate on multiple transverse modes. In this case, the upward PS is in the region where the first higher order transverse mode is already lasing while the downward PS is in the region of the fundamental mode lasing (Fig. 6.6 (right)). Nevertheless, the PS is of type I between the fundamental orthogonally polarized modes.

Type I PS has been observed in proton-implanted GaAs QW VCSELs for a fast current ramp, such that the temperature of the active region remains constant [26]. The current source consisted of a DC pre-bias and a fast (100 ns, 20 kHz) current ramp generator connected to the VCSEL through a bias-tee. Time-resolved spectral measurements showed a small (<0.05 nm) blue-shift of the lasing wavelength during the ramp, confirming that the active region temperature is constant. Figure 6.7a and b demonstrate such a fast PS. Figure 6.7a shows the polarized LI characteristics at 8°C substrate temperature and Fig. 6.7b shows a mapping of the PS in the plane of active region temperature versus injected current. The last consists of the temperature rise due to the DC-prebias self-heating and the substrate temperature that has been changed to obtain the different curves in Fig. 6.7. The dependence of the threshold current is also depicted in Fig. 6.7 showing a minimum at the temperature where the cavity resonance and the gain maximum are best matched.

Type I PS to the gain disfavored mode has been reported in [38] for proton-implanted 8 μm aperture VCSELs lasing at 845 nm, with frequency splitting between the two LP modes of 6 GHz (Fig. 6.8). At the PS point the total output power shows an abrupt drop of about 3% (see the inset of Fig. 6.8). The relaxation oscillation frequency also shows a drop at the PS current, confirming that the PS is to the mode with less gain. The PS is maintained in a temperature range of 50°C, indicating that it is not due to temperature changes.

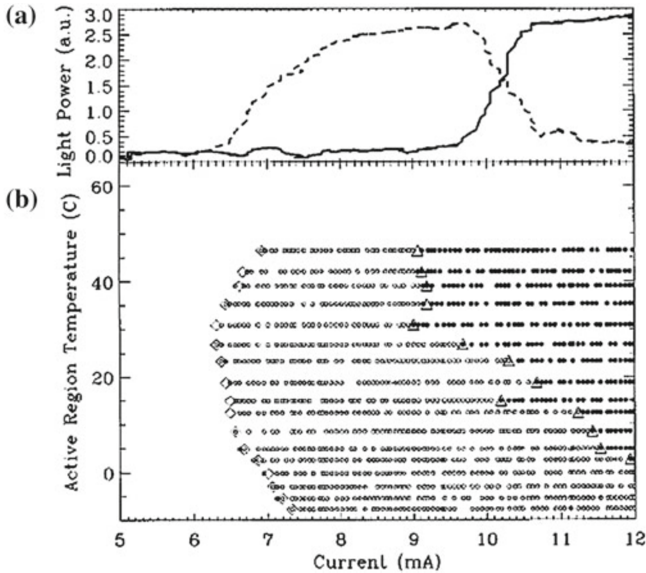

Fig. 6.7 **a** Polarized LI characteristics at 8°C substrate temperature. **b** Active region temperature vs. injected current diagram: threshold currents are indicated by *rhombs*, and PS currents by *triangles*. The *open* (*solid*) *circles* corresponds to linear *short-* (*long-*) wavelength polarization emission. Reprinted with permission from [26]. Copyright 1997, American Institute of Physics

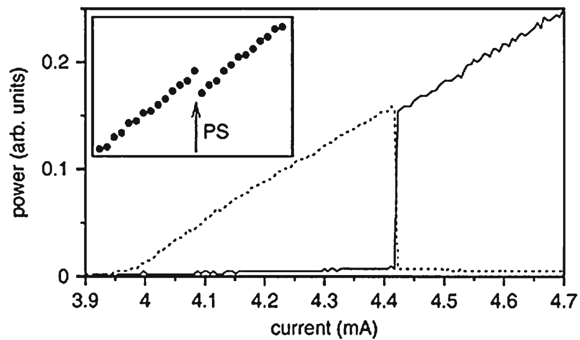

Fig. 6.8 Polarization-resolved output power vs. injection current. *Solid (dashed)* lines denote the power in the *lower (higher)* frequency mode. The *inset* shows the total output power (*dotted line*) in the vicinity of the PS [38] (© 2004 IEEE)

6.2.3 Polarization Mode Hopping

Although an abrupt PS is evident in the steady-state LI curve in Figs. 6.4 and 6.5, as a matter of fact, the VCSELs may continuously and randomly switch between the two well-defined LP states when biased in the PS region [29, 40–43]. This is illustrated in Fig. 6.9 where the time traces of the two LP modes are shifted vertically for clarity. One can see perfect anti-correlation between the two polarization-resolved

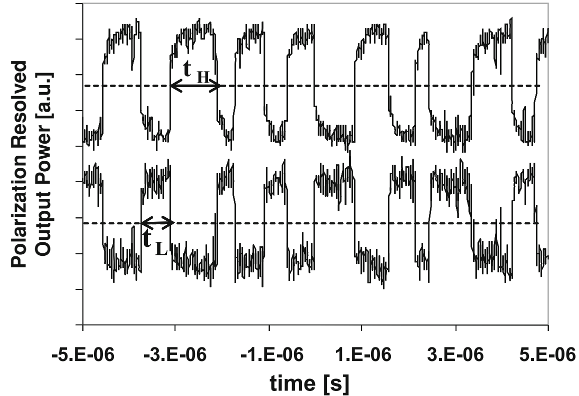

Fig. 6.9 Time trace of the polarization-resolved optical output showing polarization mode hopping behavior. The VCSEL is biased at the PS current in Fig. 6.4

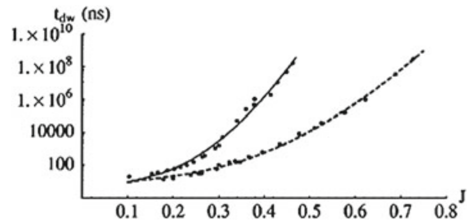

Fig. 6.10 Dwell time as a function of PS current for air-post (*dashed line*) and proton-implanted VCSELs. Reprinted figure with permission from [43]. Copyright (2003) by the American Physical Society

intensities [29]. The polarization mode hopping implies that the VCSEL is actually polarization bistable and self-switches between the two LP states by the influence of spontaneous emission noise [29, 40]. Therefore, the hysteresis region evidenced for oxide-confined VCSELs in Fig. 6.6 is also believed to exist for proton-implanted (Fig. 6.4) and air-post VCSELs (Fig. 6.5), but appears to be masked by the LP mode hopping behavior. The residence time τ_H (τ_L), the time the laser stays in the ν_H (ν_L) mode, is measured as the time interval between two consecutive crossing—upwards and downwards—of a reference level at a half the output power of the corresponding LP mode (see Fig. 6.9). It changes randomly with a mean value called dwell time.

The rather symmetric mode hopping time trace shown in Fig. 6.9 occurs only in the middle of the PS region where the dwell times of the two LP modes are equal [29, 40, 41]. Otherwise they are different: the larger one being for the ν_H (ν_L) LP mode when approaching (leaving) the PS region. If the current where the PS occurs is changed, the dwell time changes over several orders of magnitudes [42, 43]. Experimentally, scaling of the dwell time with the PS current from tens of nanoseconds to seconds has been observed (see Fig. 6.10). This phenomenon is well understood as a stochastic process of noise driven hopping in a bistable system and has been explained in two different model frameworks of polarization bistable VCSELs [42, 43].

A polarization-resolved small-signal modulation response of a proton-implanted VCSEL biased in the region of mode hopping is shown in Fig. 6.11. For a frequency of 30 MHz perfect PS is observed (Fig. 6.11 left, top trace), while at 50 MHz the

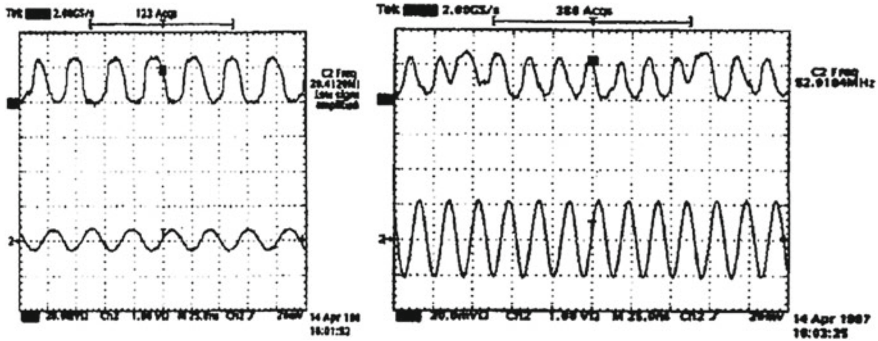

Fig. 6.11 Small-signal modulation around the PS current: the modulation signal is the *bottom trace* and the polarization-resolved optical signal is the *top trace*. Reprinted with permission from [12]. Copyright 2001, American Institute of Physics

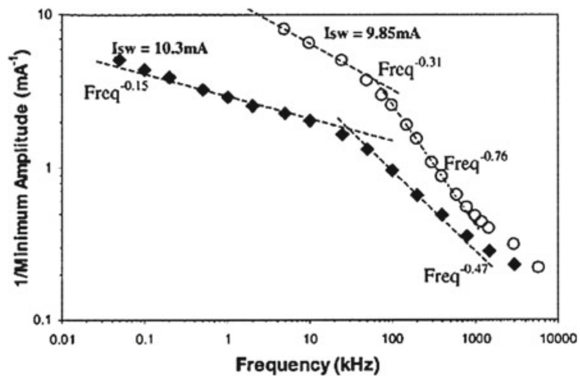

Fig. 6.12 Inverse of the minimum modulation amplitude as a function of modulation frequency for proton-implanted GaAs VCSELs. Reprinted with permission from [36]. Copyright 2002, American Institute of Physics

laser starts to miss the polarization switch from time to time being only intensity modulated at these events (Fig. 6.11 right, top trace). In such a way, one can define a maximum modulation frequency for PS which in this case is around 30 MHz. These results are in agreement with polarization modulation experiments on air-post GaAs VCSELs [21]. Together with the dwell time, which exponentially increases with PS current, the maximum modulation frequency for a given amplitude of modulation scales in a similar but reverse way. This behavior is quite similar to the mode hopping between two longitudinal modes in EELs [47]. A detailed study of the frequency response of PS has been carried out in [36]. The minimum modulation amplitude for successful PS is defined as the one at which for 80% of the modulation periods PS occurs. The PS current is modified using the uniaxial strain technique described in Sect. 6.2.1. In Fig. 6.12 the inverse of the minimum amplitude is plotted as a function of the modulation frequency for proton-implanted GaAs VCSELs [36]. Two regimes with different slopes can be clearly distinguished separated by a cut-off frequency of 90 kHz. This quite low frequency limit of PS corresponds exactly to the thermal cut-off frequency, clearly identifying a thermal mechanism responsible for

PS [21, 29, 33]. For air-post VCSELs however, the frequency response is much flatter [44] and therefore, thermal effects seem to play a minor role in PS. The PS events may synchronize better with the applied modulation signal when adding externally electrical noise to the VCSEL current, as shown in [40, 41], a typical signature of the phenomenon of stochastic resonance.

6.2.4 Type II Polarization Switching and Double Polarization Switching

The impact of the laser substrate temperature on the polarization switching of VCSELs has been studied in [7, 23, 26, 33]. Figure 6.13 shows three typical LI curves for DC operation at fixed substrate temperatures of 10, 15 and 55°C [33]. It is seen that at low substrate temperature (10°C) only type I PS takes place (a). At $T_{sub} = 15$°C (b) two types of PS occur: from ν_H mode to ν_L mode (type I PS) followed by a second one in the opposite direction (type II PS). At higher substrate temperatures $T_{sub} = 25$–55°C only type II PS takes place (c). The frequency splitting between the two orthogonal LP modes is 12 GHz and remains constant in the range of substrate temperatures for which these measurements are taken. Although observed rarely double PS is not an exception, see, e.g., the polarization-resolved LI curves reported in [7, 23, 28].

Type II PS between elliptically polarized (EP) states and through a region of dynamical instabilities has been reported in [39] for 8 µm aperture proton-implanted VCSELs lasing at 845 nm. The general EP monochromatic light can be described by two characteristic angles ([48], Chap. 1): the tilting angle ϕ of the main axis of the polarization ellipse and the ellipticity angle χ, related to the ellipticity e, i.e., the ratio of the semi-minor b axis to the semi-major a axis of the polarization ellipse,

$$e = \pm \tan(\chi) = \pm b/a, \tag{6.2}$$

where +(−)sign denotes right- (left-) handed polarization. Light is right- (left-) handed when the electrical vector traverses the polarization ellipse clockwise (counter clockwise) looking against the direction of light propagation. The Stokes parameters are determined by measuring the total light intensity, with intensities in LP bases (along x and y axes and ±45° from them) and those in the circular basis (left l and right r handed polarization) [48].

$$\begin{aligned} S_0 &= I_0 = I_x + I_y = I_{+\pi/4} + I_{-\pi/4} = I_r + I_l, \\ S_1 &= I_x - I_y, \qquad S_2 = I_{+\pi/4} - I_{-\pi/4}, \qquad S_3 = I_r - I_l. \end{aligned} \tag{6.3}$$

The normalized Stokes parameters can be written in terms of ϕ and χ as [48]

$$\boldsymbol{s} = \boldsymbol{S}/S_0 = \{\cos 2\phi \cos 2\chi, \sin 2\phi \cos 2\chi, \sin 2\chi\}, \tag{6.4}$$

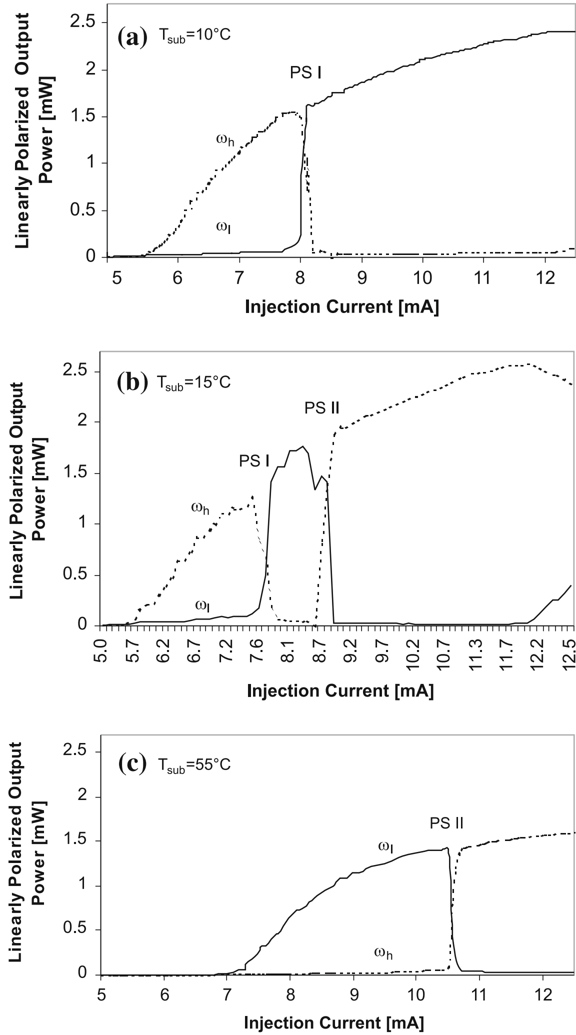

Fig. 6.13 Polarization-resolved optical output power versus DC injection current characteristic at different substrate temperatures: **a** $T_{sub} = 10°C$, **b** $T_{sub} = 15°C$ and **c** $T_{sub} = 55°C$. The *lower* (*higher*) energy mode is shown as *full* (*dashed*) line [33]

i.e., the azimuth ϕ and the ellipticity angle χ are obtained as

$$\phi = 1/2 \arctan\left(S_2/S_1\right), \qquad \chi = 1/2 \arcsin\left(S_3/\sqrt{S_1^2 + S_2^2 + S_3^2}\right). \tag{6.5}$$

Figure 6.14 shows the polarization-resolved LI curve for projection onto the main axes of the EP state at threshold. The mode with lower optical frequency starts lasing at threshold with ellipticity of 5°. The power in both LP components increases above threshold, first rather slowly but then, after a current of 7.4 mA, quite drastically. The poor suppression ratio between the two LP components after PS is due to the finite ellipticity of 10° and to the rotation by 20° of the principal axis of the polarization

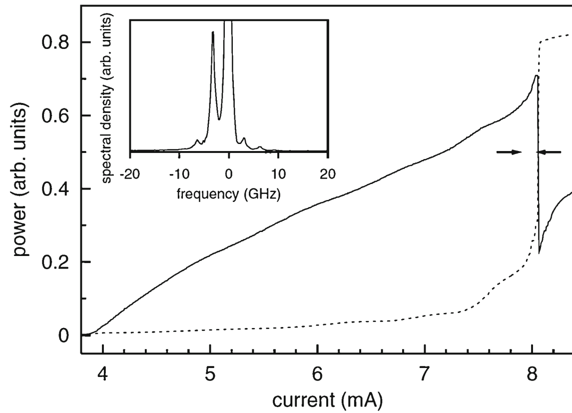

Fig. 6.14 LP-resolved output power vs. current for projection onto the main axes of the EP state at threshold. The *solid* (*dashed*) line corresponds to the *lower* (*higher*) frequency mode. The *inset* shows the optical spectrum for $I = 8.02$ mA after projection onto linear polarization, minimizing the main peak. Reprinted from [39], Copyright (2004), with permission from Elsevier

ellipse between threshold and PS. Dynamical instabilities are observed in the region denoted by arrows in Fig. 6.14, as evidenced from the optical spectrum shown in the inset. The sidebands in the optical spectrum disappear abruptly after the PS.

Double PS between EP states and through dynamical instabilities is reported in [39] when tuning the VCSEL polarization characteristics by the anisotropic strain technique described in Sect. 6.2.1. The polarization-resolved LI curve and optical spectrum are shown in Fig. 6.15. At threshold the higher frequency LP mode starts lasing. The first PS at about 6 mA is type I, between LP states and without any dynamical instability. At a current beyond 6.5 mA the ellipticity strongly increases, reaching about 22° at the second, type II PS. At a current of 6.55 mA sidebands appear in the optical spectrum as shown in the inset of Fig. 6.15. Similarly to the case of Fig. 6.14, the sidebands disappear after the PS. These results indicate that the existence of EP and dynamical states before type II PS does not depend qualitatively on the light ellipticity at threshold and the presence of preceding type I PS. The distance of the sidebands in the optical spectrum (see the inset in Fig. 6.15) is about 2.1 GHz and is also observed in the power spectrum for projection onto the LP directions corresponding to maximum and minimum time averaged power, i.e., onto the main axes of the polarization ellipse. This frequency is interpreted as the beating frequency between the different "modes", which are oscillating at adjacent frequencies, i.e., as an "effective birefringence" [39]. Such an effective birefringence is the sum of the linear birefringence observed at threshold and the non-linear contributions due to saturable dispersion and spin dynamics (see Sect. 6.3.3). Double PS in the fundamental transverse mode has also been reported for air-post GaAs QW VCSELs emitting around 850 nm [21] and oxide-confined InAlGaAs QW VCSEL emitting around 810 nm [28] however, the spectral resolution was not enough to distinguish the types of PSs.

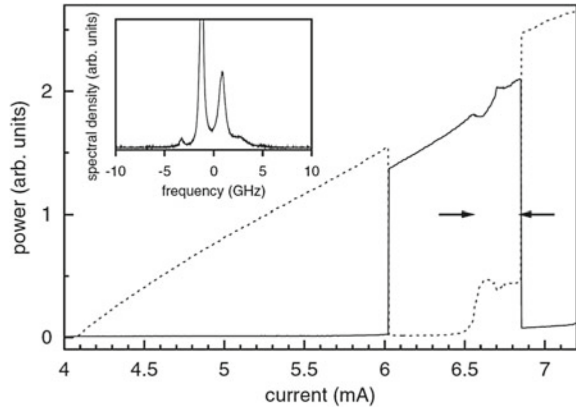

Fig. 6.15 Same as Fig. 6.14 but for a different VCSEL with an ellipticity angle $<1°$ at threshold. The *inset* shows the optical spectrum at a current of 6.66 mA after projection onto linear polarization. Reprinted from [39]. Copyright (2004), with permission from Elsevier

6.2.5 *Impact of QW Anisotropic Strain on Polarization Switching Behavior*

QW in-plane anisotropic strain has a strong impact on the polarization characteristics of VCSELs [8, 10, 13] and is utilized in order to study different types of PS in VCSELs [10, 39, 44–46]. Experimentally, it can be controllably introduced in the VCSEL cavity by the techniques described in Sect. 6.2.1. In [10], two different directions of the strain were experimentally investigated as shown in Fig. 6.16. For uniaxial tensile strain along $[1\overline{1}0]$ direction the laser is initially (at a small external stress) emitting in the low frequency (ν_L) mode. The direction of this LP state is about 20° away from the $[1\overline{1}0]$ direction (Fig. 6.16, part A-a). Increasing the external stress, the direction of this LP mode is continuously tuned towards the line of the tensile strain and remains in this orientation. Moreover, the frequency splitting between the two LP modes also increases. PS type II in the fundamental mode is first observed when the strain induced frequency splitting becomes rather large (about 25 GHz in (A-b)) and appears at quite a high current. The PS current continuously decreases as the external stress is further increased (A-c-d). A very broad region of stress-induced PS tuning exists (frequency splitting from 25 to 60 GHz). At about 60 GHz the PS point is moved to threshold (A-f) and for larger frequency splitting the laser is emitting in the higher frequency mode only, with LP oriented perpendicular to the $[1\overline{1}0]$ direction of the laser wafer.

For small uniaxial tensile strain along the [110] direction, the laser is again emitting in the low frequency (ν_L) mode oriented at about 15° away from the $[1\overline{1}0]$ direction (B-a). Now, even a very small amount of external stress changes the direction of polarization orientation much more than in the previous case. Moreover, the tuning of the polarization orientation for the low frequency mode with increasing external stress is again towards the line of the tensile strain—now the [110] direction. However, before reaching this orientation, PS is observed in a very restricted domain of external stress (frequency splitting of 4 GHz in (B-b)). This is again type II PS but this time the polarization eigenstates are oriented at about 40° degrees with respect

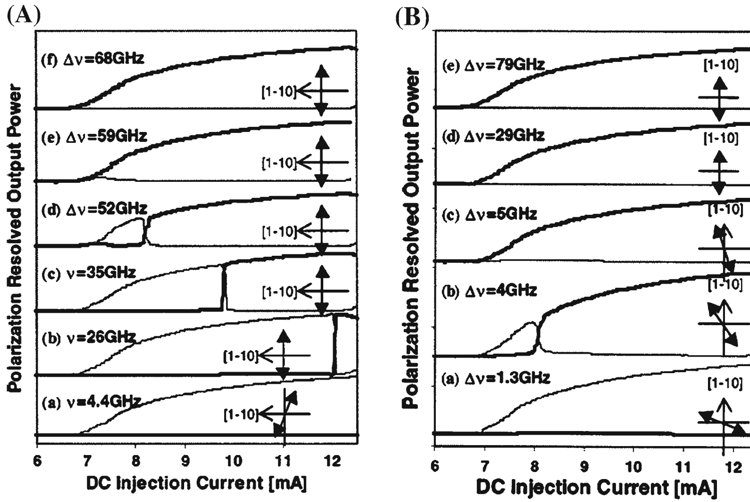

Fig. 6.16 Polarization-resolved optical output power versus DC injection current for increasing tensile strain along $[1\bar{1}0]$ (**A**) and [110] (**B**) axes. The *higher* (*lower*) frequency mode is shown by *thick* (*thin*) *solid lines*. The orientation of the higher frequency LP mode is shown, too. Reprinted with permission from [10]. Copyright 2000, American Institute of Physics

to the [110] direction. Furthermore, it is much more difficult to stress-tune the PS current and impossible to judge for the direction of this tuning. At a splitting of 5 GHz PS disappears and the laser is emitting in the higher frequency mode only. When further increasing the external stress, the polarization eigenstates are again fixed along [110] and $[1\bar{1}0]$ directions (B-d) and the higher frequency mode becomes more and more favored. No PS is observed in the whole region of frequency splitting where it did exist in the previous case (the frequency splitting between the two modes was tuned up to 80 GHz (B-e)).

The polarization mode suppression ratio (PMSR), defined as the ratio of the power of the primary polarization mode and the orthogonal polarization mode, as a function of the frequency splitting between these two modes is shown in Fig. 6.17 for different injection currents. As can be seen from this figure, PMSR changes with the splitting: initially it continuously decreases, reaches a minimum at the PS point and increases afterwards. As the current and the substrate temperature are fixed, this is a signature that the effective gain difference between the two modes has a minimum at the point of PS.

6.2.6 Polarization Fluctuations and Nonlinear Birefringence and Dichroism

Polarization fluctuations in VCSELs have been precisely characterized in a series of works [30–32, 34] and utilized to estimate the nonlinear birefringence and dichroism.

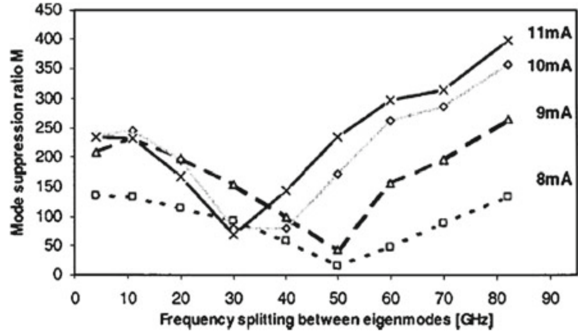

Fig. 6.17 Polarization mode suppression ratio (PMSR) as a function of the frequency splitting induced by an in-plane anisotropic strain. Reprinted with permission from [10]. Copyright 2000, American Institute of Physics

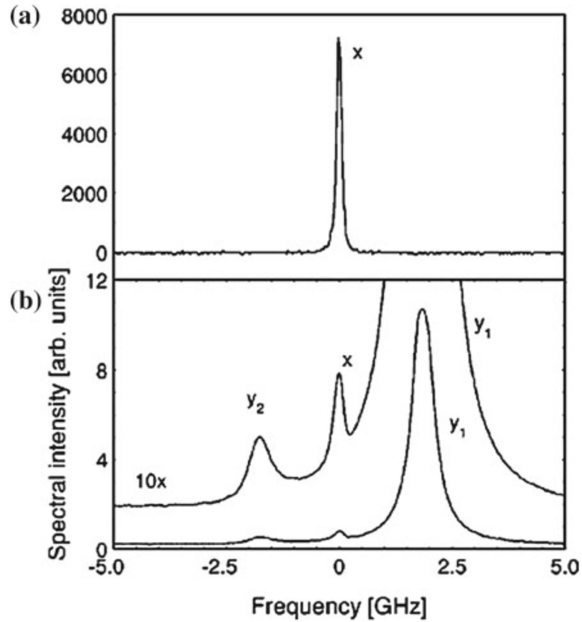

Fig. 6.18 Polarization-resolved optical spectra of a proton-implanted GaAs QW VCSEL taken with a Fabry–Perot interferometer: **a** x-LP and **b** y-LP (same arbitrary units). The latter shows the nonlasing peak at higher frequency and a weak FWM peak, as mirror image, at lower frequency. Reprinted figure with permission from [31]. Copyright (1998) by the American Physical Society

Figure 6.18 shows the polarization-resolved Fabry–Perot optical spectra of a proton-implanted VCSEL lasing around 850 nm [31].

The x-LP lasing peak, which dominates in Fig. 6.18a, is almost completely suppressed in the y-polarized spectrum in Fig. 6.18b (a very small fraction of the lasing peak is kept to serve as a marker). The three (equidistant) peaks in Fig. 6.18b are the four-wave mixing (FWM) peak (y_2), the lasing peak (x), and the nonlasing peak (y_1). The frequency difference between the lasing and nonlasing peaks gives the effective birefringence $\Delta\nu_{\mathrm{eff}} = -1.82$ GHz, whereas the difference in their spectral widths at half maximum gives the effective dichroism $\Delta\gamma_{\mathrm{eff}} = 0.22$ GHz [31]. Furthermore, the relative strength of the FWM peak, as compared to the nonlasing peak, (2.5% in Fig. 6.18) can be used to quantify the nonlinear anisotropies in the laser [31]. For

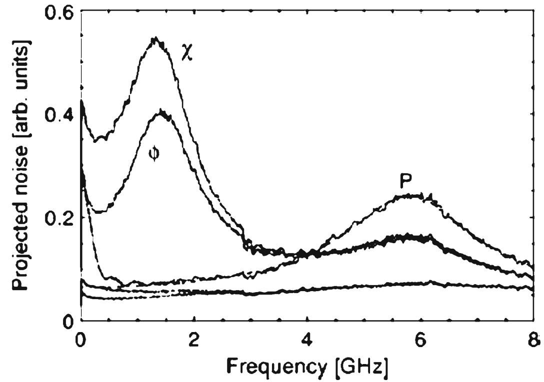

Fig. 6.19 Intensity noise of a proton-implanted VCSEL projected on: P (total intensity), χ (ellipticity angle), and ϕ (ellipticity azimuth). Reprinted figure with permission from [31]. Copyright (1998) by the American Physical Society

VCSELs with a very small $\Delta\nu_{\text{eff}}$ the FWM relative strength can be as high as 20% [31] indicating very strong nonlinearities.

Figure 6.19 shows the projected intensity noise of another VCSEL biased close to threshold [31]. The spectrum for projection onto the lasing polarization (solid curve, label P) is dominated by pure intensity noise with a broad maximum around the relaxation oscillation frequency $\nu_{\text{RO}} \approx 6$ GHz. The ϕ and χ curves show the noise spectra for polarization projections specially chosen to reveal the noise in the respective polarization angles. Note the strong noise in these polarization projections with maxima at frequency of 1.5 GHz, distinctively different from ν_{RO}. Such special projections were made in [30, 31] by an optical setup consisting of a quarter-wave plate in combination with a half-wave plate and an optical isolator, which act together as a rotatable linear polarizer. The light polarization after passing this setup can be determined by multiplying the corresponding Jones matrices ([48], Chap. 2). The quarter-wave plate is rotated by $\pi/4$ with respect to the dominant laser polarization. For projection on the main axis of the VCSEL polarization ellipse, one obtains

$$I_{\beta=0} = [1 + \sin(2\chi)]\, I_0/2, \tag{6.6}$$

with I_0 the VCSEL total output intensity. This projection is denoted by χ in Fig. 6.19 as it is sensitive to noise in the ellipticity angle χ. For a projection on an angle of $\pi/4$ the result is $I_{\beta=\pi/4} = I_0/2$, i.e., the measured fluctuations do not depend on the ellipticity χ and are solely due to fluctuations of the azimuth ϕ. Indeed, assuming a small fluctuation φ of the azimuth the detected intensity is

$$I_{\beta=\pi/4} = (1 + 2\phi)\, I_0/2. \tag{6.7}$$

This projection is denoted by ϕ in Fig. 6.19, which clearly shows how intensity noise and polarization noise add up in the projected ϕ and χ spectra; the relaxation oscillation is then less prominent because the average intensity for the polarization projections is about half the intensity for the P projection onto the lasing polarization (see (6.6) and (6.7)). It can be also seen that the noise in the ellipticity angle

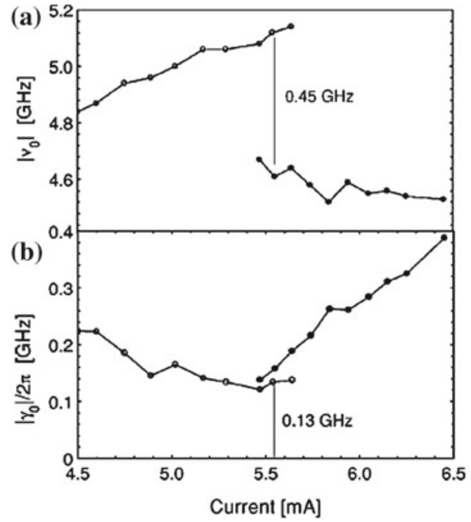

Fig. 6.20 **a** Effective birefringence and **b** effective dichroism of an air-post VCSEL as a function of current. Note the observed hysteresis and the jump in $|\nu_0|$ that occurs upon a polarization switch (around $I = 5.5$ mA). From **b** it is concluded that PS results from a current-dependent dichroism $\gamma_0(I)$. Reprinted figure with permission from [31]. Copyright (1998) by the American Physical Society

is much stronger than the one in the azimuth. By fitting the curves in Figs. 6.18 and 6.19 one can very accurately measure the effective birefringence $\Delta\nu_{\text{eff}}$, the effective dichroism $\Delta\gamma_{\text{eff}}$ and the linewidth enhancement factor α ([31] and Sect. 6.3.3).

The precise measurement of $\Delta\nu_{\text{eff}}$ and $\Delta\gamma_{\text{eff}}$ allows following their evolution with injection current, especially around the PS point [30–32]. For an air-post VCSEL the PS happens through a hysteresis of polarization-resolved intensity, also manifested as hysteresises of the effective birefringence (Fig. 6.20a) and dichroism (Fig. 6.20b). The jumps at the PS points of both ν_{eff} and γ_{eff} allow estimating the corresponding nonlinear contributions to them due to the difference in the light intensity before and after the PS.

The correlation properties of the fluctuations in the two LP modes have been characterized in [32]. The total intensity is the sum of the orthogonally LP lasing and nonlasing mode intensities, $I(t) = I_x(t) + I_y(t)$. Its spectral density is the Fourier transform of the autocorrelation function (see [3] App. XIII), i.e.,

$$S(\omega) = \int_{-\infty}^{\infty} \langle I(t)I(t+\tau)\rangle \mathrm{e}^{j\omega\tau}\mathrm{d}t = S_{xx}(\omega) + S_{yy}(\omega) + S_{xy}(\omega) + S_{yx}(\omega), \quad (6.8)$$

where the individual noise spectra $S_{ij}(\omega)$ are given by similar integrals. The cross-correlation function for the fluctuations in the two LP modes is

$$C_{xy}(\omega) = \frac{\mathrm{Re}\left[S_{xy}(\omega)\right]}{\sqrt{S_{xx}(\omega)S_{yy}(\omega)}} = \frac{S(\omega) - S_{xx}(\omega) - S_{yy}(\omega)}{2\sqrt{S_{xx}(\omega)S_{yy}(\omega)}}. \quad (6.9)$$

Figure 6.21 shows the intensity noise spectra of the lasing and nonlasing LP modes as traces in Fig. 6.20a and Fig. 6.20b, respectively. The spectrum of the lasing mode contains mode-partition noise and fluctuations due to relaxation oscillations, whereas

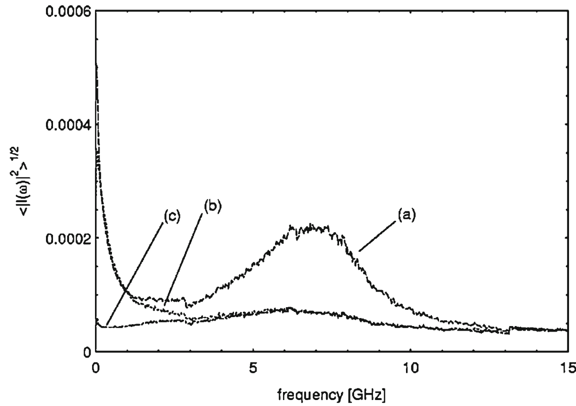

Fig. 6.21 Intensity noise spectra of the *a* lasing and *b* nonlasing modes. The lowest trace *c* is the background noise. Reprinted figure with permission from [32]. Copyright (1999) by the American Physical Society

the spectrum of the nonlasing mode only contains mode-partition noise. At low frequencies the LP mode intensity noise is relatively high, above the total intensity noise (not shown), which, according to (6.9), results in strong anti-correlation. A cross-correlation coefficient $-0.95 > C_{xy} > -1$ is measured [32], reaching a minimum at the PS current where the mode competition (and the individual polarization noise fluctuations) are strongest. A more detailed inspection of the mode-partition noise shows that the spectra are Lorentzian, having the same width for the two LP modes. At higher frequencies the relaxation oscillations are visible in the spectrum of the lasing mode, but not in the one of the nonlasing mode.

The polarization fluctuations during PS have been time-resolved in [34] by using a single-shot streak camera. The light emitted by a proton-implanted VCSEL has been projected on specific Stokes parameters, by using $\lambda/4$ and $\lambda/2$ wave plates and an optical Faraday isolator as described above. Figure 6.22 shows the experimental time traces of subsequent polarization switches, where each time the polarization is projected on one of the normalized Stokes parameters (see (6.4)). The polarization projection on s_1 shows a gradual increase whereas the projections on s_2 and s_3 show transient oscillations. Such oscillations are not surprising as the two LP modes with different optical frequency that simultaneously exist can beat when projected on polarization state different from x and y. However, the frequency of the oscillations decreases during the switch, which provides information about the optical nonlinearities involved in the process of PS [34]. The stochastic origin of the switches gives rise to a distribution of the PS time τ_{PS} (see the histogram in the inset of Fig. 6.22). The value of τ_{PS} is determined from s_1 time traces by measuring the time interval during which the intensity is between the 25 and 75% levels of the intensity after the switch. On average no difference between PS-up and PS-down times was observed. The mean value of τ_{PS} was found to be 3.7 ns.

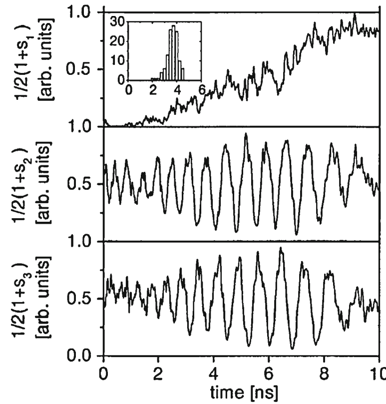

Fig. 6.22 Time-resolved measurements of the polarization during the switch. Each box shows the intensity projection on one of the Stokes parameters. The *inset* shows a distribution of transit times, defined as the passage time from 25 to 75% in the upper box curve, obtained from 120 polarization switches of the same device. Reprinted figure with permission from [34]. Copyright (2000) by the American Physical Society

The impact of the LP mode partition noise, as evidenced in Figs. 6.19 and 6.21, on the VCSEL relative intensity noise (RIN) characteristics has been investigated in [49, 50]. As shown in [50], the PMSR that can be quite high in a continuous-wave regime (more than 99%) is significantly degraded under large-signal modulation, especially for modulation frequencies larger than 100 MHz (see Fig. 6.23a). The DC prebias is adjusted so that the VCSEL operates in a single transverse mode when modulated. It has been found that it takes relatively long time to establish the dominant polarization state (see Fig. 6.23b).

The PMSR increases from 0 dB at the beginning of the square modulation pulse to its maximum value of 22 dB for a time of 2–5 ns, consistent with the characteristic time of polarization switching. As a result, the RIN is significantly degraded under large-signal modulation (Fig. 6.24). The low-frequency RIN increases with modulation frequency. The change can be as high as 25 dB for 500 MHz modulation.

Comparison of the VCSEL intensity noise to the fundamental shot noise (SN) limit has been carried out in [51–53]. In [51], the polarization cross-correlation C_{xy} is measured to be about −0.45 (−0.7) at frequency of 1 (10) MHz. Therefore, the polarization fluctuations do not cancel completely and the total intensity noise is always above the SN limit. Sub-Poissonian noise levels have been reported in [52] for a 3 μm diameter oxide-confined VCSELs with 40 dB SMSR. For frequencies ranging from 1 MHz to 5 GHz and currents from three to seven times threshold current, the noise stays at the SN limit. The results of [53] show that the amplitude squeezing is directly related to the PMSR and is only possible for the limiting case of PMSR ≈ 0 or PMSR ≈ 1. The last case has been realized in [54] for competing orthogonal LP fundamental and first order transverse modes and amplitude squeezing of 1.3 dB below the SN limit has been demonstrated.

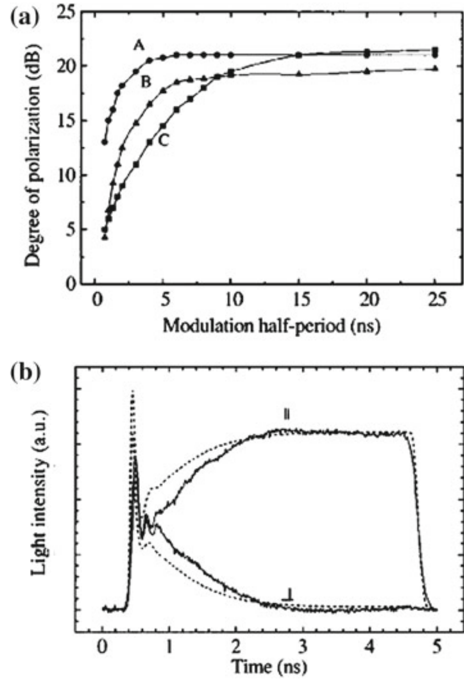

Fig. 6.23 **a** Degree of polarization plotted as a function of the half-period (pulse width) of the square-wave modulation for different VCSELs with (*A*) 850 nm emission wavelength, 8 μm aperture; (*B*) 960 nm, 12 μm; (*C*) 850 nm, 10 μm. **b** Polarization-resolved time response of a VCSEL driven with current pulses 10 ns in width. The VCSEL is biased DC at 4 mA. *Dashed lines* are calculated from the rate equation model (see Sect. 6.3.1). Reprinted with permission from [50]. Copyright 1995, American Institute of Physics

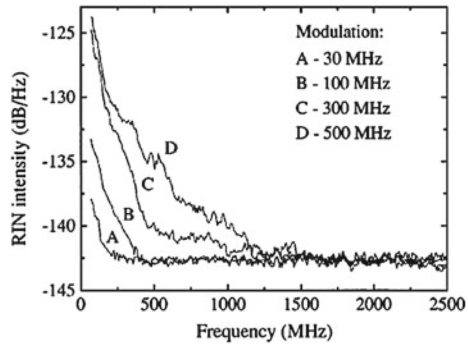

Fig. 6.24 RIN spectra for the dominant polarization under large-signal square-wave modulation. Reprinted with permission from [50]. Copyright 1995, American Institute of Physics

6.2.7 Pitchfork Type of Polarization Switching in VCSELs

In [22] and [27] a different type of polarization bistability in InGaAs VCSELs has been reported. In this case the solitary VCSEL characteristics show no evidence of PS in the whole region of injection currents, see Fig. 6.25 (left). With optical injection of a light pulse, orthogonally polarized to the VCSEL LP mode, a clear hysteresis in the polarization-resolved LI curve is observed, see Fig. 6.25 (right). At a current of $I = 3.52$ mA the wavelength of the injected light is 976.6 nm and the one of the VCSEL is 976.3 nm and does not change due to the PS. Remarkably,

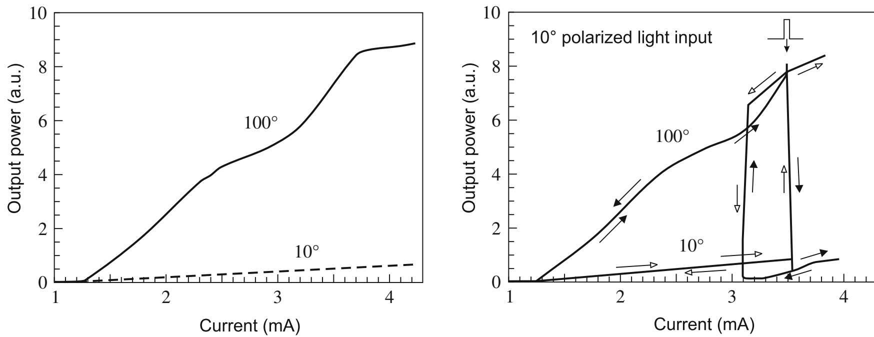

Fig. 6.25 Polarization-resolved LI curves of an InGaAs VCSEL: (*left*) solitary VCSEL and (*right*) VCSEL with injected light polarized at 10° (orthogonal to the solitary VCSEL polarization). After [22]

when the VCSEL is biased at this current its linear polarization remains fixed in the direction of the injected light polarization even when the injected light is blocked. PS induced by "orthogonal" optical injection, i.e., the linear polarization of the injected light is orthogonal to the one of the solitary VCSEL, has been known from an earlier demonstration [19]. However, in that case the solitary VCSEL is polarization bistable. As a function of the injected power two different scenarios of PS are experimentally distinguished in [19]: when the VCSEL is biased outside (inside) the bistable region the PS is reversible (non-reversible). In the last case the LP state of the VCSEL remains fixed in the direction of the injected light polarization, orthogonal to the one of the solitary VCSEL, even when the intensity of injected light is decreased to zero.

This clearly shows that, as a matter of fact, the solitary VCSEL investigated in [22] is polarization bistable. The second stable branch with orthogonal to the solitary VCSEL polarization is however, not evident in the polarization-resolved LI curve in Fig. 6.25 (left), i.e., PS can not be achieved by simply scanning the injection current of the solitary VCSEL. This second branch is however accessible by orthogonal optical injection. Such kind of polarization bistability is shown to be due to a pitchforck bifurcation [22, 27] (see also Sect. 6.3.1).

6.2.8 Voltage-Controlled Polarization Switching in Coupled-Cavity VCSELs

Nonthermal, electrically driven PS has been realized in coupled-cavity VCSELs (CC-VCSELs) in [55]. The CC-VCSELs consist of two λ-sized vertical cavities, detuned by 5% with respect to the DBR resonant wavelength, sharing a common DBR. The structure supports two longitudinal CC modes localized at $\lambda_S = 927$ nm and $\lambda_L = 953$ nm. The gain/absorption media consist of 8 nm thick InGaAs strained QWs: four in the shorter (top) cavity and two in the longer (bottom) cavity [56].

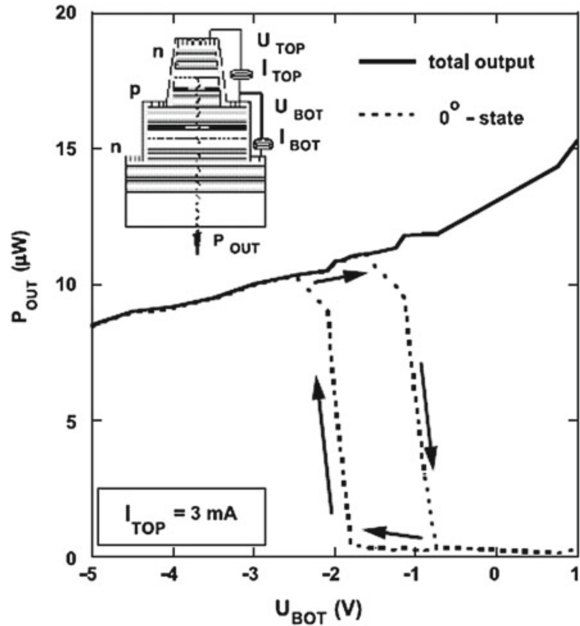

Fig. 6.26 Reverse-bias controlled polarization switching in a CC-VCSEL. The total output power is shown as a thick *solid line* and the polarization-resolved output power as a *dashed line*. The *inset* shows a schematic drawing of the CC-VCSEL [55] (© 2004 IEEE)

The CC-VCSELs have three electrical contacts that allow applying independent electrical signal of each cavity—see the inset of Fig. 6.26. In such a way, different working regimes can be achieved: single wavelength emission (either λ_S or λ_L), simultaneous dual wavelength emission, or no lasing region [57]. PS has been achieved in λ_S mode of operation when a pump current is injected in the top cavity and a reverse bias is applied to the bottom cavity [55]. This voltage driven PS is between LP states oriented along [110] and [1$\bar{1}$0] wafer axes and is with a hysteresis region of about 1 V and a high PMSR of 30 dB. The measured PS time is below 2 ns, limited by the experimental setup used in [55]. The two LP modes red-shift with the reverse bias however, the frequency splitting between them (about 13 GHz) remains constant, ruling out an electro-optically induced birefringence as a possible mechanism of PS. Instead, quantum-confined Stark effect is suggested as explanation of the observed PS [57]. The temperature dependence of polarization properties of CC-VCSELs has been investigated in details in [58].

6.2.9 Polarization Dynamics of Optically Pumped VCSELs

The polarization dynamics and the role of microscopic electron spin dynamics have been experimentally investigated in optically pumped VCSELs in [37, 59–64]. First manifestation of coherent spin dynamics in the stimulated emission has been given in [59] for InGaAs QW VCSELs lasing at 835 nm, pumped by 780 nm circularly

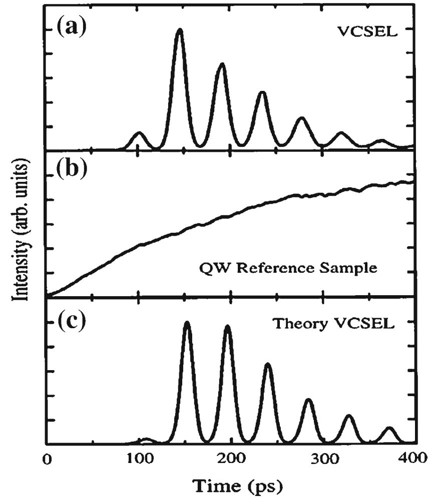

Fig. 6.27 **a** Time-resolved stimulated emission of the quantum well micro-cavity laser in a 2 T magnetic field. **b** Time-resolved emission of the quantum-well reference sample without a cavity. **c** Computed microcavity emission with parameters corresponding to the conditions of **a**. Reprinted figure with permission from [59]. Copyright (1997) by the American Physical Society

polarized light. The VCSELs are held at a low temperature of 15 K and a magnetic field B is applied in the plane of QWs, perpendicular to the light emission (Voigt geometry). Figure 6.27 shows the time-resolved stimulated emission for 2 T magnetic field in a VCSEL and in a reference QW sample without a cavity.

Pulsed laser emission at repetition frequency of 22 GHz, twice the electron Larmor frequency $\omega_L = g_e \mu_B B/\hbar$ with g_e the electron Lange factor and μ_B the Bohr magneton, is clearly seen. By using a non-equilibrium microscopic model the experimental results are explained as time-dependent modulation of gain/absorption for σ^+ and σ^- circularly polarized light by the respective carrier distribution for spin-up and spin-down electrons due to electron spin precession in the magnetic field (Fig. 6.27c).

In [60] GaAs VCSELs with bulk active region emitting at 860 nm are pumped by circularly polarized light with a wavelength of 800 nm at room temperature. As shown in Fig. 6.28, for σ^+ excitation the lasing output from the VCSEL mainly consists of σ^+ circularly polarized light and vice versa. This is attributed to the spin alignment of conduction band electrons as the valence holes are known to lose spin alignment on sub-picosecond scale because of the complexity of the valence band [64]. The electron spin-flip relaxation time has been measured in [60] by a time-resolved photoluminescence and shown to decrease with excitation power as $\tau_s \approx P_{exc}{}^{-0.7}$. At the threshold of $P_{exc} = 8.3$ mW, $\tau_s \simeq 40$ ps and the carrier density is estimated to be $N = 3$–$4 \cdot 10^{18}$ cm^{-3}.

A similar "memory" effect for the elliptical polarization of the pumped light has been found out for GaAs QW VCSELs in [61]. The ellipticity of the VCSEL output light is shown however to depend on the VCSEL linear birefringence $\Delta\nu_{brf}$ and to decrease as $\Delta\nu_{brf}$ is increased. It is also found that, although well aligned to the birefringence axes, the orientation of the VCSEL polarization can change by about 1.5° following the linear polarization of the pumped light as it is rotated by

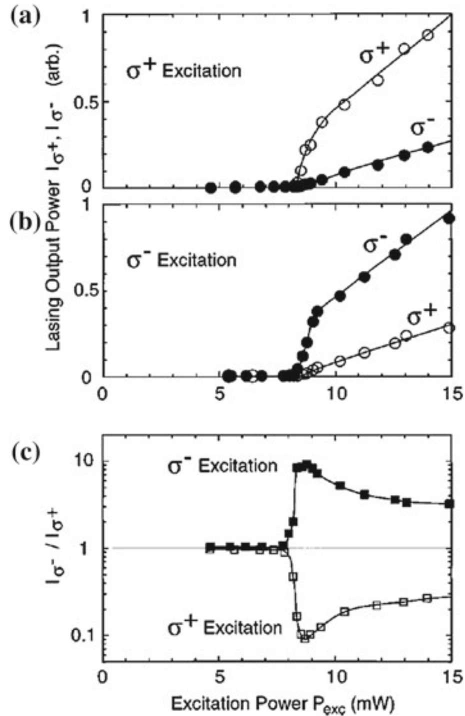

Fig. 6.28 Emission intensities of circular polarization components I_{σ^+} and I_{σ^-} vs. excitation power P_{exc}: **a** σ^+ pumping and **b** σ^- pumping. The ratio $I_{\sigma^+}/I_{\sigma^-}$ is shown as functions of P_{exc} in **c**. Here, P_{exc} denotes the time-averaged power of laser pulses with an 80 MHz repetition rate. Reprinted with permission from [60]. Copyright 1998, American Institute of Physics

90°. The spin-flip relaxation rate is estimated for the QW VCSEL used in [61] to be $\gamma_s = 300 \pm 150\,\text{ns}^{-1}$. Detailed characterization of picosecond polarization dynamics in optically pumped VCSELs at cryogenic temperatures has been carried out in [62, 63].

6.3 Physical Mechanisms and Theoretical Modeling of Polarization Dynamics in VCSELs

6.3.1 Polarization Bistability in Edge-Emitting Semiconductor Lasers and Gain Compression Model

Polarization switching in edge-emitting semiconductor lasers has been long known [65, 66] (see also [27] and the references therein). Explanation and theoretical modeling has been provided based on a gain compression mechanism in [67]. The phenomenological rate equations read

$$dP_X/dt = G_X\,(1 - \epsilon_{SX}P_X - \epsilon_{XY}P_Y)\,P_X - P_X/\tau_{PX} + \beta N/\tau, \tag{6.10}$$

$$dP_Y/dt = G_Y\,(1 - \epsilon_{SY}P_Y - \epsilon_{YX}P_X)\,P_Y - P_Y/\tau_{PY} + \beta N/\tau, \tag{6.11}$$

$$dN/dt = \eta I/eV_A - G_X(1 - \epsilon_{SX}P_X - \epsilon_{XY}P_Y)P_X \\ - G_Y(1 - \epsilon_{SY}P_Y - \epsilon_{YX}P_X)P_Y - N/\tau, \tag{6.12}$$

where P_X and P_Y are the photon densities for the *x*- and *y*-LP modes (TE and TM modes in [67]), respectively. The unsaturated gains are assumed to depend linearly on the carrier density N as $G_{X,Y} = \Gamma_{X,Y} v_{gX,Y} a_{X,Y}\left(N - N_{0X,Y}\right)$, where $\Gamma_{X,Y}$, $v_{gX,Y}$ and $a_{X,Y}$ are, respectively, confinement factors, group velocities and differential gains, and $N_{0X,Y}$ are the carrier densities at transparency for the two modes. The other parameters are: injection current I, injection efficiency η, electron charge e, volume of the active region V_A, photon and carrier lifetimes $\tau_{PX,Y}$ and τ, spontaneous emission factor β. The coefficients ϵ_{SX}, ϵ_{SY} and ϵ_{XY}, ϵ_{YX} are instantaneous self and cross gain compression terms, respectively. The approximation of instantaneous gain compression stems from the very fast intra-band relaxation of carriers, justifying the use of rate equations and quasi-equilibrium approximation, i.e., approximating the carrier distributions by Fermi–Dirac functions. As long as the dynamics of N is neglected and the gains $G_{X,Y}$ are assumed constant, the stability of the *x*- and *y*-modes can be determined following the graphical method of [68], which leads to the bistability condition [69]

$$\epsilon_{XY}\epsilon_{YX} > \epsilon_{SX}\epsilon_{SY}, \tag{6.13}$$

i.e., the so called "strong coupling" regime. It is interesting to notice that in one and the same VCSELs both strong and weak coupling regime (the sign in (6.13) reversed) can be realized simultaneously. For the two fundamental transverse modes the strong coupling regime always occurs. However, for a fundamental and an orthogonally polarized first order mode, the weak coupling mechanism results in their simultaneous lasing. This is due to the different spatial overlap of the optical modes: it is almost one for orthogonal LP modes of the same transverse order, while it is quite small for modes of different transverse order. Therefore, the modal gain cross-suppression coefficient between fundamental and first order orthogonally polarized transverse modes, that takes this spatial overlap into account, will be strongly reduced. Such a behavior is typical for VCSELs and can be evidenced, for instance, in the experimental results shown in Fig. 6.4.

The origin of the nonlinear gain is spectral hole burning [68, 70, 71], spatial hole burning [72] and carrier heating effects [73]. The relative contribution from these effects depends on the gain medium and on the device geometry. For the case of TE/TM polarizations the spectral hole burning effect has been calculated on the base of density matrix approach and $\boldsymbol{k} \cdot \boldsymbol{p}$ theory in [74] for bulk active material in the waveguiding configuration of [66] including strain contributions. In this way, the phenomenological model (6.10)–(6.12) has been supported by first-principle calculations, revealing the proper carrier density, strain and frequency dependence of the nonlinear gain contributions. Different experimental situations of lasing in a single polarization, in two polarizations, polarization switching and polarization bistability have been reproduced in [74] by using a few free parameters only, most

importantly the strain and the different losses of the two LP modes. For QW active material the nonlinear gain has been calculated in [75, 76].

The rate equations (6.10)–(6.12) have been used to model polarization dynamics in VCSELs in several works [27, 43–45, 50, 53, 77–80]. The large-signal modulation response has been modeled and compared to the experimental results in [50]. The VCSEL parameters, taken from the experiment, are the same for the two modes and the self and cross gain compression coefficients are also equal. The only difference is in the modal losses $\alpha_X - \alpha_Y = 0.1\,\text{cm}^{-1}$, which leads to a small difference in the photon lifetimes, defined as $\tau_{PX,Y} = (v_{gX,Y}\alpha_{X,Y})^{-1}$. Very good agreement with the experiment is evident from Fig. 6.23b, explaining the strong degradation of the degree of polarization for modulation frequencies higher than 100 MHz observed in Fig. 6.23a. In such a way, the increase of the polarization-resolved relative intensity noise in VCSELs (Fig. 6.24) is explained as an effect of the fluctuations in the maximum degree of polarization reached during each current pulse.

Langevin noise sources for the two LP modes have been introduced in the two-mode model in [53] and analytical expressions for the amplitude noise in each LP mode have been derived. It is concluded that generation of amplitude squeezed states of light in VCSELs is only possible in the two limiting cases: ideal two-polarization mode laser (PMSR $\simeq$ 1) and ideal single-polarization-mode laser (PMSR $\simeq$ 0); see the last part of Sect. 6.2.6.

According to the experimental results presented in Sects. 6.2.5 and 6.2.6, the gain/loss difference between the two LP mode of VCSELs changes with the injection current and PS takes place at the gain/loss equalization point (see Figs. 6.17 and 6.20). Assuming a linear dependence of the differential gains $a_{X,Y}$ on current, the two-mode model can be significantly simplified (reduced) by using the facts that the parameters for the two LP modes are nearly the same and that the photon and carrier lifetimes differ by about 3 orders of magnitude [77]. The bistability condition derived in the reduced model is

$$\epsilon_{XY} + \epsilon_{YX} > \epsilon_{SX} + \epsilon_{SY}, \tag{6.14}$$

and the PS time, i.e., the time the x-mode takes to attain half of its final intensity during a switch from the y-LP mode to the x-LP mode is

$$t_{1/2} = \tau_{PX}\left(\Gamma_Y a_Y \tau_{PY}/(\Gamma_X a_X \tau_{PX}) - 1\right)^{-1} \ln\left(P_X(0)/P_Y(0)\right). \tag{6.15}$$

The PS time is proportional to the photon lifetime and inversely proportional to the relative gain/loss difference between the two LP modes. There is a weaker logarithmic dependence on the initial conditions $P_{X,Y}(0)$. The relative gain/loss difference between the two LP modes is of the order of 10^{-3} (dichroism of about $0.12\,\text{ns}^{-1}$ in Fig. 6.20b divided by the estimated cavity loss rate of $\kappa = 120\,\text{ns}^{-1}$ [31]), resulting in a PS time of about 10 ns, in agreement with the experimental results in Sect. 6.2.6 (see Fig. 6.22a). An analytical expression for the dwell time in the polarization mode hopping regime is derived in [43] as

$$t_{\text{dw}} = 4/\left(J^2\sqrt{\pi R_{\text{sp}}/\delta^3}\,\exp\left(J^2/(4R_{\text{sp}})\right)\right), \tag{6.16}$$

where J is the reduced current above threshold, R_{sp} is the normalized spontaneous emission rate and $\delta = \epsilon_{XY} - \epsilon_{SY} = \epsilon_{YX} - \epsilon_{SX}$ (the bistability condition is $\delta > 0$). In Fig. 6.10 the analytical results (the solid and the dashed lines) are compared with the experimental result for both proton-implanted and air-post VCSELs showing a very good agreement. In a similar fashion, the polarization modulation response and stochastic polarization switching times are treated theoretically in [44, 45]. Different PS scenarios possible in the two-mode gain compression model are discussed in [78] and are similar to the ones in EELs.

Saturation of the internal optical losses that are due to heavy-hole–split-off band transitions in the p-doped DBR of the VCSEL has been considered in [79, 80] and incorporated in an "effective net-gain" compression term, so that

$$\epsilon_{S/C} = \epsilon_{gS/C} - (\Gamma_P/\Gamma)\,(\alpha_{P0}/g_{\text{th}})\,\epsilon_{PS/C}, \tag{6.17}$$

where $\epsilon_{gS/C}$, and $\epsilon_{PS/C}$, are the self/cross gain/absorption compression coefficients; Γ and Γ_P are the longitudinal confinement factors in active layer and p-doped DBR layers, g_{th} is the threshold gain value and α_{P0} the linear absorption coefficient. The physical origin of this saturation mechanism is the hole burning effect in the carrier momentum space for transitions between heavy-hole and split-off band because of the polarization dependence of the TME (see Sect. 6.1). Anisotropy of linear optical gain and losses due to directional current flow in VCSELs has been considered in [81, 82].

An interesting case of the two-mode gain compression model, described in [83], is the so called pitchfork bistability shown in Fig. 6.29. The parameters in (6.10)–(6.12) are [83]: $v_{gX} = v_{gY} = 6.7 \cdot 10^9$ cm/s; $\Gamma_X = 0.15$, $\Gamma_Y = 0.1505$; $a_X = a_Y = 3.25 \cdot 10^{-16}\,\text{cm}^2$; $N_{0X} = N_{0Y} = 10^{18}\,\text{cm}^{-3}$, $\tau = 3$ ns, $\tau_{PX} = 3$ ps, $\tau_{PY} = 2.989$ ps and $\epsilon_{SX} = \epsilon_{SY} = 1 \cdot 10^{-17}\,\text{cm}^3$, $\epsilon_{XY} = \epsilon_{YX} = 2 \cdot 10^{-17}\,\text{cm}^3$. In this case, as the current pump rate is increased, the solutions for the two LP modes bifurcate at a critical point and form branch A. Branch B is obtained only by injection of optical trigger pulse with TM (y) polarization [83]. Experimentally, such a "hidden" bistability has been indeed observed in VCSELs [22] (see Fig. 6.25 in Sect. 6.2.7). A very fast polarization bistable switching with PS time of 7 ps has been demonstrated when the VCSEL is triggered by ps optical pulses of two orthogonal polarizations [27].

6.3.2 Different Physical Mechanisms Can Lead to Net Gain Equalization in VCSELs

Based on the experimental findings presented in Sect. 6.2, different physical mechanisms that can lead to net gain equalization for the LP modes in VCSELs have been considered. They can be divided in two main groups: the first one takes into account the modification of the material gain and losses with the injection current

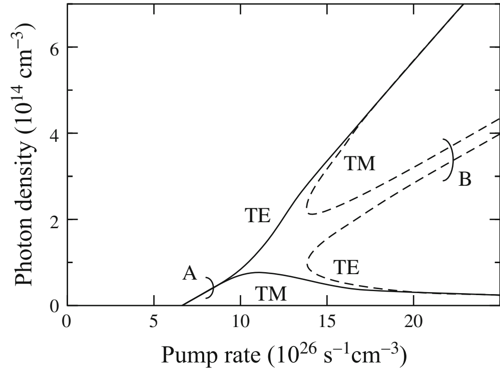

Fig. 6.29 Pitchfork bistability demonstrated numerically in [83]. TE/TM polarization coresponds to X/Y polarization in (6.10)–(6.12). The parameters are listed in the text. After [83]

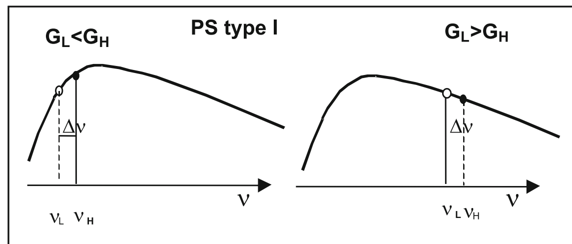

Fig. 6.30 Schematic representation of the material gain and the two LP cavity modes: the gain curve red-shifts with current heating giving rise to type I PS

(temperature) and the second considers such modifications for the modal gain, determined by the overlap of optical field with carrier distribution in the QW.

A specific feature of VCSELs is the enhanced heating due to the current flow through the DBRs, which leads to gain red-shift. As VCSELs support a single longitudinal cavity mode, which also red-shifts but about 3 times slower, its relative detuning to the gain maximum changes with current. This thermal mechanism has been put forward in [7, 23] to explain PS in VCSELs by considering two orthogonal LP modes with slightly different wavelengths. Then, due to a slightly larger gain, the VCSEL will operate on the higher frequency mode (H) at the lower frequency side of the gain maximum and vice versa (see Fig. 6.30). This has indeed been observed experimentally in [7, 23]. Such a thermal mechanism explains type I PS when transiting the gain maximum.

Not only the gain g , but also the internal losses α_p, which are mainly due to intervalence band absorption (IVBA) in the heavily p-doped DBR depend on the photon energy [33]. The higher frequency mode will be lasing if $g_{\mathrm{H}} = \alpha_{p\mathrm{H}}$ and $g_{\mathrm{L}} < \alpha_{p\mathrm{L}}$, which mutually subtracted and divided by the small difference $\Delta\nu = \nu_{\mathrm{H}} - \nu_{\mathrm{L}}$ can be written as $dg/d\nu > d\alpha_p/d\nu$. At the PS point the gains of the two LP modes are simultaneously equal to the losses and $dg/d\nu = d\alpha_p/d\nu$. As the IVBA decreases with the photon energy, i.e., $d\alpha_p/d\nu < 0$, the PS will be shifted to the higher energy side of the gain maximum where $dg/d\nu < 0$. The behavior of the gain and loss derivatives is shown in Fig. 6.31 as a function of the temperature rise of the VCSEL. The gain derivative is plotted for different initial positions on the gain curve, corresponding

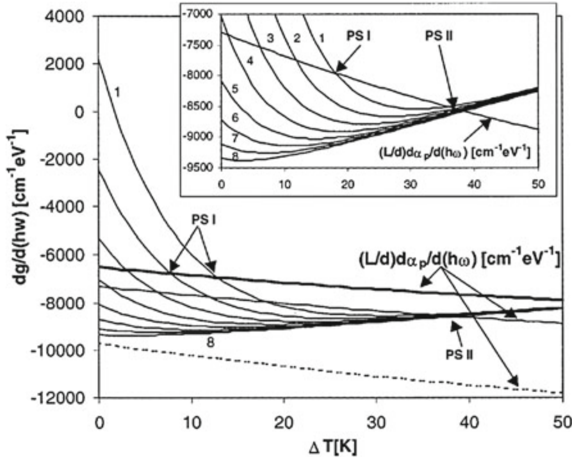

Fig. 6.31 Dependence of the gain derivative with respect to the photon energy on ΔT, which is the difference between the active region temperature at a certain current and at threshold (*solid curves 1–8*). For curve 1, $\hbar\omega_0$ is close to the gain maximum and $T_{\text{sub}} = 300\,\text{K}$. Each of the curves 2–8 corresponds to a relative increase of the substrate temperature of 4.5 K. The dependence of the loss derivative on ΔT is shown by the nearly *straight lines*. The initial points of thick and thin *solid lines* are taken at $(\alpha_p/\alpha_{tot})g \simeq 2000\,\text{cm}^{-1}$ and $T_{\text{sub}} = 300\,\text{K}$ and 350 K, respectively. The *inset* shows an enlargement [33]

to different substrate temperatures T_{sub} (solid curves 1–8). If the loss derivative also depends on the temperature, its initial value also changes with substrate temperature as illustrated by the three nearly straight lines in Fig. 6.31. PS now takes place at the crossing of the gain and loss derivatives. Depending on the laser temperature, gain offset, etc. different experimentally observed scenarios can be explained: PS type I at the higher frequency side of the gain maximum (see Sect. 6.2.2) or PS type I followed by PS type II (see Sect. 6.2.4).

The experimental results in Sect. 6.2.5 showing the strong dependence of PS on the anisotropic QW in-plane strain can also be explained in this framework, however two separate gain curves for the two LP modes need to be considered [10]. Gain calculations in presence of strain are done by using the Bir–Pikus Hamiltonian for the QW HH and LH bands [4, 5]. In Fig. 6.32a, the valence band energies of the first 3 QW levels are shown along the [110] and $[1\overline{1}0]$ axes as a function of the in-plane crystal momentum $2\pi/a_{\text{GaAs}}$ with a_{GaAs} being the lattice parameter of GaAs. The upper HH band exhibits a larger slope, and, consequently, a smaller density of states for crystal momentum $\boldsymbol{k}$ orthogonal to the direction of the tensile strain. This means that the hole population extends to a deeper level, i.e., the chemical potential (the quasi-Fermi level) goes deeper in the valence band for $\boldsymbol{k}$ along the $[1\overline{1}0]$ direction. Consequently, the overlap with the conduction states population distribution improves, or equivalently, the reduced density of states, and as a result the gain for the light linearly polarized along the $[1\overline{1}0]$ direction, increases. The resulting splitting of the gain curve is shown in Fig. 6.32b for different temperatures.

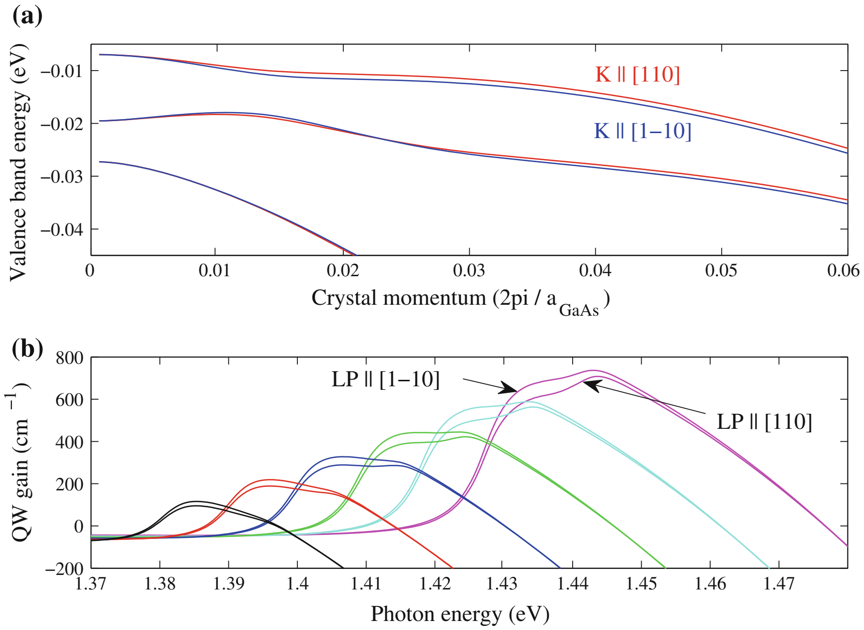

Fig. 6.32 **a** Valence band structure of a 10 nm GaAs/$Al_{0.25}Ga_{0.75}As$ QW along the [110] and [$1\bar{1}0$] axes for 0.02% tensile strain along [110]. **b** Gain for LP along the [110] and [$1\bar{1}0$] axes as a function of the photon energy for temperatures from 300 K (*magenta*) to 400 K (*black*) in steps of 20 K

It should be stressed that the gain anisotropy due to the splitting of the gain curve is much larger than the gain difference solely due to the strain-caused frequency splitting: for the case of Fig. 6.32 it is 60 and 2.5 cm^{-1}, respectively ($\Delta\nu = 42$ GHz).

In practice, one has to consider not only the material gain, but also the overlap of optical field and carrier density radial distributions, i.e., the modal gain. The modal gain can be changed due to change of optical field pattern (e.g., by thermal lensing) or of carrier distribution (e.g., by spatial hole burning). The current heating of the active region changes the transverse refractive index profile by the thermo-optic effect and leads to the creation of a waveguide (thermal lens). If one considers birefringent VCSELs, this effect is slightly different for the two LP modes. Therefore, the shorter wavelength mode may experience larger modal gain even when operating on the shorter wavelength side of the gain maximum, where its material gain is smaller [10]. With increasing injection current and active region temperature the waveguiding becomes stronger, the difference in the confinement between the two LP modes weaker, and the modal gain for the longer wavelength mode becomes larger. This mechanism explains PS type I in gain-guided VCSELs when operating at the short-wavelength side of the gain curve (see Fig. 6.4 in Sect. 6.2.2). All considered thermal PS mechanisms are consistent with the low cutoff frequency of PS modulation response in proton-implanted VCSELs (see Sect. 6.2.3).

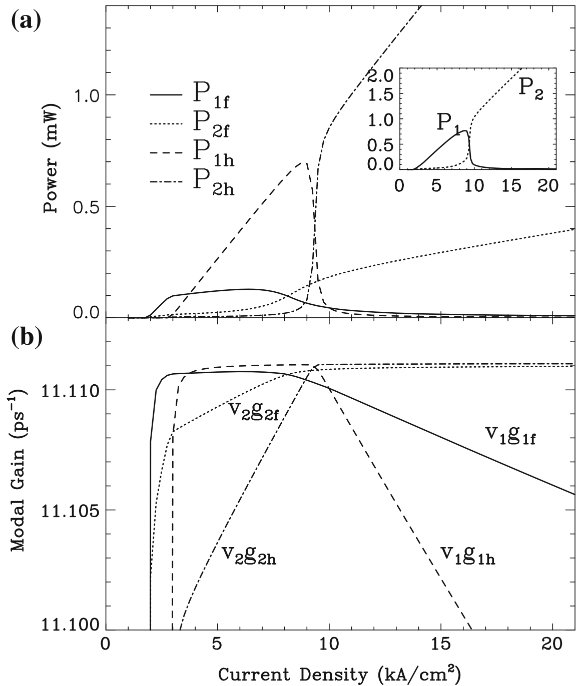

Fig. 6.33 **a** Steady-state power of the polarized transverse modes of a birefringent ($\Delta n_C = 2 \cdot 10^{-4}$) index-guided VCSEL for a refractive index step of 0.01. The total output power in each polarization appears in the inset. **b** Steady-state modal gain versus injection current density [84] (© 1997 IEEE)

An alternative modal gain equalization mechanism is provided by the spatial hole burning (SHB) effect [84]. In Fig. 6.33a, the output power of fundamental (f) and first-order (h) transverse modes are shown for the two orthogonal LP modes (denoted by 1 and 2) for an index-guided VCSEL. At low currents SHB is not significant and the carriers accumulate near the center of the device and, therefore, the gain of the better confined polarization 1 is larger for both transverse modes as seen from Fig. 6.33b. The situation changes with increasing current because SHB is deeper in the center of the device which leads to accumulation of carriers at the aperture edge and hence to an increase in the modal gain of the less confined polarization 2 for both transverse modes (Fig. 6.33b). Type I PS occurs when both transverse modes in polarization 2 reach the threshold gain.

6.3.3 Polarization Dynamics in VCSELs: The Spin-Flip Model (SFM)

A well established model of polarization dynamics in VCSELs is the spin-flip model due to San Miguel, Feng and Moloney (SFM) [85]. It considers transitions between conduction band (CB) and heavy hole valence band (HHB) and is relevant to unstrained or compressively strained QWs, i.e., when the first HH QW level

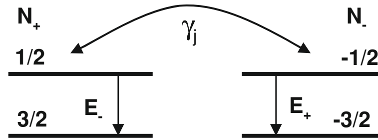

Fig. 6.34 Schematic representation of the VCSEL carrier reservoirs (CB and HH valence band), allowed transitions and spin-flip processes

has higher energy than the first LH level [5]. The projection of the total angular momentum along z (the direction of light propagation, perpendicular to the QW surface) is $J_z = \pm 1/2$ for CB and $J_z = \pm 3/2$ for HHB. Neglecting valence band-mixing, the CB and HHB carrier reservoirs can be considered as two subsystems of different spin orientation (Fig. 6.34). The allowed dipole transitions for light polarized in the plane of the QW (see Sect. 6.1) are those with $\Delta J_z = \pm 1$, i.e., those occurring within each of the two subsystems, and are associated with right (E_+) and left (E_-) circularly polarized light. The two subsystem populations N_+ and N_- are coupled through the spin-flip processes: if an excess of carriers is present in one of the two systems, their spin flips to the opposite orientation with a rate γ_j.

The SFM describes the composite system using the usual semiconductor rate equations for the two subsystems (E_-, N_+) and (E_+, N_-), complemented by amplitude (γ_a) and phase (γ_p) anisotropies that couple the two field components, and spin-flip processes that couple the two populations

$$dE_\pm/dt = \kappa\,(1+i\alpha)\,(N_\mp - 1)\,E_\pm - \left(\gamma_a + i\gamma_p\right)E_\mp, \tag{6.18}$$

$$dN_\pm/dt = -\gamma[N_\pm(1+2|E_\mp|^2) - \mu] - \gamma_j(N_\pm - N_\mp). \tag{6.19}$$

Here $\kappa = 1/(2\tau_P)$, $\gamma = 1/\tau_C$ and $\gamma_j = 1/\tau_j$, where τ_P, τ_C and τ_j are, respectively, the photon lifetime, carrier lifetime and spin-flip time; μ is the normalized injection current ($\mu \approx 1$ at threshold), and the phase–amplitude coupling, typical for semiconductor lasers, is taken into account by the linewidth enhancement factor α. The role of spin-flip becomes more manifest when the equations are written in terms of the semi-sum $N = (N_- + N_+)/2$ and -difference $n = (N_- - N_+)/2$ of the two populations, and the new spin-flip rate $\gamma_s = 2\gamma_j + \gamma$ is introduced, namely

$$dE_\pm/dt = \kappa\,(1+i\alpha)\,(N \pm n - 1)\,E_\pm - \left(\gamma_a + i\gamma_p\right)E_\mp, \tag{6.20}$$

$$dN/dt = -\gamma[N(1+|E_+|^2+|E_-|^2) + n(|E_+|^2 - |E_-|^2) - \mu], \tag{6.21}$$

$$dn/dt = -\gamma_s n - \gamma[N(|E_+|^2 - |E_-|^2) + n(|E_+|^2 + |E_-|^2)]. \tag{6.22}$$

Typical orders of magnitude of τ_P and τ_C are $\tau_P \sim 1$ ps, $\tau_C \sim 1$ ns. Should spin-flip processes occur on a time scale much faster than τ_P, the population difference n

could be adiabatically eliminated and the only relevant population variable would be N. But this is not the case: although much dependent on the QW composition and operating conditions, the time scale of spin-flip processes is intermediate between τ_P and τ_C. Hence, the complete system of equations must be considered in order to describe properly polarization dynamics in a VCSEL. This is the basic idea of SFM.

The spin-flip time for electrons has been measured at room temperature by a time-resolved pump-probe polarization-resolved absorption technique to be 32 ps for GaAs/AlGaAs [86] and 5.2 ps for InGaAs/InP [87] QWs. The spin-flip time for the holes is much faster, on a subpicosecond time scale [86, 87]. From the electron energy [86, 87], temperature [88] and excitation energy dependence of the spin-flip time the spin-flip mechanism relevant to the material system and operating conditions can be identified. For undoped GaAs QWs it is concluded that the spin-flip at room temperature is mainly governed by the D'ykonov–Perel' mechanism [89, 90], which takes into account the spin-splitting of the CB caused by the lack of inversion symmetry in III-V compounds with zincblende structure. This spin splitting can be described by introducing an intrinsic k-dependent magnetic field around which electron spins precess. The momentum scattering changes the effective magnetic field and, together with the spin precession, leads to spin dephasing. For InGaAs QWs the relevant mechanism is the one of Elliott–Yafet [91, 92], arising from the mixing of the wave functions in the conduction band with opposite spins caused by spin–orbit interaction. Electron momentum scattering caused by impurities (at low T) and phonons (at high T) couples the spin-up and spin-down states and leads to spin relaxation. Increasing the electron scattering makes the Elliott–Yafet mechanism more effective, while it decreases the effectiveness of the D'yakonov–Perel' processes. The third plausible spin-relaxation mechanism, the one of Bir–Aronov–Pikus [93, 94] resulting from the exchange interaction between electrons and holes has been shown to be dominant at low temperature (<40 K) only [88]. Much longer spin-flip times of 340 ps [95] and 280 ps [96] have been measured for InGaAs/InAlAs and InGaAs/GaAs QWs.

In the basis of the linearly polarized field components E_x and E_y, related to the circularly polarized ones by $\sqrt{2}E_\pm = E_x \pm i E_y$, the SFM reads [97, 98]

$$dE_{x,y}/dt = \kappa\,(1+i\alpha)\left[(N-1)\,E_{x,y} \pm inE_{y,x}\right] \mp \left(\gamma_a + i\gamma_p\right)E_{x,y}, \tag{6.23}$$

$$dN/dt = -\gamma[N(1+|E_x|^2+|E_y|^2) + in(E_y E_x^* - E_x E_y^*) - \mu], \tag{6.24}$$

$$dn/dt = -\gamma_s n - \gamma[n(|E_x|^2+|E_y|^2) + iN(E_y E_x^* - E_x E_y^*)]. \tag{6.25}$$

These equations admit LP and EP stationary solutions. The x-LP stationary solution is given by $E_y = 0$ and

$$E_x = \sqrt{\mu/\mu_x - 1}\,\mathrm{e}^{i\omega_x}, \qquad \mu_x = 1 + \gamma_a/\kappa, \qquad \omega_x = -\gamma_p + \alpha\gamma_a. \tag{6.26}$$

The y-LP stationary solution is given by $E_x = 0$ and

$$E_y = \sqrt{\mu/\mu_y - 1}\, \mathrm{e}^{i\omega_y}, \qquad \mu_y = 1 - \gamma_a/\kappa, \qquad \omega_y = \gamma_p - \alpha\gamma_a. \tag{6.27}$$

The EP states have very complicated implicit expressions in the general case that we do not report here. μ_x and μ_y are the thresholds of the two LP states. The *x*-LP (*y*-LP) state has the lower threshold if $\gamma_a < 0$ ($\gamma_a > 0$). This shows that the amplitude anisotropy γ_a is associated with dichroism. The frequency difference of the two modes is $\omega_y - \omega_x = 2(\gamma_p - \gamma_a) \approx 2\gamma_p$, because γ_p is usually much larger in absolute value than γ_a. Hence, γ_p in the SFM is the birefringence parameter, and, since it is usually taken positive, the *y*-LP (*x*-LP) is the high (low) frequency mode. The linear stability analysis of the LP states reveals the existence of different types of instability. The *x*-LP state is unstable with respect to a steady pitchfork bifurcation (a real eigenvalue that crosses zero) that occurs when the pump μ reaches the threshold value $\mu_{x,s}$ given by

$$\mu_{x,s} \approx 1 + \frac{\gamma_s}{\kappa\alpha - \gamma_p}\frac{\gamma_p}{\gamma}. \tag{6.28}$$

The *y*-LP state is unstable due to a Hopf bifurcation at

$$\mu_{y,H} \approx 1 + \frac{2\left(\gamma_s^2 + 4\gamma_p^2\right)}{\kappa\left(2\alpha\gamma_p - \gamma_s\right)}\frac{\gamma_a}{\gamma}. \tag{6.29}$$

A Hopf bifurcation affects also the *x*-LP state, but only for $\gamma_a > 0$, and its threshold is

$$\mu_{x,H} \approx 1 + \frac{2\left(\gamma_s^2 + 4\gamma_p^2\right)}{\kappa\left(2\alpha\gamma_p + \gamma_s\right)}\frac{\gamma_a}{\gamma}. \tag{6.30}$$

Assuming $\gamma_p > 0$, the above instabilities lead to different stability scenarios depending on the sign of γ_a. Let us consider first the case $\gamma_a < 0$, which means that the *x*-LP state (lower frequency) is selected at threshold. The stability diagram is shown in Fig. 6.35. In this case the only instabilities are the pitchfork instability of the *x*-LP state and the Hopf instability of the *y*-LP state. The threshold $\mu_{y,H}$ of the latter displays a vertical asymptote at the critical birefringence

$$\gamma_p \approx \gamma_s/2\alpha = \gamma_c. \tag{6.31}$$

The *y*-LP state is always unstable for $\gamma_p > \gamma_c$ and it is stable for $\gamma_p < \gamma_c$ only above the curve $\mu_{y,H}$. The lower part of Fig. 6.35 displays the evolution of the field intensities under a forward and backward scan of the pump parameter μ for a value of the birefringence $\gamma_p = 4\gamma$ to the left of the critical one. In the forward scan the *x*-LP state is stable from laser threshold to the instability threshold $\mu_{x,s} \sim 1.21$. The transition to the *y*-LP state (type II PS) however, is not abrupt. Elliptically polarized (EP) and unpolarized states are found before the VCSEL switches to the *y*-LP state at about $\mu = 1.37$. If now the direction of the scan is reversed, the VCSEL remains

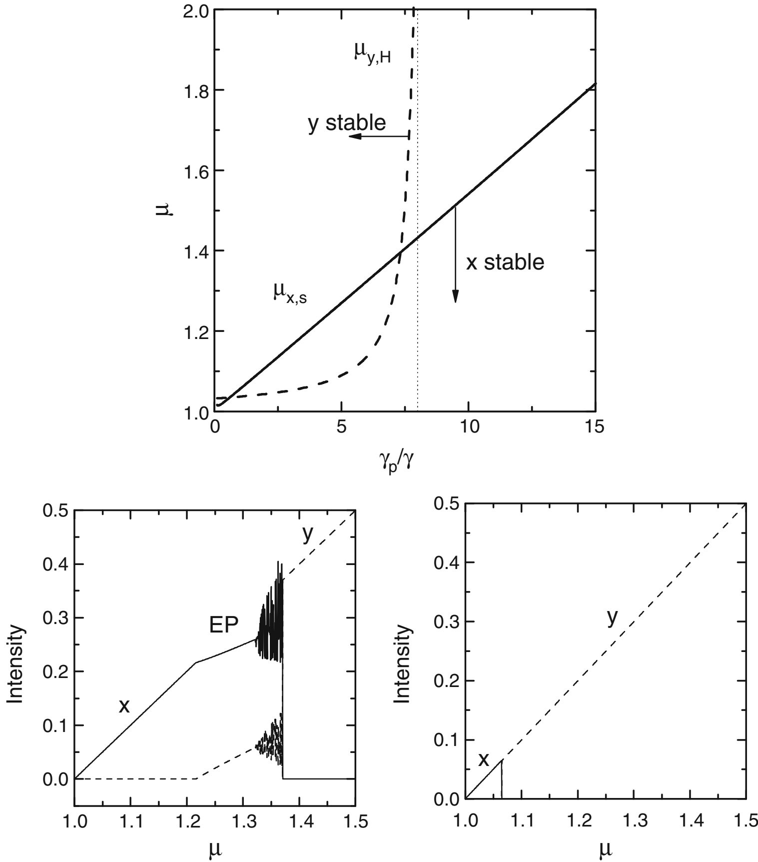

Fig. 6.35 *Top*: stability diagram for the LP solutions of the SFM with $\gamma_a = -0.1\gamma$. The x-LP state is stable below the *solid line*, the y-LP state is stable above the *dashed line*. The *vertical dotted line* indicates the critical birefringence $\gamma_c = \gamma_s/(2\alpha)$. Other parameters are: $\kappa = 300\gamma$, $\gamma_s = 48\gamma$, and $\alpha = 3$. *Bottom*: evolution of the field intensity under a forward (*left*) and a backward (*right*) scan of the pump parameter μ and $\gamma_p = 4\gamma$. The forward scan shows a type II PS mediated by EP and unpolarized states

in the y-LP state until the Hopf instability threshold $\mu_{y,H} \sim 1.065$ is crossed (type I PS). A relatively large bistability range exists where the y-LP state coexists with the x-LP state, the EP state and an unpolarized state.

If $\gamma_a > 0$ the state selected at threshold is the y-LP state. The stability domains of the two LP states are shown in Fig. 6.36. The x-LP state is stable in the region delimited by the two curves $\mu_{x,s}$ and $\mu_{x,H}$, which cross at $\gamma_p \sim 2\alpha\gamma_a$. The y-LP state is always stable for $\gamma_p < \gamma_c$ and it is stable for $\gamma_p > \gamma_c$ only below the curve $\mu_{y,H}$. Therefore, the interesting dynamics now occurs when $\gamma_p > \gamma_c$, as shown in the lower part of Fig. 6.36, where we chose $\gamma_p = 10\gamma$. In the forward scan, the VCSEL switches from the y-LP to the x-LP state (type I PS) at $\mu_{y,H} \sim 1.16$. Increasing

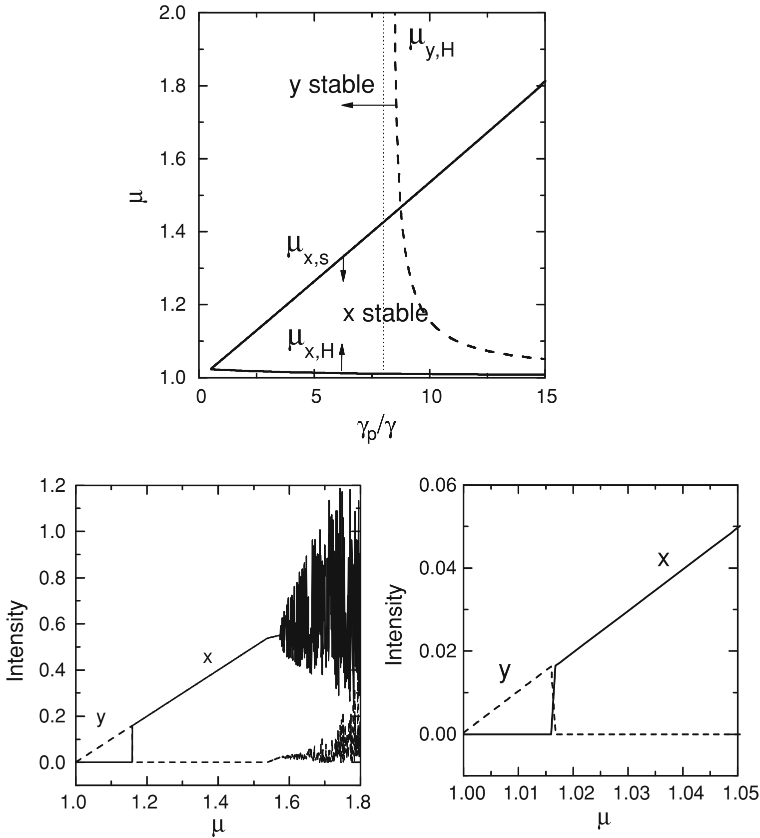

Fig. 6.36 *Top*: stability diagram for the same parameters as in Fig. 6.35 and $\gamma_a = 0.1\gamma$. The x-LP state is stable in between the two *solid lines*, while the y-LP state is stable below the *dashed line*. *Bottom*: evolution of the field intensity under a forward (*left*) and a backward (*right*) scan of the pump parameter μ and $\gamma_p = 10\gamma$. A type I PS in the forward scan is visible

further the pump the x-LP state also becomes unstable at $\mu_{x,H} \sim 1.54$. Similarly to the previous case, an EP state followed by an unpolarized state are observed. Yet, as in this case the y-LP state is always unstable for large μ, the VCSEL never switches to the y-LP state. If the pump is reduced starting form the unpolarized state, the same EP and x-LP states are observed as in the forward scan, but now the x-LP state is stable up to very small values of the pump. The VCSEL returns to the y-LP state only at $\mu_{x,H} \sim 1.017$. In this case there is a large range of pump values for which both LP states are stable.

Summarizing, the main features of the SFM are:

– for $\gamma_a < 0$ and $\gamma_p < \gamma_c$ a type II PS is observed increasing the pump;
– for $\gamma_a > 0$ and $\gamma_p > \gamma_c$ a type I PS is observed increasing the pump;
– the PS for increasing pump is always towards the gain disfavored mode;

– large bistability domains exist for intermediate pump between the two PS;
– the critical birefringence $\gamma_c = \gamma_s/(2\alpha)$ which separates the two cases represents a combination of the two main ingredients of the model: spin-flip processes (γ_s) and saturable dispersion (α).

The SFM has been extensively studied and further elaborated and hereafter we give a brief account of the main results. Systematic investigation of the role of optical anisotropies has been carried out in [99]. A period doubling sequence has been identified in the dynamical instability of the EP state shown above that leads to unpolarized emission. Circular anisotropy caused by optical activity has been ruled out because of the helicity reversal upon light reflection by the laser mirrors. However, circular anisotropy σ_c caused by the Faraday effect (magnetic field along light propagation direction) results in a term $\pm i\sigma_c E_\pm$, added to the right side of (6.20) [99, 100]

$$dE_\pm/dt = \kappa\,(1 + i\alpha)\,(N \pm n - 1)\,E_\pm - \left(\gamma_a + i\gamma_p\right) E_\mp \pm i\sigma_c E_\pm. \tag{6.32}$$

Such a circular anisotropy is shown [99] to convert the LP states given by (6.26) and (6.27) in EP ones, which are however unstable close to threshold. The previous EP steady-states found in a small domain above $\mu_{x,s}$ are now stable from threshold until a certain value of the pump and their ellipticity increases with the pump. The PS between EP states accompanied by dynamical instabilities is investigated in [100].

The general case of misaligned amplitude and phase anisotropies has been discussed in [101]. The misalignment converts the LP states in EP ones, and the orientation and ellipticity (especially the ones of the nonlasing mode) may strongly change with the injection current at large misalignments. This explains the experimental results shown in Sect. 6.2.4 on PS between EP states.

The important role of polarization fluctuations caused by the spontaneous emission noise has been pointed out in [102] and analytical expressions for the solution of Langevin SFM equations written in terms of Stokes components have been provided. It has been pointed out that time-resolved polarization measurements could provide information for all time scales and anisotropies involved. Langevin noise is considered in [103], too, where the limit $\kappa\,(\mu - 1)\,\gamma/\gamma_s \ll \gamma_p \ll \gamma_s$, i.e., VCSEL with a relatively high spin-flip rate and operating not too far from threshold, is discussed. In this limit, if amplitude anisotropies are ignored ($\gamma_a = 0$) and the lasing mode is the one at high frequency ($\omega_y = \gamma_p$), the complex conjugated eigenvalues describing polarization fluctuations are

$$\lambda = -\kappa\,(\mu - 1)\,\gamma/\gamma_s \pm i\left[2\gamma_p + \alpha\kappa\,(\mu - 1)\,\gamma/\gamma_s\right]. \tag{6.33}$$

The imaginary part of the eigenvalues determines the frequency at which resonance peaks in the optical spectrum occur, and the real part determines the width of these peaks. Adding to λ the contribution $i\gamma_p$ of the lasing mode, (6.33) predicts the existence of two peaks with the same width at frequencies ω_{sp} and ω_{conj}

$$\omega_{\mathrm{sp}} = -\gamma_p - \alpha\kappa\,(\mu - 1)\,\gamma/\gamma_s, \qquad \omega_{\mathrm{conj}} = 3\gamma_p + \alpha\kappa\,(\mu - 1)\,\gamma/\gamma_s. \tag{6.34}$$

The peak centered at ω_{sp} is the spontaneous emission peak associated with the nonlasing mode. The peak at ω_{conj} is due to four-wave mixing between the lasing and nonlasing modes. Equation (6.34) shows that the frequency of the spontaneous emission peak is red-shifted with respect to that of the low frequency mode ($\omega_x = -\gamma_p$) by an amount $\alpha\kappa\,(\mu - 1)\,\gamma/\gamma_s$ proportional to the optical power $\mu - 1$ and inversely proportional to γ_s. If we repeat the calculation for the case of a VCSEL operating on the low frequency mode, we obtain the same red-shift for the spontaneous emission peak associated with the high-frequency mode. This means that the frequency separation between the lasing and nonlasing modes, due to the nonlinear effects, is larger (smaller) than $2\gamma_p$ when the lasing mode is the one with high (low) frequency. The same results have been obtained independently in [104].

The nonlinear polarization anisotropy $\alpha\kappa\,(\mu - 1)\,\gamma/\gamma_s$ has been measured in [30] in proton-implanted VCSELs observing: (i) the red-shift of the nonlasing mode, (ii) the four-wave mixing peak, and (iii) the correlations between polarization fluctuations. The measured value $\alpha\kappa\,(\mu - 1)\,\gamma/\gamma_s = 3$–$4\,\text{ns}^{-1}$ allows to estimate $\gamma_s = 100 - 800\gamma$ using $\kappa = 133 - 600\,\text{ns}^{-1}$, $\mu \approx 2$ and $\alpha = 3$–4. The approach has been generalized in [31] for the case of misaligned birefringence and dichroism and analytical expressions for the strength of the polarization fluctuations for polarization projections along the azimuth and ellipticity (see Sect. 6.2.6) have been obtained. All this allowed, as shown in Sect. 6.2.6 (see Figs. 6.19, 6.20), the predictions of the SFM to be experimentally confirmed [30–32], and to estimate the relevant VCSEL parameters.

Two consecutive PS in the same VCSEL (see Sect. 6.2.4, Fig. 6.13) have been explained by extending the SFM to include a more realistic temperature dependent QW gain in order to account for the misalignment of the LP cavity modes with the gain maximum and their relative shifts [105]. This extended model has also been used in [39] to explain PS through elliptical states and dynamical instabilities (see Sect. 6.2.4, Figs. 6.14, 6.15).

The interplay of polarization and transverse mode dynamics has been studied using the SFM, extended to different degree of complexity in a number of works [106–110] and its impact on the intensity noise has been analyzed in [111].

The SFM has been supported by a full microscopic model developed in [112, 113] and based on a rigorous vectorial solution of the Maxwell equations coupled to the generalized semiconductor Bloch equations. Valence band mixing is taken into account for the first HH and LH subbands, as well as how they are impacted by an anisotropic strain in the QW. Spatial hole burning, carrier heating due to Fermi blocking and many-body effects are considered in a self-consistent manner. The stability diagrams for the LP states, calculated as a function of the anisotropic strain in [112] fully confirm the validity of the SFM given by (6.20–6.22): PS appears in exactly the same fashion as a result of combined action of birefringence and saturable dispersion. In order to reduce the complexity of the fully microscopic model, a macroscopic model has been derived in [113] by linearization around the VCSEL working point, while all coefficients are obtained on the base of the microscopic model. In [114] analytical expressions for the optical susceptibility of uniaxially stressed QWs have been derived in free-carrier and low temperature

approximations following [105]. The PS behavior obtained by this simplified model [46] agrees well with the experimental results presented in Sect. 6.2.5.

The SFM has been modified to consider the in-plane component of the carrier momentum in the QW in [115], where the impact of hole in the momentum alignment for the LP states has been considered. This impact has been shown to be rather small due to the much larger relaxation rate of the momentum than that of the spin.

The effect of the HH–LH band mixing and the fact that the hole spin relaxes on a sub-picosecond time scale, much faster than the CB electrons, have been studied in [116]. It was found that the effect of the valence band mixing is rather small, while the one of the instantaneous valence band spin-flip could be significant. The reason is that the gain and dispersion coefficients of the CB electrons which only participate in the polarization dynamics in that case are very different from those of the total population.

The SFM has been also extended to take into account the effects of spectral hole burning (SpHB) in [117]. The SpHB contribution results in a single additional term in (6.20), namely

$$dE_{\pm}/dt = \kappa\,(1+i\alpha)\,(N \pm n - 1)\,E_{\pm} - \left(\gamma_a + i\gamma_p\right)E_{\mp} - 2b\,(1+i\beta)\,|E_{\pm}|^2\,E_{\pm}, \tag{6.35}$$

where the coefficients b and β are obtained from the microscopic model. Equation (6.35) provides a direct link to the two-polarization-mode gain compression model discussed in Sect. 6.2.4. In the LP basis it reads

$$\begin{aligned} dE_{x,y}/dt = {} & \kappa\,(1+i\alpha)\left[(N-1)\,E_{x,y} \pm inE_{y,x}\right] \mp \left(\gamma_a + i\gamma_p\right)E_{x,y} \\ & - b\,(1+i\beta)\left[\left(\left|E_{x,y}\right|^2 + 2\left|E_{y,x}\right|^2\right)E_{x,y} - E_{y,x}^2 E_{x,y}^*\right], \end{aligned} \tag{6.36}$$

i.e., SpHB leads to self and cross gain compression, with the coefficient of cross-compression which is twice those of self-compression and four-wave mixing. Quite importantly, the model of [117] predicts double PS for $\gamma_a > 0$, as shown in Fig. 6.37. Double PS requires that the y-LP state has two stability domains: one close to threshold (as in Fig. 6.36) and one for values of the pump larger than $\mu_{x,s}$. This second stability domain actually exists also in the standard SFM, but only for very large values of the pump. SpHB makes it accessible to lower pump rates. The first PS in Fig. 6.37 is of type I and it is followed by a type II PS through elliptical states and dynamical instabilities in the typical SFM scenario. Double PS of such order has indeed been observed experimentally in proton-implanted VCSELs (see Sect. 6.2.4 and Fig. 6.15).

Asymptotic reduction of the SFM to two equations only has been suggested in [118] for the parameter region $|\gamma_a| \ll |\gamma_p| < 1$. It allows for analytical studies of the elliptically polarized steady state and periodic solutions and identifies the bifurcation sequence in the PS transitions. These transitions depend on unstable limit cycles and stable EP states as well as time-periodic states may appear as alternate attractors to the x-LP and y-LP states.

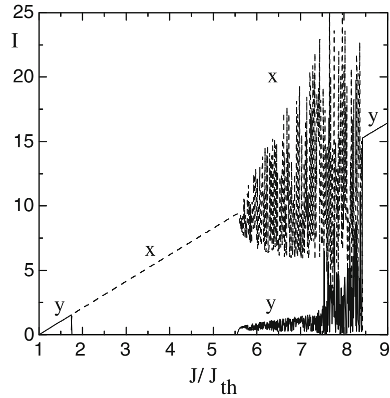

Fig. 6.37 Forward scan of the pump current for $\kappa = 534\gamma$, $\alpha = 1.22$, $\gamma_a = 0.25\gamma$, $\gamma_p = 57\gamma$ and dipole dephasing rate $10^4\gamma$ leading to $b = 0.48$ and $\beta = 0.05$. A type I PS y to x is followed by a type II PS x to y

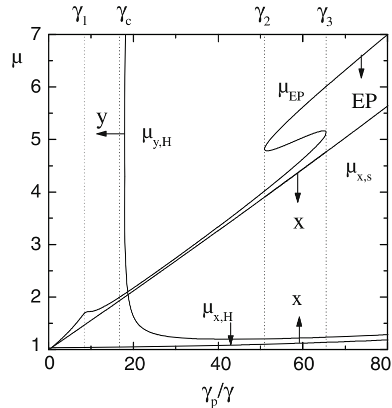

Fig. 6.38 Complete stability diagram for the LP and EP stationary solutions of the SFM. $\gamma_a = 0.1\gamma + 0.01\gamma_p$. The other parameters are $\kappa = 600\gamma$, $\gamma_s = 100\gamma$, and $\alpha = 3$

A complete study of the EP states in the SFM, valid for any γ_p, has been carried out in [119]. An implicit expression for the Hopf bifurcation of the EP states has been derived and revealed interesting phenomena for large birefringence, of the order of the spin-flip relaxation rate. The threshold μ_{EP} for the EP solution is plotted together with the instability thresholds of the LP solutions $\mu_{x,s}$, $\mu_{x,H}$, and $\mu_{y,H}$ in Fig. 6.38.

The stability domain of the EP solution displays some unexpected features: a maximum at a characteristic value of the birefringence $\gamma_1 \sim \gamma_c/2$ and an S-shaped form between the birefringence values $\gamma_2 \sim 3\gamma_c$ and γ_3, i.e., two disjoint stability domains. Numerically, it was shown in [119] that these domains are accessible when decreasing the pump leading to the conclusion that among the three Hopf bifurcations of the EP state that exist for $\gamma_2 < \gamma_p < \gamma_3$, two (the smallest and the largest) are supercritical, while the other (the intermediate one) is subcritical. It was also shown that the pitchfork bifurcation $\mu_{x,s}$ is subcritical if $\alpha < 1$. In that case there is bistability between the EP and x-LP states below $\mu_{x,s}$. All these interesting theoretical predictions remain to be found experimentally.

The modulation properties of light polarization have been investigated in the framework of the SFM in [120–122]. In [120, 121], it has been shown that the PS bifurcation is delayed when the speed of the current ramp is increased, an example of critical slowing down in a dynamical system operated close to a bifurcation point. Nevertheless, the SFM predicts high-speed PS modulation which can be used to rule out the thermal mechanisms, as has been done for the case of Fig. 6.7 [26] in Sect. 6.3.2. However, alternative nonthermal mechanism as saturable inter-valence band absorption [79] or gain compression due to carrier heating and spectral hole burning as discussed in Sect. 6.3.2 might also be possible. The small-signal polarization response has been investigated in [122] for both type I and type II PS as a function of the spin-flip rate. In the case of a dominant LP the small-signal modulation response is similar to the relative intensity noise characteristics calculated numerically and analytically in [123]. However, for small γ_s, in the region of dynamical instabilities, a multi-peaked modulation response with frequencies varying with injection current has been observed.

6.4 Conclusions and Perspective Applications of Polarization Dynamics of VCSELs

In this chapter we wrapped up the recent results on polarization dynamics of solitary VCSELs, especially the occurrence and dynamical characteristics of polarization switching (PS). The first two parts were devoted to the experimental findings on polarization dynamics of VCSELs. Due to the emission of light perpendicular to the surface of the quantum well and the usually symmetric vertical resonator there is no a priori intrinsic polarization anisotropy mechanism in VCSELs. Small residual strain and electro-optic effect explain the emission of linearly polarized light with a common orientation along [110] or [$1\overline{1}0$] crystallographic directions. Experimentally, PS between the two fundamental transverse modes with linear and orthogonal to each other polarization (LP) is observed. It could happen, with increasing the injection current, from higher to lower frequency mode (PS type I) or in the opposite way—from lower to higher frequency mode (PS type II). Such PS is observed for all different types of VCSELs: proton-implanted, oxide-confined and air-post. It could happen through a region of a noise driven polarization mode hopping or a hysteresis. In the first case, the dwell time scales several orders of magnitude with the injection current. In some VCSELs PS happens between elliptically polarized (EP) states rather than LP ones. The orientation and ellipticity of these states may also continuously change with the current. A particular transition, reported in several experiments, is the following: LP (ν_L) $\rightarrow$ EP $\rightarrow$ dynamical instabilities $\rightarrow$ PS to LP (ν_H). Double PS in the order type I followed by type II has also been reported. Externally applied in-plane anisotropic strain strongly modifies the polarization behavior of VCSELs by introducing well controlled birefringence and dichroism. PS type II persists in a birefringence interval of about 35 GHz and can be continuously tuned in the whole region of fundamental mode emission. By current modulation around the PS point,

the cut-off frequency for PS response has been shown to be low and to coincide with the frequency of the thermal response for proton-implanted VCSELs or to be high, indicating nonthermal PS mechanisms for air-post VCSELs. Polarization bistability of pitchfork type has been observed experimentally, too.

In the third part we discussed some physical phenomena that explain these various experimental findings. Two different thermal mechanisms due to current induced self-heating of VCSELs are identified: the first considers the faster spectral red-shift of the gain curve with respect to the two LP cavity modes with slightly different wavelength. Passing through the gain maximum leads to PS type I, and passing through a net gain equalization point when considering the spectral dependence of inter-valence band absorption can lead to PS type I, double PS (type I followed by type II) or type II PS only. The second thermal mechanism is relevant to gain-guided VCSELs and modifies the modal gains of the two LP modes by the thermal lensing effect leading to PS type I. Similarly, spatial hole burning can also lead to PS type I by improving the modal gain for the longer wavelength mode with increasing injection current. To explain the abrupt switch, gain nonlinearities have been taken into account into a phenomenological two-polarization-mode gain equalization model following the earlier works on PS in edge-emitting lasers. A more comprehensive model that considers the spin-flip dynamics has been developed by San Miguel, Feng and Moloney and is called SFM (spin-flip model). SFM predicts fully isotropic VCSELs to emit linearly polarized light, with direction that diffuses on the timescale of the coherence time. Taking the birefringence into account PS type II for small birefringence and PS type I for large birefringence is predicted. The switching scenario LP (ν_L) $\rightarrow$ EP $\rightarrow$ dynamical instabilities $\rightarrow$ PS to LP (ν_H) has been first predicted and later confirmed experimentally. Recent predictions of SFM, that still await experimental confirmation, are the bistability between LP and EP states and an S shape of the EP region for large birefringence. Double PS in order type I–type II is possible with the SFM if it is combined with a thermal red-shift model or if spectral hole burning is taken into account. The SFM is indispensable for explaining the experiments on optically pumped VCSELs with circular or elliptical polarization and the coherence spin precession in the presence of a longitudinal magnetic field.

Polarization switching and instabilities are often not desirable in practice, as they cause excess noise and increasing bit error rate. Therefore many research has been done in order to stabilize the polarization, which is described in detail in Chap. 5 of this book. Alternatively, one can make use of PS in VCSELs in order to enhance its functionality or achieve better performance. Hereafter we discuss some ways how this can be done.

Digital optical signal processing with 1 and 0 states being the two orthogonal LP states has the advantage that the laser is always lasing throughout the operation and changes states without change of carrier density. Sub-nanosecond speed and high-contrast-ratio PS is easily achieved by injection of a short electrical or optical pulse. As the switching of one LP mode is always complementary to the other one, two complement logic functions are achieved in a single logic gate or complement output is available in a flip-flop circuit [124]. Flip-flop is a basic memory element in digital

systems with two stable states. It is used in clock pulsed sequential synchronous systems, changing its state Q_n to Q_{n+1} at an occurrence of a clock pulse. For example the set–reset (SR) flip-flop keeps the same state if the set and reset inputs are zero but changes to 0 or 1 when the reset or the set inputs are 1. Optical logic gates and different flip-flops based on PS are demonstrated in [124] with EEL. Nonthermal, electrically driven PS has been realized in coupled-cavity VCSELs in [55] with a switching time below 2 ns, limited by the experimental setup. All-optical flip-flop operation based on PS in VCSELs has been demonstrated in [19, 125, 126]. High repetition rates of 5.3 GHz [27] and 10 GHz [125] and low switching energy of 0.3 fJ [125] have been demonstrated and a scaling to a 100 GHz repetition rate seems feasible [27]. All-optical signal regeneration with timing jitter reduction has been demonstrated in [126] by using AND gate and reset operations performed by polarization bistable VCSELs. One-bit all-optical buffer memory with shift register function has been experimentally demonstrated in [127] using an array of polarization bistable VCSELs. Injection of spin-polarized electrons has been theoretically shown in [128] to have the capacity of reducing twice the VCSEL threshold current.

Acknowledgments Some of the works presented in this chapter have been undertaken with other past and present colleagues, as acknowledged via the relevant reference citations. KP wishes to acknowledge the FWO (Fund for Scientific Research - Flanders) and the Research Council (OZR) of the Vrije Universiteit Brussel.

References

1. H. Li, K. Iga (eds.), *Vertical-Cavity Surface-Emitting Laser Devices* (Springer, Berlin, 2003)
2. C. Wilmsen, H. Temkin, L.A. Coldren (eds.), *Vertical-Cavity Surface-Emitting Lasers* (Cambridge University Press, Cambridge, 1999)
3. L.A. Coldren, S.W. Corzine, *Diode Lasers and Photonic Integrated Circuits* (Wiley, New York, 1995)
4. W.W. Chow, S.W. Koch, M. Sargent III, *Semiconductor-Laser Physics* (Springer, Berlin, 1994)
5. S.L. Chuang, *Physics of Optoelectronics Devices* (Wiley, New York, 1995)
6. C.J. Chang-Hasnain, J.P. Harbison, G. Hasnain, A.C. Von Lehmen, L.T. Florez, N.G. Stoffel, Dynamic, polarization, and transverse-mode characteristics of vertical cavity surface emitting lasers. IEEE J. Quantum Electron. **27**, 1402 (1991)
7. K.D. Choquette, D.A. Richie, R.E. Leibenguth, Temperature dependence of gain-guided vertical-cavity surface emitting laser polarization. Appl. Phys. Lett. **64**, 2062 (1994)
8. A.K. Jansen van Doorn, M.P. van Exter, J.P. Woerdman, Elasto-optic anisotropy and polarization orientation of guided vertical-cavity surface-emitting semiconductor lasers. Appl. Phys. Lett. **69**, 1041 (1996)
9. K.D. Choquette, R.E. Leibenguth, Control of vertical-cavity laser polarization with anisotropic transverse cavity geometries. IEEE Photon. Technol. Lett. **6**, 40 (1994)
10. K. Panajotov, B. Nagler, G. Verschaffelt, A. Georgievski, H. Thienpont, J. Danckaert, I. Veretennicoff, Impact of in-plane anisotropic strain on the polarization behavior of vertical-cavity surface-emitting lasers. Appl. Phys. Lett. **77**, 1590 (2000)
11. K. Panajotov, M. Camarena, M.C. Moreno, H.J. Unold, R. Michalzik, H. Thienpont, J. Danckaert, I. Veretennicoff, G. Verschaffelt, Polarization behavior and mode structure of vertical-cavity surface-emitting lasers with elliptical surface relief. Proceedings of SPIE, vol. 4994 (2003), p. 127

12. K. Panajotov, J. Danckaert, G. Verschaffelt, M. Peeters, B. Nagler, J. Albert, B. Ryvkin, H. Thienpont, I. Veretennicoff, Polarization behavior of vertical-cavity surface-emitting lasers: experiments, models and applications. Am. Inst. Phys. Conf. Proc. **560**, 403 (2001)
13. A.K. Jansen van Doorn, M.P. van Exter, J.P. Woerdman, Tailoring the birefringence in a vertical-cavity semiconductor laser. Appl. Phys. Lett. **69**, 3635 (1996)
14. A.K. Jansen van Doorn, M.P. van Exter, A.M. van der Lee, J.P. Woerdman, Coupled-mode description for the polarization state of a vertical-cavity semiconductor laser. Phys. Rev. **55**, 1473 (1997)
15. M.P. van Exter, A.K. Jansen van Doorn, J.P. Woerdman, Electro-optic effect and birefringence in semiconductor vertical-cavity lasers. Phys. Rev. A **56**, 845 (1997)
16. P. Debernardi, G.P. Bava, C. Degen, I. Fischer, W. Elsäßer, Influence of anisotropies on transverse modes in oxide-confined VCSELs. IEEE J. Quantum Electron **38**, 73 (2002)
17. R.F.M. Hendriks, M.P. van Exter, J.P. Woerdman, A. van Geelen, L. Weegels, K.H. Gulden, M. Moser, Electro-optic birefringence in semiconductor vertical-cavity lasers. Appl. Phys. Lett. **71**, 2599 (1997)
18. D. Vakhshoori, Symmetry considerations in vertical-cavity surface-emitting lasers: prediction of removal of polarization isotropicity on (001) substrates. Appl. Phys. Lett. **65**, 259 (1994)
19. Z.G. Pan, S. Jiang, M. Dagenais, R.A. Morgan, K. Kojima, M.T. Asom, R.E. Leibenguth, G.D. Guth, M.W. Focht, Optical injection induced polarization bistability in vertical-cavity surface-emitting lasers. Appl. Phys. Lett. **63**, 2999 (1993)
20. S. Jiang, Z. Pan, M. Dagenais, R.A. Morgan, K. Kojiama, High-frequency polarization self-modulation in vertical-cavity surface-emitting lasers. Appl. Phys. Lett. **63**, 3545 (1993)
21. K.D. Choquette, K.L. Lear, R.E. Leibenguth, M.T. Asom, Polarization modulation of cruciform vertical-cavity laser diodes. Appl. Phys. Lett. **64**, 2767 (1994)
22. H. Kawaguchi, I.S. Hidayat, Y. Takahashi, Y. Yamayoshi, Pitchfork bifurcation polarization bistability in vertical-cavity surface-emitting lasers. Electron. Lett. **31**, 109 (1995)
23. K.D. Choquette, R.P. Schneider Jr., K.L. Lear, R.E. Leibenguth, Gain-dependent polarization properties of vertical-cavity lasers. IEEE J. Select. Topics Quantum Electron. **1**, 661 (1995)
24. J.E. Epler, S. Gehrsitz, K.H. Gulden, M. Moser, H.G. Sigg, H.W. Lehmann, Mode behavior and high resolution spectra of circularly symmetric GaAs-AlGaAs air-post vertical cavity surface emitting lasers. Appl. Phys. Lett. **69**, 722 (1996)
25. U. Fiedler, G. Reiner, P. Schnitzer, K.J. Ebeling, Top surface-emitting vertical-cavity laser diodes for 10-Gb/s data transmission. IEEE Photon. Technol. Lett. **8**, 746 (1996)
26. J. Martin-Regalado, J.L.A. Chilla, J.J. Rocca, P. Brusenbach, Polarization switching in vertical-cavity surface emitting lasers observed at constant active region temperature. Appl. Phys. Lett. **70**, 3350 (1997)
27. H. Kawaguchi, Bistable laser diodes and their applications: state of the art. IEEE J. Select. Topics Quantum Electron **3**, 1254 (1997)
28. C.L. Chua, R.L Thornton, D.W. Treat, R.M. Donaldson, Anisotropic apertures for polarization-stable laterally oxidized vertical-cavity lasers. Appl. Phys. Lett. **73**, 1631 (1998)
29. K. Panajotov, B. Ryvkin, J. Danckaert, M. Peeters, H. Thienpont, I. Veretennicoff, Polarization switching in VCSEL's due to thermal lensing. IEEE Photon. Technol. Lett. **10**, 6 (1998)
30. M.P. van Exter, A. Al-Remawi, J.P. Woerdman, Polarization fluctuations demonstrate nonlinear anisotropy of a vertical-cavity semiconductor laser. Phys. Rev. Lett. **80**, 4875 (1998)
31. M.P. van Exter, M.B. Willemsen, J.P. Woerdman, Polarization fluctuations in vertical-cavity semiconductor lasers. Phys. Rev. A **58**, 4191 (1998)
32. M.B. Willemsen, M.P. van Exter, J.P. Woerdman, Correlated fluctuations in the polarization modes of a vertical-cavity semiconductor laser. Phys. Rev. A **60**, 4105 (1999)
33. B. Ryvkin, K. Panajotov, A. Georgievski, J. Danckaert, M. Peeters, G. Verschaffelt, H. Thienpont, I. Veretennicoff, Effect of photon-energy-dependent loss and gain mechanisms on polarization switching in vertical-cavity surface-emitting lasers. J. Opt. Soc. Am. B **16**, 2106 (1999)
34. M.B. Willemsen, M.P. van Exter, J.P. Woerdman, Anatomy of a polarization switch of a vertical-cavity semiconductor laser. Phys. Rev. Lett. **84**, 4337 (2000)

35. T. Ackemann, M. Sondermann, Characteristics of polarization switching from the low to the high frequency mode in vertical-cavity surface-emitting lasers. Appl. Phys. Lett. **78**, 3574 (2001)
36. G. Verschaffelt, J. Albert, I. Veretennicoff, J. Danckaert, S. Barbay, G. Giacomelli, F. Marin, Frequency response of current-driven polarization modulation in vertical-cavity surface-emitting lasers. Appl. Phys. Lett. **80**, 2248 (2002)
37. Y. Matsui, D. Vakhshoori, P. Wang, P. Chen, C.-C. Lu, M. Jiang, K. Knopp, S. Burroughs, P. Tayebati, Complete polarization mode control of long-wavelength tunable vertical-cavity surface-emitting lasers over 65-nm tuning up to 14-mW output power. IEEE J. Quantum Electron. **39**, 1037 (2003)
38. M. Sondermann, M. Weinkath, T. Ackemann, Polarization switching to the gain-disfavored mode in vertical-cavity surface-emitting lasers. IEEE J. Quantum Electron. **40**, 97 (2004)
39. M. Sondermann, T. Ackemann, S. Balle, J. Mulet, K. Panajotov, Experimental and theoretical investigations on elliptically polarized dynamical transition states in the polarization switching of vertical-cavity surface-emitting lasers. Opt. Commun. **235**, 421 (2004)
40. G. Giacomelli, F. Marin, M. Gabrysch, K.H. Gulden, M. Moser, Polarization competition and noise properties of VCSELs. Opt. Commun. **146**, 136 (1998)
41. G. Giacomelli, F. Marin, I. Rabbiosi, Stochastic and bona fide resonance: an experimental investigation. Phys. Rev. Lett. **82**, 675 (1999)
42. M.B. Willemsen, M.U.F. Khalid, M.P. van Exter, J.P. Woerdman, Polarization switching of a vertical-cavity semiconductor laser as a Kramers hopping problem. Phys. Rev. Lett. **82**, 4815 (1999)
43. B. Nagler, M. Peeters, J. Albert, G. Verschaffelt, K. Panajotov, H. Thienpont, I. Veretennicoff, J. Danckaert, S. Barbay, G. Giacomelli, F. Marin, Polarization-mode hopping in single-mode vertical-cavity surface-emitting lasers: theory and experiment. Phys. Rev. A **68**, 013813 (2003)
44. G. Verschaffelt, J. Albert, B. Nagler, M. Peeters, J. Danckaert, S. Barbay, G. Giacomelli, F. Marin, Frequency response of polarization switching in vertical-cavity surface-emitting lasers. IEEE J. Quantum Electron. **39**, 1177 (2003)
45. J. Danckaert, M. Peeters, C. Mirasso, M.S. Miguel, G. Verschaffelt, J. Albert, B. Nagler, H. Unold, R. Michalzik, G. Giacomelli, F. Marin, Stochastic polarization switching dynamics in vertical-cavity surface-emitting lasers: theory and experiment. IEEE J. Select. Topics Quantum Electron. **10**, 911 (2004)
46. G. van der Sande, M. Peeters, I. Veretennicoff, J. Danckaert, G. Verschaffelt, S. Balle, The effect of stress, temperature, and spin flip on polarization switching in vertical-cavity surface-emitting lasers. IEEE J. Quantum Electron. **42**, 898 (2006)
47. M. Ohtsu, Y. Teramachi, Y. Otsuka, A. Osaki, Analysis of mode-hopping phenomena in an AlGaAs laser. IEEE J. Quantum Electron. **22**, 535 (1986)
48. R.M.A. Azzam, N.M. Bashara, *Ellipsometry and Polarized Light* (North-Holland Elsevier, Amsterdam, 1987)
49. F. Koyama, K. Morito, K. Iga, Intensity noise and polarization stability of GaAlAs-GaAs surface emitting lasers. IEEE J. Quantum Electron. **27**, 1410 (1991)
50. D.V. Kuksenkov, H. Temkin, S. Swirhun, Polarization instability and relative intensity noise in vertical-cavity surface-emitting lasers. Appl. Phys. Lett. **67**, 2141 (1995)
51. E. Goobar, J.W. Scott, B. Thibeault, G. Robinson, Y. Akulova, L.A. Coldren, Calibrated intensity noise measurements in microcavity laser diodes. Appl. Phys. Lett. **67**, 3697 (1995)
52. D. Wiedenmann, P. Schnitzer, C. Jung, M. Grabherr, R. Jäger, R. Michalzik, K.J. Ebeling, Noise characteristics of 850 nm single-mode vertical cavity surface emitting lasers. Appl. Phys. Lett. **73**, 717 (1998)
53. J.-L. Vey, C. Degen, K. Auen, W. Elsäßer, Quantum noise and polarization properties of vertical-cavity surface-emitting lasers. Phys. Rev. A **60**, 3284 (1999)
54. D.C. Kilper, R.A. Ross, J.L. Carlsten, K.L. Lear, Squeezed light generated by a microcavity laser. Phys. Rev. A **55**, R3323 (1997)

55. V. Badilita, J.-F. Carlin, M. Ilegems, M. Brunner, G. Verschaffelt, K. Panajotov, Control of polarization switching in vertical coupled-cavities surface emitting lasers. IEEE Photon. Techn. Lett. **16**, 365 (2004)
56. R.P. Stanley, R. Houdré, U. Oesterle, M. Ilegems, C. Weisbuch, Coupled semiconductor microcavities. Appl. Phys. Lett. **65**, 2093 (1994)
57. K. Panajotov, V. Badilita, J.-F. Carlin, H. Thienpont, I. Veretennicoff, Quantum confined Stark effect in coupled-cavity VCSELs. Proceedings of SPIE, vol. 5359 (2004), p. 360
58. D.M. Grasso, K.D. Choquette, Temperature-dependent polarization characteristics of composite-resonator vertical-cavity lasers. IEEE J. Quantum Electron. **41**, 127 (2005)
59. S. Hallstein, J.D. Berger, M. Hilpert, H.C. Schneider, W.W. Rühle, F. Janke, S.W. Koch, H.M. Gibbs, G. Khitrova, M. Oestreich, Manifistation of coherent spin precession in stimulated semiconductor emission dynamics. Phys. Rev. B **56**, R7076 (1997)
60. H. Ando, T. Sogawa, H. Gotoh, Photon-spin controlled lasing oscillation in surface-emitting lasers. Appl. Phys. Lett. **73**, 566 (1998)
61. R.F.M. Hendriks, M.P. van Exter, J.P. Woerdman, K.H. Gulden, M. Moser, Memory effects for polarization of pump light in optically pumped vertical-cavity semiconductor lasers. IEEE J. Quantum Electron. **34**, 1455 (1998)
62. E.L. Blansett, M.G. Raymer, G. Khitrova, H.M. Gibbs, D.K. Serkland, A.A. Allerman, K.M. Geib, Ultrafast polarization dynamics and noise in pulsed vertical-cavity surface-emitting lasers. Opt. Express **9**, 312 (2001)
63. E.L. Blansett, M.G. Raymer, G. Cui, G. Khitrova, H.M. Gibbs, D.K. Serkland, A.A. Allerman, K.M. Geib, Picosecond polarization dynamics and noise in pulsed vertical-cavity surface-emitting lasers. IEEE J. Quantum Electron. **41**, 287 (2005)
64. M.Z. Maialle, M.H. Degani, Electron-spin relaxation in p-type quantum wells via electron-hole exchange interaction: the effects of the valence-band spin mixing and of an applied longitudinal electric field. Phys. Rev. B **55**, 13771 (1997)
65. N.B. Patel, J.E. Ripper, P. Brosson, Behavior of threshold current and polarization of stimulated emission of GaAs injection lasers under uniaxial stress. IEEE J. Quantum Electron. **9**, 338 (1973)
66. Y.C. Chen, J.M. Liu, Polarization bistability in semiconductor lasers. Appl. Phys. Lett. **46**, 16 (1985)
67. Y.C. Chen, J.M. Liu, Polarization bistability in semiconductor laser: rate-equation analysis. Appl. Phys. Lett. **50**, 1406 (1987)
68. W.E. Lamb, Theory of an optical maser. Phys. Rev. **134**, A1429 (1964)
69. C. Tang, A. Schremer, T. Fujita, Bistability in two-mode semiconductor lasers via gain saturation. Appl. Phys. Lett. **51**, 1392 (1987)
70. M. Asada, Y. Suematsu, Density-matrix theory of semiconductor lasers with relaxation broadening model—gain and gain-suppression in semiconductor lasers. IEEE J. Quantum Electron. **21**, 434 (1985)
71. G.P. Agrawal, Gain nonlinearities in semiconductor lasers: theory and application to distributed feedback lasers. IEEE J. Quantum Electron. **23**, 860 (1987)
72. M. Sargent III, Theory of a multimode quasi-equilibrium semiconductor-laser. Phys. Rev. A **48**, 717 (1993)
73. A. Uskov, J. Mørk, J. Mark, Wave mixing in semiconductor-laser amplifiers due to carrier heating and spectral-hole burning. IEEE J. Quantum Electron. **30**, 1769 (1994)
74. B.M. Yu, J.M. Liu, Polarization-dependent gain, gain nonlinearities, and emission characteristics of internally strained InGaAsP/InP semiconductor lasers. J. Appl. Phys. **69**, 7444 (1991)
75. Y. Takahashi, H. Kawaguchi, Polarization-dependent gain saturations in quantum-well lasers. IEEE J. Quantum Electron. **36**, 864 (2000)
76. Y. Takahashi, H. Kawaguchi, Strain-dependence of the gain saturations in InGaAsP/InP quantum-well gain media. IEEE J. Quantum Electron. **38**, 1384 (2002)

77. J. Danckaert, B. Nagler, J. Albert, K. Panajotov, I. Veretennicoff, T. Erneux, Minimal rate equations describing polarization switching in vertical-cavity surface-emitting lasers. Opt. Commun. **201**, 129 (2002)
78. J. Albert, G. van der Sande, B. Nagler, K. Panajotov, I. Veretennicoff, J. Danckaert, T. Erneux, The effects of nonlinear gain on the stability of semi-degenerate two-mode semiconductor lasers: a case study on VCSELs. Opt. Commun. **248**, 527 (2005)
79. B.S. Ryvkin, E.A. Avrutin, M. Pessa, Polarization-dependent intersubband absorption saturation and its effect on polarization selection in vertical cavity surface-emitting lasers. J. Appl. Phys. **93**, 2353 (2003)
80. B.S. Ryvkin, E.A. Avrutin, M. Pessa, Spontaneous emission, light-current characteristics, and polarization bistability range in vertical-cavity surface-emitting lasers. J. Appl. Phys. **94**, 4267 (2003)
81. B.S. Ryvkin, E.A. Avrutin, A.C. Walker, Photon energy dependence of the sign of the current-induced absorption polarization sensitivity in degenerate semiconductors. Appl. Phys. Lett. **78**, 2655 (2001)
82. B.S. Ryvkin, E.A. Avrutin, A.C. Walker, Current-directionality-induced giant absorption dichroism in III-V semiconductors and its potential for polarization control in vertical cavity surface-emitting lasers. J. Appl. Phys. **91**, 3516 (2002)
83. H. Kawaguchi, I.H. White, M.J. Offside, J.E. Carroll, Ultrafast switching in polarization-bistable laser-diodes. Opt. Lett. **17**, 130 (1992)
84. A. Valle, L. Pesquera, K.A. Shore, Polarization behaviour of birefringent multitransverse mode vertical-cavity surface-emitting lasers. IEEE Photon. Technol. Lett. **9**, 557 (1997)
85. M. San Miguel, Q. Feng, J.V. Moloney, Light-polarization dynamics in surface-emitting semiconductor lasers. Phys. Rev. A **52**, 1728 (1995)
86. A. Tackeuchi, Y. Nishikawa, O. Wada, Room-temperature electron spin dynamics in GaAs/AlGaAs quantum wells. Appl. Phys. Lett. **68**, 797 (1996)
87. A. Tackeuchi, O. Wada, Y. Nishikawa, Electron spin relaxation in InGaAs/InP multiple-quantum wells. Appl. Phys. Lett. **70**, 1131 (1997)
88. S. Akasaka, S. Miyata, T. Kuroda, A. Tackeuchi, Exciton spin relaxation dynamics in InGaAs/InP quantum wells. Appl. Phys. Lett. **85**, 2083 (2004)
89. M.I. D'yakonov, V.I. Perel, Optical orientation in a system of electrons and lattice nuclei in semiconductors: theory. Zh. Eksp. Teor. Fiz. **65**, 362 (1973)
90. M.I. D'yakonov, V.I. Perel, Optical orientation in a system of electrons and lattice nuclei in semiconductors. Sov. Phys. JETP **38**, 177 (1974)
91. R.J. Elliott, Theory of the effect of spin-orbit coupling on magnetic resonance in some semiconductors. Phys. Rev. **96**, 266 (1954)
92. Y. Yafet, *g* factors and spin-lattice relaxation of conduction electrons, in *Solid State Physics*, vol. 14, ed. by F. Seitz, D. Turnbull (Academic Press, New York, 1963), pp. 1–98
93. G.L. Bir, A.G. Aronov, G.E. Pikus, Spin relaxation of electrons scattered by holes. Zh. Eksp. Teor. Fiz. **69**, 1382 (1975)
94. G.L. Bir, A.G. Aronov, G.E. Pikus, Spin relaxation of electrons scattered by holes. Sov. Phys. JETP **42**, 705 (1976)
95. T. Adachi, Y. Ohno, R. Terauchi, F. Matsukura, H. Ohno, Mobility dependence of electron spin relaxation time in n-type InGaAs/InAlAs multiple quantum wells. Physica E **7**, 1015 (2000)
96. K. Jarasiunas, V. Gudelis, R. Aleksiejunas, M. Sudzius, S. Iwamoto, M. Nishioka, T. Shimura, K. Kuroda, Y. Arakawa, Picosecond dynamics of spin-related optical nonlinearities in $In_xGa_{1-x}As$ multiple quantum wells at 1064 nm. Appl. Phys. Lett. **84**, 1043 (2004)
97. J. Martin-Regalado, M. San Miguel, N.B. Abraham, F. Prati, Polarization switching in quantum-well vertical-cavity surface-emitting lasers. Opt. Lett. **21**, 351 (1996)
98. J. Martin-Regalado, F. Prati, M. San Miguel, N.B. Abraham, Polarization properties of vertical-cavity surface-emitting lasers. IEEE J. Quantum Electron **33**, 765 (1997)

99. M. Travagnin, M.P. van Exter, A.K. Jansen van Doorn, J.P. Woerdman, Role of optical anisotropies in the polarization properties of surface-emitting semiconductor lasers. Phys. Rev. A **54**, 1647 (1996)
100. C. Serrat, N.B. Abraham, M. San Miguel, R. Vilaseca, J. Martin-Regalado, Polarization dynamics in a vertical-cavity laser with an axial magnetic field. Phys. Rev. A **53**, R3731 (1996)
101. M. Travagnin, Linear anisotropies and polarization properties of vertical-cavity surface-emitting semiconductor lasers. Phys. Rev. A **56**, 4094 (1997)
102. H.F. Hofmann, O. Hess, Quantum noise and polarization fluctuations in vertical-cavity surface-emitting lasers. Phys. Rev. A **56**, 868 (1997)
103. H. van der Lem, D. Lenstra, Saturation-induced frequency shift in the noise spectrum of a birefringent vertical-cavity surface emitting laser. Opt. Lett. **22**, 1698 (1997)
104. M.P. van Exter, R.F.M. Hendriks, J.P. Woerdman, Physical insight into the polarization dynamics of semiconductor vertical-cavity lasers. Phys. Rev. A **57**, 2080 (1998)
105. S. Balle, E. Tolkachova, M. San Miguel, J.R. Tredicce, J. Martin-Regalado, A. Gahl, Mechanisms of polarization switching in single-transverse-mode vertical-cavity surface-emitting lasers: thermal shift and nonlinear semiconductor dynamics. Opt. Lett. **24**, 1121 (1999)
106. J. Martin-Regalado, S. Balle, M. San Miguel, Polarization and transverse-mode dynamics of gain-guided vertical-cavity surface-emitting lasers. Opt. Lett. **22**, 460 (1997)
107. J. Martin-Regalado, S. Balle, M. San Miguel, A. Valle, L. Pesquera, Polarization and transverse-mode selection in quantum-well vertical-cavity surface-emitting lasers: index and gain-guided devices. J. Opt. B. Quantum Semiclass. Opt. **9**, 713 (1997)
108. J. Mulet, S. Balle, Spatio-temporal modeling of the optical properties of VCSELs in the presence of polarization effects. IEEE J. Quantum Electron. **38**, 291 (2002)
109. M.S. Torre, C. Masoller, P. Mandel, Transverse and polarization effects in index-guided vertical-cavity surface-emitting lasers. Phys. Rev. A **74**, 043808 (2006)
110. C. Masoller, M.S. Torre, K.A. Shore, Polarization dynamics of current-modulated vertical-cavity surface-emitting lasers. IEEE J. Quantum Electron. **43**, 1074 (2007)
111. F. Prati, G. Giacomelli, F. Marin, Competition between orthogonally polarized transverse modes in vertical-cavity surface-emitting lasers and its influence on intensity noise. Phys. Rev. A **62**, 033810 (2000)
112. D. Burak, J.V. Moloney, R. Binder, Microscopic theory of polarization properties of optically anisotropic vertical-cavity surface-emitting lasers. Phys. Rev. A **61**, 053809 (2000)
113. D. Burak, J.V. Moloney, R. Binder, Macroscopic versus microscopic description of polarization properties of optically anisotropic vertical-cavity surface-emitting lasers. IEEE J. Quantum Electron. **36**, 956 (2000)
114. G. van der Sande, J. Danckaert, I. Veretennicoff, K. Panajotov, S. Balle, Analytical approximation for the quantum-well gain and refractive-index spectra of vertical-cavity surface-emitting lasers including the effect of uniaxial planar stress. Phys. Rev. A **71**, 063801 (2005)
115. R.F.M. Hendriks, M.P. van Exter, J.P. Woerdman, How the carrier momentum influences the polarization properties of a vertical-cavity semiconductor laser. Phys. Rev. A **59**, 765 (1999)
116. F. Prati, L. Fratta, M. Travagnin, Band model for light-polarization selection in unstrained quantum-well vertical-cavity surface-emitting laser. Phys. Rev. A **62**, 033819 (2000)
117. F. Prati, P. Caccia, F. Castelli, Effects of gain saturation on polarization switching in vertical-cavity semiconductor lasers. Phys. Rev. A **66**, 063811 (2002)
118. T. Erneux, J. Danckaert, K. Panajotov, I. Veretennicoff, Two-variable reduction of the San Miguel–Feng–Moloney model for vertical-cavity surface-emitting lasers. Phys. Rev. A **59**, 4660 (1999)
119. F. Prati, P. Caccia, M. Bache, F. Castelli, Analysis of elliptically polarized states in vertical-cavity surface-emitting lasers. Phys. Rev. A **69**, 033810 (2004)
120. C. Masoller, M.S. Torre, P. Mandel, Influence of the injection current sweep rate on the polarization switching of vertical-cavity surface-emitting lasers. J. Appl. Phys. **99**, 026106 (2006)

121. J. Paul, C. Masoller, P. Mandel, Y.H. Hong, P.S. Spencer, K.A. Shore, Experimental and theoretical study of dynamical hysteresis and scaling laws in the polarization switching of vertical-cavity surface-emitting lasers. Phys. Rev. A **77**, 043803 (2008)
122. M.S. Torre, C. Masoller, Polarization-resolved modulation response of single-transverse-mode vertical-cavity surface-emitting lasers. IEEE J. Quantum Electron. **45**, 206 (2009)
123. J. Mulet, C.R. Mirasso, M. San Miguel, Polarization resolved intensity noise in vertical-cavity surface-emitting lasers. Phys. Rev. A **64**, 023817 (2001)
124. J.M. Liu, Y.C. Chen, Digital optical signal-processing with polarization-bistable semiconductor-lasers. IEEE J. Quantum Electron. **21**, 298 (1985)
125. T. Mori, Y. Yamayoshi, H. Kawaguchi, Low-switching-energy and high-repetition-frequency all-optical flip-flop operation of polarization bistable vertical-cavity surface-emitting laser. Appl. Phys. Lett. **88**, 101102 (2006)
126. T. Mori, Y. Sato, H. Kawaguchi, Timing jitter reduction by all-optical signal regeneration using a polarization bistable VCSEL. J. Lightwave Technol. **26**, 2946 (2008)
127. H. Kawaguchi, T. Mori, Y. Sato, Y. Yamayoshi, Optical buffer memory using polarization-bistable vertical-cavity surface-emitting lasers. Jpn. J. Appl. Phys. **45**, L894 (2006)
128. J. Rudolph, S. Döhrmann, D. Hägele, M. Oestreich, W. Stolz, Room-temperature threshold reduction in vertical-cavity surface-emitting lasers by injection of spin-polarized electrons. Appl. Phys. Lett. **87**, 241117 (2005)

Chapter 7
Design and Performance of High-Speed VCSELs

Yu-Chia Chang and Larry A. Coldren

Abstract Over the past several years, high-speed vertical-cavity surface-emitting lasers (VCSELs) have been the subject of intensive worldwide research due to their applications in optical interconnects and optical data networks. The performance of VCSELs, especially with respect to their high-speed characteristics, has made significant progress. In this chapter, we first present the basic theory for current-modulated VCSELs using rate equations and small-signal analysis. Factors that affect the modulation bandwidth, including the intrinsic laser responses and extrinsic parasitics, are identified. Once these limitations are known, we discuss various designs that have been implemented in VCSELs to specifically address them, followed by a review of the current high-speed VCSEL performance based on these designs at several different wavelengths, including 850 nm, 980 nm, 1.1 μm, and 1.3–1.6 μm. Finally, we consider new modulation schemes based on loss modulation in coupled-cavity VCSELs, which has the potential to reach even higher speeds.

7.1 Introduction

The rapid explosion of information has created ever increasing demands for data bandwidth. Optical fiber communication now dominates long-haul and metropolitan telecommunication networks, and it has made many in-roads into data-communication networks in campus and high-performance computing environments. However, traditional electrical signaling is still used for many tele- and data-communication links at the edge of these networks where data rates are still modest. But, even here

Y.-C. Chang (✉)· L. A. Coldren
Department of Electrical and Computer Engineering,
University of California, Santa Barbara, CA, USA
e-mail: yuchia@engineering.ucsb.edu

L. A. Coldren
e-mail: coldren@ece.ucsb.edu

R. Michalzik (ed.), *VCSELs*, Springer Series in Optical Sciences 166,
DOI: 10.1007/978-3-642-24986-0_7, © Springer-Verlag Berlin Heidelberg 2013

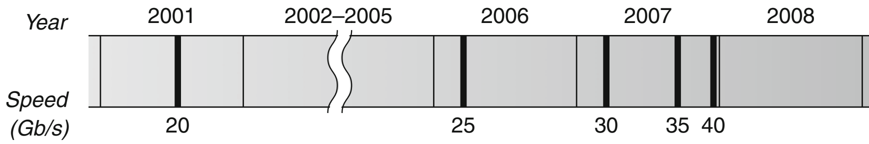

Fig. 7.1 Timeline of the first reported 20, 25, 30, 35, and 40 Gb/s direct current modulation of VCSELs

optical techniques are beginning to look more attractive as the optical component cost becomes more competitive and the bandwidth demands increase. Also as space and power dissipation become important, some fundamental limitations come into play [1]. Optics is progressively replacing many electrical links, from networks to eventually even chip-to-chip and on-chip interconnects within computers. Low-cost, power-efficient, high-speed optical sources are one of the main keys to enable this transition.

Vertical-cavity surface-emitting lasers (VCSELs) are inherently suitable for optical data transmission for various reasons. Their small volume fundamentally implies that low power consumption and high-speed operation can be realized simultaneously. Due to surface emission, VCSELs can produce a more circular output beam with less divergence, can easily be fabricated in arrays, and can support on-wafer testing. All these lead to a significant reduction of the testing and packaging costs.

Over the past several years, worldwide research efforts to improve the performance of VCSELs for optical data links have reached fruition, especially with respect to their high-speed aspects. Figure 7.1 summarizes the timeline of the first reported data rates of 20, 25, 30, 35, and 40 Gb/s for directly modulated VCSELs. In 2001, 20-Gb/s operation was reported by Kuchta et al. using oxide-confined 850-nm VCSELs [2]. Not until 2006, 25-Gb/s operation was achieved by Suzuki et al. in NEC using 1.1-μm-wavelength VCSELs [3]. One year later, data rate was further pushed to 30 Gb/s by the same group using buried tunnel junction (BTJ) VCSELs [4]. Just after six months, a data rate of 35 Gb/s was reported by Chang et al. using oxide-confined 980-nm VCSELs [5]. Three months later, the 40-Gb/s milestone was finally hit by Anan et al., again by NEC, using BTJ VCSELs [6]. So, in the year 2007, the direct modulation speed of VCSELs was pushed from 25 to 40 Gb/s, a tremendous progress.

Of at least equal importance, many system-level optical links based on VCSELs have been demonstrated in this period. For example, an aggregate data rate of 500 Gb/s has been reported using 48 channels of 10.42-Gb/s data transmitted over a parallel 12-fiber ribbon with four wavelengths per fiber [7]. These links have demonstrated that power consumption is equally important to speed, so a significant emphasis on reducing overall power-consumption/data-rate ratio is also a goal for both optical interconnects and optical data links. The total link power consumption, including driver and receiver electronics, for 500 Gb/s is 3.3 W, corresponding to a power-consumption/data-rate ratio of 6.6 mW/(Gb/s). For waveguide-based

chip-to-chip optical links, an aggregate data rate of 160 Gb/s has been reported with 4×4 VCSEL and photodiode arrays, each operated at 10 Gb/s [8]. The total link power consumption is 2.5 W, corresponding to 15.6 mW/(Gb/s). More results will be presented in Chaps. 15 and 16 of this book.

Long-wavelength VCSELs (LW-VCSELs) have made significant progress as well. Novel structures and new materials have been pursued to overcome the material challenges faced by LW-VCSELs. Based on different technologies, several groups and companies have demonstrated data transmission at 10 Gb/s over single-mode fibers (SMF) [9–13]. At this writing such components are beginning to be sampled commercially by some companies. Although intense efforts on 1300–1550 nm VCSELs are expected to continue, it is unlikely that such devices will reach the modulation bandwidths ultimately available in the shorter 850–1100 nm range due to both material and cavity volume constraints that will be discussed in the next section.

This chapter is organized as follows. Section 7.2 presents the theoretical background for current-modulated VCSELs. The device designs are covered in Sect. 7.3, and Sect. 7.4 reviews some of the high-speed VCSEL results. Section 7.5 discusses loss-modulated VCSELs, and Sect. 7.6 concludes this chapter.

7.2 Theoretical Background

Before jumping to the design of high-speed VCSELs, it is important to understand how the bandwidth of VCSELs is determined. Once various factors that can limit the bandwidth are known, the VCSEL structure can be specifically optimized to address these restrictions. In this section, the necessarily theoretical background for directly current modulating VCSELs is provided.

Just like other diode lasers, the bandwidth of VCSELs is determined by the intrinsic laser response as well as the extrinsic parasitic response. To facilitate our discussion, the cascaded two-port model for representing a diode laser, shown in Fig. 7.2, is used to separate the intrinsic laser and the parasitics [14]. The intrinsic laser is the active region where it is desirable to concentrate the current and optical modes to maximize the carrier and photon densities, which are coupled via stimulated recombination. The parasitics, defined between the intrinsic laser and the driving circuit, are split into the pad parasitics and chip parasitics at the metal contacts. The input variables in the model are the drive voltage v_{d} and drive current i_{d}. The currents entering the pad and chip parasitics are i_{p} and i_{c}, respectively. The voltage and current seen by the intrinsic laser are v_{a} and i_{a}, respectively. The output variables are the output power p and frequency shift $\Delta\nu$. For short-distance optical data links, dispersion is usually not a concern and $\Delta\nu$ will not be considered.

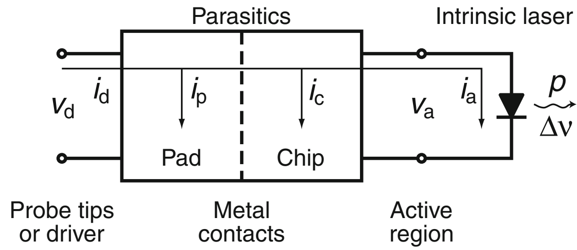

Fig. 7.2 Cascaded two-port model for VCSEL

7.2.1 *Intrinsic Laser Response*

Rate Equation Analysis

We start with the phenomenological rate equations, which describe the supply and loss of the carriers and photons within the active region [15]:

$$\frac{dN}{dt} = \frac{\eta_i I}{qV} - \frac{N}{\tau} - v_g g N_p \tag{7.1a}$$

$$\frac{dN_p}{dt} = \Gamma v_g g N_p + \Gamma R'_{sp} - \frac{N_p}{\tau_p} \tag{7.1b}$$

where N is the carrier density, N_p is the photon density, η_i is the injection efficiency, I is the terminal current, q is the electronic charge, V is the volume of the active region, τ is the carrier lifetime, v_g is the group velocity, g is the gain, Γ is the confinement factor, R'_{sp} is the spontaneous recombination rate into the mode of interest, and τ_p is the photon lifetime.

The gain g can be well approximated by a four-parameter logarithmic formula [15]

$$g(N, N_p) = \frac{g_0}{1 + \varepsilon N_p} \ln\left(\frac{N + N_s}{N_{tr} + N_s}\right) \tag{7.2}$$

where g_0 is the gain coefficient, ε is the gain compression factor, N_{tr} is the transparency carrier density, and N_s is a shift to make g equal the unpumped absorption at $N = 0$.

Once we have the rate equations ready, small-signal frequency analysis can be applied. Assume there is a small sinusoidal modulating current with an amplitude of I_1 superimposed on the steady-state bias current I_0, we have

$$I(t) = I_0 + I_1 e^{j\omega t} \tag{7.3a}$$

$$N(t) = N_0 + N_1 e^{j\omega t} \tag{7.3b}$$

$$N_p(t) = N_{p0} + N_{p1} e^{j\omega t} \tag{7.3c}$$

where N_0 and N_{p0} are the steady-state carrier and photon densities, N_1 and N_{p1} are the corresponding small-signal modulation amplitudes, and ω is the angular frequency. Substituting (7.3) into (7.1), neglecting the products of the small-signal terms, but retaining other first-order deviations, we obtain the modulation transfer function

$$H_{\text{int}}(\omega) \equiv \frac{p(\omega)}{i_a} = A_i \frac{\omega_r^2}{(\omega_r^2 - \omega^2 + j\omega\gamma)} \tag{7.4}$$

where A_i is the DC slope efficiency, $\omega_r = 2\pi f_r$ is the relaxation resonance frequency, and γ is the damping factor. This transfer function is in the form of a second-order low-pass filter with a damped resonance peak.

The relaxation resonance frequency is the natural oscillation frequency between the carriers and photons in the laser cavity and can be approximately expressed as

$$\omega_r = \left[\frac{v_g a N_{p0}}{\tau_p}\right]^{1/2} = \left[\frac{v_g a}{q V_p} \eta_i (I_0 - I_{th})\right]^{1/2} \tag{7.5}$$

where $a = \partial g / \partial N|_{th}$ is the differential gain at threshold, V_p is the mode volume, and I_{th} is the threshold current. As clearly shown in (7.4), the relaxation resonance frequency basically determines how fast an intrinsic diode laser can be modulated when the damping is not severe. Therefore, it is important to increase the relaxation resonance frequency for higher bandwidth. Examining (7.5) tells that higher differential gain a, larger photon density N_{p0}, and smaller photon lifetime τ_p can improve the relaxation resonance frequency. (But, one must be careful not to think that adding internal loss is good, because it always reduces N_{p0} more than τ_p.)

The only parameter, to the first-order approximation, in (7.5) that depends on the operating conditions is the photon density, which can be increased with higher current. A figure of merit commonly used to evaluate how efficient an intrinsic laser can be modulated is the D-factor [16]

$$D \equiv \frac{f_r}{(I - I_{th})^{1/2}} = \frac{1}{2\pi} \left[\frac{v_g a}{q V_p} \eta_i\right]^{1/2}.$$

To evaluate the device's overall high-speed performance, the related factor, modulation current efficiency factor (MCEF), is more commonly used [17]

$$\text{MCEF} \equiv \frac{f_{3\text{dB}}}{(I - I_{th})^{1/2}}$$

where $f_{3\text{dB}}$ is the 3-dB frequency, which is approximately equal to $1.55 f_r$ when the parasitics and damping are relatively small.

The damping represents the rate of energy loss in the laser cavity, which effectively reduces the strength of the resonance peak. The damping factor γ is given as

$$\gamma = v_g a N_{p0} \left[1 + \frac{\Gamma a_p}{a}\right] + \frac{1}{\tau_{\Delta N}} + \frac{\Gamma R'_{sp}}{N_{p0}} \tag{7.6}$$

where $\tau_{\Delta N}$ is the differential carrier lifetime, and

$$a_{\mathrm{p}} = -\left.\frac{\partial g}{\partial N_{\mathrm{p}}}\right|_{N_{\mathrm{p0}}} = \frac{\varepsilon g}{1 + \varepsilon N_{\mathrm{p0}}}. \tag{7.7}$$

At normal high-speed operating conditions, spontaneous-emission-related damping can be neglected, and γ increases with N_{p0}, which is proportional to f_{r}^2. The proportionality is the K-factor given as

$$K = 4\pi^2 \tau_{\mathrm{p}} \left[1 + \frac{\Gamma a_{\mathrm{p}}}{a}\right]. \tag{7.8}$$

Practically, K-factor is empirically determined by fitting γ versus f_{r}^2. As the photon density keeps increasing to a point, the modulation response becomes overdamped and the bandwidth decreases. The maximum theoretically damping-limited f_{3dB} is given as

$$f_{\mathrm{3dB}}|_{\max} = \sqrt{2}\frac{2\pi}{K} \qquad (\gamma/\omega_{\mathrm{r}} = \sqrt{2}). \tag{7.9}$$

Since K-factor increases with gain compression factor ε through a_{p}, reducing gain nonlinearity is also important to achieve high bandwidth.

Beyond the Rate Equations

The proceeding rate equation analysis is appealing due to its simplicity but still providing intuitive insights. However, many effects were not included, and we summarize some of them here.

First discovered in 1991, carrier transport in the separate-confinement heterostructure (SCH) region actually plays an important role in the dynamics of quantum-well (QW) lasers [18]. To reduce the carrier transport effects, it is necessary to minimize the time for carriers to reach and fall into QWs and maximize the time for carriers to escape back from QWs to SCH region. This can be treated with a modified set of rate equations that incorporates a second carrier reservoir [15], but we shall not go into that complexity here.

We also have implicitly assumed that the carrier and photon densities are uniform across the active region in (7.1a) and (7.1b). In reality, the photon density varies spatially as the square of the optical mode field due to the waveguiding of the cavity, which causes the stimulated emission rate to vary accordingly. This spatial nonuniformity of the stimulated emission rate results in an overdamping of the relaxation resonance frequency, which reduces the bandwidth [19]. In addition, carriers are depleted faster where the optical intensity is higher, a phenomenon referred to *spatial* hole burning, and the carrier gradient drives diffusion [20]. It has been shown that the lateral carrier diffusion does not significantly reduce the bandwidth but increases the damping [21].

In (7.2), the nonlinearity of gain was included through the gain compression factor ε. This saturation of gain at high photon density is attributed to the *spectral*

hole burning and carrier heating effects [22]. It is important to minimize the gain nonlinearity so that damping can be reduced.

Many parameters in the rate equations are actually temperature dependent. Excessively high junction temperature degrades the differential gain, reduces the injection efficiency, increases the threshold current, affects the transverse modes, and red-shifts the cavity mode and gain peak. All these lead to a reduction of the bandwidth. Therefore, thermal management is a main issue for high-speed VCSELs.

Many of the limitations on modulation bandwidth are more acute in the longer wavelength VCSELs, especially the thermal effects due to the relative importance of Auger recombination. Thermal management is even more important, but quaternary materials tend to have very poor thermal conductivities, so additional 'engineering fixes' are required. Gain materials at longer wavelengths also usually have lower inherent differential gain, and the cavity volume tends to be larger because of lower inherent index contrast for lattice-matched alloys, which either directly results in a longer mirror, or requires an intracavity contact.

7.2.2 Extrinsic Parasitic Response

When dealing with high-frequency devices, parasitics are always a concern. Parasitics divert the modulated current i_d from entering the intrinsic laser due to i_p and i_c. In most cases, it is desirable to minimize the parasitics so that the intrinsic bandwidth can be achieved.

The parasitics vary depending on the device structure. Here a typical oxide-confined VCSEL, whose cross-sectional schematic and parasitic elements are shown in Fig. 7.3, is used as an example. The pad capacitance C_p represents the capacitance between the signal and ground from the probe tips/driver to the metal contacts. The value of C_p varies from tens to hundreds of femto-farads, depending on the pad layout and the materials between the pads. The pad resistance R_p accounts for the pad loss. Since it is usually relatively small, in the ohm range, compared with the impedance of C_p at the frequency of interest, it is sometimes omitted in the small-signal model.

The mirror resistance R_{mirr} includes the resistances from both DBRs. It includes the net differential impedances of the mirror heterobarriers at the bias point. R_{sheet} represents the sheet resistance in the n-contact layer, and R_{cont} is the contact resistance for both contacts. All these resistances, usually dominated by R_{mirr}, can be grouped together into $R_m = R_{mirr} + R_{sheet} + R_{cont}$ in the small-signal model. The mesa capacitance C_{mesa} is the oxide capacitance in series with the capacitance associated with the intrinsic region below the aperture. C_{mesa} depends on the diameters of the mesa and aperture and the thicknesses of the oxide and intrinsic semiconductor layer.

The capacitance C_j represents the diode junction capacitance in the apertured area where current flows. Under normal forward bias condition, C_j is usually dominated by the diffusion capacitance, which models the modulation of the minority carriers stored in the intrinsic SCH [23]. It has been shown that the diffusion capacitance not only depends on the carrier lifetime but also depends on the design of the SCH [24].

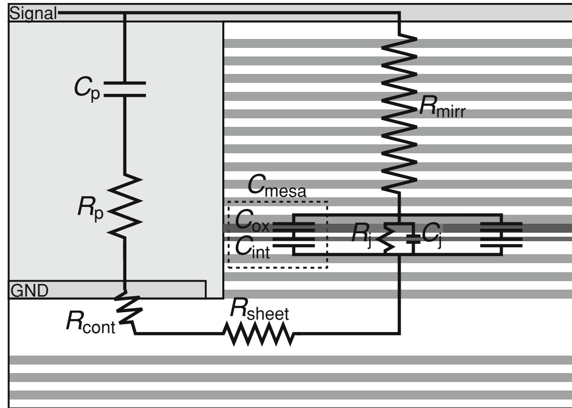

Fig. 7.3 Cross-sectional schematic of an oxide-confined VCSEL superimposed with its parasitics

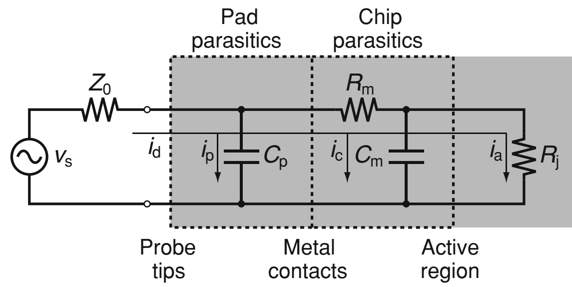

Fig. 7.4 Small-signal model with the driving source. The grayed area represents the VCSEL

For simplicity, C_{mesa} and C_j are grouped together into $C_m = C_{mesa} + C_j$. Lastly, the intrinsic laser is represented by the junction resistance R_j.

Figure 7.4 plots the small-signal model of VCSEL and the RF driving source. The VCSEL is represented by four elements, including C_p, R_m, C_m, and R_j. The RF driving source consists of a voltage source v_s and a characteristic impedance of Z_0. Here we have assumed that the device is driven by 50-Ω-terminated instruments, and Z_0 is included to account for the RF power reflection due to impedance mismatch.

The effects of the parasitics can be described by a transfer function, $H_{ext}(\omega)$ [25]:

$$H_{ext}(\omega) \equiv \frac{\text{current flowing into the intrinsic diode}}{\text{voltage from the voltage source}} = \frac{i_a(\omega)}{v_s}.$$

The frequency at which $|H_{ext}(\omega)|^2/|H_{ext}(0)|^2 = 1/2$ is defined as the parasitic 3-dB frequency ω_{rc}. This transfer function can be approximated by a single-pole low-pass filter function:

$$H_{ext}(\omega) = \frac{A_e}{1 + j\omega/\omega_0} \tag{7.10}$$

where A_e is a proportional constant and ω_0 is the parasitic roll-off frequency, which may be different from ω_{rc}.

The overall electrical modulation frequency response $H(\omega)$ is given as:

$$H(\omega) \equiv \left|\frac{p(\omega)}{v_s}\right|^2 = \left|\frac{i_a(\omega)}{v_s} \cdot \frac{p(\omega)}{i_a(\omega)}\right|^2 = |H_{ext}(\omega) \cdot H_{int}(\omega)|^2$$
$$\propto \left(\frac{1}{1+(\omega/\omega_0)^2} \frac{\omega_r^4}{\left(\omega_r^2-\omega^2\right)^2+\gamma^2\omega^2}\right). \tag{7.11}$$

This gives the commonly used three-pole equation, which is squared when considering electrical-to-electrical links, for fitting the frequency response to extract ω_r, γ, and ω_0.

7.3 Design of High-Speed VCSELs

In Sect. 7.2, we have discussed various factors that can affect the bandwidth of VCSELs based on small-signal analysis. Now we will review different designs to specifically address these limitations for better high-speed performance.

7.3.1 Active Region

The choice of active region is mainly determined by the wavelength and the substrate. However, some designs are better than the others in terms of high-speed performance. Most of them are related to the improvement in differential gain. Differential gain depends on the sensitivity of the quasi-Fermi levels (and thus gain) to small changes in carrier density [15]. To have higher differential gain, the density of states (DOS) needs to be more peaked near the band edges, and the quasi-Fermi levels, where the slopes of the Fermi functions are at their maximum, need to be aligned to the band edges.

In order to improve differential gain, a number of refinements to the active region have been explored. Originally, quantum dots (QDs) were proposed as a superior gain region because of their inherent delta-function-like DOS, which should have a huge differential gain [26], but all experimental QDs have a very broad DOS due to variable dot size and the associated inhomogenous broadening. Adding strain in the QWs reduces the anisotropy between the DOS of electron and hole as well as pushes the hole quasi-Fermi level towards the valence band edge, which improves differential gain [15, 27]. In addition, strain advantageously reduces the transparency carrier density [15]. However, gain nonlinearity and damping increase with strain due to the increased valance-band curvature [22]. *P*-doping the active region increases the carrier-carrier scattering rate and thus decreases the intraband relaxation times, which reduces the gain nonlinearity induced by spectral hole burning [27]. *P*-doping also moves the quasi-Fermi levels down to a more symmetrical position and can increase

the differential gain [15]. However, the experimentally observed improvement in differential gain due to *p*-doping is more pronounced in unstrained systems than in strained systems [28]. In short, strained QWs perform better than unstrained QWs due to higher differential gain, and *p*-doped strained QWs perform better than undoped strained QWs due to reduced gain nonlinearity.

Within the strain limit, increasing the number of QWs is generally preferable for high-speed operation due to the differential gain enhancement [29]. However, the gain enhancement factor from the standing-wave effect, unique for VCSELs, decreases with increased number of QWs and must be considered [15]. Deeper wells are also favorable for high-speed and high-temperature operation because carriers have less chance to escape from the QWs, which reduces the carrier transport effects and carrier leakage.

7.3.2 Lateral Mode Confinement and Single Modeness

Since the relaxation resonance frequency increases with the square root of the photon density, it is desirable to increase the photon density for high-speed operation. This can be done by (1) increasing the current above threshold that contributes to the number of photon, i.e., $\eta_i(I-I_{th})$, (2) reducing the mode volume, and (3) maintaining single-mode operation to insure that the photon density must increase as the current increases. For given device dimensions and bias current, single-mode devices have higher photon density because photons do not spread among the mutually orthogonal modes. Maintaining single-mode operation is also necessary for some applications which use SMF or require better beam quality. However, some past applications have desired multimode VCSELs to match multimode fibers or waveguides. Unfortunately, these are not well suited for high data rate applications. Here we will mention some approaches to achieve single-mode operation, and more details can be found in Chap. 5 of this book.

For gain-guided VCSELs without any deliberate index guiding, the lateral mode confinement is mainly provided through thermal lensing effects, which can be unstable under dynamic operation due to time-dependent temperature variation [30]. Although gain-guided VCSELs have demonstrated 14.5 GHz modulation bandwidth [31], index guiding is more common nowadays for high-speed VCSELs, both to insure single mode operation, as well as reduce the mode volume.

The most common approach to implement lateral index guiding, at least for GaAs-based VCSELs, is to use a dielectric aperture. The discovery of wet thermal oxidation of high aluminum content semiconductors provides an easy way to form thermally stable aluminum oxide inside a VCSEL cavity. Oxide-confined VCSELs have shown superior performance in many aspects due to reduced internal losses, and simultaneously providing good electrical and optical confinement. Various aperture designs have been incorporated in high-speed VCSELs, including standard quarter-wavelength-thick blunt aperture [32], double apertures [33, 34], thin aperture ($\sim$30 nm) [35], and tapered oxide aperture [36, 37].

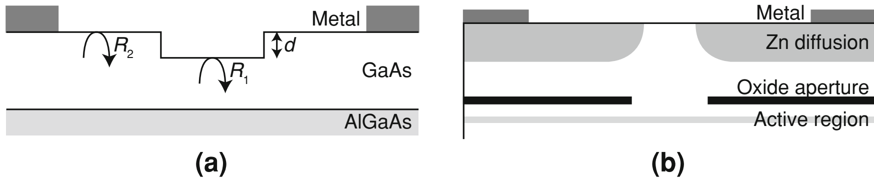

Fig. 7.5 Two approaches to achieve single-mode VCSELs. **a** Illustration of the inverted surface relief structure on the top surface of a VCSEL. Reflectivity R_2 is lower due to an extra thickness of d, and the center is etched down to restore the high reflectivity R_1 for the fundamental mode. **b** Illustration of Zn diffusion from the top surface to create a higher-order mode absorber

There are several advantages of using a tapered oxide aperture. First, it can achieve lower optical scattering losses if designed properly [38, 39]. This is because a tapered oxide aperture, if placed at the standing-wave node, can produce a nearly ideal parabolic lens that eliminates the optical scattering loss. Second, the nonlinear damping effects can be reduced for higher bandwidth by confining the current smaller than the optical mode [19, 40]. Third, the parasitic capacitance from the oxide can be lower due to the increased oxide thickness at high radii where the area is large. Fourth, the eigenmodes are Hermite–Gaussian modes, which diffract less and have no sidelobes, so that external coupling and focusing can be done more ideally. On the other hand, a tapered oxide aperture also reduces the losses that differentiate the fundamental and higher-order modes, and the devices tend to be multi-mode unless some mode-dependent loss is added. Fortunately, the higher-order modes have significantly larger diameters, so this can also be done more easily than in other cases.

Approaches have been proposed to achieve single-mode operation for larger-diameter devices, which can also be implemented for tapered-oxide-apertured devices. Many of them involve creating some mode-dependent losses, usually in the perimeter of the top mirror, to favor the more centered fundamental mode. For example, a surface relief structure, as illustrated in Fig. 7.5a, increases the mirror loss [41], or Zn diffusion, shown in Fig. 7.5b, increases the internal loss for the higher-order modes [42]. High-speed, single-mode VCSELs have been demonstrated with these two approaches [13, 43].

Aperturing using an etched tunnel junction and then performing a regrowth over it to form a BTJ, which is common for InP-based LW-VCSELs, can also provide mode confinement as well as current confinement. This is due to the larger optical cavity length, where the unetched tunnel junction material remains in the center of the cavity. Single-mode operation can be achieved with BTJ for diameters up to 7 and 9 μm at 1.3- and 1.55-μm wavelengths, respectively [44].

7.3.3 Chip Parasitics

Parasitics are one of the main limiting factors for high-speed VCSELs. As can be seen in Table 7.1, most devices have relatively close f_{3dB} and f_{rc}, indicating they are

Table 7.1 Parasitic elements for different high-speed VCSELs from the literature

Authors	Lear	AL-Omari	Chang	Lin	Suzaki	Yashik
Reference	[45]	[32]	[46]	[47]	[3]	[4]
λ (μm)	0.85	0.85	0.98	0.98	1.1	1.1
Size (μm^2)	4×4	$3.5^2\pi$	$1.5^2\pi$	$3^2\pi$	$3.5^2\pi$	$2.5^2\pi$
I_0 (mA)	N/A	4.5	4.5	6.0	7.0	4.0
C_p (fF)	41.7	62	29	22	56	33
$R_p (\Omega)$	15.9	17	0	0	0	0
$R_m (\Omega)$	28.3	45	103	34.1	63.3	38
C_m (fF)	44.3	151	87.9	152	133	130
$R_j (\Omega)$	288.7	64.4	146.5	92.0	71.6	134
f_{rc} (GHz)	36.4	21.8	22.8	22.5	23.6	21.0
f_{3dB} (GHz)	21.5	17	>20	17	20	24[a]

[a] Obtained from 5-μm-diameter devices

partially parasitic-limited. In the following, we will discuss approaches to reduce the parasitics.

Chip Parasitic Resistance

Due to the alternating layers in the DBR mirrors, VCSELs inherently have much higher series resistance, ranging from tens to hundreds of ohms, compared with edge emitters. This excess resistance can limit the modulation bandwidth due to *RC* limitations and heating. Various bandgap-engineering schemes at the DBR interfaces, mostly for the *p*-mirror, have been proposed to simultaneously achieve low resistance and loss [48, 49]. Since *n*-type materials are less lossy and resistive, *p*-down configuration has also been pursued for top-emitting VCSELs [32, 50].

To eliminate the resistances and losses from the doped semiconductor DBR mirrors, one or both intracavity contacts with (partially) undoped semiconductor mirror/abrupt interfaces, mostly for oxide-confined VCSELs [35, 36], or dielectric DBR mirror, mostly for BTJ VCSELs with a regrown *n*-spacer for lower loss [6, 51], have been used. For dielectric DBR, several periods usually provide sufficient reflectivity due to large index contrast, which helps to compress the optical modes in the longitudinal direction. However, the uniformity of current injection, lateral sheet resistance, and optical loss from the highly-doped contact layers near the active region can be issues for intracavity contacts and must be considered in the device design [39].

Chip Parasitic Capacitance

Another source of the parasitics is the shunt mesa capacitance surrounding the active region. Figure 7.6 illustrates the sources of the mesa capacitance for oxide-confined and BTJ VCSELs. For oxide-confined VCSELs, the shunt mesa capacitance is the oxide capacitance C_{ox} in series with the capacitance from the intrinsic active region below the oxide aperture C_{int}. For BTJ VCSELs, the oxide capacitance is replaced by the depletion capacitance C_{dep} from the reverse-biased *p*–*n* junction.

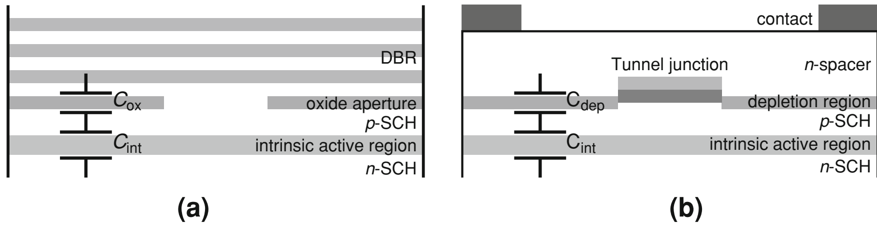

Fig. 7.6 Schematics illustrating parasitic mesa capacitance for **a** oxide-confined VCSEL and **b** BTJ VCSEL

Since all these layers are relatively thin, the mesa capacitance can be quite large. Combined with high series resistance, parasitics can greatly reduce the achievable bandwidth. To reduce the mesa capacitance, it is necessary to create additional (thick) nonconducting layers inside the mesa above or below these high-capacitance current blocking junctions, and this is commonly done using implantation [6, 37, 50]. For oxide-confined VCSELs with semiconductor mirrors, the nonconducting layers can also be formed by oxidizing additional one (double aperture) [34] or several higher aluminum layers (deep oxidation layers) [36]. This can be performed simultaneously with the oxide aperture to eliminate one fabrication step. Since the dielectric constant for the aluminum oxide is much smaller than that of the semiconductor, the total thickness of the nonconducting layers can be smaller. This reduces the funneled distance, usually at the lowest-doped layers, that current has to conduct, which is beneficial for resistance.

For edge emitters, which typically work at relatively high currents, the junction resistance is practically negligible. Therefore, the diffusion capacitance, which is in parallel with the junction resistance, can be neglected. However, this is not the case for VCSELs due to their small currents. The junction resistance and diffusion capacitance have to be considered. A graded SCH layer can potentially reduce the diffusion capacitance [23] and has been employed in high-speed VCSELs [33].

7.3.4 Pad Parasitics

Since the pad parasitics are in parallel with the current path of the intrinsic laser, it is important for these to have a high impedance, i.e., smaller pad capacitance and higher pad shunt resistance, to prevent current flowing through them.

Reasonable size pads are necessary to drive VCSELs, especially for bonding. However, the associated pad parasitics can greatly reduce the modulation bandwidth if precautions are not taken. For example, the pad capacitance for a $100 \times 100\ \mu\text{m}^2$ pad on a 200-nm-thick nitride is $\sim$3.3 pF, which is very large (see Table 7.1). To overcome this limitation, some thick low-dielectric-constant resin can be used underneath the signal pad. The two most common choices are polyimide [32, 50] and

benzocyclobutene (BCB) [34, 36], although silicon dioxide has also been used [37]. Just as a comparison, the same $100 \times 100\ \mu m^2$ pad on a 5-μm-thick BCB gives a pad capacitance of ∼47 fF, a 70 times reduction.

VCSELs grown on semi-insulating substrates can also have lower pad parasitics through co-planar transmission lines with lower microwave loss due to the removal of the resistive substrate. Similarly, removing the part of the contact layer that is underneath the signal pad also reduces the pad capacitance by enabling a higher impedance co-planar interconnecting line [5].

7.3.5 Thermal Management

Thermal management is always an important issue for high-speed devices. For VCSELs, most of the heat generated in the diode junction and DBRs is dissipated through the substrate. To more efficiently remove the heat, we can either integrate the devices on a substrate with higher thermal conductivity [52], e.g., copper which has ∼9 times of the thermal conductivity of GaAs, or provide additional heat sinking from the top surface and sidewalls using gold [53] or copper plating [54]. Compared with gold, copper is inexpensive and has high thermal conductivity, which makes it really attractive.

Figure 7.7 shows SEMs and schematic cross-section of copper-plated VCSELs [54]. The 4-μm-overlapped devices show considerably better thermal properties compared with the non-overlapped devices. This is because heat first flows laterally to the sidewalls and can eventually dissipate in the substrate through the copper, bypassing the more thermally-resistive bottom DBR. However, this relies on good thermal contact between the overlapped copper and substrate and would result a high parasitic capacitance if a thin dielectric is used. This trade-off can be addressed using flip-chip bonding so that heat can be dissipated through the bonded interface instead of the substrate, which relieves the restriction of the thickness of the dielectric layer [45].

In addition to improve heat dissipation, reducing the amount of heat generated is another way to prevent thermal degradation. Ideally, the relaxation resonance frequency should increase as the square root of the current density $J_0 = I_0/\text{Area}$. For a given current density, the temperature rise should be *lower* for smaller devices because power dissipation is roughly proportional to the area and thermal impedance is inversely proportional to the diameter [15]. However, smaller devices typically suffer from higher losses. If the size-dependent losses can be minimized, scaling the devices down should yield better performance. Size-dependent losses have been reduced by incorporating tapered apertures and this has allowed much smaller devices to be created with high bandwidths [55]. Perhaps more importantly, these smaller devices have lower currents for a given bandwidth, and a data-rate/power dissipation of 35 Gbps/10 mW has been reported [5].

Once the operating temperature is determined by the ambient temperature, heat generation and dissipation, the devices have to be optimized at that temperature.

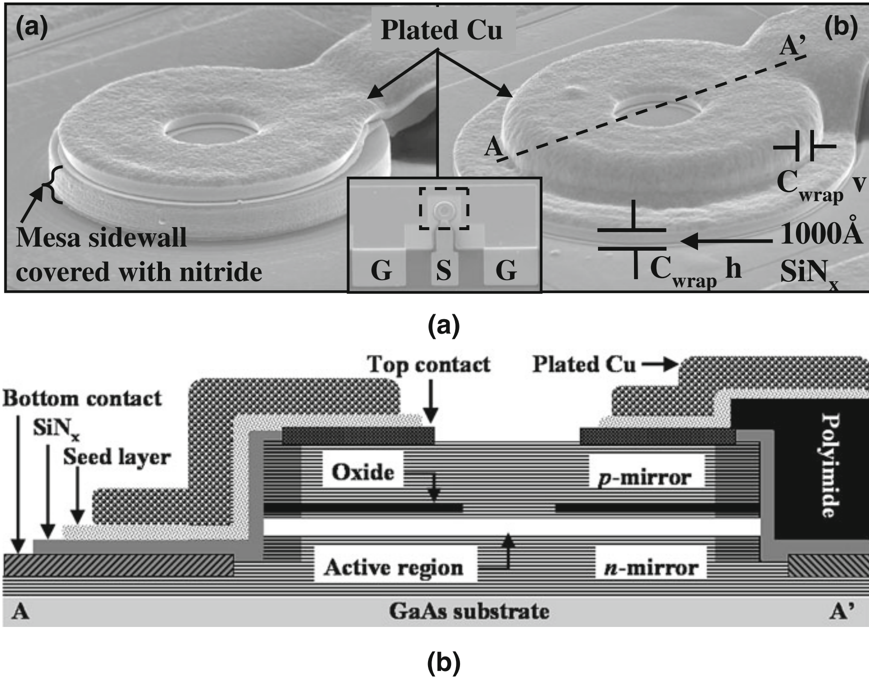

Fig. 7.7 **a** SEMs of copper-plated VCSELs. *Left*: heat sink from the top surface. *Right*: heat sink from both the top surface and sidewalls with 4-μm overlap with the substrate. **b** Cross-sectional schematic of the device [54] (© 2006 IEEE)

As the temperature increases, both the cavity mode and gain peak red-shift, but at different rates. Take 980-nm VCSELs with InGaAs QWs as an example, cavity-mode and gain peak shift at approximate 0.07 and 0.3 nm/°C, respectively [39]. By deliberately detuning the cavity-gain offset at room temperature, better high-temperature performance has been realized [56].

7.4 Performance of High-Speed VCSELs

This section reviews some of the high-speed VCSEL results at several different wavelengths. High-speed VCSELs operated at the datacom wavelengths, ranging from 0.83 to 1.1 μm, are exclusively GaAs-based and mainly for optical interconnects and short-distance optical links. Typical wavelengths include 850 nm, 980 nm, and 1.1 μm. LW-VCSELs operated at 1.3 and 1.55 μm are attractive as alternative light sources for optical links transmitting longer distances over SMF due to the low loss and dispersion of fibers at these wavelengths; both GaAs- and InP-based devices exist at the longer wavelengths.

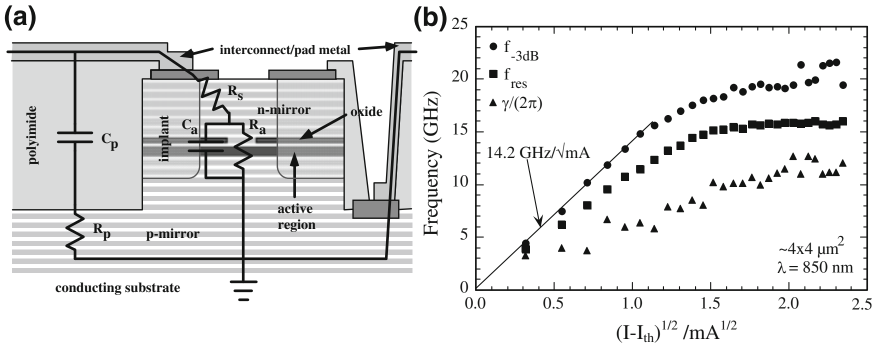

Fig. 7.8 **a** Device structure and **b** $f_{3\text{dB}}$, f_r, and $\gamma/(2\pi)$ vs. $(I-I_\text{th})^{1/2}$ for the 850-nm VCSELs with a bandwidth of 21.5 GHz [45] (© 1997 OSA)

7.4.1 850-nm VCSELs

VCSELs operating at 850-nm wavelength are probably the most mature VCSEL technology to date, because 850 nm has several fiber-based standards for short-haul datacom. Products using 850-nm VCSELs for 10 Gigabit Ethernet have been commercially available on the market for some time.

There are several active region choices for 850-nm emission including GaAs/AlGaAs [37], InGaAs/AlGaAs [34], InAlGaAs/AlGaAs [57], and InGaAsP/InGaP [58]. We will focus on the GaAs/AlGaAs and InGaAs/AlGaAs designs, which are more common nowadays.

GaAs/AlGaAs 850-nm VCSELs

The unstrained GaAs/AlGaAs multiple quantum wells (MQW) is the most common active region choice for 850-nm VCSELs, and many high-speed records were achieved with it. For example, the first VCSEL to demonstrate a bandwidth in excess of 20 GHz was achieved with this active region in 1997, and this is still the highest reported bandwidth for 850-nm VCSELs [50]. Figure 7.8 shows a cross-sectional schematic and $f_{3\text{dB}}$, f_r, and $\gamma/(2\pi)$ vs. $(I-I_\text{th})^{1/2}$ for the 4×4 μm^2 devices that achieved a 21.5-GHz bandwidth.

One of the reasons that these devices achieved a high bandwidth was their low-parasitic structure (see the first column of Table 7.1). The pad capacitance is only 42 fF using 5-μm-thick polyimide underneath the pad. The pad resistance is due to the dielectric loss of the polyimide. The series resistance is reduced to 28.3 Ω using *n*-up configuration. Despite the junction resistance is 289 Ω, high-dose proton implantation brings C_m down to 44.3 fF so that current still flows through the intrinsic laser. Since $f_\text{rc} = 36.4$ GHz, the bandwidth is not parasitic-limited. Because the relaxation resonance frequency and 3-dB frequency both saturate at about the same current, the bandwidth is limited by the intrinsic laser response. The damping-limited

bandwidth, extracted from *K*-factor, is 58 GHz. Therefore, the devices are limited by thermal effects.

The highest data rate reported for 850-nm VCSELs with GaAs QWs is 30 Gb/s at a bias current of 8 mA using 6-μm-diameter devices [37]. The maximum bandwidth is 19 GHz at that bias.

InGaAs/AlGaAs 850-nm VCSELs

One of the issues with unstrained GaAs/AlGaAs QWs is that it has lower differential gain compared with strained QWs. It has been shown that adding some indium, typically 10% or less, in the wells can double the achievable gain and differential gain [59]. In addition, the presence of indium has been shown to suppress the propagation of dark-line defects, which prevents sudden failure of the devices [60]. Data rates of 32 Gb/s [61] and 39 Gb/s [62] have been demonstrated using 850-nm VCSELs with InGaAs QWs.

The 9-μm devices which achieved 32-Gb/s operation at 25°C have a threshold current of 0.6 mA, fairly low for this size, and a slope efficiency of 0.8 W/A, which corresponds to a differential quantum efficiency (DQE) of ~55%. The parasitics are reduced using BCB, an undoped substrate, double oxide apertures, and bandgap-engineered DBRs. The series resistance is approximately 90 Ω. They also reported 25-Gb/s operation up to 85°C.

The devices that achieved a 39-Gb/s data rate have a diameter of ~6 μm, confined by an oxide aperture. BCB is used for reducing the pad parasitics, and a relatively large lower mesa for the bottom DBR is used for better heat dissipation, lower resistance, and easier manufacturing. The bias current for large-signal modulation is 9 mA, corresponding to a fairly low current density of ~10 kA/cm^2. Eye diagram at 40 Gb/s is also shown. The signal-to-noise ratio reduces from above 6.3 to 3.6, preventing error-free operation at 40 Gb/s.

7.4.2 980-nm VCSELs

Another common wavelength for high-speed VCSELs is 980 nm, which typically employs strained InGaAs/GaAs QWs. This aluminum-free active region offers high differential gain, low transparent carrier density, and superior reliability. Due to the transparency of GaAs substrates at 980 nm, bottom-emitting structure is commonly used.

InGaAs/GaAs 980-nm VCSELs

The highest MCEF for any QW-based VCSELs to date is 16.8 $GHz/mA^{1/2}$ using InGaAs/GaAs VCSELs at 970 nm [33]. One of the keys to achieve such high MCEF is the small mode volume. The dimensions of the devices are 3×3 μm^2, confined with double oxide apertures. Pad capacitance is estimated to be 40 fF for a 75×120 μm^2 bond pad. The threshold current is 0.37 mA and the DQE is 45%. The bandwidth

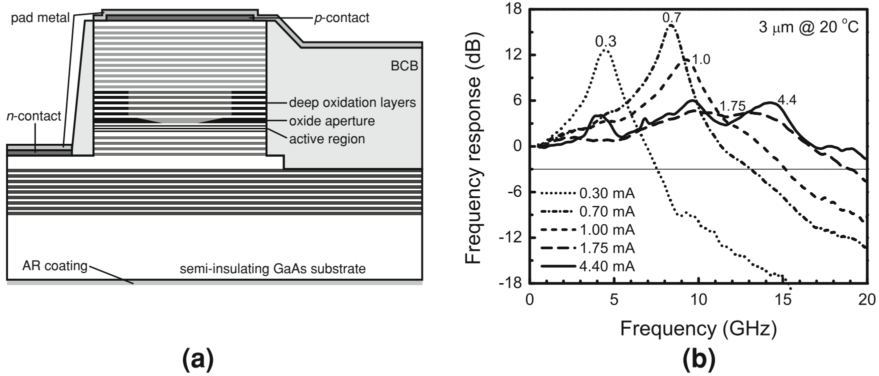

Fig. 7.9 **a** Structure and **b** frequency responses for 3-μm-diameter devices achieving 35-Gb/s operation

reaches 11.2 GHz at a bias current of only 1 mA, and the maximum bandwidth is 16.3 GHz at 4.5 mA.

The highest data rate reported for 980-nm VCSELs is 35 Gb/s using the structure shown in Fig. 7.9a [5]. Instead of the conventional quarter-wavelength-thick blunt oxide aperture, a half-wavelength-thick tapered oxide aperture is used. The taper length is carefully chosen to provide sufficient mode confinement while still maintaining low optical scattering losses [55]. This enables the smaller 3-μm devices, which typically suffer from high optical losses, to be used. The low pad capacitance of 29 fF is realized by using BCB, selectively etching off the *n*-GaAs contact layer underneath the signal pad, and shrinking the pad dimensions. Deep oxidation layers as well as the thick oxide aperture effectively reduce C_m down to ~88 fF. The devices have a threshold current of only 0.14 mA and a slope efficiency of 0.67 W/A (DQE = 0.54). The series resistance is approximately 250 Ω.

Figure 7.9b plots the frequency responses of the devices at 20°C. Due to the small size, a bandwidth of 15 GHz is achieved at a bias current of only 1 mA, corresponding to a power dissipation of 1.3 mW. The temperature rise is estimated to be 4.3°C. It is evident that small devices are more efficient and can achieve the bandwidth with lower currents and temperature rise, even with a somewhat higher series resistance than desired in this case. A bandwidth exceeding 20 GHz is also demonstrated for currents larger than 2 mA. The bandwidth is limited by multimoding above 2 mA; simulations illustrate that the maximum bandwidth would be ~25 GHz if single-mode operation were maintained. The MCEF at low biases is 16.7 GHz/mA$^{1/2}$. 35-Gb/s operation was achieved with a bias current of only 4.4 mA. This corresponds to a very high data-rate/power-dissipation ratio of 3.5 (Gb/s)/mW.

InAs QD 980-nm VCSELs

Another active region choice for 980-nm VCSELs is submonolayer deposited quantum dots, which provides higher differential gain and better temperature

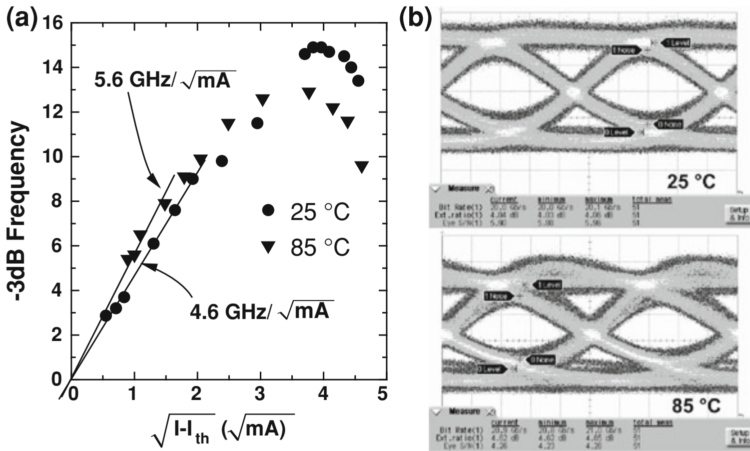

Fig. 7.10 **a** f_{3dB} vs. $(I - I_{th})^{1/2}$ and **b** 20-Gb/s eye diagrams for 6-μm QD VCSELs at 25°C and 85°C [63] (© 2006 SPIE)

insensitivity [63]. Their 1-μm single-mode devices show the highest MCEF of 19 GHz/mA$^{1/2}$ for any VCSELs to date. For their 6-μm multimode devices, the threshold currents at 25°C and 85°C are 0.29 and 0.16 mA, respectively, due to better cavity–gain alignment at elevated temperatures.

Figure 7.10 shows f_{3dB} vs. $(I - I_{th})^{1/2}$ and eye diagrams for 6-μm devices at 25°C and 85°C. The MCEF drops from 5.6 to 4.6 GHz/mA$^{1/2}$ for the temperature increased from 25°C to 85°C. The maximum bandwidth at 25°C and 85°C are 15 and 13 GHz, respectively. These bandwidths still can support 20-Gb/s operation as shown in the eye diagrams. The eye is slightly degraded at 85°C. Recently, they demonstrated 20-Gb/s operation up to 120°C using 2-μm single-mode devices [64].

7.4.3 1.1-μm VCSELs

High-speed VCSELs operating in the 1.1-μm-wavelength range have resulted from engineering the MQW InGaAs/GaAs active region to have the maximum allowable strain as well as *p*-type modulation doping [65]. The active region consists of three thin highly-strained $In_{0.3}Ga_{0.7}As/GaAs$ (5/10 nm) QWs. The GaAs barriers are modulation doped *p*-type at 2×10^{18} cm^{-3} to reduce gain nonlinearity. Two types of device structures have been reported: oxide-confined VCSELs and BTJ VCSELs.

Figure 7.11a shows their oxide-confined VCSEL structure. The 6.9-μm-diameter devices have a threshold current of 0.4 mA and a series resistance of 135 Ω. Because the mesa is relatively large at 33 μm in diameter, proton implantation is used to reduce the mesa capacitance. The pad capacitance is lowered using polyimide. The

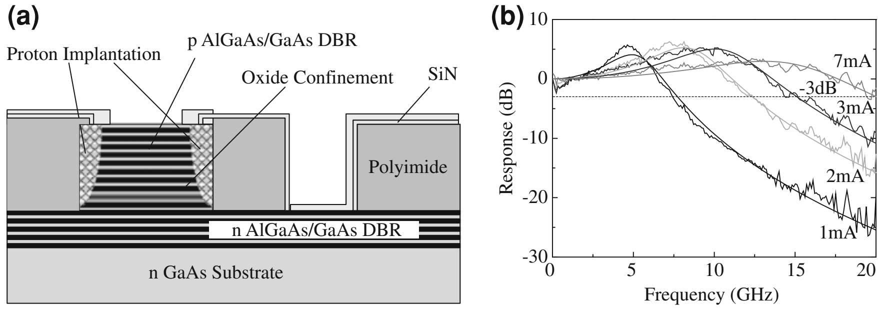

Fig. 7.11 **a** Cross-sectional schematic and **b** frequency responses of oxide-confined 6.9-µm-diameter 1.1-µm VCSELs [66] (© 2007 IEEE)

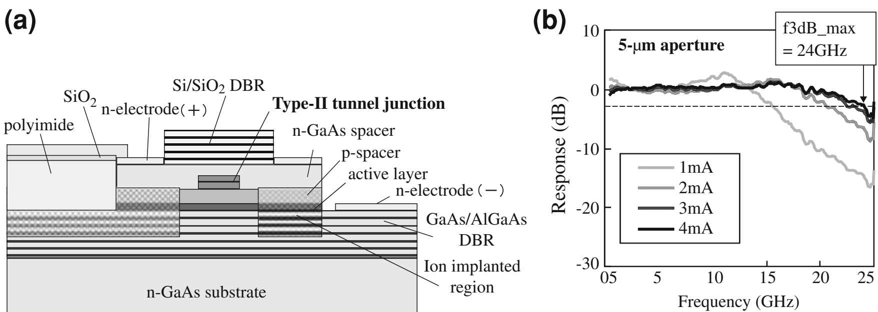

Fig. 7.12 **a** Structure and **b** frequency responses for 1.1-µm, BTJ VCSELs [67] (© 2008 OSA)

devices achieve a maximum bandwidth of 20 GHz at a bias of 7 mA, as shown in Fig. 7.11. Transmission at 30 Gb/s back-to-back and over 100-m multi-mode fiber have been done, and the power penalty is ~2 dB.

The main limiting factor in their oxide-confined devices is self-heating effect, which causes the relaxation resonance frequency to saturate at high biases. To address this limitation, a low-resistance type-II BTJ is used so that the more resistive *p*-layer can be replaced with a less resistive *n*-spacer. The devices use top-emitting, double-intracavity structure shown in Fig. 7.12a.

The electrical and optical confinement is achieved by selectively etching the tunnel junction and regrowing the *n*-GaAs spacer layer. Oxygen ions are implanted around the tunnel junction to reduce the mesa capacitance. The pad capacitance is similarly reduced using polyimide. Dielectric Si/SiO_2 DBR is used for the top mirror.

Figure 7.12b plots the frequency responses for 5-µm-diameter devices. The maximum 3-dB frequency is 24 GHz at a bias current of 4 mA, which is the highest bandwidth reported for directly current-modulated VCSELs to date. A data rate of 40 Gb/s, which is also the highest data rate for VCSELs to date, is achieved using 6-µm devices at a bias current of 5 mA.

All these results were achieved at room temperature. To improve the high-temperature performance, they have also developed a new active region with strain-compensated $In_{0.3}Ga_{0.7}As/GaAs_{0.8}P_{0.2}$ QWs [68]. By increasing the conduction-band offset, electrons are better confined at the elevated temperature. A data rate of 25 Gb/s is achieved using oxide-confined structure.

7.4.4 Long-Wavelength VCSELs

Several technologies exist for LW-VCSELs, and they will be covered in more detail in Chaps. 11 and 12 of this book. The main application of high-speed LW-VCSELs is to use for optical networks, which currently require transmission up to 10 Gb/s over SMF. Here we summarize some current high-speed results for LW-VCSELs.

GaAs-Based Long-Wavelength VCSELs

GaAs-based LW-VCSELs are attractive due to the well-established technologies of short-wavelength VCSELs such as oxide apertures and bandgap-engineered, high-index-contrast DBRs. The main challenge is the choice of the gain media that can be pseudomorphically grown on GaAs substrates to reach longer emission wavelengths. Currently, GaAs-based LW-VCSELs are mainly operated below 1.3-μm wavelength, and there are three active region candidates [69]: highly strained InGaAs QWs, GaInNAs QWs, and InAs QDs.

The structure of GaAs-based LW-VCSELs is usually pretty similar to short-wavelength VCSELs except with a different gain media. Transmission at 10 Gb/s over 9-km SMF from 25°C to 85°C has been reported using highly strained InGaAs QWs emitting at 1.28 μm [13]. The indium content of the QWs is increased to 42% to push the gain peak to 1220 nm, and the cavity mode is detuned at 1275 nm, giving a large gain-cavity offset for better high-temperature stability [70]. An inverted surface relief is patterned on the top mirror for single-mode operation. However, the threshold current seems fairly high and reduces at higher temperature due to better cavity–gain alignment. The bandwidth is mostly limited by parasitics.

LW-VCSELs based on a GaInNAs active region emitting at 1.28 μm have also demonstrated 10-Gb/s transmission over 20-km SMF [11]. These devices show good reliability and have been placed into production [11, 71].

InP-Based Long-Wavelength VCSELs

For InP-based LW-VCSELs, the mature high-reliability InAlGaAs or InGaAsP active region can be used. The main issues are (a) the lack of DBR materials which provide high reflectivity and thermal conductivity, (b) the more extreme sensitivity to elevated temperatures, and (c) the realization of lateral mode confinement.

The first of these issues was addressed with an all-epitaxial approach using lattice-matched AlGaAsSb DBRs, which offer relatively high reflectivity, and an air-gap aperture formed by selectively etching tunnel junction. These have been explored

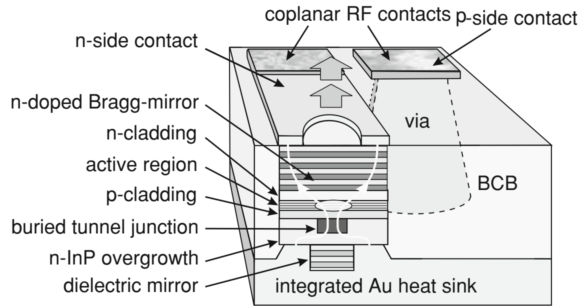

Fig. 7.13 Structure of InP-based BTJ LW-VCSEL [73] (© 2008 IEEE)

and demonstrated reasonable DC characteristics as well as 3.125-Gb/s operation up to 60°C [72]. The poor electrical and thermal conductivity of the quaternary DBRs was addressed by using *n*-type intracavity InP contact layers, but these also added to the cavity length, which increased the cavity volume, and thus, reduced the frequency response.

Another approach is to use BTJ, pioneered by Amann et al. at Walter Schottky Institute. Some of the best high-speed performance for LW-VCSELs to date are demonstrated based on this platform. Figure 7.13 shows the structure of their devices. The lateral current and mode confinement is provided by the BTJ, which also enables the regrown InP spacing layer to be *n*-type for lower loss and resistance. The back mirror consists of several periods of CaF_2/ZnS dielectric DBR and a gold termination layer, which also works as a heat sink. The device is passivated with BCB for high-speed operation.

Based on this structure, bandwidth exceeding 10 GHz has been demonstrated for both 1.3- and 1.55-μm wavelengths at room temperature [12, 51] and is limited by parasitics and thermal effects. Transmission at 10 Gb/s for 22 km and 12.5 Gb/s for 3 km have also been reported at 1.3- and 1.55-μm wavelengths, respectively.

Corning also reported LW-VCSELs with 10-Gb/s transmission for both 1.3- and 1.55-μm wavelengths up to 85°C [10]. Their devices, shown in Fig. 7.14, are based on similar BTJ technology with a dielectric top mirror. However, they use double-intracavity contacts with top emission, which greatly simplifies the device structure and can be mass manufactured more easily.

Wafer-Fused Long-Wavelength VCSELs

Both InP-based active region and GaAs-based DBRs are preferable for LW-VCSELs. Therefore, wafer fusion, pioneered by Bowers et al. at University of California, Santa Barbara, has been used to combine these two material systems. Transmission at 10 Gb/s over 10-km standard SMF has been reported [44]. The structure consists of undoped top and bottom AlGaAs/GaAs DBRs, wafer fused with InAlGaAs/InP cavity grown on an InP substrate. A tunnel junction is used for lateral confinement.

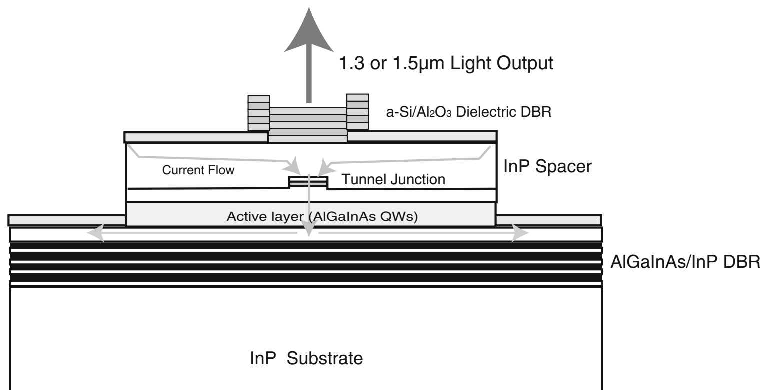

Fig. 7.14 Cross-sectional schematic of BTJ LW-VCSELs with double-intracavity contacts [74] (© 2005 IEEE)

7.5 Loss-Modulated High-Speed VCSELs

Due to inherent damping limitations, it would be very challenging for directly current-modulated VCSELs to reach bandwidth beyond 40 GHz, even after the parasitic and thermal limitations have been removed. The highest modulation bandwidth to date is still limited below 25 GHz [6]. Alternative approaches have to be pursued to extend the bandwidth, e.g., optical injection locking and loss modulation. Optically injection locked VCSELs have demonstrated an impressive modulation bandwidth of 66 GHz based on a cascaded configuration [75]. However, a separated master laser is required. Therefore, we only consider coupled-cavity loss-modulated VCSELs here.

7.5.1 Principle of Operation

All the devices that have been discussed so far are based on current modulation, which is an indirect way to modulate the photon density. Alternatively, the photon density can be modulated by varying the cavity loss, which has been theoretically predicted to have higher modulation bandwidth [76].

In the rate equations discussed in Sect. 7.2, the losses are included through the photon lifetime $\tau_\mathrm{p}^{-1} = v_\mathrm{g}(\alpha_\mathrm{i} + \alpha_\mathrm{m})$, where α_i and α_m are the internal loss and mirror loss, respectively. Here, we apply the small-signal analysis for loss modulation, similar to (7.3a), by assuming

$$\frac{1}{\tau_\mathrm{p}} = v_\mathrm{g}(\alpha_0 + \alpha_1 \mathrm{e}^{j\omega t}) = \frac{1}{\tau_{\mathrm{p}0}}(1 + m\mathrm{e}^{j\omega t}) \tag{7.12}$$

where α_0 is the steady-state total loss, α_1 is the small-signal loss modulation amplitude, $\tau_{\mathrm{p}0} = (v_\mathrm{g}\alpha_0)^{-1}$ is the steady-state photon lifetime, and $m = \alpha_1/\alpha_0$ is the loss

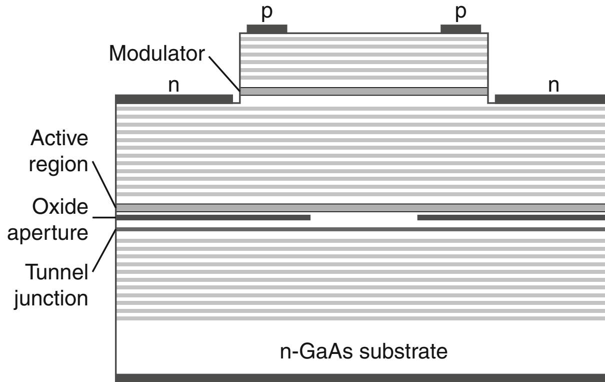

Fig. 7.15 Cross-sectional schematic of EAM-VCSEL [78]

modulation depth. Following the same procedure as we did for current modulation, the transfer function for loss-modulated intrinsic laser can be written as [77]

$$H_{\mathrm{L}}(\omega) = \frac{m}{\tau_{\mathrm{p0}}} \frac{\omega_{\mathrm{r}}^2 \tau_{\mathrm{p}} + j\omega}{(\omega_{\mathrm{r}}^2 - \omega^2 + j\omega\gamma)}. \tag{7.13}$$

The main difference between loss modulation and current modulation is the decay rate after the resonance: $1/\omega$ (20 dB/decade) for loss modulation and $1/\omega^2$ (40 dB/decade) for current modulation. In addition, the resonance peak is also stronger for loss modulation, which can be an issue for data transmission.

Two mechanisms have been used to achieve loss modulation in coupled-cavity VCSELs. One is to modulate the internal loss α_{i} using an electroabsorption modulator, and the other is to modulate the mirror loss α_{m} using an electrooptical modulator.

7.5.2 VCSELs with an Electroabsorption Modulator

Figure 7.15 shows the cross-sectional schematic of VCSEL with an intracavity electroabsorption modulator (EAM-VCSEL). It is basically a *p–n–p* configuration with a tunnel junction below the active region to reverse the polarity of the bottom contact. Reverse-biased MQW, placed at the standing-wave peak for maximal efficiency, is used as the modulator. A 17-GHz modulation bandwidth with a distinct 20 dB resonance peak has been reported [78]. The roll-off slope is ∼45 dB/decade with parasitics ($f_0 \sim 8$ GHz), showing a slower decay rate compared with current-modulated devices.

Recently, the same group demonstrated optically decoupled loss modulation in a duo-cavity VCSELs by carefully detuning the resonances of the cavities [79]. The photon density in the active region remains unchanged under loss modulation, similar

to the case of using an external modulator with a continuous-wave laser. Relatively flat frequency responses up to 20 GHz have been shown.

7.5.3 VCSELs with an Electrooptical Modulator

Another possible way of achieving loss modulation is to integrate an electrooptical modulator in the VCSEL structure (EOM-VCSEL). The refractive index of the electrooptical modulator (MQW) can be tuned by an applied voltage. If properly designed, the cavity mode of the modulator cavity can be tuned in and out of the resonance of the VCSEL cavity, which effectively modulates the mirror reflectivity, i.e., the mirror loss α_{m}. Small-signal modulation bandwidth up to 35 GHz, limited by the photodiode, has been reported with EOM-VCSELs [80].

7.6 Conclusion

The chapter provides an overview of the current status for high-speed VCSELs. We discussed the basic theory for current modulation of VCSELs, various high-speed designs, and device performance. Novel structures and new material systems have been pursued to overcome many of the bandwidth limitations to achieve higher performance. For short-wavelength VCSELs, bandwidth up to 24 GHz and a data rate of 40 Gb/s have been successfully demonstrated. For LW-VCSELs, single-mode, 10-Gb/s transmission over a wide temperature range has also been reported by several groups. We also considered loss-modulated VCSELs which are still under development and have the potential to reach even higher bandwidth. As these technologies become more mature and the supporting components such as high-speed photodetectors are ready, VCSELs will be used as low-cost, power-efficient, high-speed light sources for most optical data communications.

Acknowledgments The authors would like to thank the support of DARPA via the C2OI project and IBM and Corning via the UC-MICRO program.

References

1. D.A.B. Miller, Physical reasons for optical interconnection. Int. J. Optoelectronics **11**, 155 (1997)
2. D.M. Kuchta, P. Pepeljugoski, Y. Kwark, VCSEL modulation at 20Gb/s over 200m of multimode fiber using a 3.3v SiGe laser driver IC, in *Technical Digest LEOS Summer Topical Meeting*, Copper Mountain, CO (2001), p. 49

3. N. Suzuki, H. Hatakeyama, K. Fukatsu, T. Anan, K. Yashiki, M. Tsuji, 25-Gbps operation of 1.1-μm-range InGaAs VCSELs for high-speed optical interconnections, in *Proceedings of Optical Fiber Communication Conference*, *OFC 2006*, Anaheim, CA (2006)
4. K. Yashiki, N. Suzuki, K. Fukatsu, T. Anan, H. Hatakeyama, M. Tsuji, 1.1-μm-range tunnel junction VCSELs with 27-GHz relaxation oscillation frequency, in *Proceedings of Optical Fiber Communication Conference*, *OFC 2007*, Anaheim, CA (2007)
5. Y.-C. Chang, C.S Wang, L.A Coldren, High-efficiency, high-speed VCSELs with 35 Gbit/s error-free operation. Electron. Lett. **43**(19), 1022 (2007)
6. T. Anan, N. Suzuki, K. Yashiki, K. Fukatsu, H. Hatakeyama, T. Akagawa, K. Tokutome, M. Tsuji, High-speed InGaAs VCSELs for optical interconnects. in *Proceedings of International Symposium on VCSELs and Integrated Photonics*, paper E3, Tokyo, Japan (2007)
7. B.E. Lemoff, M.E. Ali, G. Panotopoulos, E. de Groot, G.M. Flower, G.H. Rankin, A.J. Schmit, K.D. Djordjev, M.R.T. Tan, A. Tandon, W. Gong, R.P. Tella, B. Law, D.W. Dolfi, Parallel-WDM for multi-Tb/s optical interconnects, in *Proceedings of IEEE Lasers and Electro-Optical Society Annual Meeting*, *LEOS 2005*, Sydney (2005), p. 359
8. C.L. Schow, F.E. Doany, O. Liboiron-Ladouceur, C. Baks, D.M. Kuchta, L. Schares, R. John, J.A. Kash, 160-Gb/s, 16-channel full-duplex, single-chip CMOS optical transceiver, in *Proceedings of Optical Fiber Communication Conference*, *OFC 2007*, Anaheim, CA (2007)
9. J. Cheng, C.-L. Shieh, X. Huang, G. Liu, M. Murty, C.C. Lin, D.X. Xu, Efficient CW lasing and high-speed modulation of 1.3-μm AlGaInAs VCSELs with good high temperature lasing performance. IEEE Photon. Technol. Lett. **17**(1), 7 (2005)
10. N. Nishiyama, C. Caneau, J.D. Downie, M. Sauer, C.-E. Zah, 10-Gbps 1.3 and 1.55-μm InP-based VCSELs: 85°C 10-km error-free transmission and room temperature 40-km transmission at 1.55-μm with EDC, in *Proceedings of Optical Fiber Communication Conference*, *OFC 2006*, Anaheim, CA (2006)
11. J. Jewell, L. Graham, M. Crom, K. Maranowski, J. Smith, T. Fanning, 1310 nm VCSELs in 1–10 Gb/s commercial applications, in *Vertical-Cavity Surface-Emitting Lasers X*, ed. by C. Lei, K.D. Choquette, Proceedings of SPIE, vol. 6132 (2007), p. 613204-1
12. W. Hofmann, N.H. Zhu, M. Ortsiefer, G. Böhm, Y. Liu, M.-C. Amann, High speed (> 11GHz) modulation of BCB-passivated 1.55μm InGaAlAs-InP VCSELs. Electron. Lett. **42**(17), 976 (2006)
13. E. Söderberg, J.S. Gustavsson, P. Modh, A. Larsson, Z. Zhang, J. Berggren, M. Hammar, High-temperature dynamics, high-speed modulation, and transmission experiments using 1.3-μm InGaAs single-mode VCSELs. J. Lightwave Technol. **25**(9), 2791 (2007)
14. R.S. Tucker, High-speed modulation of semiconductor lasers. J. Lightwave Technol. **3**(6), 1180 (1985)
15. L.A. Coldren, S.W. Corzine, *Diode Lasers and Photonic Integrated Circuits* (Wiley, New York, 1995)
16. D. Tauber, G. Wang, R.S. Geels, J.E. Bowers, L.A. Coldren, Large and small signal dynamics of vertical cavity surface emitting lasers. Appl. Phys. Lett. **62**(4), 325 (1993)
17. T.R. Chen, B. Zhao, L. Eng, Y.H. Zhuang, J. O'Brien, A. Yariv, Very high modulation efficiency of ultralow threshold current single quantum well InGaAs lasers. Electron. Lett. **29**(17), 1525 (1993)
18. R. Nagarajan, T. Fukushima, S.W. Corzine, J.E. Bowers, Effects of carrier transport on high-speed quantum well lasers. Appl. Phys. Lett. **59**(15), 1835 (1991)
19. Y. Liu, W.-C. Ng, B. Klein, K. Hess, Effects of the spatial nonuniformity of optical transverse modes on the modulation response of vertical-cavity surface-emitting lasers. IEEE J. Quantum Electron. **39**(1), 99 (2003)
20. J.W. Scott, R.S. Geels, S.W. Corzine, L.A. Coldren, Modeling temperature effects and spatial hole burning to optimize vertical-cavity surface-emitting laser performance. IEEE J. Quantum Electron. **29**(5), 1295 (1993)

21. S.F. Yu, W.N. Wong, P. Shum, E.H. Li, Theoretical analysis of modulation response and second-order harmonic distortion in vertical-cavity surface-emitting lasers. IEEE J. Quantum Electron. **32**(12), 2139 (1996)
22. M. Willatzen, T. Takahashi, Y. Arakawa, Nonlinear gain effects due to carrier heating and spectral hole burning in strained-quantum-well lasers. IEEE Photon. Technol. Lett. **4**(7), 682 (1992)
23. Y. Liu, W.-C. Ng, F. Oyafuso, B. Klein, K. Hess, Simulating the modulation response of VCSELs: the effects of diffusion capacitance and spatial hole-burning. IEE Proc. Optoelectron. **149**(4), 182 (2002)
24. J. Strologas, K. Hess, Diffusion capacitance and laser diodes. IEEE Trans. Electron Devices **51**(3), 506 (2004)
25. K.Y. Lau, A. Yariv, Ultra-high speed semiconductor lasers. IEEE J. Quantum Electron. **21**(2), 121 (1985)
26. Y. Arakawa, A. Yariv, Quantum well lasers—gain, spectra, dynamics. IEEE J. Quantum Electron. **22**(9), 1887 (1986)
27. J.D. Ralston, S. Weisser, I. Esquivias, E.C. Larkins, J. Rosenzweig, P.J. Tasker, J. Fleissner, Control of differential gain, nonlinear gain, and damping factor for high-speed application of GaAs-based MQW lasers. IEEE J. Quantum Electron. **29**(6), 1648 (1993)
28. A. Schönfelder, S. Weisser, I. Esquivias, J.D. Ralston, J. Rosenzweig, Theoretical investigation of gain enhancements in strained $In_{0.35}Ga_{0.65}As/GaAs$ MQW lasers via p-doping. IEEE Photon. Technol. Lett. **6**(4), 475 (1994)
29. B. Zhao, T.R. Chen, A. Yariv, The extra differential gain enhancement in multiple-quantum-well lasers. IEEE Photon. Technol. Lett. **4**(2), 124 (1992)
30. K.L. Lear, R.P. Schneider Jr., K.D. Choquette, S.P. Kilcoyne, Index guiding dependent effects in implant and oxide confined vertical-cavity lasers. IEEE Photon. Technol. Lett. **8**(6), 740 (1996)
31. Y. Satuby, M. Orenstein, Limits of the modulation response of a single-mode proton implanted VCSEL. IEEE Photon. Technol. Lett. **10**(6), 760 (1998)
32. A.N. AL-Omari, K.L. Lear, Polyimide-planarized vertical-cavity surface-emitting lasers with 17.0-GHz bandwidth. IEEE Photon. Technol. Lett. **16**(4), 969 (2004)
33. K.L. Lear, A. Mar, K.D. Choquette, S.P. Kilcoyne, R.P. Schneider Jr., K.M. Geib, High-frequency modulation of oxide-confined vertical cavity surface emitting lasers. Electron. Lett. **32**(5), 457 (1996)
34. P. Westbergh, J.S. Gustavsson, Å. Haglund, H. Sunnerud, A. Larsson, Large aperture 850 nm VCSELs operating at bit rates up to 25 Gbit/s. Electron. Lett. **4**(15), 907 (2008)
35. B.J. Thibeault, K. Bertilsson, E.R. Hegblom, E. Strzelecka, P.D. Floyd, R. Naone, L.A. Coldren, High-speed characteristics of low-optical loss oxide-apertured vertical-cavity lasers. IEEE Photon. Technol. Lett. **9**(1), 11 (1997)
36. Y.-C. Chang, C.S. Wang, L.A. Johansson, L.A. Coldren, High-efficiency, high-speed VCSELs with deep oxidation layers. Electron. Lett. **42**(22), 1281 (2006)
37. R.H. Johnson, D.M. Kuchta, 30 Gb/s directly modulated 850 nm datacom VCSELs, in *Conference on Lasers and Electro-Optics*, CLEO 2008, San Jose, CA (2008)
38. E.R. Hegblom, D.I. Babic, B.J. Thibeault, L.A. Coldren, Scattering losses from dielectric apertures in vertical-cavity lasers. IEEE J. Select. Topics Quantum Electron. **3**(2), 379 (1997)
39. L.A. Coldren, E.R. Hegblom, Fundamental issues in VCSEL design. Chap. 2 in *Vertical-Cavity Surface-Emitting Lasers*, ed. by C. Wilmsen, H. Temkin, L.A. Coldren (Cambridge University Press, Cambridge, 1999), pp. 32–67
40. Y.H. Chang, H.C. Kuo, F.-I. Lai, K.F. Tzeng, H.C. Yu, C.P. Sung, H.P. Yang, S.C. Wang, High speed (>13 GHz) modulation of 850 nm vertical cavity surface emitting lasers (VCSELs) with tapered oxide confined layer. IEE Proc. Optoelectron. **152**(3), 170 (2005)
41. Å. Haglund, J.S. Gustavsson, P. Modh, A. Larsson, Dynamic mode stability analysis of surface relief VCSELs under strong RF modulation. IEEE Photon. Technol. Lett. **17**(8), 1602 (2005)

42. C.C. Chen, S.J. Liaw, Y.J. Yang, Stable single-mode operation of an 850-nm VCSEL with a higher order mode absorber formed by shallow Zn diffusion. IEEE Photon. Technol. Lett. **13**(4), 266 (2001)
43. J.-W. Shi, C.-C. Chen, Y.-S. Wu, S.-H. Guol, C. Kuo, Y.-J. Yang, High-power and high-speed Zn-diffusion single fundamental-mode vertical-cavity surface-emitting lasers at 850-nm wavelength. IEEE Photon. Technol. Lett. **20**(13), 1121 (2008)
44. A. Syrbu, A. Mereuta, V. Iakovlev, A. Caliman, P. Royo, E. Kapon, 10 Gbps VCSELs with high single mode output in 1310 nm and 1550 nm wavelength bands, in *Proceedings of Optical Fiber Communication Conference*, *OFC 2008*, San Diego, CA (2008)
45. K.L. Lear, A.N. Al-Omari, Progress and issues for high-speed vertical cavity surface emitting lasers, in *Vertical-Cavity Surface-Emitting Lasers XI*, ed. by K.D. Choquette, J.K. Guenter, Proceedings of SPIE, vol. 6484 (2007), p. 64840J-1
46. Y.-C. Chang, L.A. Coldren, Efficient, high-data-rate, tapered oxide-aperture vertical-cavity surface-emitting lasers. IEEE J. Select. Topics Quantum Electron. **15**(3), 704 (2009)
47. C.-K. Lin, A. Tandon, K. Djordjev, S.W. Corzine, M.R.T. Tan, High-speed 985 nm bottom-emitting VCSEL arrays for chip-to-chip parallel optical interconnects. IEEE J. Select. Topics Quantum Electron. **13**(5), 1332 (2007)
48. M.G. Peters, B.J. Thibeault, D.B. Young, J.W. Scott, F.H. Peters, A.C. Gossard, L.A. Coldren, Band-gap engineered digital alloy interfaces for lower resistance vertical-cavity surface-emitting lasers. Appl. Phys. Lett. **63**(25), 3411 (1993)
49. K.L. Lear, R.P Schneider Jr., Uniparabolic mirror grading for vertical cavity surface emitting lasers. Appl. Phys. Lett. **68**(5), 605 (1996)
50. K.L. Lear, V.M. Hietala, H.Q. Hou, J. Banas, B.E. Hammons, J. Zolper, S.P. Kilcoyne, Small and large signal modulation of 850 nm oxide-confined vertical-cavity surface-emitting lasers, in *Conference on Lasers and Electro-Optics*, *CLEO'97*, Baltimore, MD (1997)
51. M. Ortsiefer, W. Hofmann, E. Rönneberg, A. Boletti, A. Gatto, P. Boffi, J. Rosskopf, R. Shau, C. Neumeyr, G. Böhm, M. Martinelli, M.-C. Amann, High speed 1.3μm VCSELs for 12.5 Gbit/s optical interconnects. Electron. Lett. **44**(16), 974 (2008)
52. D.L. Mathine, H. Nejad, D.R. Allee, R. Droopad, G.N. Maracas, Reduction of the thermal impedance of vertical-cavtiy surface-emitting lasers after integration with copper substrates. Appl. Phys. Lett. **69**(4), 463 (1996)
53. T. Wipiejewski, D.B. Young, M.G. Perers, B.J. Thibeault, L.A. Coldren, Improved performance of vertical-cavity surface-emitting laser diodes with Au-plated heat spreading layer. Electron. Lett. **31**(4), 279 (1995)
54. A.N. AL-Omari, G.P Carey, S. Hallstein, J.P. Watson, G. Dang, K.L. Lear, Low thermal resistance high-speed top-emitting 980-nm VCSELs. IEEE Photon. Technol. Lett. **18**(11), 1225 (2006)
55. Y.-C. Chang, L.A. Coldren, Optimization of VCSEL structure for high-speed operation, in *Proceedings of IEEE International Semiconductor Laser Conference*, *ISLC 2008*, Sorrento, Italy (2008), p. 159
56. D.B. Young, J.W. Scott, F.H. Peters, M.G. Peters, M.L. Majewski, B.J. Thibeault, S.W. Corzine, L.A. Coldren, Enhanced performance of offset-gain high-barrier vertical-cavity surface-emitting lasers. IEEE J. Quantum Electron. **29**(6), 2013 (1993)
57. J. Ko, E.R. Hegblom, Y. Akulova, B.J. Thibeault, L.A. Coldren, Low-threshold 840-nm laterally oxidized vertical-cavity lasers using AlInGaAs-AlGaAs strained active layers. IEEE Photon. Technol. Lett. **9**(7), 863 (1997)
58. H.C. Kuo, Y.S. Chang, F.Y. Lai, T.H. Hsueh, L.H. Laih, S.C. Wang, High-speed modulation of 850 nm InGaAsP/InGaP strain-compensated VCSELs. Electron. Lett. **39**(14), 1051 (2003)
59. T. Aggerstam, R.M.V. Würtemberg, C. Runnström, E. Choumas, Large aperture 850 nm oxide-confined VCSELs for 10 Gb/s data communication, in *Vertical-Cavity Surface-Emitting Lasers VI*, ed. by C. Lei, S.P. Kilcoyne, Proceedings of SPIE, vol. 4649 (2002), p. 19

60. S.L. Yellen, A.H. Shepard, R.J. Dalby, J.A. Baumann, H.B. Serreze, T.S. Guido, R. Soltz, K.J. Bystrom, C.M. Harding, R.G. Waters, Reliability of GaAs-based semiconductor diode lasers: 0.6–1.1 μm. IEEE J. Quantum Electron. **29**(6), 2058 (1993)
61. P. Westbergh, J.S. Gustavsson, Å. Haglund, A. Larsson, H. Hopfer, G. Fiol, D. Bimberg, A. Joel, 32 Gbit/s multimode fibre transmission using a high speed, low current density 850 nm VCSEL. Electron. Lett. **45**(7), 366 (2009)
62. S.A. Blokhin, J.A. Lott, A. Mutig, G. Fiol, N.N. Ledentsov, M.V. Maximov, A.M. Nadtochiy, V.A. Shchukin, D. Bimberg, 40 Gbit/s oxide-confined 850 nm VCSELs. Electron. Lett. **45**(10), 501 (2009)
63. F. Hopfer, A. Mutig, G. Fiol, M. Kuntz, S.S. Mikhrin, I.L. Krestnikov, D.A. Livshits, A.R. Kovsh, C. Bornholdt, V. Shchukin, N.N. Ledentsov, V. Gaysler, N.D. Zakharov, P. Werner, D. Bimberg, 20 Gb/s direct modulation of 980 nm VCSELs based on submonolayer deposition of quantum dots, in *Workshop on Optical Components for Broadband Communication*, ed. by P.-Y. Fonjallaz, T.P. Pearsall, Proceedings of SPIE, vol. 6350 (2006), p. 635003-1
64. A. Mutig, G. Fiol, P. Moser, F. Hopfer, M. Kuntz, V. Shchukin, N. Ledentsov, D. Bimberg, S. Mikhrin, I. Krestnikov, D. Livshits, A. Kovsh, 120 °C 20 Gbit/s operation of 980 nm single mode VCSEL, in *Proceedings of IEEE International Semiconductor Laser Conference*, *ISLC 2008*, Sorrento, Italy (2008), p. 9
65. N. Suzuki, H. Hatakeyama, K. Tokutome, M. Yamada, T. Anan, M. Tsuji, 1.1 μm range InGaAs VCSELs for high-speed optical interconnections, in *Proceedings of IEEE Lasers and Electro-Optical Society Annual Meeting*, *LEOS 2005*, Sydney (2005), p. 394
66. K. Fukatsu, K. Shiba, Y. Suzuki, N. Suzuki, H. Hatakeyama, T. Anan, K. Yashiki, M. Tsuji, 30-Gbps transmission over 100 m-MMFs (GI32) using 1.1 μm-range VCSELs and receivers, in *Proceedings of International Conference on Indium Phosphide and Related Materials*, Matsue, Japan (2007), p. 434
67. T. Anan, N. Suzuki, K. Yashiki, K. Fukatsu, H. Hatakeyama, T. Akagawa, K. Tokutome, M. Tsuji, *High-speed* 1.1-μm-range InGaAs VCSELs, in *Proceedings of Optical Fiber Communication Conference*, *OFC 2008*, San Diego, CA (2008)
68. H. Hatakeyama, T. Anan, T. Akagawa, K. Fukatsu, N. Suzuki, K. Tokutome, M. Tsuji, Highly reliable high speed 1.1μm-InGaAs/GaAsP-VCSELs, in *Vertical-Cavity Surface-Emitting Lasers XIII*, ed. by K.D. Choquette, C. Lei, Proceedings of SPIE, vol. 7229 (2009), p. 722902-1
69. P. Gilet, E. Pougeoise, L. Grenouillet, P. Grosse, N. Olivier, S. Poncet, A. Chelnokov, J.M. Gérard, R. Stevens, R. Hamelin, M. Hammar, J. Berggren, P. Sundgren, 1.3μm VCSELs: InGaAs/GaAs, GaInNAs/GaAs multiple quantum wells and InAs/GaAs quantum dots—three candidates as active material, in *Vertical-Cavity Surface-Emitting Lasers XI*, ed. by K.D. Choquette, J.K. Guenter, Proceedings of SPIE, vol. 6484 (2007), p. 64840F-1
70. S. Mogg, N. Chitica, U. Christiansson, R. Schatz, P. Sundgren, C. Asplund, M. Hammar, Temperature sensitivity of the threshold current of long-wavelength InGaAs-GaAs VCSELs with large gain-cavity detuning. IEEE J. Quantum Electron. **40**(5), 453 (2004)
71. J. Jewell, L. Graham, M. Crom, K. Maranowski, J. Smith, T. Fanning, M. Schnoes, Commercial GaInNAs VCSELs grown by MBE. Phys. Status Solidi C **5**(9), 2951 (2008)
72. D. Feezell, L.A. Johansson, D.A. Buell, L.A. Coldren, Efficient modulation of InP-based 1.3-μmVCSELs with AsSb-based DBRs. IEEE Photon. Technol. Lett. **17**(11), 2253 (2005)
73. W. Hofmann, M. Ortsiefer, E. Rönneberg, C. Neumeyr, G. Böhm, M.-C. Amann, 1.3μm InGaAlAs/InP VCSEL for 10G Ethernet, in *Proceedings of IEEE International Semiconductor Laser Conference*, *ISLC 2008*, paper MB3, Sorrento, Italy (2008)
74. N. Nishiyama, C. Caneau, B. Hall, G. Guryanov, M.H. Hu, X.S. Liu, M.-J. Li, R. Bhat, C.E. Zah, Long-wavelength vertical-cavity surface-emitting lasers on InP with lattice matched AlGaInAs-InP DBR grown by MOCVD. IEEE J. Select. Topics Quantum Electron. **11**(5), 990 (2005)
75. X. Zhao, D. Parekh, E.K. Lau, H.-K. Sung, M.C. Wu, W. Hofmann, M.C. Amann, C.J. Chang-Hasnain, Novel cascaded injection-locked 1.55-μmVCSELs with 66 GHz modulation bandwidth. Opt. Express **15**(22), 14810 (2007)

76. E.A. Avrutin, V.B. Gorfinkel, S. Luryi, K.A. Shore, Control of surface-emitting laser diodes by modulating the distributed Bragg mirror reflectivity: small-signal analysis. Appl. Phys. Lett. **63**(18), 2460 (1993)
77. J. van Eisden, M. Yakimov, V. Tokranov, M. Varanasi, O. Rumyantsev, E.M. Mohammed, I.A. Young, S.R. Oktyabrsky, High frequency resonance-free loss modulation in a duo-cavity VCSEL, in *Vertical-Cavity Surface-Emitting Lasers XII*, ed. by C. Lei, J.K. Guenter, Proceedings of SPIE, vol. 6908 (2008), p. 69080M-1
78. J. van Eisden, M. Yakimov, V. Tokranov, M. Varanasi, E.M. Mohammed, I.A. Young, S. Oktyabrsky, Modulation properties of VCSEL with intracavity modulator, in *Vertical-Cavity Surface-Emitting Lasers XI*, ed. by K.D. Choquette, J.K. Guenter, Proceedings of SPIE, vol. 6484 (2007), p. 64840A-1
79. J. van Eisden, M. Yakimov, V. Tokranov, M. Varanasi, E.M. Mohammed, I.A. Young, S.R. Oktyabrsky, Optically decoupled loss modulation in a duo-cavity VCSEL. IEEE Photon. Technol. Lett. **20**(1), 42 (2008)
80. A. Paraskevopoulos, H.J. Hensel, W.D. Molzow, H. Klein, N. Grote, N.N. Ledentsov, V.A. Shchukin, C. Möller, A.R. Kovsh, D.A. Livshits, I.L. Krestnikov, S.S. Mikhrin, P. Matthijsse, G. Kuyt, Ultra-high-bandwidth (>35 GHz) electrooptically-modulated VCSEL, in *Proceedings of Optical Fiber Communication Conference*, *OFC 2006* Anaheim, CA (2006)

Chapter 8
High-Power VCSEL Arrays

Jean-François P. Seurin

Abstract We review recent developments on high-power, high-efficiency two-dimensional vertical-cavity surface-emitting laser (VCSEL) arrays emitting around 808 and 980 nm. Selectively oxidized, bottom-emitting single VCSEL emitters with 50% power conversion efficiency were developed as the basic building block of these arrays. More than 230 W of continuous-wave (CW) power is demonstrated from a 5 mm × 5 mm array chip. In quasi-CW mode, smaller array chips exhibit 100 W output power, corresponding to more than 3.5 kW/cm^2 of power-density. High-brightness VCSEL pumps have been developed, delivering a fiber output power of 40 W, corresponding to a brightness close to 50 kW/(cm^2 sr). High-energy VCSEL arrays in the milli-Joule range have also been developed. Many of the advantages of low-power single VCSEL devices such as reliability, wavelength stability, low-divergence circular beam, and low-cost manufacturing are preserved for these high-power arrays. VCSELs thus offer an attractive alternative to the dominant edge-emitter technology for many applications requiring compact high-power laser sources.

8.1 Introduction

Compact, reliable, and efficient high-power lasers are needed in a variety of medical, industrial, and military applications. Today, the dominant laser source used for these tasks are semiconductor edge-emitting lasers, as they are small and very efficient in converting the input electrical power to the output optical power. Over 70% power conversion efficiency at 50 W power levels has been demonstrated [1] using edge-emitting lasers. These lasers are either used directly or indirectly as pumping sources

J.-F. P. Seurin (✉)
Princeton Optronics, 1 Electronics Drive
Mercerville, NJ 08619, USA
e-mail: jfseurin@princetonoptronics.com

R. Michalzik (ed.), *VCSELs*, Springer Series in Optical Sciences 166,
DOI: 10.1007/978-3-642-24986-0_8, © Springer-Verlag Berlin Heidelberg 2013

for other lasers, such as diode-pumped solid-state (DPSS) lasers or fiber-lasers. In the medical field, such lasers can be used for teeth whitening, hair-removal, skin-care, or for tissue welding in surgery for example. In industrial applications these lasers are used for printing, cutting, welding and marking. In the military, high-power lasers can be used as weapons, laser radars (LADAR), beacons, and illuminators. Power levels can range from a few Watts to several kilo-Watts for most applications, and mega-Watts for very high-power systems. As an extreme application, laser nuclear fusion requires several Giga-Watts [2]. Typical wavelengths range from 8xx up to 15xx nm. For example, 830 nm is the preferred wavelength for some printing applications (due to the high sensitivity of the coated printing plates at that wavelength), 808 and 880 nm wavelengths are widely used for DPSS laser applications, wavelengths in the range 900–980 nm are used for fiber-laser pumping, and $>$14xx nm wavelengths are used for some skin-care applications as well as "eye-safe" military applications.

Edge-emitting lasers, however, have several limitations such as poor intrinsic beam and spectral properties, as well as low reliability at higher operating temperatures, mainly due to catastrophic optical damage (COD) [3]. Scaling up the power also requires complex and costly assembly of individual laser bars into stacks. There have been a few attempts to develop semiconductor laser technologies to address some of these issues. These approaches aimed at coupling the light out of edge-emitter lasers in a direction normal to the standard output direction using surface grating [4] or etched 45-degree angled mirrors [5]. This allowed for much-improved beam and spectral properties and the potential for low-cost two-dimensional array fabrication for power scaling, something that is not possible using the standard edge-emitting laser technology. However, these approaches have the disadvantages of poor conversion efficiency and/or fabrication issues.

As an alternative, the VCSEL technology can be used. Historically, vertical-cavity surface-emitting lasers (VCSELs) have been mostly confined to low-power applications (a few mW at most), such as high-speed data transmission [6, 7]. These VCSELs have been used as single devices or small addressable arrays. However, there are no fundamental reasons why the VCSEL technology cannot be extended to very high-power applications by fabricating large two-dimensional (2D) arrays of low- to medium-power single-emitters.

There are relatively few reported studies on high-power VCSELs. Devices operating around 100 mW were first reported in [8]. Improvements in the epitaxial growth, processing, device design, and packaging led to VCSELs emitting several hundreds of milliwatts from single very large aperture device and from arrays [9]. More than 2 W under continuous-wave (CW) operation at $-10°$C heat-sink temperature was reported from a VCSEL array consisting of 1,000 single elements [10], corresponding to a power-density of 30 $\mathrm{W/cm^2}$. In another work [11], more than 1 W CW power and 10 W pulsed (15 ns) power was obtained at room temperature from a 19-element array. The 1 W CW power corresponded to a 1 $\mathrm{kW/cm^2}$ power-density. Finally, a record 3 W CW output power has been reported from large (350 μm-diameter aperture) single devices emitting around 976 nm [12].

The idea is to extend to high-power VCSELs most if not all the advantages that made the low-power VCSELs successful. Such advantages include low-cost manufacturing [13], reliability [14], and spectral and beam quality. For example, in applications requiring Giga-Watts of pump power [2], cost is a critical consideration, and the VCSEL technology could be a viable candidate as the pump source.

We focused our development of high-power VCSEL arrays on mainly two wavelengths, 808 and 976 nm, as they represent the bulk of wavelength needs for high-power applications. Laser sources emitting around 976 nm are very important for pumping of fiber-lasers, which have gained tremendous importance in recent years. Laser sources emitting around 808 nm are used in industrial end-pumped DPSS lasers (Nd:YAG or Nd:YVO_4) for end uses such as material cutting and processing, light welding, marking and printing [15]. Pump sources at 808 nm are also used for green laser systems in which a multi-mode 808 nm high-power source is used to pump Nd:YVO_4 glass or a semiconductor gain medium set up in an external-cavity configuration to generate a single-transverse mode at 1064 nm. Green light (532 nm) is then obtained by intra-cavity second harmonic generation using a frequency doubling crystal (such as PPLN) located inside the cavity. These can be fabricated in very compact modules as part of RGB sources for micro-projectors for example [16]. Diode pumped green lasers are also used in many other applications such as scientific instruments (interferometers), precision machining, targeting in defense applications, and for fluorescence diagnostics and spectroscopic applications in the medical field. Finally, 808 nm sources are also used in the medical field for skin-care related cosmetic applications such as hair removal [17], and as industrial and military infra-red illumination sources [18, 19].

Although plenty of work has been done on 976 nm VCSELs, we note that there are very few reports in the literature discussing 808 nm VCSELs [20], possibly due to the fact that applications for 808 nm semiconductor lasers require high-powers.

To compete with the existing edge-emitting laser technology in most applications, VCSELs need to improve their power conversion efficiency (PCE) beyond 50%. For high-power systems, the cost, size and weight are dominated by the input power supplies and refrigeration units, so high-efficiency is needed for the laser sources. The edge-emitter technology currently exceeds 70% power conversion efficiency [1]. However, unlike edge-emitters, VCSELs do not suffer from catastrophic optical damage (COD) [3], which means VCSELs can be operated reliably at high temperatures [21, 22]. In this case, the refrigeration unit can be altogether eliminated, which translates into a significant gain in overall system-level conversion efficiency, even if the VCSEL source itself has a lower conversion-efficiency than the edge-emitter source operating with a refrigeration unit [23].

Top-emitting 976 nm VCSEL devices exceeding 50% power conversion efficiency have already been demonstrated [24]. However, for high-power arrays, junction-down, bottom-emitting devices are required for efficient heat-removal [25].

The technical challenges for the development of a high-power VCSEL array can be summarized as follows: (1) Develop a high-efficiency single-device with low thermal impedance; (2) Improve the growth and process uniformity for cm-scale chips; (3) Develop the packaging for reliability and kW-level heat-removal.

This chapter first reviews the development effort of high-efficiency bottom-emitting VCSEL devices emitting around 976 nm, leading to $>50\%$ power conversion efficiencies (PCE) over a wide range of aperture sizes, as well as the development of efficient 808 nm VCSEL devices. Then, the fabrication and packaging of large VCSEL arrays is discussed and results on the array are presented. Compared to the 976 nm wavelength, the 808 nm wavelength presents the additional challenge that substrate-emission is not an option because of the strong GaAs absorption at that wavelength. Also, in a top-emitting configuration, keeping the GaAs substrate would result in unacceptable increase in thermal impedance. The GaAs substrate must therefore be removed for high-power 808 nm VCSEL arrays. For proper design of the array, we show that the PCE is preserved, with minimal drop compared to the single device performance. Record CW output power >230 W and QCW output power densities $>3.5\,\text{kW/cm}^2$ from large VCSEL arrays are demonstrated and we also show that the spectral and beam properties are preserved at the array level. Finally, results for high-brightness and high-energy arrays are presented.

8.2 Development of High-Efficiency VCSEL Devices

8.2.1 Device Structure and Fabrication

For high-power operation, efficient heat-removal is required. In the case of 976 nm devices a junction-down, bottom-emitting structure is preferred to improve current injection uniformity in the active region and to reduce the thermal impedance between the active region and the heat-spreader [9, 25]. In the case of 808 nm devices, a top-emitting geometry is considered, with substrate removal in mind. Schematics of the 976 and 808 nm VCSEL structures are shown in Fig. 8.1.

For current and optical confinement, the selective oxidation process [28] is used to create an aperture near the active region to improve performance [29]. In the case of 976 nm devices, a low-doped GaAs N-type substrate is used to minimize absorption of the output light while providing electrical conductivity for the substrate-side N-contact. The growth is performed in a MOCVD reactor. The reflectivity of the output distributed Bragg reflector (DBR) is optimized for maximum power conversion efficiency (PCE) [30]. The active region consists of InGaAs (976 nm) or InAlGaAs (808 nm) multi-quantum wells. A high-Aluminum content layer is placed near the first pair of the P-DBR to later form the oxide aperture. The placement and design of the aperture is critical to minimize optical losses [31, 32] and current spreading [33]. Band-gap engineering (including modulation doping) is used to design low-resistivity DBRs with low-absorption losses [34]. The processing of the single devices is straightforward. On the epitaxial side, Ti/Pt/Au disks (976 nm) or rings (808 nm) of different diameters are evaporated to form the P-type contacts, which at the same time act as the self-aligned mask for subsequent dry-etching (RIE) of mesas, deep enough to expose the Aluminum-rich layer. The samples are

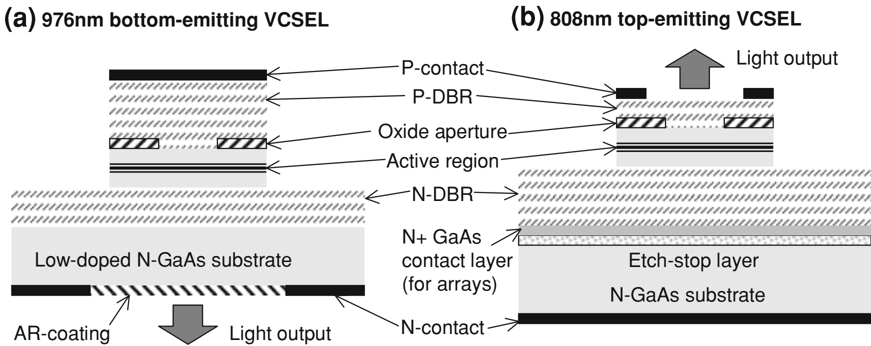

Fig. 8.1 Schematic of the selectively oxidized VCSEL single devices for **a** the 976 nm bottom-emitting structure and **b** the 808 nm top-emitting structure [26, 27]

then exposed to high humidity in a furnace (390–420°C) for the selective oxidation process. In the case of 976 nm devices, on the substrate side, the substrate is thinned to less than 150 μm thickness to minimize absorption losses and then polished to an optical finish. A Si_3N_4 anti-reflection coating is deposited using PECVD, followed by patterning, etching of the field nitride and Ge/Au/Ni/Au N-metals evaporation. Finally, the devices are cleaved and packaged on heat-spreader submounts for testing.

8.2.2 Results and Discussion

Individual devices are tested on a probe-station using a calibrated system comprising an integrated-sphere, a detector, a power-meter, a high-precision current source, and a voltmeter. A temperature-controlled stage maintains a constant heat-sink temperature. A four-point-probe measurement was used to record the voltage accurately. For accurate determination of the device power-conversion-efficiency (PCE; ratio of optical power out to electrical power in), precise calibration of the instruments is critical. For example, for devices with small threshold currents ($<$1 mA), a small offset in the current source could result in a significant error in PCE for these devices. The measurement error of our test set-up is estimated to be better than $\pm$1%.

Figure 8.2 shows the room-temperature L-I-V characteristics of high-efficiency 976 and 808 nm single VCSEL devices. For the 16 μm-diameter bottom-emitting 976 nm device, threshold current, differential slope efficiency, and differential resistance are 1 mA, 77.5%, and 47.5 Ω, respectively. A maximum PCE of 51.2% is achieved at 6.6 mA (5.7 mW). For the 15 μm-diameter top-emitting 808 nm device, threshold current, differential slope efficiency, and differential resistance are 0.98 mA, 75.2%, and 65.7 Ω, respectively, and a maximum PCE of 49.2% is achieved at 6.0 mA (5.8 mW). To the best of our knowledge, these are the highest PCE levels reported to date for 976 nm bottom-emitting and 808 nm top-emitting VCSEL devices.

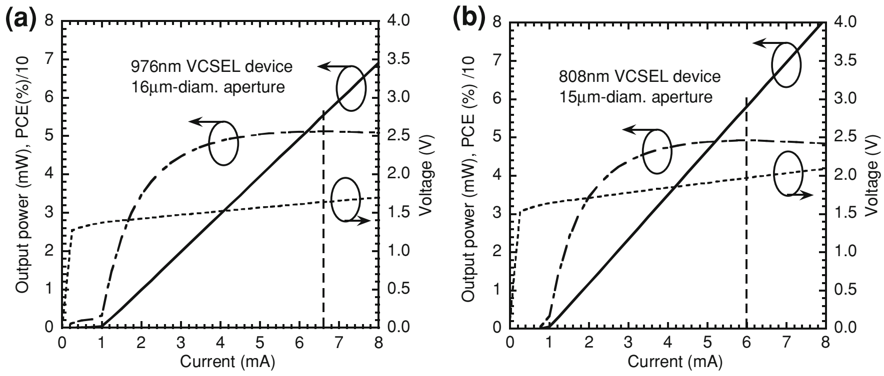

Fig. 8.2 L-I-V characteristics of **a** a high-efficiency, bottom-emitting, 976 nm VCSEL device, and **b** a high-efficiency, top-emitting, 808 nm VCSEL device [26, 27]

Fig. 8.3 Pie diagram showing the different sources of power consumption in the 976 nm bottom-emitting VCSEL device (Fig. 8.2a) operating at maximum PCE [26]

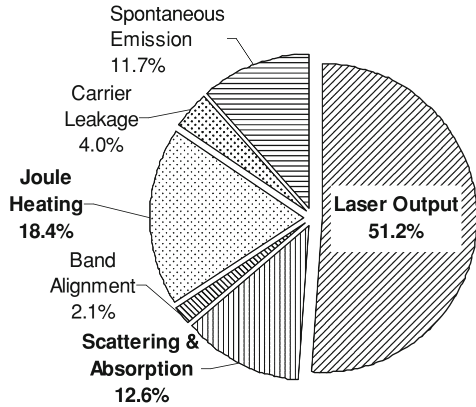

From the 976 nm device power consumption budget analysis at the maximum PCE operating point (Fig. 8.3), we find that most of the wasted power comes from Joule resistive heating (18.4%) and absorption losses (12.6%). Both account for 31% of the lost power.

It is interesting to note that overall, the power conversion efficiency numbers are similar for the 976 and 808 nm devices. Because of the increased absorption below 20% Aluminum content in AlGaAs layers at 808 nm, GaAs cannot be used as the high-index layer resulting in lower contrast DBRs, which increases the number of pairs required to achieve a certain reflectivity. For given doping levels, reducing the contrast between DBR layers also increases the field penetration depth in the DBRs, which increases absorption losses [35]. However, using lower contrast DBR layers usually means that the barrier resistance between the low and high index DBR layers will decrease, giving some room to lower the doping levels and therefore the absorption losses, especially in the P-DBR as this can compensate the negative

effects of a low contrast DBR. Therefore, we believe that it is possible to maintain the high PCE levels for VCSELs across a broad wavelength range (790–1100 nm).

To analyze the results and optimize device design (and more specifically determine the optimal output mirror reflectivity), we can extend the work of Bour and Rosen [36] to VCSELs to obtain a simple analytical expression for the maximum PCE of a device as a function of the slope efficiency, threshold current, and resistance[1]:

$$\eta_{e,\,m} = \eta_d \frac{V_\nu}{V_0}\left(1 - \frac{2}{1+\sqrt{1+\alpha}}\right). \tag{8.1}$$

where η_d is the differential slope efficiency, V_ν is the photon energy voltage (1.27 and 1.53 V for 976 and 808 nm lasers, respectively), V_0 is the zero-current intercept of the linear portion of the laser I-V characteristic (also referred to as the "turn-on voltage"), and α is a characteristic device parameter defined as $\alpha = V_0/(I_{th}R_d) = V_0/(J_{th}\rho_d)$, where I_{th} (J_{th}) and R_d (ρ_d) are the threshold current (threshold current density) and the resistance (resistivity) of the device considered, respectively. The expression in (8.1) is obtained by simply assuming that the output power and voltage vary linearly with the current after threshold, and at least up to the point of maximum power conversion efficiency. This is the case for our VCSELs, as can be seen from Fig. 8.2. In this case, the device series resistance and differential resistance are the same and referred to simply as the device resistance from now on. The problem of increasing a device's PCE then reduces to one or all of the following: increasing the slope efficiency, decreasing the resistance, and/or decreasing the threshold current. Reducing V_0 will also help increase the PCE, although the contribution is minor (V_0 has a small dependence on I_{th} and R_d).

For $\alpha >> 1$, (8.1) approximates to

$$\eta_{e,\,m} \approx \eta_d \frac{V_\nu}{V_0}\left(1 - \frac{2}{\sqrt{\alpha}}\right). \tag{8.2}$$

But in practice, the above relation is useful only for $\alpha > 50$, in which case the error in estimating the maximum wall-plug efficiency of a device is less than 5%. However, $\alpha > 50$ is rarely achieved for VCSELs. For example, for the device in Fig. 8.2, $\alpha = 28$.

To better understand how the different device parameters contribute to device's maximum PCE, we can examine the following relation derived from (8.1), which expresses the relative change in PCE as a function of the relative changes in slope efficiency and α:

$$\frac{\Delta\eta_{e,\,m}}{\eta_{e,\,m}} = \frac{\Delta\eta_d}{\eta_d} + \frac{1}{\sqrt{1+\alpha}}\frac{\Delta\alpha}{\alpha}. \tag{8.3}$$

[1] A similar approach for optimizing the VCSEL operating point was presented in [37], albeit with a slightly different formulation. In particular, the authors consider the dependence of the "electrical confinement factor" (which is essentially the internal quantum efficiency) on the output mirror reflectivity. We found this dependence negligeable for our devices and therefore tend to ignore it, as it greatly simplifies the analysis.

Clearly, α contributes significantly less than the slope efficiency to changes in PCE. For example, for a typical value of α of 24, an increase in α will contribute five times less to the increase in PCE than the same relative increase in slope efficiency. Or, put another way, to get the same improvement from a 5% relative increase in slope efficiency (from 70 to 73.5% for example), the device resistance would need to be decreased by approximately 30%. Therefore, to improve a device's PCE, it is much more critical to first work on increasing the slope efficiency rather than decreasing the threshold current or resistance. A corollary to this observation is that since the slope efficiency is directly proportional to the internal quantum efficiency (see [38] for example), it is also critical to develop a good design and growth process for the multi-quantum-well cavity. We grew top-emitting VCSEL structures with the same cavity design and growth conditions as the bottom-emitting material and extracted an internal quantum efficiency of 95% by varying the output mirror reflectivity (see [30] for example).

The α-parameter is a useful metric to quickly evaluate device performance (single devices or arrays). In practice we found that $\alpha < 10$ corresponds to poor performance (unless the slope efficiency is exceptionally high) and $\alpha > 50$ corresponds to exceptional performance for a VCSEL device (for 976 nm devices, with $V_0 \sim 1.33$ V). Furthermore, α can be obtained directly from the derivative analysis of the I-V characteristic [39, 40], without the need for any optical measurements (the threshold current is determined from the pinning of the junction voltage).[2]

To analyze the device size dependence of the maximum PCE, the size-dependent analytical expressions for the threshold current and slope efficiency derived by Hegblom et al. [33] are used. These take into account current and carrier spreading, which are a major contributor to loss of performance. These expressions are given by:

$$I_{th} = J_\infty \pi r_a^2 + \frac{I_0}{2} + r_a\sqrt{\pi I_0 J_\infty}. \tag{8.4}$$

$$\eta_d = \eta_\infty/(1 + D_0/D_a). \tag{8.5}$$

where r_a (D_a) is the device aperture radius (diameter), I_0 is a characteristic spreading current, D_0 is a characteristic spreading distance, and J_∞ and η_∞ are the threshold current density and differential slope efficiency without spreading (infinitely large aperture), respectively. The parameters J_∞ and η_∞ depend only on the structure intrinsic parameters, such as the mirror reflectivities, the internal loss (that can include such effects as aperture scattering losses for very small devices), the number of quantum wells, the confinement factor, the internal quantum efficiency and material gain parameters. Analytical expressions for J_∞ and η_∞ can be found in [38] for example.

[2] For a given device, the expression for the operating current at the maximum PCE can be derived as $I_{e,m} = I_{th}(1 + \sqrt{1+\alpha})$, and can also be obtained directly from the derivative analysis of the electrical characteristics. Also, it can be seen that—within the approximations of the present analysis—a laser's point of maximum PCE will always occur at a drive current greater than twice the threshold current.

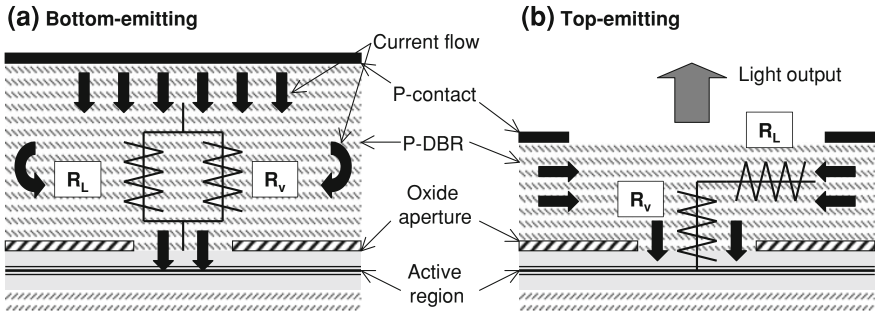

Fig. 8.4 Schematic representation of the effective resistance network for **a** a bottom-emitting and **b** a top-emitting VCSEL structure [26, 27]

For a bottom-emitting structure with the P-DBR as the back reflector, the size-dependent resistance is modeled as the sum of two resistances in parallel:

$$\frac{1}{R_d} = \frac{1}{R_L} + \frac{1}{R_V}. \tag{8.6}$$

while for a top-emitting structure with the P-DBR as the output reflector, the size-dependent resistance is modeled as the sum of the resistances in series [41]:

$$R_d = R_L + R_V. \tag{8.7}$$

where $R_L = \rho_L/(2\pi r_a)$ accounts for constriction or spreading, lateral and contact resistance (scales inversely with aperture perimeter), and $R_V = \rho_V/(\pi r_a^2)$ models a uniform vertical current flow resistance (scales inversely with aperture area). The quantities ρ_L (Ω cm) and ρ_V (Ω cm^2) are the corresponding characteristic resistivities. In practice, we found that using this model always fit our simulated and measured data very well over a wide range of aperture diameters. The two cases are illustrated in Fig. 8.4.

In the case of the bottom-emitting structure, for infinitely large apertures the resistance will scale as the aperture area, with ρ_V being essentially the vertical resistivity of the P-DBR. This situation has important implications for the scaling of the PCE with device size.

Figure 8.5 shows the threshold current and the resistance (or inverse resistance) as a function of device diameter D_a for high-efficiency 980 and 808 nm VCSEL devices. Figure 8.6 shows the differential slope efficiency as a function of device diameter D_a. Equations 8.4–8.7 are used to fit the data. The extracted characteristic parameters for these structures are given in Table 8.1. These seven parameters are sufficient to fully characterize a particular structure in terms of PCE performance.

The previous expressions can also be used directly to fit simulated results, thereby accelerating the design optimization process. In this case we deduce the parameters of Table 8.1 from more advanced simulations. For example, we determine the current

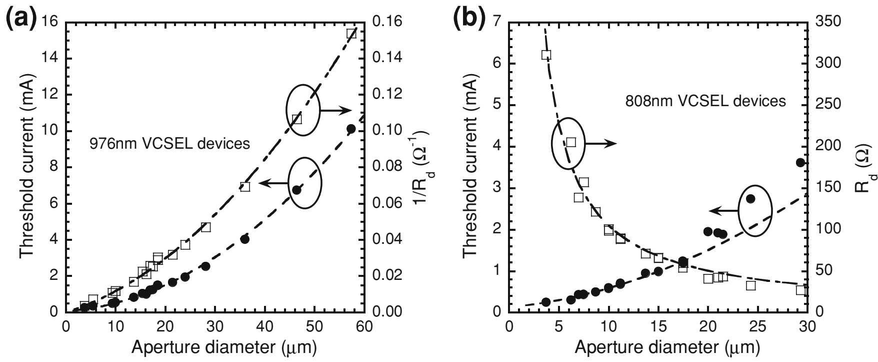

Fig. 8.5 Threshold current and resistance (or inverse resistance) for **a** bottom-emitting 980 nm devices and **b** top-emitting 808 nm devices as a function of device aperture diameter. The symbols are measured data and the lines represent best fits using the analytical formulas [26, 27]

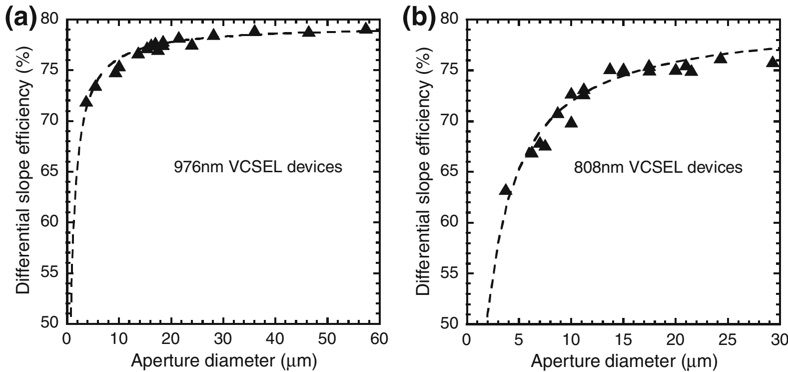

Fig. 8.6 Differential sope efficiency for **a** bottom-emitting 980 nm devices and **b** top-emitting 808 nm devices as a function of device aperture diameter. The symbols are measured data and the lines represent best fits to using the analytical formula

distribution (and the resulting carrier profile in the active region) from finite element simulations, and we can then extract I_0, D_0, ρ_V, and ρ_L for a particular design.

Using these extracted parameters and the measured value of V_0 (roughly independent of device size), α and $\eta_{e,\,m}$ (maximum PCE) are plotted against the measured data (Figs. 8.7, 8.8).

As can be seen in this case, α and $\eta_{e,\,m}$ have optimal values. The PCE characteristic is relatively flat over a wide range of device diameters, exceeding 50% in the range 10–30 μm (data). More interestingly, α and $\eta_{e,\,m}$ converge towards non-zero, constant values for infinitely large aperture diameters. These values are given by

$$\alpha_\infty = \frac{V_0}{J_\infty \rho_V} \tag{8.8}$$

Table 8.1 Extracted VCSEL characteristic parameters [26, 27]

Description	Symbol	976 nm	808 nm	Unit
Turn-on voltage	V_0	1.33	1.58	V
Threshold current density (∞)	J_∞	344	290	A/cm^2
Characteristic spreading current	I_0	0.126	0.240	mA
Vertical resistivity	ρ_V	2.52e-4	6.44e-6	$\Omega\,cm^2$
Lateral resistivity	ρ_L	0.363	0.303	Ω cm
Characteristic spreading diameter	D_0	0.431	1.14	µm
Slope efficiency (∞)	η_∞	79.5	80.1	%

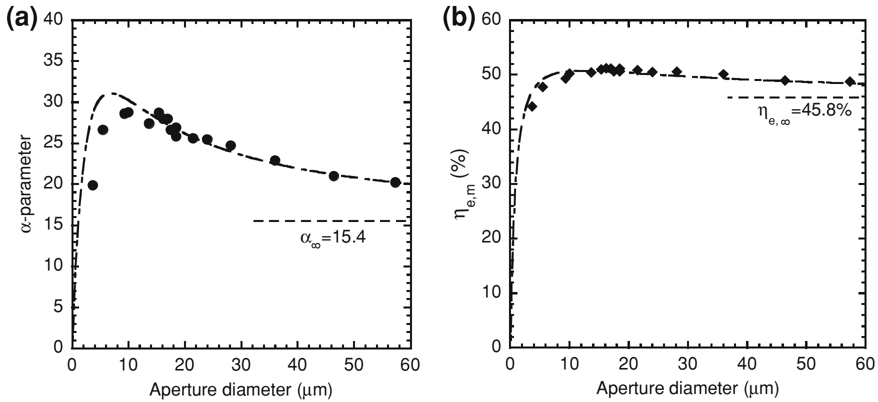

Fig. 8.7 **a** α-parameter and **b** maximum PCE as a function of device aperture diameter for 980 nm bottom-emitting devices. The symbols are data and the lines were obtained using the analytical expressions and the parameters extracted in Table 8.1 [26]

$$\eta_{e,\,\infty} = \eta_\infty \frac{V_\nu}{V_0}\left(1 - \frac{2}{1+\sqrt{1+\alpha_\infty}}\right). \tag{8.9}$$

For the 976 nm bottom-emitting devices studied in this work, using the values in Table 8.1, we obtain $\alpha_\infty \approx 15.4$ and $\eta_{e,\,\infty} \approx 45.8\%$. This result means that for a bottom-emitting geometry, a large aperture size is not necessarily a hindrance to achieving reasonably large PCE. In fact, we characterized bottom-emitting 976 nm VCSEL devices with 100 µm-diameter apertures and 48% PCE. We also note that decreasing J_∞ and the P-DBR vertical resistivity, and increasing η_∞ are a good place to start to maximize device efficiency. Furthermore, it can be shown that the existence of a local maximum for the parameter α depends only on a dimensionless quantity defined as

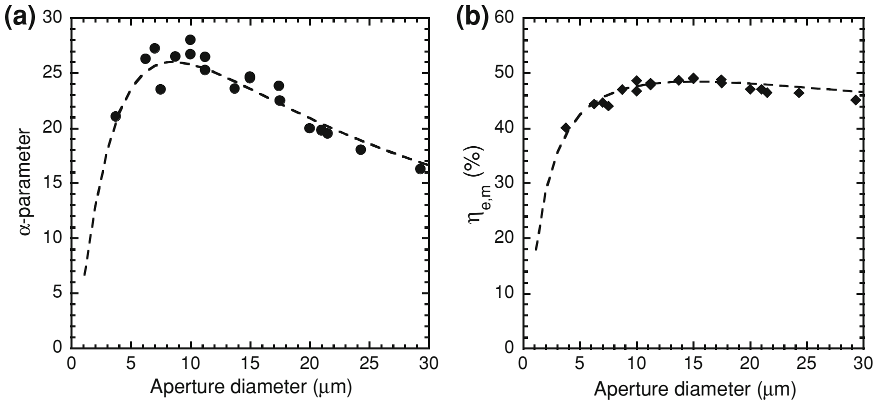

Fig. 8.8 **a** α-parameter and **b** maximum PCE as a function of device aperture diameter for 808 nm top-emitting devices. The symbols are data and the lines were obtained using the analytical expressions and the parameters extracted in Table 8.1 [27]

$$\alpha_0 = 2\frac{\rho_V}{\rho_L}\sqrt{\frac{\pi J_\infty}{I_0}}. \tag{8.10}$$

When $\alpha_0 \leq 1$, no local maximum exists for α. Instead, α_∞ is an absolute maximum, attained for infinitely large aperture diameters. On the other hand, when $\alpha_0 > 1$, a local maximum exists for α. It is always larger than α_∞ and is given by:

$$\alpha_{\text{opt}} = \alpha_\infty\left(1 + \frac{\left(\sqrt{2\alpha_0(\alpha_0 - 1) + 1} - 1\right)^2}{2\left(\sqrt{2\alpha_0(\alpha_0 - 1) + 1} + \alpha_0 - 1\right)}\right). \tag{8.11}$$

Note that for $\alpha_0 >> 1$, the above expression simplifies to

$$\alpha_{\text{opt}} \approx \alpha_\infty \frac{\alpha_0}{1 + \sqrt{2}} \approx 1.47\frac{V_0}{\rho_L\sqrt{I_0 J_\infty}}. \tag{8.12}$$

Finally, in the case $\alpha_0 > 1$ the expression for the aperture diameter at optimal α is:

$$D_\alpha = \frac{4\rho_V/\rho_L}{\sqrt{2\alpha_0(\alpha_0 - 1) + 1} - 1} \approx 0.8\sqrt{I_0/J_\infty} \quad \text{for} \quad \alpha_0 >> 1. \tag{8.13}$$

Table 8.2 summarizes the values for these derived parameters in the case of 976 nm bottom-emitting devices.

The derived and measured values for the optimal α and PCE are in good agreement. It is interesting to note that for all 976 nm devices larger than a certain diameter, the maximum PCE will lie in a relatively narrow range between $\eta_{e,\infty}$ and $\eta_{e,\text{opt}}$ (between 45.8 and 51% for the 976 nm devices studied in this work).

Table 8.2 Derived characteristic parameters for the 980 nm VCSEL material and comparison to some measured values [26]

Description	Symbol	Calc. value	Meas. value	Unit
α-parameter, infinitely large devices	α_∞	15.4	–	–
Max. PCE, infinitely large devices	$\eta_{e,\infty}$	45.8	–	%
Characteristic α_0 parameter	α_0	4.1	–	–
Optimal α (maximum)	α_{opt}	31.1	29.5	–
Device diameter at α_{opt}	D_α	6.8	11.5	μm
Optimal PCE (maximum)	$\eta_{e,\text{opt}}$	50.7	51.2	%
Device diameter at $\eta_{e,\text{opt}}$	D_η	12.4	16.0	μm

By contrast, for 808 nm top-emitting devices, the asymptotic expressions for α and $\eta_{e,\,m}$ (infinitely large diameters) are inversely proportional to the aperture diameter:

$$\alpha_\infty = \frac{4V_0}{J_\infty \rho_L D_a}. \tag{8.14}$$

$$\eta_{e,\,\infty} = \eta_\infty \frac{V_\nu}{J_\infty \rho_L D_a}. \tag{8.15}$$

and therefore converge towards zero for large diameters. The difference comes from the scaling of the resistance with large diameters: in the case of the bottom-emitting structure (the P-DBR is the high reflector), the resistance is inversely proportional to the area for large diameters, whereas for the top-emitting structure (the P-DBR is the output mirror), the resistance is inversely proportional to the diameter for large diameters, which eventually limits the PCE. Hence, for the 808 nm top-emitting devices, the lateral resistivity ρ_L becomes the limiting factor to achieving high PCE for large diameters. This issue could potentially be addressed by switching the polarity of the two DBRs, although using a P-doped DBR as the high-reflector may introduce additional absorption loss.

Overall, we found that the main obstacle to achieving high efficiency in VCSELs is lateral carrier diffusion in the active region. Current spreading can be virtually eliminated by placing the oxide aperture very close to the quantum wells and/or by proper design of the layer(s) between the aperture and the quantum wells [33]. Optical losses from the oxide aperture are mainly a concern for very small devices ($<5\,\mu$m diameter) and can be virtually eliminated by proper design and placement of the aperture [31, 32].

The problem is that lateral carrier diffusion still has a significant impact on device performance even for large devices and vanishes very slowly with increasing aperture size: from (8.4) we can see that the excess threshold current density decreases only as $1/D_a$ in the limit of very large apertures. For example, for a 20 μm-diameter device, the lateral carrier diffusion still accounts for approximately 30% of the total threshold current. Moreover, it also decreases the slope efficiency.

The lateral carrier confinement issue in VCSELs can potentially be addressed by various quantum well interdiffusion techniques [42]. Recent work using selective

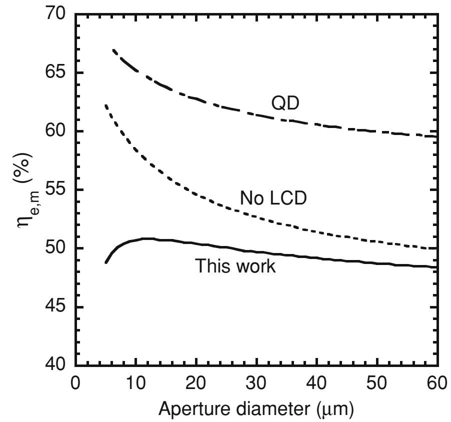

Fig. 8.9 Plot of the maximum PCE for 976 nm devices as a function of aperture diameter for various cases: for current devices ("This work"), assuming no lateral carrier diffusion ("No LCD"), and assuming a quantum-dot-based structure ("QD") [26]

quantum-well intermixing [43] has demonstrated promising results for VCSELs. Another approach involves the use of quantum dots (QD) [44], which have minimal lateral carrier diffusion. In addition, QD have very low transparency current density ($<20\,\text{A/cm}^2$) [44, 45]. Since J_∞ is directly proportional to the transparency current density, this design could greatly improve the PCE of VCSELs. However, QD can suffer from low internal quantum efficiency, possibly due to non-optimized growth conditions [46].

Using the parameters extracted in Table 8.1 as a starting point, we simulated the PCE of 976 nm devices assuming no lateral carrier diffusion (LCD) by setting $I_0 = D_0 = 0$. We also simulated the PCE for ideal quantum-dot (QD) VCSELs, with a $20\,\text{A/cm}^2$ transparency current density (corresponding to $J_\infty \approx 115\text{A/cm}^2$) and an internal quantum efficiency of 95% (we also assumed that for the QD case there was no LCD). These cases are illustrated in Fig. 8.9 for device diameters $>5\,\mu\text{m}$ since we did not include small-size loss effects in our simulations. As can be seen, some drastic improvements in PCE can be expected (PCE $>65\%$) for QD-based VCSEL structures.

8.3 2D VCSEL Array Fabrication

Processing of 2D VCSEL arrays is similar to that of single devices. A cross-section schematic of the processed sample is shown in Fig. 8.10. There are a few more processing steps such as thick plating of the N- and P-contacts for uniform current distribution within the array.

However, unlike 976 nm high-power VCSEL arrays, a junction down, bottom emitting (substrate emission) configuration is not possible for 808 nm, because of the excessive GaAs substrate absorption at that wavelength. Furthermore, a top-emitting configuration with the GaAs substrate still present (even if thinned down) would add excessive thermal impedance. Therefore, in the case of 808 nm VCSEL arrays, the GaAs substrate needs to be removed. This section describes the processing and

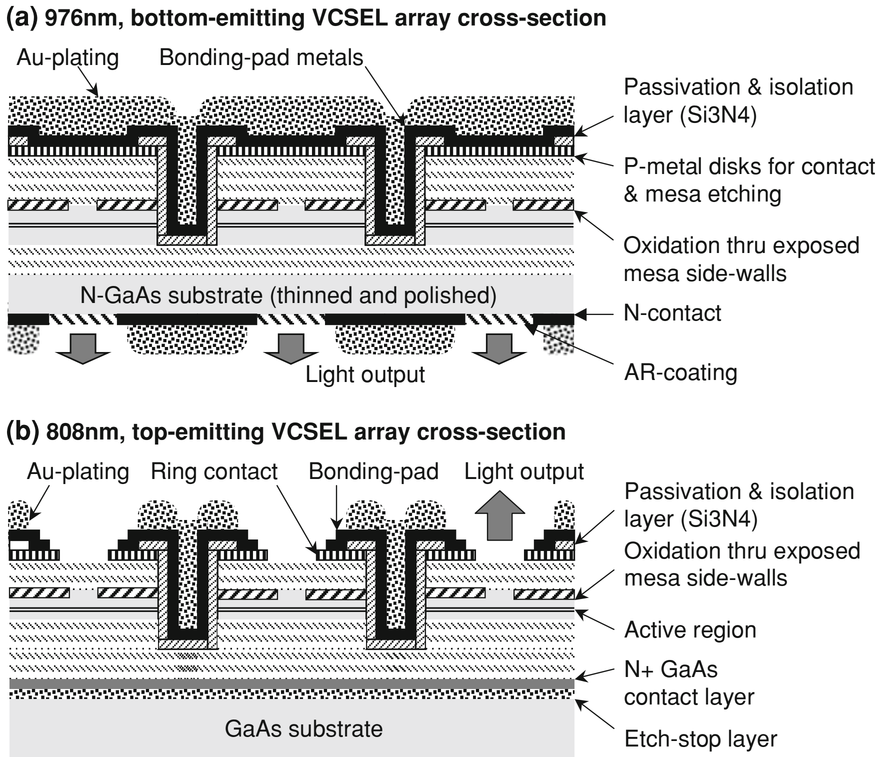

Fig. 8.10 Schematic cross-section of a 2D VCSEL array for **a** 976 nm operation, and **b** 808 nm operation [26, 27]

packaging steps of these high-power 808 nm VCSEL arrays. First, the epitaxial side of the sample is fully processed as shown in Fig. 8.10b. At this stage, the arrays are tested at the wafer level (before cleaving and separation) to check for performance and excessive dead pixels for example. Refering to Fig. 8.11 the process can be summarized as follows:

(a) Processing of the epitaxial side (Fig. 8.10b),
(b) The sample, with the epitaxial side fully processed, is bonded onto a sacrificial carrier using a special bonding agent,
(c) The GaAs substrate is removed using a selective wet-etch. The etch-stop layer is then removed using another selective wet-etch, thus exposing the N+ GaAs contact layer. At this stage, the sample is only 10 μm thick,
(d) Patterned N-metal pads are evaporated onto the N+ GaAs contact layer. Alloying temperature is minimized to avoid affecting the bonding agent, while still providing an ohmic contact. These bonding pads are then plated with Gold,
(e) The individual arrays are cleaved. Each array is still attached to its individual sacrificial carrier,

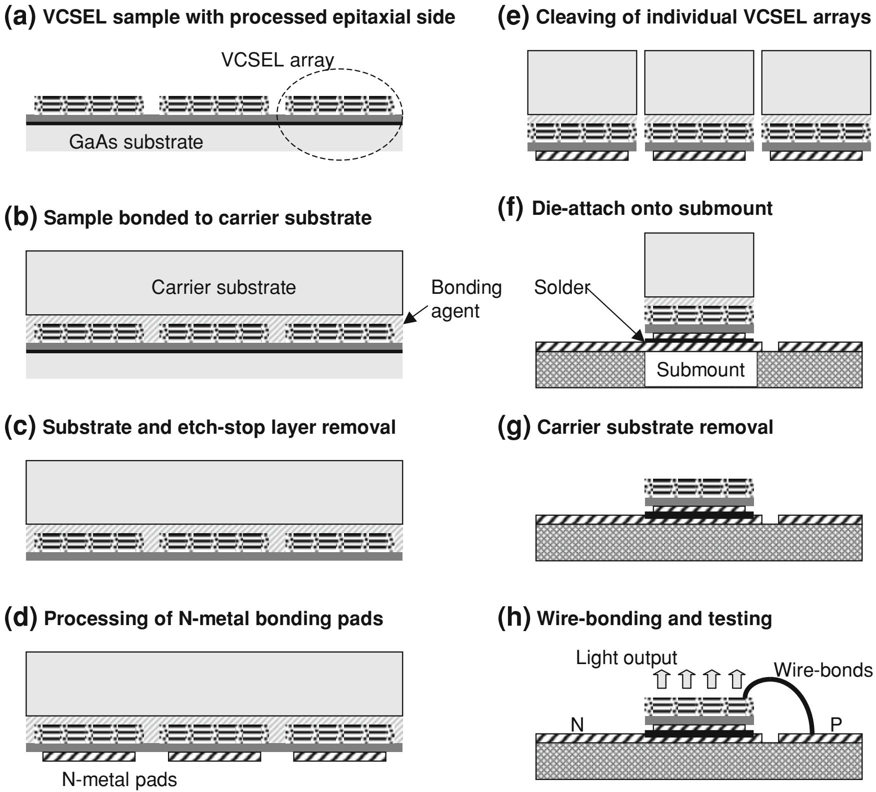

Fig. 8.11 Processing and packaging steps for 808 nm VCSEL arrays. The chip soldered on the submount is only 10 μm thick [27]

(f) Each array/carrier assembly is then soldered to a high-conductivity submount (such as diamond),
(g) The sacrificial carrier is removed and the array-on-submount assembly is cleaned,
(h) The array is wire-bonded and tested.

Even though the chips are very thin (10 μm), we successfully soldered them on diamond heat-spreading submounts. The plating thickness is optimized and an appropriate solder is chosen to account for the large CTE mismatch between diamond and GaAs. The chip-on-submount can be further packaged onto a micro-channel cooler to increase the heat removal capacity, especially for continuous-wave (CW) operation. For quasi-CW (QCW) operation, other submount materials such as BeO (better CTE match to GaAs and less costly than diamond) can be used.

We found that our selective oxidation process was extremely uniform within an array and from array to array within the same sample. Thus, we believe the selective oxidation process is well suited for VCSEL arrays even larger than 5 mm × 5 mm and for the production of these arrays.

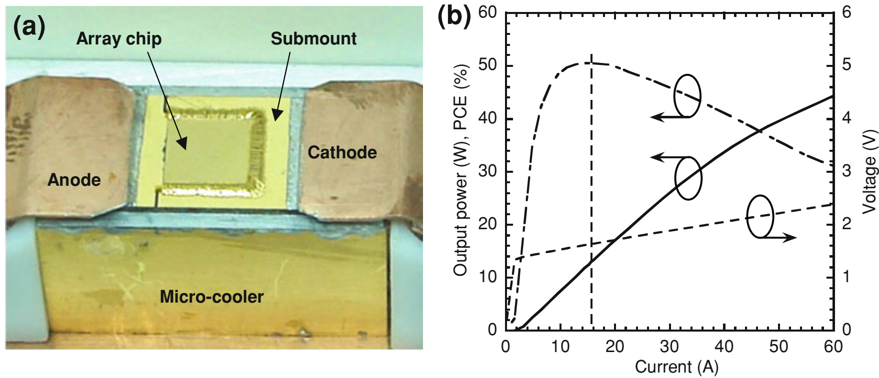

Fig. 8.12 **a** Picture of a fully packaged 976 nm, 2D VCSEL array on micro-channel-cooler and **b** CW LIV characteristics. The array achieves a maximum PCE of 51% for an output power of 13 W at 16A [26]

8.4 Results

For properly designed arrays, there is little drop in PCE compared to the single device results. Figure 8.12 shows a 976 nm, 5 mm × 5 mm VCSEL array chip fully packaged on a micro-channel cooler and the LIV characteristics of a high-efficiency array. This array achieves a maximum PCE of 51% (similar to a single device) at a CW output power of 13 W.

For higher power and power-density, arrays with more closely spaced elements were fabricated for CW and QCW (typically 1–500 μsec pulse-width and 0.1–10% duty-cycle regime) operation. Care must be taken to avoid thermal crosstalk effects [47, 48]. The results are shown in Fig. 8.13. The CW array has an emission area of 0.22 cm^2 and was operated under constant heat-sink temperature (15°C). A record 231 W output power was reached at a 320 A drive current, limited by thermal roll-over, corresponding to a power-density of 1 kW/cm^2. This array has a peak conversion efficiency >44%. The QCW chip is smaller (0.028 cm^2 area) and was designed to operate in the 100–125 A window. The chip-on-submount was not packaged on a micro-channel-cooler. Instead, it was tested directly on a temperature-controlled stage maintained at 20°C. A QCW power of 100 W is achieved at 125 A, corresponding to a record 3.5 kW/cm^2 power-density.

Figure 8.14a shows a fully packaged 3 mm × 3 mm 808 nm VCSEL array on diamond submount. The emission area is 2.8 mm × 2.8 mm and has approximately 3,000 elements. The LIV results are shown in Fig. 8.14b. The array rolls over at 58 W output power at 70 A. A peak PCE of 42% is achieved at 17 W (18 A).

Figure 8.15 shows the LIV results for a 5 mm × 5 mm 808 nm VCSEL array. The emission area is 4.8 mm × 4.8 mm and has approximately 10,000 elements. Output power exceeds 120 W (125 A). A peak PCE of 42% is achieved at 27 W output power (31 A drive current).

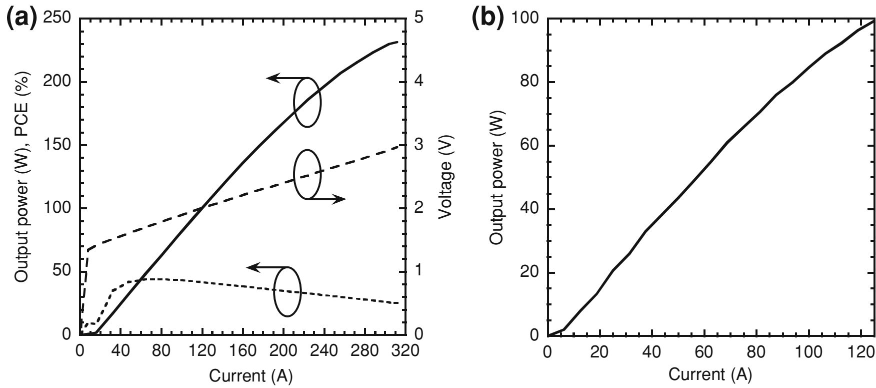

Fig. 8.13 **a** High-power 976 nm VCSEL array achieving 231 W of CW output power at 320 A. **b** High-power-density 976 nm QCW VCSEL array. At 125 A, the output power is 100 W, corresponding to a 3.5 kW/cm^2 power-density [26]

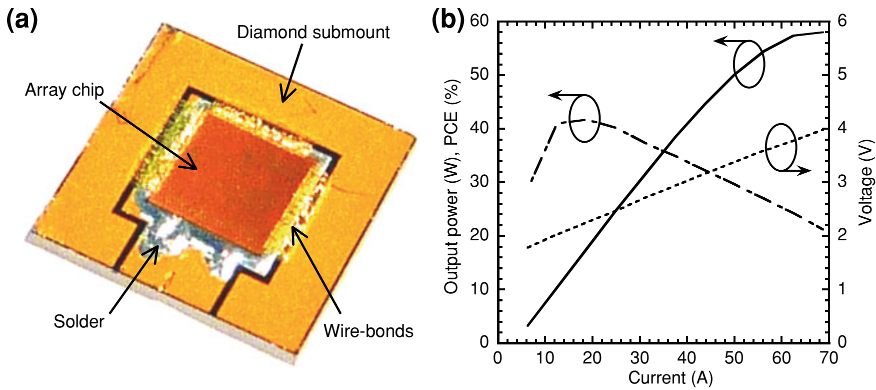

Fig. 8.14 **a** Photograph of a fully packaged 808 nm VCSEL array on diamond submount. The chip is 3 mm × 3 mm and the emission area is 2.8 mm × 2.8 mm. **b** LIV characteristics of the chip [27]

The wavelength spectrum and intensity far-field profile were measured at 100 W (125 A) for the 230 W, 976 nm array and the results are shown in Fig. 8.16. The beam is circular, with a quasi-top-hat profile. The 1/e^2 full-width divergence angle is 17°. Since such beam characteristics can be achieved without any optics, VCSEL arrays present a cost-effective solution for direct pumping applications. Also, such beam charateristics make 808 nm VCSEL arrays ideal candidates for compact, portable hair-removal [17] and infra-red illuminator [18, 19] units. In addition, in the case of illuminators, VCSEL arrays with a large number of elements (>100) have the added benefit of speckle-free emission, with no interference patterns, thus greatly improving image quality.

The spectral full-width at half-maximum (FWHM) of these arrays is only 0.8 nm, about five times less than the spectral width of edge-emitter bars or stacks (typically

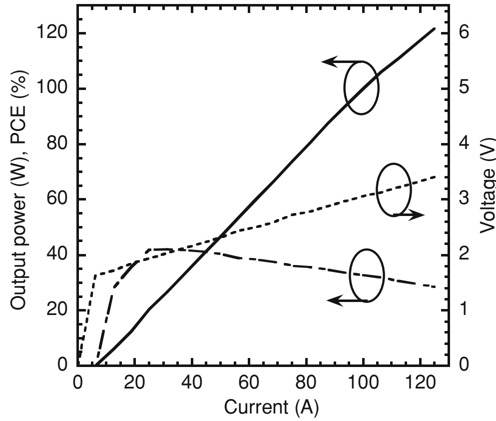

Fig. 8.15 LIV characteristics of a 5 mm × 5 mm 808 nm VCSEL array [27]

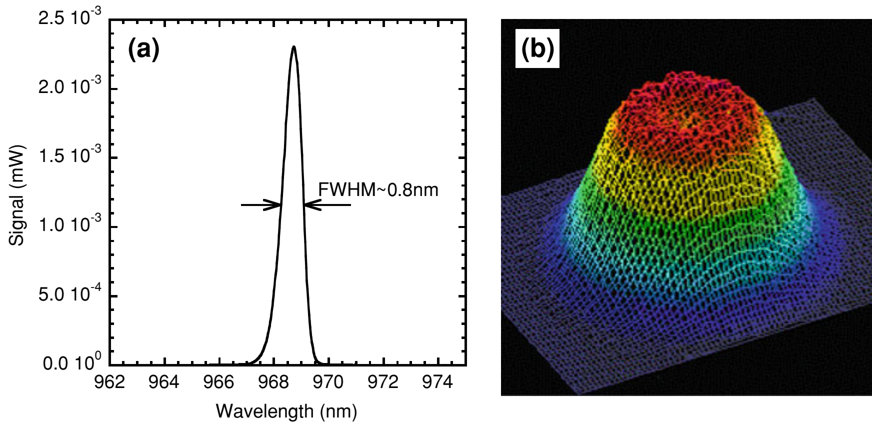

Fig. 8.16 **a** Wavelength spectrum and **b** far-field intensity distribution at a 100 W output power (125 A) from the 231 W array shown in Fig. 8.13a [26]

in the 3–5 nm range). We also measured the wavelength shift as a function of the heat-sink temperature to be 0.065 nm/K, identical to the value for single devices. This value is five times less than that of edge-emitters (typically 0.33 nm/K). Therefore, similarly to single-devices, high-power VCSEL arrays benefit from an intrinsic narrow spectrum and stable emission wavelength. This is useful for many pumping applications where the medium has a narrow absorption band.

Our current 3” production wafers have a Fabry-Pérot etalon-wavelength standard deviation of less than 1 nm. Such excellent uniformity was achieved through optimization of the growth process for these particular VCSEL structures. From thermal simulations, we expect that the spectral width will not increase significantly for larger size (cm) chips.

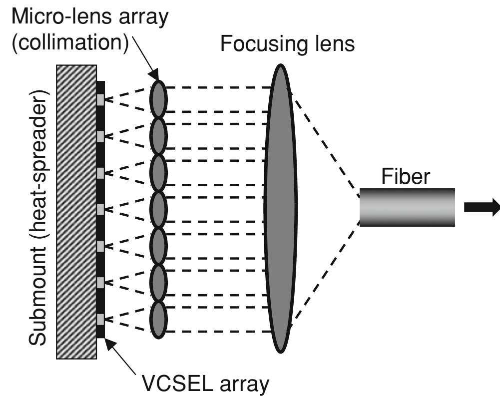

Fig. 8.17 Schematic of the high-brightness VCSEL array fiber-coupling scheme [26]

Initial reliability results on arrays operating continously (>10,000 h) at 50 W output and 30°C submount temperature show very little degradation (<8%), in agreement with previous work [11] in which the authors reported more than 10,000 operating hours for a smaller 1 W array.

8.5 High-Brightness VCSEL Arrays

Certain applications, such as fiber-lasers, require that the pump light be fiber-coupled and other applications, such end-pumping of solid-state laser rods, require that the pump light be focused into a small, low-diverging spot. In these cases, a high-brightness source is required. The brightness is the ratio of the output power to the étendue (the étendue is the product of the emitting aperture area and the solid angle into which the power is emitted). In the case of VCSELs, a high-brightness pump can be fabricated by using a 2D array of hundreds or thousands of small low-power devices, followed by a micro-lens array (with the same layout as the VCSEL array) and a focusing lens to efficiently couple the power into a fiber or a small spot (Fig. 8.17).

The purpose of the micro-lens array is to collimate the individual beams of the array, thereby filling the emission area and reducing the divergence of the overall beam. Such an approach has been successfully demonstrated in Ref. [49], in which the authors used 2D VCSEL arrays of 40×40, 10 μm-diameter-aperture, multi-mode devices. These arrays exhibited 1.2 W CW output power and the authors demonstrated coupling with 75% efficiency into a 1 mm-diameter/0.22 NA fiber, corresponding to a fiber-out brightness of $1\,\text{kW}/(\text{cm}^2\,\text{sr})$.

The brightness is very sensitive to the beam quality of the individual elements in the array, as it is inversely proportional to the square of the "M^2" parameter (beam-quality parameter) [50]. Whereas M^2 is in the range 1.2 for good single-mode devices, it can rapidly rise above 10 for multi-mode devices, severely impact-

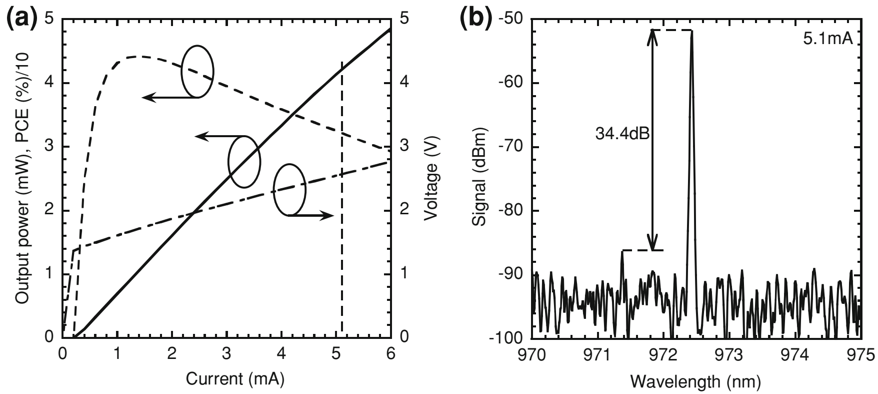

Fig. 8.18 **a** LIV characteristics of a single-mode bottom-emitting 980 nm VCSEL device. The aperture diameter is 4 µm. The device operates single-mode up to 4.2 mW (5.1 mA). **b** Wavelength spectrum at 5.1 mA showing a >34 dB SMSR [26]

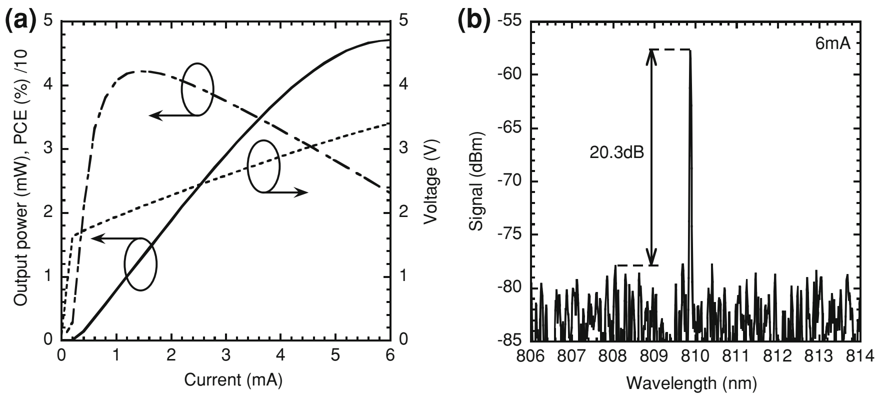

Fig. 8.19 **a** LIV characteristics of a single-mode top-emitting 808 nm VCSEL device. The aperture diameter is 4 µm. The device operates single-mode up to 4.7 mW (6 mA). **b** Wavelength spectrum at 6 mA showing a >20 dB SMSR [27]

ing the brightness of the source. To improve the brightness of 2D VCSEL arrays, we have developed small, high-efficiency single-mode devices at the 808 and 976 nm wavelengths. Typical LIV and spectral characteristics are shown in Figs. 8.18, 8.19. These devices exceed 40% PCE at 1.1–1.2 mW output power (single-mode), and exhibit >4 mW peak single-mode power, with good side-mode suppression ratio (SMSR).

Fiber-coupled pump modules were built at 976 nm for fiber-laser pumping applications. Figure 8.20 shows a completed module and the corresponding fiber-out power versus current characteristic. The fiber used has a 400 µm-diameter core and a 0.46 numerical aperture (NA). Maximum fiber-out power is 40 W, corresponding to a fiber-

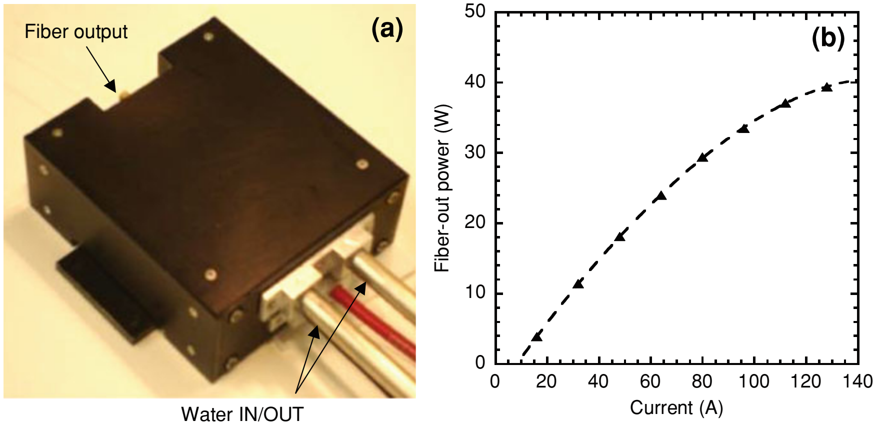

Fig. 8.20 **a** Picture of the completed high-brightness fiber-coupled VCSEL pump module. The fiber has a 400 μm-diameter core and a 0.46 numerical aperture; **b** fiber-out power characteristics [26]

out brightness of more than 48 kW/(cm^2 sr). Such high-power modules are useful for fiber-lasers because they avoid the need of multiple lower-power edge-emitter pump modules. Furthermore, these modules are intrinsically wavelength-stabilized. Recently, by increasing the single-mode power of the individual VCSEL elements in the array, a very high brightness of more than 10 MW/(cm^2 sr) has been demonstrated [50].

8.6 High-Energy VCSEL Arrays

8.6.1 VCSEL-Based Active Q-Switch

There is increased interest from the military for a compact range finder to equip the individual soldier, thus providing him with a light-weight tool for high-precision targeting engagements. One of the main components of this micro-laser-range-finder (μLRF) is the saturable absorber Cr-doped YAG (Cr^{4+} : YAG) Q-switch [51]. This Q-switch is passive. However, a pulse-coded signal would be desired for these range-finder applications. This means that the Q-switch needs to be actively turned on and off and thus a series of non-evenly-spaced pulses can be sent. This way other signals and jamming can be discriminated against.

For this purpose, we developed high-energy 5 mm × 5 mm VCSEL arrays and a power supply for 100 nsec pulses to pump the Cr crystal [52]. The fully assembled active Q-switch is shown in Fig. 8.21. Each array has an output energy of 220 μJ at a 2 kA current, corresponding to a record peak power of 2.2 kW, as shown in Fig. 8.22.

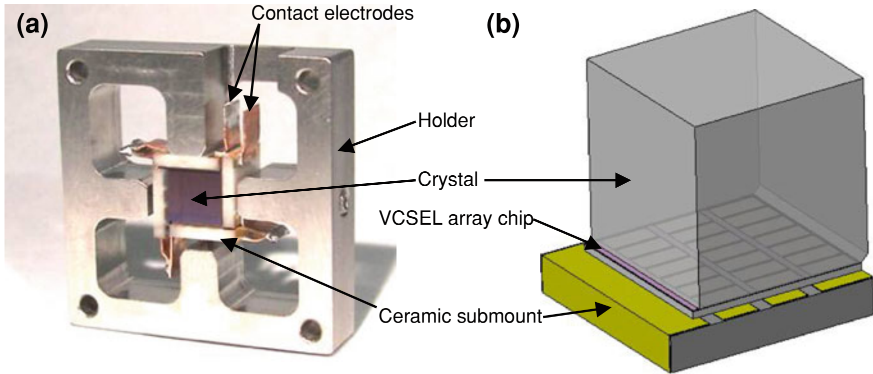

Fig. 8.21 **a** Fully assembled VCSEL-based active Q-switch module, and **b** detail showing the crystal with one of four VCSEL chip against the bottom facet [52]

Fig. 8.22 Energy and peak-power versus current (100 nsec pulse-width) for a 5 mm × 5 mm 2D VCSEL array chip [52]

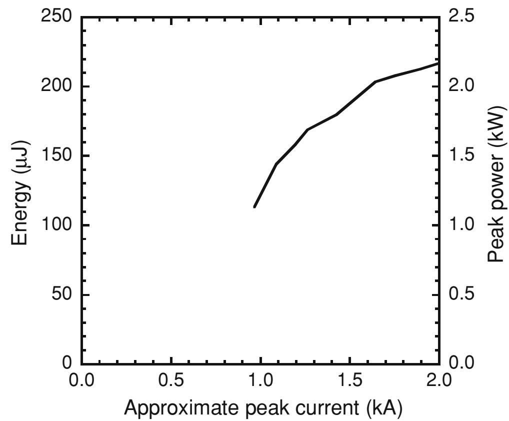

The main advantage of VCSELs is that since they are not subject to COD, they do not fail when operated at many times their roll-over CW current, at such high output energies. Also, their unique geometry and properties allow for direct assembly against the crystal facets, without the need for coupling optics or isolators. The detail in Fig. 8.21b shows how one of the VCSEL array chip is directly pressed against one of the crystal facet that is anti-reflection coated at 980 nm. In fact, the crystal is held in place by the pressure of all four VCSEL chips against its facets. The four VCSEL arrays provide a combined energy of close to 1 mJ into the crystal, thus providing a means to actively control the Q-switch.

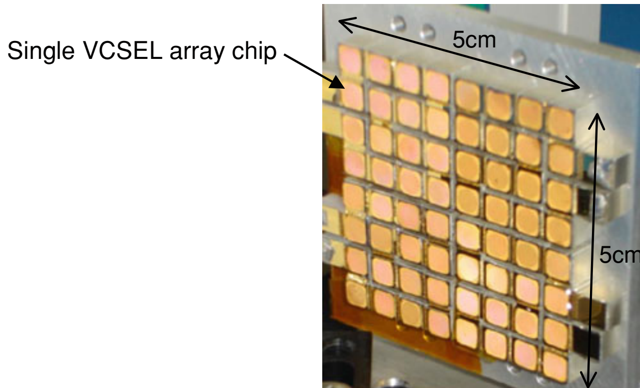

Fig. 8.23 Photograph of short-pulse array module for designator and beacon applications [52]

8.6.2 Short Pulse VCSEL Array Modules

For designator and beacon military applications, we developed large modules of VCSEL arrays operated under very short pulses (20–100 nsec). The module (Fig. 8.23) comprises 64 VCSEL arrays connected in series. Each array is 5 mm × 5 mm and mounted on a removable individual carrier for easy replacement in case it fails. The module is approximately 5 cm × 5 cm. To operate this module, a custom power source delivering a peak current of 1.5 kA with a pulse width of 30 nsec was developed. For this first generation module, non-optimized VCSEL arrays delivering 20 μJ at 1.5 kA (30 nsec pulse) were used, for a module total energy of 1.28 mJ. However, these numbers were limited by the power supply.

For designator applications, low divergence is required and the high-brightness technology discussed in Sect. 8.5 can be used. The beam divergence for designator applications from the existing array is about 24 mrad (half-angle). High-energy large array such as shown in Fig. 8.23 with narrow divergence can be made for designator applications with this technology. With new arrays this number is being reduced to 8 mrad. For beacon applications, where low-divergence is not required, the module can be used as-is. Higher-energy arrays are being developed [52].

8.7 Conclusions

It is possible to use VCSEL technology to make compact high-efficiency high-power pump sources. High-efficiency top-emitting 808 nm and bottom-emitting 976 nm VCSEL devices were developed for high-power arrays. The scaling behavior of 976 nm devices showed that even very large aperture devices maintain relatively high PCE. Large 2D arrays were fabricated and record power levels were demonstrated at 976 and 808 nm. It was also shown that many of the advantages on which low-power single VCSEL devices built their success are preserved for these high-power

VCSEL arrays. These advantages include low manufacturing costs, spectral stability and beam quality. Although the conversion efficiency of VCSELs has improved significantly in recent years ($>50\%$), it still lags a bit behind that of edge-emitters ($>60\%$ for commercial products). Still, since VCSELs can operate reliably at high temperature, the overall system efficiency could be higher using VCSELs since a refrigeration apparatus would not be needed. For the fabrication of 808 nm VCSEL arrays, a process was successfully developed in which the GaAs substrate is completely removed and the 10 μm-thick chips are soldered onto diamond submounts for efficient heat removal. These 808 nm VCSEL arrays are promising candidates for such applications as laser-based skin treatment and infra-red illumination.

High-brightness high-power VCSEL-based pump modules emitting at 976 nm were also fabricated. These units deliver 40 W out of a 400 μm/0.46 NA fiber, corresponding to a fiber-out brightness of 48 kW/(cm^2 sr) and more recent developments yielded modules with 10 MW/(cm^2 sr) brightness.

These 2D VCSEL arrays can also operate under short pulses (<200 nsec) at many times their roll-over CW current without any COD-induced failure, making them a reliable laser source for high-energy applications such as designators, beacons, and active Q-switch modules. Arrays with a record peak power of 2.2 kW under 100 nsec pulse have been demonstrated. Also, modules delivering 1.28 mJ (30 nsec pulse) have been demonstrated.

Because of their significant and unique advantages in terms of costs, reliability, and performance VCSELs could become the next technology of choice for compact and efficient high-power semiconductor laser sources for many applications.

Acknowledgments The author would like to acknowledge his colleagues at Princeton Optronics who have contributed to the work summarized in this chapter. This work was supported in part by the DARPA program on Super High Efficiency Diode Sources (SHEDS), contract # HR0011-04-C-0139.

References

1. M. Kanskar, T. Earles, T. Goodnough, E. Stiers, D. Botez, L. Mawst, 73% CW power conversion efficiency at 50 W from 970 nm diode laser bars. Electron. Lett. **41**(5), 245 (2005)
2. Lawrence Livermore National Laboratory, National Ignition Facility (LLNL, 2009), http://www.lasers.llnl.gov/about/missions/energy_for_the_future/life/
3. A. Moser, E.E. Latta, Arrhenius parameters for the rate process leading to catastrophic damage of AlGaAs-GaAs laser facets. J. Appl. Phys. **71**(10), 4848 (1992)
4. G. Evans, D. Bour, N. Carlson, R. Amantea, J. Hammer, H. Lee, M. Lurie, R. Lai, P. Pelka, R. Farkas, J. Kirk, S. Liew, W. Reichert, C. Wang, H. Choi, J. Walpole, J. Butler, W. Ferguson Jr., R. DeFreez, M. Felisky, Characteristics of coherent two-dimensional grating surface emitting diode laser arrays during CW operation. IEEE J. Quantum Electron. **27**(6), 1594 (1991)
5. R.M. Lammert, S.W. Oh, M.L. Osowski, C. Panja, P.T. Rudy, T.S. Stakelon, J.E. Ungar, Advances in high brightness semiconductor lasers, in *High-Power Diode Laser Technology and Applications IV*, ed. by M.S. Zediker. Proceedings of SPIE, vol. 6104 (2006), p. 61040I-1
6. N. Margalit, S. Zhang, J. Bowers, Vertical cavity lasers for telecom applications. IEEE Commun. Mag. **35**(5), 164 (1997)

7. K. Giboney, L. Aronson, B. Lemoff, The ideal light source for datanets. IEEE Spectr. **35**(2), 43 (1998)
8. F. Peters, M. Peters, D. Young, J. Scott, B. Thibeault, S. Corzine, L. Coldren, High-power vertical-cavity surface-emitting lasers. Electron. Lett. **29**(2), 200 (1993)
9. M. Grabherr, R. Jager, M. Miller, C. Thalmaier, J. Herlein, R. Michalzik, K. Ebeling, Bottom-emitting VCSEL's for high-CW optical output power. IEEE Photon. Technol. Lett. **10**(8), 1061 (1998)
10. D. Francis, H.-L. Chen, W. Yuen, G. Li, C. Chang-Hasnain, Monolithic 2D-VCSEL array with >2 W CW and >5 W pulsed output power. Electron. Lett. **34**(22), 2132 (1998)
11. M. Miller, M. Grabherr, R. Jager, K. Ebeling, High-power VCSEL arrays for emission in the watt regime at room temperature. IEEE Photon. Technol. Lett. **13**(3), 173 (2001).
12. L. D'Asaro, J. Seurin, J. Wynn, High-power, high efficiency VCSELs pursue the goal. Photon. Spectra **2**, 64 (2005)
13. K. Choquette, H. Hou, Vertical-cavity surface emitting lasers: moving from research to manufacturing. Proc. IEEE **85**(11), 1730 (1997)
14. J.A. Tatum, A. Clark, J.K. Guenter, R.A. Hawthorne III, R.H. Johnson, Commercialization of Honeywell's VCSEL technology, in *Vertical-Cavity Surface-Emitting Lasers IV*, ed. by K.D. Choquette, C. Lei. Proceedings of SPIE, vol. 3946 (2000), p. 2
15. A. Timmermann, J. Meinschien, P. Bruns, C. Burke, D. Bartoschewski, Next generation high-brightness diode lasers offer new industrial applications, in *High-Power Diode Laser Technology and Applications VI*, ed. by M.S. Zediker. Proceedings of SPIE, vol. 6876 (2008), p. 68760U-1
16. U. Steegmüller, M. Kühnelt, H. Unold, T. Schwarz, R. Schulz, S. Illek, I. Pietzonka, H. Lindberg, M. Schmitt, U. Strauss, Green laser modules to fit laser projection out of your pocket, in *Solid State Lasers XVII*: *Technology and Devices*, ed. by W.A. Clarkson, N. Hodgson, R.K. Shori. Proceedings of SPIE, vol. 6871 (2008), p. 687117-1
17. G. Town, C. Ash, Measurement of home-use laser and intense pulsed light systems for hair removal: preliminary report. J. Cosmet. Laser Ther. **11**(3), 157 (2009)
18. J. Geske, C. Wang, M. MacDougal, R. Stahl, D. Follman, H. Garrett, T. Meyrath, D. Snyder, E. Golden, J. Wagener, J. Foley, High power VCSELs for miniature optical sensors, in *Vertical-Cavity Surface-Emitting Lasers XIV*, ed. by J.K. Guenter, K.D. Choquette. Proceedings of SPIE, vol. 7615 (2010), p. 76150E-1
19. J.-F. Seurin, G. Xu, B. Guo, A. Miglo, Q. Wang, P. Pradhan, J.D. Wynn, V. Khalfin, W.-X. Zou, C.L. Ghosh, Efficient vertical-cavity surface-emitting lasers for infrared illumination applications, in *Vertical-Cavity Surface-Emitting Lasers XV*, ed. by J.K. Guenter, C. Lei. Proceedings of SPIE, vol. 7952 (2011), p. 795215-1
20. M. Grabherr, M. Miller, R. Jaeger, D. Wiedenmann, R. King, Commercial VCSELs reach 0.1-W CW output power, in *Vertical-Cavity Surface-Emitting Lasers VIII*, ed. by C. Lei, K.D. Choquette, S.P. Kilcoyne. Proceedings of SPIE, vol. 5364 (2004), p. 174
21. R. Morgan, M. Hibbs-Brenner, T. Marta, R. Walterson, S. Bounnak, E. Kalweit, J. Lehman, 200°C, 96-nm wavelength range, continuous-wave lasing from unbonded GaAs MOVPE-grown vertical cavity surface-emitting lasers. IEEE Photon. Technol. Lett. **7**(5), 441 (1995)
22. F. Hopfer, A. Mutig, G. Fiol, P. Moser, D. Arsenijevic, V.A. Shchukin, N.N. Ledentsov, S.S.S. Mikhrin, I.L. Krestnikov, D.A. Livshits, A.R. Kovsh, M. Kuntz, D. Bimberg, 120°C20 Gbit/s operation of 980 nm VCSEL based on sub-monolayer growth, in *Vertical-Cavity Surface-Emitting Lasers XIII*, ed. by K.D. Choquette, C. Lei. Proceedings of SPIE, vol. 7229 (2009), p. 72290C-1
23. L. D'Asaro, J. Seurin, C. Ghosh, Powerful VCSEL arrays beat the heat. Laser Focus World **43**(11), 81 (2007)
24. K. Lear, K. Choquette, R.P. Schneider Jr., S. Kilcoyne, K. Geib, Selectively oxidised vertical cavity surface emitting lasers with 50% power conversion efficiency. Electron. Lett. **31**(3), 208 (1995)

25. R. Michalzik, M. Grabherr, K.J. Ebeling, High-power VCSELs: modeling and experimental characterization, in *Vertical-Cavity Surface-Emitting Lasers II*. ed. by K.D. Choquette, R.A. Morgan. Proceedings of SPIE, vol. 3286 (1998), p. 206
26. J.-F. Seurin, C.L. Ghosh, V. Khalfin, A. Miglo, G. Xu, J.D. Wynn, P. Pradhan, L.A. D'Asaro, High-power high-efficiency 2D VCSEL arrays, in *Vertical-Cavity Surface-Emitting Lasers XII*, ed. by C. Lei, J.K. Guenter. Proceedings of SPIE, vol. 6908 (2008), p. 690808-1
27. J.-F. Seurin, G. Xu, V. Khalfin, A. Miglo, J.D. Wynn, P. Pradhan, C.L. Ghosh, L.A. D'Asaro, Progress in high-power high-efficiency VCSEL arrays, in *Vertical-Cavity Surface-Emitting Lasers XIII*, ed. by K.D. Choquette, C. Lei. Proceedings of SPIE, vol. 7229 (2009), p. 722903-1
28. J.M. Dallesasse, J.N. Holonyak, A.R. Sugg, T.A. Richard, N. El-Zein, Hydrolyzation oxidation of Al_xGa_{1-x} As-AlAs-GaAs quantum well heterostructures and superlattices. Appl. Phys. Lett. **57**(26), 2844 (1990)
29. D.L. Huffaker, D.G. Deppe, K. Kumar, T.J. Rogers, Native-oxide defined ring contact for low threshold vertical-cavity lasers. Appl. Phys. Lett. **65**(1), 97 (1994)
30. G.M. Yang, M. MacDougal, V. Pudikov, P. Dapkus, Influence of mirror reflectivity on laser performance of very-low-threshold vertical-cavity surface-emitting lasers. IEEE Photon. Technol. Lett. **7**(11), 1228 (1995)
31. A. Bond, P. Dapkus, J. O'Brien, Aperture placement effects in oxide-defined vertical-cavity surface-emitting lasers. IEEE Photon. Technol. Lett. **10**(10), 1362 (1998)
32. E. Hegblom, N. Margalit, A. Fiore, L. Coldren, High-performance small vertical-cavity lasers: a comparison of measured improvements in optical and current confinement in devices using tapered apertures. IEEE J. Select. Topics Quantum Electron. **5**(3), 553 (1999)
33. E.R. Hegblom, N.M. Margalit, B. Thibeault, L.A. Coldren, J.E. Bowers, Current spreading in apertured vertical-cavity lasers, in *Vertical-Cavity Surface-Emitting Lasers*, ed. by K.D. Choquette, D.G. Deppe. Proceedings of SPIE, vol. 3003 (1997), p. 176
34. M.G. Peters, B.J. Thibeault, D.B. Young, A.C. Gossard, L.A. Coldren, Growth of beryllium doped Al_xGa_{1-x} As/GaAs mirrors for vertical-cavity surface-emitting lasers. J. Vac. Sci Technol. B **12**(6), 3075 (1994)
35. D. Babic, S. Corzine, Analytic expressions for the reflection delay, penetration depth, and absorptance of quarter-wave dielectric mirrors. IEEE J. Quantum Electron. **28**(2), 514 (1992)
36. D.P. Bour, A. Rosen, Optimum cavity length for high conversion efficiency quantum well diode lasers. J. Appl. Phys. **66**(7), 2813 (1989)
37. G. Taylor, Q. Yang, Optimization of the operating point of a vertical-cavity surface-emitting laser. IEEE J. Quantum Electron. **32**(8), 1441 (1996)
38. L. Coldren, S. Corzine, *Diode Lasers and Photonic Integrated Circuits* (Wiley-Interscience, New York, 1995)
39. P. Barnes, T. Paoli, Derivative measurements of the current-voltage characteristics of double-heterostructure injection lasers. IEEE J. Quantum Electron. **12**(10), 633 (1976)
40. J. Li, J.-F. Seurin, S.L. Chuang, K.D. Choquette, K.M. Geib, H.Q. Hou, Correlation of electrical and optical characteristics of selectively oxidized vertical-cavity surface-emitting lasers. Appl. Phys. Lett. **70**(14), 1799 (1997)
41. K. Lear, S. Kilcoyne, S. Chalmers, High power conversion efficiencies and scaling issues for multimode vertical-cavity top-surface-emitting lasers. IEEE Photon. Technol. Lett. **6**(7), 778 (1994)
42. R. Naone, P. Floyd, D. Young, E. Hegblom, T. Strand, L. Coldren, Interdiffused quantum wells for lateral carrier confinement in VCSELs. IEEE J. Select. Topics Quantum Electron. **4**(4), 706 (1998)
43. D. Lofgreen, Y.-C. Chang, L. Coldren, Vertical-cavity surface-emitting lasers with lateral carrier confinement. Electron. Lett. **43**(3), 163 (2007)
44. D. Bimberg, N. Kirstaedter, N. Ledentsov, Z. Alferov, P. Kop'ev, V. Ustinov, InGaAs–GaAs quantum-dot lasers. IEEE J. Select. Topics Quantum Electron. **3**(2), 196 (1997)

45. G. Liu, A. Stintz, H. Li, T. Newell, A. Gray, P. Varangis, K. Malloy, L. Lester, The influence of quantum-well composition on the performance of quantum dot lasers using InAs-InGaAs dots-in-a-well (DWELL) structures. IEEE J. Quantum Electron. **36**(11), 1272 (2000)
46. N.-H. Kim, J.-H. Park, L. Mawst, T. Kuech, M. Kanskar, Temperature sensitivity of InGaAs quantum-dot lasers grown by MOCVD. IEEE Photon. Technol. Lett. **18**(8), 989 (2006)
47. E.C. Yu, M. Osinski, W. Nakwaski, M. Turowski, A.J. Przekwas, Thermal crosstalk in arrays of proton-implanted top-surface-emitting lasers, in *Physics and Simulation of Optoelectronic Devices VI*, ed. by M. Osinski, P. Blood, A. Ishibashi. Proceedings of SPIE, vol. 3283 (1998), p. 384
48. M. Grabherr, M. Miller, R. Jager, R. Michalzik, U. Martin, H. Unold, K. Ebeling, High-power VCSELs: single devices and densely packed 2-D-arrays. IEEE J. Select. Topics Quantum Electron. **5**(3), 495 (1999)
49. H.-L. Chen, D. Francis, T. Nguyen, W. Yuen, G. Li, C. Chang-Hasnain, Collimating diode laser beams from a large-area VCSEL-array using microlens array. IEEE Photon. Technol. Lett. **11**(5), 506 (1999)
50. J.-F. Seurin, G. Xu, Q. Wang, B. Guo, R.V. Leeuwen, A. Miglo, P. Pradhan, J.D. Wynn, V. Khalfin, C.L. Ghosh, High-brightness pump sources using 2D VCSEL arrays, in *Vertical-Cavity Surface-Emitting Lasers XIV*, ed. by J.K. Guenter, K.D. Choquette. Proceedings of SPIE, vol. 7615 (2010), p. 76150F-1
51. J.E. Nettleton, B.W. Schilling, D.N. Barr, J.S. Lei, Monoblock laser for a low-cost, eyesafe, microlaser range finder. Appl. Opt. **39**(15), 2428 (2000)
52. J.-F. Seurin, C.L. Ghosh, V. Khalfin, A. Miglo, G. Xu, J.D. Wynn, P. Pradhan, L.A. D'Asaro, High-power vertical-cavity surface-emitting arrays, in *High-Power Diode Laser Technology and Applications VI*, ed. by M.S. Zediker. Proceedings of SPIE, vol. 6876 (2008), p. 68760D-1

Chapter 9
High-Contrast Grating VCSELs

Connie J. Chang-Hasnain

Abstract We review a recent invention of single-layer one-dimensional high-index-contrast subwavelength grating (HCG) and its incorporation into a VCSEL structure. The HCG is approximately 50 times thinner than a conventional distributed Bragg reflector (DBR), but offers higher reflectivity with a much broader spectral width. It provides lithographically defined control of polarization, transverse mode and emission wavelength. Using this ultrathin reflector, the tunable mirror in a micromechanical HCG-VCSELs are fabricated with a 10^4 times volume reduction and more than two orders of magnitude improved tuning speed.

9.1 Introduction

Surface-emitting lasers was first proposed by K. Iga [1], however, significant advance was made possible only after epitaxy tecnology became mature enough for precision growth of tens pairs of distributed Bragg reflectors (DBRs) [2–4]. This rendition of surface emitting lasers, with active region sandwiched between two highly reflecting DBRs, are referred to as vertical cavity surface emitting lasers (VCSELs). The DBRs typically consist of layers of materials with alternating high and low refractive indices. Because of the very short gain length in VCSELs, a very high reflectivity (>99%) is required for the DBRs. Hence, the DBRs are typically very thick, consisting of 20–30 or 50–60 pairs of alternating index materials for 850 nm and 1550 nm VCSELs, respectively. A planar VCSEL structure using proton implantation was first proposed and demonstrated, which facilitated fabrication of large VCSEL arrays and multi-wavelength arrays [5, 6]. It was shown that *m*ultiple transverse *m*ode (MM) VCSEL can be obtained with

C. J. Chang-Hasnain (✉)
Department of Electrical Engineering and Computer Science,
University of California, Berkeley, CA 94720, USA
e-mail: cch@berkeley.edu

R. Michalzik (ed.), *VCSELs*, Springer Series in Optical Sciences 166,
DOI: 10.1007/978-3-642-24986-0_9, © Springer-Verlag Berlin Heidelberg 2013

a large aperture [7] and directly modulated at multiple Gbps rates. The use of MM-VCSEL as transmitter through low-cost multi-mode fiber for high speed optical interconnect applications was first suggested and demonstrated in 1991 [8]. Transmitters were developed in mid-1990s [9] and has been dominating the transceiver market for Gbps local area netowrks.

It suffices to say that DBRs remain to be the most challenging problem for the realization of VCSELs in various wavelength regimes. Recently, we reported a novel mirror to replace the DBRs. This mirror consists of a single layer of one-dimensional (1D) subwavelength grating made of materials with a large refractive index contrast, and hence the name high-contrast grating (HCG) [10–12]. The results in this seemingly extremely simple geometry are a wealth of unexplored and unexpected properties.

First of all, HCGs provide an extraordinarily broad bandwidth of high reflectivity for waves propagating in the surface-normal direction to the plane of gratings. We reported the incorporation of HCG to a VCSEL structure with a determined polarization direction [13, 14]. Single transverse mode emission was obtained with a HCG as small as 4 periods [15] and as large as 12 μm aperture [16]. We showed that VCSELs performance is not compromised with an extranordinarly large dimension variation, and even its emission wavelength can be made fairly insensitive to HCG dimensions. Yet, with an appropriate design, the HCG-VCSEL emission wavelength can be made to vary by HCG period and duty cycle. This makes it possible to make monolithic multi-wavelength VCSELs on one wafer with uniform epitaxy [17]. Simulation results show that over 100 nm wavelength span can be attained. Two dimensional lens or reflector can be made by varying the duty cycle and period of HCGs, which are desirable to control the transverse modes of VCSEL [18, 19]. Making the HCG a movable mirror in a VCSEL, tunable VCSELs with wide tuning range and rapid tuning speed can be achieved [15, 20]. Both will be useful to fabricate cost effective multi-wavelength arrays for wavelength division multiplexing (WDM) applicaitons. Finally, most recently, HCG with various material combinations have been demonstrated and incorporated into VCSELs with 980, 1,300, and 1,550 nm wavelength regimes [16, 21–24]. In this chapter, we provide a systematic review of experimental and numerical simulation results demonstrating many desirable attributes in HCG-VCSELs.

9.2 High-Contrast Subwavelength Grating (HCG)

High-Contrast Grating (HCG) is a single-layer subwavelength grating where the refractive index contrast between the grating high index region and low index region is relatively high. As a grating with a period smaller than the wavelength, known as subwavelength grating, only the 0-th order diffraction exists; all the higher diffraction orders are evanescent modes.

Several research groups studied subwavelength grating in the past a few years with the advent of subwavelength lithography for optoelectronics. It has been reported

that subwavelength gratings can be used to select the polarization and suppress higher order modes for the output light of vertical cavity surface emitting lasers (VCSELs) [25–27]. All these subwavelength gratings were fabricated on a substrate by advanced etching technology. Since the etched surface only creates a refractive index modulation on the substrate, there is *no index contrast* between the high index region of the grating and the substrate it sits on.

In this chapter, we will focus on another type of subwavelength grating: high-index-contrast subwavelength grating, or HCG, where the high index grating strips are surrounded by low index material. We will show that this novel grating structure has many unique properties with a wide range of applications.

9.2.1 HCG as Broadband Reflector

In an effort to realize an ultra-thin mirror with high reflectivity and broad spectral width, we arrived at a simple design of HCG. Figure 9.1 shows a schematic of two versions of subwavelength HCG mirrors. The HCG structure consists of a single layer of periodic grating structure with a highly refractive index material that is surrounded by low index materials. Shown in Fig. 9.1 are cases with air as the low index medium on top and between the stripes. A second low index material is used below the gratings in Fig. 9.1a [10–12], whereas the same low index material is used for case in Fig. 9.1b [12–14]. Figure 9.1a can be realized using silicon-on-insulator (SOI) substrates or GaAs on AlOx, whereas (b) on a AlGaAs substrate with a selectively removed layer, as will be described in Sect. 9.3.

The HCG is polarization sensitive by its nature of 1D periodicity. However, high reflectivoty can be designed to reflect light either with polarization along or perpendicular to the gratings, so noted transverse electric (TE) and magnetic (TM) polarization. Figure 9.1a, b are drawn with TM and TE polarized light intentionally to show the feasibility, respectively.

The design parameters for the structure include the indices of refraction of the high and low index materials, grating period (Λ), grating thickness (t), grating duty cycle (η), and, if applied, the thickness of the low index layer under the grating (t_L). The duty cycle (η) is defined as the ratio of the width of the high index material with respect to the period. Using an SOI-HCG structure, broadband (1.12–1.62 μm), high reflectivity ($R > 98.5\%$) was reported [11]. This is the widest bandwidth ($\Delta\lambda/\lambda > 35\%$), high reflectivity mirror reported by a grating structure.

Broadband reflectivity can be designed for both TE- and TM- polarized surface-normal incidence light. Figure 9.2a, b shows an example calculated reflectivity spectra for E-field parallel and perpendicular to the grating direction (y) for TM- and TE-HCGs using rigorous coupled wave analysis (RCWA) [28], respectively. As shown here, if the reflectivity is optimized for one E-field orientation (e.g. 99.5%), the reflectivity for the other direction but is mostly significantly lower, e.g. $<60\%$. This difference is very large for typical VCSELs and, hence, polarization of the lasing mode will be determined by the grating design. The HCGs in Fig. 9.2 are

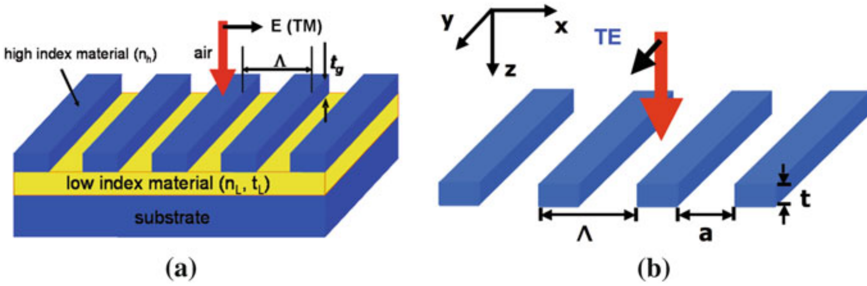

Fig. 9.1 Schematic of **a** TM polarized [10] (© 2004 IEEE), **b** TE polarized high-contrast grating (HCG) [14] (© 2009 IEEE). The gratings are fully surrounded by low index medium, which leads to the extraordinary broadband reflection. Thick vertical arrows show the light propagation directions. The thin horizontal arrows attached to them show the E-field polarization directions. In **a**, the HCG sits on a second low index medium, e.g. SiO_2 or AlOx. Whereas, in **b**, the HCG can be freely suspended

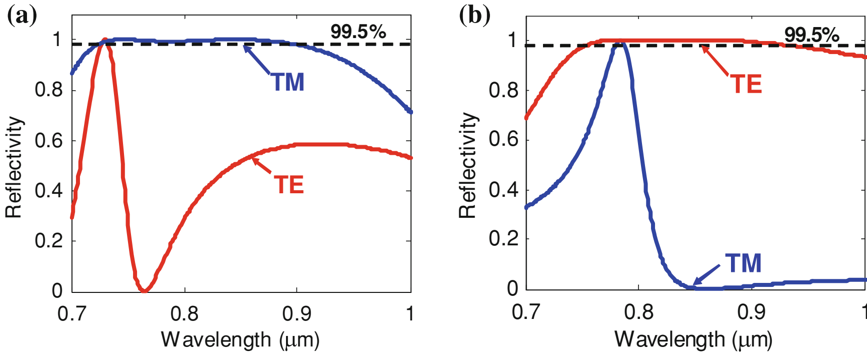

Fig. 9.2 Calculated reflectivity spectra for surface-normal incident plane waves with E-field along x and y directions for **a** TM- and **b** TE-HCG. The TM-HCG has an very high reflectivity for E-field aligned in x direction but significantly lower for y direction. The opposite is true for TE-HCG. This enables polarization selection in HCG-VCSELs [14] (© 2009 IEEE)

designed for 850 nm wavelength and consist of periodic $Al_{0.6}Ga_{0.4}As$ stripes as the high index material, surrounded by air as the low index material. It is interesting to note that the dimensions are substantially different. For TM-HCG, the grating parameters Λ, a and t are 380, 130 and 235 nm, respectively. For TE-HCG, Λ, a and t are 620, 400 and 140 nm, respectively. Depending on the specific applications, one type of HCG may be more desirable to use. Although we use $Al_{0.6}Ga_{0.4}As$/air as an example here in designing the broadband HCG mirrors, the basic principle can be applied to almost all systems with high refractive index contrast, such as Si/air/SiO_2, $GaAs/Al_2O_3$, GaN/air, and $ZnSe/CaF_2$. In general, the larger the index contrast is, the broader band it is possible to achieve.

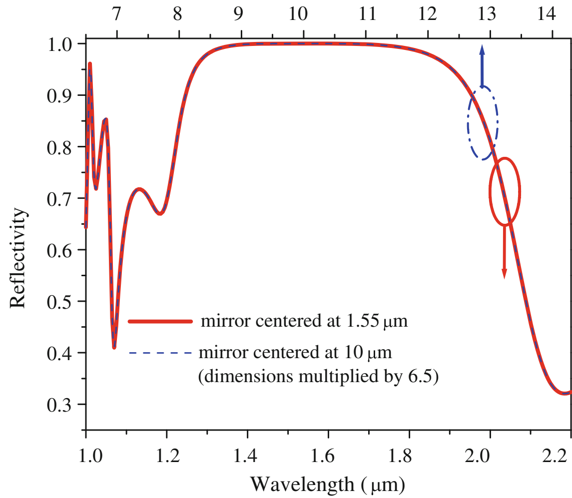

Fig. 9.3 Reflected power for light polarized perpendicularly to the grating lines. A simple scaling factor (6.5) applied to the dimensions gives completely overlapped traces. Thick line is centered at 1.55 μm while dashed at 10 μm [10] (© 2004 IEEE)

One important fact is the wavelength scalability of HCG, as illustrated by Fig. 9.3. By simply multiplying the dimensions by a constant, in this case 6.5, the reflection band shifts from centered at 1.55–10 μm wavelength range with all features and values being identical. This points out that different wavelength regime can basically use the same design. Though not a surprising result from the Maxwell's equations, nevertheless, it is important to specifically highlight.

9.2.2 Physics of HCG

The reflectivity mechanism of an HCG is described as the following. For simplicity, we consider the incident wave a surface-normal plane wave. Due to HCG period is subwavelength, only the 0-th diffraction order exists in the reflected and transmitted waves, which are plane waves. Physically, the HCG can be considered an array of short slab waveguides with the propagation direction along the z-axis. The incident wave excites multiple waveguide modes of the array. The first two or three modes are propagating modes and, hence, carry energy and are most significant. The higher order modes are below cutoff and have the form of evanescent surface-bound waves. The incident wave excites an ensemble of these modes. After propagating through the HCG thickness, each propagating mode accumulates a different phase. At the exiting plane, due to a strong mismatch to the existing plane wave (the higher order diffractions are evanescent waves), the waveguide modes reflect back not only into themselves but also couple into each other. As the modes propagate and return to the input plane, similar mode coupling occurs. Following the modes through one round trip, the reflectivity solution can be attained [29–31].

The HCG thickness determines the phase accumulated by the modes, and therefore controls their interference, making the thickness of the HCG an important

design parameter. Depending on the grating thickness, a constructive or destructive interference between these two modes could occur at the output plane which thus determines the reflectivity of the HCG [31].

Destructive interference in this case does not mean that the fields are zero everywhere. Rather, it means that the spatial mode-overlap along the bottom interface with the transmitted plain-wave is zero, yielding a zero transmission coefficient. This prevents optical power from being launched into a transmissive propagating wave, and thus causes full reflection.

There are two major index contrasts that lead to the extraordinarily broad, high reflectivity spectrum of HCG. The contrast between the grating bars and the medium in-between determines the array waveguide modes: their propagation constants, field profiles and cut-off wavelengths. With a large contrast between grating bars and space in-between, the wavelength span that an HCG has *exactly two* propagating modes is large. Furthermore, the propagation constants are rather insensitive to wavelength. These are the main reasons for the broad band. The index contrast between the HCG and the input and output planes are critical to control the coupling between the modes. A large contrast results in a strong coupling and mode mixing, which is essential for the high reflectivity as well as broad band.

Throughout this chapter, the reflectivity of HCG is simulated using the RCWA, a broadly accepted method that uses a matrix formalism to analytically solve for the reflected and transmitted diffraction orders of planar gratings. In addition, we used an FDTD commercial package for purposes of verification. We also developed analytical solution for subwavelength HCGs [29], based on mode matching between the modes inside HCG and the free space modes outside it, as discussed above. As the derivation is rather lengthy, it is not included here. Readers are encourage to read the manuscript for details [29]. We have found excellent agreement between RCWA, FDTD and our mode matching calculations.

It should be mentioned that HCG can behave as a resonator with a high quality factor (Q) and surface-normal emission, a broadband reflector for incident wave at any angle, and be used as the reflective cladding for hollow-core waveguides with ultra low propagation loss [31]. A transparent HCG can be designed to achieve tunable optical phase and used as a tailorable birefringent material. Finally, a non-periodic HCG can be designed to function as a planar, high numerical aperture, low loss, focusing reflectors and lenses [12, 18, 19, 32].

9.3 HCG-VCSEL Design and Fabrication

The HCG can be easily incorporated into a VCSEL in several ways. Figure 9.4 shows the schematic of a 850 nm VCSEL with a freely suspended AlGaAs HCG. The VCSEL consists of an HCG-based top mirror, a λ-cavity layer, and a conventional semiconductor-based bottom n-DBR mirror. The λ-cavity contains a multiple quantum well active region. The top mirror consists of two parts: an HCG and an M-pair p-doped DBR, where M is small (2∼4). The M-pair p-DBR is mainly used for

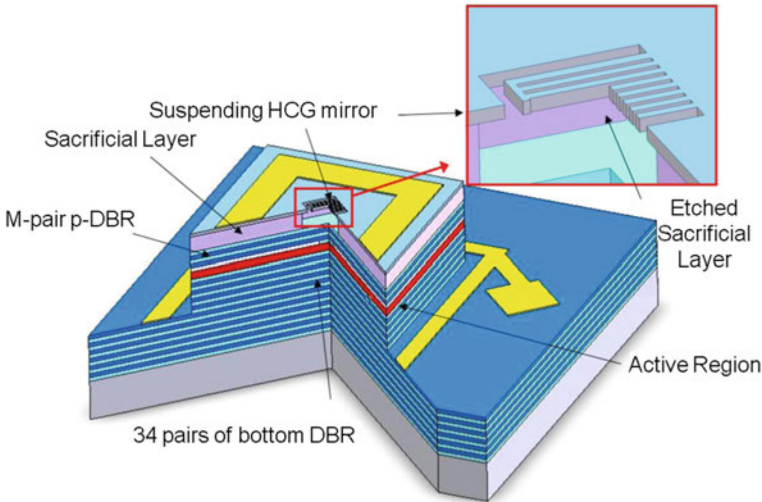

Fig. 9.4 The cross-section schematic of HCG-VCSEL. The top mirror consists of a freely-suspending HCG and M-pairs DBRs. $M = 2$ or 4. Reprinted by permission from Macmillan publishers Ltd: nature photonics [13], copyright (2007)

providing current injection into the active region while protecting the active region during the fabrication process. While the p-DBR does increase the overall reflectivity of the top mirror, the number of p-DBR pairs can be reduced or eliminated because a single-layer HCG is capable of providing sufficient reflectivity ($R > 99.9\%$) as the VCSEL top mirror. Electric current injection is conducted through the top metal contact via the p-doped HCG layer and through the bottom metal contact via the n-DBR. Current confinement of is achieved through the use of an aluminum oxide aperture.

In this chapter, majority of the discussion and data will be based design of Fig. 9.4, as there are much data on this first demonstrated structure. It is without doubt that further advances will be made on the other newly reported structures [16, 20–24].

The HCG structure used in the VCSEL top mirror can be either TM-HCG or TE-HCG. For 850 nm VCSELs in Fig. 9.4, the air gap distance between the HCG and M-pairs of DBR is designed to be $5\lambda/4$ or odd number of quarter-λ. This is a direct result of the fact that there is little field penetration into this particular HCG, a consequence of the broad band by design. As will be seen in Sect. 9.6 this needs not be the case if HCG is designed differently. The smallest lithography dimension for the HCGs is the air spacing (a); for TM-HCG, it is ~130 nm, but for TE-HCG, it is as large as 400 nm.

The fabrication process of the HCG-VCSEL in Fig. 9.4 is similar to that of a standard VCSEL, including metal depositions, mesa formation etch, thermal oxidation, and HCG definition. The HCG is patterned by electron-beam lithography on poly-methyl methacrylate (PMMA) photoresist, which provides the design flexibility in terms of the grating period and duty cycle. The lithography patterns are then

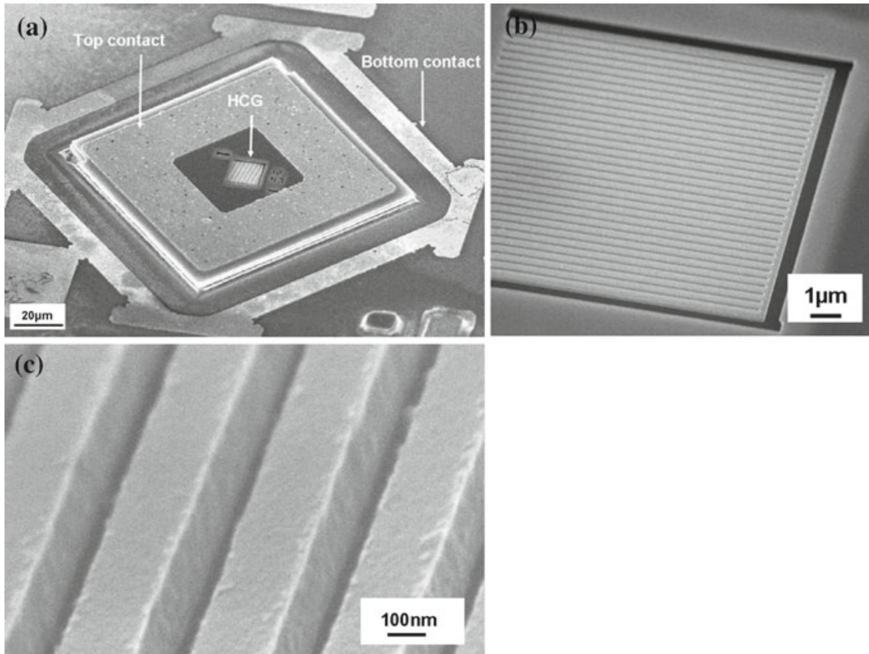

Fig. 9.5 **a** SEM image of fabricated TM-HCG-VCSEL, where the grating is aligned to the center of the device mesa. **b** Close-up SEM image of the freely-suspended grating, where a stress-relief trench is used to eliminate buckling of the grating. **c** Zoomed-in SEM image of the fabricated individual grating stripes. Reprinted by permission from Macmillan publishers Ltd: nature photonics [13], copyright (2007)

transferred through a wet or dry etching process. Finally, a selective etch process is carried out to remove the GaAs sacrificial material underneath the HCG layer and to form the freely suspending grating structure.

Scanning electron microscope (SEM) images of the fabricated HCG-VCSEL are shown in Fig. 9.5. Figure 9.5a shows the overview of a HCG-VCSEL, with top contact, bottom contact, and HCG labeled in the figure. HCG is patterned in the center of the VCSEL mesa aligned with the oxide aperture. Figure 9.5b is a close-up SEM image of the freely-suspending HCG, where a stress-relief trench is used to eliminate buckling of the grating. Figure 9.5c shows the zoomed-in SEM image of the fabricated individual grating stripes.

9.4 Optical Characteristics of HCG-VCSEL

9.4.1 Light–Current and Near Field Characteristics

Single mode, continuous-wave (CW) operation of HCG-VCSELs, was demonstrated for both TM-HCG and TE-HCG at room temperature. Figure 9.6a, b shows

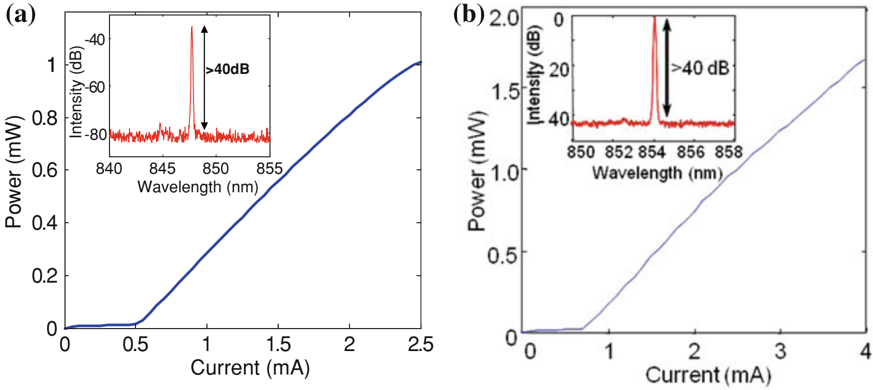

Fig. 9.6 Typical optical power vs. current for a typical **a** TM- and **b** TE-HCG-VCSEL under room temperature continuous wave operation. The inset shows the optical spectrum with 40 dB side-mode suppression ratio [14] (© 2009 IEEE)

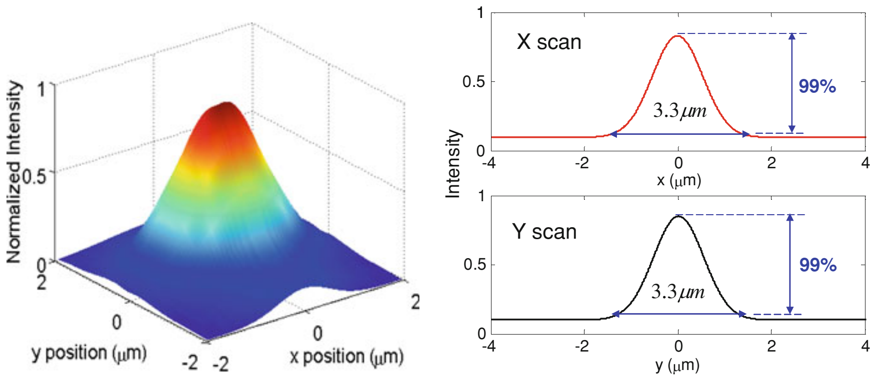

Fig. 9.7 Measured optical near-field beam profile of a TM-HCG-VCSEL. The optical emission has a symmetrical, fundamental mode Gaussian beam profile [14] (© 2009 IEEE)

typical optical output power versus input current (LI) and voltage versus current (VI) characteristics for a TM- and TE-HCG-VCSEL, respectively. The device has very low sub-mA threshold currents and output power >1 mW. Threshold current reduction is seen with HCG-VCSELs, attributed to a much lower free-carrier absorption associated with p-DBRs. The insets shows typical emission spectra. Single mode emission with a >40 dB side-mode suppression ratio (SMSR) was obtained. The high SMSR can be attributed to the optical confinement of aluminum oxide aperture and an angular dependence of HCG reflectivity.

Figure 9.7 illustrates the near-field optical characteristics of the emission beam from a typical TM-HCG-VCSEL. Despite the grating having a rectangular geometry, the optical emission output remains to be a symmetrical, fundamental mode Gaussian

profile, which is the optical mode of the laser. The beam diameter is measured to be about 3 μm, which is characterized by the width of the 99% drop in intensity. The near field intensity distribution for a TE-HCG-VCSEL is basically the same though not shown here.

9.4.2 Lithographically-Defined Polarization Control

In a conventional VCSEL, polarization modes are degenerated transverse modes. Due to the lack of polarization selection, polarization mode hopping of a VCSEL can cause mode partition noise in an optical communication link [33].The polarization state in VCSELs can be controlled by introducing anisotropy in the waveguide such that only one polarization state is supported, or by providing a polarization dependent gain or loss [34–38]. Recent progress on polarization-stable VCSELs are summarized in Chap. 5 of this book.

The inherent reflectivity difference between TM and TE polarized light in HCG results in a large polarization-dependant modal loss. In this section, we present highly effective and lithographically-defined polarization mode control in HCG-VCSEL under both CW and dynamic operation. We will use TM-HCG-VCSEL as an example. However, similar results can also be obtained for TE-HCG-VCSELs.

A TM-HCG-VCSEL emits TM polarized light with an electric field perpendicular to the grating stripes since it sees a much higher reflectivity (as shown in Fig. 9.2). Figure 9.8a shows SEM photos of 4 TM-HCG-VCSELs fabricated on the same wafer with the grating orientation aligned to different directions relative to [011] crystal plane at a 30° step while keeping the rest of the structure exactly the same. Polarization-resolved output power is measured through a polarization filter as a function of its angle relative to [011] crystal plane. Figure 9.8b shows the polarization-resolved power for the four different lasers. As the HCG is TM-polarized, the maximum output is expected at 90° from the stripe orientation. The experimental data in Fig. 9.8b indeed confirms this. For 0° orientated HCG, the maximum and minimum powers at 90 and 0°, respectively. An optical polarization suppression ratio (OPSR) as high as 30 dB is obtained. For a 30°, oriented HCG, the maximum and minimum are 120 and 30°, respectively. Similar observations are found for the 60 and 90° oriented HCGs. The 30 and 60° HCGs have a reduced mode discrimination with 20 dB OPSR, attributed to the gain anisotropy of the active region. Similar behavior is found for TE-HCG-VCSELs. This clearly demonstrates the HCG-VCSEL polarization can be lithographically determined with mode discrimination as large as 25–36 dB.

Time-dependent OPSR under large-signal direct modulation for a TM-HCG-based VCSEL was also characterized. This is a more stringent test criteria for polarization mode selection, where the laser is switched from being totally off to on. In this study, the laser was tested without a DC bias and is modulated with 5 V_{pp} rectangular pulses, with an electrical pulse width of 1 μs width and a repetition rate of 5 μs. Figure 9.9 shows the measured polarization-resolved emission spectra of a

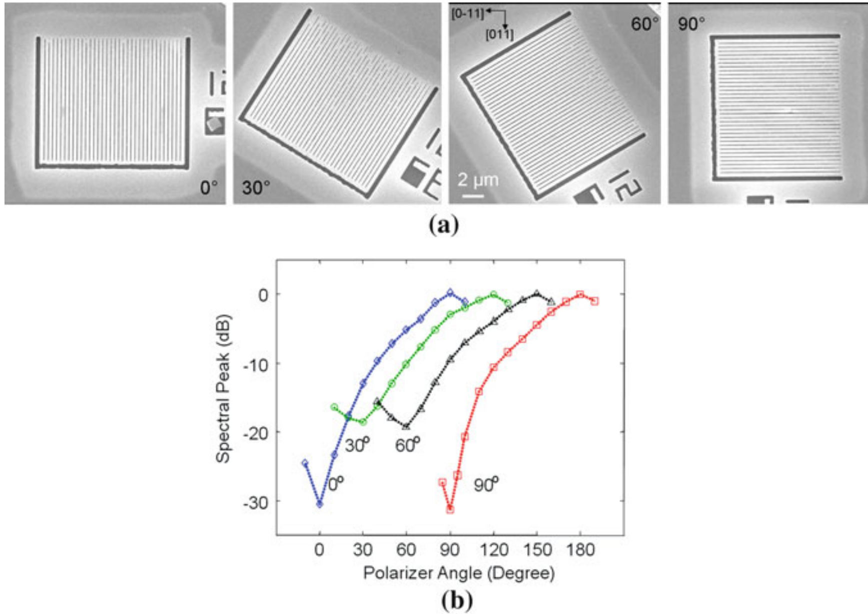

Fig. 9.8 **a** SEM photos of 4 identical TM-HCG-VCSELs fabricated on the same wafer with the grating orientation aligned to different directions relative to [011] crystal plane at a 30° step. **b** Polarization-resolved output power measured through a polarization filter as a function of its angle relative to [011] crystal plane. The maximum and minimum outputs are 90 and 0° from the stripe orientation, clearly illustrating polarization selection is determined lithographically by the HCG orientation with mode discrimination as large as 25–36 dB [30] (© 2009 IEEE)

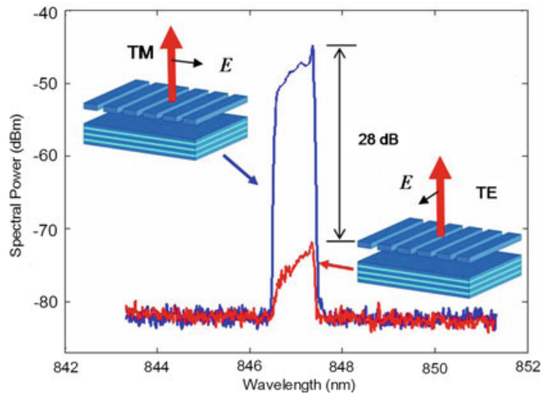

Fig. 9.9 Measured polarization-resolved optical spectra for a TM-HCG-VCSEL under a large-signal on-off modulation [30] (© 2009 IEEE)

TM-HCG-based VCSEL. A very large OPSR of 28 dB is maintained showing the effectiveness of HCG in polarization selection under dynamic modulation. Due to the large carrier transient and chirp as well as thermal heating effects under pulsed modulation, the measured spectrum was broadened in this case.

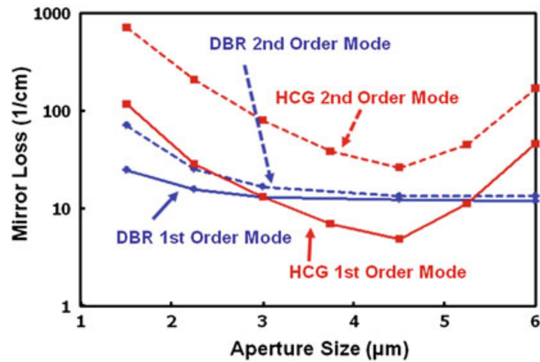

Fig. 9.10 Finite difference time-domain (FDTD) simulation of mirror loss for 1st (*solid*) and 2nd (*dotted*) order modes of a 6 μm (9 period) TE-HCG and standard top DBR (24 pairs). The 2nd order mode sees high mirror loss and will not lase in HCG case, but will lase in apertures larger than ∼3 μm in a standard VCSEL structure

9.4.3 Transverse Mode Control

A VCSEL operates with a single longitudinal mode by virtue of its extremely short cavity length. However, if the lateral diameter of the active region is large, multiple transverse mode operation typically occur [7, 39]. For many applications, the VCSEL's operation in the fundamental transverse mode is important for high system performance. Lateral transverse mode confinement of VCSEL by selective oxidation has allowed the control of modal characteristics of small-aperture (<2–3 μm) VCSELs [39]. However, the use of oxide apertures in VCSELs requires a tightly controlled oxidation process and high power operation in the fundamental mode is difficult to achieve. Considerable effort has been invested to achieve single-mode operation with high output power in VCSELs, including the use of an antiguide cavity [40], surface relief etching [37] and photonic crystal defects [41]. While these methods have shown effectiveness in controlling emission mode, they typically require additional structural complexity and stringent fabrication control.

The HCG reflectivity can be designed to vary with incident angle, which has been shown to be effective in transverse mode control. As large as 12 μm size VCSEL exhibits single fundamental mode emission with a large SMSR greater than 42 dB [16, 42]. This is in sharp contrast of oxide confined VCSEL, emitting multi-mode typically with an aperture larger than 2 μm.

Numerical simulation is performed to study the oxide aperture size dependence on the HCG-VCSELs performance, and the simulation results are very consistent with the experimental observation. Figure 9.10 shows a finite difference time-domain (FDTD) simulation of the transmitted mirror losses for the first and second order transverse modes in a standard top DBR with 24 pairs and a 6 μm size (9 periods) TE-HCG based mirror. The red lines show the mirror losses of the fundamental (solid) and the second order (dotted) mode for a 6 μm TE-HCG-mirror. When the aperture size increases, the mirror loss curve first goes down, then up, and can be explained by the following: the HCG is designed to provide higher reflectivity for surface-normal incident light than for incident lights with a small inclined angle. For a specific mode, when aperture size is large, the divergence angle is small;

a small divergence angle will experience a higher reflectivity from HCG. Therefore, the mirror loss decreases when the aperture size increases at the beginning. However, when the aperture size approaches the HCG size, due to the spreading of the light, the light close to (or outside) the edge of the HCG will experience a lower reflectivity (or little reflectivity). Therefore, when the aperture size approaches the HCG mirror size, the mirror loss of the HCG starts to increase again. For the same size oxide aperture, higher order transverse mode usually has a larger divergence angle (or larger transverse *k*-vector). Therefore, in Fig. 9.10, the mirror loss of the second order mode for the HCG-mirror is always higher than the mirror loss of the fundamental mode. In fact, for a 6 μm HCG-mirror, the mirror loss of the second order mode is so high that it never reaches the lasing condition. This explaines why HCG-VCSEL can maintain single mode operation even when the oxide aperture size is relatively large.

As a comparison, in Fig. 9.10, the mirror losses of a 22 pairs of DBR structures are plotted in blue lines. Because the DBR structure has a much weaker angular dependence for reflectivity compared to a HCG-mirror, the mirror losses for fundamental mode and 2nd order mode are very close to each other in DBR. When the aperture size is larger than 2 μm, both fundamental and 2nd order mode will reach lasing condition. Hence, the device will lase in multimode.

9.4.4 HCG Size Dependence

Since most of the simulations and analytic solutions are based on HCGs with infinite periods, it is really interesting to investigate just how many periods of grating are necessary to achieve lasing. To study the HCG size dependence, we fabricated a set of TE-HCG-VCSELs with a variation in the HCG area from 2×2 to $8 \times 8\,\mu m^2$ with a step of 620 nm (period of the TE-HCG). All the devices have a 2 μm oxide aperture. We obtained single mode CW lasing operation for all the devices with a grating area larger than $3 \times 3\,\mu m^2$. The smallest HCG has as few as 4 periods or a size of 3 μm × 3 μm × 145 nm, with a mass of just 5 pg! This means only 4 periods of TE-HCG can already provide reflectivity as high as 99.5%. Figure 9.11 shows an SEM image of the smallest working HCG-VCSEL. The alignment accuracy between the HCG and oxide aperture is estimated to be 0.5–1 μm. Hence, it is perhaps possible to have an even smaller HCG-VCSEL.

Light intensity-Current (LI) characteristics are measured for the lasing TE-HCG-VCSELs with different grating sizes. Figure 9.12 shows the LI curves of devices with different numbers of periods of TE-HCG. Device performance is fairly uniform for the devices with larger TE-HCGs. Threshold is stable at about 1 mA. Once the number of periods becomes less than 7, or the size of the HCG reaches 5 μm, the measured laser threshold current exhibits an inverse relationship to the grating area. The device threshold increases and slope efficiency decreases as the number of periods is further reduced.

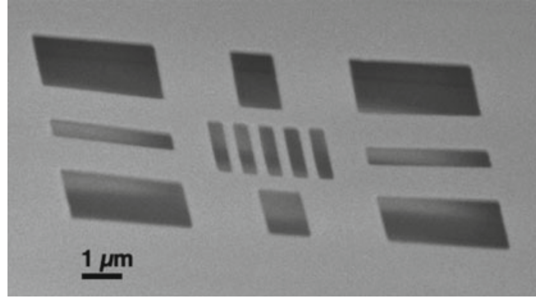

Fig. 9.11 SEM image of the freely suspended TE-HCG with only 4 periods or a size of $3 \times 3\,\mu m^2$

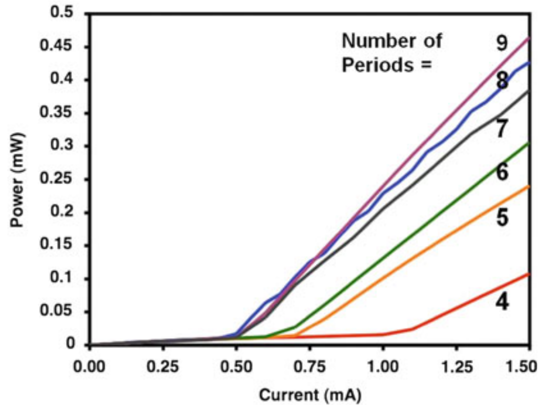

Fig. 9.12 Optical characteristics for HCG-VCSELs, showing the light intensity versus injected current for the set of identical TE-HCG-VCSELs with different grating sizes and 2 μm oxide apertures

9.5 Fabrication Tolerance

For HCG-VCSEL, the most important parameters are associated with HCG dimensions. First of all, the HCG thickness is determined by well-controlled MOCVD or MBE epitaxial growth. Hence, most of the discussion here will focus on HCG period and duty cycle, which are determined by lithography and etching.

Numerical simulation was performed for the fabrication tolerance of different parameters in the HCG structure based on rigorous coupled wave analysis. The contour plot in Fig. 9.13 shows the fabrication tolerance window for a fixed wavelength of 840 nm, where both the grating period (Λ) and grating spacing (a) are varied. From the simulated contour plot, we can see grating spacing a, the critical dimension in HCG, has about ±30% fabrication tolerance while still maintaining >99.5% reflectivity. Experimentally, a large number of HCG-VCSELs with different combinations of grating spacing and period were patterned by using electron-beam lithography. In Fig. 9.13, the white dots represent the grating spacings and periods of a large ensemble of HCG-VCSELs measured by SEM. We demonstrated that the HCG structure can have grating spacing variation from 80 to 120 nm (±20% of critical dimension

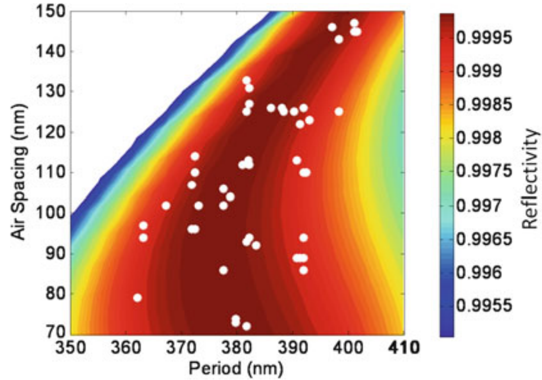

Fig. 9.13 Simulated top mirror reflectivity as a function of grating spacing and period for fixed $\lambda = 840$ nm. The white dots represent the combination of grating spacing and periods of the lasing TM-HCG-VCSELs. [14] (© 2009 IEEE)

a of 100 nm), and 40 nm variation in grating period (∼10% of the design period of 380 nm), while still providing enough reflectivity for the VCSELs to lase.

A lasing wavelength dependence study was performed for TM-HCG-VCSELs with different grating spacing from 86 to 126 nm, but the same grating period of 392 nm and an oxide aperture of 2 μm. The lasing wavelength blue-shifts as little as ∼2 nm or $\Delta\lambda/\lambda \sim 0.2\%$, when the grating spacing increases by 40%. Similarly, HCG-VCSELs with the same grating spacing (94 nm) but different grating periods, ranging from 363 to 392 nm, were also studied. The lasing wavelength red-shifts ∼2 nm when the grating period is varied by 30 nm (∼10%). All these are drastically different from conventional DBRs, where the wavelength shifts 1% with every 1% of DBR dimension change [33]. This insensitivity of VCSEL wavelength HCG parameters arises because the particular HCG structure used here has very little power penetration into the HGG, hence an extremely small phase-wavelength dependence which contributes to the effective cavity length. (In Sect. 9.6, we will discuss how to design HCG differently to achieve a large wavelength variation for multi-wavelength array.) This is in sharp contrast with a DBR structure, whose high reflectivity comes from interference of multiple reflections from different layers, and hence, by nature having a large power penetration and effective length.

To study the fabrication tolerance for HCGs with non-uniform grating spacing and period distribution within the same grating, each individual stripe of HCG was intentionally designed and fabricated with a non-uniform and random distribution. The average grating spacing size is 97 nm and the standard deviation is as large as 27 nm, nearly ±30% of the average. Similarly, we also studied gratings with a non-uniform distribution of period, having an average period of 374 nm and a standard deviation of 18 nm. Despite the large variation, a HCG-VCSEL with this random grating still lased with threshold current ∼0.55 mA [43]. Besides these designed fabrication errors, we fabricated several VCSELs with HCGs that were not completely etched through in parts or had lithographic defects. These VCSELs still lase under room temperature, CW operation with reasonable threshold currents and output powers. A SEM image of one such device where the HCG was etched with an

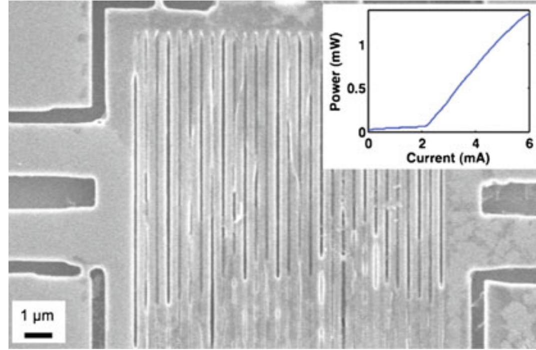

Fig. 9.14 SEM image of a TM-HCG-VCSEL patterned with underexposed photoresist. Despite obvious imperfections, the device still lased. Inset: Optical power vs. current characteristic of this device. [14] (© 2009 IEEE)

underexposed photoresist pattern is shown in Fig. 9.14, with its LI characteristics shown in the inset.

The large fabrication tolerance of the HCG structure originates from its broadband nature and wavelength scalability. HCG is a broadband high reflective mirror (in this design, the high reflectivity band $\Delta\lambda/\lambda > 12\%$ for reflectivity $>99.5\%$). Also, by varying the geometric dimension of HCG, the reflective spectrum of the HCG can be scaled accordingly to achieve a high reflectivity for a specific wavelength. This leads to the large fabrication tolerance in HCG-VCSEL fabrication.

9.6 Lithographically-Defined Multi-Wavelength HCG-VCSELs

Wavelength division multiplexing (WDM) offers an ideal way to leverage the high bandwidth of an optical fiber ($\gg$1 Tb/s) while using existing electronics operating close to 10 Gb/s. Consequently, monolithically-integrated, low cost, high-speed, multi-wavelength (MW) sources are extremely desirable for both dense and coarse WDM applications. Surface-normal emission, wafer-scale manufacturing and testing makes vertical-cavity surface-emitting lasers (VCSELs) a cost effective solution for MW sources. MW VCSEL sources can also be cost effective solutions for a wide range of applications including local area networks, etc.

All monolithically integrated MW VCSEL arrays fabricated to date utilize thickness variations either in the distributed Bragg reflector (DBR) or cavity layers to achieve different emission wavelengths. A change in the layer thickness directly translates to a change in the lasing wavelength due to the round trip phase condition of a VCSEL cavity. Thickness variations achieved by leveraging the natural non-uniformity in a molecular beam epitaxy (MBE) system [6, 44], patterned substrates [45], nonplanar metalorganic chemical vapor deposition [46], or anodic oxidation of a GaAs spacer layer [47] were reported. However, none of the previously reported

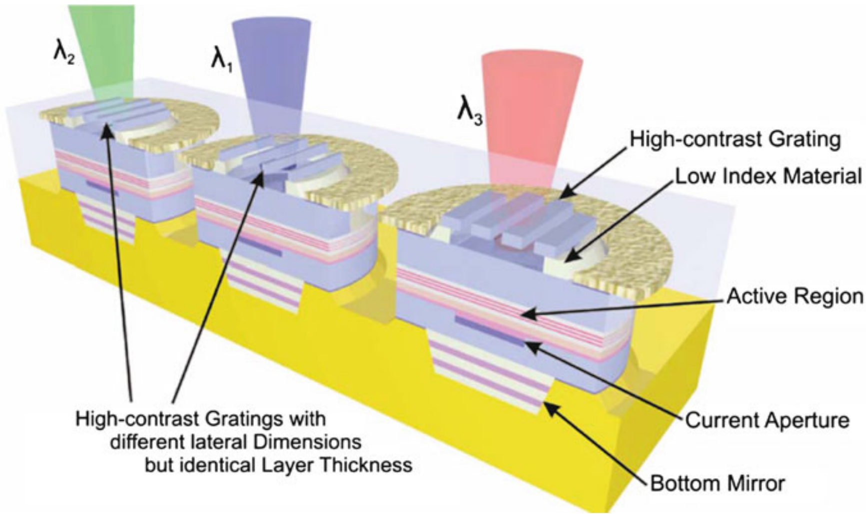

Fig. 9.15 Schematic of the proposed HCG-VCSEL array. Modifying the lateral dimensions of the HCG from VCSEL to VCSEL changes the HCG reflectivity phase, which facilitates control over the lasing wavelength of each VCSEL. Thus, a MW VCSEL array can be created

techniques led to precise control of the lasing wavelength. In addition, due to complicated fabrication processes, these techniques are not readily scalable to large arrays.

Note that the HCG discussed in previous sections are broad band reflectors, which by nature have low wavelength-dependent phase and large tolerances to grating dimension variations. With a different design, the phase (but not magnitude) of HCG reflectivity can exhibit a large dependence on dimensions, leading to a wide range of VCSEL emission wavelengths. We show HCG-VCSELs whose wavelengths are significantly varied by tuning grating period and duty cycle (ratio between grating width and period), while keeping the same epitaxy design (same layer thickness), thus enabling the fabrication of MW VCSELs array using simple lithographic means. As the laser wavelength is determined entirely by lithography, this design facilitates precise wavelength control and arbitrary physical layout.

The VCSEL structure used in this simulation is similar to that reported in [48], with the epitaxial top mirror being replaced by a HCG structure. A schematic VCSEL design is shown in Fig. 9.15. The out-coupling mirror is a HCG, lithographically formed out of a semiconductor material like InP, with an air-gap underneath. In principle, the top two layers could also be designed to be SiO_2 as the low index material and Si as the HCG as used in [10, 11].

The VCSEL wavelength is determined by the round-trip 2π phase condition (9.1) as in any Fabry-Perot cavity:

$$4\pi \frac{L_{\text{Cavity}}}{\lambda_{\text{Lasing}}} + \phi_{\text{HCG}} + \phi_{\text{DBR}} = 2\pi m, \tag{9.1}$$

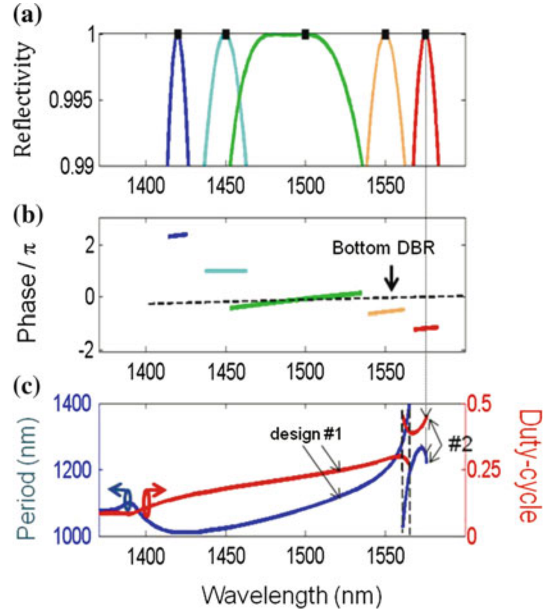

Fig. 9.16 Reflectivity **a** magnitude, and **b** phase vs. wavelength for various HCG lateral dimensions, **c** The design comprises of two parts: the first ending at 1,565 nm and the second beginning at 1,561 nm, leaving a 4 nm overlap. Each wavelength within the tuning range has at least one suitable HCG design

L_{Cavity} being the physical length of the cavity, λ_{Lasing} being the lasing wavelength, ϕ_{HCG} and ϕ_{DBR} being the reflectivity phases of the HCG and DBR mirrors, respectively, and m is an integer. Hence, to attain a large wavelength range in λ_{Lasing} with the same epitaxy, i.e. same L_{Cavity} (ϕ_{DBR} being relatively insensitive to λ_{Lasing}), we need a design of HCG whose ϕ_{HCG} can be changed greatly with grating period and duty cycle. In this case, by using a *thicker* HCG to facilitate a longer propagation length for the HCG modes (array modes), the destructive interference condition to yield a high reflectivity can be achieved with a larger wavelength dependence in phase. This leads to a possibility to significantly change λ_{Lasing} using only moderate changes in HCG lateral dimensions. Figures 9.16a, b are reflectivity magnitude and phase of HCGs with different periods and duty cycles (Fig. 9.16c), while keeping the same thickness. It is obvious that this design is highly desirable for fabricating lithographically-defined MW VCSEL arrays with an especially large wavelength wavelength range.

A reasonable HCG thickness of only 900 nm is already thick enough to provide wavelength tuning range in excess of 100 nm. The difference between the blue and red curves (designs #1 and #2) in Fig. 9.16c is the integer m in (9.1). In this case, there is a 4 nm wavelength window, at which two different HCG designs are suitable for lasing. This overlap window between two different HCG designs is necessary to make sure that the wavelength tuning range is continuous, i.e. without wavelength gaps, at which no design works. This way, when one of the designs can no longer be pushed to higher wavelengths, we can switch to a second HCG design (with different dimensions) and extend the wavelength range even further.

9.7 Tunable HCG-VCSELs

Tunable lasers are recognized as a highly desirable component for dense wavelength-division multiplexing (DWDM) systems [49]. A wavelength-tunable semiconductor laser has been constructed by combining an optical micro-electromechanical (MEM) mirror with a VCSEL [49–56]. Such mechanically tunable lasers have been extensively studied for various applications including optical networks, biomolecular sensing, chemical spectroscopy and chip-scale atomic clocks. The MEM tunable structures are desirable because they provide for a large and continuous tuning range with high precision, and fast response. The monolithic integration of VCSEL and MEMS brings together the best of both technologies and leads to an unprecedented performance in wavelength tunable lasers with simple electrical control.

Previous demonstrations of MEM tunable VCSEL used a MEM design that was relatively large, typically $\sim$200 μm long and $10-20$ μm wide. The main reason for such large size is due to the thickness of the top DBR held on the end of the micromechanical structure [49]. The wavelength tuning is accomplished by applying a voltage between the top DBR and laser active region, across the air gap. The applied bias generates an electrostatic force, which attracts the top DBR downward toward the substrate. This physical movement changes the optical length of the laser cavity and thus produces a change (blue-shift) in the laser emission wavelength. In order to achieve a large tuning range with a small voltage, the entire MEM structure must be scaled with the DBR thickness. The large mass of the movable mechanical structures translates into a slow tuning speed and high actuation power, as well as processing difficulties.

The HCG is naturally suitable for forming a tunable MEM structure. With its ultra-thin layer, 10–20 times thinner than a typical DBR, the other two dimensions of the MEM structure can be reduced by similar numbers, resulting in a 10^4 times mass reduction and close to three-order-of-magnitudes increase in tuning speed.

9.7.1 Design and Fabrication

A device schematic of the tunable VCSEL is shown in Fig. 9.17a. The device consists of an *n*-doped HCG top mirror, a sacrificial layer, two (or four) pairs of *p*-doped DBR, AlGaAs oxidation layer, a cavity layer containing the active region, and a bottom standard *n*-doped DBR mirror, all monolithically grown on a GaAs substrate. The main difference from the regular HCG-VCSELs is that, in the tunable structure, sacrificial layer (to be removed to form the airgap) is typically undoped and the HCG layer is *n*-doped, instead of both being p-doped. Electrical current injection is conducted through the middle laser *p*-contact (via 2 pairs of *p*-doped DBRs above the cavity layer) and backside *n*-contact (via substrate). An aluminum oxide aperture is formed on the AlGaAs layer just above the active region to provide current and optical confinement.

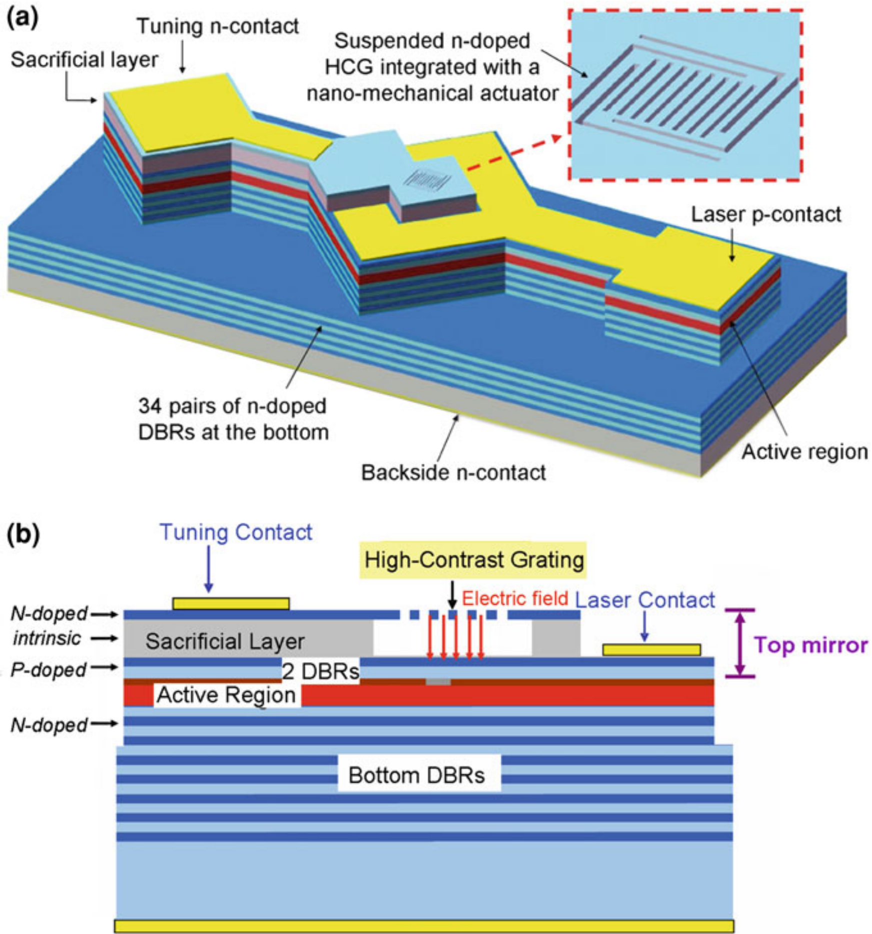

Fig. 9.17 **a** Schematic of the tunable HCG-VCSEL using the highly reflective high-contrast subwavelength grating as its top mirror. **b** Cross-section epitaxial design. The electric field generated by reverse biasing the top two contacts creates the attractive force to pull the HCG downwards, which in turn decreases the VCSEL cavity length and blue-tunes the emission wavelength [14] (© 2009 IEEE)

The cross-sectional design of the device is shown in Fig. 9.17b. The HCG is freely suspended above a variable airgap and supported via a nano-mechanical structure. Various MEM supporting structures, including cantilever, bridge, folded-beam (shown in Fig. 9.18), and membrane (4-fold supported bridge) are fabricated to experimentally study their trade-offs in voltage and tuning speed. The tuning contact is fabricated on the top *n*-doped HCG layer. The top two contacts provide a bias across the gap between the HCG and the active region. Using a reverse bias in this junction, the electric field resulted from the p-n junction charges attracts the

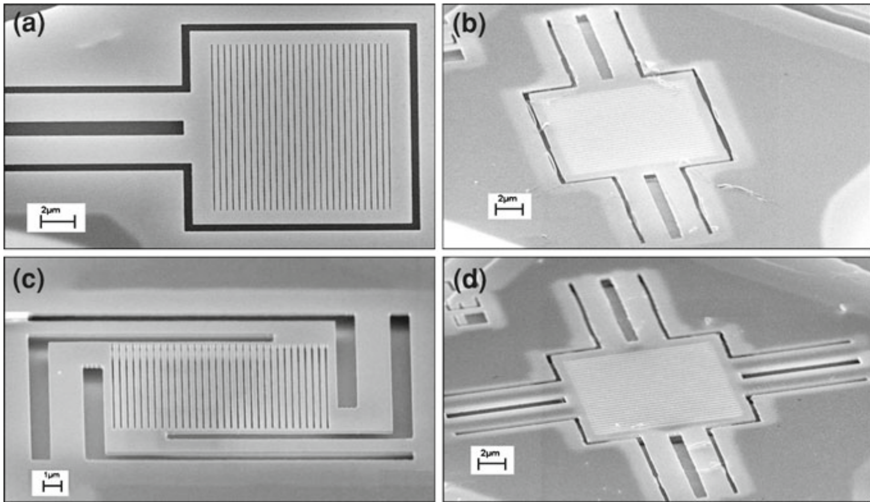

Fig. 9.18 SEM image of the freely suspended HCG-mirror with a variety of MEM structure including **a** cantilever, **b** bridge, **c** folded-beam, and **d** membrane. Reprinted by permission from Macmillan publishers Ltd: nature photonics [18], copyright (2008)

HCG downwards, which thus shortens the laser cavity length and blue-shifts the lasing wavelength. The tuning range is limited primarily by the movable distance to approximately 1/3 of the airgap and the reverse breakdown voltage [49]. More on the fabrication details can be found in Ref. [17].

9.7.2 Characteristics of Tunable HCG-VCSEL

The optical characteristics of tunable HCG-VCSELs are summarized. Figure 9.19 shows the output power and voltage versus current (LI and IV curves, respectively) for a typical tunable VCSEL with TM-HCG. The TM-HCG exhibits a very low threshold current of 200 μA and an external slope efficiency 0.25 mW/mA. We found that compared to the regular non-tunable TM-HCG-VCSEL, the threshold current was substantially lower. We attribute this to the lower free carrier absorption in the n-doped HCG. In addition, the threshold current is also significantly lower compared to standard DBR-based tunable VCSELs with 1–2 mA threshold current.

Wavelength tuning is measured by applying a reverse voltage bias across the tuning contact and the laser contact, while a constant electrical current is applied between the laser and backside contact. The reverse bias across the *pin* junction results in a negligibly small leakage current of ∼10 nA, which does not affect the operation of the VCSEL current injection. Figure 9.20 shows the measured wavelength tuning spectra of a fabricated VCSEL, where the movable HCG-mirror is integrated with a bridge nano-mechanical actuator. The laser is biased at ∼1.2 times the threshold

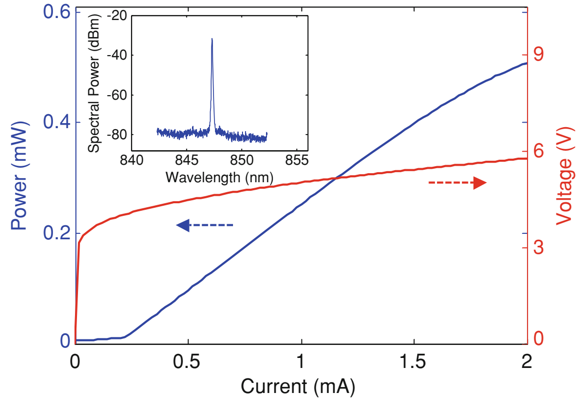

Fig. 9.19 Light-current and voltage-current curves of a typical tunable VCSEL with TM-HCG. The inset shows the measured single mode optical emission spectra with >40 dB SMSR in both cases. Reprinted by permission from Macmillan publishers Ltd: nature photonics [18], copyright (2008)

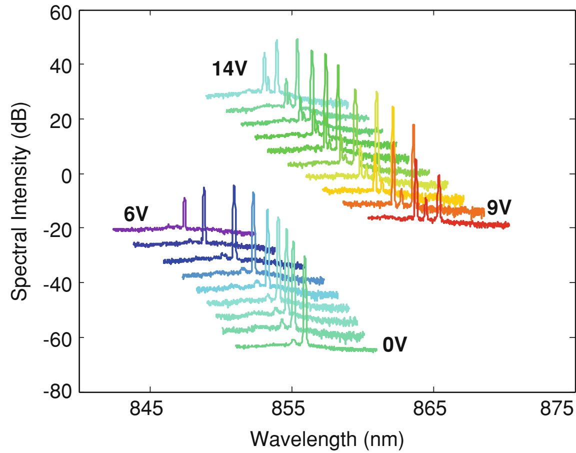

Fig. 9.20 Measured continuous wavelength tuning spectra of a tunable VCSEL, with an ∼18 nm tuning range. Spectra are vertically offset by 5 dB. Reprinted by permission from Macmillan publishers Ltd: nature photonics [18], copyright (2008)

current and actuated under various applied voltages across the tuning contact. An 8 nm continuous wavelength tuning toward the shorter wavelength is first obtained within 0–6 V of external applied voltage. The VCSEL stops lasing when the external applied voltage is further increased, as the optical loss becomes larger than the laser gain due to the phase mismatch between the HCG and M pairs of DBR. Once the voltage reaches 9 V, the device starts lasing again but at another longitudinal mode and continuously tunes again for 13 nm over the applied voltage range of 9–14 V. With the total spectral overlap, an overall continuous wavelength tuning range of 18 nm is experimentally obtained.

The mechanical response of various structures is measured by applying a sinusoidal AC modulating voltage in addition to a DC voltage, while the VCSEL is injected with constant current. The emission light is then collected by an optical fiber and sent to an optical spectrum analyzer. Since the signal integration time of

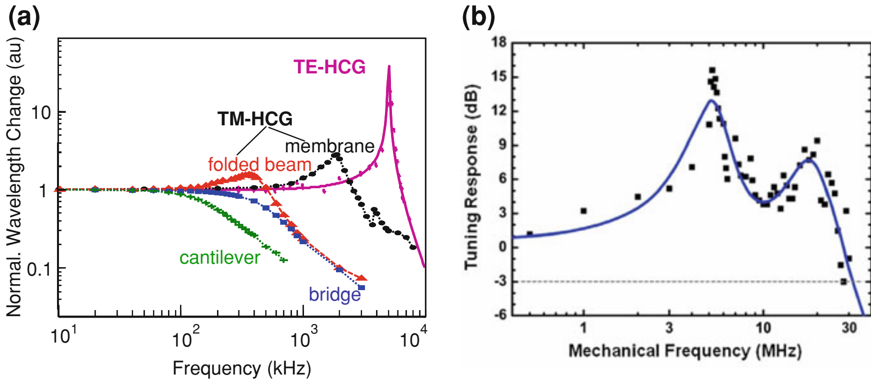

Fig. 9.21 Relative optical wavelength change of the VCSEL as a function of input frequency to the tuning contact. **a** for various TM-HCG and TE-HCG-VCSEL [30] (© 2009 IEEE) **b** for the smallest 4-period TE-HCG-VCSEL with −3 dB frequency ∼27 MHz [15]

an optical spectrum analyzer is much slower compared to the voltage modulation, a spectrally broadened emission can be observed as the nano-mechanical actuator (and hence the emission wavelength) is being modulated.

The spectral broadening is directly proportional to the magnitude of the mechanical deflection. The measured response of various structures is shown in Fig. 9.21a. For TM-HCG, we show the response for different nano-mechanical structures. The HCGs are $12 \times 12\,\mu\text{m}^2$ and the mechanical structures are typically 10 μm long. The membrane actuator exhibits the fastest mechanical resonant response with the 3 dB frequency bandwidth of 3.3 MHz, or equivalently the tuning speed of this device is calculated to be about 151 ns (inverse of half cycle of 3.3 MHz). The TE-HCG-VCSEL is also shown on the same plot. As the thickness of the HCG is reduced, the size of the HCG and mechanical structures are all further reduced.

For a $3 \times 3\,\mu\text{m}^2$ HCG with 3 μm long membrane bridges, the 3 dB frequency is increased to 27 MHz, Fig. 9.21b, with an equivalent tuning time of 18 ns. Compared to the existing DBR-based electrostatic-actuated MEM VCSEL (with tuning speed ∼10 μs), the demonstrated tunable VCSEL with an integrated mobile HCG has faster wavelength tuning speed by close to three orders of magnitude.

9.8 Summary

The recent discoveries of high-contrast gratings have led to a wealth of new research studies. By integrating the single-layer HCG with a VCSEL, many desirable and yet previously unattained properties are achieved, e.g. lithographically defined polarization control and large aperture single transverse mode. We experimentally demonstrated a very large fabrication tolerance in HCG-VCSELs with ±20% critical

dimension variation in uniform HCGs and ±30% critical dimension variation in random size HCGs. The VCSEL emission wavelength is insensitive to the lithographical variations of HCG, which makes it especially attractive for designing and manufacturing VCSELs for a fixed and desirable wavelength for any particular application. A very small HCG with only 4 grating periods is enough to support lasing. These results show that a low-cost and high-throughput fabrication process such as nano-imprint can be implemented for HCG large volume batch processing.

We present a multi-wavelength HCG-VCSEL array design, whose wavelength is determined by varying the lateral dimensions of the HCG. With this design, the VCSEL epitaxy thickness remains constant for the entire array devices, which facilitates cost-effective fabrication. The theoretically simulated wavelength range approaches 200 nm. We believe the HCG-VCSEL reported here would enable a new type of cost-effective WDM source suitable to accommodate the full bandwidth of Er-doped fiber amplifier. The same concept may be applied to fabricate multiwavelength filter and detector arrays.

We demonstrated a nano-electromechanical tunable laser by monolithically integrating the lightweight, single-layer high-index-contrast subwavelength grating as the movable top mirror of a VCSEL. The small footprint of the HCG enables the scaling down of the mechanical actuating component, which results in a drastic reduction in mass and tuning speed. By using electrostatic actuation to control the air gap below the HCG, a compact and efficient wavelength-tunable VCSEL with precise and continuous tuning range is demonstrated with ultra-low power consumption.

The high reflectivity as well as the feasibility of monolithic integration with optoelectronic devices are demonstrated. HCG design can be readily implemented on various material systems, opening the door to the fabrication of devices in vast wavelength regimes. The simplicity, wavelength-scalability, and versatility of the single-layer HCG design would provide numerous benefits when fabricating surface-normal optoelectronic devices such as VCSELs, high brightness LEDs, photo-voltaic cells, optical filters and detectors, and micro-electromechanical (MEMS) tunable devices, for a wide range of wavelengths.

Acknowledgments The author wishes to acknowledge major contributions from former and current graduate students at UC Berkeley, C. Mateus, M. Huang, Y. Zhou, C. Chase, V. Karagodsky and Y. Rao; and fruitful collaborations with Profs. Fumio Koyama and Markus Amann. She also thanks the support of a National Security Science and Engineering Faculty Fellowship and National Science Foundation through CIAN NSF ERC under grant #EEC-0812072.

References

1. K. Iga, Surface-emitting laser—its birth and generation of new optoelectronics field. IEEE J. Select. Topics Quantum Electron. **6**, 1201–1215 (2000)
2. F. Koyama, H. Uenohara, T. Sakaguchi, K. Iga, GaAlAs/GaAs MOCVD growth for surface emitting laser. Jpn. J. Appl. Phys. Part 1 **26**, 1077–1081 (1987)

3. J.L. Jewell, S.L. McCall, Y.H. Lee, A. Scherer, A.C. Gossard, J.H. English, Lasing characteristics of GaAs microresonators. Appl. Phys. Lett. **54**,1400 (1989)
4. L.A. Coldren, R.S. Geels, S.W. Corzine, J.W. Scott, Efficient vertical-cavity lasers. Opt. Quantum Electron. **24**, 105–119 (1992)
5. M. Orenstein, A. Von Lehmen, C.J. Chang-Hasnain, N.G. Stoffel, L.T. Florez, J.P. Harbison, J. Wullert, A. Scherer, Matrix addressable vertical cavity surface emitting laser array. Electron. Lett. **27**(5), 437–438 (1991)
6. C.J. Chang-Hasnain, J.P. Harbison, C.E. Zah, M.W. Maeda, L.T. Florez, N.G. Stoffel, T.P. Lee, Multiple wavelength tunable surface emitting laser arrays. IEEE J. Quantum Electron. **27**(6), 1368–1376 (1991)
7. C.J. Chang-Hasnain, J.P. Harbison, G. Hasnain, A. Von Lehmen, L.T. Florez, N.G. Stoffel, Dynamic, polarization, and transverse mode characteristics of vertical cavity surface emitting lasers. IEEE J. Quantum Electron. **27**(6), 1402–1409 (1991)
8. M.W. Maeda, C.J. Chang-Hasnain, J.S. Patel, C. Lin, H.A. Johnson, J.A. Walker, Use of a multi-wavelength surface-emitting laser array in a 4-channel wavelength-division-multiplexed system experiment. IEEE Photon. Technol. Lett. **3**(3), 268–269 (1991)
9. K.H. Hahn, M.R. Tan, S.Y. Wang, Intensity noise of large area vertical cavity surface emitting lasers in multimode optical fibre links. Electron. Lett. **30**(2), 139–140 (1994)
10. C.F.R. Mateus, M.C.Y. Huang, Y. Deng, A.R. Neureuther, C.J. Chang-Hasnain, Ultrabroadband mirror using low-index cladded subwavelength grating. IEEE Photon. Technol. Lett. **16**(2), 518–520 (2004)
11. C.F.R. Mateus, M.C.Y. Huang, L. Chen, C.J. Chang-Hasnain, Y. Suzuki, Broadband mirror (1.12–1.62 μm) using single-layer sub-wavelength grating. IEEE Photon. Technol. Lett. **16**(7), 1676–1678 (2004)
12. C.J. Chang-Hasnain, C.F.R. Mateus, M.C.Y. Huang, Ultra broadband mirror using subwavelength grating, US Patent 7,304,781
13. M.C.Y. Huang, Y. Zhou, C.J. Chang-Hasnain, A surface-emitting laser incorporating a high-index-contrast subwavelength grating. Nat. Photon. **1**, 119–122 (2007)
14. C. Chang-Hasnain, Y. Zhou, M. Huang, C. Chase, High-contrast grating VCSELs. IEEE J. Select. Topics Quantum Electron. **15**, 869–878 (2009)
15. C. Chase, Y. Zhou, C. Chang-Hasnain, Size effect of high contrast gratings in VCSELs. Opt. Express **17**, 24002–24007 (2009)
16. C. Chase, Y. Rao, W. Hofmann, C.J. Chang-Hasnain, 1550 nm high contrast grating VCSEL. Opt. Express **18**(15), 15461–15466 (2010)
17. V. Karagodsky, B. Pesala, C. Chase, W. Hofmann, F. Koyama, C.J. Chang-Hasnain, Monolithically integrated multi-wavelength VCSEL arrays using high-contrast gratings. Opt. Express **18**(2), 694–699 (2010)
18. F. Lu, F.G. Sedgwick, V. Karagodsky, C. Chase, C.J. Chang-Hasnain, Planar high-numerical-aperture low-loss focusing reflectors and lenses using subwavelength high contrast gratings. Opt. Express **18**(12), 12606–12614 (2010)
19. D. Fattal, J. Li, Z. Peng, M. Fiorentino, R.G. Beausoleil, Flat dielectric grating reflectors with focusing abilities. Nat. Photon. **4**, 466–470 (2010)
20. M.C.Y. Huang, Y. Zhou, C.J. Chang-Hasnain, A nanoelectromechanical tunable laser. Nat. Photon. **2**, 180–184 (2008)
21. P. Gilet, N. Olivier, P. Grosse, K. Gilbert, A. Chelnokov, I.-S. Chung, J. Mørk, High-index-contrast subwavelength grating, in *Vertical-Cavity Surface-Emitting Lasers XIV*, Proceedings of SPIE, vol. 7615 (2010),p. 76150J-1
22. S. Boutami, B. Ben Bakir, J.-L. Leclercq, P. Viktorovitch, Compact and polarization controlled 1.55 μmvertical-cavity surface emitting laser using single-layer photonic crystal mirror. Appl. Phys. Lett. **91**(7), 071105-1–071105-3 (2007)
23. S. Boutami, B. Benbakir, X. Letartre, J.L. Leclercq, P. Regreny, P. Viktorovitch, Ultimate vertical Fabry-Perot cavity based on single-layer photonic crystal mirrors. Opt. Express **15**(19), 12443–12449 (2007)

24. I.-S. Chung, J. Mørk, P. Gilet, A. Chelnokov, Subwavelength grating-mirror VCSEL with a thin oxide gap. IEEE Photon. Technol. Lett. **20**(2), 105–107 (2008)
25. A. Haglund, S.J. Gustavsson, J. Vukusic, P. Jedrasik, A. Larsson, High-power fundamental-mode and polarisation stabilised VCSELs using sub-wavelength surface grating. Electron Lett. **41**, 805–807 (2005)
26. S. Goeman, S. Boons, B. Dhoedt, K. Vandeputte, K. Caekebeke, P.V. Daele, R. Baets, First demonstration of highly reflective and highly polarization selective diffraction gratings (GIRO-gratings) for long-wavelength VCSELs. IEEE Photon. Technol. Lett. **10**, 1205–1207 (1998)
27. L. Zhuang, S. Schablitsky, R.C. Shi, S.Y. Chou, Fabrication and performance of thin amorphous Si subwavelength transmission grating for controlling vertical cavity surface emitting laser polarization. J. Vac. Sci. Technol. B **14**, 4055–4057 (1996)
28. M.G. Moharam, T.K. Gaylord, Rigorous coupled-wave analysis of planar-grating diffraction. J. Opt. Soc. Am. **71**, 811–818 (1981)
29. V. Karagodsky, F. Sedgwick, C.J. Chang-Hasnain, Theoretical analysis of subwavelength high contrast grating reflectors. Opt. Express **18**(16), 16973–16988 (2010)
30. V. Karagodsky, C. Chase, C.J. Chang-Hasnain, Matrix Fabry–Perot resonance mechanism in high-contrast gratings. Opt. Lett. **36**(9), 1704–1706 (2011)
31. V. Karagodsky, F.G. Sedwick, C.J. Chang-Hasnain, New physics of subwavelength high contrast gratings. in *Proceedings of Conf. on Lasers and Electro-Optics, CLEO '11.* Baltimore, MD, May 2011, paper QThD2
32. Y. Zhou, M.C.Y. Huang, C. Chase, V. Karagodsky, M. Moewe, B. Pesala, F.G. Sedgwick, C.J. Chang-Hasnain, High-index-contrast grating (HCG) and its applications in optoelectronic devices. IEEE J. Select. Topics Quantum Electron. **15**(5), 1485–1499 (2009)
33. C.J. Chang-Hasnain, VCSEL for metro communications, Chap. 13 in Optical Fiber Communications IV A: Components, ed. by I. Kaminow, T. Li (Academic Press, New York, 2002), pp. 666–698
34. A. Mizutani, N. Hatori, N. Nishiyama, F. Koyama, K. Iga, InGaAs/GaAs vertical-cavity surface emitting laser on GaAs (311)B substrate using carbon auto-doping. Jpn. J. Appl. Phys. **37**, 1408–1412 (1998)
35. S.J. Schablitsky, Z. Lei, R.C. Shi, S.Y. Chou, Controlling polarization of vertical-cavity surface-emitting lasers using amorphous silicon subwavelength transmission gratings. Appl. Phys. Lett. **69**, 7–9 (1996)
36. J.M. Ostermann, P. Debernardi, R. Michalzik, Optimized integrated surface grating design for polarization-stable VCSELs. IEEE J. Quantum Electron. **42**, 690–698 (2006)
37. A. Haglund, J.S. Gustavsson, J. Bengtsson, P. Jedrasik, A. Larsson, Design and evaluation of fundamental-mode and polarization-stabilized VCSELs with a subwavelength surface grating. IEEE J. Quantum Electron. **42**, 231–240 (2006)
38. R. Michalzik, J.M. Ostermann, P. Debernardi, Polarization-stable monolithic VCSELs, in *Vertical-Cavity Surface-Emitting Lasers XII*, ed. by C. Lei, J.K. Guenter, Proceedings of SPIE, vol. 6908 (2008), pp. 69080A-1–69080A-16
39. K.D. Choquette, K.M. Geib, C.I.H. Ashby, R.D. Twesten, O. Blum, H.Q. Hou, D.M. Follstaedt, B.E. Hammons, D. Mathes, R. Hull, Advances in selective wet oxidation of AlGaAs alloys. IEEE J. Select. Topics Quantum Electron. **3**, 916–926 (1997)
40. Y.A. Wu, G.S. Li, W. Yuen, C.J. Chang-Hasnain, C. Caneau, High-yield processing and single-mode operation of passive antiguide region vertical-cavity lasers. IEEE J. Select. Topics Quantum Electron. **3**, 429–434 (1997)
41. A.J. Danner, J.J. Raftery Jr., N. Yokouchi, K.D. Choquette, Transverse modes of photonic crystal vertical-cavity lasers. Appl. Phys. Lett. **84**, 1031 (2004)
42. M.C.Y. Huang, Y. Zhou, C.J. Chang-Hasnain, Single mode high-contrast subwavelength grating vertical cavity surface emitting lasers. Appl. Phys. Lett. **92**, 171108 (2008)
43. Y. Zhou, M.C.Y. Huang, C.J. Chang-Hasnain, Large fabrication tolerance for VCSELs using high-contrast grating. IEEE Photon. Technol. Lett. **20**, 434–436 (2008)

44. C. Chang-Hasnain, M. Maeda, N. Stoffel, J. Harbison, L. Florez, J. Jewell, Surface emitting laser arrays with uniformly separated wavelengths. Electron. Lett. **26**, 940–941 (1990)
45. L. Eng, K. Bacher, W. Yuen, J. Harris Jr., C. Chang-Hasnain, Multiple wavelength vertical cavity laser arrays on patterned substrates. IEEE J. Quantum Electron. **1**, 624–628 (1995)
46. F. Koyama, T. Mukaihara, Y. Hayashi, N. Ohnoki, N. Hatori, K. Iga, Wavelength control of vertical cavity surface-emitting lasers by using nonplanar MOCVD. IEEE Photon. Technol. Lett. **7**, 10–12 (1995)
47. T. Wipiejewski, M. Peters, E. Hegblom, L. Coldren, Vertical-cavity surface-emitting laser diodes with post-growth wavelength adjustment. IEEE Photon. Technol. Lett. **7**, 727–729 (1995)
48. W. Hofmann, E. Wong, G. Böhm, M. Ortsiefer, N.H. Zhu, M.C. Amann, 1.55 μm VCSEL arrays for high-bandwidth WDM-PONs. IEEE Photon. Technol. Lett. **20**, 291–293 (2008)
49. M.S. Wu, E.C. Vail, G.S. Li, W. Yuen, C.J. Chang-Hasnain, Widely and continuously tunable micromachined resonant cavity detector with wavelength tracking. IEEE Photon. Technol. Lett. **8**(1), 98–100 (1996)
50. C.J. Chang-Hasnain, Tunable VCSEL. IEEE J. Select. Topics Quantum Electron. **6**, 978–987 (2000)
51. S. Decai, W. Fan, P. Kner, J. Boucart, T. Kageyama, Z. Dongxu, R. Pathak, R.F. Nabiev, W. Yuen, Long wavelength-tunable VCSELs with optimized MEMS bridge tuning structure. IEEE Photon. Technol. Lett. **16**, 714–716 (2004)
52. F. Riemenschneider, M. Maute, H. Halbritter, G. Boehm, M.C. Amann, P. Meissner, Continuously tunable long-wavelength MEMS-VCSEL with over 40 nm tuning range. IEEE Photon. Technol. Lett. **16**, 2212–2214 (2004)
53. M.C.Y. Huang, K.B. Cheng, Y. Zhou, B. Pesala, C.J. Chang-Hasnain, A.P. Pisano, Demonstration of piezoelectric actuated GaAs-based MEMS tunable VCSEL. IEEE Photon. Technol. Lett. **18**, 1197–1199 (2006)
54. B. Kögel, H. Halbritter, S. Jatta, M. Maute, G. Böhm, M.-C. Amann, M. Lackner, M. Schwarzott, F. Winter, P. Meissner, Simultaneous spectroscopy of NH_3 and CO using a > 50 nm continuously tunable MEMS-VCSEL. IEEE Sens. J. **7**(11), 1483–1489 (2007)
55. H. Halbritter, C. Sydlo, B. Kögel, F. Riemenschneider, H.L. Hartnagel, P. Meissner, Impact of micromechanics on the linewidth and chirp performance of MEMS-VCSELs. IEEE J. Select. Topics Quantum Electron. **13**(2), 367–373 (2007)
56. S. Jatta, B. Kögel, M. Maute, K. Zogal, F. Riemenschneider, G. Böhm, M.-C. Amann, P. Meißner, Bulk-micromachined VCSEL at 1.55 μm with 76 nm single-mode continuous tuning range. IEEE Photon. Technol. Lett. **21**(24), 1822–1824 (2009)

Part III
From Infrared to Violet Emission

Chapter 10
Long-Wavelength VCSELs with Buried Tunnel Junction

Markus Ortsiefer, Werner Hofmann, Jürgen Rosskopf and Markus-Christian Amann

Abstract Despite the earliest work on VCSELs in the late 1970s on InP-based materials, the further realization of VCSELs beyond 1.3 μm emission wavelength has been significantly delayed for many years with respect to their short-wavelength counterparts on GaAs substrates. This chapter covers the specific challenges, solutions and application prospects of VCSELs in non-GaAs-based material systems which are suitable for achieving significantly extended wavelength ranges. By using highly advanced device concepts, since the late 1990s it became possible to overcome the fundamental technological drawbacks related with long-wavelength VCSELs such as inferior thermal properties and to realize lasers with remarkable device performance. In particular and with respect to huge application opportunities in optical communications, this chapter presents InP-based VCSELs with single-mode output powers of several milliwatts at room temperature and well beyond 1 mW at 85°C, as well as modulation frequencies far above 10 GHz in conjunction with ultra-small power consumption. While the InP-based VCSEL technology is limited to maximum emission wavelengths around 2.3 μm, even longer emission up to the mid-infrared wavelength range can be achieved with VCSELs based on GaSb. With their inherent and, compared to other laser types, superior properties like enhanced tuning

M. Ortsiefer (✉) · J. Rosskopf
VERTILAS GmbH, Lichtenbergstr. 8, 85748 Garching, Germany
e-mail: ortsiefer@vertilas.com

J. Rosskopf
e-mail: rosskopf@vertilas.com

W. Hofmann
Institut für Festkörperphysik, Technische Universität Berlin,
Hardenbergstr. 36, 10623 Berlin, Germany
e-mail: werner.hofmann@tu-berlin.de

M.-C. Amann
Walter Schottky Institut, Technische Universität München,
Am Coulombwall, 85748 Garching, Germany
e-mail: amann@wsi.tum.de

R. Michalzik (ed.), *VCSELs*, Springer Series in Optical Sciences 166,
DOI: 10.1007/978-3-642-24986-0_10, © Springer-Verlag Berlin Heidelberg 2013

characteristics, long-wavelength VCSELs are regarded as key components for applications in optical sensing.

VCSELs have emerged as high-performance commercial products with millions of annual units over the last decade [1, 2]. These devices are usually based on GaAs substrates and show emission wavelengths from approximately 0.65–1.3 μm. The ongoing success of VCSELs is particularly due to the intrinsic advantages of this laser type as compared to the edge-emitting laser diodes. The most important features of VCSELs are their low beam divergence leading to relaxed fiber alignment tolerances, the small threshold currents and high slope efficiencies leading to low electrical power consumption, and their potential for integration to 1D and 2D laser arrays. Additionally, VCSELs are usually longitudinal single-mode. However, the transverse single-mode operation as well as the polarization are difficult to control in common VCSELs. From the viewpoint of manufacturing and technology, VCSELs are superior against the edge emitters because the vertical power emission of the built-in laser resonator requires no mirror cleaving so that an on-wafer testing is possible. Finally, the small size of the devices increases the fabrication output.

All the VCSEL features described above also hold for the long wavelength range beyond 1.3 μm. In addition, for geometrical reasons, the longer wavelengths make the transverse mode and polarization control easier so that true single-mode devices with a stable polarization may be achieved even for rather large diameters of around 5–7 μm [3]. Accordingly, long-wavelength VCSELs have a tremendous meaning for a wide variety of applications, ranging from short to long range optical communications, parallel data transmission as well as optical measurement and gas sensing. In many of these applications, therefore, long-wavelength VCSELs turn out to be cost-effective and superior performance substitutes for conventional Fabry-Perot or distributed feedback (DFB) lasers.

10.1 Special Issues for Long-Wavelength VCSELs

Intensive efforts have been paid in the past to realize VCSELs also in the long wavelength regime above 1.3 μm. These efforts mainly had to deal with the intrinsic difficulties of the material systems suited for the long wavelength regime. A major drawback of long-wavelength VCSELs emitting at wavelengths of, e.g., 1.3 or 1.55 μm is that active regions cannot be grown on GaAs substrates using mature InP-based materials such as InGaAsP or InGaAlAs. While the short-wavelength GaAs-based devices benefit from the large index difference between GaAs and AlAs that gives high-reflective Bragg mirrors even with relatively small numbers of layer pairs, the long-wavelength VCSELs based on InP suffer from almost a factor of two smaller index contrast of the InGaAsP or InGaAlAs mirror layers [4]. Accordingly, larger numbers of layer pairs are required for reasonable mirror reflectivity. Together with the larger layer thicknesses due to the longer wavelength, the epitaxial mirror stacks of the InP-based VCSELs become rather thick. Considering further the small thermal conductivity of the ternary/quaternary layers being about an order of

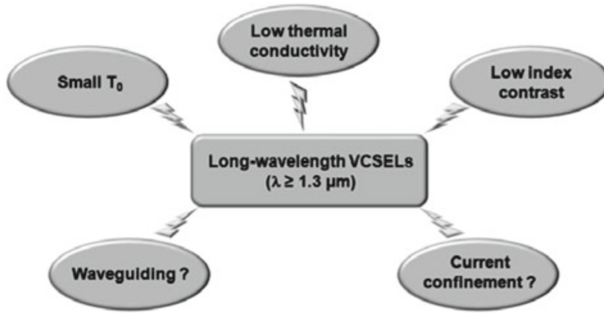

Fig. 10.1 Schematic illustration of main challenges of long-wavelength VCSEL technology

magnitude smaller than GaAs and AlAs [5], the thermal resistances of equally reflecting epitaxial mirrors for the InP-based long-wavelength VCSELs are 20–40 times larger than for their short-wavelength GaAs-based counterparts. Using AlAsSb lattice-matched on InP, the index contrast can—in principle—be increased up to about the same magnitude as in the GaAs-based materials [6]. However, the small thermal conductivity still prevents an effective heat dissipation through the corresponding epitaxial mirrors. The enhanced self-heating caused by high thermal resistances is even more critical with respect to increased temperature sensitivity of the optical gain for commonly used active regions in the long-wavelength range. Due to gain saturation, stronger electrical pumping leads to unacceptable internal temperature rise which in turn deteriorates the radiative recombination efficiency.

Furthermore, the perfected lateral steam oxidation technique of AlAs that represents an effective and well-established method in the GaAs-based devices for self-adjusted current and photon confinement [7] is not available in the InP-based material systems. In principal, steam oxidation can be applied onto AlAsSb, which can be grown lattice-matched on InP [8]. However, the performance of the oxidized regions has not yet proven to be sufficient for the realization of InP-based devices. The main challenges for the development of long-wavelength InP-based VCSELs are summarized schematically in Fig. 10.1.

As an alternative, GaAs-based approaches such as dilute nitrides, quantum dots and strained GaAsSb or InGaAs have also been considered and promising results have been achieved for both edge emitters and VCSELs around 1.3 µm [9–12]. Although there have been several developments for novel active region materials on GaAs substrates, these approaches could not demonstrate reasonable performance for wavelengths longer than 1.3 µm.

In fact, devices with remarkable performance in the long-wavelength regime have been realized by hybrid approaches based on the wafer fusion technique [13, 14]. In this approach, the superior performance of the GaAs-based epitaxial mirrors is combined with the mature InP-based active regions by bonding the latter ones onto GaAs-based mirror structures. However, the wafer fusion technique is complicated,

commonly yields large electrical resistance for current flow across the bonding interfaces and requires several epitaxial growth steps on different wafers.

A related approach is to use lattice-mismatched GaAs/AlAs on InP to improve the mirror performance [15]. While this technique offers the potential for a one-step all-epitaxial approach including the possibility for the AlAs steam oxidation, the reliability of the metamorphic layers is an important issue. The device performance obtained with this approach suffers from small efficiencies and moderate output powers of single-mode devices.

Monolithic low-threshold 1.55 μm VCSELs based on InP have been presented based on laterally etched active areas to achieve strong carrier and photon confinement [16]. The stationary characteristics including the continuous wave (cw) operation up to about 85°C are among the best results achieved so far for long-wavelength VCSELs. The reliability, however, is an issue because the contamination of the etched active region boundaries with ambient air may cause strong degradation as with the related previous mushroom-type laser diodes.

This article presents VCSELs in the long-wavelength range from 1.3–2.3 μm providing excellent performance with respect to the relevant stationary and dynamic characteristics. The approach is based on the application of buried tunnel junctions (BTJ) and hybrid dielectric-metallic mirrors that allow the simultaneous reduction of heat generation and thermal resistance and thus effectively addresses the essential challenges of the long-wavelength devices.

10.2 The Buried Tunnel Junction Concept

As stated in the preceding section, a reduction of the laser self-heating by an elaborate thermal device management is of paramount importance to realize long-wavelength VCSELs with reasonable performance. The internal device heating is usually caused by electrical resistances which are dominated by the *p*-conducting device layers. This is due to the higher effective mass and, consequently, lower mobility of holes as compared to electrons ($\mu_e/\mu_h \approx 20$) which leads to higher resistances at heterostructures such as Bragg mirrors or in current spreading layers used for lateral current injection. Furthermore, low metal contact resistances on *p*-doped materials are difficult to achieve.

A significant reduction of the electrical series resistance can be achieved by the substitution of *p*-doped layers by *n*-doped materials. Since in any case optical power generation is based on radiative recombination of electrons and holes, this implies a conversion of the charge carriers from electrons to holes.

The basic idea underlying the buried tunnel junction (BTJ) long-wavelength VCSEL is to use a laterally structured tunnel junction within the *p*-side of the laser in order to:

- convert the major part of the *p*-side confinement layers from *p*- to *n*-conduction to obtain low electrical resistance and, as a consequence, reduced heat generation

- apply low-resistive *n*-type contacts on both sides of the VCSEL
- reduce optical losses in the *n*-doped *p*-side layers
- enable the application of in-cavity lateral contacting with low spreading resistance and the use of non-conducting dielectric mirrors on the *p*-side yielding high reflectivity and significantly smaller thermal resistance than ternary/quaternary epitaxial mirrors with equal reflectivity
- achieve effective lateral current confinement
- offering the possibility to introduce strong lateral waveguiding which is self-adjusted to the current confinement.

It should be stressed that because of the conduction type inversion by the tunnel junction technique the major part of the *p*-side of the devices becomes *n*-doped and the *p*-side contacts become *n*-contacts as well. Since the heat dissipation in the BTJ-VCSEL is accomplished through the BTJ and the thermally low-resistive *p*-side dielectric mirror, the light extraction usually occurs via the *n*-side so that a common epitaxial Bragg mirror can be used on the *n*-side irrespectively of its thermal resistance.

The principal structure of a buried tunnel junction (BTJ) circular structure for electrical characterization is shown in Fig. 10.2a.

The tunnel junction consists of each one heavily *p*- and *n*-doped low-bandgap InGa(Al)As layer. The BTJ is arranged on the *p*-side of the diode and is laterally restricted to diameter D_{BTJ} which is equal to or smaller than the total diode diameter D_0. The lateral definition of the BTJ is accomplished by etching off the upper n^+-InGaAs layer and covering the remaining bottom p^+-layer by moderately doped *n*-InP in a second epitaxial run. Under applied reverse bias, therefore, a blocking p^+n-structure is established beneath the BTJ, while within the BTJ area the p^+n^+-junction shows an ohmic behavior and a very low resistance because of the tunnel effect.

Applying an equal bias onto both the BTJ and the area beneath results in an effective lateral current confinement to the BTJ area [17]. This is demonstrated in Fig. 10.2b where the current densities for 22 μm-diameter BTJ and blocking p^+n-structure, respectively, are compared.

Note that these characteristics include the voltage-current characteristic of the underlying (forward-biased) laser *pn*-heterojunction. With a typical 1.55 μm MQW laser active layer region representing the *pn*-heterojunction, laser current densities of the order of several kA/cm^2 are relevant. As can clearly be seen in this figure, the current densities of the BTJ are more than three orders of magnitude larger than for the blocking p^+n-structure beneath, and several kA/cm^2 are achieved at total voltages as low as 1 V. Consequently, the BTJ provides an excellent lateral current confinement together with a small total (contact) resistance of the order $3–7 \cdot 10^{-6}\ \Omega\,\mathrm{cm}^2$ enabling 1.55 μm devices to operate at a total bias of only about 1 V.

It should finally be noted that the epitaxial growth by MBE or MOCVD can be performed such that the thickness difference due to etching-off the area beneath the tunnel junction may be preserved up to the top epitaxial layer. As long as the thickness difference is smaller than $\lambda/4n$, this will lead to a positive effective index difference Δn_{eff} between the BTJ area and the regions laterally outside the BTJ given by [18]

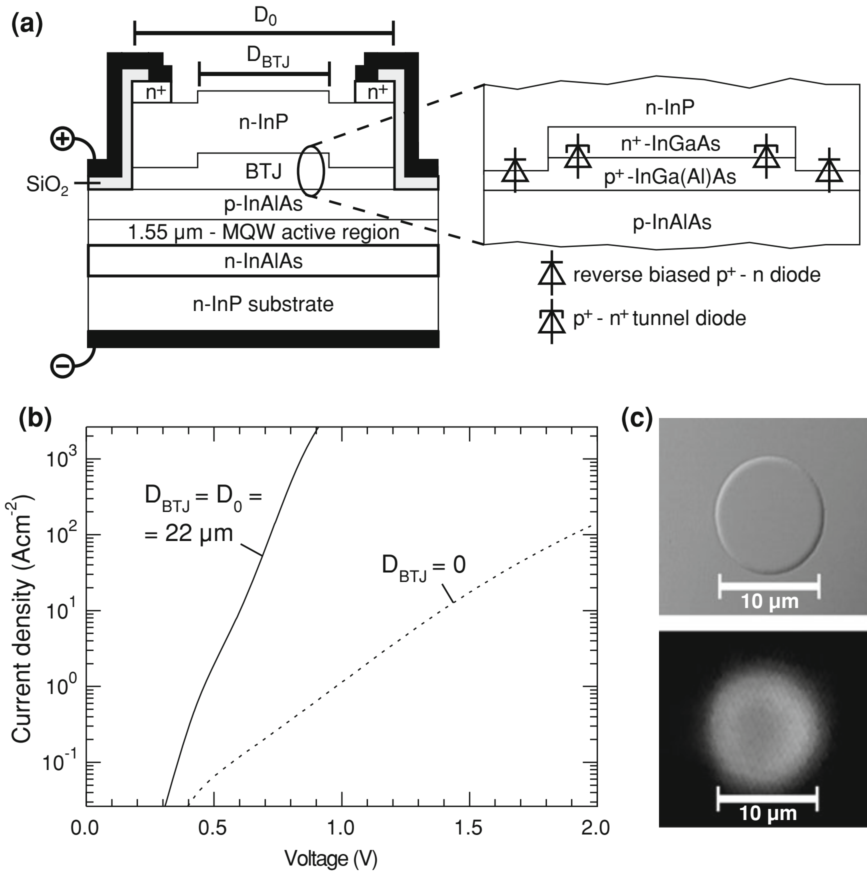

Fig. 10.2 **a** Schematic cross-section of BTJ structure including a 1.55 μm MQW diode region. **b** *IV*-characteristics of test structures with overall tunneling (*solid curve*) or overall blocking (*dotted curve*) area. **c** Optical micrograph of regrown BTJ with 10 μm diameter and near field image of light spot of BTJ test structure under applied bias

$$\frac{\Delta n_{\mathrm{eff}}}{n_{\mathrm{eff}}} = \frac{\Delta l_{\mathrm{opt}}}{l_{\mathrm{opt}}} \tag{10.1}$$

where l_{opt} and Δl_{opt} denote the optical cavity length and the difference in optical cavity length between the BTJ region and the regions outside. With typical cavity lengths around 3 μm and typical etching depths of 30 nm, the effective index difference can be of the order 1% of n_{eff}, i.e., about 0.03. Accordingly, the lateral waveguiding may be as strong as for the steam-oxide-confined short wavelength AlGaAs/GaAs VCSELs.

10.3 Device Structures and Characteristics

10.3.1 InP-Based VCSELs

Structure

Completing the test structure of Fig. 10.2 with an *n*-side epitaxial and a *p*-side dielectric mirror and mounting the device up-side down onto an integrated Au-heatsink results in the final BTJ-VCSEL shown in Fig. 10.3. To minimize parasitic contact-pad capacitances and enable flip-chip mounting, the VCSEL chip is passivated with low-ϵ benzocyclobutene (BCB) which is qualified for high-speed semiconductor device fabrication. Evidently, this structure resembles the previous Burrus-type LED that showed excellent device performance and reliability [19].

The *n*-side epitaxial DBR consists of InGa(Al)As/InAlAs quarter wavelength layer pairs with a calculated reflectivity beyond 99% against air as shown in Fig. 10.4a. The composition of the high-index InGa(Al)As layer is determined by the target emission wavelength to avoid fundamental absorption near the bandgap. For example at 1.55 μm wavelength, the Al-content and the refractive index difference between the high-index InGaAlAs and low index InAlAs layer are 10% and 0.25, respectively. The bottom dielectric mirror deserves some consideration because its reflectivity and thermal conductivity are decisive for the VCSEL performance. This mirror typically consists of a hybrid combination of only a few pairs of dielectric layers with a high index contrast in conjunction with a terminating Au-layer. Figure 10.4b shows the schematic structure and calculated reflectivity for 3.5 pairs of CaF_2/ZnS layers covered with gold.

Considering the phase shift due to the complex refractive index of Au, the optical thickness of the adjacent CaF_2 layer deviates from $\lambda/4$ in order to achieve phase-matching and maximum reflectivity. The large difference in refractive index ($\Delta n \approx 0.8$) causes a large reflection bandwidth and a high peak reflectivity of 99.9% as shown in Fig. 10.4b. While fluorides and sulfides show negligible absorption for the entire wavelength range of InP-based BTJ-VCSELs, the use of amorphous silicon (*a*-Si) offers even higher refractive index differences against fluorides ($\Delta n \approx 1.8$) and has often been applied for long-wavelength dielectric VCSEL-mirrors [20]. However, *a*-Si has a complex refractive index because of its absorption also for photon energies below the bandgap energy of crystalline Si. Photodeflection spectroscopic (PDS) investigations showed an absorption around 440 cm^{-1} at 1.55 μm wavelength. The high absorption limits the reflectivity even for a larger number of mirror pairs and leads to an additional self heating. Therefore, *a*-Si is not well suited as high index layer for the telecommunication wavelengths 1.3 and 1.55 μm. On the other hand, VCSELs with extended emission wavelengths, e.g., 2 μm, can exploit low absorption and high refractive index differences of *a*-Si containing Bragg mirrors.

The thermal resistance is dominated by the dielectric layers. For comparison, Table 10.1 shows the thermal conductivities of various III–V semiconductors and

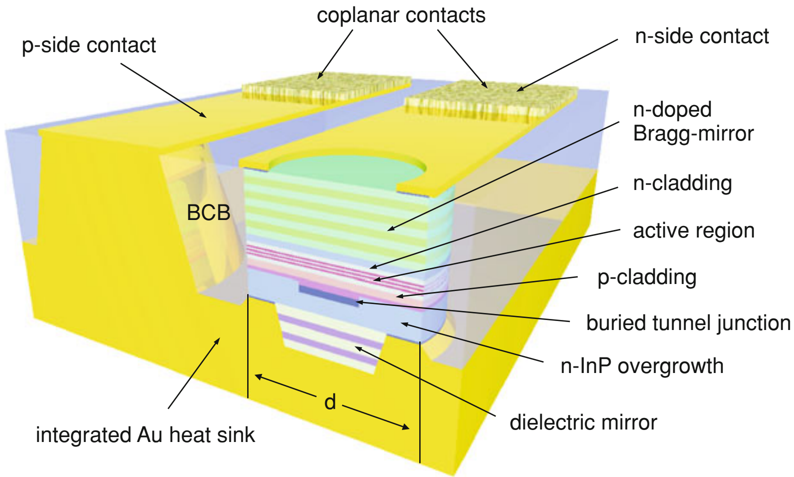

Fig. 10.3 Schematic cross section of InP-based BTJ-VCSEL with high-speed design

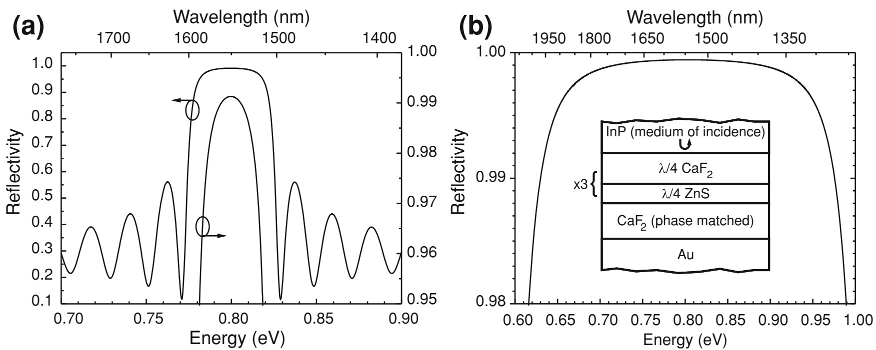

Fig. 10.4 **a** Calculated reflectivity of 32.5 pairs of an epitaxial $In_{0.53}Ga_{0.37}Al_{0.1}$ As/InAlAs DBR. **b** Calculated reflectivity and layer structure of the hybrid 3.5 pair CaF_2/ZnS-Au mirror. The medium of incidence is InP (refractive index $n = 3.17$ at 1.55 μm wavelength)

Table 10.1 Thermal conductivities for various III-V-semiconductors and amorphous dielectrics

Material	AlAs	GaAs	InP	$In_{0.53}Ga_{0.47}As$	*a*-Si	CaF_2	ZnS
$\lambda_{th}\left(\frac{W}{mK}\right)$	91	44	68	4.5	2.2	1.4	6.8

amorphous dielectrics. The latter ones have been measured by a technique as described in [21].

Again, Table 10.1 illustrates the marked decrease of thermal conductivity in the ternary alloys relative to binary GaAs, AlAs and InP. Also, the thermal conductivity of the chosen CaF_2/ZnS combination is even smaller than for the ternary InGaAs.

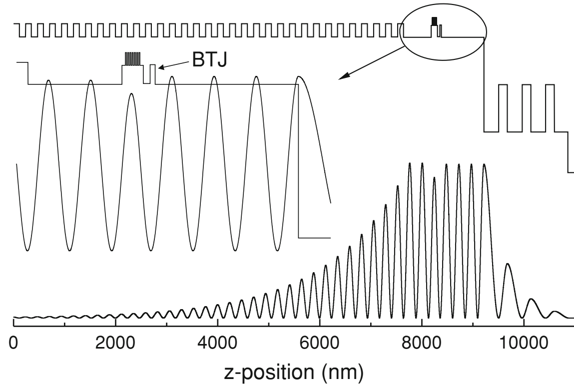

Fig. 10.5 Refractive index and longitudinal profile of optical field $|E|^2$ of BTJ-VCSEL

Because of the strong index contrast, however, only 3.5 pairs of CaF_2/ZnS layers are required so that the total thermal conductivity of the CaF_2/ZnS mirror is strikingly larger as compared to an equally well reflecting InGaAlAs/InAlAs epitaxial mirror.

A useful measure for the comparison of thermal resistances is the thermal contact resistance $\rho_{c,th}$ which is calculated as the sum over the products of thermal specific resistance, i.e., $1/\lambda_{th,i}$ for layer i, and layer thickness d_i taken over all mirror layers

$$\rho_{c,th} = \sum_{i=1}^{N} \frac{d_i}{\lambda_{th,i}} \tag{10.2}$$

where N is the number of mirror layers. The thermal resistance for a given VCSEL active region cross-section area A is then obtained as $R_{th} = \rho_{c,th}/A$. Calculating $\rho_{c,th}$ for the hybrid CaF_2/ZnS-Au mirror with a reflectivity of 99.9% gives $11 \cdot 10^{-3}\,\mathrm{K\,cm^2/W}$ while the cases of equally reflecting epitaxial mirrors on Au (18 pairs) or against InP substrate (45 pairs) yields $20 \cdot 10^{-3}\,\mathrm{K\,cm^2/W}$ and $47 \cdot 10^{-3}\,\mathrm{K\,cm^2/W}$, respectively. Taking a 10 μm diameter VCSEL and neglecting lateral heat spreading, the thermal resistances for these three mirrors are about 11200, 25000, and 60000 K/W, respectively. Assuming a small threshold current of only 2 mA, a low-resistive design with a threshold voltage of 1 V and complete conversion of electrical power into heat, the temperature increases by about 23, 50 and 120 K. Obviously, only in the first case (dielectric mirror) the temperature rise is acceptable and laser operation would occur because the small T_0-values of the InP-based long-wavelength compounds around 50–80 K prevent lasing for the latter cases. Consequently, the hybrid dielectric-Au mirror together with the low-resistive BTJ structure represents a viable solution for long-wavelength InP-based VCSELs.

A low-resistive BTJ requires a low-bandgap n^+/p^+-InGa(Al)As tunnel junction which may absorb the laser radiation due to fundamental bandgap absorption or losses by free-carrier absorption in the heavily doped tunnel junction layers. To minimize such losses in the BTJ-VCSEL, therefore, the BTJ must be placed exactly in a node of the standing optical wave as illustrated in Fig. 10.5.

As can be seen in the inset, the BTJ is placed in a node whereas the active region consisting of several quantum wells (QWs) is placed in a maximum of $|E|^2$. The figure also shows the strong decay of the field in the dielectric mirror, while $|E|^2$ decays rather slowly within the epitaxial mirror on the left side.

InP-based BTJ-VCSELs are designed for wavelengths between 1.3 and 2.3 μm using a two-step epitaxial growth process. MBE is usually used for both runs. The relevant epitaxial mirror and active region layers are adjusted in terms of composition and thickness to achieve the desired lasing wavelength. The first epitaxial run finishes with growing the heavily doped p^+-InGa(Al)As/n^+-InGa(Al)As ($n^+ \approx p^+ \approx 10^{20}\text{cm}^{-3}$) tunnel junction placed at the first node of the optical field above the active region.

After laterally defining the BTJ by dry-etching the n^+-InGa(Al)As layer, the epitaxial growth is completed by an *n*-InP layer and a thin n^+-doped InGaAs contact layer. In the following device processing, the n^+-doped InGaAs contact layer is completely removed on top the BTJ in order to avoid optical absoption losses. Removal of excess heat and lowering of series resistance is significantly enhanced by the thermally and electrically well conducting InP spreading layer. In the following processing, the hybrid dielectric mirror is deposited and covered with a gold film. An electroplating of the *p*-side contact with about 50 μm Au and the removal of the *n*-InP substrate results in the VCSEL structure of Fig. 10.3. The electroplated Au-heatsink provides mechanical stability and serves as an excellent heatsink.

Stationary Properties

Figure 10.6 shows the temperature dependent *LIV*-characteristics of 1.33 and 1.55 μm single-mode VCSELs. Due to the excellent thermal heat management, these devices exhibit cw output powers at room temperature up to 3–4 mW. At temperatures around 80°C, the output powers still exceed 1 mW. These values could be achieved with relatively small BTJ diameters of only 5 μm. As can be seen from Fig. 10.6b and 10.6d, the emission spectra show large side-mode suppression ratios (SMSR) well beyond 30 dB over the whole temperature and current range. Typical threshold currents of BTJ-VCSELs at room temperature are between 1 and 2 mA. VCSELs with BTJ diameters between 6 and 10 μm show multimode emission at least for parts of the operating range. VCSELs at 1.55 μm with large BTJ diameters of 20 μm exhibit a highly multimode emission with output powers around 12 mW.

In particular, the electrical characteristics document the superior performance of the BTJ design. The differential series resistance of typical single-mode BTJ-VCSELs is as small as 30–40 Ω which significantly reduces excess device heating and improves dynamic properties. With respect to the corresponding photon energy at 1.55 μm wavelength (≡0.8 eV), the threshold voltage is only around 100 mV higher. Taking into account additional quasi Fermi level splitting, the threshold voltage V_{th} is even close to the theoretical limit allowed by the Bernard–Duraffourg condition

$$eV_{th} \geq W_{Fc} - W_{Fv} \geq E_{ph} \geq E_g \tag{10.3}$$

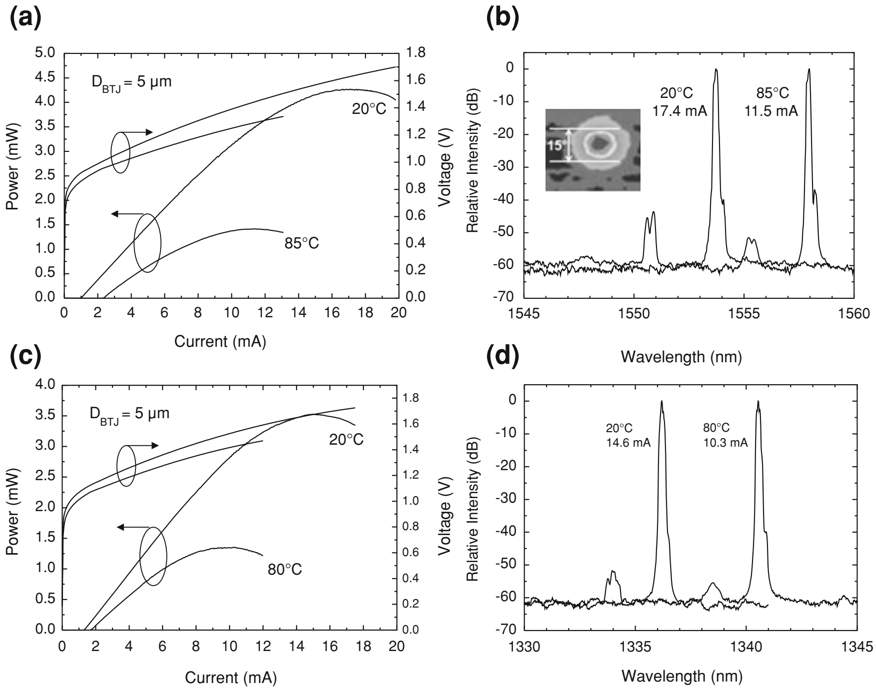

Fig. 10.6 **a** Temperature dependent *LIV*-characteristics and **b** emission spectra of 1.55 μm single-mode VCSEL together with far field intensity distribution. **c** Temperature dependent *LIV*-characteristics and **d** emission spectra of 1.33 μm single-mode VCSEL

with W_{Fc} and W_{Fv} as quasi Fermi levels for conduction and valence band, respectively, and E_g as bandgap energy.

Dynamic Properties

The characterization of BTJ-VCSELs without additional parasitics of housing and bonding wires was based on the chip design with coplanar connectivity as depicted in Fig. 10.3. The contact pad capacitances are significantly lowered by an approximately 10 μm thick, low-dielectric constant ($\epsilon \approx 2.5$) passivation layer of BCB (Benzocyclobutene). During manufacturing, the whole epi-structure is dry etched down to the substrate enabling very small chip sizes around 30 μm.

In order to verify the performance of the high-speed chip layout, parasitic responses were calculated from equivalent circuits with element values gained from impedance measurements as depicted in Fig. 10.7b. In order to minimize multiple numerical solutions, we used a three-element, first order equivalent circuit for fitting as presented in Fig. 10.7a. All VCSELs under investigation feature an identical vertical optical resonator with varying chip diameters d (c.f. Fig. 10.3). Biasing

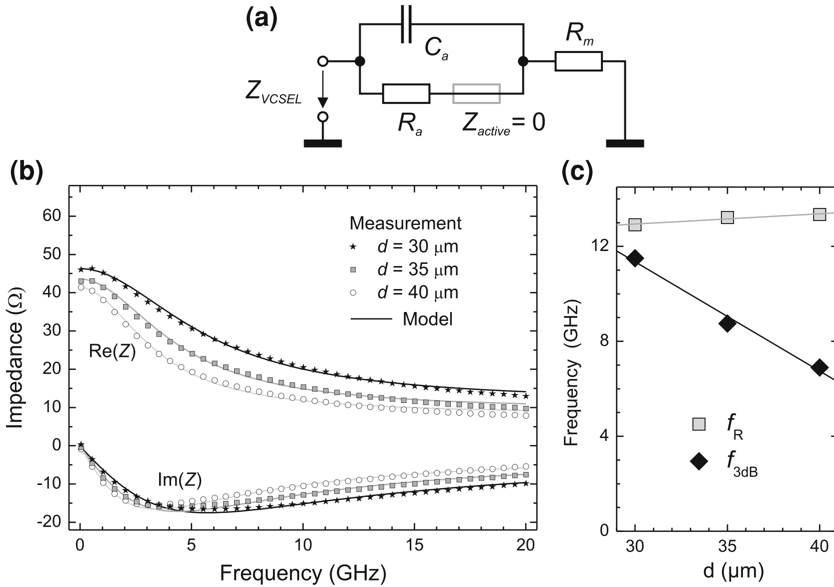

Fig. 10.7 **a** Equivalent circuit of BTJ-VCSEL. **b** Real and imaginary part of chip impedance Z against frequency for different chip diameters d. The solid lines are a fit to the three-pole filter funtion given in (10.4). **c** Dependence of resonance frequency f_R and modulation bandwidth f_{3dB} on chip diameter d

conditions were kept identical. No fluctuation of the intrinsic parameters such as the relaxation oscillation frequency were observed whereas the 3-dB modulation bandwidth f_{3dB} decreased by 50% with increasing semiconductor chip diameter as shown in Fig. 10.7c. Although the equivalent circuit contains only three elements (resistors R_m and R_a, capacitance C_a), it can model the electrical impedance of BTJ-VCSELs well and the relevant terms ($R_m = 12.4\,\Omega$, $R_a = 33\,\Omega$, $C_a = 0.76$ pF at $d = 30\,\mu$m) match the physical properties of the device. As a simple first-order equivalent circuit can model the parasitics well, this investigation also justifies to model the parasitics of these devices by a single parasitic pole.

That investigation pointed out, that the VCSELs under investigation evaluated in this investigation where still limited by the parasitic capacitances of the space charge region of the reverse biased blocking diode outside the BTJ. Especially for large d which could be favorable regarding manufacturing tolerances, this problem is obvious. Therefore the doping has been reduced to reduce these parasitics. With reduced doping-levels of the n-InP regrowth, the parasitic roll-off frequency could be improved from around 4.5 to 6.5 GHz enabling 3-dB bandwidths greater 10 GHz with a 40 μm device. The small-signal modulation performance was verified on chip level for various bias currents and temperatures. Bias currents were chosen equally spaced when plotted versus the square-root of current above threshold. The measurements were done using a HP8510C vector-network analyzer with matched

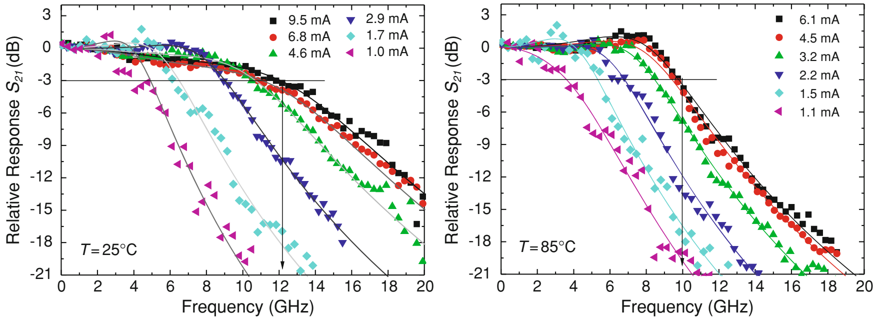

Fig. 10.8 Small signal response of 1.55 μm BTJ-VCSEL at different temperatures and bias currents

calibrated photodiode. The chip was driven with a small-signal modulation amplitude level of −6 dBm and contacted directly by a cascade microprobe. Calibration was done to the chip plane utilizing a calibration substrate. Backscattering into the device was tried to be avoided as this causes significant artifacts in the data. The frequeny response can be expressed by a three-pole filter function

$$H(f) \propto \frac{f_R^2}{f_R^2 - f^2 + j\frac{f}{2\pi}\gamma} \cdot \frac{1}{1 + j\frac{f}{f_{par}}} \tag{10.4}$$

including relaxation-oscillation frequency f_R, intrinsic damping γ and parasitics characterized by f_{par}. Curve fitting allows several intrinsic parameters such as modulation current efficiency factor and thermally limited maximum relaxation oscillation frequency to be extracted [22]. The first term of (10.4) can be directly derived by small-signal analysis of the rate equations above threshold yielding a two-parameter modulation transfer function. The second factor models the electrical chip-parasitics by a single parasitic pole, which is in agreement with the equivalent circuit given in Fig. 10.7a.

The main application for high-speed laser diodes in the wavebands around 1.3 or 1.55 μm is optical data transmission. Telecommunication standards require broadband performance in a wide temperature-range up to 85°C. Figure 10.8 shows record 3-dB bandwidths as high as 12 GHz at 25°C and 10 GHz at 85°C, respectively. This modulation bandwidth is sufficient for data-rates up to 17 Gb/s at room temperature and 12.5 Gb/s up to 85°C. Therefore, broadband optical data transmission systems at long wavelength are now also feasible with VCSELs.

VCSEL Arrays

The surface-normal topology of VCSELs facilitates the fabrication of monolithic one- (1D) or two-dimensional (2D) laser arrays with lithographically defined layout. As attractive light sources for optical interconnects including high modulation bandwidth and high coupling efficiencies into optical fibers, VCSEL arrays in the

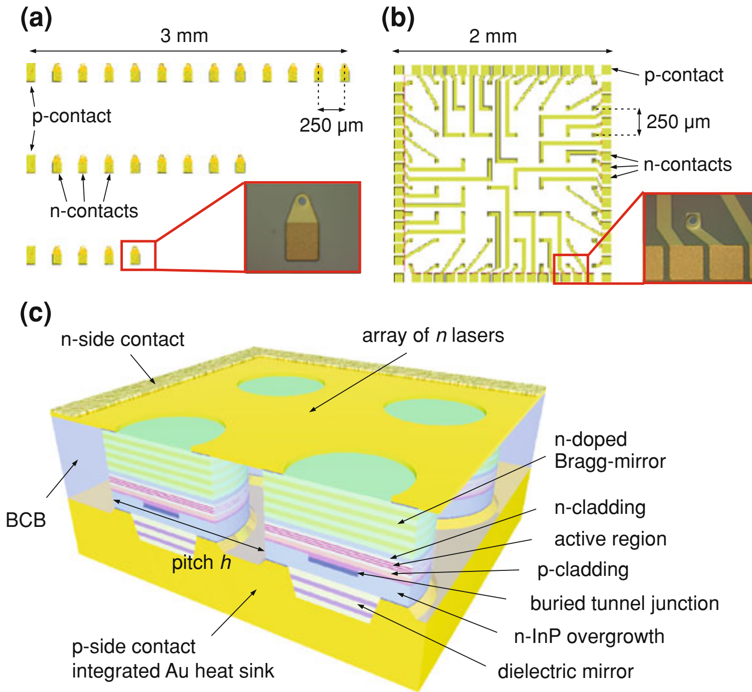

Fig. 10.9 Lithographic layout and microscope images of **a** 1×12, 1×8, 1×4 one-dimensional and **b** 8×8 two-dimensional long-wavelength VCSEL arrays for optical interconnects. **c** Schematic cross-section of high-power VCSEL array [27] (© 2008 IEEE)

wavelength-range around 850–980 nm have shown to be a source of interest for optoelectronic interconnects. High data-rates up to 12.5 Gb/s have been reported [23, 24]. Furthermore, arrays of vertical emitting near-infrared lasers in the Watt regime are now being developed with great effort to enable new applications in illumination, free-space optics, laser pumping or engraving [25]. Recently, monolithic arrays of InP-based BTJ-VCSELs for the long wavelength regime above 1.3 μm for optical interconnects and high output powers have been presented [26]. The layout of these VCSEL-arrays is shown in Fig. 10.9. The device structure is similar to the high-speed single laser design in Fig. 10.3. 1D arrays comprising 4, 8 and 12 devices for parallel links and wavelength division multiplexing (WDM) upgrade solutions and 2D arrays of 8 × 8 individually addressable lasers for optical interconnects were fabricated. All VCSELs were operating at 1.55 μm emission wavelength but any CWDM wavelength from 1.3 to 1.6 μm is feasible. The array pitch is 250 μm and the different chip dimensions can be taken from Fig. 10.9. The *p*-contact can be accessed both at the bottom and on top of each chip. This technology enables all kind of *p*- and *n*-contact pad designs for various mounting and housing technologies including flip-chip design.

The *LIV*-characteristics were found to be very homogeneous for all (up to 64) devices of the arrays. The cw output power of each VCSEL exceeds 1 mW at room temperature and the threshold current is below 1 mA. In this case the output power is limited by the very conservative design with current apertures of 4.5 μm only. Significantly higher single-mode output powers exceeding 1 mW up to 85°C are feasible. The operating voltage of these devices is as low as 1–1.5 V and therefore is compatible with CMOS driver chips. The device impedance is around 50 Ω matching RF-circuits and driver boards. The spectral homogeneity of all arrays was found to be very high. The inherent current tunability is 5 nm. All devices are single-mode with side-mode suppression ratio of more than 40 dB. The modulation bandwidth exceeds 10 GHz for bias currents as low as 4.4 mA and 10 Gb/s data rates are possible even for bias currents of 3 mA. Further, the threshold voltages of typically 0.9 V are very low compared to other device concepts. Consequently, these devices provide high bandwidth at very low energy cost.

Recently, we also developed large-scale monolithic arrays of InP-based BTJ-VCSELs for the long wavelength regime above 1.3 μm with record-high output powers. Generating higher laser powers with VCSEL arrays is an alternative to edge emitters as VCSELs do not suffer from catastrophic optical mirror damage (COMD). For high-speed applications such as free-space optics, parasitic capacitances should be kept low. Therefore we used our high-speed design also for these power devices in order to keep the potential bandwidth above 10 GHz as shown for our single devices. This leads to a structure as shown in Fig. 10.9c. Especially for large arrays of several hundreds of VCSELs, thermal crosstalk is an important issue limiting device performance. The temperature-distribution of N VCSELs as disk-source on top of a heat-sink can be expressed by

$$\Delta T(r) = 2\sqrt{\frac{g}{\pi^3}} \cdot \frac{\sqrt{N}P}{h\lambda} E \cdot \left(\frac{r}{R}\right) \tag{10.5}$$

where g denotes a geometrical factor, h is the pitch size and P is the heat dissipation from each VCSEL. The thermal conductivity of the heat sink is λ. $E(k)$ is the complete elliptic integral of the second kind and R the radius of the whole array. $\Delta T(r)$ is the additional temperature at a distance r from the center due to thermal crosstalk via the heat sink.

Figure 10.10 shows the *LIV*-characteristics of a high-power array including 900 densely packed VCSELs with a cartesian pitch. As a first preliminary approach, the array was glue-mounted to a copper heat-sink. Nevertheless, we achieved significantly high cw output powers exceeding 3 W at −11°C. Power-densities up to 130 W/cm^2 were realized. At room temperature, the array provides more than 2 W and high-temperature operation up to 70°C is applicable. The driving voltages are rather low (around 1.2 V) enabling single battery mobile operation without any driving circuit. The wall-plug efficiency at room temperature exceeds 20% in a wide range and maximum values of 25% can be observed at −11°C. From (10.5) which can be used to verify finite element solver simulations, design rules for high-power VCSEL arrays can easily be derived. Since the power at thermal roll-over decreases

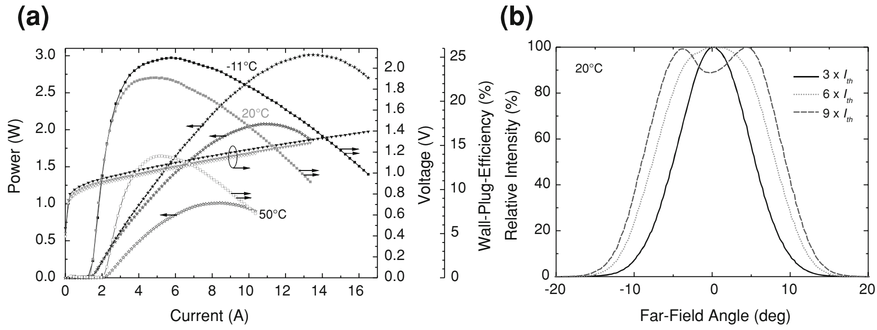

Fig. 10.10 **a** *LIV*-characteristics of 1.55 µm VCSEL-array including 900 VCSELs with 50 µm cartesian pitch. **b** Far-field angle distribution for different driving currents

linearly with temperature as can be seen in Fig. 10.10a, $\Delta T(r)$ and VCSEL power degradation can be related. Consequently, higher power densities can be achieved by an elaborate mounting of the chip, the usage of micro cavity coolers or sphisticated heat spreaders. In order to check the dependency on the array size and cancel out the mounting variations, we fabricated an array with addressable sectors and found a good agreement with (10.5). Furthermore, this array shows very homogeneous characteristics, showing equal performance with a standard deviation of less than 2.8% of all sectors.

VCSELs with Extended Wavelengths

With respect to optical sensing applications, strong demand exists for lasers with emission wavelengths well beyond the communication range ($\lambda \gg 1.55$ µm). This spectral region comprises strong absorption lines of several important species such as H_2O (1877 nm), CO_2 (2004 nm) or CO (2339 nm). The design for InP-based BTJ-VCSELs emitting at such wavelengths is basically the same as depicted in Fig. 10.3. For wavelengths beyond 1.7 µm, a maximum refractive index difference of $\approx$ 0.32 between lattice matched InGaAs and InAlAs layers can be exploited since no fundamental bandgap absorption occurs. The active region typically consists of 5 heavily strained quantum wells separated by tensile strained barriers. Figure 10.11 shows the output characteristics of two laser structures designed for emission wavelengths of 1.83 and 1.87 µm, respectively.

The dielectric back mirror of the 1.83 µm device consists of 2.5 pairs of Al_2O_3/ *a*-Si whereas the 1.87 µm VCSELs incorporates 3.5 pairs of CaF_2/ZnS. As can be seen from Fig. 10.11a, the BTJ technology enables very small apertures of only 2.5 µm diameter even at very long wavelengths together with ultralow threshold currents of only 190 µA. The 1.87 µm VCSEL comprises a thermally well conducting InP heat spreader between the expitaxial mirror and active region that lowers self heating and enables higher output powers. Devices at 1.87 µm emission wavelength

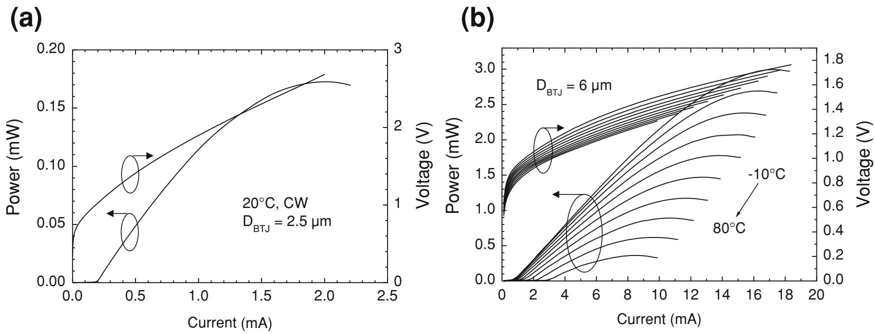

Fig. 10.11 **a** *LIV*-characteristics of 1.83 μm VCSEL with 2.5 μm BTJ diameter. **b** Temperature dependent *LIV*-characteristics of single-mode 1.87 μm VCSEL with 6 μm BTJ diameter

with an aperture diameter of 6 μm as shown in Fig. 10.11 exhibit an output power around 2 mW at room temperature. Threshold current and threshold voltage are as low as 950 μA and 0.9 V, respectively. The threshold voltage of these lasers is comparable to that of the VCSELs at 1.55 μm wavelength despite the smaller active region bandgap energy. Accordingly, the comparatively higher voltage is attributed to higher bandoffsets in the electrically conducting epitaxial mirror. Since diode lasers are usually temperature stabilized in optical sensing setups, there is no need for high temperature optimization. Accordingly, the present VCSELs have a moderate mode–gain offset around 30 nm and show a steadily increasing threshold current with temperature. The spectrum is found to be single-mode with at least 30 dB side mode suppression ratio over the relevant current and temperature range. While BTJ-VCSELs with wavelengths up to 2.05 μm have been commercially available for some years, the availability of VCSELs with even longer wavelengths is desirable for detection of, e.g., CO. This wavelength range is usually reached with mature GaSb-based interband diode lasers showing excellent optical gain performance [28]. For InP-based DFB lasers, InAs-quantum wells with homogeneous composition and large barrier thickness together with an optimized waveguide have been demonstrated for 2.3 μm wavelength [29]. However, this is not viable for VCSELs regarding a sufficient overlap of the active region with the optical field. On the other hand, calculations show that the emission wavelength can be significantly extended by using a triangular (V-shaped) quantum well design by keeping the total strain. Here, an increasing amount of indium in the center of a symmetrical quantum well lowers the transition energy. To achieve an emission near 2.3 μm wavelength, the quantum well comprises a lattice-matched InGaAs layer after the tensile strained InGaAlAs barrier followed by a graded sequence of layers with increasing indium content ending with a 1 nm thick layer of pure InAs in the center of the well [30]. This method avoids direct interfacing of tensile and heavily compressive strained layers in barriers and wells, respectively, that would deteriorate the radiative recombination efficiency. In addition, relevant growth parameters such as temperature and V/III ratio have been optimized. The high crystalline quality is confirmed by X-ray diffraction

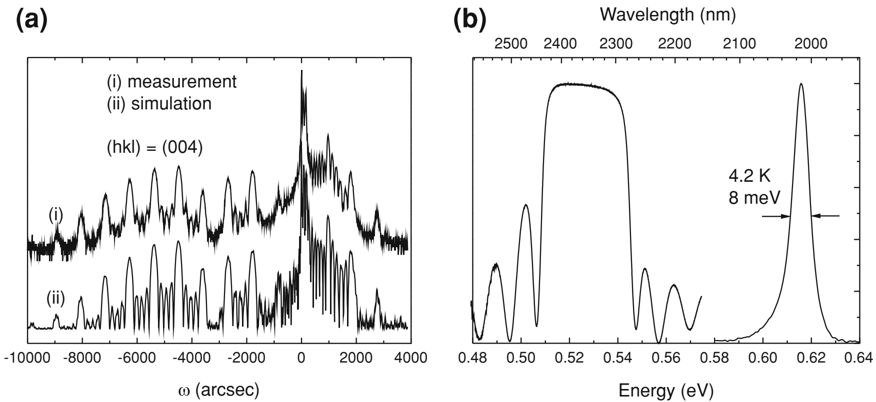

Fig. 10.12 **a** X-ray diffraction pattern and simulation of a five QW active region for 2.3 μm lasing wavelength. **b** Reflectivity of VCSEL basis structure (before regrowth) and low temperature photoluminescence measurement from a separate active region test structure

including an almost perfect match to the simulation assuming a pseudomorphic crystalline structure. Furthermore, good optical quality is derived from the small Full Width at Half Maximum (FWHM) value of the low temperature photoluminescence measurement (Fig. 10.12).

The active region as described above has been implemented in a standard BTJ design. With almost negligible absorption at 2.3 μm in amorphous silicon but exploiting a high refractive index, these VCSELs incorporate 2.5 pairs of CaF_2 /*a*-Si in the hybrid back mirror. Figure 10.13 shows the output characteristics of these electrically pumped BTJ-VCSELs at 2.36 μm emission wavelength. To the best of our knowledge, this is the longest wavelength which has been achieved so far for any interband InP-based laser. Single-mode VCSELs with BTJ diameters of 6 μm show room temperature output powers of 0.5 mW with threshold current and threshold voltage of 3.8 mA and 0.95 V, respectively. Devices with apertures of 12 μm show multimode output power in excess of 1 mW. The maximum cw operating temperature of these lasers is typically between 50 and 60°C. Compared to shorter wavelength BTJ-VCSELs, the threshold currents are increased which may be attributed to the high mode–gain offset of more than 100 nm, higher nonradiative recombination and larger optical losses.

Widely Tunable MEMS VCSEL

With their longitudinal and transverse single-mode operation, properly designed long-wavelength VCSELs represent rather ideal laser sources, the electronic wavelength tuning of which would strikingly extend their application areas. While the wavelength of a VCSEL can be tuned electrothermally via slow (<1 MHz) current changes over a couple of nanometers, many application would benefit from a larger

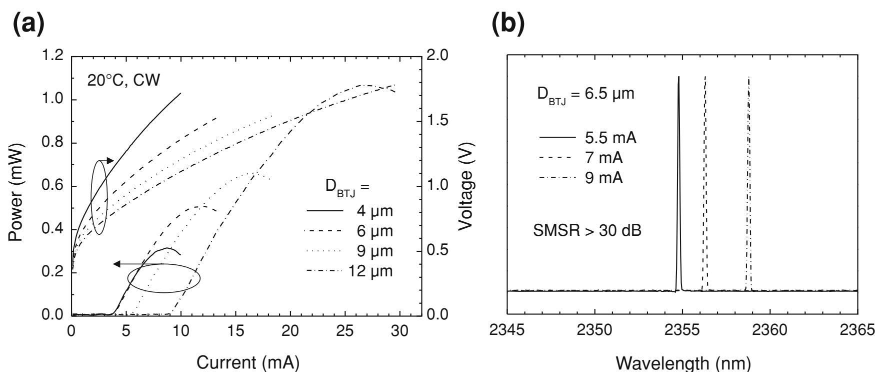

Fig. 10.13 **a** *LIV*-characteristics of 2.36 µm VCSEL with different BTJ diameters. **b** Optical emission spectra of single-mode VCSEL at various driving currents (Due to sensitivity issues at this wavelength, the lower SMSR limit can not be precisely determined while the upper limit exceeds 30 dB) [31] (© 2008 IEEE)

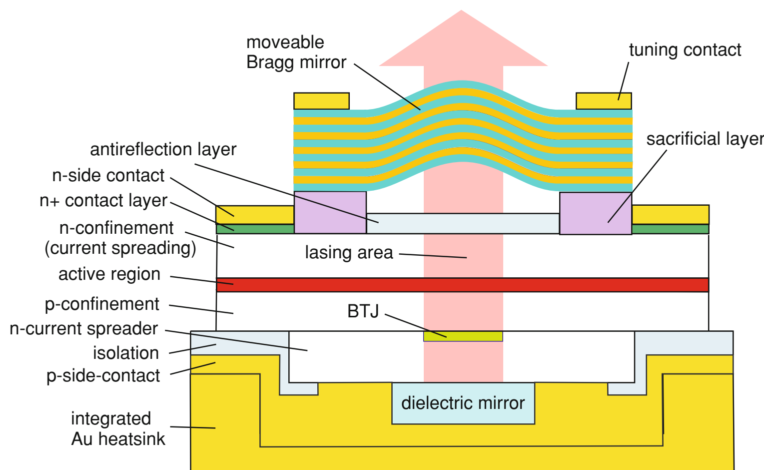

Fig. 10.14 Schematic cross-section of widely tunable MEMS BTJ-VCSEL

tuning range. One approach to accomplish this with miniaturized device structures is to use some type of micro-electro-mechanical system (MEMS) with an electro-thermally actuated mirror movement [32]. The schematic structure of a corresponding laser is depicted in Fig. 10.14. The buttom part of the device represents a 'half VCSEL'-structure with missing top DBR. The latter is made independently, either by another epitaxial step, e.g., based on GaAs/AlGaAs or can even be made entirely by dielectrics. With the exception of the *n*-side layer structure, the device technology corresponds to the above described BTJ-VCSELs.

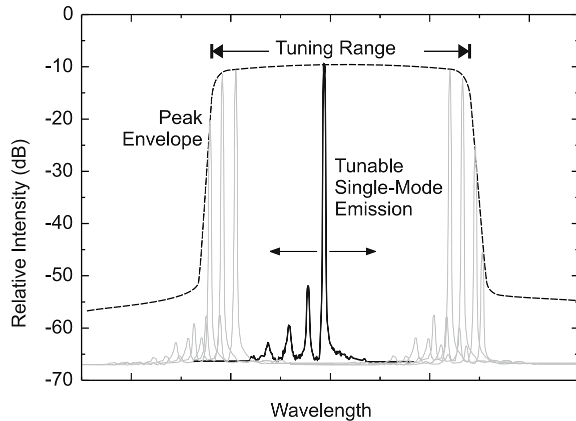

Fig. 10.15 Schematic tuning characteristic of MEMS-tunable VCSEL

The epitaxial DBR on the *n*-side is replaced by a current-spreading n-confinement layer made by *n*-doped AlGaInAs or InP, respectively. To minimize the electrical series resistance and to provide optimal transverse homogeneity of the current injection into the active region, a modulated doping profile has been used with high-doped areas placed in the nodes of the standing wave field. To avoid absorption, the n^+-contact layer is removed inside the optical path area and optionally an antireflection coating can be applied improving the tuning range.

For optimal performance and to ease adjustment of the two device parts, the moveable Bragg mirror should exhibit a curvature with a radius of curvature in the range of a couple of millimeters. In case of epitaxial GaAs/AlGaAs DBRs this has conveniently been achieved by applying an axial strain gradient using a graded lattice-mismatch of the mirror layers. The latter has been accomplished by adding 2–5 % of Indium to some of the DBR layers. Such a plane-concave resonator design can also be engineered to suppress higher-order transverse modes.

Wavelength tuning is achieved by transversely feeding a current through the slightly *n*-doped epitaxial DBR. This causes heating of the membrane structure followed by thermal expansion. The thermal expansion in turn results in a vertical movement by which the cavity length and, hence, the laser wavelength can be controlled. Since heating is proportional to the square of the tuning current, the wavelength tuning also shows a square dependence on the tuning current. According to the large free spectral range of VCSELs with their short cavities, comparatively large continuous tuning ranges can be obtained. Because of the thermal time constants, however, the tuning speed of this approach does not exceed 1 kHz. The observed tuning behaviour is schematically plotted in Fig. 10.15 showing the limitations of the tuning range by the occurence of higher-order modes and reduced fundamental mode power yielding a reduction of the SMSR.

Requiring an SMSR of at least 30 dB in most applications, continuous tuning of the order 50 nm in the 1.55 μm wavelength regime has been achieved and the simultaneous spectroscopy of NH_3 and CO using such a 1.55 μm tunable MEMS-

VCSEL was reported [33]. It should finally be noted, that the proper design of the BTJ and the MEMS-membrane enables the achievement of single-mode operation for significantly larger aperture sizes than in the non-tunable standard BTJ-VCSELs (e.g., 20 μm compared to 5 μm) [34].

10.3.2 GaSb-Based VCSELs

As has been shown in the previous section, InP-based VCSELs using highly strained QW active regions may approach maximum wavelengths around 2.36 μm. These lasers are thus suited for the spectroscopic detection of many important gases. It should be noted that the strength of the absorption lines usually strongly increases with wavelength and that many other important species exhibit relevant lines at even larger wavelengths. Accordingly, gas sensing applications would benefit from the availability of wavelength-tunable single-mode VCSELs emitting at even larger wavelengths. For these and other applications, long-wavelength VCSELs based on GaSb appear as a feasible option noting that edge-emitting GaSb-lasers have beeen presented operating at room temperature up to about 3.3 μm wavelength. However, the GaSb-based material systems such a AlGaInAsSb/GaSb revealed technologically extremely difficult features such as a bandgap blue shifting during thermal processes occuring, for instance, during epitaxial growth steps. This is particularly critical for single-mode lasers such as VCSELs where the gain peak, which is determined by the bandgap energy, requires a careful adjustment to the Bragg reflectors.

On the other hand, extensive research accomplished worldwide recently led to considerable breakthroughs on GaSb-based VCSELs in the 2.3–2.6 μm wavelength regime. Even current-tunable single-mode devices were presented that are based on the BTJ device concept [35]. A schematic cross-section of the corresponding GaSb BTJ-VCSEL structure is shown in Fig. 10.16.

As can be seen, the top-emitting VCSEL structure differs from its bottom-emitting InP-based counterpart shown in Fig. 10.3. This is because the thermal resistance of the 24 pairs AlAsSb/GaSb DBR is significantly smaller than that of the InP-based DBR structures enabling the heat sinking through the DBR and the GaSb substrate with sufficiently small active region heating. Correspondingly, the light output is emitted through the dielectric mirror consisting of 4.5 pairs of *a*-Si/SiO_2 layers. The reflectivities of the epitaxial DBR and the dielectric mirror amount to 99.8 and 99.7%, respectively. Designed for 2.3 μm wavelength, the active region consists of 5 $Ga_{0.63}In_{0.37}As_{0.11}Sb_{0.89}$ quantum wells embedded in $Al_{0.33}Ga_{0.67}As_{0.03}Sb_{0.97}$ barriers. The BTJ is made of p^+-GaSb and n^+-InAsSb which due to the broken gap alignment yield efficient tunneling even for relatively low doping levels. *LIV*-characteristics for the temperature range from −10 to 50°C are shown in Fig. 10.17a for an elliptically shaped BTJ.

The threshold voltages are just below 1 V for all temperatures. With the photon energy around 0.5 eV, the threshold voltages are still too high indicating considerable series resistances, particularly in the epitaxial DBR because of the large band offsets of the constituting layer materials. Despite the low output powers of below

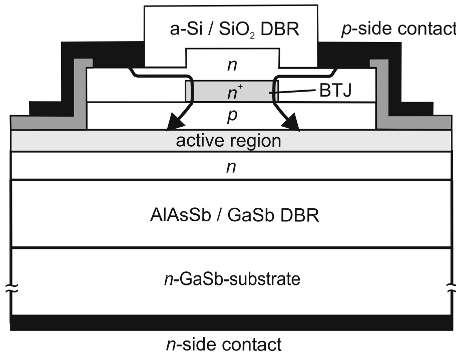

Fig. 10.16 Schematic cross-section of GaSb-based top-emitting BTJ-VCSEL [35] (© 2008 IEEE)

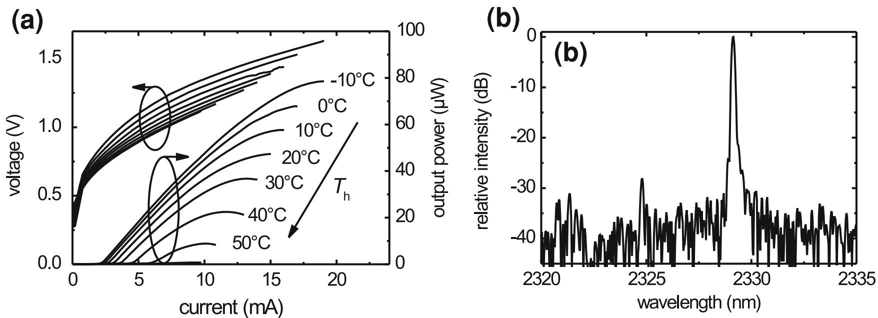

Fig. 10.17 **a** Temperature dependent *LIV*-characteristics of an elliptically shaped device (3.1 and 5.3 µm axes) and **b** room-temperature cw spectrum at a current of 11 mA [35] (© 2008 IEEE)

100 µW, these devices are well suited for tunable diode laser spectroscopy (TDLS) applications because of their large tuning ranges. With a current tuning rate around 0.7 nm/mA, the tuning ranges amount to 8 nm at −10°C and 3 nm at 50°C, respectively. The temperature tuning rate is 0.21 nm/K. The room-temperature spectrum plotted in Fig. 10.17b shows a decent SMSR of about 28 dB.

In fact, just recently the successful application of the GaSb-based single-mode BTJ-VCSELs for gas sensing at 2.3 µm has been reported [36]. Using the electro-thermal current-tuning scheme, CO and CH_4 have accurately been detected simultaneously over a short optical path length using wavelength modulation spectroscopy.

While the 2.3 µm wavelength has also been approached with the InP-based BTJ-VCSELs as shown in the previous Sect. 10.3.1, the newly established GaSb-based BTJ-VCSEL technology may straightforwardly be extended to the entire wavelength range accessible for edge-emitting GaSb-based lasers, i.e., the 2–3.3 µm wavelength range.

10.4 Applications

10.4.1 Optical Communication

Smaller form factors and lower power dissipation standards in optical communication modules gear up the need for new generations of ultralow power lasers. The 10GBASE-LR (long range) standard, to be found in the IEEE 802.3ae recommendation, describes 10G Ethernet at 1.3 μm over a link of 10 km of the widely deployed standard single mode fiber (SSMF). For the 10GBASE SR (short range) standard, 850 nm VCSELs are already used as cost-effective light sources. A prospective approach for these applications is based on long-wavelength VCSELs. For this purpose, the transmission performance of InP-based BTJ-VCSELs was evaluated under direct modulation at 10.3125 Gb/s with non-return-to-zero data ($2^{31}-1$ PRBS pattern length) over an unamplified SSMF-transmission link with a length of 10 km. With a matched photodiode receiver for the lab-environment, error-free received powers as low as −26 dBm were evaluated. To be closer to practical VCSEL-based communications solutions, we intentionally used a bit error rate (BER)-detector module with lower performance for this experiment. Figure 10.18 shows the BER-measurements for 20 and 75°C for a back-to-back (BTB) configuration and for transmission over 10 km of a SSMF. The corresponding open eye diagrams are shown as insets. Error-free operation was achieved for all configurations and no error floor was detected. Biasing conditions were set to achieve extinction ratios above 7 dB. Therefore, a slight over-shoot can be seen in the eye diagrams yielding lower bit error rates.

Further transmission experiments with VCSEL arrays in a dense wavelength division multiplexing (DWDM) configuration were performed to highlight their feasibility as directly modulated transmitters in broadband optical communication systems. Error-free transmission over 20 km of the most widely deployed SSMF links with monolithically integrated 1D arrays has been demonstrated recently at a wavelength of 1.55 μm [38]. The transmission experiment was carried out over an unamplified 20 km link of SSMF. A 12.5 GHz photodiode with a 10 GHz limiting amplifier followed by a 9.33 GHz low pass filter was used. Figure 10.19a shows the superimposed optical spectrum from four 10 Gb/s modulated channels with a spacing of 100 GHz on the ITU-grid.

The layout of these devices is presented in Fig. 10.9a. BER-measurements of all channels are shown in Fig. 10.19b providing error-free operation under all biasing conditions. Note that there was no BER-penalty in between all channels with widely spread bias from 3.3 to 7.6 mA. Corresponding eye diagrams at a BER of 10^{-9} are shown as inset. The timing jitter in eye diagrams as well as the low sensitivity may be attributed to the use of a preliminary laser-mounting used for that experiment. At a modulation rate of 10 Gb/s, the line broadening due to adiabatic chirp was measured to be less than the 100 or 50 GHz channel spacing, respectively. Different from arrays of classical edge-emitters, VCSEL-arrays can be used in an upgrade of coarse wavelength division multiplexing (CWDM) to DWDM networks due to

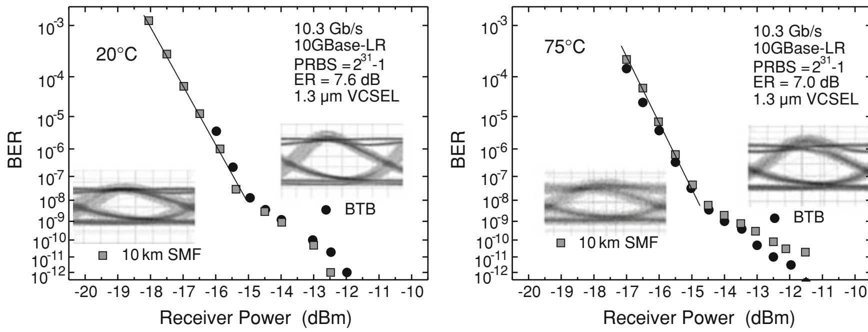

Fig. 10.18 BER measurement under BTB configuration and over 10 km of SSMF at 10.3 Gb/s (10GBASE-LR) at 20 and 75°C; corresponding eye diagrams inset [37] (© 2008 IEEE)

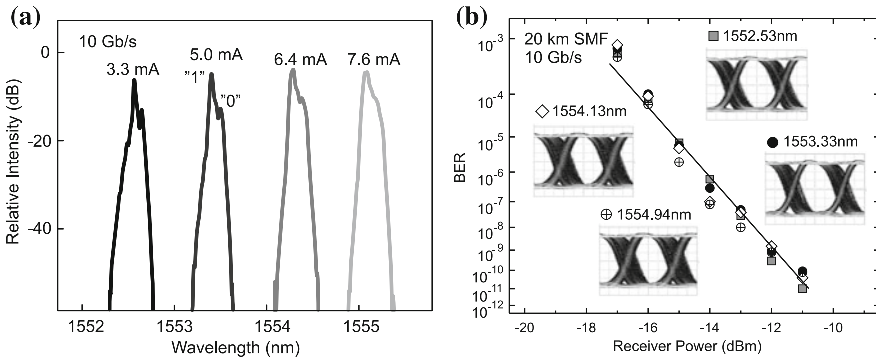

Fig. 10.19 **a** Spectrum of a 1×4 array of electro-thermally tuned 1.55 μm VCSELs under modulation at 10 Gb/s. WDM (100 GHz spacing) channels are addressed by current tuning. **b** BER-performance of 10 Gb/s modulated VCSEL array over 20 km of SSMF. WDM channels are addressed without BER-penalty. Corresponding eye diagrams are given as inset

their flat bandwidth behavior and large tuning ability. Even for DWDM grids of 50 GHz, there is no crosstalk due to adiabatic chirp. For 100 GHz/50 GHz DWDM-grid at least four, respectively eight, channels at 10 Gb/s can be addressed only by varying the laser biasing condition. Our transmission results highlight the potential of VCSELs as transmitters in CWDM access networks. Moreover, optically injection locked VCSELs can also be utilized as duplex transmitters/receivers redundantizing separate photodetectors [39].

VCSELs and VCSEL arrays at CWDM-wavelengths from 1.3 to 1.6 μm for 10G Ethernet are feasible with the BTJ technology. Error-free data transmission at 10.3 Gb/s over a link of 10 km SSMF as described in the 10GBASE LR standard is achieved up to 75°C. Together with their high bandwidth and low power consumption, these lasers are ideally suited for 10G Ethernet solutions at long range and potential candidates for 100G Ethernet with bitrates of 8 × 12 Gb/s or

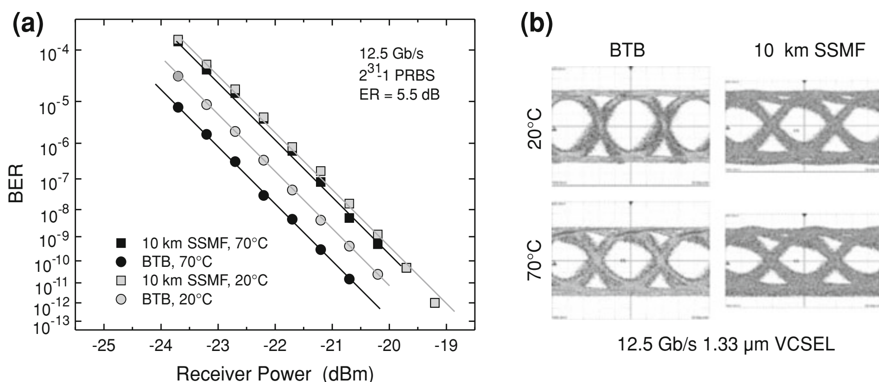

Fig. 10.20 **a** BER-curves vs. received power at different operating temperatures and transmission configurations. **b** Eye diagrams detected at the receiver in BTB-configuration and after 10 km transmission for different operating temperatures

6 × 17 Gb/s. Recently, modulation bandwidths as high as 12.5 Gb/s have been demonstrated with BTJ-VCSELs [40]. The chip is mounted in a transmitter optical sub-assembly (TOSA) module with an LC-receptacle including an optical isolator, a monitoring diode and a 50 Ω flex circuit connection. Figure 10.20 shows the results of the temperature dependent transmission experiments over different propagation lengths.

The 1.33 μm TOSA packaged VCSEL under test shows a maximum output power of 1.2 mW and is evaluated under direct modulation at 12.5 Gb/s with non return to zero (NRZ) binary data with $2^{31} - 1$ pseudo-random binary signal (PRBS) pattern length in a BTB configuration and over 10 km transmission link of SSMF (attenuation at 1.33 μm: 0.35 dB/km, dispersion at 1.33 μm: 2.5 ps/(nm·km)) without any dispersion compensation. The signal is detected by an avalanche photodiode (APD) with a sensitivity of −26 dBm at an extinction ratio (ER) of 10.2 dB. The APD is then connected to the sampling oscilloscope or to the BER-tester. The bias current is 11 mA for both 20 and 70°C and an optimal operating point is found to achieve the same extinction ratio of 5.5 dB changing the amplitude modulation.

BER-curves as a function of the received power for BTB-configuration and after 10 km of SSMF at 20 and 70°C are reported in Fig. 10.20a. At 70°C in BTB-condition, there is a slight improvement of the performances compared to 20°C which is due to an optimized operating point at high temperatures. However, after 10 km SSMF propagation no difference is visible between BER measurements at 20 and 70°C, so the requested power at the receiver is the same at both temperatures. Eye diagrams at different temperatures are shown in Fig. 10.20b. There is no difference over the considered temperature range, the eyes are open also at 70°C and there are no visible distortions even if the electronic driver is designed to work up to 11.3 Gb/s.

10.4.2 VCSEL-Based Optical Gas Sensing

TDLS Systems

Today, optical sensing by Tunable Diode Laser Spectroscopy (TDLS) is a fast emerging market. Gas sensing systems are used for a wide range of applications such as industrial process control, environmental monitoring and safety applications.

Figure 10.21 shows the absorbance of important gas lines in the discussed transitions of rotational-vibrational molecule energy states. These transitions have a defined transition energy and can be indirectly observed by the wavelength-dependent absorption of light. In TDLS systems, therefore, the laser wavelength is tuned across the gas absorption line by means of temperature or current.

The temperature shift of the wavelength is about 0.1 nm/K for lasers in the InP-based material system and about 0.2 nm/K in the GaSb-based material system. VCSELs typically exhibit an electro-thermal current tuning rate of 0.3–0.6 nm/mA, much higher than for edge emitting lasers and (continuous) tuning ranges of several nanometers are feasible to monitor several absorption lines of one gas or even multiple species. Together with single-mode operation, small linewidth and their low-cost potential, VCSELs are ideal light sources in TDLS systems.

For gas sensing purposes an appropriate package with a temperature-controlled heat-sink is used to fix the wavelength range by stabilizing the laser temperature. Wavelength tuning is then usually accomplished by electro-thermal current tuning. For VCSELs, this mechanism works up to tuning rates even in the MHz regime.

Although absorption lines at higher wavelengths usually exhibit stronger absorption, the design of a TDLS-system also has to take into account the detector performance. Up to wavelengths of 2.6 μm, uncooled easy-to-use and cost effective detectors with high sensitivity are available.

Direct Absorption Measurement

In Fig. 10.22a an *LI*-curve taken at ambient conditions of a VCSEL at 1854 nm wavelength is shown. The absorption of water vapor at this wavelength is strong enough to show significant dips in the detected power even for short path lengths.

The attenuation of a light beam passing an absorption cell is given by Lambert–Beer's law

$$I(\lambda) = I_0 \cdot e^{-\alpha(\lambda)\cdot L} \tag{10.6}$$

with $\alpha(\lambda)$ as absorption coefficient and L as absorption length. The absorption coefficient is determined by the line-strength which can be taken from the HITRAN-database [42] and the gas concentration. Measuring the light attenuation after passing an absorption cell of specific length, the concentration can be readily calculated. An appropriate calibration leads to a sub-percentage accuracy over the whole measurement range.

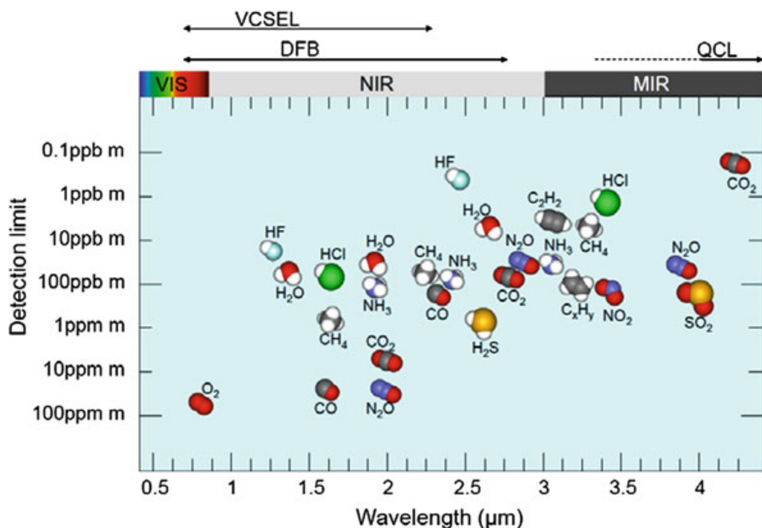

Fig. 10.21 Overview of important gas species detectable with TDLS along with underlying laser technology. The horizontal position of a specific gas corresponds to a dominant absorption line in the wavelength spectrum while the vertical position depicts the detection limit assuming an absorbance of 10^{-5} (Courtesy of Siemens AG)

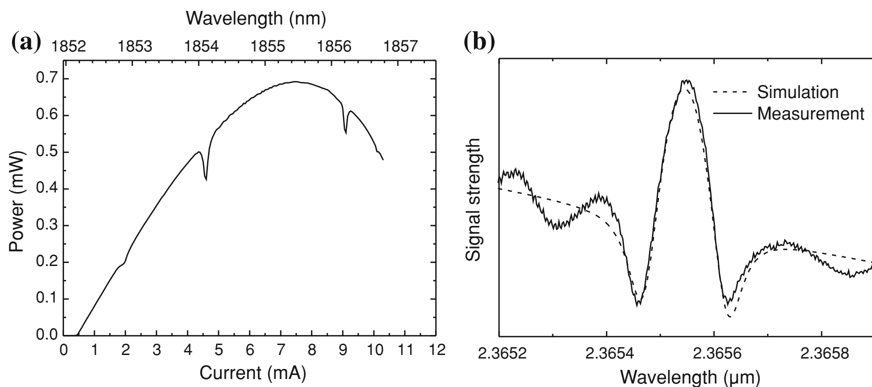

Fig. 10.22 **a** *LI*-curve of 1.85 μm VCSEL used for direct absorption measurements. The absorption dips of water vapor are clearly resolved even with short pathlengths (14 cm in this example). **b** Second harmonic spectrum of CO-measurement at 2.36 μm wavelength obtained with an InP-based BTJ-VCSEL [41]. The concentration and the absorption path length are 11 ppm and 40 cm, respectively. The oscillations are due to residual interferences [31] (© 2008 IEEE)

Wavelength Modulation Spectroscopy

For measurements with higher accuracy down to ppm-levels, more sophisticated analysis methods have to be used. The aim is to reduce residual effects from inter-

fering species, etalon fringes and to increase the signal-to-noise ratio (SNR) for achieving a better sensitivity. The path length can be increased even in compact systems by using multi-pass cells. A significant increase of sensitivity can be obtained by considering higher order detection signals originating from wavelength modulation spectroscopy techniques [41].

In a typical setup, a sinusoidal modulation is superimposed on the laser current resulting in a frequency variation. Simultaneously, the mean frequency is tuned slowly by ramping the laser current. Fourier analysis and calculation of the 2nd harmonic are then used to obtain a sensitivity level in the ppm or even ppb region [43] (see Fig. 10.22b).

10.5 Conclusion

In summary, we discussed the particular challenges for the realization of VCSELs for the wavelength range above 1 μm. We showed that for the InP-based devices the poor thermal conductivity of the ternary/quaternary alloys and the lack of efficient electrical and optical confinement are the most critical issues. The novel BTJ-VCSEL structure was described in which a buried tunnel junction gives a self-adjusted electrical and optical lateral confinement and ultra-low electrical series resistances with consequent small Joule heating. This technique, therefore, allows the application of conducting and strongly reflecting hybrid dielectric-metallic mirrors towards the integrated Au-heatsink with superior thermal properties.

Applying the BTJ technique solves most of these challenges to a fairly high degree, so that cw operation far beyond room temperature can be achieved even for wavelengths up to about 2.3 μm. Record single-mode optical power of the order of a couple of milliwatts at room temperature and even more than 1 mW at 85°C has been obtained in the 1.3 and 1.55 μm wavelength regimes. The application of elliptically shaped BTJs lifts the polarization degeneracy and yields stable single-mode operation with side mode suppression ratios of the order of 50 dB for 5 μm diameter 1.55 μm devices.

With an appropriate layout of the VCSEL chips, 3-dB bandwidths exceeding 10 GHz and large signal modulation at bit rates above 10 Gb/s are achieved. The homogeneity of neighbouring devices enables arrays for parallel data transmission such as 64 channels at 10 Gb/s each, or for enhancing output power such as 2 W at 1.55 μm for 30 × 30 arrays.

The recent progress on GaSb-based BTJ-VCSELs has yielded application-suited single mode and wavelength-tunable cw devices in the 2.3 μm wavelength range. This GaSb BTJ-VCSEL technology, furthermore, paves the way for electrically pumped single-mode VCSELs for even longer wavelengths, at least up to about 3 μm.

Finally, we demonstrated the suitability of the long-wavelength BTJ-VCSELs for applications in optical communications and gas sensing using the TDLS technique.

Acknowledgments This work has been supported by the European Union via NEMIS (contract no. FP6-2005-IST-5-031845) and the German Federal Ministry of Education and Research via NOSE (contract no.13N8772).

References

1. K. Iga, Surface emitting lasers. Electron. Commun. Jpn. Part 2 **82**, 483–493 (1999)
2. F. Koyama, Recent advances of VCSEL photonics. J. Lightwave Technol. **24**, 4502–4513 (2006)
3. R. Shau, M. Ortsiefer, J. Rosskopf, G. Böhm, C. Lauer, M. Maute, M.-C. Amann, Long-wavelength InP-based VCSELs with buried tunnel junction: properties and applications. Proceedings of SPIE, vol. 5364 (2004), pp. 1–15
4. S. Adachi, *Physical Properties of III–V Semiconductor Compounds* (Wiley, Chichester, 1992)
5. S. Adachi, Lattice thermal resistivity of III-V compound alloys. J. Appl. Phys. **54**, 1844–1848 (1983)
6. G. Tuttle, J. Kavanaugh, S. McCalmont, (Al,Ga)Sb long-wavelength distributed Bragg reflectors. IEEE Photon. Technol. Lett. **5**, 1376–1379 (1993)
7. M.H. MacDougal, P.D. Dapkus, A.E. Bond, C.-K. Lin, J. Geske, Design and fabrication of VCSEL's with Al_xO_y-GaAs DBR's. IEEE J. Select. Topics Quantum Electron. **3**, 905–915 (1997)
8. L. Legay, P. Petit, G.L.e. Roux, A. Kohl, I.F.L. Dias, M. Juhel, M. Quillec, Wet thermal oxidation of AlAsSb alloys lattice matched on InP. J. Appl. Phys. **81**, 7600–7603 (1997)
9. J.A. Lott, N.N. Ledentsov, V.M. Ustinov, Zh.I. Alferov, D. Bimberg, Continuous wave 1.3 μm InAs-InGaAs quantum dot VCSELs on gaas substrates, in *Conference on Lasers and Electro-Optics* (*CLEO*). Technical Digest (2001), p. 137
10. G. Steinle, H. Riechert, A.Y. Egorov, Monolithic VCSEL with InGaAsN active region emitting at 1.28 μm and cw output power exceeding 500 μW at room temperature. Electron. Lett. **37**, 93–95 (2001)
11. F. Quochi, J.E. Cunningham, M. Dinu, J. Shah, Room temperature operation of GaAsSb/GaAs quantum well VCSELs at 1.29 μm. Electron. Lett. **36**, 2075–2076 (2000)
12. E. Söderberg, J.S. Gustavsson, P. Modh, A. Larsson, Z. Zhang, J. Berggren, M. Hammar, High-temperature dynamics, high-speed modulation, and transmission experiments using 1.3-μm InGaAs single-mode VCSELs. J. Lightwave Technol. **25**, 2791–2798 (2007)
13. A. Black, A.R. Hawkins, N.M. Margalit, D.I. Babic Jr., A.L. Holmes, Y.-L. Chang, P. Abraham, J.E. Bowers, E.L. Hu, Wafer fusion: material issues and device results. IEEE J. Select. Topics Quantum Electron. **3**, 943–951 (1997)
14. A. Syrbu, A. Mereuta, V. Iakovlev, A. Caliman, P. Royo, E. Kapon, 10 Gbps VCSELs with high single mode output in 1310 nm and 1550 nm wavelength bands, in *Conference on Optical Fiber Communication* (*OFC*). Technical Digest (2008), pp. 1–3
15. J. Boucart, C. Starck, F. Gaborit, A. Plais, N. Bouche, E. Derouin, L. Goldstein, C. Fortin, D. Carpentier, P. Salet, F. Brillouet, J. Jaquet, 1-mW CW-RT monolithic VCSEL at 1.55 μm. IEEE Photon. Technol. Lett. **11**, 629–631 (1999)
16. S. Nakagawa, E.M. Hall, G. Almuneau, J.K. Kim, H. Kroemer, L.A. Coldren, 1.55-μm InP-lattice-matched VCSELs operating at RT under CW, in *17th IEEE International Semiconductor Laser Conference*, Monterey, USA (2000), pp. 151–152
17. M. Ortsiefer, R. Shau, G. Böhm, F. Köhler, G. Abstreiter, M.-C. Amann, Low-resistance InGa(Al)As tunnel junctions for long wavelength vertical-cavity surface-emitting lasers. Jpn. J. Appl. Phy. **39**, 1727–1729 (2000)
18. G.R. Hadley, Effective index model for vertical-cavity surface-emitting lasers. Opt. Lett. **20**, 1483–1485 (1995)

19. C.A. Burrus, B.I. Miller, Small-area double-heterostructure aluminium-gallium arsenide electroluminescent diode sources for optical-fibre transmission lines. Opt. Commun. **4**, 307–309 (1971)
20. N. Nishiyama, C. Caneau, B. Hall, G. Guryanov, M.H. Hu, X.S. Liu, M.-J. Li, R. Bhat, C.E. Zah, Long-wavelength vertical-cavity surface-emitting lasers on InP with lattice matched AlGaInAs-InP DBR grown by MOCVD. IEEE J. Select. Topics Quantum Electron. **11**, 990–998 (2005)
21. H. Wada, T. Kamijoh, Thermal conductivity of amorphous silicon. Jpn. J. Appl. Phys. **35**, 648–650 (1996)
22. A. Larsson, C. Carlsson, J. Gustavsson, Å. Haglund, P. Modh, J. Bengtsson, Direct high-frequency modulation of VCSELs and applications in fibre optic RF and microwave links. New J. Phys. **6** (2004)
23. S. Eitel, S.J. Fancey, H.P. Gauggel, K.H. Gulden, W. Bachtold, M.R. Taghizadeh, Highly uniform vertical-cavity surface-emitting lasers integrated with microlens arrays. IEEE Photon. Technol. Lett. **12**, 459–461 (2000)
24. F. Mederer, M. Grabherr, F. Eberhard, I. Ecker, R. Jäger, J. Joos, C. Jung, M. Kicherer, R. King, P. Schnitzer, H. Unold, D. Wiedenmann, K.J. Ebeling, High performance selectively oxidized VCSELs and arrays for parallel high-speed optical interconnects, in *50 Electronic Components Technology Conference*. Technical Digest (2000), pp. 1242–1251
25. J.F. Seurin, C.L. Ghosh, V. Khalfin, A. Miglo, G. Xu, J.D. Wynn, P. Pradhan, L.A. D'Asaro, High-power high-efficiency 2d VCSEL arrays. Photonics West Proc. SPIE **6908**, (2008)
26. W. Hofmann, M. Görblich, M. Ortsiefer, G. Böhm, M.-C. Amann, Long-wavelength ($\lambda = 1.55\,\mu$m) monolithic VCSEL array with >3 W cw output power. Electron. Lett. **43**, 1025–1026 (2007)
27. W. Hofmann, E. Wong, M. Ortsiefer, M. Görblich, G. Böhm, M.-C. Amann, One and two-dimensional long-wavelength VCSEL arrays for wdm applications and optical interconnects, in *21st IEEE International Semiconductor Laser Conference*, Sorrento, Italy (2008), pp. 165–166
28. C. Lin, M. Grau, O. Dier, M.-C. Amann, Low threshold room-temperature continuous-wave operation of 2.24 to 3.04 μm GaInAsSb/AlGaAsSb quantum well lasers. Appl. Phys. Lett. **84**, 5088–5090 (2004)
29. T. Sato, M. Mitsuhara, N. Nunoya, T. Fujisawa, K. Kasaya, F. Kano, Y. Kondo, 2.33-μm-wavelength distributed feedback lasers with InAs–$In_{0.53}Ga_{0.47}$ As multiple-quantum wells on InP substrates. IEEE Photonics Technol. Lett. **20**,1045–1047 (2008)
30. G. Böhm, M. Grau, O. Dier, K. Windhorn, E. Rönneberg, J. Rosskopf, R. Shau, R. Meyer, M. Ortsiefer, M.-C. Amann, Growth of InAs-containing quantum wells for InP-based VCSELs emitting at 2.3 μm. J. Cryst. Growth **301–302**, 941–944 (2007)
31. M. Ortsiefer, J. Rosskopf, E. Rönneberg, Y. Xu, K. Maisberger, R. Shau, C. Neumeyr, W. Hofmann, G. Böhm, A. Hangauer, J. Chen, R. Strzoda, M.-C. Amann, Extended near-infrared wavelength VCSELs for optical sensing, in *21st IEEE International Semiconductor Laser Conference*, Sorrento, Italy (2008), pp. 167–168
32. M. Maute, F. Riemenschneider, G. Böhm, H. Halbritter, M. Ortsiefer, R. Shau, P. Meissner, M.-C. Amann, Micro-mechanically tunable long wavelength vcsel with buried tunnel junction. Electron. Lett. **40**, 430–431 (2004)
33. B. Kögel, H. Halbritter, S. Jatta, M. Maute, G. Böhm, M.-C. Amann, M. Lackner, M. Schwarzott, F. Winter, P. Meissner, Simultaneous spectroscopy of NH_3 and CO using a 50 nm continuously tunable MEMS-VCSEL. IEEE Sensors J. **7**, 1483–1489 (2007)
34. P. Debernardi, B. Kögel, K. Zogal, P. Meissner, M. Maute, M. Ortsiefer, G. Böhm, M.-C. Amann, Modal properties of long-wavelength tunable mems-vcsels with curved mirrors: Comparison of experiment and modeling. IEEE J. Quantum Electron. **44**, 391–399 (2008)
35. A. Bachmann, K. Kashani-Shirazi, M.-C. Amann, GaSb-based electrically pumped VCSEL with buried tunnel junction operating continuous wave up to 50°C, in *21st IEEE International Semiconductor Laser Conference*, Sorrento, Italy (2008), pp. 39–40

36. J. Chen, A. Hangauer, A. Bachmann, T. Lim, K. Kashani-Shirazi, R. Strzoda, M.-C. Amann, CO and CH_4 sensing with single mode 2.3 μm GaSb-based VCSEL, in *Conference on Lasers and Electro-Optics* (CLEO). Technical Digest (2009), p. 143
37. W. Hofmann, M. Ortsiefer, E. Rönneberg, C. Neumeyr, G. Böhm, M.-C. Amann, 1.3 μm InGaAlAs/InP VCSEL for 10 G Ethernet, in *21st IEEE International Semiconductor Laser Conference*, Sorrento, Italy (2008), pp. 11–12
38. W. Hofmann, E. Wong, G. Böhm, M. Ortsiefer, N.H. Zhu, M.-C. Amann, 1.55 μm VCSEL arrays for high-bandwidth WDM-PONs. IEEE Photon. Technol. Lett. **20**, 291–293 (2008)
39. L. Chrostowski, B. Faraji, W. Hofmann, M.-C. Amann, S. Wieczorek, W.W. Chow, 40 GHz bandwidth and 64 GHz resonance frequency in injection-locked 1.55 VCSELs. IEEE J. Select. Topics Quantum Electron. **13**, 1200–1208 (2007)
40. M. Ortsiefer, W. Hofmann, E. Rönneberg, A. Boletti, A. Gatto, P. Boffi, J. Rosskopf, R. Shau, C. Neumeyr, G. Böhm, M. Martinelli, M.-C. Amann, High speed 1.3 μm VCSELs for 12.5 Gbit/s optical interconnects. Electron. Lett. **44**, 974–975 (2008)
41. A. Hangauer, J. Chen, R. Strzoda, M. Ortsiefer, M.-C. Amann, Wavelength modulation spectroscopy with a widely tunable InP-based 2.3 μm vertical-cavity surface-emitting laser. Opt. Lett. **33**, 1566–1568 (2008)
42. L.S. Rothman et al., The HITRAN 2004 molecular spectroscopic database. JQSRT **96**, 139–204 (2005)
43. P.W. Werle, P. Mazzinghi, F. D'Amato, M. De Rosa, K. Maurer, F. Slemr, Signal processing and calibration procedures for in situ diode-laser absorption spectroscopy. Spectrochim. Acta Part A **60**, 1685–1705 (2004)

Chapter 11
GaInNAs(Sb) Long-Wavelength VCSELs

James S. Harris, Hopil Bae and Tomás Sarmiento

Abstract The push to provide high-speed optical network access directly to the end user is creating both significant pressure for the development of low-cost, high-speed access terminals as well as opportunities for development of entirely new technological approaches compared to those now used in the optical backbone networks. One of the most challenging is that of providing low-cost, long wavelength, single mode lasers that can be directly modulated at 10 Gbit/s, operate un-cooled in ambient environments and are easily packaged and coupled to fiber. Long wavelength vertical cavity surface emitting lasers (VCSELs) on GaAs certainly have the potential to meet these challenges. The development of MBE growth of GaInNAsSb on GaAs, issues of VCSEL design and successful demonstration of low threshold edge emitting lasers and the first 1530 nm monolithic VCSELs in GaInNAsSb on GaAs are described.

11.1 Introduction

The incredible growth of the Internet and data transmission are now pushing the bandwidth requirements for metro (MAN), local (LAN) and storage (SAN) area networks to unprecedented performance levels. Much of this is now being driven by individuals exchanging large files with high resolution photos and videos, and the quest to provide video on demand for high definition digital movies. Providing high bandwidth fiber to the home (FTTH) will stress all of these networks, but most critically, those at the local or lowest level (the last mile). Low cost, long wavelength, single mode vertical cavity lasers (VCSELs) that can be directly modulated at $\geq$10 Gbit/s, operate un-cooled in ambient environments and are easily packaged and coupled to fiber are an essential element to enable this optical revolution. While initial

J. S. Harris (✉) · H. Bae · T. Sarmiento
Department of Electrical Engineering, Stanford University, 420 Via Ortega,
Stanford, CA 94305, USA
e-mail: harris@snow.stanford.edu

R. Michalzik (ed.), *VCSELs*, Springer Series in Optical Sciences 166,
DOI: 10.1007/978-3-642-24986-0_11, © Springer-Verlag Berlin Heidelberg 2013

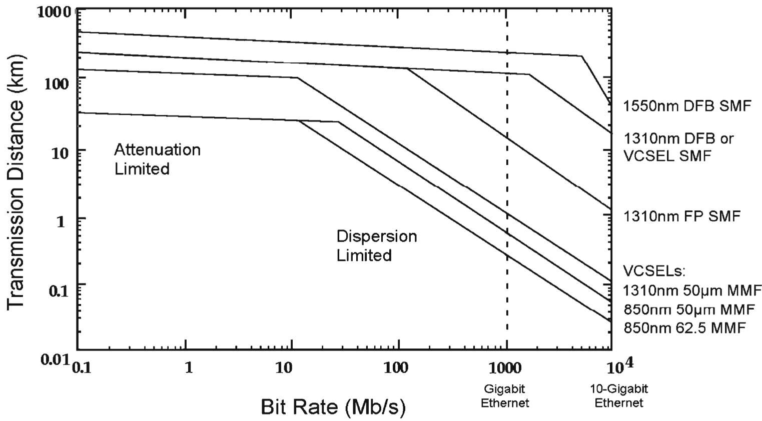

Fig. 11.1 Repeater-less transmission distance for different sources [1]

LANs could utilize GaAs based, 850 nm VCSELs that had most of the above requisite properties, the bit rate push from 100 Mbit/s to 1 Gbit/s to 10 Gbit/s in the newest systems make longer wavelength low-cost lasers essential. The requirement for such longer-wavelength lasers is illustrated in Fig. 11.1. For 850 nm VCSELs at 100 Mbit/s, the transmission distance is 7–8 km, certainly suitable for LANs, however, at 10 Gbit/s, the transmission distance is about 50 m, not even useful for a small, intra-building LAN [1, 2].

While InGaAsP/InP based Bragg grating and distributed feedback (DFB) lasers have been the sources for long-haul, 1.55 μm optical fiber backbone networks for the past three decades and clearly meet the distance criteria in Fig. 11.1, their cost is still far too high to meet the demands of hundreds of million lasers that might be utilized in MANs, LANs and FTTH links in a modern data communications network architecture. Low-cost VCSELs operating in the 1.3–1.55 μm wavelength range can certainty be a revolutionary enabler for high speed optical MANs, LANs and FTTH.

In addition to the low-cost VCSELs, there is an additional network challenge in order to realize low cost, high bandwidth networks, and that is that a much greater portion of the low loss fiber bandwidth must be made accessible to enable coarse wavelength division multiplexing (CWDM) to be utilized. This requirement comes from the necessity to operate the lasers un-cooled (i.e., no thermoelectric cooler) and directly modulated. These two requirements translate into much larger bandwidths required per channel (∼25 nm) compared to current dense WDM (DWDM) systems (∼0.1 nm) employed in the fiber backbone. The primary driving force for DWDM systems was the development of the Er-doped fiber amplifier (EDFA), which enabled all channels within its gain region to be amplified in parallel. Unfortunately, the EDFA gain region is only about 10% of the available low loss fiber region, which is illustrated in Fig. 11.2 [3]. While there is work ongoing to extend the EDFA gain into L-Band, there are still large areas of the fiber not utilized because of lack of suitable amplifiers. This provides a second, equally compelling driving force to realize better

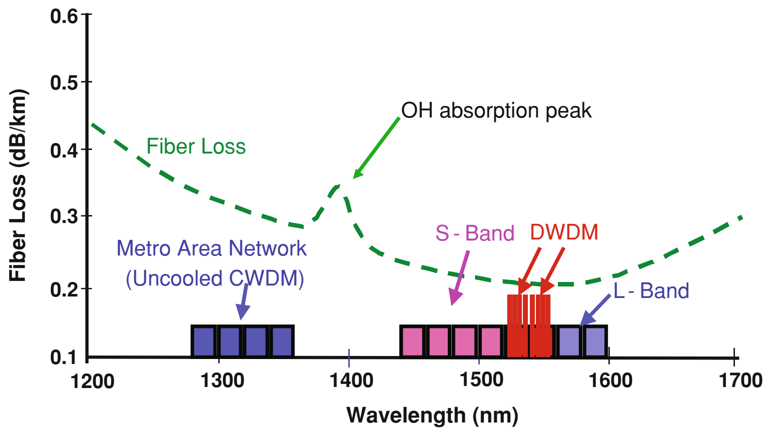

Fig. 11.2 Loss spectrum of optical fibers and CWDM/DWDM wavelengths

high power semiconductor lasers in the 1.3–1.6 μm wavelength region to serve as pump lasers for Raman amplifiers, which can work throughout the entire fiber low loss region. The sole reason that EDFAs rather than Raman amplifiers dominate the fiber backbone was availability of excellent, reliable, high power 980 nm InGaAs pump lasers for EDFAs while there were no comparable pump lasers for Raman amplifiers.

The above challenges and opportunities have certainly not gone unnoticed to device and materials scientists and there has been an intense effort to realize low cost, long wavelength VCSELs between 1.3 and 1.6 μm over the past decade [1]. Semiconductor lasers operating in the 1.3–1.6 μm region require materials with bandgaps between 0.95 and 0.78 eV. The potential candidate alloys are shown in Fig. 11.3. One of the requirements for alloy semiconductors is that they must be reasonably closely lattice matched to readily available binary substrates (GaAs or InP). The potential choices are thus defined by the intersection of the horizontal lines defining wavelength with the vertical lines below GaAs and InP defining lattice match. For many years it was believed that there was no suitable alloy adequately lattice-matched to GaAs that would emit at >1.1 μm. So InGaAsP on InP was the only materials system available for the communications wavelengths and 100% of the long wavelength communications lasers today are fabricated from this system.

However, the InGaAsP/InP system has several critical limitations to be used for VCSELs in the long wavelength range, which include [4]: a) no good combination of alloys that are lattice matched and produce a large difference in refractive index with reasonable thermal conductivity for the distributed Bragg reflectors (DBRs) required for VCSELs, b) T_0, the temperature coefficient of laser threshold current, is quite low compared to InGaAs/GaAs, the dominant combination for high power EDFA pump lasers and c) the thermal conductivity of the DBR mirror or cladding layers is inferior to GaAs based structures, resulting in greater junction heating under operation. The InGaAsP limitations pushed exploration of several approaches, which can be divided

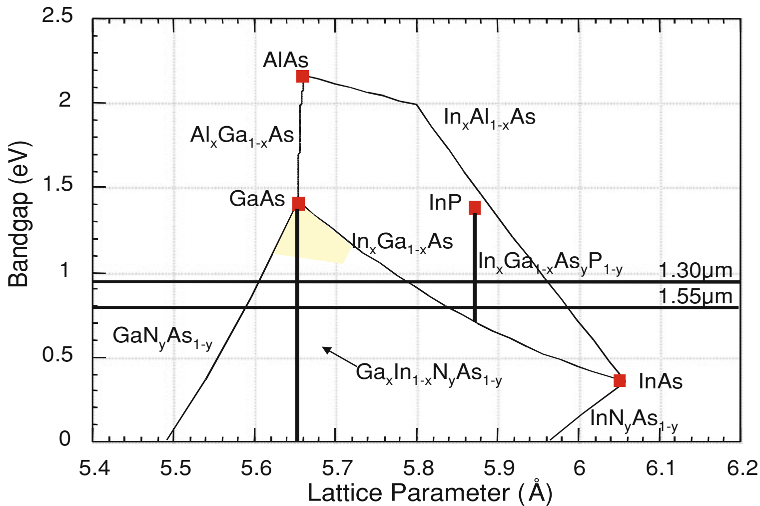

Fig. 11.3 Bandgap versus lattice constant for typical III-V compounds [1]

into two "camps" [1]; 1) those using InGaAsP/InP quantum well active regions, but alternative non-epitaxial approaches for the DBR mirrors and 2) those based upon GaAs/AlAs DBR mirror technology, but a new active gain region of materials closely lattice matched to GaAs. InGaAsP QW based VCSELs have been fabricated using metal mirrors [5], wafer bonded AlAs/GaAs mirrors [6], combined InGaAsP/InP and AlAs/GaAs metamorphic mirrors [7], AlGaAsSb/AlAsSb mirrors [8] and dielectric mirrors [9]. GaAs-based VCSEL approaches include InAs quantum dot active regions [10], GaAsSb/InGaAs Type II quantum wells [11], until Kondow et al. [4] discovered much to everyone's surprise, that GaInNAs was an attractive candidate because its bandgap could be reduced sufficiently to reach the desired wavelength regions, and most importantly, it could be grown on GaAs. This discovery was clearly far from obvious from the known properties of all other III–V ternary and quaternary alloys where a smaller lattice constant was usually correlated with a larger bandgap.

The large electronegativity of N and its small covalent radius cause a very different behevaior in the energy band properties when N is added to GaAs or GaInAs, compared to other III–V alloys. Because of nitrogen's differences, it forms a localized level within the band structure, but above the bandgap minimum of GaAs as illustrated in Fig. 11.4. Because the energy of this localized level cannot cross the parabolic conduction band of GaAs, bonding and anti-bonding orbtital bands are formed, one moving downward and the other upward, as best described by Shan et al. [12, 13] and known as the band anti-crossing (BAC) model. Thus instead of forming a III–V alloy with a larger bandgap, one achieves a very dramatic decrease of bandgap with a smaller lattice constant as illustrated in Figs. 11.3 and 11.4.

The success of these discoveries has catapulted this new material into a prominent position for the development of a broad range of long-wavelength VCSEL and

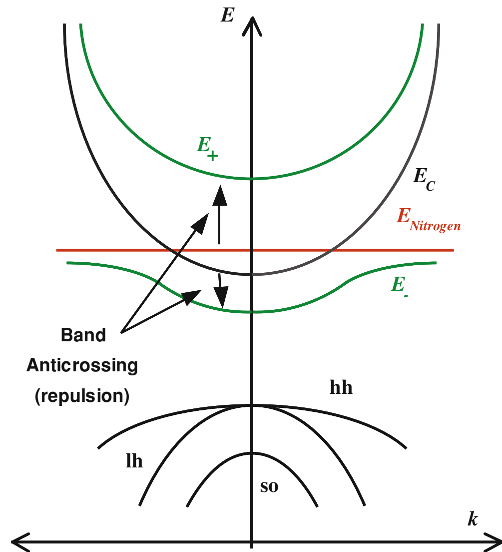

Fig. 11.4 Illustration of band anti-crossing model [12]

high-power edge-emitting lasers that we believe will be the foundation of lower cost optical networks because they not only produce the low-cost VCSELs that have been a key focus, but they enable both Raman and semiconductor optical amplifiers (SOAs) that will provide gain throughout the 1.3–1.6 μm wavelength region, enabling the use of the full low loss fiber bandwidth which will be crucial to employ lasers that are un-cooled and directly modulated.

Research on GaInNAs has revealed several additional factors vis-a-vis InGaAsP/InP that could prove decisive in the race to produce low cost, long wavelength VCSELs and high power Raman pump lasers. First, for the same bandgap material, the conduction band well is deeper [4, 14, 15] and the electron effective mass is larger in GaInNAs [15, 16], thus providing better confinement for electrons and better match of the valence and conduction band densities of states. This leads to a higher T_0, higher operating temperature, higher efficiency and higher output power [14].

Second, most of the energy band engineering used to minimize heterojunction voltage drops use intermediate graded layers of $Al_xGa_{(1-x)}$ As or AlAs/GaAs superlattices, all of which are lattice matched to GaAs and do not require difficult compositional control over both column III and column V constituents in a quaternary layer, such as InGaAsP, to maintain lattice match [1], thus improving device fabrication yield.

Third, compositional control and uniformity of GaInNAs grown by MBE [17–22] is relatively easy compared to MOVPE [23–31] or to AsP control in InGaAsP [32, 33]. This will translate into better yield and far easier scale up to larger wafers for lower cost.

Fourth, VCSELs can be fabricated using AlAs oxidation for current and optical aperture confinement. Fifth, GaInNAs on GaAs provides easy monolithic integration with GaAs high-speed electronics that will be essential to provide low-cost, high-speed integrated electronic drivers for direct laser modulation in high-speed transceivers in dense local area and FTTH networks.

Finally, one element that was initially believed to be quite straightforward and a significant advantage was use of the well-developed GaAs/AlGaAs DBR technology, which has been very successful for low cost 850 nm VCSELs. This has turned out to be one of the larger challenges in realizing long wavelength VCSELs because of the conflicting requirements of low electrical resistance through the DBR (high doping) and low optical loss, which becomes even more challenging with longer wavelength because free-carrier loss scales with λ^2 and doping. There have been several approaches to this problem and are discussed in later sections.

11.2 Growth Issues of GaInNAs(Sb)

While the above discussion highlights the advantages of the GaInNAs/GaAs system over the InGaAsP/InP or GaAsSb/GaAs systems, there were still very significant challenges for GaInNAs to produce useful, reliable lasers at 1.3–1.6 μm. The first and foremost challenge was the very low solubility of nitrogen into the InGaAs matrix. This is due to the different basic crystal structures of the constituent alloys and their regions of growth compatibility: InGaN is a hexagonal (wurtzite) crystal grown at relatively high temperatures while InGaAs is a cubic(zincblende) crystal grown at relatively low temperatures, creating a miscibility gap in the alloys [18, 20–22, 24, 34, 35]. Hence, as either or both N and growth temperature increase, phase segregation occurs and the material breaks up into microscopic regions of InGaAs and InGaN. In order to overcome this problem, the growth has to be done at much lower growth temperatures and under metastable growth conditions within the miscibility gap region of the GaInNAs alloy.

MOVPE [32] has been the primary choice for commercial production of light sources such as 850 nm VCSELs, 980 nm InGaAs EDFA pump lasers or 1.55 μm InP-based DFB lasers. InP-based systems were dominated by MOVPE because valved P-crackers did not exist at the outset and early MBE attempts to grow InP-based materials presented a fire hazard when phosphorus was exposed to air. MOVPE also had advantages over MBE for GaAs-based 850 nm VCSELs, due to higher growth rate and particularly much easier growth of the grading/doping interfaces for low resistance AlGaAs/GaAs DBR mirrors [1]. However, MOVPE growth of GaInNAs is far more challenging than earlier GaAs and InP based systems, because growth must be done at much lower temperatures. When compared to MOVPE growth of N-based wide bandgap systems which use ammonia as the N source, the growth temperature for GaInNAs is too low to achieve reasonable cracking of either ammonia or arsine [28, 29, 31, 36–38]. New sources with difficult precursor reactions and highly non-linear incorporation ratios greatly complicate the growth compared to

work on earlier III–V materials systems. There are also strong precursor reactions between N and Al, complicating the growth process for lasers that often require AlGaAs layers. In addition, the higher growth temperatures limit the N incorporation where micro-phase segregation [23, 29] begins and makes it extremely challenging to reach the N compositions needed to produce lasers beyond 1.3 μm. Carbon and hydrogen atoms from organic precursors also complicate the growth, and hydrogen atoms were found to be especially problematic [39–43]. Despite these difficulties, very low threshold GaInNAs-based 1.3 μm lasers grown by MOVPE have been demonstrated. However, the best results and only commercial long-wavelength VCSELs have come from MBE growth, especially for the 1.55 μm wavelength range [44–49].

MBE is certainly not without its challenges in growing these metastable alloys. Kondow's first work [4, 50] utilized a N plasma source added to a gas source MBE system. This system provided the insight into the potential for GaInNAs, but the issues of H incorporation and its effect on the material [39–41] were difficult to resolve. There is also a very strong composition sensitivity to growth temperature [28–31] due to the low arsine cracking efficiency. Solid source MBE with an atomic N plasma source has proven to be by far the simplest and most effective system to enable growth at the lowest temperatures and over the largest range of N and In compositions [51, 52].

Growth temperature is the single most critical parameter controlling growth [18, 20, 53]. When growth temperature exceeds a critical value, MBE growth begins to change from 2-D, layer-by-layer growth to 3-D island growth with microphase-segregation [23, 29], and this problem is more severe as we add more In or N to increase the wavelength. The window for good epitaxial growth is quite narrow compared to other III–V alloys. Many reports have indicated that $420°\text{C} < T < 460°\text{C}$ maintains 2-D epitaxial growth over the greatest range of small N compositions [18, 53–55].

Along with lower growth temperature, high group-V flux has also been considered to be essential to maintain high quality growth [20, 56], and low threshold edge emitting lasers have indeed been succesfully demonstrated by growing under high group-V flux. However, significant improvement in luminescence efficiency and laser performance at longwer wavelengths has been reported by employing lower group-V fluxes than previously considered optimum, when the growth temperature is lowered [57] or Sb is incorporated [58].

Also instrumental for demonstrating GaInNAs 1.3–1.6 μm lasers were other growth improvements such as addition of Sb [59–66], use of GaNAs barriers [2, 18, 20, 23, 67–71], removal of ion damage [72–76], and post-growth annealing [1, 2, 18, 19, 66, 68, 77–87].

The addition of Sb to GaInNAs to make GaInNAsSb was a very important step to reaching wavelengths greater than 1.5 μm [59–66]. Before introduction of Sb, the quality of GaInNAs showed rapid degradation going beyond 1.3 μm with more In and N added to increase the wavelength [1, 23, 30, 31]. Sb was found to act as a surface surfactant to maintain the 2-D layer-by-layer growth at higher In and N compositions than could be achieved without Sb, helping to achieve significantly

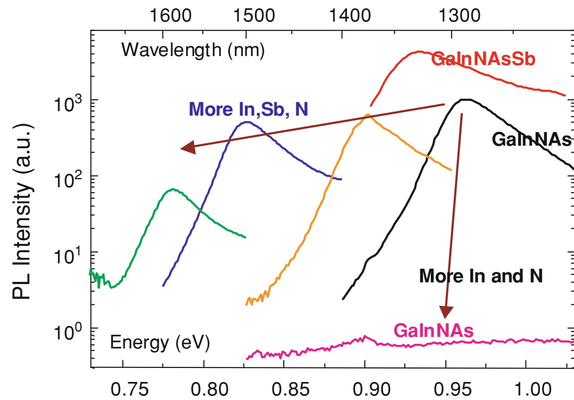

Fig. 11.5 Improved PL efficiency and extended wavelength by addition of Sb [64](© 2002 IEEE)

higher luminescence efficiency at longer emission wavelengths [59–62] as illustrated in Fig. 11.5. It has also been found [63–65] that not only does the Sb act as a surfactant, but that Sb is also incorporated into dilute nitride alloys, which further helps reaching longer wavelengths.

The GaAsN barriers provided significant advantage for growth of GaInNAs QWs by providing strain compensation for the QW/barrier pair, because the barrier is under tensile strain while the QW is under heavy compressive strain [2, 18, 20, 23, 67–71]. This strain compensation improved luminescence efficiency of QWs and also facilitated the growth of multiple QWs. The smaller bandgap of the GaNAs barriers also lowered the QW confinement energy, providing an additional advantage for reaching longer wavelengths [18]. Strain compensation through GaAsP barriers was also shown to be important for MOVPE-grown lasers [37, 88].

In MBE, reactive nitrogen is provided by an ion plasma discharge, which could produce energetic ions that damage the growing material. There have been reports [72– 74] of reduced ion damage during growth by applying a voltage across deflection plates at the exit of the plasma source to deflect ions away from the substrate. Removal of ion damage by deflection plates was an important improvement for achieving low threhold 1.55 μm lasers [45, 46, 75]. Protecting the wafer surface by arsenic capping was also helpful in improving the growth quality [89].

Annealing in both GaInNAs and GaInNAsSb has a completely unique behavior [1, 2, 18, 19, 66, 68, 77–87] compared to all similar III–V semiconductor alloys: there is a dramatic increase in photoluminescence (PL) efficiency and a significant blue shift (50–100 nm) in wavelength which was illustrated in Fig. 11.6. The major mechanism for the PL efficiency improvement is believed to be the removal of non-radiative deep level traps [90–94], which result from the very low growth temperature required to incorporate N and In. The origin of the blue shift under annealing was initially hypothesized to be indium [68, 69, 85] or nitrogen [1, 18, 20] outdiffusion from the quantum wells, but later research indicates that change in nearest-neighbor configuration of nitrogen during annealing explains this blue shift more effectively [80], especially when the QW is of high quality with fewer point defects [55, 95–98].

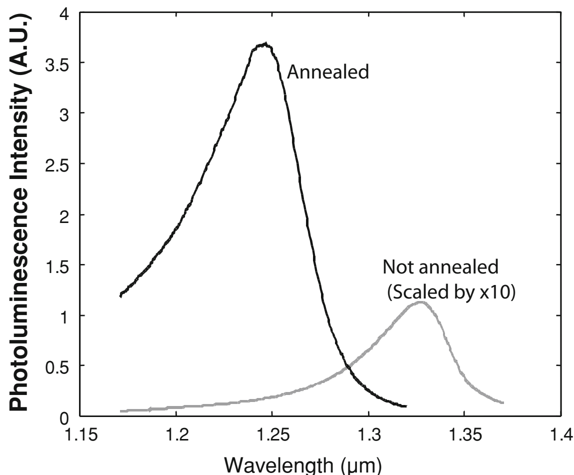

Fig. 11.6 PL intensity improvement and wavelength blue shift by annealing

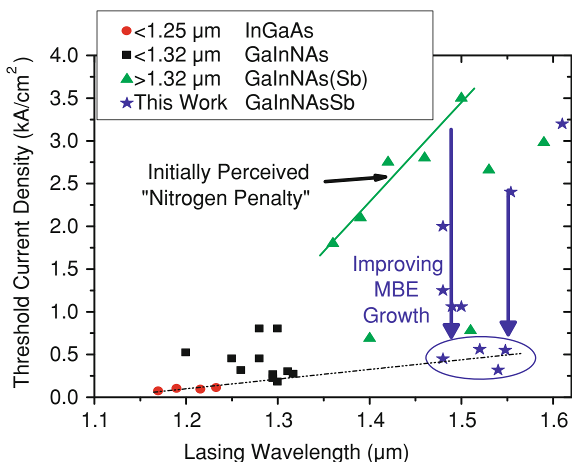

Fig. 11.7 Plot of Jth with lasing wavelength reported for GaInNAs(Sb)-based edge-emitting lasers. Adapted from [46] and references therein (© 2007 IEEE)

Due to intense efforts from many research groups, the quality of GaInNAs and GaInNAsSb epitaxy has improved dramatically as illustrated in Fig. 11.7. For 1.3 μm GaInNAs lasers, edge-emitting lasers have been reported with room-temperature threshold current densities as low as 150–300 A/cm^2 for MQW lasers and 250–320 A/cm^2 for SQW lasers [54, 88, 96, 99–101]. Threshold current density as low as 318 A/cm^2 has also been achieved for 1.55 μm GaInNAsSb lasers [46]. T_0 values above 100 K are routinely reported for 1.3 μm GaInNAs lasers [102–105], and high CW ouput power of >8.9 W has been reported [106]. T_0 values for 1.55 μm GaInNAsSb lasers tend to be significantly lower (∼60K) probably due to Auger recombination in the QW, or carrier leakage and defect recombination in the GaNAs barriers. However, pulsed output power close to 1 W has been routinely achieved from 20 μm-wide edge-emitting lasers [44, 46]. In summary, the quality of GaInNAs(Sb)

epitaxy has reached a very high and useful level despite significant challenges. By combining such high quality QWs with the already established AlAs/GaAs DBR technology, 1.3 μm VCSELs were realized quite early on in the research on GaInNAs [52, 107–109] and 1.55 μm VCSELs have been realized more recently [47, 57, 110]. More details are discussed in the following sections.

11.3 1.3 μm GaInNAs VCSELs

As discussed in previous sections, the primary advantage of GaInNAs for VCSEL applications is that it enables light emission at long wavelengths for materials grown on GaAs substrates, so that we can use the DBR technology based on AlGaAs layers, which is already a proven and well-established technology for 850 and 980 nm VCSELs. By using GaInNAs material as the active layer, 1.3 μm or longer-wavelength VCSELs can be grown monolithically in one reactor, and processed exactly in the same way as short-wavelength VCSELs. This all-monolithic growth and the maturity of the DBR and processing technology can lead to lower production cost and better reliability.

Although the GaAs/AlAs-based DBR technology is very well established for short wavelength VCSELs, different optical properties of the DBR materials at long wavelengths pose additional challenges for long wavelength VCSELs. First, the contrast in the refractive index for the DBR layers is slightly smaller at longer wavelengths, albeit only slightly, necessitating a few additional mirror pairs to provide a given reflectivity. A more prominent problem is that the free-carrier absorption and inter valence band absorption (IVBA) increase proportionately to λ^2. The problem is compounded even further by the roughly proportional increase in the thickness of each DBR layer ($=\lambda/4n$) for longer wavelengths. Lower doping has to be used to limit the optical loss, but then the electrical resistance increases, which increases the operating voltage and device heating, which significantly degrades performance, including high-speed operation. This problem has indeed made the realization of 1.55 μm VCSELs quite challenging, especially when combined with the growth challenges for GaInNAs(Sb) QWs for 1.55 μm emission. However, this has proven not to be an insurmountable barrier to realizing commercially viable 1.3 μm VCSELs, as discussed below.

The first GaInNAs VCSELs were optically pumped VCSELs at 1.22 μm and 1.25 μm by Larson et al. [107, 108]. They were grown using gas-source MBE and employing a dielectric DBR for the top reflector. Despite the novelty of the material and its unique growth challenge stemming from the low N solubility, it took a surprisingly short time from the first report of bandgap reduction by N incorporation [111] until the first VCSEL report. Moreover, these first VCSELs operated continuous-wave at room temperature, which was a very promising sign of the viability of GaInNAs material.

Next to follow were electrically pumped VCSELs, first in pulsed mode [52, 112], and soon room-temperature continuous wave operation [113]. The GaInNAs QWs,

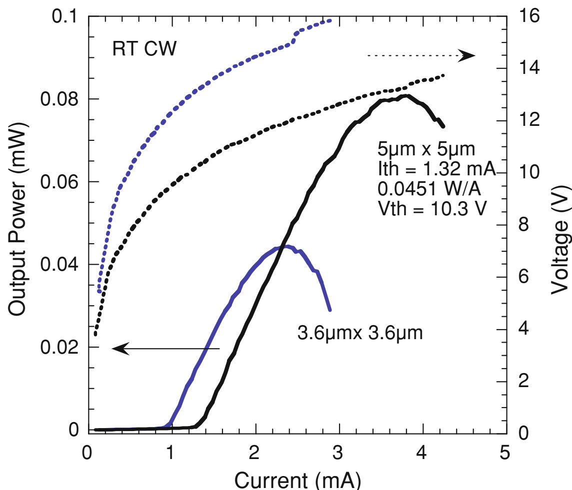

Fig. 11.8 Output power versus current for the first elecrically-pumped room-temperature(RT) continuous-wave(CW) 1200 nm GaInNAs VCSEL [113] (© 2000 IEEE)

the top p-DBR and the botom n-DBR were all grown by gas source [112] or solid source [52, 113] MBE. Due to the difficulty in MBE of smooth interface grading for minimum electrical resistance, the threshold voltage was very high (>10 V) although the threshold current was already quite reasonable at 1.3 mA for a 5 × 5 μm aperture [113]. The CW output power was also limited to about 0.08 mW at room temperature [113], as illustrated in Fig. 11.8. This figure also illustrates another challenge in that the threshold current does not scale with device size due to non-radiative recombination and leakage around the oxide barrier, both of which represent a larger fraction of the current as the aperture decreases.

Employing tunnel junctions to replace the p-DBR with an n-DBR to reduce both the optical loss and the electrical resistance, significantly lower voltage and increased output power (∼0.8 mW) [109, 114] were obtained at 1.3 μm for 2 μm-aperture VCSELs grown by solid source MBE. They also achieved OC-48 capability with these VCSELs, which means the VCSELs can be used for transmitting 2.488 Gbit/s data over short reach (SR, ∼2 km) or intermediate reach (IR-1, ∼15 km) links. However, the threshold voltage (>3 V) was still much higher than the bandgap of the active layer.

More recently, low resistance (65 Ω) and high output power (>4 mW) for 1.27 μm GaInNAs VCSELs was demonstrated by using a buried tunnel junction technique [115], where the upper half of a VCSEL is regrown over a tunnel junction mesa defined by lithography and etching, eliminating the additional electrical resistance and the aperture-size controllability issue related to the oxide aperture [116, 117]. A very high modulation bandwidth of 19 GHz was reported using this technique for 1.1 μm InGaAs/GaAs VCSELs [118], so it can be reasonably expected that such high speed modulation can be realized soon for 1.3 μm VCSELs by using buried tunnel junctions.

MOVPE (also known as MOCVD) is usually more suitable for mass production due to its high throughput and is especially suited for growing VCSELs becasue of its ability to easily grow smoothly graded interfaces for minimum electrical resistance DBRs. Although MOVPE growth of GaInNAs is more challenging than MBE growth, it didn't take too long until the first MOVPE VCSEL was demonstrated, either optically pumped [119] or electrically pumped [120]. The first electrically pumped MOVPE VCSEL operated continuous-wave at room temperature at 1.26 μm wavelength, and exhibited a low threshold voltage of 2.8 V, largely due to the smooth grading in the p-DBR interfaces by MOVPE. Since then, many groups have reported high-performance 1.3 μm VCSELs using MOVPE growth and a graded p-DBR, routinely achieving low threshold current (1–2 mA), low threshold voltage (<2 V), high output power (0.8 mW or higher) [30, 121, 122], and 2.5 Gbit/s modulation [121].

10 Gbit/s modulation was achieved by using intra-cavity contacts to get rid of DBR-related absoprtion and resistance, first by MBE [123] and then MOVPE [124] at 1.3 μm wavelength. They achieved very low operating voltage (1.06 V at threshold [124]), low threshold current (1.22 mA), and high output power (1.5 mW) all at the same time for CW and single-mode emission. The same group later reported high CW output (∼1 mW) up to 90°C and promising reliability result, i.e., no degradation for 1500 hours at 90°C [48] and projected MTBF of 13 million hours at 40°C [125, 126]. 10 Gbit/s modulation was also reported for tunnel-junction based 1.31 μm VCSELs grown by MBE [49] with a wavelength as long as 1338 nm, further corroborating the viability of the GaInNAs material and VCSELs based on it for commercial communications applications.

Another interesting possibility is to grow GaInNAs QWs by MBE and grow DBRs by MOVPE to take advantage of the strength of each growth technique. Shimizu et al. reported [127] low threshold voltage (1.2 V), low differential resistance (60 Ω), and low threshold current density (3.6 kA/cm^2) 1.3 μm VCSELs by using graded-interface DBRs grown in MOVPE and GaInNAsSb QWs grown by gas source MBE. On the other hand, Louderback et al. reported successful linear and parabolic interface grading in the DBR layers even by MBE growth, and their VCSELs [128] exhibited a low threshold current of 0.95 mA, single-mode output power of 0.7 mA and low threshold voltage of 1.93 V. Such grading operation was not regarded as 'production worthy' for MBE due to excessive Al/Ga shutter wear [1], but newer generations of MBE machines are capable of growing with a dozen or more sources, so multiple-step grading is readily possible without shutter wear and with nearly the same effectiveness as grading by MOVPE.

11.4 1.55 μm GaInNAsSb VCSELs

The realization of 1.55 μm GaAs-based VCSELs presents significant challenges for both the distributed Bragg reflector (DBR) design and the active region growth.

DBR Mirror Design

The design of DBRs involves the optimization of the doping profile and the hetero-interface grading scheme to balance the competing requirements of high reflectivity, low optical loss, low electrical resistance and low thermal impedance. The doping profile defines the tradeoff between electrical resistance and optical loss: increasing the doping concentration reduces the resistance but increases the optical loss and reduces the reflectivity. This tradeoff is dramatically more pronounced at 1.55 μm compared to 850 nm or 1.3 μm because the free-carrier absorption scales as λ^2. Furthermore, at 1.55 μm inter-valence-band absorption (IVBA) adds significantly to the total absorption of p-type materials. The limitations are thus particularly severe for p-doped DBRs. Not only is the absoprtion higher for p-doped materials but the resistance of p-doped DBRs is also higher due to lower hole mobilities that reduces bulk conductivity and larger effective masses that limit tunneling and thermionic emission currents across the potential barriers at the heterointerfaces. Additionally, the valence band discontinuties are, in general, larger and hence the potential barriers for holes are higher, further increasing the resistance of p-doped compared to n-doped AlAs/GaAs DBRs.

Knowing these challenges, different groups chose different approaches to the p-DBR problem to demonstrate the first 1300 nm VCSEL. The three approaches are illustrated in Fig. 11.9 and are respectively, (a) conventional graded and doped n- and p-DBRs with current through both DBRs [113], (b) p^{++}/n^{++} tunnel junction combined with 2 n-type DBRs with current through both DBRs [109, 114] and (c) an intracavity contacts and undoped DBRs [129]. The fundamental trade-offs boil down to (a) known technology, but high operating voltage and very low power due to heating, (b) complex processing and unknown reliability for the tunnel junction and (c) limited output power and mode hoping due to current crowding. Very recently a fourth alternative approach has emerged, which is to replace the p-type DBR with a high contrast grating [130] that might be used in combination with either of the above three approaches because it provides very high reflectivity with essentially a single layer such that the poor conductivity and high absorption in p-type material are very significantly reduced, thus opening up a much greater design space. While this has only been demonstrated at 850 nm, it is based upon GaAs/AlAs mirrors and we are working with Prof. Chang-Hasnain's group at UC-Berkeley to demonstrate this approach at 1550 nm.

Our initial focus has been to utilize the conventional p- and n-type DBR structures (a) and minimize the resistance problems as much as possible. To lower the potential barriers that limit carrier transport, the hetero-interfaces are usually graded. Several grading schemes including linear, uniparabolic [131], and parabolic [132] have been investigated. These grading methods are easily implemented in MOVPE by varying the gas flow rates. In MBE the grading schemes are more challenging but can be implemented by digital alloying [133] or by changing the group-III cell temperatures [134]. The disadvantage of the former technique is the large number of shutter operations that degrade the shutter mechanism while the disadvantage of the latter is poor reproducibility due to the difficulty in obtaining stable and reproducible fluxes

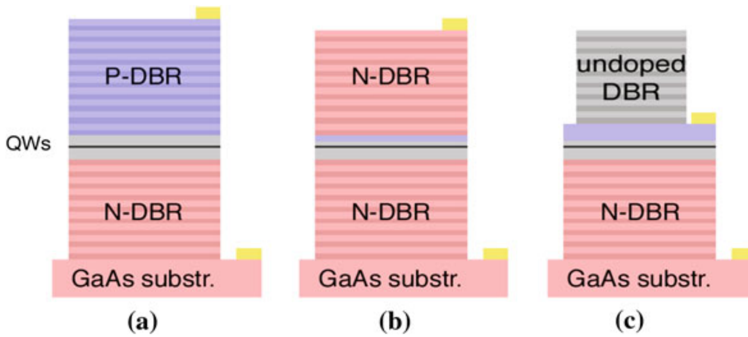

Fig. 11.9 **a** Conventional structure with n- and p-doped DBRs. **b** Structure with a tunnel junction and two n-DBRs. **c** Intracavity structure

after changing the cell temperatures. When multiple group-III sources are available step grading can be used to approximate a given profile [135].

Another complication arises from the fact that the index contrast of the Al(Ga)As/GaAs material system is reduced at longer wavelengths and hence more mirror pairs are needed to achieve a given reflectivity. The larger number of pairs, the thicker $\lambda/4$ layers and the limited doping imposed by the higher absorption at 1.55 μm contribute to both higher electrical resistance and higher thermal impedance. The higher resistance means that more Joule heating is generated and the higher thermal impedance means that the heat generated is dissipated less efficiently. This self-heating effect limits the output power and significantly degrades VCSEL performance.

Active Region Design

The emission wavelength of GaInNAs can be extended from 1.3 μm to 1.55 μm by increasing the nitrogen content above 4% and the indium content to approximately 40%. These relatively high nitrogen and indium concentrations require very low growth temperatures ($\leq$390°C) to prevent phase segregation and, consequently, near-stoichiometric arsenic-to-group-III flux ratios must be used to minimize the introduction of point defects, such as arsenic antisites and gallium vacancies, that incorporate readily at low growth temperatures. Despite the difficulties in the growth and the significant concentration of defects, edge emitting [57] and distributed feedback [136] lasers emitting in the 1.5 μm range have been demonstrated. However, no GaInNAs VCSELs emitting in this wavelength range have been reported to date and the significant decrease in PL intensity and rapid increase in laser thresholds for $\lambda > 1.45$ μm [57] suggest that realizing a VCSEL at $\lambda > 1.5$ μm will be extremely difficult.

As discussed in Sect. 11.2, antimony acts as a reactive surfactant, reducing the surface diffusion length and supressing phase segregation. Therefore, GaInNAsSb can

be grown at higher temperatures than GaInNAs and hence higher arsenic-to-group-III flux ratios can be used. In addition, with higher In composition, the incorporation of Sb is relatively insensitive to Sb flux, the Sb is acting primarily as a surface surfactant with mono-layer surface coverage and thus incorporation is relatively constant as long as the surface coverage is maintained and, thus precise Sb flux control is not required. Higher As and Sb fluxes can be used and do not require precise control since the nitrogen concentration is determined by the group III growth rate, thus only the indium and gallium fluxes require precise control, no different than the growth of ternary alloys like InGaAs or AlGaAs. The quinary GaInNAsSb system under these growth conditions thus behaves like a 'quasi-ternary' system.

1.55 μm VCSELs

Given the difficulties outlined in the previous paragraphs, it is not surprising that the development of 1.55 μm VCSELs has been extremely challenging and slow to achieve success. The first electrically-injected GaInNAsSb VCSEL operating beyond 1.31 μm was reported by Wistey et al. [110]. This device operated only in pulsed mode at 1.46 μm when cooled to −10°C. A similar device emitting at 1534 nm when cooled to −48°C was later demonstrated [45]. Optically-pumped C-band VCSELs using dielectric (SiO_2/TiO_2) top mirrors have also been reported [137]. Recently, we have achieved 1528 nm electrically-injected GaInNAsSb VCSELs operating in pulsed mode at room temperature and continuous wave up to 20°C [138]. The growth, fabrication and characterization of these devices is described in detail in the following paragraphs.

The top-emitting VCSEL structures were grown monolithically by solid-source molecular beam epitaxy (MBE) on n-type GaAs substrates. The bottom, silicon-doped mirror consists of a 31-pair AlAs/GaAs DBR followed by a 4-pair $Al_{0.91}Ga_{0.09}As$/GaAs DBR. The top mirror is composed of a 24-pair $Al_{0.91}Ga_{0.09}As$/GaAs carbon-doped DBR. To reduce series resistance, the heterointerfaces were graded in six steps over 30 nm for the p-DBR and in three steps over 5 nm for the n-DBR. A 40 nm $Al_{0.98}Ga_{0.02}As$ layer for selective oxidation was integrated into the first AlGaAs layer above the cavity. The active region is centered in a 1-λ thick GaAs cavity and consists of three 7 nm $Ga_{0.59}In_{0.41}N_{0.028}As_{0.946}Sb_{0.026}$ quantum wells with 20 nm $GaN_{0.033}As_{0.967}$ barriers designed for peak photoluminescence at 1540 nm after optimal annealing. The VCSEL structure was nominally designed to operate at 1530 nm.

The VCSELs were *ex-situ* annealed after growth at 670°C for 7 min in a rapid thermal annealing furnace under a flowing nitrogen ambient. The annealing conditions were optimized taking into account the long *in-situ* annealing that occurs during the growth of the top DBR. Device fabrication consists of Ti-Pt-Au evaporation and lift-off to form ring p-contacts. Next, mesas are defined by dry etching. Wet

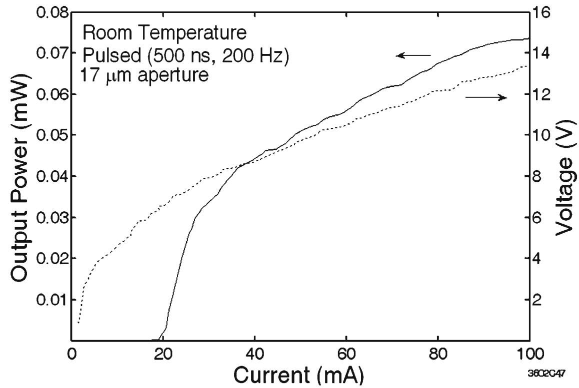

Fig. 11.10 Pulsed room-temperature LIV curve of a 17 µm aperture VCSEL

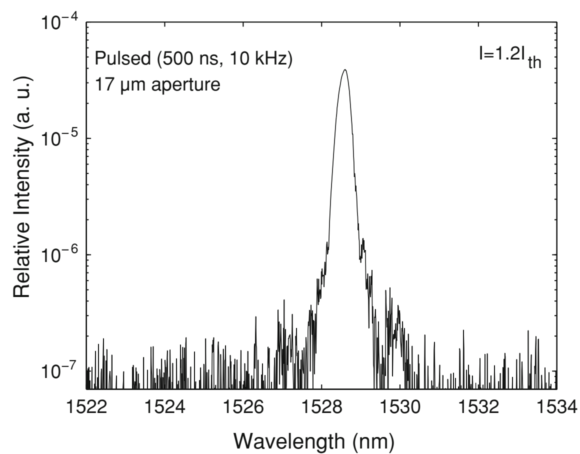

Fig. 11.11 Optical spectrum of a 17 µm aperture VCSEL at 1.2-times threshold

oxidation is then used to form the oxide aperture. Finally, the n-contact Au-Ge-Ni-Au is evaporated on the backside and annealed at 420°C for 1 min.

Figure 11.10 shows the pulsed room-temperature (25°C) light output power and voltage versus current (L–I–V) curves of a device with a 17 µm diameter current aperture. The threshold voltage is 5.9 V and the threshold current at 25°C is 18.18 mA, which corresponds to a threshold current density of 8.3 kA/cm^2. By comparison, edge-emitting lasers using a similar active region have threshold current densities in the 2.0 kA/cm^2 range [139]. The optical spectrum measured at 1.2 times the threshold current is shown in Fig. 11.11. The emission wavelength is 1528 nm.

Continuous-wave (CW) operation was observed for small-aperture devices at 15°C and lower temperatures. Figure 11.12 shows the CW L–I curves of a 7 µm diameter current aperture device at different temperatures. At 15°C the threshold current is 2.87 mA, which corresponds to a threshold current density of 7.5 kA/cm^2. The peak output power is severely limited by heating effects, mainly due to the high series resistance of the p-type DBR.

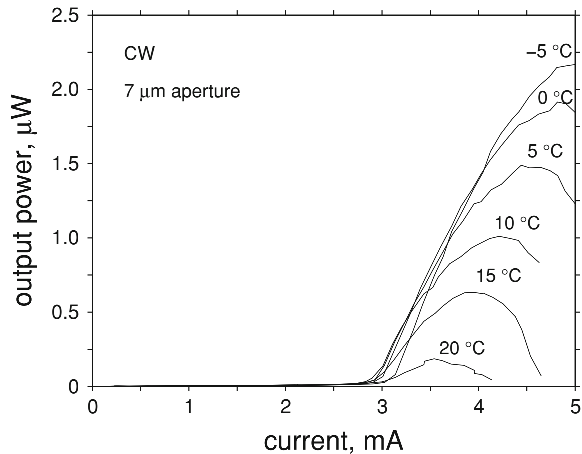

Fig. 11.12 Continuous wave L-I curves for a 7 μm aperture VCSEL at different temperatures

By using a tunnel junction to convert electrons into holes the p-type DBR can be replaced by an n-type DBR, which has lower electrical resistance and lower absorption losses. Another possibility is to use the tunnel junction in an intracavity contacted structure similar to those developed for InP-based VCSELs [116, 140–142]. In these VCSELs current cofinement is achieved by either selectively etching the tunnel junction [142, 143] or using epitaxial regrowth of a buried tunnel junction (BTJ) [116, 140]. The regrowth step necessary to form the BTJ adds complexity to the fabrication process while the undercut tunnel junction presents mechanical stability concerns. In contrast to InP-based VCSELs, GaAs-based VCSELs can use AlAs oxidation to provide carrier and optical confinement. This greatly simplifies the fabrication process.

11.5 Summary

Fiber to the home (FTTH) and broadband metro and local area networks (MANs and LANs) that can deliver high-speed access to the desktop will require very large numbers of low-cost lasers that can be operated without thermoelectric temperature control and be directly modulated at 10 Gbit/s. They will also have to cover the entire low-loss fiber region from 1.3–1.6 μm to enable coarse wavelength division multiplexing (CDWM) architectures that will allow direct modulation and operation over a wide temperature range. Because of the proven low-cost fabrication, high-speed capability and reliability of 850 nm GaAs-based VCSELs, longer-wavelength devices based upon the same fundamental materials technology are extremely attractive for these large scale, low-cost applications. The challenge is thus to extend the quantum well active region and optimize VCSEL design to operate between 1.3 and 1.6 μm. We have made significant progress in meeting both the

materials and device design challenges to realize such devices and certainly 1.3 μm devices can be commercially realized. As described in Sect. 11.4, there are still some remaining challenges to realize useful VCSELs at >1.3 μm and particularly out to 1.55 μm. Fortunately, progress in the materials and fabrication areas have enabled very good performance for edge emitting lasers at 1.55 μm and results on VCSELs provide a far more clearly defined set of challenges to optimize the design and one should expect that low-cost, GaAs-based VCSELs covering the entire 1.3–1.55 μm wavelength range will become available in the next 1–5 years, depending entirely upon the level of effort that is invested into overcoming these final obstacles.

References

1. J.S. Harris, GaInNAs long-wavelength lasers: progress and challenges. Semicond. Sci. Technol. **17**(8), 880–891 (2002)
2. J.S. Harris, R. Kudrawiec, H.B. Yuen, S.R. Bank, H.P. Bae, M.A. Wistey, D. Jackrel, E.R. Pickett, T. Sarmiento, L.L. Goddard, V. Lordi, T. Gugov, Development of GaInNAsSb alloys: growth, band structure, optical properties and applications. Physica Status Solidi (b) **244**(8), 2707–2729 (2007)
3. P. Kaiser, Photonic network trends and impact on optical components. *Advanced Semiconductor Lasers and Applications/Ultraviolet and Blue Lasers and Their Applications/Ultralong Haul DWDM Transmission and Networking/WDM Components, 2001 Digest of the LEOS Summer Topical Meetings*, p. 2 (2001)
4. M. Kondow, K. Uomi, A. Niwa, T. Kitatani, S. Watahiki, Y. Yazawa, GaInNAs: a novel material for long-wavelength-range laser diodes with excellent high-temperature performance. Jpn. J. Appl. Phys. **35**(Part-1, 2B), 1273–1275 (1996)
5. H. Soda, K. Iga, C. Kitahara, Y. Suematsu, GaInAsP/InP surface emitting injection lasers. Jpn. J. Appl. Phys. **18**(12), 2329–2330 (1979)
6. V. Jayaraman, J.C. Geske, M.H. MacDougal, F.H. Peters, T.D. Lowes, T.T. Char, Uniform threshold current, continuous-wave, singlemode 1300 nm vertical cavity lasers from 0 to 70°C. Electron. Lett. **34**(14), 1405–1407 (1998)
7. W. Yuen, G.S. Li, R.F. Nabiev, J. Boucart, P. Kner, R.J. Stone, D. Zhang, M. Beaudoin, T. Zheng, C. He, K. Yu, M. Jansen, D.P. Worland, C.J. Chang-Hasnain, High-performance 1.6 μm single-epitaxy top-emitting VCSEL. Electron. Lett. **36**(13), 1121–1123 (2000)
8. E. Hall, G. Almuneau, J.K. Kim, O. Sjolund, H. Kroemer, L.A. Coldren, Electrically-pumped, single-epitaxial VCSELs at 1.55 μm with Sb-based mirrors. Electron. Lett. **35**(16), 1337–1338 (1999)
9. S. Uchiyama, N. Yokouchi, T. Ninomiya, Continuous-wave operation up to 36°C of 1.3-μm GaInAsP-InP vertical-cavity surface-emitting lasers. IEEE Photon. Technol. Lett. **9**(2), 141–142 (1997)
10. J.A. Lott, N.N. Ledentsov, V.M. Ustinov, N.A. Maleev, A.E. Zhukov, A.R. Kovsh, M.V. Maximov, B.V. Volovik, Z.I. Alferov, D. Bimberg, InAs-InGaAs quantum dot VCSELs on GaAs substrates emitting at 1.3 μm . Electron. Lett. **36**(16), 1384–1385 (2000)
11. O. Blum, J.F. Klem, Characteristics of GaAsSb single-quantum-well-lasers emitting near 1.3 μm. IEEE Photon. Technol. Lett. **12**(7), 771–773 (2000)
12. W. Shan, W. Walukiewicz, J.W.A. III, E.E. Haller, J.F. Geisz, D.J. Friedman, J.M. Olson, S.R. Kurtz, Effect of nitrogen on the band structure of GaInNAs alloys. J. Appl. Phys. **86**(4), 2349–2351 (1999)
13. W. Shan, W. Walukiewicz, J.W. Ager, E.E. Haller, J.F. Geisz, D.J. Friedman, J.M. Olson, S.R. Kurtz, Band anticrossing in GaInNAs alloys. Phys. Rev. Lett. **82**(6), 1221–1224 (1999)

14. M. Kondow, S. Natatsuka, T. Kitatani, Y. Yazawa, M. Okai, Room-temperature continuous-wave operation of GaInNAs/GaAs laser diode. Electron. Lett. **32**(24), 2244–2245 (1996)
15. M. Hetterich, M.D. Dawson, A.Y. Egorov, D. Bernklau, H. Riechert, Electronic states and band alignment in GalnNAs/GaAs quantum-well structures with low nitrogen content. Appl. Phys. Lett. **76**, 1030–1032 (2000)
16. P.N. Hai, W.M. Chen, I.A. Buyanova, H.P. Xin, C.W. Tu, Direct determination of electron effective mass in GaNAs/GaAs quantum wells. Appl. Phys. Lett. **77**(12), 1843–1845 (2000)
17. J.S. Harris, Tunable long-wavelength vertical-cavity lasers: the engine of next generation optical networks?. IEEE J. Select. Topics Quantum Electron. **6**(6), 1145–1160 (2000)
18. S.G. Spruytte, M.C. Larson, W. Wampler, C.W. Coldren, H.E. Petersen, J.S. Harris, Nitrogen incorporation in group III-nitride-arsenide materials grown by elemental source molecular beam epitaxy. J. Cryst. Growth **227**(228), 506–515 (2001)
19. S.G. Spruytte, C.W. Coldren, J.S. Harris, W. Wampler, P. Krispin, K. Ploog, M.C. Larson, Incorporation of nitrogen in nitride-arsenides: origin of improved luminescence efficiency after anneal. J. Appl. Phys. **89**(8), 4401–4406 (2001)
20. S.G. Spruytte, MBE Growth of Nitride-Arsenides for long-wavelength optoelectronics. PhD thesis, Stanford University, 2001
21. H. Riechert, A. Ramakrishnan, G. Steinle, Development of InGaAsN-based 1.3 μm VCSELs. Semicond. Sci. Technol. **17**, 892–897 (2002)
22. J.C. Harmand, G. Ungaro, L. Largeau, G.L. Roux, Comparison of nitrogen incorporation in molecular-beam epitaxy of GaAsN, GaInAsN, and GaAsSbN. Appl. Phys. Lett. **77**(16), 2482–2484 (2000)
23. S.G. Spruytte, C.W. Coldren, A.F. Marshall, M.C. Larson, J.S. Harris, MBE growth of nitride-arsenide materials for long wavelength optoelectronics. Spring MRS meeting 5S1, W8.4 (2000)
24. C. Jin, Y. Qiu, S.A. Nikishin, H. Temkin, Nitrogen incorporation kinetics in metalorganic molecular beam epitaxy of GaAsN. Appl. Phys. Lett. **74**(23), 3516–3518 (1999)
25. M. Kawaguchi, E. Gouardes, D. Schlenker, T. Kondo, T. Miyamoto, F. Koyama, K. Iga, Low threshold current density operation of GaInNAs quantum well lasers grown by metalorganic chemical vapour deposition. Electron. Lett. **36**(21), 1776–1777 (2000)
26. S. Sato, S. Satoh, Metalorganic chemical vapor deposition of GaInNAs lattice matched to GaAs for long-wavelength laser diodes. J. Cryst. Growth **192**(3–4), 381–385 (1998)
27. A. Mereuta, G. Saint-Girons, S. Bouchoule, I. Sagnes, F. Alexandre, G.L. Roux, J. Decobert, A. Ougazzaden, (InGa)(NAs)/GaAs structures emitting in 1–1.6 μm wavelength range. Opt. Mater. **17**(1–2), 185–188 (2001)
28. W. Stolz, Alternative N-, P- and As-precursors for III/V-epitaxy. J. Cryst. Growth **209**(2), 272–278 (2000)
29. A. Hasse, K. Volz, A.K. Schaper, J. Koch, F. Höhnsdorf, W. Stolz, TEM Investigations of (GaIn)(NAs)/GaAs Multi-Quantum Wells grown by MOVPE. Cryst. Res. Technol. **35**, 787 (2000)
30. T. Takeuchi, Y.-L. Chang, M. Leary, A. Tandon, H.-C. Luan, D. Bour, S. Corzine, R. Twist, M. Tan, 1.3 μm InGaAsN vertical cavity surface emitting lasers grown by MOCVD. Electron. Lett. **38**(23), 1438–1440 (2002)
31. Z. Pan, T. Miyamoto, D. Schlenker, S. Sato, F. Koyama, K. Iga, Low temperature growth of GaInNAs/GaAs quantum wells by metalorganic chemical vapor deposition using tertiary-butylarsine. J. Appl. Phys. **84**(11), 6409–6411 (1998)
32. G.B. Stringfellow, *Organometallic Vapor Phase Epitaxy: Theory and Practice* (Academic Press, Boston, 1989)
33. R. LaPierre, B.J. Robinson, D.A. Thompson, Group V incorporation in InGaAsP grown on InP by gas source molecular beam epitaxy. J. Appl. Phys. **79**, 3021 (1996)
34. J.O. Neugebauer, C.G.V. de Walle, Electronic structure and phase stability of $GaAs_{1-x}N_x$ alloys. Phys. Rev. B **51**(16), 10568–10571 (1995)

35. I.H. Ho, G.B. Stringfellow, Solubility of nitrogen in binary III-V systems. J. Cryst. Growth **178**, 1–7 (1997)
36. M. Kawaguchi, T. Miyamoto, E. Gouardes, D. Schlenker, T. Kondo, F. Koyama, K. Iga, Lasing characteristics of low-threshold GaInNAs lasers grown by metalorganic chemical vapor deposition. Jpn. J. Appl. Phys. **40**, L744–L746 (2001)
37. N. Tansu, L.J. Mawst, Low-threshold strain-compensated InGaAs(N) ($\lambda = 1.19-1.31\,\mu$m) quantum-well lasers. IEEE Photon. Technol. Lett. **14**(4), 444–446 (2002)
38. N. Jikutani, S. Sato, T. Takahashi, A. Itoh, M. Kaminishi, S. Satoh, Threshold current density analysis of highly strained GaInNAs multiple quantum well lasers grown by metalorganic chemical vapor deposition. Jpn. J. Appl. Phys. **41**(1,2B), 1164–1167 (2002)
39. A. Polimeni, H.G. Baldassarri, H.M. Bissiri, M. Capizzi, M. Fischer, M. Reinhardt, A. Forchel, Effect of hydrogen on the electronic properties of $In_xGa_{1-x}As_{1-y}N_y$/GaAs quantum wells. Phys. Rev. B **63**(20), 201304 (2001)
40. I.A. Buyanova, M. Izadifard, W.M. Chen, A. Polimeni, M. Capizzi, H.P. Xin, C.W. Tu, Hydrogen-induced improvements in optical quality of GaNAs alloys. Appl. Phys. Lett. **82**, 3662–3664 (2003)
41. A. Polimeni, G. Baldassarri, M. Bissiri, M. Capizzi, A. Frova, M. Fischer, M. Reinhardt, A. Forchel, Role of hydrogen in III-N-V compound semiconductors. Semicond. Sci. Technol. **17**, 797 (2002)
42. A.J. Ptak, S. Kurtz, S.W. Johnston, D.J. Friedman, J.F. Geisz, J.M. Olson, Defects in GaInNAs: What we've learned so far, *National Center for Photovoltaics and Solar Program Review Meeting* Proceedings (2003)
43. A.J. Ptak, S.W. Johnston, S. Kurtz, D.J. Friedman, W.K. Metzger, A comparison of MBE- and MOCVD-grown GaInNAs, J. Cryst. Growth **251**(1–4), 392–398 (2003)
44. S.R. Bank, M.A. Wistey, L.L. Goddard, H.B. Yuen, V. Lordi, J.S. Harris, Low threshold, continuous wave, 1.5 μm GaInNAsSb lasers grown on GaAs. IEEE J. Quantum Electron. **40**(6), 656–664 (2004)
45. M.A. Wistey, S.R. Bank, H.P. Bae, H.B. Yuen, E.R. Pickett, L.L. Goddard, J.S. Harris, GaInNAsSb/GaAs vertical cavity surface emitting lasers at 1534 nm. Electron. Lett. **42**(5), 282–283 (2006)
46. S.R. Bank, H. Bae, L.L. Goddard, H.B. Yuen, M.A. Wistey, R. Kudrawiec, J.S. Harris, Recent progress on 1.55-μm dilute-nitride lasers. IEEE J. Quantum Electron. **43**(9), 773–785 (2007)
47. T. Sarmiento, H. Bae, T.D. O'Sullivan, J.S. Harris, 1528 nm GaInNAsSb/GaAs vertical cavity surface emitting lasers. *Conference on Lasers and Electro-Optics*, p. CTuY4, (2009)
48. L.R. Thompson, L.M.F. Chirovsky, A.W. Jackson, R.L. Naone, D. Galt, S.R. Prakash, S.A. Feld, M.V. Crom, J.G. Wasserbauer, M.D. Lange, B. Mayer, D.W. Kisker, Performance of monolithic 1.3 μmVCSELs in telecom applications. Proceedings of SPIE, vol. 4649 (2002), pp. 25–30
49. R.H. Johnson, V. Blasingame, J.A. Tatum, B.-S. Chen, D.T. Mathes, J.D. Orenstein, T.-Y. Wang, J.K. Kim, H.-K. Kwon, J.-H. Ryou, G. Park, E. Kalweit, H. Chanhvongsak, M.D. Ringle, T. Marta, J. Gieske, Long-wavelength VCSELs at honeywell. Proceedings of SPIE, vol. 4994(1) (2003), pp. 222–234
50. M. Kondow, K. Uomi, K. Hosomi, T. Mozume, Gas-Source molecular beam epitaxy of GaN_xAs_{1-x} using a N radical as the N source. Jpn. J. Appl. Phys. **33**(2,8A), L1056–L1058 (1994)
51. M. Fischer, M. Reinhardt, A. Forchel, GaInAsN/GaAs laser diodes operating at 1.52 μm. Electron. Lett. **36**(14), 1208–1209 (2000)
52. C.W. Coldren, M.C. Larson, S.G. Spruytte, J.S. Harris, 1200 nm GaAs-based vertical cavity lasers employing GaInNAs multiquantum well active regions. Electron. Lett. **36**(11), 951–952 (2000)
53. S.R. Bank, H.B. Yuen, M.A. Wistey, V. Lordi, H.P. Bae, J.S. Harris, Effects of growth temperature on the structural and optical properties of 1.55 μm GaInNAsSb quantum wells grown on GaAs. Appl. Phys. Lett. **87**(2), 021908 (2005)

54. D. Gollub, S. Moses, A. Forchel, Comparison of GaInNAs laser diodes based on two to five quantum wells. IEEE J. Quantum Electron. **40**(4), 337–342 (2004)
55. J.A. Gupta, P.J. Barrios, G.J. Pakulski, G.C. Aers, J.A. Caballero, D. Poitras, X. Wu, Properties of GaInNAsSb narrow ridge waveguide laser diodes in continuous-wave operation at 1.55 μm. Proceedings of SPIE, vol. 6485(1) (2007), p. 64850S
56. Y. Qiu, S.A. Nikishin, H. Temkin, V.A. Elyukhin, Y.A. Kudriavtsev, Thermodynamic considerations in epitaxial growth of $GaAs_{1-x}N_x$ solid solutions. Appl. Phys. Lett. **70**(21), 2831–2833 (1997)
57. G. Jaschke, R. Averbeck, L. Geelhaar, H. Riechert, Low threshold InGaAsN/GaAs lasers beyond 1500 nm. J. Cryst. Growth **278**, 224–228 (2005)
58. S.R. Bank, H.B. Yuen, H. Bae, M.A. Wistey, A. Moto, J.S. Harris, Enhanced luminescence in GaInNAsSb quantum wells through variation of the arsenic and antimony fluxes. Appl. Phys. Lett. **88**(24), 241923 (2006)
59. X. Yang, M.J. Jurkovic, J.B. Heroux, W.I. Wang, Molecular beam epitaxial growth of InGaAsN:Sb/GaAs quantum wells for long-wavelength semiconductor lasers. Appl. Phys. Lett. **75**, 178 (1999)
60. H. Shimizu, K. Kumada, S. Uchiyama, A. Kasukawa, 1.2μm range GaInAs SQW lasers using Sb as surfactant. Electron. Lett. **36**(16), 1379–1381 (2000)
61. J.C. Harmand, G. Ungaro, J. Ramos, E.V.K. Rao, G. Saint-Girons, R. Teissier, G.L. Roux, L. Largeau, G. Patriarche, Investigations on GaAsSbN/GaAs quantum wells for 1.3–1.55 μm emission. J. Cryst. Growth **227**(228), 553–557 (2001)
62. K. Volz, V. Gambin, W. Ha, M.A. Wistey, H. Yuen, S. Bank, J.S. Harris, The role of Sb in the MBE growth of (GaIn)(NAsSb). J. Cryst. Growth **251**(1–4), 360–366 (2003)
63. W. Ha, V. Gambin, M. Wistey, S. Bank, K. Seongsin, J.S. Harris, Multiple-quantum-well GaInNAs-GaNAs ridge-waveguide laser diodes operating out to 1.4 μm. IEEE Photon. Technol. Lett. **14**(5), 591–593 (2002)
64. V. Gambin, W. Ha, M. Wistey, H. Yuen, S. Bank, S. Kim, J.S. Harris, GaInNAsSb for 1.3–1.6 μm long wavelength lasers grown by molecular beam epitaxy. IEEE J. Select. Topics Quantum Electron **8**, 795–800 (2002)
65. H.B. Yuen, S. R. Bank, M. A. Wistey, W. Ha, A. Moto, and J. S. Harris, An Investigation of GaNAs(Sb) for Strain Compensated Active Regions at 1.3 and 1.55 μm. *45th Electronic Materials Conference*, 2003
66. S.R. Bank, H.B. Yuen, H. Bae, M.A. Wistey, J.S. Harris Jr, Overannealing effects in GaInNAs(Sb) alloys and their importance to laser applications. Appl. Phys. Lett. **88**(22), 221115 (2006)
67. A.Y. Egorov, D. Bernklau, B. Borchert, S. Illek, D. Livshits, A. Rucki, M. Schuster, A. Kaschner, A. Hoffmann, G. Dumitras, M.C. Amann, H. Riechert, Growth of high quality InGaAsN heterostructures and their laser application. J. Cryst. Growth **227**(228), 545–552 (2001)
68. E.-M. Pavelescu, T. Jouhti, C.S. Peng, W. Li, J. Konttinen, M. Dumitrescu, P. Laukkanen, M. Pessa, Enhanced optical performances of strain-compensated 1.3-μm GaInNAs/GaNAs/GaAs quantum-well structures. J. Cryst. Growth **241**(1–2), 31–38 (2002)
69. E.-M. Pavelescu, C.S. Peng, T. Jouhti, J. Konttinen, W. Li, M. Pessa, M. Dumitrescu, S. Spânulescu, Effects of insertion of strain-mediating layers on luminescence properties of 1.3-mu m GaInNAs/GaNAs/GaAs quantum-well structures. Appl. Phys. Lett. **80**(17), 3054–3056 (2002)
70. W. Ha, V. Gambin, S. Bank, M. Wistey, H. Yuen, K. Seongsin, J.S. Harris, Long-wavelength GaInNAs(Sb) lasers on GaAs. IEEE J. Quantum Electron. **38**(9), 1260–1267 (2002)
71. J.S. Harris, The opportunities, successes and challenges for GaInNAsSb. J. Cryst. Growth **278** (1–4), 3–17 (2005)
72. L.H. Li, Z. Pan, W. Zhang, Y.W. Lin, X.Y. Wang, R.H. Wu, W.K. Ge, Effect of ion-induced damage on GaNAs/GaAs quantum wells grown by plasma-assisted molecular beam epitaxy. J. Cryst. Growth **223**(1–2), 140–144 (2001)

73. Z. Pan, L. Li, W. Zhang, X. Wang, Y. Lin, R. Wu, Growth and characterization of GaInNAs/GaAs by plasma-assisted molecular beam epitaxy. J. Cryst. Growth **227**(228), 516–520 (2001)
74. L.H. Li, Z. Pan, W. Zhang, Y.W. Lin, X.Y. Wang, R.H. Wu, Quality improvement of GaInNAs/GaAs quantum wells grown by plasma-assisted molecular beam epitaxy. J. Cryst. Growth **227–228**, 527–531 (2001)
75. M.A. Wistey, S.R. Bank, H.B. Yuen, H. Bae, J.S.Harris Jr, Nitrogen plasma optimization for high-quality dilute nitrides. J. Cryst. Growth **278**(1–4), 229–233 (2005)
76. M.A. Wistey, S.R. Bank, H.B. Yuen, J.S. Harris Jr, M.M. Oye, A.L. Holmes Jr, Using beam flux monitor as Langmuir probe for plasma-assisted molecular beam epitaxy. J. Vac. Sci. Technol. A**23**(3), 460–464 (2005)
77. M. Albrecht, V. Grillo, T. Remmele, H.P. Strunk, A.Y. Egorov, G. Dumitras, H. Riechert, A. Kaschner, R. Heitz, A. Hoffmann, Effect of annealing on the In and N distribution in InGaAsN quantum wells. Appl. Phys. Lett. **81**(15), 2719–2721 (2002)
78. J.-M. Chauveau, A. Trampert, M.-A. Pinault, E. Tourni, K. Du, and K. H. Ploog, Correlations between structural and optical properties of GaInNAs quantum wells grown by MBE. J. Cryst. Growth, **251** (1–4), 383–387 (2003)
79. V. Gambin, V. Lordi, W. Ha, M. Wistey, T. Takizawa, K. Uno, S. Friedrich, J. Harris, Structural changes on annealing of MBE grown (Ga, In)(N, As) as measured by X-ray absorption fine structure. J. Cryst. Growth **251**(1–4), 408–411 (2003)
80. V. Lordi, V. Gambin, S. Friedrich, T. Funk, T. Takizawa, K. Uno, J.S. Harris, Nearest-neighbor configuration in (GaIn)(NAs) probed by X-Ray absorption spectroscopy. Phys. Rev. Lett. **90**(14), 145505 (2003)
81. G. Ciatto, F. Boscherini, F. D'Acapito, S. Mobilio, G.B.H.H Polimeni, A.M. Capizzi, D. Gollub, A. Forchel, Atomic ordering in (InGa)(AsN) quantum wells: an In K-edge X-ray absorption investigation. Nucl. Instrum. Methods Phys. Res. Sect. B Beam Interact. Mater. Atoms **200**, 34–39 (2003)
82. S. Kurtz, J. Webb, L. Gedvilas, D. Friedman, J. Geisz, J. Olson, R. King, D. Joslin, N. Karam, Structural changes during annealing of GaInAsN. Appl. Phys. Lett. **78**(6), 748–750 (2001)
83. I.A. Buyanova, G. Pozina, P.N. Hai, N.Q. Thinh, J.P. Bergman, W.M. Chen, H.P. Xin, C.W. Tu, Mechanism for rapid thermal annealing improvements in undoped GaN_xAs_{1-x}/GaAs structures grown by molecular beam epitaxy. Appl. Phys. Lett. **77**(15), 2325–2327 (2000)
84. T. Kageyama, T. Miyamoto, S. Makino, F. Koyama, K. Iga, Thermal annealing of GaInNAs/GaAs quantum wells grown by chemical beam epitaxy and its effect on photoluminescence. Jpn. J. Appl. Phys. **38**(Part 2, 3B), L298–L300 (1999)
85. L. Wei, M. Pessa, T. Ahlgren, J. Decker, Origin of improved luminescence efficiency after annealing of Ga(In)NAs materials grown by molecular-beam epitaxy. Appl. Phys. Lett. **79**, 1094–1096 (2001)
86. H.P. Bae, S.R. Bank, H.B. Yuen, T. Sarmiento, E.R. Pickett, M.A. Wistey, J.S. Harris, Temperature dependencies of annealing behaviors of GaInNAsSb/GaNAs quantum wells for long wavelength dilute-nitride lasers. Appl. Phys. Lett. **90**(23), 231119 (2007)
87. M. Kondow, T. Kitatani, S. Shirakata, Annealing in GaInNAs system. J. Phys. Condens. Matter **16**(31), S3229–S3244 (2004)
88. N. Tansu, N.J. Kirsch, L.J. Mawst, Low-threshold-current-density 1300-nm dilute-nitride quantum well lasers. Appl. Phys. Lett. **81**(14), 2523–2525 (2002)
89. M.A. Wistey, S.R. Bank, H.B. Yuen, L.L. Goddard, T. Gugov, J.S. Harris Jr, Protecting wafer surface during plasma ignition using an arsenic cap. J. Vac. Sci. Technol. B**23**, 1324–1327 (2005)
90. P. Krispin, S.G. Spruytte, J.S. Harris, K.H. Ploog, Electrical depth profile of p-type GaAs/Ga(As, N)/GaAs heterostructures determined by capacitance–voltage measurements. J. Appl. Phys. **88**(7), 4153–4158 (2000)

91. P. Krispin, S.G. Spruytte, J.S. Harris, K.H. Ploog, Origin and annealing of deep-level defects in p-type GaAs/Ga(As,N)/GaAs heterostructures grown by molecular beam epitaxy. J. Appl. Phys. **89**, 6294–6298 (2001)
92. N.Q. Thinh, I.A. Buyanova, W.M. Chen, H.P. Xin, C.W. Tu, Formation of nonradiative defects in molecular beam epitaxial GaN_xAs_{1-x} studied by optically detected magnetic resonance. Appl. Phys. Lett. **79**(19), 3089–3091 (2001)
93. A.Y. Polyakov, N.B. Smirnov, A.V. Govorkov, A.E. Botchkarev, N.N. Nelson, M.M.E. Fahmi, J.A. Griffin, A. Khan, S.N. Mohammad, D.K. Johnstone, V.T. Bublik, K.D. Chsherbatchev, M.I. Voronova, Kasatochkin V.S. Studies of deep centers in dilute GaAsN and InGaAsN films grown by molecular beam epitaxy. Solid State Electron. **46**(12), 2155–2160 (2002)
94. P. Krispin, V. Gambin, J.S. Harris, K.H. Ploog, Nitrogen-related electron traps in Ga(As,N) layers ($<3\%$ N). J. Appl. Phys. **93**, 6095–6099 (2003)
95. J.L. Harris, A.C. Bryce, O. Kowalski, J. Marsh, T. Jouhti, M. Pessa, and M. Hopkinson, Selective quantum well intermixing of 1.22 and 1.55 μm GaInNAs laser material, in *Conference on Lasers and Electro-Optics/International Quantum Electronics Conference and Photonic Applications Systems Technologies*, p. CTuJ7, Optical Society of America, (2004)
96. M. Hopkinson, C.Y. Jin, H.Y. Liu, P. Navaretti, R. Airey, 1.34 μm GaInNAs quantum well lasers with low room-temperature threshold current density. Electron. Lett. **42**(16), 923–924 (2006)
97. M. Kondow, T. Kitatani, Molecular beam epitaxy of GaNAs and GaInNAs. Semicond. Sci. Technol. **17**(8), 746–754 (2002)
98. D.V. Lang, Deep-level transient spectroscopy: a new method to characterize traps in semiconductors. J. Appl. Phys. **45**(7), 3023–3032 (1974)
99. G. Adolfsson, W. Shumin, M. Sadeghi, J. Bengtsson, A. Larsson, J.L. Jun, V. Vilokkinen, P. Melanen, Effects of lateral diffusion on the temperature sensitivity of the threshold current for 1.3-μm double quantum-well GaInNAsGaAs lasersl. IEEE J. Quantum Electron. **44**(7), 607–616 (2008)
100. J. Kasai, T. Kitatani, K. Adachi, K. Nakahara, and M. Aoki, Growth of low-threshold GaInNAs/GaAs triple-quantum-well lasers. J. Cryst. Growth **301–302**, 545–547 (2007)
101. Y.Q. Wei, M. Sadeghi, S.M. Wang, P. Modh, A. Larsson, High performance 1.28 μm GaInNAs double quantum well lasers. Electron. Lett. **41**(24), 1328–1330 (2005)
102. S. Sato, S. Satoh, High-temperature characteristic in 1.3-μm -range highly strained GaInNAs ridge stripe lasers grown by metal-organic chemical vapor deposition. IEEE Photon. Technol. Lett. **11**(12), 1560–1562 (1999)
103. M.R. Gokhale, P.V. Studenkov, J. Wei, S.R. Forrest, Low-threshold current, high-efficiency 1.3-μm wavelength aluminum-free InGaAsN-based quantum-well lasers. IEEE Photon. Technol. Lett. **12**(2), 131–133 (2000)
104. C.S. Peng, T. Jouhti, P. Laukkanen, E.-M. Pavelescu, J. Konttinen, W. Li, M. Pessa, 1.32-μm GaInNAs-GaAs laser with a low threshold current density. IEEE Photon. Technol. Lett. **14**(3), 275–277 (2002)
105. Y. Wei, J.S. Gustavsson, M. Sadeghi, S. Wang, A. Larsson, P. Savolainen, P. Melanen, P. Sipilä, Uncooled 2.5 Gb/s operation of 1.3 μm GaInNAs DQW lasers over a wide temperature range. Opt. Express **14**(7), 2753–2759 (2006)
106. D. Bisping, D. Pucicki, S. Höfling, S. Habermann, D. Ewert, M. Fischer, J. Koeth, A. Forchel, High-temperature high-power operation of GaInNAs laser diodes in the 1220–1240-nm wavelength range. IEEE Photon. Technol. Lett. **20**(21), 1766–1768 (2008)
107. M.C. Larson, M. Kondow, T. Kitatani, Y. Yazawa, M. Okai, Room temperature continuous-wave photopumped operation of 1.22 μm GaInNAs/GaAs single quantum well vertical cavity surface-emitting laser. Electron. Lett. **33**(11), 959–960 (1997)
108. M.C. Larson, M. Kondow, T. Kitatani, K. Tamura, M. Okai, Photopumped lasing at 1.25 μm of GaInNAs-GaAs multiple-quantum-well vertical-cavity surface-emitting lasers. IEEE Photon. Technol. Lett. **9**(12), 1549–1551 (1997)

109. K.D. Choquette, J.F. Klem, A.J. Fischer, O. Blum, A.A. Allerman, I.J. Fritz, S.R. Kurtz, W.G. Breiland, R. Sieg, K.M. Geib, J.W. Scott, R.L. Naone, Room temperature continuous wave InGaAsN quantum well vertical-cavity lasers emitting at 1.3 μm. Electron. Lett. **36**(16), 1388–1390 (2000)
110. M.A. Wistey, S.R. Bank, H.B. Yuen, L.L. Goddard, J.S. Harris, Monolithic, GaInNAsSb VCSELs at 1.46 μm on GaAs by MBE. Electron. Lett. **39**(25), 1822–1823 (2003)
111. M. Weyers, M. Sato, H. Ando, Red shift of photoluminescence and absorption in dilute GaAsN alloy layers. Jpn. J. Appl. Phys. **31**(Part 2, 7A), L853–L855 (1992)
112. M.C. Larson, M. Kondow, T. Kitatani, K. Nakahara, K. Tamura, H. Inoue, K. Uomi, GaInNAs-GaAs long-wavelength vertical-cavity surface-emitting laser diodes. IEEE Photon. Technol. Lett. **10**(2), 188–190 (1998)
113. M.C. Larson, C.W. Coldren, S.G. Spruytte, H.E. Petersen, J.S. Harris, Low-threshold oxide-confined GaInNAs long wavelength vertical cavity lasers. IEEE Photon. Technol. Lett. **12**(12), 1598–1600 (2000)
114. A.W. Jackson, R.L. Naone, M.J. Dalberth, J.M. Smith, K.J. Malone, D.W. Kisker, J.F. Klem, K.D. Choquette, D.K. Serkland, K.M. Geib, OC-48 capable InGaAsN vertical cavity lasers. Electron. Lett. **37**(6), 355–356 (2001)
115. Y. Onishi, N. Saga, K. Koyama, H. Doi, T. Ishizuka, T. Yamada, K. Fujii, H. Mori, J. Hashimoto, M. Shimazu, and T. Katsuyama, High power and low resistive GaInNAs-VCSELs with buried tunnel junctions, *21st IEEE International Semiconductor Laser Conference (ISLC)*, pp. 53–54 (2008)
116. M. Ortsiefer, S. Baydar, K. Windhorn, G. Bohm, J. Rosskopf, R. Shau, E. Ronneberg, W. Hofmann, M.-C. Amann, 2.5-mW single-mode operation of 1.55-μm buried tunnel junction VCSELs. IEEE Photon. Technol. Lett. **17**(8), 1596–1598 (2005)
117. N. Nishiyama, C. Caneau, J. Downie, M. Sauer, C.-E. Zah, 10-Gbps 1.3 and $1.55 - \mu$m InP-based VCSELs: 85 °C 10-km error-free transmission and room temperature 40-km transmission at 1.55-μm with EDC. Optical Fiber Communication Conference, p. PDP23 (2006)
118. N. Suzuki, T. Anan, H. Hatakeyama, M. Tsuji, Low resistance tunnel junctions with type-II heterostructures. Appl. Phys. Lett. **88**(23), 231103 (2006)
119. A. Wagner, C. Ellmers, F. Höhnsdorf, J. Koch, C. Agert, S. Leu, M. Hofmann, W. Stolz, W.W. Rühle, (GaIn)(NAs)/GaAs vertical-cavity surface-emitting laser with ultrabroad temperature operation range. Appl. Phys. Lett. **76**(3), 271–272 (2000)
120. S. Sato, N. Nishiyama, T. Miyamoto, T. Takahashi, N. Jikutani, M. Arai, A. Matsutani, F. Koyama, K. Iga, Continuous wave operation of 1.26 μm GaInNAs/GaAs vertical-cavity surface-emitting lasers grown by metalorganic chemical vapour deposition. Electron. Lett. **36**(24), 2018–2019 (2000)
121. C.S. Murray, F.D. Newman, S. Sun, J.B. Clevenger, D.J. Bossert, C.X. Wang, H.Q. Hou, R.A. Stall Development of 1.3 μm oxide-confined VCSELs grown by MOCVD. Proceedings of SPIE, vol. 4649 (2002), pp. 31–38
122. A. Yue, K. Shen, R. Wang, J. Shi, Low threshold current 1.3-μm GaInNAs VCSELs grown by MOVPE. IEEE Photon. Technol. Lett. **16**(3), 717–719 (2004)
123. G. Steinle, F. Mederer, M. Kicherer, R. Michalzik, G. Kristen, A.Y. Egorov, H. Riechert, H.D. Wolf, K.J. Ebeling, Data transmission up to 10 Gbit/s with 1.3 μm wavelength InGaAsN VCSELs. Electron. Lett. **37**(10), 632–634 (2001)
124. A. Ramakrishnan, G. Steinle, D. Supper, C. Degen, G. Ebbinghaus, Electrically pumped 10 Gbit/s MOVPE-grown monolithic 1.3-μm VCSEL with GaInNAs active region. Electron. Lett. **38**(7), 322–324 (2002)
125. S.R. Prakash, L.M.F. Chirovsky, R.L. Naone, D. Galt, D.W. Kisker, A.W. Jackson, Reliability of 1.3 micron VCSELs for metro area networks. Proceedings of SPIE, vol. 4994 (2003), pp. 44–54
126. D.W. Kisker, L.M.F. Chirovsky, R.L. Naone, J.M.V. Hove, J.M. Rossler, M. Adamcyk, N. Wasinger, J.G. Beltran, D. Galt, 1.3-μm VCSEL production issues. Proceedings of SPIE, vol. 5364 (2004), pp. 146–157

127. H. Shimizu, C. Setiagung, M. Ariga, Y. Ikenaga, K. Kumada, T. Hama, N. Ueda, N. Iwai, A. Kasukawa, 1.3-μm -range GaInNAsSb-GaAs VCSELs. IEEE J. Select. Topics Quantum Electron. **9**(5), 1214–1219 (2003)
128. D.A. Louderback, M.A. Fish, J.F. Klem, D.K. Serkland, K.D. Choquette, G.W. Pickrell, R.V. Stone, P.S. Guilfoyle, Development of bottom-emitting 1300-nm vertical-cavity surface-emitting lasers. IEEE Photon. Technol. Lett. **16**(4), 963–965 (2004)
129. G. Steinle, H. Riechert, A.Y. Egorov, Monolithic VCSEL with InGaAsN active region emitting at 1.28 μm and CW output power exceeding 500 μW at room temperature. Electron. Lett. **37**(2), 93–95 (2001)
130. M.C. Huang, Y. Zhou, C.J. Chang-Hasnain, A surface-emitting laser incorporating a high-index-contrast subwavelength grating. Nat. Photonics **1**(2007), 119–122 (2007)
131. K.L. Lear, R.P.S. Jr, Uniparabolic mirror grading for vertical cavity surface emitting lasers. Appl. Phys. Lett. **68**(5), 605–607 (1996)
132. M.G. Peters, B.J. Thibeault, D.B. Young, J.W. Scott, F.H. Peters, A.C. Gossard, L.A. Coldren, Band-gap engineered digital alloy interfaces for lower resistance vertical-cavity surface-emitting lasers. Appl. Phys. Lett. **63**(25), 3411–3413 (1993)
133. K. Tai, L. Yang, Y.H. Wang, J.D. Wynn, A.Y. Cho, Drastic reduction of series resistance in doped semiconductor distributed Bragg reflectors for surface-emitting lasers. Appl. Phys. Lett. **56**(25), 2496–2498 (1990)
134. M. Hong, D. Vakhshoori, J.P. Mannaerts, Y.-F. Hsieh, Low resistivity vertical-cavity surface emitting lasers grown by molecular- beam epitaxy using sinusoidal-composition grading in mirrors and in situ nonalloyed ohmic contacts. J. Vac. Sci. Technol. B **13**(2), 758–761 (1995)
135. G.W. Pickrell, D.A. Louderback, M.A. Fish, J.J. Hindi, H.C. Lin, M.C. Simpson, P.S. Guilfoyle, K.L. Lear, Compositional grading in distributed Bragg reflectors, using discrete alloys, in vertical-cavity surface-emitting lasers. J. Cryst. Growth **280**(1–2), 54–59 (2005)
136. D. Bisping, S. Hofling, D. Pucicki, M. Fischer, A. Forchel, Room-temperature singlemode continuous-wave operation of distributed feedback GaInNAs laser diodes at 1.5 μm. Electron. Lett. **44**(12), 737–738 (2008)
137. N. Laurand, S. Calvez, H.D. Sun, M.D. Dawson, J.A. Gupta, G.C. Aers, C-band emission from GaInNAsSb VCSEL on GaAs. Electron. Lett. **42**(1), 29–30 (2006)
138. T. Sarmiento, H.P. Bae, T.D. O'Sullivan, J. Harris, GaAs-based 1.53 μm GaInNAsSb vertical cavity surface emitting lasers. Electron. Lett. **45**(19), 978–979 (2009)
139. H. Bae, T. Sarmiento, and J. S. Harris, Experimental investigation of temperature dependence of 1.55 μm GaInNAsSb/GaNAs QW lasers grown in MBE. *IEEE 21st International Semiconductor Laser Conference (ISLC)*, pp. 59–60 (2008)
140. N. Nishiyama, C. Caneau, B. Hall, G. Guryanov, M.H. Hu, X.S. Liu, M.-J. Li, R. Bhat, C.E. Zah, Long-wavelength vertical-cavity surface-emitting lasers on InP with lattice matched AlGaInAs-InP DBR grown by MOCVD. IEEE J. Select. Topics Quantum Electron. **11**(5), 990–998 (2005)
141. S. Nakagawa, E. Hall, G. Almuneau, J.K. Kim, D.A. Buell, H. Kroemer, L.A. Coldren, 1.55-μm InP-lattice-matched VCSELs with AlGaAsSb-AlAsSb DBRs. IEEE J. Select. Topics Quantum Electron. **7**(2), 224–230 (2001)
142. C.-K. Lin, D.P Bour, J. Zhu, W.H Perez, M.H Leary, A. Tandon, S.W Corzine, M.R.T Tan, High temperature continuous-wave operation of 1.3- and 1.55-μm VCSELs with InP/air-gap DBRs. IEEE J. Select. Topics Quantum Electron. **9**(5), 1415–1421 (2003)
143. D. Feezell, D.A. Buell, L.A. Coldren, Continuous-wave operation of all-epitaxial InP-based 1.3 μm VCSELs with 57 % differential quantum efficiency. Electron. Lett. **41**(14), 803–804 (2005)

Chapter 12
Red Emitting VCSEL

Michael Jetter, Robert Roßbach and Peter Michler

Abstract This chapter describes the progress in development of vertical-cavity surface-emitting lasers (VCSEL) emitting in the red spectral region around 650 nm for data transmission over polymer optical fibers (POF). First, growth issues of red VCSEL using two different material systems, namely AlGaAs and AlGaInP, are introduced. In particular, the optical and electrical state-of-the-art characteristics as low threshold currents ($\leq$1 mA) and high output powers (several mW) are presented with a special focus on emission wavelength. Also the thermal budget and heat removal in the devices are pointed out with regard to the geometry of the VCSEL. Small-signal modulation response in terms of maximum resonance frequency in dependance on temperature behavior are discussed. Applications of these devices in optical interconnects are described and digital data transmission at data rates up to 2.1 Gbit/s over step-index POF is reported. These properties make red emitting VCSEL perfectly suited for high-speed low power consuming light sources for optical data communication via POF. By introducing InP quantum dots as gain material in red emitting VCSEL nearly temperature independent record low threshold current densities of around 10 A/cm^2 could be observed.

12.1 Introduction

Vertical-cavity surface-emitting lasers (VCSEL) captivate with their circular beam profile, low beam divergence and low threshold current. In the last decades GaAs based devices emitting in the near infrared (around 850 nm) have become successfully commercially available mostly as transmitters for data communication. However, for

M. Jetter (✉) · R. Roßbach · P. Michler
Institut für Halbleiteroptik und Funktionelle Grenzflächen,
Universität Stuttgart, Allmandring 3,
70569 Stuttgart, Germany
e-mail: michael.jetter@ihfg.uni-stuttgart.de

R. Michalzik (ed.), *VCSELs*, Springer Series in Optical Sciences 166,
DOI: 10.1007/978-3-642-24986-0_12, © Springer-Verlag Berlin Heidelberg 2013

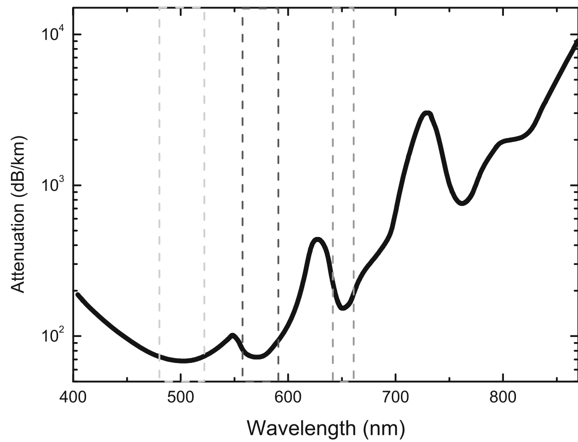

Fig. 12.1 Attenuation versus wavelength of standard step index (SI) POF [6]. The *dashed lines* indicate the regions of attenuation minima in the visible spectral range

applications where pointing, scanning, beam alignment, or display are important the visibility of VCSEL is essential. Also the shortened wavelength holds advantages in performance for optical imaging applications as laser printing or optical recording where higher resolutions due to smaller spot sizes are produced. To move to these shorter wavelengths aluminum can be incorporated into the GaAs quantum wells to increase their band gap. Even though AlGaAs provides a direct band gap for wavelength down to about 640 nm, the adverse effects of oxygen and its associated non-radiative deep levels as well as population of the indirect minima inhibit laser performance rapidly below 750 nm. Here, for visible wavelengths below 700 nm the AlGaInP system, which can be grown lattice matched to GaAs, provides the opportunity to fabricate Al-free ternary GaInP quantum wells. Decreasing the wavelength in this material system is attended by a reduction of the carrier confinement energy leading to a higher temperature sensitivity. This is one of the major concerns for red emitting VCSEL. In particular, for their major application as optical data transmitters in polymer optical fiber (POF) network systems it is essential to move their wavelength down to 650 nm reaching a rather narrow minimum of attenuation of the POF (Fig. 12.1). In this area the true red emitting VCSEL can prove its superiority to the commonly used light emitting diodes (LEDs) due to much higher modulation bandwidth (GHz), lower power consumption and easy fiber coupling due to the circular beam profile and additionally low divergence.

The fast epitaxial development of red VCSELs in the 1990s resulted in the first demonstration of an undoped photopumped VCSEL structure consisting of an AlGaInP active region embedded in AlGaAs distributed Bragg reflectors (DBRs) by Schneider in 1992 [1]. In the following years doped structures were fabricated fighting doping and heat dissipation problems ending in an electrically pulsed VCSEL device in 1993 [2, 3] and shortly afterwards in continuous wave lasing at room temperature [4, 5].

12.2 VCSEL Structure

In contradiction to AlGaAs based VCSEL which where mostly grown by molecular beam epitaxy (MBE) the AlGaInP system, providing direct band gap energies of 1.9 up to 2.35 eV, is grown almost exclusively by metal-organic vapor-phase epitaxy (MOVPE). This material system is well established for high-brightness LEDs, red edge-emitting lasers, and especially for red VCSEL.

12.2.1 AlGaInP Active Zone

For emission wavelengths around 650 nm $(Al_xGa_{1-x})_{0.51}In_{0.49}P$ grown lattice matched to GaAs is used providing the highest quantum efficiencies at the high carrier densities required for laser operation. At the desired wavelengths AlGaInP exhibits the higher bandgap and greater Γ and X band separation in comparison to AlGaAs material. The active layer consists of a 1-λ optical cavity made of $(Al_{0.33}Ga_{0.66})_{0.51}In_{0.49}P$ barriers and $(Al_{0.55}Ga_{0.45})_{0.51}In_{0.49}P$ spacer layers where compressively strained GaInP quantum wells (QWs) are embedded. For p-doping of the active zone both Mg and Zn can be used. However, due to the high activation energies relatively low hole concentrations ($< 10^{18}$ cm^{-3}) can be achieved. In addition, these dopants trend to diffusion, especially during the long growth times and high temperatures for a complete device structure. For better doping efficiency in the AlGaInP system substrates oriented 6° towards the [111]A direction are used [7]. The miscut also contributes to a higher confinement energy for the QWs as a result of the more disordered growth of the barrier material. The disordering is supported by relatively high growth temperatures around 750°C [8]. This results in a higher band gap energy ($\Delta E \approx 70$–100 meV) compared to the growth on exact orientated substrates [9].

12.2.2 Distributed Bragg Reflectors

To avoid absorption in the red spectral region $Al_{0.50}Ga_{0.50}As/AlAs$ mirror pairs instead of GaAs/AlAs have to be used for the bottom n-type distributed Bragg reflector (DBR). The small refractive index step between both materials necessitates a high number of mirror pairs to achieve sufficient reflectivity. Therefore, usually 45 or more $\lambda/4$-pairs of $Al_{0.50}Ga_{0.50}As/AlAs$ are grown to achieve a stopband width of around 40 nm. For n-type doping Si from Si_2H_6 or SiH_4 is used. Mostly disilane is chosen due to its independence of the incorporation site on substrates with miscut [10, 11]. To achieve better heatspreading near the cavity the topmost layer of the bottom DBR can be made of optically matched AlAs with a thickness of $(2k + 1)\lambda/4$ without disturbing the mirror reflectivity (Fig. 12.2). The layer thickness and its binary com-

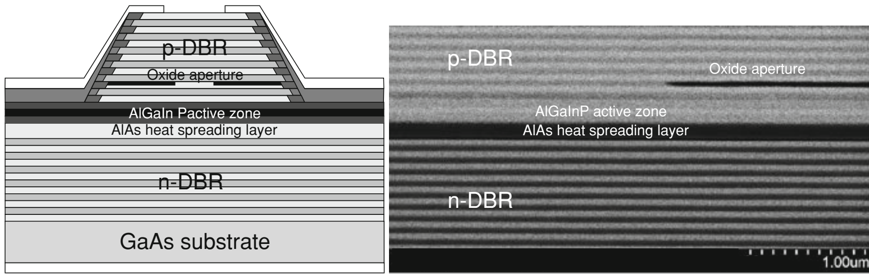

Fig. 12.2 Illustration of a VCSEL structure with oxide aperture and AlAs heat spreading layer underneath the AlGaInP active zone. A scanning electron microscope (SEM) cross-section picture of a VCSEL cleaved in the middle of the mesa reveals the high structural integrity

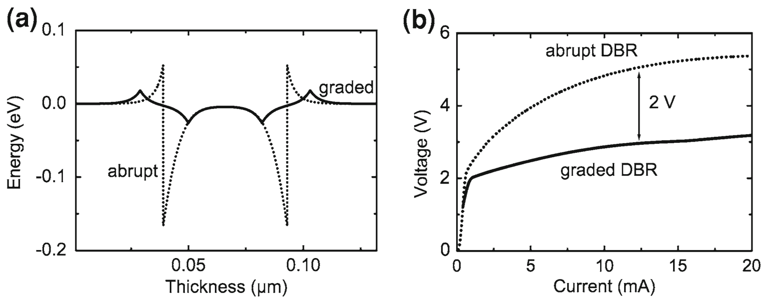

Fig. 12.3 **a** Simulation of band bending in p-type DBRs ($Al_{0.50}Ga_{0.50}As/Al_{0.95}Ga_{0.05}As$, $p = 10^{18}\,cm^{-3}$) with abrupt (*dotted line*) and linearly graded interfaces (*solid line*) over a grading distance of 0.1 λ. **b** Current-voltage characteristics of VCSEL with abrupt (*dotted line*) and linearly graded (*solid line*) interfaces. The voltage drop can be reduced by 2 V [14]

position leads to a better heat dissipation in comparison to the ternary AlGaAs and the DBR superlattice [12].

The top p-type DBR consists of more than 30 $\lambda/4$-pairs of $Al_{0.50}Ga_{0.50}As/Al_{0.95}Ga_{0.05}As$ with linearly graded interfaces to reduce the electrical series resistance. Former studies have shown that the band bending at abrupt interfaces causes high barriers of around 160 meV for the holes which can be reduced by the gradual change in the composition (Fig. 12.3a) [13]. By increasing the grading length the barrier height decreases, but reflectivity decreases also and an additional number of DBR-pairs have to be inserted to level out these losses. With this method it is possible to reduce the voltage drop of a VCSEL with graded DBR compared to the comparable VCSEL structure with abrupt DBR by 2 V (Fig. 12.3b).

To further decrease the ohmic resistivity of the p-type DBR the carrier concentration has to be increased. The p-dopants normally show a high tendency for diffusion, which could lead to a shift of the p-n-junction of the device or even worse disturb the quantum wells [15]. Because of its lower diffusion coefficient compared to Zn, carbon is the almost ideal p-dopant in the AlGaAs material system [16]. A very

elegant method for C-doping is the intrinsic carbon doping with the rest adducts of the metal-organic precursors (e.g. trimethylgallium $(CH_3)_3Ga$). With this method carbon concentrations in $Al_xGa_{1-x}As$ up to $10^{20}\,cm^{-3}$ could be demonstrated [17, 18]. In the normal growth mode of AlGaAs the parameters are chosen to suppress the C-incorporation. By lowering both V/III ratio and growth temperature, the incorporation of carbon can be increased [18]. Unfortunately, oxygen incorporation is also supported at these unfavorable growth conditions. Therefore, using an external carbon source as CBr_4 is more established due to its flexibility in controlling carrier concentration while growing at ideal growth conditions for the device achieving doping levels up to $5 \times 10^{19}\,cm^{-3}$ [19, 20].

In the first years of development of red VCSEL AlGaInP was used to fabricate visible DBRs avoiding the use of different material systems for the DBRs (AlGaAs) and the active zone (AlGaInP) [21]. It seemed that the epitaxial growth is complicated by the need to precisely control two distinct material systems, with very different p-type doping characteristics. In addition, the design and growth of the optical cavity/DBR interfaces is complicated by uncertainty in the band lineups and refractive index profiles at these interfaces. However, the VCSEL device structure imposes stringent requirements for composition and thickness control to maintain precise optical thicknesses (to within 1% absolute). This issue complicates the use of AlGaInP-based DBRs because of the additional difficulty in composition control and lattice matching in very thick ($>10\,\mu m$) structures composed of In-containing quaternary compounds. Furthermore, because of the low refractive index differential available with this system [22] compared to AlGaAs [23], only narrow stopband widths could be fabricated with more than 60 mirror pairs for the bottom DBR.

12.2.3 Oxide Aperture

The invention of native-oxide defined apertures [24, 25] allows to fabricate VCSEL with well defined thermal budget as well as well defined wave guiding. To realize an oxide aperture, the advantage of high oxidation selectivity of the $Al_xGa_{1-x}As$ material system can be used. A few percent change in the aluminum content for $x_{Al} \geq 90\%$ leads to a drastic change of the oxidation rate by more than an order of magnitude [26]. In Fig. 12.4 a SEM cross-section picture of a VCSEL mesa structure is shown where the development of the oxide aperture in the Bragg layer stack due to the high selectivity can be directly observed by the darker contrast. In addition to the definition of photon and carrier confinement, there is also the possibility to control the scattering losses in the cavity, improving spectral mode quality and photon losses, by positioning the oxide aperture in a field node of the standing wave field inside the VCSEL structure [27, 28].

In fact, due to the short cavity length, VCSEL can oscillate in a single longitudinal mode. However, the modal behavior depends strongly on the transverse dimension of the device and on the confinement mechanism. In VCSEL with oxide aperture diameters of around $6\,\mu m$, only the fundamental transverse mode is supported by the

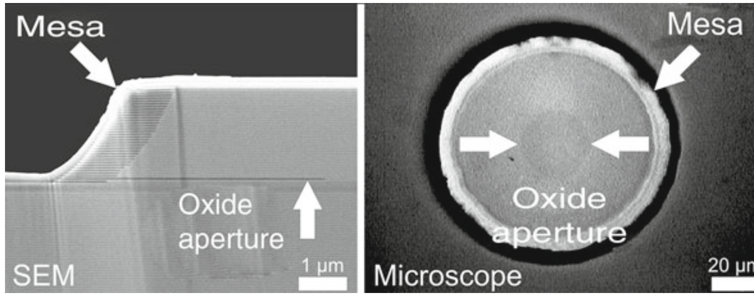

Fig. 12.4 Cross-section and top view of a VCSEL mesa with oxide aperture, captured with a scanning electron and plain optical microscope, respectively

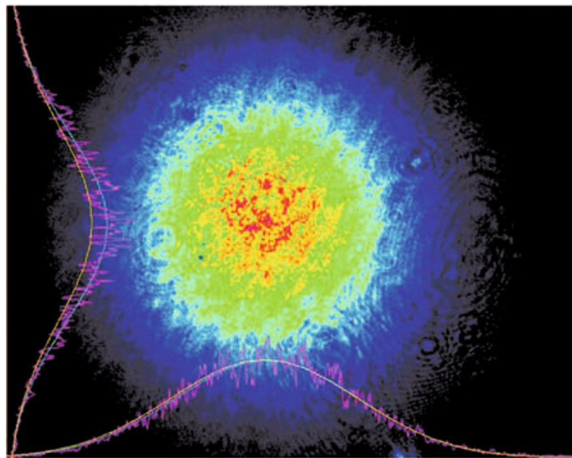

Fig. 12.5 Beam profile of a 655 nm VCSEL with an aperture diameter of around 6 μm in single transverse mode operation

cavity, but, due to the small active region, the emitted power is, in general, quite low (∼1 mW) [29]. In Fig. 12.5 the beam profile of a 655 nm VCSEL with an aperture diameter of 6 μm is shown. Both in vertical and in horizontal direction the beam shape exhibits gaussian profile. On the other hand, VCSEL with bigger aperture diameters offer higher optical power, but single-mode operation is possible only over a limited range of injection currents close to threshold [30].

12.2.4 In-Situ Reflection Measurement

As the complete laser structure contains around 180 layers, it is very sensitive to key device parameters as layer thickness, stop band tuning and cavity resonance. Therefore it is essential to control these critical properties of the VCSEL during growth. For this purpose *in-situ* reflectance measurement setups are used [31–35].

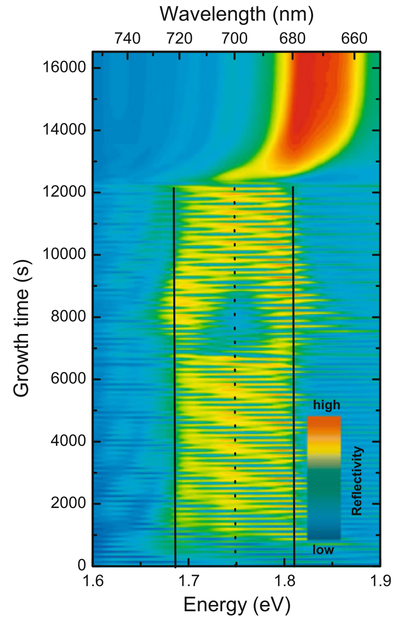

Fig. 12.6 Reflectivity fingerprint during growth of a 660 nm VCSEL: *red* indicates high reflectivity, *blue* low reflectivity. The *black lines* accentuate the stopband edges of both bottom and top DBR. The *dashed line* in between indicates the spectral position of the cavity resonance [31]

In Fig. 12.6 the development of the reflectance of the bottom and top DBR of a red VCSEL versus energy is shown. During the growth of the n-DBR the stop band, the region with strong reflectance, shows up at around 1.75 eV (708.5 nm) at a growth temperature of 750°C. After the growth of the cavity at around 7,500 s a characteristic minimum in the reflectance (cavity resonance) can be seen at 1.75 eV. Due to the limited resolution of the setup this feature disappears with increasing number of top mirror pairs. Finally, at around 12,500 s the structure cools down after the growth and the maximum of the reflectance shifts to the desired value of 670 nm (1.85 eV) at room temperature.

12.3 Device Characteristics of Red VCSEL

High temperature sensitivity of light output power is still a big challenge for red VCSEL. In addition, the POF attenuation spectrum in Fig. 12.1 shows a quite narrow dip around 650 nm and the carrier confinement in the AlGaInP material system decreases with almost every nanometer below 670 nm resulting in an even higher temperature sensitivity. Record output power was presented for 673 nm devices of nearly 12 mW and for short wavelength VCSEL at 650 nm of around 4 mW [30, 36, 37]. Here, long wavelength VCSEL show continuous-wave (CW) lasing at temperatures up to 80°C (666 nm) and 650 nm devices up to 65°C [37–40]. In Fig. 12.7a typical P(I)-curves are plotted for different temperatures of a 660 nm VCSEL

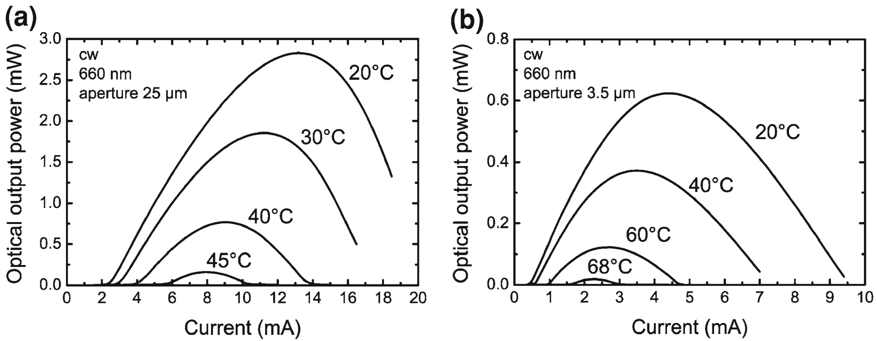

Fig. 12.7 Typical input–output characteristics of two 660 nm VCSEL devices (80 μm mesa diameter) at different temperatures. VCSEL (**a**) has an aperture diameter of 25 μm (threshold current $I_{th} = 2.5$ mA, 20°C) and VCSEL (**b**) of 3.5 μm ($I_{th} = 500$ μA, 20°C)

device. The big aperture of 25 μm leads to a maximum output power of nearly 3 mW due to the large pumped area of the active zone. Simultaneously, the maximum operating temperature is only 45°C which is caused by the high current which is needed to achieve lasing operation as current density defines the lasing threshold. In contradiction, the P-I curves of a further device with a smaller aperture diameter of 3.5 μm is shown in Fig. 12.7b. The smaller pumped volume leads to smaller threshold currents and therefore the heat generation is reduced resulting in a maximum operating temperature of nearly 70°C. However, the maximum output power is also decreased down to <1 mW which is adequate for POF applications and simultaneously ensures eye-safety for the user.

12.3.1 Heat Dissipation Model

In order to gain a deeper insight into the temperature influence over the performance of red VCSEL, the whole device has been simulated using a two-dimensional cylindrical heat dissipation model [41]. The model includes ohmic heating of the device as well as photonic cooling, taking into account specific T_0 ($\approx$100 K) and T_1 ($\approx$80$-$100 K) values of the threshold current rise and quantum efficiency fall with temperature, respectively. Especially the influence of the oxide aperture width (D_a) on the internal heating was analyzed. This model reveals that the thermal resistivity R_{th} strongly depends on the diameter of the active region D_a and on the diameter ratio of active to passive mesa D_a/D_s according to

$$R_{th} = \frac{4d}{\pi k D_s^2} + \frac{1}{2kD_a} \cdot \left(1 - \frac{D_a}{D_s}\right)^{3/2} \tag{12.1}$$

where D_s is the outer mesa diameter (see Fig. 12.4), d the thickness of the device and k the thermal conduction coefficient. The resulting R_{th} versus the aperture size

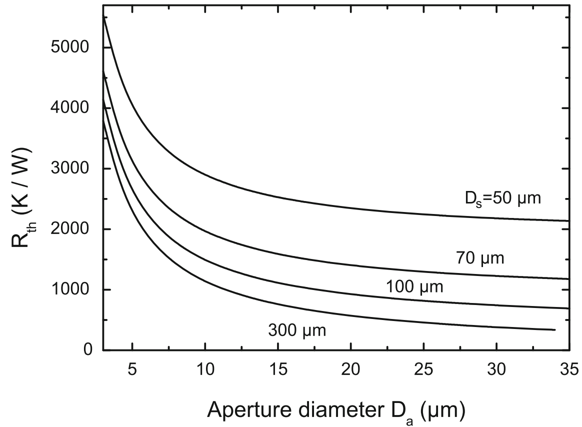

Fig. 12.8 Simulation of thermal resistance R_{th} versus aperture diameter D_{a} for different mesa diameters D_{s} according to (12.1)

D_{a} for different mesa diameters is plotted in Fig. 12.8. With increasing aperture diameter the thermal resistance R_{th} decreases as well as for increasing outer mesa diameters. However, there is no drastic improvement of R_{th} neither for larger mesa sizes ($D_{\mathrm{s}} > 100\,\mu\mathrm{m}$) nor wider apertures ($D_{\mathrm{a}} > 25\,\mu\mathrm{m}$). This results indicates that the ratio $D_{\mathrm{a}}/D_{\mathrm{s}}$ must be properly chosen.

With these calculations the internal temperature can be figured out

$$T_{\mathrm{int}} - T_{\mathrm{HS}} = R_{\mathrm{th}} \cdot \left[U_0 I + R_{\mathrm{s}} I^2 - P_{\mathrm{opt}} \right] \qquad (12.2)$$

depending on current density j (with $j = 4I/(\pi D_{\mathrm{a}}^2)$) for different aperture sizes D_{a}, with T_{HS} as the heat sink temperature, U_0 the forward voltage, R_{s} the series resistance and P_{opt} the photonic cooling. In Fig. 12.9a the calculated data of the internal temperature is shown as a function of current density for different outer mesa and aperture diameters. Small mesa diameters and big apertures sizes lead to an increased self-heating of the device (dashed curve in Fig. 12.9a). This combination allows only small current densities to achieve a given internal temperature (dashed horizontal line, 40°C). By reducing the aperture diameter (12.1) predicts a higher thermal resistivity. But the applied current is decreased simultaneously reducing ohmic heating and therefore a higher current density can be achieved. An enlargement of the mesa diameter leads to an improved heat spreading keeping the device at low internal temperatures at high current densities. In summary, big mesa diameters support heat spreading and therefore low internal temperatures could be found. Due to small apertures widths only small currents are needed to achieve lasing and additional current induced heat generation is suppressed.

To compare the calculated results with real devices, VCSEL were fabricated with the same outer mesa and aperture diameters as for the simulation. Figure 12.9b shows the dependence of the internal temperature as function of the current density for these different devices. The internal temperature of red VCSEL is determined by measuring the emission wavelength. From the temperature shift of the reflectivity

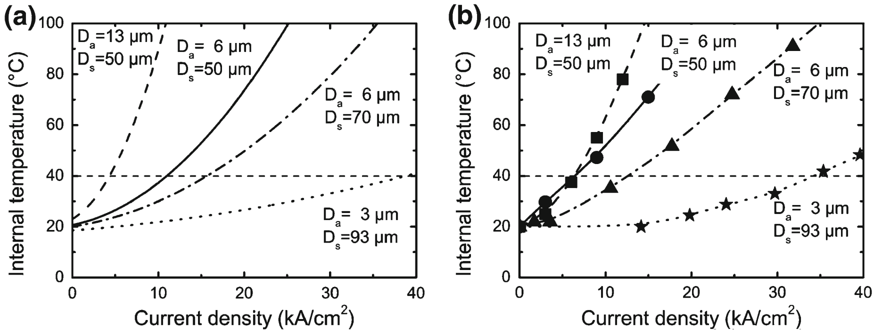

Fig. 12.9 Comparison of **a** calculated and **b** measured internal temperatures of 660 nm VCSEL devices with different outer mesa diameters and aperture sizes. Big mesas and small aperture diameters allow the highest current densities at a given internal temperature (*dashed horizontal line*)

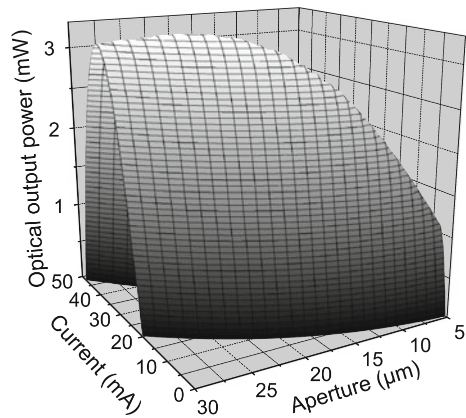

Fig. 12.10 Simulated input–output characteristics for different aperture diameters at a given outer mesa diameter of 90 µm

dip of the *in-situ* control of the epitaxial growth (Fig. 12.6), the relation between wavelength and temperature is deduced to 0.04 nm/K [31]. Figure 12.9b displays the excellent agreement of the experimental data with calculations confirming that smaller aperture sizes increase the internal temperatures most slowly with rising current density.

With this model the theoretical maximum output power $P_{\max}$ in dependence of the aperture size for a given mesa diameter can be calculated. The model predicts a maximum output power (∼3 mW) at around $D_a = 20\,\mu$m aperture size (Fig. 12.10) for a device with a mesa diameter of 90 µm. Going from the maximum to smaller apertures, R_{th} increases and limits dramatically the light output, which results also from the decrease of the active device area. By increasing the aperture diameter the operating current has to be increased to achieve comparable current densities, resulting in strong heating by the series resistance. This heating begins to limit $P_{\max}$ of the devices and leads to a decrease of the optical output power.

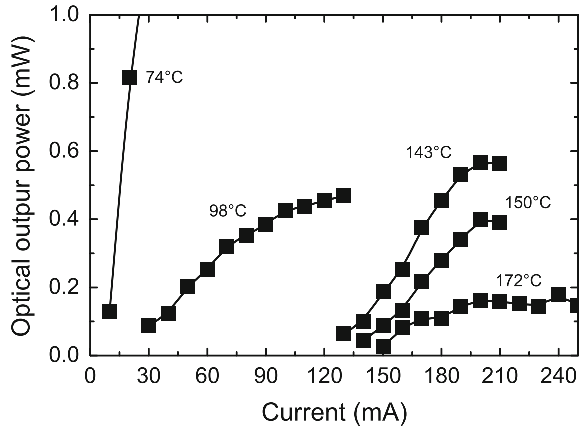

Fig. 12.11 Optical emission characteristics for an AlGaInP-based 660 nm VCSEL device under pulsed electrical excitation (200 Hz repetition rate, 0.3 μs pulse width) at different temperatures

12.3.2 High Temperature Results

The high temperature optical properties of AlGaInP based VCSEL can be analyzed if the influence of ohmic heating in the p-cladding region during CW operation can be neglected. By applying short pulses to achieve lasing operation at elevated temperatures, the internal temperature can be kept near to the heat sink temperature and the intrinsic thermal properties can be obtained. Therefore, output power under pulsed operation is measured as a function of heatsink temperature. Devices with 8.8 μm aperture size and an outer mesa diameter of 88 μm are mounted on a copper block which was heated by a heating coil. The temperature is measured on the copper surface right beneath the laser chip and $P(I)$-curves were recorded with 0.3 μs short pulses and a repetition frequency of 200 Hz [42]. The Cu heatsink temperature and thus the temperature of the VCSEL could be varied in a range between room temperature and more than 170°C (Fig. 12.11). At this maximum temperature the device exhibits a maximum output power of >0.1 mW (660 nm). Even though the threshold current was $I_{\mathrm{th}} = 150\,\mathrm{mA}$, which is nearly two orders of magnitude higher than at room temperature, this shows the capability of red AlGaInP VCSEL for future applications even in rough environment when efficient heat removal will be employed.

12.3.3 Modulation Bandwidth

Fast data communication is one key application for VCSEL. In 1996 red VCSEL (670 nm) achieved over 2 GHz in small-signal bandwidth measurements [44]. So far, small-signal resonance frequencies f_{r} have been reported for 670 nm devices of 11 GHz [45] and for 656 nm VCSEL of 3.75 GHz [46], respectively. As the parasitic resistance-capacity-product limits the modulation bandwidth, it is essential to

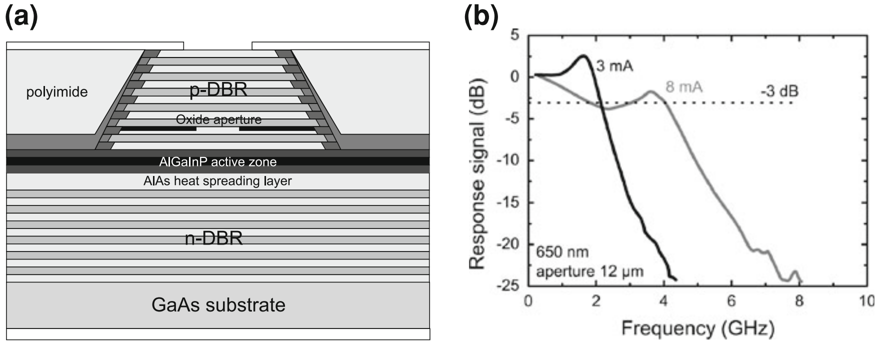

Fig. 12.12 **a** Schematic cross-sectional view of a high-frequency (HF) optimized VCSEL. **b** Modulation response of a 650 nm VCSEL with 12 µm aperture diameter under various bias currents ($I_{th} = 2.6$ mA). [43]

reduce the resistance of the VCSEL, mainly of the top p-type DBR as described in Sect. 12.2.2. Additionally, changing the VCSEL design (Fig. 12.12a) by using a 3 µm layer of polyimide [47] for passivation, the parasitic capacitance can be reduced. With this method modulation bandwidths of more than 5 GHz [48] for a 650 nm VCSEL with 3.5 µm aperture diameter were achieved (Fig. 12.12b).

Using rate equations, an analytic model [49] was fit to the modulation response against frequency data for each bias condition to extract the resonance frequency and damping factor. The result is shown in Fig. 12.13a. The slope of this graph gives a K-factor of 0.36 ns obtained using the relationship [50]:

$$\gamma = K \cdot f_r^2 + \frac{1}{\tau} \tag{12.3}$$

where f_r is the resonance frequency, γ is the damping factor and τ is the carrier lifetime.

$$f_{max,-3\,dB} = \frac{2\sqrt{2}\pi}{K} \tag{12.4}$$

leads to a maximum possible intrinsic −3 dB cut-off frequency of 25 GHz estimated from the K-factor [45].

12.3.4 Modulation Limits

From the light-current characteristics the photon density S_0 can be evaluated. The data follows the relationship [49]:

$$\omega_r = \sqrt{\frac{v_{gr}\Gamma_r \frac{dg}{dn}}{(1-\beta)\tau_{ph}}}\sqrt{S_0}. \tag{12.5}$$

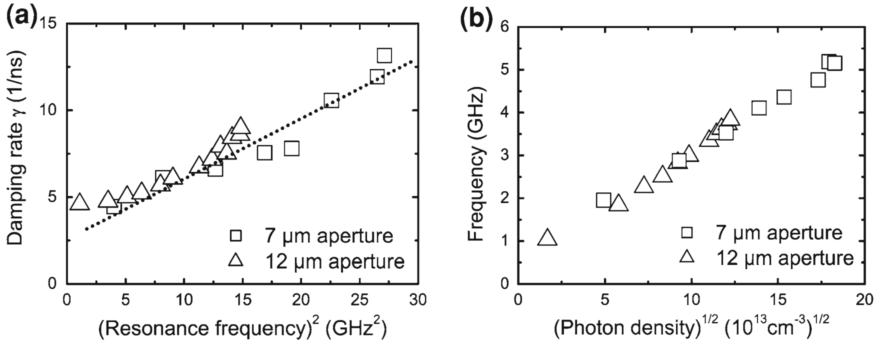

Fig. 12.13 **a** Damping rate γ versus square of the resonance frequency f_r to evaluate the K-factor. **b** Resonance frequency against square root of the photon density ($\sqrt{S_0}$) of VCSEL with 7 µm and 12 µm oxide aperture [48]

v_{gr} is the group velocity, $\frac{dg}{dn}$ is the differential gain coefficient, Γ_r is the filling factor of the standing wave, β is the spontaneous emission factor and τ_{ph} is the photon lifetime. Using parameters appropriate for these devices, a differential gain coefficient of 1.15×10^{-16} cm^2 can be estimated. Figure 12.13b also reveals that the maximum modulation bandwidth of a VCSEL depends mainly on one parameter: the photon density S_0 inside the quantum wells, as expected from rate equation analysis.

By observing the temperature shift of the emission wavelength as mentioned in Sect. 12.3.1 the intrinsic temperature in dependence on the DC drive current density of the VCSEL with different aperture diameters can be analyzed. Figure 12.14a shows the result against current density. As expected from analysis of (12.2), the device with a smaller aperture size allows higher current densities at a given temperature.

From rate equations S_0 is found to be proportional to current density:

$$S_0 = \frac{\Gamma \tau_{ph}}{eV}(I_0 - I_{th}). \tag{12.6}$$

Γ is a filling factor, e is the elementary charge, and V is the active volume.

The knowledge of the internal temperature and optical output power allows to plot directly the temperature versus current density (Fig. 12.14b). The internal temperature increases with photon density and current density, respectively, until the temperature induced carrier loss in the quantum wells limits recombination. Therefore, the photon density decreases at higher internal temperature in close analogy to the roll-over of the output power at high currents. In Fig. 12.14 the VCSEL with smaller aperture has the higher current density or photon density at a constant internal temperature (dashed horizontal line). This diagram shows that smaller oxide aperture sizes cause higher photon densities due to a better temperature behavior. By improving the temperature behavior of the VCSEL it is possible to improve its modulation limit.

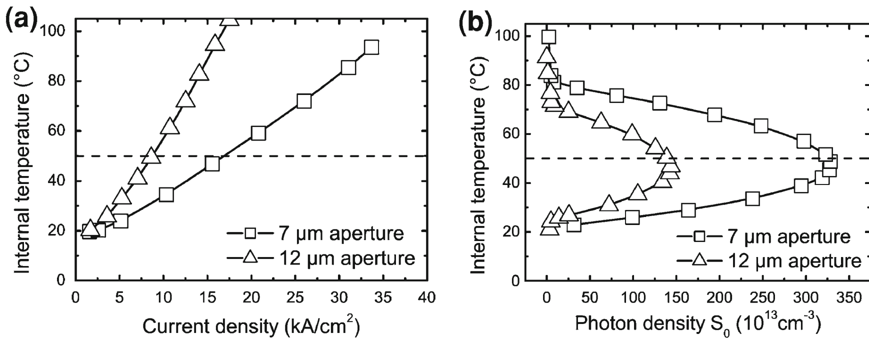

Fig. 12.14 **a** Internal temperature of two different 650 nm VCSEL as a function of driving current density. **b** Behavior of photon density for increasing DC drive currents and therefore increasing temperatures in the device. For temperatures above 50°C (*dashed horizontal line*) the photon density decreases [43]

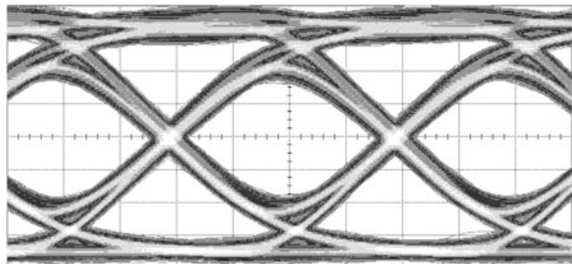

Fig. 12.15 Eye pattern at 1.25 Gbit/s modulation bandwidth (660 nm VCSEL) over 5 m step-index POF measured at the POF Application Center in Nuremberg. The time unit per division is 200 ps. The vertical scale is 35 mV per division

12.3.5 Data Transmission

The FTTH (fiber to the home) council Europe predicts that in 2012 about 15 millions households will be equipped with broadband glass fiber connections with data rates in the Gbit/s range [51]. To offer this bandwidth to the end user device, convenient in-house networks have to be developed. Here, the data communication with a red VCSEL as the opto-transmitter via POF is preferable due to user-friendly handling (visible light), easy fiber coupling (1 mm fiber core diameter) and mechanical stability. Therefore, the modulation performance in combination with perfect wavelength matching to the POF attenuation minimum at 650 nm is of great importance.

Only a few years after the development of red 670 nm VCSEL large-signal modulation bandwidths of 1.5 Gbit/s were reported [44]. Data rates of 1.25 Gbit/s at temperatures of up to 60°C could be measured over 1 m SI-POF with 665 nm devices [52]. With even shorter wavelength VCSEL (660 nm) it is possible to achieve data rates of 1.25 Gbit/s via 5 m SI-POF at temperatures from 20°C (Fig. 12.15) up to 55°C [53]. Finally, the same device offered maximum error-free data transmission up to 2.1 Gbit/s [54].

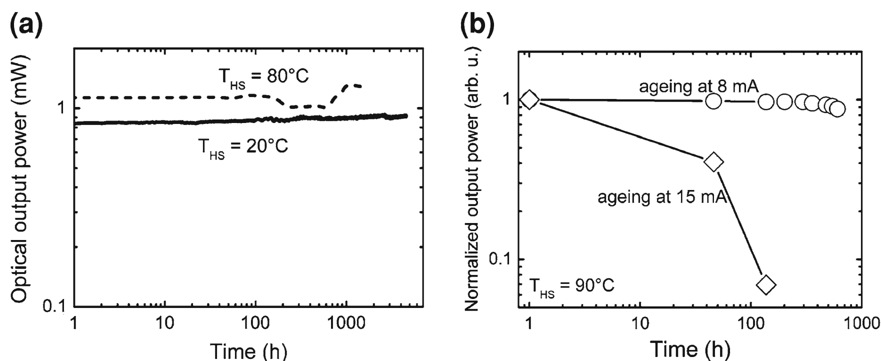

Fig. 12.16 Lifetime measurements of 660 nm VCSEL driven at **a** constant small currents around 3–4 mA and different temperature and **b** at constant temperatures (90°C) driven at different currents

12.3.6 Reliability

Reliability plays a major role in every application. At an operating temperature of 20°C and a constant current of 4 mA red 660 nm VCSEL show no degradation over a continuous operating time of more than 4,500 h (solid line in Fig. 12.16a) [52]. Accelerated ageing studies are difficult as the devices do not show reasonable output powers at elevated temperatures (>80°C). Therefore, reliability investigations have to be done in a cyclic manner. The devices are driven at a certain current and temperature has to be brought down periodically to room temperature to determine the optical output power. No device failures or significant power losses (occasional jumps possibly due to modal instabilities) were observed even for devices that were operated for more than 1,400 h at 80°C at a small current of 3 mA (dashed line in Fig. 12.16a). In Fig. 12.16b the maximum optical output power during high stress ageing studies are shown. At temperatures of around 90°C and high currents, the device driven at 15 mA degrades very fast in the first 100 hours in comparison to the other one operated at 8 mA (Fig. 12.16b). The high current density leads to fast ageing of red VCSEL devices with an ageing acceleration factor which was found to be [55]

$$\lambda_I = \left(\frac{I_\mathrm{a}}{I_\mathrm{op}}\right)^5, \tag{12.7}$$

where I_a is the ageing current for accelerated ageing, I_op is the moderate operating current and λ_I the resulting ageing acceleration factor. Visual inspection of the electroluminescence in the apertures of seriously degraded devices has revealed a consistent failure signature in the form of a dark spot at the periphery of the current aperture [30]. This failure signature exhibits always the same orientation with respect to the crystal axes. The authors suspect that a plausible explanation may be some form of conductivity anisotropy in the semiconductor layers due to the

off-axis substrate orientation, leading to localized current crowding and accelerated defect formation [56, 57].

12.4 Quantum Dot Based Red Emitting VCSEL

For a laser device with low threshold current, it is essential to decrease the pumped mode volume by using an oxide aperture above the cavity [58] and thereby decreasing the active volume for lowest power consumption. By using zero-dimensional quantum dots (QDs) as the active medium of semiconductor lasers, theory has predicted splendid properties compared to higher dimensional media [59, 60], such as low thresholds and broader gain spectra. In the In(Ga)As/GaAs material system, which emits in the near-infrared spectral region, laser physics and development have reached a high level and are best understood [61]. Low threshold current densities j_{th} of around 113 A/cm^2 for micropillar lasers in the InGaAs/GaAs material system with a QD density of $5 \times 10^9\ \text{cm}^{-2}$ were achieved [62]. World record transparency current density value of 6 A/cm^2 for one QD layer with a QD density of $1 \times 10^{11}\ \text{cm}^{-2}$ in the InGaAs/GaAs material system was reached [63]. It is also preferable to fabricate QDs at shorter wavelengths as active emitters for on-board optical interconnects and polymer optical fiber (POF) applications or as single-photon emitters as common silicon-based avalanche photo diodes have their highest photon detection efficiency in the red spectral range [64–66]. InP QDs embedded in AlGaInP barrier material are capable of emitting light in the red up to the green spectral range [67–69]. For such InP/AlGaInP QDs as active layer for edge-emitting lasers with emission wavelengths around 660 nm, j_{th} of around 300 A/cm^2 (single QD layer) at room temperature were achieved [70, 71]. In comparison, multiple quantum well VCSELs in the red spectral region and GaInP/AlGaInP material system exhibit low j_{th} values in the range of around 2 kA/cm^2 at 293 K [39].

A single layer of self-assembled InP-QDs was grown using the Stranski–Krastanow growth mode [72] by depositing several monolayers (ML) of InP. The QDs were sandwiched in between $(\text{Al}_{0.20}\text{Ga}_{0.80})_{0.51}\text{In}_{0.49}\text{P}$ as barrier material surrounded by a one wavelength-thick $(\text{Al}_{0.55}\text{Ga}_{0.45})_{0.51}\text{In}_{0.49}\text{P}$ cavity spacer [73]. The growth was interrupted for 20 s directly after the deposition of the QDs in order to ripen the QDs. Atomic force microscope measurements were used to determine the surface density of the QDs of around $5.5 \times 10^{10}\ \text{cm}^{-2}$. To form a current aperture for electrical pumping, an $\text{Al}_{0.98}\text{Ga}_{0.02}\text{As}$ oxidation layer was inserted above the cavity. The oxide aperture leads to a number of QDs of 5×10^3 to 1×10^5 lying spatially under the respective aperture opening while the pumped volume is expected to be larger due to current spreading between the active region and the current constriction layer. Post-growth standard lithography, wet oxidation and evaporation of ohmic contacts were used to fabricate single VCSEL devices. A ring contact with 20 μm opening window was used for current injection through the upper DBR [74].

An overview spectrum in Fig. 12.17 shows the laser emission line at 290 K due to the cavity resonance positioned at 653 nm. The input–output characteristics of

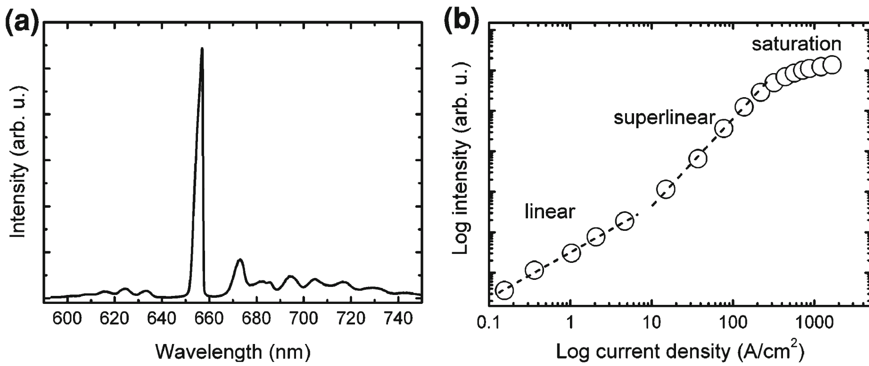

Fig. 12.17 **a** Overview emission spectra of an electrically pumped red emitting InP-QD based VCSEL with an aperture diameter of around 16 µm at room temperature. **b** Input–output characteristics of the QD-VCSEL shown in **a**. The change from linear to super-linear regime around and above j_{th} of 10 A/cm^2 is a strong hint on lasing. At 300 A/cm^2 the intensity begins to saturate due to the low quantity of QDs contributing to the lasing mode

a QD-based VCSEL is given in Fig. 12.17. As the current density is continuously increased from 1×10^{-2} A/cm^2 to around 10 A/cm^2 in Fig. 12.17, the integrated intensity over all modes increases linearly. The further increase in current density results in a super-linear increase in integrated intensity whose position was identified as j_{th} of the laser. Finally, even higher current densities result in saturation of output power. This can be explained due to the fact that the number of QDs which match optically and spatially to the mode is reduced and underlies the probability to be under the electrically pumped area. At the current stage of development, the overall efficiency of such InP-QD based VCSEL was estimated to be below 1%.

Finally, j_{th} was evaluated out of Fig. 12.17 for temperatures in a range from 100 to 290 K. The results are shown in Fig. 12.18. It appears that j_{th} is nearly temperature independent which might originate from a broad gain contribution of the QD ensemble in general and besides from three-dimensional carrier confinement as predicted [60]. Also, lowest j_{th} values of around 10–30 A/cm^2 were observed.

As mentioned above, only 5×10^3 to 1×10^5 InP-QDs are lying spatially under the aperture opening while the number of QDs that match spectrally to the cavity resonance is between around 7 and 160. This is due to the large QD ensemble with its broad emission spectra of around 170 meV and cavity detuning being in a range of around 114 meV at 300 K as shown in Fig. 12.18. The surprising effect that such a small number of QDs can exhibit enough gain to lasing might be explained by non-resonant dot-cavity coupling mechanisms [75–77]. In Ref. [77], the authors showed in detail that 2–4 QDs in a photonic crystal cavity being optically pumped provide sufficient gain for lasing and they reason that with cooperation from the surrounding non-resonant QDs emission into the lasing mode becomes feasible. In this case, a perfect spectral dot-cavity alignment is not essentially needed.

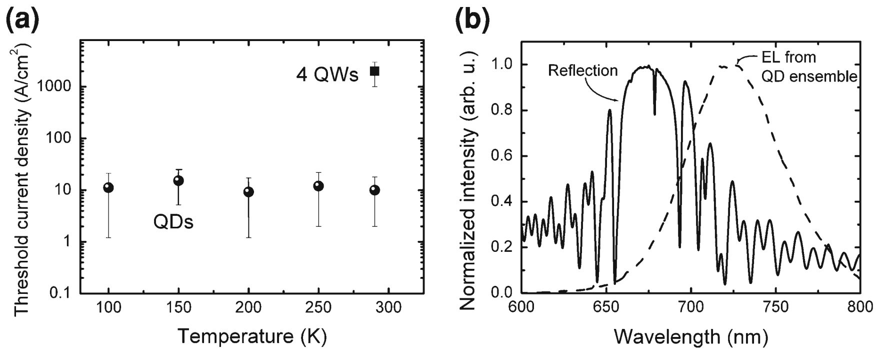

Fig. 12.18 **a** j_{th} of a red InP quantum dot VCSEL and a common quantum well based VCSEL with four quantum wells as a function of temperature. The measurement shows that j_{th} of the QD VCSEL is nearly constant over the investigated temperature range. **b** Reflection measurement and electroluminescence spectra from the QD-VCSEL. The electroluminescence was taken to the edge of the sample to avoid influences of the microcavity while the reflection was measured from the top of the sample. A large detuning of cavity resonance and QD electroluminescence maximum was observed

12.5 Conclusion

In summary, the particular challenges for the optimization and realization of red-emitting AlGaInP based VCSEL were discussed. Up to now devices with remarkable CW output powers of up nearly 12 mW at 673 nm and around 4 mW at 650 nm were fabricated. Lasing was shown even at 80°C for 666 nm devices and up to 65°C for 650 nm VCSEL. Using a heat dissipation model the temperature behavior could be improved by choosing appropriate mesa and aperture geometries. Under pulsed excitation AlGaInP VCSEL are capable of lasing even at 170°C. In view of data transmission 670 nm devices achieved resonance frequencies of 11 GHz and 5.7 GHz for 650 nm VCSEL. From a K-factor analysis a maximum modulation bandwidth of around 25 GHz could be estimated. Large-signal modulation bandwidth measurements of red VCSEL showed error-free data rates of 1.25 Gbit/s even at 60°C over POF. Reliability tests showed that red VCSEL are suitable for applications even in harsher environment. By replacing GaInP quantum wells by InP quantum dots as gain material in red emitting VCSEL nearly temperature independent record low threshold current densities of around 10 $\mathrm{A/cm^2}$ could be observed.

12.6 Outlook

Red AlGaInP VCSEL have been successfully developed in the last 15 years showing high output powers and improved temperature behavior as well as high modulation bandwidths. However, in the past for each special requirement a different VCSEL

design was processed. For practical usage especially in red VCSEL's major application as transmitters in POF based optical networks, it has to combine all the required specifications in one device. To achieve high data rates red AlGaInP VCSEL have to perfectly match the POF attenuation minimum at 650 nm. Unfortunately, with almost every nanometer below 670 nm the laser performance degrades and temperature sensitivity increases. Many investigations and calculations have shown that controlling the heat generation and heat removal results in a threefold improvement. With a lower thermal budget in the device and enhanced heat dissipation the temperature sensitivity can be reduced. This results in higher output powers and increased achievable current densities at higher temperatures which imply higher modulation bandwidths. Using quantum dots as the active material the threshold current will be decreased to very low values with a very low temperature sensitivity. This remedial action may reduce the heat generating current and may lead to red emitting VCSEL with high performance in all mentioned required specifications.

Acknowledgments The authors would like to thank Erich Kohler for assistance with the MOVPE growth and Marcus Eichfelder, Michael Wiesner, Susanne Weidenfeld, Monika Ubl, and Hedi Gräbeldinger for help with the device processing.

References

1. R.P. Schneider, R.P. Bryan, J.A. Lott, G.R. Olbright, Visible (657 nm) InGaP/InAlGaP strained quantum well vertical-cavity surface-emitting laser. Appl. Phys. Lett. **60**, 1830 (1992)
2. J.A. Lott, R.P. Schneider, Electrically injected visible (639–661 nm) vertical cavity surface emitting laser. Electron. Lett. **29**, 830 (1993)
3. R.P. Schneider, J.A. Lott, Cavity design for improved electrical injection in InAlGaP/AlGaAs visible (639–661 nm) vertical-cavity surface-emitting laser diodes. Appl. Phys. Lett. **63**, 917 (1993)
4. J.A. Lott, R.P. Schneider, K.D. Choquette, S.P. Kilcoyne, J.J. Figiel, Room temperature continuous wave operation of red vertical cavity surface emitting laser diodes. Electron. Lett. **29**, 1693 (1993)
5. R.P. Schneider, K.D. Choquette, J.A. Lott, K.L. Lear, J.J. Figiel, K.J. Malloy, Efficient room-temperature continuous-wave AlGaInP/AlGaAs visible(670 nm) vertical-cavity surface-emitting laser diodes. IEEE Photon. Technol. Lett. **6**, 313 (1994)
6. T. Kaino, M. Fujiki, S. Nara, S. Oikawa, Fabrication of a low-loss plastic optical fiber, U.S. Patent 4,381,269 (26 Apr. 1983)
7. J.-H. Lin, M.-J. Jou, C.-Y. Chen, B.-J. Lee, Effect of substrate misorientation on the optical properties and hole concentration of $Ga_{0.5}In_{0.5}P$ and $(Al_{0.5}Ga_{0.5})_{0.5}In_{0.5}P$ grown by low pressure metalorganic vapor phase epitaxy. J. Cryst. Growth **124**, 415 (1992)
8. Q. Liu, W. Prost, F.J. Tegude, Investigation of growth temperature dependent GaInP ordering in different crystal planes using X-ray diffraction and photoluminescence. Mat. Sci. Eng. B **44**, 91 (1997)
9. J.-R. Dong, S.-J. Chua, Y.-J. Wang, H.-R. Yuan, Substrate orientation dependence of In composition of AlGaInP epilayers grown by MOCVD. J. Cryst. Growth **269**, 408 (2004)
10. E. Veuhoff, T.F. Kuech, B.S. Meyerson, A study of silicon incorporation in GaAs MOCVD layers. J. Electrochem. Soc. **132**, 1958 (1985)
11. W.G. Breiland, M.E. Coltrin, J.R. Creighton, H.Q. Hou, H.K. Moffat, J.Y. Tsao, Organometallic vapor phase epitaxy (OMVPE). Mater. Sci. Eng. R **24**, 241 (1999)

12. J. Piprek, T. Tröger, B. Schröter, J. Kolodzey, C.S. Ih, Thermal conductivity reduction in GaAs–AlAs distributed Bragg reflectors. IEEE Photon. Technol. Lett. **10**, 81 (1998)
13. P. Zhou, J. Cheng, C.F. Schaus, S.Z. Sun, K. Zheng, E. Armour, C. Hains, W. Hsin, D.R. Myers, G.A. Vawter, Low series resistance high-efficiency GaAs/AlGaAs vertical-cavity surface-emitting lasers with continuously graded mirrors grown by MOCVD. IEEE Photon. Technol. Lett. **3**, 1041 (1991)
14. R. Rossbach, T. Ballmann, R. Butendeich, F. Scholz, H. Schweizer, M. Jetter, Red VCSEL for automotive applications, in *Photonics in the Automobile*. Proceedings of SPIE, vol. 5663 (2004), pp.135–146
15. T. Lin, K. Zheng, C. Wang, X. Ma, Photoluminescence study of AlGaInP/GaInP quantum well intermixing induced by zinc impurity diffusion. J. Cryst. Growth **309**, 140 (2007)
16. B.T. Cunningham, L.J. Guido, J.E. Baker, J.S. Major, N. Holonyak, G.E. Stillman, Carbon diffusion in undoped, n-type, and p-type GaAs. Appl. Phys. Lett. **55**, 687 (1989)
17. F. Dimroth, U. Schubert, F. Schienle, A. Bett, High C-doping of MOVPE grown thin $Al_xGa_{1-x}As$ layers for AlGaAs/GaAs interband tunneling devices. J. Electron. Mater. **29**, 47 (2000)
18. T.F. Kuech, J.M. Redwing, Carbon doping in metalorganic vapor phase epitaxy. J. Cryst. Growth **145**, 382 (1994)
19. E. Richter, P. Kurpas, D. Gutsche, M. Weyers, Carbon doped GaAs grown in low pressure-metalorganic vapor phase epitaxy using carbon tetrabromide. J. Electron. Mater. **24**, 1719 (1995)
20. K. Tateno, Y. Kohama, C. Amano, Carbon doping and etching effects of CBr_4 during metalorganic chemical vapor deposition of GaAs and AlAs. J. Cryst. Growth **172**, 5 (1997)
21. R.P. Schneider, J.A. Lott, InAIP/InAlGaP distributed Bragg reflectors for visible vertical cavity surface-emitting lasers. Appl. Phys. Lett. **62**, 2748 (1993)
22. H. Tanaka, Y. Kawamura, H. Asahi, Refractive indices of $In_{0.49}Ga_{0.51-x}Al_xP$ lattice matched to GaAs. J. Appl. Phys. **59**, 985 (1986)
23. S. Adachi, GaAs, AlAs, and $Al_xGa_{1-x}As$: Material parameters for use in research and device applications. J. Appl. Phys. **58**, R1 (1985)
24. D. Huffaker, D. Deppe, K. Kumar, T. Rogers, Native-oxide defined ring contact for low threshold vertical-cavity lasers. Appl. Phys. Lett. **65**, 97 (1994)
25. K.D. Choquette, R.P. Schneider, M.H. Crawford, K.M. Geib, J.J. Figiel, Continuous wave operation of 640–660 nm selectively oxidised AlGaInP vertical-cavity lasers. Electron. Lett. **31**, 1145 (1995)
26. K.D. Choquette, R.P. Schneider, K.L. Lear, K.M. Geib, Low threshold voltage vertical-cavity lasers fabricated by selective oxidation. Electron. Lett. **30**, 2043 (1994)
27. E. Hegblom, B. Thibeault, R. Naone, L. Coldren, Vertical cavity lasers with tapered oxide apertures for low scattering loss. Electron. Lett. **33**, 869 (1997)
28. A. Bond, P. Dapkus, J. O'Brian, Aperture dependent loss analysis in vertical-cavity surface-emitting lasers. IEEE Photon. Technol. Lett. **11**, 397 (1999)
29. T.M. Calvert, J.D. Lambkin, B. Corbett, A.F. Phillips, G.M. Crean, Fabrication of low-threshold red VCSELs. Mater. Sci. Semicond. Process. **3**, 517 (2000)
30. K. Johnson, M. Hibbs-Brenner, High output power 670 nm VCSELs, in *Vertical-Cavity Surface-Emitting Lasers XI*. Proceedings of SPIE, vol. 6484 (2007), pp. 6484–6504
31. R. Roßbach, T. Ballmann, R. Butendeich, H. Schweizer, F. Scholz, M. Jetter, Red VCSEL for high-temperature applications. J. Cryst. Growth **272**, 549 (2004)
32. H. Hou, H. Chui, K. Choquette, B. Hammons, W. Breiland, K. Geib, Highly uniform and reproducible vertical-cavity surface-emitting lasers grown by metalorganic vapor phase epitaxy with in situ reflectometry. IEEE Photon. Technol. Lett. **8**, 1285 (1996)
33. M. Zorn, K. Haberland, A. Knigge, A. Bhattacharya, M. Weyers, J.T. Zettler, W. Richter, MOVPE process development for 650 nm VCSELS using optical in-situ techniques. J. Cryst. Growth **235**, 25 (2002)

34. K. Haberland, M. Zorn, A. Klein, A. Bhattacharya, M. Weyers, J.T. Zettler, W. Richter, In-situ determination of interface roughness in MOVPE-grown visible VCSELs by reflectance spectroscopy. J. Cryst. Growth **248**, 194 (2003)
35. M. Zorn, A. Knigge, U. Zeimer, A. Klein, H. Kissel, M. Weyers, G. Tränkle, MOVPE growth of visible vertical-cavity surface-emitting lasers (VCSELs). J. Cryst. Growth **248**, 186 (2003)
36. A. Knigge, R. Franke, S. Knigge, B. Sumpf, K. Vogel, M. Zorn, M. Weyers, G. Tränkle, 650-nm vertical-cavity surface-emitting lasers: laser properties and reliability investigations. IEEE Photon. Technol. Lett. **14**, 1385 (2002)
37. A. Knigge, A. Zorn, A. Weyers, G. Tränkle, High-performance vertical-cavity surface-emitting lasers with emission wavelength between 650 and 670 nm. Electron. Lett. **38**, 882 (2002)
38. T.E. Sale, G.C. Knowles, S.J. Sweeney, A.Onischenko, J.E.F. Frost, S.M. Pinches, J.Woodhead, -180 to $+80$°C CW lasing in visible VCSELs, in *Conference Digest 17th IEEE International Semiconductor Laser Conference, 2000*, pp. 15–16
39. T. Calvert, B. Corbett, J.D. Lambkin, 80°C continuous wave operation of AlGalnP based visible VCSEL. Electron. Lett. **38**, 222 (2002)
40. A. Knigge, M. Zorn, J. Sebastian, K. Vogel, H. Wenzel, M. Weyers, G. Tränkle, High-efficiency AlGalnP/AlGaAs vertical-cavity surface-emitting lasers with 650 nm wavelength. IEE Proc. Optoelectron. **150**, 110 (2003)
41. W. Nakwaski, M. Osinski, Thermal resistance of top-surface-emitting vertical-cavity semiconductor lasers and monolithic two-dimensional arrays. Electron. Lett. **28**, 572 (1992)
42. R. Roßbach, R. Butendeich, T. Ballmann, B. Raabe, M. Jetter, H. Schweizer, F. Scholz, 160°C pulsed laser operation of AlGaInP-based vertical-cavity surface-emitting lasers. Electron. Lett. **39**, 1654 (2003)
43. T. Ballmann, R. Rossbach, M. Jetter, M. Berroth, H. Schweizer, Analysis of the modulation behaviour of red VCSELs, in *Nanophotonics for Communication: Materials and Devices*. Proceedings of SPIE, vol. 5597 (2004), pp. 102–108
44. D. Kuchta, R. Schneider, K. Choquette, S. Kilcoyne, Large- and small-signal modulation properties of red (670 nm) VCSELs. IEEE Photon. Technol. Lett. **8**, 307 (1996)
45. J.A. Lehman, R.A. Morgan, D. Carlson, M.H. Crawford, K.D. Choquette, High-frequency modulation characteristics of red VCSELs. Electron. Lett. **33**, 298 (1997)
46. A. Knigge, M. Zorn, H.J. Unold, F. Mederer, M. Weyers, G. Tränkle, High-performance vertical-cavity surface-emitting lasers with emission wavelengths from 650 nm to 670 nm. in *Conference Digest 18th IEEE International Semiconductor Laser Conference*, 2002, pp. 7–8
47. R.S. Geels, S.W. Corzine, J.W. Scott, D.B. Young, L.A. Coldren, Low threshold planarized vertical-cavity surface-emitting lasers. IEEE Photon. Technol. Lett. **2**, 234 (1990)
48. T. Ballmann, R. Roßbach, R. Butendeich, B. Raabe, M. Jetter, F. Scholz, H. Schweizer, Analog modulation of 650-nm VCSELs. IEEE Photon. Technol. Lett. **18**, 583 (2006)
49. L.A. Coldren, S.W. Corzine, *Diode Lasers and Photonic Integrated Circuits* (Wiley, New York, 1995)
50. K. Petermann, *Laser Diode Modulation and Noise* (Kluwer Academic Publishers, Berlin, 1991)
51. FTTH council, http://www.ftthcouncil.eu/ (2011)
52. G. Duggan, D.A. Barrow, T. Calvert, M. Maute, V. Hung, B. McGarvey, J.D. Lambkin, T. Wipiejewski, Red vertical cavity surface emitting lasers (VCSELs) for consumer applications, in *Vertical-Cavity Surface-Emitting Lasers XII*. Proceedings of SPIE, vol. 6908 (2008), p. 69080G-1
53. M. Wiesner, M. Eichfelder, R. Roßbach, M. Jetter, P. Michler, Red and fast vertical-emitting semiconductor laser for POF application, in Kommunikationskabelnetze, Beiträge der 15. ITG-Fachtagung. ITG-Fachberichte **212**, 157–160 (2004)
54. M. Jetter, R. Roßbach, P. Michler, Red VCSELs for high-speed data communication via POF. Photonik International **1**, 33 (2009)

55. T. Sale, D. Lancefield, B. Corbett, J. Justice, Ageing studies on red-emitting VCSELs for polymer optical fibre applications, in *Conference Digest 19th IEEE International Semiconductor Laser Conference*, 2004, pp. 75–76
56. R.S. Goldman, H.H. Wieder, K.L. Kavanagh, K. Rammohan, D.H. Rich, Anisotropic structural, electronic, and optical properties of InGaAs grown by molecular beam epitaxy on misoriented substrates. Appl. Phys. Lett. **65**, 1424 (1994)
57. J. Chung, J. Chen, P.-K. Ko, C. Hu, M. Levi, The effects of low-angle off-axis substrate orientation on MOSFET performance and reliability. IEEE Trans. Electron Devices **38**, 627 (1991)
58. K. Iga, Vertical-cavity surface-emitting laser: its conception and evolution. Jpn. J. Appl. Phys. **47**, 1 (2008)
59. M. Asada, Y. Miyamoto, Y. Suematsu, Gain and the threshold of three-dimensional quantum-box lasers. IEEE J. Quantum Electron. **22**, 1915 (1986)
60. Y. Arakawa, H. Sakaki, Multidimensional quantum well laser and temperature dependence of its threshold current. Appl. Phys. Lett. **40**, 939 (1982)
61. D. Bimberg, Quantum dots for lasers, amplifiers and computing. J. Phys. D Appl. Phys. **38**, 2055 (2005)
62. S. Reitzenstein, T. Heindel, C. Kistner, A. Rahimi-Iman, C. Schneider, S. Höfling, A. Forchel, Low threshold electrically pumped quantum dot-micropillar lasers. Appl. Phys. Lett. **93**, 061104 (2008)
63. R.L. Sellin, C. Ribbat, M. Grundmann, N.N. Ledentsov, D. Bimberg, Close-to-ideal device characteristics of high-power InGaAs/GaAs quantum dot lasers. Appl. Phys. Lett. **78**, 1207 (2001)
64. P. Michler, ed., *Single Quantum Dots – Fundamentals Applications and New Concepts* (Springer, Berlin, 2003)
65. M. Reischle, G.J. Beirne, W.-M. Schulz, M. Eichfelder, R. Roßbach, M. Jetter, P. Michler, Electrically pumped single-photon emission in the visible spectral range up to 80 K. Opt. Express **16**, 12771 (2008)
66. M. Reischle, C. Kessler, W.-M. Schulz, M. Eichfelder, R. Roßbach, M. Jetter, P. Michler, Triggered single-photon emission from electrically excited quantum dots in the red spectral range. Appl. Phys. Lett. **97**, 143513 (2010)
67. S.P. DenBaars, C.M. Reaves, V. Bressler-Hill, S. Varma, W.H. Weinberg, P.M. Petroff, Formation of coherently strained self-assembled InP quantum islands on InGaP/GaAs(001). J. Cryst. Growth **145**, 721 (1994)
68. R. Roßbach, W.-M. Schulz, M. Reischle, G.J. Beirne, M. Jetter, P. Michler, Red to green photoluminescence of InP-quantum dots in $Al_xGa_{1-x}InP$. J. Cryst. Growth **298**, 595 (2006)
69. R. Roßbach, W.-M. Schulz, M. Eichfelder, M. Reischle, G.J. Beirne, M. Jetter, P. Michler, Red to orange electroluminescence from InP/AlGaInP quantum dots at room temperature. J. Cryst. Growth **310**, 5098 (2008)
70. W.-M. Schulz, M. Eichfelder, R. Roßbach, M. Jetter, P. Michler, Low threshold InP/AlGaInP quantum dot in-plane laser emitting at 638 nm. Appl. Phys. Exp. **2**, 112501 (2009)
71. W.-M. Schulz, M. Eichfelder, R. Roßbach, M. Jetter, P. Michler, InP/AlGaInP quantum dot laser emitting at 638 nm. J. Cryst. Growth **315**, 123 (2011)
72. I.N. Stranski, L. Krastanow, Zur Theorie der orientierten Aussscheidung von Ionenkristallen aufeinander. Sitz. Ber. Akad. Wiss., Math.-naturwiss. Kl. Abt. IIb **146**, 797 (1938)
73. W.-M. Schulz, R. Roßbach, M. Reischle, G.J. Beirne, M. Bommer, M. Jetter, P. Michler, Optical and structural properties of InP quantum dots embedded in $(Al_xGa_{1-x})_{0.51}In_{0.49}P$. Phys. Rev. B **79**, 035329 (2009)
74. M. Eichfelder, W.-M. Schulz, M. Reischle, M. Wiesner, R. Roßbach, M. Jetter, P. Michler, Room-temperature lasing of electrically pumped red-emitting $InP/(Al_{0.20}Ga_{0.80})_{0.51}In_{0.49}P$ quantum dots embedded in a vertical microcavity. Appl. Phys. Lett. **95**, 131107 (2009)

75. S. Ates, S.M. Ulrich, A. Ulhaq, S. Reitzenstein, A. Löffler, S. Höfling, A. Forchel, P. Michler, Non-resonant dot-cavity coupling and its potential for resonant single-quantum-dot spectroscopy. Nature Photon. **3**, 724 (2009)
76. M. Kaniber, A. Laucht, A. Neumann, J.M. Villas-Bôas, M. Bichler, M.-C. Amann, J.J. Finley, Investigation of the nonresonant dot-cavity coupling in two-dimensional photonic crystal nanocavities. Phys. Rev. B **77**, 161303 (2008)
77. S. Strauf, K. Hennessy, M.T. Rakher, Y.-S. Choi, A. Badolato, L.C. Andreani, E.L. Hu, P.M. Petroff, D. Bouwmeester, Self-tuned quantum dot gain in photonic crystal lasers. Phys. Rev. Lett. **96**, 127404 (2006)

Chapter 13
GaN-Based VCSELs

Shing-Chung Wang, Tien-Chang Lu, Hao-Chung Kuo and Jun-Rong Chen

Abstract This chapter first briefly reviews the background of the development of GaN-based edge-emitting lasers and key technical issues and approaches. Then we present the design considerations and fabrication technology for the development of GaN-based vertical-cavity surface-emitting lasers (VCSELs). The technical issues and approaches for fabricating high-quality and high-reflectivity GaN distributed Bragg reflectors (DBRs) are discussed. The trade-offs among the three kinds of GaN microcavity structures are compared. Fabrication processes and key performance characteristics of hybrid and double dielectric microcavities for optically pumped GaN VCSELs are presented. The key approaches to achieve electrically pumped GaN VCSELs are analyzed and recent developments in electrically pumped GaN VCSELs are described. The future prospects of enhancing the GaN VCSEL performance and operation temperature are discussed. Finally the emerging applications for nitride-based VCSELs are briefly described.

13.1 Introduction

Gallium nitride and its most relevant alloys such as InGaN and AlGaN have many unique properties suitable for fabrications of various photon emission devices including light-emitting diodes (LEDs) and edge-emitting laser diodes (LDs). By varying the alloy composition, different photon emission can be obtained over a wide range of energy from 0.7 to 6.2 eV, covering the wavelength range from infrared to ultraviolet. In addition, the GaN-based materials have large exciton binding energy of about

S.-C. Wang, T.-C. Lu (✉), H.-C. Kuo · J.-R. Chen
Department of Photonics and Institute of Electro-Optical Engineering, National Chiao Tung University,
1001 University Road, Hsinchu 300, Taiwan
e-mail: timtclu@mail.nctu.edu.tw

R. Michalzik (ed.), *VCSELs*, Springer Series in Optical Sciences 166,
DOI: 10.1007/978-3-642-24986-0_13, © Springer-Verlag Berlin Heidelberg 2013

26 meV for bulk GaN layers [1] and about 40−50 meV for quantum-well (QW) structures [2]. This property has attracted much attention in the research field of single-photon emitters [3] and dynamical Bose–Einstein condensates [4]. Besides, the GaN material has large LO phonon energy making it a potential candidate for development of high temperature quantum cascade laser [5].

However, there are several key technical issues in realization of nitride-based laser devices. These include no suitable GaN substrate material, difficulty in p-doping, and relatively high defect densities of epitaxially grown films. In 1989, Akasaki and co-workers first realized the p-type GaN films by using Mg-doping as an acceptor impurity and activated the Mg acceptors by post low-energy electron-beam irradiation treatment [6]. Subsequently, the first GaN-based homojunction LED was reported by Akasaki et al. in 1992 [7]. Thereafter, ultra-bright InGaN/GaN double-heterostructure LEDs were demonstrated by Nakamura et al. in 1994 [8]. Most of these LED devices reported were grown on foreign substrate such as sapphire. In 1996, first GaN-based edge-emitting laser with InGaN multiple quantum wells (MQWs) was reported by Nakamura et al. [9]. This laser was operated at room-temperature (RT) under continuous-wave (CW) conditions with a relatively short lifetime. The lifetime and output power of the laser diodes were later improved to more than 10,000 h and 420 mW in 1998 [10, 11]. These breakthroughs in the edge-emitting laser performance were attributed to the improvement of crystal quality and the p-type conductivity control [12, 13]. The edge-emitting GaN-based LDs have since been rapidly developed and currently been developed successfully into commercial applications such as high density optical storage systems. However, the development of GaN-based vertical-cavity surface-emitting lasers (VCSELs) has been relatively slow even though the idea of such a VCSEL has been proposed by Iga et al. since 1979 [14]. In the following, we will discuss those critical technical issues limiting the development of GaN-based VCSELs and describe the key approaches to these issues in detail.

VCSELs have become one kind of most important semiconductor lasers due to many inherent advantages and promising applications [15–17]. In contrast with the well-developed GaAs- and InP-based red and infrared VCSELs, the lasing action of GaN-based VCSELs is mostly reported under optical pumping conditions. There are three critical difficulties in fabricating electrically pumped GaN VCSELs. One is the lack of suitable substrates, leading to much higher defect densities in GaN films. Another is the difficulty in growing high-quality and high-reflectivity GaN-based distributed Bragg reflectors (DBRs) due to the large lattice mismatch between GaN and AlN layers. The other is to obtain low-resistive p-type GaN layers, originated from the high activation energy of Mg dopants. Despite the material quality or fabrication problems, the desirable breakthrough in the realization of GaN-based VCSELs makes many research groups devoted to the growth and fabrication of GaN-based VCSELs. The first demonstration of the RT optically pumped GaN-based VCSELs has been reported by Redwing et al. in 1996 [18]. The fully epitaxial VCSEL structure consists of a 10 μm GaN active region sandwiched between 30-period $Al_{0.12}Ga_{0.88}N/Al_{0.4}Ga_{0.6}N$ DBRswith the reflectivity values of about 84–93% from

the theoretical prediction. The relatively low reflectivity results in the high threshold pumping energy of $\sim 2.0\,\mathrm{MW/cm^2}$ and the employment of thick GaN gain layer. Furthermore, Arakawa et al. fabricated an $In_{0.1}Ga_{0.9}N$ VCSEL and observed the lasing action at 77 K in 1998 [19]. The 3-λ cavity made of an $In_{0.1}Ga_{0.9}N$ active layer was grown on 35-pair $Al_{0.34}Ga_{0.66}N/GaN$ DBRs with the reflectivity of 97%. The top-DBR consisting of 6-pair TiO_2/SiO_2 multi-layer providing the reflectivity of 98% was evaporated on the top of the active layer to form the hybrid VCSEL structure (i.e., the VCSEL structure consisting of a semiconductor grown mirror and a dielectric deposited mirror). The emission linewidth significantly decreased from 2.5 to 0.1 nm after the threshold condition. Thereafter, Song et al. demonstrated a VCSEL structure consisting of InGaN MQWs and 10-pair SiO_2/HfO_2 top and bottom DBR by using laser lift-off technology in 1999 [20]. Since the reflectivity of top and bottom DBRs were 99.5 and 99.9%, respectively, the cavity quality factor (Q-factor) is larger than 600 in their experiments. In the same year, Someya et al. reported the RT lasing at blue wavelengths in hybrid GaN-based VCSELs [21]. Lasing action was observed at a wavelength of 399 nm under optical excitation and the emission linewidth decreased from 0.8 nm below threshold to less than 0.1 nm above threshold. In 2005, crack-free fully epitaxial nitride microcavity using lattice-matched AlInN/GaN DBRs has been reported by Carlin et al. [22]. The optical cavity was formed by a $3\lambda/2$ GaN cavity surrounded by lattice-matched AlInN/GaN DBRs with reflectivity values close to 99%. The cavity mode was clearly resolved with a linewidth of 2.3 nm. Other optically pumped results reported in recent years are aimed at improving the device performance and investigating the physical mechanisms [23–30]. In this chapter, we will take the research results from Wang's group as the examples to describe the performance characteristics of optically pumped GaN-based VCSELs by employing a double dielectric DBR VCSEL structure [27, 28] and a hybrid DBR VCSEL structure [29, 30]. It was not until 2008 that the first electrically pumped GaN VCSEL was demonstrated at 77 K under CW operation by Wang et al. [31] and recently the RT CW GaN VCSEL was also reported by Nichia Corporation [32].

In this section, we present the brief development history of GaN-based VCSELs and describe the recent breakthroughs in demonstration of optically pumped and electrically pumped GaN-based VCSELs. In following Sect. 13.2, we discuss the design considerations and fabrication of GaN-based VCSELs. The issues and technical approaches of fabrication of high-reflectivity GaN DBRs are highlighted. The trade-offs among the three kinds of typical GaN microcavity structure are also described. In Sects. 13.3 and 13.4, we present the fabrication processes and performance characteristics of optically pumped and electrically pumped GaN VCSELs respectively. In Sect. 13.5, the critical approaches to achieve electrically pumped GaN VCSELs are analyzed and the future prospects of enhancing the laser performance and operation temperature are discussed. Finally in Sect. 13.6, we summarize this chapter and briefly discuss the emerging applications for nitride-based VCSELs.

13.2 Design and Fabrication of GaN-Based VCSELs

The evolution of nitride-based light-emitting devices suffered many obstacles, such as the absence of lattice-matched substrates [33], low activation ratio of p-type (Al)GaN [34], large mobility difference between electrons and holes [35], crystal-structure- and strain-induced quantum-confined Stark effect (QCSE) [36], etc. These problems have been widely investigated in nitride-based LEDs and LDs. Nevertheless, the most difficult challenge for nitride-based VCSELs is the lattice-mismatched nitride-based DBRs. High-quality and high-reflectivity DBRs are necessary to achieve threshold condition due to the relatively short gain region of a VCSEL [15, 16]. In general, there are three kinds of material systems used in nitride-based DBRs, including AlN/GaN, Al(Ga)N/(Al)GaN, and AlInN/GaN. The AlN/GaN DBRs offer the highest refractive index contrast among the III-nitride compounds and provide highly reflective structures together with a large stopband width. However, the large lattice mismatch between AlN and GaN is up to 2.4%, which generally results in a tensile strain and the formation of cracks. These cracks tend to grow into V-shaped grooves and seriously affect the reflectivity of the DBR due to scattering, diffraction, and absorption. To prevent the formation of cracks, the $Al_xGa_{1-x}N/Al_yGa_{1-y}N$ system is usually used to reduce the strain in the whole DBR structure. Nevertheless, the refractive index contrast decreases with increasing Al composition in GaN or Ga composition in AlN, which leads to a reduced stopband width and the requirement of increased number of pairs to achieve high reflectivity. An alternative approach was proposed by Carlin and Ilegems [37]. They demonstrated high-reflectivity AlInN/GaN DBRs near lattice matched to GaN. The 20-pair DBRs exhibited a peak reflectivity over 90% and a 35 nm stopband width at 515 nm. Although this kind of DBR has been reported, the growth of high-quality AlInN film is difficult due to the composition inhomogeneity and phase separation in AlInN, which results from large mismatch of covalent bond length and growth temperature between InN and AlN [38]. The related progress in the growth of highly reflective nitride-based DBR can be found in the review paper [39].

In order to obtain high-reflectivity and large-stopband DBRs for nitride-based VCSELs, Wang's group is keeping on the study of growing high-quality AlN/GaN DBRs. In their previous study, they reported the growth of crack-free AlN/GaN DBRs with insertion of 5.5 periods of AlN/GaN superlattice (SL) [40]. Figure 13.1 shows cross-sectional transmission electronic microscopy (TEM) images of the SL DBR structure. The lighter layers represent AlN layers while the darker layers represent GaN layers. The interfaces between AlN and GaN layers are sharp and abrupt in low-magnification TEM image, as shown in Fig. 13.1a. The arrows indicate the SL insertion positions. Figure 13.1b shows the cross-sectional TEM image of one set of 5.5-pairs AlN/GaN SL insertion layers under high magnification. Detailed observations by this TEM image reveal that the V-shaped defects in the AlN layers are always observable at the GaN-on-AlN interfaces and filled in with GaN. These V-shaped defects have been reported earlier and could be due to various origins such as stacking mismatch boundaries and surface undulation [41]. The GaN/AlN SL

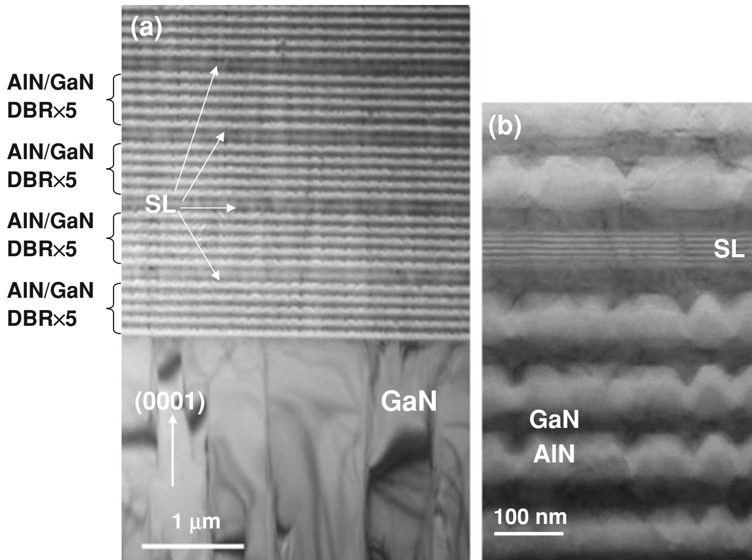

Fig. 13.1 **a** Low-magnification cross-sectional TEM image of the SL DBR structure. **b** High-magnification cross-sectional TEM image of the SL DBR structure. The 5.5-pair AlN/GaN SL can be observed clearly

insertion layers were ended by one more AlN layer to identify the changing from the AlN layer to the GaN layer. Here a set of GaN/AlN SL insertion layers can be seen as a quasi alloy of an $Al_xGa_{1-x}N$ layer for a low refractive index quarter-wave layer in the DBR structure. The effect of the SL insertion layers on the structural characteristics of the nitride DBRs is relevant to the mechanism of strain relaxation. The relaxation process of AlN/GaN SL layers keeps relatively better coherency, i.e., GaN and AlN SL layers are fully strained against each other. Therefore, the SLs behave like effective bulk layers which have in-plane lattice constant between bulk GaN and AlN DBR layers [42]. The subsequent growth of five-pair AlN/GaN DBR could follow the AlN/GaN SLs, which will make the DBR layers suffer relatively smaller strain as compared with DBR layers grown on bulk GaN layer. Consequently, the insertion of the SL layers during the growth of the DBR layers could act as strain buffers between DBRs and the underlying GaN bulk layer because the in-plane lattice constants of the SL layers are close to those of the AlN layers in the DBRs.

Another consideration of the VCSEL design is the thickness and position of the InGaN/GaN MQWs inside the GaN microcavity. Typically, the cavity length of VCSELs is on the order of few half operating wavelengths. In such a short cavity device, the electromagnetic waves would form standing wave patterns with nodes (electromagnetic wave intensity minima) and anti-nodes (electromagnetic wave intensity maxima) within the GaN microcavity. The location of the InGaN/GaN MQWs with respect to the anti-nodes can significantly affect the coupling of laser mode with the cavity field. The proper alignment of the MQWs region with the

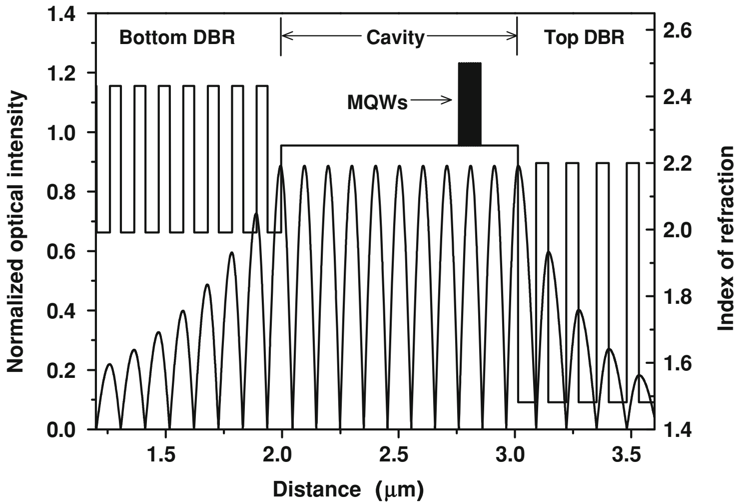

Fig. 13.2 Schematic representation of the relation between refractive index and longitudinal optical field for a typical hybrid DBR VCSEL

anti-nodes of the cavity standing wave field patterns will enhance the coupling and reduce laser threshold condition. As a result, the precise layer thickness control in the VCSEL fabrication is important. Wang's group used ten pairs InGaN/GaN MQWs to form a $\lambda/2$ optical thickness to fully overlap with one standing wave pattern in order to have more thickness tolerance during the fabrication and to have a higher longitudinal confinement factor with respect to the total cavity length. Figure 13.2 shows the refractive index value in each layer and the simulated standing wave patterns inside the hybrid DBR VCSEL structure. Since the bottom AlN/GaN DBR and the GaN cavity are epitaxially grown, the precise layer thickness can be controlled by the in-situ monitoring system. By fixing a specific monitor wavelength, the thickness of each quarter-wavelength GaN and AlN, and GaN cavity can be precisely controlled by following the reflectance signals during the metal organic chemical vapor deposition (MOCVD) growth. The total reflectance signal at 460 nm for the half-cavity structure is shown in Fig. 13.3. The relative reflectivity is gradually saturated with increasing number of DBR pairs, as shown in Fig. 13.3a. The AlN/GaN SL layers are inserted in to AlN/GaN DBR at the time indicated as SL. The cavity thickness and positions of MQWs can also be in-situ monitored by observing the oscillation periods during the growth, as shown in Fig. 13.3b. After the growth of nitride-based half cavity, an eight-pair of Ta_2O_5/SiO_2 dielectric mirror was deposited by electronic beam evaporation as the top DBR reflector to form the hybrid microcavity.

Because of the difficulty of growing high-quality and high-reflectivity nitride-based DBRs, the possible design of GaN based blue-VCSELs has been proposed by Iga in 1996 [43]. The corresponding structural designs for nitride-based VCSELs can be classified into three major types, as shown in Fig. 13.4. The first one is

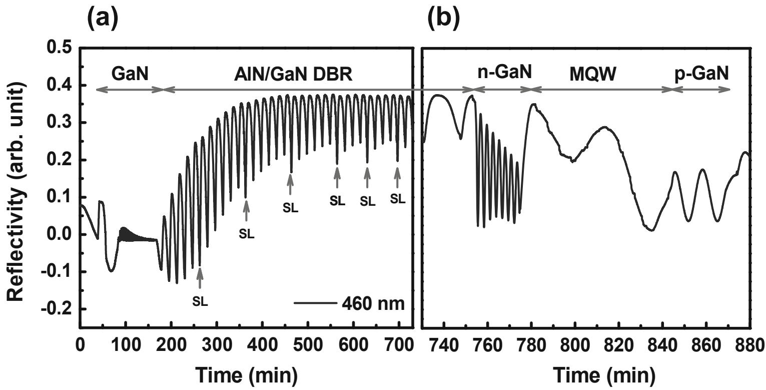

Fig. 13.3 **a** In-situ normal reflectance measurement during the growth of the AlN/GaN DBR and GaN microcavity with InGaN/GaN MQWs by a fixed measurement wavelength of 460 nm. The AlN/GaN superlattices are inserted into AlN/GaN DBR at the time indicated as SL. **b** Enlarged part of reflectance signals during the growth of the GaN microcavity consisted of n-GaN, InGaN/GaN MQWs and p-GaN layers

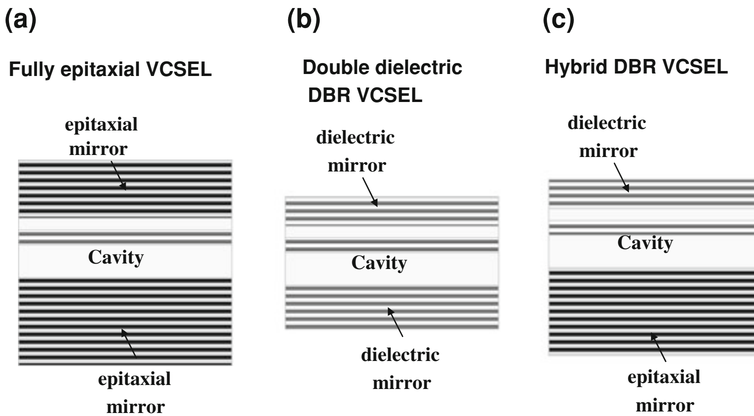

Fig. 13.4 Three kinds of GaN-based VCSEL structures. **a** Fully epitaxial VCSELs. **b** Double dielectric DBR VCSELs. **c** Hybrid DBR VCSELs

monolithic grown vertical resonant cavity consisting of epitaxially grown III-nitride top and bottom DBRs (Fig. 13.4a). The advantage of the fully epitaxial microcavity is the controllable cavity thickness which is beneficial to fabricate microcavity structure. However, VCSELs require extremely high-reflectivity DBRs (i.e., high cavity Q-factor). The fully epitaxial nitride microcavity is very difficult to achieve this requirement although the related results have been reported [22, 44]. The second one is vertical resonant cavity consisting of dielectric top and bottom DBRs (Fig. 13.4b). The double dielectric DBR VCSELs can exhibit high cavity Q-factors because of the high-reflectivity DBR, which are relatively easy to fabricate. The large refractive

index contrast in dielectric materials can make high-reflectivity and large-stopband DBR with less number of pairs. The drawback of the double dielectric DBR VCSEL is the difficulty of controlling the cavity thickness precisely and the complicated fabrication process due to the employment of laser lift-off technique [27]. In addition, the thickness of the GaN cavity should keep as thick as possible to avoid the damage of the InGaN/GaN MQWs during the laser lift-off process. Such a thick cavity length could increase the threshold condition and reduce the microcavity effect. Although the cavity layer can be polished and thinned using chemical-mechanical polishing (CMP) technique, the smooth surface is another key issue for high-quality GaN cavity [32]. The third one is the VCSEL structure combining an epitaxially grown DBR and a dielectric type DBR which compromises the advantages and disadvantages of the above two VCSEL structures (Fig. 13.4c) [29, 30]. The hybrid DBR VCSEL can eliminate the complex process and keep the feasibility of coplanar contacts with dielectric DBR mesas for the future electrically pumped VCSEL applications. The major requirement for the fabrication of hybrid DBR VCSEL is to grow high-reflectivity and high-quality nitride-based DBRs. Wang's approaches to the realization of GaN-based VCSELs are mainly based on the double dielectric DBR VCSELs and the hybrid DBR VCSELs. The device performances of these two VCSEL structures will be analyzed and discussed in the following sections.

13.3 Optically Pumped GaN-Based VCSELs

13.3.1 Optically Pumped Hybrid DBR VCSEL

The hybrid DBR GaN-based VCSELs were grown in a low-pressure high-speed rotating-disk MOCVD system. Two-inch diameter (0001)-oriented sapphire substrates were used for the growth of AlN/GaN DBR and cavity. During the growth, trimethylgallium (TMGa), trimethylindium (TMIn) and trimethylaluminum (TMAl) were used as group III source materials and ammonia (NH_3) as the group V source material. Then, the growth process was as follows. The substrate was thermally cleaned in hydrogen ambient for 5 min at 1100°C, and then a 30 nm thick GaN nucleation layer was grown at 500°C. The growth temperature was raised up to 1100°C for the growth of a 2 μm GaN buffer layer. Then the 29 pairs of AlN/GaN DBR with six AlN/GaN superlattice insertion layers were grown under the fixed chamber pressure of 100 Torr similar to the previous reported growth conditions [40]. In order to reduce the tensile strain between the AlN and GaN, they inserted one superlattice into each five DBR periods at first twenty pairs of DBR. Then the superlattice was inserted into each three DBR periods for the remaining nine pairs of DBR to reduce the tensile strain. The overall AlN/GaN DBRs has 29 pairs with six superlattice insertion layers. On top of this 29-pair AlN/GaN DBR is a 790 nm-thick Si-doped n-type GaN cladding layer. The MQW active region consists of ten 2.5 nm-thick $In_{0.2}Ga_{0.8}N$ QWs and 7.5 nm-thick GaN barrier layers. A 120 nm-thick Mg-doped

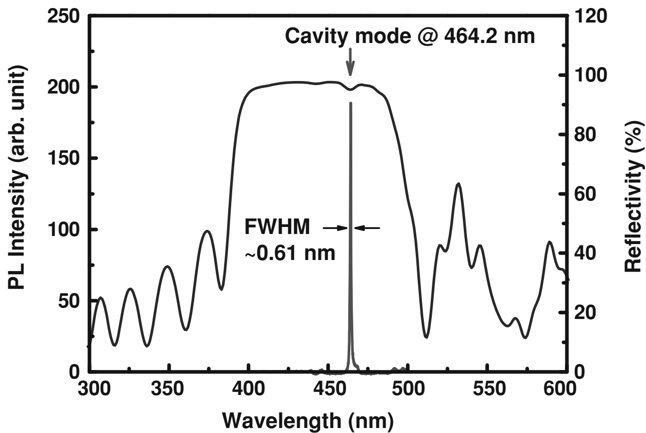

Fig. 13.5 Room-temperature reflectivity spectrum and PL spectrum of whole GaN-based microcavity

p-type GaN cladding layer was grown on top of the MQWs to form a 5-λ cavity in optical thickness for center wavelength of 460 nm. Here, they chose 460 nm as the designed lasing wavelength mainly due to the consideration of the higher absorption of the indium tin oxide (ITO) layer at shorter wavelength for the further electrically pumped GaN VCSELs. Besides, the grown epilayer thickness is easier to monitor at this wavelength by the in-situ monitor system. After the growth of nitride-based half cavity, an eight pairs of Ta_2O_5/SiO_2 dielectric mirror was deposited by electronic beam evaporation as the top DBR reflector to form the hybrid microcavity.

The experimental results obtained from the performance characteristics of optically pumped VCSELs provide useful information for further development of electrically pumped VCSELs. It allows the estimation of the threshold condition of the designed VCSEL structure and provides better understanding of the material properties. From the reflectivity spectrum of the full VCSEL structure, the accuracy of the cavity thickness can be assured. Figure 13.5 shows the RT reflectivity spectrum of whole microcavity under near normal incidence. The peak reflectivity is about 97% with a large stopband of 70 nm originated from the large refractive index contrast between Ta_2O_5 and SiO_2 layers. The irregular long wavelength oscillations of the reflectivity spectrum arise from the modulation of the respective top and bottom DBR spectra. On the other hand, the short wavelength oscillator is relatively regular, which only results from the top dielectric DBR since the short-wavelength light is absorbed by GaN layer. The photoluminescence (PL) emission spectrum of the full microcavity was measured at room temperature and shown in Fig. 13.5 as well. The excitation source is a 325 nm He-Cd laser and the cavity resonance mode at 464.2 nm with a full-width at half-maximum (FWHM) value of 0.61 nm is clearly observed. The cavity mode dip is located at reflectivity curve corresponding to the emission peak. This indicates that the InGaN/GaN MQWs emission peak was well aligned

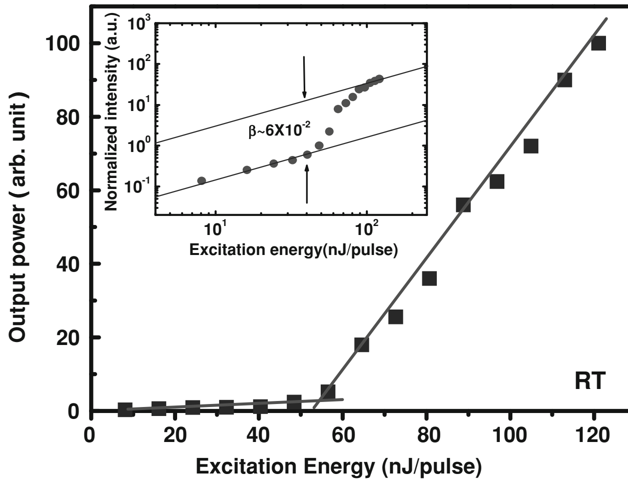

Fig. 13.6 Laser emission intensity as a function of the exciting energy at room temperature conditions for the hybrid DBR VCSEL. (*Inset*) Laser emission intensity versus pumping energy in logarithmic scale. The difference between the heights of the emission intensities before and after the threshold corresponds roughly to the value of β. The dash lines are guides for the eye

with the hybrid microcavity. The cavity Q-factor was estimated from the $\lambda/\Delta\lambda$ to be about 760.

To examine the lasing action, they measured the emission intensity of the hybrid microcavity with increasing pumping power using a microscopic optical pumping system. The optical pumping of the samples was performed using a frequency-tripled Nd:YVO_4 355 nm pulsed laser with a pulse width of $\sim$0.5 ns at a repetition rate of 1 kHz. The pumping laser beam with a spot size ranging from 30 to 60 μm was incident normal to the VCSEL sample surface. The light emission from the VCSEL sample was collected using an imaging optic into a spectrometer/CCD (Jobin-Yvon Triax 320 Spectrometer) with a spectral resolution of $\sim$0.1 nm for spectral output measurement. Figure 13.6 shows the emission intensity at RT from the hybrid GaN-based VCSEL as a function of the excitation energy. A distinct threshold characteristic can be found at the threshold excitation energy of $\sim$55 nJ corresponding to an energy density of 7.8 mJ/cm^2. Then the laser output increased linearly with the pumping energy beyond the threshold. A dominant laser emission line at 448.9 nm appears above the threshold pumping energy.

The laser emission spectral linewidth reduces as the pumping energy above the threshold energy and approaches 0.17 nm at the pumping energy of 82.5 nJ. In order to extract the spontaneous coupling factor β of this cavity from Fig. 13.6, they normalized the vertical scale and re-plotted it in a logarithm scale as shown in the inset in Fig. 13.6. The difference between the heights of the emission intensities before and after the threshold roughly coincides with the value of β [45]. The β value of this hybrid GaN-based VCSEL estimated from the inset of Fig. 13.6 is

about 6×10^{-2}. The alternative approach to estimating the β value is based on the approximation equation which can be expressed by [46, 47]

$$\beta = \frac{F_p}{1 + F_p} \tag{13.1}$$

with

$$F_p = \frac{3}{4\pi^2} \frac{Q}{V_c/(\lambda/n)^3} \tag{13.2}$$

where F_p is the Purcell factor, Q is the cavity quality factor, λ is the laser wavelength, V_c is the optical volume of laser emission, and n is the refractive index. Since the photoluminescence spectrum of the hybrid DBR VCSEL showed a narrow emission peak with FWHM of 0.61 nm, cavity quality factor was estimated to be 760. The refractive index is 2.45 for the GaN cavity. For the estimation of the optical volume, they used the spot size of the laser emission image which was about 3 μm and the cavity length of about 9.5λ with considering the penetration depth of the DBRs. By using these parameters, the Purcell factor of about 2.9×10^{-2} was obtained and they estimated the β value to be about 2.8×10^{-2}, which has the same order of magnitude as the above β value estimated from the inset in Fig. 13.6. This β value is three order of magnitude higher than that of the typical edge emitting semiconductor lasers (normally about 10^{-4}–10^{-5} [47]) indicating the enhancement of the spontaneous emission into a lasing mode by the high quality factor microcavity effect in the VCSEL structure. The variation of the laser emission intensity with the angle of the polarizer was also measured and showed nearly a cosine square variation. The result shows that the laser beam has a degree of polarization of about 89%, suggesting a near linear polarization property of the laser emission.

13.3.2 Optically Pumped Dielectric DBR VCSEL

The schematic fabrication flowchart for dielectric DBR VCSELs is shown in Fig. 13.7. The layer structure of the GaN-based cavity, grown on a (0001)-oriented sapphire substrate by MOCVD is described as followed: a 30 nm nucleation layer, a 4 μm GaN bulk layer, MQWs consisting of 10 periods of 5 nm GaN barriers and 3 nm $In_{0.1}Ga_{0.9}N$ wells, and a 200 nm GaN cap layer. The peak emission wavelength of the MQWs for the as-grown sample was obtained to be 416 nm. Then, the dielectric DBR consisting of 6-pair SiO_2/TiO_2 was evaporated on the top of GaN-based cavity. The stopband center of the DBR was tuned to 450 nm. The reflectivity of the SiO_2/TiO_2 DBR at 414 nm is obtained to be 99.5%. Next, in order to enhance the adhesion between the epitaxial layers and silica substrate, an array of disk-like patterns with the diameter of 60 μm was formed by standard photolithography process and the SiO_2/TiO_2 DBR mesas were formed by the buffer oxide etcher. The wafer

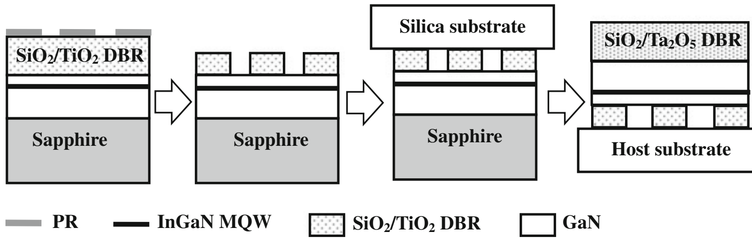

Fig. 13.7 Schematic process flowchart of the dielectric DBR VCSELs incorporating two dielectric DBRs fabricated by the laser lift-off technique

was then mounted onto a silica substrate, which is nearly transparent to the wavelength of the excitation light and the VCSEL. A KrF excimer laser radiation at 248 nm was guided into the sample from back side of the sapphire to separate the sapphire from the epitaxial layers [48]. After the laser lift-off process, the sample was dipped into the H_2SO_4 solution to remove the residual Ga on the exposed GaN buffer layers. In the next step, the sample was lapped and polished by diamond powders to smooth the GaN surface since the laser lift-off process left a roughened surface. The mean surface roughness of the polished GaN surface measured by the atomic force microscopy (AFM) is about 1 nm over a scanned area of $20 \times 20\ \mu m^2$. However, to prevent the possible damage of the quality in MQWs during the lapping process, the 4 μm GaN bulk layer was preserved. Finally, the second DBR consisting of 8-pair SiO_2/Ta_2O_5 was deposited on the top of the polished GaN surface. The reflectivity of the SiO_2/Ta_2O_5 DBR at 414 nm is 97%. The stopband center of the DBR was also tuned to 450 nm. The thickness of the whole epitaxial cavity was equivalent to the optical thickness of 24.5 emission wavelengths. The optical thickness of the MQWs covered nearly half of the emission wavelength right between two adjacent nodes.

Figure 13.8 shows the laser emission intensity from the dielectric DBR VCSEL as a function of the pumping energy at room temperature conditions. A clear evidence of threshold condition occurred at the pumping energy of $E_{th} = 270$ nJ corresponding to an energy density of 21.5 mJ/cm^2. The output laser intensity from the sample increased linearly with the pumping energy level beyond the threshold energy. The estimated carrier density at the threshold is in the order of 10^{20} cm^{-3} assuming that the pumping light with the emission wavelength of 355 nm has experienced a 60% transmission through the SiO_2/Ta_2O_5 DBR layers and undergone a 98% absorption in the thick GaN layer. According to the report by Park [49], the gain coefficient of InGaN at this carrier density level is about 10^4 cm^{-1}. Wang et al. estimated the threshold gain g_{th} of the VCSEL using the equation $g_{\text{th}} \geq 1/(\xi L_a) \times \ln(1/(R_1 R_2))$, where ξ is the axial enhancement factor, L_a is the total thickness of the InGaN MQWs, and R_1 and R_2 are the reflectivities of the dielectric DBRs. Since the active region covers half of the emission wavelength, ξ is unity. They obtained an estimated gain coefficient of about 10^4 cm^{-1} which is consistent with the above g_{th} value estimated from the carrier density. This also proved that the quality of the MQWs had been kept after the laser lift-off and lapping process. The inset shown in Fig. 13.8 is the

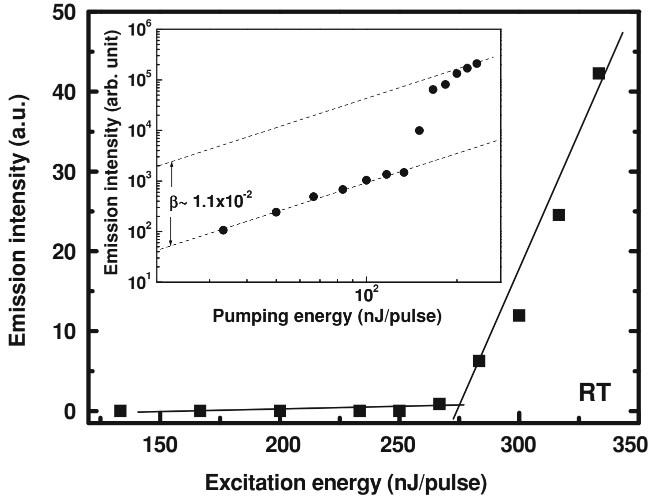

Fig. 13.8 Laser emission intensity as a function of the exciting energy at room temperature conditions for the dielectric DBR VCSEL. *Inset*: Laser emission intensity versus pumping energy in logarithmic scale. The difference between the heights of the emission intensities before and after the threshold corresponds roughly to the value of β. The dash lines are guides for the eye

laser emission intensity as the function of pumping energy in a logarithmic scale. From the logarithmic data, the spontaneous coupling factor β was estimated from the difference between the heights of the emission intensities before and after the threshold condition. The estimated β was about 1.1×10^{-2}. Since the cavity volume of this dielectric DBR VCSEL is large than the above hybrid DBR VCSEL, the Purcell factor and the spontaneous coupling factor shall be lower accordingly.

Figure 13.9 shows the evolution of the VCSEL emission spectrum with the pumping energy at room temperature. When the pumping energy is below the threshold, the spontaneous emission spectrum shows multiple cavity modes. The mode spacing is about 7 nm corresponding to a cavity length of 4.3 μm, which is nearly equal to the thickness of the epitaxial cavity. The linewidth of a single cavity mode is 0.8 nm as shown in the inset of Fig. 13.9. The cavity quality factor estimated from the linewidth is about 518. Considering the optical absorption of GaN layer, an estimated effective cavity reflectivity based on this Q-factor is about 97%, which is close to the cavity reflectivity formed by the two dielectric DBRs. This result indicates the laser cavity structure was nearly intact after the laser lift-off process. As the pumping energy increased above the threshold, a dominant laser emission line appeared at 414 nm with a narrow linewidth of about 0.25 nm. The lasing wavelength is located at one of cavity modes near the peak emission wavelength of the InGaN MQWs. The laser emission polarization contrast between two orthogonal directions was measured as well. A degree of polarization of about 70% is estimated. The lower degree of polarization in comparison to the hybrid DBR VCSEL could be due to the smaller Q-factor for this dielectric DBR VCSEL.

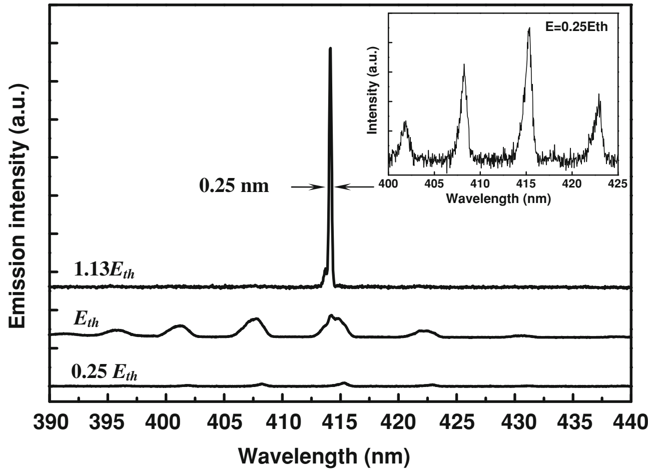

Fig. 13.9 Emission spectra from the dielectric DBR VCSEL at various pumping energy. The lasing emission wavelength is 414 nm with a linewidth of 0.25 nm. *Inset*: Rescaled emission spectrum under pumping power of 0.25 E_{th}

13.4 Electrically Pumped GaN-Based VCSELs

13.4.1 Electrically Pumped HybridDBR VCSEL

To fabricate the VCSEL structure for electrical excitation, additional processes for current injection are necessary. Since the epitaxially grown bottom AlN/GaN DBR was un-doped and non-conductive, the epitaxially grown wafer should be further processed to form the intra-cavity co-planar p- and n-contacts for current injection. First, the mesa region was defined by photo-lithography and etched using an inductively coupled plasma reactive ion etching system with Cl_2/Ar as the etching gases to expose the n-GaN layer for the n-contact formation. Then a 0.2-μm thick SiN_x layer was used as the mask to form a current injection and light emitting aperture of 10 μm in diameter, which was then deposited an ITO as the transparent contact layer. Since the ITO locates just next to the VCSEL microcavity, the thickness of 240 nm corresponding to 1-λ optical length ($\lambda = 460$ nm) has to be accurate to match the phase condition and reduce the microcavity anti-resonance effect. The ITO was annealed at 525°C under the nitrogen ambient to reduce the contact resistance as well as to increase transparency thus reducing the internal cavity loss. A high transmittance of about 98.6% at $\lambda = 460$ nm was measured for the deposited ITO after the annealing. Then the metal contact layer was deposited by the electron beam evaporation using Ti/Al/Ni/Au (20/150/20/1000 nm) and Ni/Au (20/1000 nm) as the n-type electrode and p-type electrode to form co-planar intra-cavity contacts, respectively. Finally, an eight-pair Ta_2O_5/SiO_2 dielectric DBR (measured reflectivity of about 99% at $\lambda = 460$ nm) was deposited on top of the ITO layer to

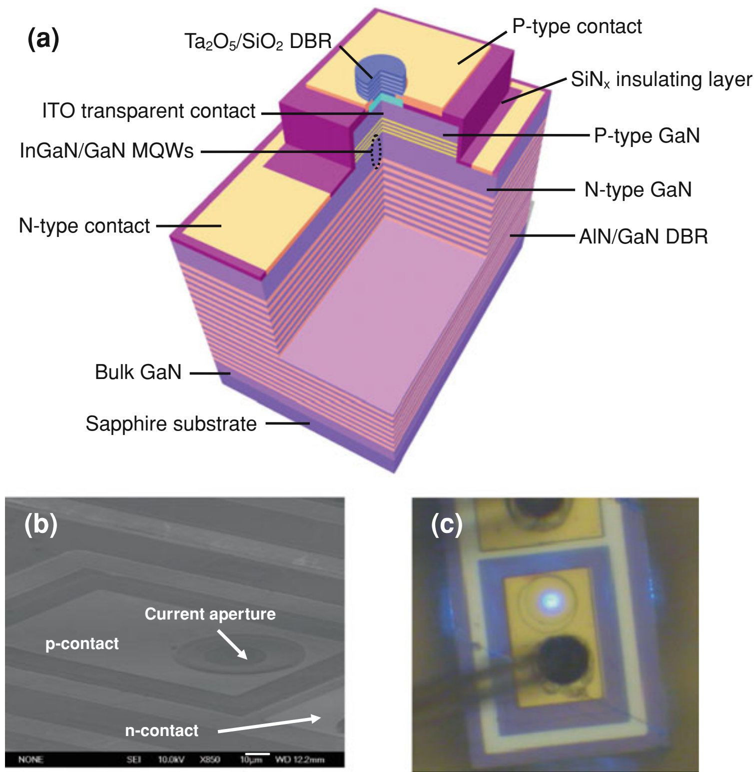

Fig. 13.10 Structure of electrically pumped hybrid GaN VCSEL. **a** The schematic diagram of the intra-cavity GaN VCSEL. **b** SEM image for the VCSEL with the intra-cavity with two co-planar p- and n-contacts for current injection. **c** The vertical surface emission image of a GaN VCSEL chip at an injection current of 1 mA. The crack line under the p-contact wire bond was occurred during the chipping process

form the top DBR mirror and complete the full hybrid microcavity VCSEL device. Figure 13.10a shows the schematic of the electrically pumped hybrid GaN-based VCSEL structure. Figure 13.10b shows the scanning electron microscopy (SEM) image of the completed VCSEL devices. For VCSEL performance characterization, the fabricated VCSEL devices were diced into an individual device size of $120\,\mu m \times 150\,\mu m$ and packaged into the TO-can. The packaged VCSEL device was mounted inside a cryogenic chamber for testing under the 77 K condition. Figure 13.10c shows the optical microscopy image of a GaN VCSEL sample device at an injection current of 1 mA. The GaN VCSEL sample was placed inside a liquid nitrogen cooled chamber at 77 K and tested under CW current injection condition using a CW current source (Keithley 238). The emission light was collected by a $25\,\mu m$ diameter multimode fiber using a microscope with a 40× objective (numerical aperture = 0.6) and fed into the spectrometer (Triax 320). The system has a focal distance

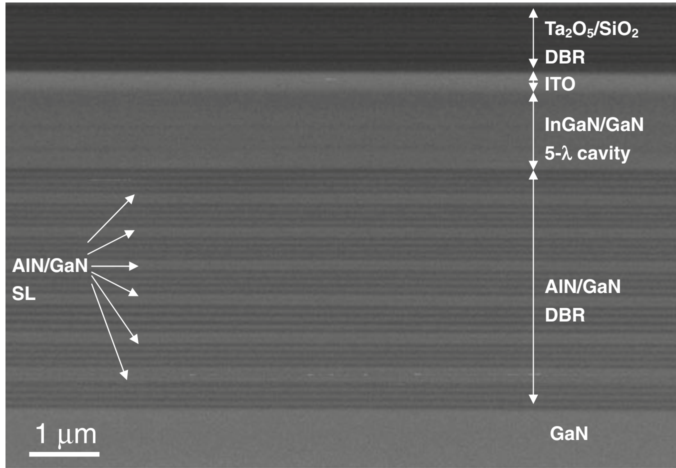

Fig. 13.11 Cross-sectional SEM image of the whole hybrid GaN-based VCSEL structure with hybrid DBRs, MQWs, and ITO layer

of 320 mm and a grating of 1800 lines/mm with a spectral resolution of 0.15 nm. The output from the spectrometer was detected by a charge-coupled device (CCD) to record the emission spectrum. The spatial resolution of the imaging system was about 1 μm as estimated by the diffraction limit of the objective lens. The cross-sectional SEM image of the whole hybrid VCSEL structure is shown in Fig. 13.11.

Figure 13.12a shows the reflectivity spectra of crack-free 29-pair AlN/GaN DBR with six SL insertion layers and 8-pair Ta_2O_5/SiO_2 DBR, respectively. A high peak reflectivity of 99.4% with a spectral bandwidth of ~25 nm was observed from the 29-pair AlN/GaN DBR. The flat-topped stopband indicates the high crystal quality of the AlN/GaN DBRs. The 8-pair Ta_2O_5/SiO_2 DBR shows a peak reflectivity of about 99% at 460 nm. The hybrid microcavity quality factor Q of the fabricated GaN VCSEL without the ITO layer was estimated from the PL spectrum of the VCSEL structure as shown in Fig. 13.12b. The VCSEL structure was also excited by a CW 325 nm He-Cd laser with a laser spot size of about 1 μm in diameter. From the PL emission peak of 454.3 nm and a narrow linewidth of 0.21 nm, the cavity Q-factor can be calculated by $\lambda/\Delta\lambda$ to be about 2200. This Q value is larger than that of the previous optically pumped VCSEL structure, which may originates from the improvement of AlN/GaN DBR reflectivity and the better sample quality. On the other hand, the Q value is slightly higher than the value obtained from the whole VCSEL structure with intra-cavity ITO contact layer due to the additional absorption loss of the ITO.

Figure 13.13a shows the light output power versus injection current and current-voltage characteristics (typical L-I-V characteristics of a laser) of the VCSEL sample at 77 K. The turn-on voltage is about 4.1 V, indicating the good electrical contact of

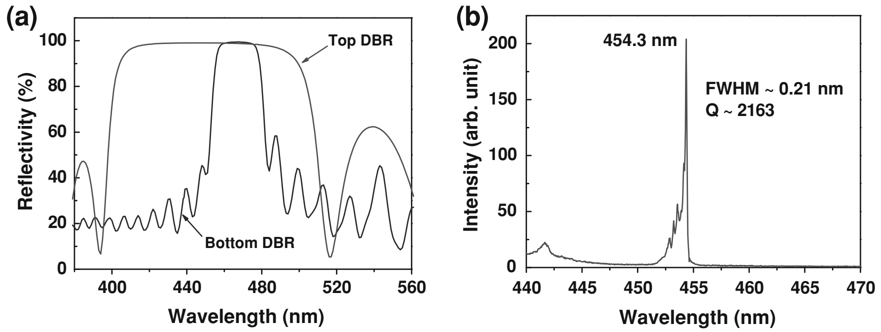

Fig. 13.12 **a** The reflectivity spectra of top and bottom DBRs show that the highest peak reflectivity of bottom and top DBR is about 99.4 and 99%, respectively. **b** The PL spectrum of the GaN VCSEL structure excited by a CW He-Cd laser (325 nm) at room temperature

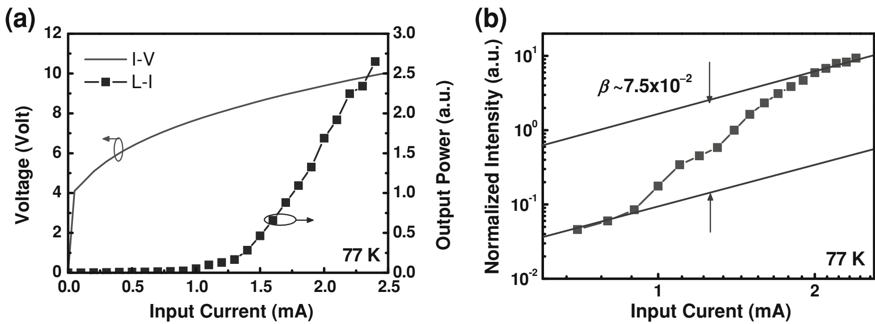

Fig. 13.13 **a** The light output intensity versus injection current and current-voltage characteristics of GaN VCSEL measured under the CW condition at 77 K. **b** The logarithm light output intensity as a function input current at 77 K. The two solid lines are guides for the eye

the ITO transparent layer and the intra-cavity structure. The series resistance of the VCSEL is about 1200 Ω at the driving current of 2.5 mA due to the small current injection aperture. The laser light output power showed a distinct threshold characteristic at the threshold current I_{th} of about 1.4 mA then increased linearly with the injection current beyond the threshold. The threshold current density is estimated to be about 1.8 kA/cm^2 for a current injection aperture of 10 μm in diameter. The corresponding threshold carrier density is about 2.6×10^{19} cm^{-3}, estimated by assuming that the carrier lifetime of InGaN MQW is 6.4 ns and the internal quantum efficiency is 0.9 at 77 K [50]. However, according to the observation from CCD image, the injected carriers are not uniformly spreading over the whole 10 μm current aperture, resulting in the spatial non-uniformity in the emission intensity [28]. The actual area for carrier localizations appearing in the current aperture should be much smaller than the 10 μm current aperture. The carrier localization area was estimated to be about 30 − 50% of the total aperture. Then the carrier density for the

lasing spots should be in the range of 5.2–8.7 $\times$ 10^{19} cm^{-3}. Furthermore, they also estimated the threshold gain coefficient g_{th} of the current injection VCSEL operated at 77 K using the equation:

$$g_{\text{th}} \geq \frac{L_{\text{eff}} - d_a}{d_a} \langle \alpha_i \rangle + \frac{1}{2d_a} \ln \left(\frac{1}{R_1 R_2} \right) \quad (13.3)$$

where L_{eff} is the effective cavity length, $\langle \alpha_i \rangle$ is the average internal loss inside the cavity, d_a is the total thickness of the multiple quantum well and R_1, R_2 are the reflectivities of the top and bottom DBR mirrors, respectively. Since the internal loss inside the cavity mainly came from the ITO absorption, a threshold gain coefficient value was obstained to be about 8.8 $\times$ 10^3 cm^{-1}, which is a reasonable value for the carrier density in the range of 5.2–8.7 $\times$ 10^{19} cm^{-3}. Furthermore, the spontaneous emission coupling factor β of the VCSEL sample was estimated from Fig. 13.13b, which is the logarithm plot of the Fig. 13.13a. The extracted β value is about 7.5 $\times$ 10^{-2} for the GaN VCSEL. Moreover, the β value was also estimated from the Purcell factor F_p using the approximation equation as that shown in expressions (13.1) and (13.2). The cavity Q value is about 1800 based on the emission linewidth of 0.25 nm near the threshold. The optical volume V_c is estimated to be about 1.2 $\times$ 10^{-11} cm^3 for an emission spot size measured to be about 3 μm. The cavity length is about 10.5λ considering the thickness of the ITO and the penetration depth of the DBRs. By using these parameters, a Purcell factor could be estimated to be about 7.9 $\times$ 10^{-2} and an estimated β value of about 7.4 $\times$ 10^{-2} was then obtained. This value is close to that obtained above from Fig. 13.13b. The high β value of the microcavity VCSEL could be responsible for low threshold operation of the laser.

Figure 13.14 shows the laser emission spectrum at various injection current levels. A dominant single laser emission line at 462.8 nm appears above the threshold current. The inset in Fig. 13.14 shows the light emission linewidth at various injection current levels. The laser emission spectral linewidth reduces suddenly with the injection current above the threshold current and approaches the spectral resolution limit of 0.15 nm at the injection current of 1.7 I_{th}. Another inset in Fig. 13.14 shows the CCD image of the spatial laser emission pattern across the 10 μm emission aperture at a slightly below the threshold injection current of 1 mA. The non-uniform emission intensity across the emission aperture with several bright emission spots was observed. Earlier report showed that InGaN MQWs tend to have indium inhomogeneity [51]. Therefore, the non-uniformity in the emission intensity across the aperture could be due to the indium non-uniformity that creates non-uniform spatial gain distribution in the emitting aperture. Actually, the lasing action mainly arises from those spots with brightest intensity as indicated in the inset of Fig. 13.14. The spatial dimension of these bright spot clusters is only about few μm in diameter. Similar result was also observed and reported recently for the optically pumped GaN VCSELs [28]. The polarization characteristics and far-field pattern (FFP) of the laser emission were also measured. The laser emission has a degree of polarization of about 80% and the FWHM of the FFP is about 11.7° in both horizontal and vertical directions.

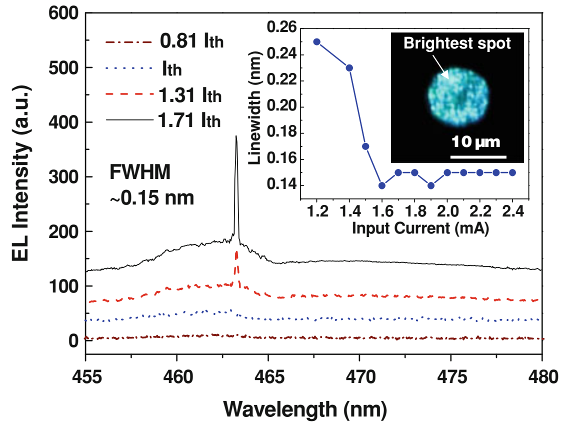

Fig. 13.14 The laser emission spectrum at different injection current levels measured at 77 K. *Inset*: The light emission linewidth at various injection current levels and the CCD image of the emission from the aperture

The further breakthrough of CW electrically pumped hybrid DBR VCSELs has been achieved at RT by Wang's group in 2010 [52, 53]. A thin ITO layer of 30 nm and a thin heavily doped p-type InGaN contact layer are the main improvements in device structures for reducing the optical loss and the contact resistance. Moreover, an AlGaN electron blocking layer on the top of the InGaN MQWs was employed to prevent the electron leakage current [54]. At 300 K, the laser has a threshold current at 9.7 mA corresponding to 12.4 kA/cm^2. The laser emission wavelength is 412 nm with a linewidth of about 0.5 nm. The laser has an estimated spontaneous emission coupling factor of about 5×10^{-3}.

13.4.2 Electrically Pumped Dielectric DBR VCSEL

The RT CW electrically pumped dielectric DBR VCSEL was firstly demonstrated by Nichia Corporation in 2008 [32]. The VCSEL structure was grown on a (0001)-oriented sapphire substrate by MOCVD. The active region consisted of two-pair 9 nm-thick InGaN QWs and 13 nm-thick GaN barrier layers. For the purpose of electrical pumping, an 8 μm current aperture was formed by photolithography process. They employed a 50 nm ITO layer as a p-type contact and current spreading layer. Subsequently, an 11.5-pair SiO_2/Nb_2O_5 DBR was deposited to form the backside mirror. The sample was then bonded on a Si substrate and the sapphire substrate was removed by laser lift-off technique. Then, the n-type GaN was thinned to be about 7λ using CMP technique. Finally, a 7-pair SiO_2/Nb_2O_5 DBR was formed to complete the VCSEL structure. Figure 13.15 shows the schematic sketch of the GaN-based dielectric DBR VCSEL with a vertical current injection configuration.

Figure 13.16a shows the light output intensity versus injection current and current-voltage characteristics of the dielectric DBR VCSEL. The lasing behavior was clearly observed and the threshold current was 7.0 mA. The output power was about 0.14 mW

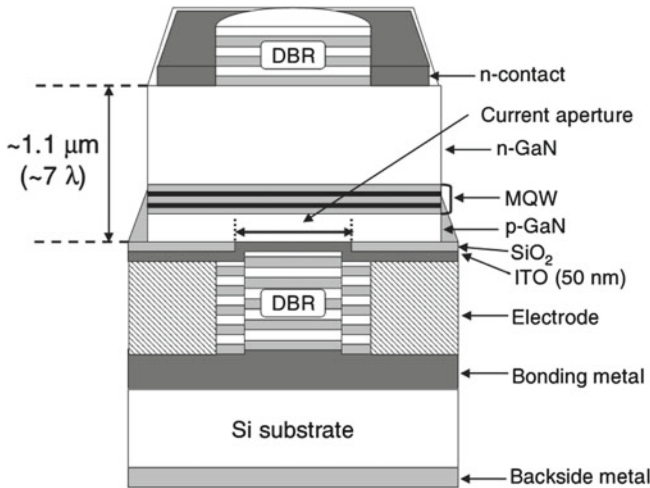

Fig. 13.15 Schematic sketch of the GaN-based dielectric DBR VCSEL with a vertical current injection configuration [32]

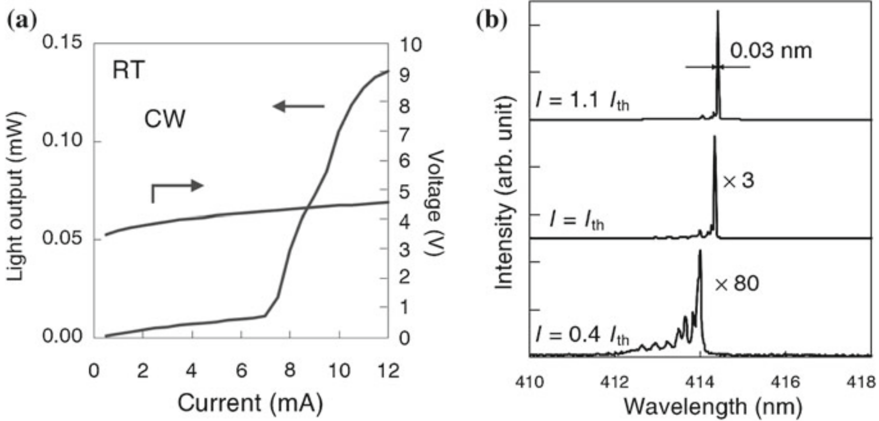

Fig. 13.16 **a** The light output intensity versus injection current and current-voltage characteristics of the dielectric DBR VCSEL. **b** The laser emission spectrum at different injection current levels measured at RT [32]

at an injection current of 12 mA. Figure 13.16b shows the laser emission spectrum at different injection current levels measured at RT. The spontaneous emission peak with many higher-order transverse modes is observed when the input current is lower than the threshold current. The peak intensity of the fundamental transverse mode is increased and the emission linewidth becomes narrower with increasing input current. When the input current is about 1.1 $I_{\rm th}$ the lasing wavelength is 414.4 nm and the FWHM is about 0.03 nm.

13.5 Future Perspectives

The lasing action of GaN-based hybrid DBR VCSELs by optical pumping at RT and CW electrical pumping at 77 K were demonstrated by Wang et al. in 2008 and the RT CW electrically pumped dielectric DBR VCSEL was reported by Higuchi et al. in the same year. Recently, Wang's group also demonstrated CW electrically pumped GaN-based hybrid DBR VCSELs at RT in 2010. The next challenge of the GaN-based VCSELs is to improve the laser performance. The difficulties in improving hybrid DBR VCSEL structures may be due to several important issues. The current crowding in the intracavity contacted structure is an important problem which induces a high operation voltage and heat generation. It is well known that the performance of semiconductor laser will degrade with the increasing device temperature because of the broadening gain spectra, increased nonradiative recombination, and electron leakage. These heat-induced problems are especially serious in nitride-based VCSELs due to the relatively large thermal resistance in multi-layer DBR and the smaller size of current aperture [52], and QCSE-induced electron current leakage [54]. In addition, heat dissipation limited by the poor thermal conductivity of the sapphire substrate significantly affects the device performance. These issues should be the main physical mechanisms limiting the breakthrough of lasing action. The advanced design for improving the laser performance of GaN VCSELs will be an important issue. It has been reported that the use of polarization-matched InGaN/AlInGaN MQWs enables an independent control over interface polarization charges and bandgap and has been suggested as a method to reduce electron leakage current [56]. On the other hand, conventional GaAs-based VCSELs mostly use the wet oxidation technique to achieve effective index guiding structures. However, the design of intra-cavity structure has the problems with an effective confinement of an optical field in a radial direction of standard nitride-based VCSELs [57]. Additionally, several technical issues should be considered. These include the design of a transparent and good current spreading contact structure for carrier injection, improvement of the spatial uniformity of InGaN MQW active region because of relative small light emission aperture of the current injection device, enhancement of p-type GaN layer conductivity, and further increase of the high reflectivity of DBRs for the reduction of threshold current. It is necessary to overcome these problems to achieve high-performance RT CW GaN-based VCSELs.

13.6 Summary

We have presented an overview of the current state of the art in the development of GaN-based VCSELs. The technical approaches, fabrication processes, and key performance characteristics of optically pumped and electrically pumped GaN-based VCSELs are introduced in this chapter. The design considerations and fabrication technology of two types of GaN-based VCSEL structures: hybrid DBR VCSELs and

double dielectric DBR VCSELs have discussed. The first CW electrically pumped GaN VCSEL has been demonstrated at 77 K by Wang's group in 2008. The laser action occurred at a threshold current of 1.4 mA with an emission wavelength at 462.8 nm in blue wavelength. In the same year, Nichia reported RT CW GaN VCSEL by using wafer bonding and laser lift-off. The threshold current was about 7 mA at an emission wavelength of 414 nm. These electrically pumped GaN VCSELs are only the first step to achieve high-performance RT CW GaN VCSELs, which is a future challenge for all the researchers devoted to the development of GaN VCSELs.

Acknowledgements The authors would like to thank Prof. Kenichi Iga of Tokyo Institute of Technology, Prof. Anthony Siegman and Prof. Yoshihisa Yamamoto of Stanford University for their valuable technical discussion and comments.

References

1. K. Kornitzer, T. Ebner, K. Thonke, R. Sauer, C. Kirchner, V. Schwegler, M. Kamp, M. Leszczynski, I. Grzegory, S. Porowski, Photoluminescence and reflectance spectroscopy of excitonic transitions in high-quality homoepitaxial GaN films. Phys. Rev. B **60**, 1471 (1999)
2. G. Christmann, R. Butté, E. Feltin, A. Mouti, P.A. Stadelmann, A. Castiglia, J.-F. Carlin, N. Grandjean, Large vacuum Rabi splitting in a multiple quantum well GaN-based microcavity in the strong-coupling regime. Phys. Rev. B **77**, 085310 (2008)
3. S. Kako, C. Santori, K. Hoshino, S. Götzinger, Y. Yamamoto, Y. Arakawa, A gallium nitride single-photon source operating at 200 K. Nat. Mater. **5**, 887 (2006)
4. S. Christopoulos, G. Baldassarri H. von Högersthal, A. Grundy, P.G. Lagoudakis, A.V. Kavokin, J.J. Baumberg, G. Christmann, R. Butté, E. Feltin, J.-F. Carlin, N. Grandjean, Room-temperature polariton lasing in semiconductor microcavities. Phys. Rev. Lett. **98**, 126405 (2007)
5. G. Sun, R.A. Soref, J.B. Khurgin, Active region design of a terahertz GaN/$Al_{0.15}Ga_{0.85}N$ quantum cascade laser. Superlattice. Microstruct. **37**, 107 (2005)
6. H. Amano, M. Kito, K. Hiramatsu, I. Akasaki, P-type conduction in Mg-doped GaN treated with low-energy electron beam irradiation (LEEBI). Jpn. J. Appl. Phys. **28**, L2112 (1989)
7. I. Akasaki, H. Amano, K. Itoh, N. Koide, K. Manabe, GaN based UV/blue light-emitting devices. Inst. Phys. Conf. Ser. **129**, 851 (1992)
8. S. Nakamura, T. Mukai, M. Senoh, Candela-class high-brightness InGaN/AlGaN double-heterostructure blue-light-emitting diodes. Appl. Phys. Lett. **64**, 687 (1994)
9. S. Nakamura, M. Senoh, S.-I. Nagahama, N. Iwasa, T. Yamada, T. Matsushita, Y. Sugimoto, H. Kiyoku, Room-temperature continuous-wave operation of InGaN multi-quantum-well structure laser diodes. Appl. Phys. Lett. **69**, 4056 (1996)
10. S. Nakamura, M. Senoh, S.-I. Hagahama, N. Iwasa, T. Yamada, T. Matsushita, H. Kiyoku, Y. Sugimoto, T. Kozaki, H. Umemoto, M. Sano, K. Chocho, High-power, long-lifetime InGaN/GaN/AlGaN-based laser diodes grown on pure GaN substrates. Jpn. J. Appl. Phys. **37**, L309 (1998)
11. S. Nakamura, M. Senoh, S.-I. Nagahama, N. Iwasa, T. Yamada, T. Matsushita, H. Kiyoku, Y. Sugimoto, T. Kozaki, H. Umemoto, M. Sano, K. Chocho, Violet InGaN/GaN/AlGaN-based laser diodes with an output power of 420 mW. Jpn. J. Appl. Phys. **37**, L627 (1998)
12. S. Nakamura, M. Senoh, T. Mukai, Highly p-typed Mg-doped GaN films grown with GaN buffer layers. Jpn. J. Appl. Phys. **30**, L1708 (1991)
13. S. Nakamura, N. Iwasa, M. Senoh, T. Mukai, Hole compensation mechanism of p-type GaN films. Jpn. J. Appl. Phys. **31**, 1258 (1992)

14. H. Soda, K. Iga, C. Kitahara, Y. Suematsu, GaInAsP/InP surface emitting injection lasers. Jpn. J. Appl. Phys. **18**(12), 2329 (1979)
15. K. Iga, Surface-emitting laser—its birth and generation of new optoelectronics field. IEEE J. Select. Topics Quantum Electron. **6**, 1201 (2000)
16. W.W. Chow, K.D. Choquette, M.H. Crawford, K.L. Lear, G.R. Hadley, Design, fabrication, and performance of infrared and visible vertical-cavity surface-emitting lasers. IEEE J. Quantum Electron. **33**, 1810 (1997)
17. E. Towe, R.F. Leheny, A. Yang, A historical perspective of the development of the vertical-cavity surface-emitting laser. IEEE J. Select. Topics Quantum Electron. **6**, 1458 (2000)
18. J.M. Redwing, D.A.S. Loeber, N.G. Anderson, M.A. Tischler, J.S. Flynn, An optically pumped GaN-AlGaN vertical cavity surface emitting laser. Appl. Phys. Lett. **69**, 1 (1996)
19. T. Someya, K. Tachibana, J. Lee, T. Kamiya, Y. Arakawa, Lasing emission from an $In_{0.1}Ga_{0.9}N$ vertical cavity surface emitting laser. Jpn. J. Appl. Phys. **37**, L1424 (1998)
20. Y.-K. Song, H. Zhou, M. Diagne, I. Ozden, A. Vertikov, A.V. Nurmikko, C. Carter-Coman, R.S. Kern, F.A. Kish, M.R. Krames, A vertical cavity light emitting InGaN quatnum well heterostructure. Appl. Phys. Lett. **74**, 3441 (1999)
21. T. Someya, R. Werner, A. Forchel, M. Catalano, R. Cingolani, Y. Arakawa, Room temperature lasing at blue wavelengths in gallium nitride microcavities. Science **285**, 1905 (1999)
22. J.-F. Carlin, J. Dorsaz, E. Feltin, R. Butté, N. Grandjean, M. Ilegems, M. Laügt, Crack-free fully epitaxial nitride microcavity using highly reflective AlInN/GaN Bragg mirrors. Appl. Phys. Lett. **86**, 031107 (2005)
23. H. Zhou, M. Diagne, E. Makarona, A.V. Nurmikko, J. Han, K.E. Waldrip, J.J. Figiel, Near ultraviolet optically pumped vertical cavity laser. Electron. Lett. **36**, 1777 (2000)
24. S.-H. Park, J. Kim, H. Jeon, T. Sakong, S.-N. Lee, S. Chae, Y. Park, C.-H. Jeong, G.-Y. Yeom, Y.-H. Cho, Room-temperature GaN vertical-cavity surface-emitting laser operation in an extended cavity scheme. Appl. Phys. Lett. **83**, 2121 (2003)
25. T. Tawara, H. Gotoh, T. Akasaka, N. Kobayashi, T. Saitoh, Low-threshold lasing of InGaN vertical-cavity surface-emitting lasers with dielectric distributed Bragg reflectors. Appl. Phys. Lett. **83**, 830 (2003)
26. E. Feltin, G. Christmann, J. Dorsaz, A. Castiglia, J.-F. Carlin, R. Butté, N. Grandjean, S. Christopoulos, G. Baldassarri, H. von Högersthal, A.J.D. Grundy, P.G. Lagoudakis, J.J. Baumberg, Blue lasing at room temperature in an optically pumped lattice-matched AlInN/GaN VCSEL structure. Electron. Lett. **43**, 924 (2007)
27. J.-T. Chu, T.-C. Lu, H.-H. Yao, C.-C. Kao, W.-D. Liang, J.-Y. Tsai, H.-C. Kuo, S.-C. Wang, Room-temperature operation of optically pumped blue-violet GaN-based vertical-cavity surface-emitting lasers fabricated by laser lift-off. Jpn. J. Appl. Phys. **45**, 2556 (2006)
28. J.-T. Chu, T.-C. Lu, M. You, B.-J. Su, C.-C. Kao, H.-C. Kuo, S.-C. Wang, Emission characteristics of optically pumped GaN-based vertical-cavity surface-emitting lasers. Appl. Phys. Lett. **89**, 121112 (2006)
29. C.-C. Kao, Y.C. Peng, H.H. Yao, J.Y. Tsai, Y.H. Chang, J.T. Chu, H.W. Huang, T.T. Kao, T.C. Lu, H.C. Kuo, S.C. Wang, Fabrication and performance of blue GaN-based vertical-cavity surface emitting laser employing AlN/GaN and Ta_2O_5/SiO_2 distributed Bragg reflector. Appl. Phys. Lett. **87**, 081105 (2005)
30. C.-C. Kao, T.C. Lu, H.W. Huang, J.T. Chu, Y.C. Peng, H.H. Yao, J.Y. Tsai, T.T. Kao, H.C. Kuo, S.C. Wang, C.F. Lin, The lasing characteristics of GaN-based vertical-cavity surface-emitting laser with AlN–GaN and $Ta_2O_5SiO_2$ distributed Bragg reflectors. IEEE Photon. Technol. Lett. **18**, 877 (2006)
31. T-C. Lu, C.-C. Kuo, H.-C. Kuo, G.-S. Huang, S.-C. Wang, CW lasing of current injection blue GaN-based vertical cavity surface emitting laser. Appl. Phys. Lett. **92**, 141102 (2008)
32. Y. Higuchi, K. Omae, H. Matsumura, T. Mukai, Room-temperature CW lasing of a GaN-based vertical-cavity surface-emitting laser by current injection. Appl. Phys. Exp. **1**, 121102 (2008)
33. F.A. Ponce, D.P. Bour, Nitride-based semiconductors for blue and green light-emitting devices. Nature **386**, 351 (1997)

34. J. Li, T.N. Oder, M.L. Nakarmi, J.Y. Lin, H.X. Jiang, Optical and electrical properties of Mg-doped *p*-type $Al_xGa_{1-x}N$. Appl. Phys. Lett. **80**, 1210 (2002)
35. E. Petrolati, A.D. Carlo, The influence of mobility unbalance on GaN based vertical cavity surface emitting lasers. Appl. Phys. Lett. **92**, 151116 (2008)
36. S. Chichibu, T. Azuhata, T. Sota, S. Nakamura, Spontaneous emission of localized excitons in InGaN single and multiquantum well structures. Appl. Phys. Lett. **69**, 4188 (1996)
37. J.-F. Carlin, M. Ilegems, High-quality AlInN for high index contrast Bragg mirrors lattice matched to GaN. Appl. Phys. Lett. **83**, 668 (2003)
38. T. Fujimori, H. Imai, A. Wakahara, H. Okada, A. Yoshida, T. Shibata, M. Tanaka, Growth and characterization of AlInN on AlN template. J. Cryst. Growth **272**, 381 (2004)
39. R. Butté, E. Feltin, J. Dorsaz, G. Christmann, J.-F. Carlin, N. Grandjean, M. Ilegems, Recent progress in the growth of highly reflective nitride-based distributed Bragg reflectors and their use in microcavities. Jpn. J. Appl. Phys. **44**, 7207 (2005)
40. G.S. Huang, T.C. Lu, H.H. Yao, H.C. Kuo, S.C. Wang, C.-W. Lin, L. Chang, Crack-free GaN/AlN distributed Bragg reflectors incorporated with GaN/AlN superlattices grown by metalorganic chemical vapor deposition. Appl. Phys. Lett. **88**, 061904 (2006)
41. H.K. Cho, J.Y. Lee, G.M. Yang, Characterization of pit formation in III-nitrides grown by metalorganic chemical vapor deposition. Appl. Phys. Lett. **80**, 1370 (2002)
42. S. Einfeldt, H. Heinke, V. Kirchner, D. Hommel, Strain relaxation in AlGaN/GaN superlattices grown on GaN. J. Appl. Phys. **89**, 2160 (2001)
43. K. Iga, Possibility of green/blue/UV surface emitting lasers, in *International Symposium Blue Laser and Light Emitting Diodes*, No. Th-11, 263 (Mar. 1996)
44. X.H. Zhang, S.J. Chua, W. Liu, L.S. Wang, A.M. Yong, S.Y. Chow, Crack-free fully epitaxial nitride microcavity with AlGaN/GaN distributed Bragg reflectors and InGaN/GaN quantum wells. Appl. Phys. Lett. **88**, 191111 (2006)
45. R.J. Horowicz, H. Heitmann, Y. Kadota, Y. Yamamoto, GaAs microcavity quantum-well laser with enhanced coupling of spontaneous emission to the lasing mode. Appl. Phys. Lett. **61**, 393 (1992)
46. Y. Yamamoto, S. Machida, Microcavity semiconductor laser with enhanced spontaneous emission. Phys. Rev. A **44**, 657 (1991)
47. S. Kako, T. Someya, Y. Arakawa, Observation of enhanced spontaneous emission coupling factor in nitride-based vertical-cavity surface-emitting laser. Appl. Phys. Lett. **80**, 722 (2002)
48. W.S. Wong, T. Sands, N.W. Cheung, M. Kneissl, D.P. Bour, P. Mei, L.T. Romano, N.M. Johnson, Fabrication of thin-film InGaN light-emitting diode membranes by laser lift-off. Appl. Phys. Lett. **75**, 1360 (1999)
49. S.-H. Park, Crystal orientation effects on many-body optical gain of wurtzite InGaN/GaN quantum well lasers. Jpn. J. Appl. Phys. **42**, L170 (2003)
50. A. Kaneta, K. Okamoto, Y. Kawakami, S. Fujita, G. Marutsuki, Y. Narukawa, T. Mukai, Spatial and temporal luminescence dynamics in an $In_xGa_{1-x}N$ single quantum well probed by near-field optical microscopy. Appl. Phys. Lett. **81**, 4353 (2002)
51. B. Witzigmann, V. Laino, M. Luisier, U.T. Schwarz, G. Feicht, W. Wegscheider, K. Engl, M. Furitsch, A. Leber, A. Lee, V. Härle, Microscopic analysis of optical gain in InGaN/GaN quantum wells. Appl. Phys. Lett. **88**, 021104 (2006)
52. T.-C. Lu, S.-W. Chen, T.-T. Wu, P.-M. Tu, C.-K. Chen, C.-H. Chen, Z.-Y. Li, H.-C. Kuo, S.-C. Wang, Continuous wave operation of current injected GaN vertical cavity surface emitting lasers at room temperature. Appl. Phys. Lett. **97**, 071114 (2010)
53. H.-C. Kuo, T.-C. Lu, Z.-Y. Li, T.-T. Wu, P.-M. Tu, C.-H. Chiu, S.-W. Chen, S.-C. Wang, C.-Y. Chang, Toward a high-performance, low-power microprojector with a surface-emitting blue laser. SPIE Newsroom, June 14 (2012). doi:10.1117/2.1201205.004195
54. Y.-K. Kuo, Y.-A. Chang, Effects of electronic current overflow and inhomogeneous carrier distribution on InGaN quantum-well laser performance. IEEE J. Quantum Electron. **40**, 437 (2006)

55. M.H. MacDougal, P.D. Dapkus, A.E. Bond, C.-K. Lin, J. Geske, Design and fabrication of VCSEL's with Al_xO_y-GaAs DBR's. IEEE J. Select. Topics Quantum Electron. **3**, 905 (1997)
56. J. Piprek, R. Farrell, S. DenBaars, S. Nakamura, Effects of built-in polarization on InGaN-GaN vertical-cavity surface-emitting lasers. IEEE Photon. Technol. Lett. **18**, 7 (2006)
57. M.F. Schubert, J. Xu, J.K. Kim, E.F. Schubert, M.H. Kim, S. Yoon, S.M. Lee, C. Sone, T. Sakong, Y. Park, Polarization-matched GaInN/AlGaInN multi-quantum-well light-emitting diodes with reduced efficiency droop. Appl. Phys. Lett. **93**, 041102 (2008)
58. P. Maćkowiak, R.P. Sarzała, M. Wasiak, W. Nakwaski, Nitride VCSEL design for continuous-wave operation of higher-order optical modes. Appl. Phys. A **77**, 761 (2003)

Part IV
VCSEL Applications

Chapter 14
VCSEL-Based Transceivers for Data Communications

Kenneth P. Jackson and Clint L. Schow

Abstract The data communications (datacom) transceiver market has experienced tremendous growth over the last fifteen years due in large part to the use of vertical-cavity surface-emitting lasers (VCSELs) and multimode optical fibers. This chapter reviews the evolution of 850 nm laser-based datacom transceivers beginning with the early use of AlGaAs edge-emitters to the adoption of VCSELs where their unique attributes have enabled significant performance enhancements and cost reductions in transceiver designs.

14.1 Introduction

In 2009 over 18 million 850 nm wavelength VCSEL-based datacom transceivers were sold resulting in revenue of almost US$ 500 million. The size and scope of this market has grown tremendously over the last fifteen years, driven primarily by the use of VCSELs. VCSEL technology, along with the use of multimode optical fibers, have been key enablers for low-cost optical interconnects. These low cost optical interconnects are attractive solutions for a wide range of data communications applications including storage and local area networks (SANs and LANs) as well as system interconnects for high performance computing (HPC).

VCSELs for datacom transceivers have evolved from the early days when they were used as replacements for short wavelength edge-emitting lasers to today,

K. P. Jackson (✉)
Emcore Corporation, 10420 Research Road SE, Bldg 2,
Albuquerque, NM 87123, USA
e-mail: kenneth_jackson@emcore.com

C. L. Schow
IBM T. J. Watson Research Center, 1101 Kitchawan Rd., M.S. 38-127,
Yorktown Heights, NY 10598, USA
e-mail: cschow@us.ibm.com

R. Michalzik (ed.), *VCSELs*, Springer Series in Optical Sciences 166,
DOI: 10.1007/978-3-642-24986-0_14, © Springer-Verlag Berlin Heidelberg 2013

where the advantages of VCSELs allow cost and performance optimizations, not readily achievable with traditional 1,300 or 1,550 nm wavelength sources and single-mode optical fiber technologies.

In this chapter, VCSEL-based transceivers are reviewed. Beginning with the earliest developments of datacom transceiver designs using edge-emitting lasers, to the introduction of VCSELs, this chapter focuses on the requirements and the unique attributes of VCSELs which have enabled low-cost, high volume, manufacturable transceivers. This chapter will also discuss present and future transceiver developments which continue to lower the cost and further increase the performance of these solutions for an expanding range of applications.

14.2 Early Datacom Transceivers

The use of 850 nm wavelength VCSELs for datacom transceivers has its origins in the mid 1980s when the growth in computer processing speeds drove the need for even higher speed interconnects [1]. Fiber-optic interconnects offered advantages in terms of distance and bulk. Light-emitting diodes (LEDs) were the technology of choice used in these early implementations. However, they were mostly limited to data rates of a few hundred Mb/s and the optical power coupled in to the fiber was relatively low. Increasing the speed of these devices generally resulted in lower emitted optical powers requiring high efficiency fiber coupling and high-sensitivity (~ -30 to -35 dBm), wide bandwidth receivers which led to higher cost transceivers. Laser-based solutions, on the other hand, were capable of launching higher optical powers while operating at greater modulation speeds. This enabled longer distance links, or more importantly, links having multiple fiber connections and higher overall link loss. The use of laser sources in optical interconnects simplified receiver designs and ultimately led to lower cost solutions. Unfortunately, most of the lasers available were optimized for long-distance telecommunications applications and were therefore expensive. In contrast to telecommunication links, most data communications links are relatively short and the optical-to-electrical conversion costs can be a significant fraction of the overall link cost that also includes fiber and fiber installation.

In the 1980s, audio compact discs (CDs) were gaining in popularity and fueled significant investments in the manufacturing infrastructure of 780 nm wavelength, edge-emitting AlGaAs lasers. This investment resulted in low-cost lasers which could also be used for multimode fiber data links [2]. These edge-emitting sources were designed to have an optical self-pulsation. This self-pulsation resulted in devices having a relatively low coherence (Fig. 14.1) which minimized noise arising from optical back-reflections in the disc reading system. This self-pulsation effect was also helpful in minimizing modal noise in multimode optical fiber data links. Telecommunications applications demanded lasers with narrow spectral line widths in order to minimize chromatic dispersion to achieve long link distances. This narrow spectral width results in a relatively coherent source (Fig. 14.2) which when used in

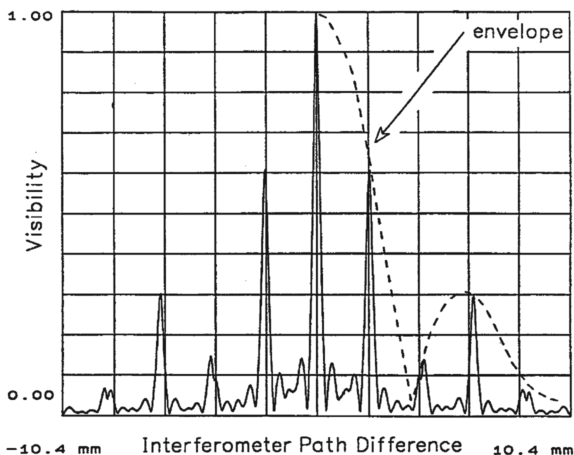

Fig. 14.1 Fringe visibility as a function of optical path length difference for a self-pulsating, 780 nm AlGaAs edge-emitting laser. Fringe visibility is a measure of the source coherence length, which for this type of source is relatively low. Low coherence minimizes the effects of modal noise making such sources attractive solutions for multimode fiber data links

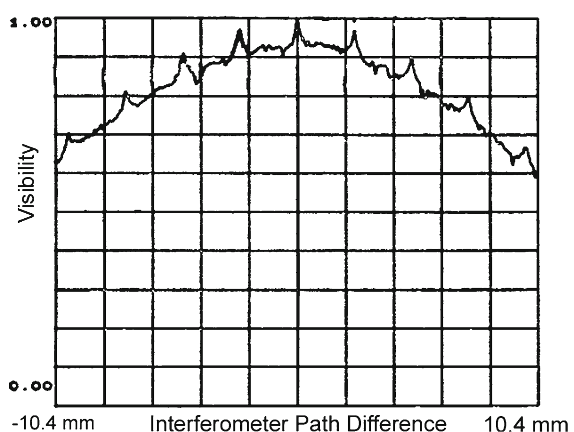

Fig. 14.2 Fringe visibility (coherence) as a function of optical path length difference for a narrow linewidth, telecom-grade, edge-emitting laser. The envelope of the visibility is relatively high (i.e. high coherence) making this type of source unsuitable for multimode data links where mode selective loss may be present

a short distance multimode fiber link having multiple optical connectors, will suffer from "bit-error-rate-floors" arising from the time-varying effects of the source and mode-selectivity in the fiber network [3]. Self-pulsating, edge-emitting lasers greatly minimized this phenomenon and along with their relatively low-cost quickly became the sources of choice for short distance data communications interconnects. Figure 14.3a shows an oscilloscope response for a self-pulsating laser modulated at a data rate of 220 Mb/s. Because the frequency of the optical self-pulsation is higher than the bandwidth of the receiver at the remote end, the resulting waveform at the receiver output is free of deleterious modulation or noise effects (see Fig. 14.3b). This type of laser was common for datacom transceivers operating at 220, 266 and 531 Mb/s (see Fig. 14.4), the latter two data rates being part of the ANSI Fibre Channel standard for quarter- and half-speed physical link definitions, respectively [4].

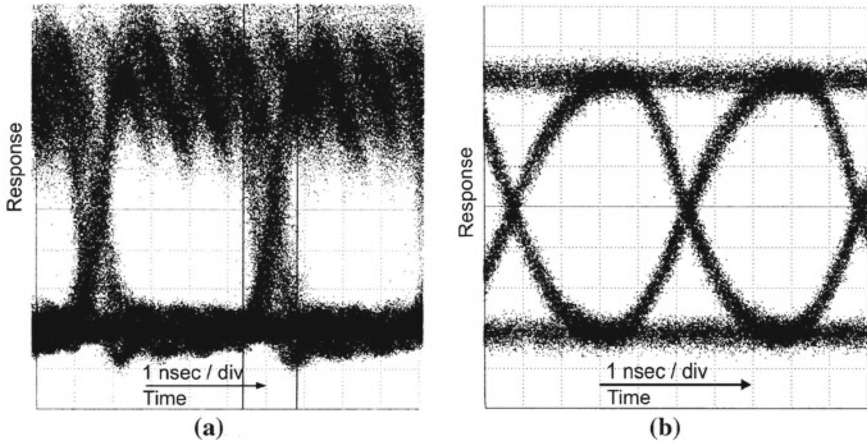

Fig. 14.3 **a** Transmitted optical eye diagram for a self-pulsating, edge-emitting, AlGaAs, 780 nm laser modulated at 220 Mb/s. Signal captured using a wide-bandwidth optical-to-electrical converter. **b** Electrical eye diagram from a 220 Mb/s multimode data link receiver after filtering the waveform from **a**. (Courtesy of D. Siljenberg)

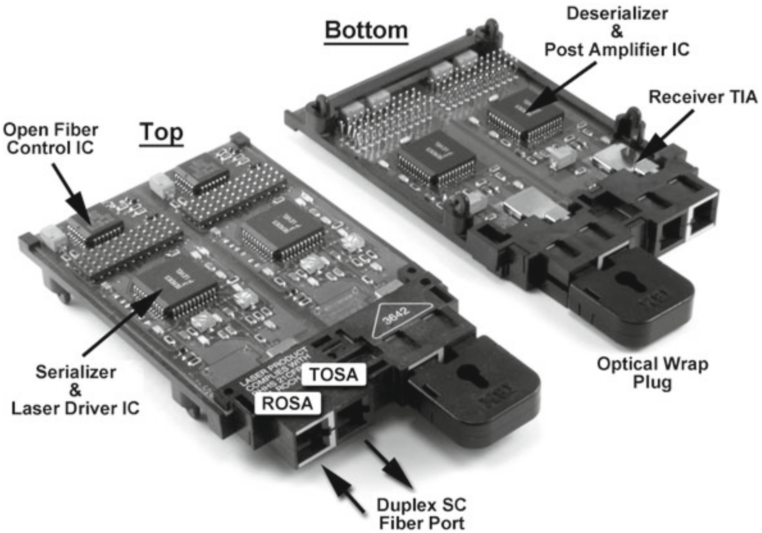

Fig. 14.4 Example of an early optical data link card (circa 1991) which used a self-pulsating edge-emitting, 780 nm, AlGaAs laser. The module shown is a "dual" card in that entire duplicate transceiver functions were located on the same PC board. One-half of the module provided full-duplex (bi-directional) data transfers at a rate of 220 Mb/s

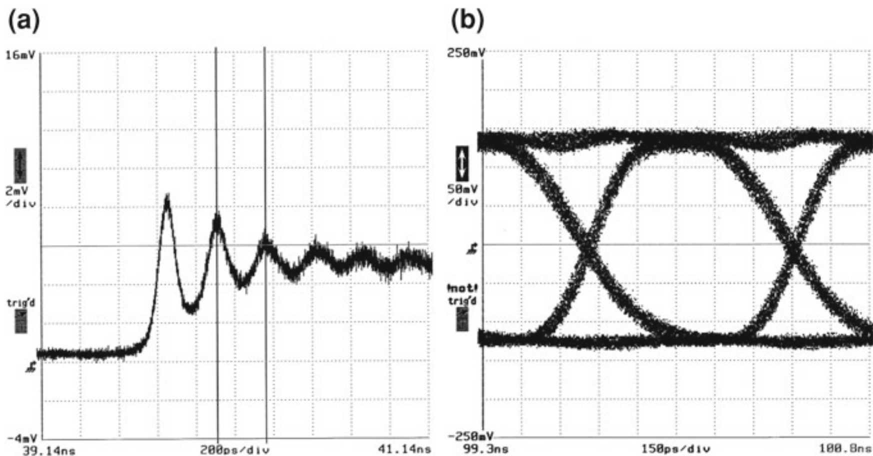

Fig. 14.5 **a** Modulated waveform of an edge-emitting, AlGaAs, 780 nm laser with high frequency relaxation oscillations (rising edge of a string of “ones”). Useful data rates for this type of laser were in the one gigabit per second range where these oscillations could be filtered out by the receiver. **b** Electrical eye diagram from a one-gigabit per second multimode data link receiver after filtering the waveform from **a**

14.3 The Need for VCSELs

The ever increasing need for high data throughput required even faster laser sources. The CD-laser industry was motivated to achieve higher storage densities and so moved to shorter wavelengths, modulation speeds were a secondary concern. As the data communications industry approached data rates of 1 Gb/s in the mid 1990s, self-pulsating edge-emitting lasers, with oscillation frequencies sufficiently high to be adequately filtered by the receiver, were increasingly difficult to fabricate. As a consequence, early 1 Gb/s datacom transceivers utilized a variant of the self-pulsating laser—one that exhibited high frequency oscillations that damped out relatively quickly (on the order of a bit period). The oscillatory behavior resulted in lasers whose coherence lengths were relatively short and therefore well-suited for multimode fiber interconnects. These relaxation oscillations were sufficiently high in frequency that the receiver on the remote end adequately filtered them out providing a communications channel with high fidelity (Fig. 14.5a, b).

Unfortunately, the AlGaAs edge-emitting laser solution was short-lived. Data rates continued to increase at a rapid pace and a new low-cost laser technology was required. VCSELs were an attractive solution because they could be designed to operate at much higher speeds and over greater temperature ranges than the AlGaAs edge-emitting lasers at the time. VCSELs were also relatively inexpensive to manufacture due to wafer scale fabrication and testing in contrast to edge emitters that must be cleaved into “bars” before initial optical testing. Early VCSEL devices were fabricated with relatively large optical emission apertures having a narrow beam

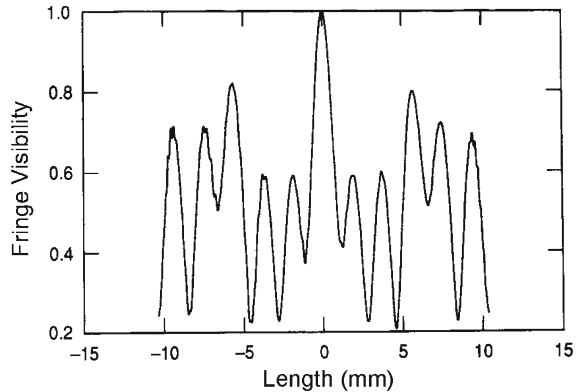

Fig. 14.6 VCSEL coherence length (fringe visibility) as a function of optical path length difference. VCSELs have relatively low coherence which minimizes modal noise making them an attractive technology for multimode fiber data links [5] (© 1994 IEEE)

divergence. This enabled the optical output to be efficiently coupled to a multimode fiber while relaxing the laser-to-fiber alignment tolerance. Large aperture VCSELs also have better thermal characteristics and higher manufacturing yields as well as low contact resistance and therefore low operating voltages, a critical requirement for operation with 3.3 V power supplies that were supplanting the previous industry standard 5 V supplies. In addition, large aperture devices emit light in multiple *transverse* spatial modes. These transverse modes are beneficial in that they reduce the coherence of the source in ways similar to the longitudinal modes of the self-pulsating edge-emitting laser (Fig. 14.6) [5, 6]. As a consequence, large aperture VCSELs are well-suited in suppressing modal noise as well as enabling simple, low-cost laser-to-fiber coupling approaches for multimode optical fiber data links.

14.4 VCSEL Technology and the Drive for Lower Costs

VCSELs and multimode optical fiber technologies enabled data communications links having significant cost advantages over long-distance, single-mode fiber based telecommunications links. However, in the continuing effort to compete with shorter length copper interconnects, the industry pushed for even lower costs, higher densities and greater modulation speeds to address the increasing data throughput needs. This drive resulted in several key developments enabling VCSEL-based transceivers to penetrate application spaces that were traditionally served by copper. These developments included changes in packaging (in part enabled by the properties of the VCSEL) and changes to the kinds of functions contained in the datacom transceiver.

Due to the circularly symmetric emission beam and large aperture of a VCSEL, the optical components that provide the laser-to-fiber coupling, commonly referred to as transmit optical subassemblies (TOSAs) could be simplified. Packages for edge-emitting lasers consisted of machined headers and lids with optically transparent, anti-reflection-coated windows (referred to as TO-56). With the use of

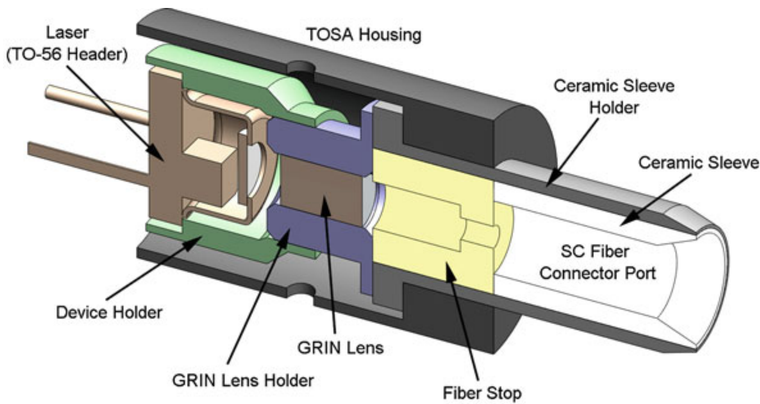

Fig. 14.7 Cross-section of an early 780 nm AlGaAs edge-emitting laser SC TOSA (transmit optical subassembly) (circa 1991). Although inexpensive relative to alternatives at the time, this approach is expensive when compared to the low-cost approaches used today with VCSELs (see Fig. 14.9). (Courtesy of D. Karst)

VCSELs and the relaxed alignment tolerances, lower-cost, stamped, TO-46 packages could be used. In addition, these TOSAs could be molded using plastic materials. Figures 14.7, 14.8, and 14.9 show the chronological evolution of TOSAs beginning with assemblies optimized for edge-emitters (Fig. 14.7) and progressing to VCSEL-based plastic TOSAs (Fig. 14.9a, b). Edge-emitting laser-based TOSAs consisted of machined stainless-steel housings with precision ceramic inserts in which the optical fiber ferrule was inserted. The various piece parts were held together using a combination of solder and laser welding. These approaches, although less expensive than the existing 1310 nm, single-mode fiber based, telecom solutions at the time, were relatively costly. VCSELs, with emission apertures about 3× larger than edge-emitters, are more tolerant of misalignments and therefore can be assembled into plastic housings using adhesives. In addition, because of the relaxed alignment tolerance, the subassembly can provide adequate fiber coupled power over a wider operating temperature range even in the presence of relatively large temperature induced refractive index changes that shift the focal point.

In the late 1990s, the basic TOSA, shown in Fig. 14.8, gave way to a smaller format leading to increased density (Fig. 14.9). Many datacom transceivers were compatible with the industry-standard SC duplex multimode fiber connector (e.g. GBICs, GLM, 1 × 9 transceiver modules). However, as the width of the electrical signal interface decreased through parallel to serial migration, a smaller optical interface was needed to match, offering narrower transceivers and thus higher densities along the edge of the host printed circuit board. A number of optical connection interfaces such as MT-RJ, MU and LC were considered. Today the dominant interface is the duplex LC (Fig. 14.9). The transceiver form factor that utilizes this optical interface is referred to as the Small Form-factor Pluggable (SFP) (Fig. 14.10). A fixed, pin-through-hole module, referred to as the Small Form-factor Fixed (SFF), is also offered.

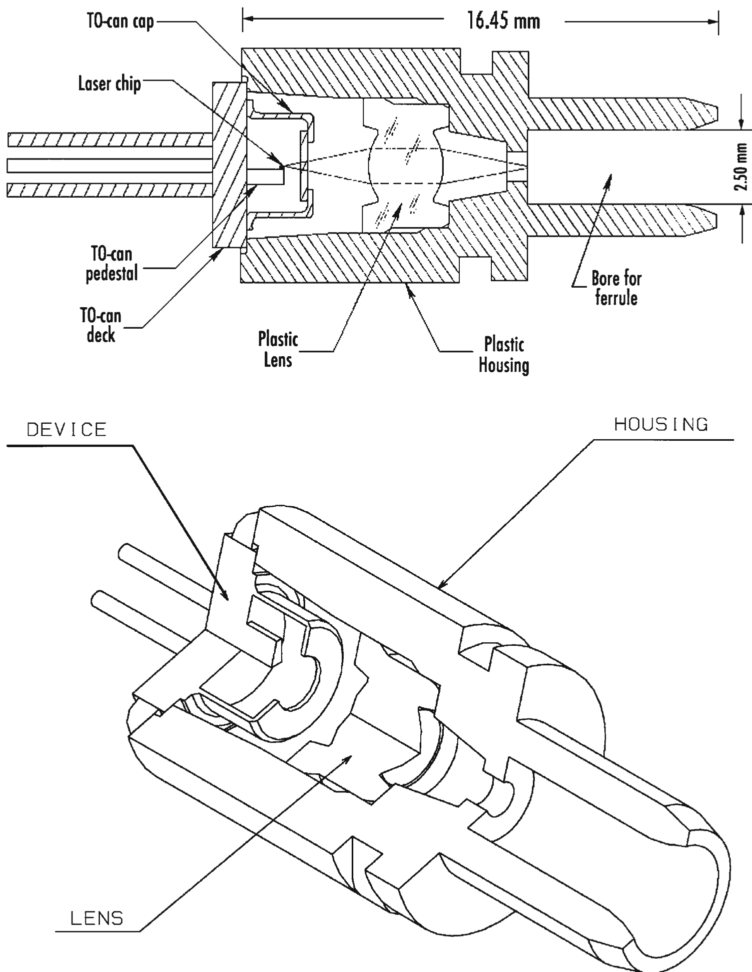

Fig. 14.8 Cost-reduced SC TOSA of Fig. 14.7. Changes in materials (molded plastic body and lens) and reduction of piece parts (down to three) led to significantly lower costs

Other significant developments leading to lower costs with higher density and performance was the removal or re-partitioning of various functions contained in the transceiver. Early on the routing of high-speed signals on a large host system printed circuit board was challenging. To minimize the risk, transceiver electrical interfaces utilized multiple, parallel, signal lines operating at modest data rates. Figure 14.11 shows a Gigabit Link Module (GLM) which accepted a two-byte wide, 10 bits/byte, 53 MHz, parallel electrical signal. The on-board serializer converted this signal to a 1 Gb/s data stream. This 1 Gb/s signal was impressed on the optical output of the laser by modulating with a laser driver circuit. The optical signal was then

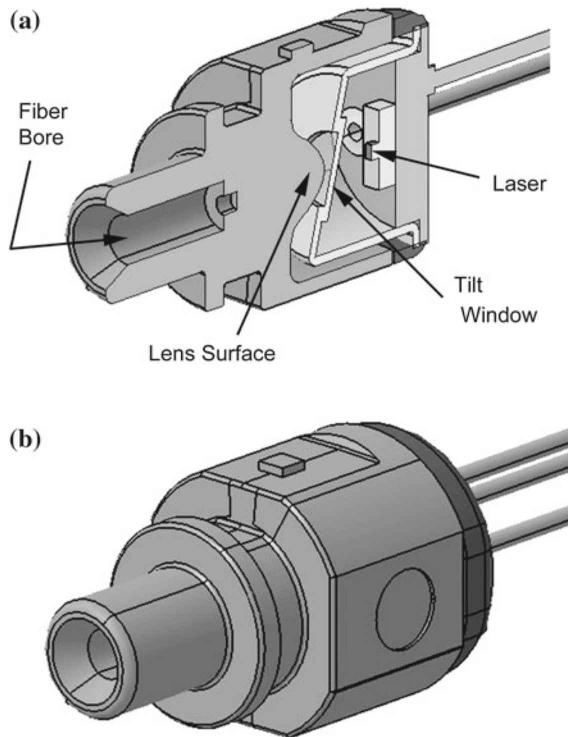

Fig. 14.9 VCSEL-based LC TOSA common in the industry today. Housing and lens are combined into a single molded piece typically made from Ultem®. **a** Cross-sectional view. **b** Overall external view. (Courtesy of D. Gaio)

Fig. 14.10 Typical small form-factor pluggable (SFP) transceiver. The LC optical connector interface along with the high-speed serial electrical interface enabled higher density transceiver interconnects. The SFP transceiver is hot-pluggable and can be installed by the end-customer [7] (Courtesy of JDSU)

coupled to a multimode optical fiber with a TOSA which accommodates the fiber connector ferrule. A duplex optical fiber allowed for simultaneous, bi-directional operation. The adjacent optical subassembly contained an optical receiver which converted the incoming 1 Gb/s optical data into an electrical signal that was then de-multiplexed or deserialized into two 10 bit wide electrical data streams. In the mid-1990s,

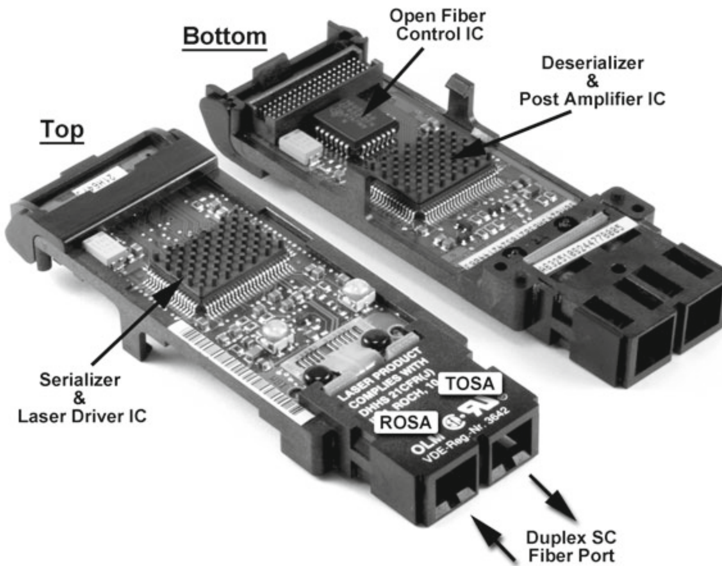

Fig. 14.11 Gigabit Link Module (GLM), circa 1995. This module is sometimes referred to as a "y-axis" pluggable as opposed to "z-axis" pluggable shown in Figs. 14.10 and 14.12. The GLM was installed at the factory and was not readily removed in the field thus limiting customer flexibility

this architecture gave way to the GBIC (GigaBit Interface Converter) (Fig. 14.12) that removed the serializing/deserializing function from the optical transceiver and integrated it into the electronics on the host side of the interface. This greatly simplified the transceiver, lowered the component costs and reduced its size, but required users to manage 1 Gb/s electrical interfaces. Unlike GLMs, GBICs were also hot-pluggable in the field, providing users greater flexibility in terms of network configuration, performance and cost optimization.

Other changes to transceiver functions involved combining the laser driver (transmit) and post-amplifier (receive) into a single integrated circuit [8]. With proper design, the transmit and receive sections can be adequately isolated resulting in negligible on-chip cross-talk. Such designs can lead to lower costs due to a single chip having fewer I/Os, fewer packages and less test complexity than the two-chip solution (Fig. 14.13a, b).

All laser-based datacom transceivers also require certifications by government agencies to ensure they adhere to specified laser safety standards. Early laser-based transceivers utilized a control circuit, referred to as Open Fiber Control in order to meet the least restrictive of the laser product safety standards ([4], App. I, pp. 308–314). The Open Fiber Control circuit (Fig. 14.14) utilized the fact that the transceiver was a duplex link, so that when light incident on the receiver portion of the transceiver was interrupted, the transmit portion was immediately turned off. The laser was then pulsed with a low duty cycle at a power level below the maximum eye safety limit.

Fig. 14.12 GigaBit Interface Converter (GBIC) module, circa 1998. The GBIC was hot-pluggable, hot-swappable in the field giving customers greater flexibility and the ability to optimize configuration and deployment costs

When the fiber connection was restored, a DC detection circuit in the receiver would detect the connection and both the near and far-end transceivers would be restored to full power, returning the link to operation. In the late 1990s, the laser safety standards were effectively relaxed as more biological data was accumulated and considered. As a result, the acceptable maximum emission limits were increased thus eliminating the need for this control circuitry. The elimination of this circuitry reduced the number of components, simplified test complexity, and ultimately led to even lower costs.

14.5 Today's VCSEL-Based Transceivers

The relentless drive for higher data rates continues unabated. Around 1999, the IEEE 802.3 standards organization began work on the next generation of Ethernet, 10 Gb/s or ten times the previous generation. As the committees debated physical form factors and interfaces for the new 10 Gb/s standard, it was determined a 4-lane, parallel interface, called XAUI, was optimal for the same reasons as the GLM noted above for 1 Gb/s data rates. The XENPAK and X2 form factors (see Fig. 14.15) were larger, in part to accommodate the longer distance solutions (e.g. 10 km) using InGaAsP-based sources required for 10 Gb Ethernet. Eventually, a narrower form factor having a serial interface (XFP) gathered momentum, which provided the customer with more ports per linear inch on the edge of the card–an important parameter from an overall system cost point of view. This XFP form factor is recently giving way to the SFP+ form factor (Fig. 14.16) which is essentially the same as the SFP form factor mentioned earlier.

It has become increasingly challenging for current datacom transceiver manufacturers to sustain a longstanding trend of cost reductions. Figure 14.17a, b shows the progression of datacom interconnects as a function of time and associated costs. Using the metric of \$ per Gb/s, cost reductions are approximately 2× every six years. But the relatively easy cost reductions have been made, for example: device changes

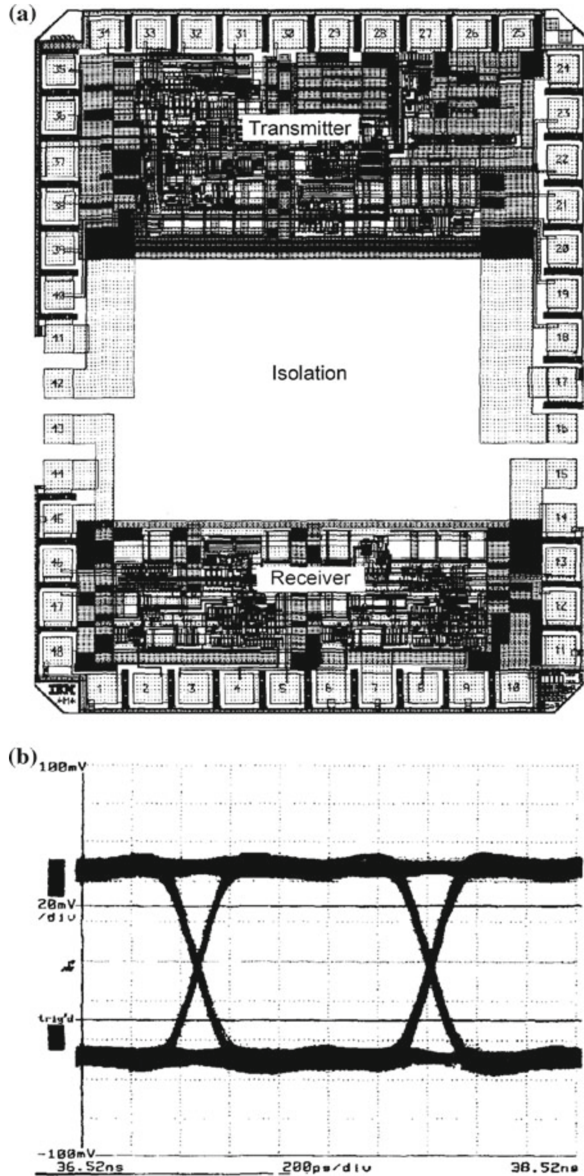

Fig. 14.13 **a** Top-level image of the combined laser driver and post amplifier chip referred to as the Media Interface Controller Chip (MICC). To minimize on-chip crosstalk the two functional blocks were separated with an isolation area. **b** Electrical eye diagram output of the laser drive section operating at 1.06 Gb/s [8] (© 1997 IEEE)

(VCSELs), material changes (plastic optics), higher levels of electronic integration, and increased yields due to better manufacturing uniformity of optoelectronic devices. Over the last few years, attention has been paid to minimizing packaging complexity and therefore cost and applying higher speed circuit technologies

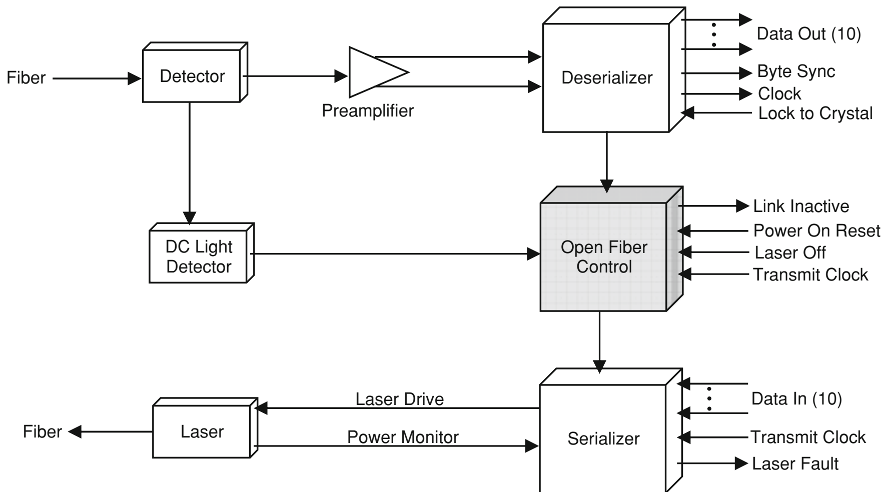

Fig. 14.14 Simplified functional block diagram showing the Open Fiber Control features of an early laser-based data communications transceiver

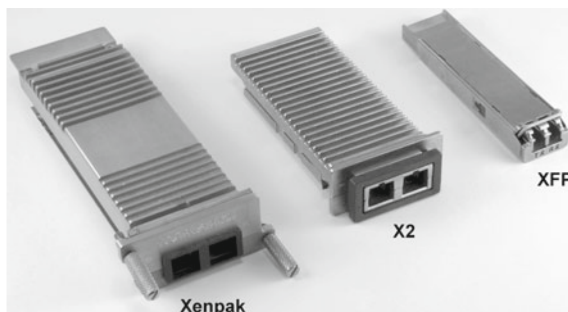

Fig. 14.15 Xenpak, X2 and XFP, 10 Gb/s transceiver Form-factors. The Xenpak and X2 transceivers have a 4-lane, parallel electrical interface at 3.125 Gb/s per lane. The optical interface is a duplex SC fiber connector. The XFP has a serial electrical interface operating at a data rate of over 10 Gb/s. The optical interface is a duplex LC fiber connector

to correct and adapt for design and/or manufacturing variations in the various components.

One example has been to eliminate unnecessary packaging components. Figure 14.18a, b show an optical receiver in which the submount/de-coupling capacitor has been eliminated so that the photodiode is placed directly on top of the transimpedance amplifier chip. With proper use of differential signals and the use of on-chip filtering, the design can perform as well as the traditional receiver utilizing multiple external components. Such designs lead to lower costs due to fewer components and less complexity. More recently, the desire to reduce packaging costs

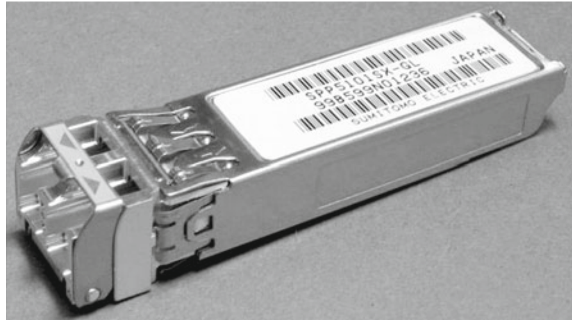

Fig. 14.16 Small Form-factor Pluggable "plus" (SFP+) transceiver. This form factor is currently used with 8 and 10 Gb/s applications and is essentially the same form factor as the one used with lower data rates (Courtesy of Sumitomo Electric Device Innovations U.S.A.)

has resulted in using approaches which are common in parallel optical interconnects (the subject of another chapter of this book). In this case, the VCSEL or PD die is placed directly on a substrate (e.g. printed circuit board) containing the laser driver. This approach eliminates the traditional TO-can and its associated terminal interfaces. These approaches subject the optoelectronic devices to an uncontrolled, non-hermetic atmosphere and VCSEL and photodiode suppliers have enhanced the ruggedness of the die so they can tolerate this potentially hostile environment. These so called "chip-on-carrier" approaches can result in even lower costs, as the number of packages and packaging interfaces are reduced or eliminated.

Another cost-reduction approach gaining in popularity is based on well-known electronic dispersion compensation (EDC), where signal distortion is removed using adaptive equalization [9–11]. In this instance, a signal may become distorted from the bandwidth-distance limitation of the multimode fiber which limits the maximum distance of the link for a given data rate. This is a key and persistent problem for datacom users in which a particular length of installed fiber can become obsolete as the data rates continue to increase. Also, signal distortion may be due to the use of long copper traces connecting host circuits to the optical transceiver modules, or the distortion may be caused by the use of lower speed and therefore lower cost components having slow rise and fall times. This EDC approach involves incorporating the equalization function in the host side electronics where the extra circuitry adds minimal complexity, power dissipation and cost.

Figure 14.19 shows an oscilloscope photograph of the eye diagram of a distorted signal, in this case, caused by the use of a relatively long length of multimode optical fiber operated at a data rate where the bandwidth of the fiber degrades the signal. As can be seen, the equalization circuitry removes the distortion and produces error-free communications. Such approaches may enable even lower cost transceiver solutions.

14.6 Future of VCSEL-Based Transceivers

While current VCSEL transceivers are offered at speeds up to 12.5 Gb/s, the development of next-generation Ethernet, Fibre Channel, and Infiniband standards continues

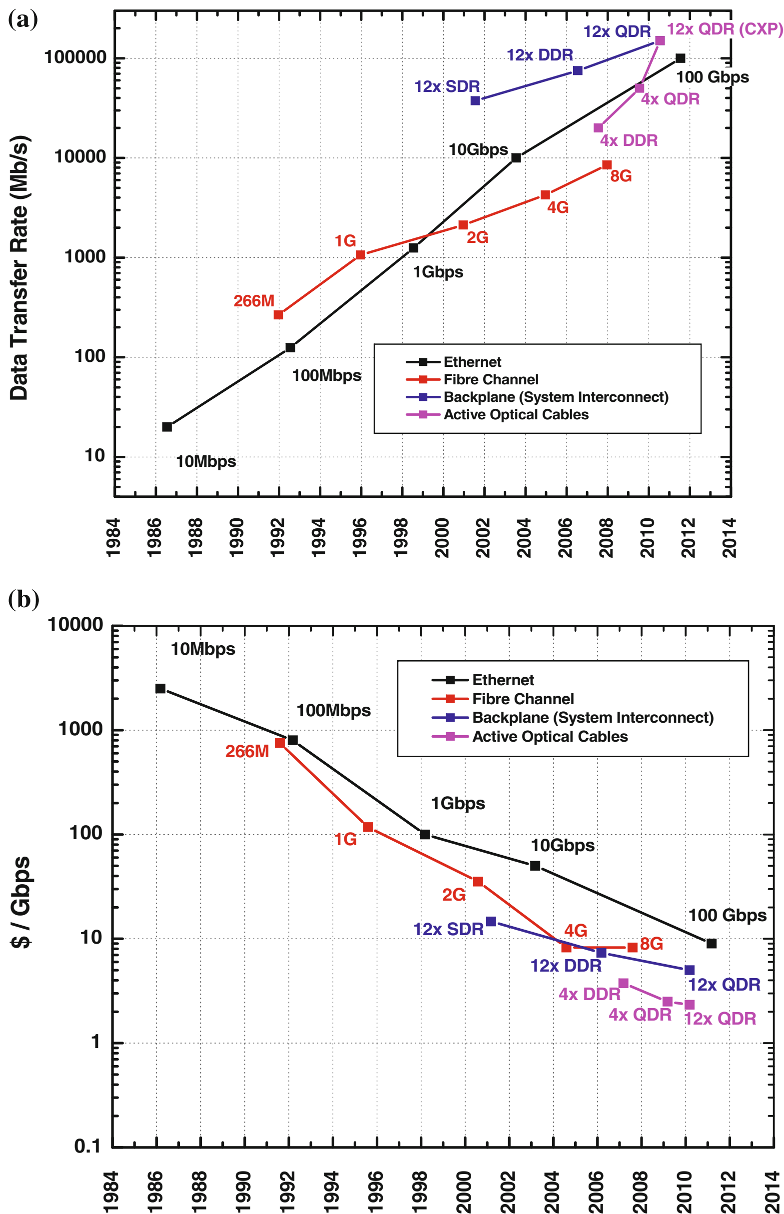

Fig. 14.17 **a** Progression of data transfer rate of transceivers over time. Date used is approximately the year in which volume shipments occurred. **b** Associated costs of transceivers normalized to cost per Gb/s. Note: Parallel interconnects denoted as 4× and 12× with Single Data Rate (SDR), Double Data Rate (DDR) and Quad Data Rate (QDR) are included for comparisons

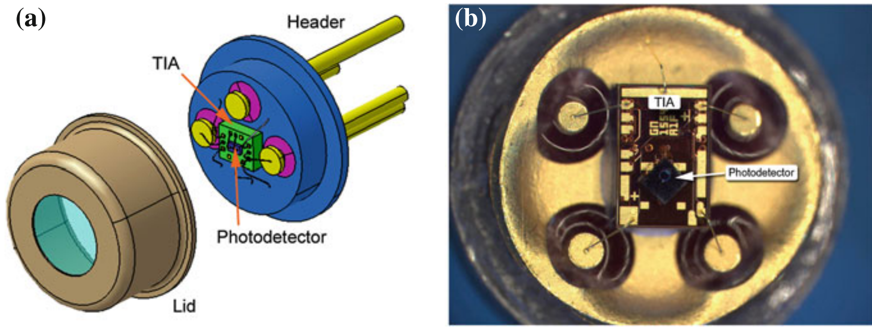

Fig. 14.18 **a** Mechanical drawing of an optical receiver used in many data communications transceivers today. The receiver consists of a photodetector placed directly on top of the transimpedance amplifier (TIA) which is placed in a TO-46 header. **b** Top view photograph of device. (Courtesy of Gennum Corporation)

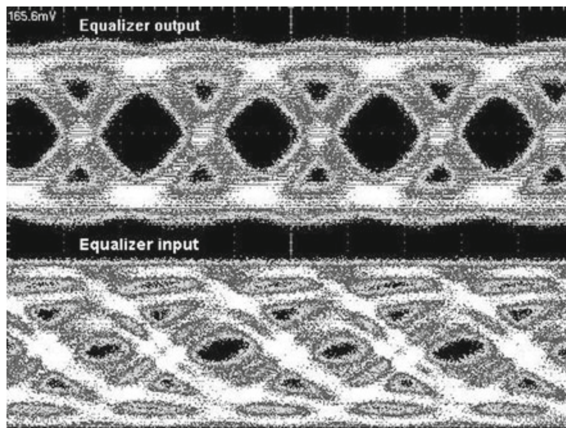

Fig. 14.19 Oscilloscope response of a 10 Gb/s data pattern showing electrical waveform input to the equalizer circuit (*bottom*) and the resulting output waveform after the equalizer removes the "channel" degradation [9] (© 2003 IEEE)

to motivate the development of higher-speed devices. Serial data rates are expected to exceed 20 Gb/s within the coming years, and many research efforts are focused on extending data rates up to 40 Gb/s. VCSELs emitting at 850 nm have been operated at data rates from 30 Gb/s [12] to 40 Gb/s [13]. Longer-wavelength devices have also achieved impressive speeds, with devices at 980 nm [14], and 1,100 nm [15] attaining 30 to 40 Gb/s data rates. These research achievements illustrate the potential of VCSELs to keep pace with ever-increasing data rates, but are not representative of true production-level devices. For commercial offerings, reliability must be proven and a range of specifications must be met with high-yield: spectral width, RIN, threshold current, series resistance, etc. Product-ready VCSELs for >20 Gb/s applications will likely require several years of development.

While worldwide high-speed VCSEL research can be expected to continue to set and break speed records, the VCSEL device itself is only one component of a transceiver module. For serial transceivers to continue to extend to higher data rates, technologies beyond the VCSELs must be improved. Improvements in key areas must be realized, including: higher-performance device and module packaging that maintains low assembly and test cost, higher bandwidth photodiodes that are compatible with low-cost coupling to MMF, and higher speed and lower-power dissipation driver and receiver electronics with higher integration and added function (e.g. equalization).

Developing low-cost receivers for $> 20\,\mathrm{Gb/s}$ links is likely to be at least as challenging as producing the corresponding VCSELs. Typically, the gain and bandwidth of transimpedance amplifiers are closely linked, and both are constrained by the photodiode capacitance. A lower photodiode capacitance translates into a smaller RC time constant that can be exploited to yield either greater bandwidth or higher transimpedance gain. However, reducing photodiode capacitance typically is achieved by shrinking the active diameter of the detector. Coupling from multimode fiber to small-diameter photodiodes then becomes more difficult to do in a cost effective manner as greater magnification is required that reduces alignment tolerances. Receiver sensitivity is also reduced as data rates are scaled due to a larger required bandwidth, resulting in less available link budget. Research efforts are underway to help alleviate some of the trade-offs in receiver circuit design, and new transimpedance amplifier architectures have been specifically designed to tolerate large photodiode capacitances [16, 17].

Reducing power consumption is also becoming a much greater priority in recent years in the design of large-scale networks and computing systems. This emphasis on low-power operation is migrating down to the transceiver level. Continuing to develop VCSELs with lower thresholds and higher slope efficiencies will help to reduce transmitter power consumption, but innovation in circuit design will also be required as data rates continue to increase. Today, nearly all analog chips for multimode transceivers are built using SiGe Bi-CMOS, a technology that has not been advancing as quickly as CMOS. Relentless scaling may begin to make CMOS advantageous for building analog driver/receiver chips, eventually supplanting Bi-CMOS as the circuit technology of choice for multimode transceiver electronics. No matter what process technology is utilized, the energy efficiency of multimode transceivers, typically expressed in mW consumed per Gb/s transferred (mW/Gb/s or pJ/bit), must be improved over current products. In addition, as data rates move beyond 20 Gb/s, accumulated jitter, contributed by the optical and the electrical links at the transceiver input and output will become a severe problem. To allow reasonable jitter budgets for system design, it is likely that some re-timing will be required in the transceivers: at least re-clocking the serial data and perhaps returning to the inclusion of complete serialization/deserialization within modules.

Finally, the unique structure of VCSELs allows them to be readily populated into large two-dimensional arrays. This feature enables a dimension of scaling not easily achieved with edge-emitting lasers: deploying parallel optical interconnects to offer higher bandwidth optical data buses. Chapter 16 of this book discusses imple-

mentations of parallel VCSEL-based optical interconnects in detail. While parallel optical interconnects are poised for rapid growth in the coming years, driven by bandwidth hungry high-end computing and networking applications, next-generation serial VCSEL transceivers will continue to be a high growth, high-volume market owing to their low production cost and continually improving performance.

References

1. N.R. Aulet, D.W. Boerstler, G. DeMario, F.D. Ferraiolo, C.E. Hayward, C.D. Heath, A.L. Huffman, W.R. Kelly, G.W. Peterson, D.J. Stigliani Jr., IBM enterprise systems multimode fiber optic technology. IBM J. Res. Dev. **36**(4), 553–576 (1992)
2. R.L. Soderstrom, T.R. Block., D.L. Karst, T. Lu, An optical data link using a CD laser. In *High-Speed Fiber Networks and Channels*, ed. by K. Annamalai. Proceedings of SPIE, vol. 1577 (1991), pp. 163–173
3. A.M.J. Koonen, Bit-error-rate degradation in a multimode fiber optic transmission link due to modal noise. IEEE J. Selected Areas in Commun. **4**(9), 1515–1522 (1986)
4. Fibre channel physical and signaling interface (FC-PH), Rev 4.3, http://www.t11.org (1994)
5. D.M. Kuchta, C.J. Mahon, Mode selective loss penalties in VCSEL optical fiber transmission links. IEEE Photon. Technol. Lett. **6**(2), 288–290 (1994)
6. K.H. Hahn, M.R. Tan, Y.M. Houng, S.Y. Wang, Large area multitransverse-mode VCSELs for modal noise reduction in multimode fibre systems. Electron. Lett. **29**(16), 1482–1483 (1993)
7. INF-8074i Specification for SFP (Small formfactor pluggable) transceiver, Rev 1.0, *SFF Committee* ftp://ftp.seagate.com/sff (May 2001)
8. S. Baumgartner, L. Freitag, M. Paschal, D. Siljenberg, An integrated 1.25 Gb/s laser driver post amplifer IC. *IEEE Custom Integrated Circuits Conference*, Sect. 2.4, pp. 17–20 (1997)
9. H. Wu, J.A. Tierno, P. Pepeljugoski, J. Schaub, S. Gowda, J.A. Kash, A. Hajimiri, Integrated transversal equalizers in high-speed fiber-optic systems. IEEE J. Solid-State Circuits **38**(12), 2131–2137 (2003)
10. D. McGhan, Electronic dispersion compensation, *Optical Fiber Communication Conference, OFC*, 2006, tutorial OWK1 (Feb. 2006)
11. A. Ghiasi, M. Dudek, Benefits of EDC and linear receivers for short reach 40/100 GE. IEEE Commun. Mag. **46**(2), S17–S21 (2008)
12. R.H. Johnson, D. Kuchta, 30 Gb/s directly modulated 850 nm datacom VCSELs, *IEEE Conference on Lasers and Electro-optics/Quantum Electronics and Laser Science*, *CLEO/QELS*. San Jose, CA, May 2008, paper CPDB2
13. S.A. Blokhin, J.A. Lott, A. Mutig, G. Fiol, N.N. Ledentsov, M.V. Maximov, A.M. Nadtochiy, V.A. Shchukin, D. Bimberg, Oxide-confined 850 nm VCSELs operating at bit rates up to 40 Gb/s. Electron. Lett. **45**(10), 501–503 (2009)
14. Y.-C. Chang, C.S. Wang, L.A. Coldren, High-efficiency, high-speed VCSELs with 35 Gb/s error-free operation. Electron. Lett. **43**, 1022–1023 (2007)
15. T. Anan, N. Suzuki, K. Yashiki, K. Fukatsu, H. Hatakeyama, T. Akagawa, K. Tokutome, M. Tsuji, High-speed 1.1 μm range InGaAs VCSELs, *Optical Fiber Communication Conference*, *OFC*, 2008, paper OThS5 (Feb. 2008)
16. S.M. Park, H.-J. Yoo, 1.25-Gb/s regulated cascode CMOS transimpedance amplifier for Gigabit Ethernet applications. IEEE J. Solid-State Circuits **39**(1), 112–121 (2004)
17. C. Kromer, G. Sialm, T. Morf, M.L. Schmatz, F. Ellinger, D. Erni, H. Jäckel, A low-power 20-GHz 52-dBΩ transimpedance amplifier in 80-nm CMOS. IEEE J. Solid-State Circuits **39**(6), 885–894 (2004)

Chapter 15
Low-Cost Optical Video Links Based on VCSELs

Hyun-Kuk Shin

Abstract The history of introduction and current status of VCSEL based optical video link modules which have emerged as one of the main applications of VCSELs are described. The structure and characteristics of VCSELs in optical video links are summarized. The technical issues of the next generation optical video links for the mass market are discussed.

15.1 Introduction

As graphic signal was digitalized in the late 1990s, DVI (Digital Visual Interface), one of several digital interfaces, has rapidly emerged as a standard of the digital graphic data transmission in PC industry [1]. With the spread of DVI, the demand of optical video link for the long distance transmission, usually referred to as the distance longer than 10 m, has also been issued.

Though the use of laser or LED was considered for a long distance transmission when almost all graphic signals were transmitted in an analog way in the past, it could not become popular due to the high cost of analog signal transmission through optical fiber. So, very thick and shielded coaxial cables were used instead of optical fiber for many years.

However, unlike analog interface whose bandwidth was only 100–200 MHz per each color, the speed of digital interface easily exceeded Gbps per color, and naturally, optical video link using semiconductor laser was introduced. As HDMI (High Definition Multimedia Interface) standard targeting the home TV market was distributed in 2002, demand for optical video link was further increased [2].

H.-K. Shin (✉)
OPTICIS Co., Ltd, Suite 304, Byucksan Technopia,
434-6 Sangdaewon-dong, Jungwon-Gu, Sungnam City,
Gyunggi-Do 462-120, Korea
e-mail: hkshin@opticis.com

R. Michalzik (ed.), *VCSELs*, Springer Series in Optical Sciences 166,
DOI: 10.1007/978-3-642-24986-0_15, © Springer-Verlag Berlin Heidelberg 2013

DVI standard was introduced right after 850 nm VCSEL was applied to Gigabit Ethernet transceiver, and the speed per channel was similar. Therefore 850 nm VCSEL applied to the optical video link module for DVI quickly. In 2000, the first optical video link module that completely supported the DVI standard was announced [3]. Since then, various optical video link modules were developed by several companies, and most of the products used 850 nm VCSEL. The concept of the optical module and technical issues will be described in Sect. 15.2, and the characteristics of the VCSELs used in the transmission of signals with regard to DVI or HDMI will be explained in Sect. 15.3.

DVI and HDMI are basically a multi-channel interfaces, and due to the advantages of VCSEL where multi-channel can be easily implemented and it is convenient in terms of package, low cost and small size optical video links could be made. And on the back of advantages of optical video links that can maintain the quality of signals regardless of the location of display equipment, diversified display systems could be configured. Accordingly, although it is not easy for us to find them sometimes, the VCSEL optical video link modules can be found in a variety of places. Some interesting application areas are shown in the Sect. 15.4.

High-resolution large screen display has rapidly been implemented, and new standards such as DisplayPort have been adopted following DVI and HDMI in order to respond to continuous increase in the speed of graphic signal transmission. The new interface requires a 10 Gbps bandwidth or higher, and the optical video link module is expected to be more critical in the design of display system.

In addition to external link module, the transmission speed of graphic signal inside the display equipment is also rapidly increasing along with higher resolution and higher refresh rate. Therefore the optical video link module that has been applied only to the industrial market and some high-end A/V system markets is expected to develop into the huge volume market for the use inside the display equipment. In order to successfully enter such mass market, further miniaturization of the module may be necessary as well as the reduction of manufacturing cost. In addition, technical breakthrough is required to reduce the number of optical fibers. The technical issues to achieve such improvements will be described in the Sects. 15.5 and 15.6.

15.2 Optical Video Link Modules for DVI and HDMI

Graphic signals in DVI and HDMI are transmitted in the format of TMDS (Transition Minimized Differential Signaling) [4]. Though a different signal format, LVDS had been widely used in the internal interface that transmits signals to LCD panel from the main board of a laptop PC or a LCD TV, TMDS was chosen as a standard of external interface owing to the function of skew compensation and other advantages. Fortunately, TMDS could make the implementation of optical link easy. LVDS signal for which DC balance was not considered cannot be easily transmitted through optical fiber without additional coding, but as 8B/10B coding is applied, the TMDS signal for which DC balance was considered to a great degree could be easily connected

Fig. 15.1 World first DVI optical video link module

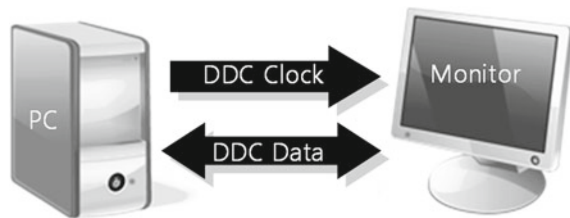

Fig. 15.2 Directionality of DDC signals in DVI

through optical link. In this regard optical video link module was developed as DVI was used to display equipment.

Figure 15.1 shows the DVI optical video link module that was commercialized for the first time in 2000. The product was made to support SXGA resolution, the highest resolution in the market at that time. Seven 850 nm oxide VCSELs and seven PIN photodiodes (PDs) were used to support transmission speed up to 1.08 Gbps per each channel.

In addition to four VCSELs corresponding to three colors and one clock, three VCSELs were used in order to transmit DDC (Display Data Channel) signals. The function of DDC signal is to read the information of a display device and enables graphic source to transmit appropriate graphic signals, and its protocol complies with IC widely used in the bus between ICs [5, 6].

As DDC signals consist of two-way channels including Clock and Data, the clock is used only in one direction in most display devices (Fig. 15.2).

In order to support bi-directional data channel, two pairs of VCSEL-PD and uni-directional clock channel, one pair of VCSEL-PD is used. The DC balance was not considered at all, but since the highest speed is only 400 kbps, optical transmission is possible. However, due to the presence of bi-directional signal, it is impossible to connect electric signals to optoelectronic device directly, and it requires additional circuit part that determines the direction of signal.

The optical transmission block of the Fig. 15.1 product is shown in Fig. 15.3. As there is a circuit part that detects the direction of signal transmission between source or display and VCSEL operation part, VCSEL connected to source or display is turned on, and accordingly, the direction of data transmission is determined. The

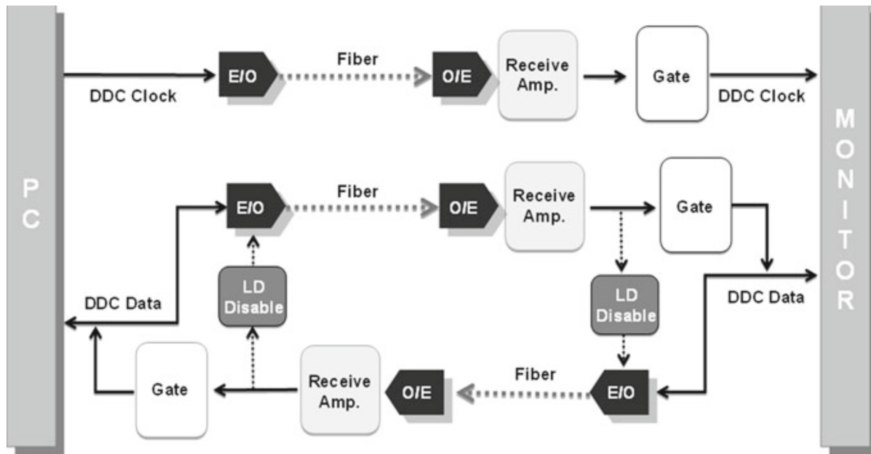

Fig. 15.3 The schematic of optical transmission of DDC signals

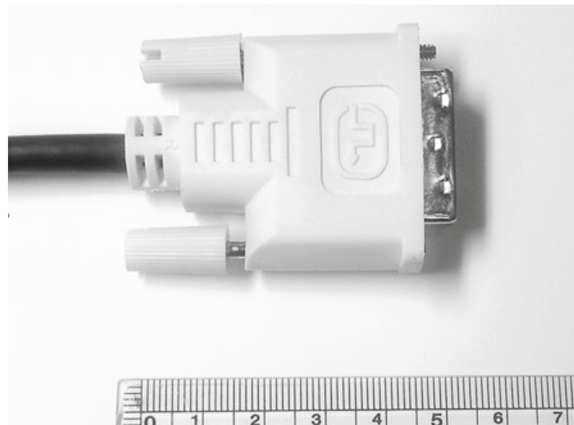

Fig. 15.4 Size of a copper DVI cable

fact that Gbps graphic signals and kbps DDC signals can be transmitted through the use of the same VCSEL well demonstrates that VCSEL has wide range of application as well as price competitiveness.

The product of Fig. 15.1 looked like a copper cable and could be conveniently used in a way of 'plug and play'. It led various active optical cable products which were released afterwards by several companies.

One of the most important design points in the active optical cable product is limitation of size. It is natural for customers to want the same size of the DVI optical active cable as the DVI copper cable. Otherwise, it is not easy to directly connect to display related devices with many ports. The size of typical DVI copper cable, which

Fig. 15.5 An example of optical connector for optical video link

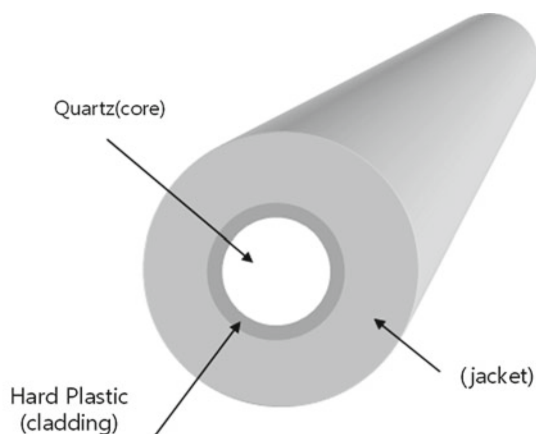

Fig. 15.6 Structure of H-PCF

is shown in Fig. 15.4 is not so big, usually 49 mm(L) × 40 mm(W) × 16 mm(H). Considering the space for DVI connector and control circuit of DDC signal in addition to seven channels OE/EO conversion part, there remains little room in pure optical packaging. Therefore it can hardly contain the popular TO packages, and so direct coupling is frequently used between VCSEL and optical fiber. Figure 15.5 shows the example of VCSEL package structure used in the actual product. VCSEL chip is positioned one after another within a narrow partition in order to block optional crosstalk and coupled with fiber bundle.

Another important issue in the active optical cable product is to select fiber or cable. In order to implement small size products, passive alignment process is advantageous. So a larger core optical fiber such as hard core polymer clad fiber (H-PCF) was used initially (Fig. 15.6).

Such a fiber, with core diameter 200 μm or larger, does not require alignment and polishing, so it is advantageous at a time of mass production. But since the price of the fiber is usually higher than multi mode optical fiber (MMF) and because of large

Fig. 15.7 Optical video link module for DVI using hybrid cable

core, the efficiency of light incident on PD may be very low without lens. For this reason, MMF was used recently more often than H-PCF.

In the case of MMF, passive alignment is possible in principle, but in that case, great precision might be required in making packaging components. If low-price parts are used instead of high-price precision parts, alignment of multiple channels should be done in a small space.

In order to overcome the difficulties described in the above, plastic optical fiber (POF) with core diameter around 100 μm can be used as a tradeoff between H-PCF and MMF. The development of perfluorinated POF that can support the speed of multi Gbps with loss being 0.06 dB per meter or lower in the band of 850 nm opened a new possibility in optical video link [7].

Among various optical fibers, MMF is most commonly used, and it seems due to the consideration of the price, availability and packaging cost. However, if the price of POF is reduced significantly, the POF may be widely used owing to the advantages of POF such as flexibility of fiber and easy coupling with laser output.

On the surface, active cable products look similar to copper cable products, but since it has optical conversion part, it requires separate power supply for the operation of TX and RX. In particular, all optical products are divided into transmitter part (TX) and receiver part (RX) and need separate power supplies.

In order to remove such inconvenience, optical video link module that includes electric wires in a cable for transmission of power and low speed DDC signal was commercialized right after as shown in Fig. 15.7. The product used hybrid cable including optical fiber and electric wire was not technologically improved but provided better function of unified power supply. In particular, if sufficient electric current is supplied in the graphic source, it can be operated without a separate power adapter, which is very convenient for users.

In addition to 4-strip fiber optic that connects 4 VCSEL-PIN PDs, a hybrid cable that consists of 5 pairs of UTP (Unshielded Twisted Pair) wires is used. Many strips in UTP are for DDC, power transmission and GND.

Fig. 15.8 Optical video link module transmitting graphic signals only

The product of active optical cable like that in Fig. 15.1 or 15.7 was accepted by the market well, maybe due to its familiar look and ease of use. However, in some cases, it requires a lot of time and money to install or remove the product since it cannot go through the conduit due to the large size of modules at both ends. Therefore there was demand, from system integrators, for a function to attach or detach optical fiber so that they can install the fiber through conduit easily.

In order to respond to such demand, a product where optical fiber can be attached or detached while optoelectronic conversion part was connected to source or display was soon introduced.

A product in which fiber can be attached or detached that transmits only the graphic signals through the use of a 4-channel LC patch cord was announced in 2001 Fig. 15.8. Due to the restriction in size, LC connectors are more widely used than ST and SC form factors. 850 nm VCSEL TO package is used, and the structure is not much different from what is frequently used in a VCSEL transceiver.

The concept of a breakout cable with solid jacket where 4 LC ferrules are placed at both ends was very convenient, and it resolves problems in system installation and construction.

One of the problems of such product was that there was no space to send and receive DDC signals while 4 TO packages were already being inside.

In order to send the suitable data without the channel for DDC, a method to store the appropriate information of display device on TX part of the optical video link module and to enable a graphic source to send appropriate data communicating with TX part was developed.

The optical video link module that transmits DVI signals went through numerous improvements, and currently, many companies are manufacturing various products for a wide range of applications.

How the optical video link module is being used will be described in Sect. 15.4.

In DVI, the optical video link module has been recognized to be efficient in a long-distance transmission, but it was not rapidly distributed in HDMI that was established after DVI targeting the consumer market in 2002.

Table 15.1 Comparison between DVI and HDMI

	DVI	HDMI
Height (mm)	15.5	10.0
Length (mm)	48.8	34.8
Width (mm)	39.5	20.0
Maximum number of pixels	1600×1200	1920×1080
Additional signals other than graphic	DDC	DDC,CEC
Encryption	No	Yes
DDC check	once at beginning	every 200 μs

Fig. 15.9 Optical video link for HDMI

One of main reasons was that optical parts technology was not good enough to supply the optical video link module suitable for HDMI.

From the perspective of the optical video link module, difference between DVI and HDMI can be summarized as in Table 15.1.

Size may be one of the most serious restrictions on the design of the optical video link module for HDMI. As seen in the table, the allowed volume of optic conversion part for HDMI is reduced down to a quarter or even smaller size compared to DVI's.

For the purpose of drastic reduction in size, the development of a small package that enables passive alignment between VCSEL array and fiber array has become one of the most important issues. Recently several companies announced the development 4-channel or 8-channel optoelectronic conversion modules which are integrated in a small package. In several cases of such modules, VCSEL or PD array are mounted on silicon optical bench and coupled with fiber ribbon through passive alignment [8]. However, despite numerous attempts, packaging that can implement HDMI size has not yet been commercialized.

Fig. 15.10 Optical and CAT5 video link for HDMI

In order to avoid the size problem prior to the completion of a new technology, a product with optoelectronic conversion part in the middle of cable as seen in Fig. 15.9 was commercialized in 2005. Some products avoided the problem of size by using the short copper cables to connect optical module with display equipments. Either way, 4 pairs of VCSEL-PIN PD were used, and both types of products show that we can hardly solve the size problem with the present status of technology.

As described in Table. 15.1 another difference between HDMI and DVI is that, in HDMI, DDC should be communicated without any interruptions. And moreover there is an additional bi-directional channel, called CEC, in HDMI. There are several ways to meet such differences, adding more VCSEL channels or implementing MUX/DEMUX of different signals and so on. In any case, it results in increasing the size. After all, the box type product as seen in Fig. 15.10 was announced first.

High speed graphic signals are transmitted by four VCSELs and low speed bi-directional signal by CAT5 cable, so it adopts an eclectic method. Transmitting all signals including HDMI by small optical module is a task to be done in the future. For the transmission of two signal groups of different characteristics in small module, a combination of optical and wireless may be considered in the future. In such concept, VCSEL and optical fiber may be used for high speed graphic signal and wireless communication for low speed DDC or CEC signal [9].

Finally let us consider the difference of bandwidth problem. Bandwidth is determined by the number of pixels, the number of color bits and refresh rate. As for the number of pixels, there is not much difference between HDMI and DVI, around 2 million pixels for highest resolution.

However, there is considerable difference in color bits. HDMI that started with 24 bit color like DVI has expanded the number of color bits up to 48 bits along with the establishment of HDMI 1.3 standard in 2006 [2].

Accordingly, it requests 2.97 Gbps per channel at a total of 8.8 Gbps much higher from existing 1.485 Gbps per channel at a total of 4.4 Gbps. From the perspective of optical transmission, the range can be easily covered, but in the future when all signals are transmitted through one optical fiber, cost will be burdensome. In addition, a next-generation large screen display with 4–8 million pixels that goes beyond 1080p or UXGA is expected to be commercialized, and a higher bandwidth

is likely to be necessary. In this regard, up to 30 Gbps of high speed parallel optical interconnection may be introduced.

15.3 VCSEL in Display Interconnection Module

As mentioned in the introduction, 850 nm VCSEL was chosen as the most suitable light source of the optical video link because the transmission distance was less than 1 km in most display systems and multi channel optical link was used with the transmission speed one to two Gbps per each channel. Though similar characteristics were required for VCSEL in optical video link compared with VCSEL transceivers in datacom market, whereas a difference in priority exists.

One of the biggest differences is again the limit of the packaging size. As mentioned in the previous section the size of optical video link might be determined by that of copper cable in the market. To implement four or seven channels optical transmission module in a size of DVI connector, we can hardly use TO package, and even more difficult for HDMI. Accordingly, as described in the previous section, direct coupling in small size package without lens was often used.

In that case, we need package structure that can adjust coupling efficiency of multiple channels while maintaining the distance between VCSEL and optical fiber at 200 μm or less. As for VCSEL, we may need to have a small divergence angle for high coupling efficiency frequently necessary for the transmission quality. The small divergence angle is often from small operating current, and so we need to try to reduce the driving current.

On the other hand, in order to acquire sufficient optical output power in this low driving current, the large slope of the light versus current (L–I) curve may be desirable. For a large L–I slope, the reflectivity of top mirror may be reduced a little bit. In the products in Figs. 15.1 and 15.7 the transmissivity of top mirror was almost doubled by the deposition of SiN on the top mirror.

In the case of direct coupling between VCSEL and optical fiber, another important issue is the degradation of high frequency signal transmission quality. Without lens, the coupling efficiency may be different depending upon the transverse modes. The higher order transverse modes usually have smaller coupling efficiency compared with the lower order modes. Differences in coupling efficiency among transverse modes may increase overshoot and increase/reduce rising time causing the degradation of high speed data transmission quality.

In order to get the better signal transmission quality, it is desirable to raise the bandwidth of VCSEL higher than actual data transmission rate. High frequency characteristics of VCSEL can be expressed in many different variables, and one of them, relaxation oscillation frequency (ROF) expresses high frequency modulation characteristic of VCSEL in an appropriate way. One of simple ways to improve ROF is to reduce the size of active area of VCSEL, and it can be easily applied. VCSEL with better high frequency characteristic may compensate the degradation of transmission quality caused by simple packaging.

In most optical communication modules, APC (Automatic Power Control) circuit is used to maintain the constant optical output power from VCSEL in various environments. It adjusts the drive current of VCSEL depending upon the output current of PD for power monitoring on which a portion of optical output of VCSEL is incident. The PD for power monitoring is usually located near to VCSEL and it captures the light reflected by the cap window of the package. If the temperature rises, optical output of VCSEL is reduced and optical input of monitor PD is reduced. If output electric current of monitor PD is reduced, diver IC increases input electric current of VCSEL to maintain optic output constantly.

Though the APC circuit is desirable for the reliable operation of VCSEL over the wide range of temperatures, it is not easy to apply it to optical video link module due to a limited space. Without APC, VCSEL in optical video link module operates at a constant drive current. Therefore, we should limit the change of optical output power of VCSEL as temperature changes over operating temperature range, usually 0 to 50°C or −10 to 70°C depending upon the application. According to the experience of the author, the maximum allowed change of optical output power was about 1 dB.

One of the most critical issues without APC is related with the threshold current. The threshold current usually changes with temperature. Without APC the fixed operating current may become lower than the threshold current at a certain temperature. In such case, we may not get the suitable high frequency response of VCSEL and so the eye pattern may be jeopardized suddenly. To avoid the problem, we needed to set the low value of drive current higher than the threshold current all over the operating temperature range. It means that we increase the low value of VCSEL drive current at some temperature, and accordingly extinction ratio (ER) may be reduced.

Fortunately, optical video link, transmitting signals between two designated points, can do the job well with lower ER than optical data communication. In order to obtain higher ER, the threshold current should be small so that the low value of VCSEL drive current can be small as well as the temperature variation of the threshold current itself becomes small.

In the case oxide type VCSEL, the less oxidation diameter means the lower threshold current and the larger ROF. Therefore we may obtain the better high frequency characteristics, the better temperature characteristics and larger ER by making the oxide diameter small. However, the smaller active area makes the VCSEL more sensitive to external stimulation including electrostatic damage, and it may reduce the lifetime of VCSEL. In this regard, appropriate tradeoff is necessary to find a suitable value of oxide diameter.

In Fig. 15.11 the temperature variations of threshold current and optical output power of VCSEL with oxide diameter of 10 μm is shown. As the temperature increases to 70°C from normal temperature, the change of optical output power is less than 1 dB. Figure 15.12 shows the high frequency characteristics of VCSEL. ROF is measured to be about 8 GHz, much higher than the necessary bandwidth, 1–2 Gbps.

Though, as described above, 850 nm VCSEL has been used in most optical video links, a long wavelength 1.3 μm VCSEL, which is being rapidly commercialized, may be considered as a promising light source too [10]. In some applications, we

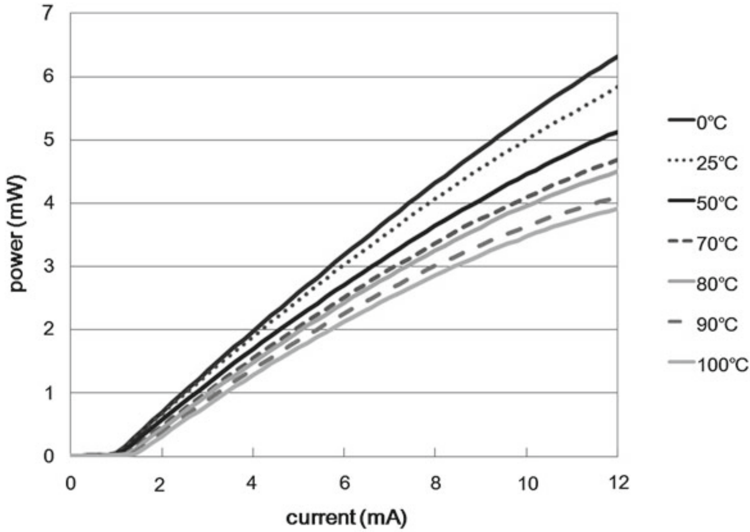

Fig. 15.11 Temperature characteristics of small aperture VCSEL

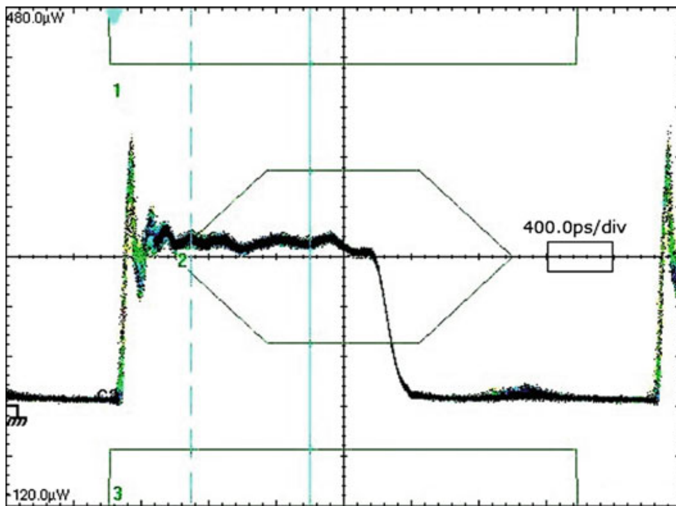

Fig. 15.12 Temporal response of a VCSEL showing relaxation oscillations (no electrical filtering has been applied)

need longer transmission distance about a few kilometers using long wavelength laser and single mode optical fiber. Moreover, considering that most installed optical fibers are single mode fibers, it may become appealing to system integrators.

In addition, at a time of sending graphic signals through single channel optical fiber, which will be discussed in Sect. 15.5, the data speed becomes several times

higher than before. With multi mode optical fiber, the transmission distance may be limited considerably. In this regard, a combination of long wavelength VCSEL and single mode fiber which can maintain hundreds of meters of transmission distance may be preferred to 850 nm VCSEL and multi mode fiber. Due to its higher price in the early time of commercialization, the application of long wavelength VCSEL may be limited to high end system that requires a long distance transmission. As the price gap is narrowed along with the development of mass production technologies, it is expected to replace 850 nm VCSEL in most single fiber products.

15.4 Applications of Optical Video Links

Recently, the number of large screen display systems has rapidly increased. As the prices of LCD/PDP panels are dramatically reduced the price of flat-screen display equipment has continuously decreased too. Accordingly, large display systems are installed in many places. One of the most important issues in such display systems is a connectivity problem that is to connect and control the display equipments of the system. The low cost optical video link module based on VCSEL is a key component of the digital connectivity to enable an effective configuration of the display system.

This section introduces several interesting applications of optical video links and describes some design points of them. The applications introduced might not be the most important ones in the market at the moment, but they could be interesting ones with good potential in the future.

15.4.1 Train Display System

Figure 15.13 shows the picture of display equipments in the metro train. System composition is shown in Fig. 15.14. Similar systems can be used not only in metro train but also in other transportations like ships or airplanes.

Graphic signals stored in the server in an engine room are transmitted to display equipments in passenger cars. In typical metro trains, the distance between two adjacent cars is 30–50 m and TV is installed in two locations in each car. Therefore the typical connection distance of optical video link would be about 30 m. In the train, there are many kinds of copper cables for power, control signals and sensors, and so minimal number of optical fibers is usually preferred.

In the system of Fig. 15.13 electrical serialization was used to reduce the number of fibers to two. Since the resolution of the TV was not so high, the transmission speed was about 2 Gbps per channel even after the reduction of the number of fiber channels.

Another issue is the operating temperature. The temperature within the train can be much higher than 50°C which is the maximum operating temperature of most optical video link products. If you think about the subway train without an air-conditioner in the summer, you may imagine how high the temperature can go up. In some cases, it

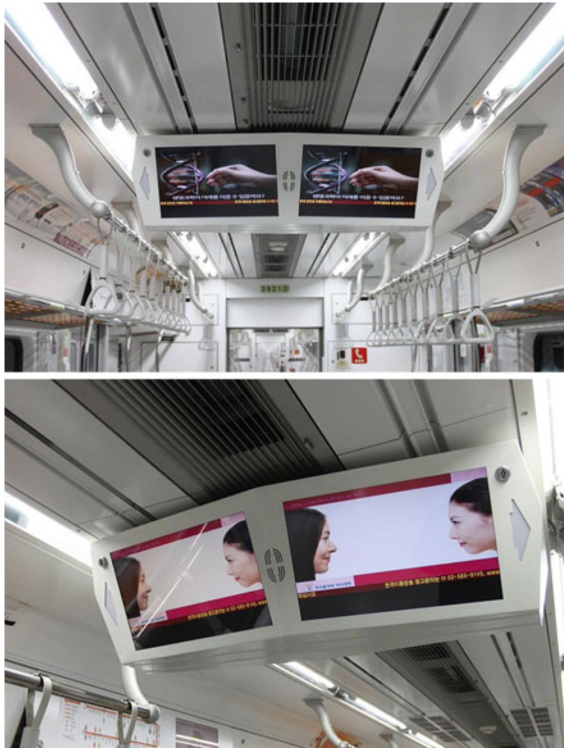

Fig. 15.13 The picture of display system inside metro train

can be 80°C or higher. Moreover, the temperature inside optical module can be even higher by 10 to 15°C. So, it is desirable to use VCSEL with very stable characteristics according to temperature change.

15.4.2 Elevator System

This kind of system is to provide multimedia information including weather and advertisements in a building from the displays installed in a lobby and elevator.

Figure 15.15 shows the simple concept of the system, and Fig. 15.16 shows an example of a display in an elevator connected by optical video link. In the elevator display systems, they want to use pre-installed optical fiber, which is usually single mode fiber. In addition, the number of available optical fibers is quite limited, so optical video link in this system should use one single mode fiber in most cases.

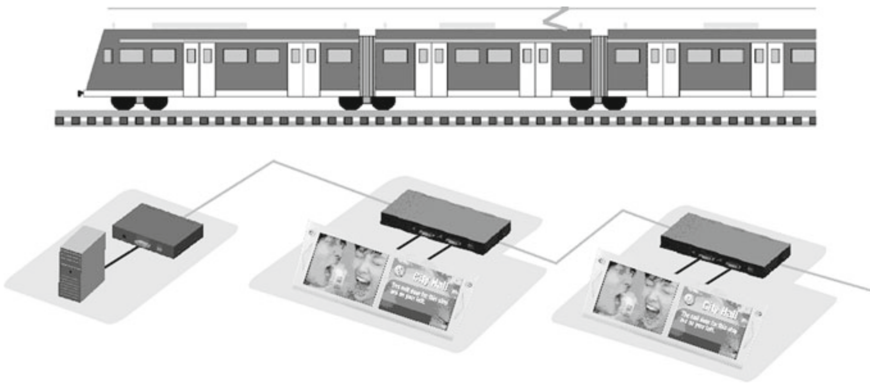

Fig. 15.14 The concept of display system in train using optical video link

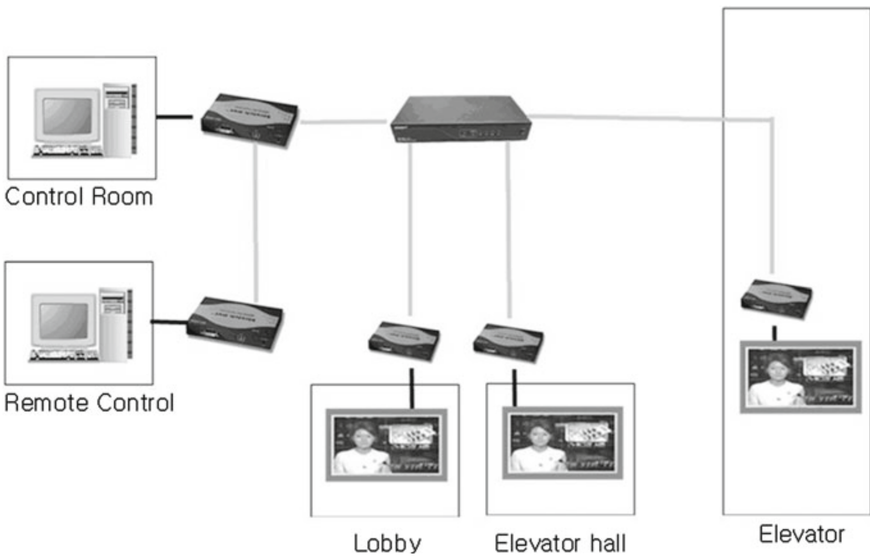

Fig. 15.15 The concept of elevator display system using optical video links

Since the display is small in an elevator, the resolution is low. Moreover, the refresh rate may be low too, for example 30 Hz instead of normal 60 Hz. It means that the bandwidth can be at most ∼2 Gbps after serialization of the graphic data.

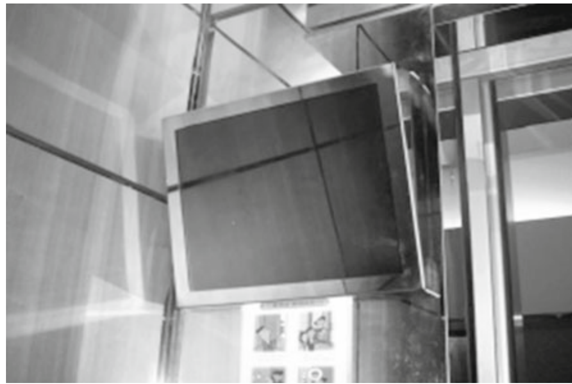

Fig. 15.16 Display inside elevator connected by optical video link

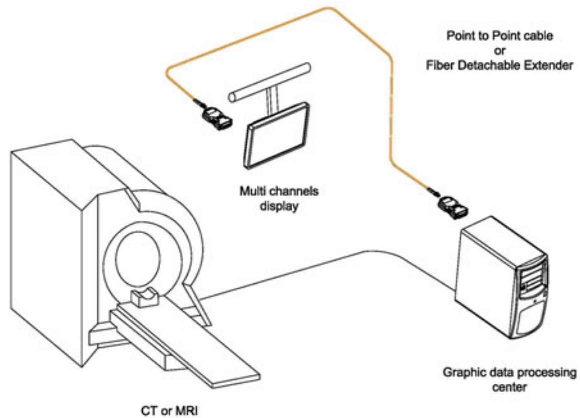

Fig. 15.17 Medical system using optical video links

15.4.3 Medical Application

There have been developed many kinds of medical equipments which need high resolution large screen display equipments. For examination, there are CT, MRI, PET and digital X-ray systems. For surgery, we may find high definition endoscope. These systems adopt highest resolution display equipments. Figure 15.17 shows application of optical video link in CT or MRI.

Since the noise caused by EMI can result in fatal consequences, copper hybrid cable is not allowed to be used in many cases, and so, optical video links without copper, such like Figs. 15.1 or 15.8 are used. Excellent EMI characteristics and high reliability are required. Thus more attention to the reliability of VCSEL in this application is essential.

In addition to the above-mentioned applications, optical video link is being used in more and more new applications. In the stadium of Olympic opening ceremony, in

major international airports and in the train station, we can find, large screen displays connected by optical video links using 850 nm VCSEL.

15.5 Reduction of the Number of Fibers

Most optical video link modules described by now use optical fibers of four channels or more. It was natural since DVI and HDMI had four channels of graphic signals. But, in real applications, it is not so convenient, especially for average consumers, to plug many lines of optical fibers. In addition smaller number of optical fibers looks better, and as mentioned in the previous section there might be a limitation on the number of usable optical fibers. So there has been strong demand for the reduction of the number of fiber channels. The reduction of the number of optical fibers has been one of the key issues in optical telecommunication market, and WDM and TDM were commercialized many years ago. It is interesting that there are similar attempts again in very short distance data transmission like optical video links.

Like optical telecommunication, the similar technologies have been suggested to reduce the number of fibers in the optical video links, and some products have already been commercialized.

The product using CWDM technology will be described first. Figure 15.18 shows optical video link module transmitting DVI graphic signals with one channel optical fiber. It contains CWDM module, where GaAs VCSEL of four different wavelengths around 850 nm are used [11]. If 770–860 nm wavelength is used, the wavelength spacing is about 30 nm, large enough in most applications. Though CWDM is not a new technology, it may be important that it can be implemented in such a small size.

Since the number of channels is four in the product of Fig. 15.18 there is no channel for DDC or CEC in HDMI. To transmit all the signals of DVI/HDMI in one optical fiber, we may need two more channels in CWDM, one from TX to RX and the other in the reverse direction. The 6 channels CWDM technology for such purpose has also been announced and is expected to be commercialized soon. There are also many efforts by several companies to develop low cost CWDM technologies for optical video links.

In addition to CWDM, serialization/de-serialization (SER/DES) technologies have also been developed to reduce the number of optical fibers. It serializes DVI/HDMI graphic signals into one channel, and additional signals like DDC, serial data, audio and USB can be mixed too. One of the main issues of SER/DES for optical video links may be the minimization of redundant data. If it fails to reduce the redundant data, the required bandwidth may become too high and the result would be high cost solution not suitable for optical video links.

The transmission speed after the serialization depends upon the SER/DES technology. In Fig. 15.19 there is shown an example of one-fiber HDMI optical link using SER/DES developed by a small venture company. By reducing the redundant data, they succeeded in reducing the transmission bandwidth by about 4 Gbps. An opti-

Fig. 15.18 Optical video link using internal CWDM optical sub-assembly

cal bi-directional transceiver is used for the transmission of the bi-directional DDC signal.

The above-mentioned one-fiber optical video link is what the industry should pursue in the future. But currently, it may cost much compared with the existing multi-fiber products, and the application of one-fiber optical video link might be limited to high end display systems such as broadcasting system or military system. Low cost one-fiber optical video link as the next generation product is dealt in the next section.

15.6 Optical Video Link for a Mass Market

Optical video links based on VCSEL is in a very early stage of the commercialization, and they are used only in the small portion of connections between display

Fig. 15.19 One-fiber optical video link for HDMI

equipments. In this section, I would like to deal with technical issues to enter a mass consumer market beyond special niche applications.

First of all, let us discuss the potential of active optical cable. HDMI is more suitable than DVI for such mass market since it was designed for consumer electronics. As mentioned in Sect. 15.2, we should have appropriate optical component technologies in order to make a small size and low cost active optical cable for consumer use.

In consideration of HDMI connector size, the area of array packaging component can hardly be larger than $7 \times 3\ \text{mm}^2$, and its thickness not more than 2.5 mm. And, the area of VCSEL drive IC or amplification IC may not be larger $5 \times 5\ \text{mm}^2$, which means the pitch of lead should be smaller than 50 μm.

In addition, there is little room for optical alignment, and if we use multi mode optical fiber as before, the precision of optical packaging should be maintained 5 μm or less. For such precision packaging, we may need the array packaging components with the precision of $2-3$ μm, and the uniformity of optical output power of VCSEL array should be small, for example within $\pm 10\%$. In such a small size packaging, optical and electrical crosstalk between the adjacent channels may matter as the speed is increased. The speed of 5 Gbps/channel transmission may be necessary not in the distant future with increased resolution and color-depth. The component technologies used in active optical cables for Infiniband, which have been commercialized recently may be useful in the development of HDMI optical cable too [12].

If low price HDMI active optical cables are commercialized, consumers may buy them like high end copper cables such as component cables. The technologies for such active optical cables may be applied to a wide range of digital interfaces so that the market of active optical cable can be expanded much more and furthermore. It has been forecasted that, in the near future, the market of HDMI active optical

Table 15.2 Requirements of optical video links for TV

	External optical video link	Internal optical video link
Number of fibers	1 to 4	1
Target price	~ $100	$10 ~ 30
Power consumption	<~ 3 W	not so important
Size	small	thin
Additional signals	not necessary	serial data (RS etc.)

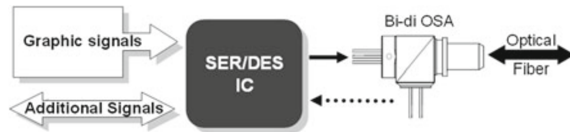

Fig. 15.20 One-fiber option using SER/DES and a bi-directional optical sub-assembly (OSA)

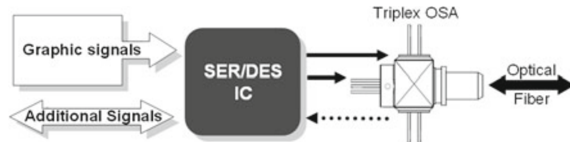

Fig. 15.21 One-fiber option with SER/DES and optical triplexer

cables would grow very fast [13]. In order to enter such a promising market, we need to develop the technologies as described above.

Active optical cable is still outside the display equipment and may be still high end product, not a consumer one. The next step for a consumer mass market may be to put optical video link inside TV to connect with other display equipments, as considered by several major TV manufacturers.

For such application to be installed inside TV, the number of optical fiber must be one. The general requirements of optical video link inside TV are summarized and compared with those for ordinary external optical video links in Table 15.2.

Optical module should be thin to be used inside TV since flat panel TV is becoming thinner and thinner. The thickness of optical module may be required to be as thin as 7–8 mm. As for the implementation of single fiber, we can do the job with CWDM or with SER/DES. With CWDM technology only, we can hardly meet the target price. It may be a very difficult task to make CWDM module with six or more wavelengths at such a low price. Therefore we had better make use of SER/DES technology to reduce the number of fibers.

Using SER/DES technology for optical video link inside TV we may have two possibilities as shown in Figs. 15.20 and 15.21 .

In Fig. 15.20 we have just one channel for data transmission, and a bi-directional optical transceiver is used for optical communication. In this case, the 5–10 Gbps bandwidth may be used and it means that transceiver may cost much.

Not to use very high speed optical transceiver as well as high speed silicon ASIC, we may use two channels for the transmission of data as in Fig. 15.21 where we

need an optical triplexer instead of a bi-directional optical transceiver. The decision between the two options would be made depending upon the cost structure. In the long run, the approach of Fig. 15.20 will prevail owing to its simple optical structure. We may expect the price of 5 or 10 Gbps bi-directional optical transceiver would be reduced considerably in the near future.

However, if the resolution of display increases, we will face the same problem again, then between 20 Gbps bi-directional optical transceiver and 10 Gbps optical triplexer.

It may be important which structure would be chosen for the first generation product. It may become a de-facto standard so that the same concept may be easily adopted for a higher resolution too. Moreover, owing to the mass production of the same structure, the low price key components can be supplied well.

Another interesting application of optical video link inside TV may be to transmit the graphic signals from main board to LCD panel. It is a kind of internal board to board interface. At this moment, electrical wires are used to send the data in LVDS form [14]. It does not contain bi-directional signals, just from main board to LCD panel, and the fiber may be fixed to the module or detachable. It is simpler interface than HDMI and we may have more design freedom except for the lower target price than HDMI optical video link inside TV.

The main issue is bandwidth and the number of wires. With increase in resolution, the number of electric wires has increased too, and with two many number of wires, it may cause a difficulty in TV design. The typical number of electric wires of such internal interface is 10 pairs at the condition of 1080p resolution, 10 bit per color and 60 Hz refresh rate. As the refresh rate of the flat panel TV is rapidly increasing from 60–120 Hz recently and 240 or 480 Hz in the near future, we can estimate the increase of the number of necessary electrical wires. It may increase up to 80 pairs at a refresh rate of 480 Hz, and even more if we want to have more color bits as HDMI 1.3 defines.

Accordingly, there would be a strong demand for a simple optical video link to be used for internal interface between main board and LCD panel inside TV. The commercialization of this kind of very short distance optical link may not be so simple. It has to compete with low price copper technology of which the production technology is improved continuously. However, considering that the required bandwidth of internal interface rapidly increases, optical video link may be used for internal interface not in the distant future.

We have examined the possibility of consumer mass market of optical video links. HDMI active optical cable is expected to enter the consumer market in the near future, but it is still the high end product with limited applications. As the bandwidth of display interface increases, optical video link would be used inside TV. With the current technologies, we may be able to develop optical video link to be used inside TV regardless of internal LVDS or external HDMI interface. The development of manufacturing technology of optical video link may determine when it may be used in volume competing with low cost copper wires.

15.7 Conclusion

A variety of optical video link modules, that is being used or is expected to be applied in the future, have been described. We focused on DVI video links for industry market as well as HDMI ones for consumer applications. Besides them, there are several kinds of digital video interfaces available including LVDS, SDI and DisplayPort. It means that we can expect bigger potential of market from optical video links [15, 16].

Since the commercialization of DVI optical video link was done in 2000, optical video links have been applied to high end systems. But the application area has been expanded rapidly so that we can find optical video link in a variety of applications as described before. In part, it was because that the demand of bandwidth rapidly increased as the resolution of the display became higher and higher. And in part, it was owing to the nice characteristics of 850 nm VCSEL with which low cost and small size packaging was made possible, and so, the price competitive optical video links were developed.

After the introduction of optical video links with multiple number of optical fibers, there have been much effort to develop the technologies to reduce the number of optical fibers. VCSEL CWDM and SER/DES may be the key technologies to reach the target of single-fiber optical video link, and some products are alread-commercialized.

As the bandwidth of internal/external interfaces of digital TV increases, there may be an opportunity for optical video link to be used inside TV. To make such a potential be a real market, we need a thin and low price VCSEL bi-directional transceiver or VCSEL triplexer together with a suitable SER/DES technology running the bandwidth 5 to 10 Gbps.

Up to now, 850 nm VCSEL was used in most optical video links where the transmission distance was not longer than several meters. As the number of optical fibers is reduced, long wavelength 1.3 μm VCSEL may become another candidate of the light source in optical video links. It may give us enough transmission distance even with the higher bandwidth through a single optical fiber. In the long run, when the manufacturing cost of 1.3 μm VCSEL is reduced enough, it is highly probable for it to replace 850 nm VCSEL currently being used.

References

1. Digital Visual Interface, Rev 1.0, http://www.ddwg.org/downloads.asp
2. http://www.hdmi.org/manufacturer/specification.aspx
3. H.K. Shin, Optical interfaces using VCSEL array, in *Proceedings of International Symposium on Ultra-parallel Optoelectronics,* Kawasaki, Japan, pp. 68–71, Feb. 2000
4. VESA TMDS Standard, in DDWG Promoters, *Digital Visual Interface, DVI*, rev. 1.0, Apr. 1999, http://www.ddwg.org/lib/dvi_10.pdf (in the document, TMDS is spelled T.M.D.S.)
5. http://www.nxp.com/products/interface_and_connectivity/i2c/i2c_bus_repeaters_hubs_extenders/PCA9507.html#overview

6. Enhanced Display Data Channel (E-DDC), Standard-Version 1.2, http://www.vesa.org/vesa-standards/standards-summaries/
7. G. Giaretta, W. White, M. Wegmuller, T. Onishi, High-speed (11 Gbit/s) data transmission using perfluorinated graded-index polymer optical fibers for short interconnects (<100 m). IEEE Photon. Technol. Lett. **12**(3), 347–349 (2000)
8. S.H. Hwang, S.H. Lee, H.-H. Park, Optical subassembly with 57°-angled fiber array and silicon optical bench for VCSEL array and parallel optical transmitter module, in *Optoelectronic Materials and Devices*, ed. by Y.H. Lee, F. Koyama, Y. Luo, Proceedings of SPIE, vol. 6352 (2006), pp. 63520W-1–63520W-7
9. S.J. Mac Mullan, S.S. Fastert, T.S. Rao, B. Patel, System, method and apparatus for wireless delivery of content between a generalized content source and a generalized content sink, Patent WO/2006/101801 (2006)
10. J. Jewell, L. Graham, M. Crom, K. Maranowski, J. Smith, T. Fanning, 1310 nm VCSELs in 1–10 Gb/s commercial applications, in *Vertical-Cavity Surface-Emitting Lasers X*, ed. by C. Lei, K.D. Choquette. Proceedings of SPIE, vol. 6132 (2006), pp. 613204-1–613204-9
11. http://www.components.omron.com/components/web/webfiles.nsf\protect\LY1\textdollarFILES/techgroup.html?ID=GTAA-6WGVQY
12. http://www.emcore.com/fiber_optics/emcoreconnects
13. Active Optical Cables Market Report 2009 by IGI Group
14. http://focus.ti.com/paramsearch/docs/parametricsearch.tsp?family=analog&familyId=531&uiTemplateId=NODE_STRY_PGE_T
15. http://www.smpte.org/standards
16. http://www.vesa.org/vesa-standards/free-standards/

Chapter 16
Progress in VCSEL-Based Parallel Links

Daniel M. Kuchta

Abstract This chapter covers most aspects of VCSEL-based parallel optical links during the period of 2000–2010, a period of tremendous advancement in this field both in research and in commercial deployment. Section 16.1 introduces the topic. Commercial activities are covered in Sect. 16.2. Section 16.3 covers research activities in this field. Deployment of these technologies in large systems, supercomputers and test beds is discussed in Sect. 16.4. Advances in multi-fiber, multicore fiber and multi-fiber connectors for parallel links is the topic of Sect. 16.5. Section 16.6 discusses reliability for parallel links and its application to large systems. Finally, Sect. 16.7 concludes the chapter with future applications for VCSEL-based parallel links.

16.1 Introduction

VCSEL-based parallel optical links have come a long way since their commercial introduction in the late 1990s. By November 2008, the top 3 supercomputers listed on the TOP500.org website [1] and more notably, the world's first two petaflop machines all used VCSEL-based parallel optical links for high speed input/output (I/O). The commercial market has also come a long way in the past 10 years although not nearly as far as predicted. In 1997 there was essentially no market for VCSEL-based parallel links as most companies sold hundreds of units mostly for evaluation purposes. The market size in 1998 was estimated at US$59M with a fantastic 5 year growth projection of almost US$900M by 2003 [2]. Today's market(US$80M in

---

D. M. Kuchta
IBM T. J. Watson Research Center, 1101 Kitchawan Rd., M.S. 38-123,
Yorktown Heights, NY 10598, USA
e-mail: kuchta@us.ibm.com

R. Michalzik (ed.), *VCSELs*, Springer Series in Optical Sciences 166,
DOI: 10.1007/978-3-642-24986-0_16, © Springer-Verlag Berlin Heidelberg 2013

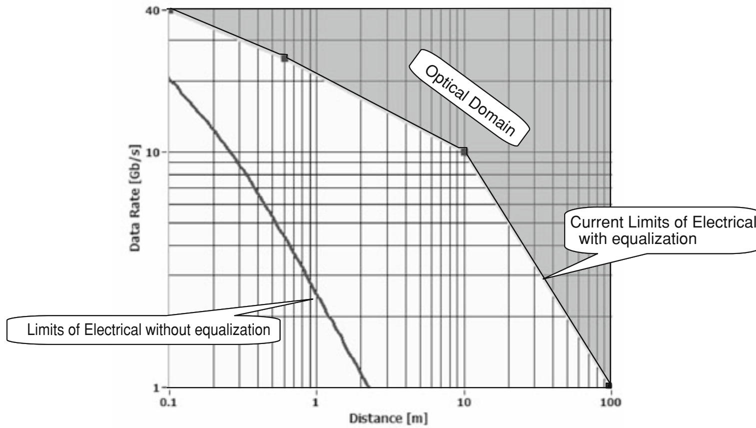

Fig. 16.1 Current limits of electrical cabling technology as a function of distance and data rate

2008) is about a factor of 10 lower than that projection due in part to the "Telecom Bubble" of the early 2000s which affected all companies producing and researching parallel links and in part due to advances in copper cable and connector technology which proved to be lower in cost. By late 2008, there was a prediction that the market for parallel links will reach US$2.4B in the next 5 years.[1] While this prediction may not be realized due to the recession of 2009, the trend in consumption of parallel links is certainly growing with an estimated consumption of 50K units in 3Q07 to 100K units in 3Q08.[2]

Today VCSELs are a key solution for most of the major serial datacom standards: Fibre Channel 1, 2, 4, 8G, Ethernet 1, 10 GbE and recently 100 Gigabit Ethernet (GbE). VCSEL-based parallel links have been adopted by several parallel datacom standards: InfiniBand (IB) SDR, DDR, and QDR, and Ethernet 40 and 100 GbE and they will almost certainly be a part of emerging higher data rate standards such as IB EDR (up to 12 channels parallel at 26 Gb/s/ch) and Fibre Channel 16 G (14.025 Gb/s).

On the research front, quite a few groups have demonstrated direct modulation of single VCSELs above 30 Gb/s [3–9] so there is room for VCSELs to grow and participate in even higher data rate standards yet to be proposed (e.g., Fibre Channel 32 G is expected to be 28 Gb/s).

The data rate–distance products for both serial and parallel VCSEL links has grown, partially due to faster VCSELs and photodiodes but also due to multimode fiber tuned to the VCSEL's wavelength (OM3 fiber bandwidth peaks around 850 nm) and smaller core multimode fiber (~26–32 μm). Figure 16.1, shows the approximate boundary between all electrical and optical interconnects in terms of speed and distance. This boundary has historically moved to the right over time due to improvements in electrical interconnects (equalization, low loss dielectrics, surface

[1] Information Gatekeepers Inc. (2009) Active optical cables market report.

[2] Lightcounting Transceiver Market Survey Results Q3-2008.

mount connections, back drilled and/or blind vias), but cost, size, and flexibility pressures from optical solutions have slowed this movement recently as system designers choose optical over electrical for distances that electrical can cover. DDR IB active cables (described later in Sect. 16.2) are one example of this.

It has been 10 years since a book chapter on VCSEL-based parallel links was published [10]. During that period there were not any general review papers on this topic although there were a few papers that did cover the subject a bit in general [11, 12] and a few papers that reviewed activities within a particular company [13–15] or country [16]. This chapter will pick up from where Hahn and Giboney left off in ∼1999–2000 and cover both commercial and research activities in VCSEL-based parallel links, Sects. 16.2 and 16.3, deployment of these technologies in large systems and test beds, Sect. 16.4, cables and connectors for parallel links, Sect. 16.5, reliability for parallel links, Sect. 16.6, and future applications, Sect. 16.7.

16.2 Commercial VCSEL-Based Parallel Links Since ∼2000

At the turn of the century the fiber optic industry was white hot with many companies offering VCSEL-based serial link products and quite a few of them were also offering parallel link products. It was a period when new opto companies seemed to be created on a monthly basis. Dr. Ingo Schmale maintained the website www.paralleloptics.org from late 2000 until 2005 which proved to be a very useful resource for keeping track of the many new companies and their parallel link offerings during this hectic period.[3] Table 16.1 lists many of the products that were at one time available and compares several technical parameters: maximum data rate, number of channels, area, volume, energy efficiency, wavelength, receiver sensitivity, jitter and miscellaneous features. Unfortunately, primarily due to the burst in the telecom bubble, almost all of these products are no longer available and most of these companies either do not exist or no longer sell fiber optics.

Infineon (spun off from Siemens) had the strongest presence early on with its line of Paroli parallel links [15].[4,5] These devices were all based on 850 nm VCSELs that were coupled to fiber through a block of ribbon fiber that was polished at 45° and mounted over the VCSELs (similar to the OETC package concept of the early 1990s [17]). One of the first offerings had a 22 channel wide electrical interface that was multiplexed up to 11 optical channels plus a clock at 1 Gb/s. It was one of the very few to incorporate an electrical multiplexer (MUX). All other parallel link modules did a straight 1:1 electrical to optical (E to O) and O to E conversion. The early Paroli links used an SMC fiber connector (simplex MT ferrule based) but

[3] Web page: http://www.paralleloptics.org which now only exists on internet archives such as http://www.archive.org.

[4] Paroli V23814-K1306-M230 datasheet.

[5] Paroli V23832-T1231-M1 and V23832-R211-M1 datasheet.

Table 16.1 Comparison of commercially available VCSEL-based parallel links (UI: unit interval, TJ: total jitter)

Company	# of channels	Max. data rate (Gb/s)	Area (mm^2)	Volume (mm^3)	Energy (mW/Gb/s)	λ (nm)	Distance (m)	Rx sensitivity (dBm)	Jitter	Notes	Refs.
Infineon Paroli I	12	1.25	1,282	16,315	600*	850	75	−18	83 ps, Tx = 0.43 UI	DC coupled synchronous link, 22 electrical I/O *Includes Serdes	[15], footnote 4
Infineon Paroli II	12	2.5	961	8,074	60	850		−16	Tx = 0.35 UI, Rx = 0.39 UI		footnote 5
Cielo	8	2.5	1,147	14,567	1,000	1,310	25,000				footnotes 6, 7
Teraconnect TeraLink-24	24	3.2	1,742	19,468	88.5	850	300	−12	Tx = 110 ps, Rx = 90 ps		footnote 10
Teraconnect TeraLink-48	48	3.2	4,125	68,085	88.5	850	300	−12	Tx = 110 ps, Rx = 90 ps		footnote 11
Xanoptix XTM-16	8 + 8	3.125	1,043	13,038		850	1,100	−13	TJ = 0.72 UI max. at test point 4[a]		footnote 12
Xanoptix XTM-24	12 + 12	3.125	1,043	13,038		850	1,100	−14	TJ = 0.72 UI max. at test point 4[a]		footnote 12
Xanoptix XTM-32	16 + 16	3.125	1,209	15,116		850	1100	−14	TJ = 0.72 UI max. at test point 4[a]		footnote 12
Xanoptix XTM-48	24 + 24	3.125	1,209	15,116		850	1100	−14	TJ = 0.72 UI max. at test point 4[a]		footnote 12
Xanoptix XTM-72	36 + 36	3.125	1,209	15,116	72	850	1,100	−14	TJ = 0.72 UI max. at test point 4[a]		footnotes 12, 13
Alvesta 3100	4 + 4	2.5			100	850	300	−16	Tx = 121 ps max., Rx = 153 ps max.		[b]
Alvesta 3200	4 + 4	3.1875			100	850	100				[c]

[a] Test point 4 (TP4) as defined in the IEEE 802.3 standards [b] Alvesta 3100 product datasheet [c] Alvesta 3200 product datasheet

(countinued)

Table 16.1 (continued)

Company	# of channel	Max. data rate (Gb/s)	Area (mm^2)	Volume (mm^3)	Energy (mW/Gb/s)	λ (nm)	Distance (m)	Rx sensitivity (dBm)	Jitter	Notes	Refs.
Gore nLighten-1200	12	1.5	1,320	13,200	205	850	200	−18	300 ps	Leadframe package	[18]
Gore nLighten-2100	12	2.7	658	8,630	76	850	600			SNAP12	[19]
Gore nLighten-2200	12	3.3				850	600	−16		Polymer light pipe coupler	[20]
Mitel	12	2.5	732	7,470	123	850	300	−18	Tx = 106 ps, Rx = 204 ps	Leadframe package	[d]
Paracer	4+4	3.125			60	850	300			Hot pluggable 40 pin edge connector	[e]
Paracer	12	2.7	738	9,160	65	850	300	−16	Tx = 100 ps, Rx = 120 ps	SNAP12	[f]
Paracer	12	2.7			65	850	300			40 pin edge connector	[g]
Aralight	36	3.125	1,613	24,580	58	850	300	−15	0.3 UI	Substrate removed VCSELs	[21–23], footnote 9
SNAP12 MSA	12	2.7	901	14,014	100	850	600	−16	Tx = 0.33 UI, Rx = 0.39 UI		[h]
Reflex Photonics	12	3.5	845	9,292	48	850	300	−16	Tx = 100 ps, Rx = 100 ps	SNAP12	[24]
POP4 MSA	4+4	2.7	901	14,014	122	850	600	−11.7	Tx = 120 ps, TJ = 0.7 UI		[25]

[d] Mitel Inc. MFT62340-J datasheet, Feb. 2000 [e] Paracer Inc. PR2200 product brief [f] Paracer Inc. PR2800 series data sheet dated 6/18/2002 [g] Paracer Inc. PR2000, P1225P1Tx, P1225P1Rx product briefs, ca. 2002 [h] SNAP12 specifications, Appendix to SNAP12 multi-source agreement, rev. 1.1, May 15, 2002

(countinued)

Table 16.1 (continued)

Company	# of channels	Max. data rate (Gb/s)	Area (mm^2)	Volume (mm^3)	Energy (mW/Gb/s)	λ (nm)	Distance (m)	Rx sensitivity (dBm)	Jitter	Notes	Refs.
OptoIC Technology	12	3.3	390			850	300			BGA or MEG-Array	[i]
OptoIC Technology	4+4	3.2	390		80	850	300			BGA or MEG-Array	[i]
Corona/Emcore OptoCube	12	3.3	253	1,960	52	850	600	−14	Tx = 80 ps, Rx = 70 ps		[j]
Blaze/Omron	4	3.5	170	1,187	52	778, 800, 825, 850	200	−14		CWDM	footnote 16
Blaze	8	0.156	170	1,187	118	780–865, $\Delta\lambda = 12$ nm	2000	−13.5	TJ = 0.46 UI	CWDM, 1 Gb/s serial input	[26, 27]
Xloom AVDAT 4x	4+4	5	668	9,355	50	850	100		IB DDR compliant	Solder to PCB	footnote 17
Peregrine PE97201	4+4	2.7	900	14,000	38	850	600	−17.5		Rad. hardened to 10^5 rad	[28], footnote 15
Harting Pareos	4	10	712	10,688	30	850				Parecon 30 pin connector	[29]
IB DDR active cable	4+4	5	1,032	12,690	60	850	100		TJ = 0.60 UI	CX4 electrical interface	footnote 19
120 G SNAP12	12	10	717	9,255	43	850	50			MEG-Array connector with different pin assignments	[30]
12x QDR/100-GbE active cable	12+12	12.5			10	850	100		IB QDR compliant	CXP interface	footnote 20
Avago Technologies	12	10	72	360	50	850	80	−10.4		PRIZM coupler	[31]

[i] http://www.optoictech.com website

[j] OptoCube 40-S transmitter and receiver datasheets, rev. 030320-btc

Fig. 16.2 Early Paroli I module [15] (© 2000 IEEE)

later versions were built around the MTP/MPO connector. Figure 16.2 shows the early Paroli module with the lead frame package interface.

The VCSEL-based parallel link offered by Cielo Inc. was unique in that it is the only one built around long wavelength (1,310 nm) VCSELs and single mode ribbon fiber.[6,7]

In late 2001, Emcore Inc., Picolight Inc., and Gore Inc. came together and created the "SNAP12" multi-source agreement which ended up driving the entire industry to a common packaging format and outer dimensions. Many companies would offer a SNAP12 compliant product without actually signing on to the multi-source agreement (MSA). The SNAP12 parallel module had a 100 pin, 1.27 mm pitch, Z pluggable MEG-Array connector as the electrical interface.[8] The optical interface was a 12 fiber MTP/MPO connector. In between these two interfaces most companies inserted a flexible printed circuit board to bend the electrical signals 90° and permit the optical signals to be aligned in a straight path with a simple lens to the VCSELs and photodiodes. The SNAP12 concept was a separate Tx and Rx module although in roughly the same time period, Agilent Inc. and Zarlink Inc. founded the POP4 MSA (with Primarion, Emcore and OptoIC as supporting members) which put 4 VCSELs and 4 photodiodes into the SNAP12 package to create a 4 + 4 transceiver. The SNAP12 and POP4 are still available today from a few vendors with data rates up to 10 and 5 Gb/s/ch respectively. A top and bottom view of a SNAP12 module is shown in Fig. 16.3.

---

[6] Cielo Inc., Preliminary Product Brief dated March 2001. The author personally witnessed this technology demonstrated on the Exhibit Floor of an OFC conference.

[7] Compoundsemiconductor.net article dated 26 June 2001.

[8] MEG-Array Connector System (2002) Datasheet and application notes. FCI USA, Etters, PA. Web page: http://www.fciconnect.com.

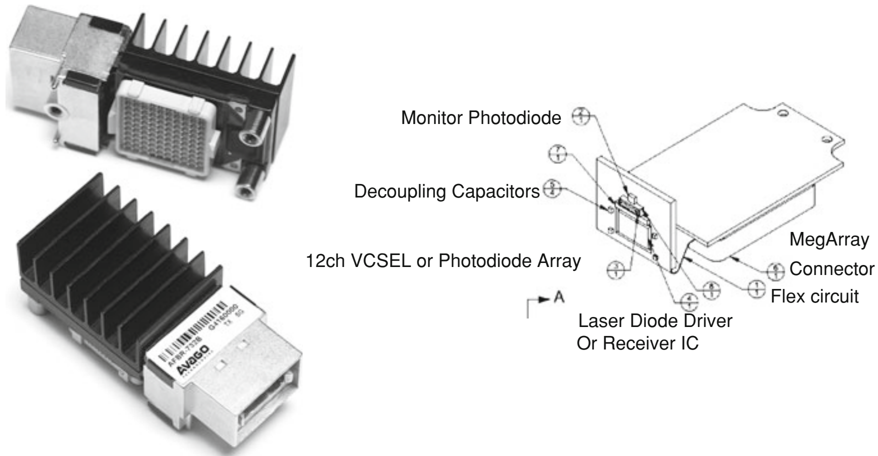

Fig. 16.3 *Left*: SNAP12 modules showing top and bottom view (courtesy Avago Technologies Inc.), *right*: typical internal components

A number of companies were in competition for high fiber count parallel links: Aralight, Xanoptix, and Teraconnect. Their internal packaging concepts were very similar. They used an electrical flex to bend the electrons and flip-chip mounted the 850 nm VCSELs directly on to the driving IC then thinned the VCSEL substrate to permit light emission though the substrate. Aralight and Teraconnect would offer separate Tx and Rx modules of 36 and 24 channels respectively.[9,10] [21–23]. Aralight's optical interface was three 12 ribbon fiber pigtails with three 12 channel MTP connectors. Teraconnect offered a 24 fiber pluggable MTP interface. The TeraLink-48 was two separate 24 fiber interfaces and was essentially a 24 Tx and 24 Rx packaged side by side.[11] A very notable exception to these high fiber count modules were the ones produced by Xanoptix.[12,13] The Xanoptix XTM-72 had a 2D array of 36 VCSELs and of 36 photodiodes flip-chip mounted (separately) onto a transceiver IC with subsequent substrate removal. The optical interface was the pluggable 72 fiber MTP which remains one of the highest fiber count connectors to date. The Xanoptix 2D VCSEL array was actually four times larger than the fiber count as four closely spaced VCSELs were coupled to each fiber. The additional 3 VCSELs were provided both to increase yield and to increase reliability through sparing. The electrical interface for the Xanoptix and Teraconnect high fiber count

[9] Aralight Inc. ARL-36 series product brochure.

[10] Teraconnect Inc. TeraLink-24 TC-T24T-320E and TC-T24R-320E datasheet.

[11] Teraconnect Inc. TeraLink-48 TC-T48T-320E and TC-T48R-320E datasheet.

[12] Tyco Electronics Fiber Optics Catalog #1307895, revised 9-2004, High Speed PARA-OPTIX Transceivers.

[13] Tyco Electronics technical datasheet #TDS1511223, XTM-72 PARA-OPTIX Transceiver, revision 5, dated 7 May 2004.

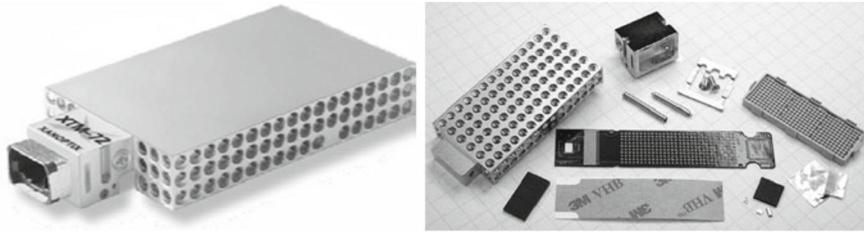

Fig. 16.4 *Left*: Xanoptix XTM-72 module, *right*: XTM-72 internal components view (reprinted with the permission of Tyco Electronics Corporation, US)

Fig. 16.5 Image of TeraLink-24 showing the MTP interface on one end and the 200 pin MEG-Array connector on the other (from [32])

modules was the 300 pin version of the FCI MEG-Array. The Xanoptix parallel link modules are also notable as they appeared to be one of the first to offer an adjustable amplitude and pre-emphasis on the optical receiver's electrical interface. Figure 16.4 shows the 72 fiber Xanoptix module along with an unassembled version showing the internal components, most notably the flex. Figure 16.5 shows the TeraLink-24 module.

The OptoCube produced by Corona (later acquired by Emcore) remains one of the smallest and lowest profiles of the parallel link modules produced in this time period. The OptoCube electrical interface was the 1 mm pitch Z pluggable socket, HiLo^{TM}, made by ISI Inc.[14] although the very first version had a solder ball interface. The external optical interface accepted a bare MT ferrule which was held in place with a clip. Internally the OptoCube was also unique as the VCSELs and photodiodes were mounted face down on a glass substrate with patterned electrical traces which was scribed into two pieces held together by the metal from the electrical traces. The piece of glass with the OE's on it was bent up 90° to mate with the MT ferrule. The

[14] Interconnect Systems Inc. HiLo board to board interconnect system, http://www.isipkg.com.

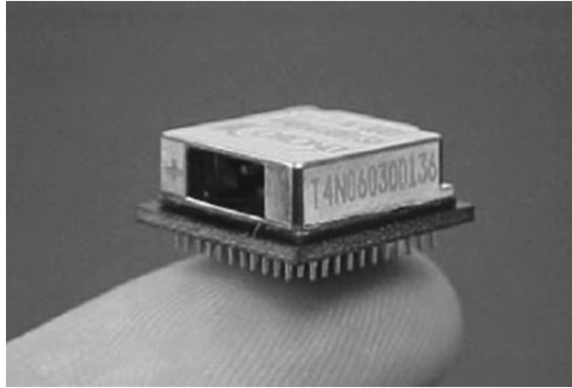

Fig. 16.6 Image of the OptoCube module with the pin grid array interface (courtesy Emcore Inc.)

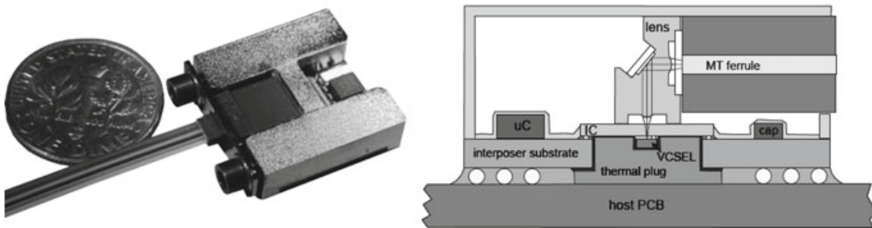

Fig. 16.7 *Left*: 4 channel radiation hardened VCSEL transceiver, *right*: cross section showing component location and optical coupling path [28] (© 2005 IEEE)

horizontal portion of the glass substrate was connected by wire bonds to the driver or receiver IC. Figure 16.6 shows an image of the OptoCube with the pin grid array interface.

In early 2002 Peregrine Inc. came out with an 850 nm 4+4 transceiver module constructed of VCSELs and photodiodes that are flip-chip mounted face down on a Si on sapphire transceiver IC.[15] Since sapphire is transparent at 850 nm the light can be emitted and detected through the IC substrate. A few years later Peregrine would offer what appears to be the only radiation hardened parallel link based on 850 nm VCSELs in both a SNAP12-like package and a smaller version for harsh environments [28]. Figure 16.7 is an image of the radiation hardened 4 channel transceiver and a cross section showing the internal components and the optical coupling path.

Although technically a parallel link but one without parallel fiber, Blaze Inc. (later Aduro and now Omron) entered the parallel market very early with a coarse wavelength division multiplexing (CWDM) offering based on VCSELs with wavelengths ranging from ~780 to 865 nm.[16] At one point they claimed to have had a 12 fiber

[15] Peregrine Semiconductor Inc. PE97201 Product brief and press release dated 6/8/2004.

[16] Aduro Inc. Afterburner SX4-Tx, SX4-Rx technical specification Rev. 1.3 and 1.4, 11/1/2003.

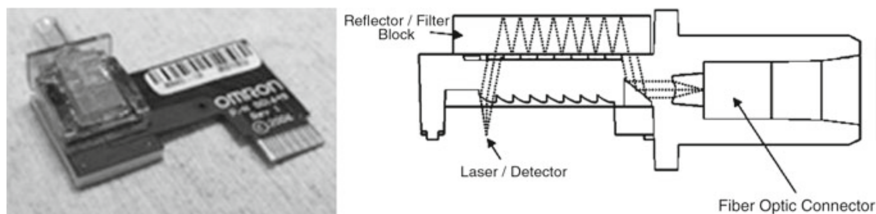

Fig. 16.8 *Left*: Complete 4 wavelength VCSEL transmitter on flex, *right*: cross section of wavelength MUX with ray tracing [26] (© 2001 IEEE)

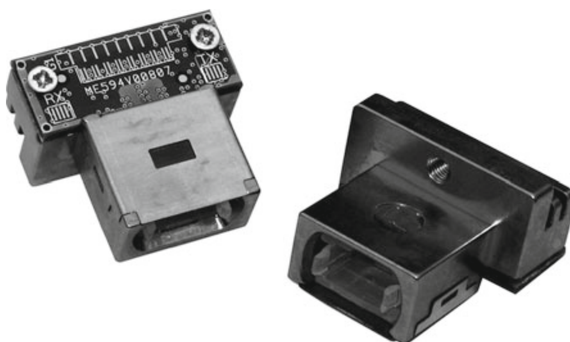

Fig. 16.9 Xloom AVDAT 4x transceiver designed to directly replace an electrical CX4 connector (courtesy Xloom Inc.)

version with 4 wavelengths per fiber at 3.125 Gb/s for a total throughput of 150 Gb/s [26, 27]. Figure 16.8 shows a recent implementation of the 4 wavelength version along with a cross section of the wavelength MUX and the optical path of one of the VCSELs.

Xloom Inc. has created a POP4-like parallel transceiver but with a package and footprint that is designed to directly replace a copper cable connector at the edge of a printed circuit board.[17] This parallel link becomes a direct replacement for copper cables. Figure 16.9 shows both sides of this copper replacement transceiver.

Avago Technologies recently announced a new, very small (10 × 12ch) 120 Gb/s VCSEL-based parallel link technology called "MicroPod" [31]. The MicroPod sets the record for commercial parallel optical bandwidth density. The outer dimensions are $8 \times 9 \times 5\,\text{mm}^3$ and were designed in such a manner to permit placement of the next module as close as 1 mm away. Key to the size reduction was the use of a new right angle photon turning connector called PRIZM LightTurn developed by US Conec Ltd.[18] Figure 16.10 shows an image of the MicroPod.

---

[17] Xloom Communications Inc. AVDAT 4x Product brief.

[18] US Conec Ltd. website: http://www.usconec.com.

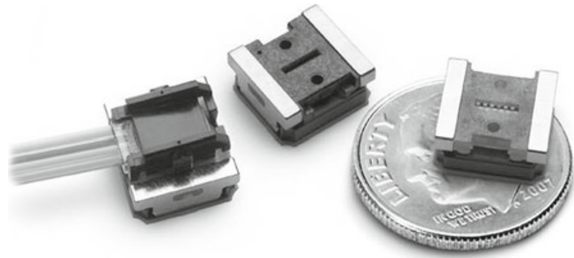

Fig. 16.10 Avago Technologies Inc. MicroPod module. This is the smallest VCSEL-based parallel module currently available commercially (courtesy Avago Technologies Inc.)

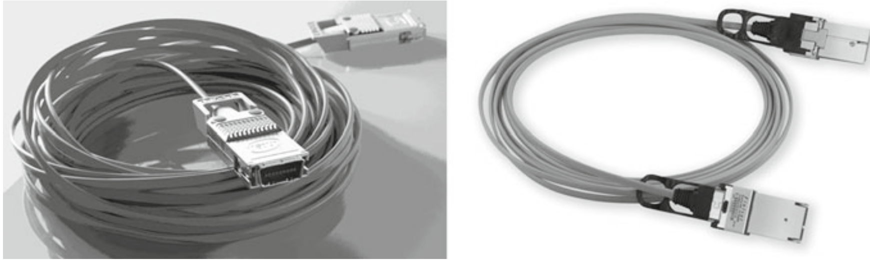

Fig. 16.11 Two examples of active cable, *left*: DDR IB with CX4 connector interface (courtesy Emcore Inc.) and *right*: 12ch QDR IB with CXP connector interface (courtesy Finisar Inc.)

The newest entry to the parallel market is a technology known as "active cable".[19,20] Active cable has an electrical interface on each end but a non-removable optical interface in-between. The optical ribbon is permanently attached; there are no optical connectors in the path. These cables are designed to plug directly on to copper cable ports that have the ability to supply power. There are several advantages to making active optical cable. One is that the optical interface no longer has to be interoperable with other vendors nor does it have to meet any standards specifications. Only the electrical interfaces must meet the standards. In between, the actual optical technology used (e.g. OE devices and fiber type), can be hidden from the user. The active cable concept is similar to the Seamless Migration link that Gore prototyped in the mid-1990s but without the removable optical interface [33]. Although most of the active cables used today use 850 nm VCSELs and multimode glass fiber there are some that are not VCSEL-based [34]. Another advantage is that the optical interface does not need to be eye safe since it is closed and tradeoffs can be made to the optical interfaces to lower costs and increase yield since the vendor controls both ends of the optical link. The active cable concept is seen as a stepping stone for users and systems that are not quite ready to put optics deeper in the system or have a need for a mixture of copper and optics in the same system, perhaps for cost reasons (Fig. 16.11).

[19] Emcore Inc., Emcore Cable Connects, High performance 20 Gbps optical cables, product specification. See also Zarlink Inc. ZLYNX ACTIVE OPTICAL CABLE ZL60615 specification.

[20] Finisar Inc. C.Wire product brief. See also Hitachi Cable Ltd. Infinigreen product specification.

16.3 Research Activities in VCSEL-Based Parallel Links

The last decade also saw a lot of research into VCSEL-based parallel optical links. Table 16.2 lists many of the notable research efforts in parallel optical links and compares properties such as number of channels, maximum data rate, area, volume, energy efficiency, VCSEL wavelength, distance, receiver sensitivity, crosstalk and jitter.

At the end of the 1990s HP (later Agilent) was completing its DARPA sponsored PONI project [35, 36]. This effort developed a 12 channel separate Tx and Rx module, 850 nm, VCSEL-based parallel link with ICs juxtaposed to the OEs, attached to a flex and aligned normal to an MT-based optical connector. The electrical interface was a ball grid array intended to be directly soldered to a printed circuit board. Between the fiber connector and the OEs was an image fiber face plate. Data rates as high as 1.25 Gb/s/ch were demonstrated. This technology would later be commercialized as the SNAP12[21] with the BGA replaced by the demountable MEG-Array connector and the image fiber coupler replaced with a lens array.

Also at the end of the 1990s IBM had an internal effort to commercialize a 12 channel 850 nm VCSEL-based transceiver called LITEBUS [37]. Although nominally based on the earlier Jitney project [38], LITEBUS used substantially different packaging technologies, while retaining just the 850 nm VCSEL array and the GaAs MSM OEIC TIA (metal–semiconductor–metal optoelectronic integrated circuit transimpedance amplifier). Similar to PONI, the VCSELs and detectors were mounted on a flex bent up 90° to aligned fibers but these fibers were mounted in a Si V-groove coupler. The ICs were mounted on the other end of the flex. The module had a BGA interface and was intended to be soldered to a printed circuit board. error-free operation with all 24 channels operating (12 Tx + 12 Rx) at 1.25 Gb/s for a total throughput of 15 Gb/s was achieved. Unfortunately, due to the downturn in the fiber optics industry and a lack of a real market for parallel optics at that time, LITEBUS was never commercialized. Figure 16.12 shows the LITEBUS transceiver package.

McGill University, in collaboration with BAE Systems, produced a number of very high channel count parallel links starting with a 256 channel device and later demonstrating one with 1,080 VCSELs and 1,080 photodiodes mounted on a single IC [39–41]. These efforts are among the first to directly solder VCSELs and photodiodes on top of CMOS ICs. Because these OEs are 850 nm, their substrates had to be removed or thinned substantially to permit the light to exit (or enter). The large IC with 1,080 VCSELs and photodiodes was configured as 540 channels using differential optical signaling. Although the channel counts were very high and single channel operation could be demonstrated above 400 Mb/s, multi-channel operation was limited to much lower data rates. One interesting side note of this work is the use of an FPGA as a flexible low cost parallel pattern generator. Much of this technology would later appear commercially in the transceivers produced by Xanoptix and Teraconnect.

[21] http://www.snapoptics.org now only available at http://www.archive.org.

Table 16.2 Comparison of research activities in VCSEL-based parallel links (UI: unit interval, TJ: total jitter)

Company or project name	Year	# of channels	Max. data rate (Gb/s)	Area (mm^2)	Volume (mm^3)	Energy (mW/Gb/s)	λ (nm)	Distance (m)	Rx sensitivity (dBm)	Cross-talk (dB)	Jitter	Refs.
PONI	1997–1999	12	1.25	Tx = 560, Rx = 560	5,600	133	850		−20		0.7 UI at Tx	[35, 36]
POSH	2001–2004	12	9	Tx = 850, Rx = 1280	11,440, 16,640	50	990	100	−12.4	Rx = 1.3	0.3 UI	[42–44]
Furukawa	2007	4	10	165	660		850					[45]
Furukawa	2007	12	5	100	1,000	190	850	40	−11.0	None		[45]
Furukawa	2009	12	10.3	169	1,183		1,050	650	−10			[46]
Lucent	2000	4 CWDM	10				815–835	310	−12	1 dB optical		[48]
AIST	2008	12	10	100	600		850		−9.6		TJ = 0.56 UI	[53–55, 85]
MAUI	2003–2006	48 CWDM	10.4	80		6	990–1,080			2.5		[49–52]
NEC	2007	12	10	20	20			3	−8			[57, 58]
NEC	2008	4+4	10	196		12–20	850	50	−15	Tx = 0.3, Rx = 2.0		[59]
NEC	2005	4+4	10	196	196	38	850	30	−9.6	Tx = 0.6, Rx = 0.7		[60]
NEC	2001	4+4	3.125	64		100	850	50	−13			[61]
NEC	2010	12	20	126		14.5	1,100	50	−9			[62]
NGK	2008	4	10	42			850		−12.2		TJ = 0.4 UI	[63]
NGK	2008	12	10	70	210	Tx = 12.5	850					[64]
IBM	1999	12+12	1.25	1,440	14,112		850	400				[37]
IBM, Picolight	2003–2005	12	10.3	720	9,206	18	850	300	−14	Tx = 0−2, Rx = 0.5−2	TJ = 0.45 UI	[65–67]
IBM	2003–present	16+16	15.0	17		4.6–13.5	985	0.15 (polymer waveguide)	−8.3		2.6 ps rms	[68–70]
IBM	2003–present	48	Tx = 20, Rx = 14	100		10	985		−10.8 (10 Gb/s), −8 (12.5 Gb/s)		TJ = 0.55 UI	[71]

(continued)

Table 16.2 (continued)

Company or project name	Year	# of channels	Max. data rate (Gb/s)	Area (mm^2)	Volume (mm^3)	Energy (mW/Gb/s)	λ (nm)	Distance (m)	Rx sensitivity (dBm)	Cross-talk (dB)	Jitter	Refs.
IBM	2003–present	24 + 24	12.5	66		11	850		−13 (10 Gb/s), −10 (12.5 Gb/s)			[72]
Toshiba	2006	12 + 12	10.7	19.8	19.8		850?				Tx = 0.3 UI	[73]
Toshiba	2008	12	13.5				850?					[74]
LLNL	2002	40 CWDM	1.25	1.2			825, 845, 977, 988					[47]
McGill Univ.	2000–2003	256 + 256	0.4	100		96	850	0.1 (free space)	−4			[39]
McGill Univ.	2000–2003	512 + 512	Tx = 0.25 Rx = 0.05	110		150	850	0.75 (free space)				[40, 41]
StorLite	2006	4 + 4	10	100			850	0.1 (polymer waveguide)			TJ = 0.34 UI	[75]
Peregrine	2004	4 + 4	2.7	173		102	850		−15		Tx = 0.13 UI	[76, 77]
Peregrine	2004	4 + 4	0.5	6		79	850	0.7 (free space)				[78]

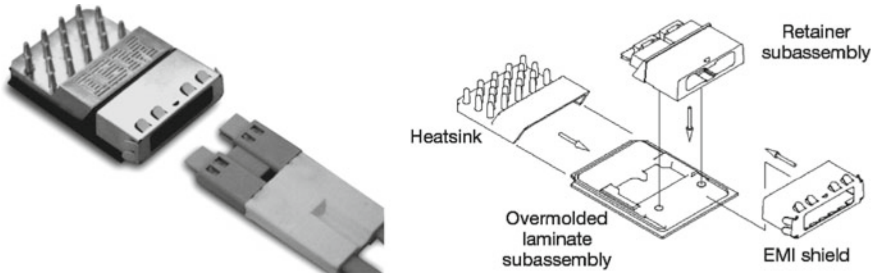

Fig. 16.12 *Left*: IBM 12 channel parallel transceiver ca. 2000 showing dual ribbon cable, *right*: exploded parts view [37] (© 2000 IEEE)

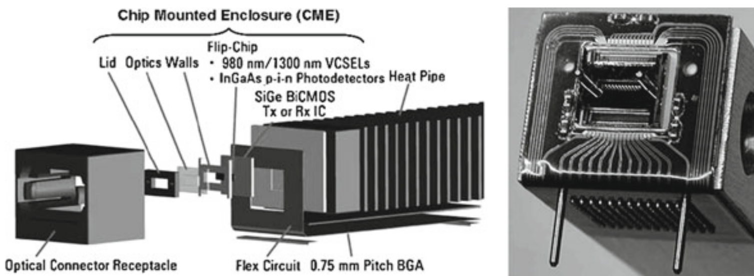

Fig. 16.13 *Left*: Exploded parts view of POSH module [79] (© 2005 IEEE), *right*: assembled POSH receiver [43] (© 2004 IEEE)

Agilent Laboratories followed their PONI project with a corporate sponsored project with the acronym POSH (Parallel Optical Super Highway) [42, 43]. POSH was similar to PONI in terms of the electrical package (BGA to PCB and internal flex circuit) but changed the optics in several key ways. The biggest change was from wire bonded 850 nm OEs to flip-chip soldered 990 nm VCSELs and photodiodes. There were also changes in the optical coupler to a polymer or pyrex refractive lens (half diffractive vortex lens for the transmitter) and changes in the heat sink to a heat pipe design. To balance the front end of the receiver IC, POSH used a 2×12 photodiode array with one row dedicated as a dummy load. Although intended as a 12 channel 10 Gb/s/ch link, the demonstrated performance only reached 9 Gb/s/ch due to lower than desired receiver bandwidth. POSH was one of the first parallel projects to start reporting crosstalk which becomes noticeable at the 10 Gb/s/ch data rate. The measured crosstalk was negligible on the Tx and 1.3 dB on the Rx. Figure 16.13 shows an exploded parts view of the POSH technology and a completed POSH receiver.

NEC has been actively involved in parallel link research and pre-commercialization efforts throughout this decade and continuing forward. NEC ended the 1990s with a parallel link based on 1.3 μm edge emitter arrays [80] and emerged at the

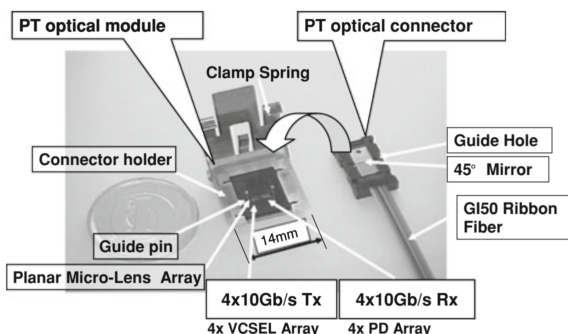

Fig. 16.14 NEC PETIT module with clamp spring (courtesy NEC)

beginning of this decade with an 850 nm VCSEL-based transceiver called MCM-type OIP [61]. This was a large 304 pin PQFP intended to house an LSI chip. Its optical interface was 6 + 6 at 1.25 Gb/s/ch and used a polymer waveguide with a 45° mirror as the coupler to fiber. This effort did not last long and was quickly succeeded by NEC's PETIT parallel link [60, 81]. PETIT started out as a 4 + 4 at 3.125 Gb/s/ch using 850 nm VCSELs and MSM PDs. Originally there was no laser diode driver IC, only a TIA IC for the receiver. The PETIT module did not bend electrons for the opto coupler but rather bent photons. It used the low profile "PT" connector which was an array of 12 fibers with a 45° turning mirror.[22] An image of the PETIT module within a clamping spring and the PT connector are shown in Fig. 16.14. A later version of PETIT separated the Tx and Rx into separate housings with a 60 pin pluggable electrical interface with IC included in the Tx and Rx. The ultimate version of PETIT merged the Tx and Rx plus ICs into a single package with a 62 pin BGA interface and increased the per channel speed to 10 Gb/s [59, 60]. The MSM PD was replaced with a PIN PD. The VCSELs, PDs, and ICs were flip-chip mounted on a resin film which was transparent to 850 nm and a planar micro-lens array was inserted between this resin film and the PT connector. Figure 16.15 shows an image of the inside of the PETIT module and a cross section showing the internal components and the optical path through the resin film. Other features such as optical pre-emphasis on the Tx and adjustable electrical amplitude and pre-emphasis on the Rx were added. Recently NEC has increased the channel count to 12 and moved back to separate packages for Tx and Rx, this time using a very compact LTCC with the ICs on the top and the VCSELs and photodiodes mounted on the sides to wrap-around electrical traces [57, 58]. The PT connector has been replaced with fibers in V-grooves on a Si optical bench. Figure 16.16 shows an image of this version of the NEC parallel optical link. Very recently, NEC has set the record for 12 channel high speed link performance at 20 Gb/s/ch using a very compact $9 \times 14\,\text{mm}^2$ package with IC, microcontroller, and VCSEL or PD mounted on an alumina substrate [62]. The optical output is normal to this substrate.

[22] Japan Printed Circuit Association Standard No. JPCA-PE03-01-06S-2005.

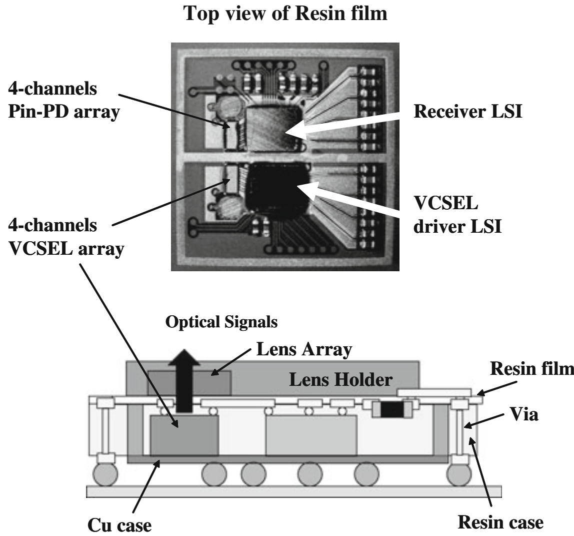

Fig. 16.15 Picture and cross section of NEC PETIT module showing internal components and the optical path through the resin film [60] (© 2005 IEEE)

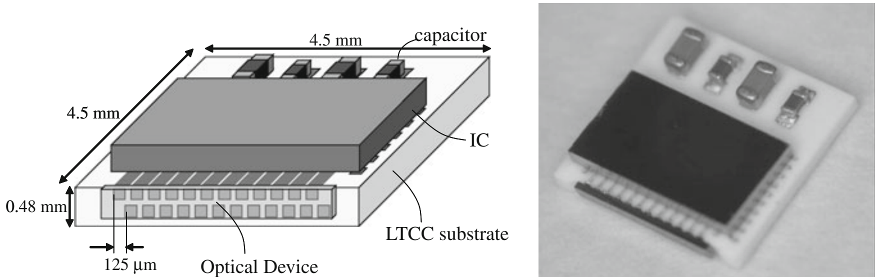

Fig. 16.16 *Left*: Drawing of NEC 12 channel parallel link module on LTCC substrate showing dimensions. The VCSELs are mounted on the edge of the LTCC, *right*: picture of the module [58] (reprinted with permission from JIEP)

Research efforts into parallel links using multiple wavelengths per fiber started off the decade with activities such as Lucent's 4 × 10 Gb/s/ch CWDM demonstration using 4 VCSELs with 7 nm separation starting at 815 nm [48]. A few years later, Lawrence Livermore National Laboratory (LLNL) would publish a 40 channel parallel link also using 4 wavelengths, 825, 845, 977 and 988 nm and a combination of proximity coupling (2 VCSELs side by side coupled into 1 fiber) and optical filters as splitters/combiners [47]. But the biggest CWDM effort during this period by far and one that does not appear to have been surpassed in many of the key performance metrics, even today, is Agilent's DARPA sponsored MAUI project [49–52].

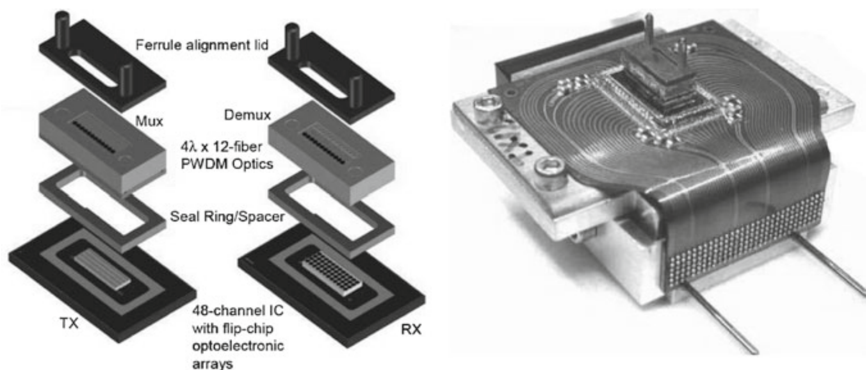

Fig. 16.17 *Left*: Exploded view of MAUI Tx and Rx OSAs, *right*: MAUI Tx assembly on flex showing BGA connection point [50] (© 2005 IEEE)

The MAUI project adopted much of the technology developed under the POSH project but instead of one 12 channel VCSEL array flip-chip bonded to the IC, it bonded four 12 channel arrays for a total of 48 channels, again relying on the transparent substrate at 980 nm. It also inserted an optical MUX and demultiplexer into the fiber coupler based on dichroic filters. There were four discrete wavelengths with a 30 nm separation starting at 980 nm. The MAUI link also set the bar for energy efficiency at 6 mW/Gb/s. The OSA (separate Tx and Rx) were mounted on a flex circuit with a 180 pin BGA interface on a 0.5 mm pitch. The sub-components that comprise the MAUI OSA and an assembled MAUI Tx are shown in Fig. 16.17. For testing all 48 channels, Agilent used a custom pseudorandom bit sequence generator ASIC for speeds up to 6 Gb/s/ch. At 10 Gb/s/ch they split and amplified the signal from a high speed bit error rate tester. They reported a crosstalk penalty of 2.5 dB at 10 Gb/s/ch with all 48 channels operating simultaneously but unfortunately not all channels were error-free at this rate due to the receiver IC. Error-free 48 channel operation was achieved at 9 Gb/s/ch yielding a 432 Gb/s link over 12 multimode fibers. Agilent did not take the MAUI technology in to commercialization and there is very little current research activity into CWDM parallel links. A recent effort in this area is a demonstration of a 1.5 μm wavelength 12 channel VCSEL array with 4 nm spacing [82, 83]. Presumably this will be used for a parallel link, perhaps over single mode fiber.

IBM had an internal research effort in collaboration with Picolight Inc. to explore the limits of the SNAP12 packaging starting in late 2002 [65]. To the extent possible, much of the SNAP12 technology was preserved, e.g., optical coupler, MEG-Array connector, assembly steps and heat sinking. The flex circuit was redesigned to support 10 Gb/s/ch and the ICs were replaced first with high speed SiGe circuits and later with lower power CMOS [66, 67]. A fully functioning error-free link at 120 Gb/s over 300 m of OM3 fiber was demonstrated. Key to this demonstration was the development of a low cost multi-channel pattern generator and error detector built around 10 GbE PHY ASICs. This low cost tester also permitted a detailed crosstalk

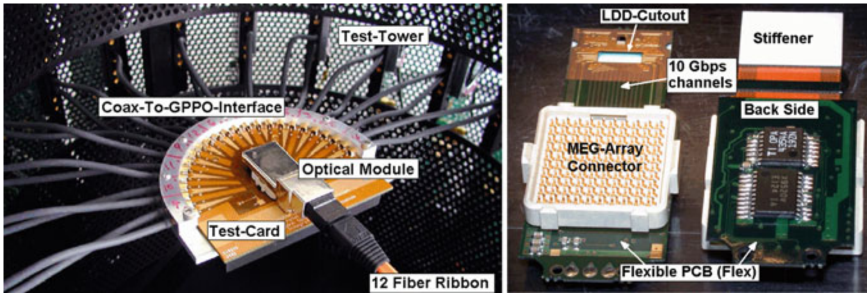

Fig. 16.18 *Left*: 120 Gb/s transmitter on low cost tester, *right*: internal view of modified flex circuit [65] (© 2003 IEEE)

investigation as individual channels could be turned on and off as aggressors or victims. Figure 16.18 shows a fully assembled 120 Gb/s transmitter mounted on the low cost testing stations and an internal view of the front and back side of the modified flex circuit. Frequency domain techniques were also used to characterize the crosstalk of the individual link components. The flex circuit and MEG-Array connector were found to have <40 dB crosstalk out to 20 GHz. The VCSELs on the other hand were found to have much higher crosstalk if they were common cathode type and very low crosstalk for the semi-insulating substrate isolated contact type. The coupling between neighboring VCSELs was found to be primarily electrical in nature, with little or no optical crosstalk. The electrical crosstalk exhibited a capacitive type characteristic due to the coupling of all bond pads through the conductive substrate. All photodiodes studied were constructed on semi-insulating substrates and thus had very low crosstalk. Receiver crosstalk which tends to be the largest component of link crosstalk was found to be due to coupling within the IC. Today, a SNAP12 link at 10 Gb/s/ch is commercially available from Avago Technologies (formerly Agilent, formerly HP) [30].

About the same time that the IBM–Picolight interaction was completed, IBM started its DARPA sponsored Terabus project with Agilent [71]. This effort was one of the first, aimed at parallel links faster than 10 Gb/s/ch. In addition, the channel density exceeded the 250 μm limit of conventional glass fiber pitch density. The original Terabus link was comprised of a separate 48 channel Tx and 48 channel Rx. The 2D-arrays of substrate emitting 985 nm VCSELs included an integrated lens array etched on the substrate side. A similar substrate illuminated companion 2D PIN PD array was fabricated, also with an integrated substrate lens array. The 985 ± 5 nm wavelength specification was carefully chosen as a balance between PIN PD Urbach absorption tails from the InP substrate [84] which extend out past 970 nm and the longer wavelength absorption tails from polymer waveguide materials that extend down to 1,000 nm from the long wavelength side. The 2D OE arrays were flip-chip soldered to CMOS ICs using fluxless AuSn solder which is more likely to be manufacturable and more reliable than the previous flip-chip efforts that used PbSn and In solders [44, 39]. The CMOS ICs were subsequently flip-chip soldered

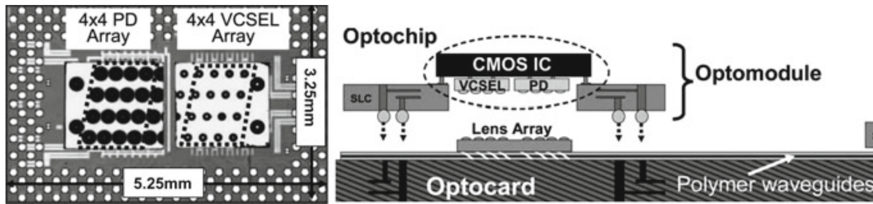

Fig. 16.19 *Left*: Image of Terabus 16+16 channel transceiver IC showing flip-chip mounted VCSEL and photodiode array, *right*: cross section schematic view of Terabus packaging scheme [68] (© 2009 IEEE)

to a Si carrier which was to be attached to a parallel circuit board containing a 1D array of polymer waveguides, 45° turning mirrors and a 2D coupling lens array. Open eyes were obtained from the 48 channel Tx at data rates up to 20 Gb/s/ch (operated one at a time) and up to 14 Gb/s/ch from the 48 channel Rx. A second generation of the Terabus link moved away from the separate Tx and Rx to a 16+16 channel transceiver that was packaged on an organic carrier instead of a Si carrier [68–70]. The new transceiver IC had two variations, a 15 Gb/s/ch version that operated at 9 mW/Gb/s (Tx + Rx power) and a lower power 10 Gb/s/ch version that operated at <5 mW/Gb/s. An image of this 16+16 channel transceiver and a schematic view of the Terabus packaging concept is shown in Fig. 16.19. Ultimately the Terabus project moved away from the 985 nm OEs to 850 nm. There were several reasons for this, one was a larger selection of low loss polymers for the waveguides and the other was a larger selection of vendors already producing reliable low-cost VCSELs and PDs at 850 nm. The first 850 nm Terabus link was a 24+24 channel transceiver at 12.5 Gb/s/ch with ICs and OEs flip-chip mounted on a silicon carrier with optical vias (holes) for coupling the light through the silicon carrier to the printed circuit board mounted below [72].

While Terabus was transmitting 850 nm light through holes in silicon, another DARPA sponsored parallel link project involving the University of Delaware and Peregrine Inc. flip-chip bonded 850 nm OEs to a silicon-on-sapphire CMOS IC and transmitted the light through the transparent sapphire substrate [78]. These designs were all 4+4 transceivers starting at 500 Mb/s/ch with a wider 16 channel electrical interface and eventually ending up with a 2.7 Gb/s/ch interface [76, 77]. One interesting feature of the silicon-on-sapphire technology is the ability to integrate a Si monitor PD in the emission path of the VCSEL.

In an effort to bring parallel links ever closer to the VLSI ICs that are the source of the very high speed data, Toshiba has developed a miniature package which they call the “OE Ferrule” [73, 74]. This package mounts VCSEL or PD arrays on a lead frame that is part of a plastic ferrule holding the fiber ribbon. This OE ferrule is then wire bonded to an laser diode driver or TIA IC to complete the EO-to-OE conversion. Data rates up to 10.7 Gb/s/ch were demonstrated including the ICs and up to 13.5 Gb/s/ch without the ICs. The “OE Ferrule” is shown in Fig. 16.20 alongside a regular MT ferrule for size comparison.

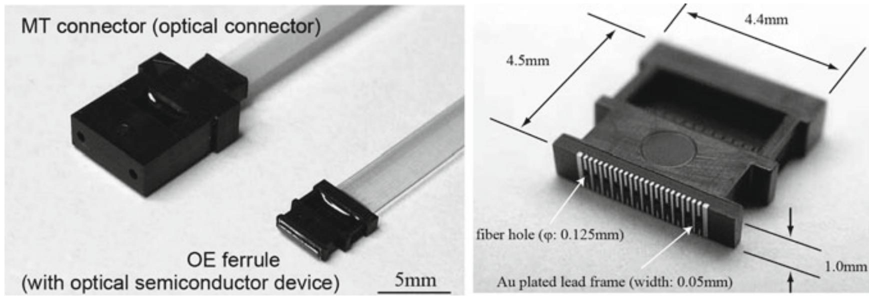

Fig. 16.20 *Left*: A comparison of the Toshiba "OE Ferrule" with a regular MT ferrule, *right*: close-up of the "OE Ferrule" showing dimensions and VCSEL attachment contacts [74] (© 2008 IEEE)

In an effort to reduce the vertical height of fiber-based parallel link modules, AIST embarked on two separate efforts. The first was an approach similar to several others which involved the use of 45° mirrors cut on to the end of fibers in a Si V-groove block structure [54]. The difference here is that higher index ($\Delta n = 1.9\%$) graded-index 50 μm core diameter (GI-50) fiber was used. A 4 channel 10 Gb/s/ch 850 nm link was demonstrated [55]. Later, this high numerical aperture (NA) fiber would be used in a 90° coupler with the fiber bent in a very tight 2 mm bend radius [85]. The higher NA fiber is used to reduce the bending loss from such a tight bend. The outer glass diameter is also reduced to 125 μm to maintain fiber reliability for such a tight bend. A 12 channel separate Tx and Rx was demonstrated [53]. The total height of the module, including the fiber connector is only 6 mm. Figure 16.21 shows several views of the components comprising AIST's low profile parallel link.

While almost all of the fiber-based parallel modules have the fibers coming off the top or the side of the module, NGK developed a pin grid array package with the fiber connector on the pin (bottom) side of the package [63]. This concept has optical vias, in the form of a 40 μm core waveguide inserted into holes in the plastic package. A 4 channel 10 Gb/s/ch separate Tx and Rx using 850 nm VCSELs and PDs was demonstrated. This packaging concept is shown in Fig. 16.22. The coupling losses due to the optical vias appear to be a bit large, 1.5 dB. Recently, NGK appears to have moved away from this concept with a completely different package: VCSELs wire bonded to a ceramic submount with electrical through-vias attached on the edge of another ceramic package which has metallization on one edge [64]. A 12 channel 850 nm Tx at 10 Gb/s/ch was demonstrated.

Another research effort in parallel links using tight bend radius fiber was undertaken by Furukawa. Nicknamed u-POEM (see Fig. 16.23), they demonstrated a 12 channel 5 Gb/s/ch separate Tx and Rx parallel link using 850 nm VCSELs and photodiodes and ICs mounted on a ceramic carrier [45]. A 0.5 mm pitch LGA is used to make contact to a printed circuit board. The optical coupler is comprised of butt-coupled fibers on a 250 μm pitch with a tight 5 mm 90° bend. The tight bend fiber is a special 50/80/250 (core/clad/overcoat) MMF on a 250 μm pitch with $\Delta n = 2\%$. This high NA fiber had a low bending loss of <0.5 dB for 5 mm bend

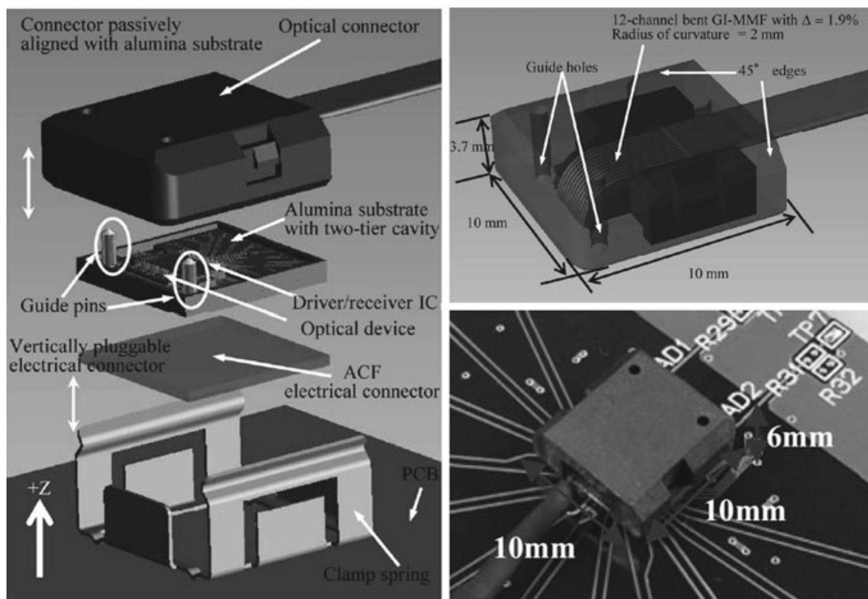

Fig. 16.21 *Left*: Exploded view of the components comprising AIST's low profile 12 channel parallel module [56] (© 2009 IEEE), *upper right*: transparent view of the optical connector showing the tight bend radius fiber [56] (© 2009 IEEE), *lower right*: image of the assembled module on a test card [85] (© 2008 IEEE)

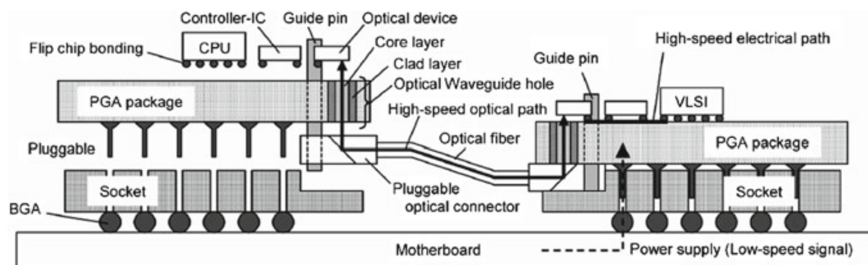

Fig. 16.22 Conceptual view of NGK's parallel link package with an optical via in the package and a fiber connector beneath the package [63] (© 2005 IEEE)

radius but also had a low bandwidth of 200 MHz × km which appears to be adequate at 10 Gb/s provided the link length is limited to ~20 m. Another version of the u-POEM did not use the tight fiber bend coupler but rather an array of fibers on a 125 μm pitch with a 45° mirror polished on the end. This version was a separate 4 channel Tx and Rx on a 250 μm pitch (using every other fiber) and operated up to 10 Gb/s/ch. Recently, Furukawa appears to have moved away from the use of 850 nm

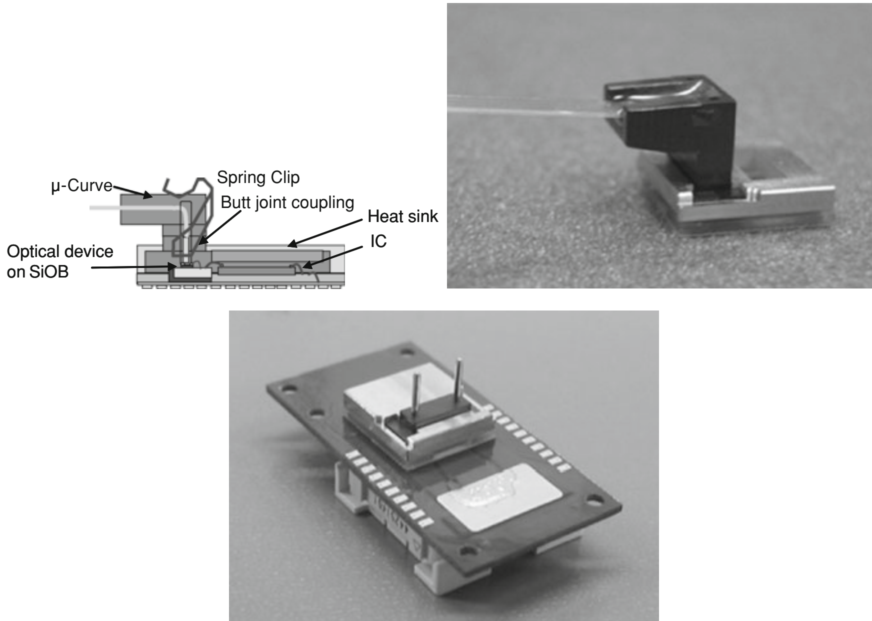

Fig. 16.23 *Left*: Conceptual view of Furukawa's u-POEM V-pack module, *center*: image of u-POEM with connector attached, *right*: pluggable version of u-POEM. (courtesy Furukawa Electric Co., Ltd.)

VCSELs to a longer 1,100 nm wavelength. This move appears to be based in part due to the higher BW of InGaAs quantum-well-based VCSELs, high bandwidth of OM2 fibers at this wavelength, and a potential to realize lower power dissipation [46]. A 12 channel separate Tx and Rx at 10 Gb/s/ch has been packaged similar to the u-POEM with the tight bend radius fiber although the bend radius of the fiber coupler was reduced from 5 mm to a very tight 1 mm.

There have been several research efforts to extend the flex-based packaging concepts to longer lengths of flex that permit the optical interface to fit into spaces much smaller than the electrical interface. One such example is a collaboration between IBM and Intexsys Photonics which placed 12 channel 850 nm OEs and ICs (separate Tx and Rx) at the end of a liquid crystal polymer flex (for lower electrical loss). The flex assembly was shaped to fit into a hole in a printed circuit board containing embedded polymer waveguides [86]. Another example is a collaboration between Xyratek and UCL called the StorLite project which placed a 4 + 4 10 Gb/s/ch 850 nm VCSEL transceiver at the end of a fairly long flex so that it could reach and connect to an optical backplane containing polymer waveguides [75].

16.4 Deployment of Parallel Links in Large Systems and Test Beds

An important step in the progress of the development of VCSEL-based parallel links is the move away from the lab bench bit error rate (BER) testing and into system test beds and ultimately into real systems. This section will describe a number of system test beds and several real very large scale High Performance Computing (HPC) systems that use parallel optical links for high speed I/O.

The first HPC system to use VCSEL-based parallel optics in a significant way was IBM's Advanced Simulation and Computing (ASC) Purple system installed at Lawrence Livermore National Laboratory starting in 2005.[23] By June 2006 this system was ranked #3 on the Top500.org list and was operating at over 100 Teraflops. The ASC Purple system has over 12,000 Power5 processors interconnected as a Symmetric Multiprocessor (SMP) system using IBM's proprietary Federation switch and interconnect fabric.[24] The interconnect fabric links are 12 + 12 at 2.5 Gb/s/ch. For cost reasons, copper cables were used for links shorter than 20 m. But for longer distances, optical links with SNAP12 modules at either end were employed. The ASC Purple system comprised 17,000 links totaling over 140 miles of which approximately 3,000 were optical links with individual lengths ranging from 20–80 m. VCSEL-based parallel optics were chosen for the distance capability in this application. Figure 16.24 shows the ASC Purple system and the rear view of one of the racks.

In an effort to study the issues associated with bringing parallel optics ever closer to the processor, Agilent teamed with IBM to create two system test beds with parallel optical links attached to the top surface (processor side) of a ceramic multichip module (MCM). The first test bed used a repackaged version of the POSH module with the flex redesigned to attach to much smaller (0.2 mm) and tighter pitch (0.5 mm) pads on the MCM surface [87]. Test signals were applied to the top of the MCM and error-free operation at 8 Gb/s/ch was demonstrated over an MCM-to-MCM link. The second test bed incorporated many more channels using the MAUI optical link hardware [79]. Some of these channels went to test pads on the MCM while others were routed through the MCM and LGA to a mother board with a test ASIC with InfiniBand ports. The test signals applied to the top of the MCM were demonstrated at 8 Gb/s/ch and the ASICs established a 4x SDR (2.5 Gb/s/ch) IB link through the optics (limited by the speed of the IB SDR interface). Figure 16.25 shows several views of this test bed hardware.

Another HPC system that was an early adopter of parallel optical links is the Mare Nostrum System at the Barcelona Supercomputing Center in Spain.[25] By June 2005, the fully configured system debuted at #5 on the Top500.org list and was the fastest

[23] Lawrence Livermore National Laboratory website: https://asc.llnl.gov/computing_resources/purple/.

[24] IBM Redbook. An Introduction to the New IBM Eserver pSeries High Performance Switch, http://www.redbooks.ibm.com/redbooks/pdfs/sg246978.pdf.

[25] Barcelona Supercomputing Center: http://www.bsc.es/.

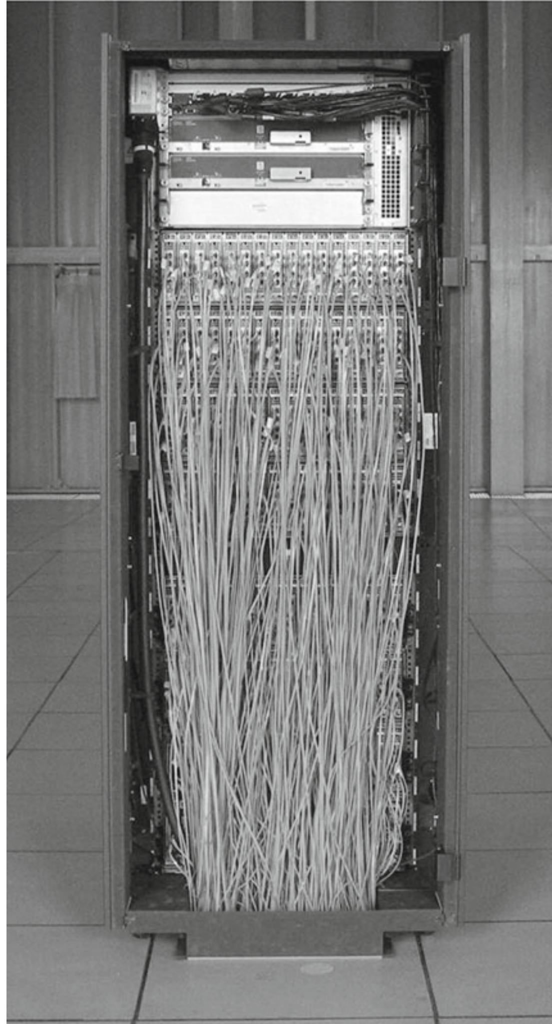

Fig. 16.24 *Top*: ASC Purple installation at Lawrence Livermore National Laboratory (photo courtesy of LLNL), *bottom*: rear view on ASC Purple rack showing the optical fibers [79] (© 2005 IEEE)

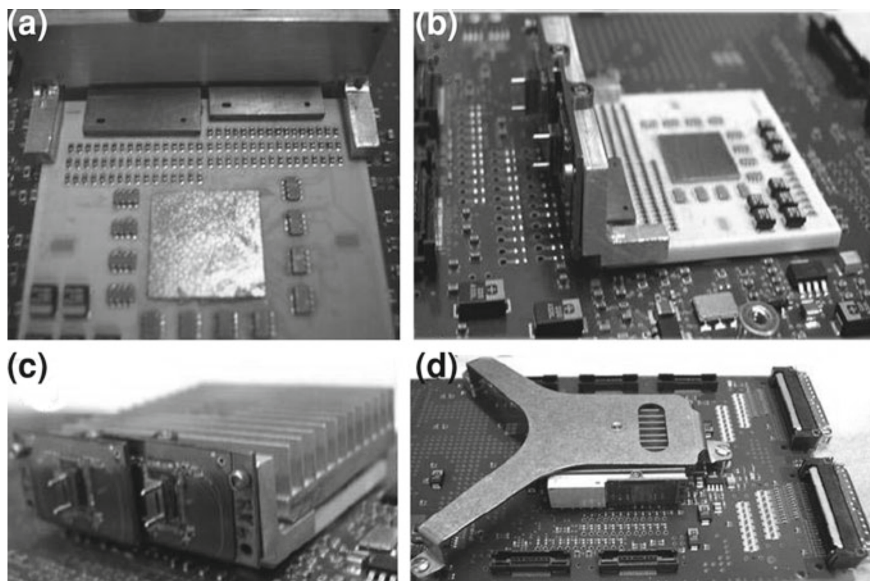

Fig. 16.25 **a** Rear view of ceramic carrier showing ASIC and MAUI flex attachment points, **b** side view, **c** optics attachment view and, **d** entire test bed board [79] (© 2005 IEEE)

computer in Europe at 62 Teraflops. Mare Nostrum is based on IBM's Blade Center and comprises 2,560 JS21 blades each containing two dual core PowerPC 970MP processors for a total of 10,240 CPUs. The system uses a Myrinet network to connect the blade chassis to the 12 Myrinet switches.[26] This connection is achieved using approximately 5000 of the POP4 optical links (4 + 4 at 2.5 Gb/s/ch 850 nm VCSELs). The optical links were chosen due to the interconnect length and the ease of cable management from the optical ribbon fiber. Figure 16.26 shows the Mare Nostrum installation and a view of the Myrinet switches with the ribbon fibers.

Pushing above the 2.5 Gb/s rate of the previous systems and test beds, IBM put together a system trial of a 3.2 GB/s SMP link over optics [88]. The system used IBM's model x460 which has 4 CPU sockets per chassis and 3 high speed SMP ports to connect up to 8 chassis to form a 32 socket SMP. Two VCSEL-based parallel link solutions were investigated. The first used six SNAP12 modules placed at the rear of the chassis (farthest from the CPUs) and the other used four of Emcore's OptoCube modules and a fiber shuffle to place the optics deep into the center of the system closer to the CPUs. The OptoCube version also placed the very low speed (<100 kHz) system service signals on to the fiber ribbon using a fiber shuffle. Both versions were subjected to a variety of system tests and performed equally well. Many of the tests were run with different electrical amplitudes and pre-emphasis settings that were part of the electrical SMP ports used to drive the copper cables. It was

[26] Myricom Inc.: http://www.myri.com/.

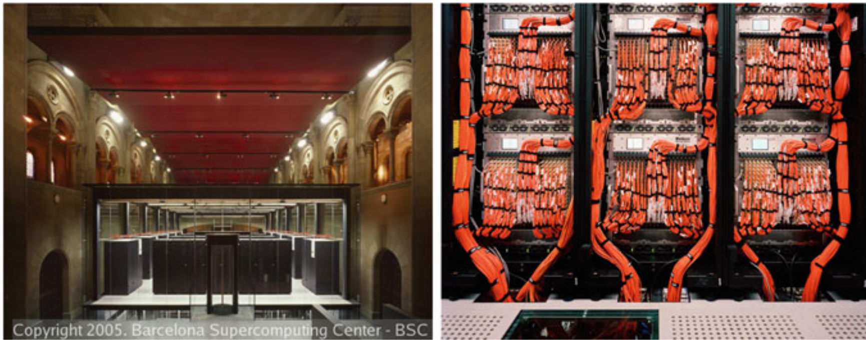

Fig. 16.26 *Left*: Mare Nostrum installation at the Barcelona Supercomputing Center, *right*: parallel fibers exiting the Myrinet switches (courtesy of Barcelona Supercomputing Center, see footnote 25)

ultimately found that the optical links could be operated error-free with the electrical signaling amplitudes dialed down to their minimums and the pre-emphasis turned off. At this setting, copper cables do not work. A 7 W power savings was realized under these conditions resulting in a net power savings for the optical link. This is one of the first cases where optics could be shown to be a lower power solution than an electrical cable. The SNAP12 version was eventually used in a TPC-E benchmark test with two x460 chassis configured as an 8-way SMP with five ServerRaid-6M SCSI adapters in one chassis (forces increased traffic over the optical link) and external connections to a rack containing 4 TB of disk storage. The TPC-E test simulates the online transaction processing work load of a brokerage firm with 100,000 users generating multiple transactions per second.[27] The benchmark test found the system with 2.5 m fiber links performed the same as the 2.9 m copper links. Going to distances much longer than copper cables can support, the performance dropped to 98% at 12.5 m and 92% at 45.2 m. Although performing well in the system test bed, neither optical solution was commercialized due to the cost compared with the copper cables. Figure 16.27 shows the model x460 system, a view with the cover removed showing the optical SMP link and a view of the OptoCube version of the SMP link.

There have been several system demonstrations and test beds using VCSEL-based parallel links, blind mate connectors and optical backplanes. NEC in particular envisioned optical backplanes with parallel optical links and used the term "generation-free" to emphasize that while electrical backplanes need to be re-characterized or replaced with each change in data rate, optical ones do not. NEC demonstrated this generation-free concept by building a large switch card with a switch LSI IC mounted on an MCM and surrounded by four of its PETIT modules (2 Tx and 2 Rx) [89]. Each MCM could have up to 160 + 160 Gb/s of optical I/O. Four of these MCMs were mounted on a card which had 3 blind mate optical connectors

[27] Transaction Processing Performance Council Benchmark E, http://www.tpc.org/tpce/default.asp.

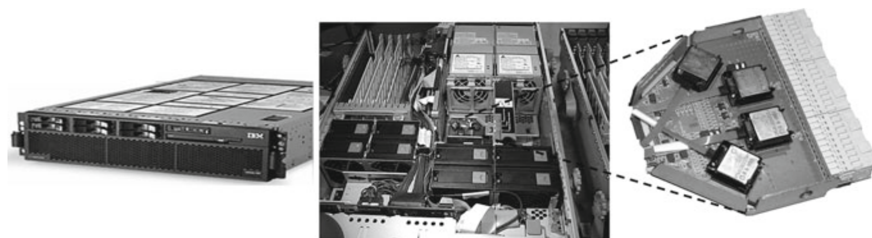

Fig. 16.27 *Left*: IBM eServer model 460, *center*: 3 port optical SMP link embedded in the center of the system, *right*: enlarged view showing Emcore OptoCube optical modules

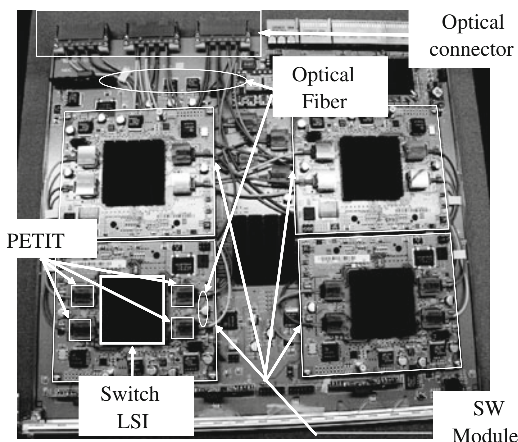

Fig. 16.28 NEC 160 Gb/s switch card with 4 switch LSI modules each surrounded by 4 PETIT modules. Three blind mate optical connectors are located on the *top left* to mate with an optical backplane (reprinted from [89] with permission from SPIE)

on the back edge, each of which held 4 MT ferrules. Figure 16.28 shows an image of this switch card. A special optical backplane was developed by AIST for this test bed which used tight bend radius 50/80/125 MMF to reduce the vertical height of the blind mate receptacle from 39.5 mm to 23 mm. The tight bend fiber also allowed the connectors to be placed on a tighter pitch. NEC later packaged five PETIT modules around a 20 $\times$ 20 cross-point switch and demonstrated 10 Gb/s/ch transmission though the optical backplane and switch [90]. A block diagram and picture of this cross-point switch module is shown in Fig. 16.29.

IBM pursued a hybrid approach to the optical backplanes through a prototype Blade Center system that had both a high speed electrical backplane and an optical pass through fabric [91]. This approach acknowledged that for short blade-to-blade communication within the same chassis, the lowest cost approach would be a wired connection but for the longer chassis-to-chassis connections the cost effective way appears to be optical. To demonstrate this concept a Blade Center-H chassis was

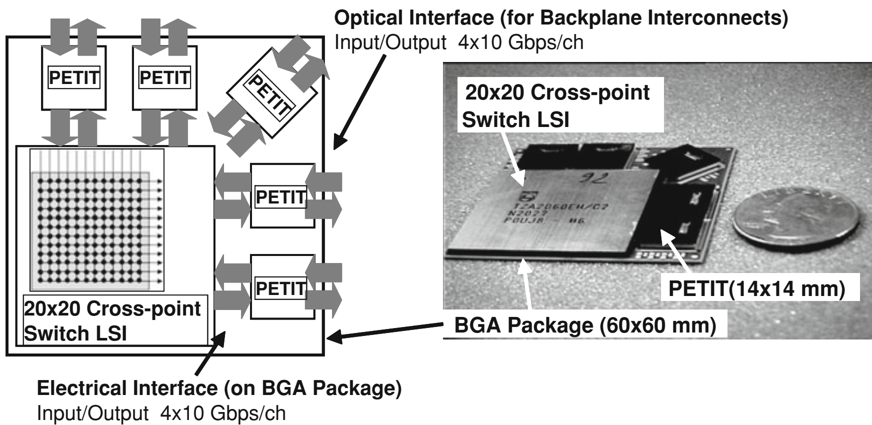

Fig. 16.29 *Left*: Block diagram of NEC's 20 × 20 cross-point switch LSI surrounded by 5 PETIT modules, *right*: photograph of the switch module showing its small size [60] (© 2005 IEEE)

modified to have a row of 14 optical blind mate connectors (one per blade) placed behind the electrical midplane. Short ribbon jumpers connected the midplane connectors to 8 quad MT adapters on the rear of the chassis. A DDR IB daughter card was modified to replace the two 20 Gb/s IB electrical interfaces with a pair of modified POP4 optical modules. The POP4 optical modules had to be modified since the space between the daughter card and the blade was 13 mm at its maximum and could not accommodate the large POP4 package with a protruding MTP connector. DDR IB connections were made between blades up to 41 m of fiber (twice the distance of the longest copper cable for DDR IB) and various MPI benchmark tests were performed.[28] It was found that the 200 ns latency of the longer fiber cable could only be noticed when the packet size was less than 1 kB. A small Linux cluster using several blades across two modified chassis and a SDR IB switch was put together to demonstrate an all optically connected cluster. A view from the rear of the modified Blade Center chassis and an image of the optical DDR IB daughter card is shown in Fig. 16.30.

In mid-2008 IBM announced that it had built the world's first Petaflop (10^{15} flops) HPC system, known as the Roadrunner system [92]. This system, installed at Los Alamos National Laboratory, was built of ~270 racks holding some ~1000 Blade Center chassis with over 3000 triblade nodes. (A triblade is an AMD Opteron blade with 2 Cell blades attached as accelerators.) All the chassis are connected to IB switch racks optically, using about 55 miles of active optical cables (close to 5000 individual links). Each active cable contains a 4 channel 850 nm Tx and 4 channel Rx at each end with a 12 channel optical ribbon in between. The active cable has a DDR IB electrical connector and gets its electrical power through this connector as well. The choice of active optical cable over an active electrical cable was made for several

[28] Open MPI organization, http://www.open-mpi.org/.

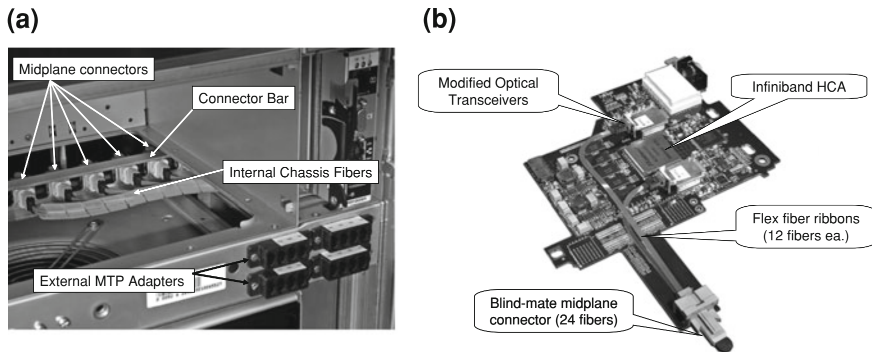

Fig. 16.30 *Left*: Internal view of modified Blade Center chassis showing blind mate optical connectors and ribbon fiber routing, *right*: optically enabled DDR IB daughter card for blades (reproduced with permission from APEX/JJAP [91])

reasons. The primary reason appeared to be the cost of the technology. Other reasons included a lower BER specification (10^{-15} while active copper cables specified 10^{-12}), no exposed optical connector to get dirty or damaged, a tighter bend radius and smaller cable bulk to permit easier routing and to not block as much of the cooling air. The 5000 optical cables also helped in meeting the electromagnetic emissions compliance requirements. The 100 m distance specification also permitted greater flexibility in the layout of the machine room floor. The Roadrunner system was ranked #1 on the TOP500.org list in June 2008 and would retain that ranking for 3 more ranking cycles. Figure 16.31 shows a front view of two compute racks from Roadrunner and a rear view of one of the switch racks.

Around the same time that IBM announced the Roadrunner system, there was a second Petaflop system announced by Cray Inc. called Jaguar, built for the Dept. of Energy[29] and a smaller system (487 Gflops) built for NASA, by SGI, called Pleiades.[30] These two systems occupied the #2 and #3 positions on the TOP500.org list and notably, they also used active optical cable for their high speed interconnects. The Jaguar system used 3000 active optical cables with lengths ranging up to 60 m. Active optical cable was chosen as the only solution for cable to interconnect this large system which is spread over 2 floors. The Pleiades system has 24 miles of high speed cabling of which 20 are active optical cable which was chosen primarily for distance. The active optical cable in Pleiades is a combination of DDR and QDR data rates. The maximum length of copper cabling in Pleiades is 7 m. A view of NASA's Pleiades supercomputer is shown in Fig. 16.32.

Around the time of publication of this book, IBM will have announced a new HPC system building-block that is entirely interconnected by VCSEL-based parallel links. This system is called Power 775. The basic unit of this system is a drawer that

---

[29] National Center for Computational Sciences located at the Oak Ridge National Laboratory, http://www.nccs.gov/computing-resources/jaguar/.

[30] NASA Advanced Supercomputing Division, http://www.nas.nasa.gov/.

Fig. 16.31 *Left*: Front view of two compute racks from IBM's Roadrunner system showing 4 Blade Center chassis each with 3 triblades and an active optical cable, *right*: rear view of an IB switch rack showing 2 switches and ∼532 active optical cables

Fig. 16.32 A view of NASA's Pleiades supercomputer showing active optical cables connecting compute racks (photo courtesy of NASA)

contains 256 processor cores which are electrically connected to 8 hub switch chips. The hub switch chips connect optically to hub switches in different drawers using the Avago MicroPod [31], see Fig. 16.10. Each hub switch chip is surrounded by 56 MicroPods for a total bandwidth of more than 3 Tb/s. Each drawer contains up to 448 MicroPods and more than 5000 fibers [93]. This system, if fully configured,

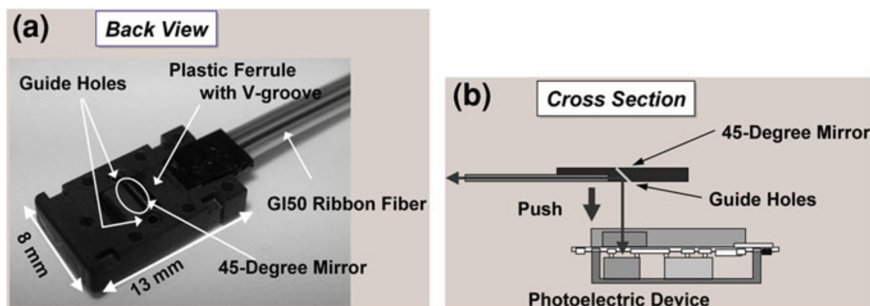

Fig. 16.33 *Left*: Back view of the PT connector, *right*: conceptual side view showing how the PT connector would work with a VCSEL-based optical module [94] (© 2008 IEEE)

2048 drawers, would contain over 5 million VCSELs and fibers and would consume, roughly, what was the world market volume for parallel links just 2 years hence. The decision to use VCSEL-based parallel links in this system was based on a number of factors. One was IBM's sucessful experience with VCSEL links in it's three prior systems: ASC Purple, Mare Nostrum, and Roadrunner. Others were the low cost of the parallel link solution and also the low power dissipation. But the main reason was the ability to package the parallel links in such a manner that allowed them to be placed directly on the ceramic carrier and in very close proximity to the hub switch chips. An electrical cable with this packaging density and bandwidth does not exist.

16.5 Fibers and Connectors for Parallel Links

In an effort to increase bandwidth density both at the OE module and that of the bulkhead/bezel, a number of different avenues have been and are being pursued. At the OE module level custom connector interfaces which are smaller than an MTP pluggable connector have been prototyped such as the NEC PETIT PT connector (footnote 22), Toshiba "OE Ferrule" [73], MU with tight bend radius [95], PRIZM LightTurn (footnote 18) and MT ferrule only with metal clip [96]. Figure 16.33 shows an image and a conceptual side view of the PT connector and Fig. 16.34 shows the Furukawa μ-Joint ferrule compared to a standard MT ferrule. In manufacturing there are a number of connector-less active cable vendors, Emcore, Zarlink, and Finisar for example, which produce internal OE sub-assemblies which are somewhat smaller than an MTP interface. Internally some of these designs may still use the MT ferrule. In addition, there are other efforts to increase OE module density by directly coupling to waveguides on printed circuit boards, e.g., Terabus [71], and StorLite [75].

At the bulkhead/bezel, efforts to increase density typically use higher fiber count MT ferrules in an MTP or MPX connector. Ferrules with as many as 72 fibers can be obtained today although they are not at the minimum in terms of the cost per

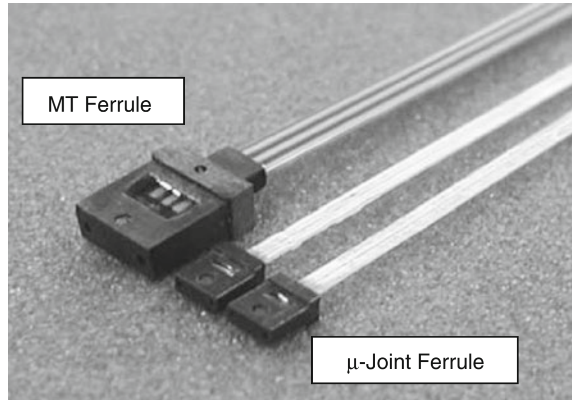

Fig. 16.34 Size comparison of the standard MT ferrule with fibers on a 250 μm pitch and Furukawa's μ-Joint ferrule with fibers on a 125 μm pitch (courtesy Furukawa Electric Co., Ltd.)

fiber due primarily to the lack of volume and perhaps also due to yield. Other size reductions at the bezel/bulkhead use the multi-fiber MU connector which is much smaller than the MT-based connectors. Fiber ribbons with 50/80 fiber on a 125 μm pitch have been prototyped but have yet to appear commercially perhaps due to a lack of a standard. Figure 16.34 shows a size comparison of the standard MT ferrule and a new ferrule with fibers on a 125 μm pitch. CWDM is one another approach to reducing fiber bulk by putting different channels on separate wavelengths in the same fiber. Another approach is to put more cores into a single 250 μm diameter fiber. Four 10 μm cores on a 62.5 μm pitch has been demonstrated within a 125 μm diameter glass fiber [97] and 37 10 μm cores on a 31.25 μm pitch has been demonstrated within a 250 μm diameter photonic crystal fiber [98]. Recently, there was a VCSEL-based multimode, multicore fiber demonstration using a 7 core fiber with 26 μm diameter graded-index cores on a 39 μm pitch hexagonal pattern. A custom matching 6 channel 850 nm VCSEL array was coupled to a 100 m sample of this fiber with each channel running simultaneously at 20 Gb/s for a total single fiber bandwidth of 120 Gb/s [99].

The fibers and connectors for parallel links have not made as much progress over the last 10 years as the optoelectronic modules at each end of the link. Polymer waveguides on printed circuit boards or flex circuits have already been realized at a density that glass fibers may have difficulty reaching (e.g., 30 μm cores on a 62.5 μm pitch), but have yet to be commercialized. Ribbon fiber pitch could probably be pushed down by another factor of two to 62.5 μm but going below that level does not seem likely. One of the early 30 Gb/s VCSEL link demonstrations used a special graded-index 32 μm core diameter (GI-32) multimode fiber [100]. Smaller cores are useful for these higher data rates since the photodiode diameter needs to be below 30 μm to achieve the desired bandwidth. A 30–32 μm core fiber could be coupled to a 20–30 μm diameter photodiode with a simple lens and still have some alignment tolerance. A VCSEL can also be coupled with good efficiency into a 30 μm core fiber. If the cladding for smaller core fiber can be reduced to a 10 μm wide annulus around the core, then fiber diameters could be as small as 50 μm and ribbons could

have a 62.5 μm pitch. But, this is perhaps the limit for glass fiber density as the fiber becomes very fragile and connectorization becomes more difficult.

16.6 Reliability for Parallel Links

The reliability of parallel links used in large systems is a primary concern for a number of reasons. One is that there is a real need to keep the system up and running for as long as possible and to minimize the number of application restarts. Another is that the cost of field replacement can be high and field replacement is often very difficult if not impossible.

This section will look at the reliability requirement for VCSELs in parallel links. VCSEL failure physics and analysis can be found in many references [101–105]. Although photodiodes, ICs, packages and fibers can also fail, VCSELs are often the sole focus of reliability discussions as their failure rates tend to dominate the overall failure rate and in parallel links can add up to be more than the sum of all the other components together.

There are three modes of VCSEL failure: infant mortality, normal wearout and random failures. It is assumed that a suitable burn-in and screening process is in place with mature VCSEL manufacturers so that infant mortalities will not be in the field population and are thus left out of this discussion. VCSEL wearout has been shown to follow log-normal statistics. The failure rate λ is time dependent and is given by

$$\lambda(t) = \frac{\sqrt{2}\,\exp\left\{-(\ln^2(t/t_{\rm m}))/(2\sigma^2)\right\}}{\sqrt{\pi}\,t\sigma\,\mathrm{erfc}\left\{(\ln(t/t_{\rm m}))/(\sqrt{2}\sigma)\right\}}.$$

The cumulative survivor function R is $R(t) = 0.5\,\mathrm{erfc}\{(\ln(t/t_{\rm m}))/(\sqrt{2}\sigma)\}$ and the cumulative failure function F is $F = 1 - R$. The failure rate is characterized by two parameters, $t_{\rm m}$, the median time to fail (not the same as the mean time between fails MTBF) and σ, the spread (variance) of the distribution. σ is related somewhat to the quality of the VCSEL manufacturing line. A small σ means that the fails will be closely spaced in time around the median time. A large σ means that the fails will be spread out in time most notably to earlier times. σ generally varies between 0.3 (for mature well tuned processes) to 0.8 (for a new device still undergoing development) for today's oxide-confined VCSELs. When plotted on a log-normal plot, the VCSEL cumulative failure distribution ideally appears as a straight line, see for example Fig. 16.35. The mean time to failure (MTTF) (which is related to the median time by MTTF $= t_{\rm m}\ \exp\{\sigma^2/2\}$) is often quoted in hundreds of years or millions of hours (for ambient temperatures around 40°C) and is an impressive number. However, due to the log-normal behavior, failures can often be seen in as little as one year. When engineers review VCSEL log-normal plots they often look at the early tails of the distribution and in particular either the time to 1% fails or time to 0.1% fails. In Fig. 16.35, the time to 1% fails is 2×10^5 hrs. VCSELs are assumed to be independent devices

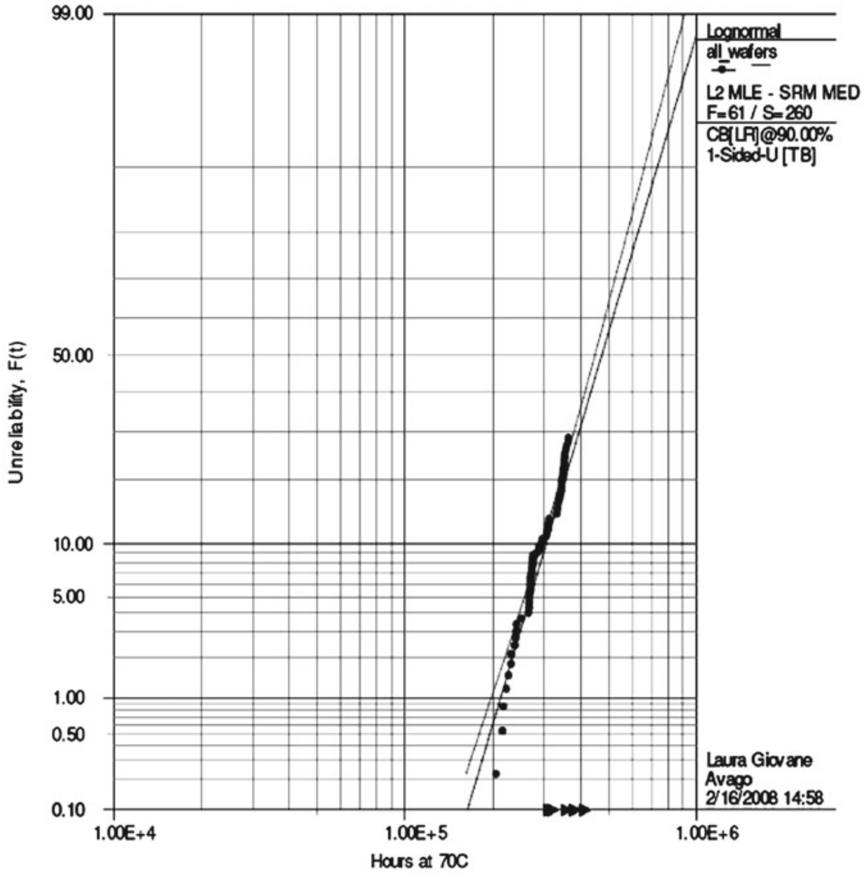

Fig. 16.35 Example accelerated reliability data plotted on a log-normal plot. In this example $\ln(t_m/(1\,\mathrm{hr})) = 13.07$ and $\sigma = 0.34$ (reprinted from [106] with permission from SPIE)

(failures are not correlated). This appears to be borne out by the field experience. The exception is when devices have experienced an electrostatic discharge (ESD) event. In this case, the fails are correlated. A collection of N devices with log-normal fail rate will have an overall cumulative failure function of $F = 1 - R^N$.

Table 16.3 shows a comparison of the time to 1% cumulative fails for serial and parallel (12 channel) links using data for 1996 proton-implanted 1 Gb/s VCSELs ($t_m = 2.3 \times 10^5$ hrs, $\sigma = 1.57$) and 2008 oxide-confined 10 Gb/s VCSELs ($t_m = 2.3 \times 10^5$ hrs, $\sigma = 0.34$). Back in 1996 it would have been rather costly to have deployed 12 channel parallel links as the replacement rate would have been unacceptably high. With today's VCSEL wearout characteristics, replacement due to wearout in the first 10 years should be rather rare. It is at this level of

Table 16.3 A comparison of array wearout lifetimes between early proton-implanted VCSELs and today's oxide-confined VCSELs

	1996: 1 Gb/s proton-implanted VCSEL, 70°C, 10 mA	2008: 10 Gb/s oxide-confined VCSEL, 70°C, 7 mA
1% cumulative fails $(1 - R)$	0.7 years	24.8 years
1% cumulative fails $(1 - R^{12})$	0.2 years	18.8 years

reliability that the random defect level dominates. Random defects are VCSEL device imperfections that are able to go undetected through the normal burn-in and screening processes. Random defects are characterized by a constant failure rate λ which is often converted to FIT (failures in time). 1 FIT represents 1 failure in 10^9 (1 billion) device hours. FIT is a convenient figure to work with as the total failure rate due to random defects of a parallel link is simply the sum of the individual FIT rates of all of the components. The reliability function R becomes $R(t) = \exp\{-\lambda t\}$. In the early days of serial link deployment, the random defect level was often overlooked or ignored. For example suppose 10^5 serial links were deployed for 1 year, i.e., ~1 billion device hours. At a VCSEL FIT of 20, about 20 devices would have failed due to random defects. Typically, if the 10^5 links were distributed to many customers, each customer would likely see one or fewer random fails per year. But future HPC machines could have as many as 10^5 parallel (10–12 channels) links in a single system. Then the 20 FIT level per VCSEL would result in 4 link fails every week! This is unacceptable and would have a big impact on system performance. One approach to dealing with this is to reduce the FIT level through enhanced screening and higher quality production. But even at a FIT level of 2 per VCSEL, about 2 links per month would need replacement in a large system, which is still rather costly. The other approach is to use sparing. Here, the high speed link is designed to be 10 or 11 lanes wide with the 12 channel module having one or two spare lanes. In the case of an 11 channel link with 1 spare the reliability function R_{11} is given by (see also [107])

$$R_{11}(t) = R(t)^{11} + 11\, R(t)^{10} \int\limits_{x=0}^{x=t} f(x) R(t-x) \mathrm{d}x,$$

where $f(t)$ is the failure probability density function which is given by

$$f(t) = \frac{\exp\{-(\ln^2(t/t_\mathrm{m}))/(2\sigma^2)\}}{\sqrt{2\pi}\sigma t}$$

for log-normal wearout and $f(t) = \lambda\ \exp\{-\lambda t\}$ for random defects. R_{11} needs to include both the wearout and random defect effects, but for the early deployment period (first 5 years) where the random defects dominate, the wearout statistics can

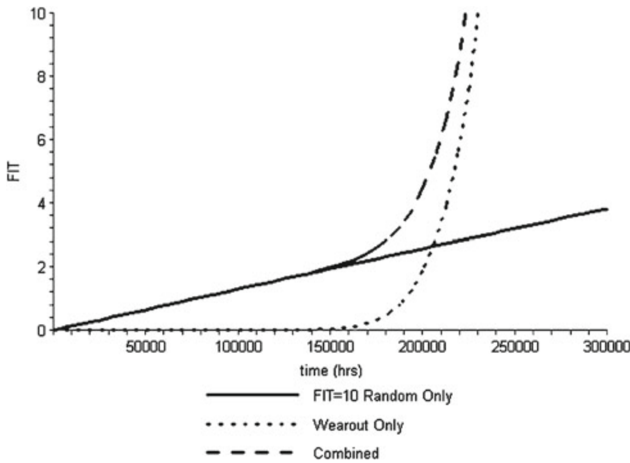

Fig. 16.36 Effective FIT rate versus time for a 12 channel parallel link module with one spare channel and an individual FIT = 10 for each VCSEL, $t_{\mathrm{m}} = 10^6$ hrs, $\sigma = 0.5$

be dropped and R_{11} becomes $R_{11}(t) = \exp\{-11\lambda t\}(1 + 11\lambda t)$. The failure rate with sparing becomes time dependent. Note there is a subtlety here depending on whether the spare is a hot or a cold spare. The case for R_{11} shown here is for a cold spare but the difference between hot and cold sparing for VCSELs can be shown to be insignificant if the wearout reliability is high. For a large system with 10^5 parallel links, each consisting of 11 lanes with 1 spare and 20 FIT per VCSEL, the expected fail rate is approximately linear with time and reaches 1.1 fails/year at the end of 3 years. Figure 16.36 plots an example calculation of the effective module FIT for the case of a 12 channel module with one spare, an individual VCSEL FIT of 20, $t_{\mathrm{m}} = 10^6$ hrs and $\sigma = 0.5$. The combined FIT is linear with time for the first 15 years then increases rapidly as wearout starts to become noticeable.

In practice the total FIT rate of a parallel link will be the sum of all the components in the link, many of which cannot be easily spared (e.g., driver and TIA ICs). Figure 16.37 shows a sample calculation of the cumulative failures over time for a system comprising 1,000 links. Each link is assumed to be 12 channels with one spare, an individual VCSEL FIT = 20, $t_{\mathrm{m}} = 10^6$ hrs, $\sigma = 0.5$ and a total unspared component FIT = 50. In this case, 2 links are expected to have failed by the end of the first 5 years. With sparing, the VCSEL no longer becomes the dominant source of unreliability in parallel optics links.

16.7 Outlook for VCSEL-Based Parallel Links

This moment in time appears to be an inflection point in the use of parallel optical links for a number of reasons. One is that parallel optical links are able to com-

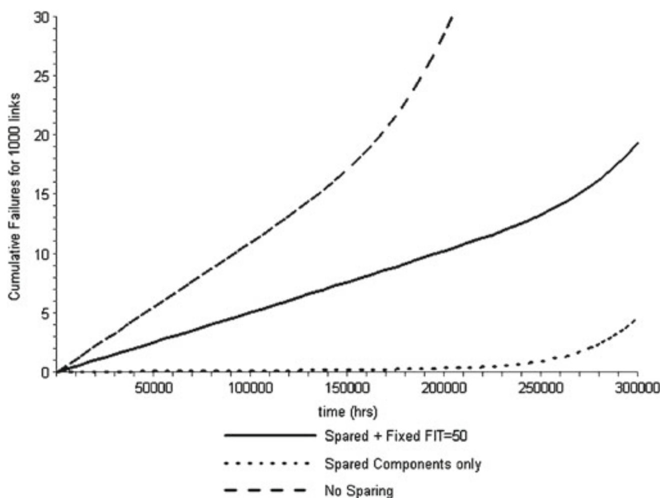

Fig. 16.37 Cumulative failures over time for a system compromising 1,000 links. Each link is defined as a 12 channel module with 1 spare, an individual VCSEL FIT = 20, $t_\mathrm{m} = 10^6$ hrs, $\sigma = 0.5$ and total unspared component FIT = 50

pete economically with copper cables at shorter distances than ever before and copper cables are running into distance limitations that put severe constraints on system layout. Another reason is that the next generation of Ethernet, 100-Gigabit Ethernet (100-GbE) is about to complete its standard specifications, which, for the first time, does not include a serial PMD (physical layer, medium dependent) but rather contains a series of parallel PMDs [108]. Of particular interest for VCSEL-based parallel links are the 40 Gbase-SR4 and 100 Gbase-SR10 specifications. These two call for either 4 or 10 lanes at 10 Gb/s over OM3 multimode fiber with distances up to 100 m. Both of these standards will be initially served by active optical cable offerings. The 4 channel version will use cables based on the QSFP MSA[31] and the 12 channel will use cables based on the CXP specification from the InfiniBand Trade Association (IBTA).[32] InfiniBand has had 4-wide and 12-wide parallel link specifications in its standard since its first release but specified only the electrical connector interface. Very few companies implemented the 12 channel version. One exception is IBM which used 12 channel DDR IB links for its Parallel Sysplex application.[33] Many companies implemented the 4 channel DDR and QDR IB interfaces which have seen volume use of active cables. Now, with the release of the CXP specification, IB links will likely be deployed in 12x width and the CXP active

[31] QSFP specifications used to be available at http://www.qsfpmsa.org which has been disbanded.

[32] InfiniBand[TM] Architecture Specification Release 1.2.1 Annex A6: 120 Gb/s 12x Small Form-factor Pluggable (CXP). Available from the IBTA at http://www.infinibandta.org.

[33] IBM Redbook. IBM System z10 Business Class Technical Overview, http://www.redbooks.ibm.com/redbooks/pdfs/sg247632.pdf, pp. 101–104.

cables, now bi-directional 12 + 12 over 24 fibers, will also be used for 100-GbE using 10 of the 12 channels with 2 as spares or used for system management functions.

InfiniBand has increased its data rate with each new specification by factors of 2. The next generation, called FDR, will be 14 Gb/s/ch and the generation after that, called EDR for Enhanced Data Rate, will likely be 26 Gb/s/ch and will include both 4x and 12x widths. The FDR standard is expected to be finalized by 2011 and EDR by 2013 and will be readily satisfied by high speed VCSEL technology. Beyond EDR is HDR, expected to be specified at 40 Gb/s/ch. This too seems to be within the reaches of directly modulated VCSELs although devices capable of >30 Gb/s are at the state of current research efforts (see also Chap. 7 of this book).

Ethernet increases the bandwidth of successive generations by factors of 10. The next generation after 100-GbE would thus be 1-TbE (Terabit Ethernet). Again, a VCSEL-based parallel solution seems plausible with 48 fibers at 22 Gb/s/ch although a bi-directional optical cable would be a bit unwieldy with 96 fibers. A revival of VCSEL-based CWDM , in the style of the Agilent MAUI project [52], or the use of multicore fiber may be a reasonable solution to keep the fiber count near 24 or 48 fibers.

The research trends in parallel links indicate that they are certainly headed for higher speed, small package size, and lower energy per bit. It is possible that the link width may increase slightly to 16+16 to accommodate parallel I/O connections such as PCI Express. The trend also shows parallel links moving closer to the ICs which are the source of data and toward use in shorter connections which are currently the domain of copper wiring. At a certain point the density and speed increases will move parallel links away from glass fibers to polymer waveguides on printed circuit boards or flex for very short (<1 m) board-to-board and MCM-to-MCM interconnects.

In summary, although VCSEL-based parallel links have come a long way since the early research demonstrations in the 1990s, they have only relatively recently seen serious field deployment. Deployment is at a turning point where the bandwidth and distance demands could use all of the benefits offered by parallel optics. If the cost comes down enough, people in the not so distant future will wonder what copper cables were once used for.

References

1. http://top500.org/
2. J. Montgomery, S. Montgomery, Parallel optical links fill integrated-circuit niches. Laser Focus World **35**(4), 57–59 (1999)
3. R.H. Johnson, D.M. Kuchta, 30 Gb/s directly modulated 850 nm datacom VCSELs. *Conference on Lasers and Electro-Optics and Quantum Electronics and Laser Science, CLEO/QELS 2008*, May 2008, post-deadline paper CPDB2
4. S.A. Blokhin, J.A. Lott, A. Mutig, G. Fiol, N.N. Ledentsov, M.V. Maximov, A.M. Nadtochiy, V.A. Shchukin, D. Bimberg, 850 nm VCSELs operating at bit rates up to 40 Gbit/s. Electron. Lett. **45**(10), 501–502 (2009)

5. J. Sakai, A. Noda, M. Yamagishi, T. Ohtsuka, K. Sunaga, H. Sugita, H. Takahashi, M. Oda, H. Ono, K. Yashiki, H. Kouta, 20 Gbps/ch optical interconnection between SERDES devices over distances from chip-to-chip to rack-to-rack. *34th European Conference on Optical Communication, ECOC 2008*, Sep. 2008, paper We.2.D.5
6. H. Hatakeyama, T. Akagawa, K. Fukatsu, N. Suzuki, K. Yashiki, K. Tokutome, T. Anan, M. Tsuji, 25 Gbit/s-100 °C operation and high reliability of 1.1-μm-range VCSELs with InGaAs/GaAsP strain-compensated MQWs. *Conference on Lasers and Electro-Optics and Quantum Electronics and Laser Science, CLEO/QELS 2008*, May 2008, paper CMW3
7. K. Fukatsu, K. Shiba, Y. Suzuki, N. Suzuki, T. Anan, H. Hatakeyama, K. Yashiki, M. Tsuji, 30 Gb/s over 100-m MMFs using 1.1-μm range VCSELs and photodiodes. IEEE Photon. Technol. Lett. **20**(11), 909–911 (2008)
8. P. Westbergh, J.S. Gustavsson, A. Haglund, A. Larsson, F. Hopfer, G. Fiol, D. Bimberg, A. Joel, 32 Gbit/s multimode fibre transmission using high-speed, low current density 850 nm VCSEL. Electron. Lett. **45**(7), 366–368 (2009)
9. Y.-C. Chang, C.S. Wang, L.A. Coldren, High-efficiency, high-speed VCSELs with 35 Gbit/s error-free operation. Electron. Lett. **43**(19), 1022–1023 (2007)
10. K. Hahn, K. Giboney, VCSEL-based fiber-optic data communication, in *Vertical Cavity Surface Emitting Lasers*, ed. by C. Wilmsen, H. Temkin, L. Coldren (Cambridge University Press, Cambridge, 1999)
11. A.F.J. Levi, Optical interconnects in systems. Proc. IEEE **88**(6), 750–757 (2000)
12. J. Trezza, J. Iamartino, H. Bagheri, C. DeCusatis, Parallel optical interconnects for enterprise class server clusters: needs and technology solutions. IEEE Commun. Mag. **41**(2), S36–S42 (2003)
13. L.A. Buckman Windover, Parallel-optical interconnects and their applications. *Tech. Digest Opt. Fiber Commun. Conf., OFC/NFOEC*, 2005, paper OWH4
14. D.W. Dolfi, Multi-channel optical interconnects for short-reach applications, *Proceedings of the 53rd Electronic Components and Technology Conference, ECTC*, May 2003, pp. 1032–1039
15. K. Drögemüller, D. Kuhl, J. Blank, M. Ehlert, T. Kracker, J. Höhn, D. Klix, V. Plickert, L. Melchior, I. Schmale, P. Hildebrandt, M. Heinemann, F.P. Schiefelbein, L. Leininger, H.-D. Wolf, T. Wipiejewski, A. Ebberg, Current progress of advanced high speed parallel optical links for computer clusters and switching systems, *Proceedings of the 50th Electronic Components and Technology Conference, ECTC*, May 2000, pp. 1227–1235
16. K. Kurata, Review of optical interconnect (on board or others) development in Japan, *IEEE Lasers and Electro-Optics Society Ann. Meet., LEOS 2008*, Nov. 2008, pp. 517–518
17. Y.-M. Wong, D.J. Muehlner, C.C. Faudskar, D.B. Buchholz, M. Fishteyn, J.L. Brandner, W.J. Parzygnat, R.A. Morgan, T. Mullally, R.E. Leibenguth, G.D. Guth, M.W. Focht, K.G. Glogovsky, J.L. Zilko, J.V. Gates, P.J. Anthony, B.H. Tyrone Jr., D.H. Ireland, T.J. Lewis Jr., D.F. Smith, S.F. Nati, D.K. Lewis, D.L. Rogers, H.A. Aispain, S.M. Gowda, S.G. Walker, Y.H. Kwark, R.J.S. Bates, D.M. Kuchta, J.D. Crow, Development of a high-density 32-channel 16-Gb/s optical data link for optical interconnection applications for the optoelectronic technology consortium (OETC). J. Lightwave Technol. **13**(6), 995–1016 (1995)
18. W.L. Gore Associates Inc., nLighten nL1202-1.6 data sheet, issued 11/2001
19. W.L. Gore Associates Inc., nLighten 2100 product brief, 2002
20. W.L. Gore Associates Inc., nLighten 2200 product brief, 2002
21. A.V. Krishnamoorthy, L.M.F. Chirovsky, W.S. Hobson, R.E. Leibengath, S.P. Hui, G.J. Zydzik, K.W. Goossen, J.D. Wynn, B.J. Tseng, J. Lopata, Vertical-cavity surface-emitting lasers flip-chip bonded to gigabit-per-second CMOS circuits. IEEE Photon. Technol. Lett. **11**(1), 128–130 (1999)
22. A.V. Krishnamoorthy, K.W. Goossen, L.M.F. Chirovsky, R.G. Rozier, P. Chandramani, S.P. Hui, J. Lopata, J.A. Walker, L.A. D'Asaro, 16 × 16 VCSEL array flip-chip bonded to CMOS VLSI circuit. IEEE Photon. Technol. Lett. **12**(8), 1073–1075 (2000)

23. C. Cook, J.E. Cunningham, A. Hargrove, G.G. Ger, K.W. Goossen, W.Y. Jan, H.H. Kim, R. Krause, M. Manges, M. Morrissey, M. Perinpanayagam, A. Persaud, G.J. Shevchuk, V. Sinyansky, A.V. Krishnamoorthy, A 36-channel parallel optical interconnect module based on optoelectronics-on-VLSI technology. IEEE J. Select. Topics Quantum Electron. **9**(2), 387–399 (2003)
24. Reflex Photonics, Inc., Product Data Sheet SN-970-004-00, rev. 1.1, Mar. 2007
25. POP4 MSA Technical Specification, rev. 1.0, 4 Sep. 2002
26. E.B. Grann, Low cost CWDM optical transceivers, *Proceedings of the 51st Electronic Components and Technology Conference, ECTC*, May/June 2001, pp. 26–29
27. E.B. Grann, K. Herrity, B.C. Peters, W. Wiedemann, Datacom applications for new VCSEL technologies, Proceedings of SPIE, vol. 3946 (2000), pp. 165–169
28. C. Kuznia, Aerospace transceivers built with flip-chip VCSEL packaging, *IEEE Conference on Avionics Fiber-Optics and Photonics*, Sep. 2005, pp. 39–40
29. Pareos 4×10 Gbps high speed parallel optical link, preliminary technical information bulletin, Nov. 2002
30. Avago Technologies Inc., part number AFBR-810BxxxZ, product brief AV02-1760EN—24, Aug. 2009
31. M.H. Fields, J. Foley, R. Kaneshiro, L. McColloch, D. Meadowcroft, F.W. Miller, S. Nassar, M. Robinson, H. Xu, Transceivers and optical engines for computer and datacenter interconnects, *Tech. Digest Opt. Fiber Commun. Conf., OFC/NFOEC*, 2010, paper OTuP1
32. Teraconnect Inc. TeraLink^{TM}-24, 76 Gbps opto-electronic interconnect modules datasheet, TC_0166_Rev_a1, 2002
33. C. Theorin, S. Kilcoyne, F. Peters, R. Martin, M. Donhowe, Seamless migration to VCSEL-based optical data links, in *Vertical-Cavity Surface-Emitting Lasers*, ed. by K.D. Choquette, D.G. Deppe, Proceedings of SPIE, vol. 3003 (1997), pp. 120–130
34. Blazar 40 Gbps Optical Active Cable. http://www.luxtera.com/documents.html
35. K. Giboney, P. Rosenberg, A. Yuen, J. Straznicky, S. Corzine, L. Buckman, D. Dolfi, The PONI optoelectronic platform, *IEEE Lasers and Electro-Optics Society Ann. Meet., LEOS '99* **1**, Nov. 1999, pp. 25–26
36. P. Rosenberg, K. Giboney, A.Yuen, J. Straznicky, D. Haritos, L. Buckman, R. Schneider, S. Corzine, F. Kiamilev, D. Dolfi, The PONI-1 parallel-optical link, *Proceedings of the 49th Electronic Components and Technology Conference, ECTC*, June 1999, pp. 763–769
37. L. Freitag, J. Kuczynski, P. Fortier, F. Guindon, M. Letourneau, B. Chan, J. Sherman, G. Johnson, D. Demangone, M. Mentzer, D. Naghski, B. Trostle, Packaging aspects of the Litebus^{TM} parallel optoelectronic module, *Proceedings of the 50th Electronic Components and Technology Conference, ECTC*, May 2000, pp. 1259–1265
38. J.D. Crow, J.-H. Choi, M.S. Cohen, G. Johnson, D. Kuchta, D. Lacey, S. Ponnapalli, P. Pepeljugoski, K. Stawiasz, J. Trewhella, P. Xiao, S. Tremblay, S. Ouimet, A. Lacerte, M. Gauvin, D. Booth, W. Nation, T.L. Smith, B.A. DeBaun, G.D. Henson, S.A. Igl, N.A. Lee, A.J. Piekarczyk, A.S. Kuczma, S.L. Spanoudis, The Jitney parallel optical interconnect, *Proceedings of the 46th Electronic Components and Technology Conference, ECTC*, May 1996, pp. 292–300
39. D.V. Plant, M.B. Venditti, E. Laprise, J. Faucher, K. Razavi, M. Chateauneuf, A.G. Kirk, J.S. Ahearn, 256-channel bidirectional optical interconnect using VCSELs and photodiodes on CMOS. J. Lightwave Technol. **19**(8), 1093–1103 (2001)
40. M.B. Venditti, E. Laprise, J. Faucher, P.-O. Laprise, J.E.A. Lugo, D.V. Plant, Design and test of an optoelectronic-VLSI chip with 540-element receiver–transmitter arrays using differential optical signaling. IEEE J. Select. Topics Quantum Electron. **9**(2), 361–379 (2003)
41. M. Chateauneuf, M.B. Venditti, E. Laprise, J. Faucher, K. Razavi, F. Thomas-Dupuis, A.G. Kirk, D.V. Plant, T. Yamamoto, J.A. Trezza, W. Luo, Design, implementation, and characterization of a 2D bidirectional free-space optical link. Proceedings of SPIE, vol. 4089 (2000), pp. 530–538

42. K. Giboney, J. Simon, L. Mirkarimi, B. Law, G. Flower, S. Corzine, M. Leary, A. Tandon, C. Kocot, S. Rana, A. Grot, L. Kun-Jing, L. Buckman, D. Dolfi, Next-generation parallel-optical data links, *IEEE Lasers and Electro-Optics Society Ann. Meet., LEOS 2001* **2**, Nov. 2001, pp. 859–860
43. J. Simon, L. Buckman Windover, S. Rosenau, K. Giboney, B. Law, G. Flower, L. Mirkarimi, A. Grot, C.K. Lin, A. Tandon, G. Rankin, R. Gruhlke, D. Dolfi, Parallel optical interconnect at 10 Gb/s per channel, *Proceedings of the 54th Electronic Components and Technology Conference, ECTC*, June 2004, pp. 1016–1023
44. L.A. Buckman Windover, J.N. Simon, S.A. Rosenau, K.S. Giboney, G.M. Flower, L.W. Mirkarimi, A. Grot, B. Law, A. Tandon, C.K. Lin, R.W. Gruhlke, X. Hui, G. Rankin, M.R.T. Tan, D.W. Dolfi, Parallel-optical interconnects >100 Gb/s. J. Lightwave Technol. **22**(9), 2055–2063 (2004)
45. M. Iwase, M. Shiino, T. Yagi, M. Tanaka, K. Takakahashi, Y. Nekado, H. Nasu, M. Morimoto, H. Aoyagi, K. Suematsu, H. Miyazaki, M. Shinoda, N. Nishimura, I. Shimotakahara, R. Sugizaki, T. Oyama, T. Ozawa, N. Okada, K. Yujobo, Optical components for high-density optical inter-connect system: OptoUnity. Furukawa Review, no. 32, 26–33 (2007)
46. Y. Ishikawa, H. Nasu, Y. Nekado, K. Takahashi, Y. Ikegami, 1.1-μm-range 12 channels × 10-Gbit/s transmission over 600 m MMF using high-density optical modules, *Tech. Digest Opt. Fiber Commun. Conf., OFC*, Mar. 2009, paper OTuK1
47. R.R. Patel, S.W. Bond, M.D. Pocha, M.C. Larson, H.E. Garrett, R.F. Drayton, H.E. Petersen, D.M. Krol, R.J. Deri, M.E. Lowry, Multiwavelength parallel optical interconnects for massively parallel processing. IEEE J. Select. Topics Quantum Electron. **9**(2), 657–666 (2003)
48. R. Michalzik, G. Giaretta, K.W. Goossen, J.A. Walker, M.C. Nuss, 40 Gb/s coarse WDM data transmission with 825 nm wavelength VCSELs over 310 m of high performance multimode fiber, *26th European Conference on Optical Communication, ECOC 2000* **4**, Sep. 2000, pp. 33–34
49. B.E. Lemoff, M.E. Ali, G. Panotopoulos, G.M. Flower, B. Madhavan, A.F.J. Levi, D.W. Dolfi, MAUI: enabling fiber-to-the-processor with parallel multiwavelength optical interconnects. J. Lightwave Technol. **22**(9), 2043–2054 (2004)
50. B.E. Lemoff, M.E. Ali, G. Panotopoulos, E. de Groot, G.M. Flower, G.H. Rankin, A.J. Schmit, K.D. Djordjev, M.R.T. Tan, A. Tandon, W. Gong, R.P. Telia, B. Law, D.W. Dolfi, 500-Gbps parallel-WDM optical interconnect, *Proceedings of the 55th Electronic Components and Technology Conference, ECTC*, May/June 2005, pp. 1027–1031
51. B.E. Lemoff, M.E. Ali, G. Panotopoulos, E. de Groot, G.M. Flower, G.H. Rankin, A.J. Schmit, K.D. Djordjev, M.R.T. Tan, A. Tandon, W. Gong, R.P. Tella, B. Law, D.W. Dolfi, Parallel-WDM for multi-Tb/s optical interconnects, *IEEE Lasers and Electro-Optics Society Ann. Meet., LEOS 2005*, Oct. 2005, pp. 359–360
52. B.E. Lemoff, M.E. Ali, G. Panotopoulos, E. de Groot, G.M. Flower, G.H. Rankin, A.J. Schmit, K.D. Djordjev, M.R.T. Tan, A. Tandon, W. Gong, R.P. Tella, B. Law, L.-K. Chia, D.W. Dolfi, Demonstration of a compact low-power 250-Gb/s parallel-WDM optical interconnect. IEEE Photon. Technol. Lett. **17**(1), 220–222 (2005)
53. A. Suzuki, T. Ishikawa, Y. Wakazono, D. Nagao, T. Hino, Y. Hashimoto, H. Masuda, S. Suzuki, M. Tamura, T.-I. Suzuki, K. Kikuchi, Y. Okada, H. Nakagawa, M. Aoyaghi, T. Mikawa, 10-Gb/s × 12-ch downsized optical modules with electrical conductive film connector, *Proceedings of the 58th Electronic Components and Technology Conference, ECTC*, May 2008, pp. 250–255
54. Y. Wakazono, A. Suzuki, D. Nagao, T. Ishikawa, T. Hino, Y. Hashimoto, H. Masuda, S. Suzuki, M. Tamura, T. Suzuki, K. Kikuchi, H. Nakagawa, M. Aoyagi, T. Mikawa, A study on coupling efficiency between VCSEL and 45°-angled mirror component for low-cost and high-density 10 Gbps/ch optical parallel link module, *IEEE Lasers and Electro-Optics Society Ann. Meet., LEOS 2007*, Oct. 2007, pp. 678–679

55. S. Atsushi, S. Kenji, W. Yoshitsugu, S. Shuji, Y. Takayuki, M. Hiroshi, S. Kazuhito, K. Masao, I. Osamu, K. Katsuya, N. Hiroshi, O. Yoshikuni, A. Masahiro, Low-cost and high-density 10 Gbps/ch optical parallel link module for multi-terabit router application, *32rd European Conference on Optical Communication, ECOC 2006*, Sep. 2008, paper We4.2.3
56. A. Suzuki, T. Ishikawa, Y. Wakazono, Y. Hashimoto, H. Masuda, S. Suzuki, M. Tamura, T.-I. Suzuki, K. Kikuchi, H. Nakagawa, M. Aoyagi, T. Mikawa, Vertically pluggable and compact 10-Gb/s $\times$ 12-channel optical modules with anisotropic conductive film for over 100-Gb/s optical interconnect system. J. Lightwave Technol. **27**(15), 3249–3258 (2009)
57. M. Oda, J. Sakai, H. Takahashi, H. Kouta, Chip-to-chip optical interconnection for next-generation high-performance systems, *IEEE Lasers and Electro-Optics Society Ann. Meet., LEOS 2007*, Oct. 2007, pp. 638–339
58. J. Sakai, A. Noda, K. Nakano, K. Maeda, H. Takahashi, T. Ohtsuka, C. Tanaka, H. Ono, J. Tsuchida, H. Yamaguchi, H. Kouta, LSI-to-LSI signal transmission at 10Gb/s/ch using ultra-high density optoelectronic modules, *Proceedings of International Conference on Electronics Packaging (ICEP)*, 2007, paper TC4-1
59. R. Kuribayashi, I. Hatakeyama, D. Inami, T. Hino, T. Sugimoto, K. Kurata, Adaptive quad 10-Gbps optical I/O module for power-minimized interconnection, *Proceedings of International Conference on Electronics Packaging (ICEP)*, 2009, paper 14B2-1-1
60. K. Miyoshi, I. Hatakeyama, J. Sasaki, K. Yamamoto, M. Kurihara, T. Watanabe, J. Ushioda, Y. Hashimoto, R. Kuribayashi, K. Kurata, A 400 Gbps backplane switch with 10 Gbps/port optical I/O interfaces based on OIP (optical interconnection as IP of a CMOS library), *Tech. Digest Opt. Fiber Commun. Conf., OFC/NFOEC*, Mar. 2005, paper OWB1
61. T. Yoshikawa, I. Hatakeyama, K. Miyoshi, K. Kurata, J. Sasaki, N. Kami, T. Sugimoto, M. Fukaishi, K. Nakamura, K. Tanaka, H. Nishi, T. Kudoh, Optical interconnection as an IP macro of a CMOS library, *Hot Interconnects 9*, Aug. 2001, pp. 31–35
62. K. Yashiki, Y. Hashimoto, M. Oda, N. Suzuki, K. Yamamoto, M. Kurihara, T. Sugimoto, H. Hatakeyama, J. Sakai, T. Akagawa, K. Narita, H. Ono, K. Fukatsu, K. Tokutome, H. Kouta, M. Tsuji, I. Ogura, A. Noda, T. Anan, Y. Suzuki, K. Kurata, 240-Gb/s on-board optical transmitters and receivers, *Tech. Digest Opt. Fiber Commun. Conf., OFC/NFOEC*, Mar. 2010, paper OTuM4
63. Y. Takagi, T. Ohno, T. Horio, A. Suzuki, T. Kojima, T. Takada, S. Iio, K. Obayashi, M. Okuyama, Optoelectronic package having low-loss optical waveguide hole with core–clad structure for chip-to-chip interconnection. IEEE Photon. Technol. Lett. **20**(24), 2033–2035 (2008)
64. Y. Takagi, T. Horio, T. Ohno, A. Suzuki, T. Kojima, T. Takada, S. Iio, K. Obayashi, M. Okuyama, Compact and 10-Gb/s $\times$ 12-channel optical transmitter for optical interconnection with high heat-dissipation capability using alumina substrates. IEEE Photon. Technol. Lett. **21**(4), 248–250 (2009)
65. D.M. Kuchta, Y.H. Kwark, C. Schuster, C. Baks, C. Haymes, J. Schaub, P. Pepeljugoski, L. Shan, R. John, D. Kucharski, D. Rogers, M. Ritter, J. Jewell, L.A. Graham, K. Schrodinger, A. Schild, H.M. Rein, 120-Gb/s VCSEL-based parallel-optical interconnect and custom 120-Gb/s testing station. J. Lightwave Technol. **22**(9), 2200–2212 (2004)
66. D. Kuchta D. Kucharski Y. Kwark R. John, 120Gb/s VCSEL-based parallel optical links, *8th International Symposium on Contemporary Photonics Technology (CPT 2005)*, Tokyo, Japan, 2005, pp. 169–172
67. D. Kuchta, D. Kucharski, Y. Kwark, R. John, C. Schuster, $>$100 Gb/s VCSEL-based parallel optical links, *10th OptoElectronics and Communications Conference (OECC 2005)*, Seoul, Korea, July 2005, pp. 266–267
68. F.E. Doany, C.L. Schow, C.W. Baks, D.M. Kuchta, P. Pepeljugoski, L. Schares, R. Budd, F. Libsch, R. Dangel, F. Horst, B.J. Offrein, J.A. Kash, 160 Gb/s bidirectional polymer-waveguide board-level optical interconnects using CMOS-based transceivers. IEEE Trans. Adv. Packag. **32**(2), 345–359 (2009)

69. C.L. Schow, F.E. Doany, O. Liboiron-Ladouceur, C. Baks, D.M. Kuchta, L. Schares, R. John, J.A. Kash, 160-Gb/s, 16-channel full-duplex, single-chip CMOS optical transceiver, *Tech. Digest Opt. Fiber Commun. Conf., OFC/NFOEC*, Mar. 2007, paper OThG4
70. C.L. Schow, F.E. Doany, C. Chen, A.V. Rylyakov, C.W. Baks, D.M. Kuchta, R.A. John, J.A. Kash, Low-power 16 $\times$ 10 Gb/s bi-directional single chip CMOS optical transceivers operating at <5 mW/Gb/s/link. IEEE J. Solid-State Circ. **44**(1), 301–313 (2009)
71. L. Schares, J.A. Kash, F.E. Doany, C.L. Schow, C. Schuster, D.M. Kuchta, P.K. Pepeljugoski, J.M. Trewhella, C.W. Baks, R.A. John, L. Shan, Y.H. Kwark, R.A. Budd, P. Chiniwalla, F.R. Libsch, J. Rosner, C.K. Tsang, C.S. Patel, J.D. Schaub, R. Dangel, F. Horst, B.J. Offrein, D. Kucharski, D. Guckenberger, S. Hegde, H. Nyikal, C.-K. Lin, A. Tandon, M. Trott, G.R. Nystrom, D.P. Bour, M.R.T. Tan, D.W. Dolfi, Terabus: Terabit/second-class card-level optical interconnect technologies. IEEE J. Select. Topics Quantum Electron. **12**(5), 1032–1044 (2006)
72. F.E. Doany, C.L. Schow, C.K. Tsang, N. Ruiz, R. Horton, D.M. Kuchta, C.S. Patel, J.U. Knickerbocker, J.A. Kash, 300-Gb/s 24-channel bidirectional Si carrier transceiver Optochip for board-level interconnects, *Proceedings of the 58th Electronic Components and Technology Conference, ECTC*, May 2008, pp. 238–243
73. H. Hamasaki, H. Furuyama, H. Numata, C. Takubo, Novel optoelectronic LSI packaging suitable for standard FR-4 printed wiring board with bandwidth capability of over 1 Tbps, *Proceedings of the 56th Electronic Components and Technology Conference, ECTC*, May/June 2006, pp. 298–302
74. H. Uemura, H. Hamasaki, H. Furuyama, H. Numata, C. Takubo, H. Shibata, Extremely-compact and high-performance (160Gbps = 20GB/s) optical semiconductor module using lead frame embedded optoelectronic ferrule, *Proceedings of the 58th Electronic Components and Technology Conference, ECTC*, May 2008, pp. 1936–1940
75. I. Papakonstantinou, D.R. Selviah, K. Wang, R.A. Pitwon, K. Hopkins, D. Milward, Optical 8-channel, 10 Gb/s MT pluggable connector alignment technology for precision coupling of laser and photodiode arrays to polymer waveguide arrays for optical board-to-board interconnects, *Proceedings of the 58th Electronic Components and Technology Conference, ECTC*, May 2008, pp. 1769–1775
76. P. Gui, F.E. Kiamilev, X.Q. Wang, X.L. Wang, M.J. McFadden, M.W. Haney, C. Kuznia, A 2-Gb/s 0.5-μm CMOS parallel optical transceiver with fast power-on capability. J. Lightwave Technol. **22**(9), 2135–2148 (2004)
77. J. Ahadian, M. Englekirk, M. Wong, T. Li, R. Hagan, R. Pommer, C. Kuznia, A quad 2.7 Gb/s parallel optical transceiver, *IEEE Radio Frequency Integrated Circuits (RFIC) Symposium*, June 2004, pp. 13–16
78. F.E. Kiamilev, P. Gui, M.J. MacFadden, X. Wang, N. Waite, M.W. Haney, C. Kuznia, A source-synchronous double-data-rate parallel optical transceiver IC. IEEE Trans. Very Large Scale Integration (VLSI) Systems. **13**(7), 833–842 (2005)
79. E.G. Colgan, B. Furman, J.H. Magerlein, J. Schaub, C. Schow, D. Stigliani Jr., J. Torok, A. Benner, D. Becker, G. Katopis, J. Abshier, W. Dyckman, B.E. Lemoff, M.E. Ali, G. Panotopoulos, E. de Groot, G.M. Flower, G.H. Rankin, A.J. Schmit, K.D. Djordjev, M.R.T. Tan, A. Tandon, W. Gong, R.P. Telia, B. Law, S.A. Rosenau, L.A. Buckman Windover, D.W. Dolfi, Direct integration of dense parallel optical interconnects on a first level package for high-end servers, *Proceedings of the 55th Electronic Components and Technology Conference, ECTC*, May/June 2005, pp. 228–233
80. T. Yoshikawa, S. Araki, K. Miyoshi, Y. Suemura, N. Henmi, T. Nagahori, H. Matsuoka, T. Yokota, Skewless optical data-link subsystem for massively parallel processors using 8 Gb/s $\times$ 1.1 Gb/s MMF array optical module. IEEE Photon. Technol. Lett. **9**(12), 1625–1627 (1997)
81. K. Kurata, T. Yoshikawa, I. Hatakeyama, K. Miyoshi, K. Tanaka, S. Dhomae, H. Tanaka, A 16 $\times$ 16 crosspoint switch module with 3.125-Gbit/port optical I/O interfaces based on OIP (optical-interconnection as IP) design concept, in *Active and Passive Optical Components for WDM Communications II*, Proceedings of SPIE, vol. 4870 (2002), pp. 78–83

82. W. Hofmann, M. Görblich, G. Böhm, M. Ortsiefer, L. Xie, M.-C. Amann, Long-wavelength 2-D VCSEL arrays for optical interconnects, *Conference on Lasers and Electro-Optics and Quantum Electronics and Laser Science, CLEO/QELS 2008*, May 2008, paper CMW7
83. W. Hofmann, E. Wong, G. Böhm, M. Ortsiefer, N.H. Zhu, M.C. Amann, 1.55-μm VCSEL arrays for high-bandwidth WDM-PONs. IEEE Photon. Technol. Lett. **20**(4), 291–293 (2008)
84. M. Beaudoin, A.J.G. DeVries, S.R. Johnson, H. Laman, T. Tiedje, Optical absorption edge of semi-insulating GaAs and InP at high temperatures. Appl. Phys. Lett. **70**(26), 3540–3542 (1997)
85. T. Ishikawa, A. Suzuki, Y. Wakazono, D. Nagao, T. Hino, Y. Hashimoto, H. Masuda, S. Suzuki, M. Tamura, T.-I. Suzuki, K. Kikuchi, Y. Okada, H. Nakagawa, M. Aoyagi, T. Mikawa, High-density and low-cost 10-Gbps × 12ch optical modules for high-end optical interconnect applications, *Tech. Digest Opt. Fiber Commun. Conf., OFC/NFOEC*, Feb. 2008, paper OMK6
86. L. Dellmann, C. Berger, R. Beyeler, R. Dangel, M. Gmur, R. Hamelin, F. Horst, T. Lamprecht, N. Meier, T. Morf, S.Oggioni, M. Spreafico, R. Stevens, B.J. Offrein, 120 Gb/s optical card-to-card interconnect link demonstrator with embedded waveguides, *Proceedings of the 57th Electronic Components and Technology Conference, ECTC*, May/June 2007, pp. 1288–1293
87. S.A. Rosenau, J. Simon, L.A. Buckman Windover, B. Law, G.M. Flower, E. DeGroot, A. Grot, M.J. Nystrom, C.-K. Lin, A. Tandon, K. Djordjev, M.R.T. Tan, L.W. Mirkarimi, R.W. Gruhlke, H. Xia, G. Rankin, M.E. Ali, B.E. Lemoff, K.S. Giboney, D.W. Dolfi, E.G. Colgan, B. Furman, J. Magerlein, J. Schaub, D. Stigliani Jr., J. Torok, D. Becker, G. Katopis, W. Dyckman, D. O'Connor, Novel packaging of parallel-optical interconnects for high-end servers, *Tech. Digest Opt. Fiber Commun. Conf., OFC/NFOEC*, Mar. 2005, paper OThU6
88. D. Kuchta, C. Baks, E. Mintarno, D.N. de Araujo, M. Cases, Optical high speed symmetric multi-processor link implementation, *Proceedings of the 56th Electronic Components and Technology Conference, ECTC*, May/June 2006, pp. 1573–1577
89. S. Yanagimachi, Y. Hidaka, J. Higuchi, T. Yoshikawa, A. Iwata, Generation-free platform architecture with a flexible and scalable optical interconnection system, Proceedings of SPIE, vol. 6376 (2006), pp. 63760H-1–63760H-8
90. I. Hatakeyama, K. Miyoshi, J. Sasaki, K. Yamamoto, M. Kurihara, T. Watanabe, J. Ushioda, Y. Hashimoto, R. Kuribayashi, K. Kurata, A 400 Gb/s backplane switch with 10 Gbps/port optical I/O interfaces, in *Active and Passive Optical Components for WDM Communications V*, Proceedings of SPIE, vol. 6014 (2005), pp. 60140J-1–60140J-7
91. D.M. Kuchta, Y. Taira, C. Baks, G. McVicker, L. Schares, H. Numata, Optical interconnects for servers. Jpn. J. Appl. Phys. **47**, 6642–6645 (2008)
92. D. Grice, H. Brandt, C. Wright, P. McCarthy, A. Emerich, T. Schimke, C. Archer, J. Carey, P. Sanders, J.A. Fritzjunker, S. Lewis, P. Germann, Breaking the petaflops barrier, IBM J. Res Dev. **53**(5), 1:1–1:16 (2009)
93. A.F. Benner, D.M. Kuchta, P.K. Pepeljugoski, R.A. Budd, G. Hougham, B.V. Fasano, K. Marston, H. Bagheri, E.J. Seminaro, D. Hui Xu Meadowcroft, M.H. Fields, L. McColloch, M. Robinson, F.W. Miller, R. Kaneshiro, R. Granger, D. Childers, E. Childers, Optics for high-performance servers and supercomputers, *Tech. Digest Opt. Fiber Commun. Conf., OFC/NFOEC*, Mar. 2010, paper: OTuH1
94. T. Hino, R. Kuribayashi, Y. Hashimoto, T. Sugimoto, J. Ushioda, J. Sasaki, I. Ogura, I. Hatakeyama, K. Kurata, A 10 Gbps × 12 channel pluggable optical transceiver for high-speed interconnections, *Proceedings of the 58th Electronic Components and Technology Conference, ECTC*, May 2008, pp. 1838–1843
95. N. Nishimura, K. Suematsu, M. Shinoda, M. Shiino, High-density multi-fiber connectors for optical interconnection. Furukawa Rev. **34**, 13–16 (2008)
96. Reflex Photonics Inc., LightABLE parallel modules, product brief LA-970-034-00, rev. 1.0, Oct. 2008

97. B. Rosinski, J.W.D. Chi, P. Grosso, J. Le Bihan, Multichannel transmission of a multicore fiber coupled with vertical-cavity surface-emitting lasers. J. Lightwave Technol. **17**(5), 807–810 (1999)
98. D.M. Taylor, C.R. Bennett, T.J. Shepherd, L.F. Michaille, M.D. Nielsen, H.R. Simonsen, Demonstration of multi-core photonic crystal fibre in an optical interconnect. Electron. Lett. **42**(6), 331–332 (2006)
99. B.G. Lee, D.M. Kuchta, F.E. Doany, C.L. Schow, C. Baks, R. John, P. Pepeljugoski, T.F. Taunay, B. Zhu, M.F. Yan, G.E. Oulundsen, D.S. Vaidya, W. Luo, N. Li, 120-Gb/s 100-m transmission in a single multicore multimode fiber containing six cores interfaced with a matching VCSEL array, *IEEE Photonics Society Summer Topical Meeting Series*, 2010, pp. 223–224
100. K. Fukatsu, K. Shiba, Y. Suzuki, N. Suzuki, H. Hatakeyama, T. Anan, K. Yashiki, M. Tsuji, 30-Gbps transmission over 100 m-MMFs (GI32) using 1.1 μm-range VCSELs and receivers, *Proceedings of the 19th International Conference on Indium Phosphide and Related Materials, IPRM*, Matsue, Japan, May 2007, paper WeB3-4
101. R.W. Herrick, Degradation in vertical cavity lasers, Ph.D. dissertation, University Microfilms, Ann Arbor, Michigan (1997)
102. S. Xie, R.W. Herrick, D. Chamberlin, S.J. Rosner, S. McHugo, G. Girolami, M. Mayonte, S. Kim, W. Widjaja, Failure mode analysis of oxide VCSELs in high humidity and high temperature. J. Lightwave Technol. **21**(4), 1013–1019 (2003)
103. R.W. Herrick, Failure analysis and reliability of optoelectronic devices, in *Microelectronics Failure Analysis Desk Reference*, 5th edn. (ASM International, Materials Park, Ohio, 2004), pp. 230–254
104. D.T. Mathes, R. Hull, K.D. Choquette, K.M. Geib, A.A. Allerman, J.K. Guenter, B. Hawkins, R.A. Hawthorne, Nanoscale materials characterization of degradation in VCSELs, Proceedings of SPIE, vol. 4994 (2003), pp. 67–82
105. C.J. Helms, I. Aeby, W. Luo, R.W. Herrick, A. Yuen, Reliability of oxide VCSELs at Emcore, Proceedings of SPIE, vol. 5364 (2004), pp. 183–189
106. C. Ji, J. Wang, D. Söderstrom, K.L. Chen, R. Murty, M. Keever, L. Giovane, J.K. Hwang, G.H. Koh, J. Tan, J. Chu, High volume 850 nm oxide VCSEL development for high bandwidth optical data link applications, Proceedings of SPIE, vol. 7229 (2009), pp. 722904-1–722904-11
107. W.B. Joyce, P.J. Anthony, Failure rate of a cold- or hot-spared component with a lognormal lifetime. IEEE Trans. Reliability **37**(3), 299–307 (1988)
108. IEEE P802.3ba 40Gb/s and 100Gb/s Ethernet Task Force, http://www.ieee802.org/3/ba/

Chapter 17
VCSELs for Optical Mice and Sensing

Martin Grabherr, Holger Moench and Armand Pruijmboom

Abstract A real mass application for VCSELs is their use in optical mice and sensing. As illumination source for sensing applications VCSELs offer a better performance than LEDs. The even more advanced approach of laser self-mixing interference sensors allows a next step in integration, accuracy and new application fields. This chapter summarizes the major requirements towards VCSELs in illumination for sensing applications and gives typical specifications. A detailed description of the production process and the achieved reproducibility makes clear that these VCSELs are ideally suited for production in large quantities. In the second half of the chapter the self-mixing interference method is described in more detail and a highly integrated two axes laser Doppler interferometer is shown. This product is designed for a laser mouse but offers a number of other sensing applications.

17.1 Introduction

Optical mice for computers are mass products with billions of mice sold already. The market of lasers for computer mice and optical finger navigation devices for, e.g., smartphones exceeds the datacom laser market in numbers and is the second largest

M. Grabherr (✉)
Philips Technologie GmbH U-L-M Photonics,
Lise-Meitner-Str. 13, 89081 Ulm, Germany
e-mail: martin.grabherr@ulm-photonics.de

H. Moench
Philips Research Laboratories, Weisshausstr. 2, 52066 Aachen, Germany
e-mail: holger.moench@philips.com

A. Pruijmboom
Philips Laser Lighting Systems, Hurksestraat 2c, 5652 AJ Eindhoven, The Netherlands
e-mail: armand.pruijmboom@philips.com

R. Michalzik (ed.), *VCSELs*, Springer Series in Optical Sciences 166,
DOI: 10.1007/978-3-642-24986-0_17, © Springer-Verlag Berlin Heidelberg 2013

laser market behind optical storage. Strong further growth is expected because of the superior performance of the laser based input devices.

From a computer user point of view the replacement of the mechanical ball based mouse by the optical mouse was an important step forward mainly because it helped to reduce reliability and contamination issues related to the mechanical mouse. In the optical mouse a light source (LED) illuminates a patterned surface (mouse pad or desk) and a CMOS sensor plus image processing analyses the movements between subsequent image frames. The technology relies on visible structures on the surface and is limited in the maximum detectable velocity by the frame rate of the sensor system and the pitch of repetitive patterns [1].

The LED illumination can be replaced by laser illumination yielding several advantages. The coherent laser light induces a speckle pattern, which creates a detectable structure even on a uniform surface or superimposed to a repetitive pattern. Therefore the laser mouse offers a more reliable tracking independent from the surface structure. Furthermore the laser illumination allows for simpler optics and higher system efficiency and therefore reduced (battery-) power consumption.

A more advanced approach is based on self-mixing interference in the laser cavity and uses the laser not only as light source but also as detection and demodulation system [2]. This technology is described in detail in Sect. 17.3. The VCSEL technology allows the integration of a photodiode underneath the VCSEL structure. This system can replace a laser illumination and a separate CMOS detector (both with independent optics) by just one VCSEL device with a lens in front. Based on the physical nature of the observed effect (Doppler interferometry) the system is completely independent of the surface structure and allows reliable detection over a wide range of velocities. This technology allows the integration of a two axes laser Doppler velocity sensor including optics and signal processing electronics into a package of less than 0.2 cm^3 volume [3]. While this system makes a superior mouse it can also enable many applications beyond the mouse.

In the following sections we describe the major requirements towards the VCSELs used in mouse applications as well as design and processing aspects. The major goal is to define a structure that can be mass-produced with high yield and reliability.

17.2 VCSELs as Ideal Illumination Source for the Optical Mouse

The emission profile of the VCSEL is circular and reasonably small divergent. This reduces the requirements on the optics in the illumination path and allows a simple system.

VCSELs offer very low threshold currents and therefore low power consumption. This is especially important for battery powered devices.

In the mouse application the laser illuminates the surface underneath the mouse and a speckle pattern is created on this surface. Changes in this pattern related to different modes emitted by the laser will create disturbing artefacts and have to be

avoided. This means that the laser has to emit only in one single mode and with stable polarization.

17.2.1 General Requirements and Benefits of VCSELs Over Edge Emitters

Different from edge emitters VCSELs emit only one single longitudinal mode. Single-transverse-mode operation can be achieved if the diameter of the active area is made small enough. Due to the advantageous current confinement by wet thermal oxidation electro-optical characteristics of these devices are most attractive for applications that require close to ideal laser sources with minimized power dissipation. Having the disadvantage of a relatively high effective index step incorporated into the optical cavity which is unavoidable in oxide confined VCSELs results in only small active diameters that allow for single-mode operation. Active diameters of only 4 μm are challenging to manufacture with high yields due to the very low tolerance in aperture diameter, which must be controlled within ±0.25 μm. Another challenge is the very high sensitivity to electrostatic discharge (ESD) of these devices which demands for an extremely well controlled production environment.

The laser output power should stay below the eye safety limit of 0.5 mW. This is well feasible in a small diameter single-mode VCSEL.

17.2.2 VCSEL Production and Typical Characteristics

High volume production of single-mode VCSELs requires both, reproducible supply of epitaxial wafers and superior control of unique semiconductor processing technology [4]. At Philips U-L-M Photonics the epitaxial wafers are grown by solid source MBE . The reactor is capable of growing five 3-inch wafers in parallel. Special geometries of wafer holders and effusion cells result in good homogeneity of the cavity resonance across the 3 inch VCSEL wafers. In azimuthal direction, the homogeneity of the resonance dip is extremely good and values stay within a ±0.5 nm range (±0.06%) as shown in Fig. 17.1.

In radial direction, variation is slightly increased and taking edge exclusion area not into account, wavelength variation amounts to ±1.5 nm (±0.2%). The stable material flux in the reactor enables a small wavelength variation from run to run. For 20 runs, representing 100 wafers or roughly 3 million devices, the wavelength variation is as small as ±3 nm.

Frequently, optical gain and doping profiles are checked on calibration wafers, but most of the feedback to epitaxial growth is derived from quality checks during processing, like spatially resolved reflectance measurements, transmission line model (TLM) measurements, and temperature dependent threshold current characteristics.

Compared to standard datacom VCSEL technology, the aperture size of the devices must be controlled extremely well. As a first major requirement the mesa

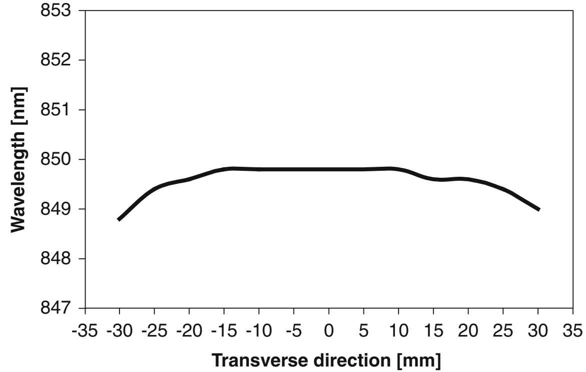

Fig. 17.1 Azimuthal cavity resonance variation of MBE grown 850 nm VCSEL structure

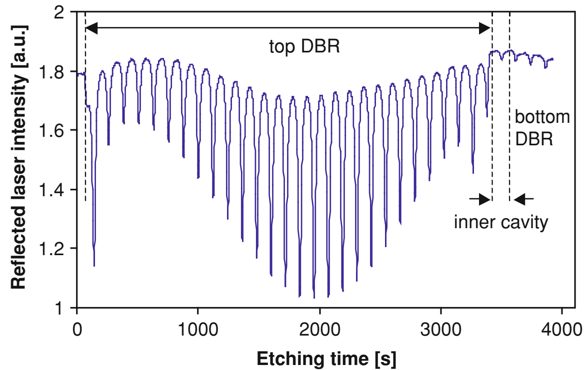

Fig. 17.2 In-situ signal obtained from surface reflection of the processed wafer

etching that exposes the sidewall of the highly aluminum containing confinement layer must be controlled well in terms of mesa geometries. Precise control of mesa height and mesa diameter is achieved by advanced reactive-ion etching (RIE) using in-situ control (Fig. 17.2) and self aligned hard mask technology.

Secondly, important parameters for the subsequent oxidation process are process temperature and material composition. Temperature homogeneity across the wafer during the formation of the apertures must be better than ±0.5°C. Ga content of the current blocking layer is much more crucial [5], but can be controlled epitaxially very well. Oxide layer thickness is chosen to be larger than 30 nm although contribution to optical confinement is rather strong, but oxidation rates are much more sensitive on thickness variations for thinner layers [6]. Finally carbon concentration plays an important role for the homogeneity of the current confinement layer and needs to be controlled precisely with variations of less than ±5% during the growth of the current confinement layer, too.

High volume production needs a further reduction of costs and the main cost driver needs to be addressed: the footprint of the chip. Today, typical VCSEL chips are still based on a $250 \times 250\,\mu\text{m}^2$ footprint cell. This is mainly due to limitations in dicing and die attach. As a first step scribe and break has been chosen for die separation,

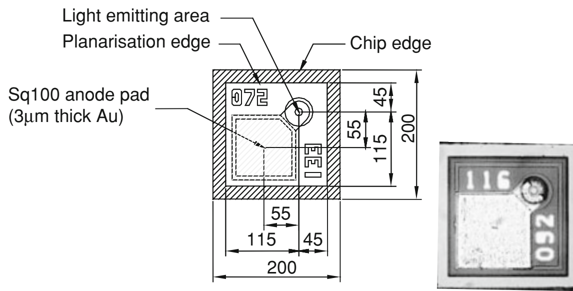

Fig. 17.3 Layout of small surface area VCSEL and photograph

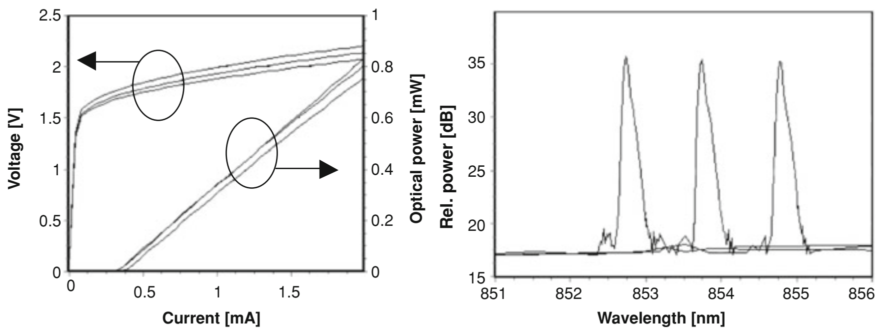

Fig. 17.4 LIV curves (*left*) and single-mode spectra (*right*) of devices from 3 different positions across the wafer

since typical dicing streets already consume 25% of the chip area. In addition Philips U-L-M Photonics has established dicing processes that allow for further reduction of the footprint down to 200 × 200 μm^2 (Fig. 17.3), which gives a direct increase of parts on wafer by another factor of 1.56. All in all the number of parts on wafer can be increased by almost a factor of 2 compared to common technology.

The light–current–voltage (LIV) characteristics across the 3 inch wafer are very homogeneous as can be seen in Fig. 17.4. Typical values are 0.4 mA threshold current, 0.6 W/A slope efficiency, and 1.5 mA as typical operating current which is given by the eye safety limit of approx. 0.5 mW. Corresponding operating voltages are in the range of 2–2.2 V. In the following, the most extreme variation across the wafer along the maximum gradient is depicted. All variations of process parameters like oxide aperture, doping profiles and wavelength variations sum up to only slight variation of threshold current in the order of 100 μA and only 150 mV operating voltage at 2 mA laser current. The output power at 2 mA laser current ranges between 0.7 and 0.9 mW. The LI curves do not show any kinks, which indicates that no significant amount of power is transported in higher order modes within the entire current range up to 2 mA. The spectra in Fig. 17.4 show that the side-mode suppression ratio is more than 10 dB even at maximum laser current.

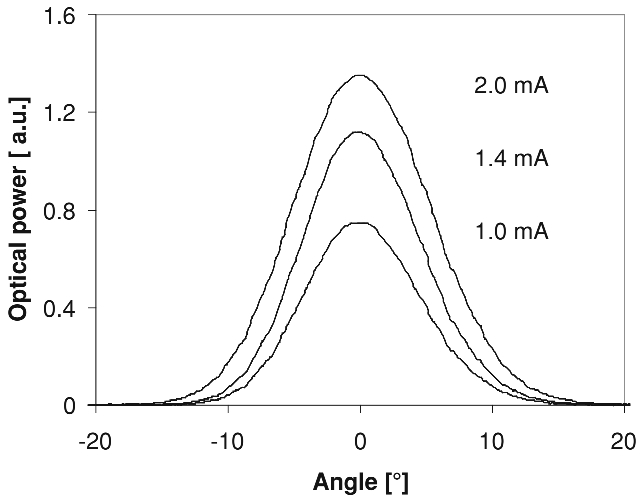

Fig. 17.5 Far-field distribution for different currents

The far-field distribution measured using a pin hole and a photodiode in a 20 cm distance shows nice Gaussian single-mode characteristics as can be seen in Fig. 17.5. The beam divergence typically amounts to 12° FWHM and is pre-defined by the small size of the current aperture and the wave guiding given by the oxide aperture.

The three typical lifetime regimes of a product lifecycle are the infant mortality period, followed by the intrinsic failure period, and finally the wear out phase. During the first hours of operation, the failure rate can be elevated due to processing defects, mechanical stress, etc. By carrying out burn-in procedures these so called early failures can be screened out. For the presented single-mode VCSELs, a burn-in of 16 h at 100°C ambient temperature and operation at maximum ratings results in a detected early failure rate of 200 ppm. The intrinsic or random failure rate is as low as 10 FIT (failures in time) based on several 100 million total test hours. The wear out behaviour is characterized by a pretty well defined time slot where all devices fail, and can be described by a lognormal distribution (Fig. 17.6) with small standard deviation, which typically amounts to 0.25. The failure mechanism can be accelerated by increasing the ambient temperature which allows for significantly reduced testing time. The according activation energy has been compiled into 0.7 eV. At 50°C ambient temperature the mean time to failure (MTTF) value is far in excess of 10,000 hours. Particular attention has to be taken for ESD protection. Due to the small aperture size of only 4 μm in diameter, oxide confined single-mode VCSELs show ESD damage threshold of only 50 V. Though challenging, assembly is still controlled in standard industrial environment.

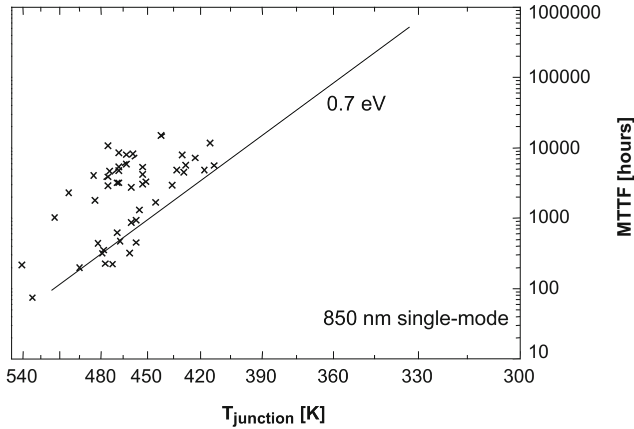

Fig. 17.6 Wear out behavior for single-mode VCSELs. Each data point represents an ensemble of 30 devices under test

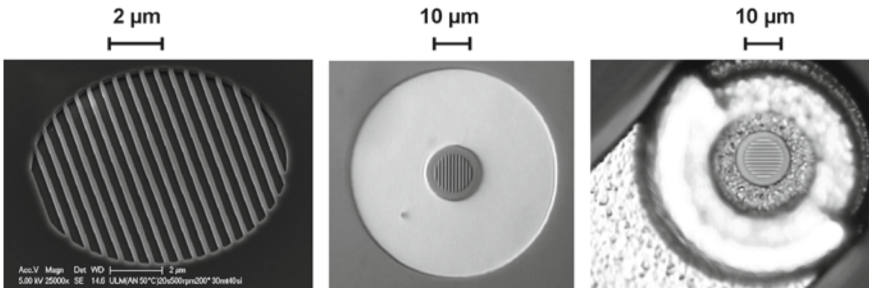

Fig. 17.7 Photographs of the surface grating on top of the mesa (*left*), the mesa (*center*) and the VCSEL structure (*right*)

17.2.3 Polarization Stabilization

Polarization controlling elements that can be implemented in VCSEL processing have been investigated, as more applications demand for single-polarization laser emission on top of single-mode operation. In general the ideas are based on breaking the symmetry of the circular cavity. Eliptically shaped mesa and apertures, higher-order substrates, or external mechanical stress are among the proposed approaches. In all these cases the effect of polarization control is too weak or the drawback for electro-optical performance is too strong. These topics are discussed extensively in Chap. 5 of this book.

We use an approach developed by Ulm University (see Chap. 5 of this book) that makes use of a shallow etched surface grating (Fig. 17.7) [7] which offers multiple advantages. No change in the established manufacturing platform for conventional single-mode VCSELs is required and the additional technological steps, like nano-

imprint-lithography (NIL) [8], can easily be implemented into the existing process flow. The polarization control mechanism is strong enough to guarantee the polarization behavior by design. The pattern of surface grating is calculated and designed by a full vectorial model [9] in a way that the polarization control is strong enough and at the same time no negative impact on output power is induced.

17.3 SMI Laser Doppler Interferometry

Optical feedback interferometry or self-mixing interferometry (SMI) is a well-known sensing principle for velocity and distance measurements. In conventional laser applications, optical feedback is unwanted, since it enhances the intensity noise of the laser, increases the linewidth, and can even lead to chaotic behavior of the laser. Sometimes the non-linear response of the laser to optical feedback is beneficial. For example, feedback provided by an external mirror is used for laser mode selection or linewidth narrowing [10]. This is also the case in optical feedback interferometry. Here, interference inside the cavity between laser light and external feedback is used. For a thorough treatment giving a theoretical background and an overview of this field we refer to the literature [11].

The main advantage from a cost-perspective point of view of self-mixing over other arrangements of interferometry, is that several functions are provided by the laser. The laser is not only the source of coherent light, but also an active filter due to its narrow optical bandwidth. Moreover, the active medium of the laser cavity acts as an amplifier and finally as an optical mixer. This makes the laser sensitive to extremely small fractions of feedback. We obtained reliable SMI signals with a fraction as small as $\sim 10^{-4}$ of the laser output back-reflected onto the laser mirror. Based on the SMI technology remote measurements have been achieved over a distance up to several meters, on a wide variety of surfaces and independent from contamination from other light sources.

17.3.1 Velocity Measurement

If the laser is aimed at a scattering object (see Fig. 17.8), a small portion of the scattered light reflects back into the cavity where it mixes with the strong laser field. When the movement of the object has a component along the direction of the laser beam, the phase of the reflected light continuously shifts with respect to the original laser light, resulting in a periodic variation of the feedback into the laser cavity at a frequency, equal to the Doppler frequency, according to [12]

$$f_{\text{Doppler}} = \frac{2v \cdot \cos\phi}{\lambda}. \tag{17.1}$$

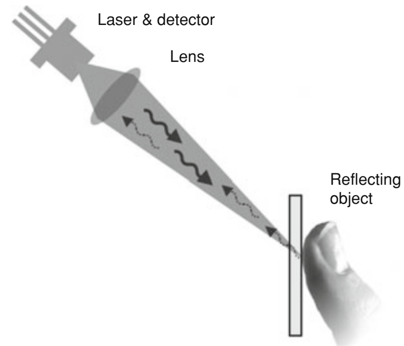

Fig. 17.8 Coherent laser light aimed at a moving surface is scattered back partially in the direction of source

Here $v \cdot \cos\phi$ is the velocity component along the direction of the laser beam in Fig. 17.8, and λ the wavelength of the undisturbed laser. Thus the feedback from this moving object generates a changing interference signal inside the laser cavity with this Doppler frequency, and hence the laser output power is modulated with a frequency, from which the velocity of the scattering object can be derived, according to (17.1).

In reality, the exact response of the laser on the external feedback is more complicated, due to the coupling between the electric field and the carrier density. When the amount of feedback is low, this non-linear effect is small and the laser output modulation is sinusoidal. As the feedback increases, the shape of the signal becomes more and more inharmonic.

17.3.2 Direction of Motion and Distance

In the manner described above, one can only determine the magnitude of the velocity. In principle it is possible to detect the direction of motion from the inharmonic shape of the self-mixing signal. It is however easier to use a frequency modulation technique. In a semiconductor laser, a current modulation also leads to a shift in the wavelength of the emitted light. As a result, when changing the injection current I, the phase of the light will increase by 360° for every additional wavelength that fits on the round-trip length d from the source to surface and back to the source. Every 360° phase rotation causes one minimum and one maximum in the power P of the emitted light. The number of these "undulations" Δn as a function of the wavelength variation is $\Delta\lambda$ given by

$$\Delta n = \Delta\lambda \frac{d}{\lambda^2}. \tag{17.2}$$

A decrease in wavelength has a similar effect as a scattering object moving away from the source, whereas an increase in wavelength mimics an object moving towards

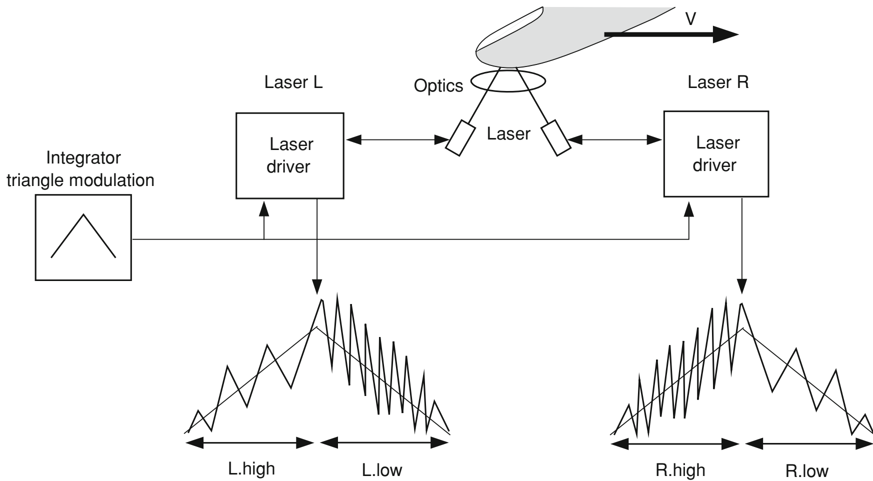

Fig. 17.9 Modulation of the laser current and resulting power fluctuations depending on the direction of movement of the scattering object

the source. If a triangular modulation of the laser current is used (see Fig. 17.9), the wavelength will decrease and increase periodically, mimicking periodical movements away from and towards the source. The power measured by a monitor diode will vary in time with the frequency of this triangular modulation, but now with superposed on it, the undulations with a frequency f_0, which can be determined from (17.2) by

$$f_0 = \frac{d\lambda}{dI} \cdot \frac{dI}{dt} \cdot \frac{d}{\lambda^2}. \tag{17.3}$$

The subscript in f_0 denotes that the scattering object does not move. In this case, the undulation frequency is the same during the up- and down-segment of the triangular modulation. An additional change of the frequency, by the Doppler frequency, occurs for a moving object. When the object is moving away, the Doppler frequency will add to f_0 during a decrease in wavelength, while it is subtracted from f_0 when the wavelength increases:

$$f_{\text{up}} = f_0 - f_{\text{Doppler}}; \quad f_{\text{down}} = f_0 + f_{\text{Doppler}}. \tag{17.4}$$

Note that (17.3) can also be used to directly determine from f_0 the distance $d/2$ to a stationary scattering object. To determine the distance to a moving object, f_0 must be derived from (17.4) and can be expressed as

$$f_0 = \left(f_{\text{up}} + f_{\text{down}}\right)/2. \tag{17.5}$$

17.4 VCSEL as Integrated Laser Doppler Interferometer

Vertical cavity surface emitting lasers are ideal light sources for self-mixing interferometry from both an economic as well as functional point of view. Because they can be made by wafer-scale processing, they are relatively inexpensive as compared to edge-emitting lasers. Due to its extremely short cavity length of the order of the wavelength, a VCSEL operates in a single longitudinal mode, which avoids signal distortions due to mode beatings. It has low power consumption and the circular output beam allows simpler optics than for side-emitting lasers.

An integrated device has been developed on the basis of our VCSEL technology, which combines laser and photodiode in one monolithic device. The specific requirements for velocity and distance measurement with the SMI technology have been translated into specifications for the VCSEL itself.

17.4.1 VCSEL with Integrated Photodiode

An advanced approach for integrating a photodiode (PD) with a VCSEL structure is placing the PD inside the cavity without additional contact or spacer layer. Actually the PD is integrated into the bottom DBR which now consists of a first part of 16 n-DBR layer pairs and 2 p-doped DBR pairs followed by the 100 nm thick absorbing GaAs layer, which is placed symmetrically around an antinode of the standing wave pattern in order to get maximum responsivity and maximum contrast of stimulated versus spontaneous emission [13]. The bottom reflector is completed by additional 22 pairs of n-doped DBR layer pairs. The intra-cavity contact in the central n-doped DBR part is used as both, VCSEL cathode and monitor anode. The additional pn-junction between VCSEL cathode and PD anode is not shortened, but driven in forward direction and thus just adding an additional voltage drop to the monitor diode bias voltage. The resulting three-terminal device comprises a p-i-n-p-i-n structure as described in Fig. 17.10. The according top-view photograph of a real device is shown on the right-hand side.

The LIV characteristics of the VCSEL with integrated intra-cavity photodiode (Fig. 17.11) show low threshold currents of 0.6 mA up to 30°C ambient temperature. Typical operating currents of 2 mA provide up to 0.5 mW single-mode output power. The according voltage drop across the laser structure is less than 2 V at room temperature. In conclusion, there is no substantive drawback for the performance of the VCSEL by integrating the intra-cavity photodiode in comparison to standard single-mode VCSELs (see Fig. 17.4).

In Fig. 17.12 the laser output power is again depicted versus the laser current (lower part of the diagram) for three ambient temperatures, −10, 30, and 80°C. The according monitor current, measured for the intra-cavity photodiode is plotted versus the same laser current scale.

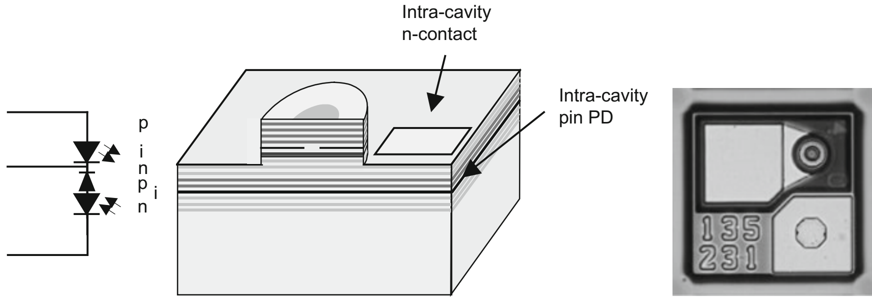

Fig. 17.10 Schematic of a VCSEL with integrated intra-cavity photodiode and according top-view picture of a processed die with a small footprint of $200 \times 200\,\mu\text{m}^2$

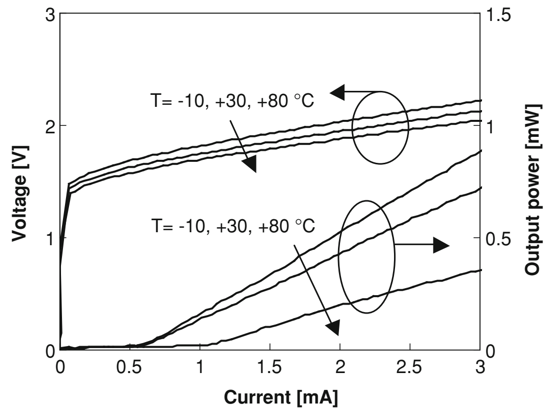

Fig. 17.11 Temperature dependent LIV characteristics of a VCSEL with integrated intra-cavity photodiode

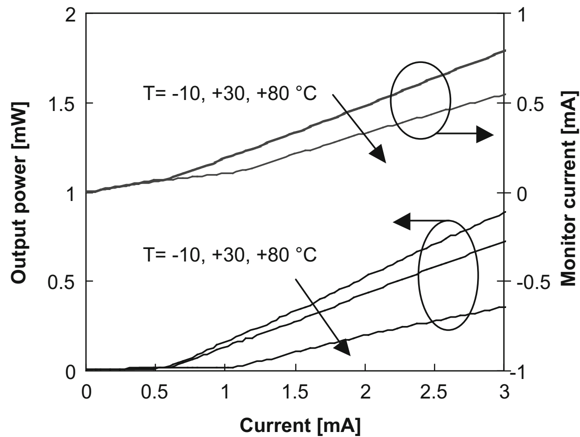

Fig. 17.12 Monitor current and output power versus laser current for a VCSEL with integrated intra-cavity photodiode. Please note that the curves for 10 and 30°C are on top of each other and occur as a single line

Below laser threshold, the monitor current is increasing linearly with laser current due to the contribution of spontaneous emission to the emitted light. Above threshold, the monitor current is increasing far stronger with output power, as the contribution of stimulated emission to the monitor current is dominant. This is due to the intra-cavity approach and the positioning of the absorption layer in an antinode of the standing wave pattern. The monitor currents are in the order of several 100 μW and can easily be processed for power monitoring or self-mixing. In combination with the excellent linearity of the monitor signal with output power the dominating stimulated emission is most advantageous for laser power tracking.

17.4.2 Single-Mode VCSEL

For use in self-mixing interference sensors, it is beneficial to use single-transverse-mode VCSELs. Figure 17.13 shows the optical spectrum of such a VCSEL. The fundamental mode has a peak at 857 nm and the first higher order peak turns up at a wavelength approximately 0.6 nm smaller. The side-mode suppression ratio (SMSR), defined as the ratio between the fundamental mode and the first side-mode, is about 23 dB at 1.0 mA for this VCSEL.

Both peaks will contribute to a self-mixing signal with roughly the same frequency, but with random phases. The resulting self-mixing undulation signal $U(t)$ detected by, e.g., a monitor diode, will be the linear addition of the signals resulting from each peak:

$$U(t) = A_0 \cos\left(\frac{4\pi vt}{\lambda} + 2\pi f_{0_0} t + \phi_0\right) + A_1 \cos\left(\frac{4\pi vt}{\lambda} + 2\pi f_{0_1} t + \phi_1\right), \tag{17.6}$$

where v is the speed of the object, λ is the wavelength, and f_{0_0} and f_{0_1} are the undulation frequencies for a still object resulting from the fundamental mode and first side-mode, respectively. A_0 and A_1 are the electrical undulation signal amplitudes of the detector and these are proportional to the optical power of main and side-mode, respectively. The optical frequency offset of the peaks is so high ($\gg$1 GHz) that mixing of the peaks does not result in an additional detector signal at base-band frequencies. As the two laser modes are spatially orthogonal, their speckle patterns are independent and therefore ϕ_0 and ϕ_1 are uncorrelated phase offsets. If the two modes are narrowly spaced, we can rewrite this equation as:

$$U(t) = A_0 \cos\left(\frac{4\pi vt}{\lambda} + 2\pi f_0 t + \phi_0\right) + A_1 \cos\left(\frac{4\pi vt}{\lambda} + 2\pi f_0 t + \phi_1(t)\right). \tag{17.7}$$

Here $\phi_1(t)$ includes the time dependent phase offset due to the small difference between f_{0_0} and f_{0_1}. In case ϕ_0 equals ϕ_1, the undulation amplitude is $\mathrm{A}_0 + \mathrm{A}_1$. When they differ by π the amplitude is $A_0 - A_1$. Therefore, the peak-to-peak variation in undulation amplitude as a fraction of the undulation of the fundamental

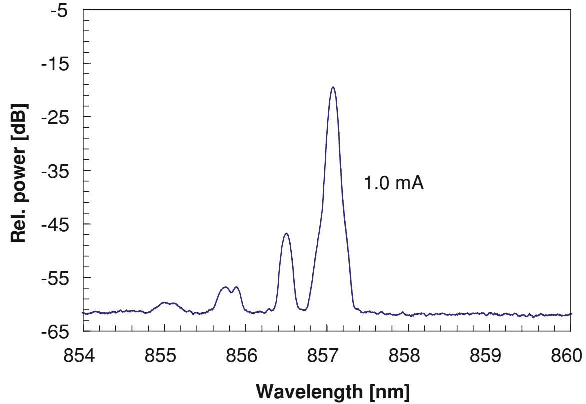

Fig. 17.13 Optical spectrum of a single-mode VCSEL

frequency is $2A_1/A_0$. The fractional peak-to-peak variation in the electrical power of the undulation signal is given by $((A_0 + A_1)^2 - (A_0 - A_1)^2)/A_0^2 = 4A_1/A_0$. Using $\mathrm{SMSR} = 10\log(A_0/A_1)$ dB, this can be written as $4{\cdot}10^{-\mathrm{SMSR}/(10\,\mathrm{dB})}$. This means for instance, that if a 50% (or 3 dB) peak-to-peak variation is considered acceptable to the sensor system, a lower limit of 9 dB for SMSR should be used.

17.4.3 *dλ/dI* Requirements

Another important VCSEL design parameter for the use in laser self-mixing sensors is $d\lambda/dI$. It results from the resistive heating of the laser when a current is applied and therefore depends on its specific heat, its volume, and its electrical resistance. The very small volume of a VCSEL is therefore very beneficial for using it for self-mixing interferometry. The electrical resistance depends on the VCSEL aperture. Figure 17.14 shows $d\lambda/dI$ and SMSR as measured on VCSELs with differently designed aperture diameters.

It can be seen from Fig. 17.14 that for large wavelength swing and high SMSR the VCSEL diameter should be made as small as possible. The smallest aperture that can be used will be limited by the yield at which it can be made reliably and by degradation properties that become worse for the smallest apertures.

17.4.4 Philips "Twin-Eye" Product

One of the unique features of the Philips Twin-Eye integrated laser self-mixing interference sensor is its very small form factor of less than 0.2 cm^3 (see Fig. 17.15). It employs two VCSELs to measure the velocity in x- and y-direction and the height

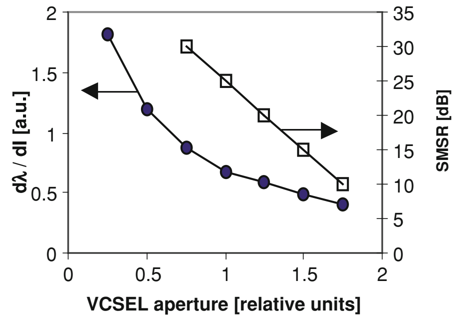

Fig. 17.14 $d\lambda/dI$ and SMSR as measured on VCSELs with different aperture diameters

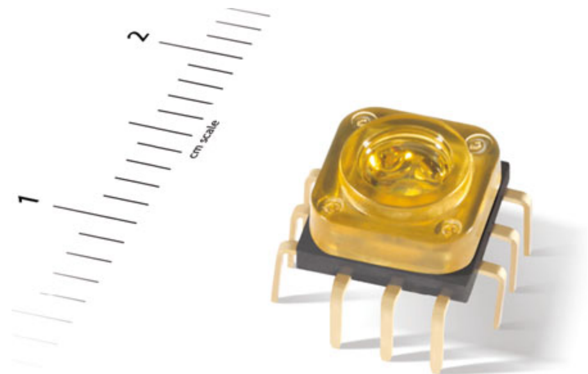

Fig. 17.15 Philips Twin-Eye laser sensor in its 0.2 cm^3 small package

above the surface, as described above. The integrated photodiode measures the fluctuations in laser power and the photocurrent is injected into an application-specific integrated circuit (ASIC). The ASIC converts this signal into a digital signal and applies a fast Fourier transformation (FFT) to determine the undulation frequency and thus the speed relative to a scattering surface. It also allows automatic current saving mechanisms for battery powered applications and guarantees eye safety without any manual adjustment of the laser current.

The system-in-package (SiP) includes capacitors for high- and low-pass filters. On top of the package a lens is placed that is made of material resistant to hand and wave soldering. The lens has two inner spheres, which share the outer sphere. The VCSELs are placed off-axis with respect to the inner spheres such that the two beams exit the lens with an angle of 90° with respect to each other and an angle of 30° with respect to the surface normal (see Fig. 17.16). As the sensor aims at applications in, e.g., computer mice, the focal point is designed a few millimeters above the lens. As a result, the sensor is only sensitive to surfaces in its vicinity. This is, however, not a fundamental limit.

The ASIC includes control systems to give a predictable resolution as a function of speed, in a regime from 0.1 mm/s to 4 m/s (Fig. 17.17). The resolution stays very high and constant even for relatively high velocities. Unlike pattern recognition based

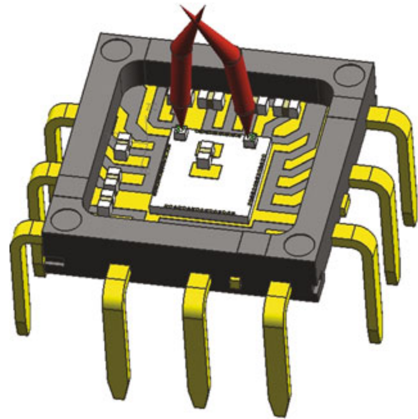

Fig. 17.16 Drawing of the package, two VCSELs on top of the ASIC and the orthogonal laser beams

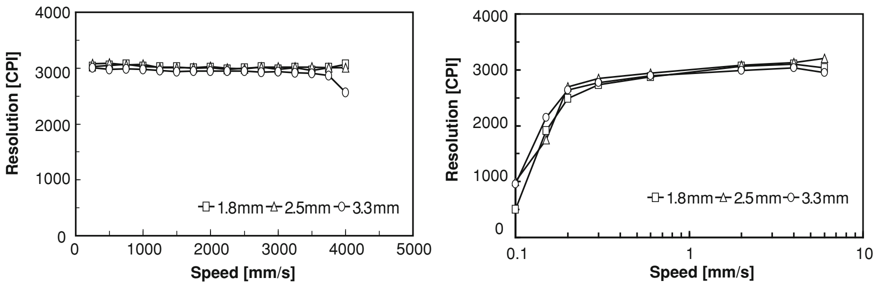

Fig. 17.17 The resolution in counts per inch (CPI) of the Twin-Eye laser sensor as a function of speed, for different distances of the sensor to the surface. The figure shows a predictable resolution in a speed regime from 0.1 mm/s to 4 m/s, independent of the distance. The resolution data represents the averages of measurements over 3 different X–Y directions, with angles between 0 and 360°, which are chosen differently for every height

optical mice the SMI based laser sensor does not require an excessively increasing computing speed for higher velocities.

17.5 More SMI Applications

SMI based laser Doppler interferometry offers unique advantages especially in combination with the VCSEL with an integrated photodiode described above. With an appropriate optics it allows remote measurements up to a few meters (the ultimate limit is half the coherence length of the VCSEL). We were able to realize measurements on a wide variety of targets down to a diffuse reflectivity below 0.1%. Furthermore the measurement is not disturbed by any surface pattern nor by environmental light. Laser Doppler interferometry allows to measure velocity and distance simultaneously.

Besides the use as input device, many other applications can be envisioned where contactless measurement is required. This includes diverse topics like velocity measurement in automotive applications [14], flow measurements [15] or range finders [16].

17.6 Summary

Lasers have found a major market in computer and smartphone input devices. Used as a light source in standard optical mice a VCSEL offers optimum performance in terms of mode and polarization stability, power consumption and lifetime. Advanced manufacturing technology allows reliable, high yield production of tens of millions of VCSELs.

Self-mixing interference based laser Doppler interferometry enables a further step in product integration. The VCSEL with an integrated photodiode acts as a light source, a spectral filter, a detector and a demodulator simultaneously. This measurement technology combines remote measurements of velocity and distance at high accuracy. The VCSEL based device has been optimized to optimally match the needs of SMI based measurements. Furthermore an integrated product has been brought to the market which combines the measurement along two orthogonal axes, all optics and signal processing electronics in a package with a volume of less than $0.2\,\text{cm}^3$.

References

1. http://en.wikipedia.org/wiki/Computer_mouse
2. M.J. Rudd, A laser velocimeter employing the laser as mixer-oscillator. Rev. Sci. Instrum. **1**, 723–726 (1968)
3. A. Pruijmboom, M. Schemmann, J. Hellmig, J. Schutte, H. Moench, V. Pankert, VCSEL-based miniature laser-Doppler interferometer, Proceedings of SPIE, vol. 6908 (2008), pp. 69080I-1–69080I-7
4. D. Wiedenmann, M. Grabherr, R. Jaeger, R. King, High volume production of single-mode VCSELs, Proceedings of SPIE, vol. 6132 (2006), pp. 613202-1–613202-12
5. K.D. Choquette, R.P. Schneider Jr., K.L. Lear, K.M. Geib, Low threshold voltage vertical-cavity lasers fabricated by selective oxidation. Electron. Lett. **30**(24), 2043–2044 (1994)
6. R.L. Naone, L.A. Coldren, Surface energy model for the thickness dependence of the lateral oxidation of AlAs. J. Appl. Phys. **82**(5), 2277–2280 (1997)
7. M. Grabherr, R. King, R. Jäger, D. Wiedenmann, P. Gerlach, D. Duckeck, C. Wimmer, Volume production of polarization controlled single-mode VCSELs, Proceedings of SPIE, vol. 6908 (2008), pp. 690803-1–690803-9
8. M. Verschuuren, H.v. Sprang, 3D photonic structures by sol-gel imprint lithography. Mater. Res. Soc. Symp. Proc. **1002**, N03–N05 (2007)
9. P. Debernardi, An efficient electro-thermo-optical model for vectorial and 3D VCSEL simulation, Proceedings of SPIE, vol. 7229 (2009), pp. 72290D-1–72290D-15
10. K. Petermann, *Laser Diode Modulation and Noise* (Kluwer, Dordrecht, 1988)

11. G. Giuliani, M. Norgia, S. Donati, T. Bosch, Laser diode self-mixing technique for sensing applications. J. Opt. A: Pure Appl. Opt. **4**, 283–294 (2002)
12. M. Liess, G. Weijers, C. Heinks, A. van der Horst, A. Rommers, R. Duijve, G. Mimnagh, A miniaturized multidirectional optical motion sensor and input device based on laser self-mixing. Meas. Sci. Technol. **13**, 2001–2006 (2002)
13. M. Grabherr, P. Gerlach, R. King, R. Jaeger, Integrated photodiodes complement the VCSEL, Proceedings of SPIE, vol. 7229 (2009), pp. 72290E-1–72290E-9
14. X. Raoul, T. Bosch, G. Plantier, N. Servagent, A double-laser diode onboard sensor for velocity measurements. IEEE Trans. Instr. Meas. **53**(1), 95–101 (2004)
15. F. de Mul, M. Koelink, A. Weijers, J. Greve, J. Aarnoudse, R. Graaff, A. Dassel, Self-mixing laser-Doppler velocimetry of liquid flow and of blood perfusion in tissue. Appl. Opt. **31**(27), 5844–5851 (1992)
16. S. Shinohara, H. Yoshida, H. Ikeda, K. Nishide, M. Sumi, Compact and high-precision range finder with wide dynamic range and its application. IEEE Trans. Instr. Meas. **41**(1), 40–44 (1992)

Chapter 18
VCSEL-Based Laser Printing System

Nobuaki Ueki and Naotaka Mukoyama

Abstract There is an endless demand for improved image quality and higher speed in printer applications. To meet market requirements, in 2003 we launched DocuColor 1256 GA, the world's first VCSEL-based electrophotographic printer utilizing a 780 nm single-mode 8 × 4 VCSEL array. The printer features 2,400 dots per inch (dpi) resolution, which is still the highest level in the industry, and a speed of 12.5 pages per minute (ppm). A two-dimensional VCSEL array makes it much easier to increase the pixel density and printing speed by simultaneously scanning the 32 beams on the photoconductor in the light exposure system. Adopting VCSELs as a light source also contributes to reduced power consumption, because the operating current of VCSELs is extremely small and the wall-plug efficiency is very high. In this chapter, we explain the key technologies of VCSELs in light exposure system of laser printer, as well as their required characteristics to assure high image quality.

18.1 Introduction

FUJI XEROX began research and development on single-mode VCSEL arrays in 1995 to investigate the possibility of using them as a novel light source for laser printing system. Following extensive work on prototype array fabrication, qualification (reliability) studies, and development of sub-systems in electrophotographic, or so-called xerographic, processes, we demonstrated the first VCSEL-based light exposure system [1, 2].

The main component of the light exposure system is called a raster output scanner (ROS). A schematic diagram of a xerographic polygon ROS system is shown in Fig. 18.1; it comprises a laser, a polygon mirror, and an $f - \theta$ lens.

N. Ueki—Deceased

N. Mukoyama
Optical System Business Development, Fuji Xerox Company, Ltd.,
430 Sakai, Kanagawa 259-0157, Japan

R. Michalzik (ed.), *VCSELs*, Springer Series in Optical Sciences 166,
DOI: 10.1007/978-3-642-24986-0_18, © Springer-Verlag Berlin Heidelberg 2013

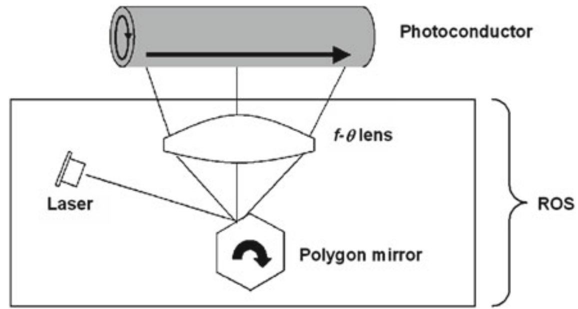

Fig. 18.1 Schematic diagram of xerographic polygon ROS system

The modulated laser light containing the image information is radiated onto the polygon mirror. The polygon mirror is rotated with a motor and reflects the laser beam to the $f - \theta$ lens. The $f - \theta$ lens scans the beam across the entire photoconductor region, generating an electrostatic latent image. The photoconductor is rotated and the scanning sequence repeated continuously until a latent image of the entire page is created. A collimator lens, a cylindrical lens, or a reflection mirror, which are not illustrated, may also be located in the light path to precisely adjust the beam to the appropriate location. Charged toner is then supplied and attached to the photoconductor by electrostatic force, and this toner is then transferred to the paper and fused thermally or mechanically.

The main parameters that determine the image resolution and printing speed are the rotational frequency and the number of facets in the polygon mirror, and the number of light beams from multiple sources. These parameters are related by [3]

$$R = \frac{60VD}{Nm}, \tag{18.1}$$

where R (rpm) is the polygon mirror rotational frequency, V (mm/s) is the printing speed, D (dot/mm) is the print density, N is the number of facets in the polygon mirror, and m is the number of beams guided to the photoconductor.

It is reasonable to assume that R of the polygon mirror should be set higher if we want to improve the resolution or increase the printing speed. However, there are practical limits to the rotational frequency due to the motor's mechanical stability. For example, to develop a printer with 2,400 dpi resolution and 500 mm/s printing speed using a single laser beam, the required polygon mirror rotational frequency would exceed 230,000 rpm. This is far beyond the capability of currently available polygon mirror motors. In addition, this approach involves numerous problems, including increased mechanical vibrations to the lens, which deteriorates the printer's reliability, as well as causing vibration noise and increasing the printer's power consumption and temperature.

As found from (18.1), increasing m is an alterative solution, without the need to increase the polygon mirror rotational frequency. Several light exposure systems using multiple discrete edge-emitting lasers have been proposed before [3, 4]. However, these methods make use of fiber arrays or waveguides to adjust the individual beams, and this is a tedious task. Adopting monolithic edge-emitting

lasers instead of discrete lasers is one possible solution. In fact, edge-emitting lasers containing two or four monolithic light sources are available on the market. However, when considering a higher number of beams, VCSELs have an advantage over edge-emitting lasers in that two-dimensional arrays can be produced with greater ease. This VCSEL-ROS strategy should significantly improve the image resolution or the printing speed, and this was the main motivation of our work.

18.2 VCSELs for Printer Applications

In this section, we describe the requirements of VCSELs for ROS system in printers. Although the parameters taken into account have quite similar requirements to those of conventional edge-emitting lasers, the actual target values differ according to the ROS specifications.

First, the laser wavelength is an important factor to determine the optical design of the system. The region at which the photoconductor possesses the highest and most stable sensitivity mainly determines the laser wavelength to be adopted. Inorganic photoreceptors, such as amorphous silicon and/or As_2Se_3, are sensitive in the visible wavelength region, whereas phthalocyanine pigments, which are widely used organic photoconductor (OPC) materials, show the highest sensitivity in the near-infrared region. We selected VCSELs emitting in the 780 nm region based on our wide experience in handling this type of photoconductor.

Second, each VCSEL must emit a Gaussian-like beam profile and operate in a single transverse mode. This is because the beam shape is directly reflected in the image profile. A multimode beam profile is difficult to focus and will result in fluctuations in the latent image.

The VCSEL must also emit sufficient output power to produce a latent image at the photoconductor. In an ROS system, the power from a single beam is described by [3]

$$P = \frac{4\pi f}{N\eta m} VS, \tag{18.2}$$

where P (mW) is the power required per beam, f (mm) is the focal length of the $f - \theta$ lens, S (mJ/mm^2) is the sensitivity of the photoconductor, and η is the light transmission efficiency from the laser to the photoconductor. Equation (18.2) means that the power emitted from a single beam can be relaxed by increasing the number of laser beams. Although the output power of a single-mode VCSEL tends to be smaller than that of an edge-emitting laser due to the relatively small active region, the array design can compensate for this drawback.

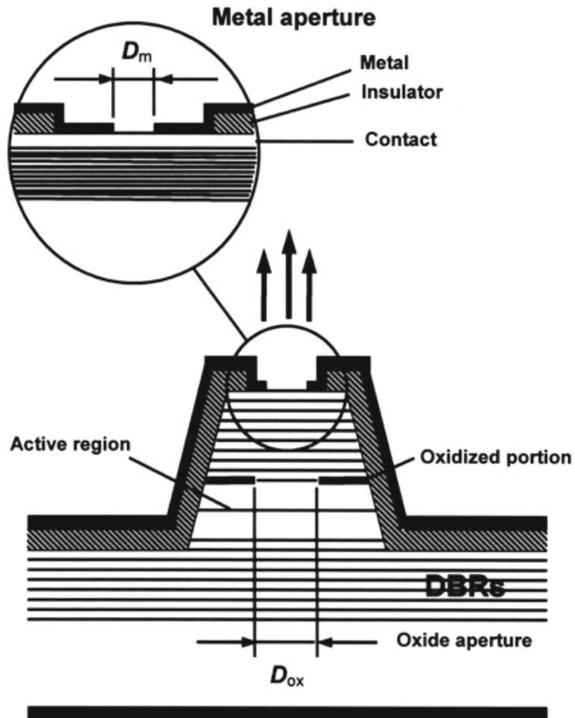

Fig. 18.2 Schematic cross-sectional structure of an oxide-confined VCSEL with a contact-metal aperture. Inset depicts a magnified view of the metal-aperture region

18.3 Structure and Characteristics of VCSEL Array

Next we describe the structure of the VCSEL array and its characteristics.

A cross-sectional view of a single-mode VCSEL is shown in Fig. 18.2. The epitaxial layers consist of $Al_xGa_{1-x}As$ semiconductor materials grown on a GaAs substrate. First, 40.5 pairs of $Al_{0.3}Ga_{0.7}As/Al_{0.9}Ga_{0.1}As$ layers are grown to construct the n-type distributed Bragg reflector (DBR) mirror. A one-wavelength-thick $Al_{0.6}Ga_{0.4}As$ spacer layer including three $Al_{0.11}Ga_{0.89}As$ quantum wells is then provided as an active layer to obtain a gain peak at 766 nm. Then, 24 pairs of $Al_{0.3}Ga_{0.7}As/Al_{0.9}Ga_{0.1}As$ with graded layers are grown to construct the p-DBR mirror, followed by a p-GaAs cap layer. An AlAs layer, which will later be oxidized, is included in the p-DBR mirror to compose a lateral current funneling and optical confinement region.

The mesa was fabricated by using a conventional reactive ion etching (RIE) process with chlorine mixture gas, followed by selective oxidation to the AlAs at 340°C in a wet oxidation furnace. After the oxidation process, the mesa was covered with a SiN_x passivation layer by plasma-enhanced chemical vapor deposition under low temperature. The function of the passivation layer is not only to prevent degeneration of the etched surface, but also to control the mechanical stress induced by

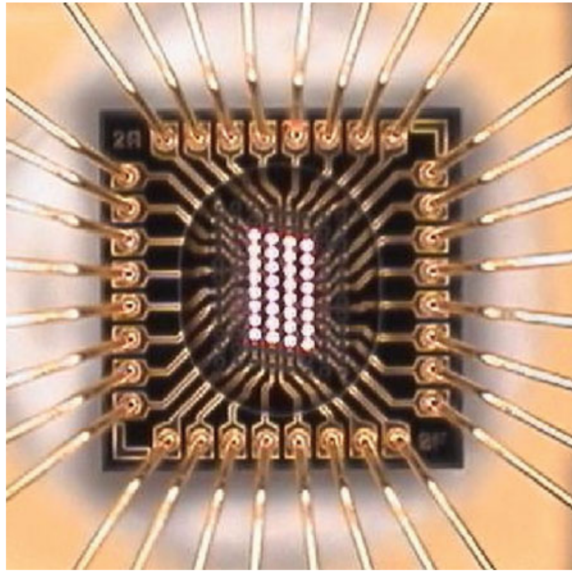

Fig. 18.3 Microscope image of an 8 × 4 single-mode 780 nm VCSEL array

the oxidized mesas. Finally, a Ti/Au p-electrode and a Au/Ge/Au n-electrode were deposited on each side of the wafer, respectively.

The contact-metal aperture was fabricated on the p-GaAs cap layer. The metal-aperture size (D_m) was adjusted to suppress the undesirable higher order lateral modes oscillating in the active region, in accordance with an oxide-aperture size (D_{ox}). It has been estimated that the round-trip loss of higher order modes is maximized when the difference between the oxide-aperture and the metal-aperture sizes is between 0 and 1.0 μm. Details of the design concept and calculation have been published elsewhere [5]. The fabricated 8 × 4 single-mode VCSEL array after the packaging process is shown in Fig. 18.3.

Figure 18.4 shows the *L–I–V* characteristics of the 8 × 4 VCSEL array at room temperature. A very low threshold current of 0.3 mA and a maximum optical output power of more than 4 mW were obtained. Single-mode operation was maintained up to 3 mW of output power for all 32 beams. The standard deviations of the threshold current and the power at 3 mA for this array were 0.5 and 5%, respectively. Due to the relatively narrow oxide-aperture size used to maintain stable fundamental mode oscillation, the differential resistance was approximately 200 Ω near 1 or 2 mW. This is a distinct feature of VCSELs for ROS compared with conventional edge-emitting lasers.

The measured spectrum of typical emission is shown in Fig. 18.5. The peak emission wavelength was around 787 nm. The side-mode suppression ratio (SMSR) exceeded 30 dB at 1.2 mW of optical output power, which is considered sufficient for use as the light source of the ROS.

Figure 18.6 is a plot of the near-field pattern (NFP) of one VCSEL operating at 1.4 mW, showing the intensity versus position at the radiation surface. The $1/e^2$

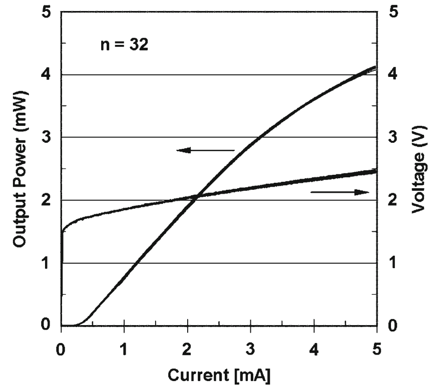

Fig. 18.4 L–I–V characteristics of the 8 × 4 VCSEL array

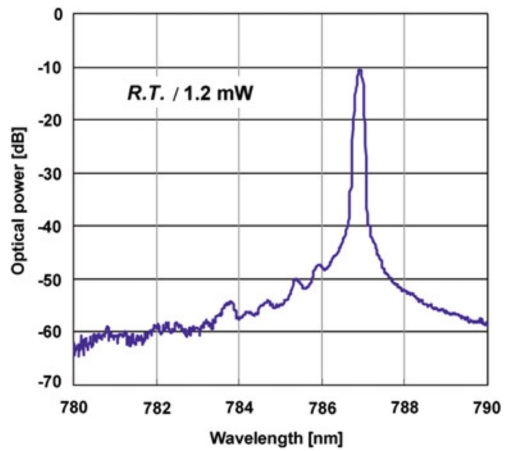

Fig. 18.5 Typical emission spectrum from a device measured at 1.2 mW

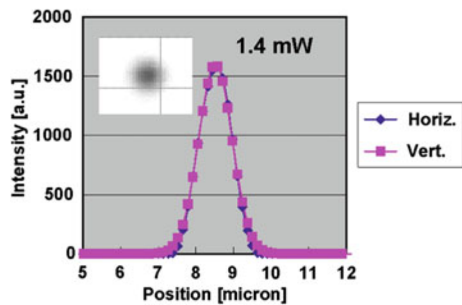

Fig. 18.6 Typical near-field pattern from one VCSEL measured at 1.4 mW. Inset depicts laser spot observed by CCD camera

mode field diameter was estimated to be less than 2 μm. The laser spot shape was nearly circular.

The two-dimensional distribution of the beam divergence angle for the 8 × 4 VCSEL array at 0.5 mW is shown in Fig. 18.7. The minimum and maximum val-

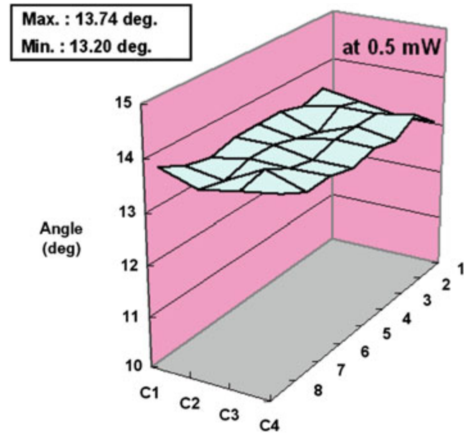

Fig. 18.7 Distribution of the beam divergence angle (FWHM) for the 8 × 4 VCSEL array at 0.5 mW

ues were 13.20 and 13.74°, respectively. Their standard deviation in the array was below 5%.

The VCSELs were produced in our fabrication line using a proprietary *in situ* monitoring method to control the oxide-aperture size [6]. As a result, highly uniform characteristics with less than 5% variation in both output power and beam divergence angle were obtained.

18.4 VCSEL Driver IC

Next we discuss the method used to drive the VCSELs for ROS.

The relation between image density, printing speed, and the time for a laser to emit a single dot is basically given by [3]

$$\frac{1}{t_{\mathrm{p}}} = \frac{4\pi f}{N}\frac{VD^2}{m}, \tag{18.3}$$

where t_{p} (s) is the time required to emit a single dot, and f (mm) is the focal length of the $f-\theta$ lens. The other symbols are the same as those in (18.1) and (18.2).

If we assume 2,400 dpi resolution, 500 mm/s speed, and 32 beams from a VCSEL, the typical time to emit a single dot is estimated to be on the order of 10 ns. However, it is relatively difficult to drive a single-mode VCSEL within 10 ns using a conventional current-drive IC. We found that the turn-on speed was not fast enough due to the VCSEL's high series resistance. This issue is schematically illustrated in Fig. 18.8a.

To reduce the turn-on time, we have investigated a voltage-drive IC instead of a current-drive one. Although the time constant was significantly reduced by using this method, we observed a gradual power rise after the VCSEL was turned on, as shown in Fig. 18.8b. It was found that the series resistance of the VCSEL was reduced due

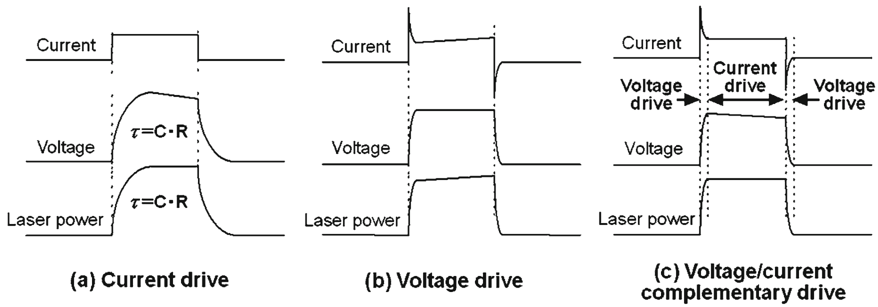

Fig. 18.8 Wave patterns of current, voltage, and laser power based on three different driving methods

to the temperature rise during turn-on, and this led to an increase in bias current, resulting in an output power rise. This power rise is unacceptable from the viewpoint of image quality [7].

To solve this problem, we developed a custom ASIC called voltage/current complementary drive IC to turn on the VCSEL rapidly without any gradual changes in the output power. This ASIC initially functions in a voltage-drive mode to rapidly turn on the VCSEL, and shifts to a current-drive mode that continuously stabilizes the output power of the VCSEL. This driving method is explained in Fig. 18.8c.

The voltage/current complementary driving method eliminates power fluctuations on the photoconductor at the initial and final points of operation, which would otherwise degrade the image quality. The improved image quality achieved by means of the voltage/current complementary drive IC was verified through sensory evaluation tests.

18.5 Image Quality

In this section, we describe an actual print sample with 2,400 dpi resolution realized by our VCSEL technology.

Figure 18.9 illustrates a comparison of the image quality of some samples achieved with a conventional 600 dpi resolution system and our novel system with 2,400 dpi resolution. The 600 dpi image exhibited some jaggy lines, whereas the 2,400 dpi image produced with the VCSELs showed smoother edges.

In addition to improved monochrome line drawing, the 2,400 dpi resolution allows excellent color gradation and halftones, though they cannot be adequately represented on the pages of this book.

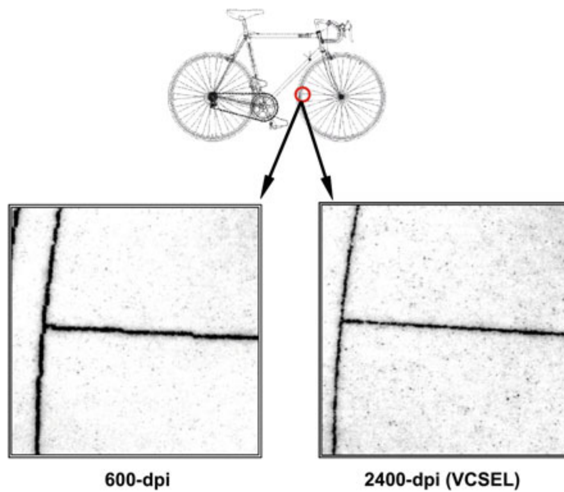

Fig. 18.9 Comparison of image quality between 600 dpi and 2,400 dpi print samples

Fig. 18.10 VCSEL-based multi-function laser printer (*left*: DocuColor 1256 GA) and on-demand publishing system (*right*: DocuColor 8000 Digital Press)

18.6 VCSEL-Based Printer Products

Examples of VCSEL-based printers are shown in Fig. 18.10. The laser printers we developed have achieved a resolution as high as 2,400 dpi, which is still the highest level performance demonstrated in electrophotographic printers. This technology is currently being extended to high-end tandem color machines (2,400 dpi, 80 ppm) to capture a share of the on-demand publishing market. The number of VCSEL arrays shipped worldwide in laser printers to date exceeds 500,000 (corresponding to more than 16 million lasing spots), and no field failures have been reported.

VCSEL-based light exposure system is undoubtedly recognized as being a key technology in meeting the market needs for high-resolution, high-speed printers.

18.7 Summary

We have developed a new light exposure system for laser printer applications utilizing 8 × 4 VCSEL arrays. By adopting a VCSEL array as a light source, the rotational frequency of the polygon mirror can be reduced while simultaneously achieving high resolution and high speed.

The VCSEL array operates in the 780 nm wavelength region in a single transverse mode up to 3 mW. The VCSEL array emits Gaussian-like beam profiles with uniform divergence angles showing a standard deviation of less than 5%. Due to our proprietary in situ oxidation monitoring process, uniform $L-I-V$ characteristics showing excellent run-to-run reproducibility were obtained.

In addition, we developed a unique voltage/current complementary drive IC to drive the VCSELs smartly with stable output power, which is the most important factor in image quality control.

We believe that VCSEL-based laser printers will satisfy the market's never-ending demand for high-quality laser printing.

Acknowledgments The authors wish to acknowledge their colleagues who developed the 8 × 4 VCSEL array, as well as the xerography engineers of FUJI XEROX, without whom it would not have been possible to realize the VCSEL-based printer product. The authors would like to specially thank Chikaho Ikeda, Hiroaki Tezuka, Jun-ichi Ichikawa, and Takaaki Sakakibara for the VCSEL-ROS development.

References

1. N. Ueki, H. Tezuka, A. Ota, Vertical-cavity surface-emitting laser diode (VCSEL)—VCSEL array and its application to the copier. J. Imaging Soc. Jpn. **44**, 149 (2005)
2. N. Mukoyama, H. Otoma, J. Sakurai, N. Ueki, H. Nakayama, VCSEL array-based light exposure system for laser printing, in *Vertical-Cavity Surface-Emitting Lasers XII*, ed. by C. Lei, J.K. Guenter. Proceedings of SPIE, vol. 6908 (2008), p. 69080H-1
3. K. Kataoka, Y. Shibayama, K. Doi, Multiple beam scanning for laser printer: application to optical fiber array method. Opt. Rev. **8**, 218 (2001)
4. A. Hamada, N. Nishida, T. Hatano, M. Mino, Characteristics of multi-beam module using waveguides of laser scanning optical systems. Opt. Rev. **10**, 544 (2003)
5. N. Ueki, A. Sakamoto, T. Nakamura, H. Nakayama, J. Sakurai, H. Otoma, Y. Miyamoto, M. Yoshikawa, M. Fuse, Single-transverse-mode 3.4-mW emission of oxide-confined 780-nm VCSELs. IEEE Photon. Technol. Lett. **11**, 1539 (1999)
6. A. Sakamoto, H. Nakayama, T. Nakamura, Fabrication control during AlAs oxidation of the VCSEL's via optical probing technique of AlAs lateral oxidation (OPTALO), in *Vertical-Cavity Surface-Emitting Lasers VI*, ed. by C. Lei, S.P. Kilcoyne. Proceedings of SPIE, vol. 4649 (2002), p. 211
7. K. Yamada, M. Ito, Influence of laser diode power fluctuation on image quality in xerographic printing, in *Proceedings of International Congress of Imaging Science 2002, ICIS '02*. Tokyo, Japan, May 2002, p. 577

Index

10-Gigabit Ethernet. *See* Ethernet, 10-Gigabit

A
Absorption, 38
    free-carrier, 29, 37, 95, 153, 329, 358, 362
    spectroscopy, 165
Active optical cable (AOC), 13, 445, 453, 455, 467, 474, 484, 502, 505, 511
Agilent, 479, 485, 488, 490, 492, 497, 512
AIST, 486, 494, 495, 501
AlAs, 22, 25, 35, 41, 328, 381
AlAsSb, 323, 341, 356
AlGaAs, 20, 24, 65, 130, 186, 215, 248, 293, 362, 380, 381, 383, 432, 435
AlGaInP, 380
AlGaN, 403
All-optical signal processing, 11, 12, 225
Alvesta, 476
Anisotropy, 219
    gain. *See* Gain anisotropy
    geometry, 159, 183
    polarization. *See* Polarization anisotropy
    refractive index, 85, 184
    strain. *See* Strain, anisotropic
    thermal, 94
Annealing, 360, 367, 416
Antiguiding. *See* Optical guiding, carrier-induced antiguiding
Antimony, 341, 360
AOC. *See* Active optical cable (AOC)
Applications, 120–122
    atomic clock, 59, 121
    automotive, 14, 537
    beacon, 264, 286, 287
    communication, 59, 120, 343, 392, 431, 449, 473
    computer mouse, 9, 13, 20, 120, 147, 156, 521
    cutting, 264, 265
    designator, 286, 287
    elevator system, 462
    gas analysis, 13, 121, 336, 341, 346
    hair removal, 265, 280
    illuminator, 264, 265, 280, 287
    LIDAR, 14, 264
    marking, 264, 265
    medical, 263–265, 287, 464
    mobile phone, 14, 521
    printing, 9, 120, 264, 265, 380, 539
    Q-switch, 284, 285, 287
    sensing, 121
    welding, 264, 265
Aralight, 477, 480
Arrays. *See* VCSEL, arrays
Amorphous silicon, 327, 336, 338
Atomic force microscopy (AFM), 166, 394, 414
Auger recombination. *See* Carrier recombination, nonradiative
Automotive. *See* Applications, automotive
Avago, 478, 480, 483, 484, 492, 504
Avalon Photonics, 157

B
Band anti-crossing (BAC) model, 356
Band mixing, 97, 214, 220, 221
Beacon. *See* Applications, beacon
Beam
    divergence angle, 48, 88, 168, 280, 282, 336, 526, 544
    profile, 47, 60, 80, 86, 89, 91, 123, 299, 384, 544

R. Michalzik (ed.), *VCSELs*, Springer Series in Optical Sciences 166,
DOI: 10.1007/978-3-642-24986-0, © Springer-Verlag Berlin Heidelberg 2013

B (*cont.*)
quality factor, 282
Benzocyclobutene (BCB), 246, 249, 250, 254, 327, 331
BeO, 278
Bernard–Duraffourg condition, 330
Bias-free data transmission. *See* Data transmission, bias-free
Bidirectional data transmission. *See* Data transmission, bidirectional
Birefringence, 85, 90, 93, 149, 152, 154, 167, 184–186
critical, 216, 219
effective, 194, 197, 199
misaligned, 185, 220
nonlinear, 196
Bistability of polarization. *See* Polarization bistability
Bit error ratio (BER), 59, 61, 343
Blue emitting VCSEL, 5, 7, 9, 405, 424
Bragg reflector (DBR), 4, 7, 24, 102, 122, 161, 266, 268, 291, 297, 302, 339, 356, 365, 381, 404, 531
dielectric, 24, 325, 327, 329, 336, 405, 413, 421
hybrid, 327, 329, 338, 410, 416
MEMS, 309, 339
peak reflectivity, 24, 29, 34
penetration depth, 26
polarisation-dependent, 158
reflection phase, 25
reflectivity spectrum, 25, 34
resistance, 239, 244, 271, 364
semiconductor, 25
Brightness, 12, 263, 266, 282–284, 286, 287
Buried tunnel junction (BTJ), 7, 8, 130, 140, 243, 244, 251, 252, 254, 324, 329, 363, 369
Burrus-type LED, 327

C
CaF_2, 254, 294, 327, 336
Carrier
diffusion, 102, 106, 187, 238, 275, 276
heating, 52, 207, 220, 223, 239
leakage, 31, 98, 101, 242, 268, 361, 363, 421, 423
recombination
heat, 96
nonradiative, 32, 46, 78, 96, 99, 104, 114, 239, 360, 361
radiative, 32, 99, 104
Catastrophic optical damage (COD, COMD), 264, 265, 285, 287, 335
Cavity
length, 26
effective, 26
mode, 34, 411
quality factor. *See* Q-factor
solitons, 11
CD laser, 12, 432, 435
Characteristic temperature. *See* T_0
Chemical-mechanical polishing (CMP), 410, 421
Chip parasitics. *See* Parasitics, chip
Cielo Inc., 479
CMOS, 43, 335, 447, 485, 491–493, 522
Coherence, 63, 120, 121, 224, 432, 435, 536
Composition grading, 34, 39, 245, 337, 357, 358, 363–365, 382
Computer mouse. *See* Applications, computer mouse
Confinement factor, 30, 51, 104, 125, 207, 209, 236
relative, 28
Connectors, 13, 433, 437, 443, 453, 455, 458, 467, 505
Conversion efficiency. *See* Efficiency, conversion
Cost, 12, 13, 20, 64, 155, 156, 162, 234, 264, 265, 278, 306, 322, 354, 431, 432, 436, 440, 441, 444, 445, 449, 470, 474, 484, 497, 503, 507, 512, 524, 528
Coupled-mode theory, 26, 80
Coupling, fiber. *See* Fiber coupling
Crosstalk, 440, 442, 467, 485, 488, 491
thermal. *See* Thermal crosstalk
Current
confinement, 22, 101, 124, 127, 140, 325, 523
crowding, 42, 100, 423
density, 32, 51, 270, 326, 361, 387, 394, 395
drive. *See* Laser diode driver, current mode
injection, asymmetric, 157
injection efficiency. *See* Efficiency, current injection
leakage. *See* Carrier leakage
spreading, 266, 270, 275, 324, 330, 340, 421
Cutting. *See* Applications, cutting
CWDM. *See* Wavelength division multiplexing, coarse (CWDM)

D
Damping, 53, 55, 56, 237, 238, 241, 333, 390
Data
  storage, 4, 12, 14, 120, 353, 404, 431, 435, 522
  transmission, 59, 333, 343, 392, 431, 449, 473
    bias-free, 6, 61, 63
    bidirectional, 10, 65
    inter-chip, 12, 42, 235, 493
    intra-chip, 13
Datacom transceivers, 6, 9, 65, 431, 455, 458, 469, 479, 485, 493
DBR. *See* Bragg reflector (DBR)
Designator. *See* Applications, designator
D-factor, 55, 237
DFB laser, 13, 322, 337, 354
Diamond, 278–280, 287
Dichroism, 91, 149, 164
  effective, 197, 199
  misaligned, 185, 220
  nonlinear, 196
Die
  attach, 278, 444, 524
  separation, 524
Differential
  gain. *See* Gain, differential
  quantum efficiency. *See* Efficiency, differential quantum
Digital visual interface (DVI), 449
Dilute nitrides, 10, 323, 360
Display data channel (DDC), 451
Displays, 12, 14, 450, 458, 461
Distributed Bragg reflector (DBR). *See* Bragg reflector (DBR)
Donut mode. *See* Mode, donut
Doping, 21, 35–37, 41, 54, 241, 251, 268, 332, 340, 358, 365, 381, 383, 404
Doppler
  frequency, 528
  interferometry, 522, 536
DPSS lasers, 264, 265, 282
DWDM. *See* Wavelength division multiplexing, dense (DWDM)
Dwell time, 190, 191, 208

E
EDC. *See* Electronic dispersion compensation (EDC)
EDFA. *See* Erbium-doped fiber amplifier (EDFA)
Edge-emitting lasers, 13, 15, 19, 21, 23, 27, 28, 30, 38, 44, 58, 93, 121, 148, 153, 182, 191, 206, 209, 244, 245, 263–265, 280, 281, 284, 287, 322, 335, 341, 343, 357, 359, 361, 368, 381, 394, 403, 431, 435, 436, 447, 488, 523, 531, 541, 543
Effective index. *See* Optical guiding, effective index analysis
Efficiency,
  conversion, 39, 263–276, 279, 282, 283, 286, 287, 335
  current injection, 31, 36, 51, 99, 207, 236
  differential quantum, 35, 36, 237, 267, 269–272, 275
  internal quantum, 269, 270, 276
Elasto-optic effect, 81, 149, 154, 155, 184
Electro-optic effect, 81, 85, 86, 91, 149, 150, 154, 155, 160, 184, 186, 257
Electron-beam lithography, 162, 297, 304
Electronic
  dispersion compensation (EDC), 64, 444
  driver. *See* Laser diode driver
Elevator system. *See* Applications, elevator system
Emcore, 431, 478, 479, 481, 482, 484, 499, 505
Emission
  linewidth, 57, 405, 412, 415, 420, 528
  spectrum, 41, 42, 48, 139, 163, 165, 166, 168, 186, 194, 280, 283, 299, 301, 312, 331, 339, 342, 344, 368, 395, 416, 421, 422, 525, 534, 544
Energy flux, 36
Epitaxy, 4, 5, 21, 281, 306, 361, 367, 381
  growth temperature, 358, 359, 381, 383, 385, 406, 410
  MBE, 4, 5, 21, 304, 306, 325, 330, 357, 359, 364, 381, 523
  MOCVD, 4, 10, 21, 266, 304, 325, 364, 408, 410
  MOVPE, 357–359, 364, 381
  uniformity, 281, 523
Erbium-doped fiber amplifier (EDFA), 354, 358
Etendue, 282
Ethernet, 158, 450, 474, 511, 512
  10-Gigabit, 63, 64, 248, 343, 441, 474
Exciton binding energy, 403
Eye diagram, 251, 343, 345, 392, 434, 435, 442

F
Far-field. *See* Beam divergence angle
Feedback. *See* Optical feedback

F (*cont.*)
Fiber
coupling, 60, 282, 436, 453, 458, 490
H-PCF, 453
laser, 264, 265, 282
multicore, 506, 512
multimode, 60, 62, 282, 506
OM3, OM4, 63, 65, 474, 491, 511
polymer optical (POF), 43, 65, 380, 392, 454
single-mode, 62, 120, 235, 242, 247, 253, 343, 436, 437
to the home, 353, 358, 392
Flip-chip bonding, 43, 246, 327, 334, 480, 482, 488, 489, 491, 492
Four-wave mixing, 197, 220, 221
Free-carrier absorption. *See* Absorption, free-carrier
Free spectral range. *See* Mode spacing, longitudinal
Free-space
optics, 334, 335
interconnects, 6, 59
Frequency doubling, 11, 265
FTTH. *See* Fiber to the home (FTTH)
Fuji Xerox, 157, 539
Furukawa, 486, 494, 496, 505, 506
Future of VCSELs, 12, 423, 444, 510

G
GaAs, 20, 25, 31, 41, 44, 54, 86, 98, 99, 122, 127, 157, 167, 186, 212, 215, 247, 248, 253, 266, 294, 328, 355, 380, 381, 485, 531, 542
GaAsSb, 323, 356
Gain
anisotropy, 5, 8, 157, 183, 209, 212
calculations, 4, 6, 44, 98, 211
compression, 52, 54, 206–209, 221, 223, 236, 238
differential, 52, 55, 207, 237, 241, 242, 249, 391
enhancement factor, 28, 242, 414
Gain guiding. *See* Optical guiding, gain guiding
modal, 104, 111, 125, 148, 149, 207, 210, 212, 213
red-shift, 44, 97, 153, 187, 210, 224, 247
threshold, 29, 34, 54, 84, 209, 414, 420
GaInNAs, 7, 10, 129, 253, 356, 362, 366
GaInNAsSb, 8, 353–370
quasi-ternary, 367
GaInP, 129, 380
GaNAs, 359–361
GaN VCSEL, 5, 7, 9, 403
Gas sensing. *See* Applications, gas analysis
GaSb, 337, 341, 346
Gaussian mode. *See* Mode, Gaussian
Gigabit
interface converter (GBIC), 437, 440
link module (GLM), 437, 440
Gore, 476, 477, 479, 484
Grading of heterointerfaces. *See* Composition grading
Grating, 91, 147, 160, 527
duty cycle, 162, 293, 307
high-index-contrast (HCG), 8, 168, 291
array waveguide modes, 296
fabrication tolerance, 304
non-periodic, 296
TE, 299
TM, 299
subwavelength, 167

H
Hair removal. *See* Applications, hair removal
HAMR (heat-assisted magnetic recording), 14
Harting, 478
HCG. *See* Grating, high-index-contrast (HCG)
HDMI (high definition multimedia interface), 449, 456, 465
Heat dissipation models. *See* Thermal modeling
He–Cd laser, 411, 418
HfO_2, 405
High-energy arrays. *See* VCSEL arrays, high-energy
Higher-index substrates, 157
Higher-order transverse mode. *See* Mode, transverse
High-index-contrast subwavelength grating (HCG). *See* Grating, high-index-contrast (HCG)
High power. *See* VCSEL, high-power
History of VCSEL research. *See* VCSEL, history of research
HITRAN, 346
Hollow-core waveguides, 10, 296
Hybrid
DBR. *See* Bragg reflector (DBR), hybrid

integration, 43
printed-circuit board. *See* Printed circuit board, hybrid electrical–optical
VCSEL. *See* VCSEL, hybrid
Hysteresis of polarization. *See* Polarization hysteresis

I
IBM, 431, 473, 485–488, 491, 492, 496–499, 501–504, 511
Illuminator. *See* Applications, illuminator
Image
processing, 12, 522
quality, 280, 546
InAlAs, 215, 327, 329, 336
InAlGaAs, 131, 194, 248, 266, 322, 327, 329, 337
InAs, 158, 250, 253, 337, 356
InAsSb, 341
Index guiding. *See* Optical guiding, index guiding
Indium tin oxide (ITO), 411, 416, 418, 421
Infant mortality. *See* Reliability
Infineon, 475
InGaAlAs. *See* InAlGaAs
InGaAs, 4, 10, 20, 34, 41, 44, 54, 63, 140, 187, 202, 204, 215, 247–249, 251, 253, 266, 323, 328, 336, 337, 355, 358, 394, 496
InGaAsP, 4, 20, 130, 140, 248, 253, 322, 354, 357, 441
InGaN, 403, 420
InP, 44, 99, 129, 131, 158, 215, 253, 307, 321, 327, 328, 346, 355, 358, 369, 394, 492
In-situ reflection measurement, 384, 408, 524, 544
Inter-valence-band absorption (IVBA), 210, 223, 224, 362, 365
Interconnects. *See* Optical interconnects
Interface grading. *See* Composition grading
Intexsys Photonics, 496
Intra-cavity contact, 24, 40, 129–131, 157, 244, 252, 254, 364, 365, 369, 416, 423, 531
Ion damage, 359, 360
ITO. *See* Indium tin oxide (ITO)
IVBA. *See* Inter-valence-band absorption (IVBA)

J
Joule heat, 95, 268

K
K-factor, 53, 54, 238, 390

L
Lambert–Beer's law, 346
LAN. *See* Local area network (LAN)
Langevin forces, 51, 56, 208, 219
Laplace equation, 99
Laser
diode driver, 438, 440, 442, 444, 447, 459, 480, 490, 493, 510
current mode, 545
voltage mode, 546
voltage/current mode, 546
lift-off, 405, 410, 414, 421
mouse. *See* Applications, computer mouse
pumping, 263–265, 280–283
Lasing threshold condition, 28, 33, 82
LED. *See* Light-emitting diode (LED)
LIDAR (light detection and ranging). *See* Applications, LIDAR
Lifetime of laser. *See* Reliability
Light
output curve. *See* Power versus current curve
Peak, 12
Light-emitting diode (LED), 5, 6, 12, 14, 20, 23, 314, 327, 380, 381, 403, 404, 406, 432, 522
Linewidth. *See* Emission linewidth
LITEBUS, 485
Local area network (LAN), 59, 120, 292, 353, 358, 431
Long-wavelength VCSELs. *See* VCSEL, long-wavelength
LP modes. *See* Modes, LP
Lucent Technologies, 486, 490

M
M^2. *See* Beam quality factor
MAN. *See* Metropolitan area network (MAN)
Marking. *See* Applications, marking
Matsushita (Panasonic), 157
MAUI, 486, 490, 491, 497–499, 512
MBE. *See* Epitaxy, MBE
McGill University, 485
Mean time to failure. *See* Reliability
Medical applications. *See* Applications, medical
Metal aperture. *See* Single-mode VCSELs, from inherently multimode, metal aperture

M (*cont.*)
Metropolitan area network (MAN), 120, 233, 353, 369
Micro-channel cooler, 278, 279
Micro-electromechanical system (MEMS). *See* Bragg reflector (DBR), MEMS
Microfluidics, 11
Microlens array, 282, 489
Micropillar lasers, 11, 394
Miscibility gap, 358
Mitel, 477
Mobile phone. *See* Applications, mobile phone
MOCVD. *See* Epitaxy, MOCVD
Modal noise, 92, 432, 436
Mode
  competition, 57, 58, 63, 109, 126, 200
  donut, 43, 48
  field diameter, 413, 420, 544
  filter, 89, 134
  fundamental, 43, 58, 113, 124, 138, 151, 162, 165, 186, 243, 302, 533, 543
  Gaussian, 47, 48, 60, 243, 384, 526, 548
  group diversity multiplexing, 64
  higher-order. *See* Mode, transverse
  Laguerre–Gaussian, 47
  longitudinal, 27, 29, 34, 35, 49, 51, 122, 312, 329, 408
  LP, 47, 60, 110, 123, 149, 184, 187, 194, 199, 207, 210, 224
  offset vs. gain peak, 31, 44, 211, 247, 253, 337, 338
  shift (thermal), 43, 45, 153, 281
  spacing
    longitudinal, 26, 340
    transverse, 42, 50
  transverse, 6, 23, 27, 40–42, 47, 50, 54, 58, 61, 89, 110, 121, 122, 124, 126, 149, 151, 162, 165, 187, 201, 207, 213, 302, 340, 436, 458, 543
  volume, 30, 237, 242, 249
Modeling, 6, 7, 10, 77, 206
Modulation, 6, 8, 10
  bandwidth, 23, 53, 235, 237, 238, 242, 244, 248, 255, 332, 333, 335, 345, 363, 389
  bias-free. *See* Data transmission, bias-free
  current efficiency factor (MCEF), 55, 237, 249–251, 333
  doping, 35–37, 99, 251, 266
  large-signal, 60, 136, 201, 208, 300, 392
  small-signal, 52, 190, 223, 236, 240, 255, 332, 389
  transfer function, 52, 237, 241, 256, 333
    parasitic, 55, 240, 333
MOST data bus, 14
Mouse, computer. *See* Applications, computer mouse
MOVPE. *See* Epitaxy, MOVPE
Multimode fiber. *See* Fiber, multimode
Multiplexing
  mode group diversity. *See* Mode group diversity multiplexing
  subcarrier, 64
  wavelength division. *See* Wavelength division multiplexing (WDM)

N
Nanocavity laser, 11
Nanoimprint lithography (NIL), 162, 314, 528
Nb_2O_5, 421
Nd:YVO_4, 265, 412
Near-field. *See* Beam profile
Near-field effects, 11, 14
NEC, 157, 234, 486, 488–490, 500–502, 505
NGK, 486, 494
NH_3, 340, 410
Noise
  quantum, 56
  relative intensity. *See* Relative intensity noise (RIN)
Nonlinear dynamics, 10
Nortel, 157
NTT, 157
Numerical aperture (NA), 283, 284, 494

O
Ohmic resistance. *See* Resistance, ohmic
OM3, OM4 multimode fiber. *See* Fiber, multimode, OM3, OM4
Omron, 478, 482
Open fiber control, 440
OPSR. *See* Orthogonal polarization suppression ratio (OPSR)
Optical
  anisotropies. *See* Anisotropy
  backplane, 12, 59, 496, 500
  computing, 12
  confinement, 35, 122–126
  data storage. *See* Data storage
  data transmission. *See* Data transmission
  feedback, 10, 63, 152, 156, 159, 160, 164, 528
  fields and modes. *See* Mode
  guiding, 122–126
    carrier-induced antiguiding, 97, 125, 128, 136

effective index analysis, 49, 79, 122, 325
effects of spatial hole burning. *See* Spatial hole burning
effects of thermal lensing. *See* Thermal lensing
gain guiding, 48, 125, 128
index guiding, 49, 123, 184, 187, 213, 242
weak guiding, 49, 50, 123, 126, 128, 149
interconnects, 5, 6, 12, 59, 234, 247, 334, 431, 445, 474, 497, 512
loss, 22, 29, 37, 40, 131, 266, 325, 338, 362, 365, 421
models, 79, 83, 97
mouse. *See* Applications, computer mouse
tweezers, 11
Orthogonal polarization suppression ratio (OPSR), 92, 157, 162, 196, 300
Opticis, 449
Oxide
aperture
formation, 41, 49, 278, 383, 524, 542
oblong shape, 86, 109, 111
confinement, 5, 6, 22, 41, 47, 48, 122, 128, 157, 266, 323, 523, 543
Oxygen sensing, 59, 155, 165

P

Parallel optical links, 5, 6, 9, 43, 59, 447, 473
test beds, 497
Parasitics,
chip, 55, 235, 239, 240, 243–245, 327, 331–333, 390
pad, 235, 239, 245
Paroli, 475, 479
Peregrine, 478, 482, 487, 493
PETIT, 489, 500, 505
Phase segregation, 358, 366
Philips, 521
Photodeflection spectroscopy (PDS), 327
Photodiode, 56, 61, 64, 235, 443, 444, 447, 474, 479, 481, 482, 485, 488, 489, 494, 506, 531
monitor, 345, 459, 480, 493, 530, 531
MSM, 65, 489
PIN, 9, 63, 65, 451, 489
Photoluminescence (PL), 338, 360, 367, 411, 413
Photon
cooling, 45
lifetime, 30, 38, 208, 237, 255
volume, 30
Photonic crystal, 10, 131, 158, 395
Picolight, 479, 486, 491, 492
Plasmonics, 11, 15, 158
Plastic optical fiber. *See* Fiber, polymer optical (POF)
Pockels effect. *See* Electro-optic effect
Polarization, 5, 6, 8, 47, 50, 57, 59, 61, 81, 126
anisotropy, 182, 220
bistability, 154, 190, 202, 203, 206–209, 224
elliptical, 185, 192–194, 205, 216–223
fluctuations, 196, 200, 201, 219, 220
higher-order modes, 151, 162, 165
hysteresis, 150, 154, 188
mode hopping, 190, 208
modulation, 191, 209, 223
orthogonal suppression ratio. *See* Orthogonal polarization suppression ratio (OPSR)
patterns, 90
suppression, 149
switching, 148, 150, 159
double, 192, 194, 221
pitchfork type, 202
stochastic, 200, 209
time, 200, 204, 208, 209
type I, 186–188, 192, 194, 210, 211, 213, 217, 218, 221, 223
type II, 187, 192, 194, 195, 211, 217, 218, 221, 223
voltage controlled, 203
Polymer optical fiber (POF). *See* Fiber, polymer optical (POF)
PONI, 485
POSH, 488
Potential grading. *See* Composition grading
Power
conversion efficiency. *See* Efficiency, conversion
density, 95, 264, 266, 279, 280
versus current curve, 23, 35, 42, 43, 46, 106, 110, 112
Poynting vector, 36
Princeton Optronics, 263
Printed circuit board, hybrid electrical–optical, 12, 59, 493, 496, 505, 506, 512
Printing. *See* Applications, printing
Projectors, 12, 265
Proton implantation. *See* VCSEL, proton-implanted
Pulsed operation, 45, 186, 201, 264, 279, 284–287, 361, 362, 367, 389, 412
Pumping. *See* Laser pumping
Purcell factor, 413, 415, 420

Q
QCSE. *See* Quantum-confined Stark effect (QCSE)
Q-factor, 34, 405, 409, 412
Q-switch. *See* Applications, Q-switch
Quantum
  dots, 6, 9, 10, 276, 323, 394
  efficiency, differential. *See* Efficiency, differential quantum
  noise, 56
  wells, 21, 28, 266, 330
    multiple, 28
Quantum-confined Stark effect (QCSE), 160, 204, 406, 423
Quasi-CW operation, 266, 278–280
Quasi-Fermi level, 39, 98, 211, 241, 330

R
Raman fiber amplifier, 355, 357
Random defects. *See* Reliability, random defects
Range finder, 284, 537
Rate equations, 36, 51, 102, 103, 207, 236, 238, 255, 333, 390
Reactive-ion etching (RIE), 266, 524, 542
Recombination. *See* Carrier recombination
Red emitting VCSEL, 5, 9, 10, 65, 379
Reflex Photonics, 477
Relative intensity noise (RIN), 56, 152, 155, 198, 200, 201, 220, 223
Relaxation oscillations, 187, 198, 435, 460
Reliability, 5, 263–265, 282, 285, 287, 393, 404, 459, 507, 526
  random defects, 509, 526
Resistance, ohmic, 4, 34, 39, 41, 55, 129, 239, 244, 267–272, 275, 324, 330, 340, 341, 358, 362, 363, 365, 367, 382, 545
Resonance
  condition, 27, 34
  frequency, 52, 237, 332, 333, 389, 458
Resonator, asymmetric, 159
Rollover, thermal. *See* Thermal rollover

S
SAN. *See* Storage area network (SAN)
Sapphire, 404, 410, 414, 423, 482, 493
Saturable dispersion, 194, 219, 220
Sb, surfactant, 359, 366
Selective oxidation. *See* Oxide confinement
Self-mixing, 522, 528, 533, 534
Self-pulsation, 432
Semiconductor disk laser. *See* VECSEL
SFF, 437
SFP, 437
SFP+, 441
Side-mode suppression ratio (SMSR), 43, 128, 130–137, 201, 283, 299, 302, 312, 330, 340, 525, 533, 543
  computation of, 109
Siemens, 347, 475
Silicon-on-insulator (SOI), 293, 493
Silicon photonics, 13
Single-mode fiber. *See* Fiber, single-mode
Single-mode VCSELs, 7, 23, 42, 49, 53, 57, 58, 60–65, 119–140, 149, 155, 165, 242, 243, 282–284, 299, 302, 330, 337, 342, 383, 523, 533, 543
  from inherently multimode, 132–137
    antiguided, 136
    antiresonant reflecting waveguide (ARROW), 136
    coupled resonators, 137
    disordered aperture, 134, 243
    extended cavity, 133
    implant/oxide aperture, 133
    metal aperture, 134, 140, 417, 543
    surface relief, 108, 135, 138, 158, 165, 243
  inherently single-mode, 127–132
    buried heterostructure, 129
    buried tunnel junction, 130
    holey structure, 132
    oxide aperture, 128
    photonic crystal, 131
    tapered oxide aperture, 129
    undercut aperture, 131
Single-photon emitters, 394, 404
SiO_2, 252, 294, 307, 326, 341, 405, 408, 411, 421
SiO_2/Ta_2O_5. *See* Ta_2O_5/SiO_2
SiO_2/TiO_2, 367, 405, 413
Slope efficiency. *See* Efficiency, differential quantum
Slow light, 11
Small-signal modulation. *See* Modulation, small-signal
Smartphone. *See* Applications, mobile phone
Smart pixel, 6
SMSR. *See* Side-mode suppression ratio (SMSR)
SNAP12, 477–480, 482, 485, 491, 497, 499
Solid angle (in sr), 282, 284, 287
Sparing of VCSELs, 480, 509

Spatial hole burning, 36, 43, 48, 97, 113, 126, 128, 154, 187, 207, 212, 213, 220, 238
Spectral hole burning, 52, 55, 207, 221, 223, 239, 241
Spin
  control, 11
  relaxation, 105, 215
Spin-flip
  model, 105, 154, 213–223
  time/rate, 205, 206, 214, 215, 219, 222, 223
Spontaneous emission, 5, 6, 41, 50, 51, 56, 57, 61, 413, 421
  factor, 51, 207, 391, 412, 415, 420
Standing-wave pattern, 27, 34, 49, 123, 329, 408
Steam oxidation. *See* Oxide aperture formation
Stimulated emission, 51, 104, 205
Stop-band width, 25, 381, 406, 411
Storage area network (SAN), 120, 353, 431
Strain, 50, 85, 86, 93, 151, 164, 241, 253, 340, 406, 407
  anisotropic, 184, 194, 195, 211, 220
  biaxial, 183
  compressive, 4, 41, 183, 184, 213, 251, 336, 360, 381
  tensile, 183, 184, 195, 212, 336, 360, 406, 410
  uniaxial, 191, 195
Subcarrier multiplexing. *See* Multiplexing, subcarrier
Substrate
  higher-index, 157
  removal, 45, 266, 276, 277, 330, 480
Superlattice, 35, 406, 410
Supermodes, 90
Surface
  grating. *See* Grating
  relief. *See* Single-mode VCSELs, from inherently multimode, surface relief
System-in-package, 535

T

Ta_2O_5/SiO_2, 408, 411, 414, 417, 418
T_0, 329, 355, 357, 361, 386
TDLAS. *See* Tunable diode laser spectroscopy (TDLS)
Temperature
  characteristics of light output, 46, 163, 166, 331, 336, 337, 342, 369, 386, 389, 532
  coefficient of threshold current. *See* T_0
  equation, 94
  profiles, 96
  turn-off, 46
Temperature-dependent phenomena, 97
Terabus, 492
Teraconnect, 476, 480, 481, 485
Test beds. *See* Parallel optical links, test beds
Thermal
  conductivity, 45, 94, 246, 322, 327, 328, 335, 386, 423
  crosstalk, 279, 335
  lensing, 36, 43, 47, 48, 50, 97, 113, 125, 154, 212, 242
  modeling, 43, 93, 97, 329, 335, 386
  resistance, 45, 265, 266, 276, 323, 325, 327, 329, 341, 387
  rollover, 23, 45, 93, 96, 109, 114, 127, 133, 187, 285, 335, 391
  shift
    of gain. *See* Gain, red-shift
    of mode. *See* Mode shift (thermal)
Threshold
  condition. *See* Lasing threshold condition
  current, 31, 35, 44, 267, 269–272, 275, 299, 303, 311, 330, 363, 419, 459
    density, 31, 361
  gain. *See* Gain, threshold
  voltage, 330, 363
Thunderbolt, 13
TiO_2/SiO_2. See SiO_2/TiO_2
TMAl, 410
TMDS (transition minimized differential signaling), 450
TMGa, 410
TMIn, 410
TOSA. *See* Transmitter optical sub-assembly (TOSA)
Toshiba, 487, 493, 505
Train display system. *See* Displays
Transceiver. *See* Datacom transceivers
Transfer matrix method, 33
Transimpedance amplifier (TIA), 443, 447, 485, 489, 493, 510
Transmitter optical sub-assembly (TOSA), 345, 436–439
Transparency
  carrier density, 31, 52, 241
  current density, 276, 394
Tunable
  diode laser spectroscopy (TDLS), 165, 342, 346
  lasers. *See* VCSEL, tunable
Tunnel junction. *See* Buried tunnel junction (BTJ)

U
U-L-M Photonics, 157, 521
Uniformity of epitaxy. *See* Epitaxy, uniformity

V
VCSEL,
  air-post, 22, 187, 191, 199, 209
  array, 43, 88, 263–266, 270, 276–287, 306, 333, 343, 456, 480, 491, 492, 509, 542
    high-energy, 263, 266, 284, 286, 287
  bottom-emitting, 23, 41, 42, 45, 160, 249, 263, 265–268, 271, 277, 283, 286, 328
  high-power, 23, 42, 263–266, 276, 277, 281, 284, 286, 287
  history of research, 3, 10
  hybrid, 10, 131, 254, 323, 328, 405
  long-wavelength, 5, 7, 10, 13, 235, 239, 253, 254, 321, 353
  mesa-etched, 22
  multimode, 42, 61, 62, 132, 165, 242, 330
  multi-wavelength, 292, 306
  oxide-confined, 5, 6, 22, 40, 83, 100, 108, 122, 128, 149, 163, 186, 223, 239, 242, 266, 297, 302, 367, 383, 459, 507, 508, 523, 542
  proton-implanted, 4–6, 20, 22, 47, 127, 133, 137, 186, 188, 190, 200, 209, 212, 220, 245, 248, 508
  single-mode. *See* Single-mode VCSELs
  top-emitting, 42, 160, 267, 271, 275, 277, 283, 341, 367, 382, 417, 422, 525, 532, 542
  tunable, 6, 8, 10, 91, 309, 338
  wearout. *See* Reliability
VECSEL, 4, 11, 12
Vectorial optical models, 83
Vertilas, 321
Voltage/current complementary drive. *See* Laser diode driver, voltage/current mode
Voltage drive. *See* Laser diode driver, voltage mode

W
Wafer fusion, 5, 10, 13, 131, 254, 323
Wallplug efficiency. *See* Efficiency, conversion
Wavelength
  detuning. *See* Mode offset vs. gain peak
  division multiplexing (WDM), 5, 6, 10, 59, 64, 292, 306, 334
    coarse (CWDM), 64, 334, 355, 465, 478, 482, 486, 487, 490, 491, 506, 512
    dense (DWDM), 309, 343, 354
  modulation spectroscopy, 121, 342, 347
  tuning. *See* VCSEL, tunable
Welding. *See* Applications, welding
Wet thermal oxidation. *See* Oxide aperture formation

X
X2, 441
Xanoptix, 476, 480, 481, 485
XAUI, 441
XENPAK, 441
XFP, 441
Xloom, 478, 483
X-ray diffraction, 337
Xyratek, 496

Z
Zarlink, 479, 484, 505
ZnS, 254, 294, 328, 336